ACCM 12

12TH ASIAN - AUSTRALASIAN CONFERENCE ON COMPOSITE MATERIALS

ORGANIZERS

Zhejiang University
Chinese Society for Composite Materials

Blossom Water Museum Hotel, Hangzhou, PR China
25-28 April, 2023

Chairs' Welcome

General Chair

Prof. Hua-Xin PENG

Zhejiang University

Honorary Chair

Prof. Shanyi DU

Harbin Institute of Technology

On behalf of the Asian-Australasian Association for Composite Materials (AACM), we sincerely welcome you to join us at the 12th Asian-Australasian Conference on Composite Materials (ACCM12) to be held from 25th to 28th April 2023 in Hangzhou.

Under the leadership of the AACM established in 1997, ACCM series has developed as one of the largest composites conference in the world promoting scientific research, technological development and industrial applications in the field of composite materials.

The theme of ACCM12 is "Composites for Quality of Life". ACCM12 will feature a 3-day program of divergent range of themes in composite research, and will showcase plenary and keynote talks, academic exchange, international networking, topical sessions/symposia and social activities including Banquet and Awards Ceremony. It promises to provide a valuable platform for scientists, engineers, postgraduates and other professionals to share, discuss and critically examine the most recent progress and trends in Composites Materials, Design Manufacturing and Applications.

Hangzhou, the home for ACCM12, renowned as "Paradise on Earth", is also preparing to host The 19th Asian Games.

We look forward to welcoming you at ACCM12 in Hangzhou in April 2023 !

Senior Advisory Committee

Debes Bhattarcharyya
Litong Zhang
Nobuo Takeda
Ze Zhang
Tongyi Zhang
Wei Yang
Xiangbao Chen
Jae Youn
Michael R Wisnom
Shanyi Du
Tsu-Wei Chou
Woo II Lee
Yiu-Wing Mai

International Scientific Committee

Alan KT Lau
Jifeng Xu
Liwu Liu
Takashi Ishikawa
Biqiong Chen
Jihua Gou
Masaki Hojo
Tao Zhang
Byung Sun Kim
Jinglei Yang
Mingqiu Zhang
Tong Earn Tay
Brian Falzon
Johann Kastner
Min Li
Xiaodong He
Bo Su
John D. Whitcomb
Miroslav Cerny
Xinghong Zhang
Chun Wang
John Summerscales
Murray Scott
Xinlin Qing
Chang-Mou Wu
John Zhanhu Guo
Naiqin Zhao
Xinran (Sharon) Xiao
Chun-Gon Kim
Joong Hee Lee
Norman Wereley
Yanju Liu
Di Zhang
Jun Takahashi
Paul Robinson
Yihui Zhang
Dongsheng Li
Jung-Il Song
Paul Weaver
Yoji Okabe
Fabrizio Scarpa
Jung-Ryul Lee
Pedro P. Camanho
Yuantong Gu
Guoxing Lu
Kevin Potter
Qibing Pei
Yudong Huang
Hee June KIM
K.H. Leong
Qing-ping Sun
Zhanjun Wu
Hao Wang
Laifei Cheng
Qingsheng Yang
Zhanwei Liu
Huiming Cheng
Lars Berglund
Ramesh Talreja
Zhishen Wu
Hyonny Kim
Lee Harper
Satoshi Kishimoto
Zhong Zhang
Huimin Xie
Lin Geng
Shaoyun Fu
Zhongmin Xue
Jian Lu
Lin Ye
Shengping Sheni
Zhongyi Ma
Jianxiang Wang
Liqun Zhang
Shuguang Li

Organizing committee

Prof. Faxiang QIN	Zhejiang University
Professor Junwei GU	Northwestern Polytechnical University
Prof. Zhongzhen YU	Beijing University of Chemical Technology
Prof. Qiang FU	Sichuan University
Prof. Yongjin LI	Hangzhou Normal University
Prof. Lujun HUANG	Harbin Institute of Technology
Prof. Bolv XIAO	Institute of metal research, Chinese Academy of Sciences
Prof. Chunnian HE	Tianjin University
Prof. Dingbang XIONG	Shanghai Jiao Tong University
Prof. Sergey ZHEREBTSOV	Belgorod State University, Russia
Prof. Xinghong ZHANG	Harbin Institute of Technology
Prof. Guojun ZHANG	Donghua University
Prof. Dewei NI	Shanghai Institute of Ceramics, CAS
Prof. Qiangang FU	Northwestern Polytechnical University
Prof. Yanwu ZHU	University of Science and Technology of China
Prof. Quan-Hong YANG	Tianjin University
Prof. Jiaqi ZHU	Harbin Institute of Technology
Prof. Nianjun YANG	University of Siegen, Germany
Prof. Diansen LI	Beihang University
Prof. Qingqing NI	Zhejiang Sci-Tech University
Prof. Yan LI	Tongji University
Prof. Renhui QIU	Fujian Agriculture and Forestry University
Prof. Tianxi LIU	Jiangnan University
Prof. Bin DING	Donghua University
Prof. Qunfeng CHENG	Beihang University
Prof. Soo-Jin Park	Inha University, South Korea
Prof. Runhua FAN	Shanghai Maritime University
Prof. Weiqiu CHEN	Zhejiang University
Prof. Yongzheng WEN	Tsinghua University
Prof. Qinghua QIN	Xi' an Jiaotong University
Prof. Zhongming LI	Sichuan University
Assistant Professor Bo LI	Villanova University
Prof. Kun DAI	Zhengzhou University
Prof. Wei YANG	Sichuan University
Prof. Xi SHEN	The Hong Kong Polytechnic University
Prof. Haibo ZHAO	Sichuan University
Prof. Pingan SONG	University of Southern Queensland
Prof. Yingjie XU	Northwestern Polytechnical University
Prof. Hui CHENG	Northwestern Polytechnical University
Prof. Philippe Boisse	Institut National des Sciences Appliquées de Lyon
Prof. Kevin Potter	University of Bristol, UK.
Prof. Min LI	Beihang University
Dr. Weijun CUI	Commercial Aircraft Corporation of China
Dr. Quansheng MA	Weihai Guangwei Composites Co.,Ltd
Prof. Xin LIN	Northwestern Polytechnical University
Prof. Dongdong GU	Nanjing University of Aeronautics and Astronautics
Prof. Xiaoyong TIAN	Xi' An Jiaotong University
Prof. Chunze YAN	Huazhong University of Science & Technology
Prof. Xitao ZHENG	Northwestern Polytechnical University
Prof. Chunhui WANG	The University of New South Wales
Prof. Xiaohua NIE	Aircraft Strength Research Institute of China
Dr. Shengchun YANG	Aircraft Strength Research Institute
Prof. Jiande LIU	Swinburne University of Technology, Australia
Prof. Jifeng XU	COMAC Beijing Aircraft Technology Research Institute
Prof. Xuefeng YAO	Tsinghua University
Prof. Zhengming HUANG	Tongji University
Prof. Jianxiang WANG	Peking University
Prof. Raj Das	Royal Melbourne Institute of Technology
Dr. Zhongmin XUE	Sinoma Science & Technology Co.,Ltd
Prof. Peng FENG	Tsinghua University
Prof. Jihui WANG	Wuhan University of Technology
Prof. Jian SHEN	Nanjing University / Nanjing Normal University
Prof. Yizao WAN	East China Jiaotong University
Prof. Yudong ZHENG	University of Science and Technology Beijing
Prof. Shibin WANG	Huaqiao University
Prof. Yin XIAO	Queensland University of Technology
Prof. Jianguo GUAN	Wuhan University of Technology
Prof. Huanyang CHEN	Xiamen University
Prof. Shutao WANG	Technical Institute of Physics and Chemistry CAS
Prof. Jintao ZHU	Huazhong University of Science & Technology
Prof. Mingqiu ZHANG	Sun Yat-Sen University
Prof. Jinglei YANG	Hong Kong University of Science and Technology
Prof. Hesheng XIA	Sichuan University
Associate Researcher Jinrui YE	Chinese Society for Composite Materials, Beijing Institute of Technology
Assistant Prof. Wangchang LI	Zhejiang University of Technology
Assistant Researcher Yang YANG	Zhejiang University
Mr. Pengcheng JIN	Chinese Society for Composite Materials

25th April	Day 1 26th April		Day 2 27th April				Day 3 28th April			
14:00-20:00 Registration	08:00-17:00	Registration Poster/ Trade Exhibition	08:00-17:00	Poster / Trade Exhibition			08:00-12:00	Poster / Trade Exhibition		
	08:30-09:00	Opening Ceremony	08:30-10:00	Keynote Session 1	Keynote Session 2	Keynote Session 3	08:30-10:00	Keynote Session 4	Keynote Session 5	Keynote Session 6
	09:00-10:20	Plenary Session 1								
	10:20	Tea Break	10:00	Tea Break			10:00	Tea Break		
	10:40-12:00	Plenary Session 2	10:20-12:00	Concurrent Sessions 1			10:20-12:00	Concurrent Sessions 4		
	12:00	Lunch	12:00	Lunch			12:00	Lunch		
	13:30-14:50	Plenary Session 3	13:30-15:00	Concurrent Sessions 2			13:30-15:00	Concurrent Sessions 5		
	14:50-15:10	Tea Break	15:00	Tea Break			15:00	Tea Break		
	15:10-16:30	Journal Session	15:20-17:30	Concurrent Sessions 3			15:20-16:40	Concurrent Sessions 6		
	16:40-18:00	Industry Session	17:30-18:30	Poster Session			16:40-17:00	Closing Ceremony		
	18:00	Dinner	18:30-20:00	Conference Banquet						

Plenary Session

	Time	Talk Title	Speaker	Affiliation	Room	Moderator
April 26	09:00-09:40	Behaviour of Thin-ply Hybrid Composites	Michael R WISNOM	University of Bristol	Main Venue	**Dongsheng LI** Commercial Aircraft Corporation of China Ltd **Ning HU** Hebei University of Technology
	09:40-10:20	Programmable Shape Memory Composites and 4D Printing: from Aerospace to Biomedical Applications	Jinsong LENG	Harbin Institute of Technology		
	10:40-11:20	Construction of Functional Composite Materials via Organic-Inorganic Hybrid Strategy and their Applications	Meifang ZHU	Donghua University		**Limin ZHOU** Southern University of Science and Technology **Yan LI** Tongji University
	11:20-12:00	Dedicate to Professor Adrian Mouritz: Professor Adrian Mouritz's Life-long Contribution to the Composites Society	Chunhui WANG	University of New South Wales		
	13:30-14:10	Dissolving Diamond, Growing Diamond in New Ways, Protonating Diamondoid Molecules, Zeolite Templated Carbons	Rodney S. RUOFF	Ulsan National Institute of Science and Technology		**Yanwu ZHU** University of Science and Technology of China **Ning HU** Hebei University of Technology
	14:10-14:50	Open Molding Technology for Continuous Fiber Reinforced Thermoplastic Composites	Asami NAKAI	Gifu University		

Keynote Session

	Time	Talk Title	Speaker	Affiliation	Room	Moderator
April 27	08:30-09:00	Development of Function-integrated Structural Composites for Aerospace Application	Xiaosu YI	University of Nottingham Ningbo China	Room 1	**Quanhong YANG** Tianjin University **Xitao ZHENG** Northwestern Polytechnical University
	09:00-09:30	A 1000 Wh/L Lithium-ion Battery Enabled with Shrinking Graphene Caged Microparticulate Silicon Anodes	Quanhong YANG	Tianjin University		
	09:30-10:00	Control of Hierarchical Structure of Polymer Articles via "Structuring Processing"	Qiang FU	Sichuan university		

	Time	Talk Title	Speaker	Affiliation	Room	Moderator
April 27	08:30-09:00	Thermomechanical Treatment of Metal Matrix Composites	Sergey ZHEREBTSOV	Belgorod State University	Room 2	**Yusheng SHI** Huazhong University of Science and Technology **Lujun HUANG** Harbin Institute of Technology
	09:00-09:30	High-performance Fiber-reinforced Composite Materials Manufactured by Robotic Laser Additive Manufacturing Technology	Yusheng SHI	Huazhong University of Science and Technology		
	09:30-10:00	The Tsai-Wu Failure Criterion: Its Full Rationalization and Implications	Shuguang LI	University of Nottingham		

KEYNOTE SESSION

	Talk Title	Speaker	Affiliation	Room	Moderator
08:30-09:00	Application of Composite Materials in COMAC Aircraft Structures	Dongsheng LI	Commercial Aircraft Corporation of China, Ltd.	Room 3	**Jinglei YANG** The Hong Kong University of Science and Technology **Tao XIE** Zhejiang University
09:00-09:30	Green Manufacturing Technologies of Thermoplastic-based FRP Composites: Current Situation and Future Development	Jinglei YANG	The Hong Kong University of Science and Technology		
09:30-10:00	Construction, Propulsion and Applications of Micro-/nanomotors	Jianguo GUAN	Wuhan University of Technology		

	Talk Title	Speaker	Affiliation	Room	Moderator
08:30-09:00	High-performing Fiber Lithium-ion Batteries	Huisheng PENG	Fudan University, China	Room 1	**Jun MA** University of South Australia **Yongjin LI** Hangzhou Normal University
09:00-09:30	Evolutionary Polymer/Nanosheet Composites	Jun MA	University of South Australia		
09:30-10:00	Fifty Years of Carbon Fibre Composites and Their Future Opportunities	Hao WANG	University of Southern Queensland		

	Talk Title	Speaker	Affiliation	Room	Moderator
08:30-09:00	Mechanism Study on Advanced Lightning Strike Protection Composites Using a Miniature Tip Discharge Technique	Zhong ZHANG	University of Science and Technology of China	Room 2	**Yanwu ZHU** University of Science and Technology of China **Zhong ZHANG** University of Science and Technology of China
09:00-09:30	Surface Construction Technologies and Biomedical Applications of Zwitterionic Materials	Jian SHEN	Nanjing Normal University		
09:30-10:00	Analysing the Thermo-Mechanical Response of Natural Fibre Composites Under Fire	Raj DAS	Royal Melbourne Institute of Technology		

	TitleTalk Title	Speaker	Affiliation	Room	Moderator
08:30-09:00	Nano-micromechanical Analysis of the Fibre Reinforced Composites'Growth Resistance to Through-thickness Matrix Cracking	Chunhui WANG	University of New South Wales	Room 3	**Faxiang QIN** Zhejiang University **Chunhui WANG** University of New South Wales
09:00-09:30	Waves in Hyperelastic Material Structures and their Manipulations	Weiqiu CHEN	Zhejiang University		
09:30-10:00	Beyond the Wooden Table: Extending the Use of Natural Fibres and Biobased Materials to Airframe Interiors, Adaptive Structures, and Metamaterials	Fabrizio SCARPA	University of Bristol		

Room	April 27		April 28	
Room1	10:20-17:10	Session 1 Polymer Matrix Composites	10:20-16:35	Session 1 Polymer Matrix Composites
Room2	10:20-16:50	Session 2 Metal Matrix Composites	10:20-15:15	Session 2 Metal Matrix Composites
Room3	10:20-17:05	Session 3 Ceramic Matrix Composites	10:20-16:00	Session 3 Ceramic Matrix Composites
Room4	10:20-17:30	Session 4 Carbon Composites	10:20-12:10	Session 4 Carbon Composites
Room5	10:20-17:50	Session 5 Textile-Based Composites	10:20-12:00	Session 5 Textile-Based Composites
Room6	10:20-16:20	Session 6 Natural Fibers / Green Composites		
Room7	10:20-17:10	Session 7 Nanocomposites	10:20-14:50	Session 7 Nanocomposites
Room8	10:20-17:30	Session 8 Meta-Composites	10:20-15:10	Session 8 Meta-Composites
Room9	10:20-17:35	Session 9 Multi-Functional / Smart Composites	10:20-15:30	Session 9 Multi-Functional / Smart Composites
Room10	10:20-17:30	Session 10 Thermal / Fire Retardant Composites	10:20-15:20	Session 10 Thermal / Fire Retardant Composites
Room11	10:20-12:15	Session 16 Failure Criteria and Verification		
	13:30-16:20	Session 11 Automated Manufacturing		
	16:20-17:05	Session 12 Out-of-Autoclave Process		
Room12	10:20-17:10	Session 13 3/4D Printing and Emerging Technologies		
Room13	10:20-17:05	Session 14 Optimization Design/ Modeling and Simulation		
Room14	10:20-17:05	Session 15 Testing and Evaluations Simulation		
Room15	10:20-17:00	Session 17 Engineering Application		
Room16	10:20-17:40	Session 18 Biomedical Applications		
Room17	10:20-17:40	Session 19 Emerging Applications	10:20-16:45	Session 19 Emerging Applications
Room18	10:20-17:1	Session 20 Composites Repair, Self-healing, Recycling and Machining		

Conference Proceeding

ACCM 12 2023

Content

Study on deformation of composite stiffened panels with variable cross section

WANG Houbing, CHEN Limin, CHENG Linan, WEI Jingchao, LI Xinxiang

Aeronautics Science and Technology Key Laboratory of Full Scale Aircraft Structure Statics and Fatigue, Aircraft Strength Research Institute of China, Xi'an 710065, China

Abstract: In order to research deformation of composite stiffened panel with variable cross section, the part of composite adjustments panel were experimentally investigated. The results show that strain difference of rows in the specimens coincide with variable cross section of stiffener, two specimens don't buckle at limit load under axial pressure.

1 Introduction

Carbon-fiber reinforced polymer(CFRP) laminate materials are becoming increasingly common in aerospace structures due to not only strength-to-weight ratio, stiffness-to-weight, but also the advantages of fatigue resistance, corrosion resistance, durability, wave absorption and wave transmission, which can significantly reduce the use and maintenance cost of the aircraft. Composite material consumption of Boeing B-787 and Airbus A-350XWB is as high as 50% and 52%[1].

Structural stability is the focus of aircraft design. Therefore, the European Union formulated two scientific research programs: POSICOSS[2]（improved postbuckling simulation for Design of Fiber composite stiffened Fuselage structures，European Union 5th framework plan）和 COCOMAT[3-4]（improved material Exploitation at Safe Design of composite Airframe Structures by Accurate Simulation of collapse，European Union 6th framework plan）. In order to apply composite materials to aircraft structures, the stability of composite structures is studied, and reliable analysis, calculation methods and design tools are provided for design. On the basis of ensuring performance and service life, it is required to significantly reduced the research and development and use costs

At present, the research on the axial compression stability of composite stiffened panels if mainly based on the stringers with constant cross section. According to the weight reduction requirements and the structural form requirements of special parts, such as the adjustment plate, the stringers need to be designed into a structure with variable section. The variable section

includes the change of the form of the stringer, for example, some are C-shaped, some are I-shaped, and there are also changes in the section size.

In the paper, the deformation characteristics of composite stiffened panels with variable cross-section stiffener under axial compression are studied, which lays a foundation for the study of axial compression stability and bearing capacity.

2 Specimen

The specimens (Fig. 1) are composite stiffened panels, with a total of 2 pieces, and the number is T-1, T-2. The carbon/epoxy material used in this work was T300/QY8911-IIprepreg tape. The specimen includes five stringers, two stringers on both sides are I-shaped, and three stringers in the middle are C-shaped. The overall dimension of the specimen is 550×500, the skin is curved surface.

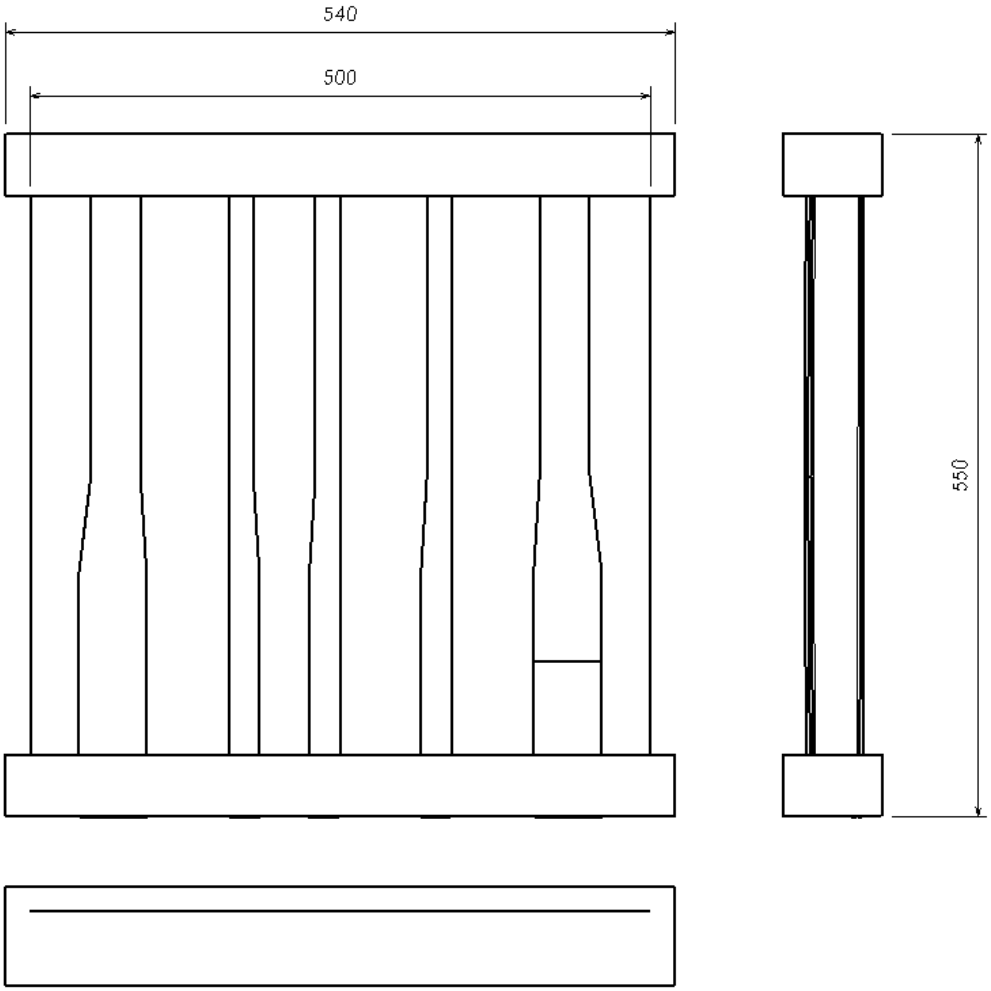

Fig.1 Sketch of specimen configuration

3 Testing

The arrangement of strain gauges is shown in Fig.2. The inner and outer sides of the skin of stiffened panels were pasted with 60 strain rosettes. Unidirectional strain gauges were pasted on the stiffeners, the number is 155 in total.

The number of the strain gauges is represented by 4 digits, the numbering method is shown in Fig.3 below. The first digit is the location code, the code of the outer side of the skin is 0, the code of the inner side of the skin, the code of the bottom flange of stringer and the web of stringer is 1, and the code of the upper flange of stringer is 3. The second digit is the line number, 5 lines in total, and 1 to 5 from top to bottom. The third and fourth digits are the serial numbers of strain gauges, 01-21 is the serial numbers of unidirectional strain gauge, and 31-49 is the serial numbers of strain rosettes.

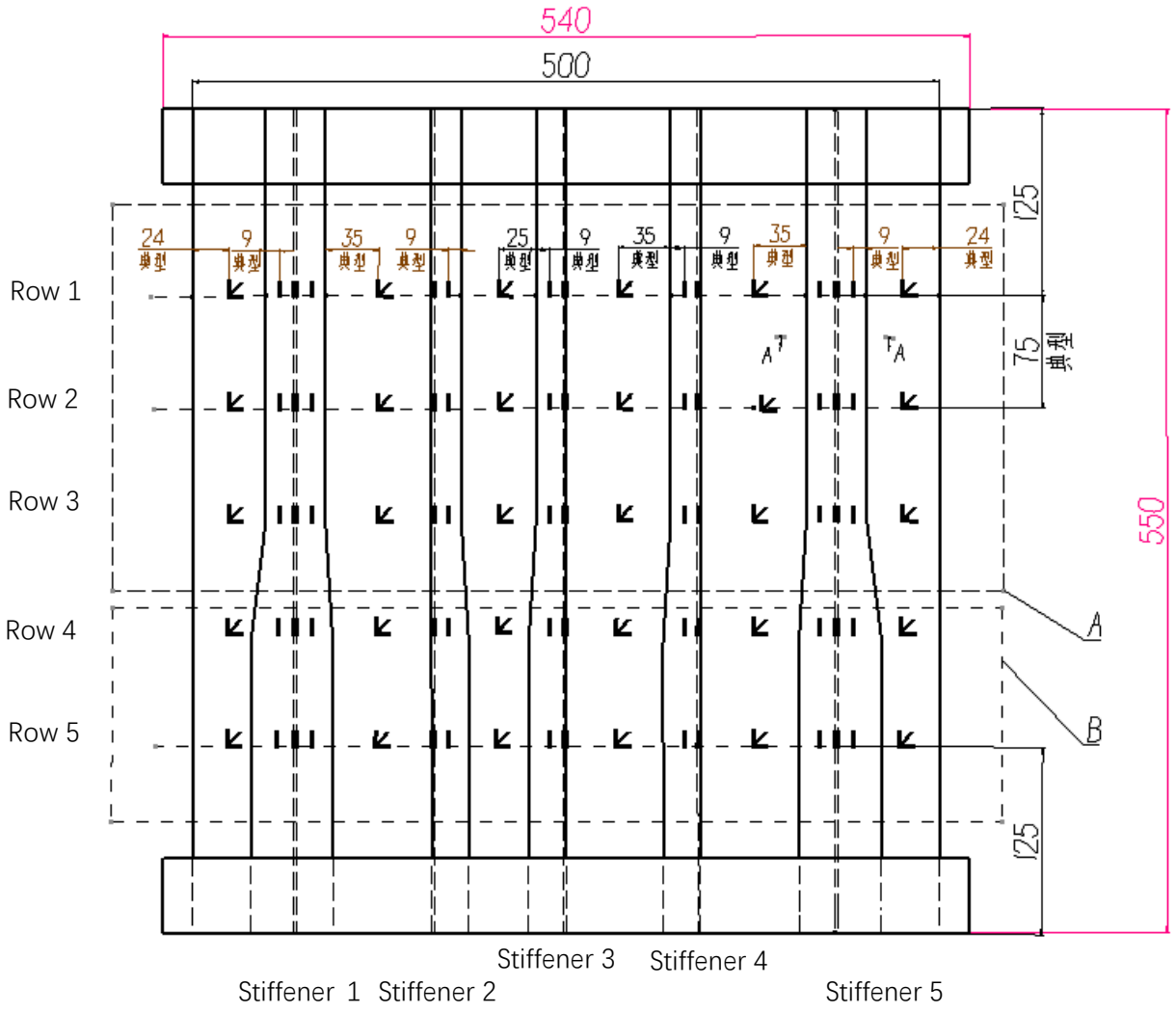

Fig.2 Strain gauge distribution on the specimen

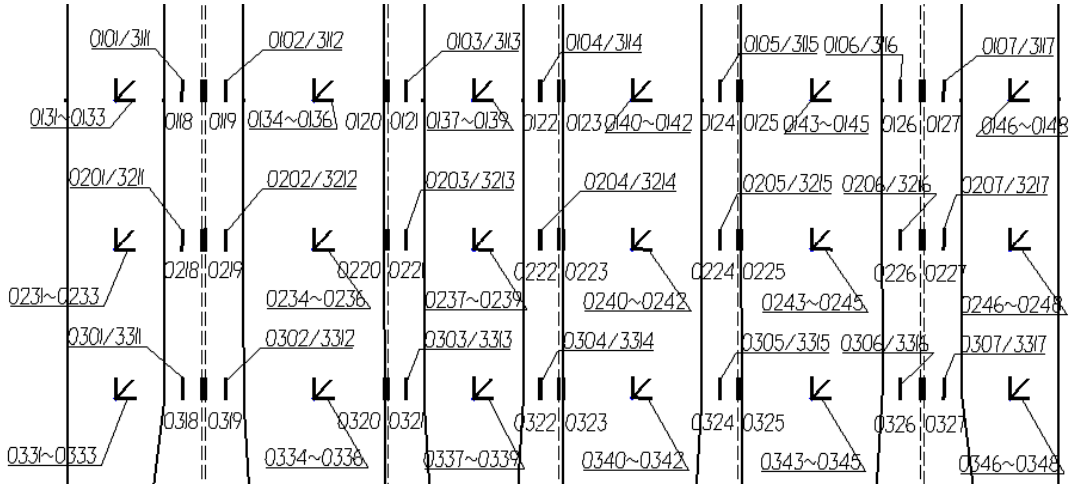

Fig.3 Strain gauge distribution in the zone A

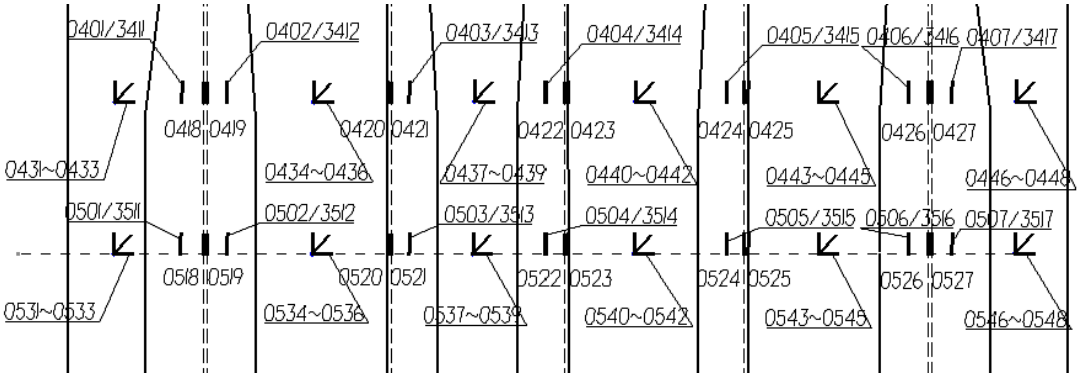

Fig.4 Strain gauge distribution in the zone B

The test was carried out on 200t compression testing machine. Before the test, the specimen was placed vertically on the support platform of test machine. To simulate side constraints of real structures, both sides of specimen were supported by two sets of knife edge clamps to constrain the normal displacement of the sides of the skin. The pressure center is 35mm on the top surface of the middle stringer. Compressive load was applied on the upper and low end faces of specimen by test machine. The support and loading methods are shown in Fig.5. The photos of the test site are shown Fig.6.

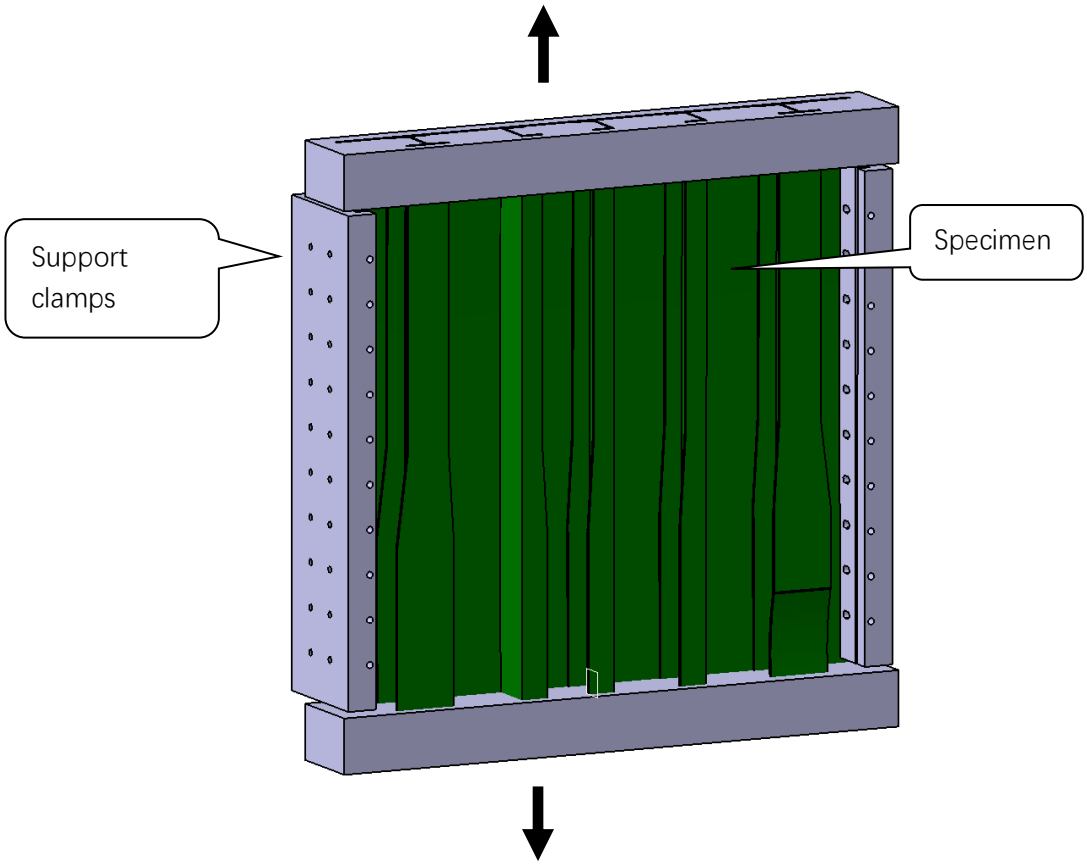

Fig.5 Schematic diagram of test support and loading

Fig.6 The photos of the test site

After the acceptance and inspection of specimens are completed, the relevant preparation was carried out, and then the tests were carried out according to the following steps.

（1） Specimen installation: Install the specimen and clamps, the load center of the

testing machine coincides with the pressure center of the specimen.

(2) Test adjustment: Take 20kN as a level, the specimen was loaded to 140kN step by step, measure strain step by step, unload at 140kN, then technical inspection was carried out, adjust the state of the loading and measuring system to make it in normal state. Analyze the strain data of the specimen, adjust the position of the specimen to make the measured strain error within the allowable range.

(3) Formal test: For specimen T-1, take 20kN as a level, the specimen was loaded to 340kN step by step. For specimen T-2, take 20kN as a level, the specimen was loaded to 380kN step by step.

4 Test results and analyses

The specimen T-1 makes a small noise when the load is 170kN, 340kN during the test. The measured maximum strain is about 2000 με when the load is 340kN. The test load-displacement curves are shown in Fig.7 below 340 kN. After the test, the specimen is undamaged through inspection.

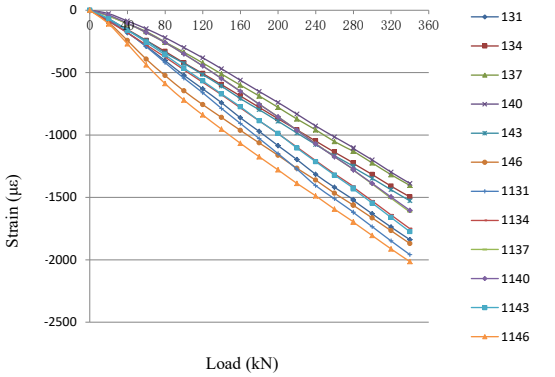

(a) Skin in row 1

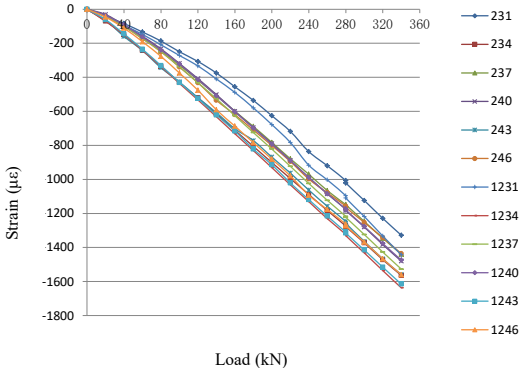

(b) Skin in row 2

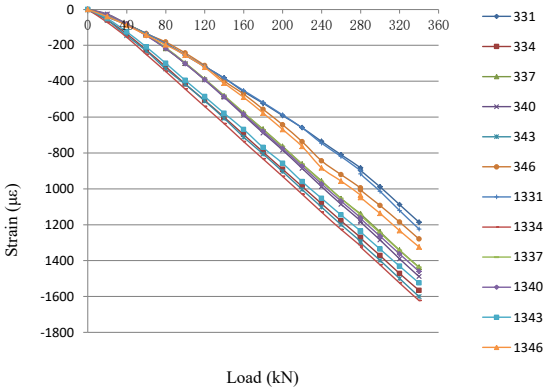

(c) Skin in row 3

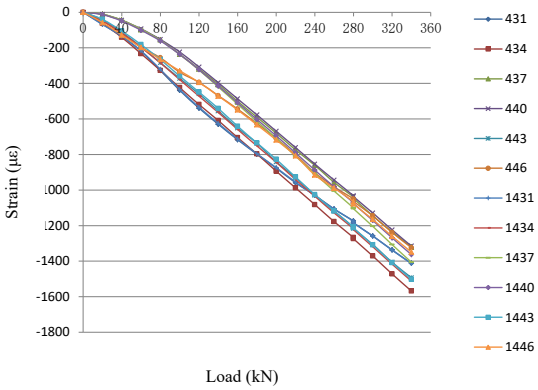

(d) Skin in row 4

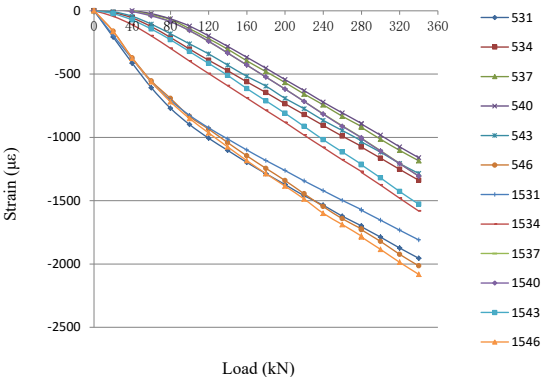

(e) Skin in row 5

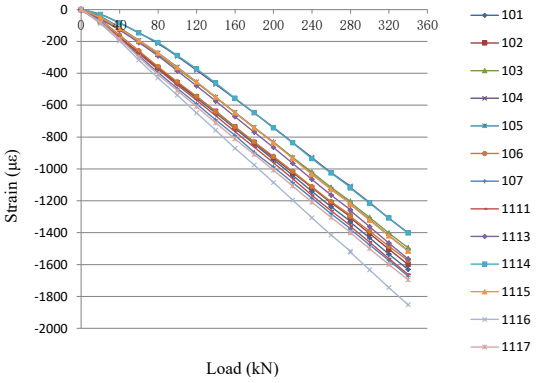

(f) Bottom part of the stringer in row 1

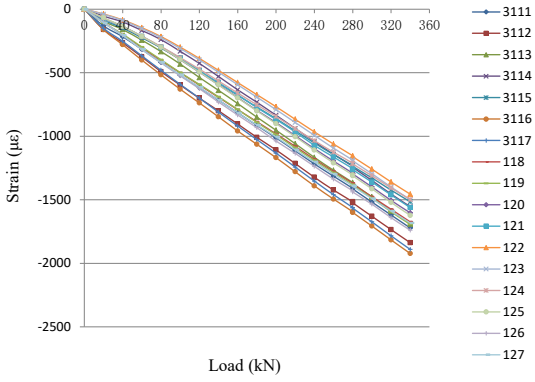

(g) Upper and Middle part of the stringer in row 1

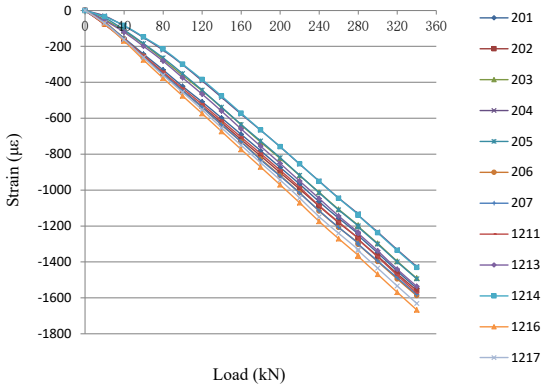

(h) Bottom part of the stringer in row 2

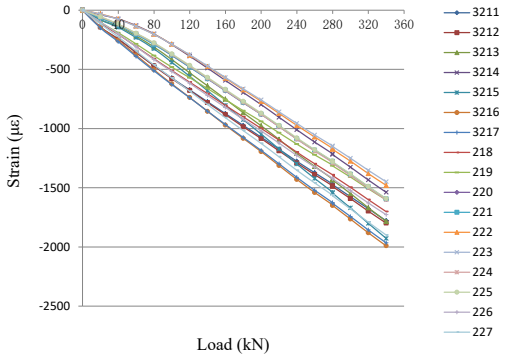

(i) Upper and Middle part of the stringer in row 2

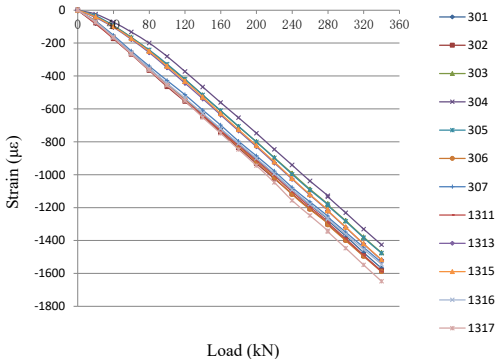

(j) Bottom part of the stringer in row 3

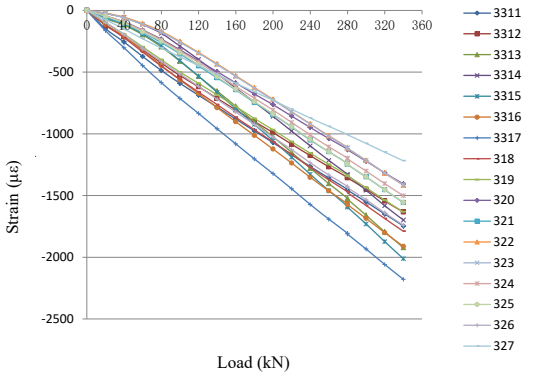

(k) Upper and Middle part of the stringer in row 3

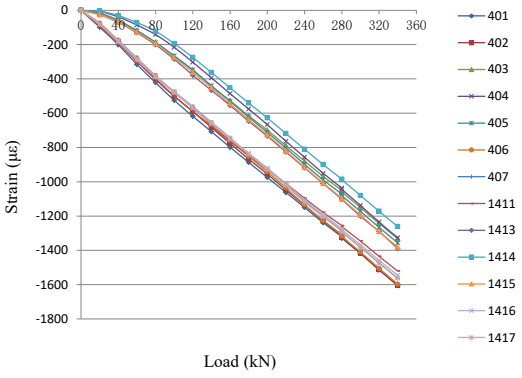

(l) Bottom part of the stringer in row 4

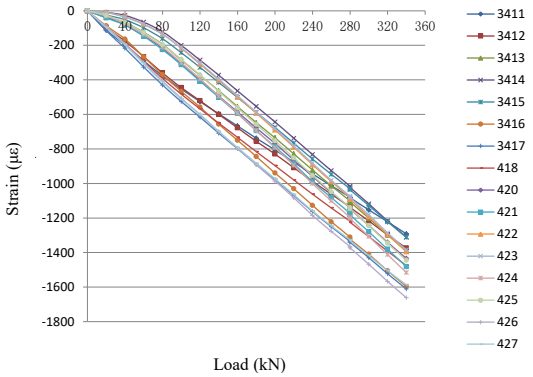

(m) Upper and Middle part of the stringer in row 4

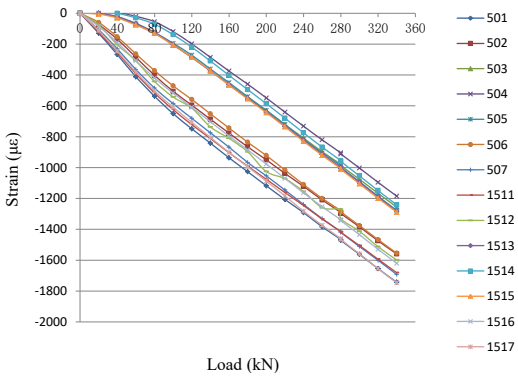

(n) Bottom part of the stringer in row 5

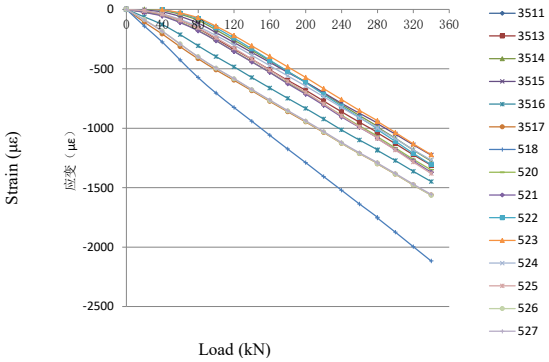

(o) Upper and Middle part of the stringer in row 5

Fig.7 Load-displacement curves of specimen T-1 in the test 340kN

The specimen T-2 makes no noise during the test. The measured maximum strain is about 2200 με when the load is 380kN. The test load-displacement curves are shown in Fig.8 below 380 kN. After the test, the specimen is undamaged through inspection.

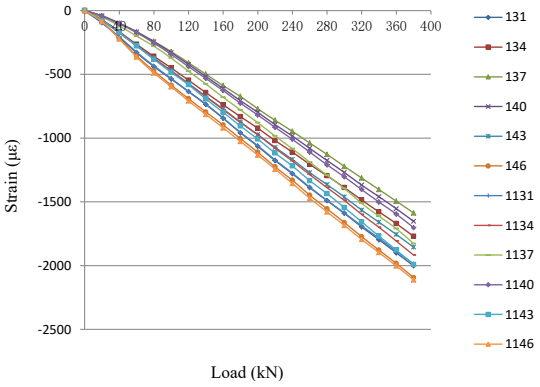

(a) Skin in row 1

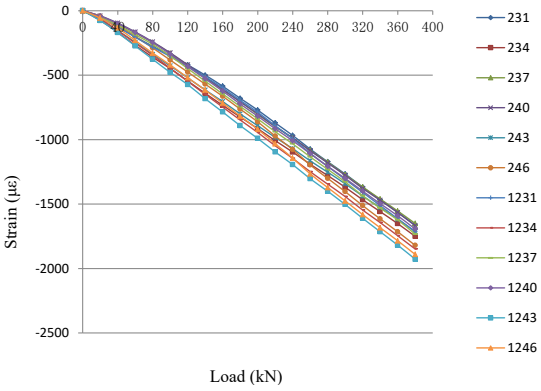

(b) Skin in row 2

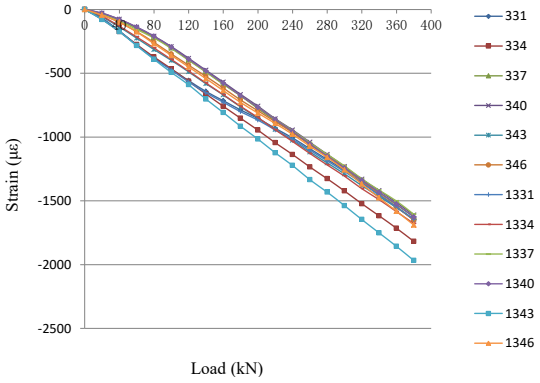

(c) Skin in row 3

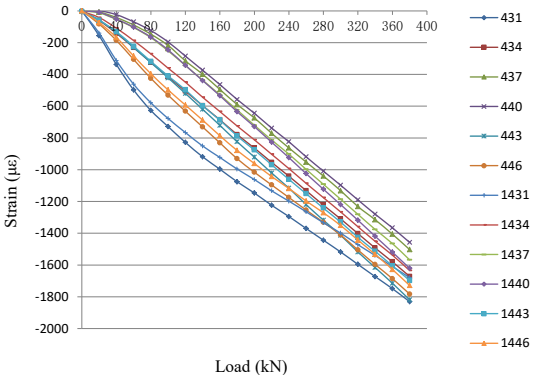

(d) Skin in row 4

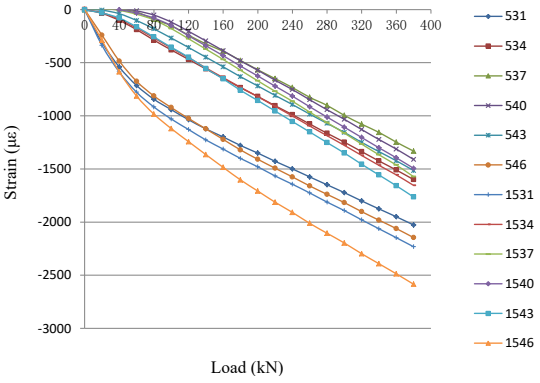

(e) Skin in row 5

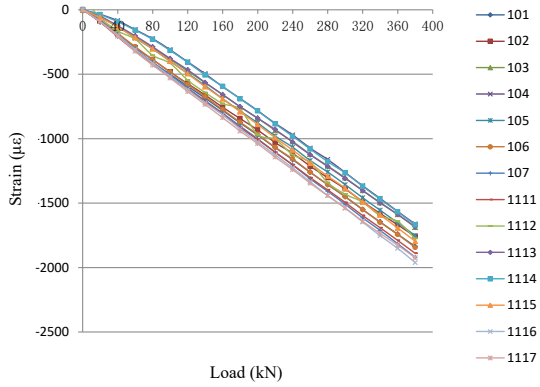

(f) Bottom part of the stringer in row 1

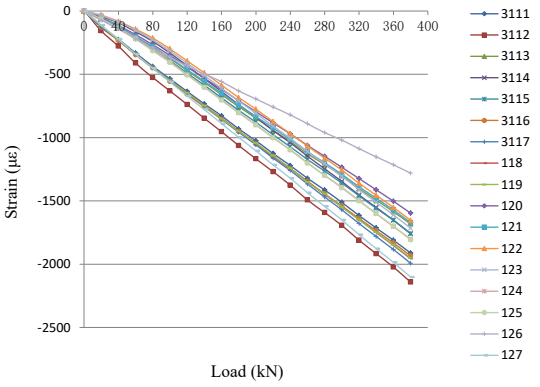

(g) Upper and Middle part of the stringer in row 1

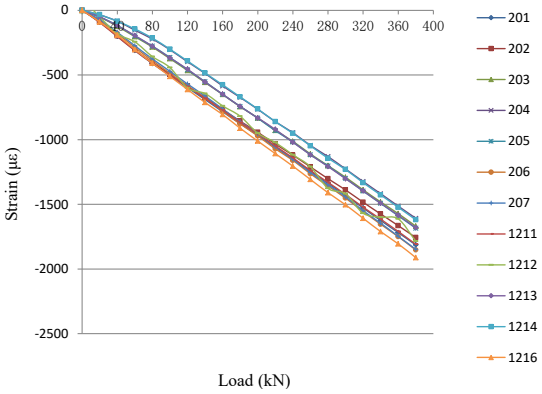

(h) Bottom part of the stringer in row 2

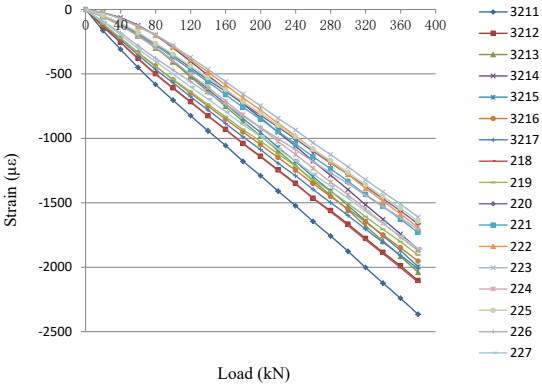

(i) Upper and Middle part of the stringer in row 2

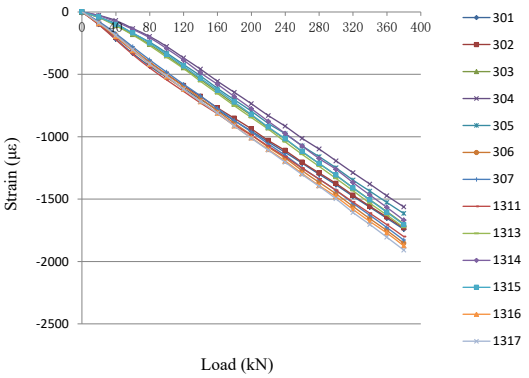

(j) Bottom part of the stringer in row 3

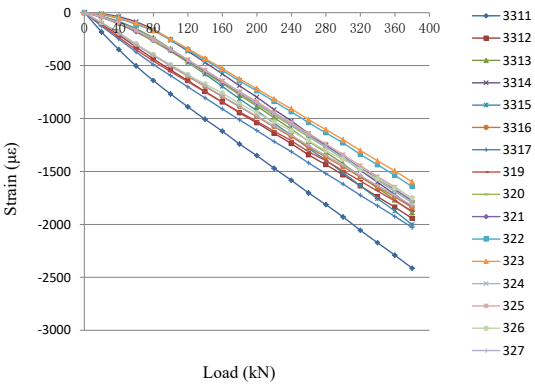

(k) Upper and Middle part of the stringer in row 3

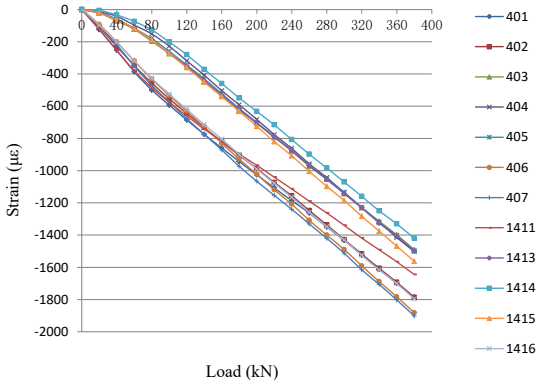

(l) Bottom part of the stringer in row 4

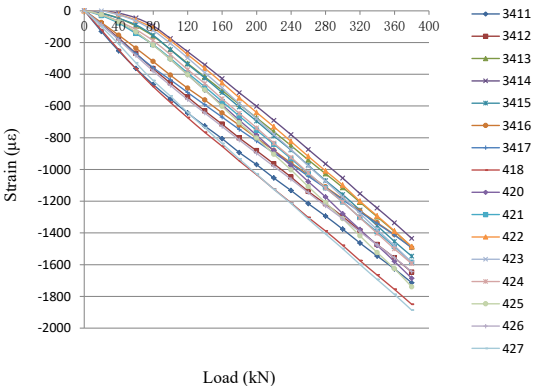

(m) Upper and Middle part of the stringer in row 4

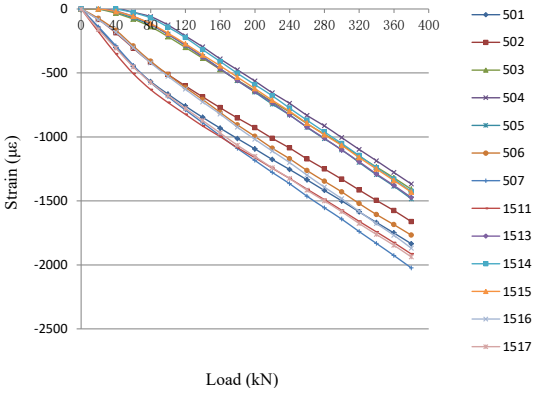

(n) Bottom part of the stringer in row 5

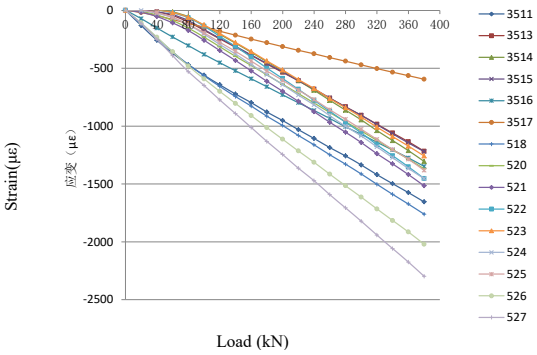

(o) Upper and Middle part of the stringer in row 5

Fig.8 Load-displacement curves of specimen T-2 in the test 380kN

The cross-sectional dimensions of the stringers are different, the stringers are narrow in row 1 and row 2, the stringers are wide in row 3 and row 4, section stiffness of the specimens are different, the strain of each row at the measurement point is slightly different. The average strain of each row of T-1 and T-2 are shown in Fig.9 and Fig.10. As can be seen from the figure: the section stiffness of row 1 is minimum, the section stiffness of row 4 is maximal. The average strain difference of the measuring points in each row is consistent with the change of the stiffeners of the specimens.

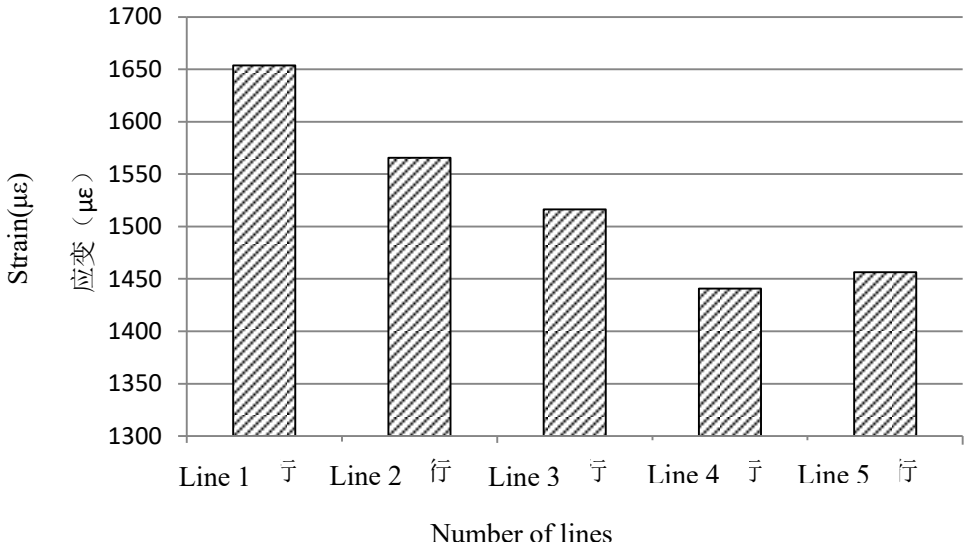

Fig.9 Average strain of each row of the specimen T-1 under load 340kN

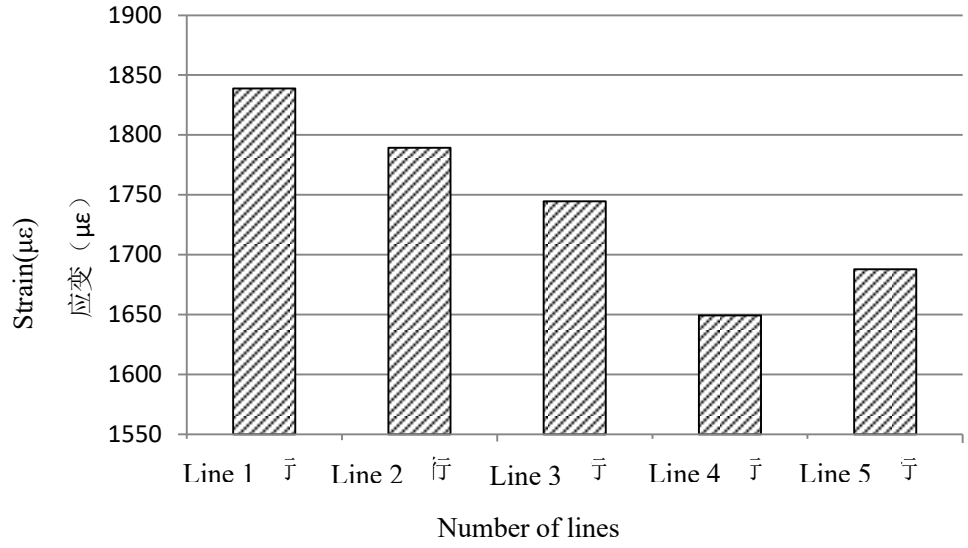

Fig.10 Average strain of each row of the specimen T-2 under load 380kN

5 Conclusion

According to the analysis of the previous test results, the following conclusions can be drawn:

(1) Except for the row 5, the strain distribution of each row of the specimens is uniform.

(2) In the limited load (340kN) test, the strain of the specimens is linear and there is no buckling.

(3) The section stiffness of row 1 is minimum, the section stiffness of row 4 is

maximal, and the average strain difference of the measuring points in each row is consistent with the change of the stiffeners of the specimens.

6 References

[1] Tang Jianmao. Current status and trends of advanced composites in aerospace[J]. Spacecraft environment engineering. 2013, 30(4): 352-359.

[2] ZIMMERMANN R，ROLFES R. POSICOSS-improved postbuckling simulation for design of fibre composite stiffened fuselage structures[J]. Composite Structures, 2006, 73: 171-174.

[3] DEFENHARDT R，ROLFES R, ZIMMERMANN R, ROHWER K. COCOMAT-improved material exploitation of composite airframe structures by accurate simulation of postbuckling and collapse [J]. Composite Structures, 2006, 73: 175-178.

[4] GHILAI G，FELDMAN E, DAVID A. COCOMAT design and analysis guidelines for CFRP-stiffened panels[J]. International Journal of Structural Stability and Dynamics, 2010, 10(4): 917-926.

CFRP Interleaved by Short/Micro-length Fibres –from laboratory testing to industrial prepreg production

*Yunsen Hu [1], Gang Han [1], Bo Tan [2], Fei Cheng [3] and Xiaozhi Hu [1]**

[1] Department of Mechanical Engineering,

University of Western Australia, Perth, WA 6009, Australia

[2] Shaoxing Baojing Composite Materials Co., Ltd, Shaoxing 312073, PR China

[3] School of Materials Science and Engineering,

Southwest University of Science and Technology, Mianyang 621000, PR China

[*] Corresponding author: E-mail address: xiao.zhi.hu@uwa.edu.au[*]

Abstract: Interleaving is effective for enhancing the delamination toughness of laminar carbon fibre reinforced polymer (CFRP) composites made from prepregs, but with concerns of the extra operation in composite forming and adverse influence on bulk compressive and flexural strengths of CFRP. This study shows that ultra-thin interleaf (< 10 μm in thickness) consisting of randomly distributed short or micro-length fibres such as aramid fibre and CNT can be combined into prepreg production so that toughened or "interleaved" prepregs can be fabricated (no need for further interleaving in composite forming). The bulk strength of CFRP can be enhanced if the coating thickness of in-plane randomly distributed short fibres over prepregs is less than 10 μm. With comparable toughening effects, short aramid fibre or aramid pulp is more cost-effective than CNT. We compare the toughening effects of short/micro-length fibres including CNT and aramid Pulp (AP) micro-/nano-fibres, and study potential challenges for technological transfer from laboratory testing to prepreg production.

Keywords: Carbon fibre reinforced polymer (CFRP); Interlaminar toughening; Interleaving; Ultra-thin interleaf; Prepreg

1 Introduction

Large thin-shell-like carbon fibre composite structures are typically constructed using carbon fibre prepregs mass-produced in industry. This laminar carbon fibre reinforced polymer (CFRP) composites have an inherent structural weakness, i.e., tendency for easy crack initiation and propagation between prepreg interfaces. Consequently, delamination along the ply interface has become one of the most frequently observed failure mechanisms in CFRP laminates under

out-of-plane loads.

Extensive efforts have been made to enhance the delamination toughness of CFRP, including the development of through-thickness reinforcement techniques such as stitching [1], tufting [2], Z-pinning [3] and 3D weaving [4], which utilise extra load carrying medium in the through-thickness direction of CFRPs to inhibit delamination growth. Although tremendous increases (more than ten-fold) in delamination toughness have been reported, these methods may degrade the in-plane properties of CFRPs and add substantial cost and complexity to manufacturing processes.

Interlaminar toughening or interleaving is a good alternative to through-thickness reinforcement methods as it is easy to be implemented. Interleaving involves the placement of extra reinforcing materials (e.g., thermoplastic or thermoset films, non-woven/woven veils) in the resin rich regions between carbon fibre plies to enhance the delamination toughness. Aramid fibre has excellent mechanical properties, chemical and thermal stabilities, making it a good candidate for interlaminar toughening. The concept of interleaving using chopped aramid fibres has been tested as early as 1994 [5].

In this paper, we study the possibility of combining the interleaving process in prepreg production for "interleaved" prepregs which are ready to be used without the need of further interleaving. That is the prepregs with an ultra-thin coating of randomly distributed short or micro-length fibres (e.g., carbon nanotubes (CNTs) or aramid pulp micro-/nano-fibres). The mechanical properties including delamination toughness, flexural strength, compressive strength and impact resistance of aramid fibre toughened CFRPs are discussed. The toughening effect of aramid fibre is also compared with other popular toughening materials such as CNT and graphene.

2 Fabrication of aramid fibre toughened CFRP

2.1 Manual distribution of short aramid fibres

In the early days [5], chopped Kevlar or aramid fibres of various lengths around 2-4, 5-7 or 13-15 mm were manually spread onto carbon fibre fabrics. While over 100% improvement in the delamination toughness had been observed, this interleaving method was laborious and highly dependent of the operator. Furthermore, it is difficult to ensure a uniform distribution of short

aramid fibres and the resultant interleaving thickness. Therefore, this effective interfacial toughening method unfortunately mainly remains in the stage of laboratory testing for mechanism studies. In principle, CNT interfacial toughening may have similar issues, e.g., uniform distribution etc.

2.2 Non-woven short aramid fibre veil

Relatively recent, unbonded non-woven veils made of short aramid fibres have been tested as thin interleaving materials as illustrated in Fig. 1. The fabrication of aramid fibre veils was similar to the traditional papermaking process, in which a sieve-like screen was used to drain water from the suspension containing un-bonded fibres. In comparison to commercially available bonded non-woven veils, these unbonded veils can potentially provide more protruding free fibre ends for the fibre bridging mechanism against delamination [6].

These non-woven veils in Fig. 1 (a) bypass the short fibre distribution stage in application, but add an extra operating step in composite forming as illustrated in Fig. 1 (b). If non-woven veils can be combined onto the carbon fibre prepreg surfaces during the prepreg production, “interleaved” prepregs or prepregs with the “random short fibre and epoxy coating” can be fabricated. In this way, the intermediate step of interleaving can be removed from composite manufacturing. Combining the two separate stages in Fig. 1 (b) and (c) is the primary objective of this study.

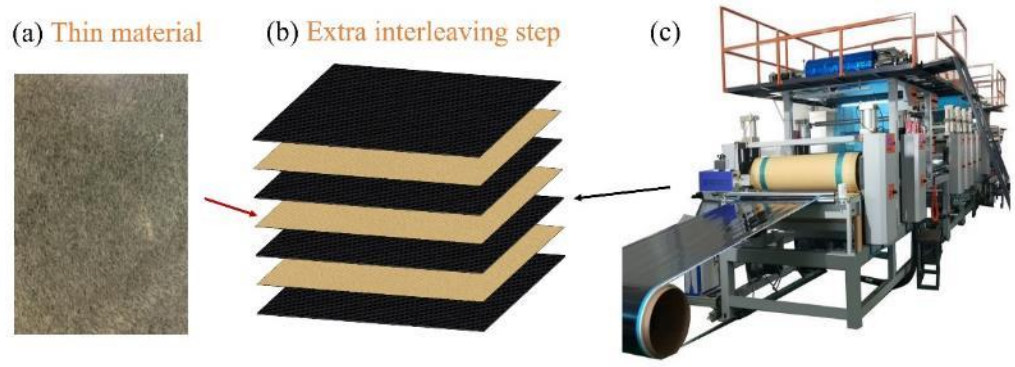

Fig. 1 (a) Thin interleaving material – unbonded non-woven aramid fibre veil. (b) Extra operation step for CFRP interleaved with aramid fibre veil. (c) From standard carbon fibre prepreg fabrication [7] to “interleaved” prepreg by combining (b) and (c) in production.

2.2 Aramid pulp micro-/nano-fibre toughened prepreg

Highly flexible aramid pulps (AP) are fibrillated fibres that retain a great strength-to-weight ratio as aramid fibre but possess shorter fibre size (0.5-1mm in length) with complicated micro-/nano-scale hierarchical structures. Recently, research in fabricating AP toughened prepregs was easily achieved by the facilitation of organic acetone solvent. AP was firstly dispersed in acetone and mixed by a high-speed blender to break up AP clusters. Then epoxy resin (without hardener) was added to the suspension and further mixed to ensure a uniform distribution. After acetone evaporation, this AP toughened resin can be used to produce CFRP. Fig. 2 shows that the AP toughened resin can be potentially used in prepreg production so that end-users can use these AP toughened prepregs just as normal prepregs.

Fig. 2 (a) Manually prepared carbon fibre prepreg with distributed aramid micro-/nano-fibres. (b) Prepreg made in industry has an ultra-thin "SAFE" coating (Short Aramid Fibre Epoxy).

3 Mechanical performance of CFRP interleaved with aramid fibre and other toughening materials

The delamination toughness of aramid fibre toughened CFRP has been measured by Sohn and Hu in 1994 [5,8]. They manually spread Kevlar 49 fibres with lengths of 5-7 and 13-15 mm and areal density of 17 g/m^2 in the mid-plane of unidirectional CFRP laminates. As shown in Fig 3 (a), The mode I and II critical strain energy release rate (G_{IC} and G_{IIC}) of aramid fibre reinforced laminates increased by approximately 100–300%. Aramid fibres have also been used to enhance the delamination toughness of CFRP/metal hybrid laminates. Sun et al. bonded CFRP to four different types of aluminium substrates and used aramid fibre veils (made from 6 mm Kevlar 49 fibres with an areal density of 12 g/m^2) to reinforce the metal/composite interfaces [9]. The aramid fibre interleaves were capable to increase the critical energy release rate G_C of asymmetric double cantilever beam (ADCB) specimens by around 50%. Although some researchers tried to introduce vertically aligned fibres (e.g., CNT) to the interlayers to hinder delamination growth through the fibre bridging mechanism (see Fig. 3 (b)) [10], the experimental results showed no advantages over those of aramid fibre toughening. The theoretical study of Huang et al. has proven that near horizontal fibres can also contribute to the fibre bridging [11]. The mechanisms of fibre bridging are illustrated in Fig. 4.

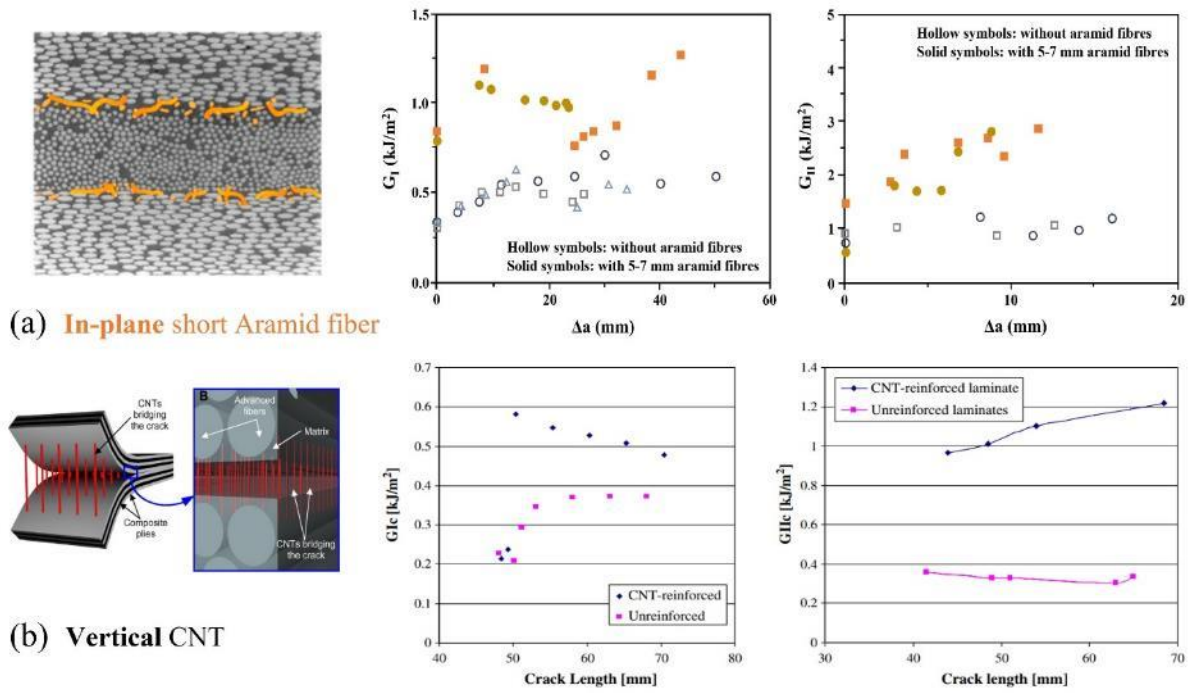

Fig. 3 (a) Short Aramid Fibre Epoxy (SAFE) between carbon fibre plies with Mode-I and Mode-II strain energy release rates [5]. In-plane SAFE toughening can be duplicated in prepreg production, as shown in Fig. 2 (b). (b) Vertical aligned CNT forest for Z-directional toughening with Mode-I and Mode-II strain energy release rates [10].

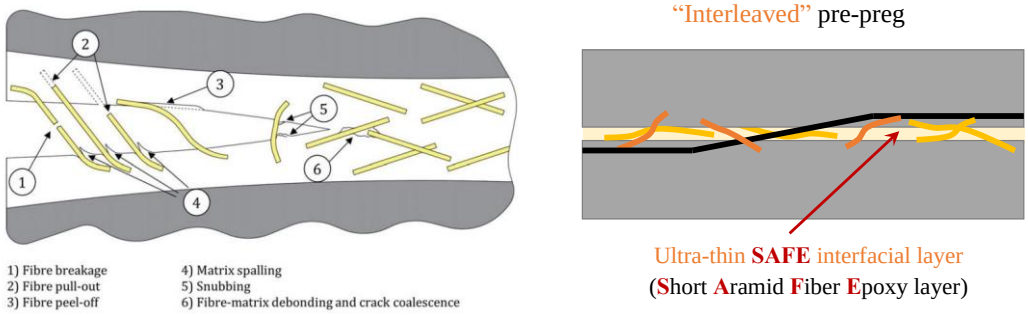

(a) **Crack-Bridging** from random short fibers in thick interfacial adhesive layer

(b) **Crack-Bridging** from continuous carbon fibers & short fibers due to ultra-thin interfacial layer

Fig. 4 (a) Crack-bridging from randomly distributed short fibres in a thick epoxy adhesive layer between carbon fibre plies [12]. (b) Crack-bridging from continuous carbon fibres trigged by short fibre bridging in ultra-thin SAFE interfacial layer (Short Aramid Fibre Epoxy layer).

Several studies have proven that the aramid fibre interlaminar toughening can effectively enhance the impact resistance of CFRPs. Yuan et al. investigated the low-velocity impact

response of twill weave CFRP laminates interleaved with non-woven aramid fibre veils (made from 3-5 mm Kevlar 49 fibres, and areal densities were 4-8 g/m^2) [13]. As shown in Fig. 4, up to 50.8% reduction in back-face deflection and inhibited in-plane delamination growth were achieved when compared with the unreinforced CFRPs. Following the low velocity impact tests, they conducted non-standard compressive after impact (CAI) tests on CFRP specimens interleaved with 8 g/m^2 non-woven aramid fibre veils. The residual compressive strength of aramid fibre toughened CFRPs was 38.6% higher than that of plain CFRPs. Ye et al. performed non-standard CAI tests on twill weave CFRPs with AP micro-/nano-fibre interlayers estimated to be around 3 and 6 g/m^2 [14]. After low-velocity impact, the residual compressive strength of AP toughened CFRPs increased by up to 86.7% compared to the plain CFRPs. In both studies, the main failure mode of plain CFRPs was delamination. By contrast, the aramid fibre/AP toughened showed shear-dominated failure, indicating improved interlaminar strength and toughness.

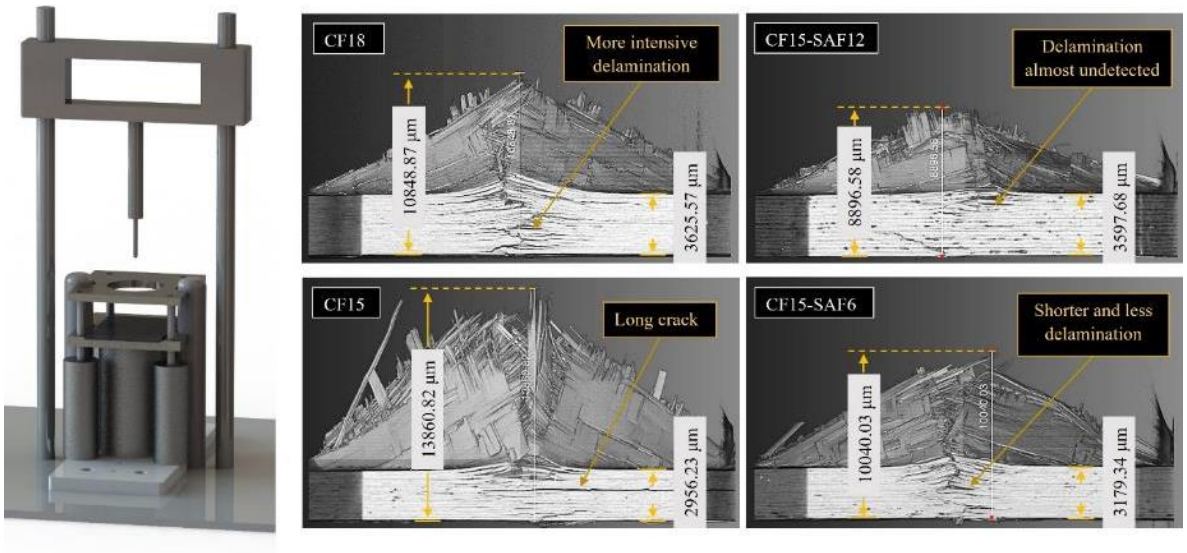

Fig. 5 Computerised tomography (CT) images of CFRPs with and without short aramid fibre (SAF) interlaminar reinforcement after low-velocity impacts [13].

Aramid fibre interlaminar toughening not only improves the residual compressive strength after impact, but also the compressive and flexural strengths even without any impact damage. As shown in Fig. 6 (a), Yuan et al. studied the flexural and flexural after low-velocity impact performance of twill weave CFRP laminates interleaved with 4 and 8 g/m^2 non-woven aramid fibre veils [15]. The flexural strength of aramid fibre toughened CFRP improved by up to 16.9%, and the residual flexural strengths after impacts were also higher than those of the plain

CFRP. Cheng et al. incorporated AP micro-/nano-fibres into interlayers of unidirectional CFRPs, and the areal density of AP reinforcement ranged from 2 to 8 g/m^2 [16]. The flexural loads of AP toughened CFRPs improved by 30% and over 100% in the longitudinal and transverse directions, respectively. The method of incorporating AP fibres is suitable for other reinforcing fillers such as poly(p-phenylene-2,6-benzobisoxazole) (PBO) fibres, CNT and graphene, and a comparison study was made by Hu et al. [17]. As can be seen in Fig 6 (b), the compressive and residual compressive after impact strengths of the CFRP with 1.6 g/m^2 AP fibres were higher than those of the plain CFRP. Although similar toughening effect may be achieved by using other reinforcing fillers such as CNT and PBO fibre, the price of aramid fibre is cheaper, making it more suitable for large-scale applications. It is worth mentioning that aramid fibre shows essentially no embrittlement or degradation at temperatures as low as −196 °C [12] and thus may be used for interlaminar toughening of CFRPs for low temperature applications. Hu et al. conducted room and low temperature flexural tests on CFRPs with 0.8-3.2 g/m^2 AP reinforcement [18]. As shown in Fig. 6 (c), the enhancement in flexural strength of CFRP with 1.6 g/m^2 AP flexural was very pronounced at -100 ℃.

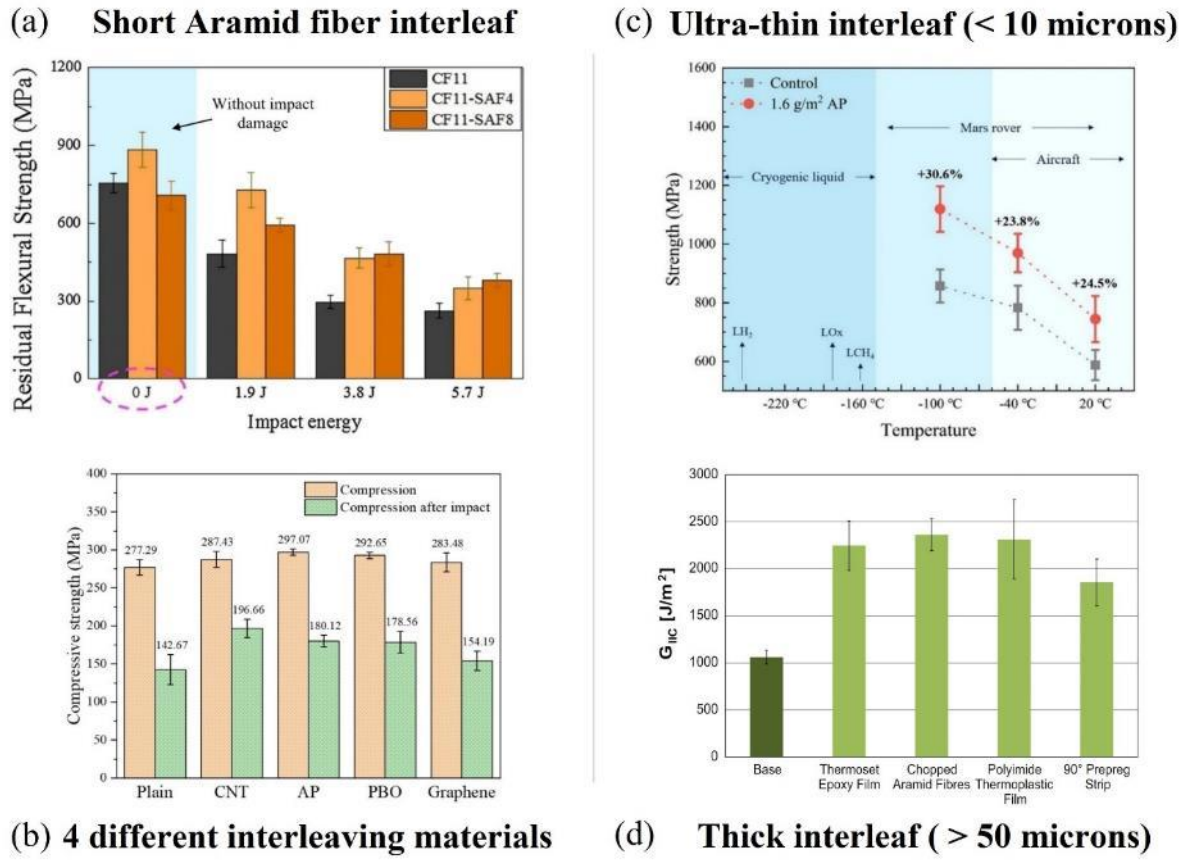

Fig. 6 (a) Residual flexural strengths of CFRPs interleaved with short aramid fibre veils of 4 and 8 grams per m^2 [15], and (b) residual compressive strengths of CFRPs interleaved by 4 different interleaving materials [17]. (c) Bulk flexural strength is improved by ultra-thin AP interleaf (around 6 microns in thickness) [18]. (d) While delamination toughness G_{II} has been improved by thick interleafs (50 – 270 microns in thickness) [19], bulk compressive strength will be reduced.

While interleaving using short or micro-length fibres, thermoplastic films and non-woven fibre veils are common interlaminar toughening methods for laminar composites and has been extensively studied by many researchers, little attention has been paid to the adverse effect on in-plane properties of CFRPs caused by thick interleaves. For example, Yasaee et al. investigated the delamination toughness of glass fibre reinforced polymers (GFRPs) interleaved with various materials [19]. The interleaf thickness of cured GFRP ranged from 50 to 270 micrometres. The experimental results given in Fig. 6 (d) showed that the G_{IIC} of aramid fibre toughened GFRPs were much higher than those of the baseline material, and the toughening effects o3f aramid fibre and thermoplastic/thermoset films were close. Although

not mentioned in their work, bulk material properties including flexural and compressive strengths of these interleaved CFRPs were likely to be reduced due to the reduction in overall volume fraction of glass fibres. The aramid fibre interlaminar toughening techniques introduced in this study including the use of non-woven short aramid fibre veils or AP micro-/nano-fibres can minimise the increase in interlayer thickness (< 10 μm) attributed to the low areal density of reinforcement and high curing pressure during the composite forming process. Therefore, even the bulk properties such as flexural and compressive strengths can be enhanced.

5 Conclusion

This study shows the interfacial toughening effects from CNT and short aramid fibres, or aramid pulps (AP) are comparable. For mass productions with less stringent requirements, AP and aramid fibres are probably more cost effective. The preliminary trials from industry show even distributions of short aramid fibres and AP (together with CNT) are possible, which is significant as all similar laboratory tests and test results can be transferred to prepreg manufacturing in principle.

In comparison with other interleaving materials including CNT and graphene, aramid fibre interlaminar toughening has been proven to be effective for enhancement of various mechanical properties including the delamination toughness, impact resistance, flexural and compressive strengths of CFRP laminates. Considering the excellent toughening effect and cost effectiveness of aramid fibres, they may potentially be incorporated in large-scale prepreg production in industry.

Reference

[1] A. Cohades, N. Hostettler, M. Pauchard, C.J.G. Plummer, V. Michaud, Stitched shape memory alloy wires enhance damage recovery in self-healing fibre-reinforced polymer composites, Compos. Sci. Technol. 161 (2018) 22–31.

[2] K.K. Verma, G. Padmakara, K.M. Gaddikeri, S. Ramesh, S. Kumar, S. Bose, The key role of thread and needle selection towards 'through-thickness reinforcement' in tufted carbon fiber-epoxy laminates, Compos. Part B Eng. 174 (2019) 106970.

[3] F. Pegorin, K. Pingkarawat, A.P. Mouritz, Comparative study of the mode I and mode II delamination fatigue properties of z-pinned aircraft composites, Mater. Des. 1980-2015. 65 (2015) 139–146.

[4] T. Huang, Y. Wang, G. Wang, Review of the Mechanical Properties of a 3D Woven Composite and Its Applications, Polym.-Plast. Technol. Eng. 57 (2018) 740–756.

[5] M.-S. Sohn, X.-Z. Hu, Mode II delamination toughness of carbon-fibre/epoxy composites with chopped Kevlar fibre reinforcement, Compos. Sci. Technol. 52 (1994) 439–448.

[6] B. Yuan, E.P.J. Wee, J.L.K. Cheong, A. Speelman, R.T.J. Long, B. Jiang, Y. Li, X. Hu, Quasi-Z-directional toughening from un-bonded non-woven veil at interface in laminar composites, Compos. Commun. 6 (2017) 20–24.

[7] ud prepreg machine_TONGLIAN PRECISION MACHINERY CO.,LTD., (n.d.). http://en.whtonglian.com/product/80.html (accessed August 24, 2022).

[8] M.-S. Sohn, X.-Z. Hu, Delamination behaviour of carbon fibre/epoxy composite laminates with short fibre reinforcement, Scr. Metall. Mater. 30 (1994) 1467–1472.

[9] Z. Sun, S. Shi, X. Hu, X. Guo, J. Chen, H. Chen, Short-aramid-fiber toughening of epoxy adhesive joint between carbon fiber composites and metal substrates with different surface morphology, Compos. Part B Eng. 77 (2015) 38–45.

[10] E.J. Garcia, B.L. Wardle, A. John Hart, Joining prepreg composite interfaces with aligned carbon nanotubes, Compos. Part Appl. Sci. Manuf. 39 (2008) 1065–1070.

[11] B.-Z. Huang, X.-Z. Hu, J. Liu, Modelling of inter-laminar toughening from chopped Kevlar fibers,

Compos. Sci. Technol. 64 (2004) 2165–2175.

[12] S. Sethi, B.C. Ray, Experimental study on the mechanical behavior and microstructural assessment of Kevlar/epoxy composites at liquid nitrogen temperature, J. Mech. Behav. Mater. 23 (2014) 95–100.

[13] B. Yuan, B. Tan, Y. Hu, J. Shaw, X. Hu, Improving impact resistance and residual compressive strength of carbon fibre composites using un-bonded non-woven short aramid fibre veil, Compos. Part Appl. Sci. Manuf. 121 (2019) 439–448.

[14] M. Ye, B. Yuan, Y. Hu, X. Hu, Compression-after-impact properties of carbon fiber composites with interlays of Aramid pulp micro-/nanofibers, Polym. Compos. 42 (2021)

[15] B. Yuan, M. Ye, Y. Hu, F. Cheng, X. Hu, Flexure and flexure-after-impact properties of carbon fibre composites interleaved with ultra-thin non-woven aramid fibre veils, Compos. Part Appl. Sci. Manuf. 131 (2020) 105813.

[16] F. Cheng, Y. Hu, B. Yuan, X. Hu, Z. Huang, Transverse and longitudinal flexural properties of unidirectional carbon fiber composites interleaved with hierarchical Aramid pulp micro/nano-fibers, Compos. Part B Eng. 188 (2020) 107897.

[17] Y. Hu, Y. Wei, G. Han, J. Zhang, G. Sun, X. Hu, F. Cheng, Comparison of impact resistance of carbon fibre composites with multiple ultra-thin CNT, aramid pulp, PBO and graphene interlayers, Compos. Part Appl. Sci. Manuf. 155 (2022) 106815.

[18] Y. Hu, F. Cheng, Y. Ji, B. Yuan, X. Hu, Effect of aramid pulp on low temperature flexural properties of carbon fibre reinforced plastics, Compos. Sci. Technol. 192 (2020) 108095.

[19] M. Yasaee, I.P. Bond, R.S. Trask, E.S. Greenhalgh, Mode II interfacial toughening through discontinuous interleaves for damage suppression and control, Compos. Part Appl. Sci. Manuf. 43 (2012) 121–128.

Micro-computed tomography characterisation of low-velocity impact damage in sandwich panel with UHMWPE facings

Bin Yang
School of Aerospace Engineering and Applied Mechanics, Tongji University, Shanghai 200092, P.R. China

Qi Zhou
School of Aerospace Engineering and Applied Mechanics, Tongji University, Shanghai 200092, P.R. China

Kunkun Fu
School of Aerospace Engineering and Applied Mechanics, Tongji University, Shanghai 200092, P.R. China

Yan Li
School of Aerospace Engineering and Applied Mechanics, Tongji University, Shanghai 200092, P.R. China

Corresponding author: Prof. Kunkun Fu, * E-mail: 1984fukunkun@tongji.edu.cn

ABSTRACT

This paper aims to investigate the low-velocity impact (LVI) responses of sandwich composites experimentally under three different impact energies (50 J, 80 J and 110 J). Polyethylene terephthalate (PET) and Polyvinyl chloride (PVC) foam cores were used as core materials, and adhesively bonded with two ultra-high molecular weight polyethylene (UHMWPE) fibres face sheets. The micro-computerized tomography (Micro-CT) was used as an inspection technique to compare and characterize internal failure status of sandwich composites, and the effect of areal densities of UHMWPE fibre fabrics and foam core materials on the impact response and failure pattern were addressed. The results show that the sandwich composite with PET foam core exhibits better impact strength and energy dissipation behaviour than that with PVC foam core.

Keywords: Low-velocity impact (LVI), UHMWPE fibre, Sandwich panel, Micro-CT, Failure pattern.

1. INTRODUCTION

Composite sandwich structures have been extensively used in aerospace, marine, wind energy and civil engineering fields, due to its high specific strength and stiffness, excellent energy-absorbing properties, corrosion and fatigue resistance [1]. A typical sandwich structure consists of two strong face sheets and a low-density core [2]. Generally, the face sheets often bear the bending and in-plane stress, while the core structures resist the transverse shear load and absorb the transverse impact energy from external objects.

A main disadvantage of sandwich composites is the poor anti impact performance. During the service life of a sandwich composite, they are likely to suffer LVI events, which often cause a complex combination of multiple failure modes involving fibre fracture, matrix crack, delamination, core crushing and face-core debonding [3][4][5]. Even if the damage caused by LVI may be hard to observe by visual inspection, the internal damage can severely weaken (up to more 70%) the residual mechanical properties of the composite structures [6][7][8]. A comprehensive understanding on the damage mechanism of composite sandwich structures under LVI is thus strongly needed for the development and validation of reliable design and selection procedures for this class of materials [9].

Various composite sandwich structures have been designed for adapting to different application situation, such as glass, carbon, aramid and Ultra-high molecular weight polyethylene (UHMWPE) fibres with polyvinyl chloride (PVC), polyurethane (PU) or polymethacrylimide (PMMI) foam cores [10]. UHMWPE textiles are generally manufactured by stacking a large quantity of fabric layers and bonded by adhesive resin under high pressures [11], which have a lot of advantages, such as low density (0.97 g/cm3, only 2/3 of aramid fibre and 1/2 of carbon fibre), high specific strength and modulus, good abrasion resistance, corrosion resistance and excellent energy absorption performance (1.8 and 2.6 times of carbon and Kevlar fibre reinforced composite, respectively) [12]. Moreover, it has been demonstrated that UHMWPE laminates are more mass efficient than common metallic and other composite materials for a wide range of thickness [12]. Lots of studies on the anti-impact performance of UHMWPE laminates have been reported [10-14]. Yang et al. [12] studied the aramid and UHMWPE-based hybrid textile composites under projectile impacts numerically and achieve the optimum design scenario for different impacts. Arora et al. [14] found that the impact resistance can be improved by filling a non-Newtonian fluid in an UHMWPE-based textile. Zulkifli et al. [15] studied the effect of plying sequence of carbon fabrics in an UHMWPE-based composite on the impact performance, and suggest that stiffer carbon fibre layer bonded on the UHMWPE laminate can greatly improve the impact performance by enhancing the bending rigidity. Hu et al. [16] found that the impact damage tolerance of the 2-dimentional UHMWPE/CF hybrid woven laminate increases by 10.1% comparing to CFRP laminate. Zhang et al. [17] studied the impact performance of UHMWPE laminates and UHMWPE encapsulated aluminium sandwich structures based on a full three-dimensional continuum model and a good design scheme was proposed to design a lightweight UHMWPE composite structure with superior impact resistance.

For a sandwich structure, the polymeric foam cores, such as polyvinyl chloride (PVC), polymethacrylimide (PMMI) and Polyethylene terephthalate (PET) have been employed in various engineering fields [18][19][20][21], due to their low cost, easy manufacturing, moisture resistance and superior thermal and sound insulation properties [10]. Caprino and Teti [22] investigated the impact response of glass fibre face sheet/PVC foam sandwich panels considering the effect of core densities, and suggested that density of cores have a great influence on the damage induced by impact. Anderson and Madenci [23] found that the carbon face sheet with a high-density core PMMI foam core sandwich structures have a higher damage resistance compared to that with a low-density foam core. Similarly, the failure of the impacted face sheet was seen to be dependent on the core material properties. Cantwell and co-workers [24][25] investigated the impact response of sandwich

composite bonded with PVC or PET foam cores with different densities and concluded that threshold energy for damage initiation [24] and the perforation energy [25] increase with the increase of the density of foams. In this paper, the sandwich structures manufactured with UHMWPE/PVC and UHMWPE/PET foam sandwich panels were designed to improve their anti-impact performance. A series of LVI tests were conducted to study the failure mechanism of sandwich structures under LVI with different energy, and the effect of areal density of UHMWPE on the impact response were analysed. The variation of impact parameters such as force and energy versus deformation and time were examined to propose the damage process of sandwich panels under different LVI.

2. MATERIALS AND EXPERIMENTS

2.1 MATERIALS

UHMWPE fabrics (supplied by Beijing Junantai Protection Technologies) were used as reinforced materials of face sheets. To examine the effect of areal densities on the LVI behaviour, the fabrics with two areal densities, i.e. 170 g/m^2 and 300 g/m^2 are selected. Epoxy resin (Epolam 2047) was cured using a hardener (Epolam 2040) with a weight ratio of 32:100. The typical properties of the hardener and epoxy resin are summarized in Table 1 and Table 2, respectively. PVC foams (Airex C70.48) with a thickness of 10 mm and PET foam (Airex T92.100) with a thickness of 11 mm were used as core materials to manufacture sandwich panels, respectively. The material densities of PET and PVC foam are 100 kg/m^3 and 130 kg/m^3, respectively. The tested mechanical properties of the two foam core materials are listed in Table 3. The layup sequence of the UHMWPE laminates was [0°/90°, 45°/-45°, -45°/45°, 90°/0°]. The naming rules of the sandwich composites are given in Table 4. The bending stiffness and strength of the sandwich composite panels and foam cores are evaluated by three-point bending test and summarized in Figure 1.

The sandwich panels were fabricated using a vacuum-assisted resin transfer moulding (VARTM) process. First, the UHMWPE fabrics and the core together with the peel plies were stacked on a steel mould. A vacuum bag was spread over the mould and was sealed off using a sealant tape. Then, the epoxy resin and hardener were mixed evenly in a beaker and vacuumized to avoid air bubbles. Next, the epoxy resin is injected into the mould by virtue of the suction offering from the vacuum pump. Finally, the curing was performed at a temperature of 25 °C for 9 h under a pressure of 0.1 MPa. Thereafter, the sandwich panel is post-cured at 70 °C for another 2 h to improve its mechanical performance of composites [26]. The sandwich panels were cooled in the air and were cut into a square shape with a dimension of 100 × 100 mm^2 using a cutting machine. The diagram of all the equipment used in VARTM technique is plotted schematically in Figure 2.

Table 1. Typical properties of the hardener

	Gel time on 100 ml at 25ºC (g/cm^3)	Pot life on 500g at 25ºC (min)	Mix viscosity at 25 ºC
EPOLAM 2047	1.16	180	220

Table 2. Typical properties of the epoxy resin

	Density at 25ºC (g/cm^3)	Viscosity at 25 ºC (cp)	Weight mixing ratio
EPOLAM 2040	1.16	1100	100

Table 3. Mechanical properties of PVC and PET foams

	Compressive modulus (MPa)	Shear modulus (MPa)	Shear strength (MPa)	Compressive strength (MPa)	Density (kg/m^3)
PVC (AIREX C70.48)	48	16	0.55	0.6	48
PET (AIREX T92.100)	90	26	0.9	1.75	100

Table 4. Parameters of the sandwich composite plates

Definition	Stacking sequences
UH300-PVC	[0º/90º/(±45º)$_{2s}$/90º/0º/(300g/m^2) PVC Foam /0º/90º(±45º)$_{2s}$/90º/0º]$_s$
UH170-PVC	[0º/90º/(±45º)$_{2s}$/90º/0º/(170g/m^2) PVC Foam /0º/90º(±45º)$_{2s}$/90º/0º]$_s$
UH170-PET	[0º/90º/(±45º)$_{2s}$/90º/0º/(170g/m^2) PET Foam /0º/90º(±45º)$_{2s}$/90º/0º]$_s$
UH300-PET	[0º/90º/(±45º)$_{2s}$/90º/0º/(300g/m^2) PET Foam /0º/90º(±45º)$_{2s}$/90º/0º]$_s$

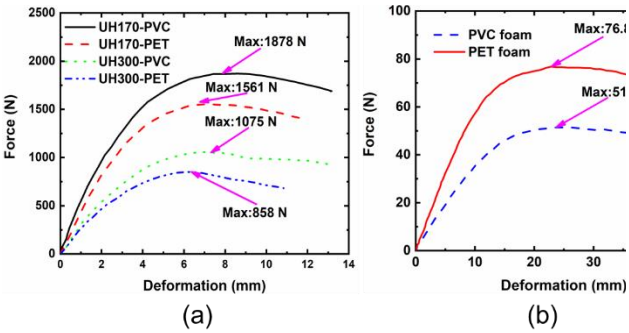

Figure 1: FORCE-DEFORMATION RELATIONSHIP OBTAINED BY THREE-POINT BENDING TEST, (A) SANDWICH PANEL, (B) FOAM CORE

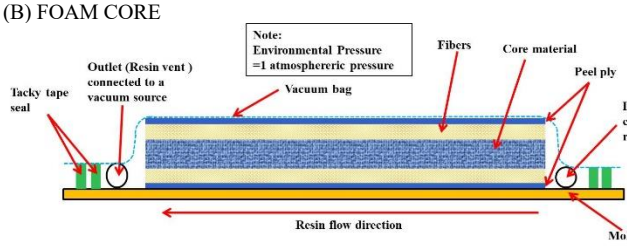

Figure 2: SCHEMATIC OF A VARTM PROCESS FOR SANDWICH COMPOSITE

2.2 SETUP FOR LVI

The LVI tests of sandwich panels were carried on a drop-weight impact testing (Instron CEAST 9350) in accordance with the ASTM D7136/D7136M-12 standard [27] as shown in Figure 3a. A hemispherical impactor with a nominal diameter of 12.7 mm was chosen (see Figure 3b). The sandwich panel was clamped on a fixture with a circular hole of 75 mm in diameter as shown in Figure 3c. All LVI tests were performed at room temperature (~ 18 oC) with impact energies of 50 J, 80 J and 110 J. The total mass of the impact assembly including impactor and added weight was 45.392 kg, resulting in impact velocities of 1.48 m/s, 1.88 m/s and 2.20 m/s. Each test was repeated for at least three times to obtain the averaged values. The time history of impact force, displacement, and energy during LVI tests were simultaneously measured by the built-in Impulse Data Acquisition Software.

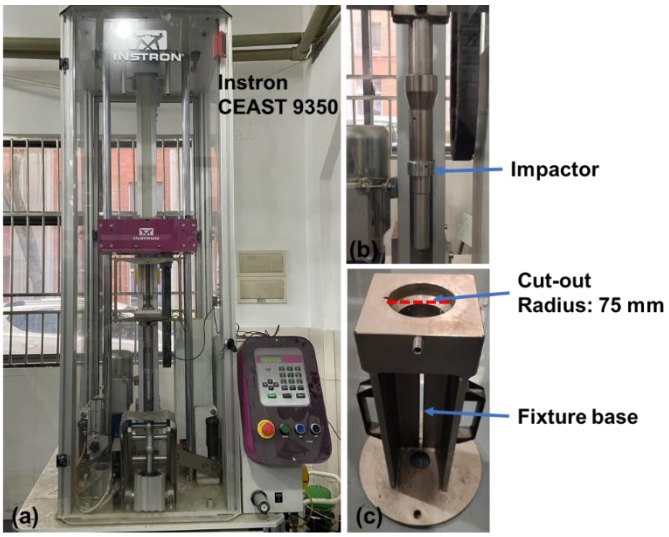

Figure 3: DROP WEIGHT SETUP: (A) OVERALL VIEW OF THE IMPACT MACHINE, (B) IMPACTOR, (C) FIXED FIXTURE

2.3 SETUP FOR MICRO-CT CHARACTERISATION

Detailed failure patterns of the impacted specimens are detected using Micro-computed tomography (Micro-CT) techniques. Micro-CT devices can provide a good damage view through the thickness for materials especially for composite structures [28][29]. The impact regions of sandwich composites specimens are scanned with phoenix v|tome|x m system to determine the failure patterns. The scanning parameters of sandwich composites are listed in Table 4.

Table 4. Micro-CT scanning parameters

Scanning Parameters	Values
Source voltage	190 KV
Source current	195 µA
Image pixel size	37.3 µm
Object to source	151.1 mm
Camera to source	800 mm
Exposure	500 ms
Rotation step	0.24°
Reconstruction program	datos
Correction	8.5

3. RESULTS AND DISCUSSION

3.1 LOW-VELOCITY IMPACT BEHAVIOUR

Contact force-deformation (displacement of the impactor through the panel) curves are considered as one of the most important visual methods to understand the response of composite material to LVI loading [30]. The variation curves of contact force against deformation for UHMWPE/PVC and UHMWPE/PET sandwich composites subjected to 50

J, 80 J and 110 J impact are shown in Figures 4-6. The force-deformation curves characterizing the typical impact response can be divided into three segments, which are complete rebound, incomplete rebound and partial or complete penetration, which are common properties for the penetration response of the sandwich panels [31][32]. Firstly, the impact force increases linearly and quickly due to the elastic response of sandwich panels under LVI loading. This phenomenon suggests that the front face sheet resist the impactor before they are damaged. The slope of the ascending section of each force-deformation curve was termed as the impact bending stiffness due to its representation of the stiffness of composite panels under impact-induced bending at the beginning of the impact process [33]. Then, the contact force reaches a fluctuant and stable state due to initiation and evolution of damages. Finally, the contact force decreases gradually with the rebounding of the impactor. It is seen from Figure 4b that the slope of force-deformation curves at initial phase is quite different from each other due to the different bending stiffness of these four specimens.

The contact force-deformation curves do not fully explain the impact behaviour of composite laminates. The impact energy is one of important parameters to find out structural behaviours and discover the damage mechanisms during the impact process [34]. The impact energy versus time and deformation relationship are presented in Figure 4 b and d. The initial kinetic energy of the impactor transfers to the sandwich panel when contact begins. The impact energy increases with the deformation before reaching peak value. With descending of the impactor, a small part of the kinetic energy is absorbed by the panel and core in the form of elastic deformation, while most of it is dissipated in the form of fibre breakage, matrix crack, delamination and the friction between impactor and panel, impactor and core and among neighbouring ply (see Figures 7 and 9). The kinetic energy of the impactor has been absorbed by the sandwich panel totally when its velocity reduces to zero, and the absorbed energy reaches to its peak [35]. Thereafter, the elastic energy stored in the sandwich panel transfers back to the impactor and lead to rebound. Finally, the impact energy absorbed in the sandwich panel keep a stable value when the impactor rebounds from or stay in the panel.

Figure 7 shows visual inspection of the experimental predicted LVI damages in the sandwich panels after 110 J impact. During the impact event, parts of the specimens damaged leaving a clean hole on the front face and an obvious break on the back side. For the 110 J impact test, only the back face of UH300-PET specimen was not perforated. The white region at the back side of the impacted specimen denotes the delamination between foam core and bottom face sheet. The delamination has a circular shape, of which diameter is almost equal to the one of open hole of fixture (75 mm).

During an impact event, the impact kinetic energy is generally absorbed by sandwich panels through the elastic, plastic deformation and creation of new fracture surfaces through various failures [36] (see Figure 9). Meanwhile, crush of core material as well as cracks in it could also absorb the impact energy. Hence, impact energy is initially absorbed through elastic deformation as well as crush of foam core. This process is continued until the threshold energy of the UHMWPE face sheet is reached. At or beyond the threshold energy value, impact energy is absorbed through both elastic deformation and creation of damage by various failure modes. This damage is occurred both in the face sheet and the core material. Normally impact damage is initiated as matrix crack in the face sheet. This crack further extends to the interface between two laminates and progresses as delamination. Matrix cracks are caused by tensile or shear load in the impact event. In both cases, the cracks may propagate along transverse direction of fibres. They propagate along the thickness direction until they meet stiffer fibres in the ply, and this will lead to the development of delamination.

3.1.1 EFFECT OF AREAL DENSITY OF UHMWPE

The UHMWPE fibre fabrics with different areal densities have different mechanical properties so that the areal density has an important influence on the impact response of UHMWPE fibre cored composite materials under LVI loading. In this section, two typical UHMWPE fibre fabrics with the density of 170 g/m^2 and 300 g/m^2 are adopted. As shown in Figures 4 a and c, there is only one peak for each curve, which demonstrates that the impactor penetrates the upper face sheet and rebound from or embedded in the foam core without contacting with the bottom panel. For the impact with high impact energy (see Figures 5 and 6), there are two peaks for each curve which can demonstrate that the bottom face sheet has also been damaged due to the squeeze of impactor. It can be also found from Figures 4-6 that the areal density and the type of foam core have a little influence on the absorbed energy of sandwich panels since the impactor have embedded into the core without rebounding leading to the kinetic energy of impactor have been totally absorbed by the sandwich panel. The recorded peak force and the corresponding deformation are

summarized in Table 5. It is observed that the peak force increases with the decrease of the areal density of fibre fabric for sandwich panels with PET cores. However, in terms of the sandwich panels with PVC cores, the influence of areal density on the peak force depends on the impact energy.

3.1.2 Effect of foam core

By comparison of impact force time history curves of sandwich panels with two different foam cores, the larger impact force caused by impacting with the PVC sandwich panel is due to lower bending stiffness of PVC foam (see Figure 1). It is interesting that there are two different types of force-deformation curves, i. e, open and closed curves. The open and close curves denote the penetration and perforation status, respectively. When the impact energy increased from lower impact energy (50 J) to the higher one (110 J), the type of force-deformation curves for UH300-PET and UH300-PVC transits from the closed type to an open one, and the UH170-PVC sandwich composite has an open curve, while UH170-PET sandwich composite has a closed one. This can demonstrate that the sandwich composite with PET core has a more stronger impact resistance than that with PVC core due to higher bending strength for PET foam. Only UH300-PET sandwich composite is not perforated under 110 J impact due to the its most strong bending strength, which has been confirmed in Figure 1. From the observations of force-deformation relationships in Figures 4-6, foam core type has an apparent effect on the descending section of the curves. This is because the failure mechanism of these two foam cores under LVI loading are totally different, which is further proved in Figure 9.

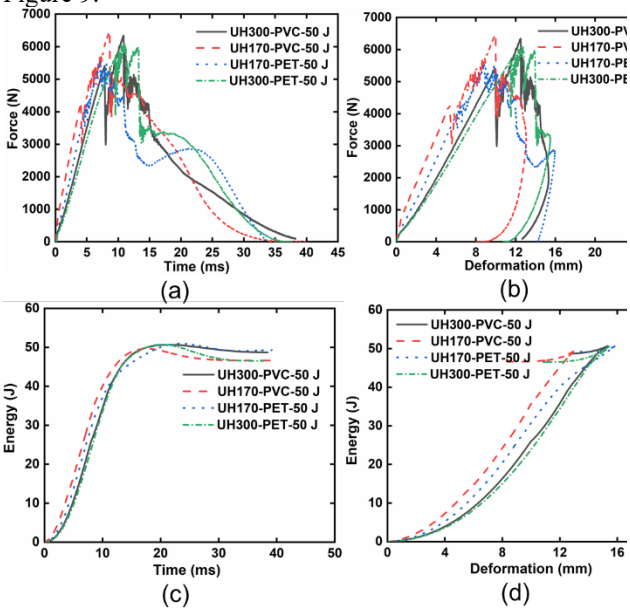

FIGURE 4: CURVES OF SANDWICH COMPOSITES UNDER 50 J IMPACT: (A) FORCE-TIME CURVE, (B) ENERGY-TIME CURVE, (C) FORCE-DEFORMATION CURVE, (D) ENERGY-DEFORMATION CURVE

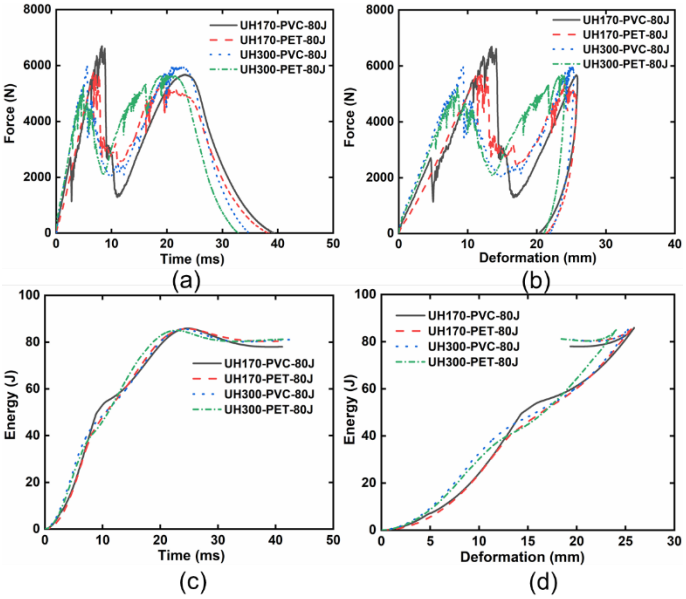

Figure 5: CURVES OF SANDWICH COMPOSITES UNDER 80 J IMPACT: (A) FORCE-TIME CURVE, (B) ENERGY-TIME CURVE, (C) FORCE-DEFORMATION CURVE, (D) ENERGY-DEFORMATION CURVE

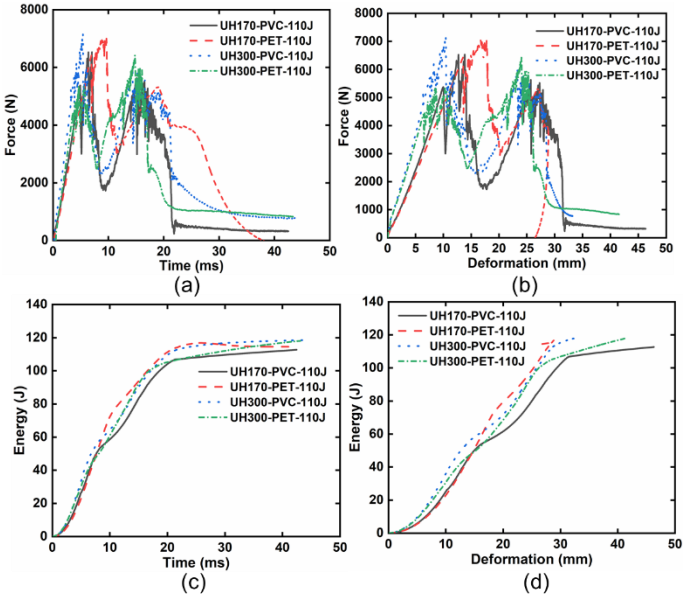

Figure 6: CURVES OF SANDWICH COMPOSITES UNDER 110 J IMPACT: (A) FORCE-TIME CURVE, (B) ENERGY-TIME CURVE, (C) FORCE-DEFORMATION CURVE, (D) ENERGY-DEFORMATION CURVE

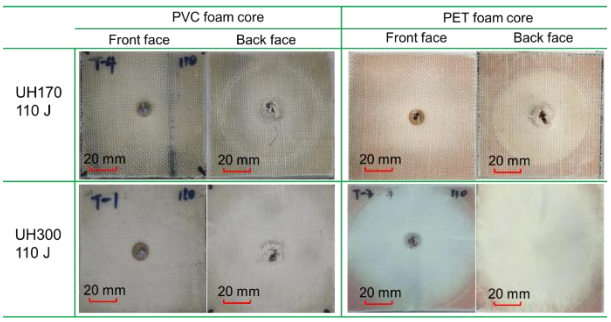

Figure 7: FAILURE PATTERN OF SANDWICH PANELS BY VISUAL INSPECTION UNDER 110 J IMPACT

Table 5 Parameters obtained at the peak of contact force during LVI events.

Impact energy	Parameters	UH300-PVC	UH170-PVC	UH300-PET	UH170-PET
50 J	Peak force / kN	6.45±0.11	6.34±0.03	5.52±0.04	6.09±0.02
80 J	Peak force / kN	5.96±0.01	6.69±0.02	5.68±0.01	5.75±0.03
110 J	Peak force / kN	7.15±0.01	6.52±0.05	6.42±0.01	7.04±0.01

3.2 Micro-CT characterization of impact damage

Micro-CT is a three-dimensional imaging technique which is used non-destructively to inspect the inner structure of an object by transmission measurements using X-rays, a large number of projection images are obtained by rotating the sample. Micro-CT complements the use of X-ray radiography by imaging detailed cross-sectional views of the specimens, thereby resolving through-thickness delamination and matrix cracks [37]. Schematic illustration of detecting the internal damage in composites using micro-CT scanning method are presented in the Figure 8. The cross-sectional images are taken in the lateral through-thickness direction of the specimens, particularly containing the delamination and crack region. There are 1400 cross-sectional slices were taken from micro-CT scanning during the actual examination. Only 5 cross-sectional micro-CT pictures were taken for evaluation due to the limited space in the paper. Slice C-C locates at the centre section of the sandwich panel, which is consistent with the symmetry plane of impact region. The length between the two adjacent slices is 0.35 mm and total scanning length from slice A-A to E-E is 1.4 mm.

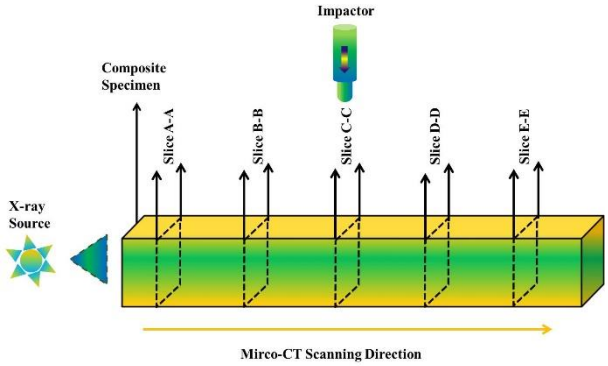

Figure 8: SCHEMATIC ILLUSTRATION OF MICRO-CT SCANNING PROCESS IN COMPOSITES AFTER LOW VELOCITY IMPACT LOADING

Figure 9 depicts the cross-sectional images of UH170-PVC and UH170-PET sandwich composites core materials after the impact with an energy of 110 J using micro-CT. Black parts in micro-CT images denote the foam core, and white parts represent the UHMWPE fibres in the sandwich composite materials. As shown, the interlaminar resin matrix near the upper surface is crushed resulting in delamination due to compression, while the resin matrix adjacent to the bottom surface is collapsed due to stretching. It can be seen that the no obvious fibre breakages at the bottom face sheet of the PET foam-based sandwich composite, while there are a lot of fibre breakage damages for the PVC foam-based composite. For the sandwich panel with PET core, the fibre fabrics at impact region have been stripped from the upper face sheet, and adhered to the bottom face sheet due to descent of the impactor.

Impact-compression zone of a sandwich panel can be illustrated by the contrast tone in every cross-section as shown in Figure 10. Davies [38] have indicated that the region on the centreline of the impactor has a lower shear stress, and in a state of through-thickness compression so that the delamination cannot occur here (see Figure 10). The delamination mainly take place at impact region with high shear stress between the upper face sheet and the outer wall of the impactor, and the more serious delamination occurs at the interface between the core and the bottom face sheet, which attributes to its smaller fracture toughness and the larger shear stress at bottom region. It is observed from Figure 10 that the deformations and failure patterns are symmetric about the slice C-C due to symmetric of loading and boundary conditions. However, the damage status at the two orthogonal sections are different, maybe it is because the manufacturing defects and nonuniformity of resin, etc., causing the anisotropy of the sandwich panel.

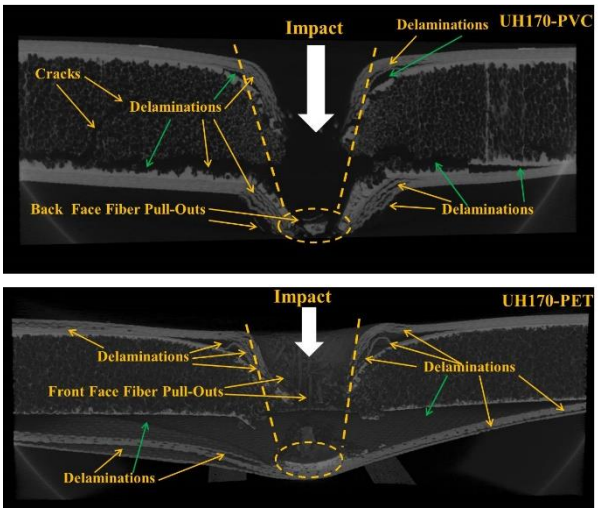

Figure 9: CROSS-SECTIONAL MICRO-CT SLICES OF SANDWICH COMPOSITES AT IMPACT CENTRE

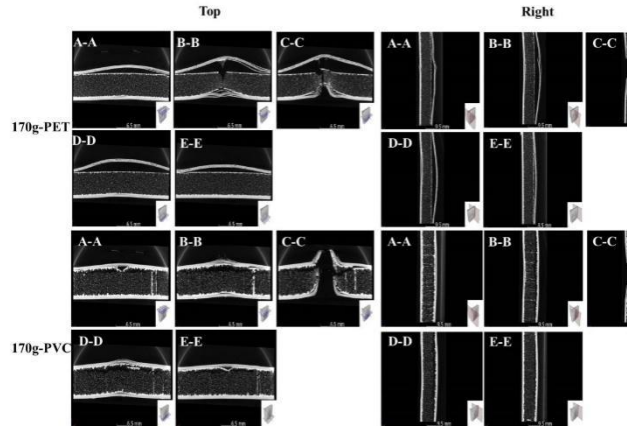

Figure 10: DAMAGE VIEWS AT DIFFERENT CROSS-SECTIONAL OF TWO SANDWICH COMPOSITE SPECIMENS FROM DIFFERENT DIRECTION (TOP AND RIGHT) AFTER 110 J IMPACT USING MICRO-CT

Figure 11 depicts the three-dimensional damage illustrations of UH170-PVC and UH170-PET sandwich composites after 110 J impact obtained from micro-CT. As depicted in Figure 11, the bright UHMWPE fibre layers has made impact compression zone more pronounced, and the three main damage patterns including fibre breakages, matrix cracks and delamination can be clearly identified. The delamination area of UH170-PVC sandwich panel is larger than that of UH170-PET panel since the bending strength of PET is stronger (see Figure 1). The composite material partially cutting from the UH170-PVC sandwich composite material is squeezed more serious than the UH170-PET, and a part of the core material of the UH170-PET sandwich composites have stacked to the bottom face sheet as shown in Figure 11d. The obvious delamination of the sandwich composite structures can be observed between each UHMWPE ply and between the upper/lower face sheets and the core material near the impact region. According to the damage status of the two foam cores, the PVC foam seems to be more brittle comparing to PET foam, and adhesion property for the PVC foam is better. The final delamination patterns for these two specimens are confined in an annular zone since the impactor has a hemisphere shape.

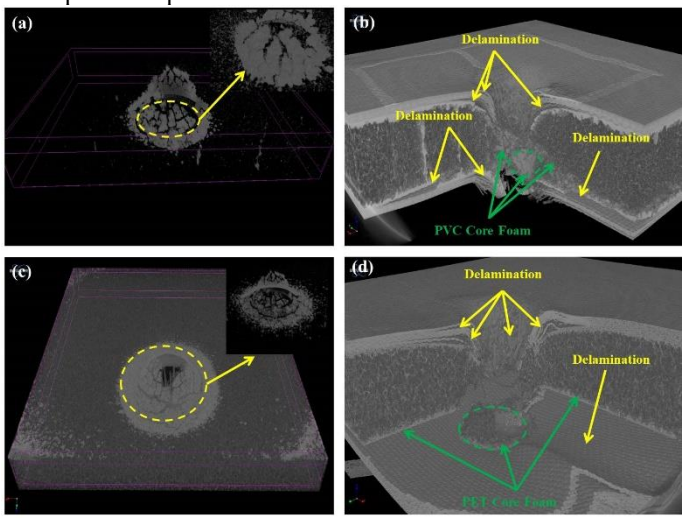

Figure 11: THREE DIMENSIONS VIEWS OF CORES OF SANDWICH COMPOSITES (110 J IMPACTED) SPECIMENS USING MICRO-CT: (A, B) PARTIAL CUTTING OF UH170-PVC SANDWICH COMPOSITES, (C, D) PARTIAL CUTTING OF UH170- PET SANDWICH COMPOSITES.

The deformation history curves and failure modes of UH170-PVC and UH170-PET sandwich composite under 110 J impact are shown in Figure 12. The UHMWPE sandwich composite experienced a complete perforation process under 110 J impact, and irreversible plastic deformation and internal damage occurred due to delamination, fibre fracture and matrix cracks. It can be clearly seen that the back face of UH170-PVC sandwich composite has been collapsed due to impact, which leads to the deformation increased over time during the whole impact event. Comparing the damage views of these two foam cores, the PET foam was squeezed more severe, meanwhile the PET foam has a higher elastic modulus and strength, which causes the PET foam can absorb more impact energy. Though the PET foam core of the sandwich composite has been penetrated, the bottom face sheet has no damages since the kinetic energy of the impactor have been dissipated by the elastoplastic deformation and damages of the upper face sheet and the foam core. The rebound mechanism of the UH170-PET core composite material has an upward trend after 25 ms, and then a downward trend, which is due to the fact that the PET foam core next to the bottom face sheet nearly turned

into its original position except internal damage regions (see Figure 12). The PVC foam in the sandwich composite have a global deformation except the internal damage region after the impactor was removed. The maximum deformation of UH170-PVC sandwich composite is 46.31 mm, which is larger than the maximum deformation of UH170-PET with a value of 28.87 mm.

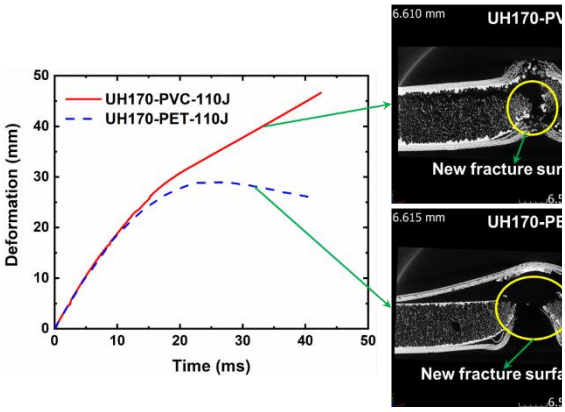

Figure 12: DAMAGE RESULTS OF SANDWICH COMPOSITES UNDER 110 J IMPACT (A) DEFORMATION-TIME CURVE (B) MICRO-CT PLOT FOR SPECIMENS

4. CONCLUSION

In this study, a series LVI tests of UHMWPE reinforced plastic composite sandwich composites plates with PVC and PET foam cores under three different impact energies (50 J, 80 J and 110 J) were conducted. The impact response results were evaluated with force-time, force-deformation, impact energy-time and impact energy-deformation. Micro-CT was adopted to deeply explore the LVI damage mechanism. Several conclusions are summarised as follows:

1. The images obtained using Micro-CT has demonstrated it is a strong tool for detecting the internal damage pattern of sandwich panels under LVI loading.
2. There is only one peak for the force-displacement curve when the impact energy is 50 J, while there are two peaks when the energy is greater than or equal to 80 J.
3. The PET foam cores in sandwich panels next to the bottom face sheet nearly turned into its original position except internal damage regions after LVI. However, the PVC foam core would have a global deformation after the impactor was removed.
4. Only the back face of UH300-PET specimen was not perforated after 110 J impact due to its best energy-absorption ability.

ACKNOWLEDGEMENTS

The authors are grateful for the financial support from the National Key Research and Development Program of China (Grant Number: 2020YFB0311500), Shanghai Pujiang Program (Grant Number: 19PJ1410000), the Fund of National Postdoctoral Program for Innovative Talents (BX20200244) and the Fellowship of China Postdoctoral Science Foundation (2020M671224).

REFERENCES

[1]. Birman V, Kardomateas GA. Review of current trends in research and applications of sandwich structures. Compos B Eng 2018;142:221–40.
[2]. Elamin M, Li B, Tan KT. Impact damage of composite sandwich structures in arctic condition. Compos Struct 2018;192: 422–33.
[3]. Zhang C, Tan K T. Low-velocity impact response and compression after impact behavior of tubular composite sandwich structures. Composites Part B: Engineering. 2020, 193, 15: 108026.
[4]. Zhu Y, Sun Y. Dynamic response of foam core sandwich panel with composite facesheets during low-velocity impact and penetration. International Journal of Impact Engineering, 2020, 139: 103508.
[5]. Palomba G, Epasto G, Crupi V, et al. Single and double-layer honeycomb sandwich panels under impact loading. International Journal of Impact Engineering, 2018, 121: 77-90.
[6]. Sun X C, Hallett S R. Failure mechanisms and damage evolution of laminated composites under compression after impact (CAI): Experimental and numerical study. Composites Part A: Applied Science and Manufacturing, 2018, 104: 41-59.
[7]. Liu H B, Liu J, Dear J P, et al. Effects of impactor geometry on the low-velocity impact behaviour of fibre-reinforced composites: an experimental and theoretical investigation. Applied Composite Materials, 2020.
[8]. Sachse R, Pickett P, Middendorf. Simulation of impact and residual strength of thick laminate composites. Composites Part B: Engineering, 2020, 195:108070.
[9]. Gurgen S. Low-velocity impact performance of UHMWPE composites consolidated with carbide particles. Archives of Civil and Mechanical Engineering, 2020, 20(2): 1-12.
[10]. Feng D, Aymerich F. Effect of core density on the low-velocity impact response of foam-based sandwich composites. Composite Structures, 2020, 239(10):112040.
[11]. Gürgen S, Kuşhan MC. High performance fabrics in body protective systems. Mater Sci Forum. 2016; 880:132–5.
[12]. Zhang R, Ni C Y, Lu T J. Ballistic performance of UHMWPE laminated plates and UHMWPE encapsulated aluminum structures: Numerical simulation. Composite Structures, 2020, 252(22): 112686.
[13]. Y. Yang, X. Chen, Investigation of failure modes and influence on ballistic performance of Ultra-

High Molecular Weight Polyethylene (UHMWPE) uni-directional laminate for hybrid design, Compos Struct. 2017, 174: 233–243.
[14]. Arora S, Majumdar A, Butola BS. Structure induced effectiveness of shear thickening fluid for modulating impact resistance of UHMWPE fabrics. Compos Struct, 2019, 210:41–8.
[15]. Zulkifli F, Stolk J, Heisserer U, Yong AT-M, Li Z, Hu XM. Strategic positioning of carbon fiber layers in an UHMwPE ballistic hybrid composite panel. Int J Impact Eng. 2019, 129: 119–27.
[16]. Hu Y, Shi Y, Liu D, et al. Damage tolerance of 2-dimentional UHMWPE/CF hybrid woven laminates subjected to low-velocity impact. Materials & Design, 2020.
[17]. Zhang R, Qiang LS, Ni CY, et al. Ballistic performance of UHMWPE laminated plates and UHMWPE encapsulated aluminum structures: Numerical simulation. Compos Struct. 2020; 252:112686.
[18]. Rajak D K, Pagar D D, Menezes P L, et al. Fiber-Reinforced Polymer Composites: Manufacturing, Properties, and Applications. Polymers, 2019, 11(10).
[19]. Fathi A, Wolff-Fabris F, Altstädt V, Gätzi R. An investigation on the flexural properties of balsa and polymer foam core sandwich structures: Influence of core type and contour finishing options. J Sandwich Struct Mater 2013;15(5):487–508
[20]. Soltani M, Moghaddam T B, Karim M R, et al. Analysis of fatigue properties of unmodified and polyethylene terephthalate modified asphalt mixtures using response surface methodology. Engineering Failure Analysis, 2015, 58(58): 238-248.
[21]. Loyens W, Groeninckx G. Ultimate mechanical properties of rubber toughened semicrystalline PET at room temperature. Polymer, 2002, 43(21): 5679-5691.
[22]. Caprino G, Teti R. Impact and post-impact behavior of foam core sandwich structures. Compos Struct 1994;29(1):47–55.
[23]. Anderson T, Madenci E. Experimental investigation of low-velocity impact characteristics of sandwich composites. Compos Struct 2000;50(3):239–47.
[24]. Hazizan MA, Cantwell WJ. The low velocity impact response of foam-based sandwich structures. Compos B Eng 2002;33(3):193–204.
[25]. Zhou J, Hassan MZ, Guan Z, Cantwell WJ. The low velocity impact response of foambased sandwich panels. Compos Sci Technol 2012;72(14):1781–90.
[26]. Lin, S., et al., Composites of UHMWPE fiber reinforced PU/epoxy grafted interpenetrating polymer networks. European Polymer Journal, 2007, 43(3):p. 996-1008
[27]. ASTM D7136/D7136M-12 standard test method for measuring the damage resistance of a fiber-reinforced polymer matrix composite to a drop-weight impact event.
[28]. D. Penumadu, F. Kim, J. Bunn. Damage of Composite Materials Subjected to Projectile Penetration Using High Resolution X-Ray Micro Computed Tomography. Experimental mechanics, 2016, 56(4): 607-616.
[29]. Fidan S, Sinmazcelik T, Avcu E, et al. Internal damage investigation of the impacted glass/glass+aramid fiber reinforced composites by micro-computerized tomography. Ndt & E International, 2012, 51(10): 1-7.
[30]. Jassim A K, Shamary A, Ozdemir O, et al. Low-velocity impact response of sandwich composites with different foam core configurations. Journal of sandwich structures and materials, 2016, 18(6): 754-768.
[31]. Y. Chen, S. Hou, K. Fu, X. Han, L. Ye, Low-velocity impact response of composite sandwich structures: modelling and experiment, Compos. Struct. 2017, 168:322–334.
[32]. Ozen, Gedikli H Aslan M, et al. Low-energy impact response of composite sandwich panels with thermoplastic honeycomb and reentrant cores, Thin-walled structures, 2020, 156: 106989.
[33]. Dahsin Liu, Basavaraju B Raju, Xinglai Dang. Impact perforation resistance of laminated and assembled composite plates. Int J Impact Eng 2000, 24(6–7): 733–46.
[34]. Zangana S, Epaarachchi J A, Ferdous W, et al. A novel hybridised composite sandwich core with Glass, Kevlar and Zylon fibres - Investigation under low-velocity impact. International Journal of Impact Engineering, 2020, 137: 103430.
[35]. Shi Y, Swait T J, Soutis C, et al. Modelling damage evolution in composite laminates subjected to low velocity impact. Composite Structures, 2012, 94(9): 2902-2913.
[36]. Kumar S J, Kumar S J. Low-velocity impact damage and energy absorption characteristics of stiffened syntactic foam core sandwich composites. Construction and Building Materials, 2020, 246: 118412.
[37]. Aryal B, Morozov E V, Wang H, et al. Effects of impact energy, velocity, and impactor mass on the damage induced in composite laminates and sandwich panels. Composite Structures, 2019, 226: 111284.
[38]. Davies GAO, Zhang X. Impact damage prediction in carbon composite structures. Int J Impact Eng 1995;16(1):149–70.

Properties of poly(butylene adipate-co-terephthalate)/thermoplastic starch filled with treated and untreated sugarcane bagasse fibre

Maisara A. M. Akhir[1,2], *S.A. Zubir*[1] *and J. Mariatti*[1*]

[1] *School of Materials and Mineral Resources Engineering, University Sains Malaysia, Nibong Tebal, Penang, Malaysia;*

[2] *Fakulti Teknologi Kejuruteraan Kimia, Universiti Malaysia Perlis (UniMAP), Perlis, Malaysia*

* Corresponding author: mariatti@usm.my

Abstract: Sugarcane bagasse composed of fibrous rind and spongy pith components are often used as a reinforcement material in concrete and plastic containers. For plastic films with thin thicknesses, sugarcane bagasse is commonly used as small grinded particles in the composite film. Incorporating this agricultural waste in the biodegradable plastic film may reduce production cost and facilitate the film's biodegradation. This present work demonstrates the formulation of poly(butylene adipate-co-terephthalate**) (**PBAT)/thermoplastic starch (TPS) (90/10) with different sugarcane bagasse fibre loadings. The effect of alkaline and silane surface treatments on tensile strength, thermal and water barrier properties were discussed. With the addition of sugarcane bagasse (5, 10, 15, and 20%), the tensile strength and elongation at break had reduced from 23.47 to 8.41 MPa, and 1135 to 55.83%., respectively. The Young's modulus also increased from 47.12 to 188.50 MPa after the addition of 20% sugarcane bagasse in PBAT/TPS matrix. There are slight improvements in tensile properties, thermal and water barrier properties, which were observed after the bagasse fibre had been treated with alkali and silane. Scanning Electron Microscope (SEM) morphology also shows that silane-treated sugarcane bagasse exhibited higher surface roughness due to lignin and hemicellulose removal. This facilitates the adhesion between the fibres and the PBAT/TPS matrix.

Keywords: Fibre composites, PBAT, tapioca starch, polymer blend, sugarcane bagasse

1. Introduction

Increasing consumer awareness on reducing waste and environmental pollution from conventional non-biodegradable plastic leads researchers to study the utilization of plant-based agricultural residues into polymer composite formulation. Employing this agricultural waste from the industry as reinforcement and filler material in the biodegradable plastic formulation

can improve the plastic stiffness apart from their high biodegradability, abundantly available, eco-friendly, renewability, lightweight alternative materials, and cheaper cost of raw material. There are opportunities to convert the agricultural residue such as sugarcane bagasse, empty fruit bunch, and fruit peel from industries from waste to wealth.

Sugarcane bagasse is one of the most produced waste derived from sugar and liquor productions. Its stalk is composed of the strong and finer long fibrous outer layer (rind) and short, soft, and spongy structured inner part (pith), which mainly consists of sucrose (Lee & Mariatti, 2008). The rind part exhibits a higher tensile strength of 8.68 MPa, Young's modulus of 2 GPa, and elongation at break of 4.24% compared to the pith part, which are 2.19 MPa, 1.2 GPa and 1.82 %, respectively (Jamali et al., 2021). Previous studies reported that the rind composites exhibited superior strength and stiffness in comparison with the pith composites (Lee & Mariatti, 2008; Wirawan et al., 2011). Due to its abundantly available, relatively high mechanical properties, low cost and large volume of production as residue, sugarcane bagasse has becomes an ideal biocomposites material to be reinforced in the polymer biocomposites formulation. Such fibrous sources can be combined with polymers to form polymer matrix composites in various forms, including woven mats, chopped fibres, and powders.

However, the utilization of natural fibres in the polymer-matrix composite is limited by their hydrophilic characteristic, high moisture absorption level, weak fibre dispersion into the matrix, poor wettability and interfacial adhesion with a hydrophobic polymer. Fibre agglomeration tends to occur during melt blending, which causes debonding and further weakens the mechanical and thermal properties. The bagasse fibre contains about 45-55% cellulose, 20–25% hemicellulose, 18–24% lignin, ash 1.3%, and other components 2.8% (Ramlee et al., 2019; Reddy & Yang, 2015). The highly crystalline and tightly packed cellulose fibres account for good chemical and mechanical properties. On the other hand, the lignin binds the hemicellulose and cellulose by ester linkages and hydrogen bonds, respectively, are the layers that hinder their interaction with the matrix. Removal of lignin, hemicellulose and other components can contribute to a high specific properties of the composite. Moreover, physical and chemical treatment, such as surface modification using coupling agents can improve fibre-matrix interfacial adhesion. Chemically treated natural fibres have the potential to be less hydrophilic and have a better bonding with the matrix. To improve interfacial strength, silane coupling agents are frequently used in polymer composites.

Poly(butylene Adipate Terephthalate) (PBAT) blended with thermoplastic starch (TPS) had been studied by number of researchers due to its competitive mechanical properties, good thermal stability and barrier properties, good biodegradability, eco-friendly, safe for food packaging, and affordable price range. Previous studies reported PBAT/TPS blend had been used as matrix reinforced with natural fibres such as oat hulls (Cardoso et al., 2018), rice husk (Yap et al., 2020), babassu mesocarp (De Moura et al., 2021; Nunes et al., 2018) and jute fibre (Yokesahachart et al., 2021). However, to the best of our knowledge, the incorporation of sugarcane bagasse fibre in PBAT/TPS blend had been rarely studied. Furthermore, limited study had been done on the effect of silane-treated bagasse on PBAT/TPS blend. Since both TPS and bagasse are hydrophilic in nature, the amount of these components is critical to ensure good barrier properties of the composite's film. Thus, this paper investigates the effect of different sugarcane bagasse fibre loadings on PBAT/TPS matrix and surface modification treatment with alkaline and GPTMS silane on the tensile, thermal, morphology and water barrier properties.

2. Materials and methods

2.1 Materials

Sugarcane bagasse was donated by the local market, after being processed to extract liquor. The outer layer of sugarcane bagasse (rind) was separated from the inner layer of sugarcane bagasse (pith). Rind parts were immersed in deionized water for 24 hr at 23 ºC and then were washed with water to remove soluble sugars and impurities. After washing, the sugarcane bagasse was dried in oven at a temperature 70 ºC for 24 hrs and then ground and sieved using kitchen sieve, removing coarse fibres. PBAT (Grade Ecoflex F Blend C1200 from BASF USA) supplied by Innovative Pultrusion Sdn. Bhd from Negeri Sembilan, Malaysia was used as a blend component and matrix. Modified tapioca starch was bought from Thye Huat Chan Sdn Bhd (Penang, Malaysia). Glycerol (85 % purity), 3-Glycidoxypropyl trimethoxysilane, sodium hydroxide, and acetic acid were purchased from Sigma-Aldrich Sdn. Bhd., Malaysia.

2.2 Fibre treatment

For treated sugarcane bagasse, sugarcane bagasse (SB) powder was soaked into 8 w/v% of NaOH mixed with distilled water for 2 hrs to remove lignin and hemicellulose during alkaline treatment. When the SB was dispersed, the pH of the mixture was adjusted to 7 using acetic acid. The SB powders were filtered and rinsed several times with distilled water. Then,

the SB powders were dried in the oven at 70ºC for 24hrs. A mixture of ethanol and deionized water (6:4) were prepared, and GPTMS (1% wt./wt.) was added dropwise and stirred. The mixtures were adjusted until pH 4 using acetic acid, and the alkaline treated SB powder were further soaked in the solution for 2 hrs. The silane-treated SB (SBT) were filtered and dried in an oven for 24 hrs.

2.3 Blend and composite preparation

Blends were prepared by melt mixing in a torque rheometer. Tapioca starch and PBAT were dried at 70 °C overnight before use to prevent excessive hydrolysis. Starch and glycerol with 70/30 wt% were dry mixed in the Haake internal mixer for 5 min at a speed of 40 rpm. Then, blends of PBAT with 10 wt% of plasticized starch were prepared in the internal mixer at a temperature of 160 °C with a rotor speed of 50 rpm for 15 min. For composite preparation, silane-treated and untreated SB fibre with 5, 10, 15, and 20 wt% were manually premixed with PBAT and TPS before the compounding process. The samples were compression molded at temperature 160°C for 5 minutes of preheating, 5 minutes of heat compression, and 3 minutes of cooling according to ASTM D638 Type IV with 1mm thickness for tensile testing.

2.3 Characterizations

The tensile properties of the composites were performed using INSTRON Universal Testing Machine according to ASTM D638. Initial grip separation was set at 30 mm gauge length, and the cross-head speed was set at 50mm/min with a 5 kN load cell operated at room temperature. Maximum tensile strength (MPa), Young's modulus, and elongation at break (%) were evaluated. Each combination of the composite was tested seven times.

The morphology of PBAT/starch (90/10) blend and reinforced SB fibre composite were obtained using ultra high resolution - scanning electron microscope (SEM) (Hitachi-Regulus, Japan). The cryo-fractured samples were coated with a thin layer of titanium and the micrographs were recorded under magnification of 200x at 3kV.

The thermal stability of the blend and composites were analyzed using thermal gravimetric analysis (TGA) (Pyris 6, PerkinElmer, USA). Approximately 18 mg of sample was used, and the tests were performed from room temperature to 600 °C under nitrogen atmosphere with heating rate of 20°C/min.

The water absorption test was conducted according to ASTM D570 using a square sample with dimension 20 x 20 x 3mm for each composite. Prior to testing, the samples were dried at

50°C for 24 hrs to a constant weight (Wi), and then cooled to room temperature in a desiccator. Each of the composites was immersed in a bottle containing distilled water for 72 hours, and then were removed and gently wiped dry with tissue paper before being weighed (W_f). The water absorption percentage was calculated using Equation (1).

$$\text{Water absorption percentage (\%)} = \frac{W_f - W_i}{W_i} \text{ x } 100\% \quad \textbf{(1)}$$

Composite film hydrophobicity was analyzed using water contact angle. The samples were cut to sample stage size and placed on the sample stages of a contact angle goniometer (Lux, DSA100, KRUSS Corporation, Hamburg, Germany). A precision syringe was used to deposit a droplet of distilled water on the film's surface. The contact angle was measured with a CCD camera and processed with an image analysis video card. The angle between the tangent and the baseline at the drop boundary was calculated automatically, and each set of samples was measured ten times before the results were averaged.

The chemical structures of PBAT/TPS (90/10) blend and different fibre loading composites were evaluated via Perkin-Elmer Frontier FT-IR spectrometer equipped with a diamond attenuated total reflectance (ATR) techniques. Bands were recorded as an average of 32 scans within the region range from 4000 to 500 cm^{-1}.

3. Result and discussion

3.1 Tensile properties

Figure 1 shows the tensile properties of the PBAT/TPS blend and composites. There is a significant reduction in tensile strength from 23.47 to 7.94MPa, and film flexibility from 1135.69 to 55.83% with the addition of SB fibre. The elongation at break of PBAT/TPS/SB composites decreased with increasing SB weight percentage due to reduced chain mobility and increased film's brittleness. Increasing the fibre fraction in the composites will decrease the amount of available PBAT for elongation and thus lead to the brittle composite film. Furthermore, the effects of silane surface treatment are more notable when 5% of SBT powder is incorporated in PBAT/TPS matrix with an improvement about 15% in tensile strength and elongation at break. This infers that the fibres had enhanced their stress transfer ability due to better interfacial bonding between the hydrophilic fibres, silane coupling agent, and hydrophobic matrix, which can be observed by SEM image in Figure 2(d). However, after the

addition of SB and SBT powder with 5% to 15% loading, there are not huge means differences in tensile strength and elongation at break with a range of 13.4 to 9.11 MPa and 739.49 to 509.68%, respectively. However, composite with 20% fibre loading shows a remarkable reduction in fibre's flexibility and strength as it drops to 55.83 and 64.41% and tensile strength of 8.25 and 8.79 MPa for both untreated and treated fibres, respectively, which might be attributed to the action of fibres acting as flaws at higher filler fraction (Chen et al., 2015). Composite with a higher amount of filler tends to agglomerate, and a limited amount of PBAT/TPS matrix to wrap the fibres has resulted in poor transmission of stress from matrix to fibre. In addition, lower tensile properties of composite with 20% SBT could be related to insufficient of GPTMS silane coupling agent to provide adequate reinforcement effect to the fibre matrix interface for higher filler concentrations.

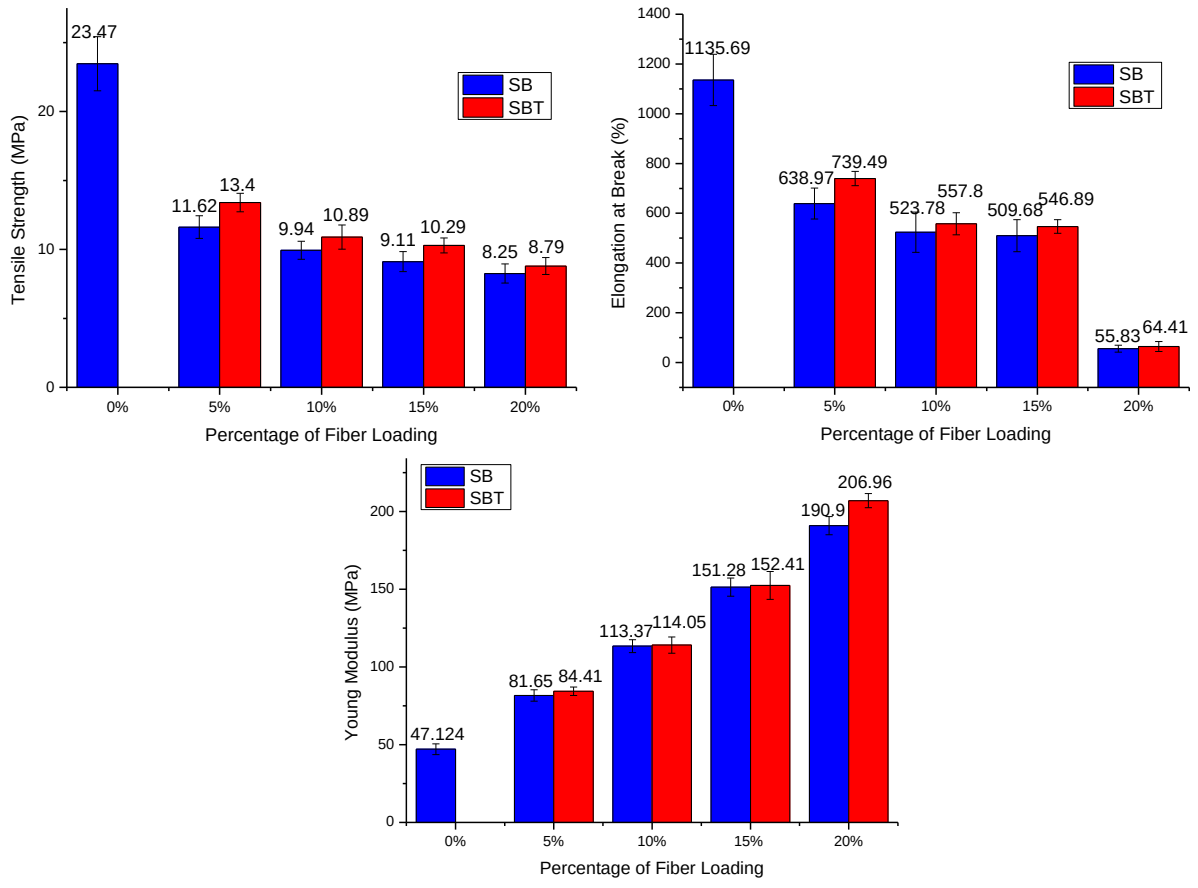

Figure 1. Tensile strength, elongation at break and Young modulus of PBAT/TPS (90/10) reinforced with 5, 10, 15, and 20% of fibre (SB=sugarcane bagasse without treatment; SBT= Treated sugarcane bagasse)

The graph also implies that the SB fibre act as filler function rather than reinforcement effect since the film strength and ductility decrease after SB addition. Nevertheless, the film's

toughness and stiffness are greatly enhanced from 47.12 to 216.86 MPa as specified as young modulus values with increasing fibre volume from 0% to 20%. The addition of SB fibres resulted in higher rigidity and hardness values of the composites compared to their matrix counterpart. It is because increasing SB fibre resulted in increasing of cellulose content which accounts for the stiffness property of the natural fibre. It can be seen that silane-treated SB filler had a slightly improvement in stiffness compared to untreated SB. This increment could be explained by the improved adhesion between cellulosic fibre and polymeric matrix due to the removal of the waxy and grassy layer from the SB fibre surface via alkaline treatment, as well as the reduced hydrophilicity via GPTMS silane treatment.

3.2 Morphological analysis

Figure 2 illustrates the SEM images of PBAT/TPS (90/10) blend, the highest (20%) and lowest (5%) loadings of composites. Figure 2 (b) and (e) show the distribution of SB fibre in PBAT/TPS matrix before starch particle removal. In contrast, Figure 2 (a), (c & d) and (f & g) are the enlarged images of composites corresponding to 0%, 5%, and 20%, respectively, after starch domain extraction, which well-distributed circles void can clearly observe in the PBAT matrix. Referring to the SEM images, the incorporation of SB fibres destroyed the surface integrity of the PBAT/TPS matrix. This could be related to the reduction of approximately half of the tensile strength and elongation at break of the composite compared to PBAT/TPS matrix. Moreover, increasing fibre contents lead to rougher and higher surface porosity, as can be correlated with stronger and enhanced film ductility of the composites with lower fibre contents than higher fibre contents.

From Figure 2 (b & c) and and (e & f), the fibre pull-out and fibre breakage in the composite samples without treatment can be seen. Furthermore, numerous gaps between the bagasse fibre and the PBAT/TPS matrix can be observed, indicating a poor interfacial adhesion between the fibre and matrix interfaces. Unlike untreated SB fibre, the surface structures of the treated SB fibre (Figure 2 (d) & (g)) displayed rougher surfaces with lesser spongy voids within the fibre. This is due to the removal of some of the hemicelluloses, lignin, pectin and wax components in bagasse fibre, which is favorable for reinforcement effect and water barrier property compared to untreated bagasse. On the other hand, the absence of fibre pull-out and reduction in gap present in the 5% SBT composites with surface modification by alkaline and silane coupling treatment in Figure 2(d) indicates better fibre-matrix affinity and good adhesion.

This is due to the fact that the addition of GPTMS can form a good siloxane network, resulting in a high tensile strength due to strong chemical interaction between the matrix and SB fibres via the presence of a cross-linked network of silane groups (Kane et al., 2016). Similar observations of silane-treated composites have been reported by Cordeiro et al. (2017) and Pereira da Silva et al. (2017), showing that GPTMS silane coupling agents improved the compatibility between the polymer matrix and fibre.

However, the appearance of a distinct debonding gap between bagasse fibre and matrix with fibre pull-out can be observed in composites with 20% SBT (Figure 2(g)). This might be due to inadequate silanization by GPTMS coupling agent to cover fibre's surface with organofunctional alkoxysilane molecules at a higher amount of fibre loading, which results in weak fibre and matrix interaction (Kane et al., 2016). The SEM image of 20% SBT agreed with the finding in tensile testing, which reveals that higher fibre volume causes significant decrement in tensile strength and elongation at break.

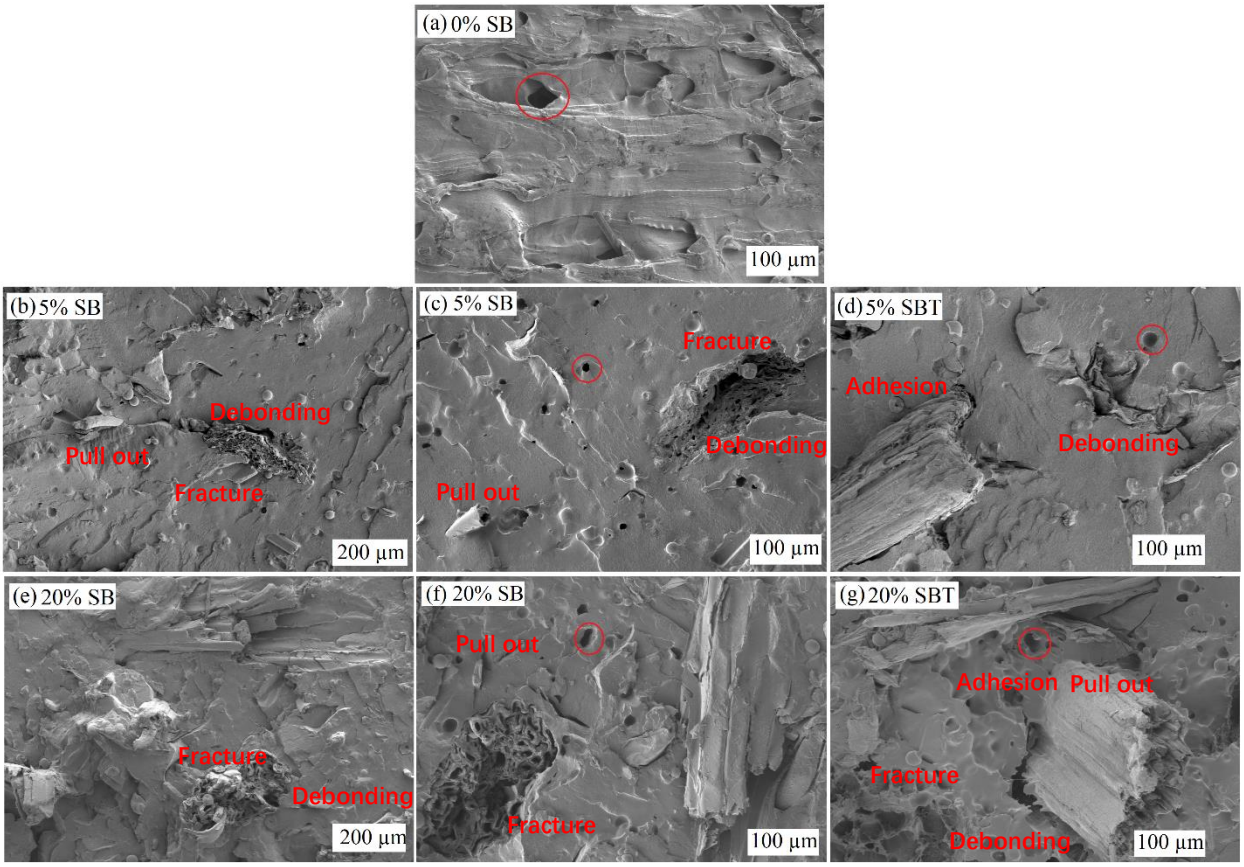

Figure 2. SEM images of PBAT/TPS (90/10) with treated and untreated SB.

3.4 TGA analysis

TGA was performed to investigate the film's limiting temperature and the influence of fibres treatment on the thermal stability of the composites. Figure 3 shows the TG and derivative thermograms (DTG) curves. From the graphs, it can be seen that there are two main zones of weight loss; one in the range of 280 to 360 °C and one between approximately 380 and 460 °C. Pure PBAT matrix is a thermally stable polymer that begins to degrade near 370 °C with high degradation rates at temperature 425 °C. Whereas PBAT/TPS (90/10) blend experienced two steps of decomposition at ~360 and 424.4 °C, representing the elimination of amylose and amylopectin components from starch, and PBAT, respectively. However, the peak at 50 – 250 °C, which indicates the glycerol and water elimination as specified by previous studies by González Seligra et al. (2016), Lendvai et al. (2017), and Liu et al. (2019) was not clearly observed in the TGA and DTG curves. This is probably due to the relatively small amount of glycerol (30%) in TPS fraction inside the PBAT/TPS (90/10) blend.

Furthermore, the weight losses at 400 °C of the pure PBAT, PBAT/TPS (90/10), and composite films with 5 and 20% treated and untreated fibres were about 95.9, 93, 81.1, 80.4, 80.3 and 73.8 %, respectively. This infers that the addition of TPS and fibres had reduced the degradation ability of the PBAT/TPS films, which were conducive to light and thermal degradation. From the TGA and DTG graphs also can be seen that upon addition of SB and SBT fibres, the sample experienced significant weight loss at 280 to 350 °C, which implies the degradation of hemicellulose and pectin, while weight loss occurred at 300 to 500 °C correspond to lignin and cellulose overlapped with PBAT decomposition event (Cardoso et al., 2018). The decreased thermal decomposition of the composites could be explained by the lower decomposition temperatures of these components compared to the matrix. Similar patterns were observed in other natural fibres such as those of SB (Vera, 2019), peach palm trees (Cordeiro et al., 2017), cotton fibre (Calabia et al., 2013), and rice husk flour (Chen et al., 2015).

Moreover, the functionalization of the fibres with GPTMS resulted in a slight shift of the main decomposition peak at 420 °C towards higher temperatures, indicating some improvement in thermal stability. This is might due to the formation of a refractory siloxane network after silanization (Kane et al., 2016). Finally, it is essential to note that the TGA results indicate that both PBAT/TPS blend and composite films are thermally stable up to temperatures around 280 °C which is compatible for packaging and agricultural mulching film application.

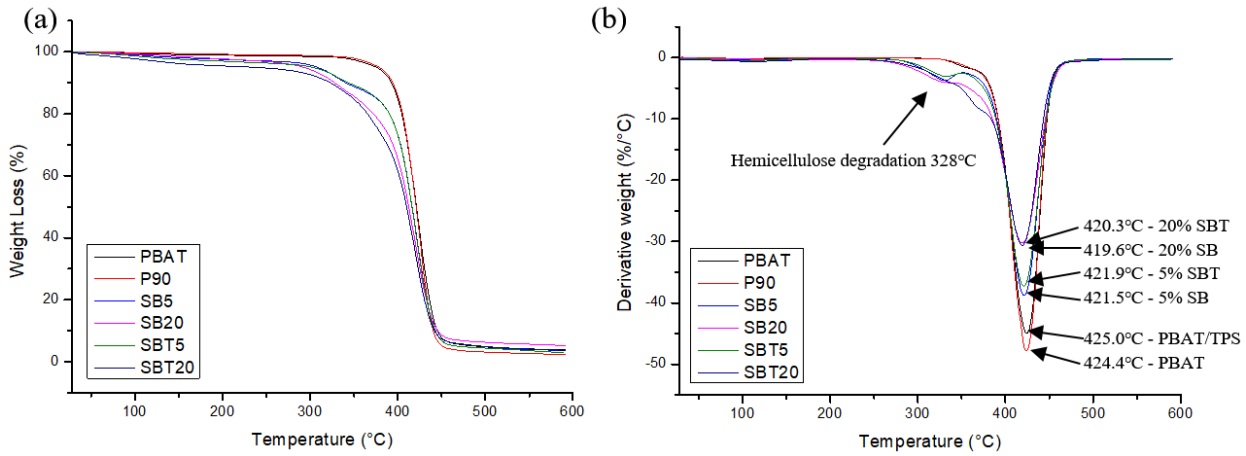

Figure 3. (a) TGA and (b) DTG of treated and untreated PBAT/TPS/SB composites.

3.5 Fourier transform infrared analysis

Figure 4 compares the FTIR spectra of 5% of untreated (SB) and treated bagasse (SBT). The spectra of both composites exhibit the main characteristic peaks at 2954 and 2850 cm-1, corresponding to asymmetric and symmetric C-H stretching of the methylene (-CH_2-) group, respectively. Peaks at 1712, 900, and 700 cm^{-1} were associated with stretching of the ester carbonyl group (C=O), bending peaks of benzene substitute, and adjacent of methylene group (-CH_2-) of PBAT, respectively. Whereas, the broad band at 3200 to 4000 cm^{-1} and the peaks between 1000 to 1200cm^{-1} are due to stretching of OH groups and C-O-C stretching present in the anhydroglucose ring from TPS and SB component.

From the spectrum, it can be seen that the change in peak at 3417cm^{-1} corresponds to the hydroxyl group from TPS component and cellulose in SB filler. The intensity of the peak increase with SBT than SB fibre indicating most of the –OH groups of the cellulose formed bonds with the silanol end group of the hydrolyzed silane. Furthermore, a tiny shoulder peak at 1120 cm-1 may indicate the presence of glycidylpropyl silane group in the treated SB composites. The shoulder peak's low intensity is due to the small amount of diluted GPTMS used in the SB silanization process. Similar observations also were found by Cordeiro et al. (2017), Kane et al. (2016) and Lule & Kim (2021) with GPTMS-treated peach palm tree, chitosan, and coffee husk fibres, respectively. The effect of alkaline treatment can be observed by the peak weakened at 1730 and 1258 cm^{-1} of film with SBT fibre indicating partial vanishment of pectin and waxes, and hemicellulose and lignin, respectively, as previously noted by Fiorentini et al. (2022), Rout et al. (2016) and Suwan et al. (2022). This result is supported by the appearance of a rough surface of SBT fibre from the SEM images due to the

removal of waxes, hemicellulose, and lignin.

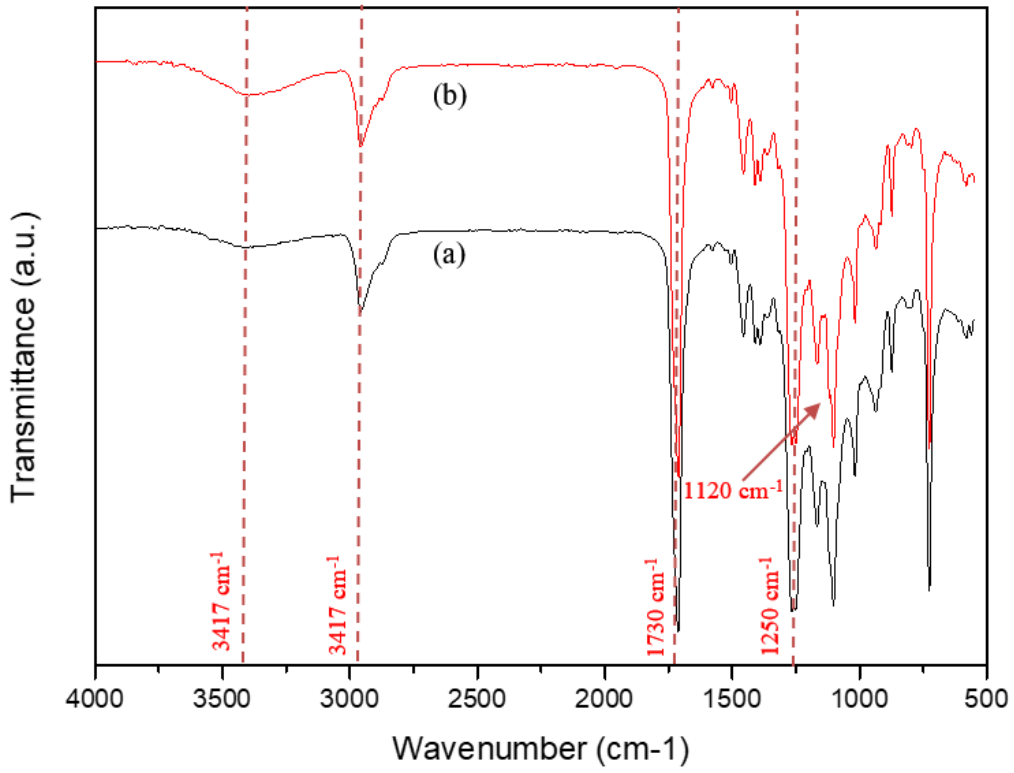

Figure 4. FTIR spectra of PBAT/TPS with (a) SB and (b) SBT fibre

3.6 Water absorption

Figure 4 shows the water absorption rate of the composites. The graph shows that all film absorbed less than 8% of water after 72 hrs of testing, indicating good water barrier property. This is because of the large percentage of PBAT content in PBAT/TPS blend (90%) which has hydrophobic characteristics wrapped in the TPS and fibre particles, which are both hydrophilic. In addition, PBAT/TPS (90/10) exhibited the lowest water absorption rate, and increased fibre contents led to a higher water absorption rate. This is due to the SB fibre surface containing many hydrophilic groups, which easily absorb moisture during the testing and cause swelling. Low barrier property of PBAT to water vapor also promotes this process.

Furthermore, the water swelling of plasticized starch particles can cause surface damage to composite materials, making it easier for water to penetrate and be absorbed by the TPS particles inside the material. As a result, increasing the fibre contents resulted in more obvious penetration and increased water absorption of the composite. Ayu et al. (2020) and Mohd Hafidz et al. (2021) also obtained similar findings upon increasing fibre loading in PBS/TPS, polyester, composites.

Moreover, it also can be observed that composites with alkaline and silane surface treatment by GPTMS had enhanced the water barrier properties of the films since the water absorption rate significantly decreased after surface treatment. Surface modification by silanization with hydrophobic moieties leads to improved adhesion of fibre surface to the matrix and causes less water absorbed. This result indicates that the silanization process reduces water absorption of the fibres and may give resistance against fungal decay. Furthermore, delignification by alkaline treatment also contributes to less water absorption since lignin has an amorphous structure and is more susceptible to water absorption (Benini et al., 2011).

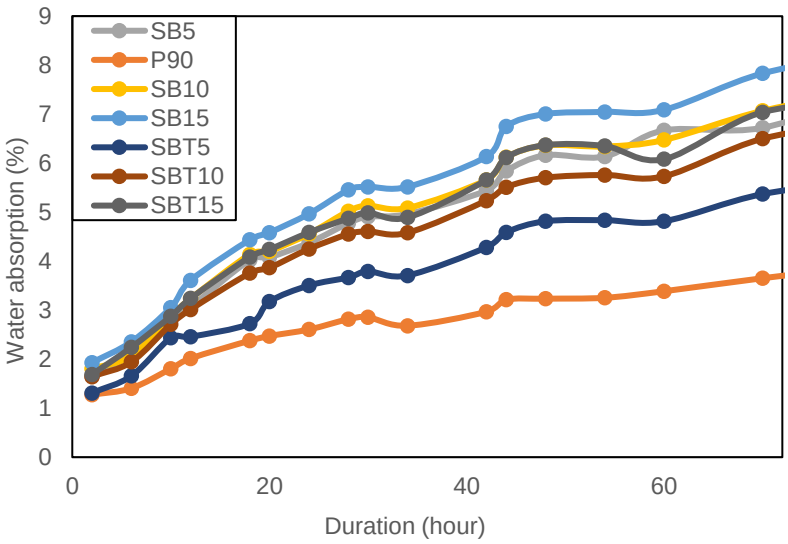

Figure 4. Water absorption rate of PBAT/TPS blend and composites.

3.7 Contact angle (CA)

Surface hydrophobicity was determined by measuring the CA of water droplets. Table 1 summarizes CA of PBAT/TPS blend and composites. PBAT/TPS (90/10) exhibits the highest CA with 92.4° followed by SB5, SB10, SB15, and SB20. Dispersion of hydrophilic SB fibres was expected to decrease CA due to increased surface hydrophilicity. Furthermore, the incorporation of fibre created rougher film's surface and corresponding reduced surface energy, leading to lower CA than matrix (Wongphan et al., 2022). As expected, treated SB (SBT) fibre has improved surface hydrophobicity as the CA value is higher than untreated SB. This is due to reduced cavities between fibre surface and matrix by hydrophobic silane surface modification, creating more homogenous fibre-matrix interface and enhancing surface hydrophobicity.

Table 1. Contact angle of PBAT/TPS blend and composites

Sample	Average contact angle	
	SB	SBT
0%	92.38 ± 3.9	
5%	77.94 ± 3.5	80.46 ± 4.6
10%	74.72 ± 7.3	77.67 ± 2.1
15%	72.22 ± 6.2	73.83 ± 3.6
20%	71.10 ± 2.4	72.20 ± 3

Conclusion

In conclusion, the presented PBAT/TPS/SB composites with 5 to 15% SB fibre loadings shows adequate tensile properties (9 to 13.4 MPa), higher thermal stability (up to 280 °C), good water barrier property (less than 8% water absorption after 72 hrs) and hydrophobicity property. Furthermore, alkaline and GPTMS silane treatments had increased SB composite's tensile strength and flexibility about 6 to 15% compared to untreated SB. The effect of silane and alkaline surface treatment by GPTMS coupling agent and NaOH can be seen in the increase in fibre surface roughness and the reduction in fibre-matrix gap in SEM image for 5% SBT, indicating better interfacial adhesion than without treatment. However, at a higher bagasse filler fraction (20%), weak coupling effect can be observed, probably due to insufficient coupling agent to fully cover the surface of the fibre. Moreover, the fibres had tendency to agglomerate leading to poor wetting of hydrophilic SB filler by hydrophobic matrix.

Acknowledgement

The authors grateful to the Universiti Sains Malaysia (Research University Grant No. 8014044) for the financial support and University Malaysia Perlis (UniMAP) for the scholarship granted to the first author. We would also like to thank Universiti Sains Malaysia (USM) and School of Materials and Mineral Resources Engineering for the use of their facilities.

References

Ayu, R. S., Khalina, A., Harmaen, A. S., Zaman, K., Isma, T., Liu, Q., Ilyas, R. A., & Lee, C. H. (2020). Characterization Study of Empty Fruit Bunch (EFB) Fibers Reinforcement in Poly(Butylene) Succinate (PBS)/Starch/Glycerol Composite Sheet. *Polymers*, *12*(7), 1571. https://doi.org/10.3390/polym12071571

Benini, K. C. C. C., Voorwald, H. J. C., Cioffi, M. O. H., & Al, E. (2011). Mechanical properties of

HIPS/sugarcane bagasse fiber composites after accelerated weathering. *Procedia Engineering*, *10*(December), 3246–3251. https://doi.org/10.1016/j.proeng.2011.04.536

Binti Mohd Hafidz, N. S., Bin Mohamed Rehan, M. S., & Binti Mokhtar, H. (2021). Effect of alkaline treatment on water absorption and thickness swelling of natural fibre reinforced unsaturated polyester composites. *Materials Today: Proceedings*, *48*, 720–727. https://doi.org/10.1016/j.matpr.2021.02.209

Calabia, B. P., Ninomiya, F., Yagi, H., Oishi, A., Taguchi, K., Kunioka, M., & Funabashi, M. (2013). Biodegradable poly(butylene succinate) composites reinforced by cotton fiber with silane coupling agent. In *Polymers* (Vol. 5, Issue 1, pp. 128–141). https://doi.org/10.3390/polym5010128

Cardoso, M. A. P., Carvalho, G. M., Yamashita, F., Mali, S., Eiras, D., Demiate, I. M., & Grossmann, M. V. E. (2018). Oat hull fibers bleached by reactive extrusion with alkaline hydrogen peroxide in thermoplastic starch/poly(butylene adipate-co-terephthalate) composites. *Polymer Composites*, *39*(6), 1950–1958. https://doi.org/10.1002/pc.24151

Chen, R. S., Ab Ghani, M. H., Ahmad, S., Salleh, M. N., & Tarawneh, M. A. (2015). Rice husk flour biocomposites based on recycled high-density polyethylene/polyethylene terephthalate blend: Effect of high filler loading on physical, mechanical and thermal properties. *Journal of Composite Materials*, *49*(10), 1241–1253. https://doi.org/10.1177/0021998314533361

Cordeiro, E. P., Pita, V. J. R. R., & Soares, B. G. (2017). Epoxy–Fiber of Peach Palm Trees Composites: The Effect of Composition and Fiber Modification on Mechanical and Dynamic Mechanical Properties. *Journal of Polymers and the Environment*, *25*(3), 913–924. https://doi.org/10.1007/s10924-016-0841-0

De Moura, C. V. R., Da Cruz Sousa, D., De Moura, E. M., De Araújo, E. C. E., & Sittolin, I. M. (2021). New biodegradable composites from starch and fibers of the babassu coconut. *Polimeros*, *31*(1). https://doi.org/10.1590/0104-1428.09519

Fiorentini, C., Bassani, A., Duserm Garrido, G., Merino, D., Perotto, G., Athanassiou, A., Peräntie, J., Halonen, N., & Spigno, G. (2022). High-pressure autohydrolysis process of wheat straw for cellulose recovery and subsequent use in PBAT composites preparation. *Biocatalysis and Agricultural Biotechnology*, *39*(January). https://doi.org/10.1016/j.bcab.2022.102282

González Seligra, P., Eloy Moura, L., Famá, L., Druzian, J. I., & Goyanes, S. (2016). Influence of incorporation of starch nanoparticles in PBAT/TPS composite films. *Polymer International*, *65*(8), 938–945. https://doi.org/10.1002/pi.5127

Jamali, V. P., Sudagar, I., Author, C., Sudha, P., Boomiraj, K., & Naik, R. (2021). Influence of sugarcane

bagasse fibres from the rind and pith on selected properties of bio-composite material. ~ *2417 ~ The Pharma Innovation Journal*, *10*(10), 2417–2422. http://www.thepharmajournal.com

Kane, S. N., Mishra, A., & Dutta, A. K. (2016). Preface: International Conference on Recent Trends in Physics (ICRTP 2016). *Journal of Physics: Conference Series*, *755*(1). https://doi.org/10.1088/1742-6596/755/1/011001

Lee, S. C., & Mariatti, M. (2008). *The effect of bagasse fibers obtained (from rind and pith component) on the properties of unsaturated polyester composites*. *62*, 2253–2256. https://doi.org/10.1016/j.matlet.2007.11.097

Lendvai, L., Apostolov, A., & Karger-Kocsis, J. (2017). Characterization of layered silicate-reinforced blends of thermoplastic starch (TPS) and poly(butylene adipate-co-terephthalate). *Carbohydrate Polymers*, *173*, 566–572. https://doi.org/10.1016/j.carbpol.2017.05.100

Liu, W., Liu, S., Wang, Z., Dai, B., Liu, J., Chen, Y., Zeng, G., He, Y., Liu, Y., & Liu, R. (2019). Preparation and characterization of reinforced starch-based composites with compatibilizer by simple extrusion. *Carbohydrate Polymers*, *223*(January), 115122. https://doi.org/10.1016/j.carbpol.2019.115122

Lule, Z. C., & Kim, J. (2021). Properties of economical and eco-friendly polybutylene adipate terephthalate composites loaded with surface treated coffee husk. *Composites Part A*, *140*(October 2020), 106154. https://doi.org/10.1016/j.compositesa.2020.106154

Nunes, M. A. B. S., Marinho, V. A. D., Falcão, G. A. M., Canedo, E. L., Bardi, M. A. G., & Carvalho, L. H. (2018). Rheological, mechanical and morphological properties of poly(butylene adipate-co-terephthalate)/thermoplastic starch blends and its biocomposite with babassu mesocarp. *Polymer Testing*, *70*(June), 281–288. https://doi.org/10.1016/j.polymertesting.2018.07.009

Pereira da Silva, J. S., Farias da Silva, J. M., Soares, B. G., & Livi, S. (2017). Fully biodegradable composites based on poly(butylene adipate-co-terephthalate)/peach palm trees fiber. *Composites Part B: Engineering*, *129*, 117–123. https://doi.org/10.1016/j.compositesb.2017.07.088

Ramlee, N. A., Jawaid, M., Zainudin, E. S., & Yamani, S. A. K. (2019). Tensile, physical and morphological properties of oil palm empty fruit bunch/sugarcane bagasse fibre reinforced phenolic hybrid composites. *Journal of Materials Research and Technology*, *8*(4), 3466–3474. https://doi.org/10.1016/j.jmrt.2019.06.016

Reddy, N., & Yang, Y. (n.d.). *NarendraaReddyy· YiqiiYang Innovative Bioo bers from Renewable Resources*.

Rout, A. K., Kar, J., Jesthi, D. K., & Sutar, A. K. (2016). Effect of surface treatment on the physical, chemical, and mechanical properties of palm tree leaf stalk fibers. *BioResources*, *11*(2), 4432–4445.

https://doi.org/10.15376/biores.11.2.4432-4445

Suwan, T., Maichin, P., Fan, M., Jitsangiam, P., Tangchirapat, W., & Chindaprasirt, P. (2022). Influence of alkalinity on self-treatment process of natural fiber and properties of its geopolymeric composites. *Construction and Building Materials*, *316*(November 2021), 125817. https://doi.org/10.1016/j.conbuildmat.2021.125817

Vera, F. L. (2019). Characterizations of Some Composite Materials. *Characterizations of Some Composite Materials*, *February*. https://doi.org/10.5772/intechopen.73357

Wirawan, R., Sapuan, S. M., Abdan, K., & Yunus, R. (2011). Tensile and impact properties of sugarcane bagasse/poly (vinyl chloride) composites. *Key Engineering Materials*, *471–472*, 167–172. https://doi.org/10.4028/www.scientific.net/KEM.471-472.167

Wongphan, P., Panrong, T., & Harnkarnsujarit, N. (2022). Effect of different modified starches on physical, morphological, thermomechanical, barrier and biodegradation properties of cassava starch and polybutylene adipate terephthalate blend film. *Food Packaging and Shelf Life*, *32*(March), 100844. https://doi.org/10.1016/j.fpsl.2022.100844

Yap, S. Y., Sreekantan, S., Hassan, M., Sudesh, K., & Ong, M. T. (2020). Characterization and Biodegradability of Rice Husk-Filled Polymer Composites. *Polymers*, *13*(1), 104. https://doi.org/10.3390/polym13010104

Yokesahachart, C., Yoksan, R., Khanoonkon, N., Mohanty, A. K., & Misra, M. (2021). Effect of jute fibers on morphological characteristics and properties of thermoplastic starch/biodegradable polyester blend. *Cellulose*, *28*(9), 5513–5530. https://doi.org/10.1007/s10570-021-03921-8

A Multi-Point Perturbation Expansion Method for Generating Random Fiber Distributions for Composite

Li Yinsong, Yang Junchao, Chai Yanan

(Aircraft Strength Research Institute of China, Xi'an)

Abstract: In order to generate the representative volume element (RVE) of composite with the random distribution of fibers, a new method named multi-point perturbation expansion (MPE) algorithm is proposed based on the perturbation algorithm and the random sequential expansion (RSE) algorithm. The algorithm overcomes the jamming limitation when generating models with fiber volume fraction greater than 60%, and also ameliorate the issue of resin-rich zone which is easily caused by the RSE algorithm.A spatial fiber distribution considering different fibers' radius is established and four statistical characteristics are analyzed. The result shows that the method proposed in this paper can effectively generate a micro-model of fiber reinforced composite with random spatial distribution of fibers.

Keyword: A.Fiber Reinforced Composite, B.Random fiber distribution, C.Statistic Characterisation.

1. Introduction

Fiber-reinforced composite laminates are widely used in the aerospace field due to their excellent properties of high specific strength and stiffness.Experimental Study on basic mechanical properties costs a lot of time and money. The numerical simulation method of composites based on micromechanics has become an important method for composite analysis[1-5], which predicts the elastic properties by averaging methods.

Researchers have proposed algorithms for generating random fiber distribution. Melro[6]'s method created model with high fiber volume fraction by moving the new fiber to the nearest neighbouring fiber. Yang [7] proposed the Random Sequential Expansion (RSE) method by generating fibers around the central fiber until the last one. Yang[8] generated a discrete fiber distribution by simulating collisions between rigid spheres, but the method cannot guarantee the periodic boundary condition.

In this paper, a multi-point perturbation expansion (MPE) method is proposed based on random perturbation algorithm and RSE method. Four statistic characterisations are analyzed on the generated microstructures and compared to experimental samples and other methods.

2. Multi-point perturbation expansion method

The perturbation method is based on a regular distribution of fiber, and a random amount of displacement perturbation is applied to each fiber to generate a fiber random distribution. The perturbation range of fibers depends on the size of the fiber volume content.The random perturbation method is efficient when generating model with low fiber volume fraction, but the jamming limit problem occur when the fiber volume fraction is over 60% and success rate of model generation is reduced. The literature [4] proposed a uniform back-off method for overlapping fibers, which reduces the probability of overlap between fibers and improves the generation efficiency of the perturbation method.

The basic idea of the RSE method[7] is to gradually expand the fibers from the center of the model to the edges until a predetermined fiber volume fraction is reached. This algorithm needs to set the appropriate control parameters l_{min} and l_{max} to determine the distance between fibers.If the value of l_{min} and l_{max} is small, the generated model tends to form "central aggregation" and "resin-rich zone" at the four corner of the RVE model, as shown in Figure 1.

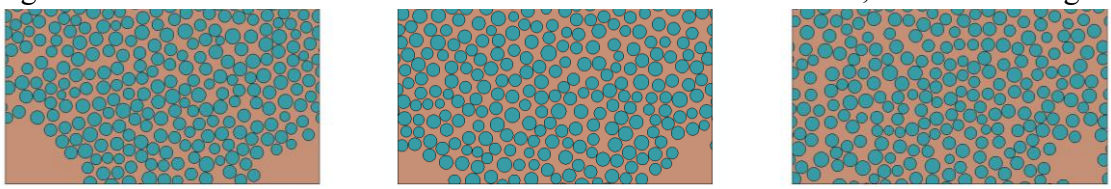

(a) $l_{\max} / \bar{R} = 0.761$ (a) $l_{\max} / \bar{R} = 1.166$ (a) $l_{\max} / \bar{R} = 1.977$

Fig 1 RVE created by RSE method with different l_{max}.

Based on above two methods, the MPE method is established and the flow chart of this algorithm is shown in Figure 2.

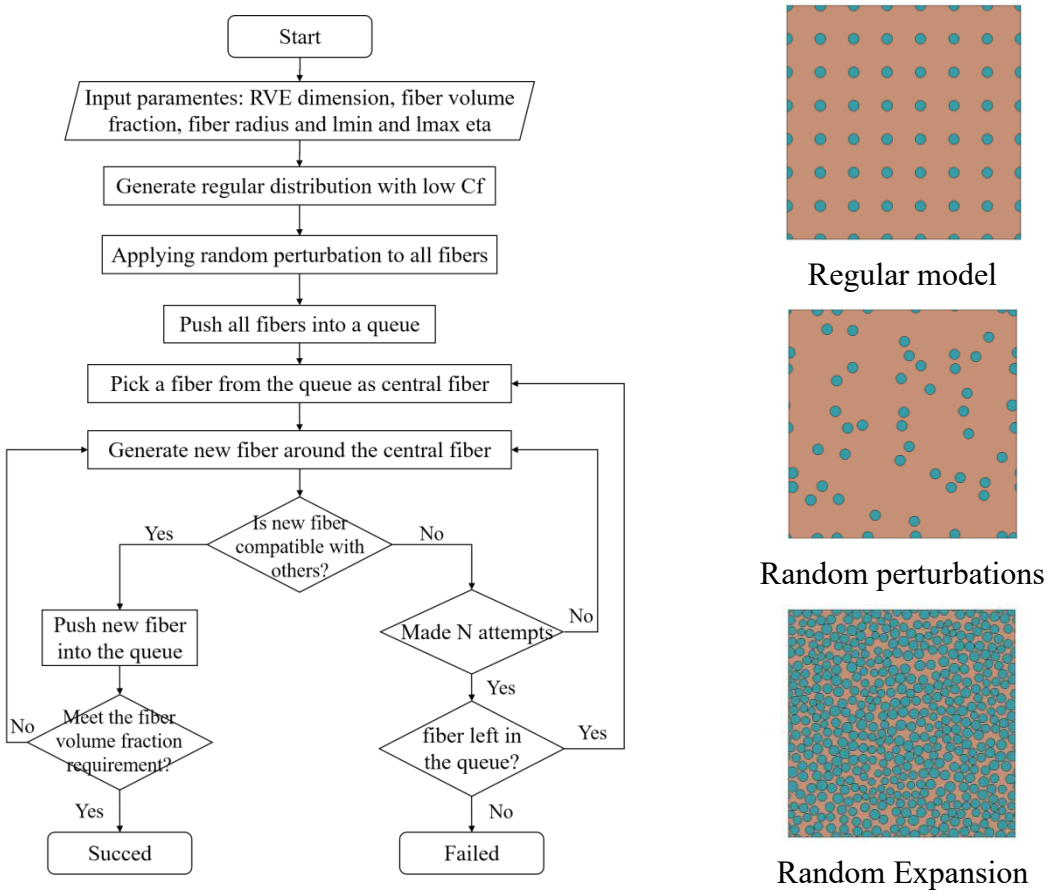

Fig 2 Flow chart of multi-point perturbation expansion method

Step 1. Generate a base model for regular distribution of fibers with low fiber volume fraction.

Step 2. Randomly select fibers for perturbation. The distribution parameter γ determines the degree of disruption of the regular model. Figure 3 shows the fiber distribution with different γ value when the fiber volume fraction c_f=40%.

(a) γ=0.3 (b) γ=0.6 (c) γ=1.0

Fig 3 Fiber distribution with different γ value

Step 3. Check for compatibility between new fibers and other fibers. For the perturbed fiber's coordinates (x_k, y_k) and other fibers' coordinate (x_i, y_i), check whether the following equation is satisfied.

$$\begin{cases} (x_k - x_i)^2 + (y_k - y_i)^2 \geq R_k + R_i + l_{\min} & i = 1,2,\mathrm{K}\ n; i \neq k \\ -R_k < x_k, y_k < W + R_k \end{cases} \tag{1}$$

where R_k and R_i is the radius of two checked fibers. If the disturbed fibers are incompatible with other fibers, regenerate new fiber until compatible. When all fibers in the regular

distribution model is disturbed, push them all into a queue.

Step 4. Pick a fiber from the queue as central fiber, generate new fibers around it according to the RSE method. New fiber's coordinate is defined by the distance ρ and angle θ. The distance ρ satisfies a specific distribution on $[R_1+R_2+l_{min}, R_1+R_2+l_{max}]$ and the angle θ satisfies a uniform distribution on $[0, 2\pi]$.R_1 and R_2 is the radius of two fibers, l_{min} / l_{max} is the minimum/maximum distance between two fibers. In this paper, l_{min} is set to $0.05R$ and l_{max} is calculated by following equation:

$$l_{\max} = \left(2\left(\sqrt{\frac{\pi}{v_f}} - 2 \right) \bar{R} - l_{\min} \right) \tag{2}$$

Step 5. Repeat step 4 until no new fibers can be generated around the central fiber. Each time a new fiber is generated, it is checked whether the new fiber is compatible with the existing fibers, and the fibers that meet the compatibility are added to the model. At the same time, the fibers located on the boundary is added to the corresponding edge respectively to meet the geometric periodicity requirement. After each addition of fibers, check whether the current fiber volume fraction meets the requirement. If so, jump out of the loop and the model is generated successfully.

3. Statistic characterisation

Five models are generated by the MPE method with the input variables: RVE dimension $W=H=165.0\mu m$, fibers' radius obey a normal distribution with a mean value $\bar{R} = 0.33\mu m$ and a stander deviation $std = 0.3106$, and parameters $\gamma = 0.8$, $l_{\min} / \bar{R} = 0.05$, $l_{\max} / \bar{R} = 0.4112$. Four statistic descriptors of the generated spatial fiber distribution are discussed to verify the validity of the proposed algorithm.

3.1. Voronoi diagram

A Voronoi diagram is a division diagram that divides a region into subregions based on a set of feature points in the plane. Based on the Voronoi diagram of the generated model, the variation coefficient of the area of the Voronoi polygon ρ_A and the variation coefficient ρ_D of the distance between fibers can be calculated. Obviously, the Voronoi polygon area and the average distance of adjacent fibers are a constants for regular distribution model without considering the boundary effects.

Table 1 Variation coefficient ρ_A and ρ_D

ρ_A	ρ_D

56%	MPE	0.2026	0.139
	RSE	0.2542	0.136
60%	MPE	0.184	0.133
	RSE	0.180	0.130

Table 1 shows that two variation coefficients ρ_A and ρ_D for two method are close, where the value of ρ_A is even smaller for MPE. It can be tentatively shown that the MPE method generates more "homogeneous" models than the RSE method at lower fiber volume fraction.

3.2. **Nearest neighbour distances**

The nearest fiber distance distribution function is a probability density function of the distance from point to its neighboring points. Figures 4 and 5 show the probability density distributions of the nearest distance and the second nearest distance for the model generated by RSE, MPE method and test value, respectively, the error lines represent the range of the calculated results for each single model.

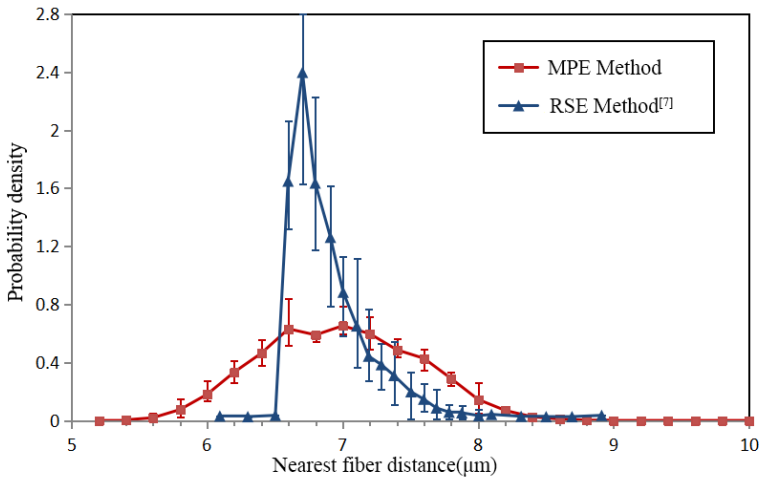

Fig 4 The nearest fiber distance distribution function

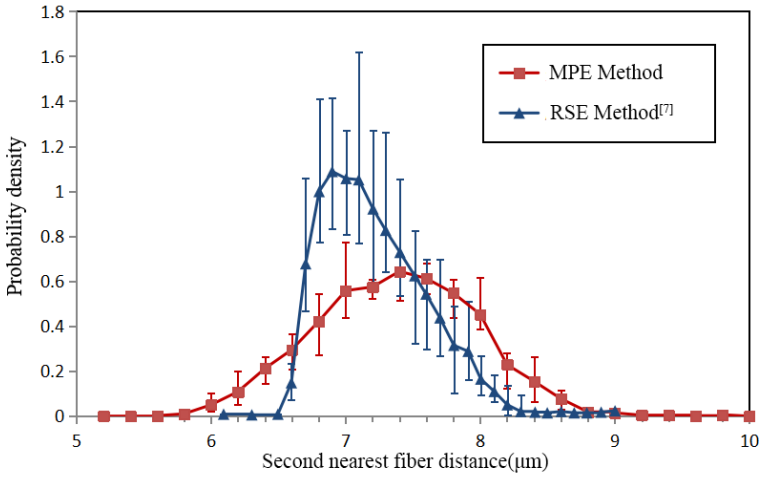

Fig 5 The second nearest fiber distance distribution function

Both the nearest and second nearest fiber distance distribution function made by MPE method are more dispersed compared to RSE method and test data. The dispersion might be caused by the distribution of fibers' radius considered in MPE models.

3.3. **Nearest neighbour orientations**

The nearest fiber orientation is determined by the orientation of the undirected line connecting the given fiber with its nearest neighbour, which is is described by the cumulative distribution function. Figure 6 shows the cumulative probability distribution function of the nearest fiber orientation of the model generated by the MPE method and the Complete Spatial Randomness (CSR) distribution. As the angle increases from 0° to 360°, the cumulative probability increases linearly from 0 to 1, indicating that the probability of the nearest fibers appearing in each direction is the same. The model generated by MPE method is proved to be a spatial randomness distribution.

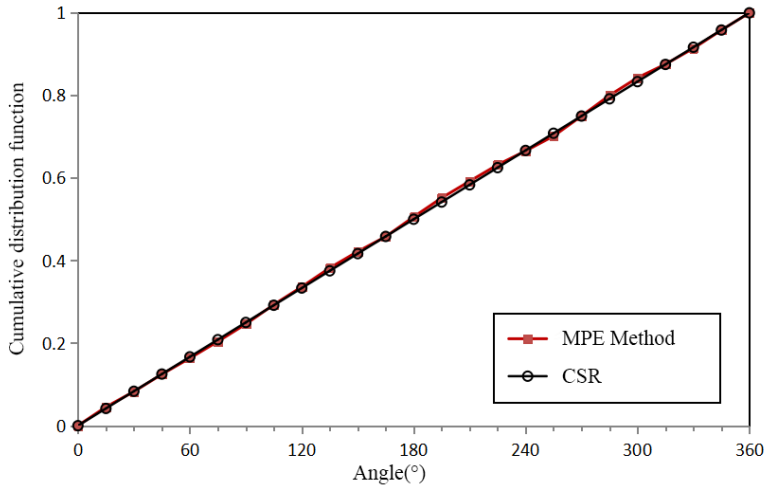

Fig 6 Nearest fiber orientation function

3.4. Second-order intensity function

The definition of second-order intensity function considering the boundary effect is shown below：

$$K(r)=\frac{A}{N^2}\sum_i\sum_{j\neq i}\frac{I\left(d_{ij}\leq r\right)}{w\left(l_i,l_j\right)} \tag{3}$$

Where A is the area of the RVE model, N is the number of fibers in the model, d_{ij} is the distance between fibers, I is an indicator function with the value 1 if the expression in the brackets is true and 0 otherwise, $w(l_i, l_j)$ is a weight function having the value 1 if the circle with centre at point i and passing by point j is completely inside the window. Otherwise, $w(l_i, l_j)$ is the ratio of the circumference contained within the window to the whole circumference of the circle.

Figure 8 shows the second-order intensity function of the model generated by MPE method. It can be seen that those points are basically located in the theoretical curve of CSR, illustrating the fiber pattern generated by MPE conforms well to a random distribution.

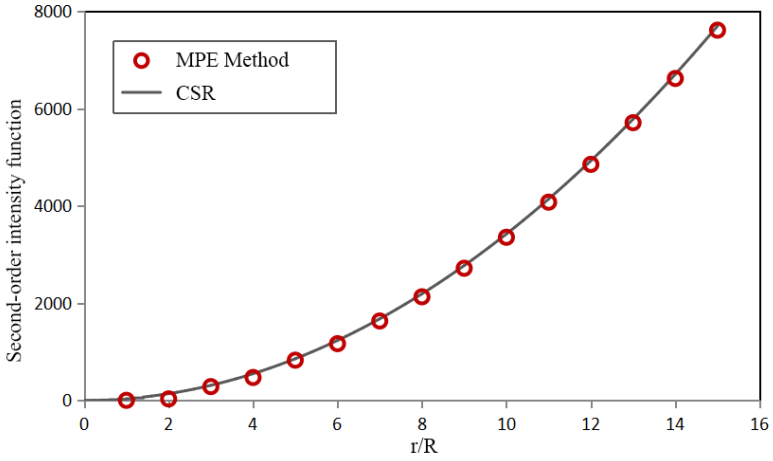

Fig 7 Second-order intensity function

4. Conclusion

Based on the random perturbation method and RSE method, a multi-point perturbation expansion method which takes into account the different fiber radius is proposed. New method avoids the jamming limitation problem and improves the success rate of RSE algorithm when the inter-fiber distance parameter is too large and the fiber aggregation problem when the parameter is too small. Four statistic characterisations are analyzed, and it's found that the fiber pattern generated by MPE fits well with the random distribution.

References

[1] Predicting Macroscopic Effective Elastic Moduli of Composites by Micro-mechanics FEM[J]. Gas Turbine Experiment and Research, 2003(03): 11-15.

[2] Liu Wanlei, Chang Xinlong, Zhang Xiaojun, eta. Analysis of Composite Transverse Mechanical Properties Based on Micromechanical Finite Element[J]. Journal of Materials Engineering, 2016, 44(11): 107–113.

[3] Peng Pai, Zhao Meiying, Wang Wenzhi. Transverse Strength Prediction of Composite Materials Via Micromechanics Model[J]. Mechanical Science and Technology for Aerospace Engineering, 2017, 36(10): 1611–1618.

[4] Peng Pai, Lu Jian. The Prediction of Composites' Elastic Constants on the Base of Fiber-Random-Distribution Model[J]. Composites Science and Engineering, 2021(03): 27–32.

[5] Wan Xiaopeng, Yang Guangmeng, Zhao Meiying. Influence of Fiber Distribution and Interfacial Strength on Transverse Compressive Strength of Unidirectional Composites[J]. Journal of Northwestern Polytechnical University, 2019, 37(03): 443–448.

[6] Melro A R, Camanho P P, Pinho S T. Generation of Random Distribution of Fibres in Long-Fibre Reinforced Composites[J]. Composites Science and Technology, 2008, 68(9): 2092–2102.

[7] Yang L, Yan Y, Ran Z, eta. A New Method for Generating Random Fibre Distributions for Fibre Reinforced Composites[J]. Composites Science and Technology, 2013, 76: 14–20.

[8] Yang Zhong. Study on Prediction of Mechanical Performance for Unidirectional Composite Considering Interphase[D]. Harbin Institute of Technology, 2010.

[9] Park S M, Lim J H, Seong M R, eta. Efficient Generator of Random Fiber Distribution with Diverse Volume Fractions by Random Fiber Removal[J]. Composites Part B: Engineering, 2019, 167: 302–316.

[10] Ismail Y, Yang D, Ye J. Discrete Element Method for Generating Random Fibre Distributions in Micromechanical Models of Fibre Reinforced Composite Laminates[J]. Composites Part B: Engineering, 2016, 90: 485–492.

[11] VaughanT J, Mccarthy C T. A Combined Experimental–Numerical Approach for Generating Statistically Equivalent Fibre Distributions for High Strength Laminated Composite Materials[J]. Composites Science and Technology, 2010, 70(2): 291–297.

[12] Soden P, Hinton M, Kaddour A. A Lamina properties lay-up configuration and loading conditions for a range of fibre-reinforced composites laminates[J]. Compos Sci Technol 1988; 58(7): 1225-1254

Microstructural evolution of Y2O3p/Mg-Zn-Gd-Zr composites during hot compression

X.H. Li [a, b], *H. Yan* [c, a, 1], *Y.P. Wang* [a, b], *R.S. Chen* [a, 2]

a. Shi-changxu Innovation Center for Advanced Materials, Institute of Metal Research, Chinese Academy of Sciences, 72 Wenhua Road, Shenyang 110016, China

b. School of Materials Science and Engineering, University of Science and Technology of China, 72 Wenhua Road, Shenyang 110016, China

c. School of Materials Science and Engineering, Shandong University of Science and Technology, Qingdao, Shandong 266590, China

Abstract:6%Y_2O_{3p}/Mg-Zn-Gd-Zr composites fabricated by stir casting were hot compressed and the microstructural evolution of the composites were systematically studied. With increasing temperatures or decreasing strain rates, the dynamic recrystallized (DRXed) grains increased while the twins decreased. At the same time, the basal textures were weakened due to the increase of dynamic recrystallized grains whose orientation was relatively random. In addition, the added micro-sized Y_2O_3 particles could promote dynamic recrystallization (DRX) due to particle stimulate nucleation (PSN) mechanism while the nano-sized precipitations in Mg-Zn-Gd alloy could retard the generation and growth of dynamic recrystallized grains due to Zener drag effect. Therefore, the DRX behavior was the synergistic effect of the micro-sized Y_2O_3 particles and nano-sized precipitations and the grain sizes of the composites could be refined efficiently. PSN mechanism and continuous DRX (CDRX) were the main DRX mechanism in the composites.

Keywords: Magnesium matrix composites; hot compression; microstructures; dynamic recrystallization

1. Introduction

As the lightest metal structural material, magnesium and its alloys can be widely used in aerospace, electronic communication, automobile transportation and other fields [1, 2]. However, the strength, modulus and wear resistance of magnesium alloys are relatively low, which limits their further applications. Adding ceramic particles to magnesium alloys to

[1] Corresponding author: H. Yan, E-mail: hyan@imr.ac.cn
[2] Corresponding author: R.S. Chen, E-mail: rschen@imr.ac.cn

fabricate particle reinforced magnesium matrix composites (PMMCs) can effectively overcome the above shortcomings of magnesium alloys [3]. In order to obtain better microstructure and mechanical properties, the PMMCs are usually processed by second hot deformation [4, 5]. Therefore, it's important to figure out the parameters that influence the microstructural and mechanical evolution during second hot deformation.

Due to simplicity and convenience, the hot compression has been used to studied the influences of parameters such as temperatures and strain rates on the microstructure of PMMCs [6, 7]. In SiC_p/AZ91 composites, the dislocations, twins and DRX of the matrix are deeply influenced by temperatures and strain rates [6]. The existence of particles in PMMCs can also influence the microstructural evolution. In SiC_p/AZ91 composites, the particle deformation zones, which are caused by mismatch between micron reinforcement and matrix during compression, are ideal sites to form DRX and this is PSN mechanism caused by micro-sized particles [7]. DRX has great influences on microstructure during compression. On the one hand, DRX mechanism of PMMCs were studied. In SiC_p/Mg-5Zn composites, the DRX mechanisms included CDRX, discontinuous DRX (DDRX), PSN and twinning DRX (TDRX) [8]. On the other hand, there are few studies on the effects of DRX on the slip of dislocations and texture evolution during compression in PMMCs. In our previous work [9], the microstructures and textures of rolled Y_2O_{3p}/Mg-Zn-Gd composites are studied. However, the effects of parameters such as temperatures, strain rates and strains on microstructural evolution of Y_2O_{3p}/Mg-Zn-Gd composites are still unclear.

Therefore, the 6%Y_2O_{3p}/Mg-Zn-Gd-Zr composites were hot compressed in this study. The influences of parameters on microstructural evolution of the compressed composites were studied and corresponding DRX mechanism was also discussed.

2. Experiments and methods

The actual chemical compositions of 6%Y_2O_{3p}/Mg-Zn-Gd-Zr composites were 6.21%Y_2O_{3p}/Mg-2.16Zn-0.45Gd-1.54Zr (wt%), which were prepared by stir casting. The diameter of Y_2O_3 particles was about 2 μm. The composites were homogenized at 480 ℃ for 14 h and then quenched in water. Cylindrical samples with a diameter of 10 mm and a height of 15 mm were cut from the homogenized composites. Isothermal uniaxial hot compression tests were carried out with temperatures from 350 ℃ to 450 ℃ and strain rates from 0.001 s^{-1} to 0.1 s^{-1}. The samples were quenched in water after hot compression to preserve the deformed

microstructures.

The optical microscopy (OM), scanning electron microscopy (SEM), electron back-scattering diffraction (EBSD) and transmission electron microscopy (TEM) were used to observe the microstructures at the central part of the plane of compression direction (CD) and radial direction (RD). X-ray diffraction (XRD) was used to analyze phases after homogenization. EBSD samples were mechanically and electrolytically polished, then analyzed by Hitachi Se3400 SEM equipped with an HKL-EBSD system operating at 20 kV. The discs for TEM were prepared by mechanical grinding and ion milling and then observed by FEI Talos F200X.

3. Results and discussion

3.1. Initial microstructure

Fig. 1 showed the microstructure of the casted and homogenized 6%Y_2O_{3p}/Mg-Zn-Gd-Zr composites. Fig. 1(a, b) showed that Y_2O_3 particles were not only distributed in the grains, but also at the grain boundaries while some Y_2O_3 particles formed clusters. Eutectic phases were distributed along grain boundaries, and these phases were mainly w ($Mg_3Zn_3Gd_2$) phases combined with Y_2O_3 particles [9]. The average grain size of casted composites was about 42 μm. After homogenization, the eutectic phases were significantly reduced, but a large number of nano-sized needle-like and ellipsoidal precipitations were formed in the grains as shown in Fig. 1(c-d). These precipitations should be precipitated at supersaturated region of alloying elements caused by segregation [10].

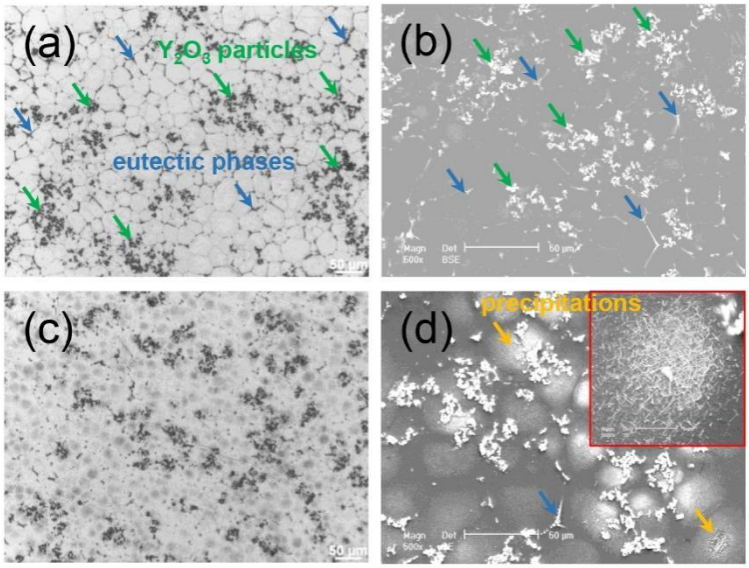

Fig. 1. The microstructure of the 6%Y_2O_{3p}/Mg-Zn-Gd-Zr composites. (a) OM, (b) SEM of casted composites; (c) OM, (d) SEM of homogenized composites.

3.2. Effect of compression temperatures and strain rates

Fig. 2 showed the optical microstructure evolution of the 6%Y_2O_{3p}/Mg-Zn-Gd-Zr composites compressed at a true strain about 0.7 but different temperatures and strain rates. When compressed at a low temperature and high strain rate such as 350 ℃ 0.1 s^{-1}, the composites showed a large number of twins in deformed grains. It could be inferred that the limited activation of dislocation slips could not effectively coordinate the deformation, therefore, the deformation was coordinated by twins at low compression temperature and high strain rate. Some fine recrystallized grains generated at grain boundaries or Y_2O_3 particles while twins gradually disappeared with increasing compression temperature or decreasing strain rate. In SiC_p/AZ91 composites, DRX preferentially generated near the particles because of PSN [7]. Therefore, the recrystallized grains generated at Y_2O_3 particles should be caused by PSN mechanism during compression. Finally, the number and size of recrystallized grains in the deformed microstructure both increased significantly. In summary, with decreasing strain rate from 0.1 s^{-1} to 0.001 s^{-1} or increasing temperature from 350 ℃ to 450 ℃, the proportion of deformed grains and twins decreased while the proportion of DRX increased obviously.

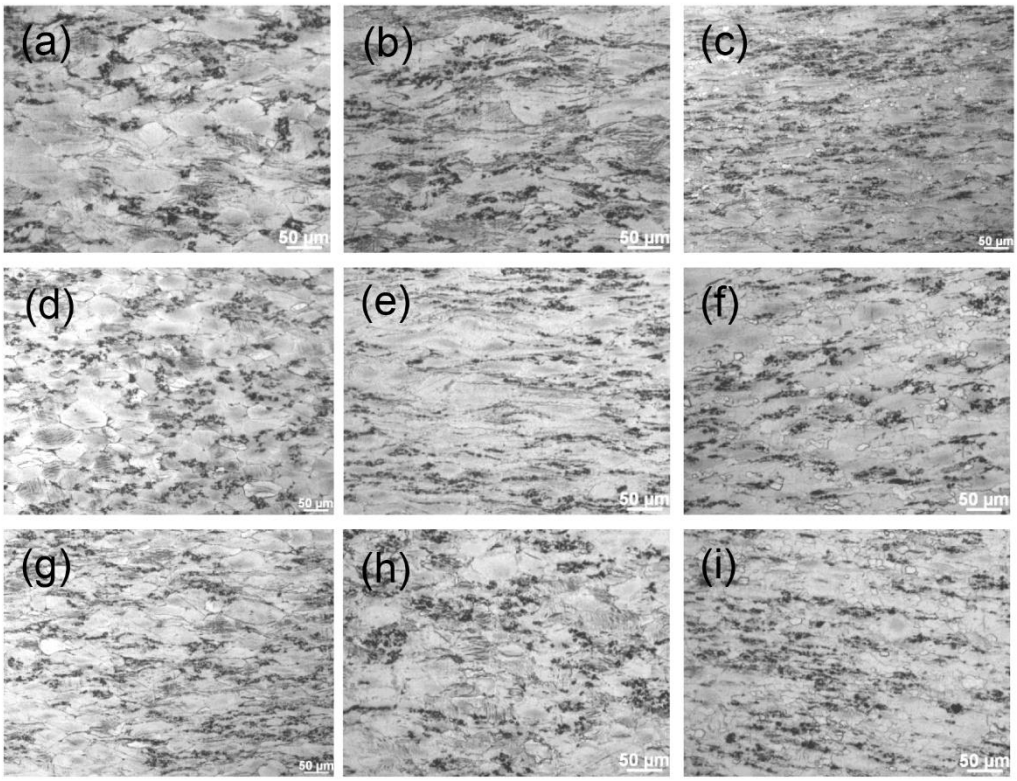

Fig. 2. Optical microstructure evolution of 6%Y_2O_{3p}/Mg-Zn-Gd-Zr composites compressed at a true strain about 0.7 but different strain rates and temperatures. (a-c) 0.1s^{-1}, (d-f) 0.01s^{-1}, (g-i) 0.001s^{-1}; (a, d, g)

350 ℃, (b, e, h) 400 ℃, (c, f, i) 450 ℃.

3.3. Effect of strains

In addition to strain rates and temperatures, the strains also had an important role in microstructure evolution as shown in Fig. 3. When compressed at a true strain of 0.2 as shown in Fig. 3(a), the original grains only slightly compressed along CD with few twins. Fine recrystallized grains generated along grain boundaries or Y_2O_3 particles with increasing compression strains to 0.9 as shown in Fig. 3(b). The microstructure was almost composed of recrystallized grains with necklace distribution of Y_2O_3 particles with increasing compression strains to 1.6 as shown in Fig. 3(c). In this study, the 1%Y_2O_{3p}/Mg-Zn-Gd-Zr composites were also used to compare with 6%Y_2O_{3p}/Mg-Zn-Gd-Zr composites. It could be found that the microstructure evolution of 1%Y_2O_{3p}/Mg-Zn-Gd-Zr composites was similar with 6%Y_2O_{3p}/Mg-Zn-Gd-Zr composites as shown in Fig. 3(d-f). However, the faction of recrystallized grains in 1%Y_2O_{3p}/Mg-Zn-Gd-Zr composites was less than 6%Y_2O_{3p}/Mg-Zn-Gd-Zr composites due to lacking the effect of Y_2O_3 particles which could promote DRX by PSN mechanism.

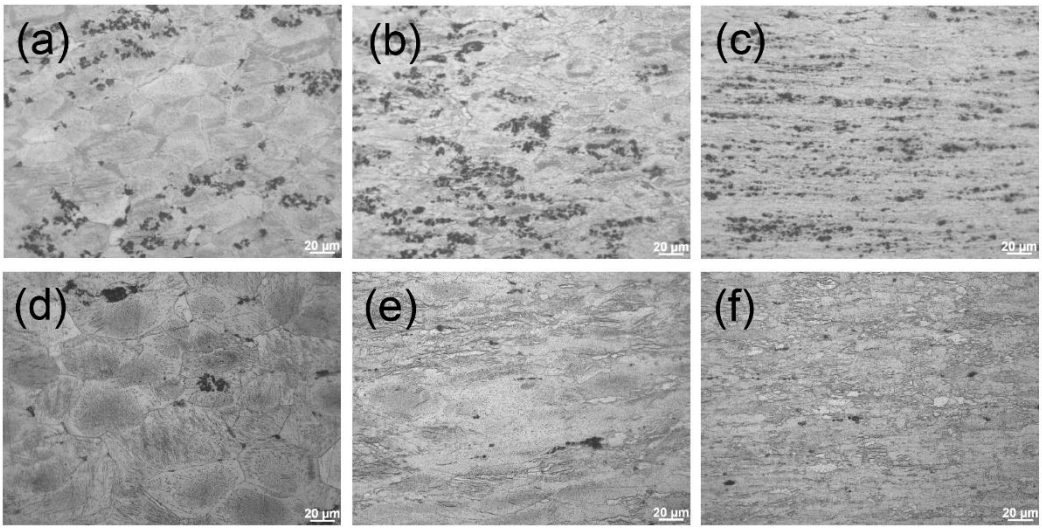

Fig. 3. Optical microstructure evolution of (a-c) 6%Y_2O_{3p}/Mg-Zn-Gd-Zr and (d-f) 1% Y_2O_{3p}/Mg-Zn-Gd-Zr composites compressed at 400 ℃, 0.001 s^{-1} but different strains: (a, d) 0.2, (b, e) 0.9 and (c, f) 1.6.

3.4. EBSD observation

In order to figure out DRX mechanism during compression, EBSD observation was used and the microstructure of 6%Y_2O_{3p}/Mg-Zn-Gd-Zr composites compressed at 400 ℃ under different strain rates was detected as shown in Fig. 4. With increasing strain rates from 0.001 s^{-1} to 0.1 s^{-1}, the proportion of deformed grains and twins increased while DRXed grains

decreased as shown in Fig. 4(a-f, h). The main reason was that when the strain rate was slow, there was sufficient time for dislocations to rearrange and form DRXed grains while there was no sufficient time under a high strain rate [6]. Fig. 4(g) showed that there were lots of dislocations around nano-sized precipitations, indicating that the dislocations were pinned by these precipitations. The compressed textures at different strain rates were still basal textures as shown in Fig. 4(j-l). The intensities of basal textures increased and the distribution became concentrated with increasing strain rates, which should be attributed to the decrease of DRXed grains. It was known that the DRX played an important role in mechanical properties and texture during compression. Therefore, it was necessary to figure out the DRX mechanism of the composites during compression. Fig. 4(i) was the enlarged area in Fig. 4 (a) that showed the deformed grains with low angle grain boundaries (LAGBs), high angle grain boundaries (HAGBs), subgrains and DRXed grains. The misorientation change of deformed grains increased to more than 15° along AB and CD, indicating that there were lots of piled-up dislocations in deformed grains that could gradually transform into subgrains. These subgrains would transform into DRXed grains after continuous compression. Therefore, when the composites were compressed at 400 ℃ 0.001s^{-1}, the DRX mechanism of the composites was CDRX, which was consistent with the DRX mechanism of extruded Mg-Zn-Gd matrix alloy [11].

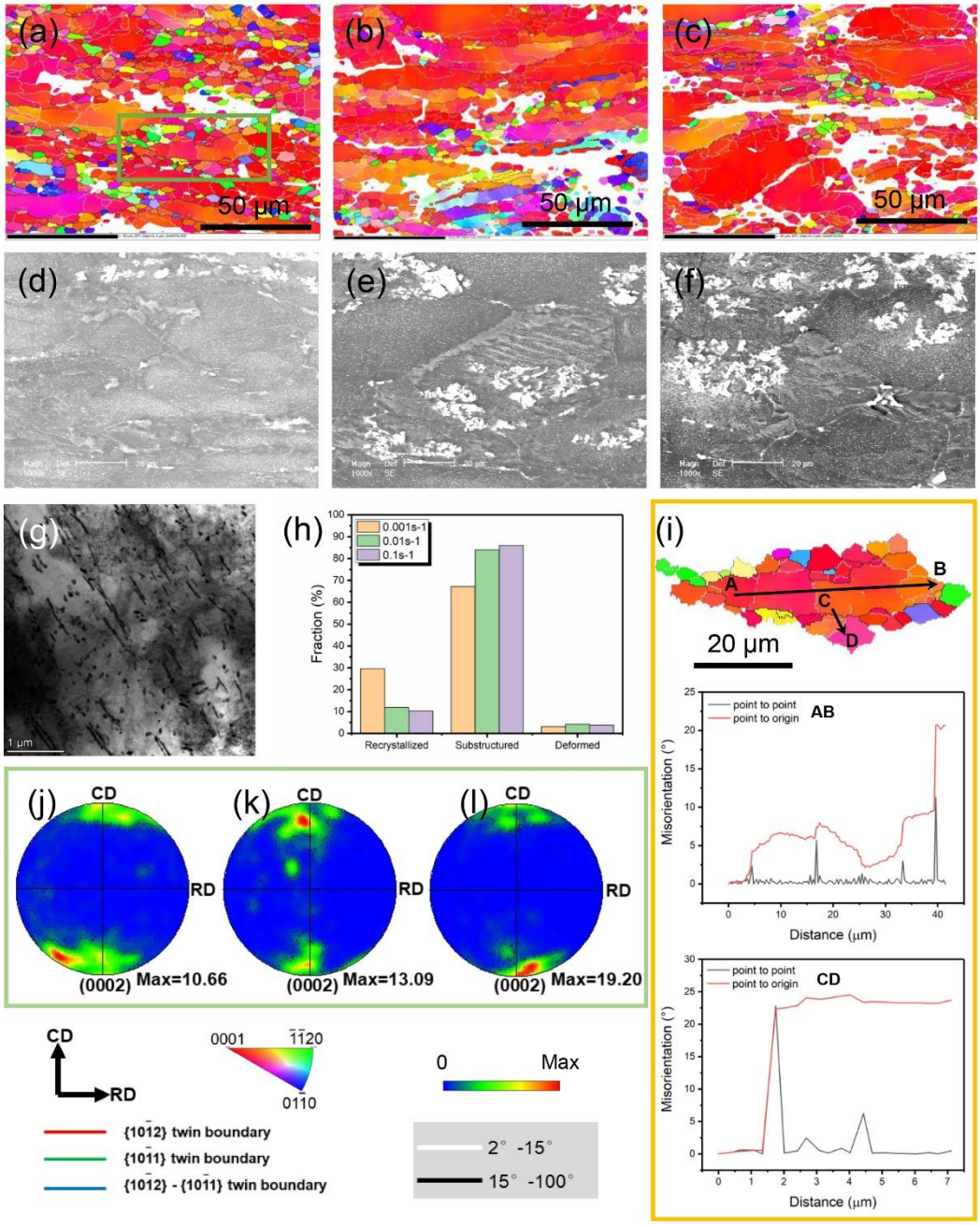

Fig. 4. Microstructure and texture of 6%Y_2O_{3p}/Mg-Zn-Gd-Zr composites compressed at 400 ℃ under different strain rates: (a, d, g, i, j) 0.001 s^{-1}, (b, e, k) 0.01 s^{-1}, (c, f, l) 0.1 s^{-1}; (a-c) IPF, (d-f) SEM, (g) TEM, (h) area fractions of deformed, substructured and recrystallized grains, (i) the enlarged IPF in Fig. 4 (a) green rectangle and line profiles of the misorientation angle along the arrow AB and CD, (j-l) (0002) pole figure.

In PMMCs, the large particles (>1 μm) could promote DRX due to the PSN mechanism while small particles (<1 μm) could retard DRX due to the Zener drag effect [12]. There were two main kinds of particles in 6%Y_2O_{3p}/Mg-Zn-Gd-Zr composites: one was the added micro-sized Y_2O_3 particles and another one was precipitated nano-sized precipitations. The more addition

of micro-sized Y_2O_3 particles in Y_2O_{3p}/Mg-Zn-Gd-Zr composites could promote DRX by PSN mechanism due to the deformation mismatch between particles and matrix alloy during compression [12]. However, the nano-sized precipitations could pin LAGBs and HAGBs due to Zener drag effect [12]. As results, the nano-sized precipitations could retard the formation of DRX. And the growth of DRXed grains was also suppressed by nano-sized precipitations due to Zener drag effect. Therefore, the nano-sized precipitations could inhibit the formation and growth of DRX. Though the Y_2O_3 particles could promote DRX, the precipitated nano-sized precipitations could retard DRX by suppressing the formation and growth of DRXed grains. In bimodal size particles reinforced PMMCs [13, 14], the grain sizes were efficiently refined through the synergy of bimodal sizes reinforcements. Therefore, the micro-sized Y_2O_3 particles and nano-sized precipitations had a synergistic effect on the DRX behavior and the grain sizes of the composites could also be refined efficiently.

4. Conclusion

The microstructural evolution of 6%Y_2O_{3p}/Mg-Zn-Gd-Zr composites compressed at different temperatures, strain rates and strains were studied. Y_2O_3 particles distributed in the grains and at the grain boundaries while some Y_2O_3 particles clusters were also found in composites. After homogenization, the eutectic phases were reduced while nano-sized precipitations were formed in the grains. With increasing compression temperature and strain or decreasing strain rate, the fraction of DRXed grains increased while the fraction of deformed grains decreased. EBSD observation showed that the DRXed grains fraction increased with decreasing strain rates, as a result, the basal textures were weakened. The added micro-sized Y_2O_3 particles could promote DRX due to the PSN mechanism, while the fine nano-sized precipitates could suppress the formation and growth of DRX due to the Zener drag effect. When the composites were compressed at 400 ℃ $0.001s^{-1}$, the DRX mechanisms of composites during deformation included PSN mechanism and CDRX mechanism.

Acknowledgments

This work was financially supported by the National Natural Science Foundation of China (No. 52271107), the Natural Science Foundation of Shandong (ZR2021ME241), the Natural Science Foundation of Liaoning Province (No. 2020-MS-004).

References

[1] S.V.S. Prasad, S.B. Prasad, K. Verma, R.K. Mishra, V. Kumar, S. Singh, The role and significance of

Magnesium in modern day research-A review, J. Magnes. Alloy. 10(1) (2022) 1-61. https://doi.org/10.1016/j.jma.2021.05.012.

[2] F.S. Pan, M.B. Yang, X.H. Chen, A Review on Casting Magnesium Alloys: Modification of Commercial Alloys and Development of New Alloys, J. Mater. Sci. Technol. 32(12) (2016) 1211-1221. https://doi.org/10.1016/j.jmst.2016.07.001.

[3] K.B. Nie, X.J. Wang, K.K. Deng, X.S. Hu, K. Wu, Magnesium matrix composite reinforced by nanoparticles – A review, J. Magnes. Alloy. 9(1) (2021) 57-77. https://doi.org/10.1016/j.jma.2020.08.018.

[4] Y.-d. Fan, K.-k. Deng, C.-j. Wang, K.-b. Nie, Q.-x. Shi, Work hardening and softening behavior of Mg–Zn–Ca alloy influenced by deformable Ti particles, Mater. Sci. Eng. A 833 (2022) 142336. https://doi.org/10.1016/j.msea.2021.142336.

[5] X. Niu, G. Li, Z. Zhang, P. Zhou, H. Wang, S. Zhang, W. Cheng, Simultaneously improving the strength and ductility of extruded bimodal size SiCp/AZ61 composites: Synergistic effect of micron/nano SiCp and submicron Mg17Al12 precipitates, Mater. Sci. Eng. A 743 (2019) 207-216. https://doi.org/10.1016/j.msea.2018.11.023.

[6] X.J. Wang, X.S. Hu, Y.Q. Wang, K.B. Nie, K. Wu, M.Y. Zheng, Microstructure evolutions of SiCp/AZ91 Mg matrix composites during hot compression, Mater. Sci. Eng. A 559 (2013) 139-146. https://doi.org/10.1016/j.msea.2012.08.054.

[7] X.J. Wang, X.S. Hu, K.B. Nie, K.K. Deng, K. Wu, M.Y. Zheng, Dynamic recrystallization behavior of particle reinforced Mg matrix composites fabricated by stir casting, Mater. Sci. Eng. A 545 (2012) 38-43. https://doi.org/10.1016/j.msea.2012.02.077.

[8] D.G. Fan, K.K. Deng, C.J. Wang, K.B. Nie, Q.X. Shi, W. Liang, Hot deformation behavior and dynamic recrystallization mechanism of an Mg-5wt.%Zn alloy with trace SiCp addition, J. Mater. Res. Technol. 10 (2021) 422-437. https://doi.org/10.1016/j.jmrt.2020.11.105.

[9] X.H. Li, H. Yan, R.S. Chen, Microstructure, texture and mechanical properties of Y2O3p/ZG21 composites after rolling and subsequent annealing, J. Alloy. Compd. 889 (2021) 161683. https://doi.org/10.1016/j.jallcom.2021.161683.

[10] Y. Tian, H. Huang, G.Y. Yuan, C.L. Chen, Z.C. Wang, W.J. Ding, Nanoscale icosahedral quasicrystal phase precipitation mechanism during annealing for Mg–Zn–Gd-based alloys, Materials Letters 130 (2014) 236-239. https://doi.org/10.1016/j.matlet.2014.05.131.

[11] M.G. Jiang, C. Xu, T. Nakata, H. Yan, R.S. Chen, S. Kamado, Enhancing strength and ductility of Mg-

Zn-Gd alloy via slow-speed extrusion combined with pre-forging, J. Alloy. Compd. 694 (2017) 1214-1223. https://doi.org/10.1016/j.jallcom.2016.10.109.

[12] R.D. Doherty, D.A. Hughes, F.J. Humphreys, J.J. Jonas, D.J. Jensen, M.E. Kassner, W.E. King, T.R. McNelley, H.J. McQueen, A.D. Rollett, Current issues in recrystallization: a review, Mater. Sci. Eng. A 238 (1997) 219-274. https://doi.org/10.1016/s0921-5093(97)00424-3

[13] M.J. Shen, X.J. Wang, M.F. Zhang, M.Y. Zheng, K. Wu, Significantly improved strength and ductility in bimodal-size grained microstructural magnesium matrix composites reinforced by bimodal sized SiCp over traditional magnesium matrix composites, Compos. Sci. Technol. 118 (2015) 85-93. https://doi.org/10.1016/j.compscitech.2015.08.009.

[14] M. Hu, S. Wei, Q. Shi, Z. Ji, H. Xu, Y. Wang, Dynamic recrystallization behavior and mechanical properties of bimodal scale Al2O3 reinforced AZ31 composites by soild state synthesis, J. Magnes. Alloy. 8(3) (2020) 841-848. https://doi.org/10.1016/j.jma.2020.02.012.

Study on interface regulation of annealed pyrolytic graphite/aluminum composites of high thermal conductivity

Y. X. Zhang [1, 2, 3], H. Guo[1, 2], Z. N. Xie[1, 2], Y. L. Liu[1, 2, 3], S. J. Du[1, 2, 3]*

[1]State Key Laboratory of Nonferrous Metals and Processes, GRINM Group Co., Ltd. China

[2]GRIMAT Engineering Institute Co., Ltd. China

[3]General Research Institute for Nonferrous Metals, China

Abstract: With the rapid development of the semiconductor industry and the continuous improvement of the heat flux density of electronic devices, hot spots caused by heat accumulation will seriously affect the reliability and life of electronic devices. Aiming to achieve a good combination between annealed pyrolytic graphite (APG) and aluminum alloy to improve the effective heat transfer at the interface, the surface of annealed pyrolytic graphite was plated with Cr and Ti elements by vacuum evaporation plating technology in this study. A novel annealed pyrolytic graphite/aluminum composite material with layered structure was fabricated by vacuum hot pressing to meet this requirement. The nanometer size of the modified layer formed on the graphite surface was controlled. The bonding method between the modified layer on the graphite surface and graphite was discussed by X-ray photoelectron spectroscopy (XPS). The effect of different carbide modified layer structures on the microstructures interface bonding of composite was investigated by transmission electron microscope (TEM) and high resolution transmission electron microscope (HR-TEM), and the intrinsic relationship between interfacial microstructure and the macroscopic thermal conductivity was revealed. As a result, the titanium/chromium modified layer formed on the surface of the annealed pyrolytic graphite exhibits a gradient distribution, and an interface structure of the APG-CrxCy/TiC-matel layer is formed between the annealed pyrolytic graphite and the metal modified layer. The annealed pyrolytic graphite is used as a thermal conductive component, which can further improve the interface bonding state of the composite material, which has high comprehensive performance, that is, the thermal diffusivity and the flexural strength are 901 $mm^2 \cdot s^{-1}$ and 141 MPa.

1. Introduce

Thermal management materials are of great significance in the electronics industry. With the rapid development of semiconductor technology, electronic devices are developing towards integration and miniaturization, the number of transistors and heat dissipation power have steadily increased. The heat dissipation generated at the chip needs to be solved urgently[1, 2]. If the generated heat cannot be dissipated in time, heat accumulation will be formed inside the device, which will lead to the failure of the device. The main solution for improving such problems is to quickly dissipate the heat generated at the hot spot to a large plane for rapid heat exchange to reduce heat on the chip surface.

At present, the research and development of such packaging materials mostly focus on ceramics and carbon-metal composite materials, and the common material systems are SiC-Al[3, 4], graphite flake-Al[5-7], graphite film-Al[8-10] and other materials, which have thermal expansion coefficients matching those of semiconductor devices and good mechanical properties, but these materials currently have the characteristics of generally low thermal conductivity in two-dimensional directions. Due to the different arrangements of carbon elements in graphite materials, its thermal conductivity can span nearly 5 orders of magnitude[11]. In packaging materials, graphite materials such as flakes, films, and fibers with thermal properties greater than 300 W/mK are widely used. Graphite materials have high anisotropy and small size, which are difficult to disperse during the preparation process, and are prone to agglomeration, which will affect the structural integrity of the material itself, and reduce the overall thermal conductivity performance of the composite material.

Using carbon materials such as highly oriented and large-sized bulk graphite as thermal conductive components can effectively solve the orientation problem by controlling its stacking with the metal matrix. Annealed pyrolytic graphite (APG)[12] has anisotropic thermal properties similar to graphite films, with a thickness of 1~2 mm, which can prepare composites with a certain size in the Z direction to reduce the interface fraction of graphite.

In carbon/aluminum composites, problems such as poor interfacial wettability and the generation of brittle phase Al_4C_3 limit the full play of the thermal conductivity of carbon materials, so the interfacial reaction must be regulated. At present, the most effective way to solve the interface problem is to modify the surface of carbon materials, by introducing Ti, Si and other carbide coatings[13-16] or Cu, Ni, Cr, Ag and other metal coatings[17-21]], which can improve the wettability with the metal and improve the adhesion between the graphite

and aluminum.

In this study, aiming to achieve a good combination between annealed pyrolytic graphite and aluminum alloy and to improve the effective heat transfer at the interface, the surface of annealed pyrolytic graphite was plated with Cr and Ti elements by vacuum evaporation plating technology. A novel layered structure of graphite/aluminum composites was prepared by vacuum hot pressing. In this study, the nanometer size of the modified layer formed on the graphite surface was controlled, and the bonding mode between the modified layer on the graphite surface and graphite was explored by X-ray photoelectron spectroscopy (XPS). The effect of layer structure on the interfacial bonding of composites was investigated by transmission electron microscopy. And the influence of Cr and Ti on the interfacial bonding of APG/Al composite was revealed.

2. Experimental

2.1 Materials and preparation

The detailed preparation process of the annealed pyrolytic graphite/aluminum composite material includes the following steps: The chromium/titanium-modified annealed graphite and the bulk aluminum alloy with the surface oxide film removed were put into a graphite mold layer by layer. The layers were put into a graphite mold, and then heated to 610°C under vacuum for 30 min, while applying pressure to obtain annealed pyrolytic graphite/aluminum composites with different interfaces.

2.2 Characterization

The surface morphology of the modified annealed graphite and the microstructure of the modified annealed graphite/aluminum composite interface were characterized using Scanning electron microscopy (SEM, JSM-7610F Plus, Hitachi, Japan) at 20 kV. The element distribution at the interface of graphite/aluminum composites was analyzed using energy dispersive spectroscopy (EDS) line scanning and surface distribution. The surface bonding of modified graphite was analyzed using X-ray photoelectron spectroscopy (XPS, Axis Supra, Japan). The interface structure samples of composite materials were prepared by Focused Ion Beam (FIB) etching. The interface structure of annealed pyrolytic graphite-aluminum composites was characterized by Transmission Electron Microscope (TEM).

High-Resolution transmission electron microscope image analysis obtained information such as the interface structure and interface reaction products of the composites. The in-plane thermal diffusivity of graphite/aluminum composites with different layer thickness ratios at room temperature was measured by LFA 457 laser thermal analyzer. The flexural strength of the composites was tested by the three-point bending method of an Instron 5569 electronic universal mechanical testing machine.

3. Results and discussion

3.1 CR element modulates the interface of annealed pyrolytic graphite /aluminum composites

Other Sections

In order to improve the interface bonding between annealed pyrolytic graphite and aluminum alloy and enhance the bonding strength between this. The paper adopts the method of vacuum micro-evaporation to modify the surface of annealed pyrolytic graphite.

Fig.1(a) shows the surface morphology of the annealed pyrolytic graphite modified by vacuum micro-evaporation coating with Cr. A uniformly distributed Cr coating is formed on the surface of the annealed pyrolytic graphite. The plating forms a chromium metallization on the graphite surface. Fig.1(b) is the measurement of the thickness of the Cr coating. It is found that the obtained Cr coating has a uniform thickness of about 750 nm under this holding time.

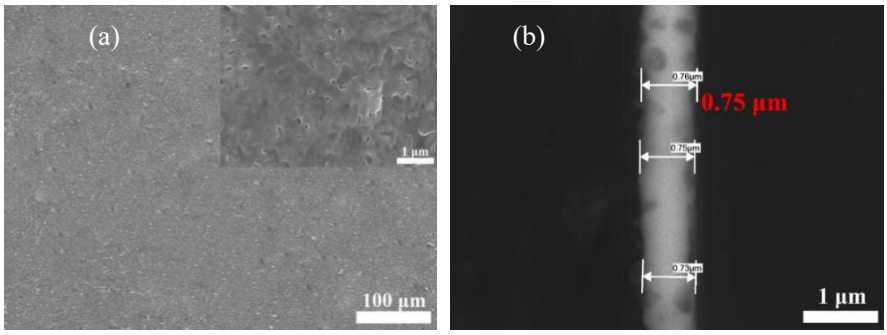

Fig.1 Morphology characterization of Cr-modified annealed pyrolytic graphite:

(a) Morphology characterization of Cr coating on the surface of annealed pyrolytic graphite (the inset is a high-magnification image); (b) Thickness of Cr coating on the surface of annealed pyrolytic graphite

The bonding method between the Cr coating and graphite was explored, and X-ray photoelectron spectroscopy (XPS) was performed on the surface of the Cr-coated annealed pyrolytic graphite sample, that is, the bonding state between the surface layers of the graphite

material was analyzed and characterized, as shown in Fig.2(a). The original annealed graphite material only has high-intensity sp2 hybridized carbon peaks and low-intensity O 1s peaks. Fig.2(b) is a comparative analysis of the fine spectrum of C 1s on the graphite surface before and after modification treatment. It is found that there is a strong sp2 hybridized C-C bond on the surface of the original annealed graphite. When the graphite surface was modified with Cr, the C 1s fine spectrum of the annealed graphite surface appeared metal carbide peaks, which further showed that the vacuum micro-evaporation Cr plating process can form a Cr element coating layer on the graphite surface. The metallurgical bond between the modified layers and the graphite substrate forms a transition layer of chromium carbides.

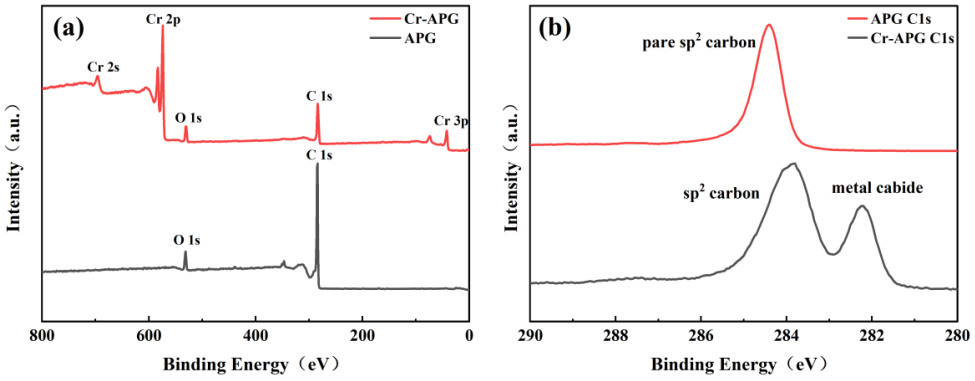

Fig.2 XPS spectrum analysis of annealed pyrolytic graphite: (a) full spectrum scan before and after chrome plating; (b) C 1s fine spectrum before and after chrome plating

In the process of vacuum micro-evaporation plating, Cr and graphite are metallurgically combined, and there is chromium carbide on the surface of annealed pyrolytic graphite, which forms a strong metallurgical bond. The distribution of surface modification layer shows annealed pyrolytic graphite-carbide-Cr distribution characteristics. The carbide layer formed between the annealed pyrolytic graphite forms a bridge between the graphite and the metal chromium, which promotes the combination of the two and makes the two closely combine. At the same time, the Cr metal layer of the outer layer can form a good combination with the metal matrix.

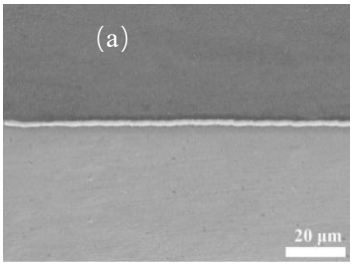

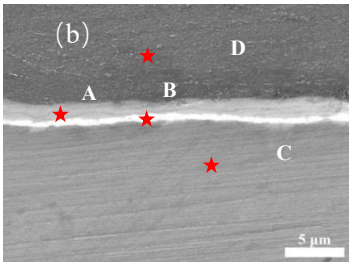

(c)

元素含量 / 区域	Al /(at.%)	Cr /(at.%)	Si /(at.%)	C /(at.%)
A	39.5	11.14	6.54	42.83
B	54.84	40.37	4.78	-
C	97.76	-	2.25	-
D	-	-	0.18	99.82

Fig.3 Interface microstructure of Cr-modified annealed pyrolytic graphite/aluminum composites: (a) Cr-modified annealed pyrolytic graphite/aluminum composite interface morphology; (b-c) phase energy spectrum analysis at different positions at the interface

The Cr-modified annealed pyrolytic graphite/aluminum composite was prepared by vacuum hot pressing. The interface microstructure is shown in Fig.3. It can be seen in Fig.3(a) that the interface between annealed pyrolytic graphite and aluminum is clear, smooth and continuous, there are obviously different contrasts between the two, and no defects such as holes are observed, indicating that the existence of the Cr modified layer significantly improves the interface bonding state between the annealed pyrolytic graphite and the aluminum alloy matrix. Fig.3(b-c) shows the phase composition at different positions at the interface, in which positions C and D are aluminum and annealed pyrolytic graphite. At the interface, the contrast can be clearly divided into two components. From the element distribution in the Fig.3, it can be seen that the interface between Cr-modified annealed pyrolytic graphite and the aluminum alloy has two distinct parts, namely C-Cr carbide phase and Cr-Al metal phase, which are distributed in the center of the graphite-aluminum interface in a parallel arrangement. The main reasons for the formation of such structures: In the process of vacuum hot pressing sintering, the Cr coating and the Al alloy are in contact with each other to cause mutual diffusion and interfacial reaction, and the Al element gradually diffuses into the Cr element to react with the Cr coating, and has a certain effect. A small amount of Al elements diffuses to the side where graphite and Cr form carbides, which forms a transition layer in a certain area. Due to the thick transition layer, it is easy to scatter in the process of heat flow transmission, thereby affecting the overall performance of the composite material.

3.2 TI element-controlled interface of annealed pyrolytic graphite /aluminum composites

There is a thick transition layer at the interface of the graphite/aluminum composite prepared from chromium-modified directional annealed graphite, which affects the heat flow and mechanical transport. Based on the interfacial thermal conductivity of different interfacial modified layers, the relationship between thermal conductivity and interfacial layer thickness, and the matching degree with the base aluminum alloy, we choose to perform Ti modification on the surface of directional annealed graphite, which can obtain thinner and better matching interface modification layers.

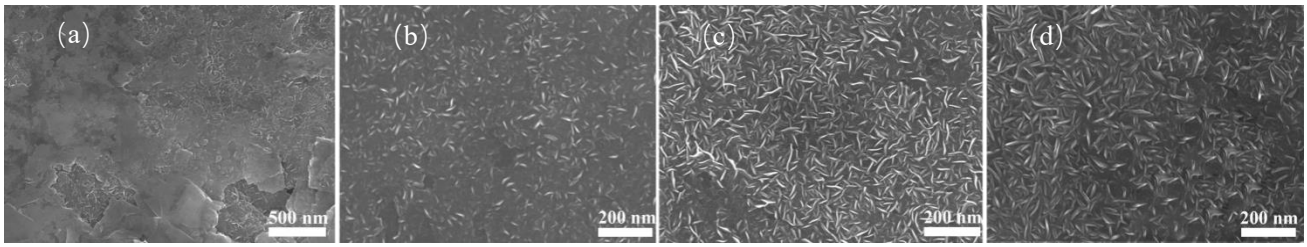

Fig.4 Micromorphology of annealed pyrolytic graphite surface of Ti-modified layers with different thicknesses: (a) 250 nm; (b) 400 nm; (c) 650 nm; (d) 900 nm

Fig.4 shows the surface microstructures of Ti-modified annealed pyrolytic graphite with different thicknesses. When the thickness of the modified layer is gradually increased, the more complete the modified layer on the surface of the annealed pyrolytic graphite, the more obvious the needle-like morphology of the coating. With the change of the thickness of different titanium modified layers, the morphology of the coating on the surface of the annealed pyrolytic graphite is complete and uniform, and the Ti layer on the surface of the annealed pyrolytic graphite is observed at high magnification to be uniform and distributed in a needle-like disorder. When the thickness of the modified layer reaches 650 nm, there is no further change in the morphology of the surface coating, but with the extension of time, the thickness gradually increases, the surface morphology of graphite becomes more disordered, and the roughness increases. In the high-magnification topography, the Ti elements are arranged in a needle-like disorder.

When the thickness of the modified layer reaches 850 nm, the diameter of the needle-like Ti element in the high-magnification topography increases, indicating that with the increase of thickness, the growth of Ti element on the graphite surface is denser, and the needle-like Ti layer is densely interlaced and connected to form a network structure. According to the calculation formula of the interface thermal resistance, it can be obtained that the thicker the interface modification layer is, the higher the interface thermal resistance is introduced. At the same time, the thermal expansion coefficient between Ti and annealed pyrolytic graphite is quite different. If the coating layer is too thick, the prepared composite material may fall off between the coating and the graphite. In order to ensure the overall thermal performance and service life of the composite material, at the current coating temperature, the coating layer of 650 nm is the optimal thickness of the modified layer of annealed pyrolytic graphite. Fig.5 shows the surface morphology of Ti-modified annealed pyrolytic graphite with a thickness of 650 nm. Observed at low magnification, the surface of

annealed pyrolytic graphite is completely covered by titanium coating. In high magnification, it is observed that the Ti modified layer on the surface of annealed pyrolytic graphite exhibits a disorderly distribution of needle-like morphology.

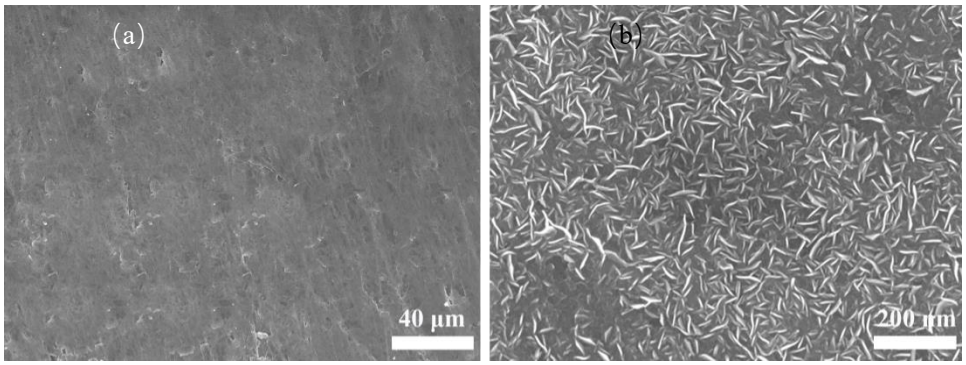

Fig.5 Surface microstructure of 650 nm Ti modified annealed pyrolytic graphite coating: (a) microstructure; (b) high magnification

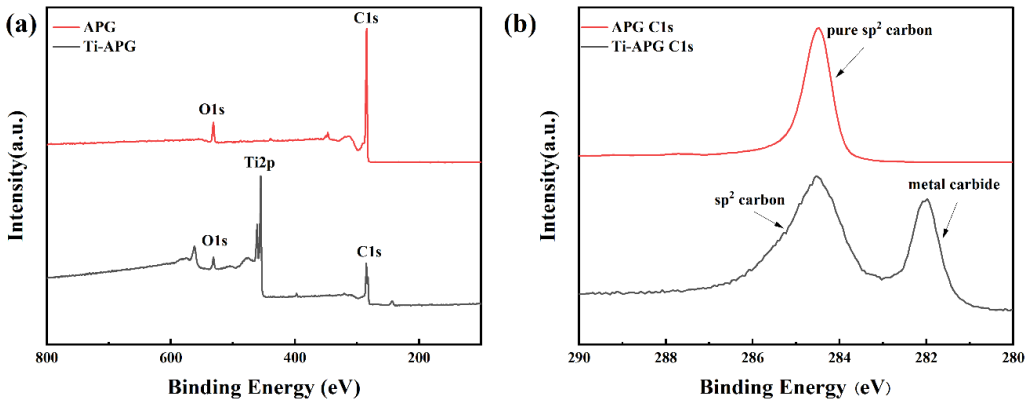

Fig.6 XPS spectrum analysis of annealed graphite: (a) full spectrum scan before and after titanium plating; (b) C 1s fine spectrum before and after titanium plating

X-ray photoelectron spectroscopy (XPS) was performed on the surface of the titanium-modified annealed pyrolytic graphite sample, that is, the bonding state between the surface layers of the graphite material was analyzed and characterized, as shown in Fig.6. It is found in Fig.6(a) that the pristine annealed graphite material only has high-intensity sp2 hybridized carbon peaks and low-intensity O 1s peaks. Fig.6(b) shows the comparison of the fine spectrum of C 1s on the graphite surface before and after the modification treatment. It is found that there is a high-strength sp2 hybridized C-C bond on the original annealed graphite surface. After the titanium modification treatment on the graphite surface, metal carbide peaks appeared in the C 1s fine spectrum of the annealed graphite surface. The metallurgical bond between the layer and the graphite substrate is presented, forming a TiC transition layer.

The fine spectrum of C 1s peak and Ti 2p of the surface layer and the titanium modified annealed graphite material after etching were compared and analyzed. Compared with the surface, the improvement is very obvious, indicating that at this depth, the carbon and titanium on the surface of the material show a certain degree of bonding, that is, the phenomenon of mutual diffusion and metallurgical bonding between the graphite and titanium coatings. The fine spectrum of Ti 2p at the binding energy of 458.70 eV was analyzed, and it was found that the bonding of Ti was mainly Ti-Ti bond. Compared with the fine spectrum of surface layer Ti 2p, the Ti-TiC combination appeared inside the etched layer.

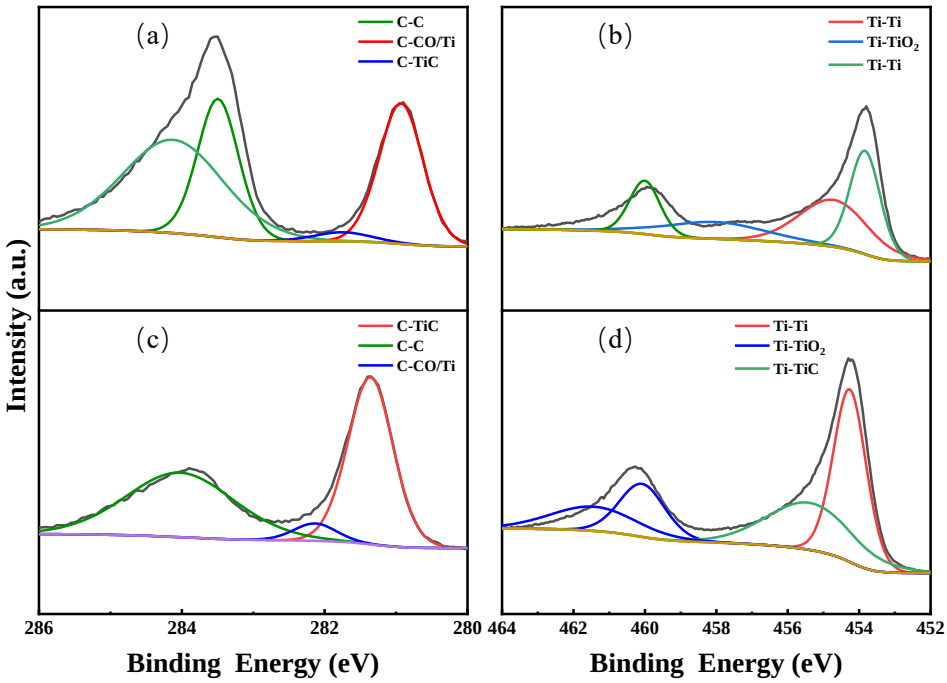

Fig.7 XPS spectra of titanium-coated annealed pyrolytic graphite surface and after etching: (a-b) Surface XPS spectrum C 1s fine spectrum, Ti 2p fine spectrum; (c-d) Internal XPS spectrum of etched layer C 1s fine spectrum, Ti 2p fine spectrum

In summary, it can be concluded that in the growth of titanium on the surface of graphite, metallurgical bonding is first formed between annealed pyrolytic graphite and Ti, that is, carbides are obtained by diffusion between the two, and the bonding strength between the interfaces is improved. With the extension of the plating time, the contact between the titanium element and the graphite decreases. During the micro-evaporation plating process, the Ti layer gradually accumulates on the surface of the annealed pyrolytic graphite to form a titanium

metal layer. It is known from the XPS spectrum analysis that the bonding process between annealed pyrolytic graphite and Ti is the combination of reaction and diffusion. During the vacuum evaporation coating process, the Ti atoms are heated under vacuum conditions to form an evaporating state, which is deposited on the surface of the graphite. It can be seen from the atomic radius of carbon that the carbon atom has a small radius and can diffuse into the interstitial space of the deposited titanium atoms to form a metallurgical bond of TiC. With the increase of the thickness of the coating, the depth of the diffusion of carbon atoms gradually decreases, and finally the orientation is formed. Finally, a surface-modified layer structure of annealed pyrolytic graphite-TiC-Ti was formed. The annealed pyrolytic graphite and the Ti modified layer are bridged by TiC, so that the two are closely combined, and the Ti in the outer layer can form a good bond for the metal matrix in the next preparation process.

Fig.8 shows the typical morphology of the titanium-modified annealed pyrolytic graphite/aluminum composite interface prepared at 590 °C and held for 30 min. There are Ti-modified layers with significantly different contrasts between the annealed pyrolytic graphite and aluminum, which are distributed in parallel strips. At the interface, compared with the interface of Cr-modified annealed pyrolytic graphite/aluminum composite material in Fig.3, the thickness of the obtained interfacial layer is thinner, and the interfacial thermal resistance introduced into the overall composite material is also smaller. At the same time, the annealed pyrolytic graphite and the aluminum alloy are closely bonded, and there are no defects such as holes. Compared with the unmodified interface, the bonding between the two is significantly improved. The carbide forming element Ti is used as the interface modification layer between the annealed pyrolytic graphite material and the aluminum alloy. At this time, as a carbide forming element, Ti will form a two-directional bridge between the graphite and aluminum, and promote the strong interface between the two. At the same time, the metal modified layer forms a barrier layer between graphite and aluminum, which physically prevents direct contact between the two and inhibits the interface reaction between the two.

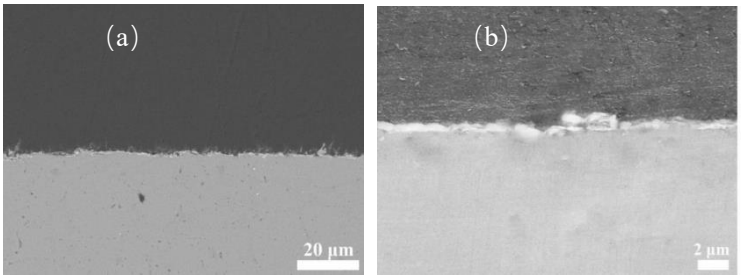

Fig.8 Typical interface structure of Ti-modified annealed pyrolytic graphite/aluminum composites: (a) interface microstructure; (b) high magnification image

Fig.9 shows the TEM bright-field image morphology of the titanium-modified annealed pyrolytic graphite/aluminum composite material, with the aluminum alloy on the left and the annealed pyrolytic graphite on the right. It can be found that the annealed pyrolytic graphite has an obvious layered structure, and there is an obvious interface layer between the graphite and the aluminum alloy. In the high magnification image, different parts of the interface area were selected for EDS point element content analysis. In the results, it was found that there were C atoms in the Ti modified layer, while there were fewer Ti atoms in the annealed pyrolytic graphite material, which was consistent with the previous analysis.

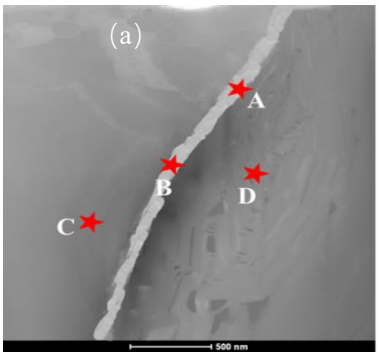

(b)

元素含量 区域	Al/ (at.%)	Ti/ (at.%)	C/ (at.%)
A	2.2	43.05	54.56
B	12.00	39.94	48.06
C	97.26	2.74	-
D	-	0.95	99.05

Fig.9 Annealed pyrolytic graphite/aluminum composite interface: (a) TEM bright field image of the interface layer; (b) EDS analysis of element distribution at the interface

The growth mechanism of the Ti modified layer on the surface of the annealed pyrolytic graphite is consistent, indicating that during the growth process of the Ti interface modified layer, the carbon atoms in the annealed pyrolytic graphite diffuse to the Ti modified layer due to the small radius, and a strong metallurgical bond is formed between the two. At the same time, at the end close to the aluminum alloy, a small amount of Ti atoms was found in the aluminum, which was also due to the diffusion of the two during the hot pressing sintering process to form an intermetallic compound.

In order to better understand the interface morphology and further confirm the interface structure of annealed pyrolytic graphite/aluminum composites, we carried out TEM characterization of the interface structure, as shown in Fig.10. It can be found that the Ti-modified layer is neatly and uniformly arranged between the graphite and the Al matrix. The inset therein shows the corresponding selected area electron diffraction (SAED) pattern. It can

be seen in the Fig.10 that the annealed pyrolytic graphite has an obvious layered microstructure, and the clear diffraction spots indicate that the annealed pyrolytic graphite has a high degree of crystallinity and graphitization, which is arranged in the orientation of the (002) crystal plane with good orientation. In the selected area electron diffraction pattern of the Al matrix, it is the image of the [111] crystal belt axis of the aluminum alloy, which corresponds to the existence of the (111) and (002) crystal planes of Al.

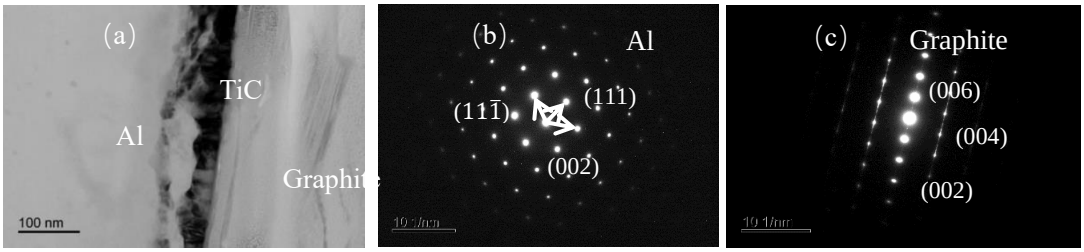

Fig.10 Ti-APG/Al composite: (a) Bright field TEM image of interface area; (b) Al SAED image; (c) APG SAED image

In this study, high-resolution transmission (HR) TEM analysis was also performed on the interfaces on both sides of the Ti-modified region, and distinct and clear interfacial bonding could be observed along the Ti interface-modified layer. The selected area electron diffraction pattern analysis of the interface layer shows that the composition of the interface layer is TiC, and the corresponding crystal plane can be known by analyzing the lattice fringe width of high-resolution images at different positions at the interface.

We carried out high-resolution transmission observation along the direction of Al-Ti-C at the interface, and the TiC-APG interface on the right near the end of the annealed pyrolytic graphite is shown in Fig.11. The lattice fringe width of one end of graphite is 0.253 nm, which corresponds to the (111) crystal plane of TiC, and the crystal plane changes compared with the near aluminum end. At the same time, there is an amorphous transition layer between TiC and annealed pyrolytic graphite, the thickness of which is about 10 nm. Fig.11 shows the Al-TiC interface, there is a small amount of lattice distortion area at this interface, which may be caused by the mutual diffusion between aluminum and TiC. The diffusion of elements at the interface can improve the relationship between the two to a certain extent. The interface bonding strength is about 0.155 nm and 0.235 nm by measuring the width of TiC lattice stripes, corresponding to the (220) crystal plane and (111) crystal plane of TiC. However, the interface between carbon and titanium carbide is an incoherent interface due to the amorphous layer in

the middle, which will promote the scattering of phonons in the process of heat transfer, increase the scattering path in the process of phonon transmission, and reduce phonons. Therefore, the thermal resistance of the interface will be increased, but due to the small thickness of the amorphous transition layer during the preparation process, the effect on the performance of the material is also small. Based on the above, the existence of the Ti modified layer prevents the direct contact between the graphite and the aluminum alloy, inhibits the generation of the brittle phase at the Al4C3 interface, and improves the interfacial bonding between the two.

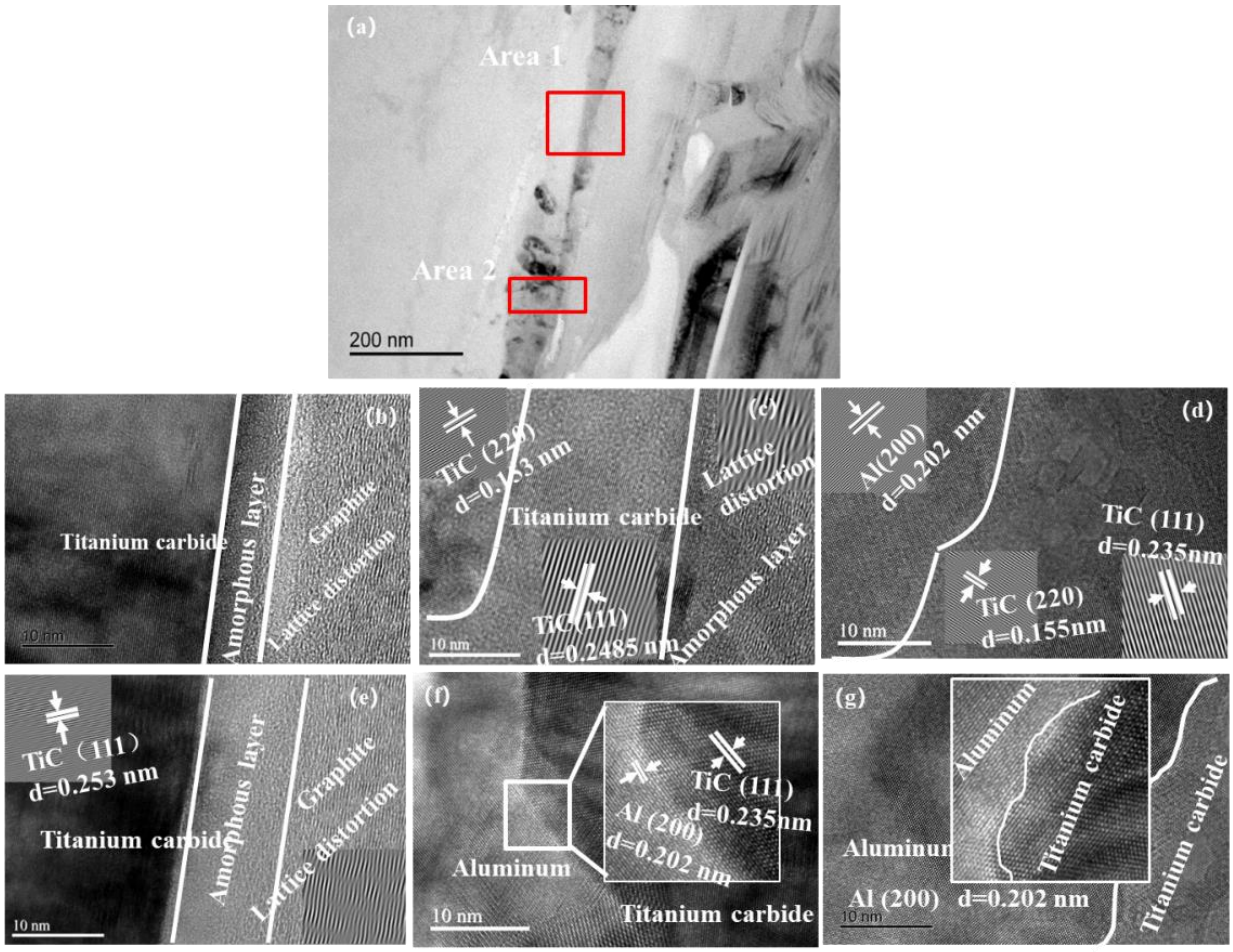

Fig.11 High-resolution images of titanium-modified annealed pyrolytic graphite/Al composite interface area: (a) bright field image of the interface; (b-d) annealed pyrolytic graphite-Ti-Al interface, region 1; (e-g) annealed pyrolytic graphite-Ti -Al interface, area 2

3.3 Performance characterization of annealed pyrolytic graphite /aluminum composites

The thermal properties of the annealed pyrolytic graphite/aluminum material and the modified material were compared, and it was found that the thermal properties were improved

to a certain extent after the Ti modification treatment. Compared with the direct combination of graphite/aluminum, the increase is nearly 19.7%. This is related to the presence of the Ti-modified layer which improves the bonding between the two, with fewer defects and less scattering during heat flow transport. However, the thermal diffusivity of the Cr-annealed pyrolytic graphite/aluminum composite prepared by the same Cr modification treatment is only 419 mm2/s, which is mainly different from the role of the interface modification layer at the interface of the composite material.

The influence of the introduction of the carbide modified layer on the properties of the composite material is mainly reflected in two aspects. On the one hand, the introduction of carbide forming elements can effectively reduce the formation of the interface brittle phase, which will increase the thickness of the interface layer to a certain extent. According to the AMM interface thermal resistance model, it can be obtained that the increase of the thickness of the interface layer will reduce the thermal conductivity of the interface. On the other hand, the shear wave velocity (vAl<vcarbide<vf) of carbides such as TiC and CrxCy formed by Ti or Cr and graphite is between graphite and aluminum, it can effectively alleviate the difficulty of heat transfer caused by the large difference in shear wave velocity, and play a coordinating role between graphite and aluminum. It can be seen in Fig.12 that the thermal diffusivity of the annealed pyrolytic graphite/aluminum composite prepared by Cr modification treatment is poor, and more interfacial phases are formed. The size of the intermetallic compound formed between Cr and Al is slightly larger than that of the Ti-Al intermetallic compound. The thickness of CrxCy formed on the graphite surface is relatively thick, which brings about a large interfacial thermal resistance and affects the improvement of the thermal performance of the composite material.

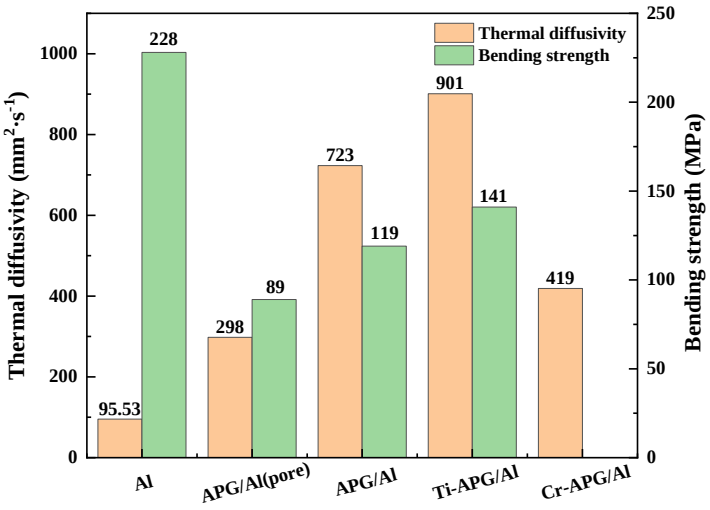

Fig.12 X-Y plane thermal diffusivity and flexural strength of annealed pyrolytic graphite/aluminum composites

In practical engineering applications, the performance of composite materials needs to take into account the requirements of both thermal conductivity and mechanical properties. Fig.12 also compares the flexural strength of the composites under different interfacial bonding states. It is found that the Ti-modified annealed pyrolytic graphite/aluminum composite has the best mechanical properties, which is mainly due to the improvement of the directional annealing under the action of the coating. The wettability between graphite and aluminum alloy can form a good meshing between the two and improve the bonding strength of the interface. At the same time, the carbide formed between the graphite and the coating has a high strength, which is equivalent to forming a reinforcement layer on the surface of the graphite, which indirectly improves the strength of annealed pyrolytic graphite.

4. Conclusion

The annealed pyrolytic graphite/aluminum composite material with good interfacial bonding and high thermal diffusivity was prepared by vacuum hot pressing. The interfacial bonding at the graphite/aluminum interface was characterized by SEM, (HR) TEM and other techniques. The relationship between the macroscopic thermal properties of the material and the microstructure of the interface was studied, and the following conclusions were drawn.

(1) The graphite surface modified layer with controllable thickness was obtained by

vacuum micro evaporation plating. By using vacuum evaporation technology, a complete Cr modified layer was uniformly formed on the graphite surface. The interface structure of APG-CrxCy-Cr is formed between the directionally annealed graphite and the Cr modified layer. The interface structure of APG-TiC-Ti was formed between directionally annealed graphite and Ti modified layer.

(2) Ti plating on the surface of directionally annealed graphite can further improve the interface bonding state of the material, effectively inhibit the formation of Al4C3 phase, and there is an amorphous transition layer with a thickness of about 10 nm between carbide and graphite, which significantly improves the interface bonding. The directionally annealed graphite/aluminum composite modified by titanium has good comprehensive properties, the thermal diffusion coefficient is 901 mm2•s-1, and the maximum bending strength is 141 MPa.

Acknowledgment

References

1. E. S. Toberer, L. L. Baranowski, C. Dames. “Advances in thermal conductivity”. *Annual Review of Materials Re-search*, 42., 179-209, 2012.
2. D. Zhang, Z. Q. Tan, D. B. Xiong, et al. “Application and prospect of metal matrix composites for thermal management: an overview”. *Materials China*, 37., 12., 994-1001, 2018.
3. X. B. He, X. H. Qu, S. B. Ren, et al. “Net-shape forming of composite packages with high thermal conductivity” . *Sci China Ser E:Technol Sci*, 52., 1., 238−242, 2009.
4. B. Guo, X. Zhang, X. Cen, et al. “Ameliorated mechanical and thermal properties of SiC reinforced Al matrix composites through hybridizing carbon nanotubes”. *Materials Characterization*, 136., 272-280, 2017.
5. D. P. Jiang, X. M. Zhu, J. K. Yu. “Enhanced thermal conductivity and bending strength of graphite flakes/aluminum composites via graphite surface modification”. *Journal of Wuhan University of Technology*, 153., 01., 13-19, 2020.
6. C. Zhou, G. Ji, Z. Chen, et al. “Fabrication, interface characterization and modeling of oriented graphite flakes/Si/Al composites for thermal management applications”. *Materials & Design*, 63.,

719-728, 2014.

7. Z. Y. Shen, G. Ji, J. F. Silvain. “From 1D to 2D arrangements of graphite flakes in an aluminum matrix composite: Impact on thermal properties”. *Scripta Materialia*, 183., 86-90, 2020.
8. C. Xue, H. BaI, P. F. Tao, et al. “Thermal conductivity and mechanical properties of flake graphite/Al composite with a SiC nano-layer on graphite surface”. *Materials & Design*, 108, 250-258, 2016.
9. Y. Huang, Q. B. Ouyang, Q guo, et al. “Graphite film/aluminum laminate composites with ultrahigh thermal conductivity for thermal management applications”. *Materials & Design*, 90., 59., 508-515, 2016.
10. J. Chang, Q. zhang, Y. Lin, et al. “Layer by layer graphite film reinforced aluminum composites with an enhanced performance of thermal conduction in the thermal management applications”. *Journal of Alloys and Compounds*, 601-609, 2018.
11. A. Balandin. “Thermal properties of graphene and nanostructured carbon materials”.*Nature Materials*, 10., 08., 569-581, 2011.
12. J. J. Kibler. “High conductivity hydride material for thermal management”. *American patent*, US. 005296310A, 1994-04-22.
13. A. T. Miranda, L. Bolzoni, N. Barekar, et al. “Processing, structure and thermal conductivity correlation in carbon fiber reinforced aluminum metal matrix compo-sites”. *Materials & Design*, 156., 329-339, 2018.
14. X. Y. Peng, Y. Huang, X. Sun, et al. “High thermal conductivity and low thermal expansion coefficient of isotropic graphite-reinforced aluminum matrix composites prepared by in situ curing of silicon aerogel”. *Journal of Materials Science: Materials in Electronics*, 31., 12., 1079-1089, 2020.
15. X. Y. Shen, X. B. He, S. B. Ren, et al. “Effect of molybdenum as interfacial element on the thermal conductivity of diamond/Cu composites”. Journal of Alloys and Compounds, 529,. 03,. 134-139, 2012.
16. J. Chang, Q. Zhang, Y. F. Lin, et al. “Layer by layer graphite film reinforced aluminum composites with an enhanced performance of thermal conduction in the thermal management applications”. *Journal of Alloys and Compounds*, 742., 601-609, 2018.
17. K. Mizuuchi, K. Inoue, Y. Agari, et al. “Processing of diamond-particle-dispersed silver-matrix composites in solid-liquid coexistent state by SPS and their thermal conductivity”. *Composites Part B Engineering*, 42., 4., 825-831, 2011.
18. C. N. Zhu, Y. S. Su, X. S. Wang, et al. “Process optimization, microstructure characterization and thermal properties of mesophase pitch-based carbon fiber reinforced aluminum matrix composites

fabricated by vacuum hot pressing". *Composites Part B: Engineering*, 2021.

19. G. H. Wu, J. Su, H. S. Gou, et al. "Study on graphite fiber and Ti particle reinforced Al composite". *Journal of Materials Science*, 44., 18., 4776-4780, 2009.
20. H. M. Zhang, X. B. He, X. H. Qu, et al. "Microstructure and thermal properties of copper matrix composites rein-forced with titanium-coated graphite fibers". Rare Metals, 32., 1., 75-80, 2013.
21. B. S. Guo, Y. Q. Chen, Z. W. Wang, et al. "Enhancement of strength and ductility by interfacial nano-decoration in carbon nanotube/aluminum matrix composites". *Carbon*, 159., 201-212, 2020,.

Microstructure and mechanical properties of SiCf/SiC-Nb2AlC composites by Si melt infiltration

Y.R. Zhou[1], J. Jiao[1], J.H. Yang[1], H. Liu[1], Y.J. Ai[1]*

[1]National Key Laboratory of Advanced Composites, AECC Beijing Institute of Aeronautical Materials, Beijing 100095, China

Abstract: In this study, a novel SiC_f/SiC-Nb_2AlC composites were prepared by the Si melt infiltration, in which Nb_2AlC phase was directly added to the SiC matrix. This method avoids the byproducts that the *in situ* synthesis would bring, and simplify the preparation process. The lamellar Nb_2AlC grains increase the strength and toughness of SiC matrix by the mechanisms such as crack deflection, grain's pull-out and fine-grain toughening. The lamellar Nb_2AlC grains as the reinforcing agents in the SiC matrix exhibit significant strengthening and toughening effect to the SiC matrix and the composites show excellent mechanical properties. The bending strength and fracture toughness of SiC_f/SiC-Nb_2AlC composites can be greatly improved.

1. Introduction

The continuous improvement of aero-engines performance imposes higher requirements on the temperature resistance and weight reduction of the materials for its hot section components. Continuous SiC fiber reinforced SiC matrix (SiC_f/SiC) composites with low density, high temperature resistance and oxidation resistance, etc have become the ideal candidate materials for the applications in hot section components of aero-engines[1-2]. For the purpose of the high toughness for the specific technological applications, the improvement of the toughness of the SiC_f/SiC composites needed to be considered. Due to the high hardness and brittleness of SiC, a second toughening phase is considered to introduce to it. The reinforcements should be stable in contact with SiC at high temperature and could improve the matrix properties [3].

The ternary carbides and nitrides with the general formula $M_{n+1}AX_n$ (M: early transition metal, A: A group element, mostly III A or IV A, X: either C and N, n=1–3) have attracted much interest, which possess a unique combination of ceramic and metal properties due to its special structure [4-5]. The layered ternary compound of Nb_2AlC has properties and remarkable resistance to oxidation at high temperature among MAX phases [6-7]. Thus,

Nb_2AlC could probably be used as a reinforcement to improve the toughness of SiC matrix.

In this study, a novel SiC_f/SiC-Nb_2AlC composites were prepared by Si melt infiltration, in which Nb_2AlC phase is directly added to the SiC matrix. This method avoids the byproducts that the in situ synthesis would bring, and simplify the fabrication process. The lamellar Nb_2AlC grains increase the strength and toughness of SiC matrix by the mechanisms such as crack deflection, grain's pull-out and fine-grain toughening. The flexural strength and fracture toughness of SiC_f/SiC-Nb_2AlC composites can be greatly improved.

2. Experimental

A mixture of Nb_2AlC powders (99.9%, average particle size <5μm) and phenolic resin were blended into absolute enthanol to prepare the mixed slurry. The 0^o unidirectional SiC fabrics were prepared by coated SiC fibers. The SiC_f/SiC-Nb_2AlC composites were prepared by the Si melt infiltration. The detailed synthesis process can be found in our previous research [8-9].

The microstructure, element distribution and fracture surface of the samples were investigated by scanning electron microscopy (SEM, Nova Nano450, FEI, USA) which equipped with a back-scattered electron (BSE) detector and energy dispersive spectroscopy (EDS). To further identify the phase constitution, the samples were crushed into a powder and analyzed by X-ray diffraction (XRD, D8 Advance, Bruker, Germany) with Cu Kα radiation. The flexural strength and fracture toughness (K_{IC}) of the as-received composites were measured by 3-point bending method and single-edge-notched beam (SENB) method on a universal testing machine (C45.105, MTS, US) at a cross-head speed of 0.5 mm/min with a loading span of 30 mm.

3. Results And Discussion

3.1 Phase identification and microstructure

Figure 1 shows the XRD pattern of the SiC_f/SiC-Nb_2AlC composites. For comparison, the pattern of the SiC_f/SiC composites fabricated by MI was also shown. It can be seen that the SiC phase was formed as a main phase in both composites. The peaks of Si phase were also noticed in the patterns. It could be attributed to the residual Si in the SiC matrix caused by Si MI process. The weak peaks of Nb_2AlC can also be observed in the SiC_f/SiC-Nb_2AlC

composites [10].

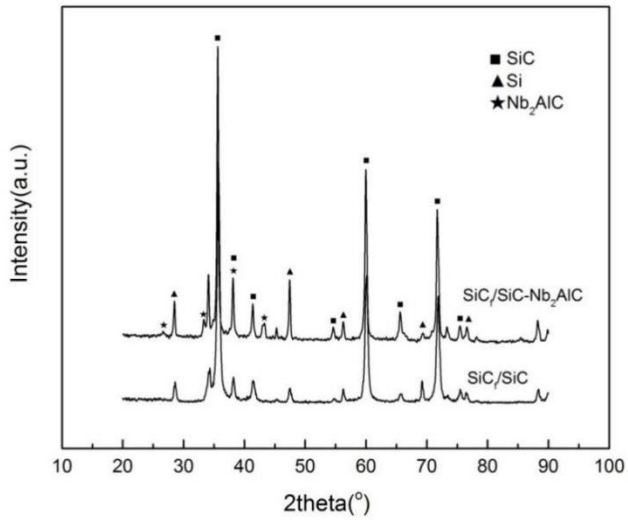

Figure 1. XRD patterns of SiC_f/SiC-Nb_2AlC and SiC_f/SiC composites

Figure 2(1) shows the BSE image of the polished surface of SiC-Nb_2AlC matrix. According to XRD results mentioned above, the deep gray area is the reaction formed SiC phase, and the light gray area is associated with the residual Si phase. The white phase is Nb_2AlC. Figure 2(2), (3) are the EDS spectrum of the marked area in Figure 2(1). As seen in Figure 2(2), the EDS result in position *A* is in accordance with SiC phases. From the spectra of Figure 2(3), the marked position *B* contains Nb, Al, C and Si elements, which means this area might be consistent with a mixture of $NbAlC_2$ and SiC.

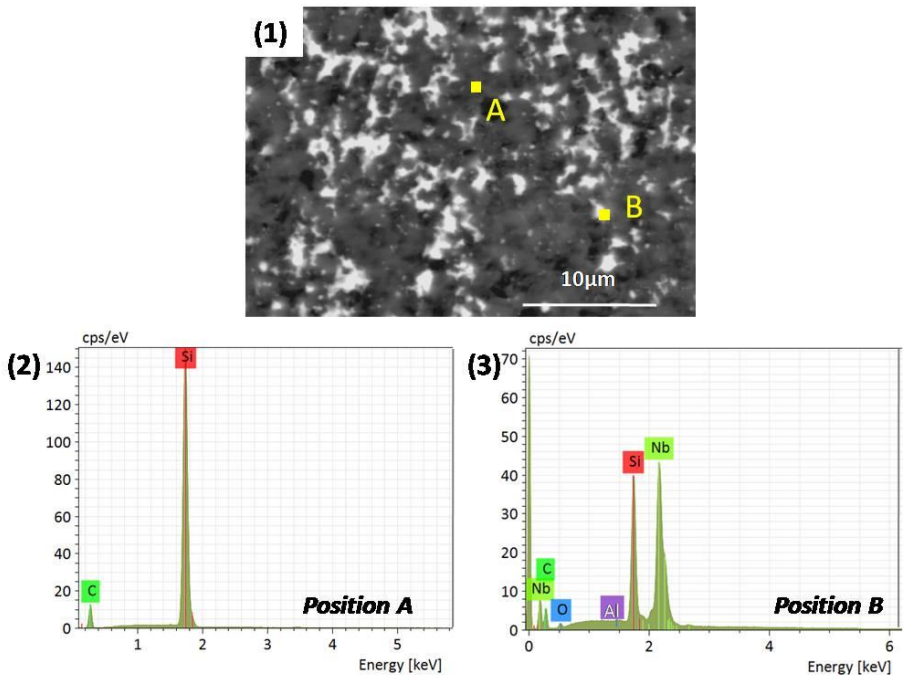

Figure 2 (1) BSE image of polished surface of SiC_f/SiC-Nb_2AlC composites and (2), (3) EDS results of the marked area in (1)

3.2 Mechanical properties and toughening mechanism of SiC_f/SiC-Nb_2AlC composites

Table 1 lists density, open porosity, flexural strength and fracture toughness of SiC_f/SiC and SiC_f/SiC-Nb_2AlC composites. It can be seen that the as-received SiC_f/SiC-Nb_2AlC composites show quite dense microstructure and great mechanical properties. The flexural strength of SiC_f/SiC-Nb_2AlC composites (971.4 MPa) is higher than that of SiC_f/SiC composites (834.3 MPa). Moreover, the fracture toughness of SiC_f/SiC-Nb_2AlC composites (24.17 $MPa \cdot m^{1/2}$) was obviously improved by adding Nb_2AlC phases to SiC matrix, compared to that of SiC_f/SiC composites (18.59 $MPa \cdot m^{1/2}$).

Figure 3 presents the load-displacement curves of SiC_f/SiC-Nb_2AlC and SiC_f/SiC composites from flexural strength test. It can be seen that both of the composites exhibit an obvious non-catastrophic failure behavior. For SiC_f/SiC-Nb_2AlC composites, the failure displacement is larger than that of SiC_f/SiC composites. This implies that with the introduction of lamellar Nb_2AlC as toughening phases, the crack mechanism occurred in the composites provided a fracture resistance to the crack propagation [11].

Table 1 Mechanical properties of the SiC_f/SiC and SiC_f/SiC-Nb_2AlC composites

Sample	Density (g/cm^3)	Open porosity(%)	Bending Strength (MPa)	Fracture Toughness ($MPa \cdot m^{1/2}$)
SiC_f/SiC	2.58	1.41	834.3	18.59
SiC_f/SiC-Nb_2AlC	2.61	1.15	971.4	24.17

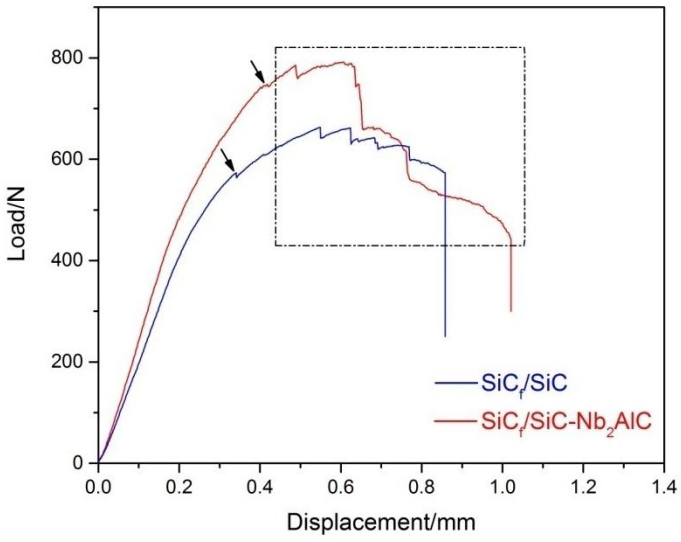

Figure 3 Load-displacement curves of SiC_f/SiC and SiC_f/SiC-Nb_2AlC composites from flexural strength test

Figure 4 presents the crack propagation path of SiC_f/SiC and SiC_f/SiC-Nb_2AlC composites after SENB test. Figure 4(1) shows the penetration crack of SiC_f/SiC composites with less-tortuous path. The crack propagation directly through the whole materials and finally leads to a catastrophic failure of structure. As can be seen in Figure 4(2), SiC_f/SiC-Nb_2AlC composites display more deflecting and tortuous propagation path. Figure 4(3) and (4) are the magnified images of the marked area in Figure 4(2). In the loading process, the fracture modes of crack deflection will absorb lots of energy and favor the improvement of flexural strength and fracture toughness of the materials [12]. Figure 5 (1) shows the fracture surface of SiC_f/SiC-Nb_2AlC composites, from which the morphology of ductile fracture occurred in Nb_2AlC toughened SiC matrix. The Nb_2AlC phase is characterized by its lamellar structure. In Figure 5(2), the pull-out of the lamellar Nb_2AlC grains was also observed, which can improve the fracture toughness of the materials. It's worth noting that neither delamination nor kinking can be observed in Nb_2AlC grains, which are relative to the direction of stress [4].

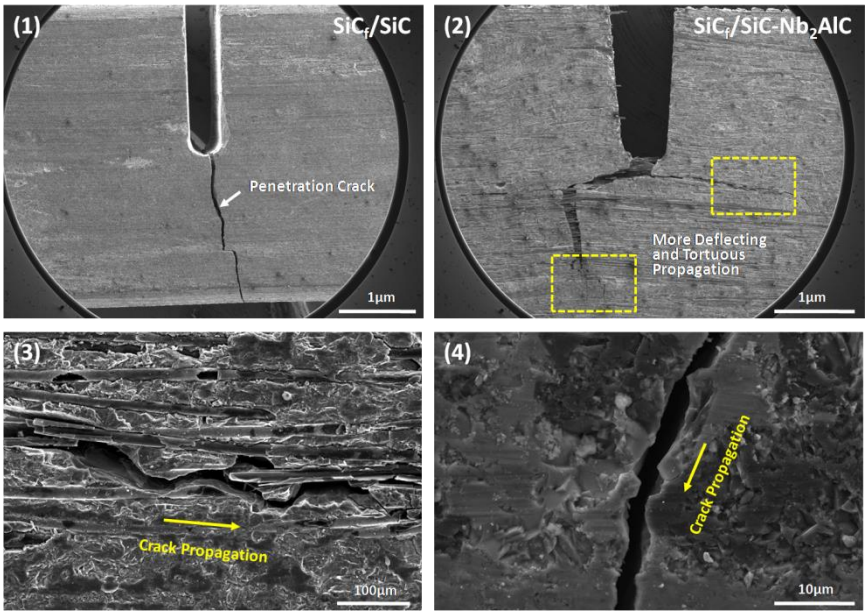

Figure 4 Crack propagation path of SiC_f/SiC and SiC_f/SiC-Nb_2AlC composites after SENB test

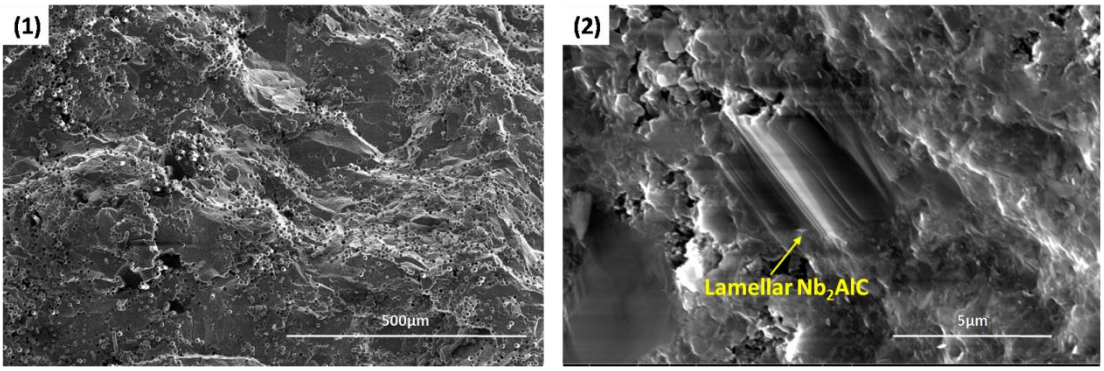

Figure 5 SEM images of (1) fracture surface of SiC_f/SiC-Nb_2AlC composites; (2) grain's pull-out

4. Conclusion

The dense SiC_f/SiC-Nb_2AlC composites were fabricated by MI method. The lamellar Nb_2AlC grains as the reinforcing agents exhibit significant strengthening and toughening effect to the SiC matrix and the composites show excellent mechanical properties. The flexural strength and fracture toughness of the SiC_f/SiC-Nb_2AlC composites reach 971.4 MPa and 24.17 MPa $m^{1/2}$ respectively, which is greatly higher than that of SiC_f/SiC composites.

References

1. J. Jiao, M.W. Chen, "New generation of high-temperature material for engine-preparation, property and application of ceramic matrix composites," *Aeronautical Manufacturing Technology*, Vol. 451, No.7, 62–69, 2014.
2. K. Rivera, J. Rhoat, T. Muth, O. J. Gregory, M. Ricci, "Novel temperature sensors for SiC-SiC CMC engine components," *Journal of Materials Research*, Vol.32, No. 17, 1–7, 2021.
3. N. P. Padture, "*In situ*-toughened silicon carbide," *Journal of the American Ceramic Society*, Vol. 77, 519–523, 1994.
4. M. W. Barsoum, T. El-Raghy, "The MAX phases: unique new carbide and nitride materials," *Journal of American Scientist*, Vol. 89, 334–343, 2001.
5. T. El-Raghy, M. W. Barsoum, "Processing and mechanical properties of Ti_3SiC_2: part I, reaction path and microstructure evolution," *Journal of the American Ceramic Society*, 82, 2849–2854, 1999.
6. I. D. Kovalev, P.A. Miloserdov, V.A. Gorshkov, D. Yu. Kovalev, "Synthesis of Nb_2AlC MAX phase by SHS Metallurgy," *Russian Journal of Non-Ferrous Metal*, Vol.61, No.1, 126–131, 2020.
7. P. A. Miloserdov, V. A. Gorshkov, I. D. Kovalev, D. Y. Kovalev, "High-temperature synthesis of cast

materials based on Nb_2AlC MAX phase," *Ceramic International*, Vol.45, 2689–2691, 2019.

8. Y. R. Zhou, J. Jian, J. H. Yang, X. X. Lv, Z. Y. Jiang, R. Yang, H. Liu, Y. Gao, "Growth of lamellar Ti_3SiC_2 in SiC matrix by the reaction of Si melt with C-TiC preform," *Materials Chemistry and Physics*, Vol. 267, 124665, 2021.
9. H. Liu, J. H. Yang, Z. M. Chen, X. D. Lang, J. Jiao, "Microstructure and properties of SiC_f/SiC composites fabricated by melt infiltration process", *Aerospace materials and technology*, Vol. 6, 48–54, 2020.
10. W. Zhang, N. Travitzky, C. F. Hu, Y. C. Zhou, P. Greil, "Reactive hot pressing and properties of Nb_2AlC," *Journal of the American Ceramic Society*, Vol. 92, No. 10, 2396–2399, 2009.
11. L. Wang, X. W. Yin, X. M. Fan, P. Greil, N. Travitzky, "$Ti_3Si(Al)C_2$-based ceramics fabricated by reactive melt infiltration with $Al_{70}Si_{30}$ alloy," *Journal of European Ceramic Society*, Vol. 34, 1493–1499, 2014.
12. Y. Cheng, C. Liu, P. Hu, B. Q. Sun, P. T. Hu, C. Ma, C. Fang, D. Y. Zhang, J. X. Feng, S. Y. Du, "Using PyC coated short chopped carben fiber to tackle the dilemma between toughness and strength of ZrC-SiC," *Ceramics International*, Vol. 45, 503–509, 2013.

Influence of Raw Material Ingredient on the Preparation of SiC Nanofibers

*Zhuo Yu Jiang[1,2], Qi Li[1,2], Yi Ran Zhou [1,2] and JianJiao[1,2]**

[1]National Key Laboratory of Advanced Composites, AECC Beijing Institute of Aeronautical Materials, Beijing 100095, China

[2]Surface Engineering Division, AECC Beijing Institute of Aeronautical Materials, Beijing 100095, China

The corresponding author's e-mail address: jiao.jian@biam.ac.cn

Abstract: In this work, the synthesis of silicon carbide (SiC) nanofibers was conduct on carbon fiber substrate by utilizing mixture powder consisting of Si and SiO_2 as raw material. During the synthesis process, SiO vapour was generated, which participated in the reaction of activated carbon source to generate SiC nanofibers. Then, the effect of mixing ratio of Si powder and SiO_2 powder on the preparation of SiC nanofibers was studied. Experimental results showed that mixture powder consisting of Si and SiO_2 reacted obviously when the experimental temperature rose above 1688K, and subsequently the SiC nanofibers were formed on carbon fiber substrate. When the mixing ratio of Si powder and SiO_2 powder was 2:1, excess Si vapour was generated at elevated temperatures and the reaction of Si vapour with carbon fiber substrate become more obvious, with the weight gain rate of carbon fiber substrate reaching a maximum of 8.8%. When the mixing ratio of Si powder and SiO_2 powder was 1:2, the weight gain rate of carbon fiber substrate was close to 5% and optimum linear homogeneity of the nanofibers was achieved.

Introduction

SiC nanowires have been suggested as reinforcement materials to enhance the strength and toughness of the composites, owing to their high strength and excellent chemical stability. When nanofibers are introduced into the brittle matrix of the composite, the crack extension distance in the matrix will be prolonged, so the matrix is effectively strengthed and toughened by the SiC nanowires. Further, the mechanical properties of the composite will be improved [1-2]. Meanwhile, the passage to the interior of the composite for oxygen molecules will be blocked due to the introduction of nanofibers, therefore another benefit of which is to improve

the oxidation resistance of the composite material at elevated temperature [3].

At present, there are many methods for SiC nanofibers preparation, such as solution blowing, chemical vapour deposition, in situ Growth, thermal evaporation process, carbon-thermal reduction process, et al [4-5]. Mostly, the nucleation and growth of SiC nanowires follow the vapor-liquid-solid (VLS) mechanism with the catalytic effect of metal monomers, such as Ni, Au, La, Fe, et al [6]. Another preparation methods follow the vapor-solid (VS) growth mechanism, which is not necessary for metal catalyst as the growth power source. During the preparation of the VS mechanism, the reaction gas is formed in the high temperature region by evaporation, chemical reduction or gas phase reaction, and is transported to the low temperature region to nucleate through the inert gas stream, which will be involved in the growth of nanofibers, which nanofibers have a high purity due to the absence of catalyst involvement in the reaction.

Wu[7] and Dai[8] have synthesized the SiC nanofibers on carbon fabrics using a catalyst-free methond with the Si and SiO_2 powder mixture as the raw material. Li[9] has fabricated the one-dimensional SiO_2@SiC shell-core nanowires on SiC substrate without any catalyst using a laser sintering method. A novel synthesis route of nano-scale and submicro-scale silicon carbide (SiC) whiskers on C/C composites was reported by Niu[10], in its research, the SiC whiskers was fabricate by the using of hydrogen silicone oil and divinylbenzene as the organic precursor. Lv[11] prepared SiC whisker-reinforced SiC ceramic matrix composites (SiC_W/SiC) by the combination of spray drying, binder jetting and chemical vapor infiltration (CVI). In addition, some researchers have also achieved the reinforcement of composites by introducing SiC nano-reinforcements. Liu[12] prepared the an oxidation protective SiC whisker-toughened mullite coating by introducing SiC nano-whisker to mullite coating precursor solution, and the results show that incorporating proper amounts of SiC whiskers can significantly improve the thermal cycling resistance of the mullite coating. However, the investigation of raw material components on the preparation effect of SiC nanofiber by VS mechanism was rarely reported, this study can provide some valuable information.

Experiment Procedure

2.1 Reaction process of synthesizing SiC nanofiber

Based on available public reports [3,13], the mixture of high-purity Si and SiO_2 powder

used as the raw materials for growth of SiC nanowires. Which maybe include two main stages of reaction process. The first step, the SiO vapour would be generated by the reaction between Si and SiO_2 powders at elevated temperatures. Under the atmosphere of SiO vapour, the reactions between gaseous SiO and carbon atoms on the surfaces of carbon fabric substrates could synthesize the SiC nuclei, which could be acted as the seeds and initiate the growth of SiC nanowires at the second step. With the growth of SiC nanowires, the carbon atoms on the surfaces of carbon fabric substrates could not ensure the continuous growth process. Thus, the continuous growth of long SiC nanowires might be supported by the other reaction between SiO and CO at the second step. At the same time, there might be occurring some secondary reactions during the reaction process in the furnace chamber, as shown in Figure 1.

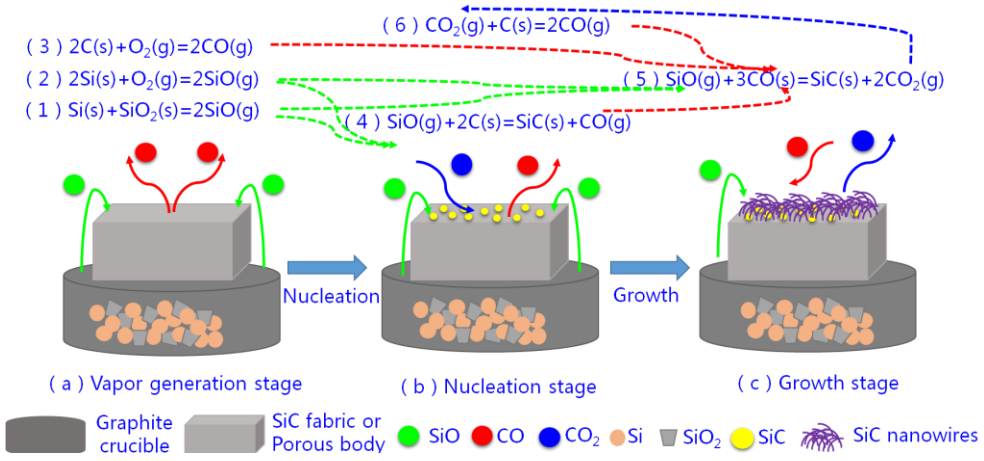

Fig.1 Schematic illustration for the growth process of SiC nanowies

2.2 Material and Procedure

Commercially available Si and SiO_2(Purity: ＞99%) powder were used as the raw materials. These powders were obtained with different molar ratios for Si:SiO_2, such as 1:2, 1:1 and 2:1. High energy ball millings were performed on these powder mixtures by a centrifugal ball mill, with a speed of 200 rpm for 10h by using WC balls (diameter:10mm) and ethanol as the milling media. Then, the ball-milled slurry dried by drying oven at 373K for 2h[13]. On the other hand, in order to obtain a source of carbon, small carbon fabric (130mm×120mm) as substrates for the growth of SiC nanofiber , which were cleaned with distilled ethanol and dried at 393K for 1h.

In the preparation of SiC nanofibers, the mixture of high-purity Si and SiO_2 was put into a graphite crucible. The carbon fabrics were suspended over the mixture powder in the graphite

crucible with a graphite lid. And then the whole assembly was placed into the center of a resistance heating furnace. The furnace was heated with heating rate of 10 K/min and maintained for 1h. During the whole reaction period, argon was introduced into the furnace to maintained constant pressure.

After deposition, the furnace was cooled down to room temperature naturally. The carbon fabric substrates were taken out of the furnace to weigh their mass, the mass change percentages (△M) of the substrates were calculated by using the following equation：

$$\triangle M=（M_1-M_0）/M_0\times 100\%$$

Where M_1 is the mass of carbon fabric after the growth of nanofibers, M_0 is the mass of carbon fabric before the growth of nanofibers.

2.3 Specimen characterizations

These powder was investigated by using differential thermal analysis in nitrogen at a heating rate of 10K/min (DTA, STA 449F3). The morphology of nanofibers were examined by scanning electron microscopy (SEM, Nova Nano SEM450). The phase composition of the nanofibers were identified by X-ray Diffraction (XRD, RigakuD-max02500) with Cu Ka radiation，the scanning range was 10°~90°. The IR spectra were collected using grating infrared spectrometer (Hitachi 285) by the KBr pellet method.

Result and discussion

The high magnification images and EDS analysis of raw material powders are presented in Fig.2. It can be seen that the morphological differences between the two kinds of powders in the mixture are more obvious, one type of spherical particle and the other type of block. The energy spectrum analysis of the two particles show that the atoms of Si and O in the spherical particles is close to 1:2, which is consistent with the stoichiometric ratio of SiO_2, indicating that the spherical particles are SiO_2 powder. The bulk particles are considered as Si powder, since the EDS results show that Si atoms in the block particles is much more than O atoms.

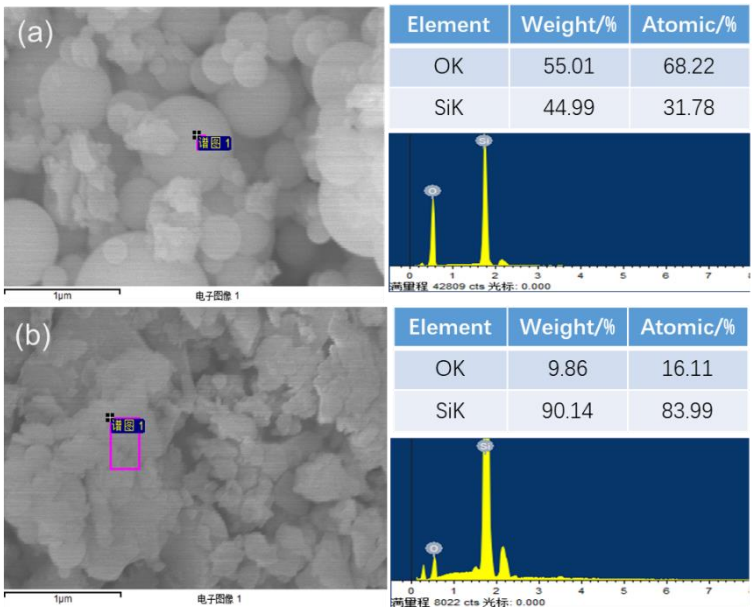

Fig.2 High magnification images and EDS analysis of raw material powders

Figure 3 shows the microscopic morphology of the mixture powders with varying molar ratios for SiO_2 to Si. Figures (a/b), (c/d) and (e/f) correspond to the molar ratios of 1:2, 1:1 and 2:1, respectively. It can also be seen that the Si and SiO_2 powders in the three kinds of mixture powders are relatively homogeneous without obvious agglomeration phenomenon.

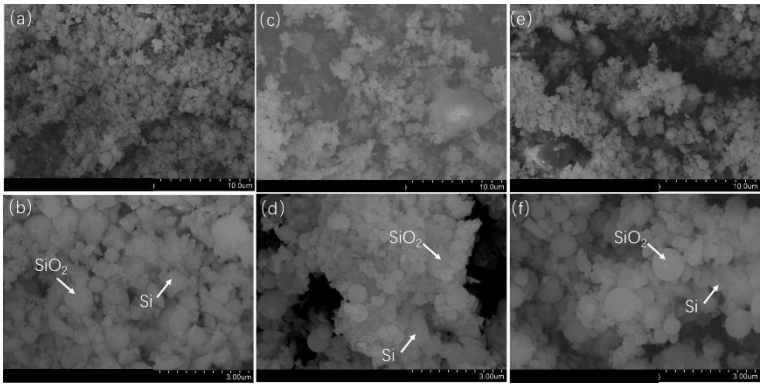

Fig.3 The microscopic morphology of three kinds of mixture powder

(a/b) $mol_{(SiO2)}$： $mol_{(Si)}$=1： 2, (c/d) $mol_{(SiO2)}$： $mol_{(Si)}$=1： 1, (e/f) $mol_{(SiO2)}$： $mol_{(Si)}$=2： 1

The result of the differential thermal analysis of the mixture powder is shown in Fig.4. As can be seen that the peak of DTA curve is located at approximately 1688K. At this temperature, the solid Si would melt and react with SiO_2. As a result, a large amount of gas phase reactants are generated [14-15]. Therefore, the process temperature for the preparation of SiC nanofibers with Si and SiO_2 as raw materials could be set at 1693K.

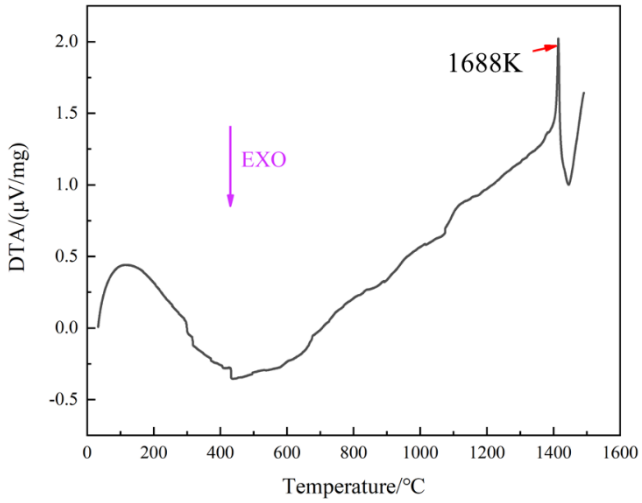

Fig.4 The differential thermal analysis of the mixture powder

Figure 5 shows the microscopic morphology of the SiC nanofibers prepared at 1693K by using three kinds of mixture powders. Figures (a/b), (c/d) and (e/f) correspond to SiC nanofibers prepared using mixture powders with molar ratios of 1:2, 1:1 and 2:1 for SiO_2 to Si, respectively. As shown in figure (a/c/e), the concentration of the nanofibers grown with the three mixture powders are close to each other under the same process conditions. However, nanofibers have different morphologies. In Figure (b), except for some of the curve, twisted and axial screw structures, the rest of the nanofibers have good diameter uniformity. However, figure (d) shows a large variation in fiber diameter and many curve structures, which have poor linear homogeneity. The linear uniformity of the nanofibers is significantly improved in figure (f), which has a diameter of about 200 nm.

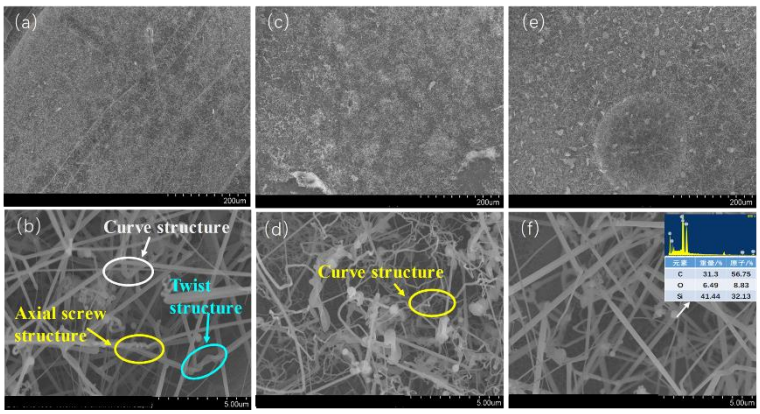

Fig.5 The images of SiC nanofibers prepared using three kinds of mixture powders

(a/b) $mol_{(SiO2)}$: $mol_{(Si)}$=1: 2, (c/d) $mol_{(SiO2)}$: $mol_{(Si)}$=1: 1, (e/f) $mol_{(SiO2)}$: $mol_{(Si)}$=2: 1

The XRD patterns of the SiC nanofibers are displayed in figure 6. As can been seen, three obvious diffraction peaks located at 35.7°, 60.1° and 71.9° are observed, corresponding to the

SiC (111), SiC (220) and SiC (311) diffraction planes, respectively. Which are well matched with the cubic structures of β-SiC crystal. Furthermore, the low intensity peaks at 2θ=33.67°are observed, which SiC nanofibers are prepared using a mixture powders with molar ratios of 1:2 and 1:1 for SiO_2 to Si, and marked with SF peaks. Which is usually caused by stacking faults formed during the growth of SiC crystals. The growth of SiC nanofibers is mainly affected by the fluctuation of reaction gas flow, reaction gas concentration gradient, temperature gradient and thermal stress. Which will lead to the formation of phase difference and misalignment of adjacent crystalline surfaces, so stacking layer dislocation is a relatively common phenomenon in the growth of SiC crystals.

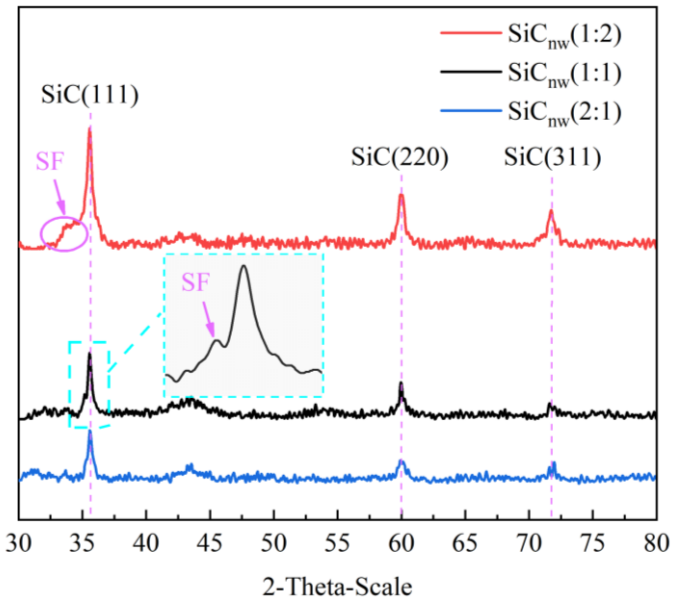

Fig.6 XRD pattern of the SiC nanofiber prepared with the three mixture powders

The FTIR spectrums of the three kinds of mixture powder after sintering at 1693K for 1hour are shown as figure 7. The characteristic peak positions are centered at 804 cm^{-1} and 1100 cm^{-1}, which are generally to assigned to stretching vibrations of S-C and Si-O-Si bonds, respectively[18]. The intensity of the S-C bond vibrational peak is significantly stronger than that of the Si-O-Si bond with the molar ratio of 1:2 for SiO_2 to Si. The vibrational peaks of Si-O-Si bond is close to that of the S-C bond with the molar ratio of 1:1 for SiO_2 to Si. The vibrational peak of the Si-O-Si bond is significantly stronger than that of the S-C bond with the molar ratio of 2:1 for SiO_2 to Si. It indicates that the residual amount of SiO_2 in the three mixture powders is gradually increasing after sintering, therefore, the mixture powder in the reaction process is sufficient. Combined with Fig. 5, it can be seen that the best linear homogeneity of the SiC nanofibers are prepared with molar ratios of 2:1 for SiO_2 to Si .

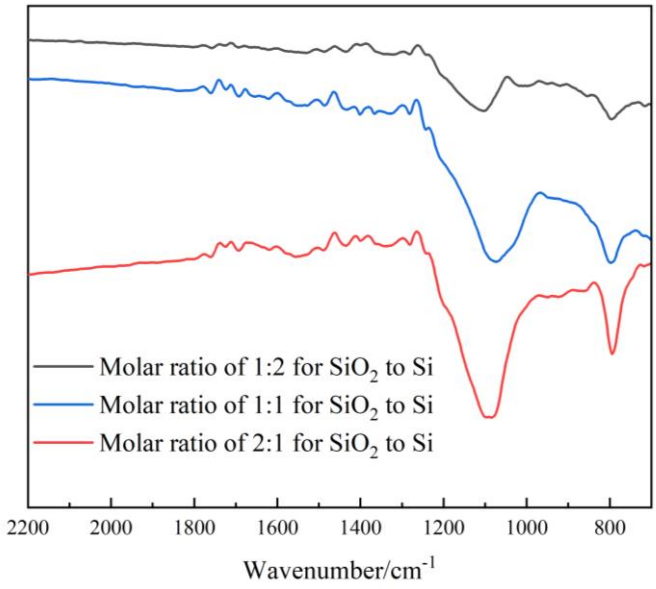

Fig.7 The FTIR curves of three kinds of mixture powders after sintering

The weight gain rates of the carbon fiber substrates are shown in Figure 8. When the mixture powder with the double amount of Si as SiO_2 is used as the raw material, this carbon fiber substrate is achieved the highest rate of weight gain and reached 8.8% after the experiment. However, the weight gain of the other two groups of carbon fiber substrates are only 4-5%. Combined with the low magnification SEM photographs (a/c/e) in Fig. 5, there is no significant difference for the density of SiC nanofibers prepared with the three kinds of mixture powders. Therefore, the higher weight gain may be due to the reaction of the fiber fabric substrate with Si vapour generated by the evaporation of excess Si powder at high temperatures.

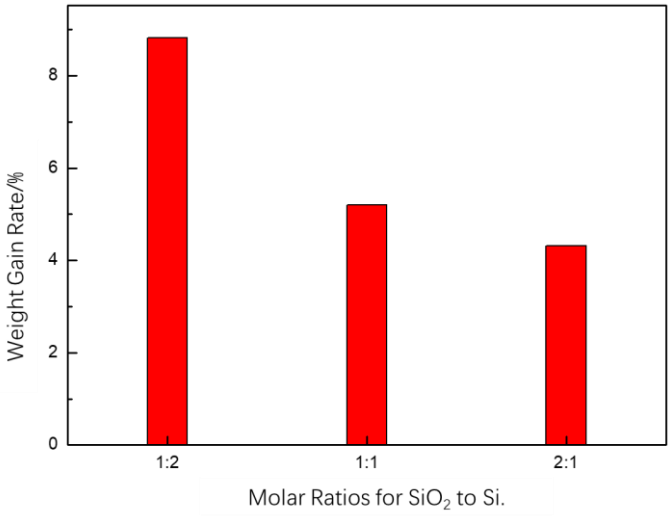

Fig.8 The weight gain rate of the carbon fiber substrates

The EDS mapping results for the element distribution of C and Si on carbon fiber

substrates are shown in Figure 9. It can be seen that two areas with significant differences in brightness are found in the high magnification photographs of the fiber surface, when which fibers have been placed in the silicon vapour environment at 1693K for 1h. The mapping results on the fiber surface show the presence of both C and Si element, which are distributed more uniformly. And the proportion of Si element is about 24.5%. This is due to the reaction between excess silicon vapor, which is generated by the evaporation of Si powder in the mixture, and carbon on the fiber surface [19]. This will cause an increase in the mass of the carbon fiber substrate without SiC nanofiber synthesis, which is detrimental to the strength of the carbon fiber substrate. Therefore, this phenomenon is more pronounced in the experimental group where the molar ratio of Si to SiO_2 is 2:1.

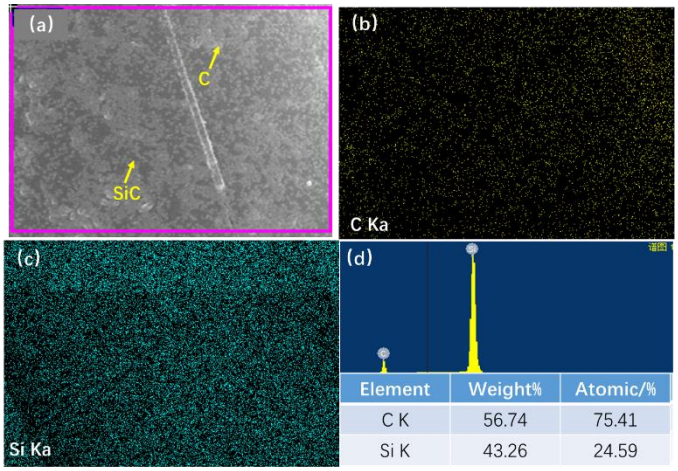

Fig.9 EDS mapping results for the element distribution of C and Si

Conclusion

In our work, we successfully prepared SiC nanofibers on carbon fiber substrate based on the vapour-solid (VS) mechanism using mixture powder consisting of Si and SiO_2 as raw material. . When the mixing molar ratio of Si powder and SiO_2 powder was greater than 1, i.e., the amount of Si powder was more than that of SiO_2 powder, excess Si vapour generated from Si powder reacted with carbon on the fiber surface. When the mixing molar ratio above was 2:1, the weight gain rate of carbon fiber substrate was the highest, which was detrimental to the strength of the carbon fiber substrate. Furthermore, the SiC nanofibers synthesized under such experimental condition(i.e., the mixing molar ratio of Si powder and SiO_2 powder was 2:1) have a spiral, bending and twisting structure in terms of microscopic morphology. These outcomes indicated that it's not an alternative option for synthesizing silicon carbide fibers

when the mixing molar ratio of Si powder and SiO_2 powder was 2:1. When the mixing molar ratio of Si powder and SiO_2 powder was 1:2, we achieved SiC nanofibers with optimum linearity and uniform fiber diameter, which should be regarded as a potential option for synthesizing silicon carbide fibers.

References

[1]Chu Y H, Fu Q G, Li H J, et al. Effect of SiC Nano-wires on the Mechanical and Oxidation Protective Ability of SiC Coating for C/C Composites, Journal of the American Ceramic Society. 2012, 95(2): 739-745.

[2]Hua Y, Zhang L, Cheng L, et al. Microstructure and High Temperature Strength of SiC_W/SiC Composites by Chemical Vapor Infiltration [J]. Materials Science & Engineering: A (Structural Materials: Properties, Microstructure and Processing), 2010, 527(21-22):5592-5595.

[3]Dai J, Sha J, Shao J, et al. In-situ Growth of SiC Nanostructures and Their Influence on Anti-oxidation Capability of C/SiC Composites, Corrosion Science, 2017, 124(0):71-79.

[4] Kim B. G., Kim B. S., Choi S. M., et al. Defect-free SiC nanowires grown from Si-deposited graphite by thermal annealing: temperature-dependent nucleus formation and nanowire growth behaviors. Crystengcomm.2016.18.5910-5915.

[5]Zeng S. J. In-situ grown SiC nanowires and its application in SiC_f/SiC composites.[D]. National University of Defense Technology.2015.

[6]Li Z.J., Gao W. D., Meng A L., et al. Large-scale synthesis of SiC nanorods via periodic VLS mechanism under Fe-assisted condition [J]. Jorunal of Functional Materials, 2009, 40(9):1549-1551.

[7]Wu Y. J., Zhang Y. F., Yang Z. X., et al. Catalyst-free method of preparing β-SiC nanowhiskers by using carbon whiskers [J]. Journal of Inorganic Materials, 2005 (03):740-744.

[8]Dai J. X., Zhang Z. F., Wang Y. C., et al. In situ growth of SiC nanofiber on carbon fibers[J]. Chinese Journal of Inorganic Chemistry, 2015, 31(12): 2379-2384.

[9]Li X , Huang J , Lu J , et al. Fabrication and characterization of SiO_2@SiC shell–core nanowire prepared by laser sintering[J]. Journal of Materials ence, 2017, 52(6):1-9.

[10] Niu F. X.. Wang Y. X. . Synthesis and characterization of nano-scale and submicro-scale silicon carbide whiskers on C/C composites [J]. Journal of Alloys and Compounds, 2017,714(0),270-277.

[11] Lv X. Y., Ye, F. Cheng L. F., et al. Fabrication of SiC whisker-reinforced SiC ceramic matrix composites based on 3D printing and chemical vapor infiltration technology, Journal of the European Ceramic Society,2019,39(11),3380-3386,

[12] Wen Z. L. Xiao P., Li Z., et al. Thermal cycling behavior and oxidation resistance of SiC whisker-

toughened-mullite/SiC coated carbon/carbon composites in burner rig tests [J]. Corrosion Science, 2016, 106(0), 179-187.

[13]Dai J, Sha J, Zu Y, et al. Synthesis and Growth Mechanism of SiC Nano fibres on Carbon Fabrics, Crystengcomm, 2017, 19(9), 1279-1285.

[14] Gao Y H, Bando Y, Kurashima K, Sato T. J Mater Sci.2002;37: 2023–2029.

[15] Rosenqvist T, Tuset JKR. Metall Mater Trans B 1987;18: 471–472.

[16]Men J, Liu Y, Luo R, et al. Growth of SiC nanowires by low pressure chemical vapor infiltration using different catalysts [J]. Journal of the European Ceramic Society, 2016:36(15),3615-3625.

[17]Fu Q.G. ,Li H.J.,Shi X. H. S, et al. Microstructure and growth mechanism of SiC whiskers on carbon/carbon composites prepared by CVD[J]. Materials Letters, 2005, 59(19-20):2593-2597.

[18] Kim R. J., Qin W. P. Wei G. D. et al. A simple synthesis of large-scale SiC-SiO_2 nanocables by using thermal decomposition of methanol: Structure, FTIR, Raman and PL characterization [J]. Journal of Crystal Growth, 2009, 311(18):4301-4305.

[19] Hart Amelia H C, Koizumi Ryota, Hamel John, et al. Velcro-Inspired SiC Fuzzy Fibers for Aerospace Applications[J]. ACS applied materials & interfaces, 2017,9 (15).13742-13750.

A novel model for predicting the equivalent elastic constants of needled C/SiC composites considering manufacturing defects

Wang Junlong[1], *Sun Shiyong*[1*], *Yang Rui*[1], *Qian Wei*[2]

[1]School of Mechanical Engineering, Dalian University of Technology, China

[2]School of Aeronautics and Astronautics, Dalian University of Technology, China

Abstract: The properties of ceramic matrix composites (CMCs) are discrete and difficult to predict owing to the heterogeneity and manufacturing defects. A novel model for predicting the equivalent elastic constants of needled C/SiC composites was proposed. The manufacturing defects caused by needling process were taken into account in the model. Based on the Micro-CT scanning method, the microstructure characteristics of the composites were analyzed by using the three-dimensional reconstruction software. Needled C/SiC composites were mainly divided into three parts: unidirectional fiber bundle layer, random short fiber layer and needled fiber bundle. Two kinds of manufacturing defects, the pores and the fiber deflections, were simplified and characterized. Two scale defects of pore, which were described as equivalent inclusion and tetrahedrons were considering in the model. The mesoscale pores were described as tetrahedrons. Two deflection angles were definite to describe the effects of fiber deflections. Three mesoscopic models were established by considering different quantity state of defects, respectively. In these models, the elastic properties of each part were predicted theoretically. Then, the models were homogenized by using periodic boundary conditions. And the equivalent elastic constants of the needled C/SiC composites were obtained. The comparison between the prediction results of the three models and the experimental data showed that the mesoscopic models considered the manufacturing defects agreed with the experimental data best. At last, discussions on the influences of different process parameters on the elastic constants of needled C/SiC composites show that the process parameter optimization should consider both out-of-plane and in-plane performance comprehensively in the preparation process.

Key words: Manufacturing defect; Pore; Fiber deflection; Periodic boundary condition

1. Introduction

Ceramic matrix composites (CMCs) are widely used in aerospace engines, nozzles and other high-temperature working environments due to their high strength and excellent heat

resistance [1]. However, the manufacturing process of depositing ceramic matrix on laminated fiber preforms can easily generate defects that lead to low interlaminar bonding strength. The process of needling in laminated preforms is an effective method to improve the interlaminar bonding strength of CMCs in the thickness direction. In addition, compared to woven CMCs, needled CMCs have broad application prospects because of their simple preparation and low manufacturing cost [2-3].

However, the manufacturing process of needled CMCs determines that the internal microstructure has a large number of manufacturing defects such as the pores and the fiber deflections. These defects are mainly caused by two aspects: (1) the manufacturing process of the preforms: needling is performed on the laminated random short fiber-web and fiber fabrics along the direction of thickness. In the process, some short fibers and long fibers are deflected in and out of the plane, forming fiber bundles in the thickness direction [4]. (2) The deposition process of ceramic matrix: the fiber preforms are placed in the reaction chamber, in which the reaction gas permeates into the preforms at high temperature and produce chemical reaction to deposit the ceramic matrix on the fiber surface [5]. During the deposition process, the fibers retain the deflection state, which is not conducive to the deposition effect of the matrix, resulting in the formation of pores with different sizes in the composites [6].

Due to technical reasons, there are inevitably manufacturing defects in needled CMCs. Moreover, the manufacturing defects have the characteristics of multi-source and multi-scale, and the ceramic matrix is greater sensitivity to defects. These two reasons make it more difficult to evaluate the performance of needled CMCs. In the production process, manufacturing defects are important indicators to control the manufacturing quality of parts. Therefore, defect characterization and performance evaluation have become the focus of current research [7]. At present, the studies on manufacturing defects of needled CMCs have focused on pores and fiber deflections. Firstly, theoretical prediction and numerical simulation are two main research methods for pores in needled CMCs. The theoretical prediction method studies the effects of porosity on the composite properties by treating pores as equivalent random inclusions [8-9]. This method is simple and efficient, but the pore morphology in needled CMCs is not considered in the analysis process. In the simulation method, the microscopic pores are observed to establish the simulation model of needled CMCs. The influences of the morphology and distribution characteristics of the pores on the composite properties are

accurately analyzed. This method has a good application for the pores of needled CMCs in a microscale, but for the analysis model with trans-scale, it is easy to produce too much calculation and other problems [10]. The research on fiber deflection defects focuses on the origin of defects and the influence law of performance. Jia et al [11]. Studied the deflection and other damage caused by needling process on fibers by simulating the needling process. Compared with the regular deflections of the woven composites, the fiber deflections of needled CMCs are unpredictable and random. Therefore, it is difficult to study the effects of fiber deflections on the properties of needled CMCs. At present, it is relatively common to study the fibers by means of observation and function characterization at the mesoscale. In this method, combined with experimental observation, some mesoscale respective volume elements with a single defect were proposed, and the stiffness characteristics of three-dimensional needled composites were predicted by means of secondary homogenization [12-14]. The results show that this method can well characterize the process characteristics such as needle arrangement and accurately predict the properties of composites. However, this method has the problems of complex modeling process and large amount of calculation.

In conclusion, the microstructure of needled CMCs presents quasi-periodic and multi-scale, and the initial defects are related to each other. The current research has not formed a comprehensive analysis model, so the influences of the original defects caused by the manufacturing process on the overall properties of composites are still worthy of further investigation.

In this paper, needled C/SiC composites were the research object. The morphology and distribution of manufacturing defects in needled C/SiC composites were analyzed on the basis of Micro-CT. A microscopic representative volume element (RVE) model of needled C/SiC composites was established by focusing on two typical defects: fiber deflections and microscopic pores. The elastic constants of needled C/SiC composites with different scale manufacturing defects predicted by combining theoretical prediction with periodic boundary conditions. Compared with the experimental results, the effectiveness of the proposed model was demonstrated. Based on this model, the effects of needling process parameters on the elastic constants of needled C/SiC composites were discussed.

2. Experiment on needled ceramic matrix composites samples

2.1 Samples preparation

The samples of needled CMCs were provided by Shenyang Institute of Metal Research, Chinese Academy of Sciences. The reinforced phase was the 0/90 ° carbon fiber preform after needling. The matrix was SiC which has been densified several times by chemical vapor infiltration process. The porosity of the composites was 10%~15%. According to the experimental standard of GJB 6475-2008, the needled C/SiC composites were cut into mechanical properties test specimens. The sample sizes were shown in Figure 1.

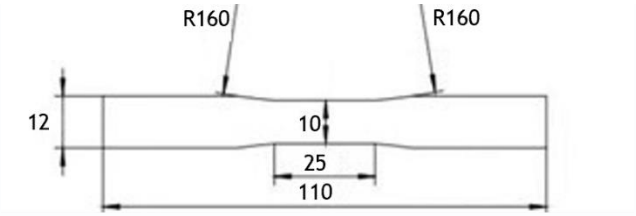

Figure. 1 Test specimens of needled C/SiC composites for mechanical properties

2.2 Determination of porosity and model parameters

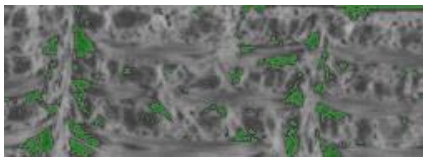

Figure. 2 Pore identification using 3D reconstruction software

Three-dimensional reconstruction software Mimics was used to analyze the slicing data of needled C/SiC composite by Micro-CT scan. In the Mimics software, the gray scale maps were employed to identify the pores as shown in Figure. 2. The mesoscale pore volume fraction was 2% through the statistics. In the area of 22.5*22.5mm², the needled fiber bundles presented uniform distribution in the thickness direction and a total of 125 bundles were identified. Therefore, the sizes of RVE were assumed. Meanwhile, the measurement tool of the software was adopted to take the average of multi-point measurement.

2.3 Experimental Process

The static tensile tests were carried out on WDW-20E material testing machine. The displacement loading method was used in static tensile test, and the loading rate was 0.1mm/s. The tests were carried out in room temperature and air atmosphere. During the test, resistance strain sensors with 10mm grid length were used to record the deformation of the material in

real time.

Figure. 3 Tensile test process

3. Finite element model of needled C/SiC composites

3.1 Microstructure of needled C/SiC composites

Needled C/SiC composites are generally prepared by depositing the matrix on the preforms by chemical vapor infiltration (CVI). Figure.4 shows the slice images of the needled C/SiC composites in different planes by Micro-CT scanning. It could be seen from the figures that according to the fiber characteristic, the needled C/SiC composites could be divided into three regions: unidirectional fiber CMCs, random short fiber CMCs and needled fiber bundles along the thickness direction. The distribution of needled fiber bundles was quasi-periodic.

It could be seen from Figure 4 (a) that the ceramic matrix failed to sufficiently to deposit on the fibers in the X-Y plane due to the extrusion of unidirectional long fibers during the needling process. There were obvious deflections of unidirectional long fiber in-plane and large-scale triangular pores around the needled fiber bundles. However, these defects were obvious in the random short fiber area. Figure.4 (b) is a slice images of the Y-Z plane. In the Y-Z plane, the needling process caused the unidirectional fiber bundle to deflect across the short fiber region along the thickness direction. The deflection fiber hindered the deposition of the ceramic matrix. Thus, large-scale umbrella shaped pores were formed. In addition, Figure. 4(a) and (b) show that a large number of micro-pores exist in other areas besides the pores near needled bundle.

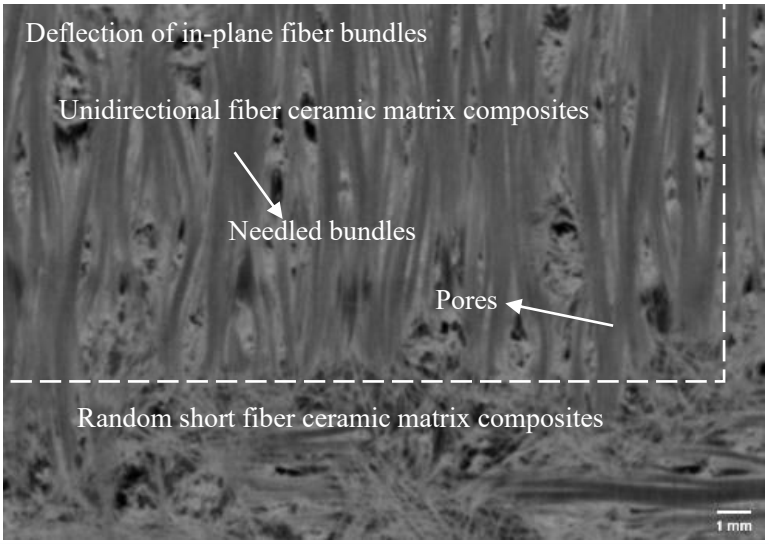

(a) Needled C/SiC composites microstructure of X-Y plane slice by Micro-CT method

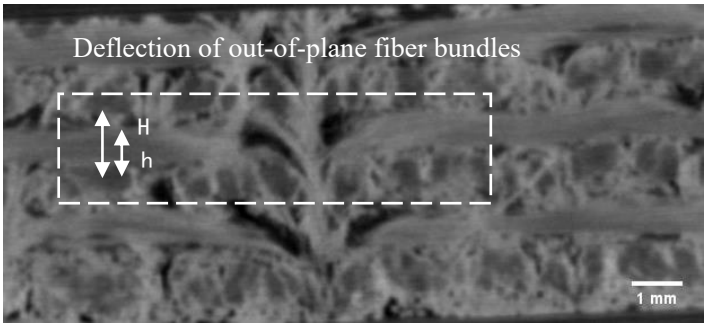

(b) Needled C/SiC composites microstructure of X-Z plane slice by Micro-CT method

Figure. 4 Microstructure of needled C/SiC composites

3.2 Model of needled C/SiC composites with manufacturing defects

Based on the observation and analysis of the above Micro-CT scanning results, the microstructure morphology and defect distribution law of the composites were obtained. The following hypotheses were proposed in this paper:(1) the needled position was uniform array distribution with periodicity. The needled fiber bundles, which were composed of long fibers and short fibers, had the same composition form and ran through the composite laminates. (2) The fiber deflection caused by needled produced mesoscale pores. The mesoscale pores only existed in the area near needling, and the fiber deflections were consistent in each layer.

Based on the above hypotheses, the RVEs of needled C/SiC composites microstructure which were divided into four parts: unidirectional fiber bundle layer, random short fiber layer,

needled bundle and mesoscale pores, were established in this paper as shown in Figure 5. The unidirectional fiber bundle layer was constituted by the unidirectional fiber and ceramic matrix. The random short fiber layer was constituted by the random short fiber and ceramic matrix. The needled bundle was the hybrid composites containing carbon short fiber and long fiber. The modeling process was as follows:

1. The cross-section shape of the needled bundle was simplified into a square. The side length of square was determined by parameter *a*. The size of the RVE was determined by parameter *L*. The thickness of random short fiber layer was determined by parameter h. The thickness of unidirectional fiber bundle layer was determined by *H-h*. The microstructure model I considering the needled bundle through the RVE was constructed, as shown in Figure 5(a).

2. Based on model I, out-of-plane deflection angle *b* and in-plane deflection angle *c* were introduced to simplify the characterization of out-of-plane and in-plane fiber deflection respectively. The in-plane deflection and the out-of-plane deflection were identified in the same region to realize the relationship between them. The microstructure model II considering the needle bundle and fiber deflection was constructed, as shown in Figure 5 (b);

3. On the basis of model II, the mesoscale pore whose morphology was characterized by *b* and *c* was further simplified as tetrahedron. Then the tetrahedral bottom area *s* in model III was expressed as:

$$S = \frac{a^2}{2\tan\frac{c}{2}}$$

In this work, it was assumed that the pore height was unchanged. And the pore only ran through a single unidirectional layer and a mesh layer, so the tetrahedral height *e* was expressed as

$$\mathrm{e} = H$$

Therefore, the single pore volume was expressed as:

$$V = \frac{1}{3}eS = \frac{a^2 H}{6\tan\frac{c}{2}}$$

According to pore morphology：

$$\tan b = \frac{2H\tan\frac{c}{2}}{a}$$

The microstructure model III considering needled bundle, fiber deflections and pores was constructed, as shown in Figure. 5(c).

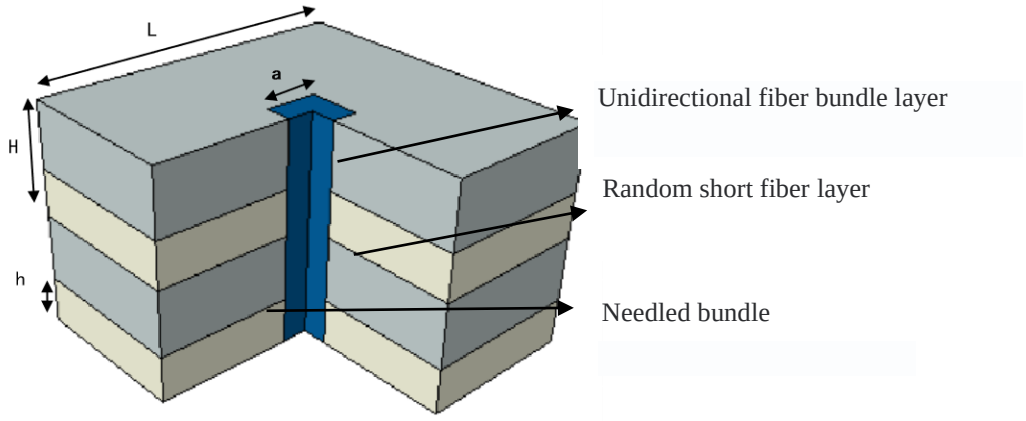

(a) Microstructural model I of acupuncture bundles

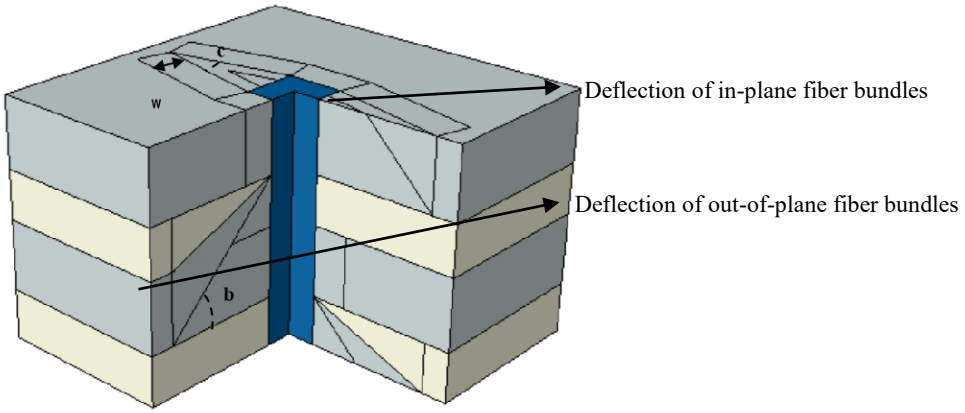

(b) Microstructural model II with acupuncture bundles and fiber deflection

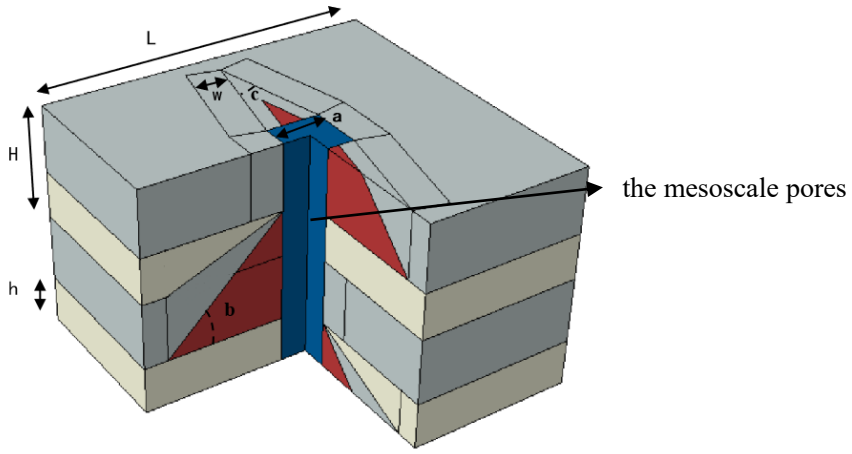

(c) Microstructural model III considering fiber bundles, deflection and porosity

Figure 5. Schematic diagram of RVE models of needled C/SiC composites with initial defects

3.3 Numerical method for predicting the elastic constants at different scales

According to the multi-scale characteristics of the manufacturing defects in needled C/SiC composites, the elastic parameters of the composites were predicted by quadratic homogenization method. In the first step, the microscopic pores were regarded as random spherical inclusions, which were uniformly mixed with the ceramic matrix to form two-phase materials. In this step, the Mori-Tanaka method was employed to study the influences of inclusion shape on the equivalent modulus [15-16]. The reduction effects of micro pores on matrix properties were taken into account in the theoretical prediction. Thus, the equivalent elastic parameters of matrix materials with pore defects were obtained. Then, considering the arrangement law of fiber reinforced phases in different regions, each region was regarded as a two-phase mixture of fibers and the above-mentioned matrix. Through the Mori-Tanaka method for long fibers and random fibers derived by Feng Xiqiao, the elastic parameters of each sub region in the RVE model were predicted. In the second step, the elastic parameters of each sub region were assigned to each part of the RVE model in 3.2. The macro elastic parameters of needled C/SiC composites were obtained by applying periodic boundary conditions on the model.

According to the experiment samples, the needled C/SiC composites were composed of carbon fiber and silicon carbide matrix. Table 1 shows the microscopic size parameters of RVE. The elastic parameters of other materials are shown in Table 2. The meso-component contents

of each region were shown in Table 3.

Table1 Microscopic size parameters of RVE

	H	h	w	L	a	b	c
Size parameters /mm	0.68	0.4	0.2	2	0.32	44°	25°

Table 2 Material properties of long and short fibers, ceramic matrix and pores

	E_1 /GPa	E_2 /GPa	E_3/ GPa	ν_{12}	ν_{13}	ν_{23}	G_{12}	G_{13}	G_{23}
Fiber	230	18.22	18.22	0.27	0.27	0.25	36.59	36.59	36.59
Matrix	350	350	350	0.3	0.3	0.3			
Chopped carbon fiber	30	30	30	0.25	0.25	0.25			

Table 3 Meso-component parameters of needled C/SiC composites

	Components	volume fraction
Unidirectional fiber bundle layer	Continuous fiber	60%
	Matrix	30%
	Pore	10%
Random short fiber layer	Continuous fiber	50%
	Matrix	40%
	Pore	10%
Needled bundle	Short fiber	30%
	Continuous fiber	30%
	Matrix	30%
	Pore	10%

4 Results and discussion

4.1 Verification of prediction model

The ply angle of needled C/SiC composite samples was 0/90°that meant in-plane parameters E1 was equal to E2, so E1 and E3 were used to evaluate the in-plane and out-of-plane properties, respectively. According to the above analysis method, the finite element method was used to predict the tensile elastic module of RVE. The material parameters of fibers, matrix and pores were substituted into the RVE model. The predicted results were compared with the experimental data.

As shown in Figure 6, among the three models proposed in 3.2, model I had the largest E1, because fiber deflections in plane were not taken into account. For model II, the in-plane performance declined slightly owing to fiber deflection, but out-of-plane deflection enhanced the out-of-plane performance. In-plane and out-plane properties of model III were obviously decreased towing to the introduction of the pores. Compared with the experimental results, the errors of E1 predicted by the three models were 8.1%, 6.8% and 2.65%, respectively. It indicated that the model III considering fiber deflection and pore defects conformed to reality better.

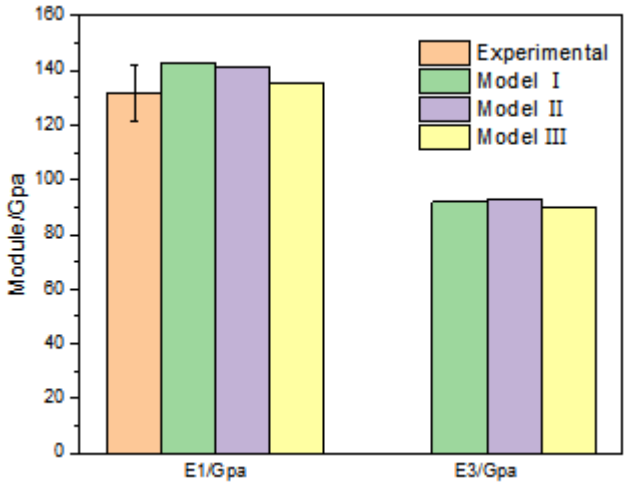

Figure.6 Comparison of prediction results and tests

4.2 Influences of needling process parameters on the composite properties

Previous study [3] and Micro-CT scanning have shown that the local microstructure of needled composites was mainly determined by the needling process of preforms. When the needle was inserted into the preforms, the needle squeezed the unidirectional fabric fibers to both sides and punctured some of them. The punctured fibers are deflected in the Z direction,

resulting in mesoscale pores and fiber deflections in the needled area. Therefore, the initial manufacturing defects caused by needling process led to the macro property changes of composites. Based on the above model III considering manufacturing defects, the effects of three process parameters, namely, needled bundles density, number of needled repeatedly and needled size, on the properties of composites were further discussed.

On the basis of the hypothesis, the needled density depended on the external dimension *L* of RVE. Figure 7 shows the effects of RVE dimension *L* on the elastic modulus of needled C/SiC composites. As shown in Figure 7(1), the increasing of RVE size led to decrease the deflection amount of in-plane fibers due to the decline of needled density. Thus, E1 increase with decreasing the deflection defects of fibers in the plane main direction. In addition, the needled fiber bundle and the out-of-plane deflection decreased with decreasing needled density in RVE, resulting in the decrease of E3, as shown in Figure. 7(2).

According to literature [17], the proportion of long fiber in the needled bundle would increase with increasing the number of needled repeatedly. Therefore, the influences of the number of needled repeatedly on the elastic properties of composites were discussed by changing the proportion of long fiber in the needled bundle. As shown in Figure 8, E1 showed a downward trend with increasing long fiber content in the needled bundle, but the value little changed, while E3 increased with increasing long fiber content. This was because the long fibers in the needled bundle were introduced from the unidirectional long fiber in the XY plane during the needled process. Therefore, needled repeatedly increased the proportion of long fibers in the needled bundle, meanwhile, reduced the proportion of long fibers in the plane. Moreover, the total content of fibers in the needled bundle was small enough to have limited effects on the in-plane performance of composites.

The needling process caused the defects of fiber deflection and meso-pore in composites. Figure.9 shows the effects of needled hole size on the properties of needled C/SiC composites. E1 presented an obvious downward trend with increasing the needled hole. The rate of decrease was from slow to fast. The in-plane deflection angle of the fiber was constant under the assumption, so the in-plane pore area and the amount of deflection fiber continued to grow with increasing the needled hole. Hence, the loss of E1 was more obvious when the needled hole continued to increase. For E3, the value climbed up and then declined with increasing

needled hole. The enhanced effects of the needled bundle on out-plane performance reached peak when the dimension of needled hole was 0.2mm-0.25mm. The reason was that more fibers into the needled bundle enhanced E3 with increasing the needled hole dimension. Meanwhile, both the fiber deflection angle in the thickness direction and the pore area also increased. Therefore, the enhanced effect of the needled bundle on E3 could not compensate for the performance degradation caused by the increase of pore area.

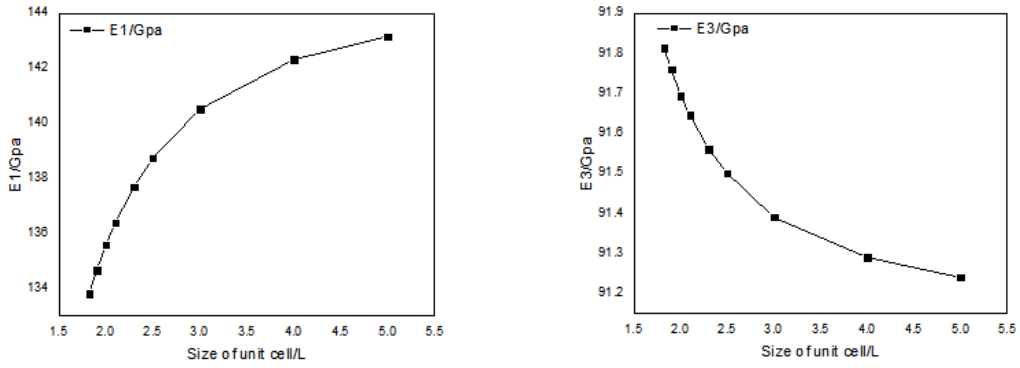

Figure. 7 Effects of RVE dimension *L* on elastic modulus of needled C/SiC composites

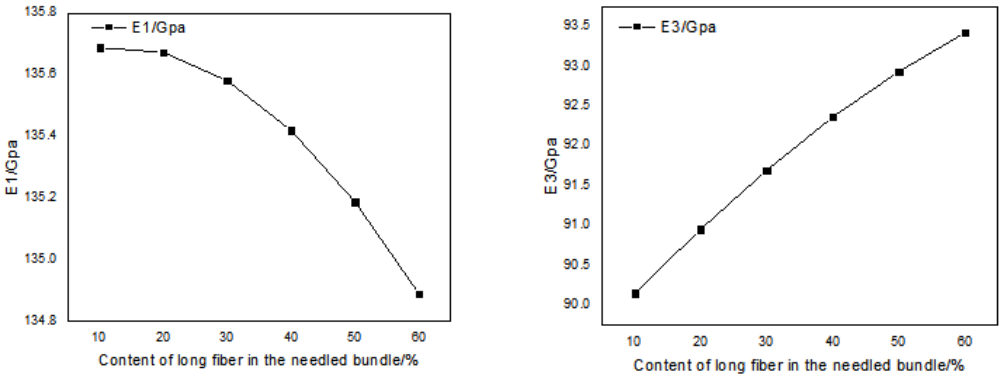

Figure 8 Effects of needled repeatedly times on elastic modulus of needled C/SiC composites

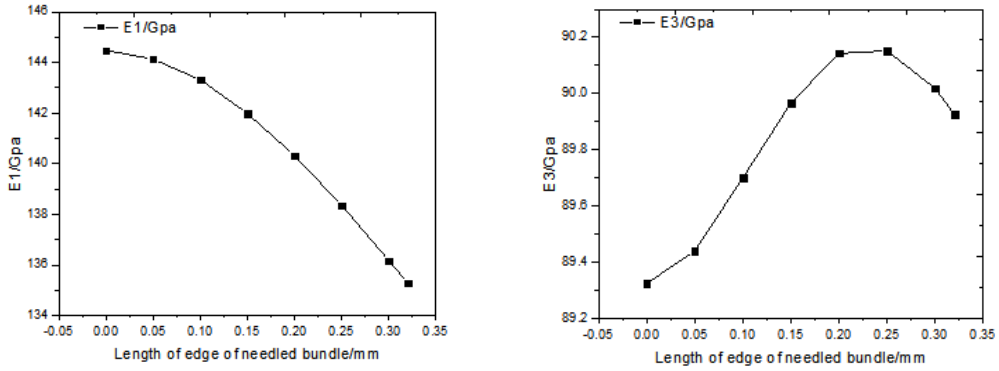

Figure. 9 Effects of needled hole size on elastic modulus of needled C/SiC composites

5 Conclusion

(1) There were obvious in-plane and out-of-plane fiber deflection and multi-scale pores in the needled C/SiC composites through microscopic observation. The process of needling caused short fibers and long fibers to deflect in and out of the plane. In the process of deposition, the fibers retain the deflection state, which is not conducive to the deposition effect of the matrix, thus resulting in the formation of pores with different scales in the composites.

(2) A RVE considering the fiber deflections and pores caused by the needling process was constructed. The basic elastic constants of fibers and matrix were calculated by using the theoretical formula. Further, three models were established to predict the elastic constants of needled C/SiC composites respectively. It was found that the predicted results of the model considering fiber deflection and porosity were in good agreement with the experimental results. It indicated that the manufacturing defects were necessary for the prediction model to evaluate the performance of needled C/SiC composites.

(3) Three needling process parameters, namely the needled bundle density, the number of needled repeatedly and the size of the needled hole, all affected the properties of the composites. And the needled density had an obvious effect. When the out-plane properties were improved by changing the process parameters, it was possible to lost the in-plane properties. Thus, the process parameter optimization should consider both out-of-plane and in-plane performance comprehensively in the preparation process.

In conclusion, the model proposed in this paper can accurately predict the properties of needled C/SiC composites and better reveal the influence mechanism of process parameters on the properties of composites. In addition, it has a potential prospect to extend the model to analyze the local damage evolution and to reveal the failure mechanism of needled C/SiC composites for further research.

Reference

[1]FANG G W，SUN J，GAO X G，et al． Micromechanical finite element analysis of effect of multilayer interphase on crack propagation in SiC /SiC composites[J].Modelling and Simulation in Materials Science and Engineering，2021,29(5) : 055010． DOI: 10. 1088 /1361-651X / abf846 ．

[2]Yuanhao Li, Zhaofeng Chen, Lixia Yang, Jiahao Liao, Tianru Guan, Qiqiao Xiao.Mechanical properties and failure mechanism of 3D needle-punched Cf/ SiC–Al composites[J]. Ceramics International.2021,47:33509-33514.

[3]Yingjie Xu, Pan Zhang, Huan Lu, Weihong Zhang. Hierarchically modeling the elastic properties of 2D needledcarbon/carbon composites[J]. Composite Structures,2015(33):148–156.

[4]Junbo Xie, Jun Liang, Guodong Fang, Zhen Chen. Effect of needling parameters on the effective properties of 3Dneedled C/C-SiC composites[J]. Composites Science and Technology.2015,117: 69-77.

[5]Choy KL ．Chemical vapor deposition of coatings[J].Progress in Materials Science,2003,48：57-170 ．

[6] Fan Kai, Lu Xuefeng, Lu Keming, et al. Research progress on pore structure of C/C composites [J]. Materials review,2019,33(13):2184-2190.

[7] PIAT R, TSUKROV I, MLADENOV N, et al. Material modeling of the CVI-infiltr-ated carbon felt I: Basic formulae, theory and numerical experiments[J]. Composites Science and Technology, 2006, 66(15): 2997-3003.

[8]Khaled H Khafagy , Siddhant Datta and Aditi Chattopadhyay. Multiscale characterization and representation of variability in ceramic matrix composites[J]. Journal of Composite Materials.2021,55(18):2431-2441.

[9]XU Y, ZHANG P, LU H, et al. Hierarch-ically modeling the elastic properties of 2D needled carbon/carbon composites[J]. Composite Structures, 2015, 133: 148-156.

[10] Wang Haibin, Zhang Weihong, Yang Jungang, et al. Calculation of Equivalent modulus of C/ C-sic braided Composites with Pore and microcrack Defects [J]. Journal of Composites,2008,(3):182-189.

[11]Yong zhenJia,Dunming Liao,Hong Cui,AlinJi,Xia Bai,Muhammad Yasir.Modelling the needling

effect on the stress concentrations of laminated C/C composites[J].Materials and Design,104(2016):19–26.

[12]QI Y, FANG G, WANG Z, et al. An improved analytical method for calculating stiffness of 3D needled composites with different needle-punched processes[J]. Composite Structures, 2020, 237(2): 111938.

[13]MENG S, SONG L, XU C, et al. Predicting the effective properties of 3D needled carbon/carbon composites by a hierarchical scheme with a fiber-based representative unit cell[J]. Composite Structures, 2017, 172: 198-209.

[14]XIE J,FANG G,CHEN Z, etal. An anisotropic elastoplastic damage constitutive model for 3D needled C/C-SiC composites[J].Composite Structures,2016,176:164-177.

[15]Feng Xiqiao, Yu Shouwen. Effect of reinforced phase shape on effective modulus of composites ()[J].
Journal of Tsinghua University (Science & Technology),2001,(11):8-10,14.

[16] Feng Xiqiao, Yu Shouwen. Effect of reinforced phase shape on effective modulus of composites () [J]. Journal of Tsinghua University (Science & Technology),2001,(11):11-14.

[17] Xie Junbo. Process Parameter Modeling of needle-punched preform and Constitutive relationship of Composite Material [D]. Harbin Institute of Technology, 2016.

Preparation and Characterazation of Hot pressed SiCf/SiC Ceramic Matrix Composites

Li Qi[1], Jiao Jian[1], Cao Lamei[2], Wei wei[1]*

1. National Key Laboratory of Advanced Composites, AECC Beijing Institute of Aeronautical Materials, Beijing, 100095, China

2. Science and Technology on Advanced High Temperature Structural Materials Laboratory, AECC Beijing Institute of Aeronautical Materials, Beijing 100095, China

Abstract: In this paper, SiC_f/SiC ceramic matrix composites were prepared by hot pressing at 1700℃with the second-generation SiC fibers as reinforcements, and their basic physical and mechanical properties were characterized. The results show that the bulk density of SiC_f/SiC ceramic matrix composite is about 2.50 g/cm^3, the open porosity is about 6.5 %. The typical values of tensile strength and tensile modulus are 261 MPa and 179 GPa respectively, and the typical values of flexural strength and flexural modulus are 621 MPa and 129 GPa respectively.

Keywords: Hot pressing, SiC_f/SiC ceramic matrix composites, mechanical properties

1. Introduction

SiC_f/SiC ceramic matrix composites (SiC_f/SiC CMC), a composite material of SiC fiber reinforced SiC ceramics, has low density (less than 3.0g/cm^3), high temperature resistance (above 1200 ºC), excellent mechanical properties and oxidation resistance, low tritium permeability, excellent irradiation stability[1,2]. And most importantly, it overcomes the brittleness of SiC ceramics. Therefore, SiC_f/SiC CMC has wide application prospects in aviation, aerospace, nuclear energy and other fields.

The preparation processes of SiC_f/SiC CMC mainly include melt infiltration process (MI)[3,4], Chemical vapor infiltration process (CVI)[5], Precursor impregnation pyrolysis process (PIP) [6], hot pressed sintering process (HP) [7-11] and so on. Among them, SiC_f/SiC CMC prepared by HP process has the advantages of high density and can be applied above 1400 ºC[12]. Since HP process usually needs to densify SiC_f/SiC CMC at a high temperature of 1800 ºC[13, 14], it is easy to damage SiC_f and thus affect the performance of SiC_f/SiC CMC. Therefore, reducing the sintering temperature is the difficulty for prepairing SiC_f/SiC CMC by HP process [15,16].

In this article, SiC_f/SiC CMC was prepared by HP process with domestic second

generation SiC fiber. Based on the in situ reaction of $ZrSi_2$, B_4C and C to form ZrB_2 and SiC above 1200 ºC, they were used as sintering additives to reduce the sintering temperature. The microstructure was analyzed by SEM. The density, tensile strength and flexural strength were tested. The results provide significant support for reducing sintering temperature in preparing SiC_f/SiC CMC by HP process.

2. Experiment

2.1 Preparation of SiC_f/SiC-HP

All the SiC fiber and powders used in this study were Commercial. β-SiC, 50 nm, 99.9 % purity; $ZrSi_2$, 100 nm, 99.5% purity; B_4C, 50 nm, 99.5 % purity; C, 100 nm, 99.5 % purity; Polyvinyl Butyral, 98% purity.

BN-coated SiC fiber were used as reinforcement for SiC_f/SiC fabrication. β-SiC powder and sintering additives with $ZrSi_2$, B_4C, C were used for matrix formation.

For the preparation of prepreg sheets, unidirectional BN-coted SiC fibers were impregnated in SiC slurry, which consists of the mixture ofβ-SiC powder and sintering additives (SiC :$ZrSi_2$: B_4C: C=70:23:4:3 wt.%) in ethanol with dissolved PVB. The prepreg sheets were dried at room-temperature and were unidirectionally stacked in a 100 mm*100 mm square graphite die, and then hot-pressed at 1700 ºC for 1 h in CO-CO_2 atmosphere under the pressure of 30 MPa。

2.2 Measurements

The density and open porosity were measured by Archimedean method, method, using distilled water as the immersion medium. The microstructures were observed using a scanning electron microscopy (SEM), The as-prepared samples were grinded and polished with diamond polisher. Three-point flexural strength and flexural modulus with 30 mm span were tested on a bending tester, the head movement rate was 0.5 mm/min. Tensile strength, tensile modulus, proportional ultimate strength and elongation at break were tested at room-temperature on a tension test machine with a displacement rate of 0.5 mm/min.

3. Results and Discussions

3.1 In-situ sintering of $ZrSi_2$, B_4C and C

In this paper, the in-situ sintering of $ZrSi_2$, B_4C and C was investigated at 1500 ºC, 1600

°C and 1700 °C, seperately. According to the reaction equation (1), $ZrSi_2$, B_4C and C can react to generate ZrB_2 and SiC.

$$2ZrSi_2+B_4C+3C=2ZrB_2+4SiC \quad (1)$$

The microstructures and elemental compositions of the sintered samples at different temperatures show that ZrB_2 phase and SiC phase have been generated after sintering at 1500 °C, however, it was not densified and remained loose(Fig. 1(a)). The sintering degree was improved significantly but still unsintered when increased the sintering temperature to 1600 °C(Fig. 1(b)). The ceramic matrix was further densified when the sintering temperature was further increased to 1700 °C(Fig. 1(c)). Based on the above reslults, it can be inferred that $ZrSi_2$, B_4C and C could complete in-situ reactive sintering at 1700 °C. By further prolongation of sintering time, sintered matrix with higher density can be obtained.

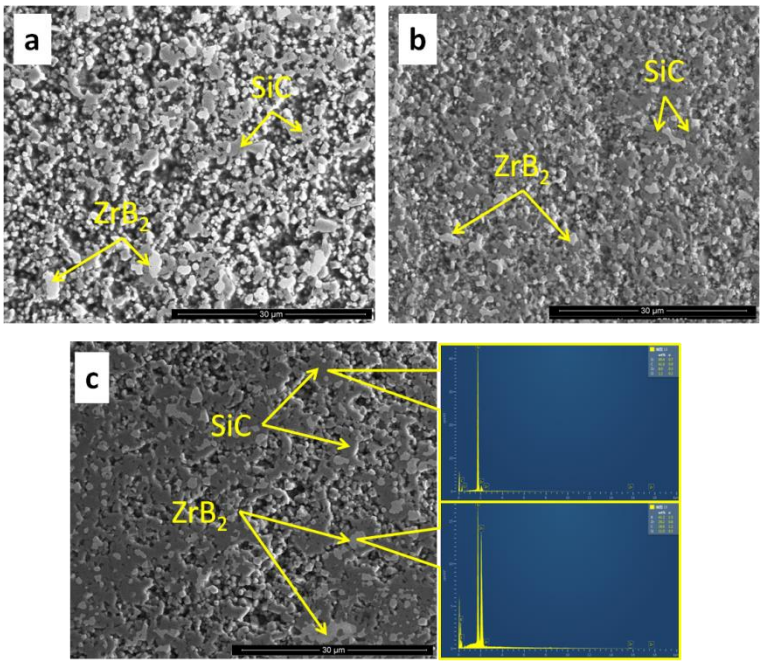

Fig. 1 Microstructures of ceramic matrix sintered at different temperatures: (a) 1500 °C ;(b) 1600 °C; (c) 1700 °C.

3.2 Microstructure of SiC_f/SiC-ZrB_2

In this paper, SiC_f/SiC CMC, referred to as SiC_f/SiC-ZrB_2, was obtained by hot pressing at 1700 °C. The density was about 2.50 g/cm^3 , the open porosity was about 6.5 % and the fiber volume fraction was about 21%(Table 1). The microstructure image (Fig. 2) shows that the dense SiC–ZrB_2 ceramic matrix has been formed, but there are still some defective holes and unsintered areas inside the fiber bundle. This is because that there are blind areas between the

fibers which is difficult to be fully filled by ceramic powders(Fig. 3). The defective holes were formed while the ceramic powders have not entered the blind areas,. When the matrix entered the blind areas in a small amount, unsintered areas were formed.

Table 1 Physical properties of $SiC_f/SiC\text{-}ZrB_2$

Physical properties	Results
Density (g/cm^3)	2.50
Prosity (%)	6.5
Fiber volume fraction (vol.%)	21

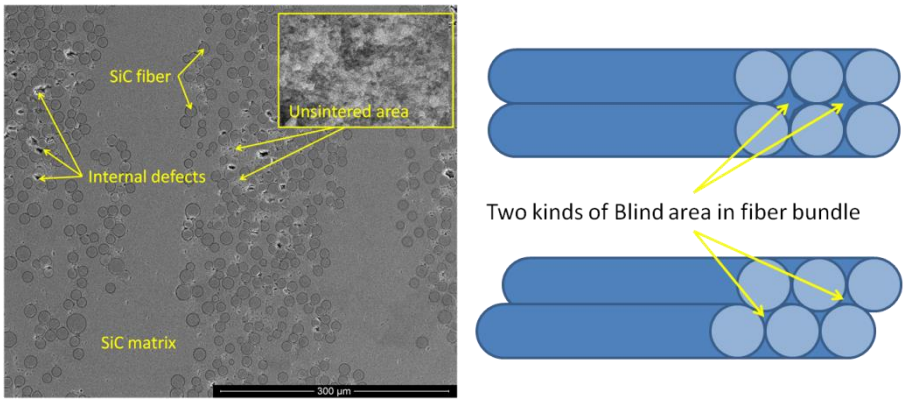

Fig. 2 SEM images of $SiC_f/SiC\text{-}ZrB_2$ and diagram of blind areas inside the fiber bundle

3.3 Mechanical properties

The mechanical properties of $SiC_f/SIC\text{-}ZrB_2$ were characterized, and the results are shown in Table 2. The flexural strength of $SiC_f/SIC\text{-}ZrB_2$ is about 621 MPa, and the flexural modulus is about 129 GPa. The flexural stress-strain curve (Fig. 3(a)) shows that a small decrease occurs when the strain is 0.55% and the stress reaches 523 MPa. When the strain increased to 0.91% and the stress increased to 621 MPa, a large decrease occurred and the CMC failed to fracture. The fracture cross section (Fig. 3(b)) shows that the fiber bundle has obvious pull-out and the ceramic matrix exhibits a brittle fracture mode.

Table 2 Mechanical properties of $SiC_f/SIC\text{-}ZrB_2$

Mechanical properties	Results
Flexural strength （MPa）	621
Flexural modulus （GPa）	129

Tensile strength（MPa）	261
Tensile modulus（GPa）	179
Proportional ultimate strength（MPa）	171
Elongation at break（%）	0.46

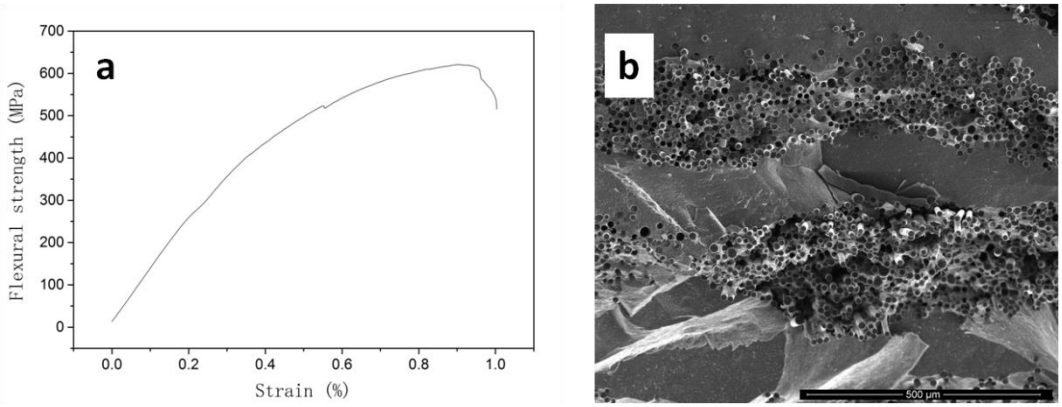

Fig. 3. Flexural stress-strain curve of SiC_f/SIC-$ZrB_2$and its fracture cross section

The tensile strength of SiC_f/SIC-ZrB_2 is about 262 MPa, the tensile modulus is about 179 GPa, the proportional ultimate strength is about 171 MPa, and the elongation at break is about 0.46 %(Fig. 4(a)). The tensile stress-strain curve could be divided into two stages. In the first stage, the tensile stress rapidly rises to 171 MPa before the strain is 0.1%, and then, with the increase of strain, the tensile stress slowly rises until the strain reaches 0.46% and the CMC failed to fracture, and the stress is up to 262 MPa. The fracture morphology (Fig. 4(b))shows that the fiber bundle has obvious pull-out and the matrix exhibits a brittle fracture mode.

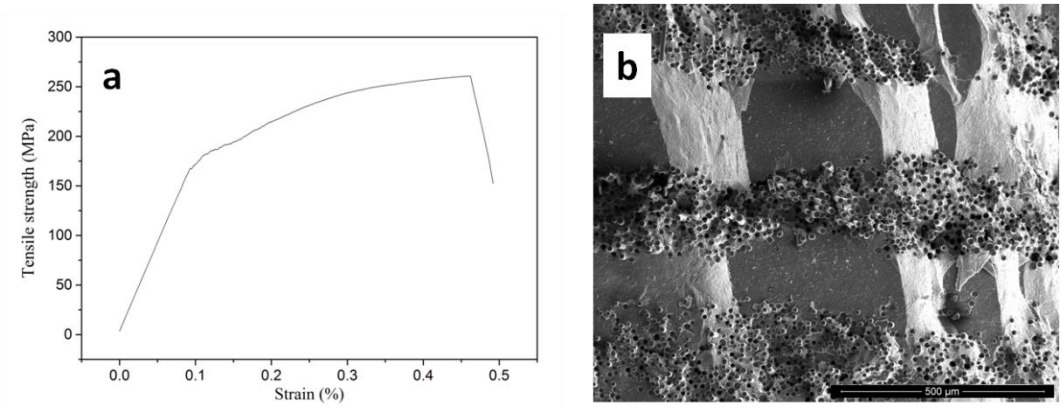

Fig. 4. Tensile stress-strain curve of SiC_f/SIC-$ZrB_2$and its fracture cross section

4. Conslusions

In this paper, SiC_f/SIC-ZrB_2 was obtained by hot pressing at 1700 °C based on the in-situ

reaction of $ZrSi_2$, B_4C and C. The bulk density of obatained SiC_f/SIC-ZrB_2 is about 2.50 g/cm^3, the open porosity is about 6.5 %. The typical values of tensile strength and tensile modulus are 261 MPa and 179 GPa respectively, and the typical values of flexural strength and flexural modulus are 621 MPa and 129 GPa respectively.

References

[1] LIU H, YANG J H, ZHOU Y R, et al. Progress in coupon tests of SiCf/SiC ceramic matrix composites used for aero engines[J]. Journal of Materials Engineering, 2018, 46(11):1-12.

[2] ZHAO S, ZHOU X G, YU J S. Research and development in fabrication and properties of SiC / SiC composites[J]. Materials Review, 2013, 27(1): 66-70.

[3] LIU H, YANG J H, CHEN Z M, LANG X D, JIAO J. Microstructure and Properties of SiCf/SiC Composite Fabricated by Melt Infiltration Process [J]. Aerospace Materials & Technology, 2020, 50(06): 48-54.

[4] WING B L，HALLORAN J W. Microstress in the matrix of a melt-infiltrated SiC/SiC ceramic matrix composite[J]. Journal of the American Ceramic Society, 2017, 100(11)：5286-5294.

[5]FENG W，ZHANG L T，LIU Y S，et al. Fabrication of SiCf-CNTs/SiC composites with high thermal conductivity by vacuum filtration combined with CVI[J]. Materials Science and Engineering a-Structural Materials Properties Microstructure and Processing，2016, 662: 506-510.

[6] KOTANI M, KONAKA K, OGIHARA S. The effect on the tensile properties of PIP-processed SiC/SiC composite of a chemical vapor-infiltrated SiC layer overlaid on the pyrocarbon interface layer[J]. Composites Part A: Applied Science and Manufacturing, 2016, 87: 123-130.

[7]DONG S, KATOH Y, KOHYAMA A. Processing optimization and mechanical evaluation of hot pressed 2D Tyranno-SA/SiC composites[J]. Journal of the European Ceramic Society, 2003, 23(8): 1223-1231.

[8] ZHOU X G, ZHANG C R, HE X B, et al. A study on the hot press of pyrolysised carbon coated carbon fiber reinforced silicon carbide composite[J]. Journal of Materials Engineering, 2000(3): 39-41.

[9] KATOH Y, KOHYAMA A, NOZAWA T, et al. SiCf/SiC composites through transient eutectic-phase route for fusion applications[J]. Journal of Nuclear Materials, 2004, 329/333: 587-591 .

[10] Tailoring the microstructure of hot-pressed SiC by heat treatment[J]. Journal f Nuclear Material, 2004, 329/333: 558-561.

[11] PARK J S, JUNG H C, OOI Y, et al. Fabrication of environmentally resistant NITE-SiCf/SiC composites[J]. IOP Conference Series: Materials Science and Engineerin, 2011, 18: 202012 .

[12] Gao Y, Jiao J. Research progress on NITE process for fabricating SiCf/SiC composites. Journal of

Materials Engineering, 2019, 47(8):33-39.

[13] DONG S M, DING Y S, JIANG D S, et al. Effects of preparation conditions on the microstructure and properties of hot pressed SiC / SiC composites [J]. Journal of Inorganic Materials, 2005, 20(4): 883-888.

[14] ZHU D, LI M F, GAO M X, et al. Research development of fabrication techniques and properties of SiCf/SiC ceramic matrix composite[J]. Materials Review, 2008, 22(3): 55-59.

[15] Lee S-H, Feng L, Chang J B: Densification of ZrB2–SiC nanocomposites prepared using ZrSi2, B4C, and C additives. Journal of Materials Research, 2017, 32(17), 3302-3308.

[16] Zhang Z F , Sha J J , Wang Y C , et al. Synthesis of nano-sized SiC-ZrB2 ceramic powder mixture by boro-carbothermal reduction method[J]. The Chinese Journal of Nonferrous Metals, 2015, 25(12), 3445-3451.

Understanding machinability improvements of ceramic matrix composites during laser-induced ablation assisted grinding

Kun Zhou, Guijian Xiao, and Xin Li

College of Mechanical and Vehicle Engineering, Chongqing University, No. 174, Shazhengjie street, Shapingba, Chongqing, 400044, China

Abstract: Ceramic matrix composites are promising high-temperature materials for key parts and components of aerospace, but they are also known as hard-to-machine materials because of the heterogeneous and hard-brittle characteristics. This study introduced laser-induced ablation assisted grinding (LIAAG), analyzed the complex physicochemical transformation behaviors of C_f/SiC composites during picosecond laser ablating, and systematically explored the grinding force, temperature, surface morphology, subsurface damage, removal mechanism and abrasive wear during LIAAG of C_f/SiC composites. It is revealed that serrated ablated groove was formed on the C_f/SiC composites after picosecond laser ablating, and the ablated product was primarily composed of SiO_2. Tangential grinding force and surface roughness could be reduced by up to 87% and 42%, respectively, through LIAAG. Besides, the surface removal morphology of C_f/SiC composites during conventional grinding (CG) was macro brittle fracture, but that in LIAAG primarily consisted of micro fracture and ductile removal. Moreover, subsurface damage of C_f/SiC composites after CG included macro crack and interface debonding, which were significantly reduced after LIAAG. Graphite crystallites of carbon fiber became disordered after LIAAG, and an amorphous structure layer with the thickness of 28 nm was found. Consequently, the grinding efficiency is observably improved and the fracture damages of C_f/SiC composites are decreased via LIAAG.

1. INTRODUCTION

Ceramic matrix composites (CMCs) are advanced structural materials in aerospace, nuclear power, rail transit and other fields, because of their advantages of high temperature resistance, high strength, oxidation resistance, corrosion resistance and low density [1]. Among them, fiber reinforced ceramic matrix composites (FRCMCs), mainly include C_f/SiC composites and SiC_f/SiC composites have shown promising applications in hot-end components of aero-engine and high-performance braking systems [2,3]. Generally, complex machining procedures are necessary for a newly fabricated

FRCMCs components to meet the size and shape requirements. However, the FRCMCs are characterized by anisotropy, heterogeneity and hard brittleness in structure and mechanical properties, which bring great challenges for their machining process, especially grinding. As reviewed by Diaz et al. [4] and An et al. [5], various forms of brittle fracture damages (primarily include matrix cracking, fiber pulling out, interface debonding) and severe diamond abrasive wear can easily occur during grinding of FRCMCs. The grinding-induced damages will significantly reduce the fatigue life of parts under extreme high-temperature and high-pressure environments, and the severe abrasive wear reduces the machining efficiency and greatly increases the manufacturing cost [6,7]. Therefore, it is of great significance to realize the low-damage and low-wear machining of FRCMCs for improving their service performance and expanding its application range.

For the last decade, many attempts have been made by scholars and engineers for overcoming the existing technical constraints of difficult machining of FRCMCs, such as laser assisted machining (LAM). LAM is based on the fact that hard and brittle materials (such as ceramics, semiconductors and glasses) soften when heated [8]. It was widely found that LAM could significantly reduce the grinding force and tool wear of FRCMCs, but played little role in improving their grinding quality [9,10]. The removal behavior of FRCMCs was still macro brittle fracture during LAM; as a result, the machining-induced damages were still visible and the surface roughness was hardly decreased. This happened because the mechanical properties including bending and tensile strength of FRCMCs changed little when heated [11,12]. Concerning highspeed machining. Consequently, the difficult-to-machine problem of FRCMCs has not been well solved at present. Besides, it can be concluded from the above research studies that the machinability of the materials cannot be significantly improved only by changing their physical properties due to the anisotropy and heterogeneity characteristics.

Recently, many experimental investigations have shown that FRCMCs occur unique microstructure and chemical transformation during laser ablating, which offers a new thought for creating the high-performance machining method. Chen et al. [13] used nanosecond and continuous-wave laser to ablate SiC_f/SiC composites and simulated the ablating temperature. It was found that the materials in the center of laser spot were directly vaporized at about 3000 ℃ temperature, and those around the laser spot occurred violent oxidation reaction, resulting in SiO_2 and recrystallized SiC affected-layer with extremely loose and porous microstructure. Jiao et al. [14] used nanosecond laser to ablate C_f/SiC composites and also found the similar chemical reaction; besides, there was a quantitative relationship between ablation depth and laser parameters (i.e., laser power, scanning speed and

scanning times). Compared with the unablated materials, the affected layer was relatively uniform and easier to be removed during grinding. Therefore, we proposed the laser-induced ablation assisted grinding (LIAAG) to improve the machinability of FRCMCs. It is worth noting that the LIAAG is essentially different from conventional laser assisted grinding (LAG); the former is the based on the chemical transformation at high laser temperatures (mostly higher than 3000 ℃), and the latter is based on softening behavior at high laser temperatures (mostly between 1000 ℃ and 2000 ℃). In previous works [15], we used a diamond grain to scratch a C_f/SiC composites workpiece ablated by continuous laser and found that the scratching force was significantly reduced, which proved the feasibility of this method. However, a final laser-induced ablation grinding test has not been performed, and the material removal mechanism, surface integrity and abrasive wear behavior during LIAAG remain to be clarified. Moreover, the effect of laser ablating mode, including scanning distance and direction on the grinding performance is also worth careful study.

The objective of this study is to explore the machining effect of LIAAG on FRCMCs. C_f/SiC composites were ablated by picosecond laser at different scanning distances and directions, which were then ground by diamond abrasive belts, that is, LIAAG tests. The microstructure on the surface and on the surface and in the section of ablated C_f/SiC composites were observed; the element distribution and chemical composition of residual materials around ablated zone were characterized; consequently, the picosecond laser-induced ablation mechanism of C_f/SiC composites was clarified. The grinding force during grinding was monitored and recorded to analyzed the general removal behavior of ablated materials. After that, the surface roughness, the micro removal morphology and residual oxide of ground surfaces were observed to investigate the effect of LIAAG on surface integrity; besides, the subsurface damage and fracture mechanism of carbon fibers during CG and LIAAG were analyzed to understand the material removal mechanism. The work is expected to provide a highly effective and practical way to solve the difficult machining problem of FRCMCs.

2. Materials and method

2.1 Workpiece material and abrasive belt

The workpiece materials used in this study was 2.5D woven C_f/SiC composites. The C_f/SiC composites fabricated through chemical vapor deposition method were provided by the Chinese Academy of Sciences. The volume fraction of caron fiber in the C_f/SiC composites is between 40% and 50%. The average diameter of these carbon fibers (covered with a pyrolytic interface layer) is

about 8 μm. In this study, 10 square samples with the dimension of 25 mm × 10 mm × 3 mm (length × width × height) made from the 2.5D woven C_f/SiC composites were prepared for LIAAG test.

Diamond abrasive belt has shown excellent wear resistance when grinding C_f/SiC composites compared with conventional ceramics and corundum abrasive materials [7]. Therefore, diamond abrasive belt (provided by VSM cooperation) is chosen to conduct the present grinding tests. The size of diamond abrasive belts is 1000 mm × 10 mm (length × width), and the granularity of abrasive grains is 60#, i.e., the diameter of diameter grains is around 250 μm. The diamond grains are cuboctahedron with two crystallographic planes, i.e., square {100} and triangular {111}, which are bonded to the cloth basement of the abrasive belt by a ceramic binder. Four diamond abrasive belts were used for grinding tests with different parameters, and a round sample would be cut from every abrasive belt after grinding for subsequent wear observation.

2.2 Experimental design

The laser processing and belt grinding tests were carried out on a self-designed picosecond laser-belt grinding testing machine, as shown in Fig. 1a. The test machine is mainly composed of two parts: laser processing station and belt grinding station. The above C_f/SiC composites workpieces are first processed on the laser processing station (Fig. 1b), followed by the belt grinding station (Fig. 1c). Some studies have shown that the material is mainly sublimated in the process of ultra-short pulse laser ablation, and the heat-affected layer (below the ablation layer) is very small [16,17], which is consistent with the idea of LIAAG proposed in this study. Therefore, this study used picosecond pulsed laser to ablate C_f/SiC composites rather than continuous-wave laser or nanosecond pulsed laser. The frequency of picosecond laser on the testing machine is 0~1000 kHz, the peak output power is 12 w, the wavelength is 1065 nm, the pulse width is 13 ps, and the spot diameter is around 15 μm. As shown in Fig. 3b, the ablation layer can be fabricated by scanning the whole surface of C_f/SiC composites sample, and the depth of which is depended on laser power and scanning times. In this study, the samples are ablated under the same laser parameter combination (the laser power is 10 w, scanning times is 500, step length is 10 μm, scanning speed is 500 mm/min) to obtain an ablation layer with uniform depth, but different scanning directions and intervals are set to investigate their effects on subsequent grinding process. The feed direction of belt grinding relative to the scanning path is therefore 0°, 45°, and 90°; three different scanning intervals are set in each direction, i.e., 100 μm, 150 μm, and 200 μm. By observing the ablation zone on the side of samples, it can be measured that the ablation depth is 332 μm.

The ablated samples are then fixed on a triaxial force sensor. To ensure that the laser-induced ablation layer can be completely removed without causing damage to the underlying materials, the grinding depth of the abrasive belt should be equal to the depth of ablation layer, i.e., 332 μm. For above 9 groups of ablated samples, the parameters of abrasive belt grinding are exactly the same, that is, grinding speed is 19.6 mm/s (up grinding), feed speed is 2 mm/s, the Shore hardness of rubber contact wheel is 65 HA, the grinding mod. Besides, to set up a control group, an unablated sample is ground for three times by abrasive belt under the same conditions. An abrasive belt is used in each series of test to compare their wear conditions, i.e., a total of 4 identical abrasive belts are used). Finally, a total 10 C_f/SiC composites samples are machined, the pictures of which before and after machining are displayed in Fig. 1d. During belt grinding, the grinding forces were recorded by the triaxial force sensor (KWR96, China), the grinding temperature was measured by a thermal imager (Fluke Ti90, USA), and the grinding chips were collected for micro morphology observations.

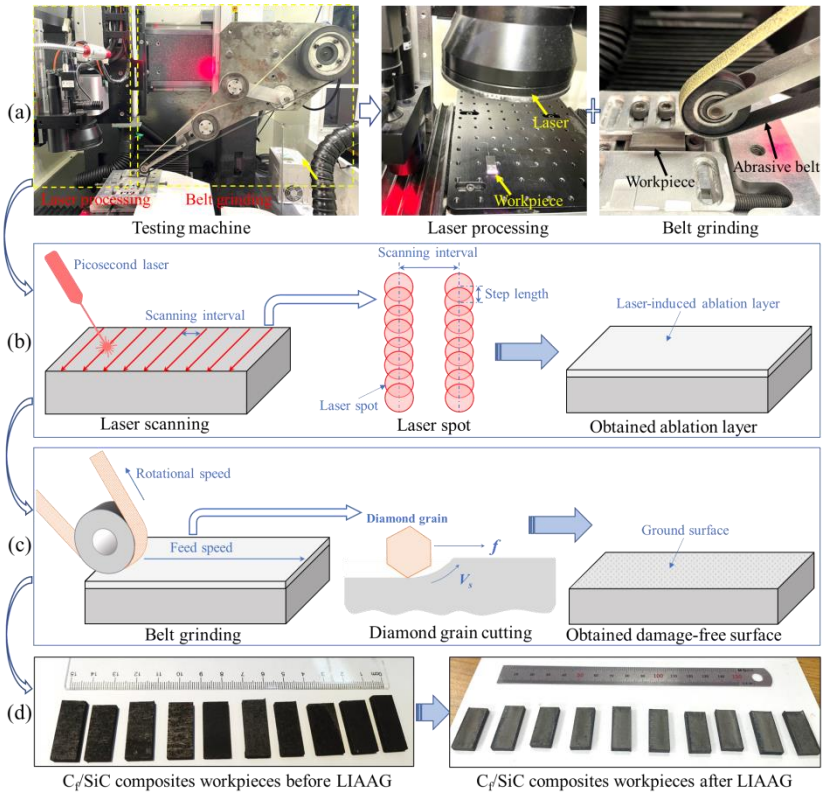

Fig. 1. LIAAG procedures: (a) LIAAG testing machine, (b) laser-induced ablation process, (c) belt grinding process, (d) C_f/SiC composites samples before and after LIAAG.

3. Results and discussion

3.1 Ablation behavior of C_f/SiC composites

To reveal the removal mechanism of C_f/SiC composites during LIAAG, it is necessary to determine the complex physicochemical transformations during laser ablating. However, most of the previous research works on laser-induced ablation behavior of FRCMCs are focused on continuous-wave laser [18,19], millisecond and nanosecond pulsed lasers, and the research on picosecond pulsed laser with

shorter pulse is rarely reported. Therefore, this study performs a thorough and detailed experimental observation on the C_f/SiC composites ablated by picosecond laser (before grinding). Fig. 2 presents the morphology of ablated surface of C_f/SiC composites. It is found from the SEM images that the material in the laser scanning path is sublimed away, and the laser-induced ablation products are form on both sides of scanning path. Macroscopically, the ablation products are clumpy, and the structure of which is loose and porous. At high magnification (more than 20000 times), it is further observed that these ablation products are composed of micron-scale particles. In addition, comparing Fig. 2a, 2b and 2c, it can be seen that at 100 μm scanning interval, the C_f/SiC composites surface is completely ablated; as the scanning interval increases to 150 μm, the ablation products are almost uniformly distributed on the C_f/SiC composites surface; as the scanning interval reaches 200 μm, the ablation products only exist at the edge ablation grooves.

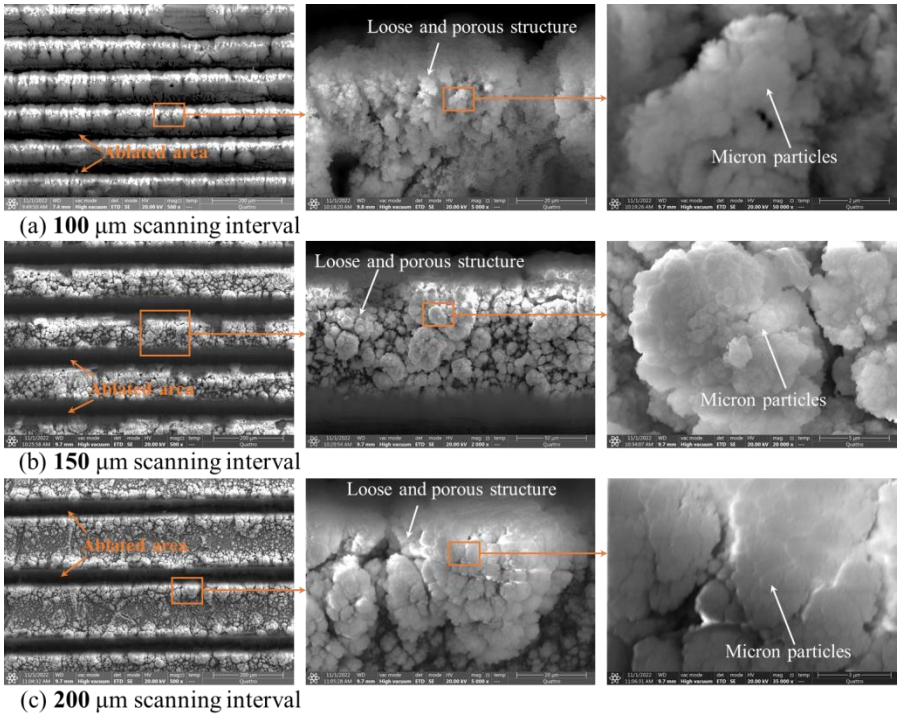

Fig. 2. SEM images of surface of ablated C_f/SiC composites.

To understand the chemical compositions of above ablation products, it is necessary to point out the elements and their distribution. Therefore, the EDS map detecting is performed as shown in Fig. 3. The unablated C_f/SiC composites is composed of carbon fiber and SiC matrix; thus, the main elements are C and Si. According to Fig. 3, a large number of O element is present on the ablated surface, and the little C element remains, especially under 100 μm scanning interval. As well known, both C and SiC can be oxidized under high-temperature conditions, resulting in gaseous carbon oxide (CO_x) and solid silicon oxide (SiO_x). It is found from the EDS map spectra that O and Si element always appear together, it can be concluded that the main component of the ablation products is (SiO_x). Table 1 lists the relative content of elements at different scanning intervals. Obviously, the content of O element at 100 μm scanning interval is higher than those at 150 μm and 200 μm. Combining Fig. 3 and Table 1, the C_f/SiC composites can be more fully oxidized during laser ablating at a smaller scanning interval, and the oxidation level becomes stable after 150 μm scanning interval.

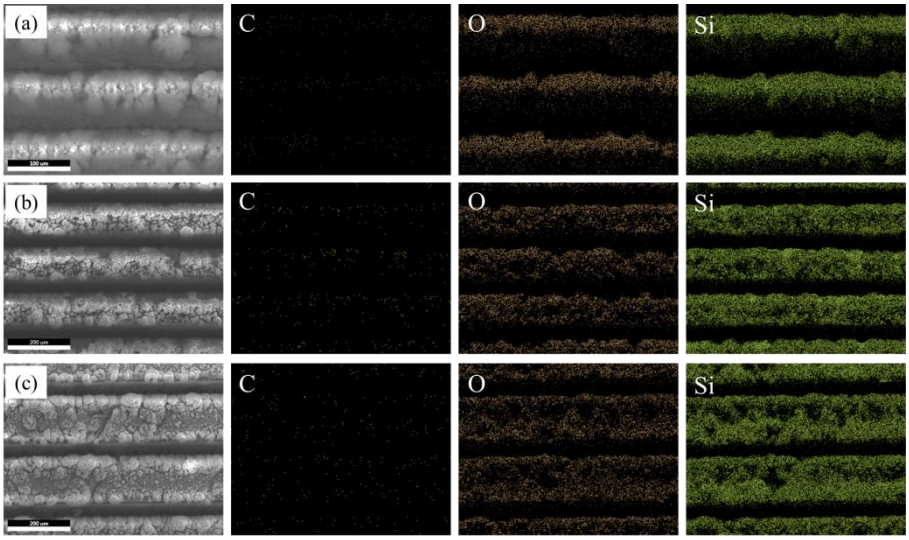

Fig. 3. EDS elements distribution on the surface of ablated C_f/SiC composites.

Table 1 Relative content of elements at different scanning intervals.

Scanning interval (μm)	Relative content (*wt.*%, *at.*%)		
	C	Si	O
100	5.34%, 8.55%	43.21%, 29.59%	51.45%, 61.86%
150	5.66%, 9.22%	46.73%, 32.55%	47.61%, 58.23%
200	4.74%, 7.79%	47.60%, 33.44%	47.65%, 58.77%

To clarify the formation mechanism of ablation products, the specific type of SiO_x should be determined through XRD and XPS. It is worth noting that the ablation products are difficult to separate from the workpiece surface, and to ensure the integrity of the workpiece, the C_f/SiC composites workpiece after laser ablating was directly detected via XRD. Fig. 4 shows the XRD spectra of ablated surface at different scanning interval. The principal diffraction peak of XRD spectra at each scanning intervals corresponds to SiC. However, it has been found in Fig. 4 that the surface materials, especially at 100 μm scanning interval, are completed ablated, i.e., there should not be SiC matrix. Chen et al. [18] also found the similar phenomenon when ablating SiC_f/SiC composites through nanosecond-pulsed and continuous-wave laser. They thought that SiC could be quickly sublimated under high laser temperatures (around 3000 ℃), the SiC vapor then be easily oxidized in the air, resulting in the formation of SiO_x. These white solid SiO_x would be attached to the edge of ablating area, which reflected off the laser beam and blocked outside oxygen. In this case, the SiC vapor below the SiO_x layer that had not been oxidized would recrystallize to form solid SiC, i.e., recrystallized SiC. It can also be seen from the XRD spectra that the SiO_x are made entirely of SiO_2 that exists in two forms, that is, amorphous and crystal. During laser-induced ablating, the SiC vapor was oxidized to form amorphous SiO_2 in the form of dust and smoke, and the amorphous formed SiO_2 near laser spot would be further crystallized under high temperature. Moreover, SiO would inevitably form when the oxidation of SiC was insufficient, but the diffraction peak of which is not seen in the XRD spectra. Many studies thought that the SiO formed in the process of laser ablation of CMCs existed in the form of gas and would be easily volatized [20]. Fig. 5 shows the XPS detecting results of ablation products in this study. The three main elements of C, O, and Si are determined in the full spectrum (Fig. 5a), and the fine spectra of C1s, Si2p, and O1s are displayed in Figs. 5b to 5d, respectively. It is found that the C1s primary peak is composed of four peaks with the binding energy (eV) of 286.50, 284.80, 287.14, and 291.30, which correspond to C-Si bond, C-C bond, C=O bond, and O-C=O bond,

respectively. The Si2p primary peak is composed of two peaks with the binding energy of 100.28 and 103.15. The binding energy of O1s primary peak is 532.58 eV, which corresponds to Si-O bond. Obviously, the Si-O bond indicates the existence of SiO_2, which was formed because of the chemical of reaction between SiC with O_2 during laser ablating. The XPS measuring results are consistent with those of XRD, and proves the above viewpoint.

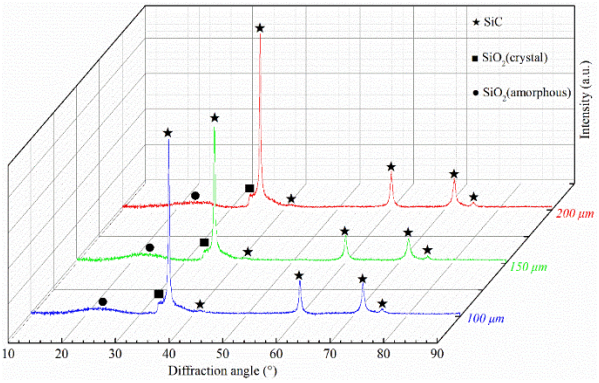

Fig. 4. XRD spectra of ablated C_f/SiC composites.

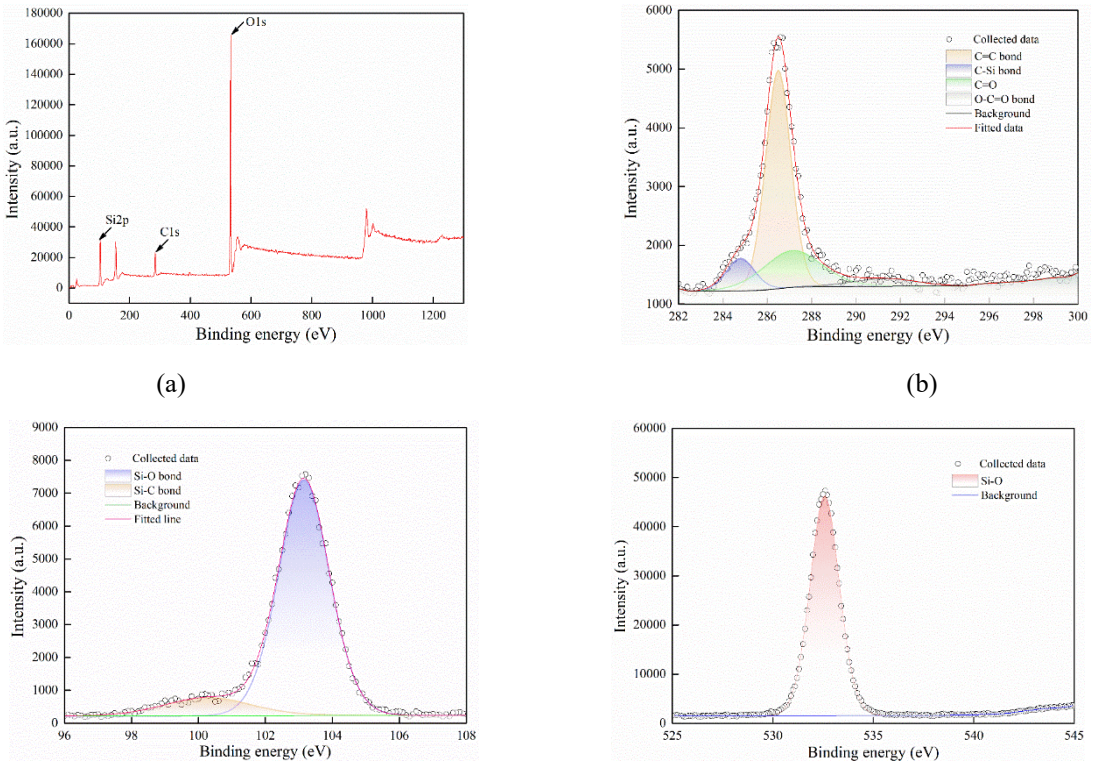

Fig. 5. XPS spectra of ablated surface: (a) full spectrum, (b) C1s peak, (c) Si2p peak, (d) O1s peak.

3.2 Grinding process analysis

After figuring out the ablation mechanism of C_f/SiC composites by picosecond laser, the next step is to compare the grinding characteristics of ablated materials and unablated materials. Dynamic monitoring of grinding force is an important method to investigate this problem, and the recorded macroscopic difference can directly show whether LIAAG improves the machinability of C_f/SiC composites. The initial grinding force signal contains a lot of system noise, and the recognizable signals processed by 0.03 HZ low pass filter are shown in Fig. 6. It can be observed from Fig. 6 that

the normal grinding force (F_n) is always higher than the tangential grinding force (F_t), and the axial grinding force (F_a) is zero under every grinding condition. Besides, the grinding force signals contain varying degrees of fluctuation, which is mainly related to the abrasive cutting and material characteristics. In this study, the grinding processes used the same abrasive belt and grinding parameters, so the material property change occurred in the LIAAG process is the only factor of grinding vibration characteristics. Comparing Fig. 6a with Figs. 6b to 6f, the vibration amplitudes during grinding of ablated workpieces are generally larger than that of unablated workpiece. Furthermore, Figs. 7b to 9d indicate that the vibration amplitude of ablated workpiece is significantly decreased with the laser scanning interval increasing from 100 to 200 μm, and Figs. 6d to 6f indicate that the vibration amplitude of 45°-ablated workpiece is slightly lower than those of 0° and 90°-ablated workpieces. The grinding vibration is caused by the intermittent cutting of many abrasive grains, and the ablated grooves of C_f/SiC composites markedly increased this type of intermittent grain cutting.

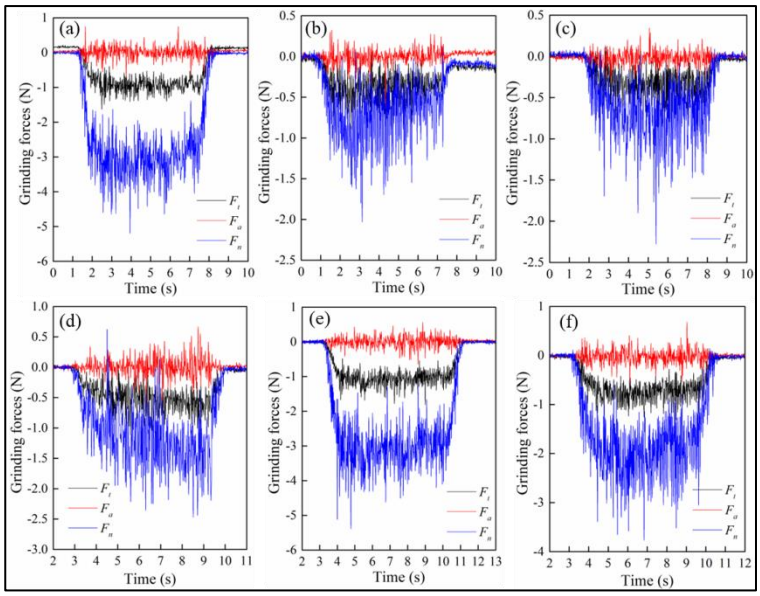

Fig. 6. Grinding force signals (processed by 0.03 HZ low pass filter): (a) unablated sample, (b) 90°/100 μm-ablated sample, (c) 90°/150 μm-ablated sample, (d) 90°/200 μm-ablated sample, (e) 45°/200μm-ablated samples, (f) 0°/200 μm-ablated sample.

Fig. 7 shows the varying trends of grinding forces with laser scanning interval and direction. The F_n and F_t during grinding of unablated sample are 4.22 N and 2.26 N, respectively, which are obviously higher than those of ablated samples. Besides, F_n and F_t can be reduced by up to 88% and 87% (when the laser scanning interval is 100 μm and the scanning direction is 90° relative to the grinding direction), respectively, proving that the LIAAG can significantly improve the machinability of C_f/SiC composites. Compared with the original C_f/SiC composites, the oxide products in the ablation layer have a very loose structure, and the blocking effect of carbon fibers after laser cutting is significantly reduced during grinding. As the laser scanning interval increases from 100 to 200 μm, F_n at 0°, 45°, and 90° increases from 0.53 to 1.37 N, 0.82 to 3.03 N, and 0.67 to 2.04 N, respectively; F_t at 0°, 45°, and 90° increases from 0.27 to 0.58 N, 0.36 to 1.09 N, and 0.33 to 0.81 N, respectively. Moreover, grinding perpendicular to the laser scanning direction will always result in the lowest grinding forces. The grinding force ratio (i.e., F_t/F_n, r) under each grinding conditions are calculated, as shown in Fig. 8b. When grinding unablated sample, r is 0.53, which is higher than those of ablated samples. As the

laser scanning interval increases, r shows a decreasing trend. In addition, the lowest grinding force ratio can be achieved when the grinding direction is at a 45° angle to the laser scanning path.

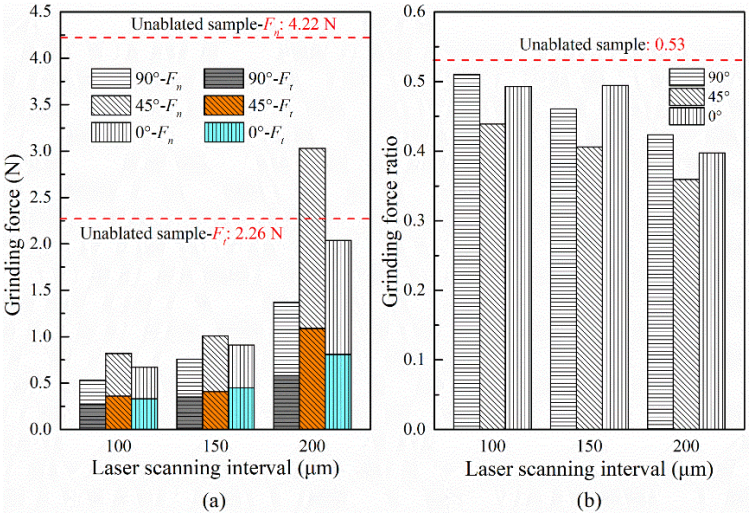

Fig. 7: (a) Grinding forces and (b) grinding force ratio.

3.3 Surface integrity of C_f/SiC composites

Surface roughness is an important aspect of evaluating the grinding surface integrity. The grinding scratches are consistent with the grinding direction, and the surface roughness parallel and perpendicular to the grinding direction are often different, so they need to be measured separately. Figs. 8a and 8b show the surface roughness of LIAAG. All the measurements are performed five times to obtain an average value. It is found that the parallel roughness is generally lower than the perpendicular roughness, and both parallel and perpendicular roughness shows increasing trend with the laser scanning interval, and are generally lower than that of CG (4.76 μm and 5.03 μm). When the scanning interval is 200 μm, the surface roughness of LIAAG is close to that of CG. Through LIAAG, the parallel and perpendicular surface roughness can be reduced by up to 54% and 42%, respectively, when the laser scanning interval is 100 μm and the scanning direction is 90°. In addition, the surface roughness at 90° scanning direction is always lower than the other two scanning directions.

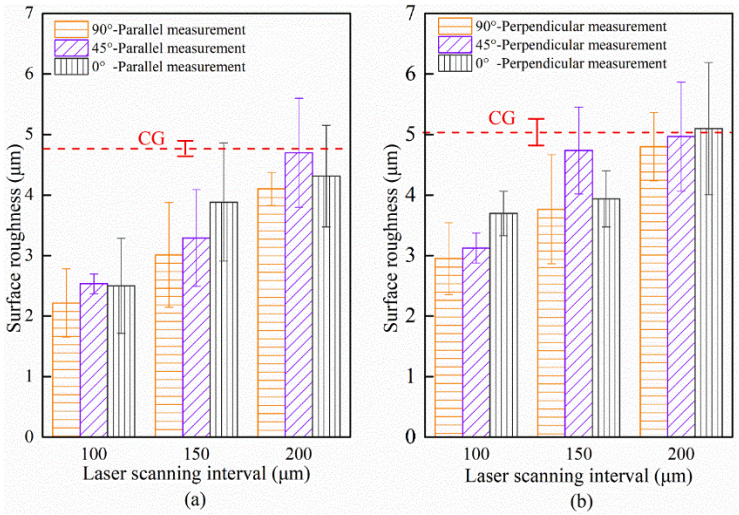

Fig. 8. Surface roughness of LIAAG: (a) measurement parallel to grinding direction, (b) measurement perpendicular to grinding direction.

To further investigate the surface integrity characteristics of C_f/SiC composites after LIAAG, the workpiece surfaces of CG and LIAAG were observed through SEM. It should be noted that the carbon fibers in 2.5D C_f/SiC composites can be divided into normal fibers and surface fibers according to their orientation, and the surface carbon fibers may be parallel or perpendicular to the motion direction of abrasive grains during grinding. Therefore, this study displayed the micro-removal morphologies of normal and surface carbon fibers, respectively. Fig. 9 shows the SEM images of surface morphology of CG samples. It is found that both normal and surface carbon fibers show typical brittle removal behavior, and macro fracture occurs in carbon fibers and SiC matrix. When grinding the normal carbon fibers, the fibers and matrix underwent an asynchronous brittle fracture, resulting in a rough grinding surface. Besides, when the grinding direction is perpendicular to the surface carbon fibers, a bundle of carbon fibers is fractured together, resulting in severe interface debonding and macro fracture damages. As shown in Fig. 9, brittle fracture is the main material removal mechanism of both normal and surface carbon fibers, but the stress condition and surface characteristics are significantly different. In normal grinding, the carbon fibers are primarily subject to shear stress, and only the interface near grinding surface is subject to tensile stress; as the grinding depth increases, these mechanical stresses are increased, and eventually a crack is formed. In this case, the crack then radially penetrated the carbon fiber, resulting in a rough and oblique fracture appearance. In perpendicular grinding, the carbon fibers suffer from both shear and tensile stress, and the whole interface suffers from high shear stress; consequently, many carbon fibers are separated from the SiC matrix at the same time of brittle fracture, the grinding-induced damages are therefore markedly larger than those in normal grinding.

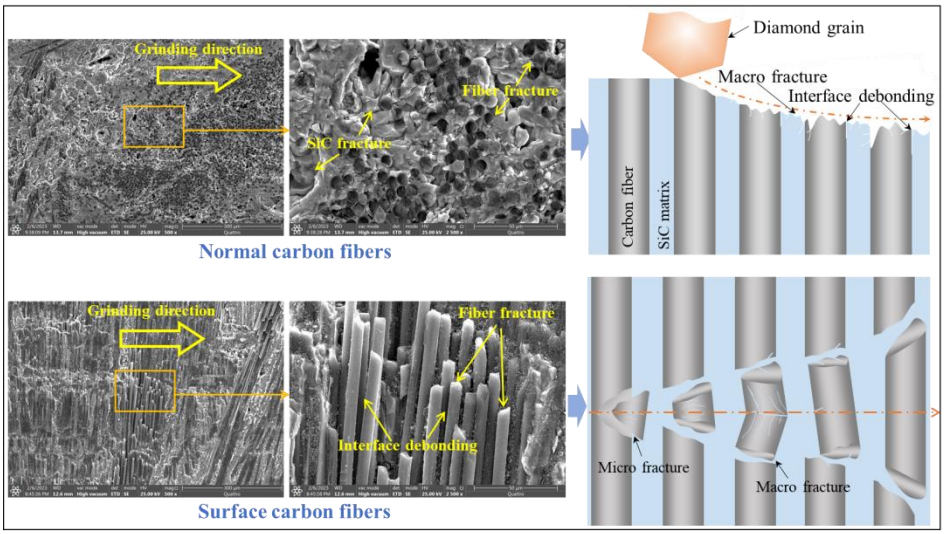

Fig. 9. Surface morphology and removal mechanism of C_f/SiC composites after CG (i.e., tests #1 in Table 3).

As a comparison, this study systematically analyzed the surface morphology of C_f/SiC composites after LIAAG. Fig. 10 shows the SEM images of LIAAG surface morphology at 90° laser scanning direction. Compared with Fig. 10, the macro fracture of surface carbon fibers is significantly reduced, and the grinding area with normal carbon fibers is generally smoother. Especially, when the laser scanning interval is 100 μm, only axial fracture with a smooth appearance is observed on the surface carbon fibers, and the SiC matrix is removed in the form of micro fracture. Besides, in the grinding area with normal carbon fibers, obvious ductile removal appearance is observed on SiC matrix, and the carbon fibers are removed in the form of micro fracture with a relatively smooth surface. According to the Zhou et al. [21], the ductile removal behavior of C_f/SiC composites could be enhanced via softer

rubber contact wheel and lower grinding depth. In this study, the grinding depth was moderate, and the Shore hardness of contact wheel was 90 HA, which was the highest hardness scale in the grinding tests of Zhou et al. [21]. Therefore, the occurrence of ductile removal of C_f/SiC composites is only related to the changes in material properties. For sure, this type of grinding surface reduces the roughness and fracture damages. Under 150 μm laser scanning interval, the surface carbon fibers start to be crushed, and the normal carbon fibers also display micro fracture. As the scanning interval increases to 200 μm, the grinding surface becomes rougher, macro fracture is seen on both surface and normal carbon fiber, and the ductile removal appearance can be rarely observed on SiC matrix. Generally, the brittle fracture damages of C_f/SiC composites during LIAAG are significantly decreased compared with those of CG, and the decrease in laser scanning interval promotes damage formation.

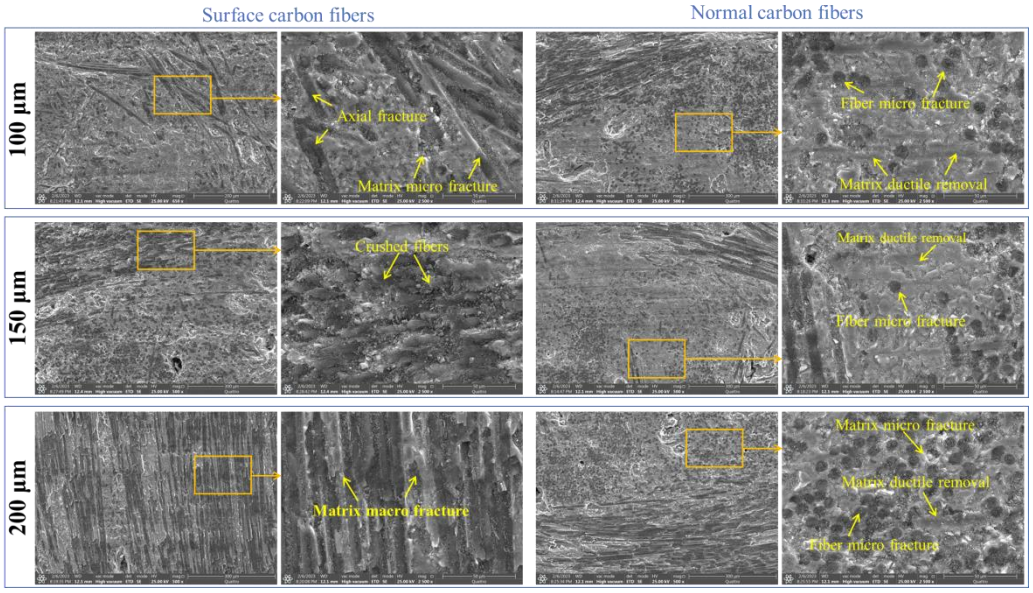

Fig. 10. SEM images of surface morphology of C_f/SiC composites after LIAAG, at 90° laser scanning direction (i.e., tests #4 in Table 3).

3.3 Subsurface damage and fracture damage

It is seen from the above surface morphology observation that the C_f/SiC composites can easily suffer from severe damage during grinding, and the damage type is more complex than that of conventional homogeneous hard-brittle materials (such as ceramics, glass, and quartz crystal), which is primarily due to the existence of continuous carbon fibers. Therefore, to further analyze the subsurface damage and fracture mechanism of C_f/SiC composites during grinding, the normal and transverse carbon fibers with a nearby SiC matrix on the ground surface of CG and LIAAG were taken out through FIB-SEM and were observed through TEM. By this way, the fracture and crack morphology in the carbon fibers, the interface debonding, the SiC matrix fracture, and chip formation is clearly displayed. It should be noted that T300 carbon fiber consists of layers of graphite crystallites and amorphous carbon, and the layers of graphite crystallites are generally parallel to the carbon fiber axis [22]. CVI-SiC matrix is composed of β-SiC, which displays columnar structure in its growing direction [23].

Fig. 11 shows the TEM images of subsurface morphology of a normal carbon fiber during CG. It is found from Fig. 11a that very uneven fractures and cracks of varying sizes are present on the subsurface of the carbon fiber. Figs. 11b to 11e are the enlarged bright field (BF) TEM images of Fig. 11a. In Fig. 11b, no cracking occurs at the interface between SiC matrix and carbon fiber, and a fractured carbon fiber with the diameter of 800 nm remains on the surface, which indicates the micro

and fracture material removal caused by abrasive grain cutting. To investigate the crystal structure of this removed carbon fiber, its high resolution (HR) TEM image was taken, as shown in Fig. 11f. In the micro grinding chip, the graphite crystallites are clearly observed, the direction of which is well-ordered along the fiber axis. Typical bright (002) diffraction spots are seen in the fast Fourier transform (FFT) result in Fig. 11f, the interplanar spacing is around 0.35 nm, indicating that the degree of graphitization of carbon fiber was not affected by CG. In Fig. 11c, micro lateral cracks (have potential to result in material removal) are seen on the subsurface. The HT-TEM image of Fig. 11c is shown in Fig. 11g. The carbon fiber near the ground surface and around the crack still retained a highly ordered graphite lamellar structure, and the electron diffraction pattern in this area (Fig. 11i) show bright (002) diffraction spots, indicating that the subsurface microstructure of carbon fiber was not affected by CG. In Fig. 11d, both material removal and long median crack are found in the carbon fiber; since graphite crystallites are well ordered along fiber axis, the median crack can easily propagate along fiber. Besides, in Fig. 11e, the interface between two carbon fibers is found to be cracked, and the crack has a tendency to continue to expand downward. The interface of C_f/SiC composites is pyrolytic carbon, which is a similar structure with graphite lamellar. HR-TEM image in Fig. 11h indicates the lamellar structure of pyrolytic carbon is also parallel to the fiber axis; in this case, the crack can be easily propagated along carbon fiber.

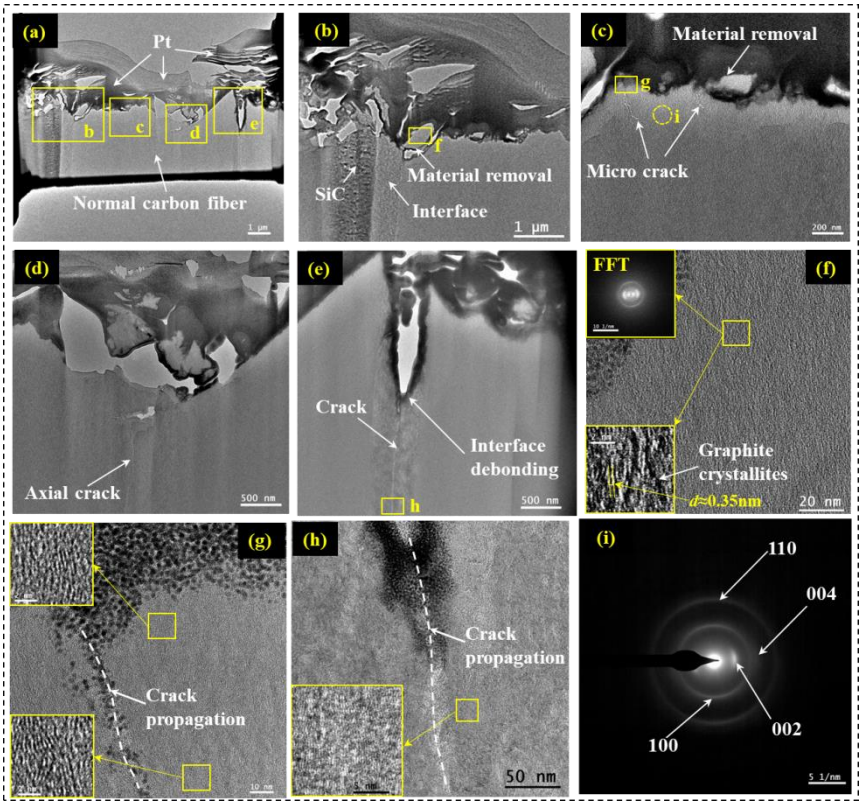

Fig. 11. TEM observation of normal carbon fiber during CG: (a) BF-TEM image of fiber subsurface, (b) to (e) enlarged BF-TEM images of (a) show crack detail, (f) HR-TEM of (b) shows well-ordered graphite crystallites in micro grinding chip, (g) HR-TEM of (c) shows well-ordered graphite crystallites near grinding surface, (h) HR-TEM of (e) shows graphite crystallites around crack, (i) electron diffraction pattern near grinding surface shows bright (002) diffraction spots.

Fig. 12 shows the TEM images of subsurface morphology of a transverse carbon fiber during CG. It

is found from Figs. 12a to 12c that the fractured carbon fiber with an uneven ground surface is almost pulled out, and obvious interface debonding is seen. Through both pulling-out and interface debonding are regarded as damages for C_f/SiC composites, their effects on material's mechanical property are different. Once the carbon fiber was pulled out or cracked, its toughening effect for SiC ceramic was lost and the mechanical property of C_f/SiC composites was decreased. On the contrary, Zheng et al. [23] thought that some degree of interface debonding allowed C_f/SiC composites occurred non-brittle failure, and its effect on mechanical property was less significant than pulling-out. Besides, the occurrence of fiber pulling-out is always accompanied by interface debonding, as shown in Fig. 12g. In Figs. 12d and 12f, median cracks are observed at the bottom of macro fractures. Fig. 12h shows the HR-TEM image of this crack in Fig. 12d, the interplanar spacing between graphite crystallites around the crack is generally increased, but the ordered structure kept unchanged. To analyze the effect of CG on graphite crystallites structure near the ground surface, a HR-TEM image was taken on the top of fractured carbon fiber (Fig. 12e), as shown in Fig. 12i. It can be clearly found that the orientation and interplanar spacing of graphite crystallites within a 1 nm of the surface is not changed. Based on these subsurface morphology observations, it can be concluded that the abrasive cutting actions during CG caused instantaneous embrittlement of carbon fibers, and no tribological action happened between these fractures and abrasive grains. In this case, the brittle damage forms are varied and the damage degree is significant, the size and morphology of the fracture are random.

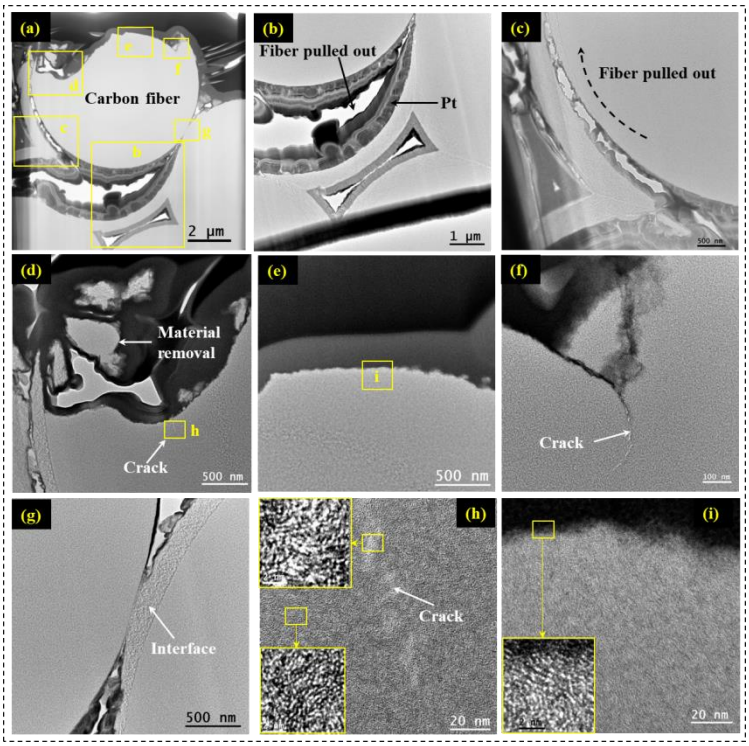

Fig. 12. TEM observation of transverse carbon fiber during CG: (a) BF-TEM image of fiber subsurface, (b) to (g) enlarged BF-TEM images of (a) show crack details, (h) HR-TEM of (d) shows graphite crystallites near crack, (i) HR-TEM of (e) shows well-ordered graphite crystallites near grinding surface.

The TEM images of subsurface morphology of near normal carbon fiber during LIAAG are shown in Fig.13 (the laser scanning interval is 100 μm, and the scanning direction is 90°). It is found from Fig. 13a that the carbon fiber shows a relative flat fracture appearance compared with Fig. 14a, and the interface debonding does not occur. In the enlarged BF-TEM images (Figs. 13b to 13e), many lateral

micro cracks are found on the subsurface. The micro cracks did not propagate downward but finally results in many micro grinding chips. Especially, some forming chips display certain orientation characteristics (Figs. 13f and 13g). To further understand the effect of LIAAG on graphene sheets structure of carbon fiber, an electron diffraction pattern was performed in the chip formation zone (Fig. 13h) and substrate zone (Fig. 13i), respectively. Both diffraction images consist of complete lattice fringes of carbon fiber, i.e., (002), (110), (004), and (100); the (002) diffraction spots in Fig. 13i show typical lattice images of T300 carbon fiber, but the (002) diffraction spots in Fig. 14h is significantly lengthened, which indicates the graphene sheets in the chip formation zone are kept but their orientations are disordered. Based on these observations, it can be inferred that the highly-ordered graphene sheets occurred deformation during cutting and friction with abrasive grains. In general, the macro brittle fracture of normal carbon fiber is significantly reduced during LIAAG, and micro fracture and deformation became the main damage form.

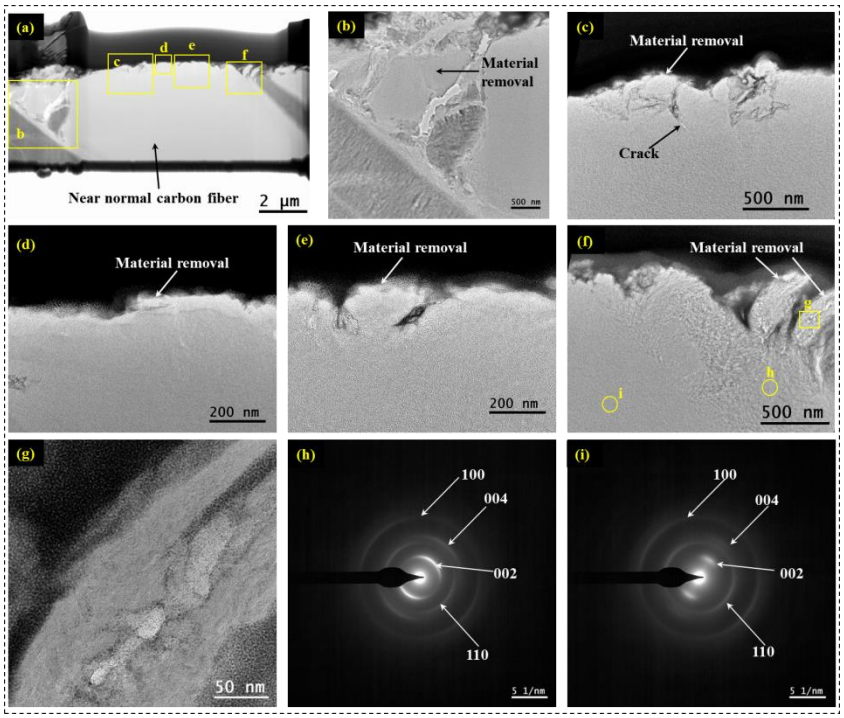

Fig. 13. TEM observation of near normal carbon fiber during LIAAG: (a) BF-TEM image of fiber subsurface, (b) to (f) enlarged BF-TEM images of (a) show crack details, (g) enlarged BF-TEM image of micro grinding chip in (f), (h) electron diffraction pattern near grinding surface indicates (002) diffraction spots lengthening, (i) electron diffraction pattern of carbon fiber substrate shows unaffected (002) diffraction spots.

The TEM images of subsurface morphology of transverse carbon fiber during LIAAG are shown in Fig. 14 (the laser scanning interval is 100 μm, and the scanning direction is 90°). In Fig. 14a, the carbon fiber shows a relative flat fracture appearance compared with that in Fig. 14a, and the interface debonding is not found. However, in the enlarged BF-TEM images (Figs. 14b to 14e), many median and lateral cracks are observed， and the longest median crack propagates to the boundary between carbon fiber core and skin (Fig. 14d). To analyze the effect of LIAAG on graphene sheets structure, the electron diffraction pattern was performed near the ground surface (the (f) area in Fig. 14c), as shown in Fig. 14f. The two bright (002) diffraction spots are observed, but they are observably lengthened, indicating the graphene sheets in this area become misoriented. It is worth noting that the

diameter of an electron diffraction pattern measuring zone is around 100 nm, and it is necessary to take a HR-TEM image of carbon fiber in this region for understanding the crystallite structure, as shown in Fig. 14g. Interestingly, an amorphous structure layer with thickness of around 28 nm is found, where the highly-ordered graphene sheets disappear. Just about 20 nm below the amorphous structure layer, the graphene sheets still be observed. The FFT results in two areas are shown in Fig. 14h and 14i, the (002) lattice image of amorphous structure layer is not found (Fig. 14h), but that below amorphous layer can be observed (Fig. 15h). Notably, the Pt plating process in FIB sample preparation is not the cause of this phenomenon, since the similar phenomenon was not found on other samples (Figs. 11 to 13). Combined with the fiber surface morphology observations in Fig. 10, it is certain that the micro fractured carbon fiber underwent significant extrusion and friction with the abrasive grains during grinding, and this high stress may be one of the reasons for the formation of amorphous layer. In the CG process (Figs. 11 and 12), it was mentioned that the carbon fibers were mainly removed in the form of macro brittle fracture, and the friction action between fibers and abrasive grains was very small, so the amorphous layer was not found.

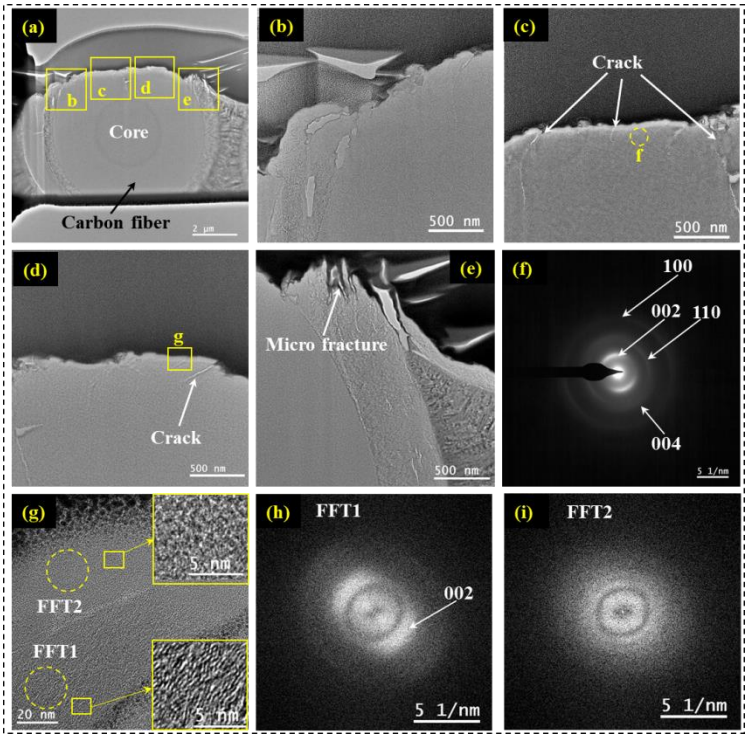

Fig. 14. TEM observation of transverse carbon fiber after LIAAG: (a) BF-TEM image of fiber subsurface, (b) to (e) enlarged BF-TEM images of (a) show crack detail, (f) electron diffraction pattern near grinding surface in (c), (g) HR-TEM image near grinding surface in (d) shows amorphous structure, (h) FFT result from (g) shows (002) diffraction spots, (i) FFT result from (g) shows fuzzy diffraction ring.

4. CONCLUSION

(1) During picosecond laser ablating, the C_f/SiC composites in the center of ablation zone is sublimated directly, and the edge materials occur violent chemical reaction, resulting in SiO_2 ablated layer with loose structure. As the laser scanning interval increases, the content of ablative products is increased.

(2) Compared with CG, the grinding force of LIAAG shows a more pronounced fluctuation, and value is observably decreased. As the laser scanning interval increases, the grinding forces have and increasing trend. The normal and tangential grinding forces can be reduced by up to 88% and 87%,

respectively through LIAAG.

(3) The surface roughness of LIAAG is significantly reduced compared with that of CG. As the laser scanning interval increases, the surface roughness is increased. Besides, the 90° laser scanning can lead to the lowest surface roughness. The parallel and perpendicular surface roughness can be reduced by up to 54% and 42%, respectively through LIAAG.

(4) The surface removal morphology of C_f/SiC composites after CG is primarily macro brittle fracture of carbon fiber and SiC matrix, and fiber pulling-out damage mostly appears. On the contrary, the C_f/SiC composites after LIAAG shows matrix ductile removal and fiber micro removal morphologies, and the brittle fracture damages are significantly decreased. In addition, the surface finishing of LIAAG has a decreasing trend with decreasing laser scanning interval.

(5) Obvious subsurface damages, including fiber pulling-out, fiber cracking, and interface debonding, occur in C_f/SiC composites after CG. Through LIAAG, the subsurface damage is significantly decreased, which primarily includes micro crack. Furthermore, the graphite crystallites of carbon fiber near LIAAG surface become disordered, and amorphous structure layer with the thickness of 28 nm is firstly found.

ACKNOWLEDGMENT

The work is supported by the National Natural Science Foundation of China (No. 52205444), the National Natural Science Foundation of Chongqing (No. CSTB2022NSCQ-MSX1128), and the China Postdoctoral Science Foundation (No. 2021M700586).

REFERENCES

1. N.P. Padture, “Advanced structural ceramics in aerospace propulsion,” *Nat. Mater.*, Vol.15, No.8, 804–809, 2016.
2. W. Hu, J.Z. Huang, C. Zhang, T.F. Ren, T.H. Guan, K. Wu, et al., “Effect of shear strain rate on interlaminar shear behavior of 2D-C/SiC composites: A damage transition from notch ends initiation to gauge section initiation,” *Carbon*, Vol.167, 770–784, 2020.
3. G. G. Luna, D. Axinte, D. Novovic, “Influence of grit geometry and fibre orientation on the abrasive material removal mechanisms of SiC/SiC Ceramic Matrix Composites (CMCs),” *Int. J. Mach. Tools Manuf.*, Vol.157, 103580, 2020.
4. O.G. Diaz, D.A. Axinte, “Towards understanding the cutting and fracture mechanism in Ceramic Matrix Composites,” *Int. J. Mach. Tool Manufact.*, Vol.118, 12–25, 2017.
5. Q. An, J. Chen, W. Ming, M. Chen, “Machining of SiC ceramic matrix composites: A review,” *Chinese J. Aeronaut*, Vol.34, No.4, 540–567, 2021.
6. F. Xue, K. Zheng, W. Liao, J. Shu, D. Miao, “Experimental investigation on fatigue property at room temperature of C/SiC composites machined by rotary ultrasonic milling,” *J. Eur. Ceram. Soc.*, Vol.41, No.6, 3341–3356, 2021.
7. K. Zhou, G. Xiao, J. Xu, Y. Huang, “Material removal behavior of C_f/SiC ceramic matrix composites as a function of abrasive wear during diamond abrasive belt grinding,” *Wear*, Vol.486–487, No.4, 204101, 2021.
8. K. You, G. Yan, X. Luo, M.D. Gilchrist, F. Fang, “Advances in laser assisted machining of hard and brittle materials,” *J. Manuf. Process.*, Vol.58, 677–692, 2020.
9. X. Dong, Y. Shin, “Improved machinability of SiC/SiC ceramic matrix composite via laser-assisted micromachining,” *Int. J. Adv. Manuf. Technol.*, Vol.90, 731–739, 2017.

10. J.C. Rozzi, M.D. Barton, “The laser-assisted edge milling of ceramic matrix composites,” *Proceedings of the ASME 2009 International Manufacturing Science and Engineering Conference*, 845–852, West Lafayette Indiana, USA, October 2009.
11. T. Cheng, X. Wang, R. Zhang, Y. Pei, S. Ai, R. He, et al., “Tensile properties of two-dimensional carbon fiber reinforced silicon carbide composites at temperatures up to 2300℃,” *J. Eur. Ceram. Soc.* Vol.40, No.3, 630–635, 2020.
12. D.T. Blagoeva, J.B.J. Hegeman, M. Jong, M.C.R. Heijna, S.M. Gonzalez de Vicente, T. Bakker, P. ten Pierick, et al., “Characterisation of 2D and 3D Tyranno SA 3 CVI SiC_f/SiC composites,” *Mater. Sci. Eng. A*, Vol.638, 305–313, 2015.
13. J. Chen, Q. An, W. Ming, M. Chen, “Investigations on continuous-wave laser and pulsed laser induced controllable ablation of SiC_f/SiC composites,” *J. Eur. Ceram. Soc.*, Vol.41, No.12, 5835–5849, 2021.
14. H. Jiao, B. Chen, Z. Deng, “Influence of laser parameters on processing microgrooves of 2.5-dimensional C/SiC composites via nanosecond laser,” *Int. J. Adv. Manuf. Technol.*, Vol.118, No.1-2, 85–101, 2022.
15. K. Zhou, J. Xu, G. Xiao, Y. Huang, “A novel low-damage and low-abrasive wear processing method of C_f/SiC ceramic matrix composites: Laser-induced ablation-assisted grinding,” *J. Mater. Process. Technol.*, Vol.302, 117503, 2022.
16. J. Zhang, S. Yuan, J. Wei, J. Li, Z. Zhang, W. Zhang, et al., “Spatio-temporal multi-scale observation of the evolution mechanism during millisecond laser ablation of SiC_f/SiC,” *Ceram. Int.*, Vol.48, 23885–23896, 2022.
17. Z. Zhai, C. Wei, Y. Zhang, Y. Cui, Q. Zeng, “Investigations on the oxidation phenomenon of SiC/SiC fabricated by high repetition frequency femtosecond laser,” *Appl. Surf. Sci.*, Vol.502, 144131, 2020.
18. J. Chen, Q. An, Q. Gong, D. Zeng, M. Chen, “Machinability improvement in milling of SiC_f/SiC composites based on laser controllable ablation pretreatment,” *J. Eur. Ceram. Soc.*, Vol.43, No.4, 1352–1365, 2023.
19. G. Zhao, Z. Nian, Z. Zhang, L. Li, N. He, “Enhancing the machinability of C_f/SiC composite with the assistance of laser-induced oxidation during milling,” *J. Mater. Res. Technol.*, Vol.22, 1651–1663, 2023.
20. J. Lee, J. Choi, D. Jang, S. Lee, T. Kim, S. Lee, “Processing-controlled radial heterogeneous structure of carbon fibers and primary factors determining their mechanical properties,” *Carbon*, Vol.206, 16-25, 2023.
21. K. Zhou, J. Xu, G. Xiao, B. Zhu, Y. Huang, “Enhancing ductile removal of C_f/SiC composites during abrasive belt grinding using low-hardness rubber contact wheels,” *Ceram. Int.*, Vol.48, No.18, 26042–26054, 2022.
22. J. Chen, Q. An, M. Chen, “Transformation of fracture mechanism and damage behavior of ceramic matrix composites during nano-scratching,” *Compos. Part A Appl. Sci. Manuf.*, Vol.130, 105756, 2022.
23. G. Zheng, H. Sano, K. Suzuki, K. Kobayashi, Y. Uchiyama, H. Cheng, “A TEM study of microstructure of carbon fiber/polycarbosilane-derived SiC composites,” *Carbon*, Vol.37, 2057–2062, 1999.

Fabrication of large aerogel-like carbon/carbon composites with excellent load-bearing capacity and thermal-insulating performance at 1800 °C

Jian Li[a, 1], *Penglei Guo*[a, b, 1], *Chenglong Hu*[a], *Shengyang Pang*[a], *Jian Ma*[a, b], *Rida Zhao*[a, b], *Sufang Tang*[a *], *and Hui–Ming Cheng*[c *]

[a] Institute of Metal Research, Chinese Academy of Sciences, Shenyang 110016, PR China

[b] School of Materials Science and Engineering, University of Science and Technology of China, Shenyang 110016, PR China

[c] Shenyang National Laboratory for Materials Science, Institute of Metal Research, Chinese Academy of Sciences, Shenyang 110016, PR China

[1] These authors contributed equally to this work.

Abstract:Carbon aerogels (CAs) are attractive candidates for the thermal protection of aerospace vehicles due to their excellent thermostability and thermal insulation. However, the brittleness and low mechanical strength severely limit their practical applications, and no significant breakthroughs in large CAs with a high strength have been made. We report a high-pressure-assisted polymerization method combined with ambient pressure drying to fabricate large, strong, crack-free carbon/carbon (C/C) composites with an excellent load-bearing capacity, thermal stability and thermal insulation. The composites are comprised of an aerogel-like carbon matrix and a low carbon crystallinity fiber reinforcement, featuring overlapping nanoparticles, macro-mesopores, large particle contact necks and strong fiber/matrix interfacial bonding. The resulting C/C composites with a medium density of 0.6 g cm^{-3} have a very high compressive strength (80 MPa), in-plane shear strength (20 MPa), and specific strength (133 MPa g^{-1} cm^3). Moreover, the C/C composites of 7.5–12.0 mm in thickness exposed to an oxyacetylene flame at 1800 °C for 900 s display very low back-side temperatures of 778–685 °C, and even better mechanical properties after the heating. This performance makes the composites ideal for the ultra-high temperature thermal protection of aerospace vehicles where both excellent thermal-insulating and load-bearing capacity are required.

Keywords: Lightweight carbon/carbon composites, aerogel, fiber-reinforced, thermal insulation, mechanical properties

With the rapid development of aerospace vehicles for higher speed and longer flight time accompanied by the restricted volume and weight of the thermal protection system (TPS), TPS working at ultra-high temperatures (higher than 1650 °C) is subjected to severe aerodynamic heating and intense mechanical stresses associated with vibration, impact and thermal loading during launch and re-entry, or in flight in the Earth's atmosphere.[1] Thermal insulation materials with good ultra-high temperature resistance and mechanical strength are therefore urgently needed. Carbon-based materials have an extremely high thermal stability to 3000 °C, which makes them the most promising candidates for lightweight aerospace materials.[2] Carbon fiber-reinforced carbon-matrix composites, also known as carbon/carbon (C/C) composites, are an outstanding example of carbon-based materials since their unique composition gives them outstanding properties such as low density, good thermal shock resistance, low thermal expansion, and excellent mechanical properties at high temperatures.[3,4] However, their uses as thermal insulation materials are limited by the high thermal conductivity (TC) caused by their compact structure and high crystallinity.

The great versatility of carbon-based materials makes it possible to design many structures with different and even contradictory properties. Carbon aerogels (CAs) with abundant mesopores and an overlapping nanoparticle network are considered as one of the promising candidates for thermal insulation at ultra-high temperatures.[5-7] They have the highest thermal stability among all the aerogels and maintain their mesoporous texture at temperatures above 2000 °C in an inert atmosphere.[8] However, they always have a poor mechanical strength due to their highly porous and weak skeletal network.[9,10] In addition, the applications of CAs have been restricted by the great difficulty in forming them in large sizes because surface tension and volume shrinkage during drying and carbonization lead to their cracking.[9,11] To reduce surface tension and prevent pore collapse, a tedious solution exchange process and/or a high-cost supercritical drying are usually necessary.[7,12]

To produce large CAs with improved robustness, three main approaches have been explored. The first is to optimize the network so that it has better structural uniformity and skeletal strength by adjusting the synthesis parameters.[5,7,9,13-17] However, the improvement is very limited due to the intrinsic skeletal structure of extremely limited connections and fragile joints of nanoparticles. The second is to form a composite structure by adding reinforcements. Many

attempts have been made to strengthen and toughen CAs by adding carbon fibers[10] and ceramic fibers.[18] However, the large shrinkage mismatch between these rigid fiber reinforcements and the organic aerogels during drying and carbonization produces a high residual tensile stress or even interlaminar cracking in the CA composites;[19,20] and the addition of fibers with a high crystallinity leads to an increase in the TC of the composites.[18] It is encouraging that large fiber-reinforced CA composites without macroscopic cracks have been produced using pre-oxidized polyacrylonitrile (PAN) fiber felt[21] or hyper-elastic carbon fiber felt.[20] The third is to increase the bulk density of the CAs since mechanical robustness is strongly related to bulk density. However, the increase of bulk density results in the smaller pore apertures and increased capillary forces, which makes the fabrication of large artefacts more difficult. Only a very few studies are available on the effect of density on the mechanical and thermal properties of CAs with medium bulk densities. The reported CAs are always small (< 50 mm) with low bulk densities (< 0.3 g cm^{-3}), high surface areas (> 600 m^2 g^{-1}), and low compressive strengths (< 1 MPa), and have been mostly investigated for potential applications in energy storage,[22-25] microwave absorption,[6] and oil-water separation.[12,26-28] Therefore, the development of large CA monoliths with high mechanical strength and low TC by a simple and economical route remains a challenge.

Here we report the development of large C/C composites with an aerogel-like carbon matrix and a low crystallinity fiber reinforcement using high-pressure-assisted polymerization combined with ambient pressure drying (APD). A 3D chopped phenolic fiber felt was used as a reinforcement precursor in a phenolic resin and cross-linker reaction system in order to improve the interfacial bonding strength through crosslinking reaction during polymerization and simultaneous shrinkage during carbonization. The prepared C/C composites have a medium bulk density, low thermal conductivity, good load-bearing ability, and can be formed into large artefacts. Their specific strength (133 MPa g^{-1} cm^{-3}) is much higher than those of recently reported CA monoliths or composites, and to the best of our knowledge, there are few reports about C/C composites with good load-bearing capacity and thermal insulation performance at ultra-high temperatures.

Results and Discussion

Preparation of C/C composites and the shrinkage match of fiber and matrix precursors

In order to prepare robust, crack-free CA monoliths with a low TC by APD, it is necessary to precisely design the pore structure as well as the skeletal strength to allow quick and safe drying and carbonization. We propose the following design principles: 1) medium bulk densities; 2) a uniform and robust skeleton; 3) suitably increased pore apertures; and 4) the introduction of a non-graphitizable reinforcement. **Figure 1** illustrates the preparation process of C/C composites. It consists of impregnation, high-pressure-assisted polymerization (curing), APD without solution exchange, and carbonization. Phenolic resin (PR) and hexamethylenetetramine (HMTA) were used as the reactive precursor and cross-linker, respectively. It has been indicated that a robust skeleton and macro-porous cells are critically important in reducing the shrinkage and collapse of the pore structure during APD.[29] Compared with the widely used resorcinol-formaldehyde (RF) reaction system, the lower steric hindrance and chain branching in the PR-HMTA system can favor the formation of relatively large polymer clusters and a robust network.[11] Furthermore, ethylene glycol (EG) with a high boiling point was used as the solvent instead of the commonly used organic solvents such as ethanol, because a higher temperature and a longer holding time are required for the polymerization of PR with HMTA in EG. This mild polymerization can further prompt the growth of polymer clusters and the interparticle connection, which are beneficial for the increase of skeletal strength. In order to strengthen and toughen the resulting porous matrix, a 3D organic phenolic fiber (PF) felt, fabricated by the needle-punching of chopped PF nets,[30] was used as the reinforcement precursor to form a composite structure. As shown in the insets a and b in **Figure 1**, most of the fibers of the felt are in the *XY* plane and the number of punching fibers in the *Z* direction is small from 3D X-ray tomography (XRT) images. The structure design is expected to keep the integrity of the felt thus increasing the interlaminar bonding and reducing heat transfer in the *Z* direction. To obtain a more uniform and robust skeleton, high-pressure-assisted polymerization was used to prevent moving or even blowing of PR solution as a consequence of the rapid release of volatile by-products at the curing temperature. As a result, APD without repeated organic solution exchange steps can be carried out. Overall, this preparation route is green and highly efficient, taking about a week, which is a third of the time needed for supercritical drying.[21,31]

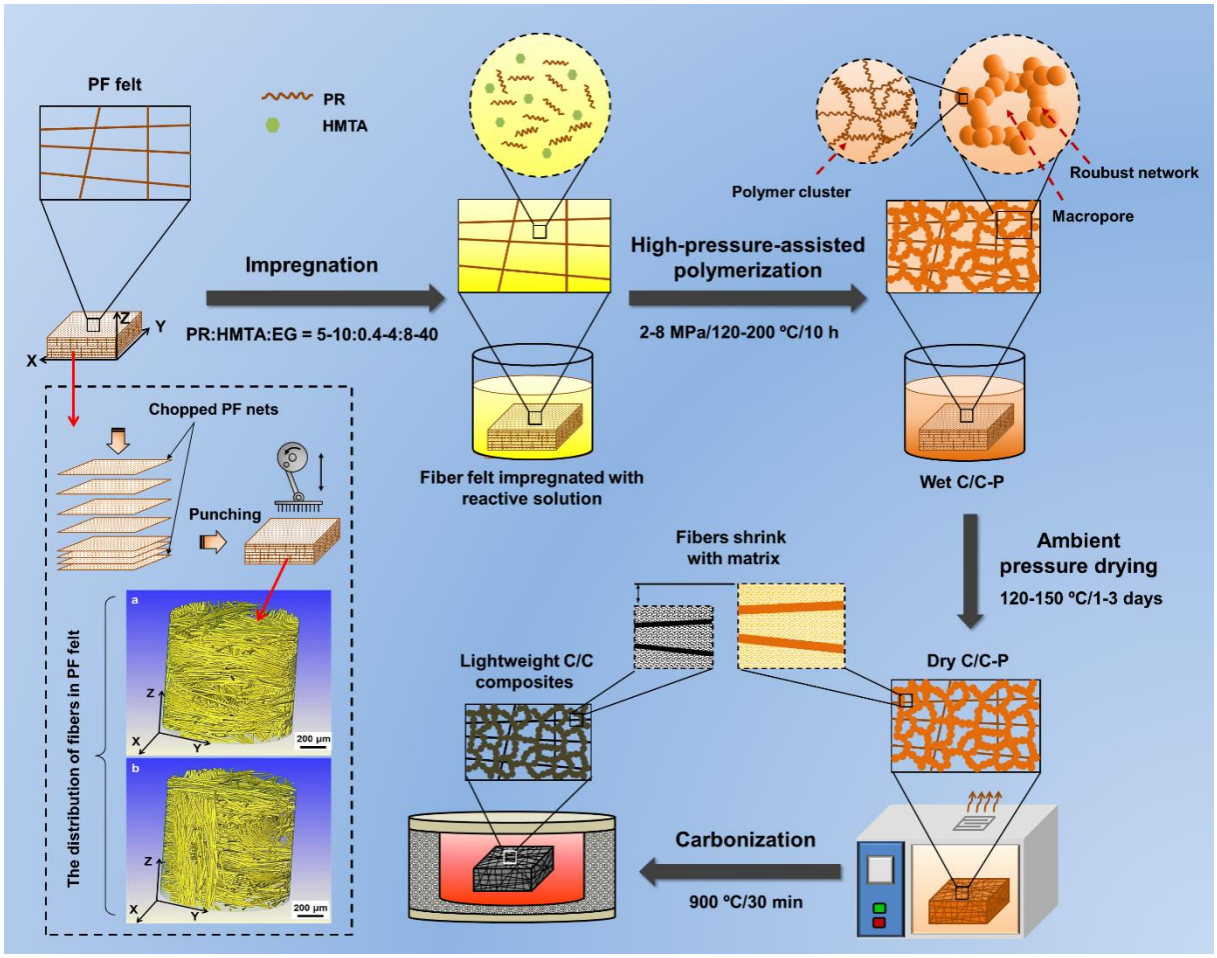

Figure 1. Preparation of C/C composites through impregnation, high-pressure-assisted polymerization, ambient pressure drying and carbonization. The insets (a) and (b) are typical 3D-XRT images of PF felt.

To ascertain the shrinkage match of the matrix and reinforcement of the C/C precursor (C/C-P) during carbonization, the pyrolysis behavior of the porous carbon precursor (PCP, pure organic monolith without reinforcement) and PF felt were investigated using thermogravimetry (TG) and differential scanning calorimetry (DSC). The corresponding TG and DSC curves are shown in **Figure 2**a. The TG curves of PCP and PF felt can be divided into four stages. In the first stage (25–95 °C), the mass losses of PCP and PF felt are 1.9% and 1.6%, respectively, due to the volatilization of absorbed moisture. In the second stage (95–450 °C), the mass loss of PCP is 22.4% due to the dehydration condensation of phenolic hydroxyl groups and carbon-nitrogen bond (C–N) breakage,[32] which is larger than that of the PF felt (10.2%). The larger mass loss is related to the volatilization of residual solution and the porous matrix with a relatively high reactivity. In the third stage (450–800 °C), the PCP and PF felt have a similar

mass loss of 27.3% and 31.5%, respectively, on account of the methylene bond (–CH_2–) breakage and dehydrocyclization of the aromatic rings.[33] In the fourth stage (> 800 °C), the measured mass losses are both less than 0.5%, indicating that the pyrolysis was almost finished at 800 °C. From the above analysis, the PCP and PF felt have

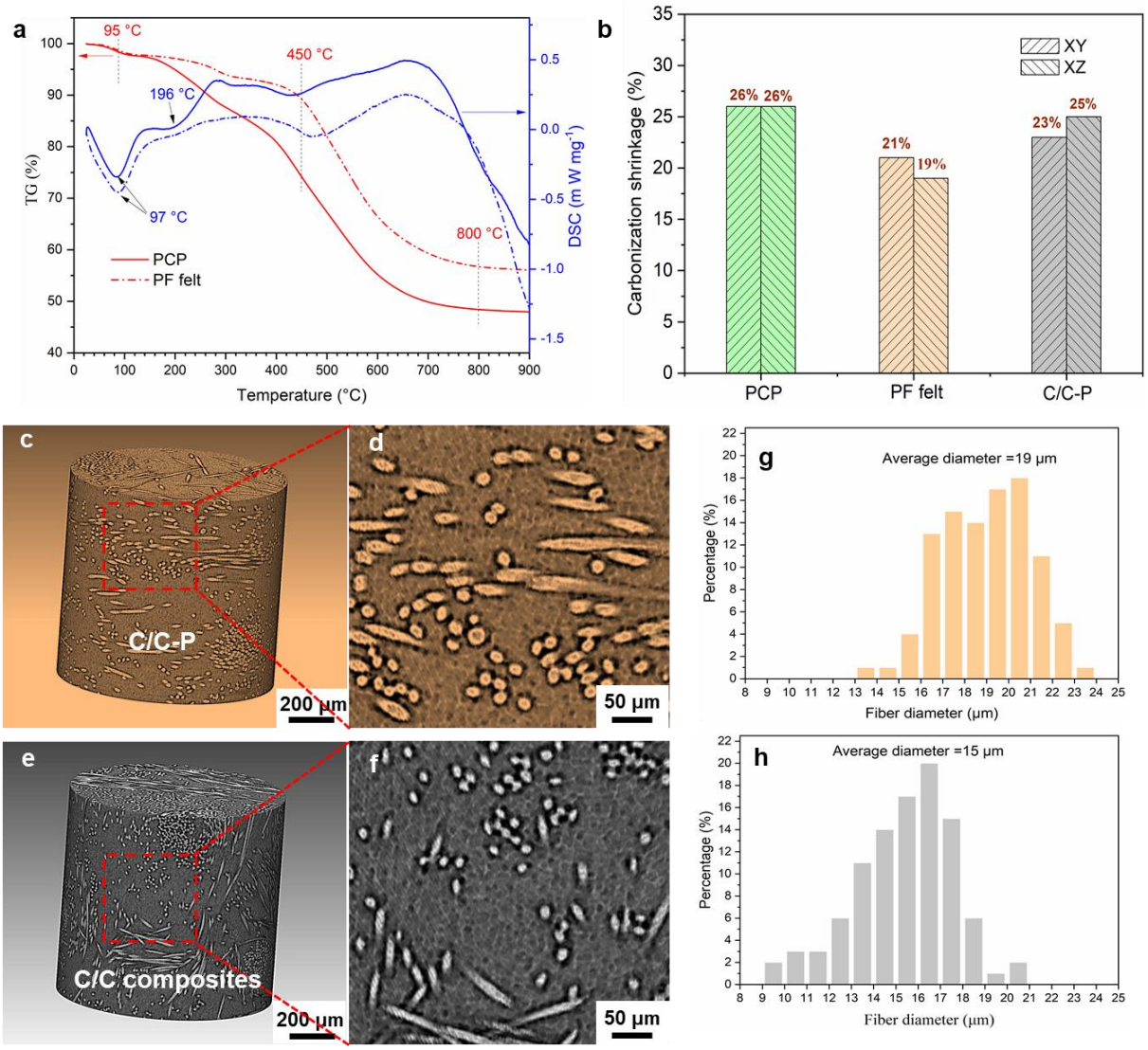

Figure 2. (a) TG and DSC curves of PCP and PF felt. (b) Carbonization shrinkages of PCP, PF felt and C/C-P in *XY* and *XZ* planes. 3D-XRT images of (c, d) C/C-P and (e, f) C/C composites. Distribution of fiber diameters in (g) C/C-P and (h) C/C composites.

quite similar trends in the TG and DSC curves throughout the pyrolysis process, implying their similar carbonization shrinkage behaviors.

Figure 2b shows shrinkages of PCP, PF felt and C/C-P carbonized at 900 °C. The PCP has the same carbonization shrinkages (26%) in the *XY* and *XZ* planes because it is isotropic, and the value is similar to those for the conventional RF aerogels (~25%).[9] The PF felt has similar

shrinkages to PCP, and those in the *XY* and *XZ* planes are 21% and 19%, respectively. The difference of shrinkages between PCP and PF felt is calculated to be 5%–7%. The good shrinkage match of the PF felt and the organic matrix is believed to improve the mechanical robustness of product and the ability to form large artefacts. To characterize the internal structure of the materials, 3D-XRT images of the C/C-P and C/C composites are shown in **Figure 2** c–f. For the C/C composites, no micro-cracks or large voids are observed due to the good shrinkage match during carbonization. **Figure 2**g,h shows the diameter distributions of PF in the radial direction before and after carbonization. The average diameter of 100 measured fibers decreases from 19 to 15 μm. The corresponding shrinkage is 21%, which is close to that of PCP. The shrinkage of PF in the axial direction was also measured at different temperatures and the results are listed in **Table 1**. For comparison, those of commercial rayon fibers and PAN fibers are also listed. Apparently, PF is the most suitable fiber reinforcement among these fibers since its carbonization shrinkage is the closest to that of PCP, especially when the carbonization temperatures are above 900 °C.

Table 1. Carbonization shrinkages of PF, rayon fiber and PAN fiber in the axial direction.

Carbonization temperature (°C)	Shrinkage (%)		
	PF	Rayon fiber	PAN fiber
600	15.5	31.3	29.8
750	17.9	33.5	30.4
900	20.4	34.1	38.4
1050	20.6	35.0	42.9
1200	20.6	35.2	43.2

Microstructure and outstanding load-bearing performance of the C/C composites

Figure 3 a–c shows SEM images of the C/C composites at different magnifications. An important feature of the composites is that there are no micro-cracks (**Figure 3**a, and **2**e,f), which is crucial for producing large artefacts. However, some micro-cracks can be found in the reported composites when using pre-oxidized PAN fibers as the reinforcement since the difference of carbonization shrinkage between fibers and RF aerogel matrix reaches 14%.[18,21]

Even interlaminar cracking is present when using rigid fibers as the reinforcement because of their distinct shrinkage mismatch.[10,20,34] More importantly, the carbon particles at the fiber/matrix interface stick firmly to the fiber surface, as shown in **Figures 3**b,c. This sharply

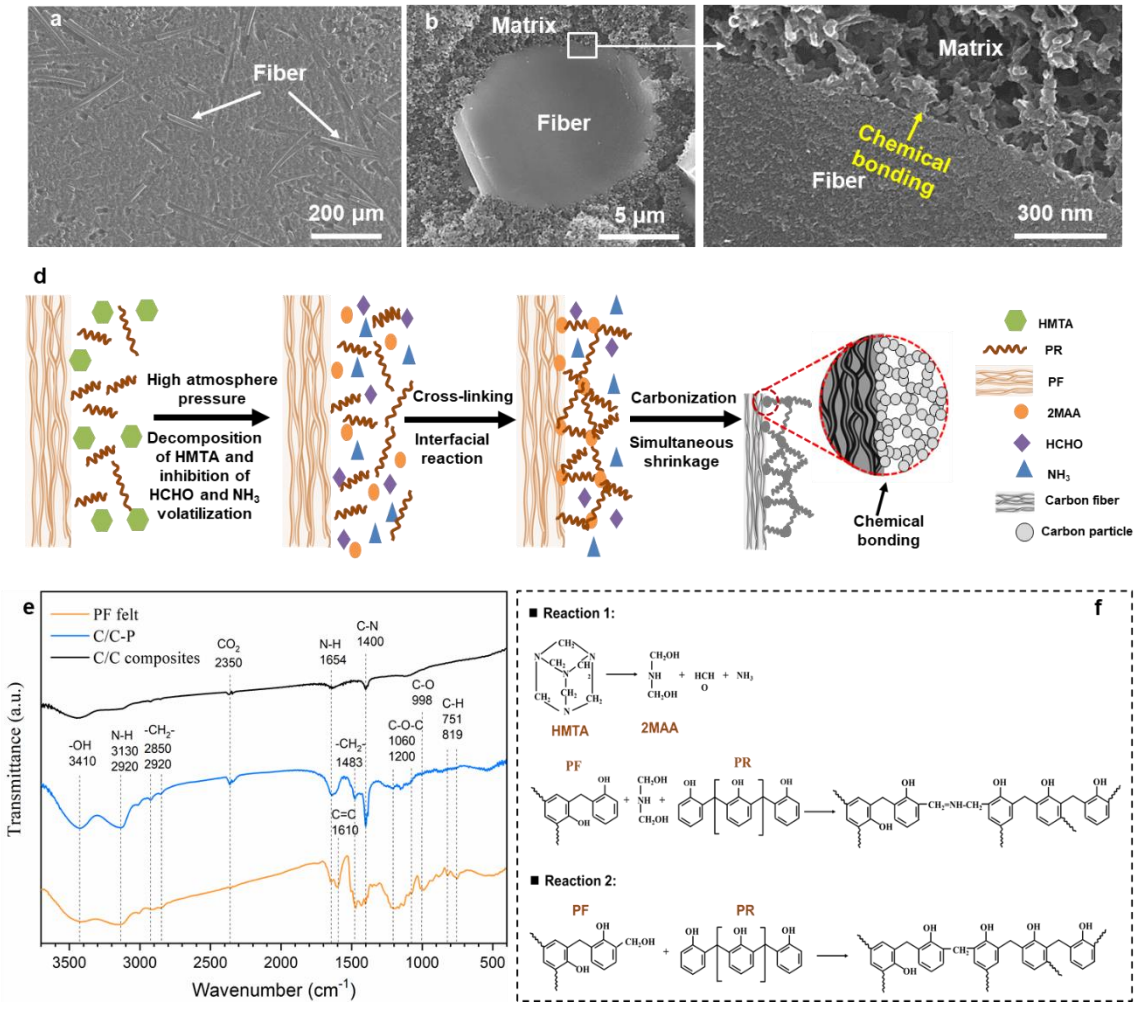

Figure 3. (a–c) SEM images of the microstructure of C/C composites at different magnifications. (d) Schematic of the interaction between PF and the reactive solution during the preparation process. (e) FTIR spectra of PF felt, C/C-P and C/C composites. (f) Chemical reactions of PF with the reactive solution during curing.

contrasts to CA composites reinforced by traditional ceramic fibers or carbon fibers, in which obvious interfacial debonding occurs due to the shrinkage mismatch of fibers and matrix during carbonization.[18] This tight fiber/matrix interfacial bonding implies that PF has reacted with the organic matrix. **Figure 3**d illustrates a related interaction between PF and the organic matrix during the composite preparation. At first, a high-pressure atmosphere is used to prevent the rapid release of volatile by-products such as HCHO and NH_3 at high temperatures, and makes

for the growth of a more uniform gel network on the fiber surface. A chemical crosslinking reaction then occurs at the interface between PF and the reactive solution, as shown by the PF and C/C-P FTIR spectra (**Figure 3**e,f). The peaks at 751 and 819 cm^{-1} for PF are attributed to hydrogen atoms in the aromatic rings with ortho- and para-positions, respectively.[11,33] When the temperature exceeds 100 °C during curing, HMTA is decomposed into 2 methyl alcohol amine (2MMA), formaldehyde (HCHO) and ammonia (NH_3).[35] The hydroxymethyl ($–CH_2OH$) of 2MMA reacts with the ortho- and para-hydrogen of PF and PR through dehydration condensation, resulting in the formation of C-N (1400 cm^{-1}). The corresponding reaction is shown in **Figure 3**f as Reaction 1. In addition, the $–CH_2OH$ (C–O, 998 cm^{-1}) of PF reacts with the ortho- and para-hydrogen of PR through dehydration condensation, resulting in the formation of $–CH_2–$ (1483, 2850, and 2920 cm^{-1}) as indicated in **Figure 3**f as Reaction 2. The much lower peaks at 751, 819, and 998 cm^{-1} for C/C-P confirm these reactions. Subsequently, the PF shrinks with the organic matrix during carbonization on account of their similar molecular structures. Overall, an interfacial chemical reaction during polymerization and simultaneous shrinkages of fiber and matrix precursors during carbonization are both necessary to obtain the strong, crack-free and large C/C composites.

Figure 4a shows morphology of the matrix of C/C composites. It exhibits a randomly stacked nanoparticles network containing abundant pores. The carbon particles are relatively uniform with a size range of 30–90 nm (**Figure 4**b). The pores are mostly mesopores and macropores with a bimodal distribution of pore diameters in the ranges of 40–60 nm and 100–120 nm (**Figure 4**c), respectively, suggesting a macro-mesoporous network. The structure configurations of traditional CAs can mainly be classified into two types: pearl-necklace and fibril configuration.[32] Unlike the RF-derived CAs with a pearl-necklace configuration,[7] the

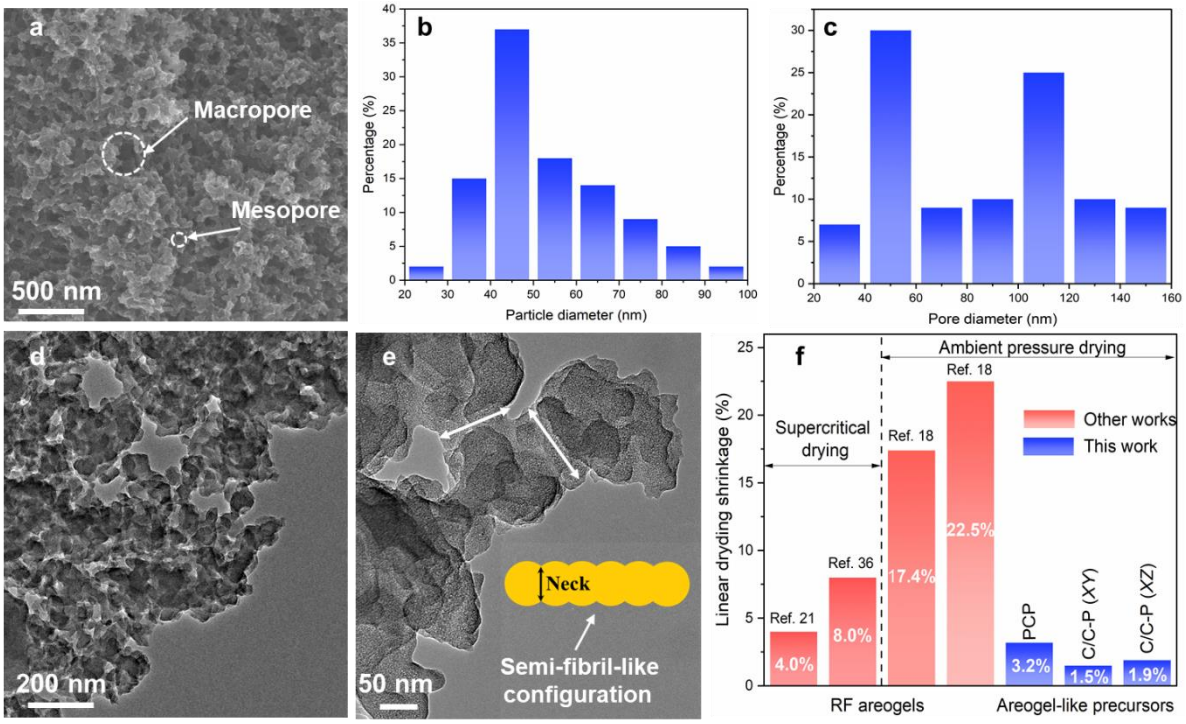

Figure 4. (a) SEM image of matrix. (b) Particle size distribution. (c) Pore diameter distribution. (d, e) TEM images. (f) Drying shrinkage of aerogel-like porous precursors in this work and RF aerogels reported in other references.

matrix of C/C composites has a typical semi-fibril-like configuration with the larger contact necks between particles (**Figure 4**d,e). In the preparation of conventional organic aerogels, necks are formed by the coagulation of polymer particles during slow gelation and grow to a certain size by dissolution and re-precipitation of polymer clusters during aging.[11] In this work, the slow polymerization of PR with HMTA in EG facilitates the formation of large polymer clusters and compact particle connection, which increases the intrinsic skeletal strength.[11,17] From the above description, the matrix has an aerogel-like network with overlapping nanoparticles, macro-mesopores, and large necks. This robust network together with the presence of macropores effectively resists capillary forces during APD, resulting in a limited drying shrinkage of PCP (3.2%) (**Figure 4**f). This is even comparable to that of RF aerogels prepared by supercritical drying (4%–8%)[21,36] and much smaller than that through APD (17%–23%).[18] Due to the introduction of the organic fiber felt, the shrinkages of C/C-P in the *XY* and *XZ* planes decrease obviously to 1.5% and 1.9%, respectively.

Figure 5a shows typical stress-strain curves of the porous carbon (PC, derived from the

carbonization of PCP) and C/C composites during compression tests, giving the respective mean compressive strengths of 96 and 80 MPa. The higher compressive strength of PC is mainly attributed to its higher bulk density (PC: ρ_{bulk} = 0.68 g cm^{-3}, C/C: ρ_{bulk} = 0.60 g cm^{-3}) caused by its larger carbonization shrinkage (Section 2.1). The PC suffers catastrophic brittle fracture with a failure strain of ~5.5%, presenting a cliff-like drop of the stress when it reaches the maximum; and has broken into many small debris scattered around the test platform. However, for the C/C composites, the stress presents a gradual decline with a ladder-like shape accompanied by a larger failure strain (~7.0%) (**Figure 5**a); and an integral block with many large cracks has remained in the center of the test platform after compression. Moreover, an obvious fiber pull-out can be found and many large dimples around the deep holes formed by the fiber pull-out are present in their fracture surface due to the good fiber/matrix interfacial bonding (**Figure 5**b). These demonstrate the increased toughness of C/C composites, therefore having a large work of fracture and a greatly improved crack tolerance. It should be clarified that it seems as if the carbon matrix is quite compact under this low magnification. In fact, the typical microstructure of aerogel materials with random and well-distributed nanoparticles and nanopores can be seen clearly under a relatively high magnification, as shown in **Figures 3**c and **4**a.

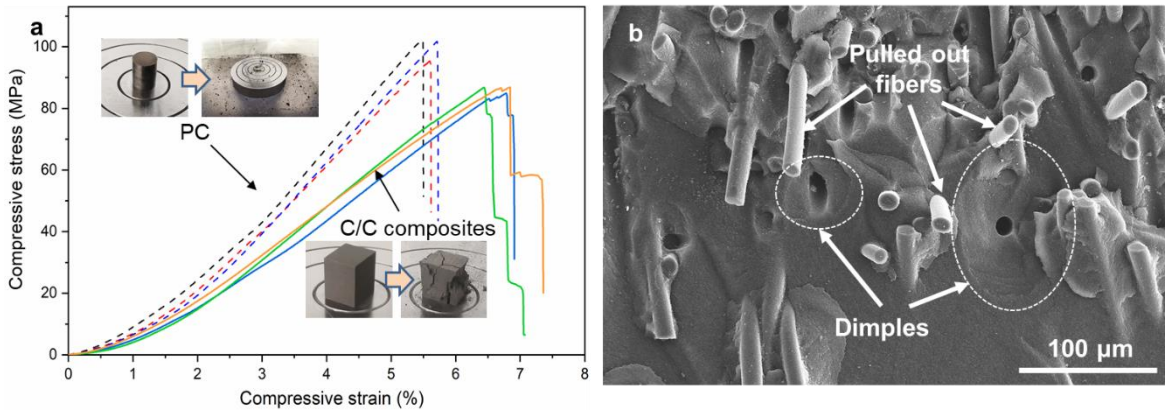

Figure 5. (a) Typical stress-strain curves of PC and C/C composites. The insets in (a) show photos of samples before and after compression. (b) SEM image of fracture surface of C/C composites.

The C/C composites have an outstanding load-bearing ability such that a curved sample with a thickness of 20 mm is capable of carrying a weight of over 80 kg (**Figure 6**a). When combined with a metal bolt, a threaded (M8 thread) C/C tablet (7 mm thick) can lift a weight of over 25

kg (**Figure 6**b). It should be noted that the nut is not installed in the assembly and the weight is all applied to the thread, thus indicating its excellent shear resistance. The interlaminar and in-plane shear strengths reach 15 and 20 MPa, respectively, as listed in **Table 2**. Moreover, the C/C composites can be formed and processed in large sizes, as shown in **Figure 6**c. The large composites with dimensions Φ400 × 80 mm were prepared, and could be cut into 140 × 140 × 1 mm^3 slices without fracture, which is definitely impossible for CAs.

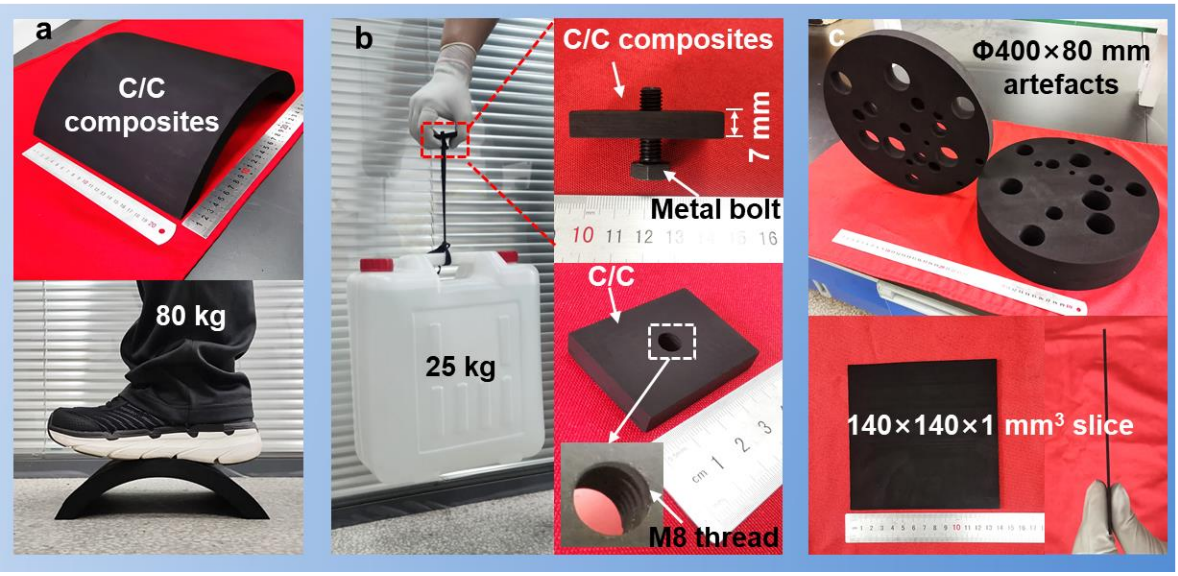

Figure 6. Demonstrations of C/C composites with (a) outstanding load-bearing ability, (b) excellent shear resistance, and (c) good ability to form and process large artefacts.

Table 2. Bulk densities, mechanical properties and TCs of the C/C composites before and after the heating tests.

No.	Properties	Before	After
1	Bulk density (g cm^{-3})	0.60	0.58
2	Compressive strength (MPa)	80±3	96±5
3	Compressive modulus (MPa)	1557±86	1707±92
4	Specific strength (MPa g^{-1} cm^3))	133	155
5	Thermal conductivity (W m^{-1} K^{-1})	0.32	0.42
6	Interlaminar shear strength (MPa)	15±2	17±3
7	In-plane shear strength (MPa)	20±4	23±5

By changing the mass ratios of PR, HMTA and EG, C/C composites with different bulk densities were obtained using the same preparation process. **Figure 7**a shows compressive strengths, specific strengths and TCs of the C/C composites in the bulk density range from 0.47 to 0.75 g cm^{-3}. Their compressive strengths, specific strengths and TCs range from 35 to 95 MPa, 74 to 133 MPa g^{-1} cm^3 and 0.22 to 0.43 W m^{-1} K^{-1}, respectively. Especially, the C/C composites with a bulk density of 0.60 g cm^{-3} exhibit the highest specific strength (133 MPa g^{-1} cm^3) while it possesses a relatively low TC of 0.32 W m^{-1} K^{-1}. The compressive strengths of our composites are 2–4 times higher than those of other reported aerogels/foams and their composites with similar bulk densities (**Figure 7**b). Detailed information on the other aerogels/foams or their composites is listed in **Table 3**.

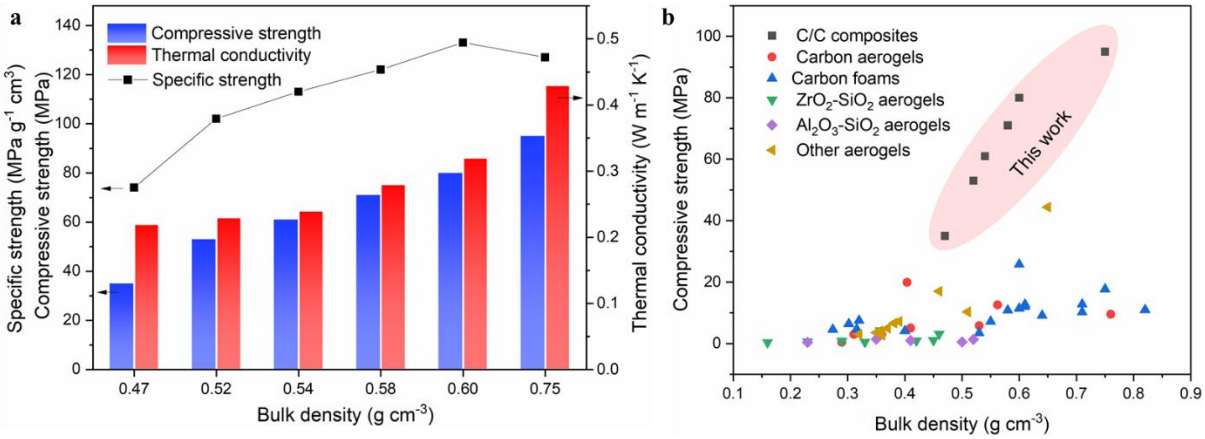

Figure 7. (a) Compressive strengths, specific strengths and TCs of C/C composites with different bulk densities. (b) Compressive strengths of C/C composites in this work and those of the aerogels/foams and their composites reported in other references.

Table 3. Bulk densities, compressive strengths and specific strengths (SS) of recently reported aerogels/foams and their composites.

Materials	Reinforcements	Matrix	ρ_{bulk} (g cm^{-3})	σ_c (MPa)	SS (MPa g^{-1} cm^3)	Ref.
CA-based lightweight composite ablators	Organic aerogel	CAs	0.76	9.5	12.50	33
			0.53	5.8	10.94	
			0.36	3.0	8.33	
Ceramic fiber-reinforced CAs	Mullite ceramic fiber	CAs	0.29	0.41	1.41	37
Graphene/CAs	Graphene oxide	CAs	0.404	19.9	49.26	38
CA monoliths	/	CAs	0.562	12.6	22.42	

CA monoliths	/ /	CAs	0.358 0.311	3.54 2.97	9.89 9.55	39
CA monoliths	/	CAs	0.41	5.0	12.20	11
SiO_2 aerogel-embedded carbon foam composite	SiO_2 aerogel	Carbon foam	0.58 0.60 0.61	10.85 11.47 12.72	18.71 19.12 20.85	40
Carbon foam reinforced with clay	montmorillonite clay	Carbon foam	0.64 0.61 0.71	9.15 12 12.8	14.30 19.67 18.03	41
Carbon foam doped with mesocarbon microbeads	mesocarbon microbeads	Carbon foam	0.75 0.82	17.7 11	23.60 13.41	42
Carbon foam monoliths	/	Carbon foam	0.55 0.71	7.2 10.2	13.09 14.37	
Potassium titanate whiskers-reinforced carbon foam	$K_2Ti_6O_{13}$ whiskers	Carbon foam	0.32	7.5	23.44	43
Aluminosilicate-reinforced carbon foams	Aluminosilicate	Carbon foam	0.302 0.316 0.274	6.39 4.71 4.56	21.16 14.91 16.64	44
Carbon foam monoliths	/	Carbon foam	0.6	25.8	43.00	45
Carbon foam monoliths	/	Carbon foam	0.4	4.1	10.25	46
Carbon foam monoliths	/	Carbon foam	0.53	3.4	6.42	47
ZrO_2-SiO_2 aerogel monoliths	/	ZrO_2-SiO_2 aerogel	0.46	3.11	6.76	48
ZrO_2-fiber-reinforced ZrO_2-SiO_2 aerogel composites	ZrO_2-fiber	ZrO_2-SiO_2 hybrid aerogel	0.16 0.23 0.29 0.33	0.36 0.65 0.82 0.53	2.25 2.83 2.83 1.61	49
Mullite fiber-reinforced and ZrO_2-SiO_2 aerogel composites	Mullite fiber	ZrO_2-SiO_2 aerogel	0.45	1.05	2.33	50
Aluminium borate whisker-reinforced Al_2O_3-SiO_2 aerogel composites	Aluminium borate whisker	Al_2O_3-SiO_2 aerogel	0.23 0.35 0.41	0.37 1.4 1.02	1.61 4.00 2.49	31
Mullite-zirconia fiber-reinforced Al_2O_3-SiO_2 aerogel composites	Mullite-zirconia fiber	Al_2O_3-SiO_2 aerogel	0.52 0.50	1.36 0.53	2.62 1.06	51
Phenolic impregnated carbon ablators	Milled carbon fiber	Phenolic resin	0.36	2.7	7.50	52
Needled carbon fiber felt/phenolic resin aerogel composite	Needled carbon fiber felt	Phenolic resin aerogel	0.370 0.320	5 3	13.51 9.38	53
Hybrid carbon-quartz fiber-reinforced phenolic-silica	Hybrid carbon-quartz fiber	Phenolic-silica aerogel	0.460	17.01	36.98	54

aerogel nanocomposite						
Lightweight carbon-bonded carbon fiber composites	Carbon fiber	Pyrolytic carbon	0.381	6.63	17.40	55
Carbon fibre–reinforced SiCO aerogel composites	Carbon fiber	SiCO aerogel	0.39	7.18	18.41	56
Carbon fibre-reinforced carbon-SiCO aerogel composites	Carbon fiber	Carbon-SiCO Hybrid aerogel	0.35 0.51 0.65	3.6 10.3 44.4	10.29 20.20 68.31	57
Carbon fibre-reinforced SiCO aerogel composites	Carbon fiber	SiCO aerogel	0.39	7.18	18.41	56
Phenolic resin/silicone hybrid aerogel composites	Carbon fiber	PR-Si hybrid aerogel	0.356	4.08	11.46	58

Excellent thermal insulating performance of C/C composites at 1800 ºC and their microstructural changes after heating

In order to investigate thermal insulation performance of the C/C composites (ρ_{bulk}: 0.6 g cm^{-3}) at ultra-high temperatures, oxyacetylene flame heating tests were carried out under an atmosphere environment using three different sample thicknesses (1#: 7.5 mm, 2#: 10.0 mm, 3#: 12.0 mm). The configuration of the fixture for the insulation test simulates an actual thermal protection system, in which the insulation material is sandwiched between a heat-resisting metal and a ceramic-matrix composite, and is also wrapped by insulation felts to prevent heat loss and cross-ventilation (**Figure 8**a). Details were given in a previous report.[20] During oxyacetylene flame heating tests (flame temperature: 1800 ± 20 °C, heating time: 900 s), the front- (T_f) and back-side (T_b) temperatures were recorded at the front surface of the ceramic-matrix composite and the back surface of the test sample, respectively. As indicated in **Figure 8**a, T_f reached 1800 ºC after heating for 100 s. For sample 1#, the highest T_b was 778 °C at about 700 s, and then remained almost constant. Furthermore, the highest T_b was 735 °C at 740 s for sample 2# and 685 °C at 820 s for sample 3#. These results demonstrate the excellent ultra-high temperature thermal insulation performance of these C/C composites, which is almost as good as that of phenolic resin impregnated carbon ablators (PICAs).[53] Generally, PICAs belong to one kind of ablative insulation materials. Therefore, in a sacrificial way, the PICAs provide thermal insulation through phase change, endothermic chemical reaction and material decomposition taking away heat produced in ablation process. This is usually accompanied by a great linear ablation rate (> 20 μm s^{-1}) and mass ablation rate.[33, 53] In this

work, the excellent thermal-insulating performance of the C/C composites benefits from their characteristics of aerogel-like structure and low crystallinity (discussed in the next paragraph). After the heating tests, the C/C sample has retained its original disc shape (**Figure 8**b). The shrinkage and mass loss are respectively less than 0.3% and 6.8%, with a

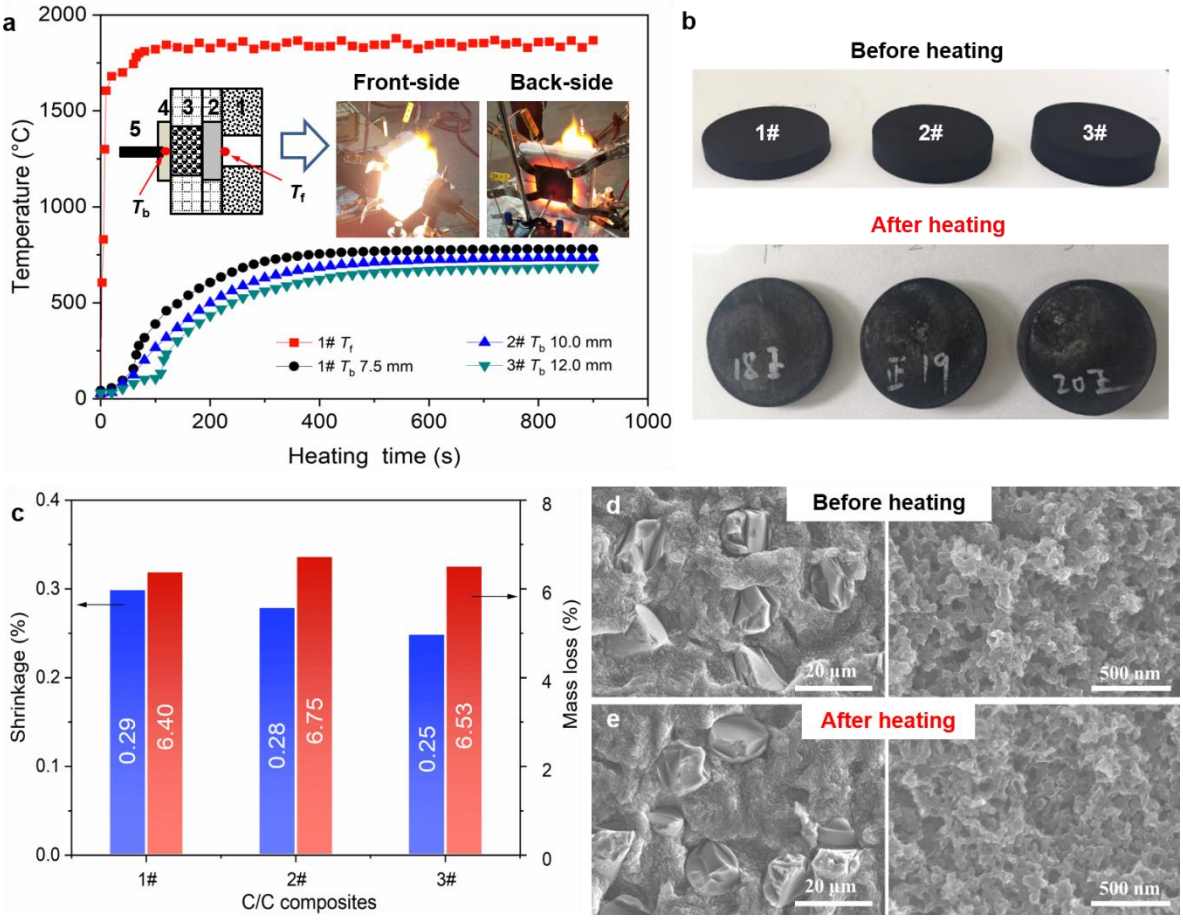

Figure 8. (a) Front- and back-side temperatures of C/C composites during oxyacetylene flame heating tests. The insets in (a) show the configuration of fixture for the test and the real-time photos of its front and back. Configuration of the fixture for heating tests includes 1. perforated insulating brick (hole diameter: 50 mm), 2. insulating felt embedded with a piece of ceramic-matrix composite (75×75×5 mm^3), 3. insulating felt embedded with the test sample (diameter: 50 mm), 4. heat resisting metal sheet (75×75×1 mm^3), 5. thermocouple. (b) Photos of C/C composites before and after heating. (c) Shrinkage and mass loss of C/C composites after heating. SEM images of C/C composites (d) before and (e) after heating.

corresponding thickness loss rate of 0.03 μm s^{-1} (**Figure 8**c), which can be mainly attributed to

their mild oxidation under the relatively enclosed test environment. Moreover, the matrix and fibers have retained their initial morphologies (**Figure 8**d,e), indicating their outstanding thermal stability at ultra-high temperatures.

Figure 9a,b shows TEM images of the C/C composites before and after the heating test. The amorphous carbon matrix becomes slightly crystallized with the interlayer spacing (d_{002}) decreasing from 0.38 to 0.37 nm, which is consistent with the XRD analysis results (0.3813 nm and 0.3749 nm) (**Figure 9**c). The d_{002} is obviously larger than that of ideal graphite (0.3354 nm), indicating the porous carbon matrix is non-graphitizable. This is still higher than

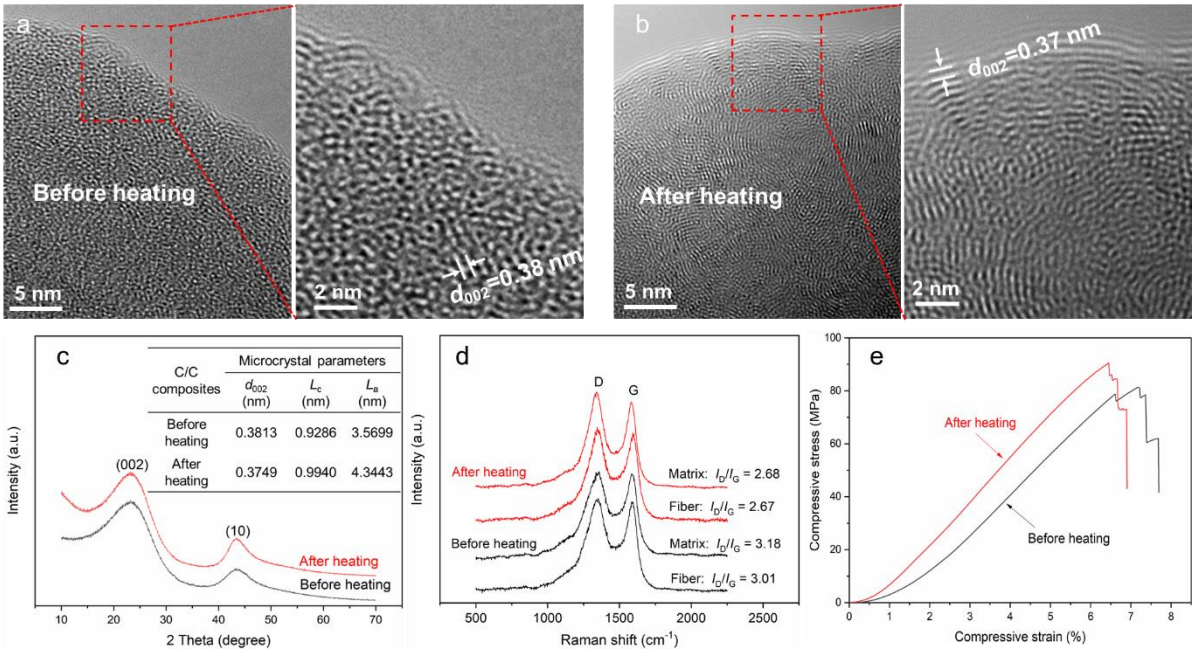

Figure 9. Characterization of C/C composites before and after heating. (a, b) TEM images. (c) XRD patterns. (d) Raman spectra. (e) Stress-strain curves during compressive test.

that of the conventional C/C composites in which d_{002} is 0.3490 nm when heat treated at 1700 °C.[59] Furthermore, Raman spectroscopy analyses were carried out to investigate the degree of graphitization of fibers and matrix of the C/C composites. As shown in **Figure 9**d, both the fiber and matrix have two characteristic peaks at about 1350 and 1590 cm^{-1}, respectively, known as the D (defect) and G (graphite) bands. The peak intensity ratio, I_D/I_G, gives an indication of the graphitic nature of the material. There is only a small decrease of I_D/I_G for both the fibers (from 3.01 to 2.67) and the matrix (from 3.18 to 2.68) after the heating, and the value is much higher than those of RF-derived CAs (I_D/I_G =0.93–1.16).[60] The I_D/I_G value of the carbon fibers derived from PF in this work is much higher than those of commercial

carbon fibers (I_D/I_G =0.15–1.80),[61] even after the heating. Therefore, PF should be an ideal reinforcement for insulating C/C composites, since carbon materials with a higher I_D/I_G value always have a lower TC. Note that the compressive strength of the composites increases from 80 to 96 MPa after the heating (**Table 2**), even though their bulk density decreases from 0.60 to 0.58 g cm^{-3} due to the mild oxidation. The typical stress-strain curves are shown in **Figure 9**e. The heated composites also have a higher compressive modulus (1707 MPa) than their original value (1557 MPa). When PR-derived CAs are heated at temperatures above 1000 °C, the rearrangement of novolac structure leads to an increase in the number of strong C=C bonds.[62] Furthermore, the defects on the surface of carbon particles start to heal at temperatures above 1200 °C, which improves the intrinsic skeletal strength of the porous carbon matrix. Meanwhile, the increase of crystallite size and perfection decreases the carrier scattering,[62] which results in an increase of TC (from 0.32 to 0.42 W m^{-1} K^{-1}) for the C/C composites (**Table 2**). However, the increase is acceptable because it only increases about 30% after the heating at 1800 °C for 900 s, and this temperature is well above the serviceable temperature of other insulation materials, such as SiO_2 aerogels (< 650 °C),[63,64] ZrO_2 aerogels (< 800 °C),[65] Al_2O_3 (< 1000 °C)[66] and Al_2O_3-SiO_2 aerogels (< 1100 °C).[67] In general, the C/C composites reported here have outstanding thermostability, thermal insulation and load-bearing capability at ultra-high temperatures.

Conclusions

We have fabricated large C/C composites with excellent load-bearing capacity, thermal stability and thermal insulation at ultra-high temperatures using a simple high-pressure-assisted polymerization method combined with ambient pressure drying. A 3D chopped PF felt was produced and used as a soft reinforcement in the PR-HMTA system. The crosslinking reaction and high-pressure-assisted polymerization favored the formation of large particle contact necks and the improved structural uniformity of organic matrix, resulting in a robust, uniform and semi-fibril-like network configuration. The strong fiber/matrix interfacial bonding was obtained due to the chemical reaction between PF and PR-HMTA and the simultaneous carbonization shrinkages of PF and organic matrix. The resultant C/C composites have macro-mesopores, large interparticle necks, strong interfacial bonding, and low degree of

crystallization. The composites with a medium bulk density have very high compressive, in-plane shear and specific strengths. The compressive strengths of our composites are 2–4 times higher than those of other reported aerogels/foams and their composites with similar bulk densities. Moreover, the C/C composites also display very low back-side temperatures and good thermal stability when exposed to a harsh ultra-high temperature environment, and even better mechanical properties after the heating. These results demonstrate their great potential as ideal ultra-high temperature thermal insulators with excellent load-bearing ability in the thermal protection system of aerospace vehicles.

Methods

Materials and preparation of aerogel-like carbon/carbon composites: Phenolic resin (PR) was supplied by Jining Baiyi Chemical Co., Ltd., China. Hexamethylenetetramine (HMTA) and ethylene glycol (EG) were supplied by Sinopharm Chemical Reagent Co., Ltd., China. 3D organic phenolic fiber (PF) felts (10–20 vol.%) were produced by needle-punching stacked chopped PF nets in *Z* direction and used as reinforcement. First, PR and HMTA were added to EG. The mass ratios of PR, HMTA and EG were (5–10) : (0.4–4) : (8–40). After magnetic stirring for 1 h, the PF felt was impregnated with this reactive solution and then cured using a high-pressure-assisted polymerization method at 2–8 MPa and 120–200 ºC for 10 h to give a wet carbon/carbon precursor (C/C-P). The wet C/C-P was directly dried at ambient pressure in an oven at 120–150 ºC for 1–3 days, and then carbonized at 900 ºC in a flowing argon atmosphere for 30 min, resulting in lightweight C/C composites. For comparison, the porous carbon precursor (PCP, *i.e.* pure organic monolith without reinforcement) and the porous carbon (PC, derived from the carbonization of PCP) were also prepared using the same procedures.

Characterization: To obtain accurate bulk densities (ρ_{bulk}), the prepared C/C composites were cut into regular cuboids with dimensions of ~100 × 100 × 20 mm^3. The volume of each cuboid was calculated by measuring its dimensions with a vernier caliper. Each sample was weighed using a balance with 0.1 mg precision. The pyrolysis behaviors of PF felt and PCP were investigated using a Jupiter thermogravimetric analyzer from room temperature to 900 °C at a heating rate of 10 °C/min under an Ar atmosphere. The shrinkages of PF felt, PCP and C/C-P

were calculated from their dimensional changes before and after carbonization. The distribution of fibers in PF felt and the 3D micromorphology of C/C-P and C/C composites were examined by 3D X-ray tomography (3D-XRT, Versa XRM-500). The microstructures of C/C composites were observed by scanning electron microscopy (SEM, Thermoscientific, Verios G4 UC) and high-resolution transmission electron microscopy (HR-TEM, FEI Tecnai F30). The chemical structures of PF felt, and C/C-P were investigated by Fourier transform infrared spectroscopy (FTIR, Bruker TENSOR 27). X-ray diffraction (XRD, D/Max-2500PC) and Raman spectroscopy (Horiba Jobin-Yvon LabRam HR800) were used to investigate the microcrystalline parameters of C/C composites. The compressive strengths (σ_c) of PC and C/C composites were measured by a SANS CMT 5205 testing machine with a strain rate of 1 mm/min. The dimension of the test samples was about Φ 10 × 15 (height) mm^3 and 10 (length) × 10 (width) × 15 (height) mm^3 for PC and C/C composites, respectively. The shear strengths of C/C composites were tested using notched samples with dimension of 30 (length) × 15 (width) × 3 (height) mm^3 using an INSTRON 55822 testing machine. Samples used to measure the interlaminar shear strength and in-plane shear strength by the compression of double-notched test pieces were prepared according to the standards of ISO 20505-2005 and GB/T 13096.3-1991, respectively. The thermal conductivity (TC) was measured by a TC 3000E apparatus (hot wire method) at room temperature in air. The thermal insulation performance was tested by oxyacetylene flame heating at 1800 ºC for 900 s while the front and back temperatures during heating were respectively measured by an infrared thermometer and a thermocouple.

Author information

Corresponding Authors

Sufang Tang – Institute of Metal Research, Chinese Academy of Sciences, Shenyang 110016, PR China; Email: sftang@imr.ac.cn

Hui–Ming Cheng – Shenyang National Laboratory for Materials Science, Institute of Metal Research, Chinese Academy of Sciences, Shenyang 110016, PR China; orcid.org/0000-0002-5387-4241; Email: cheng@imr.ac.cn

Notes

The authors declare no competing financial interest.

Acknowledgements

This work was supported by the National Natural Science Foundations of China (Grant No. U20A20242, 52022101, 52188101 & 51902315), and the Research Fund of Youth Innovation Promotion Association of CAS, China (Grant No. 2021190).

References

(1) Uyanna, O.; Najafi, H. Thermal Protection Systems for Space Vehicles: A Review on Technology Development, Current Challenges and Future Prospects. *Acta Astronaut* **2020**, *176*, 341-356.
(2) Fu, Q.; Zhang, P.; Zhuang, L.; Zhou, L.; Zhang, J.; Wang, J.; Hou, X.; Riedel, R.; Li, H. Micro/Nano Multiscale Reinforcing Strategies toward Extreme High-Temperature Applications: Take Carbon/Carbon Composites and Their Coatings As the Examples. *J. Mater. Sci. Technol.* **2022**, *96*, 31-68.
(3) Zhao, R.; Hu, C.; Wang, Y.; Pang, S.; Li, J.; Tang, S.; Cheng, H.-M. Construction of Sandwich-Structured C/C-SiC and C/C-SiC-ZrC Composites with Good Mechanical and Anti-Ablation Properties. *J. Eur. Ceram. Soc.* **2022**, *42*, 1219-1226.
(4) Jin, X.; Fan, X.; Lu, C.; Wang, T. Advances in Oxidation and Ablation Resistance of High and Ultra-High Temperature Ceramics Modified or Coated Carbon/Carbon Composites. *J. Eur. Ceram. Soc.* **2018**, *38*, 1-28.
(5) Al-Muhtaseb, S. A.; Ritter, J. A. Preparation and Properties of Resorcinol-Formaldehyde Organic and Carbon Gels. *Adv. Mater.* **2003**, *15*, 101-114.
(6) Li, Y.; Liu, X.; Nie, X.; Yang, W.; Wang, Y.; Yu, R.; Shui, J. Multifunctional Organic-Inorganic Hybrid Aerogel for Self-Cleaning, Heat-Insulating, and Highly Efficient Microwave Absorbing Material. *Adv. Funct. Mater.* **2019**, *29*, 1807624.
(7) Elkhatat, A. M.; Al-Muhtaseb, S. A. Advances in Tailoring Resorcinol-Formaldehyde Organic and Carbon Gels. *Adv. Mater.* **2011**, *23*, 2887-2903.
(8) Hanzawa, Y.; Hatori, H.; Yoshizawa, N.; Yamada, Y. Structual Changes in Carbon Aerogels with High Temperature Treament *Carbon* **2002**, *40*, 575-581.
(9) Yang, Z.; Li, J.; Xu, X.; Pang, S.; Hu, C.; Guo, P.; Tang, S.; Cheng, H.-M. Synthesis of Monolithic Carbon Aerogels with High Mechanical Strength Via Ambient Pressure Drying without Solvent Exchange. *J. Mater. Sci. Technol.* **2020**, *50*, 66-74.
(10) Petricevic, R.; Glora, M.; Fricke, J. Planar Fibre Reinforced Carbon Aerogels for Application in Pem Fuel Cells. *Carbon* **2001**, *39*, 857–867.
(11) Jia, X.; Dai, B.; Zhu, Z.; Wang, J.; Qiao, W.; Long, D.; Ling, L. Strong and Machinable Carbon Aerogel Monoliths with Low Thermal Conductivity Prepared Via Ambient Pressure Drying. *Carbon* **2016**, *108*, 551-560.
(12) Lee, J.-H.; Park, S.-J. Recent Advances in Preparations and Applications of Carbon Aerogels: A Review. *Carbon* **2020**, *163*, 1-18.
(13) Naseri, I.; Kazemi, A.; Bahramian, A. R.; Kashani, M. R. Preparation of Organic and Carbon Xerogels Using High-Temperature-Pressure Sol-Gel Polymerization. *Mater. Des.* **2014**,

61, 35-40.
(14) Meador, M. A.; Weber, A. S.; Hindi, A.; Naumenko, M.; McCorkle, L.; Quade, D.; Vivod, S. L.; Gould, G. L.; White, S.; Deshpande, K. Structure-Property Relationships in Porous 3D Nanostructures: Epoxy-Cross-Linked Silica Aerogels Produced Using Ethanol As the Solvent. *ACS Appl. Mater. Interfaces* **2009**, *1*, 894-906.
(15) Randall, J. P.; Meador, M. A.; Jana, S. C. Tailoring Mechanical Properties of Aerogels for Aerospace Applications. *ACS Appl. Mater. Interfaces* **2011**, *3*, 613-626.
(16) Nguyen, B. N.; Meador, M. A.; Tousley, M. E.; Shonkwiler, B.; McCorkle, L.; Scheiman, D. A.; Palczer, A. Tailoring Elastic Properties of Silica Aerogels Cross-Linked with Polystyrene. *ACS Appl. Mater. Interfaces* **2009**, *1*, 621-630.
(17) Aghabararpour, M.; Mohsenpour, M.; Motahari, S.; Abolghasemi, A. Mechanical Properties of Isocyanate Crosslinked Resorcinol Formaldehyde Aerogels. *J. Non-Cryst. Solids* **2018**, *481*, 548-555.
(18) Feng, J.; Zhang, C.; Feng, J.; Jiang, Y.; Zhao, N. Carbon Aerogel Composites Prepared by Ambient Drying and Using Oxidized Polyacrylonitrile Fibers As Reinforcements. *ACS Appl. Mater. Interfaces* **2011**, *3*, 4796-4803.
(19) Glora, M.; Wiener, M.; Petricevic, R.; Probstle, H.; Fricke, J. Integration of Carbon Aerogels in Pem Fuel Cells. *J. Non-Cryst. Solids* **2001**, *285*, 283-287.
(20) Guo, P.; Li, J.; Pang, S.; Hu, C.; Tang, S.; Cheng, H.-M. Ultralight Carbon Fiber Felt Reinforced Monolithic Carbon Aerogel Composites with Excellent Thermal Insulation Performance. *Carbon* **2021**, *183*, 525-529.
(21) Feng, J.; Zhang, C.; Feng, J. Carbon Fiber Reinforced Carbon Aerogel Composites for Thermal Insulation Prepared by Soft Reinforcement. *Mater. Lett.* **2012**, *67*, 266-268.
(22) Chen, Z.; Zhuo, H.; Hu, Y.; Lai, H.; Liu, L.; Zhong, L.; Peng, X. Wood-Derived Lightweight and Elastic Carbon Aerogel for Pressure Sensing and Energy Storage. *Adv. Funct. Mater.* **2020**, *30*, 1910292.
(23) Hu, X.; Zhu, J. Tailoring Aerogels and Related 3D Macroporous Monoliths for Interfacial Solar Vapor Generation. *Adv. Funct. Mater.* **2020**, *30*, 190723.
(24) Xu, X.; Zhou, J.; Nagaraju, D. H.; Jiang, L.; Marinov, V. R.; Lubineau, G.; Alshareef, H. N.; Oh, M. Flexible, Highly Graphitized Carbon Aerogels Based on Bacterial Cellulose/Lignin: Catalyst-Free Synthesis and Its Application in Energy Storage Devices. *Adv. Funct. Mater.* **2015**, *25*, 3193-3202.
(25) Schiffres, S. N.; Kim, K. H.; Hu, L.; McGaughey, A. J. H.; Islam, M. F.; Malen, J. A. Gas Diffusion, Energy Transport, and Thermal Accommodation in Single-Walled Carbon Nanotube Aerogels. *Adv. Funct. Mater.* **2012**, *22*, 5251-5258.
(26) Long, S.; Feng, Y.; Liu, Y.; Zheng, L.; Gan, L.; Liu, J.; Zeng, X.; Long, M. Renewable and Robust Biomass Carbon Aerogel Derived from Deep Eutectic Solvents Modified Cellulose Nanofiber under a Low Carbonization Temperature for Oil-Water Separation. *Sep. Purif. Technol.* **2021**, *254*, 117577.
(27) Liu, R.; Wan, L.; Liu, S.; Pan, L.; Wu, D.; Zhao, D. An Interface-Induced Co-Assembly Approach Towards Ordered Mesoporous Carbon/Graphene Aerogel for High-Performance Supercapacitors. *Adv. Funct. Mater.* **2015**, *25*, 526-533.
(28) Zhang, Y.; Wang, X.; Zheng, S.; Yang, B.; Li, Z.; Lu, J.; Zhang, Q.; Adli, N. M.; Lei, L.; Wu, G.; et al. Hierarchical Cross-Linked Carbon Aerogels with Transition Metal-Nitrogen Sites

for Highly Efficient Industrial-Level CO_2 Electroreduction. *Adv. Funct. Mater.* **2021**, *31*, 2104377.
(29) Wu, D.; Fu, R. Requirements of Organic Gels for a Successful Ambient Pressure Drying Preparation of Carbon Aerogels. *J. Porous Mater.* **2007**, *15*, 29-34.
(30) Martínez-Hergueta, F.; Ridruejo, A.; González, C.; Llorca, J. A Multiscale Micromechanical Model of Needlepunched Nonwoven Fabrics. *Int. J. Solids Struct.* **2016**, *96*, 81-91.
(31) Hou, X.; Zhang, R.; Fang, D. Novel Whisker-Reinforced Al_2O_3-SiO_2 Aerogel Composites with Ultra-Low Thermal Conductivity. *Ceram. Int.* **2017**, *43*, 9547-9551.
(32) Alshrah, M.; Tran, M. P.; Gong, P.; Naguib, H. E.; Park, C. B. Development of High-Porosity Resorcinol Formaldehyde Aerogels with Enhanced Mechanical Properties through Improved Particle Necking under CO_2 Supercritical Conditions. *J. Colloid Interface Sci.* **2017**, *485*, 65-74.
(33) Seraji, M. M.; Arefazar, A. Thermal Ablation-Insulation Performance, Microstructural, and Mechanical Properties of Carbon Aerogel Based Lightweight Heat Shielding Composites. *Polym. Eng. Sci.* **2021**, *61*, 1338-1352.
(34) Drach, V.; Wiener, M.; Reichenauer, G.; Ebert, H. P.; Fricke, J. Determination of the Anisotropic Thermal Conductivity of a Carbon Aerogel-Fiber Composite by a Non-Contact Thermographic Technique. *Int. J. Thermophys.* **2007**, *28*, 1542-1562.
(35) García, B. B.; Liu, D.; Sepehri, S.; Candelaria, S.; Beckham, D. M.; Savage, L. W.; Cao, G. Hexamethylenetetramine Multiple Catalysis As a Porosity and Pore Size Modifier in Carbon Cryogels. *J. Non-Cryst. Solids* **2010**, *356*, 1620-1625.
(36) Liang, C.; Sha, G.; Guo, S. Resorcinol±Formaldehyde Aerogels Prepared by Supercritical Acetone Drying. *J. Non-Cryst. Solids* **2000**, *271* 167-170.
(37) Yang, J.; Li, S.; Luo, Y.; Yan, L.; Wang, F. Compressive Properties and Fracture Behavior of Ceramic Fiber-Reinforced Carbon Aerogel under Quasi-Static and Dynamic Loading. *Carbon* **2011**, *49*, 1542-1549.
(38) Guo, K.; Hu, Z.; Song, H.; Du, X.; Zhong, L.; Chen, X. Low-Density Graphene/Carbon Composite Aerogels Prepared at Ambient Pressure with High Mechanical Strength and Low Thermal Conductivity. *RSC Adv.* **2015**, *5*, 5197-5204.
(39) Zhang, Z.; Zhao, S.; Chen, G.; Feng, J.; Feng, J.; Yang, Z. Influence of Acid-Base Catalysis on the Textural and Thermal Properties of Carbon Aerogel Monoliths. *Microporous Mesoporous Mater.* **2020**, *296*, 109997.
(40) Liu, H.; Xu, Y.; Tang, C.; Li, Y.; Chopra, N. SiO_2 Aerogel-Embedded Carbon Foam Composite with Co-Enhanced Thermal Insulation and Mechanical Properties. *Ceram. Int.* **2019**, *45*, 23393-23398.
(41) Wang, X.; Zhong, J.; Wang, Y.; Yu, M. A Study of the Properties of Carbon Foam Reinforced by Clay. *Carbon* **2006**, *44*, 1560-1564.
(42) Li, S.; Song, Y.; Song, Y.; Shi, J.; Liu, L.; Wei, X.; Guo, Q. Carbon Foams with High Compressive Strength Derived from Mixtures of Mesocarbon Microbeads and Mesophase Pitch. *Carbon* **2007**, *45*, 2092-2097.
(43) Luo, R.; Ni, Y.; Li, J.; Yang, C.; Wang, S. The Mechanical and Thermal Insulating Properties of Resin-Derived Carbon Foams Reinforced by $K_2Ti_6O_{13}$ Whiskers. *Mater. Sci. Eng.* **2011**, *528*, 2023-2027.

(44) Wu, X.; Liu, Y. g.; Fang, M.; Mei, L.; Luo, B. Preparation and Characterization of Carbon Foams Derived from Aluminosilicate and Phenolic Resin. *Carbon* **2011**, *49*, 1782-1786.
(45) Liu, M.; Gan, L.; Zhao, F.; Fan, X.; Xu, H.; Wu, F.; Xu, Z.; Hao, Z.; Chen, L. Carbon Foams with High Compressive Strength Derived from Polyarylacetylene Resin. *Carbon* **2007**, *45*, 3055-3057.
(46) Ford W. D. Method of Making Cellular Refractory Thermal Insulating Material. U.S. patent 3121050, **1964**.
(47) Klett J. W. Process for Making Carbon Foam. U.S. patent 6033506, **2000**.
(48) Hou, X.; Zhang, R.; Wang, B. Novel Self-Reinforcing ZrO_2-SiO_2 Aerogels with High Mechanical Strength and Ultralow Thermal Conductivity. *Ceram. Int.* **2018**, *44*, 15440-15445.
(49) Hou, X.; Zhang, R.; Fang, D. An Ultralight Silica-Modified ZrO_2-SiO_2 Aerogel Composite with Ultra-Low Thermal Conductivity and Enhanced Mechanical Strength. *Scr. Mater.* **2018**, *143*, 113-116.
(50) He, J.; Li, X.; Su, D.; Ji, H.; Wang, X. Ultra-Low Thermal Conductivity and High Strength of Aerogels/Fibrous Ceramic Composites. *J. Eur. Ceram. Soc.* **2016**, *36*, 1487-1493.
(51) Zhang, R.; Hou, X.; Ye, C.; Wang, B. Enhanced Mechanical and Thermal Properties of Anisotropic Fibrous Porous Mullite-Zirconia Composites Produced Using Sol-Gel Impregnation. *J. Alloys Compd.* **2017**, *699*, 511-516.
(52) Natali, M.; Puri, I.; Kenny, J. M.; Torre, L.; Rallini, M. Microstructure and Ablation Behavior of an Affordable and Reliable Nanostructured Phenolic Impregnated Carbon Ablator (PICA). *Polym. Degrad. Stab.* **2017**, *141*, 84-96.
(53) Cheng, H.; Xue, H.; Hong, C.; Zhang, X. Preparation, Mechanical, Thermal and Ablative Properties of Lightweight Needled Carbon Fibre Felt/Phenolic Resin Aerogel Composite with a Bird's Nest Structure. *Compos. Sci. Technol.* **2017**, *140*, 63-72.
(54) Cheng, H.; Fan, Z.; Hong, C.; Zhang, X. Lightweight Multiscale Hybrid Carbon-Quartz Fiber Fabric Reinforced Phenolic-Silica Aerogel Nanocomposite for High Temperature Thermal Protection. *Composites, Part A* **2021**, *143*, 106313.
(55) Cheng, H.; Hong, C.; Zhang, X.; Xue, H. Lightweight Carbon-Bonded Carbon Fiber Composites with Quasi-Layered and Network Structure. *Mater. Des.* **2015**, *86*, 156-159.
(56) Li, X.; Feng, J.; Jiang, Y.; Li, L.; Feng, J. Preparation and Properties of Pan-Based Carbon Fiber-Reinforced SiCO Aerogel Composites. *Ceram. Int.* **2019**, *45*, 17064-17072.
(57) Li, X.; Feng, J.; Jiang, Y.; Li, L.; Feng, J. Anti-Oxidation Performance of Carbon Aerogel Composites with SiCO Ceramic Inner Coating. *Ceram. Int.* **2019**, *45*, 9704-9711.
(58) Yin, R.; Cheng, H.; Hong, C.; Zhang, X. Synthesis and Characterization of Novel Phenolic Resin/Silicone Hybrid Aerogel Composites with Enhanced Thermal, Mechanical and Ablative Properties. *Composites, Part A* **2017**, *101*, 500-510.
(59) Kolesnikov, S. A.; Mostovoi, G. E. High-Temperature Treatment of Carbon-Carbon Composite Materials. Communication 1. Thermal Stabilization of Two-Dimensionally Reinforced Carbon-Carbon Composite Material Object Properties. *Refract. Ind. Ceram.* **2012**, *53*, 123-129.
(60) Chen, Y.; Zhang, Z.; Lai, Y.; Shi, X.; Li, J.; Chen, X.; Zhang, K.; Li, J. Self-Assembly of 3D Neat Porous Carbon Aerogels with NaCl As Template and Flux for Sodium-Ion Batteries. *J. Power Sources* **2017**, *359*, 529-538.
(61) Bukalov, S. S.; Leites, L. A.; Goloveshkin, A. S.; Trumentsev, V. A. Structure of Sp^2-

Carbon Fiber Prepared by High-Temperature Thermomechanical Treatment of Polyacrylonitrile Fiber: A Raman and X-Ray Diffraction Study. *Russ. Chem. Bull.* **2018**, *67*, 1002-1009.
(62) Allahbakhsh, A.; Bahramian, A. R. Novolac-Derived Carbon Aerogels Pyrolyzed at High Temperatures: Experimental and Theoretical Studies. *RSC Adv.* **2016**, *6*, 72777-72790.
(63) Delarosafox, N.; Gagoduport, L.; Esquivias, L. Aggregation Process in Silica Aerogels on Sintering. *J. Non-Cryst. Solids* **1995**, *193*, 534-538.
(64) Shi, F.; Wang, L. J.; Liu, J. X.; Zeng, M. Effect of Heat Treatment on Silica Aerogels Prepared Via Ambient Drying. *J. Mater. Sci. Technol.* **2007**, *23*, 402-406.
(65) Idakiev, V.; Tabakova, T.; Tenchev, K.; Yuan, Z. Y.; Ren, T. Z.; Su, B. L. Gold Catalysts Supported on Ceria-Modified Mesoporous Zirconia for Low-Temperature Water–Gas Shift Reaction. *J. Porous Mater.* **2010**, *19*, 15-20.
(66) Poco, J. F.; Satcher, J. H.; Hrubesh, L. W. Synthesis of High Porosity, Monolithic Alumina Aerogels. *J. Non-Cryst. Solids* **2001**, *285*, 57-63.
(67) Himmel, B.; Gerber, T.; Burger, H.; Holzhuter, G.; Olbertz, A. Structural Characterization of SiO_2-Al_2O_3 Aerogels. *J. Non-Cryst. Solids* **1995**, *186*, 149-158.

Ablation behavior of C/C-ZrC-SiC composites prepared by Sol-Gel method

Chen Zeng, Mingyu Zhang, Qizhong Huang*

National Key Laboratory of Science and Technology on High-strength Structural Materials, Central South University, Changsha, 410083, China

* Corresponding author: Mingyu Zhang, Email:zhangmingyu@csu.edu.cn

Abstract: Sol-Gel is a particularly efficient method to synthesize nano-sized ultra-high temperature ceramic powders. However, the Sol-Gel method is immature in its application to the preparation of anti-ablation C/C-UHTCs composites. Herein, C/C-ZrC-SiC composites with different carbon fiber preform structures were successfully prepared by the Sol-Gel method, and the microstructure, mechanical property, and ablation resistance of the composites were investigated. The results demonstrate that dense ZrC-SiC ceramics, which had a homogeneous phase distribution, were formed in the composite matrix. The obtained 3D C/C-ZrC-SiC composites delivered a flexural strength of 148.926 MPa with a bulk density of 1.98 g/cm^3, while the flexural strength of 2.5D C/C-ZrC-SiC composites is only 120.113 MPa. After being exposed to a stable oxyacetylene flame at 2800 ºC for 60 s, the mass and linear ablation rates of 3D C/C-ZrC-SiC are 0.2372 mg/(cm^2·s) and 0.0110 mm/s, respectively, which are 25.94% and 25.73% lower than those of 2.5D C/C-ZrC-SiC composites. The excellent mechanical property and ablation resistance are attributed to the firm carbon fiber preform structure and the dense ZrC-SiC ceramic matrix.

Keywords: Sol-Gel method, C/C-ZrC-SiC composites, Mechanical property, Ablation resistance.

1. Introduction

C/C-ZrC-SiC composites are a kind of representative carbon fiber reinforced carbon matrix containing ultra-high temperature ceramic composites (C/C-UHTCs), and combine the advantages of C/C composites and ZrC-SiC ceramics [1-3]. Therefore, C/C-ZrC-SiC composites possess low density, good mechanical performance, outstanding thermal shock resistance, and excellent oxidation and ablation resistance. Because of these unique properties, C/C-ZrC-SiC composites are regarded as one of the most promising structural materials in the design of thermal protection systems (TPS) for hypersonic vehicles, aircraft turbine engines,

and rocket exhaust nozzles [4, 5]. Under the high-temperature aerobic environment, SiC can be firstly oxidized to SiO_2 which has a self-healing effect to seal the cracks and pores on the surface of composites. Besides, due to the high melting point and low vapor pressure, ZrO_2 oxidized from ZrC can prevent the molten SiO_2 from being washed away by the ablation airflow.

Over the past years, various methods have been used to prepare C/C-ZrC-SiC composites, such as precursor infiltration and pyrolysis (PIP) [6, 7], chemical vapor infiltration (CVI)[8, 9], reactive melt infiltration (RMI) [10, 11], and slurry infiltration (SI) [12, 13]. However, due to the adverse factors of these methods, their applications in practical production are still limited. The complex synthesis process and low ceramic yield of the ZrC-SiC precursor make the PIP method time-consuming and high-cost. CVI process has extremely high requirements on the equipment, and the produced gases are not environmentally friendly. Since the molten metal introduced by RMI will erode the carbon fibers, the mechanical performance of the obtained C/C-ZrC-SiC composites will be seriously degraded. The limited densification of the SI method results in numerous open pores inside the composites. Recently, the Sol-Gel method combined with carbothermal reduction was developed to prepare C/C-UHTCs composites by using low-cost raw materials. Corral et al. [14] used zirconium oxychloride-hydrate, triethyl borate, and phenolic resin as raw materials to synthesize ZrB_2 sol-gel precursor, and then prepared C/C- ZrB_2-B_4C composites. Li et al. [15]successfully prepared C/C-ZrC composites by using sucrose and $ZrCl_4$ sols as sources. Chen et al. [16, 17] obtained C_f/gel preform by impregnating PVA, H_3BO_3, and glycerin solution, and then prepared C_f/SiC-ZrC-ZrB_2 composites combined with the RMI process. These studies suggest that the low-cost Sol-Gel process is a promising way to prepare C/C-ZrC-SiC composites. However, Sol-Gel usually requires a combination of other processes to ensure the excellent mechanical properties and ablation resistance of composites. Therefore, it is necessary to develop a one-step preparation process for C/C-ZrC-SiC composites by the Sol-Gel method.

In this work, we used zirconium oxychloride octahydrate ($ZrOCl_2 \cdot 8H_2O$), tetraethoxysilane (TEOS), and phenolic resin as sources to successfully prepare 2.5D and 3D C/C-ZrC-SiC composites by the one-step Sol-Gel method, and characterized the phase composition and microstructure of the composites. The influences of carbon fiber preform structure on the mechanical property and ablation resistance of C/C-ZrC-SiC composites were

investigated in detail.

2. Material and methods

2.1. Material preparation

Zirconium oxychloride octahydrate ($ZrOCl_2 \cdot 8H_2O$, 99%, Aladdin, China), tetraethoxysilane (TEOS, 98%, Macklin, China), and phenolic resin (analytical grade, Tianyu Resin, China) were used as sources to synthesize sol precursor, and the process parameters are shown in our previous work [18-21]. 2.5D carbon fiber preforms (0.45 g/cm^3) and 3D carbon fiber preforms (0.70 g/cm^3) were deposited pyrocarbon by CVI. The densities of the obtained C/C composites were 1.38 g/cm^3 (2.5D) and 1.40 g/cm^3 (3D), respectively.

Fig. 1 shows the preparation procedure of C/C-ZrC-SiC composites by the one-step Sol-Gel method. Firstly, the C/C composites with low densities were impregnated with sol under vacuum to get C/C-sol composites. Secondly, the C/C-sol composites were condensed at 60 ºC, and then dried at 200 ºC for 2 h. Then, to make the xerogel decompose fully into ZrO_2, SiO_2, and phenolic resin-derived carbon, the C/C-xerogel composites were carbonized at 600 ºC in argon. After that, the above processes, including vacuum impregnation, condensation, desiccation, and carbonization, were repeated for 3 times. Finally, the C/C-ZrO_2-SiO_2 composites were heated at 1600 ºC for 1 h in argon to obtain C/C-ZrC-SiC composites. The whole preparation process was repeated until the density growth of the C/C-ZrC-SiC composites was less than 0.01 g/cm^3.

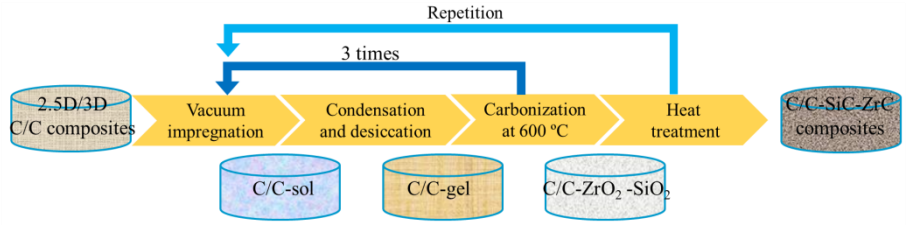

Fig. 1. The preparation schematic of C/C-ZrC-SiC composites by the one-step Sol-Gel.

2.2. Test and characterization

The densities of the C/C composites and C/C-ZrC-SiC composites were measured by the Archimedes method. The three-point bending test (Instron3369) was used to measure the flexural strength and bending modulus of C/C-ZrC-SiC composites. The span and the load velocity were 40 mm and 2.00 mm/min, respectively. Five specimens of 55 mm × 10 mm × 4 mm were tested to obtain the average value.

According to the GJB323A-96 standard, a stable oxyacetylene flame was utilized to evaluate the ablation resistance of C/C-ZrC-SiC composites. The pressure and flux of oxygen were 0.400 MPa and 1.960 L/s, and those of acetylene were 0.095 MPa and 0.696 L/s, respectively. The inner diameter of the oxyacetylene gun tip was 2 mm, and the distance between the gun tip and the sample (Φ30 mm × 10 mm) was 10 mm. And the ablation center surface temperature of composites was over 2800 ºC measured by an optical high-temperature measuring instrument (ENDURANCE 1R) in two-color mode with an error of ± 0.75 %. The samples were fixed in a water-cooled carrier and ablated for 60 s. The linear and mass ablation rates of the C/C-ZrC-SiC composites were calculated by the following formulas:

$$R_l = \frac{l_0 - l_t}{t} \quad (1)$$

$$R_m = \frac{m_0 - m_t}{S \times t} \quad (2)$$

where, R_l and R_m are the linear and mass ablation rates, respectively. The l_0 and m_0 are the thickness and mass of composites before ablation, while l_t and m_t are those of composites after ablation, respectively. The t is the ablation time, and S is the ablation surface area.

The X-ray diffractometer with Cu Kα radiation (XRD, Rigaku Dmax/2550VB+18kW) was used to determine the phase compositions of the C/C-ZrC-SiC composites before and after ablation. The scanning electron microscope (SEM, FEI Nova Nano SEM230) was used to observe the microstructure and morphology of the composites. The transmission electron microscope (TEM, Titan G2 60-300) was used to observe the microtopography and crystalline structures of the ZrC-SiC matrix.

3. Result and discussion

3.1. Microstructure and phase composition

By the one-step Sol-Gel method, the densities of 2.5D and 3D C/C-ZrC-SiC composites are up to 1.80 g/cm^3 and 1.98 g/cm^3, respectively. Since the pores in the 3D needled carbon fiber felt are more connected than those of 2.5D needled felt, the sol precursor is prone to impregnate in 3D needled felt and then transforms to ZrC-SiC ceramics at 1600 ºC. As a result, although the initial density of 2.5D and 3D C/C composites is similar, the final density of 3D C/C-ZrC-SiC composites is 0.18 g/cm^3 higher than that of 2.5D C/C-ZrC-SiC composites. Fig.2 shows the surface XRD patterns of 2.5D and 3D C/C-ZrC-SiC composites and

demonstrates that both 2.5D and 3D C/C-ZrC-SiC composites are composed of ZrC (PDF#35-0784), SiC (PDF#49-1428) and C. According to the XRD patterns, both the ZrC and SiC phases have narrow and sharp diffraction peaks, which indicate that the ZrC-SiC ceramic matrix obtained high crystallinity after heat treatment at 1600 ºC. Besides, it is worth noting that the C diffraction peak of 2.5D C/C-ZrC-SiC composites is stronger than that of 3D C/C-ZrC-SiC composites. This may be attributed to more exposed carbon fibers and pyrocarbon on the surface of 2.5D C/C-ZrC-SiC composites than 3D composites.

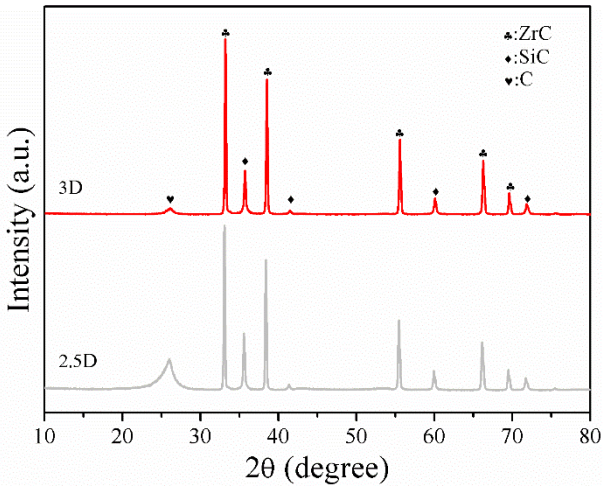

Fig.2. XRD patterns of 2.5D and 3D C/C-ZrC-SiC composites.

In order to clarify the difference of the surface between 2.5D and 3D C/C-ZrC-SiC composites, the surface SEM images of composites are shown in Fig.3. Comparing Fig.3a with Fig.3b, it can be seen that a complete ZrC-SiC coating was formed on the surface of 3D C/C-ZrC-SiC composites, while the coating of 2.5D C/C-ZrC-SiC composites was incomplete. The carbon fibers can be directly observed on the surface of 2.5D composites, as shown in Fig.3a and 3b. However, the carbon fibers of 3D composites are covered by the intact and uniform ZrC-SiC coating (Fig.3c-d). This illustrates a stronger C diffraction peak of 2.5D C/C-ZrC-SiC composites than 3D composites in Fig.2. According to Fig.3d, the coating is composed of ZrC and SiC particles, which are formed in the following two ways [6, 22]. Firstly, the sol precursor accumulated on the surface and then decomposed to ceramic particles during the repetition of the preparation process. Secondly, the gaseous SiO produced from the sol precursor would react with the carbon, mainly including pyrocarbon and phenolic resin-derived carbon, on the surface of composites to form SiC. Due to the special features of 3D needled C/C composites, the sol precursor is more likely to agglomerate on the surface of 3D C/C-ZrC-SiC composites.

The following reactions might occur in these processes:

$$ZrO_2(s) + 3C(s) = ZrC(s) + 2CO(g) \quad (1)$$

$$SiO_2(s) + 3C(s) = SiC(s) + 2CO(g) \quad (2)$$

$$SiO_2(s) + C(s) = SiO(g) + CO(g) \quad (3)$$

$$SiO(g) + 2C(s) = SiC(s) + CO(g) \quad (4)$$

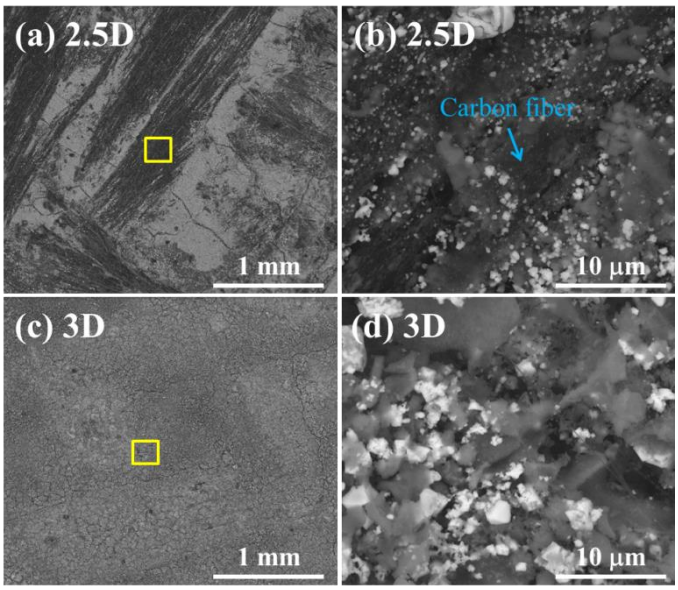

Fig.3. Surface SEM images of 2.5D and 3D C/C-ZrC-SiC composites.

Fig.4 shows the cross-section SEM images of C/C-ZrC-SiC composites. As shown in Fig.4a and Fig.4c, the 2.5D carbon fiber felt is woven of needled fiber bundles of the Z direction, the non-woven layer of the X-Y direction, and fiber webs, while the 3D carbon fiber felt is woven of carbon fiber bundles in the X, Y and Z directions. The ZrC-SiC ceramics are evenly distributed between carbon fiber bundles, with a few closed pores remaining. Moreover, due to

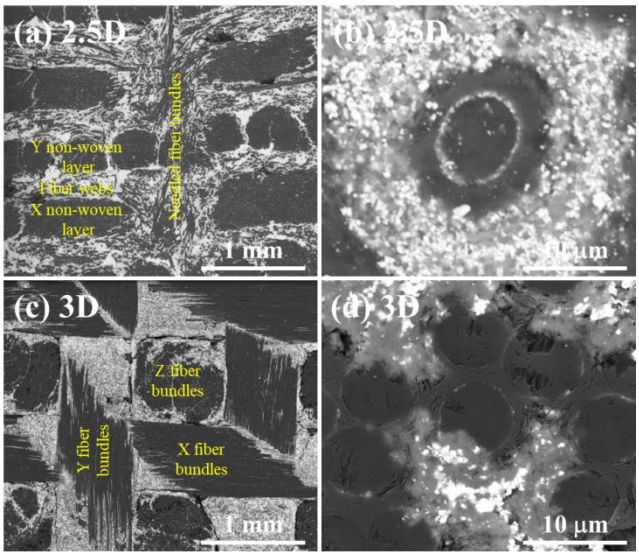

the molecular level of $ZrOCl_2 \cdot 8H_2O$, TEOS and phenolic resin achieved by the Sol-Gel method [23], the ZrC and SiC particles are uniform in size without obvious agglomeration (Fig.4b and 4c).

Fig.4.Cross-section SEM images of 2.5D and 3D C/C-ZrC-SiC composites.

To further observe the microstructure and crystalline structure of the ZrC and SiC particles transformed from sol precursor, the TEM analysis results of the ceramic particles are illustrated in Fig.5. The particles are irregular polygons, ranging in size from 50 to 300 nm, as shown in Fig.5a. According to the HRTEM image (Fig.5b), the interplanar spacings of 0.270 nm and 0.251 nm match well with the crystal planes of ZrC (111) and SiC (111), respectively, which are in good agreement with the XRD.

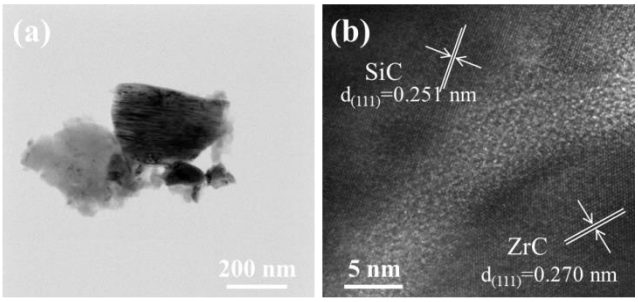

Fig.5. TEM images of the ZrC-SiC ceramic particles.

3.2 Mechanical property

To investigate the mechanical property of the C/C-ZrC-SiC composites prepared by the one-step Sol-Gel method, the three-point bending test was used to measure the flexural strength and bending modulus of the composites, and the bending load-displacement curves are displayed in Fig.6. According to the curves, the fracture models of both the 2.5D and 3D C/C-ZrC-SiC composites are pseudo-plastic fracture. However, the slope and the maximum value of the 3D C/C-ZrC-SiC curve are higher than those of 2.5D C/C-ZrC-SiC composites. The flexural strength and bending modulus of 3D C/C-ZrC-SiC composites are 148.926 MPa and 20.479 GPa, while those of 2.5D C/C-ZrC-SiC composites are 120.113 MPa and 16.113 GPa, respectively. By contrast, the flexural strength and bending modulus of 3D C/C-ZrC-SiC composites are 23.99% and 27.10% higher than those of 2.5D composites, respectively. This advantage is attributed to the high carbon fiber content and 3D needled fiber felt of 3D C/C-ZrC-SiC composites [24].

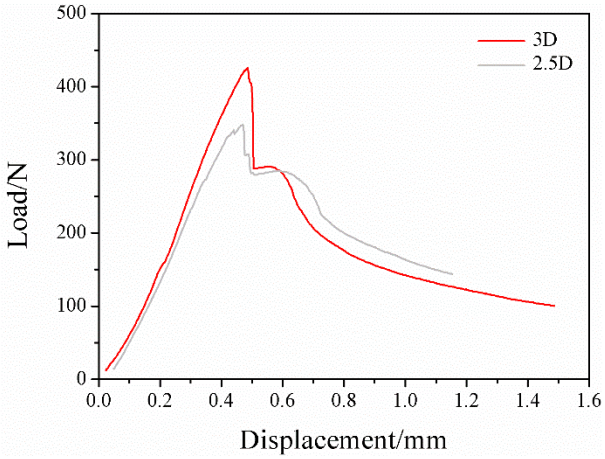

Fig.6. Bending load-displacement curves of C/C-ZrC-SiC composites.

Fig.7 displays the fracture cross-section images of 2.5D and 3D C/C-ZrC-SiC composites to further clarify the fracture behavior of the composites. Obviously, carbon fiber pullout can be seen on the fracture cross-sections of both 2.5D and 3D C/C-ZrC-SiC composites, which indicates the pseudo-plastic fracture feature of the composites. By contrast, however, both the length and quantity of carbon fiber pullout of 3D C/C-ZrC-SiC composites are more than those of 2.5D C/C-ZrC-SiC composites. According to the research, the higher fracture energy is consumed at the fibers/matrix interface, the more obvious the carbon fibers pull out. In other words, 3D C/C-ZrC-SiC composites exhibit better mechanical properties.

Fig.7. The flexural cross-section SEM morphologies of C/C-ZrC-SiC composites.

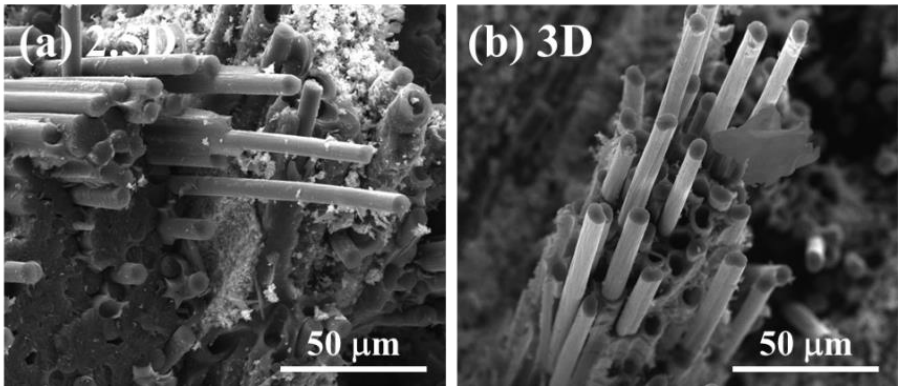

3.3 Ablation behavior

The mass and linear ablation rates of the C/C-ZrC-SiC composites after being ablated at 2800 ºC for 60 s are shown in Table 1. It can be seen that the mass and linear ablation rates of 2.5D C/C-ZrC-SiC composites are 0.3203 mg/(cm^2·s) and 0.0148 mm/s, while those of 3D C/C-ZrC-SiC composites are 0.2372 mg/(cm^2·s) and 0.0110 mm/s, respectively. By contrast,

3D C/C-ZrC-SiC composites exhibit lower mass and linear ablation rates than 2.5D C/C-ZrC-SiC composites. The main reasons why 3D C/C-ZrC-SiC composites possess better ablation resistance than 2.5D composites can be attributed to the following three points: Firstly, compared to 2.5D C/C-ZrC-SiC composites, because of more connected pores in 3D needled felt, more ZrC-SiC ceramics were introduced into 3D composites. During the ablation, the continuous ZrO_2-SiO_2 layer formed from the oxidation of ZrC and SiC can inhibit the diffusion of the oxidizing atmosphere. Secondly, 3D C/C-ZrC-SiC composites have more carbon fibers and a firmer felt structure which can effectively resist the erosion of oxyacetylene flame and provide strong support for the ZrO_2-SiO_2 layer. Thirdly, the ZrC-SiC coating formed on the surface can prevent the composites from erosion of oxyacetylene flame in a short time.

Table 1 Ablation rates of C/C-ZrC-SiC composites prepared by Sol-Gel method.

Sample	Time (s)	Ablation test	Mass ablation rate ($mg/(cm^2 \cdot s)$)	Liner ablation rate (mm/s)
2.5D	60	Oxyacetylene, surface 2800 ºC	0.3203	0.0148
3D		O_2: 1.960 L/s, C_2H_2: 0.696 L/s	0.2372	0.0110

The XRD patterns of the ablation surface are shown in Fig. 8. Due to the ablation temperature of 2800 ºC, lots of SiO_2 oxidized from SiC has evaporated into a SiO_2 gas. Moreover, the remaining molten SiO_2 presents an amorphous structure because the surface temperature rapidly decreases to room temperature. Thus, only the diffraction peaks of ZrO_2 and C were detected. Among them, the diffraction peak intensity of C is very weak, indicating that the oxide layers almost completely cover the ablated surface, especially for 3D C/C-ZrC-SiC composites.

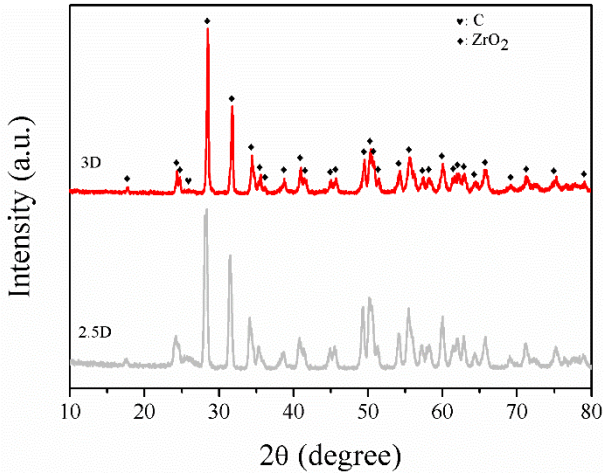

Fig.8. XRD patterns of the ablated surface of 2.5D and 3D C/C-ZrC-SiC composites.

Fig.9. presents the ablated surface images of 2.5D and 3D C/C-ZrC-SiC composites. As shown in Fig.9a and Fig.9d, the ablated surfaces of C/C-ZrC-SiC composites are covered by an oxide layer. By contrast, the oxide layer of 3D C/C-ZrC-SiC composites is more complete and uniform than those of 2.5D composites. Lots of carbon fibers can be directly observed on the ablated surface of 2.5D C/C-ZrC-SiC composites. According to the microtopographies of the ablated center (Fig.9b and 9e), the ablated center area of 2.5D composites is larger than that of 3D composites, and the amount of oxides on the ablated center of 2.5D composites is lower than that of 3D composites. Thus, 3D C/C-ZrC-SiC composites have better ablation resistance than 2.5D C/C-ZrC-SiC composites. As shown in Fig.9c and 9f, due to the scouring of high-speed oxyacetylene flame, plenty of molten oxides would flow and accumulate at the transition region, which can inhibit the expansion of the ablation center and improve the ablation resistance of C/C-ZrC-SiC composites [25].

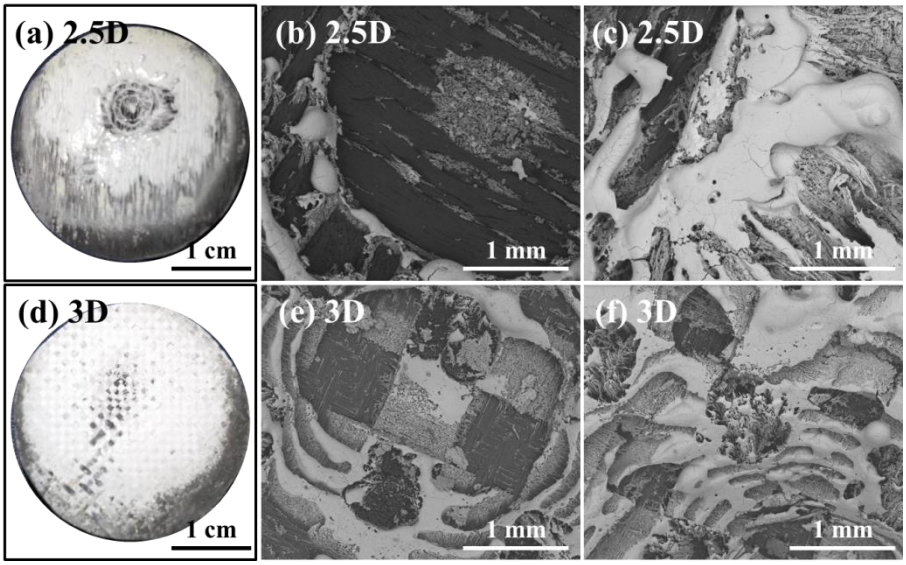

Fig.9. Ablated surface images of 2.5D and 3D C/C-ZrC-SiC composites: (a, d) Macro photographs, (b, c, e, and f) Micro topographies.

Conclusion

2.5D and 3D C/C-ZrC-SiC composites are successfully prepared by the one-step Sol-Gel method. Since the pores in the 3D needled carbon fiber felt are more connected than those of 2.5D needled felt, the sol precursor is prone to impregnate in 3D needled felt. As a result, the densities of 2.5D and 3D C/C-ZrC-SiC composites are 1.80 g/cm^3 and 1.98 g/cm^3, respectively. Besides, due to the firm 3D needled fiber felt structure and abundant carbon fibers, the flexural strength and bending modulus of 3D C/C-ZrC-SiC composites are 148.926 MPa and 20.479 GPa, which are 23.99% and 27.10% higher than those of 2.5D composites, respectively. After being ablated under a stable oxyacetylene flame at 2800 ºC for 60 s, the mass and linear ablation rates of 3D C/C-ZrC-SiC are 0.2372 mg/(cm^2·s) and 0.0110 mm/s, while those of 2.5D composites are 0.3203 mg/(cm^2·s) and 0.0148 mm/s, respectively. Thus, the 3D C/C-ZrC-SiC composites not only have good mechanical properties but also have excellent ablation resistance.

Reference:

[1] K.-z. Li, X. Jing, F. Qian-gang, L. He-jun, G. Ling-jun, Effects of porous C/C density on the densification behavior and ablation property of C/C-ZrC-SiC composites, Carbon, 57 (2013) 161-168.

[2] H. Li, L. Zhang, L. Cheng, Y. Wang, Fabrication of 2D C/ZrC-SiC composite and its structural evolution under high-temperature treatment up to 1800°C, Ceramics International, 35 (2009) 2831-2836.

[3] C. Fang, X. Yang, K. He, L. Chen, G. Zeng, A. Shi, Q. Huang, B. Huang, Microstructure and ablation properties of La_2O_3 modified C/C-SiC composites prepared via precursor infiltration pyrolysis, Journal of the European Ceramic Society, 39 (2019) 762-772.

[4] Z. Zhao, K. Li, Q. Liu, W. Li, Y. Zhang, Enhanced anti-ablation performance of carbon/carbon composites modified with ZrC-SiC, Vacuum, 156 (2018) 123-127.

[5] M.-y. Zhang, K.-z. Li, X.-h. Shi, W.-l. Tan, Effects of SiC interphase on the mechanical and ablation properties of C/C-ZrC-ZrB_2-SiC composites prepared by precursor infiltration and pyrolysis, Materials & Design, 122 (2017) 322-329.

[6] C. Liu, L. Cao, J. Chen, L. Xue, X. Tang, Q. Huang, Microstructure and ablation behavior of SiC coated C/C-SiC-ZrC composites prepared by a hybrid infiltration process, Carbon, 65 (2013) 196-205.

[7] J. Xie, K. Li, G. Sun, H. Li, Effects of precursor concentration on the microstructure and properties of ZrC modified C/C composites prepared by precursor infiltration and pyrolysis, Ceramics International, 43 (2017) 14642-14651.

[8] W. Jin, Z. Si, Y. Lu, S. Bei-zhi, W. Yi, L. Guang-de, X. Zhong-fang, C. Jie, H. Heng-ping, X. Yang, Oxidation behavior and high-temperature flexural property of CVD-SiC-coated PIP-C/SiC composites, Ceramics International, 44 (2018) 16583-16588.

[9] J. Li, R. Luo, Study of the mechanical properties of carbon nanofiber reinforced carbon/carbon composites, Composites Part A: Applied Science and Manufacturing, 39 (2008) 1700-1704.

[10] Z. Li, H. Li, S. Zhang, J. Wang, W. Li, F. Sun, Effect of reaction melt infiltration temperature on the ablation properties of 2D C/C-SiC-ZrC composites, Corrosion Science, 58 (2012) 12-19.

[11] C. Liu, Z. Su, Q. Huang, J. Chen, X. Yang, L. Cao, T. Yin, P. Zhong, Ablation behavior of

ZrC–SiC coated C/C-ZrC-SiC composites prepared by precursor infiltration pyrolysis combined with reactive melt infiltration, Journal of Alloys and Compounds, 597 (2014) 236-242.

[12] D. Zhang, P. Hu, S. Dong, X. Liu, C. Wang, Z. Zhang, X. Zhang, Oxidation behavior and ablation mechanism of Cf/ZrB_2-SiC composite fabricated by vibration-assisted slurry impregnation combined with low-temperature hot pressing, Corrosion Science, 161 (2019) 108181.

[13] D. Zhang, P. Hu, J. Feng, M. Xie, H. Zhao, X. Zhang, Characterization and mechanical properties of Cf/ZrB_2-SiC composites fabricated by a hybrid technique based on slurry impregnation, polymer infiltration and pyrolysis and low-temperature hot pressing, Ceramics International, 45 (2019) 5467-5474.

[14] E.L. Corral, L.S. Walker, Improved ablation resistance of C-C composites using zirconium diboride and boron carbide, Journal of the European Ceramic Society, 30 (2010) 2357-2364.

[15] C. Li, G. Li, H. Ouyang, J. Huang, X. Hou, Microstructure and properties of C/C-ZrC composites prepared by hydrothermal deposition combined with carbothermal reduction, Journal of Alloys and Compounds, 741 (2018) 323-330.

[16] X. Chen, S. Dong, Y. Kan, X. Jin, H. Zhou, D. Ni, D. Wang, Microstructure and mechanical properties of three dimensional Cf/SiC-ZrC-ZrB_2 composites prepared by reactive melt infiltration method, Journal of the European Ceramic Society, 36 (2016) 3969-3976.

[17] X. Chen, Q. Feng, Y. Kan, D. Ni, H. Zhou, L. Gao, X. Zhang, Y. Ding, S. Dong, Effects of preform pore structure on infiltration kinetics and microstructure evolution of RMI-derived Cf/ZrC-ZrB_2-SiC composite, Journal of the European Ceramic Society, 40 (2020) 2683-2690.

[18] C. Zeng, K. Tong, M. Zhang, Q. Huang, Z. Su, C. Yang, X. Wang, Y. Wang, W. Song, The effect of sol-gel process on the microstructure and particle size of ZrC-SiC composite powders, Ceramics International, 46 (2020) 5244-5251.

[19] C. Zeng, M. Zhang, H. He, X. Wang, K. Tong, Y. Wang, P. Xu, L. Zheng, G. Zeng, Z. Su, Q. Huang, The effect of carbon source addition order during sol-gel process on the properties of C/C-ZrC-SiC composites, Ceramics International, 47 (2021) 35366-35377.

[20] L. Zheng, C. Fang, X. Luo, Z. Zhang, M. Zhang, Q. Huang, Effect of $MgCl_2$ addition on the preparation of ZrC-SiC composite particles by sol-gel, Ceramics International, 48 (2022)

2522-2532.

[21] L. Zheng, M. Zhang, K. He, C. Fang, C. Zeng, Q. Huang, Improving the sinterability of ZrC-SiC composite powders by Mg addition, Ceramics International, 47 (2021) 18330-18338.

[22] L.-m. Huang, R.-j. Liu, C.-r. Zhang, Y.-f. Wang, Y.-b. Cao, Si/SiC optical coatings for C/SiC composites via gel-casting and gas silicon infiltration: Effects of carbon black content, Journal of Alloys and Compounds, 711 (2017) 162-168.

[23] A. Najafi, F.G. Fard, H.R. Rezaie, N. Ehsani, Synthesis and characterization of SiC nano powder with low residual carbon processed by sol-gel method, Powder Technology, 219 (2012) 202-210.

[24] Q. Li, H. Zhou, S. Dong, Z. Wang, J. Yang, B. Wu, J. Hu, Fabrication and comparison of 3D Cf/ZrC-SiC composites using ZrC particles/polycarbosilane and ZrC precursor/polycarbosilane, Ceramics International, 38 (2012) 5271-5275.

[25] D. Huang, M. Zhang, Q. Huang, L. Wang, K. Tong, Mechanical Property, Oxidation and Ablation Resistance of C/C-ZrB_2-ZrC-SiC Composite Fabricated by Polymer Infiltration and Pyrolysis with Preform of Cf/ZrB_2, Journal of Materials Science & Technology, 33 (2017) 481-486.

Effect of PDA/Fe3O4 sizing agent on the mechanical properties of carbon fiber reinforced polyamide 6 thermoplastic composites

Xiaopeng Wu [1], *Tao Huang* [1], *Weiyi Kong* [2], *Xuan Zhang* [2], *Huiming Ning* [1]

（1. College of Aerospace Engineering, Chongqing University, Chongqing 400044, P. R. China;

2. AECC Commercial Aircraft Engine Co., Ltd., Shanghai 200241, P. R. China）

Abstract: The interfacial properties between carbon fiber (CF) and polyamide 6 (PA6) thermoplastic resin were modified by a newly developed sizing agent to improve the mechanical properties of CF reinforced PA6 thermoplastic composites. Through the oxidative self-polymerization of dopamine, a polydopamine/nano ferric oxide coating (PDA/Fe_3O_4) was successfully constructed on the surface of carbon fiber. The surface properties of carbon fibers before and after modification were characterized and analyzed. The results showed that the PDA/Fe_3O_4 coating can effectively improve the surface roughness and chemical activity of carbon fibers, and enhance the mechanical engagement and chemical interaction between the fibers and the resin matrix. Compared with unmodified CF/PA6 composites, the prepared modified CF/PA6 composites exhibit excellent mechanical properties, with tensile properties increased by 27.8%. The corresponding failure characteristics and reinforcement mechanisms were also analyzed.

Keywords: Carbon fiber; polyamide 6; polydopamine; nano-Fe_3O_4; interfacial properties

1. Introduction

Carbon fiber reinforced thermoplastic composites (CFRTP) have excellent properties such as high specific strength, high specific modulus, lightweight, and recyclability, and have been widely used in automotive manufacturing, aerospace, intelligent machinery, and other industries[1,2]. Polyamide 6 (PA6) has excellent properties such as low cost, easy processing, and strong impact resistance, and is often used as a matrix material for CFRTP[3]. However, the interfacial bonding property between carbon fiber (CF) and thermoplastic resin matrix is generally weak, which which can adversely affect the mechanical properties of CFRTP. Traditional sizing methods based on coupling agent modified nanoparticles are mostly developed for thermosetting resins and may produce volatile organic compounds that are harmful to humans and the environment, so it is urgent to develop more green and sustainable sizing methods for thermoplastic resins[4]. In view of the fact that dopamine and its derivatives can self polymerize under extremely mild conditions and produce viscous polydopamine (PDA) with good adhesion to almost all types of substrates[5]. In this

paper, self-polymerization of dopamine was used to introduce a polydopamine coating on the CF surface, while low-cost ferric oxide nanoparticles were introduced to coordinate the modification of the CF surface to improve the interfacial properties of CF and PA6. The microstructure and chemical structure of the fiber surface were studied by SEM, AFM and XPS respectively. And the effect of PDA/Fe_3O_4 sizing on the mechanical properties of CF/PA6 thermoplastic composites was studied through tensile experiments.

2. Materials and experiments

The commercial sizing agent was removed from the surface of the woven carbon fabric by high-temperature desizing treatment at 600 ℃. The desized carbon fabric was recorded as CF; On the basis of desizing, dopamine hydrochloride and a mixed solution of dopamine hydrochloride and nano ferric oxide were adhered to the surface of woven carbon cloth by oxidative self polymerization, resulting in carbon cloth modified by pure polyamine and carbon cloth co-modified by polyamine and nano ferric oxide, recorded as CF/PDA and CF/PF respectively.

The CF/PA6 composite laminate was prepared by sequential lamination molding method, in which the molding temperature was 250 ℃, the molding pressure was 2 MPa, and the holding time was 10 minutes. Fiber reinforced polyamide composites were prepared and labeled as CF/PA6 (unmodified carbon fiber/polyamide 6 composite), CF-PDA/PA6 (carbon fiber/polyamide 6 composite modified by dopamine hydrochloride), and CF-PF/PA6 (carbon fiber/polyamide 6 composite modified by dopamine hydrochloride and nano ferric oxide), respectively. The composite was tested according to the corresponding tensile test standards (ASTM-D3039). The loading rate was set to 1 mm/min, and the experiment was stopped after the load decreased. Five samples were tested for each group of samples and their average values were taken.

Finally, scanning electron microscopy (SEM), optical microscopy (OM), atomic force microscopy (AFM), and X-ray photoelectron spectroscopy (XPS) were used to characterize the surface properties of the fiber and the failure mechanism of the composite.

3. Results and Discussion

3.1 Characterization of fiber surface

Through SEM and AFM observation of the surface morphology of carbon fibers before and after modification (as shown in Figure 1), it can be seen that the original CF surface after desizing treatment is relatively smooth, which is not conducive to the combination of fibers and resins. After DA self-polymerization modification, the surface roughness of CF/PDA specimen is rougher than that of the original

desizing CF. After PDA/Fe_3O_4 co-modification, the surface roughness of CF/PF specimen is further increased, which is helpful to the mechanical engagement of PA6 resin and carbon fibers. At the same time, Fe_3O_4 particles with higher modulus are uniformly distributed on the CF surface, which can effectively improve the transition modulus of the interfacial layer and better transfer the stress to the reinforcing phase CF.

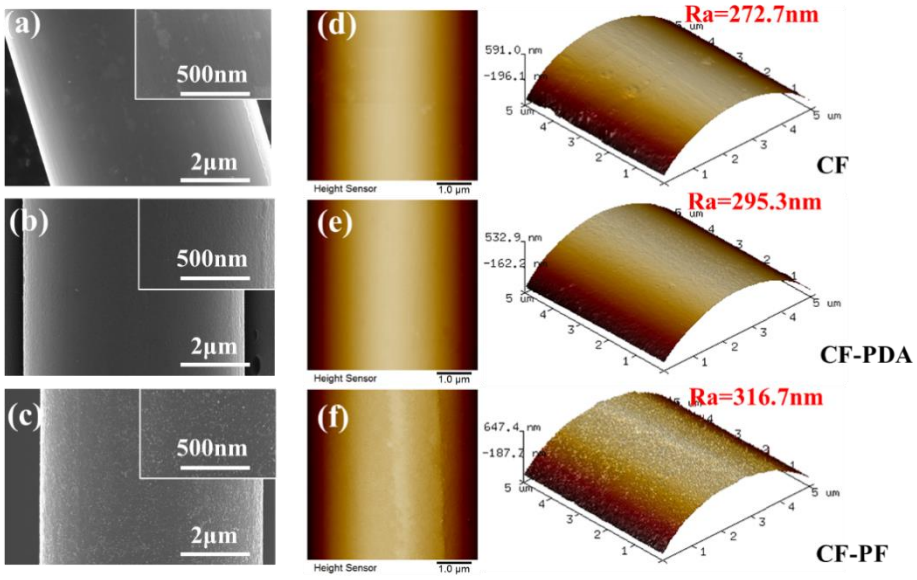

Fig.1 (a) (b) and (c): SEM images of carbon fiber surface before and after modification;
(d) (e) and (f): AFM images of carbon fiber surface before and after modification;

On the other hand, the presence of polydopamine coating and PDA/Fe_3O_4 coating on the surface of the carbon fibers were demonstrated by XPS characterization, which will provide a large number of active functional groups on the surface of the carbon fiber (as shown in Table 1). Those active functional groups can provide more active sites for interfacial adhesion and facilitate the formation of hydrogen bonds with the amide groups in polyamide 6, thereby enhancing the interfacial bonding between the fibers and the resin matrix.

Table 1 The surface functional group content of different modified CF

Carbon fiber	Surface functional group composition （At. %）							
	C-C	C-N	C-O	O=C-O	π-π	$-NH_2$	-NH	-N=
CF	85.6	/	7.1	7.3	/	/	100	/
CF-PDA	63.9	9.0	20.8	6.0	0.4	30.8	39.4	30.0
CF-PF	68.6	7.3	19.4	4.3	0.4	22.4	39.8	37.8

3.2 Mechanical Properties of Carbon Fiber/Polyamide 6 Composites

Figure 2 shows the tensile mechanical properties of CF/PA6 composites obtained by three different CF surface treatments. After testing, it can be found that modifying the CF surface does not change the elastic modulus of the fiber reinforced nylon composite, and the slopes of the three kinds of specimens were almost identical, but only improves the tensile strength and elongation of the composite. With the strengthening of the CF/PA6 interface, the tensile strength of the composite increases from 669.6 MPa at the beginning to 753.8 MPa of the CF-PDA/PA6 specimen. The tensile strength of CF-PF/PA6 specimen with the strongest interface is 855.6MPa, which is 27.8% higher than that of the CF/PA6 composite laminates made from original desizing fiber. This indicates that the interface of the original fiber is very weak and cannot meet the stress transfer requirements of CF/PA6 composites under high tensile load. After modification with PDA/Fe_3O_4, the strengthened interface facilitates the transfer of stress from the resin to the fiber, resulting in a significant improvement in the tensile strength of the composite.

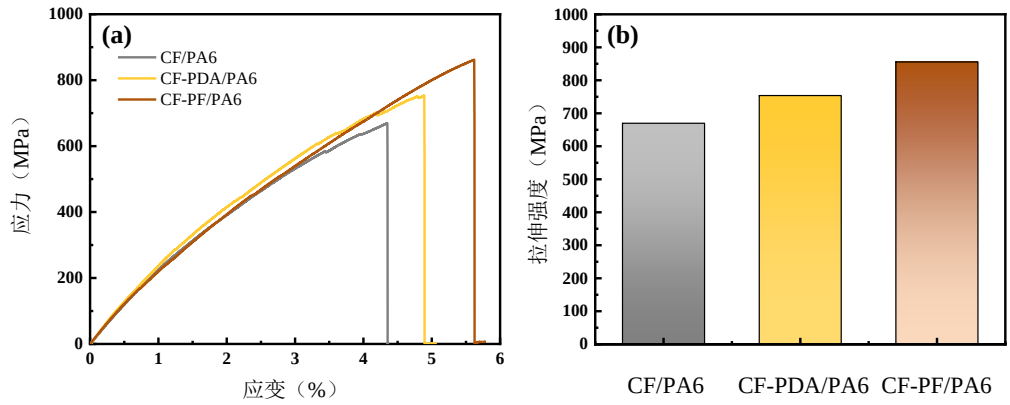

Fig. 2 Comparison of Tensile Properties of CF/PA6 Composites

After tensile testing, the fracture morphology of the composites was characterized by SEM, which allows direct determination of the attachment characteristics of the fibers and resin matrix in the composites. Figure 3 shows the specific microscopic morphology of the three three different specimens after fracture under tensile load by SEM. After tensile fracture, the exposed fiber surface of the CF/PA6 composite prepared from the original desizing CF is relatively clean and smooth, with a small amount of gaps between the fibers (Figure 3 (a) and (b)), indicating that the fibers readily debonded from the PA6 resin matrix when subjected to tensile loading. In Figure 3 (c) and (d), it can be seen that a quantitative amount of resin can be seen adhering to the surface of the fractured fibers at the exposed position, indicating that the PDA modification can initially improve the interfacial bonding of CF and PA6. In Figure 3 (f), the CF/PF surface is coated with

a thick layer of resin, and the fibers and resin are tightly bonded together. This indicates that the use of PDA/Fe_3O_4 modification has greatly improved the compatibility of inert CF with the thermoplastic resin matrix, resulting in better interfacial bonding of the prepared CF-PF/PA6 composites. The matrix phase PA6 can transfer loads to CF more effectively, while the reinforcing phase CF can also play its mechanical reinforcement role better.

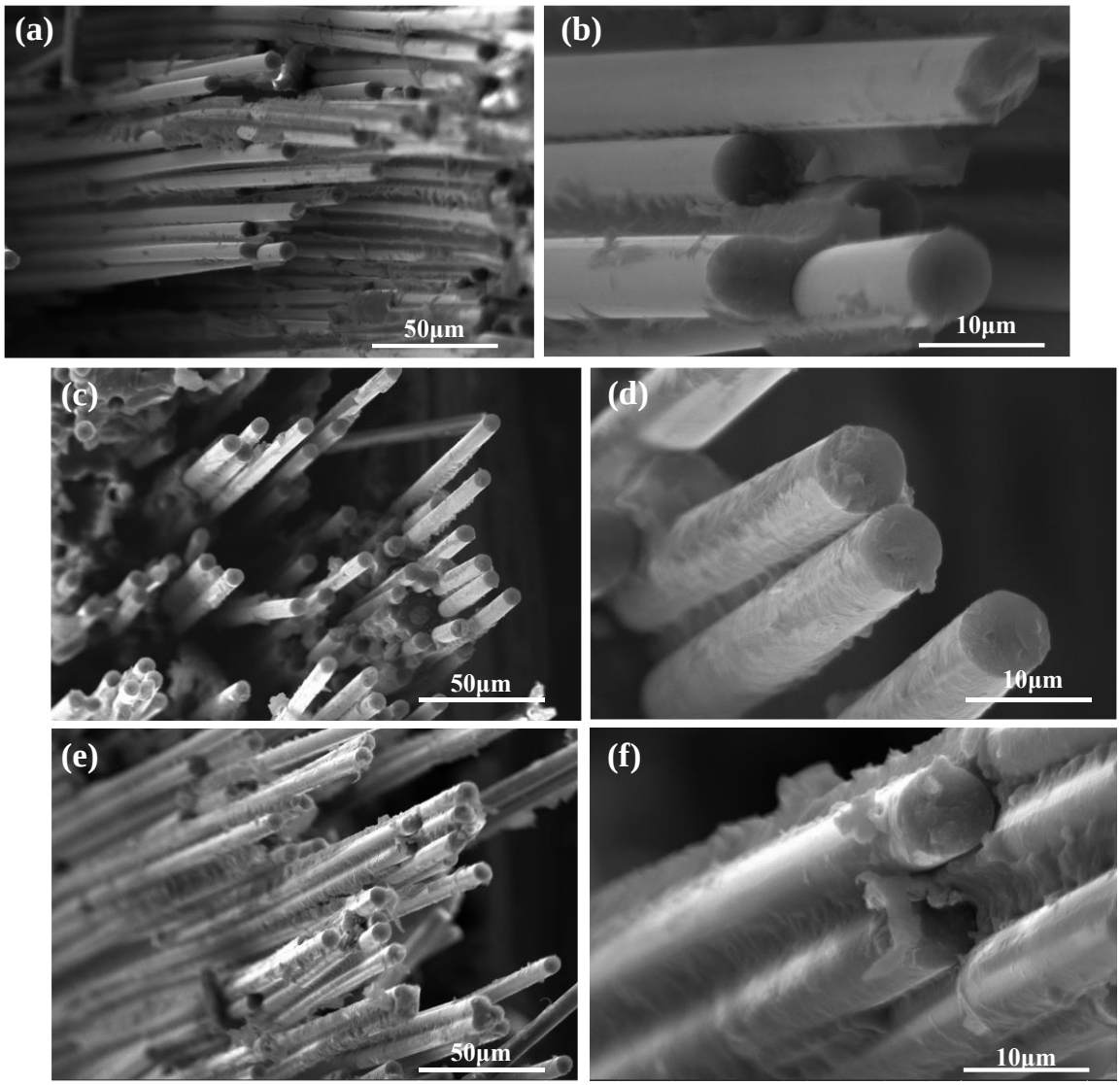

Fig.3 Tensile fracture section morphologies of composite with different modification

4. Conclusion

In this study, PDA/Fe_3O_4 coating was constructed on the surface of carbon fibers by a green and simple method using the self-polymerization of dopamine in a weak alkaline environment, and modified carbon fibers and their reinforced polyamide composites were prepared. With the introduction of PDA coating, the surface roughness of the fibers increased, while the reactive nitrogen-containing groups were introduced,

which can form strong hydrogen bonds with the amide groups in PA6 resin, which is beneficial to improve the interfacial properties of the fibers and the resin matrix; the addition of Fe_3O_4 nanoparticle further improved the roughness of the interfacial layer, while the rigid nanoparticles can improve the transition modulus of the interfacial layer, which is more beneficial to the stress transfer between the resin matrix and the fiber, thus further improving the mechanical properties of the composite. The final tensile properties of the PDA/Fe_3O_4 modified composites reached 855.6 MPa, which was 27.8% higher than that of the untreated composite laminates.

Acknowledgments

The authors would like to acknowledge the financial support provided by Shanghai Science and Technology Committee (STCSM) Sailing Program (Project No. 20YF1454000) and Standard Research Program (Project No. 20DZ2203900).

References

[1] Ma Z, Pu Y, Huang Y, et al. Improvement in interface and mechanical properties of CF/poly(ether-imide) and CF/poly(ether-ether-ketone) by aqueous sizing of reactive cationic Poly(amide-imide) with catechol pendant groups on CF. Composites Science and Technology, 2022, 230: 109754.

[2] Wegmann S, Rytka C, Diaz-Rodenas M, et al. A life cycle analysis of novel lightweight composite processes: Reducing the environmental footprint of automotive structures. Journal of Cleaner Production, 2022, 330: 129808.

[3] Kondo M Y, Montagna L S, Morgado G F D, et al. Recent advances in the use of Polyamide-based materials for the automotive industry. Polimeros, 2022, 32(2): e2022023.

[4] Xiao Y, Zou H, Zhang L, et al. Surface modification of silica nanoparticles by a polyoxyethylene sorbitan and silane coupling agent to prepare high-performance rubber composites. Polymer Testing, 2020, 81: 106195.

[5] Han W, Zhang H-P, Tavakoli J, et al. Polydopamine as sizing on carbon fiber surfaces for enhancement of epoxy laminated composites. Composites Part A: Applied Science and Manufacturing, 2018, 107: 626-32.

Molecular investigation of CNT/PP nanocomposite under dynamic loads

Ruidong Wu, Chao Wu, and Lik-ho Tam**

School of Transportation Science and Engineering, Beihang University, Beijing, China

* Corresponding authors (leo_tam@buaa.edu.cn, wuchao@buaa.edu.cn)

Abstract: Polypropylene (PP) has been widely used in various engineering fields, which are commonly subjected to dynamics loads. The limited ductility of PP under dynamic loads leads to the unexpected material failure. Carbon nanotube (CNT) with excellent mechanical properties has been regarded as an ideal reinforcement filler to improve the dynamic performance of PP materials. However, the CNT fillers form aggregation with increasing additions. In this work, the effect of CNT aggregation on the mechanical response of CNT/PP nanocomposite under dynamic loads is investigated using molecular simulation. The aggregated CNTs at different weight percentages are added into the PP matrix to generate the nanocomposite models, which are subjected to different cycles of loading-unloading dynamic compression process. By comparing the peak load and energy dissipation variations of CNT/PP nanocomposite at different weight percentages, the effect of CNT aggregation on the dynamic response of nanocomposite is examined. This study provides nanoscale insights into the CNT aggregation on the dynamic response of CNT/PP nanocomposite, which contributes to the optimized design of nanocomposite materials.

Keywords: Nanocomposite, carbon nanotube, aggregation, dynamic loads, molecular simulation

1. INTRODUCTION

During the past few decades, the advantages of polypropylene (PP) such as low density, reasonable modulus and strength, excellent chemical stability, and low cost have facilitated its wide applications in different industrial fields, including the packaging, automotive, aerospace, and construction industries [1-4]. During the long-term service-life, PP-based materials are inevitably subjected to dynamic loading due to the wind loads, vibration, and sudden bumping or strikes. However, the PP-based material possesses poor ductility, which has limited its applications as key structural components where dynamic loading conditions are of great concern. Carbon nanotube (CNT) possesses excellent structural and mechanical properties, which has been considered as a suitable nanofiller for improving the dynamic performance of PP-based material [5, 6]. Nevertheless, the enhancement induced by CNT incorporation is negatively affected by the CNT aggregation at large contents. In order to achieve the optimized design of composite material, it requires detailed investigation on the variation of dynamic properties of CNT/PP composite as affected by CNT aggregation.

In recent years, several experimental and simulation investigations have been conducted to investigate the dynamic performance of CNT/polymer composite materials [7-13]. Specifically, in previous experimental studies on the dynamic properties of CNT/PP composite under the notched impact tests, the impact strength showed an initial increasing and a subsequent decreasing trend with the increasing CNT content, and the transition appeared at around 2 wt% [7, 8]. Similar trend has been observed in another study on the impact behaviors of CNT/PP composite, where the impact strength of composite declined at CNT contents over 1.5 wt% [9]. In other studies on the dynamic compression properties of CNT/epoxy composites, both the compressive modulus and strength of composite showed obvious improvement with the CNT addition [10, 11]. Meanwhile, the energy dissipation ability of polyethylene (PE) composites during loading-unloading cycles was reported to improve with CNT incorporation [12]. Apart from experimental approaches, molecular dynamics (MD) simulation has been considered as a versatile technique for investigating the dynamic properties of CNT/polymer nanocomposite. The dynamic response of CNT/phenolic resin nanocomposite under shock compression has been explored using MD simulation, where the yield strength and deformation behavior of nanocomposite increased with increasing CNT volume fraction up to 9 vol% [13]. It is learned that the dynamic properties of composite materials under different loading cases have been investigated, which are generally enhanced with increasing CNT contents, while it could be reduced at high CNT contents. However, the effect of CNT aggregation on the mechanical degradation of composite during different loading-unloading cycles remains largely unclear.

In this study, the aim is to investigate the effect of CNT aggregation on the dynamic properties of CNT/PP nanocomposite during different loading-unloading cycles. The molecular models of CNT/PP nanocomposite with CNT aggregation at different CNT contents are constructed using coarse-grained (CG) modeling approach, which are subjected to dynamic compression for several cycles. The dynamic response of nanocomposite during different cycles is observed, including the peak load and energy dissipation. The findings of this study could be applied for designing the CNT content and composite structure to achieve the optimized dynamic response of CNT/PP composite.

2. METHODS

The simulation methods include the model construction, force field definition, model equilibration, and dynamic simulation, which are introduced as follows.

The construction of CNT/PP nanocomposite models follows the procedures as reported in our previous studies [14-16]. Specifically, both PP and CNT chains are composed of consecutively connected 1-nm CG bead, with the bead mass of 186.34 and 1953.23 amu, respectively, as shown in **Fig. 1(a)** and **(b)**. The chain length of PP and CNT is 30 and 20 nm respectively, and the ratio between the chain length is 1.5, which are within reasonable ranges in similar MD simulations [17-19]. The dimensions of nanocomposite models are selected as $30 \times 30 \times 30$ nm^3 to eliminate the size and boundary effect [17]. Periodic boundary conditions are applied in *x* and *y* axis, while non-periodic boundary condition is applied along loading direction (*z* axis), which are used to simulate the composite plate material. The CNT building blocks include the single-CNT (CNT-1) segment, three-CNT (CNT-3) segment, and seven-CNT (CNT-7) segment [20, 21]. The CNT segments further form CNT clusters with increasing number and size at CNT contents of 3 and 9 wt%, which represent the low and high CNT content case respectively, as shown in **Table 1**. The initial configuration of PP chains is set similar as those in previous MD simulations [22, 23]. The nanocomposite models are constructed by initially dispersing the CNTs in the system, and then packing the PP chains in the available space to achieve the initial packing density of 0.90 g·cm^{-3} for pure PP polymer, as shown in **Fig. 1(c)**.

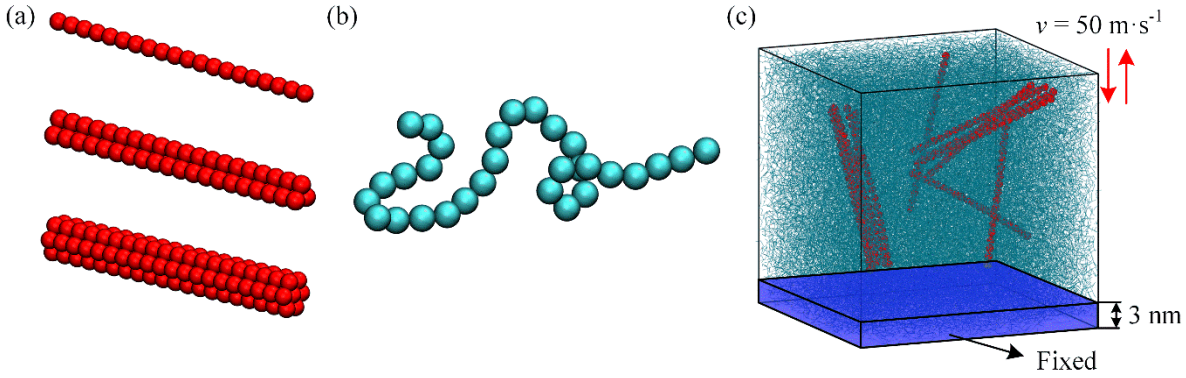

Fig. 1 (a) CNT segment and (b) PP chain are used to construct (c) 3 wt% CNT/PP nanocomposite model, where the bottom 3-nm region is fixed as the boundary and cyclic compressive load is applied on the top surface at the rate of 50 m·s^{-1}

Table 1 Setup of CNT and PP chains in the CNT/PP nanocomposite models

CNT wt%	CNT cluster C-1			CNT cluster C-2		Randomly dispersed CNTs	PP chains	Atoms
	CNT-1	CNT-3	CNT-7	CNT-1	CNT-3	CNT-1		
0	\	\	\	\	\	\		78570
3	1	1	\	2	1	3	2619	78810
9	1	1	3	5	1	3		79290

After the model construction, the interactions in the composite system are defined by the force field, as shown in **Eq. (1)**,

$$\Phi = \Phi_{\text{bonded}} + \Phi_{\text{non-bonded}} = \Phi_{\text{stretching}} + \Phi_{\text{bending}} + \Phi_{\text{vdW}} \quad (1)$$

where the bonded interactions Φ_{bonded} contain bond stretching $\Phi_{\text{stretching}}$ and angle bending Φ_{bending} interactions, and the non-bonded interaction $\Phi_{\text{non-bonded}}$ is represented by the van de Waals (vdW) interaction Φ_{vdW}. The detailed functional forms and parameters of each term have been derived in our previous papers [14-16].

With the developed molecular models and force field, the nanocomposite system is subjected to an annealing process to achieve rapid and efficient equilibration. Specifically, two Lennard-Jones (LJ) energetic walls with the strength and distance parameters of 5.0 kcal·mol^{-1} and 0.5 nm are added to the top and bottom surface of model at a distance of 0.5 nm for controlling the thickness [24-26]. The system is equilibrated in the microcanonical (NVE) ensemble for 2 ns, and then heated from 0 to 600 K and cooled down to 300 K in the canonical (NVT) ensemble, with a stepwise temperature variation of 100 K per 2 ns. Afterwards, the system is further equilibrated at 300 K in the NVT ensemble for 10 ns until fully relaxed.

After the structural equilibration, the nanocomposite model is exposed to dynamic compressive loading, where the bottom region with a thickness of 3 nm is fixed to represent the boundary and the compressive load is applied on the top surface via a planar indenter, as shown in **Fig. 1(c)**. The indenter exerts repulsive interactions on the beads of nanocomposite following **Eq. (2)**,

$$F(r) = kr^2 \quad (2)$$

where k indicates the stiffness of indenter and is selected as 20,000 kcal·mol^{-1}·nm^{-3} to represent a rigid indenter [27]; r represents the distance between the indenter plane and the bead. The commonly used loading rate in impact tests in experiments varies from 4 to 120 m·s^{-1}, and it is reported that the mechanical responses of polymer and carbon nanomaterials are not sensitive to the compressive loading rate within 5 m·s^{-1}, where the materials do not show obvious dynamic performance [25-29]. Therefore, 50 m·s^{-1} is selected as a typical loading rate for investigating the dynamic performance of CNT/PP nanocomposite. During the loading process, the model is compressed until a maximum displacement of 10 nm, which enables a reasonable deformation of 33% of the total thickness [30, 31]. Afterwards, the compression keeps for another 0.02 ns for the system relaxation, and then it is unloaded at the same rate of 50 m·s^{-1} [27]. To simulate the repeated loading-unloading process in real applications, five loading-unloading cycles are conducted, which is used in previous investigations of dynamic properties [12, 32].

3. RESULTS AND DISCUSSIONS

In order to investigate the dynamic response of pure PP and CNT/PP nanocomposite systems, the load-displacement curves of pure PP, 3 wt%, and 9 wt% CNT/PP nanocomposite during different loading-unloading cycles are firstly measured, as shown in **Fig. 2**. During loading process, the load keeps increasing with an increasing rate, which indicates that the system is more difficult to be compressed. During unloading process, the load decreases rapidly, which is lower than that at the same displacement during loading process. The load reaches zero finally and there remains certain irrecoverable deformation

after unloading. Under cyclic compression, it is observed that the load levels of the curve at the same displacement become smaller with increasing cycles and the irrecoverable deformation gradually accumulates due to the elastoplasticity of composite material. During each cycle, the system exhibits a deformation hysteresis, which dissipates the applied energy. It is noted that the load-displacement curves possess similar shapes as those observed in the nano-indentation tests, which demonstrates that the molecular model is capable of characterizing the dynamic response of CNT/PP nanocomposite [25-27].

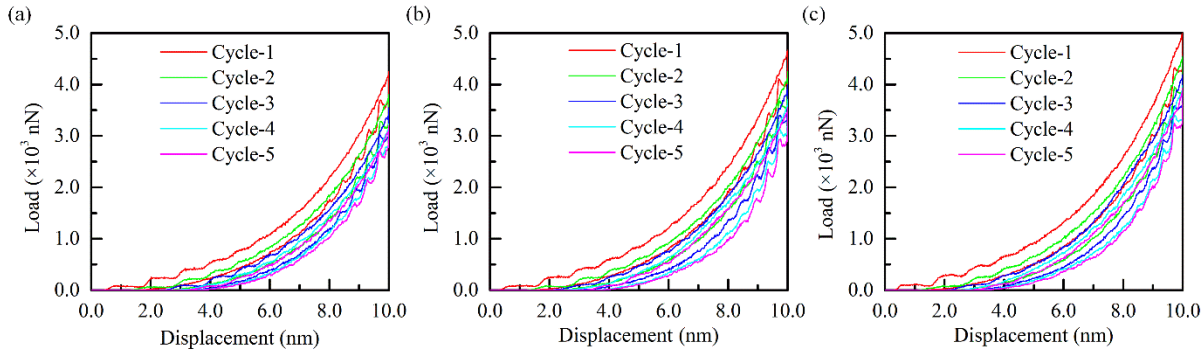

Fig. 2 Load-displacement curves of (a) pure PP, (b) 3 wt%, and (c) 9 wt% CNT/PP nanocomposite under cyclic compression

The peak load at each cycle represents the resistance to dynamic loads of material, which is measured to characterize the mechanical degradation during each cycle. The variation of peak load of the pure PP, 3 wt%, and 9 wt% CNT/PP nanocomposite cases under cyclic compression is shown in **Fig. 3(a)**. For the pure PP case, the peak load decreases continuously with increasing cycles, which indicates the rapid decline of resistance to dynamic loads. The obvious softening characteristics under dynamic compression corresponds with the experimental observation, where the polyurethane shows similar peak load decline under cyclic compression [32]. For the nanocomposite cases, the variation of peak load shows a similar decreasing trend with increasing cycles. Compared with the pure PP case, the initial peak load of 3 wt% nanocomposite shows an obvious increase, while the decreasing rate is similar, which demonstrates that the CNT incorporation greatly enhances the composite resistance, while it does not obviously affect the degradation during larger cycles. When the CNT content further increases to 9 wt%, the initial peak load further increases slightly, which demonstrates the further improved resistance, and the decline rate remains similar, as the subsequent degradation during larger cycles is not affected by the added CNTs. The results indicate that the added aggregated CNTs could continuously improve the resistance to dynamic loads, while it could not restrict the subsequent degradation during multiple cycles.

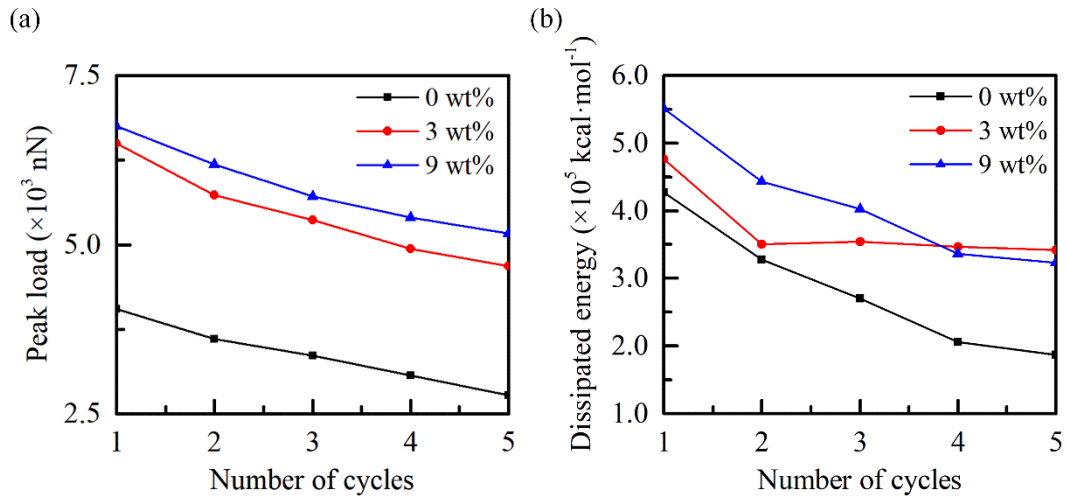

Fig. 3 Variation of (a) peak load and (b) dissipated energy of pure PP and nanocomposite systems with increasing number of cycles

Apart from the resistance to dynamic loads, the energy dissipation during each cycle is analyzed to characterize the deformation ability of nanocomposite when subjected to dynamic loads. The dissipated energy is defined as the enclosed area of the load-displacement during each cycle. The dissipated energy variation for pure PP, 3 wt%, and 9 wt% CNT/PP nanocomposite cases during different cycles is shown in **Fig. 3(b)**. For the pure PP case, it is shown that the dissipated energy shows a continuous decrease with increasing number of cycles, which indicates that the energy dissipation ability of PP degrades during multiple dynamic loading cycles. It is consistent with the experimental observation that the energy dissipation ability of polymer degrades during cyclic compression [33]. Compared with the pure PP case, the dissipated energy of 3 wt% nanocomposite shows a higher initial value, and similar decline at first two cycles, while it remains relatively stable during larger cycles, which infers that the 3 wt% CNT could obviously improve the energy dissipation ability of PP during multiple cycles. Similar finding is also reported in the experimental and simulation study of nanoclay/polyurethane composite [32]. For the 9 wt% nanocomposite case, the initial dissipated energy further increases compared with the 3 wt% case, while it continuously decreases during larger cycles and finally becomes lower than the 3 wt% case. It is learned that the formation of large CNT clusters at high CNT contents deteriorates the energy dissipation ability of nanocomposite under dynamic loading for multiple cycles.

4. CONCLUSIONS

This study investigates the effect of CNT contents on the variation of dynamic response of CNT/PP nanocomposite under cyclic compression. The CNT/PP nanocomposite models with CNT aggregation at different contents are developed using CG-MD simulations, which are subjected to cyclic dynamic compression. With increasing CNT contents, the initial peak load continuously increases, which indicates that the resistance to dynamic compression is improved. However, the decline rate of peak load during larger cycles is not obviously changed, which infers that the subsequent degradation is not affected by CNT addition. Comparatively, the degradation of dissipated energy during different cycles is significantly restricted at 3 wt%, which leads to the improved energy dissipation ability of nanocomposite compared with the pure PP case, while the degradation of dissipated energy becomes accelerated at 9 wt%, which leads to the lower energy dissipation ability of 9 wt% nanocomposite compared with the 3 wt% case after multiple

cycles. This research advances the understanding of dynamic performance of CNT/PP composite, and provides foundation for the optimized design of composite materials where dynamic loading conditions are of great concern.

ACKNOWLEDGMENTS

This work was supported by the National Natural Science foundation of China [grant numbers 51808020 and 51978025].

REFERENCES

[1] M.R. Manikantan, N. Varadharaju, Preparation and properties of polypropylene-based nanocomposite films for food packaging, Packaging Technology & Science 24 (2011) 191-209.
[2] N.O. Cabrera, B. Alcock, T. Peijs, Design and manufacture of all-PP sandwich panels based on co-extruded polypropylene tapes, Composites Part B 39(7-8) (2008) 1183-1195.
[3] K.K. Vijaya, S. Mir, A. Khaleel, An experimental evaluation of fiber reinforced polypropylene thermoplastics for aerospace applications, Journal of Mechanical Engineering 43(2) (2014) 92-97.
[4] N. Banthia, R. Gupta, Influence of polypropylene fiber geometry on plastic shrinkage cracking in concrete, Cement & Concrete Research 36(7) (2006) 1263-1267.
[5] Z.-J. Wang, D.-J. Kwon, G.-Y. Gu, H.-S. Kim, Mechanical and interfacial evaluation of CNT/polypropylene composites and monitoring of damage using electrical resistance measurements, Composites Science and Technology 81(81) (2013) 69-75.
[6] S. Ghoshal, P.H. Wang, P. Gulgunje, N. Verghese, S. Kumar, High impact strength polypropylene containing carbon nanotubes, Polymer 100 (2016) 259-274.
[7] K. Prashantha, J. Soulestin, M.F. Lacrampe, M. Claes, G. Dupin, P. Krawczak, Multi-walled carbon nanotube filled polypropylene nanocomposites based on masterbatch route: Improvement of dispersion and mechanical properties through PP-g-MA addition, eXPRESS Polymer Letters 2(10) (2008) 735-745.
[8] K. Prashantha, J. Soulestin, M.F. Lacrampe, P. Krawczak, Masterbatch-based multi-walled carbon nanotube filled polypropylene nanocomposites: Assessment of rheological and mechanical properties, Composites Science and Technology 69(11-12) (2009) 1756-1763.
[9] M.M. Zamani, A. Fereidoon, A. Sabet, Multi-walled carbon nanotube-filled polypropylene nanocomposites: high velocity impact response and mechanical properties, Iranian Polymer Journal 21(12) (2012) 887-894.
[10] P. Ma, G. Jiang, Q. Chen, H. Cong, X. Nie, Experimental investigation on the compression behaviors of epoxy with carbon nanotube under high strain rates, Composites Part B: Engineering 69 (2015) 526-533.
[11] K.S. Pandya, N.K. Naik, Energy absorption capability of carbon nanotubes dispersed in resins under compressive high strain rate loading, Composites Part B: Engineering 72 (2015) 40-44.
[12] V.M. Boddu, M.W. Brenner, J.S. Patel, A. Kumar, P.R. Mantena, T. Tadepalli, B. Pramanik, Energy dissipation and high-strain rate dynamic response of E-glass fiber composites with anchored carbon nanotubes, Composites Part B 88 (2016) 44-54.
[13] B. Arman, Q. An, S.N. Luo, T.G. Desai, D.L. Tonks, T. Cagin, W. Iii, Dynamic response of phenolic resin and its carbon-nanotube composites to shock wave loading, Journal of Applied Physics 109 (2011) 013503.
[14] C. Wu, R. Wu, W. Xia, L.-h. Tam, Understanding creep behavior of semicrystalline polymer via coarse-grained modeling, Journal of Polymer Science Part B: Polymer Physics 57(24) (2019) 1779-1791.
[15] C. Wu, R. Wu, L.-h. Tam, Coarse-grained molecular simulation of the effects of carbon nanotube

dispersion on the mechanics of semicrystalline polymer nanocomposites, Nanotechnology 32(32) (2021) 325705.
[16] C. Wu, R. Wu, L.-h. Tam, The creep behavior of semicrystalline carbon nanotube/polypropylene nanocomposite: A coarse-grained molecular study, Polymer Degradation and Stability 196 (2022) 109834.
[17] A.R. Alian, S.A. Meguid, Large-scale atomistic simulations of CNT-reinforced thermoplastic polymers, Composite Structures 191 (2018) 221-230.
[18] B. Arash, H.S. Park, T. Rabczuk, Tensile fracture behavior of short carbon nanotube reinforced polymer composites: A coarse-grained model, Composite Structures 134 (2015) 981-988.
[19] B. Arash, H.S. Park, T. Rabczuk, Mechanical properties of carbon nanotube reinforced polymer nanocomposites: A coarse-grained model, Composites Part B: Engineering 80 (2015) 92-100.
[20] A.R. Alian, S.A. Meguid, Large-scale atomistic simulations of CNT-reinforced thermoplastic polymers, Composite Structures (191) (2018) 221-230.
[21] M.J. Buehler, Mesoscale modeling of mechanics of carbon nanotubes: Self-assembly, self-folding, and fracture, Journal of Materials Research 21(11) (2006) 2855-2869.
[22] E. Panizon, D. Bochicchio, L. Monticelli, G. Rossi, MARTINI coarse-grained models of polyethylene and polypropylene, The Journal of Physical Chemistry B 119(25) (2015) 8209-8216.
[23] J. Mccarty, A.J. Clark, I.Y. Lyubimov, M.G. Guenza, Thermodynamic consistency between analytic integral equation theory and coarse-grained molecular dynamics simulations of homopolymer melts, Macromolecules 45(20) (2012) 8482-8493.
[24] H. Chen, L. Zhang, J. Chen, M. Becton, X. Wang, H. Nie, Energy dissipation capability and impact response of carbon nanotube buckypaper: A coarse-grained molecular dynamics study, Carbon 103 (2016) 242-254.
[25] J. Song, R. Kahraman, D.W. Collinson, W. Xia, L.C. Brinson, S. Keten, Temperature effects on the nanoindentation characterization of stiffness gradients in confined polymers, Soft Matter 15(3) (2019) 359-370.
[26] W. Xia, J. Song, D.D. Hsu, S. Keten, Understanding the interfacial mechanical response of nanoscale polymer thin Films via nanoindentation, Macromolecules 49(10) (2016) 3810-3817.
[27] X. Wei, Z. Meng, L. Ruiz, W. Xia, H.D. Espinosa, Recoverable slippage mechanism in multilayer graphene leads to repeatable energy dissipation, ACS Nano 10(2) (2016) 1820.
[28] M. Wisheart, Review of low-velocity impact properties of composite materials, Composites Part A: Applied Science and Manufacturing 27(12) (1996) 1123-1131.
[29] B.L. Wang, J.C. Han, S.Y. Du, Cracks problem for non-homogeneous composite material subjected to dynamic loading, International Journal of Solids & Structures 37(9) (2000) 1251-1274.
[30] E. Lezak, Z. Bartczak, Plastic deformation behavior of β phase isotactic polypropylene in plane-strain compression at elevated temperatures, Journal of Polymer Science Part B: Polymer Physics 46(1) (2008) 92-108.
[31] J.M. Kim, R. Locker, G. Rutledge, Plastic deformation of semicrystalline polyethylene under extension, compression, and shear using molecular dynamics simulation, Macromolecules 47(7) (2014) 2515-2528.
[32] L. Chen, Molecular dynamics simulation of fracture and energy dissipation in polymer/clay nanocomposites, Loughborough University, Loughborough, 2008.
[33] A. Schroer, J.M. Wheeler, R. Schwaiger, Deformation behavior and energy absorption capability of polymer and ceramic-polymer composite microlattices under cyclic loading, Journal of Materials Research 33(3) (2018) 274-289.

Effect of interlaminar toughening of short carbon fiber on structural drawing performance of composite bolt

Zesheng Huang[1], Lvtao Zhu[1,2], Wei Shen[3], Lifeng Chen[3]

(1. College of Textile Science and Engineering (International Institute of Silk), Zhejiang Sci-Tech University, Hangzhou 310018, China; 2. Shaoxing Keqiao Research Institute of Zhejiang Sci-Tech University, Shaoxing 31200, China; 3. Shaoxing Baojing Composite Material Co., Ltd, Shaoxing 31200, China)

Abstract: Carbon fiber reinforced polymer (CFRP) occupies a large proportion of composite applications. Due to its high specific strength, stiffness, and excellent corrosion resistance, CFRP has gained popularity and become recognized as a prominent material for engineering applications in the past decades. Lightweight composite alternative to conventional materials in many structural and semi-structural automotive, aerospace, and other industrial applications. In this paper, 12K T700 carbon fiber filament and epoxy resin were used to prepare carbon fiber prepreg, laminates containing short-cut carbon fiber between layers were made with it, and finished products were obtained after autoclave molding. The effects of short fiber interlaminar reinforcement on tensile, compression, bending and interlaminar shear strength of carbon fiber composite laminates were studied. The prepreg formed by resin impregnation of carbon fiber filament was made into a prefabricated body with dimensions of 150×150×125mm by five different paving methods. Bolts were embedded in the prefabricated body, and the mechanical properties of the components were tested after high-temperature curing. The experimental results show that the bolt embedded perpendicular to the plane of the prefabricated body makes the bolt have higher bond strength, and the prefabricated with short fiber lamination has stable mechanical properties.

Key words: Interlaminar toughening; Pulled off performance; CFRP

0. Introduction

Compared with traditional metal materials, the advantages of carbon fiber reinforced composites are high specific strength, high specific modulus, and low density[1]. And with the development of composite material application from secondary load-bearing structure to main load-bearing structure, the design and manufacture of large-thickness composite material components (thickness > 20mm) to replace the traditional metal component is the current research hotspot. The composite connection structure is the weak link in the

whole composite structure, and its structural strength directly affects the bearing capacity of the composite structure. The connection of composite structures has always been a bottleneck problem in these applications[2]. The common joining forms of composite structures include mechanical joining, adhesive joining, and mixed (adhesive/mechanical) joining. Among them, the bearing capacity of the adhesive connection is small. Therefore, mechanical or hybrid joints are often used in projects requiring high bearing capacity. However, because the composite material is a typical anisotropic material, its longitudinal strength and modulus are high, while the transverse and shear strength and modulus are low, resulting in a complex stress distribution around the mechanical connection hole, which increases the difficulty of calculating the load distribution of the mechanical connection of composite materials. In addition, the interlaminar strength of fiber-reinforced composites is determined by the matrix from the interface of reinforcement and matrix, so it will lead to the interlaminar debonding fracture of composites[3]. To sum up, the strength and failure of composite structure connection are mainly affected by the damage accumulation and load form of composite material, and structural failure is one of the most fatal problems of composite structures in use. Therefore, it is of great significance to improve the mechanical bonding properties of composite structures.

In the past few years, many attempts have been made to study the failure modes of mechanical connections in composite structures. There are seven main failure modes. These include tensile, shear, extrusion, tensile split, tensile failure of laminates, as well as shear and bending failure of fasteners[4]. In addition to the single failure mode mentioned above, combined failure modes may also occur in composite connections. Such as tensile-shear failure. The results show that on the premise of ensuring the safety of the connection and improving the efficiency, the tensile failure of the fastener should be avoided as far as possible through design. To improve the joint performance of composite structures, various new joint methods have been proposed, such as the Z-pinning method, stitching method, welding joint, and local winding reinforcement[5]. Among them, the Z-pinning method and the seam method rely on the reinforcement in the thickness direction to bind the composite layer and the matrix together and improve the interlayer fracture toughness and bonding strength. Welding joints are suitable for thermoplastic composites. Local winding reinforcement is mainly used in single or outrun lug joints. Although the above methods significantly improve the bonding performance of composite structures, some challenges remain with these techniques[6]. On the one hand, the residual stress and residual deformation of a welded connection reduce the bearing capacity of compressive members, and the welded structure is very sensitive to cracks, local cracks occur, easy to extend to the whole section, low temperature cold brittle problem is more prominent[7]. On the other hand, local entanglement enhances complex processes and equipment, greatly increasing manufacturing costs and limiting the spread of these reinforcement methods[8].

Short fiber toughening is a kind of method which is suitable for super-large composite components and has a good toughening effect between layers. Sohn and Hu[9] inserted thin, lightweight short aramid fibers into CFRP laminates to toughen interlaminar properties. The mechanism study shows that the toughness of modified CF/E composites is mainly improved by fiber bridging. In addition, thin (less than 20mm) non-woven SAF gauze was used to toughen the layered carbon fiber composites with weak layer interfaces in the form of self-made prepreg. It is found that aramid fiber can effectively improve the mechanical properties of rubber composites. The above study proves that short fibers can improve weak interfacial bonding by

fiber bridging between layers. However, there are few studies on the performance test of short fiber mixed in continuous fiber-reinforced composites, and most of the test methods are the two-arm suspension beam and end bending (ENF) test[10]. The compressive, bending, and interlaminar shear properties of hybrid short fiber-reinforced composite laminates are rarely studied. To improve the transverse strength of the composite structure, a pull experiment is needed. Therefore, in this paper, the compressive bending, tensile and shear properties of hybrid short carbon fiber reinforced composite laminates under different test standards were tested[11]. Then, five different lay-up designs were carried out for super-large composite components using prepregs. To further improve the mechanical properties of the joints in the composite structure, the short carbon fibers are evenly distributed between each layer of prepreg. Based on the results of the pull-out test, the influence of different paving designs of T700 staple fiber (3~5mm) /HT2-UD200 premixed was discussed in terms of fracture behavior and failure strength. The purpose of this study was to explore a simple and economical method to improve the strength of the carbon fiber/resin interface and the bonding properties of composite structures, and to improve their overall reliability.

1. Experiment

1.1 Experimental materials and equipment

T700 /HT2 unidirectional strip prepreg and T700 grade short fiber (3-5 mm) /HT2 premix are used to prepare composite laminates. The carbon fiber is T700-12K grade carbon fiber made in China. The main mechanical properties are shown in Table 1. HT2 is an epoxy resin independently developed by Shaoxing Baojing Composites Co., LTD. T700 /HT2 unidirectional strip prepreg index is shown in Table 2. HEC with the specification of 40000S was used as a dispersant of short carbon fiber. Bolts for the test are carried out according to GB/T3098.1, and M30 × 70/12.9 bolts are selected. The insert material is tapered 30CrMnSi.

CREE-601C-30 small plate vulcanizing machine; Electronic rotary mixer; Instron universal material testing machine; Hot pot.

Table 1 Properties of T700-12k[a] carbon fiber used in the study.

Order number	Density (g / cm^3)	Tensile modulus (GPa)	Tensile strength (MPa)	Break elongation rate / %
Measured value	1.78	210	4400	18

[a]As reported by the material supplier, Shaoxing Baojing Composite Material Co., Ltd.

Table 2 One-way carbon fiber/epoxy resin.

Order number	Preprep surface density (g / m^2)	Fiber surface density (g / m^2)	Resin content /%	Fugitive constituent / %
Measured value	306	214	30.1	0.513

1.2 Preparation of short carbon fiber dispersion

The chopped carbon fibers are small and clustered together, so the fibers need to be pre-dispersed so that they can be inserted between the layers before they are prepared. HEC (hydroxyethyl cellulose) is a non-ionic surfactant, which has a good dispersion effect on fibers and particles. A small amount of it can be dissolved in water to form a colloidal solution with a certain viscosity. In the dispersion experiment, wash a beaker with a capacity of 1 L, weigh 1.5g short carbon fiber (3-5 mm) and put it into the beaker, and add about 600 mL of clean water into the beaker. Put the beaker into the stirring device, and insert the stirring

paddle into the middle position below the liquid level to start the stirring device. In the slow stirring state, add the HEC that has been weighed into the beaker slowly until HEC is completely dissolved in water. At this time, the stirring speed should be increased to enter the stage of efficient dispersion of short carbon fiber, and the stirring speed should be continued at 800 r/min for 30 min. After mixing, a filter funnel was used to filter the dispersed carbon fiber. The dispersed carbon fiber is dried for later use. See Figure 1 for a schematic diagram.

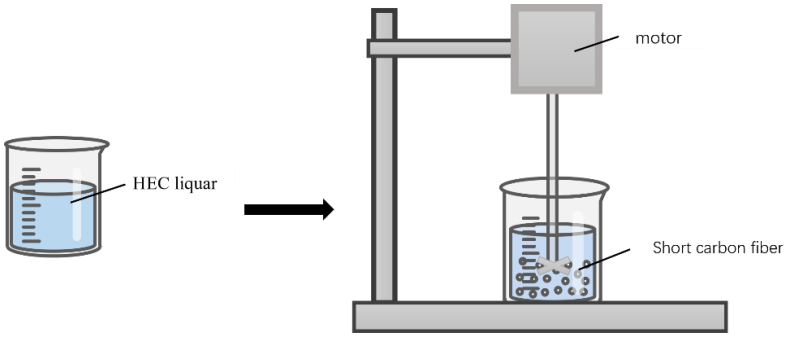

Figure. 1 Schematic diagram of staple fiber dispersion

The following is the laminate and component preparation test flow:

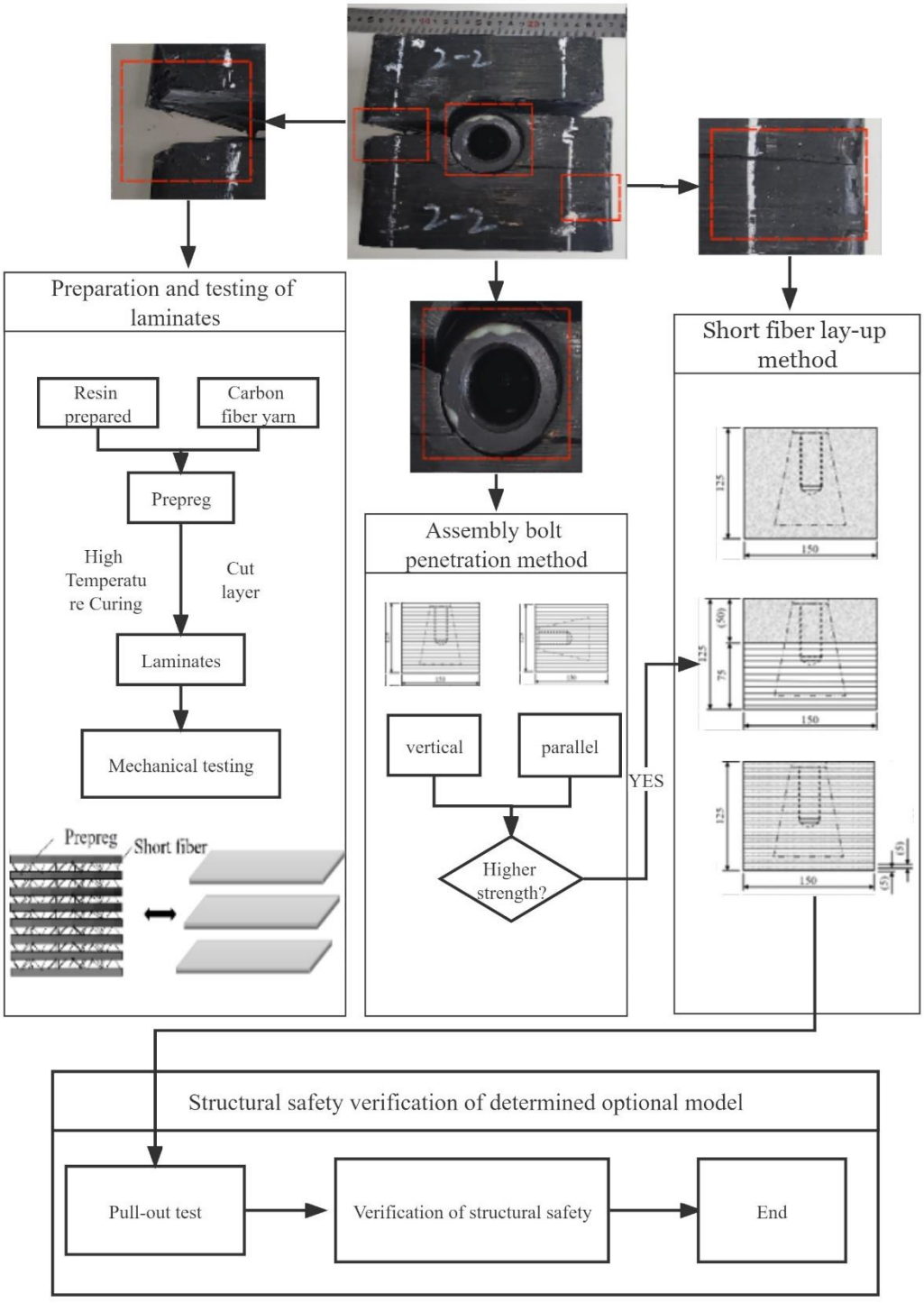

1.3 Preparation and testing of laminates

T700 /HT2 unidirectional strip prepreg was used to lay laminate. 8 layers of prepreg were laid at the Angle of [0/45/90/-45/0]8s. Short-cut carbon fiber was evenly spread between layers, as shown in Figure 2. The result is a preform containing a cut carbon fiber between layers. Repeat the above steps three times to obtain three samples with the same process parameters for different mechanical properties testing. Place the laminate in an autoclave to form.

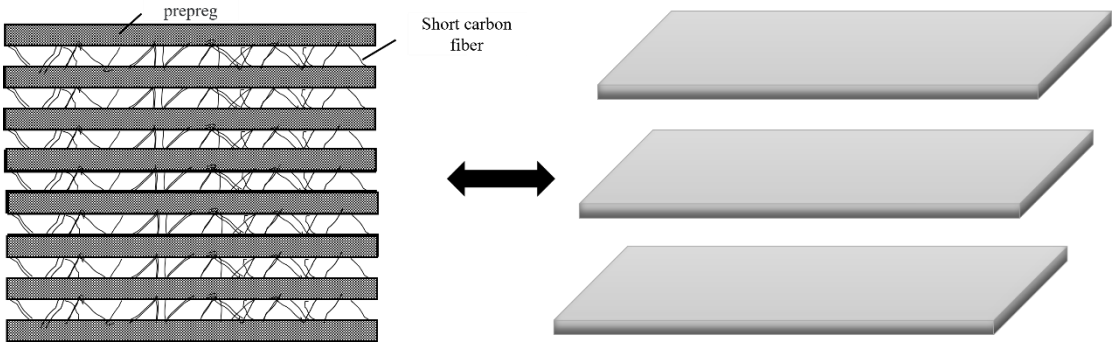

Figure. 2 Structure of composite laminate with short-carbon fiber toughening.

The sandwich structure is adopted, with carbon fiber prepreg sheet at the top and bottom, and short-carbon fiber layer in the middle.

According to ASTM 3039/D3039M-08, ASTM D3410/D3410M-03, ASTM D5379/D5379M-05, ASTM D7264/D7264M-07, the cured carbon fiber laminate is machined. Processed into standard tensile, bending, compression and interlaminar shear specimens. Before the start of the experiment, the initial state of the test parts shall be visually inspected, and obvious defects shall not be allowed in the test parts. Then nondestructive testing is carried out on the test parts. Test parts that pass NDT can only be used for experiments. Tensile, bending, compression and interlaminar shear tests were carried out on an electronic universal material testing machine. The loading speeds of tensile, bending and interlaminar shear tests were 5, 10 and 2mm/min, respectively.

1.4 Component preparation and testing

T700/HT2-UD200 unidirectional belt and T700 short fiber (3~5 mm)/HT2-UD200 premix were used to lay the components and pre-embed bolts at the Angle of [0/±45/90] ns. The components were laid and the bolts were pre-embedded according to five plans. The total layer thickness of the component is 125 mm. The thickness direction allows the layer of 25 ~ 30 mm thick plate in advance, and then through the prepreg, the multiple plates are bonded into the overall thickness of 125 mm thick plate. See Table 3 for 5 one-way belt and premix placement methods and bolt embedment schemes, 3 for each scheme and 15 components in total. The embedment mode of bolts perpendicular to the laminate plane is shown in Figure 3, and the embedment mode of bolts parallel to the laminate plane is shown in Figure 4. Place components into the autoclave to form.

Table 3 Component layering angles

	One-way prepreg and premix laying	Bolt pre-buried direction and laminate plane relationship	Schematic (mm) One-way prepreg Short fiber premix
Scheme 1	One-way prepreg	vertical	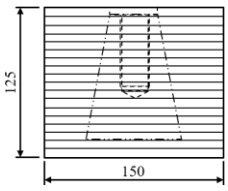
Scheme 2	One-way prepreg	parallel	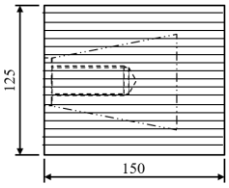

Scheme 3	Short fiber premix	vertical	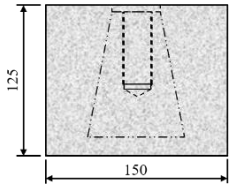
Scheme 4	75 mm thick One-way prepreg，50 mm Thick Short fiber premix (Premix near the head of the bolt)	vertical	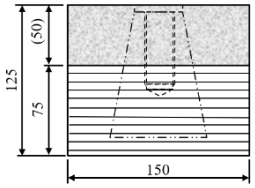
Scheme 5	5 mm premix alternating with 5 mm One-way prepreg	vertical	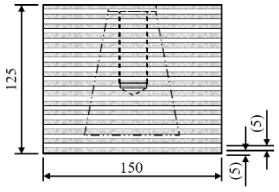

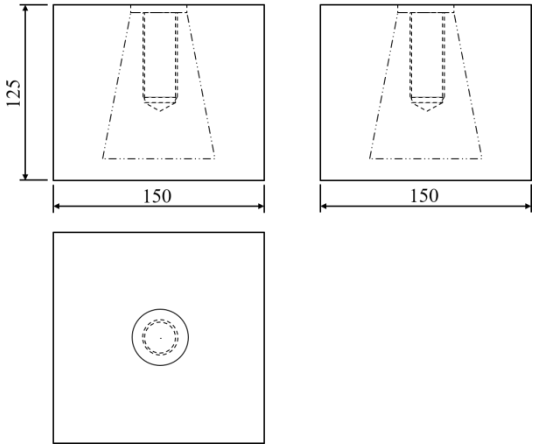

Figure. 3 Three views of bolt embedded perpendicular to the laminate plane

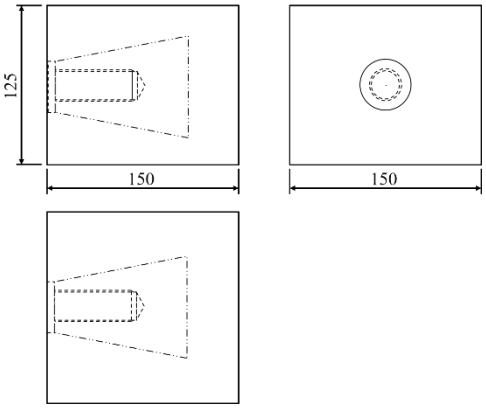

Figure. 4 Three views of bolt embedded parallel to the laminate plane

The mechanical properties of assembly bolts are calculated according to ASTM D7332/ D7332M-07EL. Before the start of the experiment, the initial state of the test parts shall be visually inspected, and obvious defects shall not be allowed in the test parts. Then nondestructive testing is carried out on the test parts. Test parts that have passed non-destructive testing can only be used for experiments. Time, displacement, and load data were recorded during the experiment.

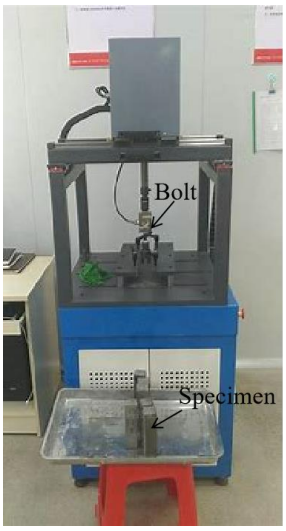

Figure. 5 Test machine and specimen

2. Result and Discussion

2.1 Laminate

2.1.1 Tensile property

The laminate containing short carbon fiber was subjected to a 90° tensile test, and its ultimate bearing capacity could be determined by the tensile strength and elastic modulus of the material after analysis of the test results. See Figure.6 for the 90° tensile sample. It can be seen from Figure. 6 that all the specimens after 90° tensile fracture with rough fracture surface.

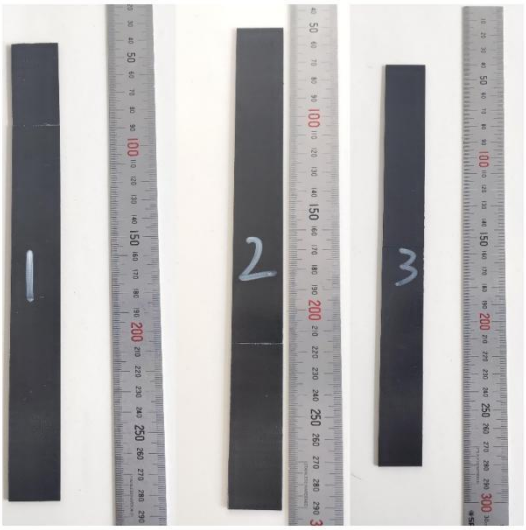

Figure. 6 Tensile specimens

2.1.2 Compressive property

The compressive strength and compressive elastic modulus of the material can be used to measure its ability to resist compressive load without damage. The compressive strength and compressive elastic modulus of the material are analyzed by the 0° compression test (reinforced sheet) and 90° compression test (unreinforced sheet). The 0° compression sample (attached stiffener) is shown in Figure. 7. As can be seen from Figure. 7, bending deformation occurs in all samples after 0° compression, among which the bending degree of Specimen 2 is larger. Figure. 8 shows the 90° compression sample (unreinforced sheet). It can be seen from Figure. 8 that bending deformation occurs in all samples after 90° compression. Samples 1, 2 and

3 are from left to right.

Figure. 7 0° compression specimens

Figure. 8 90° compression specimens

2.1.3 Bending property

The bending strength and elastic modulus of the material can be used to measure the in-plane mechanical properties of the laminate containing chopped carbon fiber. The specimen bent at 90° is shown in Figure. 9. It can be seen in Figure. 9 that all the specimens fractured after bending, and the fracture interface presented a rough shape.

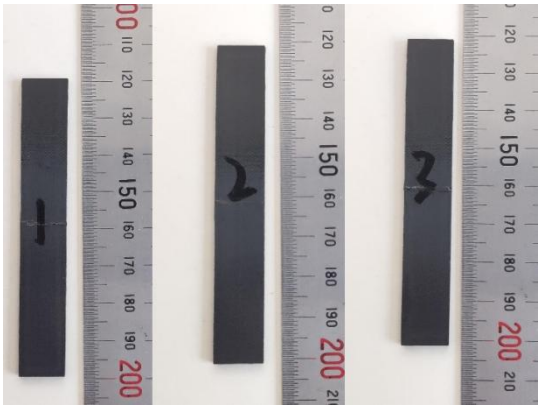

Figure. 9 Bending specimens

2.1.4 Shear property

Interlaminar shear tests were carried out on laminates containing chopped carbon fiber, and the interlaminar shear strength of the laminates could be used to characterize the interlaminar properties. The sample of interlaminar shear is shown in Figure 10. It can be seen from Figure 10 that obvious cracks can be observed on the surface of the sample after interlaminar shear, but no fracture occurs on the sample.

In terms of the mechanism of interlaminar reinforcement, the overall toughness of composite material under interlaminar interaction can be improved by adding short fibers, and the interlaminar shear strength of composite material can be improved by the bridging force.

Figure. 10 Shear specimen

Table 4 The summary of mechanical properties on short carbon fiber reinforced polymer composite.

	90°Tensile strength /MPa	90°Tensile modulus/GPa	bending strength /MPa	bending modulus/GPa	interlaminar shear strength /MPa	0°compression strength/ MPa	0°compression modulus /GPa	90°compression strength/ MPa	90°compression modulus/ GPa
av.	29.5	8.66	1621	125	83.5	1224	114	164	9.2

2.2 Module

2.2.1 Effect of bolt penetration mode on mechanical properties of components

In the pull-out test of five groups of components, the time displacement relationship is shown in Figure 11, the displacement load relationship is shown in Figure 12, and the tensile strength of component bolts is shown in Table 6. Figures 13 and 14 respectively show the components of plan 1 and Plan 2, which are made of one-way strips without cutting carbon fiber between the layers. The assembly bolts of Scheme 1 are embedded in the assembly perpendicular to the laminate plane, and the bolts of Scheme 2 are embedded in the assembly parallel to the laminate plane. The bolts of components 1-3 were broken after the bolt pulling out test, and some bolts were still buried in the components. The bolts of components 2-3 were pulled out after the bolt pulling out test, and obvious cracks were observed in the components. According to the analysis in Figure. 11, before 40 s, the bolt of component 2-3 had a greater displacement than the bolt of component 1-3 at the same time. At about 40 s, the bolt of component 2-3 was completely pulled out, while the bolt of component 1-3 remained in the component until about 90 s before the bolt broke. As analyzed from Figure. 12, the maximum load of component 1-3 is 744.760 kN, and that of component 2-3 is 296.696 kN. Comparing the test results of the two components, it can be concluded that the bolt embedment mode perpendicular to the laminate plane makes the bolt and component have higher bond strength.

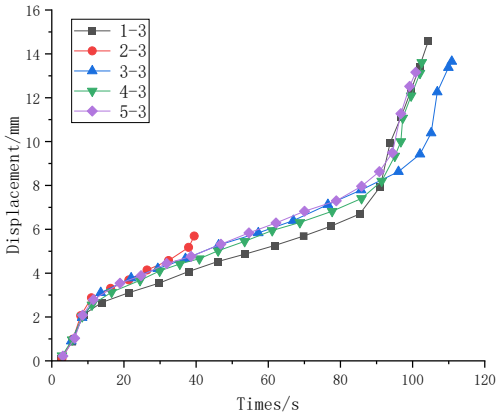

Figure. 11 Time-displacement curve of component pull-out test

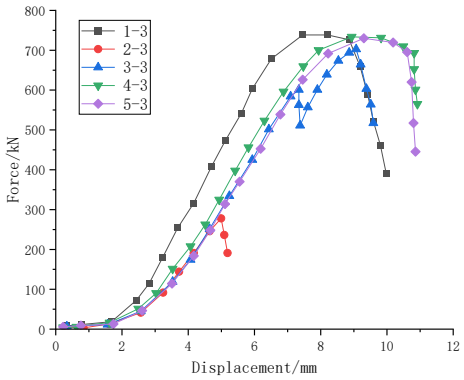

Figure. 12 Displacement-load curve of component pull-out test

Table 5 Component bolt tensile strength and breaking force

	Tensile strength of bolts (MPa)	Pull-off force（KN）
1-3	1327.56	744.760
2-3	Bolt pulled out	296.696
3-3	1312.41	736.263
4-3	1318.53	739.697
5-3	1308.84	734.257

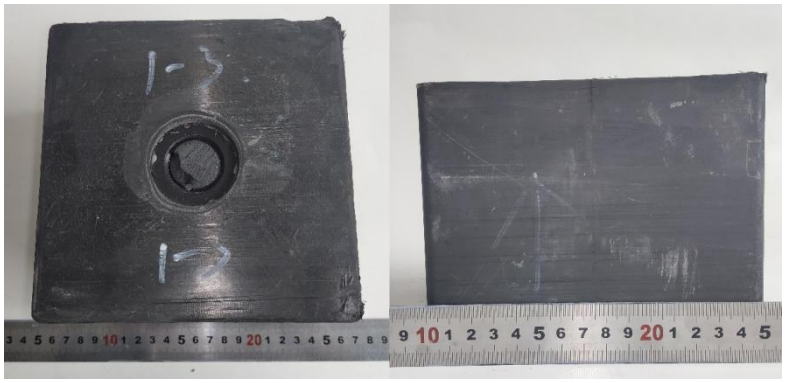

Figure 13 Component 1-3

Figure 14 Component 2-3

2.2.2 Effects of different short fiber laying methods on mechanical properties of components

Figures 15, 16, and 17 are components of plan 3, plan 4, and plan 5 respectively. Bolts are embedded in the components perpendicular to the laminate. Plan 3 is made entirely of premix; In plan 4, the thickness of the one-way belt is 75 mm, and the thickness of premixed material is 50 mm (premixed material is close to the bolt head). Plan 5 is composed of 5 mm premix and 5 mm unidirectional strips stacked alternately. The bolts of components 3-3, 4-3, and 5-3 were fractured after the bolt pulling test, and some bolts were still buried in the components.

According to the analysis in Figure. 15, by comparing the components embedded perpendicular to the laminate with four bolts, it can be found that before 90 s, the displacement of component 5-3 is the largest and that of component 1-3 is the smallest, and the displacement of component 3-3, component 4-3 and component 5-3 are very close. The bolt of component 1-3 broke the earliest, component 3-3 broke the latest, and component 4-3 and component 5-3 broke at a similar time.

According to Figure. 12, the displacement-load curve can be roughly divided into three parts :(1) in the first stage, at the beginning of the experiment, the curve rises with a low slope; (2) In the second stage, as the load continues to rise, the curve increases with a high slope until the load reaches the maximum value; (3) The third stage is the drop zone of the load. The load drops slowly first because the bolt cracks, and then the bolt completely breaks, and the load drops rapidly. The curve of component 3-3 decreased slightly at about 7.3s and then continued to rise. Since components 3-3 are all laid with staple fiber premix, voids and other defects will inevitably occur in the production process. According to literature, the performance of composite materials is affected by the porosity of composite materials, and the interlaminar shear strength, tensile strength, compressive strength, and bending strength all decrease with the increase of porosity. Component 3-3 has a higher porosity than other components, resulting in poor performance in bolt pull tests. The bolt of assembly 1-3 has the highest tensile strength of 1327.56 MPa. The bolt of assembly 5-3 has the

lowest tensile strength of 1308.84 MPa.

It can be seen from the above comparison that components 1-3 laid with unidirectional strips have the highest bolt tensile strength and the lowest bolt displacement throughout the test. Among components, 3-3, 4-3, and 5-3 containing chopped carbon fiber, component 5-3, which consists of 5 mm premix stacked alternately with 5 mm unidirectional strips, has the lowest tensile strength.

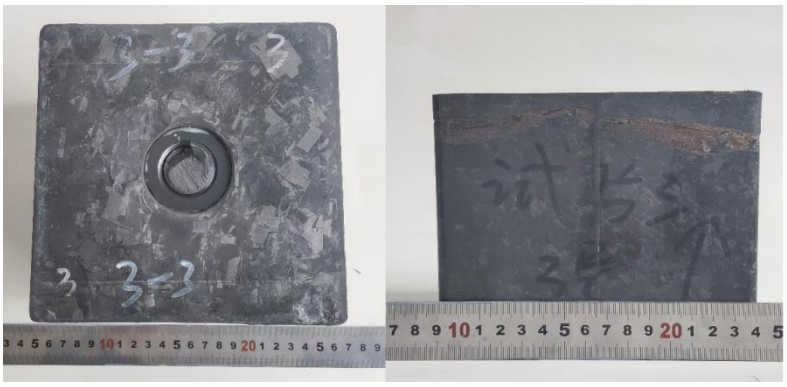

Figure 15 Component 3-3

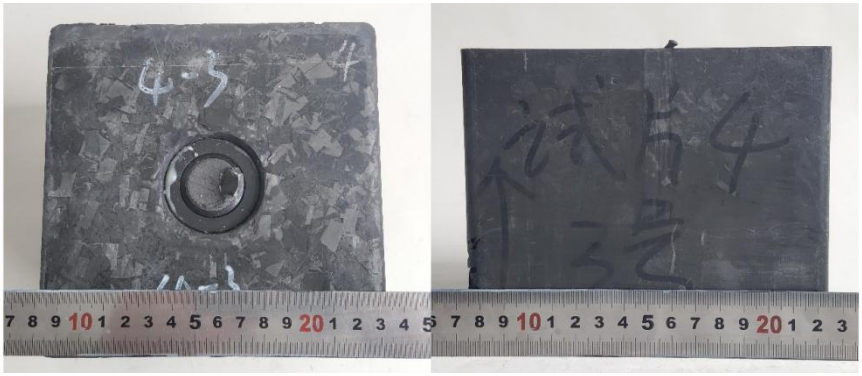

Figure 16 Component 4-3

Figure 17 Component 5-3

3. Conclusion

For carbon fiber reinforced resin matrix composites in pulled out prone to delamination failure under the action of faults, this topic based on the mechanism of short fiber layers increase with epoxy resin as the matrix resin, with carbon fiber filament yarn as the reinforcing fiber, the preparation of the interlaminar toughening of the chopped carbon fiber composite material laminate, and carries on the tensile, compression, bending and interlaminar shear strength of the performance test, The effect of short fiber interlaminar toughening on mechanical properties of carbon fiber composite laminates were studied. Then, 150×150×125 mm components with different paving methods were prepared with prepreg formed by resin impregnation

of carbon fiber filaments. Bolts were embedded in the components, and the mechanical properties of bolts were tested for pulling out. The interlaminar reinforcement of short fibers was studied to improve the connection performance of super-large composite components. The main conclusions are as follows:

(1) Rocket shell joint was simulated by a bolt pulling out a test. In the component made of one-way belt laying, the bolt embedded perpendicular to laminate has better mechanical properties than the bolt embedded parallel to laminate, the bolt is more difficult to pull out, and the bolt and assembly have higher binding strength.

(2) Among the five components laid in different ways, the bolt tensile strength of components 1-3 made of the unidirectional belt is the highest, which is 1327.56mpa, and the bolt fracture is the earliest; The tensile strength of component 4-3 with 75 mm of unidirectional belt and 50 mm of premixed material (premixed material is close to the bolt head) is only second to that of component 1-3, which is 1318.53 MPa.

Short fiber interlayer toughening technology, as an important method to improve the interlayer properties of composite materials, has attracted much attention for its ability to improve the interlayer toughness of composite materials while minimizing the reduction of overall strength. The research results are expected to be applied to the development of solid rocket motor case joints, which is of great significance to the development of aerospace technology.

There are still many deficiencies in the experimental process and research analysis of this paper. It is hoped that the following points can be improved in the subsequent research:

(1) Limited by the test equipment, the cutting uniformity and uniform distribution of chopped carbon fiber have not been well solved.

(2) There are experimental errors in the performance test of carbon fiber assembly bolt pulling out.

(3) No mesoscopic analysis of component and laminate failure samples was performed.

References

[1] ZHANG X, CHEN Y, HU J. Recent advances in the development of aerospace materials[J/OL]. Progress in Aerospace Sciences, 2018, 97: 22-34.

[2] MA Z, QI Y, LIU W, et al. A comparative study of pull-out performance of bolted joints in pultruded FRP with drilled holes or punched holes[J/OL]. Mathematical Biosciences and Engineering, 2019, 16(5): 4213-4228.

[3] RAMAKRISHNAN M U, MALLICK P K. Static and fatigue behavior of a carbon-fiber SMC-R composite under combined tensile and shear stresses[J/OL]. POLYMER COMPOSITES, 2022, 43(4): 2350-2361.

[4] CHEN J, TUO W, WAN C, et al. Shear test method for and mechanical characteristics of short basalt fiber reinforced polymer composite materials[J/OL]. JOURNAL OF APPLIED POLYMER SCIENCE, 2018, 135(16).

[5] WANG B, DONG N, DING G. Mode I interlaminar fracture toughness of CFRP laminates reinforced with short aramid fibers[J/OL]. Journal of Adhesion Science and Technology, 2020, 34(23): 2522-2536.

[6] KORHONEN O, FORSMAN N, OSTERBERG M, et al. All-cellulose composites via short-fiber dispersion approach[J]. ABSTRACTS OF PAPERS OF THE AMERICAN CHEMICAL SOCIETY, 2019, 257.

[7] LEE S W, CHANG S H. Experimental investigation of pull-through force of wing-type fastening inserts co-cured in long fiber prepreg sheet (LFPS)[J/OL]. COMPOSITE STRUCTURES, 2018, 206: 978-986.

[8] OU Y, GONZÁLEZ C, VILATELA J J. Interlaminar toughening in structural carbon fiber/epoxy composites interleaved with carbon nanotube veils[J/OL]. Composites Part A: Applied Science and Manufacturing, 2019, 124: 105477.

[9] SOHN M S, HU X Z. Delamination behaviour of carbon fibre/epoxy composite laminates with short fibre reinforcement[J/OL]. Scripta Metallurgica et Materialia, 1994, 30(11): 1467-1472.
[10] ZHAO Z K, DU S S, LI F, et al. Mechanical and tribological properties of short glass fiber and short carbon fiber reinforced polyethersulfone composites: A comparative study[J/OL]. COMPOSITES COMMUNICATIONS, 2018, 8: 1-6.
[11] SUN Z, CHEN H, SONG Z, et al. Three-point bending properties of carbon fiber/honeycomb sandwich panels with short-fiber tissue and carbon-fiber belt interfacial toughening at different loading rate[J/OL]. Composites Part A: Applied Science and Manufacturing, 2021, 143: 106289.

Optimized Design of Plant Fiber Reinforced Composites on Interior Structure of Subway

S. L. Tan[1], and Q. Li[1]*

[1]School of Aerospace Engineering and Applied Mechanics, Tongji University, Shanghai, P.R.China

Abstract: The material optimization design of subway body structure provides an effective solution to the noise reduction and environmental protection problems of subway. Plant fiber reinforced composites as interior structure not only have a certain bearing capacity, but also can absorb noise and vibration, which is more cost-effective than the traditional interior board with only decorative role. In this paper, hybrid fiber technique was employed and the composite mechanics laminates theory was applied on ABAQUS finite element software to establish a subway interior panel model. The bending properties of carbon fiber/flax fiber hybrid composites under five different stacking sequences based on the Hashin failure criterion were calculated to obtain the optimal stacking sequence. Based on the complex stiffness approach in the damping analysis of composites, the damping properties of carbon fiber/flax fiber hybrid composites with five different stacking sequences were simulated. The influences of the stacking sequences on the damping properties of hybrid composites was analyzed. Through computational comparison, the results showed that the hybrid composites can effectively balance the mechanical and damping properties that meet the requirements of subway body structure, and the stacking sequence has a significant impact on the performances. The composites prepared by mixing flax fiber with carbon fiber and placing flax fiber in the outermost layer have better damping properties, while the bending properties are significantly improved compared with pure flax fiber reinforced composites.

1. INTRODUCTION

With the development of urban rail transportation, the number of subway vehicles is increasing. The noise pollution and energy consumption problems generated by subway operations are becoming more and more serious. So the noise reduction and environmental protection of subway vehicles have become a core issue of great concern to the industry [1]. The selection of subway body structure

materials provides an effective solution to these problems. Plant fibers not only have high specific strength and modulus, low density, low price, and abundant sources but also are eco-friendly and renewable resources [2]. The application of plant fiber reinforced composites for subway body structure can improve the train speed and energy efficiency, effectively reduce the wear and impact between wheels and rails, and enhance the vibration resistance and noise prevention of the train, thus reducing the vehicle life cycle cost [3].

Hybrid composites have significant advantages over single fiber reinforced composites, especially in terms of mechanical properties [4]. Zhang et al. [5] investigated the hybrid effect of the composites made from natural and synthetic fibers. It was found that the tensile properties of flax/glass fiber reinforced composites were improved with increasing glass fiber content. At the same fiber volume content, the stacking sequence had a significant effect mainly on the tensile strength and tensile failure strain, and almost no effect on the tensile modulus. The fracture toughness and interlaminar shear strength of the hybrid composites were even higher than those of the glass fiber reinforced composites due to the better interfacial bonding after hybridization, and a positive hybridization effect appeared. In addition, Almansour et al. [6] prepared flax fiber reinforced composites and flax/basalt hybridized vinyl ester composites, and Ramanath et al. [7] mixed banana and jute fibers with glass fibers to prepare hybrid composites. All results showed that the interlaminar fracture toughness of the composites could be effectively improved by hybridizing plant fibers.

As mentioned earlier, composites have high damping properties that improve the vibration damping and noise reduction of trains. Ben et al. [8] studied the effect of hybridization, stacking sequences, and fiber orientation on the damping properties of unidirectional carbon/flax fiber reinforced epoxy composites. By comparing the damping performances of different hybrid laminates, it was found that the vibration behavior depends mainly on the stacking sequences of the carbon and flax fiber layers. It was also observed that the dynamic properties depend on the fiber orientation and the content of flax and carbon fibers. The loss factor increases with the increase in the volume content of flax fibers. In addition, the damping properties of hybrid composites in which the outer layer is a flax fiber layer are significantly higher than those of hybrid composites in which the inner layer is a flax fiber layer for the same volume content of flax fibers. Assarar et al. [9] investigated the effects of stacking sequences and hybridation on the damping properties of flax/carbon twill epoxy composites. It was shown that the position of flax fiber layers within the hybrid composite plays a major role in damping properties. Moreover, the damping ratio of flax fiber reinforced composites was one order of magnitude higher than that of carbon fiber reinforced composites, which proved that it is practical to improve the damping properties of carbon fiber reinforced composites by hybridizing flax fibers.

Plant fibers are mainly composed of cellulose, lignin, hemicellulose, pectin, waxes, etc. Unlike the single chemical composition of man-made fibers, plant fibers can be regarded as a polymer composite with cellulose microfibrils as the reinforcement and lignin and hemicellulose as the matrix, which has a unique multilayer microstructure. The multilayered structure of plant fibers brings a new damping mechanism for plant fiber-reinforced composites that are different from that of man-made fiber-reinforced composites [10]. Yan [11] and Kumar [12] studied the damping performances of flax fiber reinforced epoxy composite tubes and short sisal/banana fiber reinforced polyester composites, respectively. They concluded that the cavity structure of plant fibers helps to consume the composite

during vibration. Le Guan et al. [13] found that the damping coefficient of flax fiber reinforced composites treated with polyol was greater than that of untreated flax fiber and aramid or carbon fiber composites prepared under similar conditions. They attributed the relatively higher damping behavior of polyol-treated flax fiber reinforced composites to a stick-slip mechanism. The mechanism involves the cyclic breaking and recombination of hydrogen bonds between the polyol and the lamellae or microfibrils within the lamellae of the cell walls. The multilayered structure of plant fibers can also promote energy dissipation during vibration.

2. NUMERICAL ANALYSIS

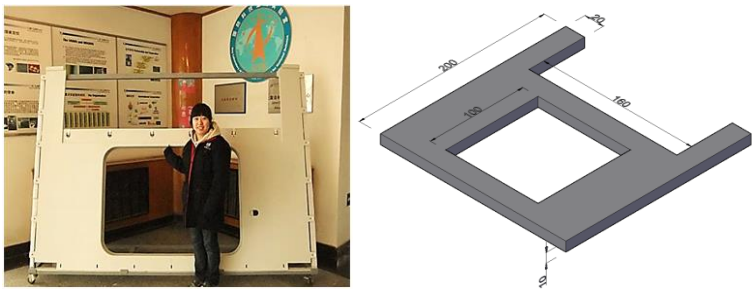

Fig. 1. Physical picture and schematic diagram of the geometric model dimensions of the subway interior panel (unit: mm).

The subway interior panel of Kunming Metro Line 1 made by plant fiber reinforced composites and the geometric model of the subway interior panel by using 3D deformable shell plane modeling are shown in Fig. 1.

2.1 FE Model for Analysis of Bending Properties

Material properties of carbon fiber/epoxy composites and flax fiber/epoxy composites are established in the property module. The stacking angle and thickness of the composite laminate are defined by the Composite layup implementation of the conventional shell type. The number of plies and fiber stacking Sequences of the laminate is shown in Table ● 1. In table 1, denotes carbon fiber ○ plies and denotes flax fiber plies. The single ply thickness of carbon fiber/epoxy composite is 0.125 mm, the single ply thickness of flax fiber/epoxy composite is 0.25 mm, and the fiber stacking angle is 0°for both. The overall fiber volume content of the composites was 60 % for all the different stacking Sequences. The cell type was chosen as four-node reduced continuous shell cell S4R, and the model contained a total of 4520 cells.

Table 1 Carbon fiber/flax fiber hybrid composite laminates with different stacking Sequences (thickness 10 mm).

Laminates	Ply number ratio(flax/carbon)	Stacking sequence
C80	0/80	80
C20F20C20	20/40	20 20 20
F15C20F15	30/20	15 20 15

F10C10F10C10F10	30/20	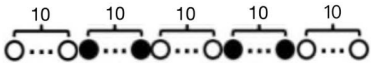
F40	40/0	

Due to the irregular geometry of the laminate, the area is first divided into regular shapes and then a quadrilateral mesh is realized by specifying the number of nodes for each side length. The constraints of the actual subway interior panel are simulated by limiting the three translational degrees of freedom at the four corners of the bottom surface. The discrete rigid cylinder is used to transfer the displacement with a 2 mm displacement load applied to the centerline of the surface. The type of interaction between the discrete rigid cylinder and the surface of the subway interior panel is face-to-face contact, and the tangential friction coefficient of the contact surface is 0.4. The analysis step of the finite element calculation is the dynamic display analysis step. The established finite element model is shown in Fig. 2.

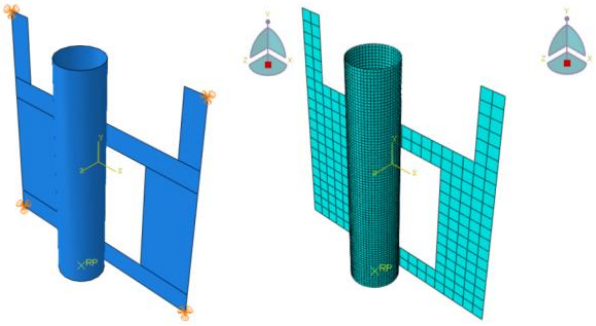

Fig.2. Isometric side view of the finite element model of the subway interior panel.

2.2 FE Model for Analysis of Damping Performance

It was shown that the damping ratio calculated by the logarithmic decay method is closer to the damping ratio of the composite itself than the half-power bandwidth method, and the air damping has little effect on its measured value [14]. The damping ratio of the unidirectional carbon fiber/flax fiber hybrid composites is calculated according to the logarithmic decay method for different stacking sequences. The damping ratio of 1.1875% and 1.78125% are obtained for carbon fiber/epoxy composites and flax fiber/epoxy composites, respectively, at the frequency of 20 Hz. The ratio of the imaginary part parameters to the real part parameters in the user-defined subroutine UMAT is the damping ratio. Input user material, non-independent variables are 2.

Create mesh parts, edit mesh, and generate solid composite layers. The analysis steps of finite element calculation include the static general analysis step, frequency extraction analysis step, and complex frequency extraction analysis step. The modal extraction method uses Lanczos method. The boundary conditions are created in the initial state. The nodes of the bottom side are completely fixed. The static general analysis step is passed, the frequency extraction analysis step is inherited from the base state, and the complex frequency extraction analysis step is built into the mode. The established finite element model is shown in Fig.3.

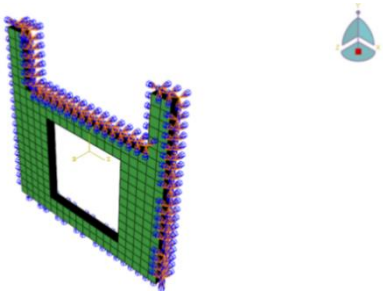

Fig.3. Isometric side view of the finite element model of the subway interior panel model.

2.3 Effect of Grid Density

The density of cell meshing is an important criterion to measure the accuracy of FEA results. To qualitatively analyze the effect of cell mesh division density on the accuracy of FEA results, carbon fiber/epoxy composites were selected and designed in three forms in equal proportions, 2.5×2.5, 5×5, and 10×10, with a cell aspect ratio of 1[15]. The calculated results of the first-order intrinsic frequency and first-order damping ratio of the carbon fiber/epoxy composites concerning the mesh density are given in Table 2. The results show that the computational results roughly converge with the encryption of the cell mesh. However, considering the time cost of calculation, a cell mesh size of 10×10 is chosen as the finite element meshing standard in this study. The cell type is chosen as S4R, and the model contains a total of 16,320 cells.

Table 2 First-order inherent frequency and first-order damping ratio of carbon fiber/epoxy composite laminates at different mesh densities.

Cell grid size	First-order inherent frequency(rad/time)	First-order damping ratio
10×10	12926	1.2077%
5×5	12431	1.2097%
2.5×2.5	12155	1.2115%

3. RESULTS AND DISCUSSIONS

3.1 Effect of Stacking Sequence on Bending Properties of Carbon Fiber/Plant Fiber Hybrid Composites

The fully analyzed in-plane stress fields of the composites for five different stacking sequences are shown in Fig. 4.

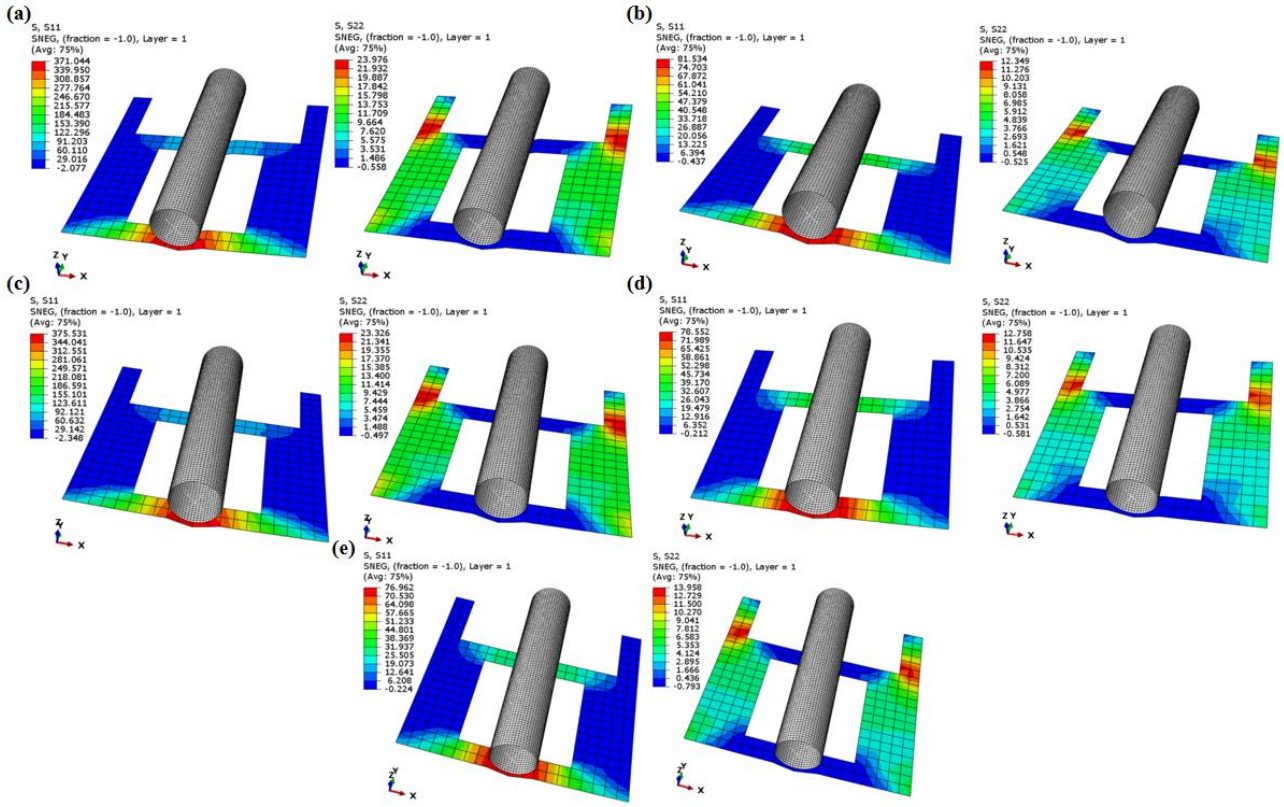

Fig.4. In-plane stress field of composites with different stacking sequences (unit: MPa): (a) Pure carbon fiber/epoxy composite, (b) Pure flax fiber/epoxy composite,(c) The stacking sequence is C20F20C20 hybrid composite,(d) The stacking sequence is F15C20F15 hybrid composite,(e) The stacking sequence is F10C10F10C10F10 hybrid composite.

From Fig.4, it can be seen that the maximum values of S11 and S22 of carbon fiber/epoxy composites are 371.044 MPa and 23.976 MPa, respectively. The maximum values of S11 and S22 of flax fiber/epoxy composites are 81.534 MPa and 12.349 MPa, respectively. The bending strength and bending modulus of pure carbon fiber/epoxy composites are much higher than those of pure flax fiber/epoxy composites due to the high strength and stiffness of carbon fiber and the weak strength and modulus of flax fiber. For carbon fiber/flax fiber hybrid reinforced epoxy composites, when the total volume fraction of fibers is the same under different stacking sequences, the influence of the stacking sequence on the bending properties is obvious. Specifically, the more the flax fiber layer is laid to the outer layer, the worse the bending property. This is because when the hybrid composite is subjected to bending load, the fibers in the upper and lower layers of the laminate are subjected to maximum compressive stress and maximum tensile stress, respectively, and less shear stress. The fibers near the middle layer are mainly subjected to maximum shear stress and less compressive and tensile stress. When the outer layer of carbon fiber with higher strength and stiffness is replaced by flax fiber with lower strength and modulus, the flax fiber layer cannot withstand greater bending load and lead to earlier damage, thus significantly weakening the ability of the hybrid composite to resist bending damage. So the bending performance of the hybrid composite is lower than that of carbon fiber/epoxy composite but better than that of flax fiber/epoxy composite. Therefore, among the three stacking sequences of hybrid composites, the stacking sequence of the C20F20C20 hybrid composite has the best bending property with the maximum values of 375.531 MPa and 23.326 MPa for S11 and S22, respectively.

3.2 Effect of Stacking Sequences on the Damping Performance of Carbon Fiber/Plant Fiber Hybrid Composites

Fig.5 shows the first 10 modes of vibration of the composites for different stacking sequences calculated by FEM.

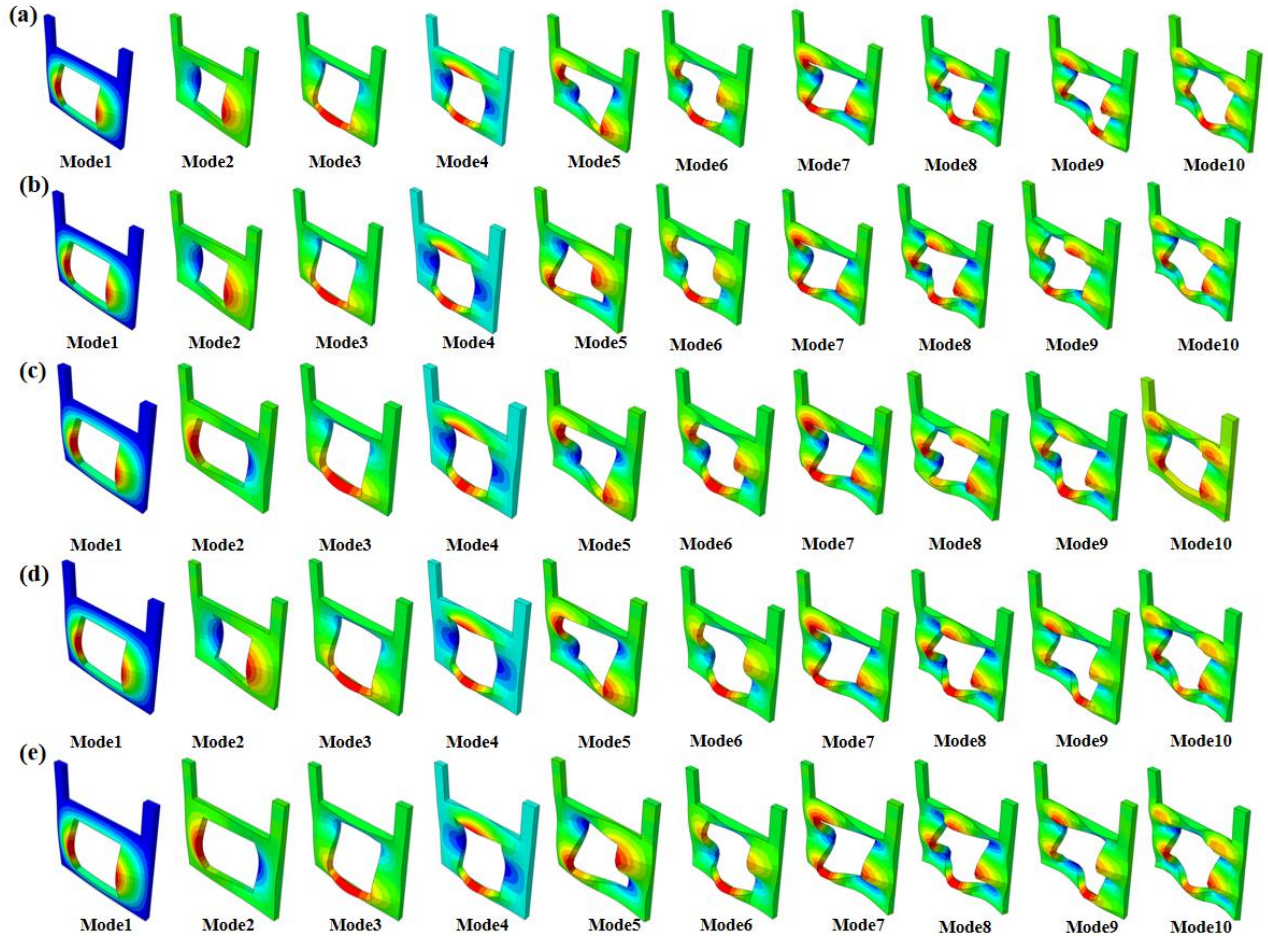

Fig.5. First 10 modes of vibration of composite materials with different stacking sequences: (a) Pure carbon fiber/epoxy composite,(b) Pure linen fiber/epoxy composite,(c) The stacking sequence is C20F20C20 hybrid composite,(d) The stacking sequence is F15C20F15 hybrid composite,(e) The stacking sequence is F10C10F10C10F10 hybrid composite.

From Fig.5, it can be seen that the mode of vibration of the composite laminate at the 5th, 8th, 9th, and 10th are different for different stacking sequences. It indicates that under the same constraint conditions, the effect of the change of stacking sequence on the mode of vibration tends to occur first in the higher mode.

The finite element calculated values of the first order mode damping ratio of the composites for different stacking sequences are shown in Table 3.

Table 3 Calculated finite element values of the first-order modal damping ratio of composites with different stacking sequences.

Laminates	Damping ratio	Stacking sequence
C80	1.21%	80
C20F20C20	1.32%	20 20 20

F15C20F15	1.69%	
F10C10F10C10F10	1.66%	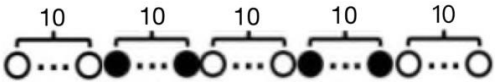
F40	1.80%	

From Table 3, it can be seen that carbon fiber/epoxy composites have the lowest damping ratio and flax fiber/epoxy composites have the highest damping ratio. This is because the interface between each internal wall layer and micro fibrillated sub-layers brought about by the multilayer structure of flax fibers provides more channels for energy dissipation compared to carbon fibers, making the damping performance of flax fiber reinforced composites much higher than that of carbon fiber reinforced composites. Ben et al.[8] prepared unidirectional carbon/flax fiber reinforced epoxy composite laminates with different stacking sequences by forming a vacuum process and carried out free vibration tests with pulse technique to investigate the dynamic behavior. It was found that the damping coefficient of pure flax fiber laminates was significantly higher than that of pure carbon fiber laminates. He attributed this difference mainly to the viscoelasticity of flax fibers, structural properties, and the content of each component in the fiber: cellulose (70%), hemicellulose (15%), lignin (2.5%) and pectin (1%), and the interface between the fiber and the fiber, and between the fiber and the matrix.

For the carbon fiber/flax fiber hybrid reinforced epoxy composites, when the total volume fraction of composite fibers is the same for different stacking sequences, the stacking sequence has a certain effect on the damping ratio. The damping ratio of the hybrid composite gradually increases as the flax fibers are laid down toward the outer layer. Hybridizing flax fiber can effectively improve the damping performance of carbon fiber reinforced composites, and placing the flax fiber in the outermost layer has the most advantage to improve the damping ratio of the hybrid composites. This is because the bending property of carbon fiber is higher and the damping performance is lower, the bending modulus of flax fiber is lower and the damping performance is higher. So the stacking sequence of carbon fiber and flax fiber has a considerable effect on the damping ratio of carbon fiber/flax fiber hybrid reinforced epoxy composites. Secondly, when the outer layer of carbon fiber is replaced by flax fiber, the flax fiber layer is subjected to the maximum compressive stress or tensile stress during vibration, producing the maximum axial compressive or tensile deformation. The maximum elastic strain is generated within the S2 layer of the cell wall, which plays a major role in the mechanical properties of flax fiber, resulting in the most interfacial frictional dissipation energy. Therefore, the damping performance of the hybrid composite F15C20F15 is higher than that of the hybrid composite C20F20C20 and alternating layers F10C10F10C10F10 when the total volume fraction of composite fibers is the same in different stacking sequences.

3.3 Analysis of the Variation Pattern Between Bending Properties and Damping Performance of Carbon Fiber/Plant Fiber Hybrid Composites

Comparing Fig.4 with the data in Table 3, it can be seen that the bending properties of pure carbon fiber/epoxy composites are higher while the damping performance is lower, and the bending modulus of pure flax fiber/epoxy composites is lower while the damping performance is higher. For the carbon fiber/flax fiber hybrid reinforced epoxy composites, when the total volume fraction of fibers is the same for different stacking sequences, the tendency for lower bending property and higher damping

performance is generally observed. When the outer layer of carbon fiber is replaced by flax fiber, the bending deformation of flax fiber is larger than when it is placed in the inner layer, and the restraint of carbon fiber is relatively smaller, which makes the damping performance of carbon fiber/flax fiber hybrid reinforced epoxy composites relatively higher. The results of this paper are in general agreement with those of Huang Xiaolei [14], Ben[8], and Assarar [9], who used unidirectional or twill flax fiber hybrid to improve the damping performance of carbon fiber reinforced composites.

The use of a lower modulus flax fiber hybrid can improve the damping performance of carbon fiber reinforced composites. Flax fibers are laid on the outermost layer so that the lower modulus flax fibers undergo greater bending deformation, and more interfacial frictional dissipation energy is generated inside the flax fibers, which is most advantageous to improve the damping ratio of the hybrid composites. In summary, it is determined that the optimal stacking sequence to meet the requirements of the mechanical properties and damping performance of the subway interior panel model is the hybrid composite with the stacking sequence of F10C10F10C10F10.

4. CONCLUSIONS

In this paper, the composite mechanics laminates theory is applied, and the large general finite element software ABAQUS is used to establish the structural mechanics model of composite materials. Based on the Hashin failure criterion of composite laminates, the bending properties of carbon fiber/plant fiber hybrid composites with five different stacking sequences are calculated to obtain the optimal stacking sequence. Using the complex stiffness approach in composite damping analysis, the damping performance of carbon fiber/plant fiber hybrid composites with five different stacking sequences is simulated, and the influence of the stacking sequences on the damping performance of hybrid composites is analyzed. The relationship between damping performance and bending properties of hybrid composites is investigated through computational comparison to determine the optimal stacking sequence design to meet the requirements of mechanical and damping performance of subway body structure. Important findings include:

(1) The bending property of pure carbon fiber/epoxy composites is much better than that of pure flax fiber/epoxy composites. When the total volume fraction of fibers in different stacking sequences is the same, the influence of the stacking sequence on the bending property is obvious, specifically, the more the flax fiber layer is laid to the outer layer, the worse the bending property.

(2) Under the same constraint conditions, the effect of the change of stacking sequence on the vibration pattern tends to occur first in the higher order modes. The carbon fiber/epoxy composite has the lowest damping ratio and the flax fiber/epoxy composite has the highest damping ratio. When the total volume fraction of fibers of the composite under different stacking sequences are the same, the stacking sequence has a certain effect on the damping ratio, and the damping ratio of the hybrid composite gradually increases as the flax fibers are laid down toward the outer layer. Flax fiber hybrid can effectively improve the damping performance of carbon fiber reinforced composites, and placing the flax fiber in the outermost layer has the most advantage to improve the damping ratio of the hybrid composites.

(3) For carbon fiber/flax fiber hybrid reinforced epoxy composites, the lower the bending property, the higher the damping performance when the total volume fraction of fibers is the same for different stacking sequences. The use of a lower modulus flax fiber hybrid can improve the damping performance of carbon fiber reinforced composites. Flax fibers are laid on the outermost layer so that the lower

modulus flax fibers undergo greater bending deformation, and more interfacial frictional dissipation energy is generated inside the flax fibers, which is most advantageous to improve the damping ratio of the hybrid composites. In summary, it is determined that the optimal stacking sequence to meet the requirements of the mechanical properties and damping performance of the subway interior panel model is the hybrid composite with the stacking sequence of F10C10F10C10F10.

ACKNOWLEDGMENTS

This research is supported by the Fundamental Research Funds for the Central Universities from Tongji University.

REFERENCES

1. X. Li,N. Zhang,"Application of New Composite Materials in the Lightweight Design of Metro Vehicles," *Urban Rail Transit Research*, Vol.10, No.24, 272-273, 2021.
2. Y. Li,Q. Li,"Mechanical High Performance and Multifunctionalization of Plant Fiber Reinforced Composites," *Journal of Solid Mechanics*,Vol.03, No.38, 215-243, 2017.
3. X. D. Kang,X. B. Gong,and J. Zhao,"Research and Application of Lightweight Body Structure Materials for Urban Rail Transit Vehicles," *Urban Rail Transit Research*, Vol.06, No.23, 177-180, 2020.
4. G. L. Shen,*Mechanics of Composite Materials*,Tsinghua University Press,2013.
5. Y. L. Zhang,Y.Li,and H.Ma,"Tensile and Interfacial Properties of Unidirectional Flax/Glass Fiber Reinforced Hybrid Composites," *Composites Science & Technology*, Vol.11, No.88,172-177 , 2013.
6. F. A. Almansour,H. N. Dhakal,and Z. Y. Zhang,"Effect of Hybridization on the Mode II Fracture Toughness Properties of Flax/Viny1 Ester Composites," *Polymer Composites*, Vol.8, No.38,1732-1740 , 2017.
7. B. Vijaya Ramnath, R. Sharavanan,and M. Chandrasekaran,"Experimental Determination of Mechanical Properties of Banana Jute Hybrid Composite," *Fiber and Polymers*, Vol.1, No.16,164-172 , 2015.
8. M. B. Ameur,A. E.Mahi,and J. L. Rebiere,"Damping Analysis of Unidirectional Carbon/Flax Fiber Hybrid Composites," *International Journal of Applied Mechanics*, Vol.5, No.10, 1-16, 2018.
9. M. Assarar, W. Zouari,and H. Sabhi, "Evaluation of the Damping of Hybrid Carbon-Flax Reinforced Composites," *Composite Structures*, Vol.132,148-154 , 2015.
10. Y. Li,T. Yu,and Y. O. Shen, *Plant fiber reinforced composites*,Science Press,2021.
11. L. Yan, N. Chouw, and K. Jayaraman, "On Energy Absorption Capacity,Flexural and Dynamic Properties of Flax/Epoxy Composite Tubes," *Fibers and Polymers*, Vol.6, No.15, 1270-1277, 2014.
12. K. Senthil Kumar, I. Siva,and P. Jeyaraj, "Synergy of Fiber Length and Content on Free Vibration and Damping Behavior of Natural Fiber Reinforced Polyester Composite Beams," *Materials&Design*, Vol.04, No.56,379-386 , 2014.
13. M. Le Guen a, R. H. Newman,and A.Fernyhough, "Tailoring the Vibration Damping Behaviour of Flax Fibre-reinforced Epoxy Composite Laminates via Polyol Additions," *Composites Part A: Applied Science and Manufacturing*, Vol.67, 37-43, 2014.
14. X. L. Huang, "The Optimization Research on the Damping Property of Hierarchical Carbon Fiber Reinforced Composites," Tongji University,2016.

15. Y. Q. Liu,, “Finite Element and Experimental Study on Damping Properties of Composite Materials and Structures Using a Complex Modulus-Based Approach,” Tongji University,2017.

In situ Raman spectroscopic study of plant fiber under tension deformation

Zhen Huang[a], *Yan Li*[a,*], *Kunkun Fu*[a]

[a] School of Aerospace Engineering and Applied Mechanics, Tongji University, Shanghai 200092, P.R. China

[*]E-mail: liyan@tongji.edu.cn

Abstract: In this paper, the crystallinity of cellulose, microfibril angle (MFA) and the tensile properties of hemp, sisal, coir fiber were investigated by X-ray diffraction (XRD) analysis and single fiber tensile tests. Typical brittle failure mode for hemp and sisal fiber and ductile failure mode for coir fiber were founded from their stress-strain curve and scanning electron microscope (SEM) images of fracture morphologies after tensile tests. Both tensile strength and tensile modulus decrease with the diameter increases. The deformation mechanism of plant fibers was investigated in situ, combining tensile test and Raman spectroscopy measurement. The characteristic Raman peak located at 1095 cm-1 and 1610 cm-1 are recorded as a function of tensile deformation of the plant fibers. The shift rate of Raman peak at 1095 cm-1 of hemp and sisal fiber keep constant during tensile deformation. However, the Raman peak shift rate of coir fiber decreases with the tensile deformation, which indicates the multi-interface damage mechanism of the plant fibers.

Keywords: plant fiber; tensile properties; in situ Raman spectroscopy; deformation mechanism;

1. Introduction

In the recent decades, plant fibers as an alternative reinforcement in polymer composites have attracted lots of attention due to their advantages over conventional man-made fibers such as low cost, comparable specific strength, reduced energy consumption, less health risk, renewability, recyclability and bio-degradability[1-3]. At the present time, the plant fiber reinforced composites are used mainly in non-structural applications such as, packaging, seat back, dashboard. However, in field of construction and aerospace, especially for the last mentioned application, the plant fiber reinforced composites appear to be poorly exploited due to the lacking of comprehensive insights of the specific mechanical property in plant fibers. Thus, before the plant fiber reinforced composites are potentially used in high performance application, it is essential to gain an accurate understanding of the structure-property relationship in such plant fibers. On the other hand, the plant fibers with superior mechanical properties inspire innovative ideas for fabricating biomimetic composites [4, 5].

Plant fibers including hemp, sisal, flax, coir, jute, bamboo and many others, have been extensively investigated [6, 7]. The major chemical constituents of natural fibers are cellulose,

hemicellulose and lignin. The structural characterization revealed that plant fibers possess the hierarchical structure across multiple length scales. On the mesoscopic scale, single plant fiber is made up of numerous elementary fiber. On the microscopic scale, the elementary fibers are regarded as laminated tube-like structure with several layers (cell wall) surrounding an empty cavity in the middle (lumen)[8]. The cell wall of elementary fibers consists of a primary cell wall layer (P) and a secondary cell wall layer (S), the latter of which is subdivided into three sub-layers referred to as S1, S2 and S3[9, 10]. The cellulosic microfibrils reinforce in amorphous hemicellulose and lignin. The angle of the parallel cellulose microfibrils to the longitudinal cell axis is called the cellulose microfibril angle (MFA), which plays a significant impact on the macro-mechanical properties of the plant fibers[11, 12]. on the nanoscopic scale, cellulose molecule chains aggregate into well packed crystalline regions and random non-crystalline regions to form cellulose microfibrils.

The complicate hierarchical structure of plant fibers calls for the use of advanced, sophisticated experimental methods to correctly relate the microstructure of plant fibers to their mechanical properties. Raman spectroscopy is an effective method to investigate the micro-mechanical behavior of a wide range of materials including synthesized and natural materials [13, 14]. The technique relies on the Raman bands corresponding to the vibrational modes of bonds in the material. And the bands shift rate changes upon stress or strain which varies with the internal structure of material. Li et al. [15] used in situ Raman spectroscopy to investigate the deformation mechanism of carbon nanotube fiber (CNF)under uniaxial tensile loading, showing that deformation of the CNF has experienced different stages such as elasticity, strengthening, damage and fracture. Eichhorn et al.[16]utilized Raman spectroscopy to probe the deformation mechanism of cellulose fibers, showing that the shift rate of 1095 cm^{-1} Raman band was proportional to the cellulose fibers modulus.

However, the such approach to investigate the deformation mechanism of native plant fibers has rarely been undertaken. In this paper, the tensile properties of hemp, sisal and coir fibers are tested and compared via single fiber tests. The in situ Raman spectroscopy measurements give insights into their structure-property relationship and the deformation mechanisms of plant fibers.

2. Experimental

2.1 Materials and pre-treatment

Hemp, sisal and coir fiber are extracted from different part, i.e. stem, leaf and fruit of plant respectively. The plant fibers used for this work supplied by Dongfang Sisal Group Co. LTD. The plant fibers were soaked in deionized water to wash their surface from impurities and then dried in a vacuum drying oven at 80℃ for 8h before tests.

2.2 X-ray diffraction (XRD) analysis

The crystalline structure of plant fibers was characterized by XRD analysis. The powered plant fibers were mounted on D8 Discover diffractometer (Burker, Germany). The intensity of Cu-Kα radiation with a wavelength of 0.154 nm was selected and the diffraction angle was scanned over the range of 10°-80° (2θ angle) with a scanning rate of 2°/min. Based on the XRD

data, the crystallinity index (I_C) of plant fibers was calculated using following expression:

$$I_c = \frac{I_{002} - I_{AM}}{I_{002}} \times 100\% \tag{1.1}$$

where I_{002} represents maximum intensity of diffraction of the (002) lattice plane at a 2θ angle between 22° and 23°, and I_{AM} represents the minimum intensity of diffraction of the amorphous material at a 2θ angle between 18° and 19°[17].

2.3 Tensile tests on plant fibers

Before the tensile tests, the diameter of plant fiber was firstly examined using optical microscopy as shown in figure 1. The average diameter was counted by taking three measurements along the fiber. The cross-sectional area is calculated by assuming a circular cross-section for determining of tensile properties of plant fibers The single fiber glued to paper frame was clamped on a universal testing machine equipped with a 500 N capacity load cell to conduct the tensile tests. The fracture morphology of the plant fibers was observed by scanning electron microscope (SEM) after tensile tests.

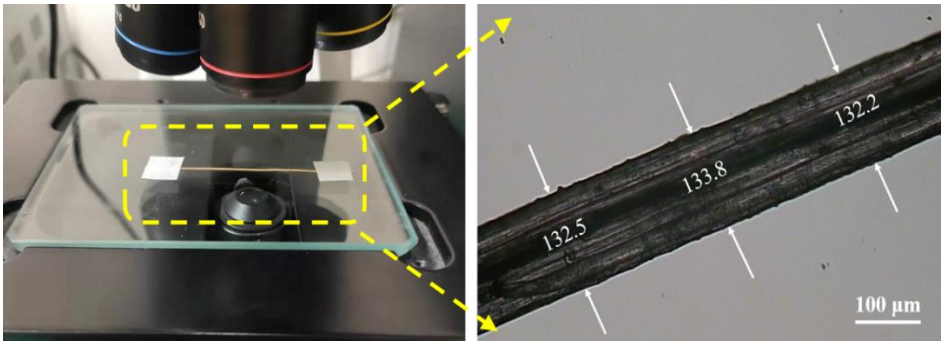

Figure 1. Optical microscopy and the measurement of fiber diameter

2.4 In situ Raman spectroscopy measurements

In situ Raman measurement on single plant fiber were carried out via a Renishaw 1000 Raman imaging spectrometer equipped with a home-built uniaxial tensile tester allowed the spectra to be recorded under macroscopic strain. A near-IR laser with a wavelength of 785 nm was used to record spectra from single plant fibers [18]. Both incident and scattered laser beam was polarized parallel to fiber axis. Prior to the measurements, the single plant fiber glued on paper frame was tightly mounted on the tensile tester with screw grips as shown in figure 2. After the edge of the frame was cut, the fiber was controlled to be stretched to failure. Each step of straining increment required 150 s, which included 120 s for exposure and 30 s for the focusing.

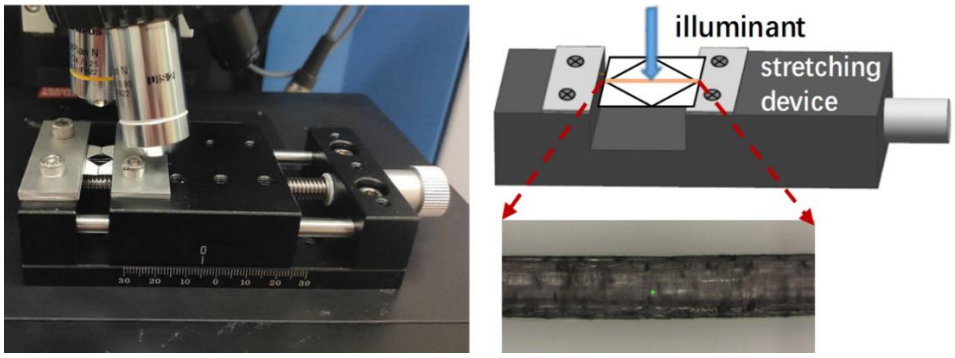

Figure 2. Schematic diagram of in suit Raman spectrum tests

3. Results and discussion

3.1 Cellulose crystallinity of plant fibers

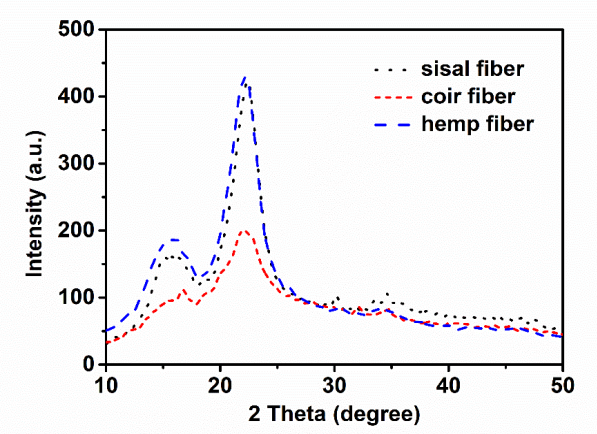

Figure 3. The X-ray diffraction pattern of plant fibers

The X-ray diffraction patterns of hemp, sisal and coir fibers are displayed in Figure. 3. It can be observed that the major crystalline peak of each kind of plant fibers occurred at around 2θ=22.4° and 2θ=16.8°, which represents the cellulose crystallographic plane (002) and (001), respectively. The peak at around 18.5° indicates the presence of amorphous materials like lignin, hemicellulose, pectin, and amorphous cellulose in the fiber. In order to quantity crystalline cellulose content of the plant fibers, the crystallinity index is calculated according to the Segal method []. Table 1 presents the detailed results of the crystallinity index estimations. The estimated values for hemp, sisal and coir fiber are 72.22%, 69.70% and 54.73%, which are well correlated with the results of biochemical composition analysis reported by literatures [19, 20]. The cellulose content is considered an indicator of the rigidity and an important factor on the mechanical behavior of the plant fibers discussed in following section.

Table 1. Crystallinity index of hemp, sisal and coir fiber

Fiber variety	I_{AM}=(2θ=18.5°)	I_{002}=(2θ=22.4°)	Crystallinity index (%)
Hemp fiber	117.5	423.3	72.3
Sisal fiber	140.5	430.5	67.4
Coir fiber	90.1	200.7	55.1

3.2 Tensile properties of plant fibers

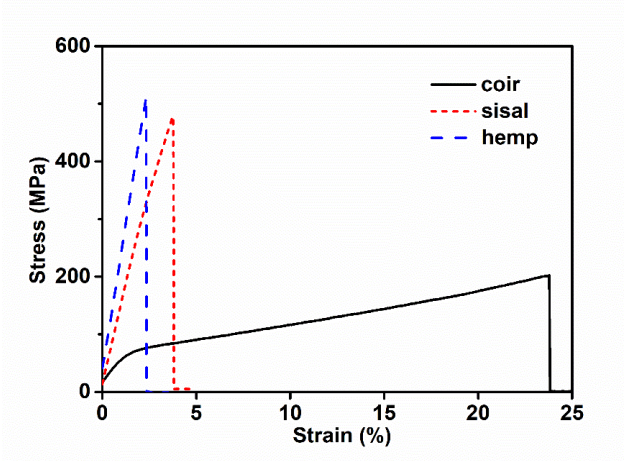

Figure 4. Typical tensile stress–strain curves of plant fibers.

Typical stress-strain curve of plant fibers is shown in Figure 4. As can be seen, sisal and hemp fiber show a linear elastic behavior without a definite yield point. On the other hand, coir fiber shows a linear region in the beginning of the loading and then shows plastic behavior until fiber failure at high strain to failure. The tensile modulus, strength and strain at failure of the plant fibers are calculated as shown in Table 2. It can be seen that the coir fibers have high strain at failure, but the lower strength and stiffness as hemp and sisal fibers due to the difference in their MFAs. The MFA of plant fibers can be calculated by the following equations[21, 22]:

$$\varepsilon = \ln\cdot\left(1+\frac{\Delta l}{l_0}\right) = -\ln\left(\cos\alpha\right) \tag{1.2}$$

where ε is the strain at failure of plant fibers. l_0 represents the length of microfibril which initially forms an angle α with the fiber axis. Δl represents the fiber lengthening caused by the changing in the orientation of the microfibrils. The calculated MFAs of plant fibers are shown in table 2. It is indicated that the smaller MFAs for hemp and sisal fibers lead to high modulus of elasticity, whereas the stiffness is substantially decreased for coir fibers with higher MFA [23, 24]. Figure 5 shows the evolution of the tensile strength and modulus of the single fibers according to their diameter. It seems that the smaller the diameter, the higher the modulus and the strength for each kind of the plant fibers, which is attributed to the lesser defect existed in the single fiber with smaller diameter.

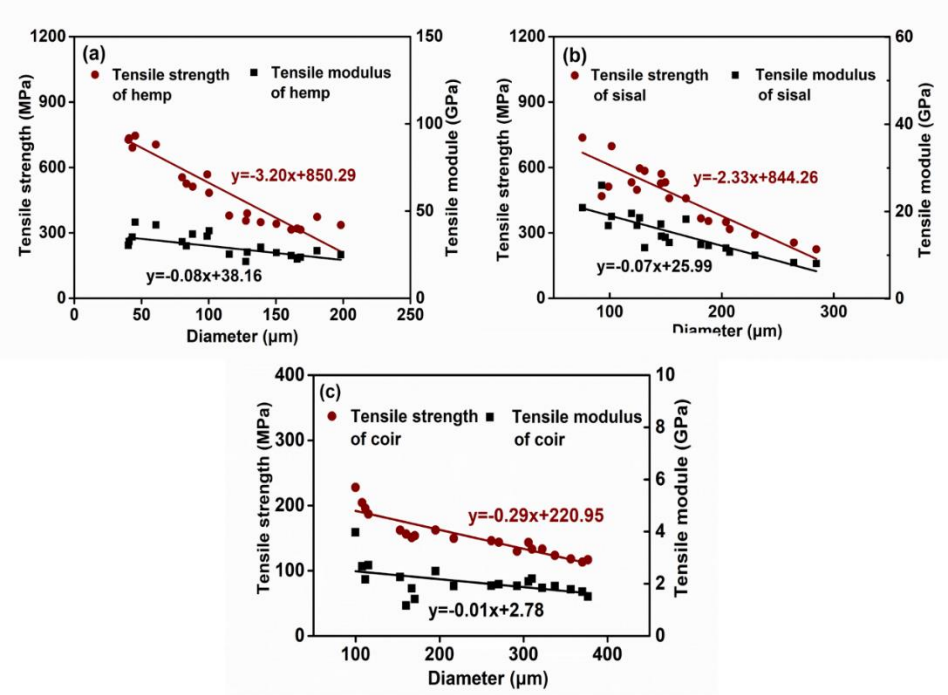

Figure 5. Evolution of the tensile strength and modulus of the plant fibers according to their mean diameter: (a) hemp fiber; (b) sisal fiber; (c) coir fiber

Table 2. comparison of the tensile properties of plant fibers

Fiber variety	Diameter (μm)	Tensile strength (MPa)	Tensile modulus (GPa)	Strain at failure (%)	MFA (°)
Hemp fiber	40.3-198.3	314.1-813.6	21.2-43.6	1.5-3.3	9.6-14.0
Sisal fiber	75.7-284.4	224.5-736.6	8.1-20.8	2.2-8.7	12.0-23.5
Coir fiber	99.8-322.2	103.7-282.5	1.2-4.7	17.2-45.9	31.8-47.9

3.3 In situ Raman spectroscopy analysis of plant fibers

Typical Raman spectra for plant fibers are shown in Figure 6. It can be seen that Raman peaks located at 1098 cm^{-1} corresponding to the cellulose C-O-C ring stretching mode appear in hemp, sisal and coir fiber. Moreover, an obvious peak occurred at 1620 cm^{-1} corresponding to amorphous component (hemicellulose, lignin) was appeared in coir fiber, which indicated the lower crystallinity of cellulose.

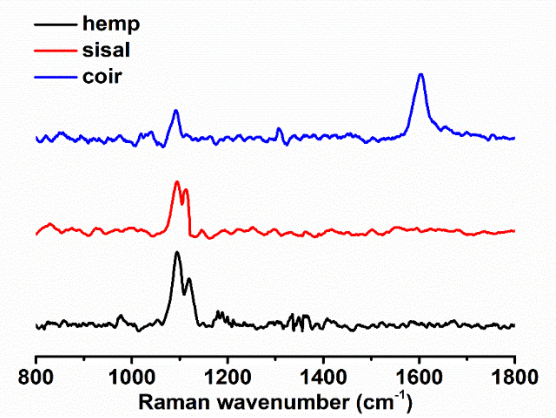

Figure 6. Comparison of Raman spectra for plant fibers measured before deformation

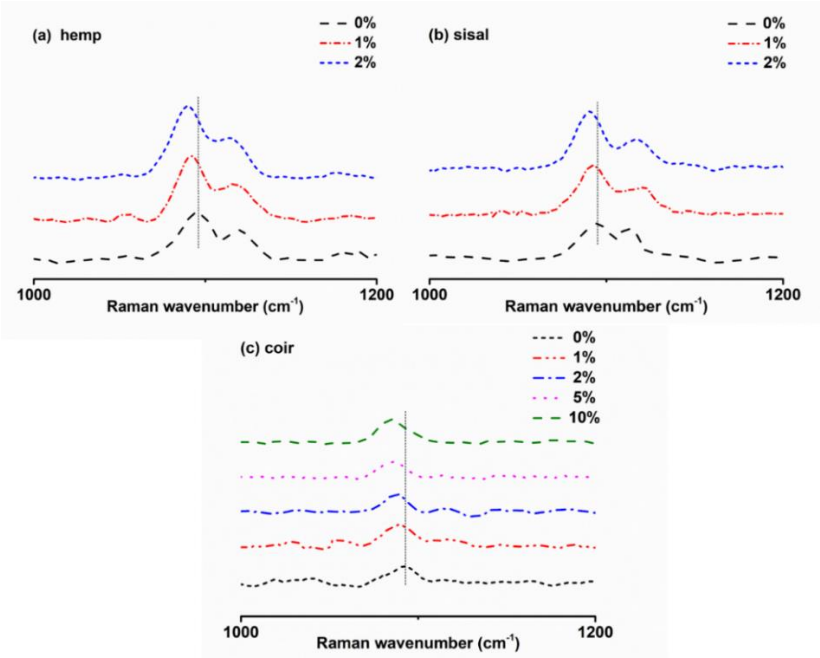

Figure 7. Typical shift in the Raman peak located at 1098 cm^{-1} for plant fibers: (a) hemp; (b) sisal; (c) coir

Figure. 7 shows the shifts for 1098 cm^{-1} Raman peak of plant fibers upon uniaxial deformation in tension. It can be seen that the Raman peaks shift to lower wavenumbers for hemp, sisal and coir fiber. Moreover, the Raman peak of hemp and sisal fiber shift approximately linear with the tension strain and a non-linear shift was observed for coir fiber as shown in Figure 8. The Raman peak shifts rates of hemp and sisal fiber keep constant with value of -1.32 ± 0.18 cm^{-1}/% and -1.12 ± 0.10 cm^{-1}/%, respectively. The shift rate of coir fiber initially is -0.85 cm^{-1}/% within 3% stain then the shift rate decreases until to failure. The results indicate the distinct internal stress of fibers during the tensile deformation.

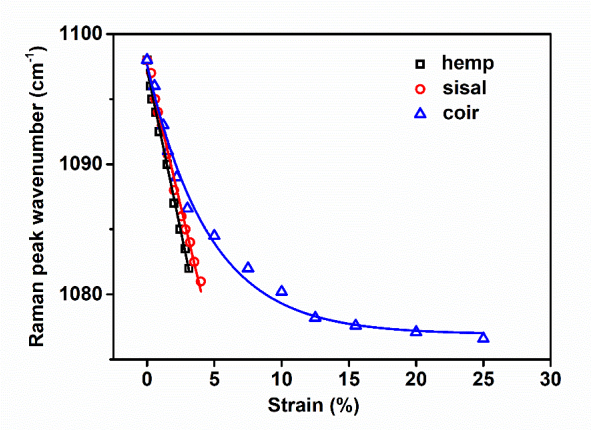

Figure 8. Raman peak shifts for the 1098 cm^{-1} plotted as a function of applied strain

3.4 Deformation mechanism of plant fibers

The deformation mechanism of plant fibers is analyzed based on macroscopic single fiber tensile test and microscopic in situ Raman spectrum test. Figure 8 shows that the Raman peak shift rates are invariant at the initial stage, which indicates the effective stress transfer inside of plant fibers. Then with the strain increasing, hemp and sisal fibers display the high and stable

Raman shift rate during the whole deformation. However, the declined Raman peak shift rate of coir fiber indicates the poor stress transfer caused by the interface sliding between the element fibers. After the yield point, the cellulose microfibrils are gradually uncoiled due to the re-arrangement of the amorphous components existed at the interface between the microfibrils. In the end, the re-aligned of the cellulosic microfibrils induces more cracks and stress concentration, which results in the final fracture of technical fiber.

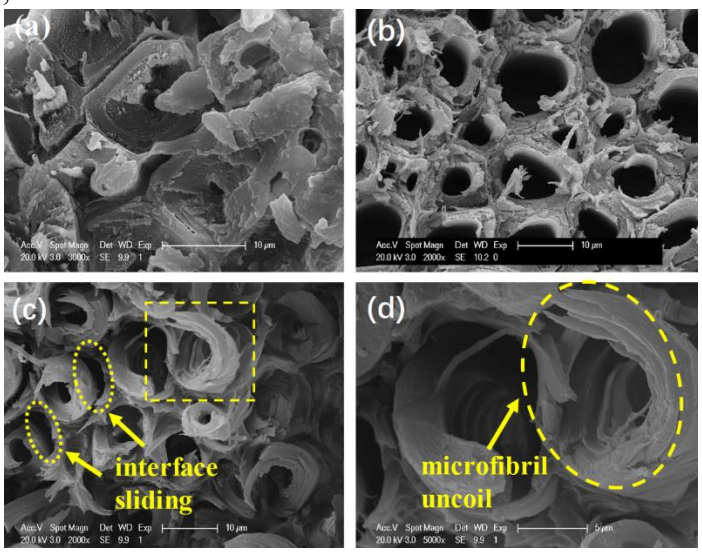

Figure 9. Fracture surfaces of plant fibers after tensile tests: (a) hemp fiber; (b) sisal fiber; (c) and (d) coir fiber;

In addition, the fracture surface of plant fiber gives some evidences to the mechanism as shown in figure 9. It can be seen that the fracture surfaces of hemp and sisal fibers are more smooth than that of coir fiber. Meanwhile, fewer cracks and defects exist at the interfaces between hemp and sisal element fibers. Whereas, obvious cracks and defects are observed in coir fiber and the cellulose microfibrils are uncoiled like helical spring which is attributed to the high intrinsic MFA. Generally, a multi-interface damage mechanism of plant fibers is proposed as shown in figure 10. At the first stage, the interfacial slips initially occur between elemental fibers at the mesoscale. Then, the interfacial slips between cellulose microfibrils accompany with microfibrils uncoil occur at the microscale.

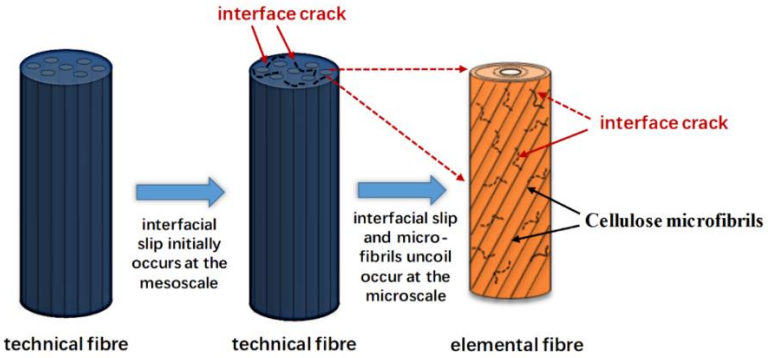

Figure 10. Schematic diagram of the multi-interface damage mechanism of plant fibers

4. Conclusion

Generally, the structure-property relationship and deformation mechanisms of hemp, sisal and coir fiber are investigated. The main conclusions are summarized as follows:

(1) The mechanical properties of plant fibers are mainly dependent on the cellulose content and the MFA. The higher cellulose content and lower MFA, the higher tensile strength and tensile modulus.

(2) The Raman peak shift rate of hemp and sisal fibers are high and stable during the whole deformation. It indicates that the stress transmission is effective due to the high interface strength between element fibers. The declined Raman shift rate of coir fiber indicates the poor loading transfer

(3) The interface sliding and the reorientation of the microfibrils is the main toughen mechanism of the plant fibers under tension deformation.

Acknowledgements

The authors acknowledge the financial support from the National Science Foundation of China (grant no. 51873153), the Shanghai International Science and Technology Cooperation Fund Project (grant no. 19520713000), and the Fundamental Research Funds for the Central Universities (grant no. 22120200054).

Reference

[1] Pickering KL, Efendy MGA, Le TM. A review of recent developments in natural fibre composites and their mechanical performance. Composites Part a-Applied Science And Manufacturing. 2016;83:98-112.

[2] Li Y, Ma H, Shen YO, Li Q, Zheng ZY. Effects of resin inside fiber lumen on the mechanical properties of sisal fiber reinforced composites. Composites Science And Technology. 2015;108:32-40.

[3] Sanjay MR, Madhu P, Jawaid M, Senthamaraikannan P, Senthil S, Pradeep S. Characterization and properties of natural fiber polymer composites: A comprehensive review. Journal of Cleaner Production. 2018;172:566-81.

[4] Haldar S, Bruck HA. Mechanics of composite sandwich structures with bioinspired core. Composites Science And Technology. 2014;95:67-74.

[5] Stanzl-Tschegg SEJMS, C E. Wood as a bioinspiring material. 2011;31(6):p.1174-83.

[6] Al-Oqla FM, Sapuan SMJJoCP. Natural fiber reinforced polymer composites in industrial applications: feasibility of date palm fibers for sustainable automotive industry. 2014;66(mar.1):347-54.

[7] Boopalan M, Niranjanaa M, Umapathy MJJCPBE. Study on the mechanical properties and thermal properties of jute and banana fiber reinforced epoxy hybrid composites. 2013;51B(aug.):54-7.

[8] Sadrmanesh V, Chen Y. Simulation of tensile behavior of plant fibers using the Discrete Element Method (DEM). Composites Part a-Applied Science And Manufacturing. 2018;114:196-203.

[9] George M, Mussone PG, Bressler DCJIC, Products. Surface and thermal characterization of natural fibres treated with enzymes. 2014;53:365-73.

[10] Gibson, L. JJJotRSI. The hierarchical structure and mechanics of plant materials. 2012;9(76):2749-66.
[11] George M, Chae M, Bressler DCJPiMS. Composite materials with bast fibres: Structural, technical, and environmental properties. 2016;83(OCT.):1-23.
[12] Huang JL, Liu WY, Zhou F, Peng YJ. Stiffness variability analysis of maize fiber bundles via multiscale simulation. Journal of Materials Science. 2017;52(13):7917-28.
[13] Eichhorn SJ, Young RJ. Deformation micromechanics of natural cellulose fibre networks and composites. 2003;63(9):1225-30.
[14] Zhou J, Sun G, Zhan Z, An J, Zhang Y, Zhang Y, et al. Polarization behaviors of twisted carbon nanotube fibers. Journal of Raman Spectroscopy. 2012;43(9):1221-6.
[15] Li Q, Kang YL, Qiu W, Li YL, Huang GY, Guo JG, et al. Deformation mechanisms of carbon nanotube fibres under tensile loading by in situ Raman spectroscopy analysis. Nanotechnology. 2011;22(22).
[16] Eichhorn SJ, Sirichaisit J, Young RJ. Deformation mechanisms in cellulose fibres, paper and wood. Journal of Materials Science. 2001;36(13):3129-35.
[17] Roncero MB, Torres AL, Colom JF, Vidal T. The effect of xylanase on lignocellulosic components during the bleaching of wood pulps. Bioresource Technology. 2005;96(1):21-30.
[18] Wanasekara ND, Michud A, Zhu C, Rahatekar S, Sixta H, Eichhorn SJ. Deformation mechanisms in ionic liquid spun cellulose fibers. Polymer. 2016;99:222-30.
[19] Tran LQN, Minh TN, Fuentes CA, Chi TT, Van Vuure AW, Verpoest IJIC, et al. Investigation of microstructure and tensile properties of porous natural coir fibre for use in composite materials. 2015;65:437-45.
[20] Wang B, Sain M, Oksman KJACM. Study of Structural Morphology of Hemp Fiber from the Micro to the Nanoscale. 2007;14(2):89-103.
[21] Tran LQN, Minh TN, Fuentes CA, Chi TT, van Vuure AW, Verpoest I. Investigation of microstructure and tensile properties of porous natural coir fibre for use in composite materials. Industrial Crops And Products. 2015;65:437-45.
[22] Lefeuvre A, Bourmaud A, Morvan C, Baley C. Elementary flax fibre tensile properties: Correlation between stress-strain behaviour and fibre composition. Industrial Crops And Products. 2014;52:762-9.
[23] Bourmaud A, Beaugrand J, Shah DU, Placet V, Baley C. Towards the design of high-performance plant fibre composites. Progress in Materials Science. 2018;97:347-408.
[24] Fiore V, Scalici T, Valenza A. Characterization of a new natural fiber from Arundo donax L. as potential reinforcement of polymer composites. Carbohydrate Polymers. 2014;106:77-83.

Bioinspired chromotropic composite sensor for discriminable strain/temperature/pressure multimodal sensing

Heng Zhang[1], Xi Shen[1,2], and Jang-Kyo Kim[1,3]

[1] Department of Mechanical and Aerospace Engineering, The Hong Kong University of Science and Technology, Clear Water Bay, Kowloon, Hong Kong, China.

[2] Department of Aeronautical and Aviation Engineering, The Hong Kong Polytechnic University, Hung Hom, Kowloon, Hong Kong, China.

[3] School of Mechanical and Manufacturing Engineering, University of New South Wales, Sydney, NSW 2052, Australia.

Abstract: Enabling simultaneous detection and differentiation of physical stimuli using an all-in-one sensing system remains a daunting challenge. This work reports rational design of a bioinspired chromotropic composite sensor which can concurrently monitor in-plane strain/temperature/pressure stimuli by integrating mechanochromic, thermoresistive and triboelectric sensing principles. Ultrahigh stimuli discriminability is achieved by tailoring the material properties and multilayer design to deliver an extremely sensitive response to a selective external stimulus while highly insensitive to unwanted ones. This integrated single sensor facilitates the mutually-discriminating trimodal sensing with accurate measurements and quantitative mapping, offering new insights into emerging interactive e-skin system.

1. INTRODUCTION

Highly flexible multimodal sensors are essential to differential complex stimuli from surrounding environment involved in emerging wearable sensing applications.[1, 2] Numerous nanocomposites and structures are evaluated to improve the sensing capabilities with high sensitivity, low detection limit and superior stability.[3] However, currently available multimodal sensing always suffers from inescapable mutual interference between different sensing layers.[4] Most of the sensors without signal fusion are bimodal, such as pressure and temperature, strain and temperature, and so on.[5] Developing a multimodal sensor capable of measuring more than two stimuli in a single unit is still challenging. To overcome the above challenges, this work, for the first time, reported a novel flexible chromotropic composite sensor that simultaneously detects and discriminates in-plane strain, temperature and pressure through integrating mechanochromic, thermoresistive and triboelectric sensing principles.

2. Results and discussion

2.1 Fabrication of chromotropic composite sensor

The chromotropic film was fabricated by assembling Fe_3O_4@C photonic crystal particle arrays into

gelatin/ polyvinyl alcohol (PVA) matrix. The strain sensing of wavelength signal leverages the inherent merits of structural color of orderly arranged magnetic particles to exhibit interactive color-switching in the full visible spectrum. Meanwhile, the polymer chains of the hybrid hydrogels were aligned upon the driving force from the directional freezing. This temperature-sensitive ionic hydrogel with well-aligned polymer chains facilitated an ultrahigh temperature sensitivity thanks to the thermoresistive effect. To achieve the strain-unperturbed and temperature-insensitive pressure sensing of voltage signal, the triboelectric structure was constructed by assembling multilayers of a prepared chromotropic film, a wrinkle-patterned polydimethylsiloxane (PDMS) friction layer with gradient modulus and a CNT-based elastic electrode. Hence, the integrated chromotropic composite sensor exhibited excellent strain/temperature/pressure multimodal sensing and stimuli discriminability by means of recoding the reflectance wavelength, resistance and voltage signals, as shown in Fig. 1.

2.2 Discriminable multimodal sensing performance

For in-plane strain sensing, the freestanding chromotropic sensor gradually switched from red to violet as the applied strain increases from 0 to 100% (Fig. 2a). The corresponding reflectance wavelength shifted from 680 nm to 430 nm during elongation, as indicated in Fig. 2b. When the chromotropic composite sensor was stretched to mixed strain and temperature stimuli (Fig. 2c), the wavelength changes during 110% stretching remained consistent regardless of different temperatures varying from 10 to 40 ℃. Furthermore, as the sensor was stretched with 40% in-plane strain and pressed with 500 Pa at the same time (Fig. 2d), the dark red changed to light green (at wavelength of 567 nm) and the reflectance wavelength in the region of the pressure source was further reduced to a dark green color (at wavelength 528 nm). The accurate in-plane strain stimulus information could therefore be retrieved by detecting the wavelength of the region surrounding the pressure source.

The thermoresistive mechanism of the composite sensor was employed to measure the temperature stimulus. Its temperature-dependent performance was qualified by the resistance at different temperatures, as shown in Fig. 3a. Due to the acceleration of ion mobility, the resistance decreases exponentially from 221.5 to 16.5 kΩ when the temperature goes from 0 to 50 ℃, which indicates an ultrahigh sensitivity to temperature. The further boosted ionic conduction of aligned polymer chains contributed to the higher temperature sensitivity compared with the random and perpendicular networks (Fig. 3b). To decouple the temperature information from mixed temperature/strain stimuli, the signal separation of strain modulation, which is based on the low strain sensitivity and stable relative resistance variation, could be employed to achieve ultrahigh strain insensitivity (Fig. 3c). Also, the pressure-insensitive property was verified in the stable resistance signal upon increasing pressure from 0 to 1.5 kPa (Fig. 3d).

The highly sensitive pressure sensing which is based on the triboelectric effect of contact/separation mode exhibited an increased voltage output upon the increased pressure loading (Fig. 4a). The enlarged triboelectric voltage output stemmed from the large contact area between the chromotropic hydrogel film (electrode) and wrinkle-patterned friction surface when the sensor was subjected increasing pressure, which was verified by the numerical simulation (Fig. 4b). Additionally, due to the gradient modulus design, the sensor exhibited a constant voltage output upon the 1 kPa stimulus when it was further stretched 100% strain (Fig. 4c), indicating the excellent strain insensitivity of pressure sensing. The temperature-insensitive performance was shown in the quite stable voltage when the sensor under the pressure of 1 kPa was subjected to different temperature environments (fig.

4d).

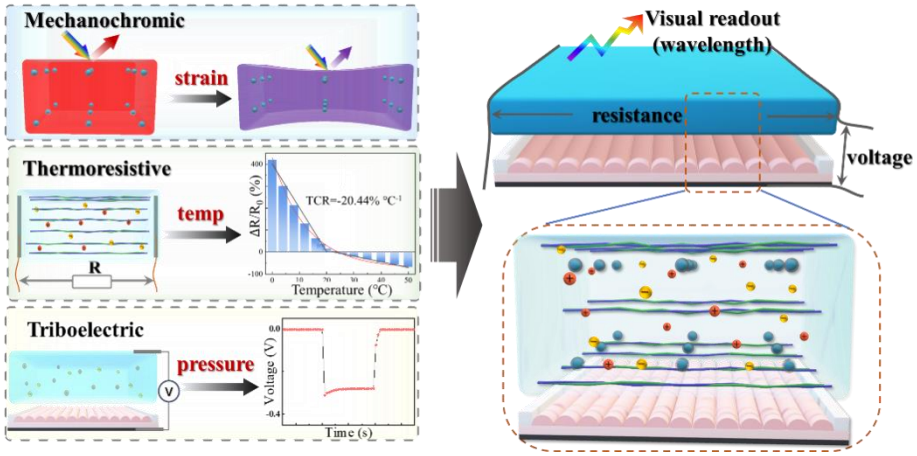

Fig. 1. Illustration of chromotropic composite sensor of integrated mechanochromic, thermoresistive and triboelectric sensing mechanisms by means of the strain-sensitive wavelength, temperature-sensitive resistance and pressure-sensitive voltage signal, respectively.

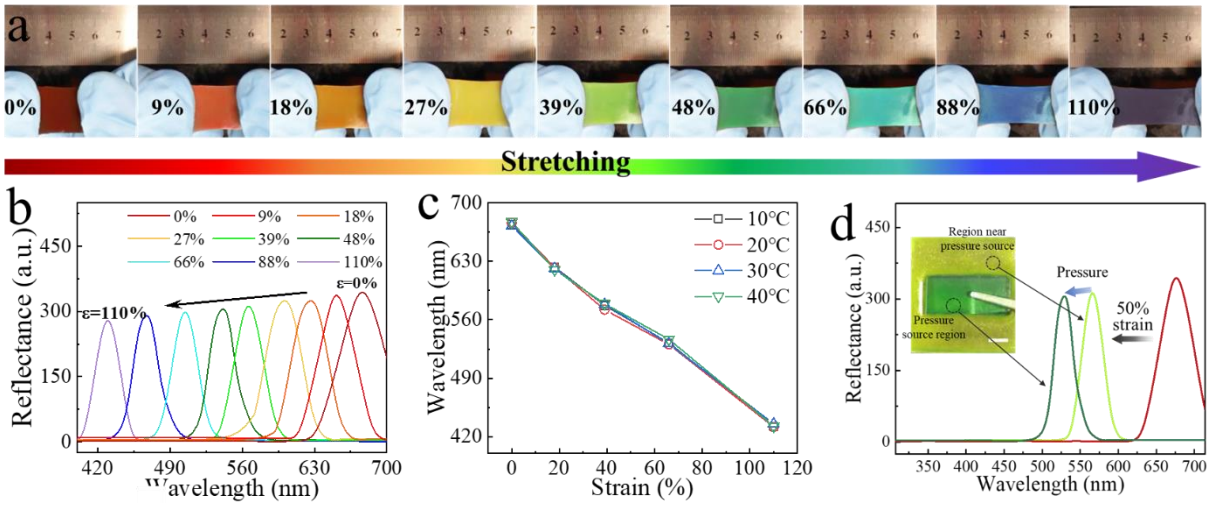

Fig. 2. (a) Photographs of the chromotropic sensor at different strains ranging from 0 to 110% (scale bar = 1 cm). (b) The corresponding reflectance spectra at different strains. (c) Reflectance wavelength of the structural-colored sensor stretched to 110% strain at different temperatures. (d) Reflectance spectra of the chromotropic sensor with initial dark red under a combination of 50% in-plane strain and 500 Pa pressure.

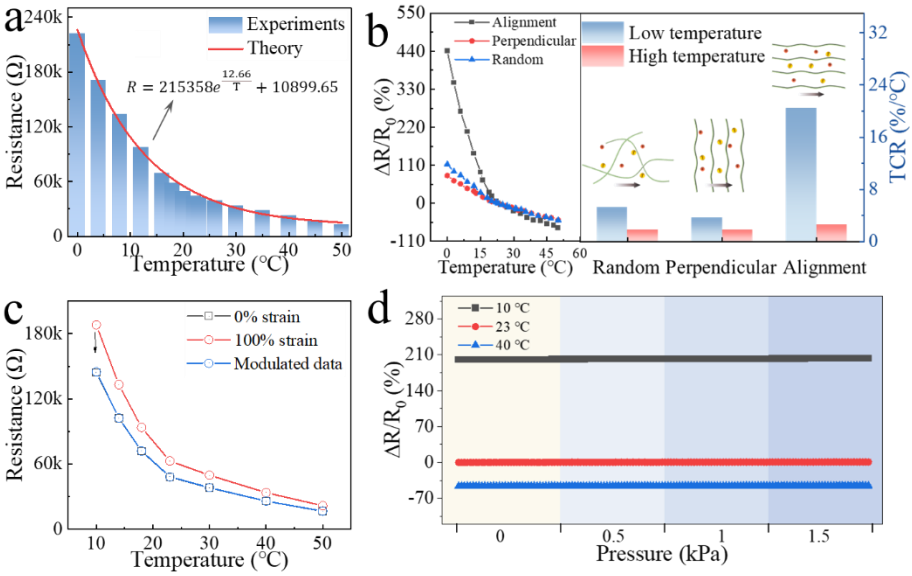

Fig. 3. (a) Resistance signal of the chromotropic composite sensor recorded at different temperatures. (b) Temperature sensitivity comparison of sensors with aligned, perpendicular and random polymer chain structures. (c) Resistance signal of composite sensor upon different temperatures when subjected to 100% strain with and without signal modulation. (d) Relative resistance signal of different temperatures upon increasing temperature from 0 to 1.5 kPa.

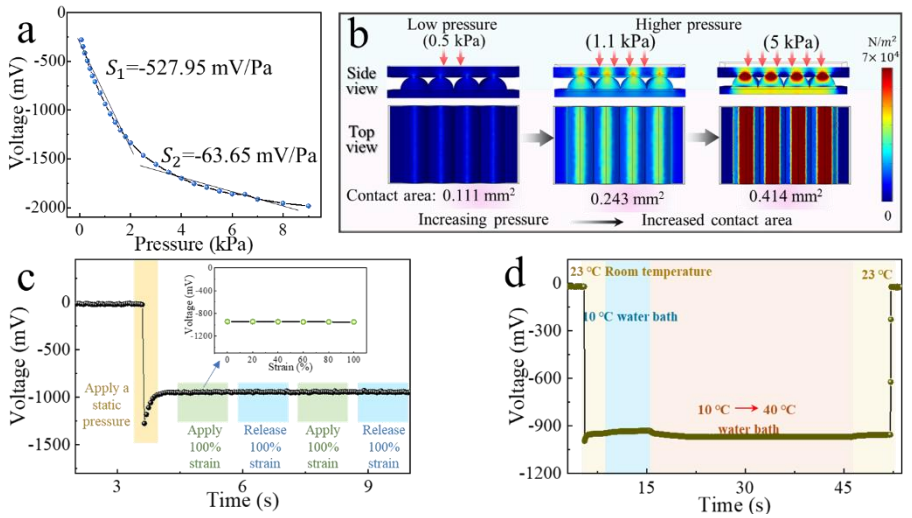

Fig. 4. (a) Voltage signal of increased pressure stimulus. (b) FEM results of the increased contact area between the chromotropic film and wrinkle-patterned friction layer upon increased pressure. (c) Voltage signal of pressure sensing in response to a constant pressure, followed by 100% strain stretching/releasing cycles. (g) Voltage output of the composite sensor when temperature is varied from 10 to 40 °C.

3. CONCLUSION

In summary, a bioinspired chromotropic composite sensor with stimuli discriminability was designed to decouple strain, temperature and pressure stimuli via integrating mechanochromic, thermoresistive and triboelectric multiple sensing principles. These three distinct functionalities selectively contribute to highly sensitive strain sensing with wavelength signal, temperature sensing with resistance signal

and pressure sensing with voltage signal while upholding high insensitivity to extraneous ones. The discriminable multimodal sensor would find potential applications in the areas of human-machine interaction, prosthesis and robotics.

REFERENCES

[1] I. You, D. G. Mackanic, N. Matsuhisa, J. Kang, J. Kwon, L. Beker, J. Mun, W. Suh, T. Y. Kim, J. B. H. Tok, Z. N. Bao, U. Jeong, *Science* **2020**, 370, 961.

[2] D. Jung, C. Lim, H. J. Shim, Y. Kim, C. Park, J. Jung, S. I. Han, S. H. Sunwoo, K. W. Cho, G. D. Cha, D. C. Kim, J. H. Koo, J. H. Kim, T. Hyeon, D. H. Kim, *Science* **2021**, 373, 1022.

[3] H. Zhang, D. Liu, J. H. Lee, H. M. Chen, E. Kim, X. Shen, Q. B. Zheng, J. Yang, J. K. Kim, *Nano-Micro Lett* **2021**, 13, 122.

[4] J. H. Lee, E. Kim, H. Zhang, H. Chen, H. Venkatesan, K. Y. Chan, J. Yang, X. Shen, J. Yang, S. Jeon, J. K. Kim, *Adv. Funct. Mater.* **2022**, 32, 2107570.

[5] G. Y. Bae, J. T. Han, G. Lee, S. Lee, S. W. Kim, S. Park, J. Kwon, S. Jung, K. Cho, *Adv. Mater.* **2018**, 30, 1803388.

Modelling of Electrical Properties of Microscale Self-enclosed Ionic Liquid Enhanced Soft Composites

Chuang Feng[3]*, Yucheng Fan*

College of Civil Engineering, Nanjing Tech University, Nanjing 211816, China

Abstract: The incorporation of room temperature ionic liquid (IL) as inclusions for dielectric elastomer composites currently generate great interest due to their potential applications in soft actuator and optical-related devices. Experiments have shown that the electrical properties of IL enhanced soft composites (ILESCs) are dependent on AC (alternating current) frequency of the electrical loading. This current work develops a mixed micromechanical model with incorporation of electrical double layer (EDL) to predict the electrical properties of the ILESCs while revealing the physical mechanisms (including crowding and overscreening structure, percolation threshold, interfacial tunneling, MWS polarization) that underpin the phenomena. Particularly, the Bazant-Storey-Kornyshev (BSK) phenomenological theory is integrated into EDL surface diffusion model for the first time to evaluate the influence of crowding and overscreening effects. The results show excellent agreement with experimental data of IL enhanced PDMS composites over the frequency range from 1 Hz to 10 GHz. Parametric analysis from the perspective of designing is conducted to explore the optimization of ILESCs with high dielectric constant and frequency-dependent stability. It is found that IL with smaller size and aspect ratio significantly increases the dielectric constant of the ILESCs before the critical dipole relaxation frequency. Increasing the surface charge density of the matrix and replacing of diluted electrolyte with IL delays the frequency-facilitated dielectric response, which is beneficial to maintain the dielectric stability of the ILESCs in the low-frequency band.

Keywords： Polymer-matrix composites, Electrical properties, Micro-mechanics, Ionic liquid

Corresponding Author

[3] E-mail: chuang.feng@njtech.edu.cn (C. Feng)

1. Introduction

The unique light weight, high flexibility, adjustable stiffness and transparent properties of poly(dimethylsiloxane) (PDMS) membranes make them a versatile material for use in a variety of fields and applications, such as, flexible electronics [1], artificial camouflage [2], soft robotics [3] and biomedicine [4]. However, the low permittivity of single PDMS will limit its effectiveness in dielectric elastomers (DEs) for actuators and sensors as electroactive polymeric. In recent years, there has been a growing interest in utilizing room-temperature ionic liquids (ILs) as fillers in DE materials to improve their electrical properties. The use of IL fillers circumvents the problem of solid functional phase induced hardening of elastomers, while the unique energy storage mechanism of ILs enhances the dielectric frequency stability of the resulting materials. Ankit et al. [5] utilized room temperature ILs as functional fillers to enhance the dielectric constant by means of mobile ions as conductors, while Shi et al. [6] utilized liquid electrolytes such as aqueous salt solutions, organic solutions, and ILs, and observed that IL enhanced PDMS showed better dielectric properties than other liquid electrolytes.

However, the theoretical investigation of the electrical properties of IL enhanced soft composites (ILESCs) remains limited, and classical homogenization theory and micromechanical models based on solid fillers are inadequate in accurately predicting the frequency-dependent electrical properties of ILESC. Ankit et al. [5] used Bruggeman and Yamada theories to predict the dielectric constant of ILESCs. These models/theories are not fully applicable to ILESCs due to the polarization occurred in the electric double layer (EDL) with crowding and overscreening effects. Hence, to accurately predict the frequency-dependent electrical properties of ILESCs and elucidate the underlying physical mechanism of the support phenomenon, it is crucial to develop a comprehensive micromechanical model that considers the impact of various factors, such as crowding and overscreening effects in EDL, interfacial tunneling, and Maxwell-Wagner-Sillars (MWS) polarization. The Bazant-Storey-Kornyshev (BSK) theory is used to describe the crowding and over-screening effects of the EDL in IL, and it is integrated into the surface diffusion model to calculate the contributions of the Stern and diffusion layers and investigate their coupling effects. The MWS polarization is also considered to describe the sudden change in electrical properties after the percolation threshold. The above factors and effects are incorporated into the Mori-Tanaka (MT) micromechanical framework to predict the frequency-dependent electrical properties of microscale self-enclosed IL-reinforced soft composites.

2. Mixed Micromechanical Modelling

2.1. Framework of Modelling

As shown in Fig. 4, the orientation of the IL fillers in the local coordinate system is defined by two Euler angles, Ψ and Φ. Based on MT micromechanics theory, the effective complex conductivity tensor $\boldsymbol{\sigma}_{\text{eff}}^{*}$ of the ILESCs can be determined by averaging the terms over all orientations considering EDL and MWS polarization in the representative volume element (RVE) as [7, 8]

$$\boldsymbol{\sigma}_{\text{eff}}^{*}=\boldsymbol{\sigma}_{\text{m}}^{*}+\frac{n}{4\pi}\int_{0}^{2\pi}\int_{0}^{\pi}\left[(\boldsymbol{\sigma}_{\text{IL}}^{*}-\boldsymbol{\sigma}_{\text{m}}^{*})\boldsymbol{A}_{\text{IL}}+\varsigma(\boldsymbol{\sigma}_{\text{EDL}}^{*}-\boldsymbol{\sigma}_{\text{m}}^{*})\boldsymbol{A}_{\text{EDL}}+\xi(\boldsymbol{\sigma}_{\text{int}}^{*}-\boldsymbol{\sigma}_{\text{m}}^{*})\boldsymbol{A}_{\text{int}}\right]\sin(\Phi)d\Phi d\Psi \tag{1}$$

All tensors mentioned above are provided in the global coordinate system (x_1, x_2, x_3). Any quantities obtained in the local coordinate system (x_1', x_2', x_3') for each phase must be converted to the global coordinate system by $\boldsymbol{\sigma}_{i}^{*}=\boldsymbol{U}^{\text{T}}\boldsymbol{\delta}_{i}^{*}\boldsymbol{U}$, which is complex conductivity tensor of "i" (=m, IL, EDL and int) phase in the global coordinate system. The transformation matrix is [9]

$$\boldsymbol{U}=\begin{bmatrix}\cos\Phi\cos\Psi & -\sin\Psi & \sin\Phi\cos\Psi\\ \cos\Phi\sin\Psi & \cos\Psi & \sin\Phi\sin\Psi\\ -\sin\Phi & 0 & \cos\Phi\end{bmatrix} \tag{2}$$

In Eq. (1), n denotes the volume fraction of the IL filler. $\boldsymbol{\delta}_{\text{m}}^{*}=\sigma_{\text{m}}^{*}\cdot\mathbf{I}$ is the complex electrical conductivity tensors of the isotropic matrix. $\mathbf{I}$ is the Kronecker delta tensor and $\boldsymbol{\sigma}_{\text{m}}^{*}$ is the complex electrical conductivity of the matrix written as $\sigma^{*}{}_{\text{m}}=\sigma_{\text{m}}+2\pi f_{\text{AC}}\varepsilon_{\text{m}}\text{j}$. σ_{m} and ε_{m} are the original electrical conductivity and dielectric permittivity of matrix, respectively. j is the imaginary number, and f_{AC} is the AC frequency (Hz) of the applied electrical field. The superscript * represents a complex quantity of its counterpart subjected to AC electrical loading. $\boldsymbol{\delta}_{\text{IL}}^{*}=\sigma_{\text{IL}}^{*}\cdot\mathbf{I}$, $\boldsymbol{\delta}_{\text{EDL}}^{*}=\sigma_{\text{EDL}}^{*}\cdot\mathbf{I}$ and $\boldsymbol{\delta}_{\text{int}}^{*}=\sigma_{\text{int}}^{*}\cdot\mathbf{I}$ are the complex electrical conductivity tensors of IL filler, EDL and interface between the fillers, respectively. $\varsigma=1-\frac{(a_1-t_{\text{EDL}})^3}{a_1^3}$ is volume ratio of the EDL with t_{EDL} being the thickness of the EDL, which is normally within 10~100 nm [10]. ξ is the percentage of the IL fillers forming conductive networks. The precise determination of these variables is expounded in subsequent sections.

The concentration tensor of the electric field $\boldsymbol{A}_i$ in the global coordinate system are [9, 11, 12]

$$\boldsymbol{A}_i = \boldsymbol{U}^{\mathrm{T}} \tilde{\boldsymbol{A}}_i \boldsymbol{U} \left\{ (1-n)\mathbf{I} + \frac{n}{4\pi} \int_0^{2\pi} \int_0^{\pi} \left\{ \boldsymbol{U}^{T} \tilde{\boldsymbol{A}}_i \boldsymbol{U} \right\} \sin(\Phi) d\Phi d\Psi \right\}^{-1} \tag{3}$$

where $\tilde{\boldsymbol{A}}_i$ is the concentration tensor in the local coordinate system of IL filler ("*i*" = IL), EDL ("*i*" = EDL) and interface ("*i*" = int), i.e.

$$\tilde{\boldsymbol{A}}_i = \tilde{\boldsymbol{T}}_i \left\{ (1-n)\mathbf{I} + n\tilde{\boldsymbol{T}}_i \right\}^{-1} \tag{4}$$

where $\tilde{\boldsymbol{T}}_i = \left\{ \mathbf{I} + \boldsymbol{S}_i (\tilde{\boldsymbol{\sigma}}_{\mathrm{m}}^{*})^{-1} (\tilde{\boldsymbol{\sigma}}_i^{*} - \boldsymbol{\sigma}_{\mathrm{m}}^{*}) \right\}^{-1}$ with $\boldsymbol{S}_i$ being the Eshelby tensor of the "*i*" phase, i.e.

$$\boldsymbol{S}_i = \begin{bmatrix} S_{11}^i & 0 & 0 \\ 0 & S_{22}^i & 0 \\ 0 & 0 & S_{33}^i \end{bmatrix} \tag{5}$$

The elements of the Eshelby tensor, which depend on the aspect ratio of the "*i*" phase, are [12]

$$\begin{aligned} S_{11}^i = S_{22}^i &= \frac{\alpha_i}{2(1-\alpha_i^2)^{3/2}} \left[\arccos \alpha_i - \alpha_i (1-\alpha_i^2)^{1/2} \right] \\ S_{33}^i &= 1 - 2S_{22}^i \end{aligned} \tag{6}$$

For ellipsoid-shaped IL filler, the aspect ratio is $\alpha_{\mathrm{EDL}}=\alpha_{\mathrm{IL}}=a_2/a_1$ with a_1 and a_2 being the lengths along x_1' and x_2' directions, respectively. the aspect ratio of interface is $\alpha_{\mathrm{int}}=((2\text{-}\pi/3)a_1+d_{\mathrm{int}})/4a_1$ with d_{int} being average separation distance of IL filler. The complex conductivity of IL filler ("*i*" = IL), EDL ("*i*" = EDL) and interface ("*i*" = int) is as follows

$$\begin{cases} \sigma_{\mathrm{IL}}^{*} = \sigma_{\mathrm{IL}} + 2\pi f_{\mathrm{AC}} \varepsilon_{\mathrm{IL}} \mathrm{j} \\ \sigma_{\mathrm{EDL}}^{*} = \sigma_{\mathrm{s}}^{*} + \sigma_{\mathrm{d}}^{*} \\ \sigma_{\mathrm{int}}^{*} = \sigma_{\mathrm{int}}^{\mathrm{frequency}} + 2\pi f_{\mathrm{AC}} \varepsilon_{\mathrm{int}}^{\mathrm{frequency}} \mathrm{j} \end{cases} \tag{7}$$

where σ_{IL} and $\varepsilon_{\mathrm{IL}}$ are the original electrical conductivity and dielectric permittivity of matrix, respectively. σ_{s}^{*} and σ_{d}^{*} are the complex conductivity of Stern layer and diffuse layer in EDL. $\sigma_{\mathrm{int}}^{\mathrm{frequency}}$ and $\varepsilon_{\mathrm{int}}^{\mathrm{frequency}}$ are frequency-dependent electrical conductivity and dielectric permittivity of interface.

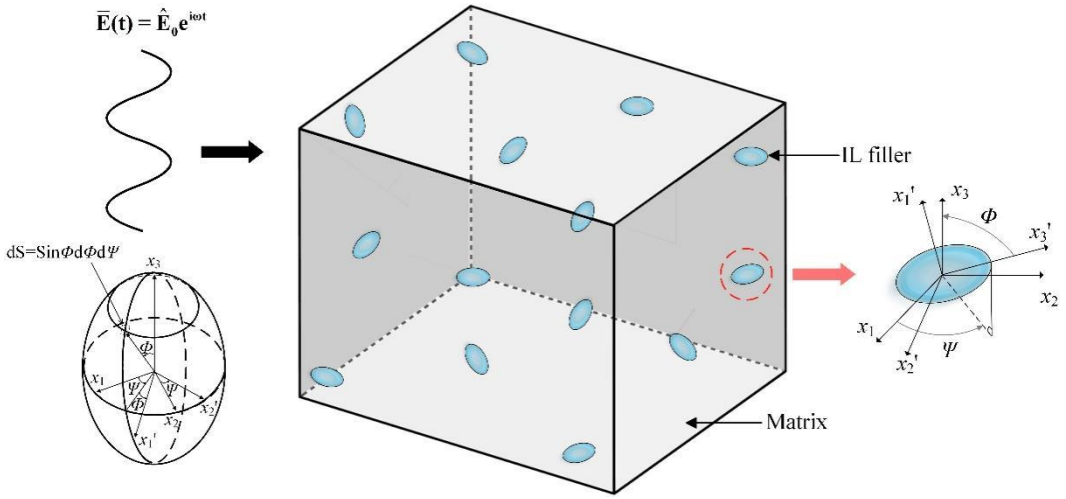

Fig. 4 Sketch of microscale RVE containing IL fillers.

2.2. Electric Double Layer

For charged elastomer matrix containing IL filler, an EDL phenomenon is observed inside the liquid as shown in Fig. 5. Such EDL consists of Stern and diffuse layer. Here we use Σ_s and Σ_0 to denote the surface charge densities in the Stern layer and in the matrix closed to the Stern layer, respectively. In the diffuse layer, we use Σ_d to denote the effective surface charge density within the range.

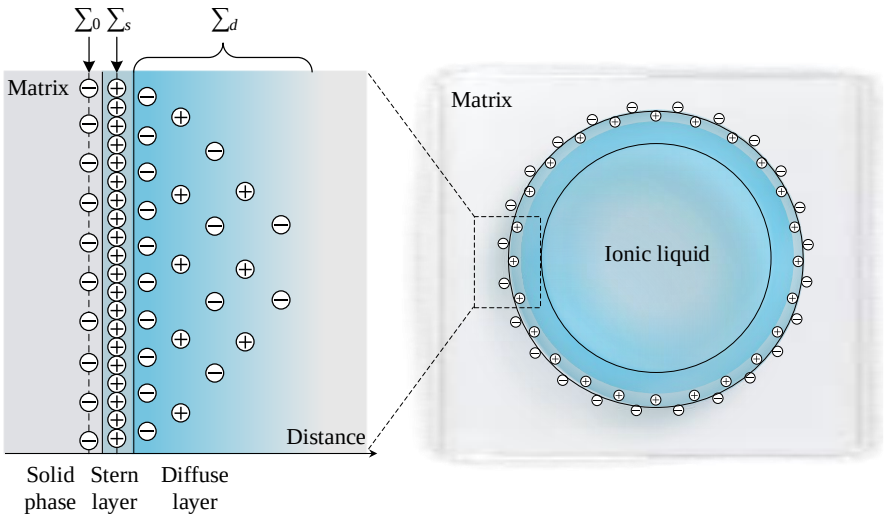

Fig. 5 Electric double layer structure of IL filler.

For ILs with only anions and cations, the classical Poisson-Boltzmann theory is no longer applicable. Therefore, the BSK phenomenological theory is used to modify the classical Poisson-Boltzmann theory as

$$\varepsilon_{\mathrm{IL}}\nabla^2\phi = -\bar{\rho}_{\mathrm{e}}(r) = -\int dr'\rho_{\mathrm{e}}(r)w_{\mathrm{s}}(r-r') \tag{8}$$

where $\varepsilon_{\mathrm{IL}}$ is the permittivity of the IL filler, ϕ is the electrostatic potential, ρ_{e} and $\bar{\rho}_{\mathrm{e}}$ are the charge density and weighted charge density of ionic centers, respectively, and w_{s} is the weighting function, which can be simplified to $w_{\mathrm{s}} \approx 1+l_{\mathrm{s}}^2\nabla^2$ where $\ell_{\mathrm{s}}=d/(24)^{0.5}$ with d being the ionic diameter. The BSK model is reduced to [13]

$$\varepsilon_{\mathrm{IL}}\nabla^2\phi = -\rho_{\mathrm{e}} - l_{\mathrm{s}}^2\nabla^2\rho_{\mathrm{e}} \tag{9}$$

At low surface potential, the differential form of the equation for surface potential displays limiting linear response behavior, which matches the behavior of the full integral equation far from the solid-liquid surface asymptotically. This asymptotic behavior is accurate enough to compute the equivalent surface charge density through integral homogenization. The potential is determined as follows [13]

$$\phi = \phi_{d/2}\left[A_1\exp\left(-k_1\left(x-d/2\right)\right)+A_2\exp\left(-k_2\left(x-d/2\right)\right)\right] \tag{10}$$

where the constants are

$$\begin{aligned} k_1 &= \frac{1+\sqrt{1-4(l_{\mathrm{s}}/\lambda_{\mathrm{D}})^2}}{2\lambda_{\mathrm{D}}(l_{\mathrm{s}}/\lambda_{\mathrm{D}})^2},\ k_2 = \frac{1-\sqrt{1-4(l_{\mathrm{s}}/\lambda_{\mathrm{D}})^2}}{2\lambda_{\mathrm{D}}(l_{\mathrm{s}}/\lambda_{\mathrm{D}})^2} \\ A_1 &= \frac{k_2+l_{\mathrm{s}}^2k_2^3}{k_2-k_1+l_{\mathrm{s}}^2(k_2^3-k_1^3)},\ A_2 = \frac{k_1+l_{\mathrm{s}}^2k_1^3}{k_1-k_2+l_{\mathrm{s}}^2(k_1^3-k_2^3)} \end{aligned} \tag{11}$$

In Eq. (11), λ_{D} is the Debye screening length, which can be approximated as [14]

$$\lambda_{\mathrm{D}} \approx \sqrt{\frac{\varepsilon_{\mathrm{IL}}k_BT\pi d^3}{6Z^2e^2\Phi_{\max}}} \tag{12}$$

where Φ_{max}=0.63 represents the maximum packing fraction of randomly packed ionic spheres, Z denotes the ion valence, k_B and e represent the Boltzmann constant and elementary electric charge, respectively, and T is the absolute temperature.

The equivalent surface charge densities of the Stern and the diffuse layers, Σ_s and Σ_d, can be obtained by integrating the charge density distribution function over the range of the distance, i.e.

$$\Sigma_s = \int_0^{Px} \left| -\varepsilon_{IL} \nabla^2 \phi \right| dx,\ \Sigma_d = \int_{Px}^{+\infty} \left| -\varepsilon_{IL} \nabla^2 \phi \right| dx \tag{13}$$

where P denotes the point separating Stern and diffuse layers as shown in Fig. 6. The sum of the corresponding shaded areas in Fig. 6 are the absolute equivalent surface charge density.

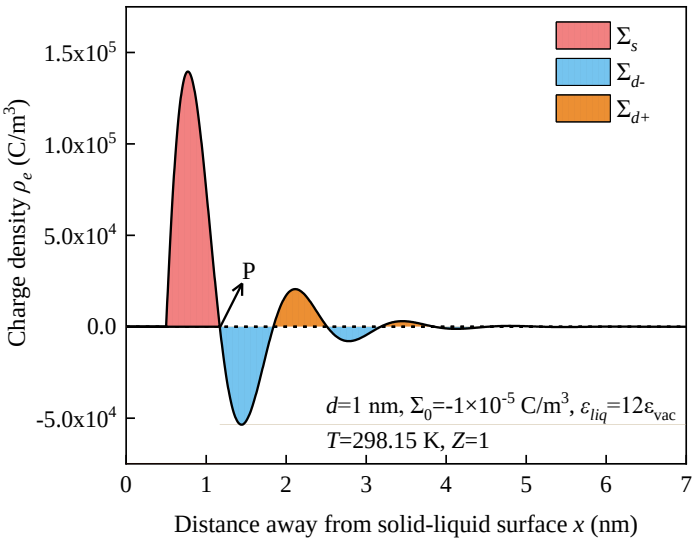

Fig. 6 Charge density distribution of EDL structure of IL filler.

The frequency-dependent complex electrical conductivity of the Stern layer can be calculated by Schwarz's surface diffusion formula as [15]

$$\sigma_s^* = \iota_s \frac{2\pi t_s f_{AC} \mathrm{j}}{1 + 2\pi t_s f_{AC} \mathrm{j}} \frac{\int |\mathbf{E}(r)|^2 \, dS}{\int |\mathbf{E}(r)|^2 \, dV} \tag{14}$$

where $\boldsymbol{E}(r)$ is the local electric field at location r and dS and dV indicate the integration of the expression over the surface and the volume of the IL filler, respectively. The rate of diffusion of the counterions along the solid-liquid surface determines the relaxation time $t_s=(a_1)^2/2D$ with the diffusion coefficient $D = \mu_+ k_B T/e$ and $\iota_s = Z_+^2 \mu_+ |\Sigma_s|$ with Z_+ and μ_+ being the valence and ionic mobility of the counterions (cations here), respectively [15].

Compared to the Stern layer, the diffuse layer contains both counterions and coions, resulting in a more complex polarization phenomenon. This polarization effect has been examined and verified by Dukhin and Shilov [16]. The frequency-dependent complex conductivity of the diffuse layer after polarization can be obtained using the Maxwell-Wagner framework, given by [17]

$$\sigma_d^*(\omega) = \sigma_{IL}^* \frac{1 + 2 f_d(\omega)}{1 - f_d(\omega)} \tag{15}$$

where σ^*_{IL} is the complex conductivity of the IL. The reflection coefficient f_d in Eq. (15) is [18]

$$f_d(\omega) = \frac{\sigma_d / \sigma_{IL} - 1}{\sigma_d / \sigma_{IL} + 2} - \frac{3Y}{2} \frac{(\sigma_{d+} - \sigma_{d-})^2}{\sigma_m^2 \left[\sigma_d / \sigma_{IL} + 2\right]^2} \left[1 - \frac{2\pi t_d f_{AC} \mathrm{j}}{1 + \sqrt{4\pi t_d f_{AC} \mathrm{j} / Y + 2\pi t_d f_{AC} \mathrm{j}}} \right] \tag{16}$$

where the coefficient Y and the relaxation time of diffuse layer t_d are

$$Y = \frac{\left[\sigma_{\mathrm{d}} / (2\sigma_{\mathrm{IL}}) + 1\right]\sigma_{\mathrm{IL}}^2}{(\sigma_{\mathrm{d}+} + \sigma_{\mathrm{IL}})(\sigma_{\mathrm{d}-} + \sigma_{\mathrm{IL}})},\ \tau_{\mathrm{d}} = \frac{a_1^2 Y}{2D} \tag{17}$$

The surface conductivity of coions and counterions in the diffuse layer is $\sigma_{\mathrm{d}\pm}=\pm 2\mu_{\pm}\Sigma_{\mathrm{d}\pm}/a_1$.

2.3. Interfacial Tunneling and MWS Polarization

Maxwell–Wagner–Sillars (MWS) polarization leads to the accumulation of charges around the filler and numerous micro capacitors are connected as shown in Fig. 7a. Once volume fraction reaches the threshold, as depicted in Fig. 7b, the conduction by quantum tunneling and the micro capacitors by MWS polarization will endow the interface with comparable electrical properties. According to Deng and Zheng [19], the percentage of the IL fillers forming conductive networks ξ can be estimated as

$$\xi = \begin{cases} 0, & (n < n^*) \\ \dfrac{(n)^{1/3} - (n^*)^{1/3}}{1 - (n^*)^{1/3}}, & (n^* \le n < 1) \end{cases} \tag{18}$$

where n^* is the percolation threshold, depends on the geometry of the IL fillers, i.e. [20]

$$n^* = \frac{9S_{33}^{\mathrm{IL}}(1 - S_{33}^{\mathrm{IL}})}{2 + 15S_{33}^{\mathrm{IL}} - 9\left(S_{33}^{\mathrm{IL}}\right)^2} \tag{19}$$

where S_{33}^{IL} is the element of the Eshelby tensor of IL as defined in Eq. (6).

For neighboring IL fillers, the electrical properties can be simulated as equivalent circuit as shown in Fig. 7c. The quantum tunneling and the MWS polarization can be simulated as a resistor (R_{IL} or R_{int}) together with a capacitor (C_{IL} or C_{int}) connected in parallel. Such circuit units for the ILs and the interphase are connected in series to simulate the contributions of the overall quantum tunneling and MWS polarization. By using Simmons' derivation [21] and Dyre function [22], The interfacial electrical conductivity can be considered by

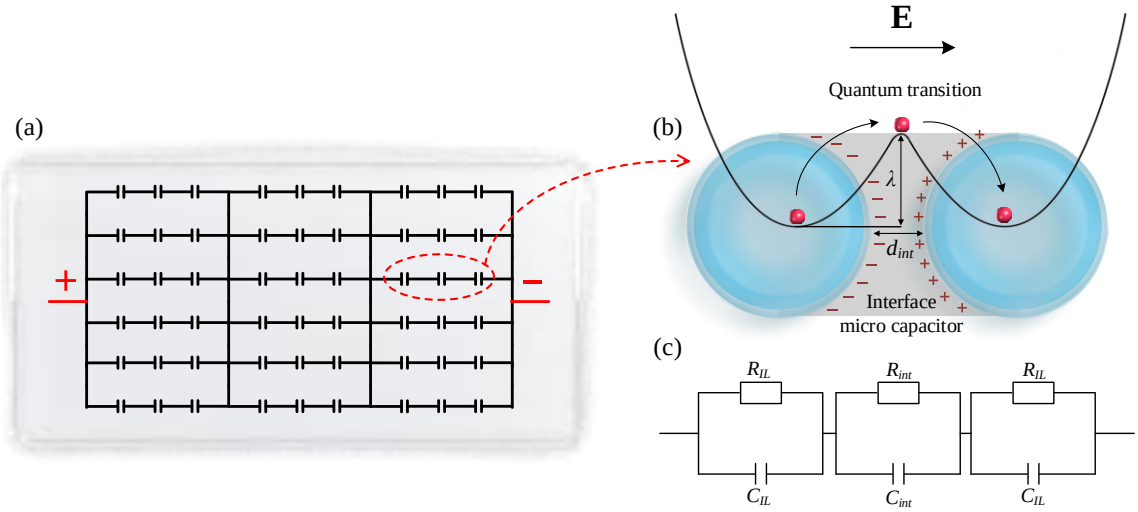

Fig. 7 Schematic of (a) connection of numerous micro capacitors in the composites, (b) quantum tunneling and MWS polarization and (c) equivalent circuit containing interface properties.

$$\begin{cases} \sigma_{\mathrm{int}}^{\mathrm{frequency}}(f_{\mathrm{AC}}) = \dfrac{e^2(2g\kappa)^{1/2}}{\hbar^2 \exp\left(\dfrac{4\pi d_{\mathrm{g}}}{\hbar}(2g\kappa)^{1/2}\right)} p(f_{\mathrm{AC}}) \\ p(f_{\mathrm{AC}}) = \dfrac{2\pi f_{\mathrm{AC}} t_\sigma (\arctan 2\pi f_{\mathrm{AC}} t_\sigma)}{\left[0.5\ln(1 + (2\pi f_{\mathrm{AC}} t_\sigma)^2)\right]^2 + \arctan^2\left(2\pi f_{\mathrm{AC}} t_\sigma\right)} \end{cases} \tag{20}$$

where κ is the potential barrier height of the matrix material, g and e are the mass and electric charge of an electron, respectively, and $\hbar$ is the Planck's constant. d_g is the critical separation distance between adjacent IL fillers in conductive networks which can be taken as d_g=1.8 nm [11]. This average separation distance d_{int} is determined as $d_{int}=d_g(n^*/n)^{1/3}$. t_σ denotes the characteristic time of the conduction process. For MWS polarization, Debye's theory can be used to illustrate the AC frequency dependency of the permittivity, i.e. [23]

$$\varepsilon_{\text{int}}^{\text{frequency}} = \varepsilon_{\text{m}} \Big/ \tau(n, n^*, \gamma_\infty^\varepsilon) + \frac{\varepsilon_{\text{m}} \Big/ \tau(n, n^*, \gamma_{\text{static}}^\varepsilon) - \varepsilon_{\text{m}} \Big/ \tau(n, n^*, \gamma_\infty^\varepsilon)}{1 + 4\pi^2 f_{\text{AC}}^2 t_\varepsilon^2} \tag{21}$$

where t_ε is the relaxation time of Debye theory. $\gamma_{\varepsilon\ \text{static}}$ and $\gamma_\infty^\varepsilon$ are the corresponding scale parameters for the formation of micro capacitors at static and infinite frequency. The resistance-like function τ can be written as

$$\tau\left(n, n^*, \gamma\right) = \frac{\arctan\left(\dfrac{1-n}{\gamma}\right) - \arctan\left(\dfrac{n-n^*}{\gamma}\right)}{\arctan\left(\dfrac{1-n^*}{\gamma}\right) + \arctan\left(\dfrac{n^*}{\gamma}\right)} \tag{22}$$

3. Results and Discussion

In this section, the developed mixed micromechanical model is validated by comparing predicted results with experimental data for ILESCs. The physical quantities as involved in present work are listed in Table 1. PDMS is selected as the matrix. Its electrical conductivity and dielectric constant are σ_m=1.72×10^{-12} S/m [24] and ε_m=3.7ε_{vac} [5], respectively. The surface charge density of PDMS is Σ_0=1.81×10^{-4} C/m^2 [25]. The IL fillers are 1-ethyl-3-methylimidazolium bis(trifluoromethylsulfonyl)imide ([EMIM][TFSI]) and 1-propyl-3-methyl-imidazolium-bis(fluorosulfonyl)imide ([PrMIm][NTf2]) [5, 6]. The electrical conductivity and dielectric constant of [EMIM][TFSI] are σ_{liq}=0.4 S/m and ε_{liq}=12ε_{vac} [26, 27], respectively. The values for [PrMIm][NTf2] are σ_{liq}=0.5 S/m and ε_{liq}=14ε_{vac} [28, 29], respectively. Ion valence and mobility are $Z_\pm$=1 and $\mu_\pm$=1.5×10^{-7} m^2·s^{-1}·V^{-1} [30], respectively. The diameter of the ionic particle is d=0.5 nm [31]. The thickness of EDL is taken as t_{EDL}=4×10^{-8} m. The potential barrier height for polymer matrix is κ=5.0 eV [11]. The relaxation time of Debye theory is τ_ε=2×10^{-3} s and the characteristic time of the conduction τ_σ=10^{-4} s. The scale factor denoting nanocapacitor formation at infinite AC frequency and static state are $\gamma_\infty^\varepsilon$=1.5×10^{-7} and $\gamma_{static}^\varepsilon$=2.8×10^{-13} [32], respectively.

Table 1 Physical parameters used in present work

Physical quantity	Value
Mass of electron g	9.10938291×10^{-31} kg
Electric charge of an electron e	−1.602176565×10^{-19} C
Planck's constant $\hbar$	6.626068×10^{-34} m^2·kg/s
Permittivity of vacuum ε_{vac}	8.854187817×10^{-12} C^2/(J·m)
Absolute temperature at room temperature T	298.15 K

3.1. Validation Study

Fig. 8 presents a comparison between the experimental data [5, 6] and the theoretical predictions of electrical conductivity and dielectric constant obtained through the mixed MT model. The effective conductivity of the composite is observed to increase with the AC frequency. The predicted results of the frequency-dependent dielectric constant, as shown in Fig. 8b, are consistent with the experimental data. The variation of the dielectric constant is found to be negligible in the frequency range of 1 Hz to 10^6 Hz. However, beyond 10^6 Hz, the predicted dielectric constant decreases with the AC frequency, and this decrease is more pronounced for higher filler volume fractions. This phenomenon can be attributed to the enhanced polarization effect of the electric double layer (EDL) resulting from the incorporation of the IL filler. The volume fraction of EDL increases with the increase of IL filler, and the charge stored by EDL polarization reaches relaxation at 10^6 Hz.

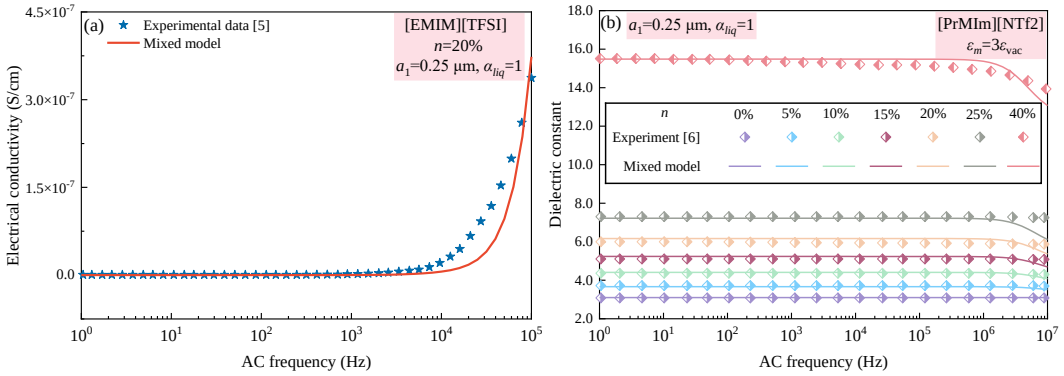

Fig. 8 Comparisons between experimental data and present modelling results for (a) electrical conductivity and (b) dielectric constant of IL-PDMS with changing AC frequency.

3.2. Parametric Analysis

The effect of the aspect ratio of ellipsoidal IL filler on the electrical conductivity and dielectric constant was investigated, as presented in Fig. 9a. The results showed that the electrical conductivity increased as the aspect ratio decreased. This can be attributed to the formation of conductive networks by the uniform dispersion of smaller aspect ratio fillers, resulting in increased quantum tunneling and electrical conductivity. On the other hand, the aspect ratio of the IL fillers had a significant effect on the dielectric constant, particularly when the aspect ratio was relatively small, at AC frequencies below 10^8 Hz. This was due to the more pronounced electric double layer (EDL) polarization effect and increased charge polarization for slender fillers. However, as the AC frequency exceeded 10^8 Hz, the effect of the IL's aspect ratio diminished, as the MWS polarization dominated the dielectric constant instead of the EDL polarization.

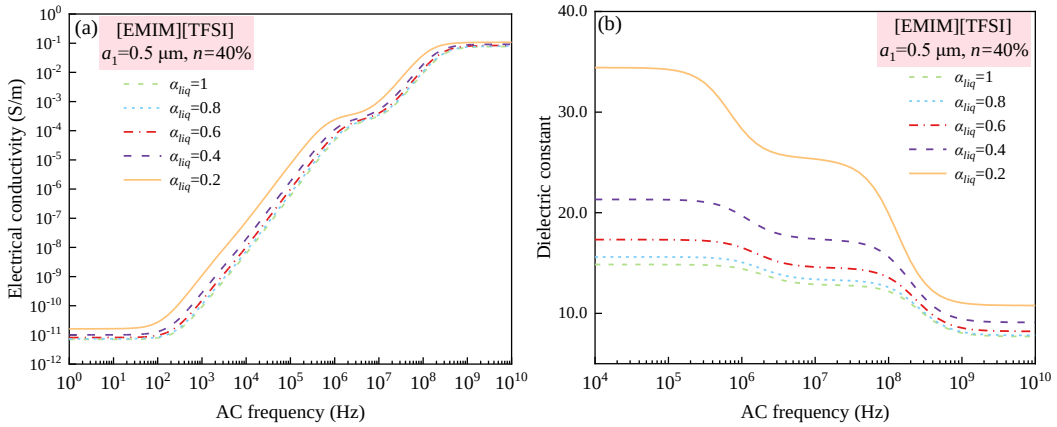

Fig. 9 Effect of IL filler's aspect ratio on electrical properties IL enhanced composites (a) electrical conductivity; (b) dielectric constant.

The electrical conductivity and dielectric constant of the composites with IL and diluted electrolyte fillers are compared and analyzed in Fig. 10. The electrical conductivity of the diluted electrolyte enhanced composites shows several significant variations as the AC frequency increases, while the electrical conductivity of the IL enhanced composites increases significantly within a certain range. On the other hand, the dielectric constant of the IL enhanced composites remains constant over a wide range of AC frequencies, whereas the dielectric constant of the diluted electrolyte enhanced composites undergoes a sudden drop as the AC frequency increases. These results indicate that the IL enhanced composites with a larger and more stable dielectric constant are more favorable for the development of dielectric elastomer-based materials and structures.

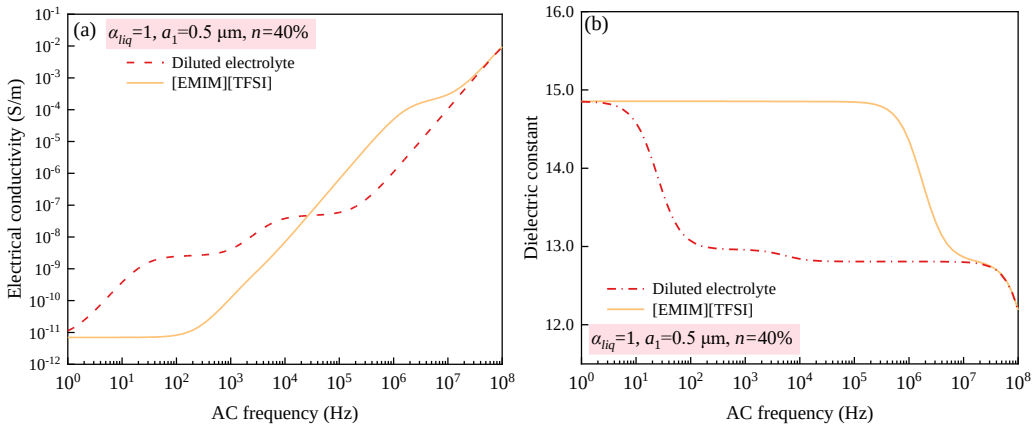

Fig. 10 Comparison of electrical properties of diluted electrolyte and IL enhanced composites (a) electrical conductivity; (b) dielectric constant.

4. Conclusion

This study presents a mixed micromechanics model to predict the frequency-dependent electrical conductivity and dielectric constant of ILESCs. The model incorporates three contributions, namely uniformly dispersed ionic liquid, EDL effects including crowding and overscreening, and MWS polarization. The theoretical predictions of the model are compared with experimental data, demonstrating excellent performance in predicting the frequency-dependent electrical properties of ILESCs. The study further reveals that decreasing the aspect ratio of the ellipsoidal ionic liquid enhances the electrical properties of the composites. Specifically, slender ellipsoidal ionic liquid fillers are more effective in enhancing the electrical properties of ILESCs at low AC frequency due to more obvious EDL polarization effects and greater charge polarization. Compared to composites enhanced with diluted electrolyte, ILESCs exhibit larger and more stable electrical properties over a wide AC frequency range, indicating their potential for developing dielectric elastomer-based materials and structures that require high dielectric constant.

Acknowledgement
The authors greatly acknowledge the financial support from Innovative and Entrepreneurial Talents of Jiangsu Province.

References

[1] Dagdeviren C, Joe P, Tuzman OL, Park K-I, Lee KJ, Shi Y, et al. Recent progress in flexible and stretchable piezoelectric devices for mechanical energy harvesting, sensing and actuation. Extreme Mech Lett 2016;9:269-81.

[2] Meng Z, Huang B, Wu S, Li L, Zhang S. Bio-inspired transparent structural color film and its application in biomimetic camouflage. Nanoscale 2019;11(28):13377-84.

[3] Chen D, Pei Q. Electronic muscles and skins: a review of soft sensors and actuators. Chem Rev 2017;117(17):11239-68.

[4] Heo C, Park H, Kim Y-T, Baeg E, Kim YH, Kim S-G, et al. A soft, transparent, freely accessible cranial window for chronic imaging and electrophysiology. Sci Rep 2016;6(1):1-11.

[5] Ankit, Tiwari N, Ho F, Krisnadi F, Kulkarni MR, Nguyen LL, et al. High-k, ultrastretchable self-enclosed ionic liquid-elastomer composites for soft robotics and flexible electronics. ACS Appl Mater Interf 2020;12(33):37561-70.

[6] Shi L, Zhang C, Du Y, Zhu H, Zhang Q, Zhu S. Improving dielectric constant of polymers through liquid electrolyte inclusion. Adv Func Mater 2021;31(8):2007863.

[7] Benveniste Y. A new approach to the application of Mori-Tanaka's theory in composite materials. Mech Mater 1987;6(2):147-57.

[8] Dunn M, Ledbetter H. Elastic moduli of composites reinforced by multiphase particles. 1995.

[9] Seidel GD, Lagoudas DC. A micromechanics model for the electrical conductivity of nanotube-polymer nanocomposites. J Compos Mater 2009;43(9):917-41.

[10] Islam MM, Alam MT, Ohsaka T. Electrical double-layer structure in ionic liquids: a corroboration of the theoretical model by experimental results. J Phys Chem C 2008;112(42):16568-74.

[11] Feng C, Jiang L. Micromechanics modeling of the electrical conductivity of carbon nanotube (CNT)–polymer nanocomposites. Compos Part A Appl Sci Manuf 2013;47:143-9.

[12] Landau LD, Bell J, Kearsley M, Pitaevskii L, Lifshitz E, Sykes J. Electrodynamics of continuous media: elsevier; 2013.

[13] de Souza JP, Goodwin ZA, McEldrew M, Kornyshev AA, Bazant MZ. Interfacial layering in the electric double layer of ionic liquids. Phys Rev Lett 2020;125(11):116001.

[14] Bazant MZ, Storey BD, Kornyshev AA. Double layer in ionic liquids: Overscreening versus crowding. Phys Rev Lett 2011;106(4):046102.

[15] Schwarz G. A theory of the low-frequency dielectric dispersion of colloidal particles in electrolyte solution1, 2. J Phys Chem 1962;66(12):2636-42.

[16] Dukhin SS, Shilov VN, Bikerman J. Dielectric phenomena and double layer in disperse systems and polyelectrolytes. J Electrochem Soc 1974;121(4):154C.

[17] Bücker M, Flores Orozco A, Undorf S, Kemna A. On the role of Stern-and diffuse-layer polarization mechanisms in porous media. J Geophys Res Solid Earth 2019;124(6):5656-77.

[18] Shilov V, Delgado A, Gonzalez-Caballero F, Grosse C. Thin double layer theory of the wide-frequency range dielectric dispersion of suspensions of non-conducting spherical particles including surface conductivity of the stagnant layer. Colloids Surf A Physicochem Eng Asp 2001;192(1-3):253-65.

[19] Deng F, Zheng Q-S. An analytical model of effective electrical conductivity of carbon nanotube composites. Appl Phys Lett 2008;92(7):071902.

[20] Wang Y, Shan JW, Weng GJ. Percolation threshold and electrical conductivity of graphene-based nanocomposites with filler agglomeration and interfacial tunneling. J Appl Phys 2015;118(6):065101.

[21] Simmons JG. Generalized formula for the electric tunnel effect between similar electrodes separated by a

thin insulating film. J Appl Phys 1963;34(6):1793-803.
[22] Dyre JC. A simple model of ac hopping conductivity in disordered solids. Phys Lett A 1985;108(9):457-61.
[23] Debye P. Results of a kinetic theory of dielectrics. Phys Z 1912;13:976-1000.
[24] Gao X, Huang Y, Liu Y, Kormakov S, Zheng X, Wu D, et al. Improved electrical conductivity of PDMS/SCF composite sheets with bolting cloth prepared by a spatial confining forced network assembly method. RSC Adv 2017;7(24):14761-8.
[25] Peng J, Zhang H, Zheng Q, Clemons CM, Sabo RC, Gong S, et al. A composite generator film impregnated with cellulose nanocrystals for enhanced triboelectric performance. Nanoscale 2017;9(4):1428-33.
[26] Chen Y, Cai Y, Thomsen K, Kontogeorgis GM, Woodley JM. A group contribution-based prediction method for the electrical conductivity of ionic liquids. Fluid Phase Equilib 2020;509:112462.
[27] Weingaertner H. The static dielectric permittivity of ionic liquids. J Mol Liq 2014;192:185-90.
[28] Liu Q, Zhao L, Ma L, Chu J, Wang J, Zang Y. Hydroxyethyl Group Effect on Properties of Bis [(trifluoromethyl) sulfonyl] imide-Type Ionic Liquids. J Chem Eng Data 2020;65(10):4780-9.
[29] Huang M-M, Jiang Y, Sasisanker P, Driver GW, Weingärtner H. Static relative dielectric permittivities of ionic liquids at 25 C. J Chem Eng Data 2011;56(4):1494-9.
[30] Umecky T, Saito Y, Matsumoto H. Ion Mobility of 1-Ethyl-3-methylimidazolium Tetrafluoroborate and 1-Ethyl-3-methylimidazolium Bis (trifluorosulfonyl) amide Ionic Liquids. ECS Transactions 2010;25(39):23.
[31] Lian C, Liu K, Van Aken KL, Gogotsi Y, Wesolowski DJ, Liu H, et al. Enhancing the capacitive performance of electric double-layer capacitors with ionic liquid mixtures. ACS Energy Lett 2016;1(1):21-6.
[32] Xia X, Wang Y, Zhong Z, Weng GJ. A frequency-dependent theory of electrical conductivity and dielectric permittivity for graphene-polymer nanocomposites. Carbon 2017;111:221-30.

Interface Engineering of MXene towards High Performance Polymer Composites

Yongqian Shi, Kexin Chen, Zixiao Wang*

College of Environment and Safety Engineering, Fuzhou University, 2 Xueyuan Road, Fuzhou 350116, P. R. China.

E-mail address: shiyq1986@fzu.edu.cn

1.1 Introduction

Polymers has been widely utilized in the electronic industry, transportation, household and cosmetics. However, polymers are highly flammable and usually generates a great amount of smoke and toxic gaseous species, which are harmful to victims escape from fire. Therefore, developing highly effective flame retardant polymeric materials with the release of low toxic fumes during burning still keep a huge challenge. In response to these challenges, tremendous efforts have been made to improve the flame retardant properties of polymeric materials by adding nanofillers. Titanium carbide (MXene, $Ti_3C_2T_x$), a recently emerging two-dimensional (2D) material, has attracted increasing attention owing to its tunable surface functional groups, super metallic conductivity, outstanding intercalation ability and mechanical ability, etc. Besides, $Ti_3C_2T_x$ exhibits distinguished flame retardancy in polymeric materials due to its excellent physical barrier effect and catalytic charring.

1.2 Research achievements

In our group, we successfully synthesized a series of functionalized MXenes to fabricate high performance polymer composites. Firstly, inorganic modified MXene. (1) $Ti_3C_2T_x$/Nano-Cu hybrid smoke suppressant was added into TPU to prepare TPU nanocomposites. The as-

synthesized $Ti_3C_2T_x$/Nano-Cu hybrid exhibited excellent smoke and toxic gaseous products suppression function during combustion of the TPU (See Figs. 1-2). For example, the TPU/$Ti_3C_2T_x$/Nano-Cu-2.0 nanocomposite exhibited decreased PSPR, TSR, PCOPR and COTY by 66.7%, 23.2%, 51.8% and 52.9%, respectively, compared with pure TPU. (2) $Ti_3C_2T_x$-rGO hybrid was successfully prepared via hydrogen bonding induced assembly of $Ti_3C_2T_x$ and rGO, and subsequently incorporated into TPU via solvent mixing and melt blending methods. Owing to the catalytic charring effect of $Ti_3C_2T_x$-rGO hybrid, the TPU/$Ti_3C_2T_x$-rGO-2.0 nanocomposite showed improved thermal stability at high temperature (See Fig. 3). (3) $Ti_3C_2T_x$@MCA was successfully prepared by engineering the surface of $Ti_3C_2T_x$ via supramolecular assembly. The significantly improved mechanical and fire-safe performances of TPU/$Ti_3C_2T_x$@MCA-3.0 were superior to those of TPU nanocomposites filled with other nano-additives (See Figs. 4-5).

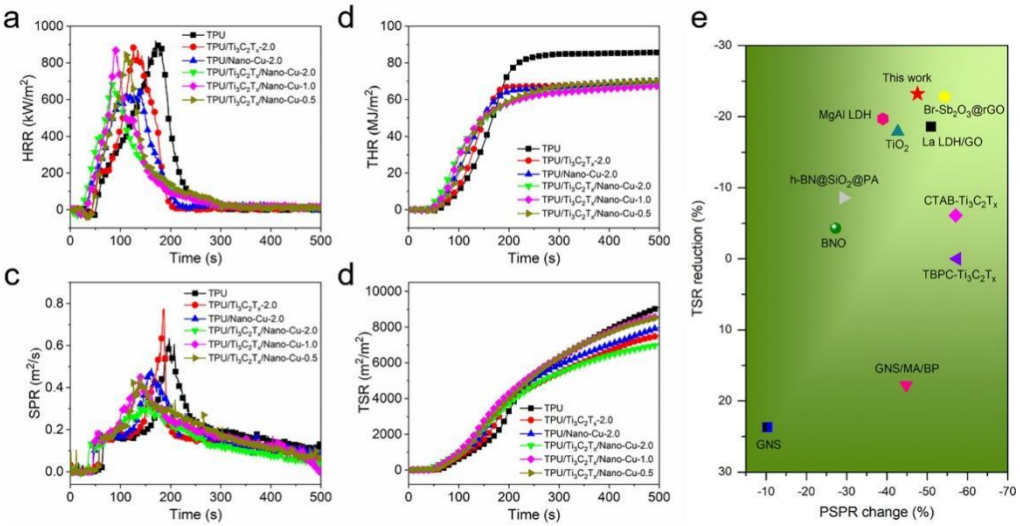

Fig. 1. (a) HRR, (b) THR, (c) SPR and (d) TSR curves of TPU and its nanocomposites; (e) Comparisons of PSPR and TSR reductions with previous work.

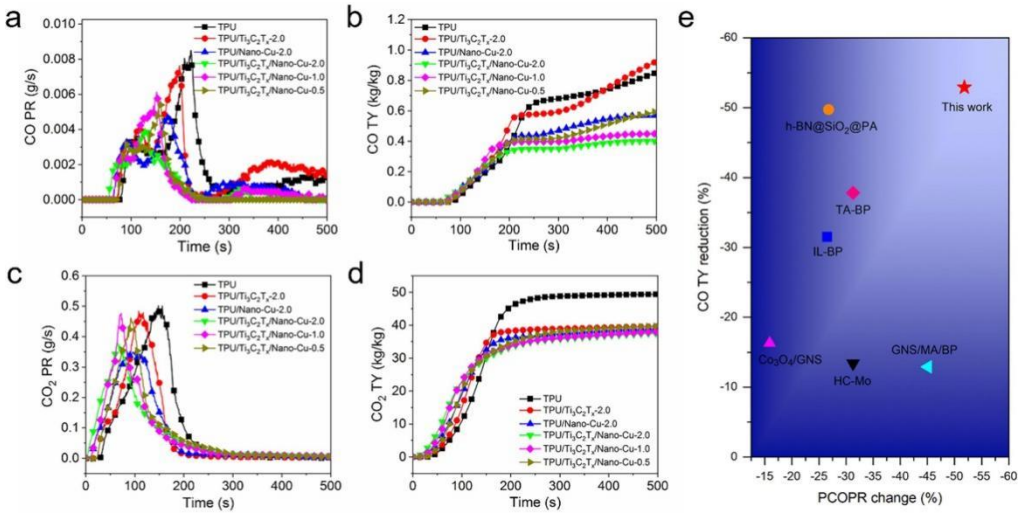

Fig. 2. (a) COPR, (b) COTY, (c) CO_2PR and (d) CO_2TY curves of TPU and its nanocomposites; (e) Comparisons of PCOPR and COTY reductions with previous work.

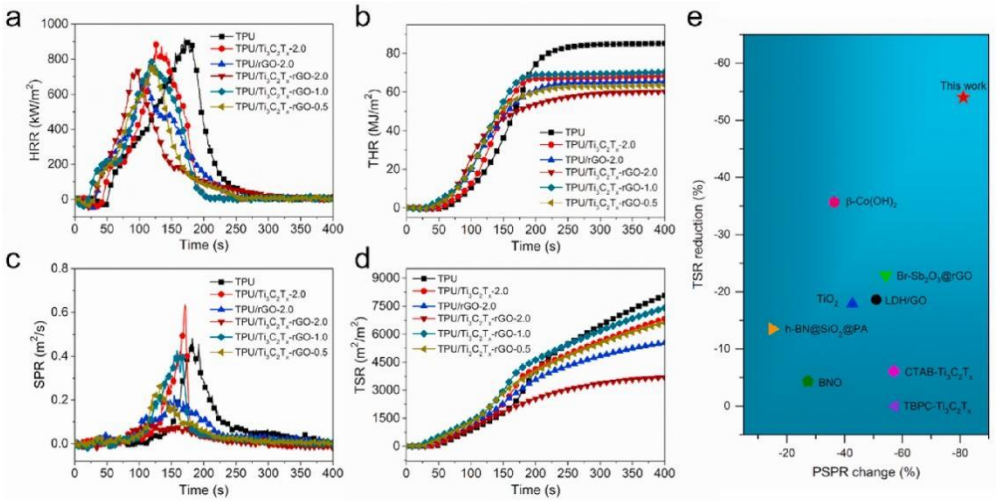

Fig. 3. (a) HRR, (b) THR, (C) SPR and (d) TSR curves of TPU and its nanocomposites; (e) Comparisons of PSPR and TSR reductions with previous work.

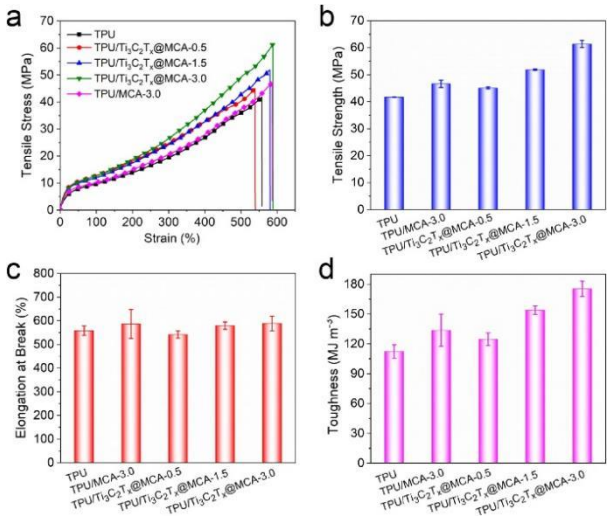

Fig. 4. Mechanical performances of as-prepared TPU and its nanocomposites. (a) Typical stress-strain curves; (b) Tensile strength, (c) Elongation at break, and (d) Tensile toughness.

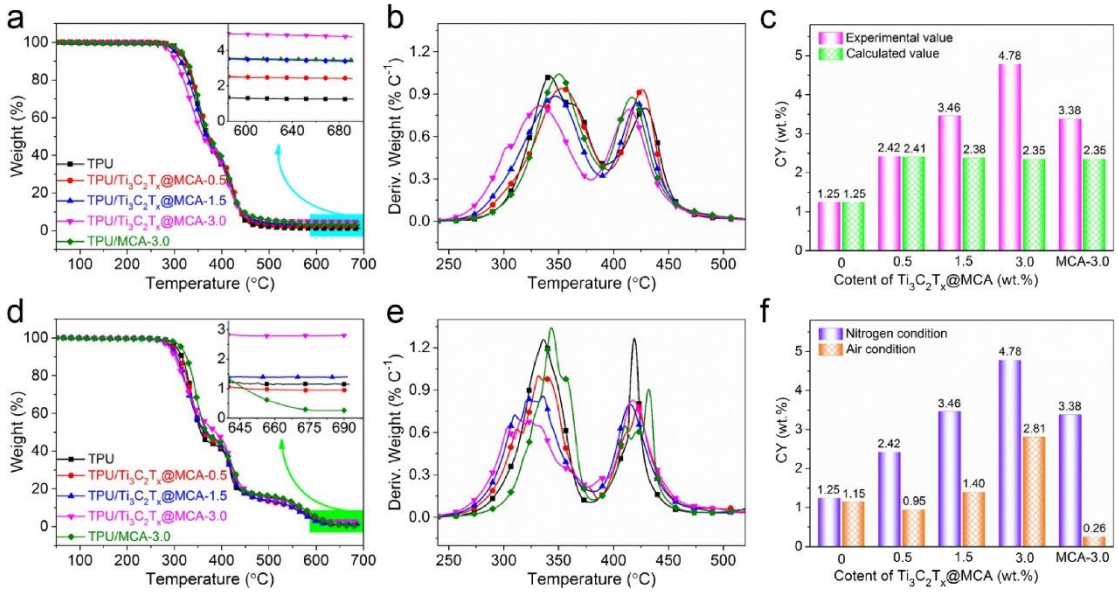

Fig. 5. (a) Thermal properties evaluation of TPU and its nanocomposites: (a) TG and (b) DTG curves under nitrogen condition; (c) Comparisons between experimental value and calculated value of char residues; (d) TG and (e) DTG curves under air condition; (f) Comparisons of char yield under nitrogen with that under air condition. Notes: CY^{cal} represents the calculated value; CY^{Exp} refers to the experimental value; CY means char yields at 700 ºC.

Secondly, organically modified MXene. (1) The $Ti_3C_2T_x$-PPPA hybrid was synthesized via the esterification and the hydrogen bonding induced assembly. The thermal stability of TPU was improved by the addition of $Ti_3C_2T_x$-PPPA hybrid. After the incorporation of 1.0 wt% $Ti_3C_2T_x$-PPPA, the PHRR, THR, TSR and COTY of the TPU nanocomposite were decreased by 24.5%, 32.6%, 54.4% and 36.8%, respectively (See Fig. 6). (2) With the incorporation of 2.0 wt% $Ti_3C_2T_x$-D-H nanohybrid, the PHRR, TSR and COTY of TPU nanocomposites were decreased by 27.3%, 43.8% and 36.7%, respectively (See Fig. 7). Besides, compared to pure TPU, TPU/$Ti_3C_2T_x$-D-H-2.0 nanocomposite displayed significantly improved strength (+32.8%) and toughness (+56.8%) (See Fig. 8).

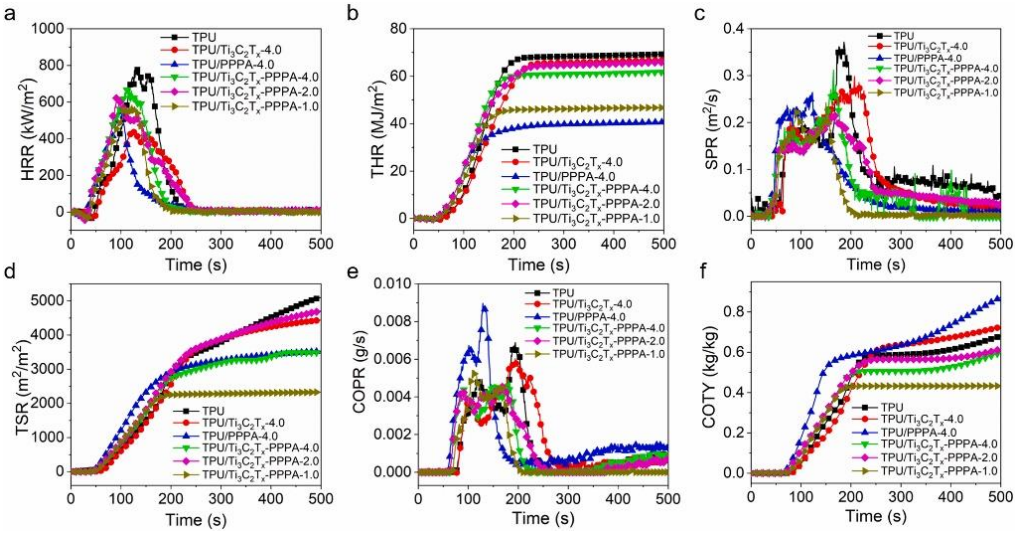

Fig. 6. (a) HRR, (b) THR, (c) SPR, (e) TSR, (e) COPR and (f) COTY curves of TPU and its nanocomposites.

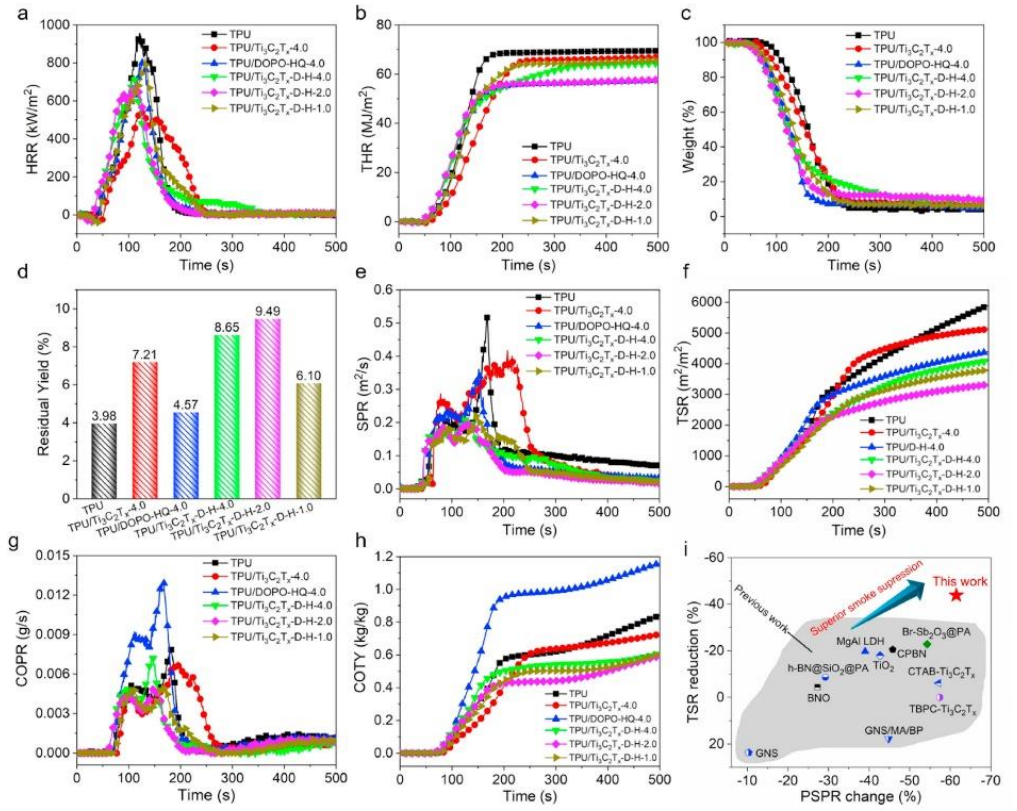

Fig. 7. (a) HRR, (b) THR, (c, d) char residues, (e) SPR, (f) TSR, (g) COPR, and (h) COTY curves of TPU and its nanocomposites; (i) Comparisons of PSPR and TSR reductions with prior reports.

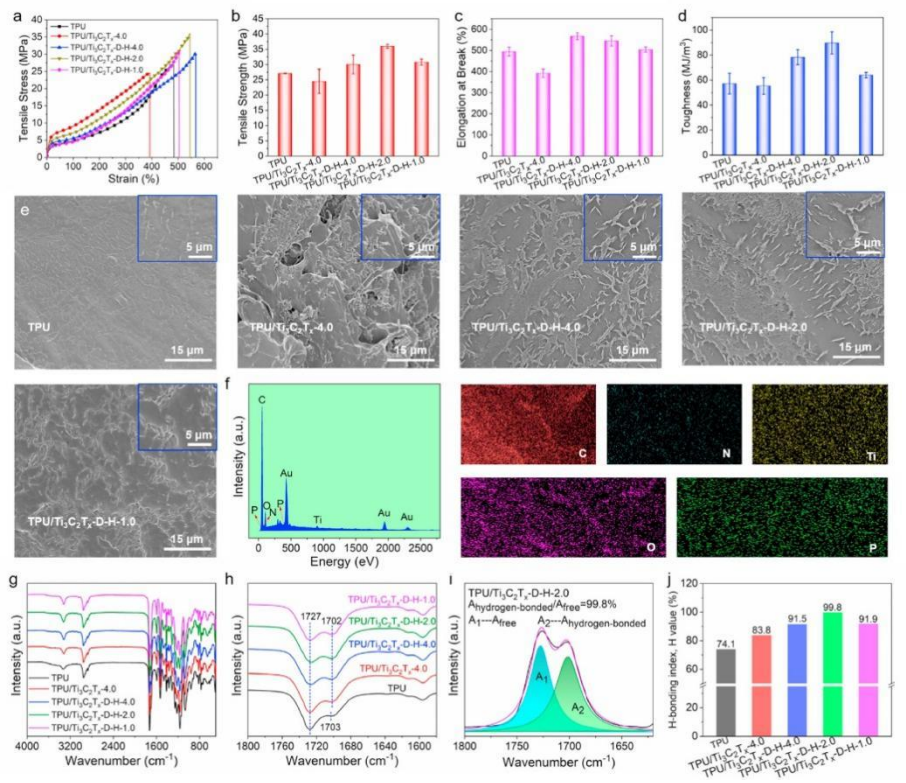

Fig. 8. Mechanical properties of TPU and its nanocomposites: (a) Stress-strain curves; (b) Tensile strength, (c) Elongation at break, and (d) Tensile toughness; (e) SEM images of the stretch-fractured surfaces for TPU and its nanocomposites; (f) SEM mapping images of the stretch-fractured surface for TPU/$Ti_3C_2T_x$-D-H-2.0; (g-i) FTIR spectra and (j) H-bonding index of TPU and its nanocomposites.

Thirdly, Synergistic flame retardant. (1) The TPU/APP@CS@$Ti_3C_2T_x$ composites were fabricated via the melt blending method and exhibited outstanding thermal stability. The THR, TSR, COTY and CO_2TY of TPU/9.5APP@CS@0.5$Ti_3C_2T_x$ composite were remarkably declined by 73.0%, 77.3%, 75.3% and 75.3%, respectively, compared to those of pure TPU (See Fig. 9). (2) Exfoliated $Ti_3C_2T_x$ nanoflakes were successfully modified with HDBAC. Then, the PLA/HDBAC-$Ti_3C_2T_x$/SiAPP composites were fabricated using melt blending method. The characterization results showed that the addition of a small amount of HDBAC-$Ti_3C_2T_x$ could significantly improve the flame retardant properties of PLA/SiAPP composites (See Fig. 10). For instance, compared to that of pure PLA, the residual carbon of PLA/2.0HD-TC/13.0SiAPP increases from 0.61 wt% to 10.33 wt%.

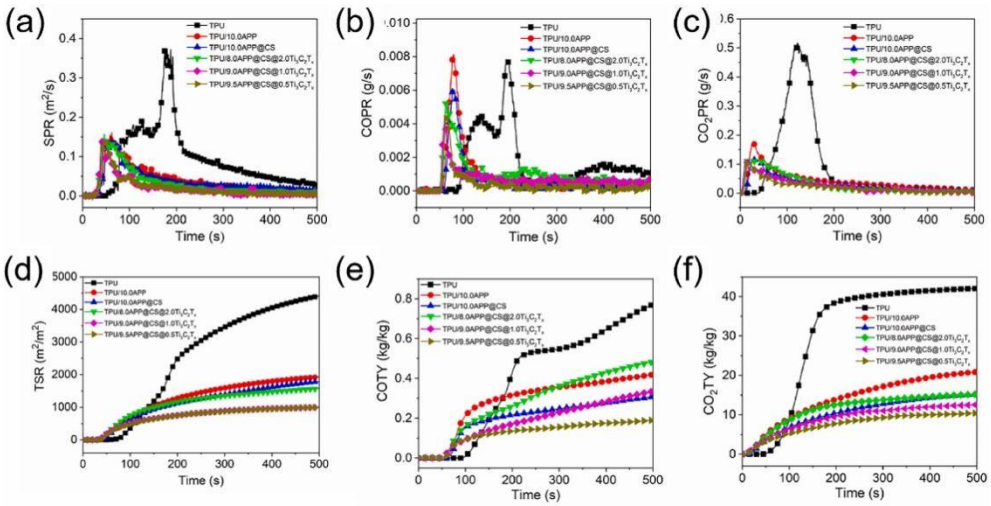

Fig. 9. (a) SPR, (b) COPR, (c) CO_2·PR, (d) TSR, (e)COTY and (f) CO_2TY curves of TPU and its composites.

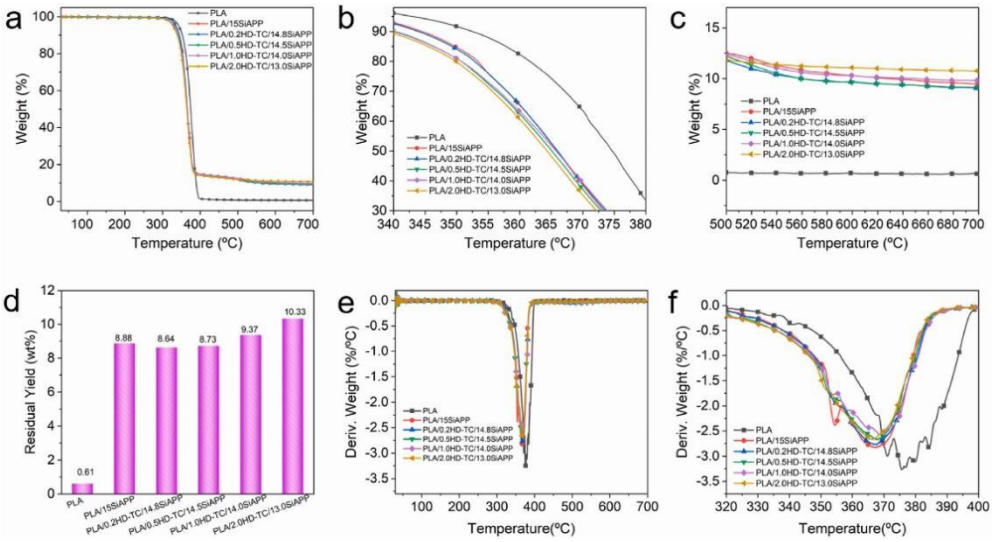

Fig. 10. (a, b and c) TG, (e, f) DTG curves and (d) char yield at 700 ºC of PLA and its composites.

Generally, MXene plays a huge role in enhancing the flame retardant properties of polymer matrices, such as TPU, PLA. MXene nanosheets function in the condensed phase via the "labyrinth effect" of nanosheets and the catalytic effect of TiO_2 nanoparticles in situ generated on the surface and edges of $Ti_3C_2T_x$ nanosheets, which can slow down the release of combustible gases into gas zone, protect the underlying polymer material from heat, and promote the charring.

1.3 Research perspectives

Though application of MXene and its derivatives in flame retarding polymeric materials has received increasing interest from the researchers, several key points are urgent to overcome. (1) MXene-based multifunctional integrated polymer composites should be further explored, e.g., electromagnetic shielding, fire alarm, flame retardant properties, and mechanical properties. (2) MXene hybrids with smaller additions and stronger performance improvements need to be further investigated. (3) The interaction mode and high-performance mechanism of MXene-based hybrids with the polymer matrix need an in-depth investigation.

Referrences

1. Yongqian Shi*, Chuan Liu, Libi Fu, et al. Highly efficient MXene/Nano-Cu smoke suppressant towards reducing fire hazards of thermoplastic polyurethane. *Composites Part A*, 2021, 150: 106600.
2. Chuan Liu, Wei Wu, Yongqian Shi*, et al. Creating MXene/reduced graphene oxide hybrid towards highly fire safe thermoplastic polyurethane nanocomposites. *Composites Part B*, 2020, 203: 108486.
3. Yognqian Shi, Chuan Liu, Zaipeng Duan, et al. Interface engineering of MXene towards super-tough and strong polymer nanocomposites with high ductility and excellent fire safety. *Chemical Engineering Journal*, 2020, 399: 125829.
4. Chuan Liu, Dong Yang, Mengnan Sun, Guojun Deng, Binghao Jing, Ke Wang, Yongqian Shi*, et al. Phosphorous-Nitrogen flame retardants engineering MXene towards highly fire safe thermoplastic polyurethane. *Composites Communications*, 2022, 29: 101055.
5. Chuan Liu, Kui Xu, Yongqian Shi*, Jiawei Wang, Suning Ma, Yuezhan Feng, et al. Fire-safe, mechanically strong and tough thermoplastic Polyurethane/MXene nanocomposites

with exceptional smoke suppression. *Materials Today Physics*, 2022, 22: 100607.

6. Chuan Liu, Ansheng Yao, Kexin Chen, Yongqian Shi*, et al. MXene based core-shell flame retardant towards reducing fire hazards of thermoplastic polyurethane. *Composites Part B*, 2021, 226: 109363.
7. Yongqian Shi*, Zixiao Wang, Chuan Liu, et al. Engineering titanium carbide ultra-thin nanosheets for enhanced fire safety of intumescent flame retardant polylactic acid. *Composites Part B*, 2022, 236: 109792.

Experiment and Numerical Simulation for Peanut Shell-based Flame Retardant combined with manganese oxide for Epoxy Resin

Jing Liang[1], Anthony Chun Yin Yuen[1,], Timothy Bo Yuan Chen[1], Wenhao Yang[2], Wei Wang[1], Shuilai Qiu[2], Yuan Hu[2], Guan Heng Yeoh[1,3]*

[1] School of Mechanical and Manufacturing Engineering, University of New South Wales, Sydney, NSW 2052, Australia;

[2] State Key Laboratory of Fire Science, University of Science and Technology of China, 96 Jinzhai Road, Hefei, Anhui 230026, PR China;

[3]Australian Nuclear Science and Technology Organisation (ANSTO), Locked Bag 2001, Kirrawee DC, NSW 2232, Australia

[*] Correspondence: c.y.yuen@unsw.edu.au; Tel.: +61 2 9385 5697; fax: +61 2 9663 1222. (A.Y.)

Abstract: Benefited by intrinsic structural properties such as the aspect ratio and heat barrier effect, two-dimensional (2D) nano-based flame retardants have shown outstanding fire performance. Herein, we reported a flake-like structure carbon derived from peanut shell (CPS) used as flame retardant for epoxy resin and exhibited a similar physical barrier effect. To further enhance the flame-retardancy of the peanut shell, CPS was designed to combine with green transition metal manganese utilising a facile method. Cone calorimeter results show that with 3wt.% addition of this flame retardant, peak heat release rate (pHRR) and total heat release (THR) can decrease dramatically by 60.2% and by 53.9%, respectively. To further comprehend the combustion process and reconstruct the cone calorimetry flaming process, a computational fluid dynamics (CFD) model was utilised and a surface regression model was uniquely embraced to simulate the fire phenomena, including thermal degradation, charring, radiation feedback and combustion of the polymer composite. The results indicate that numerical prediction is a good agreement with experimental data.

Keywords: Epoxy resin; flame retardant; peanut shell; computational fluid dynamics (CFD) model; pyrolysis kinetics.

NOMENCLATURE

A	Pre-exponential factor
c_i	Mass fraction

E_a	Activation energy
n_i	Exponent factor
R	Reaction rate
v_s	Mass fraction of the pyrolysis residue
T_s	Solid temperature
T_p	Temperature of each reaction peak
α	Conversion factor
β	Heating rate
r	Thermal degradation rate of the pyrolyzing solid

1. Introduction

In recent years, 2D nanomaterials have drawn muh attetion for the development of flame retardants (FRs). 2D nanofillers such as graphene[1,2], Layered Double Hydroxides (LDH) [3] and Hexagonal Boron Nitride (h-BN)[4] have shown excellent fire retardant efficiency due to their barrier effect and the ultra-high aspect ratio[5,6].With increasing concern on ecological health, the development of biobased materials aroused the enthusiasm of many scholars. Some explorated biomass derived carbon used as FRs for polymer matrix[7,8]. It was found that after high-temperature treatment, the biomass-derived carbon with stable backbones can lead to acceptable thermal stability and improve polymer's fire behaviours[9]. Lately, some reported studies[10,11] predicts that peanut shell derived carbon with a 2D structure is likely to be a potential FR candidate. Therefore, the effectiveness of carbonised peanut shell-based flame retardant was firstly explored for EP in our previous work[12]. In this study, to further enhance the green features while maintaining a good flame retardancy of EP, the FR is prepared by combing manganese dioxide (MnO2)[13] with CPS using a facile method.

On the other hand, the burning of EP nanocomposite involves multiple coupled and non-linear physical and chemical phenomena. While full-scale fire experiments can be performed to assess fire behaviour, they are highly costly, destructive, and produce many pollutants [14]. With the uprising of computational power and modelling technology, computational fluid dynamics (CFD) based fire models have become increasingly important for fire and materials assessment studies. To realise the fire phenomena, much effort has been made in the improvement of gas-phase models involving the fluid interactions with the fire dynamics, radiation, and turbulence[15-17]. In this work, a robust numerical approach incorporating large-eddy-simulation (LES) modelling techniques were applied[18], coupled with an in-house solid pyrolysis module that utilised the extracted thermal degradation kinetics of the underlying samples. A CFD model was built for a cone calorimeter scenario considering combustion, sub-grid-scale turbulence, radiation and soot formation, to fundamentally describe the fire behaviours involving thermal decomposition of the solid, combustion process, and charring formation of EP and its composite. The main targets of the study in this paper are as follows: (1) To develop a safe, green, and economic flame retardant: carbon derived from peanut shell combined with MnO2 by a facile method as shown in Figure 1; (2) To assess the flame retardancy, charring performance and the emissions of EP composite by conducting a series of benchmark fire tests and characterization methods;

(3) To better understand the FR mechanism, a multiphase CFD model coupled with critical chemical kinetics extracting from the pyrolysis process is applied and validated by comparing the heat release rate with cone calorimeter result.

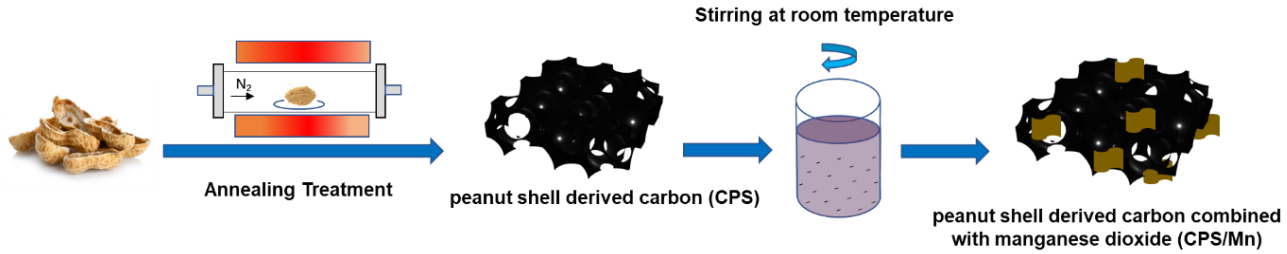

Figure 1. Schematic for fabrication process of EP/CPS/Mn

2. Experimental results

2.1 Characterisation

The micromorphology of the raw peanut shell, carbonized peanut shell (CPS), and this carbon combined with manganese dioxide (CPS/Mn) were observed by SEM. Fig 2 (a) & (b) show that before grinding, both PS and CPS own layered porous structures. In Figure 2(c), manganese dioxide can be found to grow on the surface of a carbonized peanut shell. Its element mapping image Fig. 2(d) demonstrate that the C, O, Mn elements are dispersed on the surface of CPS. Figure 2 (e) shows the XRD data of CPS/Mn. A board diffraction peak that occurs at around 21 can be observed, which appropriates graphite (002) [19]. It indicates the formation of graphite structure to some degree, ascribing to typical amorphous carbon. In addition, the reflection peaks at 18.6, 27.7 and 36.4 in the XRD pattern can be assigned to MnO_2 crystal planes (002) (003) and (100) [21, 27].

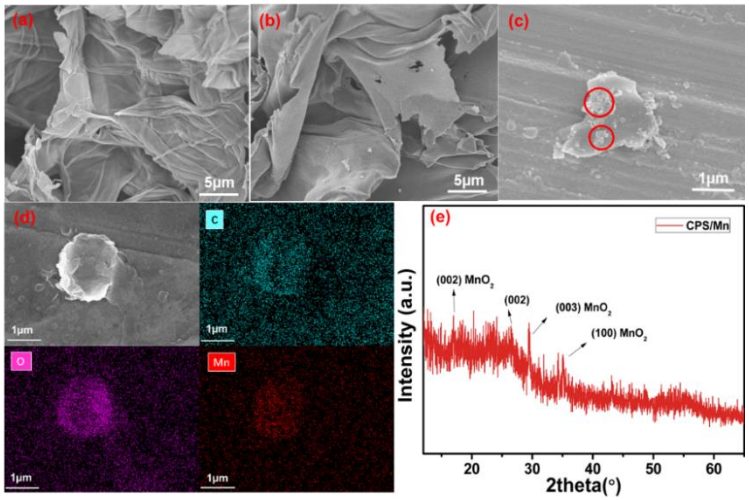

Figure 2. SEM images of (a) raw PS, (b) CPS, (c) CPS/Mn (Manganese dioxide marked by red circles), (d) element mappings for CPS/Mn, and (e) XRD patterns of CPS/Mn

2.2 Thermal stability

Thermal gravimetry (TG) and differential thermal degradation (DTG) curves of neat EP and EP/CPS/Mn are revealed in Figure 3. The correspongding detailed data are listed in Table 1. The beginning of the degradation

is widely characterized as temperature $T_{5\%}$, which denotes the temperature when the sample loses 5% of its initial weight [21]. T_{max} refers to the temperature at the peak of degradation. In Figure 3 (a), EP and EP/CPS/Mn show similar thermal decomposition behaviour. Only one peak in the DTG curve can be observed, which is mainly accredit to the breaking of macromolecular chains[22]. Compared to EP, CPS combined with MnO_2 leads to a slight decrease of $T_{5\%}$ and T_{max} and bring a bit earlier start of the thermal degradation. Whereas, the char residue of EP/CPS/Mn increases significantly, from 15.87% to 21.04%. Furthermore, Figure 3 (b) DTG curve illustrates that the addition of CPS/Mn into EP can reduce the maximum mass loss rate from 1.63%/min to 1.53%/min, restraining mass loss during the pyrolysis process.

Table 1. TGA data of EP and EP/CPS/Mn

Samples	Under nitrogen		
	$T_{-5\%}$ (℃)	T_{max} (℃)	Char residue at 800 ℃ (%)
EP	361.96	377.38	15.87
EP/CPS/Mn	337.05	363.54	21.04

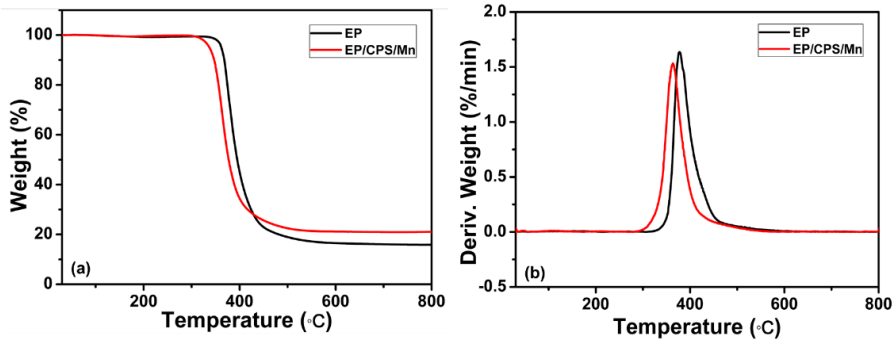

Figure 3. (a) TG and (b) DTG results for neat EP and EP/CPS/Mn under N2 at a heating rate of 10℃/min.

2.3 Cone Calarometer test

Critical parameters in cone calorimeter test were measured and displayed in Fig 4. (a-d). What needs illustration is that the calorimeter test data for neat EP are cited from our previous work[12]. The curves display that after ignition, neat EP burns fast and reach high PHRR and THR, with the numerical value of 1313 kw/m^2 and 102 MJ/m^2, respectively[12]. While for EP/CPS/Mn, 3 wt.% addition of FR brings a little earlier initiation of HRR, THR &TSR. However, compared with neat EP the corporation of CPS/Mn leads to a significant drop of pHRR to 523 kw/m^2 (appropriate 60.2% reduction) and THR to 47 MJ/m^2 (appropriate 53.9% reduction). The value of SPR also decreased by 14.2%, from 2501 m^2/m^2 to 2147 m^2/m^2. The results indicate that the loading of CPS/Mn can markedly lower the fire risk of EP.

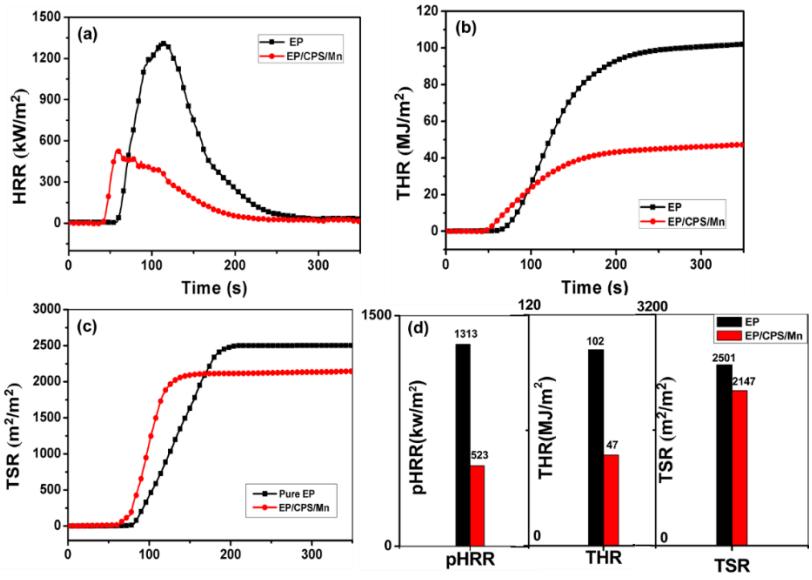

Figure 4. (a) HRR, (b) THR, (c) TSR as a function of the burning time, (d) summarised cone calorimeter data for EP and EP/CPS/Mn.

2.4 Charring Formation Performance

Figure 5 displays the digital photos of char residue and corresponding SEM interior & exterior images. In the digital photos Fig 5 (a)[12], fragile char residue can be observed for pure EP. For EP/CPS/Mn, char residue is promoted effectively, covering with yellow substance, and becoming compact, due to the catalysis effect of MnO_2. In Fig 5 (b-c), we can see multiple cracks and wrinkles on the surface and large size holes inside the char residue of pure EP. While for EP/CPS/Mn in Fig 5(e-f), the exterior char residue is denser, and the interior displays a porous structure with a smaller size. The compact charring formation can help to inhabit heat and volatile gas infiltration, which leads to better thermal stability and fire performance.

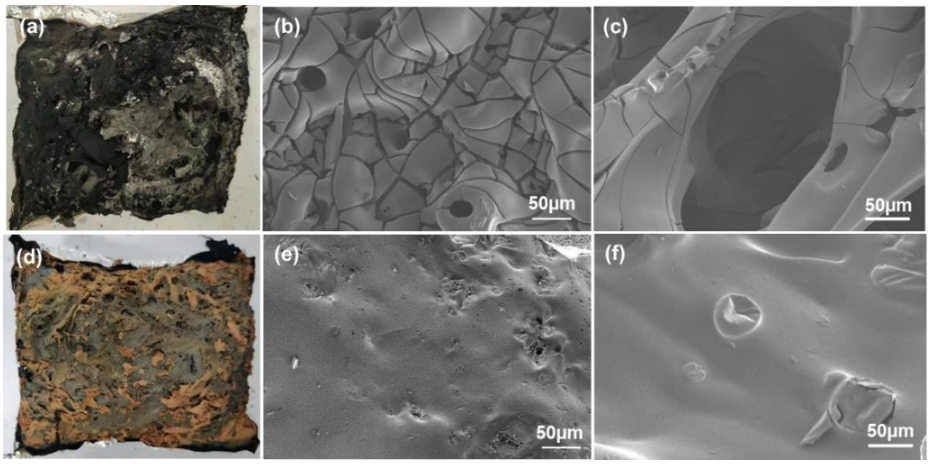

Figure 5. Digital char residue photos of (a)pure EP[12] and (d)EP/CPS/Mn, SEM images for char residue: interior (b) & exterior(c) for EP and interior (e) &exterior (f) for EP/CPS/Mn.

XPS C1s spectra of char residue of EP (cited from our previous work [12]) and EP/CPS/Mn are displayed in Fig 6 (a) and (b). The characteristic bands at 288.4, 286.8 and 284.6eV belong to C=O (carboxylic groups), C-O (ether and/or hydroxy), and C-C (aromatic and aliphatic species), respectively[23]. The thermal

oxidation resistance of the char residue can be compared by calculating the values of Cox/Ca. The lower Cox/Ca value of EP/CPS/Mn (0.43) than pure EP (0.7) means more aromatic and aliphatic carbons in char residue, suggesting the addition of CPS/Mn postpone the oxidation of materials and better fire retardancy [24].

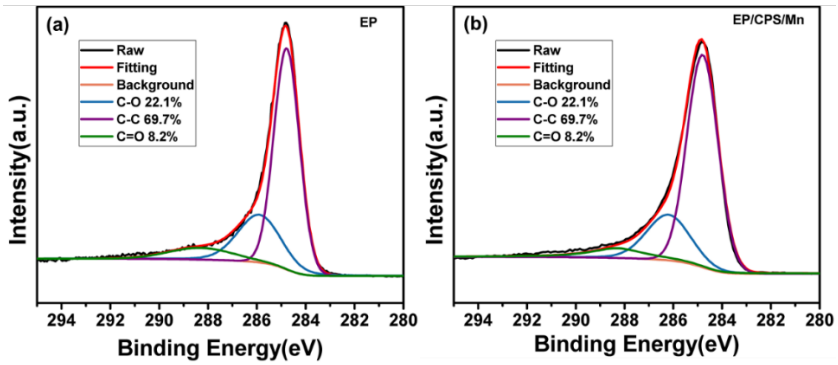

Fig 6. XPS C1s spectra of interior char residue for (a) pure EP and (b) EP/CPS/Mn.

2.5 Gaseous Volatiles Analysis

The release gases of EP (cited from our previous work [12]) and EP/CPS/Mn are investigated by TG-FTIR under nitrogen. Fig 7 (a) displays the FTIR spectra of pyrolysis products at the peak of degradation. Characteristic FTIR signals show that EP and EP/CPS/Mn have similar evolved gaseous volatiles, including kinds of hydrocarbons, CO, CO_2 and aromatic compounds[32, 33]. Fig 7 (b-f) show total volatiles intensity and FTIR absorbance of gaseous products versus temperature. Compared with neat EP, it can be found that much lower gaseous products for EP/CPS/Mn although the start of releasing the volatiles is a little bit earlier. Moreover, the results show that with the addition of CPS/Mn, EP composite release much less volatiles than neat EP. The reduction of toxic gas such as CO is meaningful, which can be beneficial for fire rescue operations. Furthermore, hydrocarbons and aromatic compounds are combustible gases. The simultaneous suppression of these gaseous products can lead to a drop of fuel for combustion and smoke formation [27].

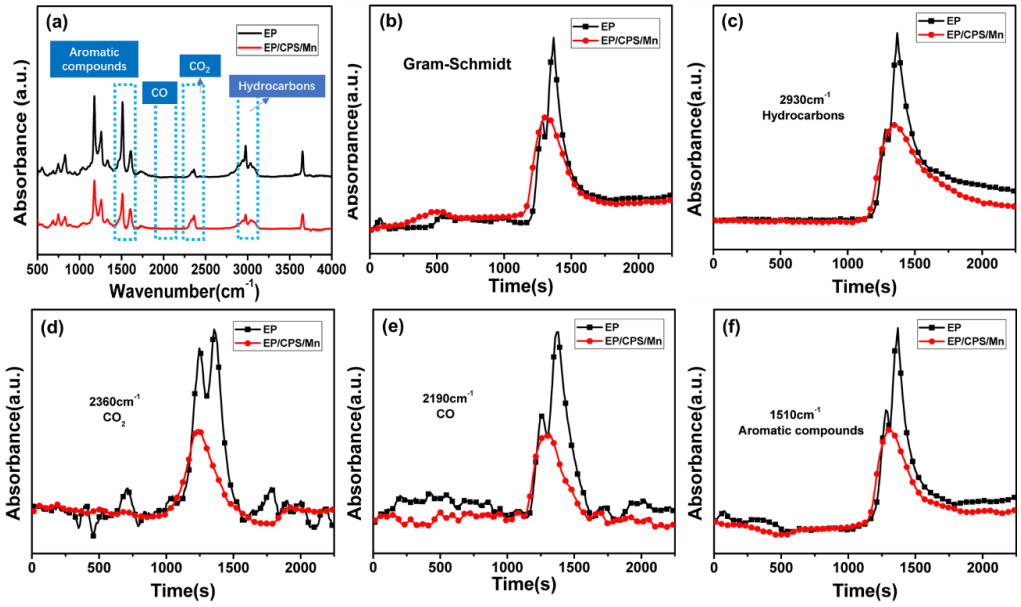

Figure 7. (a) FTIR spectra of pyrolysis gaseous products at the peak of decomposition, (b) Gram-Schmidt curves, (c–f) Absorbance of hydrocarbons, CO_2, CO and aromatic compounds

3. Numerical method and results

A Large Eddy Simulation (LES) based pyrolysis model developed from our previous works [28, 35] was applied. It is tailor-made for fire field pyrolysis simulation uniquely embraced with subgrid-scale (SGS) turbulence, combustion, soot formation and radiation sub-modelling components. The Favre-filtered transport equations for mass, momentum and energy are resolved under the low Mach number assumption[28].

3.1 Pyrolysis Model

The thermal degradation rate of the pyrolyzing solid is determined from an Arrhenius expression:

$$r = (1 - v_s)\, A\, exp\left(-\frac{E_a}{RT_s}\right)(1-\alpha)^n$$

where A is the pre-exponential factor, E_a is the activation energy, v_s is the mass fraction of the pyrolysis residue and α is the conversion factor. The solid temperature T_s is resolved using a one-dimensional heat equation that takes into account solid conduction, net heat gain/loss due to chemical reactions during solid decomposition and radiative heat transfer.

3.2 Turbulence, Combustion and Radiation Models

The turbulence modelling was handled by the Smagorinsky SGS model with a default value of 0.2 for the Smagorinsky constant[37, 38]. It is a highly robust model that has been widely employed and validated for a wide range of numerical fire studies[39-41]. The combustion was implemented via the strained laminar flamelet approach for non-premixed flame incorporating GRI-Mech version 3.0. The soot formation was modelled using the Moss-Brooke two-equation model[33]. For radiation, the standard filtered radiative transfer equations (FRTE) for non-scattering grey gas was solved by the discrete ordinates method (DOM)[34].

3.4. Validation of pyrolysis kinetics

The kinetic parameters were approximated from the derivative thermogravimetry (DTG) data[35,44]. The method is based on the Kissinger-Akahira-Sunose (KAS) method [18]combined with a genetic algorithm (GA). The pyrolysis kinetics for pure EP and CPS/Mn/EP are shown in Table 2. The numerical simulation was validated against heat release rate (HRR) results from the cone calorimeter tests. The numerical predictions and experimental HRR and THR profiles are shown in Figures 8 & 9. It can be found that the HRR profiles are in agreement with the numerical results. The general trends and the burning durations were captured in the simulation. In terms of THR, both results for EP and EP/CPS/Mn were successfully predicted with a relative error of 6.5% and 2.3% compared to the experiments, respectively. The results demonstrated that the burning behaviour of EP and EP/CPS/Mn were reasonably captured in the adopted fire model.

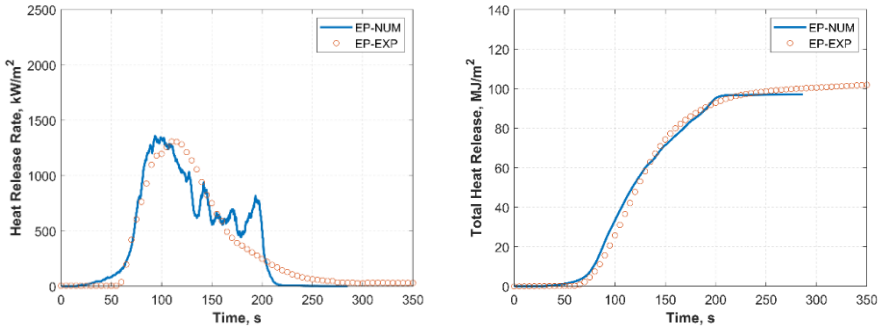

Figure 8. Plot of the numerical and experimental heat release rate curves for Pure EP

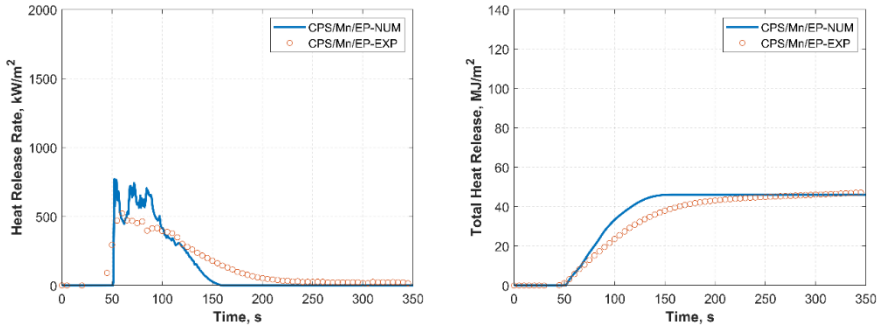

Figure 9. Plot of the numerical and experimental heat release rate curves for EP/CPS/Mn

Table 2. Pyrolysis kinetics of pure epoxy (EP) and EP/CPS/Mn

Sample	E_i	A_i	c_i	n_i
Pure EP	1.650E+05	1.640E+11	1	1.28
EP/CPS/Mn	2.14E+05	4.84E+15	1	2.3

3.5 Flame visualization, ignition time and burning duration

The flaming behaviour of the EP samples from the cone calorimeter simulations is presented in Figure 10. The first time step with visible flame was observed at approximately t = 50 s, which was 33.3% earlier than the experimental ignition time of 75 s. The discrepancy can be attributed to the approximation errors introduced in the pyrolysis kinetic extracted from TGA and the time of ignition & extinction recorded

manually based on flame observation. What's more, the combustion model applied is derived from the mixture fraction. This means that there will be instantaneous heat release when fuel is emitted from the solid surface, while in reality, there will be an initial built-up of fuel before ignition from the ignition spark. After ignition, the flame fully develops by t = 100 s, gradually reducing until extinguishing at 219s. The numerical predictions were 21.9% earlier than the experimental time of 281s. The discrepancy may be attributed to the prolonged small amount of HRR at the decline phase of the fire in the experiment due to the smouldering flame of the char residue. These char oxidation effects were not considered during the simulation. Despite these discrepancies at ignition and extinction of the flame, the overall flaming profile was aptly captured by the fire model, as demonstrated by the HRR comparisons shown in Figures 8 and 9. The detailed comparisons of the ignition time, burn duration and extinguishment are summarised in Table 3. In summary, the numerical results highlight the fire model's capability to provide detailed predictions of the ignition/extinction, flame spread, and combustion during the pyrolysis process. It can also present temporal visualization of the fluctuating flame motion at the surface of the burning material.

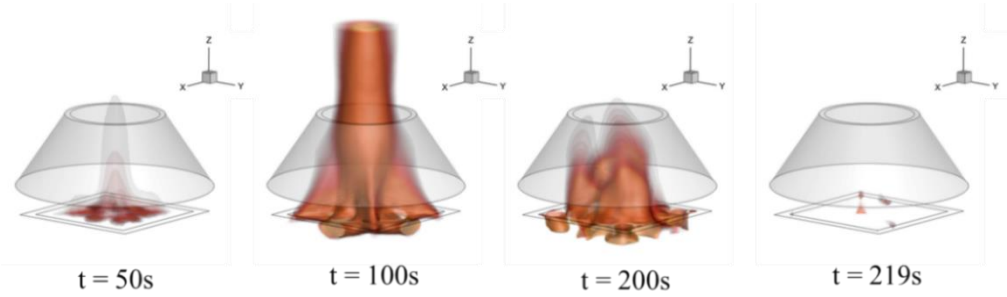

Figure 10. Three-dimensional flame visualization for 35kW/m^2 cone calorimeter simulation for EP.

Table 3. Comparison of experiment and model predictions for ignition time, burning duration, extinguishment, and total heat release rate (THR) for EP and EP/CPS/Mn.

	Experiment	Model	Relative Error
Pure EP			
Ignition time	75s	50s	33.3%
Burn duration	206s	169.4s	17.8%
Extinguishment	281s	219.4s	21.9%
Total heat release (THR)	103.76827	97	6.5%
EP/CPS/Mn			
Ignition time	61s	51.3	15.9%
Burn duration	161s	107.1	33.5%
Extinguishment	222s	158.4	28.6%
Total heat release (THR)	47.18	46.1	2.3%

4. CONCLUSIONS

In this paper, an eco-friendly and green flame retardant, peanut shell derived carbon combined with manganese oxide was developed to improve the fire performance of epoxy resin. The results illustrate that the sample encapsulates a sheet-like structure due to the layer structure of the peanut shell. The thermal stability and flame behaviour were assessed by TGA and cone calorimeter test. Compared with neat EP, 3wt.%

addition of CPS/Mn leads to a significant increase of charring during the pyrolytic reaction and dramatic reduction of peak heat release rate and total heat release rate, respectively by 60.2% and by 53.9%. Furthermore, a systematic in-house LES-based numerical modelling was applied, including kinetics extracted by the genetic algorithm to account for the fundamental thermal degradation rate. The computational and experimental results indicate that good agreement has been achieved for TG characterization, HRR and THR from the cone calorimeter. What's more, this model can describe the change of some key parameters over time during the pyrolysis process, including the ignition/extinction, flame spread and combustion, and also capture the flickering flame motion. As for the future perspective of this research work, this numerical model can be upscaled to realistic fire scenarios for building material evaluation and fire tenability analyses.

REFERENCES

[1] G. Huang, J. Gao, X. Wang, H. Liang, C. Ge, How can graphene reduce the flammability of polymer nanocomposites?, Mater. Lett. 66 (2012) 187–189. https://doi.org/10.1016/j.matlet.2011.08.063.

[2] Y.R. Lee, S.C. Kim, H. Il Lee, H.M. Jeong, A. V. Raghu, K.R. Reddy, B.K. Kim, Graphite oxides as effective fire retardants of epoxy resin, Macromol. Res. 19 (2011) 66–71. https://doi.org/10.1007/s13233-011-0106-7.

[3] S. Elbasuney, Surface engineering of layered double hydroxide (LDH) nanoparticles for polymer flame retardancy, Powder Technol. 277 (2015) 63–73. https://doi.org/10.1016/j.powtec.2015.02.044.

[4] W. Cai, N. Hong, X. Feng, W. Zeng, Y. Shi, Y. Zhang, B. Wang, Y. Hu, A facile strategy to simultaneously exfoliate and functionalize boron nitride nanosheets via Lewis acid-base interaction, Chem. Eng. J. 330 (2017) 309–321. https://doi.org/10.1016/j.cej.2017.07.162.

[5] X. Wang, E.N. Kalali, D.-Y. Wang, Two-Dimensional Inorganic Nanomaterials: A Solution to Flame Retardant Polymers, Nano Adv. (2016). https://doi.org/10.22180/na155.

[6] X. Yue, C. Li, Y. Ni, Y. Xu, J. Wang, Flame retardant nanocomposites based on 2D layered nanomaterials: a review, J. Mater. Sci. 54 (2019) 13070–13105. https://doi.org/10.1007/s10853-019-03841-w.

[7] K. Babu, G. Rendén, R.A. Mensah, N.K. Kim, L. Jiang, Q. Xu, Á. Restás, R.E. Neisiany, M.S. Hedenqvist, M. Försth, A. Byström, O. Das, A review on the flammability properties of carbon-based polymeric composites: State-of-the-art and future trends, Polymers (Basel). 12 (2020) 1–19. https://doi.org/10.3390/polym12071518.

[8] A.C.S. Omega, Intumescent-grafted bamboo charcoal : A natural nontoxic fire-retardant filler for polylactic acid (PLA) composites Intumescent-grafted bamboo charcoal : A natural nontoxic fire-retardant filler for polylactic acid (PLA) composites, (2021).

[9] S. Matta, M. Bartoli, A. Frache, G. Malucelli, Investigation of different types of biochar on the thermal stability and fire retardance of ethylene-vinyl acetate copolymers, Polymers (Basel). 13 (2021). https://doi.org/10.3390/polym13081256.

[10] M.F. Wu, C.H. Hsiao, C.Y. Lee, N.H. Tai, Flexible Supercapacitors Prepared Using the Peanut-Shell-Based Carbon, ACS Omega. 5 (2020) 14417–14426. https://doi.org/10.1021/acsomega.0c00966.

[11] J. Ding, H. Wang, Z. Li, K. Cui, D. Karpuzov, X. Tan, A. Kohandehghan, D. Mitlin, Peanut shell hybrid sodium ion capacitor with extreme energy-power rivals lithium ion capacitors, Energy Environ. Sci. 8 (2015) 941–955. https://doi.org/10.1039/c4ee02986k.

[12] J. Liang, W. Yang, A.C.Y. Yuen, H. Long, S. Qiu, I.M. De Cachinho Cordeiro, W. Wang, T.B.Y. Chen, Y. Hu, G.H. Yeoh, Peanut shell derived carbon combined with nano cobalt: An effective flame

retardant for epoxy resin, Molecules. 26 (2021) 1–14. https://doi.org/10.3390/molecules26216662.

[13] W. Wang, Y. Kan, B. Yu, Y. Pan, K.M. Liew, L. Song, Y. Hu, Synthesis of MnO2 nanoparticles with different morphologies and application for improving the fire safety of epoxy, Compos. Part A Appl. Sci. Manuf. 95 (2017) 173–182. https://doi.org/10.1016/j.compositesa.2017.01.009.

[14] T.B.Y. Chen, A.C.Y. Yuen, G.H. Yeoh, W. Yang, Q.N. Chan, Fire risk assessment of combustible exterior cladding using a collective numerical database, Fire. 2 (2019) 1–14. https://doi.org/10.3390/fire2010011.

[15] T.B.Y. Chen, A.C.Y. Yuen, C. Wang, G.H. Yeoh, V. Timchenko, S.C.P. Cheung, Q.N. Chan, W. Yang, Predicting the fire spread rate of a sloped pine needle board utilizing pyrolysis modelling with detailed gas-phase combustion, Int. J. Heat Mass Transf. 125 (2018) 310–322. https://doi.org/10.1016/j.ijheatmasstransfer.2018.04.093.

[16] C. Wang, A.C.Y. Yuen, Q.N. Chan, T.B.Y. Chen, Q. Chen, R. Cao, H.L. Yip, S. Kook, G.H. Yeoh, Influence of eddy-generation mechanism on the characteristic of on-source fire whirl, Appl. Sci. 9 (2019). https://doi.org/10.3390/app9193989.

[17] A.C.Y. Yuen, G.H. Yeoh, S.C.P. Cheung, Q.N. Chan, T.B.Y. Chen, W. Yang, H. Lu, Numerical study of the development and angular speed of a small-scale fire whirl, J. Comput. Sci. 27 (2018) 21–34. https://doi.org/10.1016/j.jocs.2018.04.021.

[18] A.C.Y. Yuen, T.B.Y. Chen, C. Wang, W. Wei, I. Kabir, J.B. Vargas, Q.N. Chan, S. Kook, G.H. Yeoh, Utilising genetic algorithm to optimise pyrolysis kinetics for fire modelling and characterisation of chitosan/graphene oxide polyurethane composites, Compos. Part B Eng. 182 (2020) 107619. https://doi.org/10.1016/j.compositesb.2019.107619.

[19] T. Qiu, J.G. Yang, X.J. Bai, Y.L. Wang, The preparation of synthetic graphite materials with hierarchical pores from lignite by one-step impregnation and their characterization as dye absorbents, RSC Adv. 9 (2019) 12737–12746. https://doi.org/10.1039/c9ra00343f.

[20] W. Wang, Y. Pan, H. Pan, W. Yang, K.M. Liew, L. Song, Y. Hu, Synthesis and characterization of MnO2 nanosheets based multilayer coating and applications as a flame retardant for flexible polyurethane foam, Compos. Sci. Technol. 123 (2016) 212–221. https://doi.org/10.1016/j.compscitech.2015.12.014.

[21] B. Lin, A.C.Y. Yuen, T.B.Y. Chen, B. Yu, W. Yang, J. Zhang, Y. Yao, S. Wu, C.H. Wang, G.H. Yeoh, Experimental and numerical perspective on the fire performance of MXene/Chitosan/Phytic acid coated flexible polyurethane foam, Sci. Rep. 11 (2021) 1–13. https://doi.org/10.1038/s41598-021-84083-2.

[22] K. Zhou, J. Liu, Y. Shi, S. Jiang, D. Wang, Y. Hu, Z. Gui, MoS2 nanolayers grown on carbon nanotubes: An advanced reinforcement for epoxy composites, ACS Appl. Mater. Interfaces. 7 (2015) 6070–6081. https://doi.org/10.1021/acsami.5b00762.

[23] W. Wang, H. Pan, Y. Shi, Y. Pan, W. Yang, K.M. Liew, L. Song, Y. Hu, Fabrication of LDH nanosheets on β-FeOOH rods and applications for improving the fire safety of epoxy resin, Compos. Part A Appl. Sci. Manuf. 80 (2016) 259–269. https://doi.org/10.1016/j.compositesa.2015.10.031.

[24] S. Bourbigot, M. Le Bras, R. Delobel, L. Gengembre, XPS study of an intumescent coating, Appl. Surf. Sci. 120 (1997) 15–29. https://doi.org/10.1016/s0169-4332(97)00239-0.

[25] S. Qiu, B. Zou, T. Zhang, X. Ren, B. Yu, Y. Zhou, Y. Kan, Y. Hu, Integrated effect of NH2-functionalized/triazine based covalent organic framework black phosphorus on reducing fire hazards of epoxy nanocomposites, Chem. Eng. J. 401 (2020) 126058. https://doi.org/10.1016/j.cej.2020.126058.

[26] P.J. Wang, D.J. Liao, X.P. Hu, N. Pan, W.X. Li, D.Y. Wang, Y. Yao, Facile fabrication of biobased P–N–C-containing nano-layered hybrid: Preparation, growth mechanism and its efficient fire retardancy in epoxy, Polym. Degrad. Stab. 159 (2019) 153–162. https://doi.org/10.1016/j.polymdegradstab.2018.11.024.

[27] D. Wang, Q. Zhang, K. Zhou, W. Yang, Y. Hu, X. Gong, The influence of manganese-cobalt oxide/graphene on reducing fire hazards of poly(butylene terephthalate), J. Hazard. Mater. 278 (2014) 391–400. https://doi.org/10.1016/j.jhazmat.2014.05.072.

[28] A.C.Y. Yuen, G.H. Yeoh, Numerical simulation of an enclosure fire in a large test hall, Comput. Therm. Sci. 5 (2013) 459–471. https://doi.org/10.1615/ComputThermalScien.2013005954.

[29] A.L.K. Cheung, E.W.M. Lee, R.K.K. Yuen, G.H. Yeoh, S.C.P. Cheung, Capturing the pulsation frequency of a buoyant pool fire using the large eddy simulation approach, Numer. Heat Transf. Part A Appl. 53 (2008) 561–576. https://doi.org/10.1080/10407780701678414.

[30] J.X. Wen, K. Kang, T. Donchev, J.M. Karwatzki, Validation of FDS for the prediction of medium-scale pool fires, Fire Saf. J. 42 (2007) 127–138. https://doi.org/10.1016/j.firesaf.2006.08.007.

[31] G. Maragkos, B. Merci, On the use of dynamic turbulence modelling in fire applications, Combust. Flame. 216 (2020) 9–23. https://doi.org/10.1016/j.combustflame.2020.02.012.

[32] T.B.Y. Chen, A.C.Y. Yuen, G.H. Yeoh, V. Timchenko, S.C.P. Cheung, Q.N. Chan, W. Yang, H. Lu, Numerical study of fire spread using the level-set method with large eddy simulation incorporating detailed chemical kinetics gas-phase combustion model, J. Comput. Sci. 24 (2018) 8–23. https://doi.org/10.1016/j.jocs.2017.10.022.

[33] A.C.Y. Yuen, G.H. Yeoh, V. Timchenko, T.B.Y. Chen, Q.N. Chan, C. Wang, D.D. Li, Comparison of detailed soot formation models for sooty and non-sooty flames in an under-ventilated ISO room, Int. J. Heat Mass Transf. 115 (2017) 717–729. https://doi.org/10.1016/j.ijheatmasstransfer.2017.08.074.

[34] A.S. Jamaluddin, P.J. Smith, Predicting Radiative Transfer in Rectangular Enclosures Using the Discrete Ordinates Method, Combust. Sci. Technol. 59 (1988) 321–340. https://doi.org/10.1080/00102208808947103.

[35] A.C.Y. Yuen, T.B.Y. Chen, G.H. Yeoh, W. Yang, S.C.P. Cheung, M. Cook, B. Yu, Q.N. Chan, H.L. Yip, Establishing pyrolysis kinetics for the modelling of the flammability and burning characteristics of solid combustible materials, J. Fire Sci. 36 (2018) 494–517. https://doi.org/10.1177/0734904118800907.

Improving flame retardant and EMI shielding properties of PLA/PCL composites using catalytic imidazolium modified CNTs and ammonium polyphosphate

Zhenfeng Wang, Tong Yan, Jiaying Tu, Rui Cheng, Pei Xu, Yunsheng Ding**

Department of Polymer Science and Engineering, School of Chemistry and Chemical Engineering, and Anhui Key Laboratory of Advanced Functional Materials and Devices, Hefei University of Technology, Hefei 230009, China

ABSTRACT: The flame retardants and electromagnetic interference (EMI) shielding performance were enhanced by using imidazolium-functionalized polyurethane (IPU) modified multi-walled carbon nanotubes (CNTs) and ammonium polyphosphate (APP) for polylactic acid (PLA)/polycaprolactone (PCL) composites. The PLA/PCL/10APP/8CNT/1.6IPU composite containing 10 wt% APP and 8 wt% imidazolium modified CNTs reached the limiting oxygen index (LOI) value of 30.3 % and passed the V-0 rating in UL-94 tests. Moreover, the peak of the heat release rate (*p*HRR) and total heat release (THR) for this composite reached around 302 kW/m^2 and 64 KJ/m^2, which were decreased by 39.1 % and 15.8 % compared with that of PLA/PCL/10APP composite. The improved flame retardancy was attributed to the interplay of catalytic, barrier, and condensed char forming of imidazolium-modified CNTs and APP. IPU expanded to the phase interface between PLA and PCL as an interfacial compatibilizer and regulated the migration of more CNTs to disperse at the two-phase interface. The dispersion of imidazolium-modified CNTs and co-continuous phase structure of the composites can establish continuous conductive pathways. The PLA/PCL/APP/CNT/IPU composite obtained a higher conductivity than that of the PLA/PCL/APP/CNT composite and whose EMI SE reached 33.9 dB. This work offered a novel methodology for fabricating composites with excellent EMI SE and flame-retardant properties, which were promising candidates for next-generation sustainable and protective plastics.

Keywords: Polylactic acid; Polymer-matrix composites; Electromagnetic interference

* Corresponding author.

E-mail addresses: chxuper@hfut.edu.cn (P. Xu), dingys@hfut.edu.cn (Y. Ding).

shielding; Interface/interphase; Flame retardant

1. Introduction

Due to excellent tensile strength, easy availability, biodegradability, and processability, polylactic acid (PLA) was considered to have the most potential to alleviate environmental problems caused by traditional petroleum-based polymers [1-4]. However, PLA has shortcomings such as poor toughness and high flammability that seriously hinder its further large-scale application in packaging, electronic, and electrical engineering fields [5,6]. Polymer blending was considered to be the simplest and most effective way to improve mechanical properties, and the flexible polymers such as poly(butylene adipate-co-terephthalate) (PABT), polybutylene succinate (PBS), and polycaprolactone (PCL) can be used to improve the toughness of PLA [7-10]. Due to good biocompatibility, biodegradability, and high toughness, PCL had been used to toughen PLA [11]. However, the compatibility between PLA and PCL was poor, which resulted in an insignificant increase in the toughness of the blends [12]. Therefore, extensive efforts have been made to overcome this deficiency, and the compatibilizer copolymers containing ionic liquid moiety contributed to boosting the miscibility. Wang et. al had been used successfully the poly(methoxy poly(ethylene glycol) monomethacrylateco-1-vinyl-3-ethylimidazolium bromide) and poly(ε-caprolactone)-b-poly(ethylene glycol) block copolymer containing ionic liquid group for improving the compatibility of PLA/PCL blends [13,14].

Despite the tremendous potential of PLA, it was faced with severe intrinsic flammability and melt dripping during combustion as typical linear aliphatic polyester [15-17]. The vast studies showed that the ammonium polyphosphate (APP) was considerably effective in improving the

flame retardancy of PLA [18-23]. Phosphorus flame retardants could facilitate the carbonization of the polymer during combustion and form dense and complete carbon layers to effectively protect underlying material and prevent free radical reactions. Li et al. introduced a biobased unsaturated polyester and APP via dynamic vulcanization into PLA substrates and found that only 20 wt% APP can make PLA exhibit a high LOI of 27% and pass the UL-94 V0 test [20]. However, PLA/APP composites can not fundamentally solve the characteristics of polyester easy to melt drops. With the booming development of nanotechnology, multi-walled carbon nanotubes (CNTs) were very helpful to improve the flame retardancy as well as melt-drop resistance of PLA because of the increase of the melt viscosity and physical barrier effect of CNTs [24-26]. Yang et al. applied calcium-magnesium phytate and acid-modified CNTs as flame retardants for PLA, indicating that the *p*HRR of PLA composites was reduced by 35 % [25]. In recent years, research interest has been gradually transferring to the combination of carbon-based fillers and APP that significantly improved thermal stability and flame retardancy of polymers [21,27,28]. Yue et al. introduced aminated CNTs electrostatically coated with APP and intumescent flame retardant (IFR) into PBS, which found that the THR of PBS/19%IFR/1%CNT@APP-1 composite was reduced by 79.6% [28]. Imidazolium ionic liquids (ILs) can facilitate CNTs dispersion owning to strong cation-π interactions between imidazolium ILs and CNTs without changing the structural features and physical characteristics of CNTs [29,30]. Additionally, CNTs decorated with imidazolium chloride can play a catalytic role [31]. Interestingly, some ILs containing functional phosphorus groups can act as an efficient flame retardant [32-34]. Our previous work also focused on promoting flame retardant PLA through melt blending with CNTs modified by tri(1-hydroxyethyl-3-methylimidazolium

chloride) phosphate due to the ionic-π stacking interaction between ILs and CNTs [31].

Electromagnetic interference (EMI) shielding has become an urgent concern in contemporary society with the prosperous development of electronic and telecommunications devices [35-38]. Conductive polymer composites (CPCs) containing conductive fillers i.e., carbon black, carbon fiber, and CNTs, were attractive in low density, lightweight, designed flexibly, and resistant to corrosion compared with traditional metal-based EMI shielding materials [39,40]. However, conventional CPCs could only achieve excellent EMI shielding effectiveness (SE) with high conductive fillers loadings, which could lead to high cost, difficult fabrication, and deteriorated mechanical properties [41]. Thus, lots of strategies such as constructing double percolation and segregated structures had been designed to significantly improve the EMI shielding with lower content of conductive fillers [42]. The EMI SE of POK/PVDF/CNTs composites was remarkably improved because the CNTs selective positioned in the POK stage, which was favorable for the improvement of conductivity [43]. PLA/PCL/CNTs composites with co-continuous structure had high EMI SE because of the selective targeting of CNTs in the PCL phase and PLA/PCL interface [44,45].

Herein, halogen-free imidazolium-functionalized polyurethane (IPU) was fabricated by the facile one-pot from IPDI, [bimd][Br], OH-PCL-OH, and the subsequent ion exchange of $H_2PO_4^-$, and its chemical structure was characterized. The combination of APP, CNTs, and IPU was incorporated into PLA/PCL composites to improve flame retardancy and EMI shielding properties. CNTs modified by IPU not only acted as conductive fillers based on excellent conductivity and high aspect ratio to enhance EMI SE but also were considered as a nano-flame retardant to reduce the inflammability. Furthermore, the collaborative mechanisms with flame

retardancy and EMI shielding of PLA/PCL composites were also evaluated.

2. Experimental section

2.1. Materials

Polylactic acid (PLA 6201D) was from Nature Works Co. Ltd., USA. Polycaprolactone (PCL CAPA6800) was purchased from Solvay Ltd., Belgium. Multi-walled carbon nanotubes (CNTs, diameter 10-20 nm, aspect ratio 1000-1500) were provided by Nanjing XFNANO Materials Tech Co., Ltd., China. APP (P % = 32.0 wt %, JLS-APP-103N) was provided by Hangzhou JLS Flame Retardants Chemical Co., Ltd., China. Synthesis and characterization of imidazolium-functionalized polyurethane (IPU) containing PCL chain segment and IPU modified CNTs are shown in Fig. S1-S5.

2.2. Sample preparation

Table 1. Component of PLA/PCL composites.

Sample	PLA:PCL=5:5 (g)	CNT (g)	IPU (g)	APP (g)	Total (g)
PLA/PCL/10APP	22.5:22.5	0	0	5	50
PLA/PCL/15APP	21.3:21.2	0	0	7.5	50
PLA/PCL/10APP/6CNT	21.0:21.0	3	0	5	50
PLA/PCL/10APP/8CNT	20.5:20.5	4	0	5	50
PLA/PCL/10APP/4CNT/0.8IPU	21.3:21.3	2	0.4	5	50
PLA/PCL/10APP/6CNT/1.2IPU	20.7:20.7	3	0.6	5	50
PLA/PCL/10APP/8CNT/1.6IPU	20.1:20.1	4	0.8	5	50

Samples were fabricated using a torque rheometer. Briefly, PLA, PCL, APP, CNTs, and IPU with a specific mass ratio were mixed in an XSS-300 torque rheometer at 180 ℃ and 50 rpm for 6 min. After that, the composites were molded by hot-pressing into standard samples for 10

min under 190 ℃ and 5 MPa. Table 1 displays the composition of the PLA/PCL composites with different formulations.

2.3. Characterization

The thermogravimetric analysis (TGA) tests had been proceeded by Netzsch TG 209 F3 instrument with an N_2 atmosphere, whose temperature range was from 40 to 700 ℃ and a heating rate was 10 ℃ min^{-1}. The limited oxygen index (LOI) values can be obtained by an oxygen index meter (JF-3, Jiangning, CHN) following ISO 4589 and each sample was 130×6.5×3.2 mm^3 in size. UL-94 tests had been carried out with a CZF-2 vertical burning test instrument (Jiangning, China) and the size of 100×13×3 mm^3 following ASTM D3801. The cone calorimeter test (CCT) was evaluated by cone calorimeter device (VOUCH, China) following ISO 5660 using a heat flux of 50 kW/m^2 and the specimen was 100×100×3 mm^3 in size. The tensile tests were carried out on a universal testing machine (CMT4304, MTS) following ISO-527 using a speed of 5 mm min^{-1}. Morphologies of fractured surfaces of PLA/PCL composites were characterized using SEM (JEOL, JSM-6490LV), and TEM (JEM-2100F, JEOL). Morphologies of char layers were observed with SEM. The Raman spectroscopy had been obtained by a Raman spectrometer (LABRAM-HR), whose excitation wavelength was 532 nm. TG-IR measurements were carried out on PerkinElmer TGA 4000 attaching Spectrum Two FT-IR spectrometer and the sample was heated from 30 to 700 ℃ at a heating rate of 10 ℃/min under N_2 flow. A vector network analyzer (N5247A, Agilent Technologies) was used to obtain the EMI SE at 8.2-12.4 GHz and each specimen with 8×8×1 mm^3 in size. S parameters were used to assess the EMI SE shielding behavior of the samples, including SE_T (total shielding effectiveness), SE_R (reflection loss), and SE_A (absorption loss).

3. Results and discussion

3.1. Flame-retarding properties

Firstly, the effect of imidazolium modified CNTs and APP on PLA/PCL composites was conducted to study by LOI and UL-94 test, and specific data excited in Table 2. Although the LOI was slightly improved to 24.8 % after the incorporation of 15wt % APP, the UL-94 rating was categorized in V-1 due to the serious dripping [20,21]. As the loading of CNTs rose from 6wt % to 8wt %, LOI of PLA/PCL composite increased from 28 % to 30 %, and the UL-94 rating achieved V-0 without any dripping. In addition, imidazolium-modified CNTs increased the LOI value of PLA/PCL composites. The LOI of PLA/PCL/10APP/4CNT/0.8IPU increased to 27.9 %, similar to that of PLA/PCL/10APP/6CNT. The cation-π interaction between CNTs and ionic liquid groups of IPU improved the dispersion of the CNTs. The dispersion of the CNTs and the acidic $H_2PO_4^-$ of IPU resulted in the enhancement of fire resistance [29]. To directly observe the melt-dripping phenomenon of PLA/PCL composites, the digital photograph after LOI testing is shown in Fig. 1. PLA/PCL/APP samples had melt-dripping behavior. The introduction of imidazolium-modified CNTs effectively inhibited the occurrence of molten droplets, which greatly reduced the risk of secondary damage from combustible polymers [21,34].

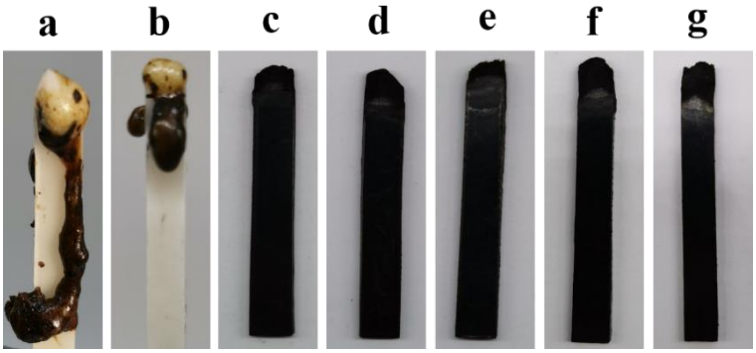

Fig. 1. Photos of the residual samples after LOI test from (a) PLA/PCL/10APP, (b)

PLA/PCL/15APP, (c) PLA/PCL/10APP/6CNT, (d) PLA/PCL/10APP/8CNT, (e) PLA/PCL/10APP/4CNT/0.8IPU, (f) PLA/PCL/10APP/6CNT/1.2IPU, (g) PLA/PCL/10APP/8CNT/1.6IPU composites.

Table 2. LOI and UL94 results for PLA/PCL composites.

Samples	LOI (%)	UL-94	
		Drip	Rating
PLA/PCL/10APP	23.5	Yes	V-2
PLA/PCL/15APP	24.8	Yes	V-1
PLA/PCL/10APP/6CNT	28.0	Yes	V-1
PLA/PCL/10APP/8CNT	30.0	No	V-0
PLA/PCL/10APP/4CNT/0.8IPU	27.9	Yes	V-1
PLA/PCL/10APP/6CNT/1.2IPU	28.8	No	V-1
PLA/PCL/10APP/8CNT/1.6IPU	30.3	No	V-0

3.2. Morphology of PLA/PCL composites

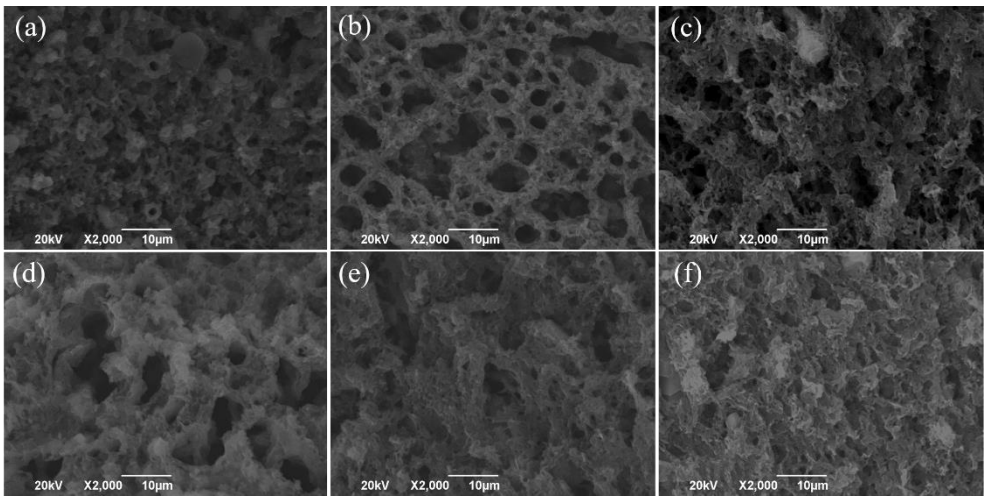

Fig. 2. SEM micrographs for the cryogenically fractured surfaced of (a) PLA/PCL/10APP, (b) PLA/PCL/10APP/6CNT, (c) PLA/PCL/10APP/8CNT, (d) PLA/PCL/10APP/4CNT/0.8IPU, (e) PLA/PCL/10APP/6CNT/1.2IPU, (f) PLA/PCL/10APP/8CNT/1.6IPU composites after glacial acetic acid etching.

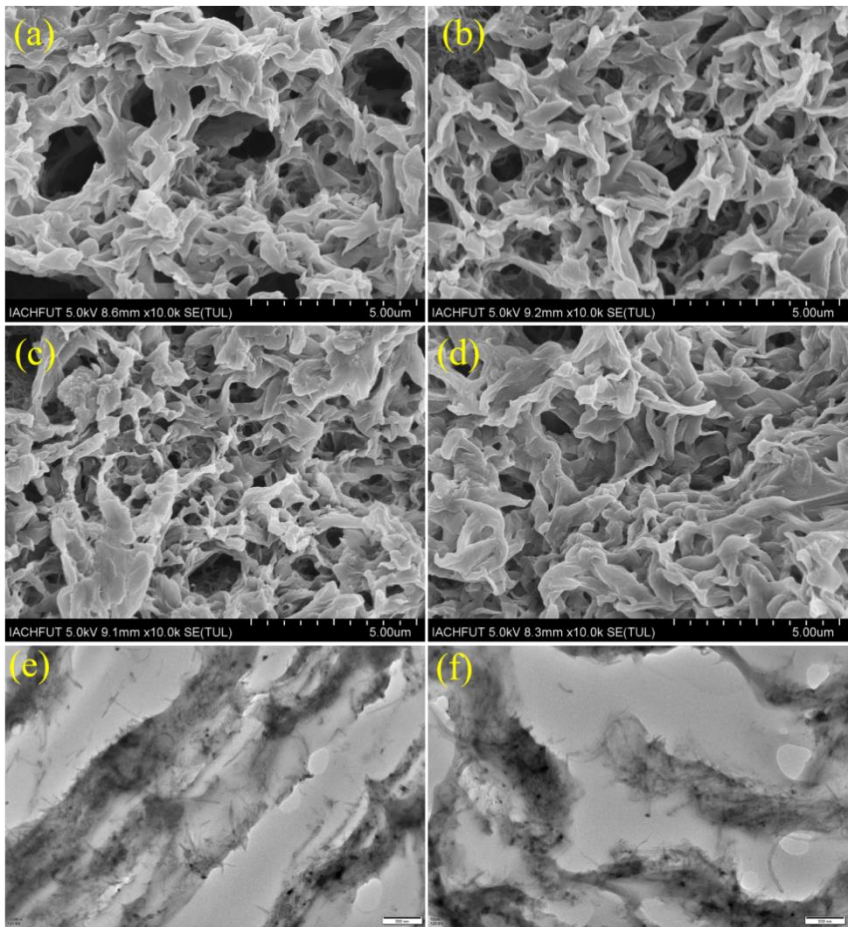

Fig. 3. FESEM images of (a) PLA/PCL/10APP/6CNT, (b) PLA/PCL/10APP/8CNT, (c) PLA/PCL/10APP/6CNT/1.2IPU, (d) PLA/PCL/10APP/8CNT/1.6IPU composites after glacial acetic acid etching; TEM images of (e) PLA/PCL/10APP/8CNT, (f) PLA/PCL/10APP/8CNT/1.6IPU composites.

The morphology of PLA/PCL composites is displayed in Fig. 2 and 3(a-d). All specimens in SEM images were immersed in glacial acetic acid for 24 h, and then PCL was completely etched. The TEM images of PLA/PCL composites are presented in Fig. 3(e-f). PLA/PCL/APP and PLA/PCL/APP/CNT exhibited typical co-continuous phase structure as the blending ratio of PLA and PCL were the same [14]. The size of continuous PCL phase in PLA/PCL/APP/CNT enlarged with the addition of CNTs content from 0 to 8 % as CNTs were distributed in the high viscous PLA phase and then shifted to the low viscous PCL phase [45]. The size of continuous

PCL phase in PLA/PCL/APP/CNT/IPU decreased with the increase of CNTs from 4 to 8 %. IPU containing PCL chain segments were mainly located in PCL phase and extended to the PLA/PCL interface due to the acidic ionic liquid structure of IPU. After introducing IPU, the interfacial between APP and polymer in PLA/PCL/APP/CNT/IPU composites was more uniform and compatible, indicating that the APP had good dispersion and uniform distribution in the matrix (Fig. S6). When APP and CNTs were localized in the PCL phase, the IPU distributed on the interface can act as compatibilizers and interface emulsifiers because the acidic ionic liquid in IPU can catalyze transesterification between PLA and PCL [31]. The enlarged difference between the two phases′ viscosity and cation-π interactions between CNTs and IPU can lead to a transfer of CNTs to the PCL domains [30]. As shown in Fig. 3(a-d), there were no CNTs in any samples, showing that the CNTs mainly existed in the PCL phase. As shown in Fig. 3(e-f), the position of the CNTs decorated by IPU was conductive to diminish the dimensions of the co-continuous phase. CNTs remained within the PCL matrix, and the traces in PLA/PCL/APP/CNT/IPU were more uniformly dispersed compared with that in PLA/PCL/APP/CNT. IPU can promote the dispersion of CNTs because of the strong cation-π interaction between carbon ring and imidazole cation ring (Fig. S7). In general, the introduction of IPU compatibilizers can restrain the phase separation between incompatible blend interfaces, leading to a reduction in the size of the PCL domain [13,14].

3.3. Thermal analysis of PLA/PCL composites

Fig. 4 shows the TGA and DTG analyses of PLA/PCL composites, with the key data in Table 3. PLA/PCL/APP exhibited a two-step degradation process from 300-450 ℃, which corresponded to the decomposition of PLA and PCL, sequentially [46,47]. With the increase of

the APP, the $T_{5\%}$ of PLA/PCL/15APP composites reduced, while carbon residual increased because PLA was sensitive to acids, and the catalysis action of phosphorus-containing APP flame retardants during heating promoted dehydration and carbonization [19]. The incorporation of CNTs significantly enhanced the thermal stability and resulted in one-step degradation of PLA/PCL/APP/CNT composites, resulting from the network structure and barrier effect of the CNTs and the catalysis effect of APP on PLA. The storage modulus (G') of the composites improved with the CNTs loading, and a plateau was exhibited in the low-frequency region, indicating that CNTs network was formed inside the composites (Fig. S8). In more detail, the $T_{5\%}$ of PLA/PCL/10APP composite occurs at 326.0 ℃, while the $T_{5\%}$ of PLA/PCL/10APP/6CNT and PLA/PCL/10APP/8CNT shifts to 326.2 and 327.9 ℃, respectively. As CNTs prevented the movement of polymer segments and increased the difficulty of arranging the polymer chains, leading to an increase in the $T_{5\%}$ of PLA/PCL/APP/CNT [48]. In addition, the residual yield of PLA/PCL/APP/CNT composites increased with increasing CNTs content, indicating that CNTs effectively promoted the heat transfer of heat throughout the polymer groups and inhibit the thermal decomposition of the PLA/PCL matrix [49]. The physical barrier effect of CNTs could restrain the transmission of decomposition products in the composites, which was beneficial to the suppression of melt droplets and flame propagation.

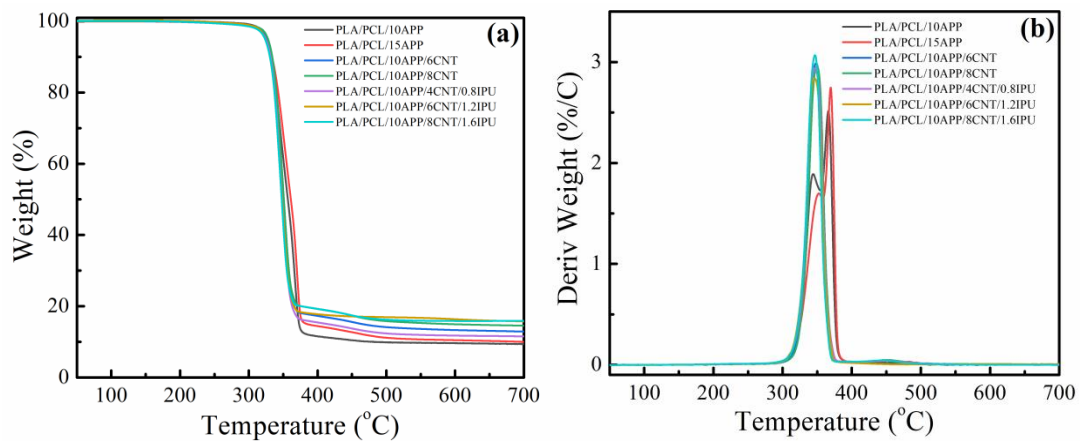

Fig. 4. (a) TGA and (b) DTG curves of PLA/PCL composites.

Table 3. TGA and DTG data of PLA/PCL composites.

	$T_{5\%}$ (°C)	$T_{50\%}$ (°C)	Tmax (°C)		Carbon residual (%)
PLA/PCL/10APP	326.0	356.7	344.5	366.5	9.1
PLA/PCL/15APP	325.1	361.1	351.9	370.2	10.0
PLA/PCL/10APP/6CNT	326.2	350.0	348.0		12.9
PLA/PCL/10APP/8CNT	327.9	350.9	349.5		14.5
PLA/PCL/10APP/4CNT/0.8IPU	324.5	348.6	346.0		11.5
PLA/PCL/10APP/6CNT/1.2IPU	323.6	348.2	346.4		15.7
PLA/PCL/10APP/8CNT/1.6IPU	323.5	347.7	347.8		15.9

$T_{5\%}$: initial decomposition temperature, $T_{50\%}$: midpoint decomposition temperature, T_{max}: maximum decomposition temperature.

Concerning the PLA/PCL/APP/CNT/IPU composites, the values of $T_{5\%}$ and $T_{50\%}$ were gradually decreased because of the poor thermal stability of IPU. However, the addition of IPU increased significantly the mass of PLA/PCL composite residue and the T_{max} moved to a modestly higher temperature. The $T_{5\%}$ of PLA/PCL/APP/CNT/IPU composites decreased coupled with an increase in T_{max} slightly. The decomposition of IPU containing phosphoric acid accelerated the formation of coke under low temperature, leading to its elevated residual carbon.

The catalysis effect and decomposition products of IPU promoted the carbon formation of flame retardants at low temperatures, and the residual carbon layer protected the PLA/PCL substrate due to its barrier effect [32]. The melting point of PLA did not change significantly, but the crystallinity gradually improved with the addition of CNTs and IPU, showing that the crystallization ability of PLA was vastly increased (Fig. S9 and Table S1).

3.4. Flame retardant mechanism

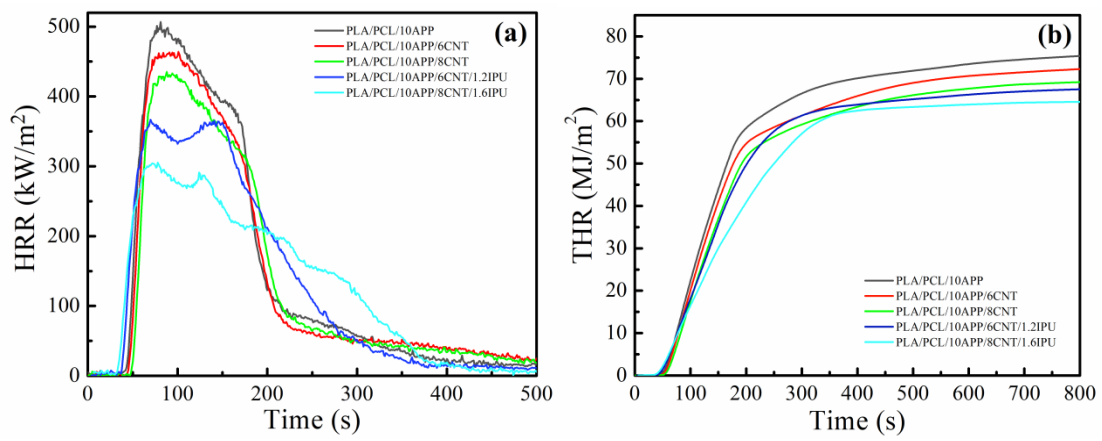

Fig. 5. (a) Heat release rate and (b) total heat release curves of PLA/PCL composites.

Table 4. CONE data for PLA/PCL composites.

Sample	TTI (s)	pHRR (kW/m^2)	T_P (s)	THR (MJ/m^2)
PLA/PCL/10APP	41	496	83	76
PLA/PCL/10APP/6CNT	42	460	91	73
PLA/PCL/10APP/8CNT	45	434	94	69
PLA/PCL/10APP/6CNT/1.2IPU	38	362	70	67
PLA/PCL/10APP/8CNT/1.6IPU	34	302	72	64

To find whether the CNTs and IPU can be beneficial to advancing the flame retardant of PLA/PCL composites, a cone calorimeter, a helpful solution to reflect the actual combustion behavior in real-world fire conditions had been used. In Fig. 5, the HRR and THR curves of PLA/PCL blends are exhibited, and the detailed cone calorimetry is in Table 4. It was clear that

after ignition at 41 s PLA/PCL/10APP composite burned quickly, suggesting relatively high flammability with the *p*HRR achieving 496 kW/m^2. By contrast, the *p*HRR value of PLA/PCL/APP/CNT and PLA/PCL/10APP/IPU composites was reduced tremendously, demonstrating that the addition of CNTs or imidazolium modified CNTs into PLA/PCL matrix slowed the combustion rate combustion rates and suppressed the heat release sufficiently [30]. Among the samples, the *p*HRR value of PLA/PCL/10APP/8CNT and PLA/PCL/10APP/8CNT/1.6IPU reached around 434 and 302 kW/m^2, which were decreased by 12.5 and 39.1 % compared with that of PLA/PCL/10APP. Furthermore, it was clear that the heat release rate (HRR) curve of PLA shifted toward lower temperature, meanwhile, HRR curves of PLA/PCL/APP/CNT/IPU composites became even flatter. After introducing 8 wt% CNTs into PLA/PCL matrix, the ignition time (TTI) was delayed to 45 s because CNTs can enhance the thermal stability of PLA/PCL, which coincided with thermogravimetric results (Fig. 4). However, the TTI value of PLA/PCL/10APP/8CNT/1.6IPU was shortened to 34 s because IPU accelerated the early decomposition of the PLA/PCL matrix [2].

The THR curves against a time of PLA/PCL composites are displayed in Fig. 5b. As you can see, the total heat released by the PLA/PCL/10APP composite was 76 MJ/m^2, and the PLA/PCL/10APP/8CNT composite released 69 MJ/m^2, but PLA/PCL/10APP/8CNT/1.6IPU only released 64 MJ/m^2. As mentioned earlier, the $H_2PO_4^-$ group in IPU accelerated the initial degradation of the PLA matrix, resulting in the faster carbonization process of PLA/PCL/APP/CNT/IPU composites. The degraded substrate material was involved in the charring process, contributing to forming the continuous and dense char layers during the fire test for PLA/PCL/APP/CNT/IPU composites. This higher quality char layer effectively

reduced the transfer of heat, oxygen, and mass from the material surface to the flame area because of the catalytic, barrier, and condensed char forming of imidazolium-modified CNTs and APP [50].

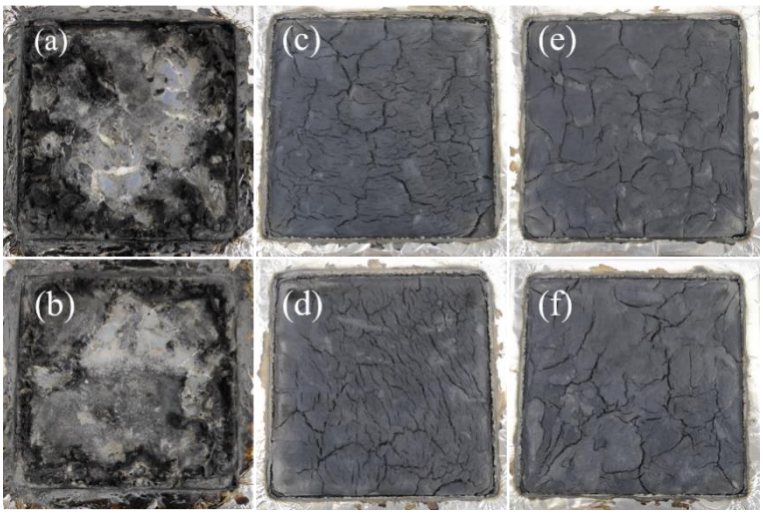

Fig. 6. Digital photos of residual char for (a) PLA/PCL/10APP, (b) PLA/PCL/15APP, (c) PLA/PCL/10APP/6CNT, (d) PLA/PCL/10APP/6CNT/1.2IPU, (e) PLA/PCL/10APP/8CNT, (f) PLA/PCL/10APP/8CNT/1.6IPU composites.

The digital photographs of PLA/PCL composite carbon residue after CCT are displayed in Fig. 6. The PLA/PCL/APP samples had a very thin and fragmented char residue layer, but PLA/PCL/APP/CNT and PLA/PCL/APP/CNT/IPU had interconnected and dense residual chars. Specifically, the PLA/PCL/APP/CNT showed a complete char structure despite some cracks (Fig.6c and 6d). For PLA/PCL/APP/CNT/IPU composites, more evident compact and continuous char layers with fewer cracks were observed, indicating the CNTs rigid network and barrier effect, as a consequence the heat exchange and mass exchange between vapor and solid phases were restricted [51].

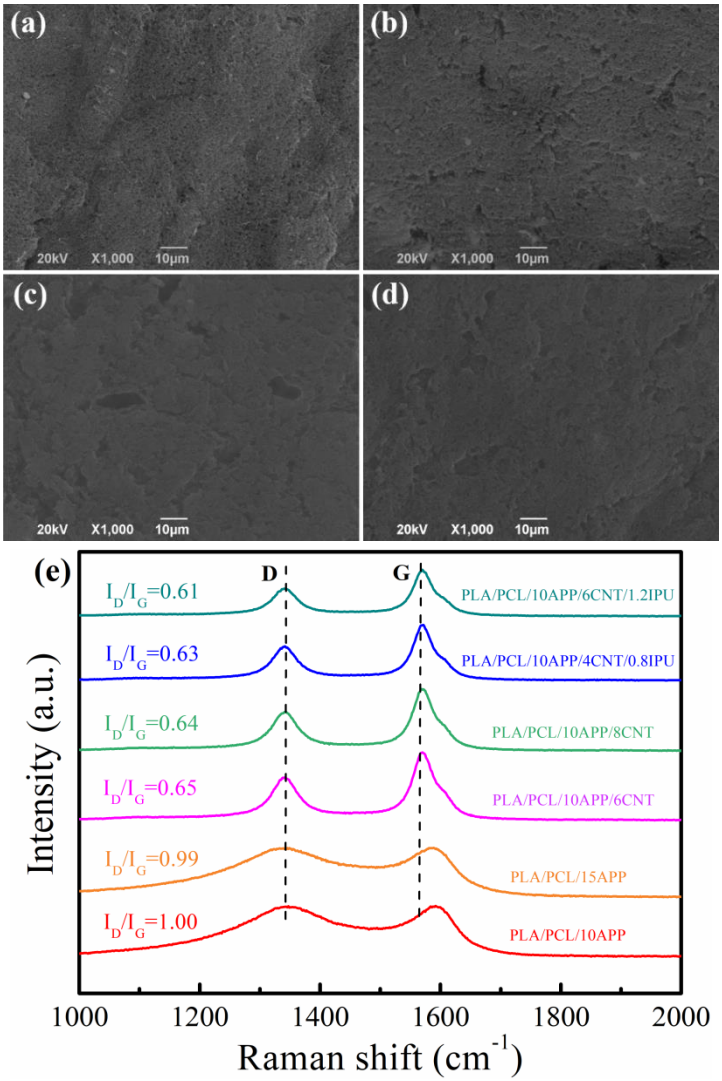

Fig. 7. SEM images of the char residues for (a) PLA/PCL/10APP/6CNT, (b) PLA/PCL/10APP/8CNT, (c) PLA/PCL/10APP/6CNT/1.2IPU, (d) PLA/PCL/10APP/8CNT/1.6IPU composites after CONE tests; (e) Raman spectra of the PLA/PCL composites residues after CONE test.

The SEM microstructures of char layers of PLA/PCL composites were displayed in Fig. 7. For the PLA/PCL/10APP/6CNT and PLA/PCL/10APP/8CNT, the char formed after combustion was relatively intact with obvious holes, so further burning cannot be prevented effectively. The char layers were different after incorporating IPU. The PLA/PCL composites containing IPU presented much more complete, denser and continuous char residue because

ionic liquids groups in IPU can catalyze carbon formation, dispersed CNTs can form barriers to protect the bottomed PLA/PCL matrix from heat and air erosion and prevent the emission of combustible gas, leading to reducing the flammability of PLA/PCL composites [31]. To further verify the quality and graphite-like structure, the Raman spectra of the char layers after CCT had been analyzed, shown in Fig. 7e. The peaks at approximately 1350 (D-band) and 1580 (G-band) cm^{-1} were attributed to amorphous and graphitized carbons in the char layers, respectively [52]. The degree of graphitization can be determined as the ratio of intensities of D to G bands (I_D/I_G), and generally, the lower I_D/I_G value, the higher level of graphitization of the residuals. The I_D/I_G value of PLA/PCL/APP/CNT/IPU composites was lowest than other samples, suggesting a higher graphitization degree of the char residue in PLA/PCL/APP/CNT/IPU composite and more hexagonal like carbon order. So such improvement in char quality was beneficial to the enhanced flame retardance due to the synergistic catalytic effect of CNTs and IPU [21].

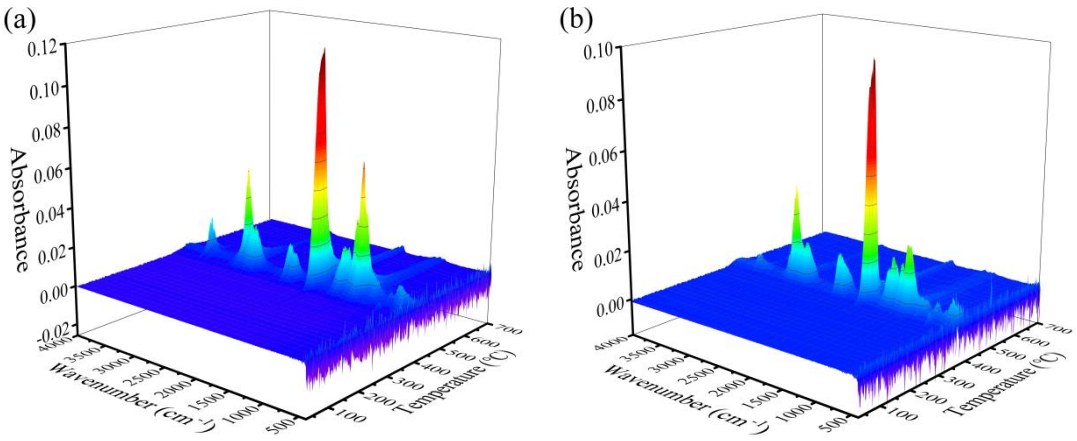

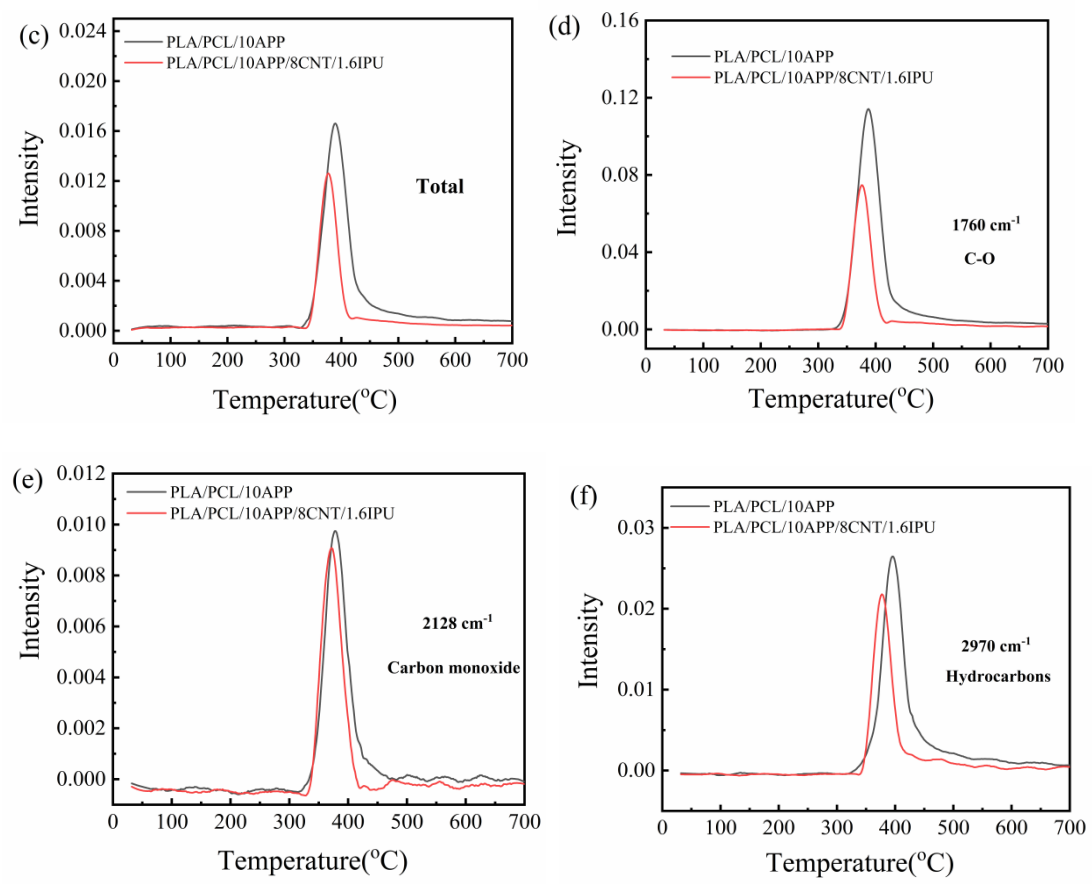

Fig. 8. 3D images of TG-IR spectra of (a) PLA/PCL/10APP and (b) PLA/PCL/10APP/8CNT/1.6IPU composites; absorption peak intensities of PLA/PCL/10APP and PLA/PCL/10APP/8CNT/1.6IPU (c) total absorption, (d) C−O containing compounds,(e) carbon monoxide, and (f) hydrocarbons in N_2 condition.

Based on the compositional analysis of gaseous products during the combustion process, the TG-IR analysis of PLA/PCL/10APP and PLA/PCL/10APP/8CNT/1.6IPU composites under nitrogen atmosphere was used to investigate the gaseous-phase mechanism, with the spectra presented in Fig. 8. The gas-phase products of the PLA/PCL/10APP/8CNT/1.6IPU composite were similar to those of PLA/PCL/10APP. However, the corresponding absorption peak intensity decreased significantly with the increase of imidazolium-functionalized CNTs content (as shown in Fig. 8c-f), suugesting that imidazole-functionalized CNTs can inhibited the

decomposition of volatile substances during heating [22,23]. Due to the synergistic effect between APP and imidazolium-functionalized CNTs, an isolation char layer quickly formed to effectively protected the matrix from decomposition, thereby improving the flame retardancy of PLA/PCL composites.

A proposed flame retardant mechanism for PLA/PCL/APP/CNT/IPU composites is shown in Fig. 9. In the gas phase, the suppressing flames effect could be relaxed by APP. As non-flammable gases, the NH_3 and H_2O were continuously freed to dilute the concentration of combustible gases, and release PO and HPO· radicals to capture H· and HO· radicals. The compact and coherent char formation of the PLA/PCL matrix was probably given rise to two processes in the condensed phase. On the one hand, APP decomposed polyphosphoric acid and phosphoric acid during combustion, which promoted matrix dehydration into carbon to protect the matrix [20]. The addition of CNTs increased the viscosity of PLA, which not only inhibited the droplet effect but also slowed down the spread of flame. On the other hand, IPU containing acidic ionic liquids and its decomposed compounds had strong catalytic carbonization and catalyzed the formation of char layers [30,31].

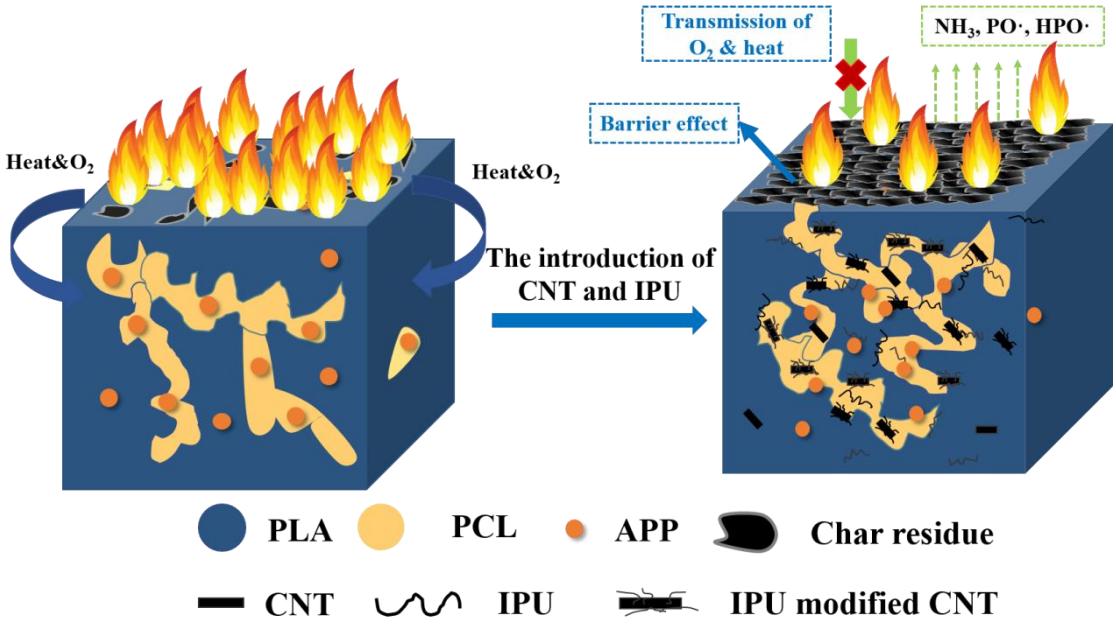

Fig. 9. Possible schematic representations of PLA/PCL/APP/CNT/IPU flame retardancy mechanism.

3.5. EMI shielding properties

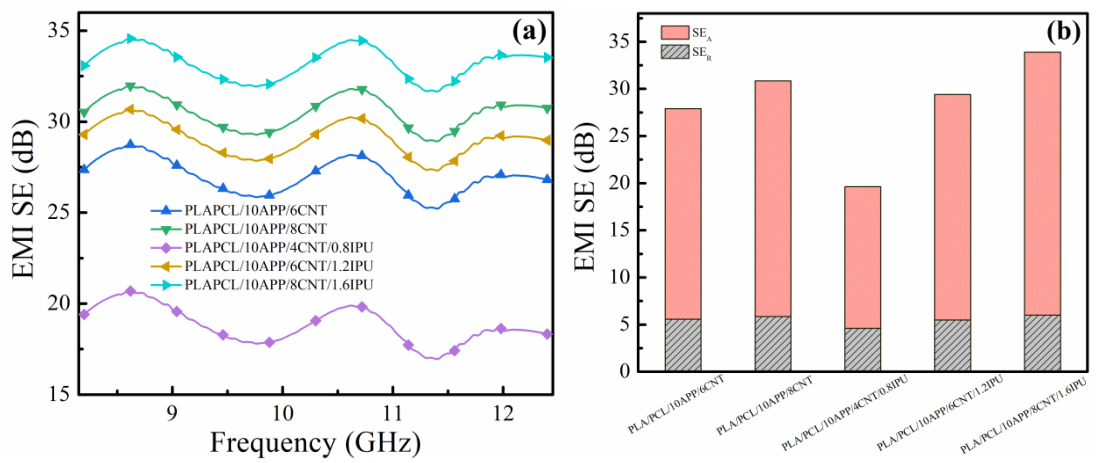

Fig. 10. (a) EMI SE of PLA/PCL/APP/CNT and PLA/PCL/APP/CNT/IPU composites in the frequency range of X band; (b) comparison of SE_R and SE_A of PLA/PCL/APP/CNT and PLA/PCL/APP/CNT/IPU composites at 9.0 GHz.

Because of the distinguished electrical conductivity of CNTs, the electrical conductivity of all composites increased with the increase of CNTs content (Fig. S10). It was noteworthy that the composites containing IPU showed higher electrical conductivity than that of the

composites without IPU. IPU expanded to the phase interface between PLA and PCL as an interfacial compatibilizer and regulated the migration of more CNTs to disperse at the two-phase interface, so the composite material containing IPU had a more complete conductive path [29]. The EMI SE curves of the PLA/PCL composites with different CNTs and IPU loadings with the range of 8.2-12.4 GHz in Fig. 10. The EMI SE of all composites increased with increasing the content of CNTs because vast charge carriers of CNTs can interact with incoming waves and dissipate electromagnetic energies [49]. The wavy relationship between EMI SE and frequency was ascribed to the heterogeneity of the size inhomogeneity of the discrete conducting network running through the polymer [29]. When the addition of CNTs was 6 wt%, the EMI SE of PLA/PCL/10APP/6CNT and PLA/PCL/10APP/6CNT/1.2IPU composite was to 27.9 and 29.4 dB at 9.0 GHz, respectively. Further improving the CNTs content reached 8 wt%, the SE_T of PLA/PCL/10APP/8CNT and PLA/PCL/10APP/8CNT/1.6IPU composites reached 30.8 and 33.9 dB, respectively. PLA/PCL/APP/CNT/IPU composites provided higher SE_T, which was consistent with the conductivity when compared with PLA/PCL/APP/CNT composites. It suggested that IPU can promote the dispersion of CNTs, act as compatibilizers and induce co-continuous structure. More conductive network structures formed in the composites can improve the EMI SE properties of the composite [29].

To further understand the EMI shielding mechanism, the contribution of SE_A and SE_R are shown in Fig. 10b. It was intuitive that the SE_A values of PLA/PCL composites overpassed the SE_R values. For the PLA/PCL/10APP/8CNT/1.6IPU composite, the SE_T, SE_A, and SE_R were 33.9 dB, 27.90 dB, and 6.0 dB, respectively. The enhanced SE_A may be associated with an

improved conductive network and interfacial dielectric polarization, which dissipated EM waves through attenuating electromagnetic radiations into thermal and internal electrical energies [49]. The stronger conductive network provided a higher SE_A value with the further introduction of CNTs and IPU. The slowly increased SE_R originated from the interactions between incident electromagnetic waves and mobile carriers on the material surface [53]. The remarkable EMI SE performances were attributed to the extremely assembled conductive network of CNTs fillers, which efficiently multiple scatters, reflects, and absorbs incident radiation.

3.6. Mechanical properties

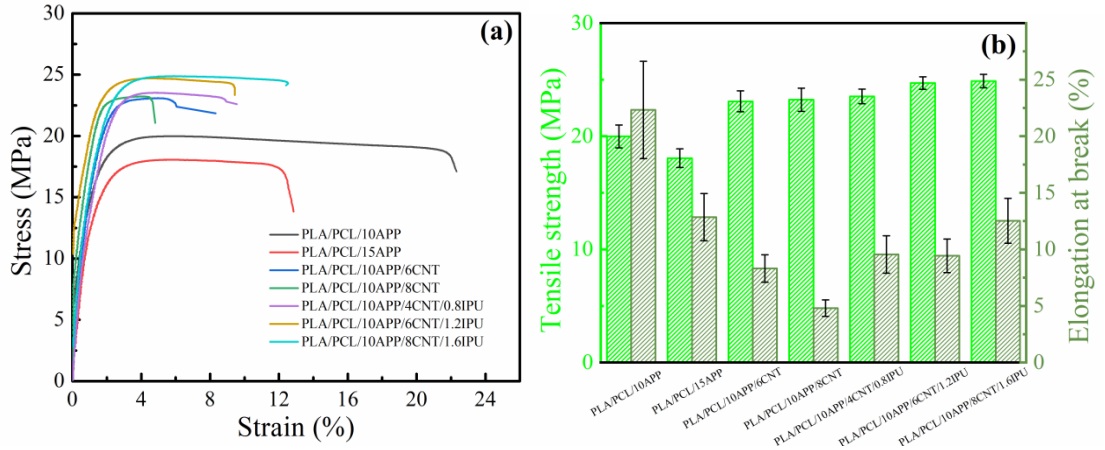

Fig. 11. (a) The typical stress-strain curves of PLA/PCL composites, (b) the mechanical properties of PLA/PCL composites.

The stress-strain curves and the tensile results of PLA/PCL composites are shown in Fig. 11. It was obvious that the incorporation of CNTs contributes to the improvement of tensile strength of the PLA/PCL/APP/CNT due to the stiffness of the conductive fillers [49]. Generally speaking, the dispersed states of CNTs, the interfacial force of the two phases, and the phase morphology play a significant role in obtaining distinguished mechanical properties [54,55]. It was noteworthy that the tensile strength of the samples containing IPU was better at the same

CNTs content. In addition, the elongation at break of PLA/PCL/APP/CNT/IPU composites increased with the increase of CNTs, while PLA/PCL/APP/CNT showed a decreased trend. Not only the PCL particles disappeared, but also the fibers became denser and longer on the tensile fracture surface with the addition of IPU. The PLA/PCL/10APP/8CNT/1.6IPU composite showed the most tightly arranged fiber structure (Fig. S11). The improved mechanical properties mainly depended on the fine dispersion of CNTs, the increased interfacial adhesion, and co-continuous morphology between PLA and PCL phase.

4. Conclusion

IPU modified CNTs and APP led to enhancing flame retardancy and EMI SE of PLA/PCL composites. PLA/PCL/10APP/8CNT/1.6IPU composite reached up to 30.3 % in the LOI test and passed V-0 rating in the UL-94 test coupled with disappeared melt-dripping. In the cone calorimeter, the *p*HRR and THR reached 302 kW/m^2 and 64 MJ/m^2, which were decreased by 39.1 and 15.8 % in cone calorimeter testing, respectively. The enhanced flame retardancy was attributed to the interplay of catalytic, barrier, and condensed char forming of imidazolium-modified CNTs and APP in the PLA/PCL composites. IPU can promote the dispersion of CNTs, act as compatibilizers and induce co-continuous structure. The dispersion of imidazolium-modified CNTs and co-continuous phase structure of the composites can establish continuous conductive pathways. Furthermore, the obtained PLA/PCL/10APP/8CNT/1.6IPU displayed a remarkable EMI SE of 33.9 dB, which was sufficient to meet the practical needs of many electronic devices. This study can present a novel way to the designation excellent EMI SE and flame-retardant properties with wide application.

Author statement

Zhenfeng Wang: Experiments, Investigation, Writing-original draft. **Tong Yan:** Formal analysis, Investigation. **Jiaying Tu:** Methodology. **Rui Cheng:** Formal analysis, Validation. **Pei Xu:** Methodology, Data curation, Writing-review & editing. **Yunsheng Ding:** Supervision.

Declaration of competing interest

The authors declare that they have no known competing financial interests or personal relationships that could have appeared to influence the work reported in this paper.

Acknowledgments

This research was supported by the National Natural Science Foundation of China (51603060), the key technological project of Anhui provincial department of economy and information technology (JB20054) and the industrial guidance fund project of Bengbu city and Hefei University of Technology (JZ2020YDZJ0334).

References

[1] Y.W. Jia, X. Zhao, T. Fu, D.F. Li, Y. Guo, X.L. Wang, Y.Z. Wang, Synergy effect between quaternary phosphonium ionic liquid and ammonium polyphosphate toward flame retardant PLA with improved toughness, Composites, Part B 197 (2020) 108192-108203.

[2] J. Feng, X. Xu, Z. Xu, H. Xie, P. Song, L. Li, G. Huang, H. Wang, One-pot, solvent- and catalyst-free synthesis of polyphosphoramide as an eco-benign and effective flame retardant for poly(lactic acid), ACS Sustainable Chem. Eng. 8(44) (2020) 16612-16623.

[3] W. Hu, Y. Zhang, Y. Qi, H. Wang, B. Liu, Q. Zhao, J. Zhang, J. Duan, L. Zhang, Z. Sun, B. Liu, Improved mechanical properties and flame retardancy of wood/PLA all-degradable biocomposites with novel lignin-based flame retardant and TGIC, Macromol. Mater. Eng. 305(5) (2020) 1900840-1900850.

[4] D. Gao, X. Wen, Y. Guan, W. Czerwonko, Y. Li, Y. Gao, E. Mijowska, T. Tang, Flame retardant effect and mechanism of nanosized NiO as synergist in PLA/APP/CSi-MCA composites, Compos. Commun. 17 (2020) 170-176.

[5] G. Urtekin, S. Hazer, A. Aytac, Effect of eggshell and intumescent flame retardant on the thermal and mechanical properties of plasticised PLA, Plastics, Rubber and Composites 50(3) (2020) 127-136.

[6] M. Niu, Z. Zhang, Z. Wei, W. Wang, Effect of a novel flame retardant on the mechanical, thermal and combustion properties of poly(lactic acid), Polymers (Basel) 12(10) (2020) 2407-2423.

[7] Y. Han, J.W. Shi, L.X. Mao, Z. Wang, L.Q. Zhang, Improvement of compatibility and mechanical performances of PLA/PBAT composites with epoxidized soybean oil as compatibilizer, Industrial & Engineering Chemistry Research 59(50) (2020) 21779-21790.

[8] B. Xue, H.Z. He, Z.X. Huang, Z. Zhu, F. Xue, S. Liu, B. Liu, Fabrication of super-tough ternary blends by melt compounding of poly(lactic acid) with poly(butylene succinate) and ethylene-methyl acrylate-glycidyl methacrylate, Composites, Part B 172 (2019) 743-749.

[9] A. Ostafinska, I. Fortelny, J. Hodan, S. Krejcikova, M. Nevoralova, J. Kredatusova, Z. Krulis, J. Kotek, M. Slouf, Strong synergistic effects in PLA/PCL blends: impact of PLA matrix viscosity, J Mech Behav Biomed Mater 69 (2017) 229-241.

[10] Y. Ahmadzadeh, A. Babaei, A. Goudarzi, Assessment of localization and degradation of ZnO nano-particles in the PLA/PCL biocompatible blend through a comprehensive rheological characterization, Polym. Degrad. Stab. 158 (2018) 136-147.

[11] A. Ostafinska, I. Fortelny, M. Nevoralova, J. Hodan, J. Kredatusova, M. Slouf, Synergistic

effects in mechanical properties of PLA/PCL blends with optimized composition, processing, and morphology, RSC Adv. 5(120) (2015) 98971-98982.

[12] T. Takayama, M. Todo, H. Tsuji, Effect of annealing on the mechanical properties of PLA/PCL and PLA/PCL/LTI polymer blends, J Mech Behav Biomed Mater 4(3) (2011) 255-60.

[13] P. Wang, Y. Zhou, P. Xu, Y. Ding, Effect of P[MPEGMA-IL] on morphological evolution and conductivity behavior of PLA/PCL blends, Ionics 25(7) (2019) 3189-3196.

[14] P. Wang, P. Xu, H. Wei, H. Fang, Y. Ding, Effect of block copolymer containing ionic liquid moiety on interfacial polarization in PLA/PCL blends, J. Appl. Polym. Sci. 135(16) (2018) 46161-46167.

[15] J. Zhan, L. Song, S. Nie, Y. Hu, Combustion properties and thermal degradation behavior of polylactide with an effective intumescent flame retardant, Polym. Degrad. Stab. 94(3) (2009) 291-296.

[16] X. Wen, Z. Liu, Z. Li, J. Zhang, D.Y. Wang, K. Szymańska, X. Chen, E. Mijowska, T. Tang, Constructing multifunctional nanofiller with reactive interface in PLA/CB-g-DOPO composites for simultaneously improving flame retardancy, electrical conductivity and mechanical properties, Compos. Sci. Technol. 188 (2020) 107988-107998.

[17] K. Wu, Y. Hu, L. Song, H. Lu, Z. Wang, Flame retardancy and thermal degradation of intumescent flame retardant starch-based biodegradable composites, Industrial & Engineering Chemistry Research 48(6) (2009) 3150-3157.

[18] X. Jin, S. Cui, S. Sun, X. Gu, H. Li, J. Sun, S. Zhang, S. Bourbigot, The preparation of an intumescent flame retardant by ion exchange and its application in polylactic acid, ACS

Appl. Polym. Mater. 1(4) (2019) 755-764.

[19] X. Jin, S. Cui, S. Sun, X. Gu, H. Li, X. Liu, W. Tang, J. Sun, S. Bourbigot, S. Zhang, The preparation of a bio-polyelectrolytes based core-shell structure and its application in flame retardant polylactic acid composites, Composites, Part A 124 (2019) 105485-105504.

[20] D.F. Li, X. Zhao, Y.W. Jia, L. He, X.L. Wang, Y.Z. Wang, Dual effect of dynamic vulcanization of biobased unsaturated polyester: simultaneously enhance the toughness and fire safety of poly(lactic acid), Composites, Part B 175 (2019) 107069-107080.

[21] H. Yang, Y. Guan, L. Ye, S. Wang, S. Li, X. Wen, X. Chen, E. Mijowska, T. Tang, Synergistic effect of nanoscale carbon black and ammonium polyphosphate on improving thermal stability and flame retardancy of polypropylene: a reactive network for strengthening carbon layer, Composites, Part B 174 (2019) 107038-107047.

[22] Y. Zhang, Z. Xiong, H. Ge, L. Ni, T. Zhang, S. Huo, P. Song, Z. Fang, Core–shell bioderived fame retardants based on chitosan/alginate coated ammonia polyphosphate for enhancing flame retardancy of polylactic acid, ACS Sustainable Chem. Eng. 8(16) (2020) 6402-6412.

[23] Z. Xiong, Y. Zhang, X. Du, P. Song, Z. Fang, Green and scalable fabrication of core–shell biobased flame retardants for reducing flammability of polylactic acid, ACS Sustainable Chem. Eng. 7(9) (2019) 8954-8963.

[24] X. Ji, D. Chen, Q. Wang, J. Shen, S. Guo, Synergistic effect of flame retardants and carbon nanotubes on flame retarding and electromagnetic shielding properties of thermoplastic polyurethane, Compos. Sci. Technol. 163 (2018) 49-55.

[25] W. Yang, B. Tawiah, C. Yu, Y.-F. Qian, L.L. Wang, A.C.-Y. Yuen, S.-E. Zhu, E.-Z. Hu,

T.B.-Y. Chen, B. Yu, H.-D. Lu, G.H. Yeoh, X. Wang, L. Song, Y. Hu, Manufacturing, mechanical and flame retardant properties of poly(lactic acid) biocomposites based on calcium magnesium phytate and carbon nanotubes, Composites, Part A 110 (2018) 227-236.

[26] J. Zhang, Q. Kong, D.Y. Wang, Simultaneously improving the fire safety and mechanical properties of epoxy resin with Fe-CNTs via large-scale preparation, J. Mater. Chem. A 6(15) (2018) 6376-6386.

[27] Y. Zhou, Y. Lin, B. Tawiah, J. Sun, R.K.K. Yuen, B. Fei, DOPO-decorated two-dimensional MXene nanosheets for flame-retardant, ultraviolet-protective, and reinforced polylactide composites, ACS Appl Mater Interfaces 13(18) (2021) 21876-21887.

[28] J. Yue, C. Liu, C. Zhou, X. Fu, L. Luo, L. Gan, X. Yang, J. Huang, Enhancing flame retardancy and promoting initial combustion carbonization via incorporating electrostatically surface-functionalized carbon nanotube synergist into intumescent flame-retardant poly(butylene succinate), Polymer 189 (2020) 122197-122204.

[29] G. Sang, J. Dong, X. He, J. Jiang, J. Li, P. Xu, Y. Ding, Electromagnetic interference shielding performance of polyurethane composites: a comparative study of GNs-IL/Fe3O4 and MWCNTs-IL/Fe3O4 hybrid fillers, Composites, Part B 164 (2019) 467-475.

[30] Y. Hu, P. Xu, H. Gui, X. Wang, Y. Ding, Effect of imidazolium phosphate and multiwalled carbon nanotubes on thermal stability and flame retardancy of polylactide, Composites, Part A 77 (2015) 147-153.

[31] H. Liu, J. Chen, L. Chen, Y. Xu, X. Guo, D. Fang, Carbon nanotube-based solid sulfonic

acids as catalysts for production of fatty acid methyl ester via transesterification and esterification, ACS Sustainable Chem. Eng. 4(6) (2016) 3140-3150.

[32] F. Xiao, K. Wu, F. Luo, Y. Guo, S. Zhang, X. Du, Q. Zhu, M. Lu, An efficient phosphonate-based ionic liquid on flame retardancy and mechanical property of epoxy resin, J. Mater. Sci. 52(24) (2017) 13992-14003.

[33] X. Chen, C. Ma, C. Jiao, Synergistic effects between [Emim]PF_6 and aluminum hypophosphite on flame retardant thermoplastic polyurethane, RSC Adv. 6(71) (2016) 67409-67417.

[34] H. Gui, P. Xu, Y. Hu, J. Wang, X. Yang, A. Bahader, Y. Ding, Synergistic effect of graphene and an ionic liquid containing phosphonium on the thermal stability and flame retardancy of polylactide, RSC Adv. 5(35) (2015) 27814-27822.

[35] W. Yuan, H. Liu, X. Wang, L. Huang, F. Yin, Y. Yuan, Conductive MXene/melamine sponge combined with 3D printing resin base prepared as an electromagnetic interferences shielding switch, Composites, Part A 143 (2021) 106238-106249.

[36] Q. He, R. Chen, S. Li, Z. Wang, F. Wen, B. Wang, J. Mu, Excellent thermally conducting modified graphite nanoplatelets and MWCNTs/poly(phenylene sulfone) composites for high-performance electromagnetic interference shielding effectiveness, Composites, Part A 143 (2021) 106280-106289.

[37] C. Ge, G. Wang, G. Zhao, C. Wei, X. Li, Lightweight and flexible poly(ether-block-amide)/multiwalled carbon nanotube composites with porous structure and segregated conductive networks for electromagnetic shielding applications, Composites, Part A 144 (2021) 106356-106364.

[38] W.Y. Wang, X. Ma, Y.W. Shao, X.D. Qi, J.H. Yang, Y. Wang, Flexible, multifunctional, and thermally conductive nylon/graphene nanoplatelet composite papers with excellent EMI shielding performance, improved hydrophobicity and flame resistance, J. Mater. Chem. A 9(8) (2021) 5033-5044.

[39] H. Fang, W. Ye, K. Yang, K. Song, H. Wei, Y. Ding, Vitrimer chemistry enables epoxy nanocomposites with mechanical robustness and integrated conductive segregated structure for high performance electromagnetic interference shielding, Composites, Part B 215 (2021) 108782-108791.

[40] X. Jia, B. Shen, L. Zhang, W. Zheng, Construction of shape-memory carbon foam composites for adjustable EMI shielding under self-fixable mechanical deformation, Chem. Eng. J. 405 (2021) 126927-126936.

[41] S. Yang, Y.Y. Wang, Y.N. Song, L.C. Jia, G.J. Zhong, L. Xu, D.X. Yan, J. Lei, Z.M. Li, Ultrathin, flexible and sandwich-structured PHBV/silver nanowire films for high-efficiency electromagnetic interference shielding, J. Mater. Chem. C 9(9) (2021) 3307-3315.

[42] Z. Lv, X. Huang, D. Fan, P. Zhou, Y. Luo, X. Zhang, Scalable manufacturing of conductive rubber nanocomposites with ultralow percolation threshold for strain sensing applications, Compos. Commun. 25 (2021) 100685-100693.

[43] Y. Yang, C. Feng, Y. Zhou, X. Zha, R. Bao, K. Ke, M. Yang, C. Tan, W. Yang, Achieving improved electromagnetic interference shielding performance and balanced mechanical properties in polyketone nanocomposites via a composite MWCNTs carrier, Composites, Part A 136 (2020) 105967-105999.

[44] K. Zhang, H.O. Yu, Y.D. Shi, Y.F. Chen, J.B. Zeng, J. Guo, B. Wang, Z. Guo, M. Wang, Morphological regulation improved electrical conductivity and electromagnetic interference shielding in poly(l-lactide)/poly(ε-caprolactone)/carbon nanotube nanocomposites via constructing stereocomplex crystallites, J. Mater. Chem. C 5(11) (2017) 2807-2817.

[45] J. Huang, C. Mao, Y. Zhu, W. Jiang, X. Yang, Control of carbon nanotubes at the interface of a co-continuous immiscible polymer blend to fabricate conductive composites with ultralow percolation thresholds, Carbon 73 (2014) 267-274.

[46] B. Najaf Oshani, S.M. Davachi, I. Hejazi, J. Seyfi, H.A. Khonakdar, A. Abbaspourrad, Enhanced compatibility of starch with poly(lactic acid) and poly(varepsilon-caprolactone) by incorporation of POSS nanoparticles: study on thermal properties, Int J Biol Macromol 141 (2019) 578-584.

[47] B. Zhu, T. Bai, P. Wang, Y. Wang, C. Liu, C. Shen, Selective dispersion of carbon nanotubes and nanoclay in biodegradable poly(epsilon-caprolactone)/poly(lactic acid) blends with improved toughness, strength and thermal stability, Int J Biol Macromol 153 (2020) 1272-1280.

[48] Y. Zhou, L. Lei, B. Yang, J. Li, J. Ren, Preparation and characterization of polylactic acid (PLA) carbon nanotube nanocomposites, Polym. Test. 68 (2018) 34-38.

[49] H. Li, D. Yuan, P. Li, C. He, High conductive and mechanical robust carbon nanotubes/waterborne polyurethane composite films for efficient electromagnetic interference shielding, Composites, Part A 121 (2019) 411-417.

[50] W. Yang, W.J. Yang, B. Tawiah, Y. Zhang, L.L. Wang, S.E. Zhu, T.B.Y. Chen, A.C.Y. Yuen,

B. Yu, Y.F. Liu, J.Y. Si, E.Z. Hu, H.D. Lu, K.H. Hu, Q.N. Chan, G.H. Yeoh, Synthesis of anhydrous manganese hypophosphite microtubes for simultaneous flame retardant and mechanical enhancement on poly(lactic acid), Compos. Sci. Technol. 164 (2018) 44-50.

[51] Y. Yang, L. Haurie, J. Wen, S. Zhang, A. Ollivier, D.Y. Wang, Effect of oxidized wood flour as functional filler on the mechanical, thermal and flame-retardant properties of polylactide biocomposites, Ind. Crops Prod. 130 (2019) 301-309.

[52] J. Jing, Y. Zhang, Z.P. Fang, D.Y. Wang, Core-shell flame retardant/graphene oxide hybrid: a self-assembly strategy towards reducing fire hazard and improving toughness of polylactic acid, Compos. Sci. Technol. 165 (2018) 161-167.

[53] Z. Zeng, M. Chen, H. Jin, W. Li, X. Xue, L. Zhou, Y. Pei, H. Zhang, Z. Zhang, Thin and flexible multi-walled carbon nanotube/waterborne polyurethane composites with high-performance electromagnetic interference shielding, Carbon 96 (2016) 768-777.

[54] B. Wu, Q. Zeng, D. Niu, W. Yang, W. Dong, M. Chen, P. Ma, Design of supertoughened and heat-resistant PLLA/elastomer blends by controlling the distribution of stereocomplex crystallites and the morphology. Macromolecules 2019;52(3):1092-103.

[55] T. Yu, T. Tuerhongjiang, C. Sheng, Y. Li, Phosphorus-containing diacid and its application in jute/poly(lactic acid) composites: Mechanical, thermal and flammability properties. Composites Part A-Appl S 2017;97:60-6.

Online monitoring and controlling applied pressure during thermal expansion process using silicon rubber mandrel

Ruiqi Guo[1], Yizhuo Gu[2], Gaopeng Wang[1], Min Li[1], Shaokai Wang[1]*

1. Key Laboratory of Aerospace Advanced Materials and Performance (Ministry of Education), School of Materials Science and Engineering, Beihang University, Beijing 100191, China;

2. Research Institute for Frontier Science, Beihang University, Beijing, 100191, China

Correspondence to: Y. Gu (E-mail: benniegu@buaa.edu.cn)

Abstract: For the fabrication of rubber and composite products with closed structures, thermal expansion method is often used to apply pressure with silicon rubber mandrel under heating. However, it is difficult for controlling the thermal expansion stress, because of unknown thermal expansion process. In this work, a negative feedback regulation system for online monitoring and controlling thermal expansion stress was established with cylindrical silicon rubber mandrel. It was used to forming rubber heat-insulating layer inside metal cylinder. The thermal expansion stress was monitored with the aid of flexible film pressure sensor and was input into a heating unit for adjusting the thermal expansion stress. For the optimized silicon rubber core, the temperature difference between inside and outside surfaces of the core was less than 5 ºC, and the thermal expansion pressure was stabilized at 0.6 MPa. Uniform thickness of rubber heat-insulating layer, good surface smoothness and bonding quality were obtained. This proposed method provides a new avenue for controlling forming quality during thermal expansion processing.

Key words: Thermal expansion method, Negative feedback regulation, Online monitoring, Silicon rubber mandrel.

1. Introduction

As a low-density and heat-resistant organic material, rubber is widely used in aerospace thermal protection structures. To prevent heat from entering the structure, thermal insulation layer made of rubber is often pasted on the inner wall of shell structure under heat and pressure. During this process, the pressure can be easily applied by silicon rubber mandrel, which has high thermal expansion coefficient and yields enough thermal expansion stress under heating.

Using the same principle, polymer matrix composite with enclosed structure can be fabricated, such as box structure and hat-stiffened panel[1-4]. The thermal expansion stress is influenced by heating temperature, process gap setting, and material properties of silicone rubber core mold, including bulk expansion coefficient and elastic modulus [4, 5]. Thus, it is difficult to accurately calculate and control the thermal expansion pressure. It is essential to control thermal expansion behavior of silicon rubber core mold to improve processing quality[6, 7].

Typically, an industrial oven serves as heating source of the thermal expansion process. However, low thermal conductivity of silicon rubber results in hysteresis in heat transfer, which generates insufficient thermal expansion stress in the silicon rubber core. In order to solve this hysteresis issue, Schneider[8] proposed a silicon rubber core with an integrated heating source, which can directly control the temperature of silicon rubber. Sala[9] investigated the thermal expansion process by means of analysis, numerical and experimental methods. The manufacturing process was optimized and hollow composite products with autoclave-class-quality was produced. Based on the Maxwell equation, Kim et al.[10] developed the Kohlr-ausch-Williame-Watts equation to describe the thermal expansion behavior of silicon rubber. The thermal expansion stress calculated using this equation agrees well with the experiment. Currently, the thermal expansion stress is primarily controlled based on experience and trial-and-error method. It is challenging to accurately measure and control the thermal expansion stress.

In this study, a thermal expansion stress in-situ monitoring and regulation system was designed and built with the aid of flexible film pressure sensor. It was used to forming rubber heat-insulating layer inside metal cylinder. A closed-loop experimental procedure for thermal expansion process was developed to study the variations of temperature and thermal expansion stress under different heating modes and mandrel structures. The effects of different heating modes and mandrel structures on temperature and pressure distributions were investigated. The result shows that the optimal temperature uniformity and product quality are achieved using the heating method that combines an industrial oven and hollow heating mandrel.

2. Experimental

2.1 Materials

Liquid silicon rubber R10301 was used to prepare silicon rubber core, which was purchased from China Bluestar Chenguang Co., Ltd. These silicone rubbers are two-component liquid

type, in which component A is liquid silicone rubber and component B is vulcanizing agent. The mass ratio of two components for preparing silicone rubber core mold is 10:1. It was then evenly mixed and placed in a vacuum oven for vacuumizing (20min) for defoaming. Then the liquid was poured into the mold and vulcanize at room temperature for 24h. It was then heated in an industrial oven at 100 ℃ for 1h and 200 ℃ for 1h. After vulcanization of the silicon rubber, it was cooled down below 40℃ and was then removed from mold cavity. Thermal insulation layer was prepared with asbestos filled Nitrile Butadiene Rubber (NBR), which was produced by China Bluestar Chenguang Co., Ltd. Heating wire used for internal heating source in silicon rubber core was manufactured by Yancheng Shengjie machine factory. It had the diameters of 3.5 mm and the power of 110V/600W. Flexible film pressure sensor was high-temperature type HT201-H, which was produced by Teskan, Inc. Hollow heating metal mandrel and heating tube were processed by Haoyu electric heat Co., Ltd. with diameters of 88 mm and 16.5 m, respectively.

2.2 Establishment of Online-Monitoring and Regulation System

The setup of online-monitoring and regulation system is described in Fig. 1(a). This system includes pressure monitoring and control system, temperature monitoring and control system, heating control system and core heating system. Among them, the pressure monitoring and control system, the temperature monitoring and control system and the heating control system were integrated into a pressure control cabinet, which controlled the core heating system. The core heating system was a precast cylindrical silicon rubber core, as shown in Fig. 1(b). Three heating wires and three armored thermocouples (TC_{in1}, TC_{in2}, TC_{in3}) were embedded in the front, middle and rear areas along the axial direction of the cylindrical core. In addition, three flexible film pressure sensors (PS_1, PS_2, PS_3) and two monitoring thermocouples (TC_{out1}, TC_{out2}) were fixed on the outer surface of the cylindrical core to monitor the temperature and thermal expansion stress of the rubber heat-insulating layer. The pressure sensors are connected to the pressure transmitter (MFF) in the pressure test system. The pressure transmitter converts the thermal expansion stress into a voltage signal (0~5VDC) and sends it to the three master control instruments (UP instruments) of the pressure control cabinet. This voltage set value is manually input into the three UP instruments, and the regulator performs PID (Proportional Integral Derivative) automatic control. Its output (4~20mA) is connected to the three auxiliary control instruments (FB instruments) for controlling heating power. During the operation of the

pressure control cabinet, a specified pressure value (voltage set value) is set on the master control in advance. Then the present voltage value of the master control increases from 0 V to the set value. At the same time, the FB instrument receives the 4~20mA current signal from UP instrument and regulates the heating power according to the temperature condition obtained from the three thermocouples in the core. Based on these, a negative feedback closed-loop control system is established, which can online monitor and control the thermal expansion stress of the silicon rubber during thermal expansion process.

Fig. 1 Schematic of the setup of (a) monitoring and regulation system, (b) Core heating system

2.2.1 Pressure test system

The pressure test system is responsible for collecting the thermal expansion stress signal in the thermal expansion process and converting it into electrical signal. The corresponding illustration of the pressure test system is shown in Fig. 2, including high-temperature Flexiforce HT201-H flexible film pressure sensor, pressure signal demodulation device and calibration

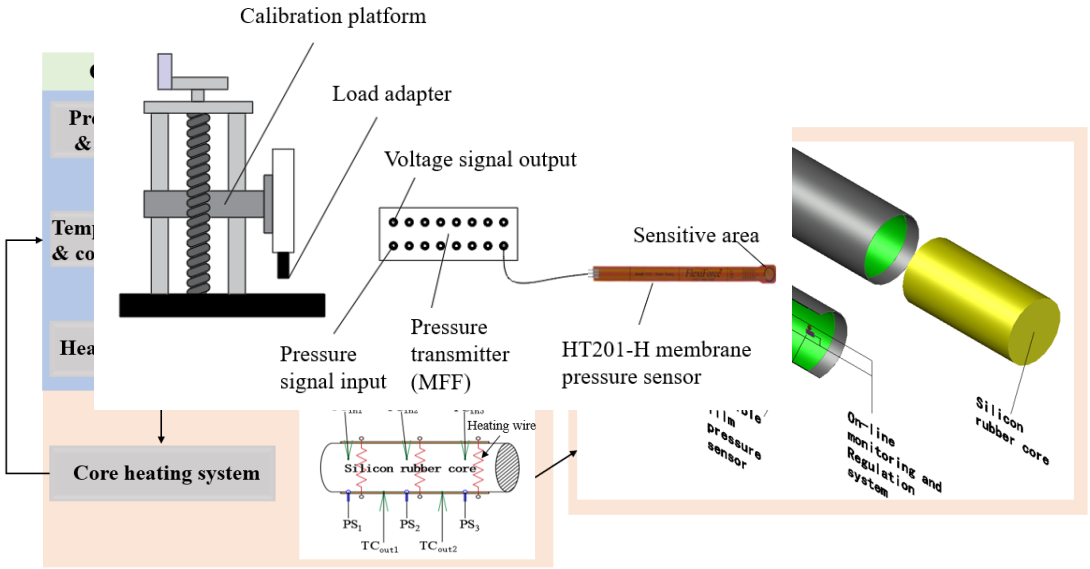

platform. The Flexiforce film pressure sensor is equivalent to a variable resistor in the circuit. When the sensitive area of sensor is under pressure, the resistance changes accordingly. Using this principle, when external force is applied to the sensing area of sensor, the resistance rapidly decreases. Through conversion and fitting, the pressure value can be obtained.

Fig. 2 Schematic illustration of the setup of the pressure test system

2.2.2 Pressure control cabinet

The composition of pressure control cabinet is shown in Fig. 3(a), including master control

instruments (UP1~UP3 digital regulators), auxiliary control instruments (FB1~FB3 digital regulators), ammeters, temperature monitoring instrument (MAC), mimic board (DOP107EG). The master control instruments receive the thermal expansion stress signal during the thermal expansion process, and output 4~20mA current signal to the auxiliary control instrument through PID operation. The auxiliary control instrument regulates the heating output power, and then regulates the thermal expansion stress. The ammeters are used to monitor the current of each heating zone. The temperature monitoring instrument MAC is used to monitor the temperature near the pressure sensor, and convert the voltage signal into the thermal expansion stress signal through the linear relationship between the voltage and thermal expansion stress of each sensor at a specified temperature. The mimic board (DOP107EG) is used to display the real-time working condition of the system, including temperature of each heating zone, current value and set value of thermal expansion stress of each zone, as shown in Fig. 3(b). The real-time process curve of the temperature and thermal expansion stress is also displayed in the mimic board, as shown in Fig. 3(c).

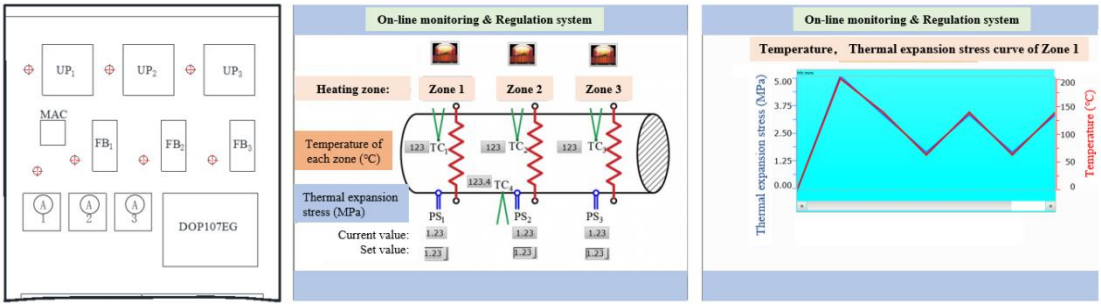

Fig. 3 Schematic of the setup of pressure control cabinet: (a) instrument panel, (b) main section of the mimic board, (c) real-time curve of temperature and thermal expansion stress.

2.2.3 Core heating system

The core heating system is the source of thermal expansion stress. Its composition is shown in Fig. 4, including silicon rubber core, rubber heat-insulating layer, heating wires, thermocouples, flexible film pressure sensors and the metallic cylindrical mold. The silicon rubber core was made of R10301 liquid silicon rubber by means of casting process. Spiral heating wires and three armored thermocouples (TC_{in1}, TC_{in2}, TC_{in3}) were embedded in the core along the axial direction, while three flexible film pressure sensors (PS_1, PS_2, PS_3) and

two monitoring thermocouples (TC_{out1}, TC_{out2}) were fixed on the outer surface of the core. Using these sensors, the axial thermal expansion stress uniformity and the axial/circumferential temperature distribution of the core can be obtained. Then the insulation rubber layer was wrapped on the outside surface of the silicon rubber core. In order to optimize the core heating system, different structure of silicon rubber core was studied, including a solid core with three heating wire embedded in three zones (type A), a solid core with one heating wire embedded in a single zone (type B), and a hollow core with metal heating mandrel (type C).

Type A: Solid core with three heating wires embedded in three zones. The heating wire was embedded in the three zones of the silicon rubber core. Its specification was 110V/600W and

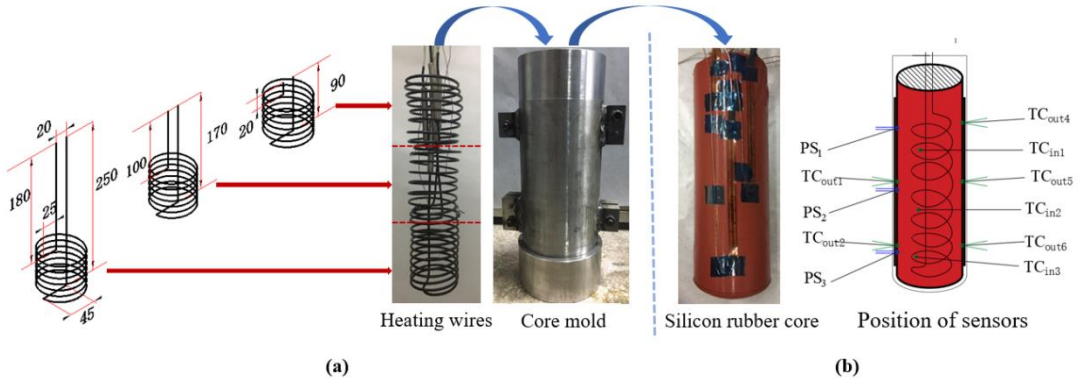

the size is shown in Figure 4(a), a spiral-shaped heating wire with the inner diameter of 70 mm and the turn number of 7. The height of the heating wires for three zones were 90mm, 170mm and 250mm, respectively. In order to heat the silicon rubber core evenly without local overheating, three spiral armored heating wires were hung at equal intervals along the axial direction. The solid core with embedded armored heating wires and thermocouples were then fabricated in the core mold by means of casting process. The location of thermocouples and flexible pressure sensor is shown in Fig. 4(b).

Fig. 4 Schematic of the silicon rubber core fabrication: (a) three-zone heating wire and assembly and fabrication of the silicon rubber core, (b) fabricated silicon rubber core with sensors

Type B: Solid core with one heating wire embedded in a single zone. On the premise of good uniformity of temperature and thermal expansion stress, the core with a single heating wire embedded was prepared, the three heating zones were controlled simultaneously. Two kinds of single heating wires with different specifications were designed. The diameter of the first heating wire is 70mm, which is consistent with the diameter of the three-zone heating wire. In addition, a heating wire with larger diameter was designed to improve heat transfer efficiency,

which was the 100mm diameter heating wire.

Type C： Hollow core with metal heating mandrel. It is composed of metal heating mandrel with round holes, heating tubes and silicon rubber mantle, as shown in Fig. 5(a). Six heating tubes were inserted into the round holes on the metal heating mandrel. The internal thermocouples (TC_{in1}, TC_{in2}, TC_{in3}) were embedded in the preset groove on the outer surface of metal heating mandrel. The silicon rubber mantle was wrapped on the metal heating mandrel

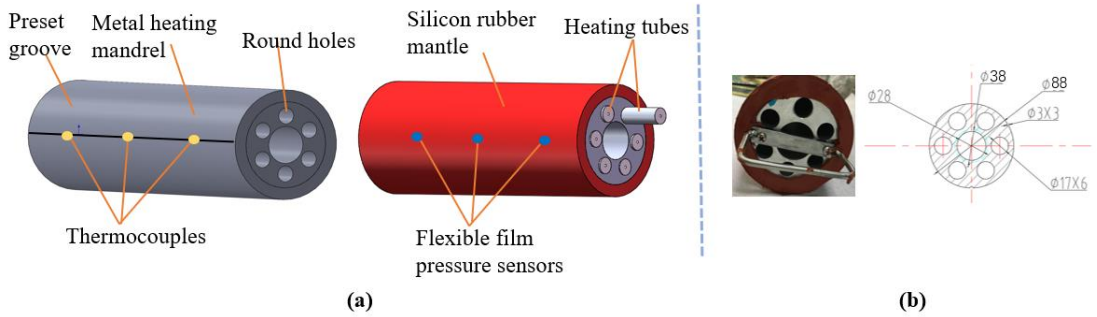

and the pressure sensors were pasted on the outer surface of the mantle. Based on the dimension of core mold and rubber heat-insulating layer, the theoretical process gap between the hollow core and the rubber heat-insulating layer is 1mm. Therefore, it is essential to determine the radius of the metal heating mandrel and the thickness of the silicon rubber mantle. The outer and inner diameter of the metal heating mandrel was 88mm, 38mm, respectively. The diameter of the round hole on the metal heating mandrel was 17mm. The diameter of the heating tube was 16.5mm and the length was 300mm, as shown in Fig 5(b). The specification of the heating tube was 110V/300W. Six heating tubes were inserted into the metal heating mandrel and connected with the control cabinet in parallel. Then a silicon rubber mantle of 12mm thick was poured on the outer surface of the metal heating mandrel. Finally, the prepared silicon rubber core with hollow heating mandrel is shown in Fig. 5(b).

Fig. 5 Schematic of (a) hollow core with metal heating mandrel, (b) dimension of hollow core

2.3 Experiment of thermal expansion process

Using the established thermal expansion stress monitoring and control system and different silicon rubber cores, thermal expansion processes were carried out to form the rubber heat-insulating layer inside metal cylinder. The outer surface of the silicon rubber core was wrapped with a rubber insulation layer and placed in the metal cylinder. This experiment studied temperature variation and thermal expansion stress distribution throughout the process.

According to different types of core heating system and heating methods, five processing

methods were adopted, in order to investigate the optimal processing condition, as shown in Table 1.

Table 1 Configuration of processing methods

Methods	Silicon rubber core type	External heating	Internal heating
Method 1	A	Industrial oven	None
Method 2	A	None	Three-segment heating wire (70cm)
Method 3	B	Industrial oven	Single heating wire (70cm)
Method 4	B	Industrial oven	Single heating wire (100cm)
Method 5	C	Industrial oven	Hollow core with metal heating mandrel

The set temperature of industrial oven was set to 160 °C. The upper temperature limit of the control cabinet's auxiliary control instrument was set to 180 °C, and the process began with the collection of process parameters. The experimental devices used in these methods are shown in Table 2.

Table 2 Information of experimental devices

Name	Model	Manufacturer Internal heating
Pressure control cabinet	Self-developed	Beijing Nanan Automation Co., Ltd
Vacuum oven	DZF-6050	Beijing Luxi technology Co., Ltd
Industrial oven	DRP-8803	Suzhou DERIP oven manufacturing Co., Ltd

The vulcanization quality of the rubber heat-insulating layer was analyzed through surface smoothness, thickness uniformity, density and hardness. In addition, tensile test was performed to evaluate the tensile strength and elongation at break of the layer.

3. Results and discussion

3.1 Testing of the thermal expansion stress-temperature feedback mechanism

In order to verify the negative thermal expansion stress temperature feedback ability of the system, one of the heating zones is used for the test, as shown in Fig. 6. The voltage value represents the thermal expansion stress. When the present voltage value is lower than the

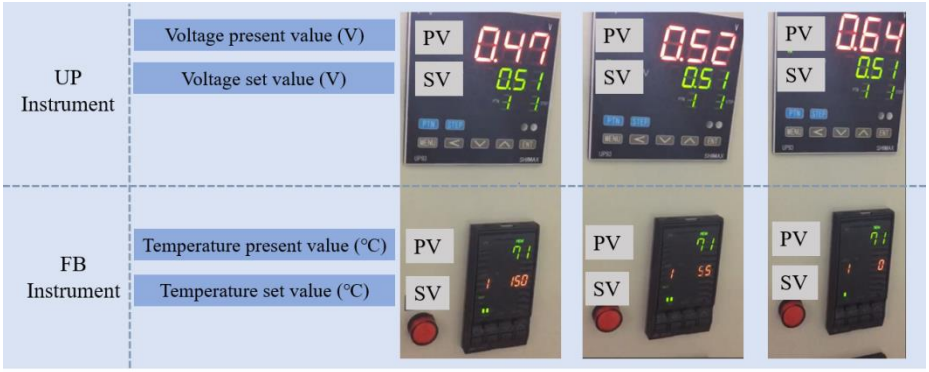

voltage set value, the temperature set value reaches the upper limit 150 ℃ (full heating power output), and the temperature set value gradually rises from 71℃ to 150 ℃, as shown in Fig. 6(a). When the present voltage value is higher than the voltage set value, the temperature set value decreases to 55 ℃, as shown in Fig. 6(b). As the thermal expansion stress increases greatly, the voltage present value is much higher than the set value and the temperature reduces to 0 ℃, as shown in Fig. 6(c). The heating output power is 0W and the heating ceases. These experiments indicates that the thermal expansion stress-temperature feedback is functional and sensitive.

Fig. 6 Test results of thermal expansion stress-temperature feedback mechanism in the case of (a) Voltage set value < Voltage present value (b) Voltage set value > Voltage present value (c) Voltage set value >> Voltage present value

3.2 Influence of processing methods

Method 1 In the case of heating only in the industrial oven, it is possible to determine the temperature and thermal expansion stress according to the locations of the embedded thermocouple and pressure sensors. Fig. 7(a) presents the test results of the heating process. Ten hours are needed for the entire heating and cooling process. The internal and surface temperatures of the silicon rubber core can reach 160 °C in 5 to 6 hours, indicating that the heat transfer rate is low. In addition, the monitored temperature of the internal thermocouple lags behind that of the surface thermocouple by 15 °C. In terms of the thermal expansion stress test

results, the thermal expansion stress changes slightly during the initial stage of heating due to the presence of a process gap. When the temperature hits about 120 °C, the thermal expansion stress (PS_3) quickly increases to more than 3MPa, which matches the forming thermal expansion stress required by the insulation layer, but PS_1 and PS_2 changes are relatively moderate and the pressure value is low. After 1 hour at a steady temperature, the heating is stopped when the temperature hits 150 °C, and the thermal expansion stress in each zone starts to decrease until it reaches 0 MPa.

Method 2 In the case of the heating with 70cm long three-segment heating wires, the results of the temperature and thermal expansion stress during the process are shown in Fig. 7(b). The heat transfer effect decreases in comparison to the heating outcomes of the industrial oven heating method 1. The surface temperature and interior temperature of the silicon rubber core can reach 100 °C, and it can take 4 hours for the surface to achieve that temperature. The thermal expansion can range from 3.5 MPa to 12MPa. The low uniformity of pressure along the silicon rubber core leads to low thickness uniformity and the squeeze-out of the rubber heat-insulating layer.

Method 3 The closed-loop experiment of Method 3 is shown in Fig. 7(c). Compared to the results of Method 2, the surface temperature of silicon rubber core can follow its internal temperature and the temperature difference is smaller. The surface temperature of the silicon rubber core rises to 150 °C in 3 hours. In the constant temperature stage, the thermal expansion stress measured by the pressure sensor fluctuates by 0.5 MPa.

Method 4 The results of the thermal expansion process are shown in Fig. 7(d). At 51min, the internal temperature of the insulation layer reaches the vulcanization temperature, the maximum thermal expansion stress measured by the pressure sensor is 5MPa. The stress in isothermal stage decreases and stabilizes at the range of 3.5~3.9MPa. This heating method has a high thermal expansion stress, so some rubber bulges out of the cylinder, as shown in Fig.8(a). Fig. 8(b)(c) demonstrates the inner and outer surfaces of the insulation layer fabricated using this method. Both the inner and outer surfaces exhibit high quality and uniformity, as well as good surface smoothness and compactness.

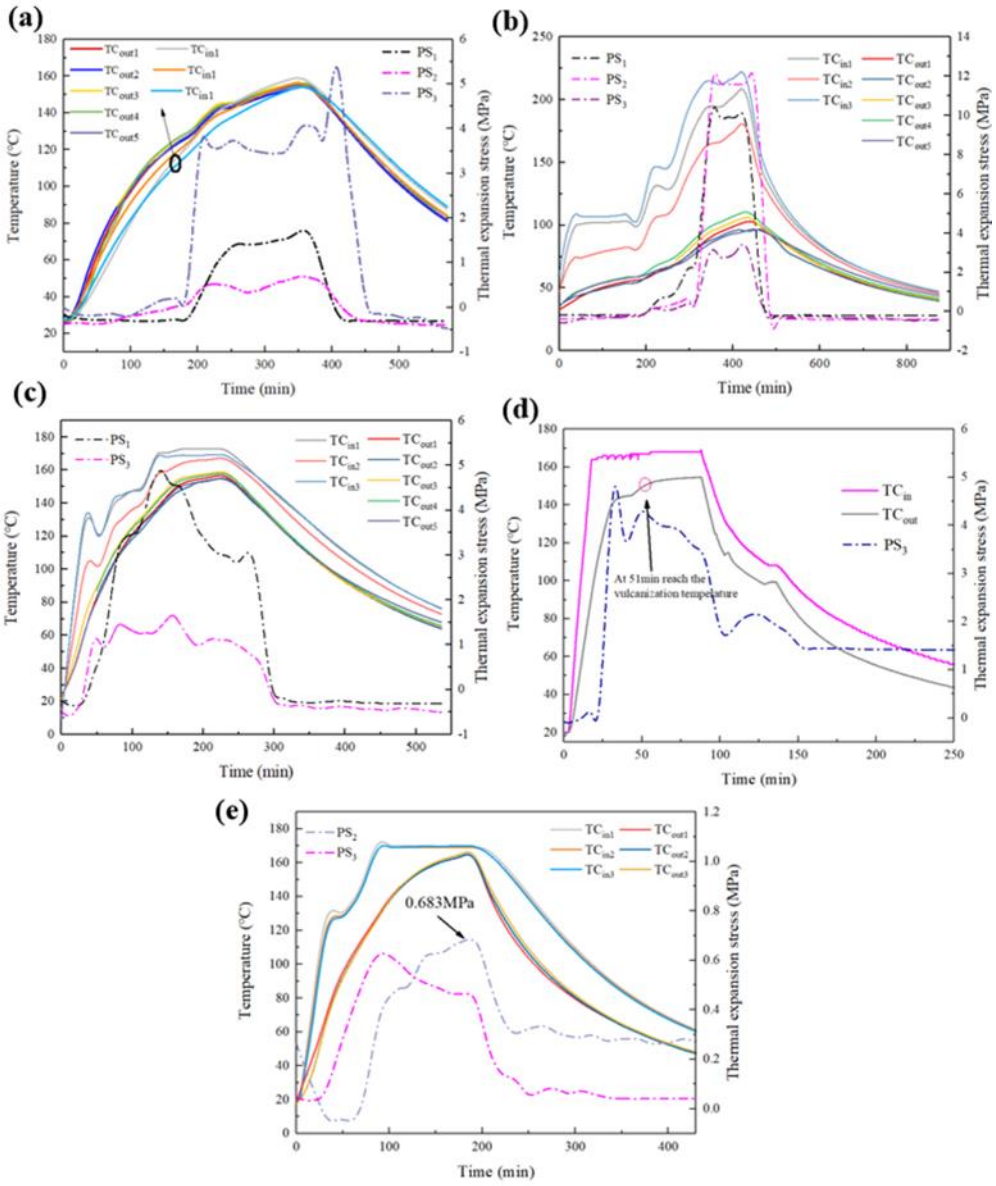

Fig. 7 Typical temperature-time and thermal expansion stress-time curve by (a) Method 1 (b) Method 2 (c) Method 3 (d) Method 4 (e) Method 5

Method 5 The core with hollow heating mandrel was used in combination with the industrial oven to perform the thermal expansion process. The results of the temperature and thermal expansion stress during the process are presented in Fig. 7(e). The results demonstrate that the inner and outer surfaces of the hollow heating mandrel core exhibit excellent temperature uniformity and significantly increases heat transfer efficiency. At the isothermal temperature stage, the temperature of the inner surface of the insulation layer (the outer surface of the core, TC_{out}) reaches the vulcanization temperature at 120 minutes, and the expansion pressure monitored by the two flexible film pressure sensors is stable at the range of 0.5~0.7 MPa. The

fabricated insulation layer exhibit high quality and uniformity on inner and outer surface, as well as good surface smoothness and compactness, can meet the demand of use.

Fig. 8 (a) The rubber bulged out under unduly high thermal expansion stress (b), the surface status of (b) inner surface (c) outer surface of the fabricated insulating rubber layer

Table 3 shows the resultant process parameters of different process. In Method 1, the heating rate is low, and it takes 5.3h for the system to reach the vulcanization temperature. As for Method 2, the internal-heating-method leads to a huge temperature difference. The internal temperature does not reach the vulcanization when the external temperature is 220°C. The ranges of thermal expansion stress for Method 1 and 2 are large. In Method 3, the heating rate is 0.9°C/min, which means the heat transfer efficiency has improved in contrast to Method 2. However, the fluctuation of thermal expansion stress is still high. In Method 4, the heating rate is greatly improved, but the thermal expansion stress is too high, resulting in rubber bulging out. As for Method 5, the heating rate and temperature difference are appropriate, and the thermal expansion stress is relatively stable.

Table 3 Comparison of the processing parameters of differernt process

Method	Heating rate/ °C/min	Time to vulcanization temperature / h	Max. temperature difference / °C	Range of thermal expansion stress / MPa
Method 1	0.5	5.3	14.6	0.4~5.3
Method 2	0.3	Not reached	111.4	3.4~12.2
Method 3	0.9	2.8	30.7	1.3~4.8
Method	2.9	0.9	21.8	3.5~4.0

4				
Method 5	1.3	2.0	30.2	0.5~0.7

The insulation layer fabricated by Method 5 possesses the most remarkable quality. Thus, a series of performance test and nondestructive testing (NDT) are performed on this insulation layer, including thickness, tensile strength, elongation at break, density and hardness. Table 4 shows the performance indexes and test results. The performance test results meet the requirements, and the ultrasonic non-destructive testing results show no debonding at the testing positions of the insulation layer, indicating good molding quality uniformity of the insulation layer.

Table 4 Performance index and test results of insulation layer using Method 5

Test items	Requirement	Test Results
Thickness	1.5 ~ 1.8 mm	1.518 ± 0.013 mm
Tensile strength	≥ 4 MPa	7.43 ± 0.14 MPa
Elongation at break	≥ 200 %	534 ± 37.4 %
Density	≤ 1.26 g/cm^3	1.24 g/cm^3
Hardness	59~75 Shore A	70 Shore A

4 Conclusion

This paper successfully established an online monitoring and regulation of thermal expansion stress in thermal expansion process. By collecting the thermal expansion stress during the process, controlling the output power the core heating system and then the thermal expansion stress of the silicon rubber core, the closed loop negative feedback control of the monitoring and regulation system can be achieved. It is important that the flexible film pressure sensor is used to monitor the thermal expansion pressure and adjust heating output, resulting in appropriate thermal expansion pressure.

The results show that process methods only using industrial oven or internal heat source lead to high thermal expansion stress and low heat transfer efficiency in the heating process. The surface temperature of the rubber insulation layer takes 5.3 hours to reach the vulcanization temperature. When external heat source (industrial oven) and internal heat source (heating wire/tube) are combined, the heat transfer efficiency is significantly improved and the thermal

expansion stress is relatively stable. Among them, the solid core with embedded heating wire combined with industrial oven produces high thermal expansion stress (more than 4MPa), but it is unstable and some rubber bulges out of the cylinder mold. Although the processing method using hollow core with metal heating mandrel combined with industrial oven produces a low thermal expansion stress (0.5~0.7MPa), this stress during the constant temperature stage is stable and controllable. The surface of formed thermal insulation layer is smooth with no debonding and high thickness uniformity. The proposed process scheme is suitable for thermal expansion processing with silicon rubber mandrel.

Reference

[1] Wu Decai LX. Research on resin pressure in prepreg stack during thermal expansion process with silicone rubber for the composite M-Stiffener. Jiangsu Science & Technology Information. 2012;No.24.

[2] Jeong KSO, Se Hoon. Development of the composite flexspline for a cycloid-type harmonic drive using net shape manufacturing method. Composite Structures. 1995;32(1-4):557-65.

[3] King R. A production engineers view of advanced composite materials. Materials & Design. 1982;3(4):515-22.

[4] Weibo Zhang XL, Min Li, Yizhuo Gu. Experimental and Numerical Studies on Compaction of Carbon Fiber Composite Joint With Variable Cross-section Using Thermal Expansion Process. POLYMER COMPOSITES. 2018;DOI 10.1002.

[5] Zuoguang Z JH, Zhijie S , et al. Thermal Expansion Process for Manufacturing of Stitched Sandwich Structures[J]. Journal of Reinforced Plastics & Composites, 2009, 29(9):1418-1427.

[6] H. Canfranc, J.L. Darrieux, C, U.S. Patent 5571, 357 (1996).

[7] Mulle M, Zitoune R, Collombet F, Robert L, Grunevald YH. Embedded FBGs and 3-D DIC for the stress analysis of a structural specimen subjected to bending. Composite Structures. 2009;91(1):48-55.

[8] Walter SC, Harry, S Reinert. A General Look at Thermal Expansion Moulding. Society for the Advancement of Materials, Process Engineering. 1976;649.

[9] G S. Advances in elastomeric tooling technology[J]. Materials & Design. 1996;17(1): 33-42.

[10] Kim D O KSW, Lee J H, et al. Thermally-expandable elastomer molding process for thermoset composite materials[J]. Composites Part A: Applied Science and Manufacturing. 2006;37(11): 2121-2127.

Research on RTM Process Technology of High-precision Load Connecting Frame Structure with Special-shaped Variable Cross-section by internal cross bars

T. Xu, H. S. Wu, and L. Ma

Beijing Spacecrafts, China

Abstract: Aiming at the research and development technology of high-precision load connecting frame structure with special-shaped variable cross-section reinforced by internal cross bars, the two-step weaving and stitching fiber preform forming process scheme and the general RTM product forming process scheme of load connecting frame are discussed by using the comparison method; The virtual simulation of RTM glue injection process is studied by using ESI Group software, which guides the design of RTM molding design; The key points of product implementation, such as the glue injection and curing process of the product and the quality control of the technological process, are analyzed, and the performance of the final formed product is evaluated. Through the process research, we have broken through the key molding technologies, such as the two-step fiber preform molding technology of weaving and stitching, the RTM molding design and processing technology of complex special-shaped composite materials, and the split molding, secondary bonding and combination finishing processing. The results show that the formed products have better forming quality, dimensional accuracy and thermal cycle dimensional stability. The nondestructive testing results of composite parts show that the internal structure of the product is good, the fiber volume fraction is controlled at (55±3)%, the flatness of the important surface of the product is 0.05 mm and 0.03mm respectively, and the dimensional accuracy of the important interface is controlled within ±0.02 mm. After the thermal cycle test, the dimensional stability is good, and all indicators of the product meet the user's requirements, It provides a technical basis for design and manufacture of high-precision and high stiffness composite structures for deep space exploration and manned spaceflight.

1 Introduction

The The antenna deployment arm is an important part of the satellite antenna. When the satellite is launched, the antenna is folded and pressed to the star. After the satellite enters the predetermined orbit, the antenna deployment arm drives the whole antenna to deploy

stably and accurately to the correct working position[1]. The joint load connection frame is an important structural member for the load connection and load force transmission of the rotary joint in the antenna deployment arm. It is exposed to the space when it is in service, and must undergo the cold and hot alternating environment, as well as the influence of space environmental factors such as electrons, protons and ultraviolet radiation. Therefore, it has higher requirements for its structural accuracy, mechanical performance and space environment resistance. In order to improve the stiffness of the unfolding arm joint load connection frame, reduce the structural weight, make full use of the high modulus and high strength characteristics of m55j fiber, and supplement the in-plane performance, the special-shaped composite parts are formed by the braiding stitching RTM process, which has unique advantages. The stitching reinforced structure of braided stitched composite structure in the thickness direction can not only achieve structural integrity, but also overcome the shortcomings of traditional laminated structure with low inter laminar strength, good fatigue resistance, damping and shock absorption, high impact toughness, high damage resistance, and nearly zero thermal expansion coefficient. It is suitable for structures with high dimensional stability requirements in high and low temperature alternating environments[2-4]. RTM molding process is a process of molding in a closed mold, which has the advantages of high dimensional accuracy of products, integrated molding of complex structures, high fiber content, and low porosity of products. In foreign countries, many RTM composite parts have been applied in V-22 "Osprey" and F-22 "Raptor" fighter projects, Airbus R & D program, aerospace Commission ATR program and missile program[5-6]. Compared with the development of RTM molding technology in foreign countries, China started relatively late. In recent years, China has also made certain progress in RTM resin, resin filling flow process and numerical simulation in the mold cavity[7-11], preform manufacturing technology, RTM equipment and glue injection process control, RTM Mold Design and manufacturing technology[12-21]. With the development of RTM technology, materials, processes and equipment, the ultimate goal is to develop products that meet various performance requirements with low manufacturing costs.

Based on the research and development task of the joint load connector, this paper studies the feasibility of the joint load connector using the braiding stitching RTM molding process, expounds the braiding stitching RTM molding technology of the joint load connector from

the aspects of the braiding stitching process scheme of the product, the design of the molding mold, and the quality control of the process, and completes the compound processing of the mechanism structural parts. Finally, the structural parts meeting the design requirements are developed.

2 Experimental

2.1 Raw materials and facilities

(1) Domestic high modulus carbon fiber, ccm55j-6k, Weihai development Fiber Co., Ltd;

(2) Epoxy resin, BS-2, independently developed and prepared by Beijing Spacecrafts

(3) Aramid sewing thread, 30s/3 joint stock, navy blue, Yantai Taihe new materials Co., Ltd;

(4) RTM injection machine, pr70v; Customized by Siemens.

(5) Constant temperature oven

(6) High temperature resistant silicone sealing strip

2.2 Technological process

2.2.1 Weaving and sewing of products

It is easy to change the direction and position of the original reinforced material design by manual laying of fiber reinforced composite in RTM cavity. At present, with the development of composite braiding technology, more and more complex fiber preforms can be pre braided by braiding machines, which greatly reduces the cost of manual laying and improves the forming accuracy. However, due to the poor weaving process of m55j high modulus carbon fiber, a two-step weaving stitching scheme is selected, which can not only increase the inter laminar mechanical properties of the final composite products, but also have lower requirements on the weaving process. First, m55j carbon fiber is woven into two-dimensional plain weave cloth, and then it is layered in a quasi isotropic layered manner (0 / + 45 / - 45 / 90) ns. Then, high-performance sewing thread with high strength, low density, heat resistance, radiation resistance and other excellent properties is used to sew the layers through the control of sewing process parameters. The number of fiber bundles needs to be properly supplemented at the corners to avoid stress concentration in the molding and bearing

process, So as to ensure the performance required by the design. As shown in Fig. 1, it is a physical view of the preform.

Fig.1 a physical view of the preform

2.2.2 Injection molding

BS-2 resin is selected. The viscosity of the resin is less than 1 pa·s at 80 ℃, which has good reactivity, low shrinkage, good compatibility with preform reinforcement materials,

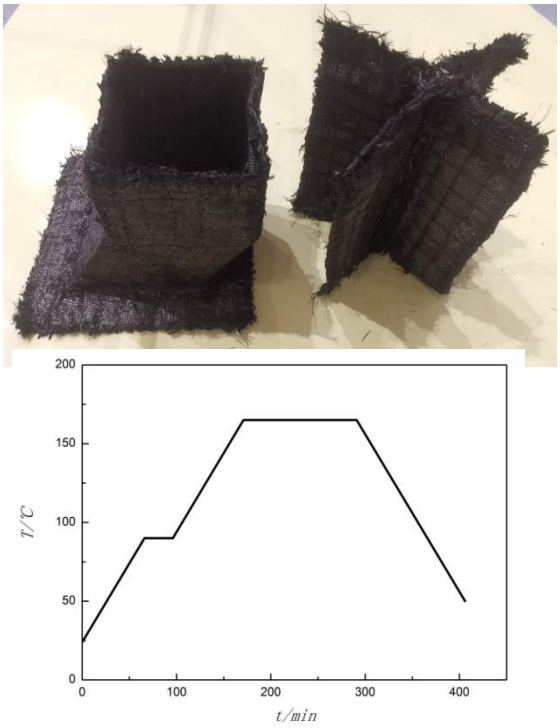

toughness and fracture elongation can meet the design requirements. The injection equipment can achieve heating and constant temperature, mixing and metering functions, and accurate control of injection pressure, which can meet the requirements of RTM injection system. Select the curing system shown in Fig. 2 to cure the RTM parts after the glue injection.

Fig.2 Curing system of product

2.3 Test method

The inspection of composite products is the core content of evaluating product forming technology. Through the evaluation of the physical effect of the molded product, the best molding process parameters are determined to further verify the feasibility of the molding technology. The inspection of composite structures is mainly carried out from non-destructive inspection, fiber volume fraction, dimensional accuracy of parts, dimensional stability of thermal cycle test and so on.

2.3.1 Nondestructive testing

Low frequency ultrasonic nondestructive testing instrument and X-ray testing instrument are used to test the internal molding quality of the composite joint load connector with reference to the class B requirements of GJB2895-97 《General Specification for Carbon Fiber Composite Laminates and Laminated Parts》.

2.3.2 Fiber volume fraction

The fiber volume fraction of the product is measured by weighing method. Respectively record the quality of the molded fiber preform and the quality of the product after RTM glue injection and curing. After calculation, the fiber volume fraction of the product is obtained. The calculation formula is as follows:

$$V_f = \frac{m_f \times \rho_r}{(m_c - m_f) \times \rho_f} \quad (1)$$

Where, ρ_r is the density of epoxy resin and ρ_f is the density of domestic carbon fiber.

2.3.3 Product dimensional accuracy detection

After the joint load connector braiding sewing RTM real product molding machine is completed, use a CMM to test the flatness of assembly surface 1 and assembly surface 2, the parallelism of assembly surface 1 and assembly surface 2 on both sides, and the coordinate dimension accuracy of important installation interface points on both sides to verify whether they meet the design requirements.

2.3.4 Evaluation of thermal cycle test

High and low temperature thermal cycle tests shall be carried out for the joint load connector products according to the design requirements. At least 3 temperature measuring points shall be used to track the thermal cycle test of the joint load connector products. After the thermal cycle test is completed, the flatness of the assembly surface 1 and the assembly surface 2 shall be re measured with a coordinate measuring instrument to detect whether there are changes before and after the thermal cycle test, so as to evaluate the dimensional stability after the thermal cycle test.

3 Results and discu

3.1 Analysis of product structure characteristics

As an important part of the deployable arm joint, the joint load connecting frame is an important connecting piece for the connection, bearing and force transmission of the composite deployable arm rod and the high-precision rotary joint, and is a kind of high-precision composite structural member with internal cross reinforcement and variable cross-section. The overall envelope size is 295 mmx220 mmx232 mm, the overall design thickness is 8 mm, and the thickness of the central cross stiffened part is 4 mm. The bottom flange mounting surface is the assembly surface 1, and the upper special-shaped opening mounting surface is the assembly surface 2. See Fig. 3 for the specific product.

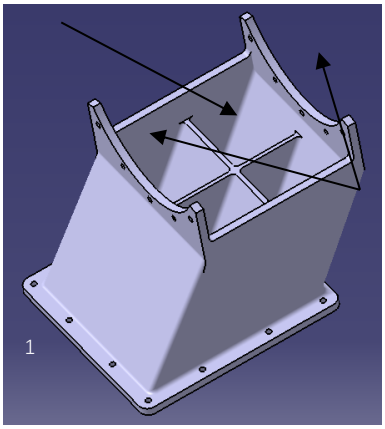

1 - assembly surface 1; 2- Cross rib flange support; 3 - assembly surface 2

Fig.3 Diagram of joint load connection structure

The joint load connecting frame products mainly have the following requirements:

(1) The flatness of assembly surface 1 is ≤ 0.06 mm, and the dimensional accuracy tolerance of installation interface is required to be ± 0.05 mm;

(2) Flatness of assembly surface 2 ≤ 0.03 mm, parallelism of both sides ≤ 0.03 mm, and dimensional accuracy tolerance of installation interface is required to be ± 0.02 mm;

(3) Perpendicularity between assembly surface 1 and assembly surface 2 ≤ 0.03 mm;

(4) The fiber volume fraction shall meet 55 ± 3%;

(5) Ultrasonic nondestructive testing was carried out on the product, and the defects met the requirements of GJB2895-97B;

(6) The product is subject to high and low temperature thermal cycle test to ensure that the assembly plane still meets the above flatness requirements after the thermal cycle test.

3.2 Selection of process plan

The dimensional accuracy, form and position accuracy and mechanical properties of the formed products shall be given priority in the selection of composite product forming process plan. On this basis, it is also necessary to consider the braiding stitching processability, RTM mold closing processability, demoulding operability, etc. For the joint load connection frame described in this paper, the bottom flange mounting surface is assembly surface 1, the upper special-shaped mounting surface is assembly surface 2, and the middle cross reinforcement is a stiffening structure. Assembly surface 1 and assembly surface 2 have very high requirements for dimensional accuracy. Therefore, the overall dimensions of the blank are guaranteed by the net size molding of the mold design, but the key interface is the allowance in the composite blank state, the flatness and parallelism are guaranteed by fine grinding and fine machining, and the mechanical properties are guaranteed by the weaving stitching RTM molding process. There are two main process schemes, one is the overall molding scheme, and the other is the split molding secondary bonding scheme. Table 1 shows the comparison of the two molding schemes. It can be seen from the table that both the overall forming scheme and the split forming secondary bonding scheme can meet the user's requirements for ensuring the mechanical properties and interface accuracy. However, the overall forming sewing mold design is particularly complex, the sewing process and the design of the sewing layer are particularly complex, and the RTM forming mold design is particularly complex, with poor processability, difficult forming, and difficult demoulding. However, bubbles, dry spots, and resin rich zone defects are more likely to occur. Therefore, in this paper, the product is divided into two parts: the joint load connection frame body and the cross rib flange support. The blanks are formed separately, and then the key interfaces are combined after the secondary bonding scheme as the main process scheme to ensure the mechanical requirements and interface accuracy requirements of the product.

Tab.1 Comparison of two molding methods

Molding method	Sewing mold design	Sewing ply design	RTM mold design	RTM molding process	Demoulding process	Mechanical property	Interface accuracy assurance
Integral forming	Extremely complex	Extremely complex	Extremely complex	Poor processability, forming	Difficulty	Meet requirements	Meet requirements

			difficulty				
Split forming secondary bonding	complex	complex	complex	Good	Good	Meet requirements	Meet requirements

3.3 Design of Forming Mold

The mold design of composite structure is closely related to the process plan. The process plan of the joint load connecting frame of this product is a secondary bonding plan for the split forming of two parts, so RTM forming mold is also divided into two sets of mold processing.

The design of RTM process mould for composite products is mainly affected by the decision of process plan and the product model of net size forming of product blanks. The design of die directly affects the shape, size, surface quality and porosity of composite structure. The material, structural form, sealing method, position and quantity of glue injection port and glue outlet, clamping device of the RTM mold directly affect the performance and quality of the final part. The structural form of the mold is related to the mold lifting, gas discharge and mold clamping. Reasonable design is the key to ensure the molding quality.

RTM mold design mainly includes the following contents:

(1) Selection of mold materials: RTM mold materials include steel, aluminum, cast iron, organic glass and some composite materials. As the size accuracy of the product is required to be high, and the number is multiple, all parts of the product mold are made of 45 steel, and the quenching and tempering treatment is HRC28-32.

(2) Determination of net size forming three-dimensional model: according to the control of product blank allowance, the three-dimensional model is processed. At this time, the dimension of the inner cavity of the tooling is determined by the overall dimension of the product blank model. The inner cavity formed after the assembly of the whole set of tooling is the real size of the blank formed by the product RTM. The threaded holes and pin holes of the blank parts of the joint load connection frame body are not machined, and 10-15 mm machining allowance is left on one side of the flange flanging profile at the bottom, and 1

mm machining allowance is left on the thickness direction of the bottom flange. The opening position is reduced by 10-15 mm on one side, and the circular opening and slot are rounded to form the same plane, with 5 mm allowance at the highest point. As shown in Figure 4, it is a schematic diagram of products and blanks.

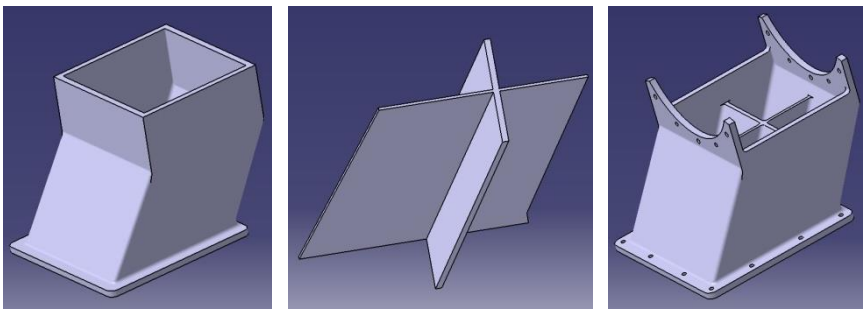

(a) Body blank (b) Cross rib blank (c) Final product

Fig.4 Diagram of product and preform

(3) Block processing of complex molds: In order to meet the requirements of RTM molding and demoulding of products, the molds should be reasonably divided to ensure that the products can be loaded smoothly during mold installation and demoulded smoothly. The body mold is divided into four upper, middle and lower core molds. To facilitate demoulding, the middle mold is divided into two left and right molds. The cross rib mold is divided into three upper, middle and lower parts, excluding the core mold. In order to facilitate demoulding, the middle mold is divided into four parts, front, rear, left and right.

(4) Treatment of sealing channel: The sealing method of the mold in RTM molding process plays a very important role in the entire molding process. Usually, different types of sealing strips are used to seal the mold. The sealing strips used include O-shaped, rectangular and other shapes, and the material is usually silicone rubber. When designing the sealing structure of the mold, in order to ensure the airtightness of the RTM molding tooling, the tooling needs to be provided with a sealant groove. The width and depth of the sealant groove are determined according to the specification of the sealant strip. The sealant groove layout needs to ensure the overall sealing of the tooling cavity. The distance between the sealant tank and the product area is more than 7mm~10mm, which can neither be too far nor too close. Too close will affect the structural connection strength and sealing effect, and too far will easily cause resin flash. Ensure sufficient safety distance to enable it to bear the injection pressure of glue injection.

(5) Treatment of repeated disassembly and positioning: In order to meet the requirements of repeated disassembly and positioning of the mold, sufficient threaded holes shall be arranged everywhere on the tooling. Considering the size envelope of the product, M8 threads and Φ 10 The positioning pin shall be positioned to ensure that the form and position accuracy of the mold and the assembly clearance are less than 0.1 mm.

(6) Handling of convenient demoulding: To facilitate the demoulding of tooling, the segmented tooling needs to be provided with a demoulding ejection threaded hole. Because the product is a hollow special-shaped variable angle section structure, the demoulding design is more complex. Therefore, after the mold design is completed, CATIA software should be used to simulate the curing process. The CATIA software should be used to analyze the movement path of the mold during demoulding, reasonably select the separation surface, and disassemble the entire molding mold to ensure that the product can demould smoothly after curing. The metal core mold plays a supporting role. In order to ensure the demoulding, the mold is designed into a combined structure, and the metal blocks are connected with the main structure through screw connection, glue connection and other connection forms. When the product is demoulded, the metal blocks are taken out according to the preset demoulding track.

(7) Treatment of glue flow channel: RTM molding tooling shall be reserved with glue injection port, glue outlet and glue flow channel. The specific quantity and position can be adjusted according to the actual product. The design of resin flow channel includes the setting of glue injection port and glue outlet, which is the core of RTM mold design. The design of glue injection port and glue outlet on the mold is related to the flow direction of resin flow front in the mold cavity. The injected resin enters the mold cavity through the glue injection port on the RTM mold, and the gas in the mold cavity is discharged through the glue outlet on the mold. This paper uses ESI Group special process simulation software to carry out the process simulation of the glue injection process. First, for the product model, single point glue injection mode is selected. The glue injection port is designed at the center of the obtuse flange flanging at the bottom of the product, and the glue outlet is located at the center of the abnormal opening on the upper part of the product. In this glue injection mode, the glue injection completion time is about 5684s.In order to save the glue injection time, improve the production efficiency, improve the design of the glue injection port, select the bottom

four point glue injection method, the glue outlet design is still designed as a single point aggregation glue, and consider the product molding margin. Under this glue injection mode, the glue injection time is rapidly reduced to 1673.9s. Therefore, in order to save time, improve the resin service life, reduce costs, and improve efficiency, the improved glue injection runner design is selected.

As shown in Figure 5, it is the schematic diagram of the forming tooling of the joint connecting frame.

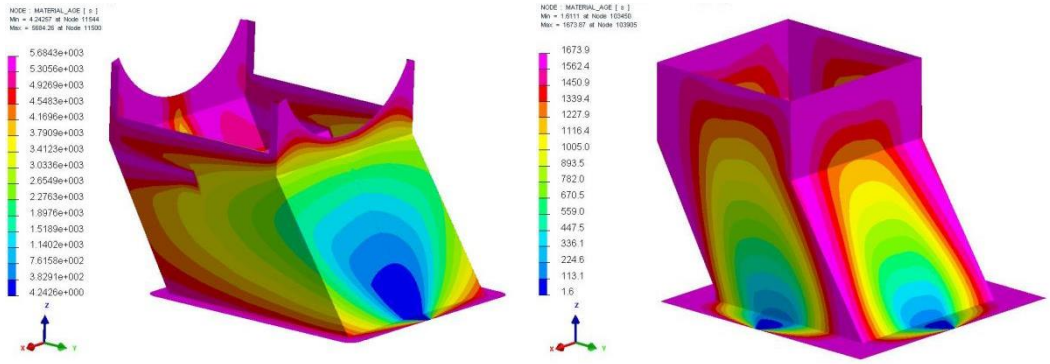

(a) Single point glue injection simulation of products (b) Four point glue injection simulation of product blanks

Fig.5 Diagram of ESI Group process simulation

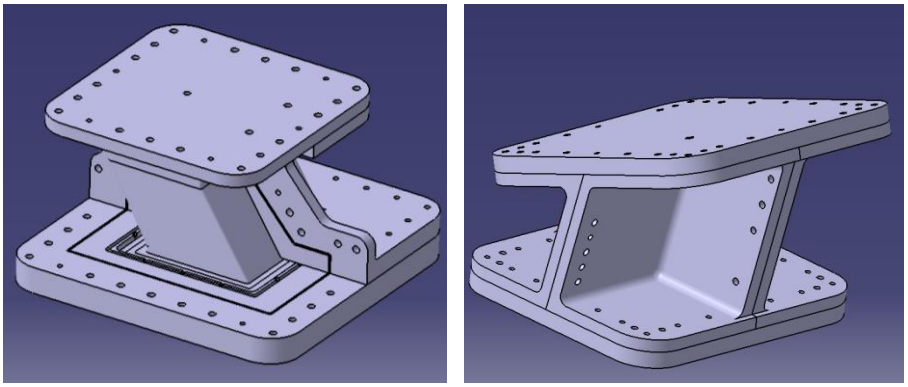

(a) Mould of joint load connection frame body (b) Mould of cross stiffened flange support

Fig.6 Diagram of forming mould of joint load connection structure

3.4 Quality control of process

Quality and process control is a key to the successful application of composite RTM process. The quality control of RTM process mainly includes dimensional accuracy control and thermal deformation control.

(1) Fiber volume fraction control: RTM is a closed grinding process for net size forming,

and the inner cavity of the mold is the actual size of the product blank. The fiber volume fraction of the final product can be controlled by strictly controlling the quality of the braided stitched fiber preform. Therefore, the fiber volume fraction requirement of the formed product can be guaranteed by controlling the fiber preform quality within ±30 g of the theoretical quality.

(2) Dimension and precision control: the main technical difficulty of joint composite parts is that the dimensional tolerance and form and position tolerance required by the product are very high, and it is difficult to achieve one-time molding of composite parts. Therefore, it must be realized through the forming of blank parts, numerical control processing of parts, secondary bonding and combined processing of components. In this paper, the joint load connecting frame product is formed by weaving stitching RTM process, the shape envelope is near net size forming, and the shape dimension of the blank is guaranteed by the mold; However, the high-precision key interface dimensions are guaranteed by numerical control processing, including: the flatness of bottom assembly surface 1, the flatness and parallelism of upper assembly surface 2, the position of two large openings on the assembly surface and each connecting hole are guaranteed by the processing accuracy of the numerical control machine tool.

(3) Thermal deformation control: the machining tool shall be selected strictly during the composite material machining process, the precision grinding and finishing speed shall be controlled, and the machining stress during the machining process shall be reduced. After the machining is completed, the CMM shall be used to measure and record the flatness of assembly surface 1 and assembly surface 2. According to the design requirements, the thermal cycle test shall be carried out to remove the machining stress. After the thermal cycle test, measure and record the flatness of the assembly surface 1 and 2 with the CMM again. If it is not suitable, the machine tool shall be used for fine grinding and finishing again to ensure that it meets the requirements.

3.5 Final performance of the product

Joint load connection frame weaving stitching RTM physical objects after knitting, sewing, glue injection, curing, demoulding, correction, bonding and machining are shown in Figure 7.

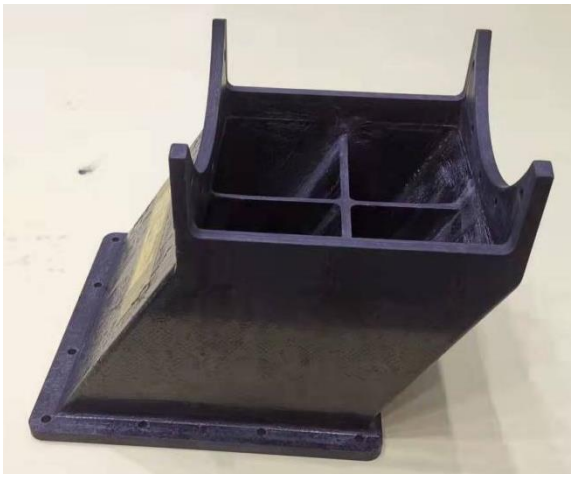

Fig.7 Diagram of real part of joint load connection structure

The results of nondestructive testing on the internal forming quality of composite joint load connection frame show that there are no surface bubbles, dry spots, resin rich areas, surface depressions, folds, scratches, cracks, inclusions and other defects inside the parts, and the internal quality meets the requirements of Class B in GJB2895-97 General Specification for Carbon Fiber Composite Laminates and Laminates. After accurate weighing and calculation, the fiber volume fraction of the structural member meets 55±3%, which is within the reasonable range specified in the design. Through the inspection of the forming accuracy of the braided stitched RTM physical product of the joint load connection frame, the dimensional accuracy of the product meets the design requirements, including the flatness of the assembly surface 1 and the transfer surface 2 are 0.05 mm and 0.03 mm respectively, the parallelism of the two sides of the assembly surface 2 is 0.03 mm, and the dimensional accuracy of the important installation interface is ±0.02 mm. All of its indicators meet the design requirements, further verifying the rationality of the process plan. The high and low temperature thermal cycle test was carried out for the joint load connecting frame products according to the design requirements. During the test, the joint load connecting frame products did not show any water condensation or dew condensation. After the thermal cycle test, the CMM was used to detect the flatness of the arm assembly and mounting surfaces and the rotary joint assembly and mounting surfaces, which were 0.05 and 0.03 respectively. The thermal cycle test process did not change, and the products met the design and use requirements.

4 Conclusion

The joint load connection frame can realize the molding of complex composite structural parts

by using the weaving suture RTM molding process and the split molding and secondary bonding scheme. The results show that this set of process plan can solve the molding problem of complex special-shaped hollow stiffened variable angle section high-precision multi-faceted interface composite structural parts, mainly in the following aspects:

(1) The weaving stitching two-step scheme, which can not only increase the interlaminar mechanical properties of the final composite products, but also lower the requirements for the weaving process, is used to realize the molding of fiber preforms. It can not only make full use of the high modulus and high strength characteristics of M55J fiber, but also supplement the in-plane performance, and ensure the molding stiffness and mechanical properties of the molded products;

(2) The key to ensure the successful development of the joint load connecting frame is to adopt the block design of the combined mold, the optimization design of the sealing channel and the glue flow channel, the design of repeated disassembly and positioning, and the demoulding design;

(3) The split forming secondary bonding process scheme is adopted, and then the combination of key finishing interfaces as the main process scheme can ensure the mechanical requirements and interface accuracy requirements of the product, and all technical indicators of the final product meet the design index requirements;

(4) ESI Group digital simulation software can be used to guide the design of mold injection runner and optimize the design of RTM molding mold, but the mold still needs to be designed manually. Later, a rapid design system for mold structure based on 3D entities can be established, which can automatically determine or manually determine the parting surface, automate the addition of standard components, parametric modification, interference inspection and other functions, reduce design errors from the design source and reduce the number of mold trials, Improve the automatic production efficiency of RTM products.

References

1. Z. Y. Li, “Three-Dimensional Parametric Modeling and Statics Analysis of Hoop Truss Deployable Satellite Antenna,” Northwestern Polytechnical University, 2004.
2. C. Y. Yang, J. X. Ma, L. Ma, “Finite element analysis of 3D woven composites multidirectional joint,” Materials Science and Technology, Vol.23, No.6, 24-28, 2015.
3. S. Ju, J. C. Zeng, D. Z. Jiang, “Study Progress in Composite Truss-joint,” Materials Reports, Vol.20, No.12,

28-31, 2006.

4. Y, J. Jing, X. Wei, Y. Zhang, “Development and Application Status of Three-dimensional Knitting Composite Material,” Cotton Textile Technology, Vol.49, No.11, 79-84, 2019.
5. Q. L. Mei, Y. D. Ji, X. C. Chen, “Development of Liquid Molding Process and Equipment for Composite Materials,” Fiber Reinforced Plastics/Composites, No.9, 52-62, 2014.
6. D. Zhan, “Study on RTM Molding Process of Skin of the Wing Composite Scale Model,” Dalian University of Technology, 2017.
7. J. Luo, Z. Liang, C. Zhang, “Optimum tooling design for resin transfer molding with virtualmanufacturing and artificial intelligence,”Composites: Part A, No.32, 877–888, 2001.
8. Seong Taek Lim, Woo Il Lee, “An analysis of the three-dimensional resin-transfermold filling process,” Composites Science and Technology, No.60, 961–975, 2000.
9. M.R. Shahnazari, A. Abbassi, “Numerical Modeling of Mold Filling and Curing in Non-Isothermal RTM Process,” IJE Transactions A: Basics, Vol.17, No.4, 395-404, 2004.
10. L. Trevino, K. Rupel, W. B. Young, “Analysis of Resin Injection Molding in Molds With Paeplaced Fiber Mats. I: Permeability and Compressibility Measurements,” Polymer Composites, Vol.12, No.1, 20-29, 1991.
11. W. B. Young, K. Rupel, K. Han, “Analysis of Resin Injection Molding in Molds With Preplaced Fiber Mats. II: Numerical Simulation and Experiments of Mold Filling,” Polymer Composites, Vol.12, No.1, 30-38, 1991.
12. B. Y,“Research on Numercal Simulation and Defect Prediction for The Filling Process of Resin Transfer Molding,” Harbin Institute of Technology, 2015.
13. L. Y. Zuo, W. P. Wu, X. L. Wang, “Process and Simulation of Complicated Composites RTM Integrity Technology,” Aeronautical Manufacturing Technology, No.1, 96-103, 2016.
14. A. A. Zhao, W. K. Yang, F. Yu, “RTM Process for Large-Scale and High-Performance Composite Components,” Journal of Nanjing University of Aeronautics & Astronautics, Vol.52, No.1, 39-47, 2020.
15. Y. P. Li, P. L. Guo, L. Su, “Simulation Research on Design of Front Strake Flow Passage of RTM Process Composite Based on PAM-RTM Software,” Trainer, No.2, 18-23, 2018.
16. D. Y. Yu, X. J. Ding, F. Liang, “Research Progress of RTM Process for Advanced Resin Matrix Composites, ” Fiber Composites, No,3, 94-98, 2021.
17. L. Zhao, N. M. Xiao, “Research and Development Review of Advanced Resin Matrix Composite Molding Process Simulation Software,” Software Guide, Vol.20, No.10, 1-6, 2021.

18. C. X. Yuan, L. M. Gao, K.Chen, “RTM Processing of the A-shaped Composite Stiffened Frame ” Fiber Reinforced Plastics/Composites, No.1, 77-79, 2017.
19. X. Y. Chen, Z. Wang, J. L. Bu, “Process Simulation and Verification of Carbon Spar Cap by VARTM Process,” Composites Science and Engineering, No.7, 110-113, 2020.
20. J. P. Peng, “Application of RTM Technology in Aviation Manufacturing,” Engineering & Technology, No.6, 223, 2018.
21. S. C. Jiang, J. W. Bao, L. W. Zhang, “Research Progress of Liquid Molding Resin Matrix Composites and Its Technology,” Aeronautical Manufacturing Technology, Vol.64, No.5, 70-81,102, 2021.

A review of research progress of out-of-autoclave prepreg process

Quansheng MA, Wenyi WANG
Beijing Lankeyingsheng Aviation technology CO., Ltd, Beijing, China

Abstract: The Out-of-Autoclave (OOA) prepreg process, which can manufacture primary and secondary structural composite parts with the same quality and performance as the autoclave process, has been developed in the aerospace field in order to reduce the cost, improve production efficiency and product more large parts. Compared with the autoclave process, OOA process has lower investment and operation cost, wider range of curing equipment, tool and materials can be used, and can manufacture super large structural parts that exceed the size of existing large autoclaves. This paper summarizes the research progress of the process of OOA prepreg. Furthermore, the form of OOA prepreg, the debulking, fiber consolidation, formation of defects and cure cycle of the process of OOA prepreg are investigated. Finally, the future development of OOA prepreg materials and processes is discussed.

Keywords: out-of-autoclave; prepreg; voids; out-life; cure cycle

1 Introduction

The high manufacturing cost of composites has become one of the main obstacles to its further application [1]. At present, low-cost composite material technology has become a key issue in the field of composite material development and research. In order to reduce costs, the aerospace field has developed out of autoclave (OOA) process to manufacture aerospace structural parts [2].

OOA process specifically refers to the process that can produce high-quality (low defect, high performance) composite material parts without autoclave [3]. Compared with the autoclave curing, OOA process has several potential advantages, such as lower capital investment and operation cost, wider range of curing equipment, tool and materials available, and can manufacture super large structural parts exceeding the size of existing large autoclaves [4]. Many manufacturing processes of composite materials, including liquid composites molding and pultrusion molding, can be classified as out of autoclave process. This paper focuses on the new generation of vacuum bag only (VBO) prepreg process for high-performance applications.

1. OOA PREPREG

In the vacuum bag process, the maximum vacuum pressure is only 0.1MPa. If the common prepreg is used, when the thickness of the composite laminate exceeds 1.5mm, the lower pressure cannot prevent the growth of the voids in the laminate, which will bring serious product quality problems. OOA prepreg, which is different from the autoclave prepreg, is sometimes called "breathing" prepreg. To achieve low porosity and tight dimensional tolerances, OOA prepregs rely on specific microstructural features and processing techniques. During manufacturing, the prepreg is designed to be partially impregnated with resin rich and dry fiber areas. OOA prepregs possess a partially-impregnated microstructure that includes

both dry and resin-rich regions (Figure 1). The dry fiber area serves as engineering air channel during cure, so as to entrapped air, vaporized moisture, and/or other volatiles present in the laminate prior to resin gelation. The dry regions of the initial prepreg microstructure form a permeable internal network that allows air transport during the initial, low temperature stages of cure. Then, at high temperature, they are evacuated by resin from external resin-rich regions[5].

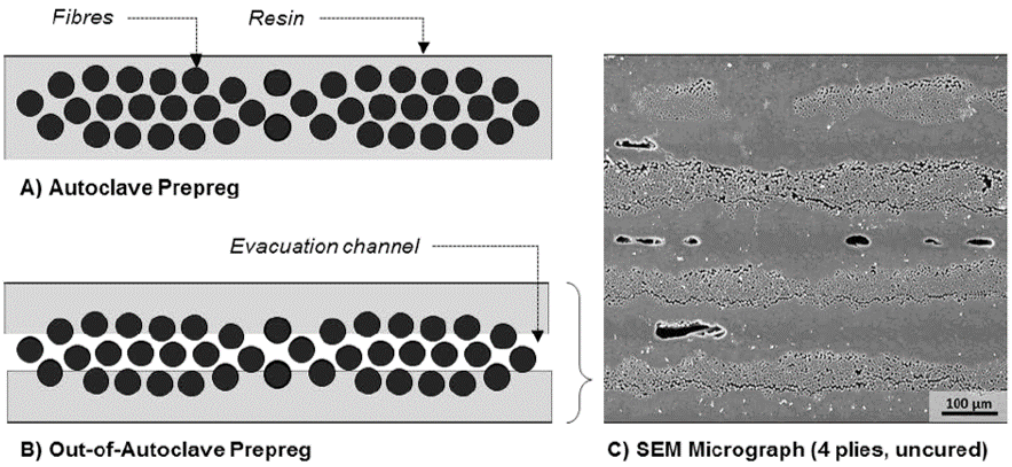

Fig. 1 Schematics of the impregnation paradigms of unidirectional (A) autoclave prepregs and(B) OOA prepregs, and (C) SEM micrograph of a four-layer laminate of uncured unidirectional prepreg (Cytec Cycom 5320-1, T40-800B).

For aerospace and other high-performance applications, zero-bleeding materials are often required to maintain strict control of resin content and maintain resin pressure. In terms of OOA prepreg resin matrix, because it is partially impregnated with fibers, it is required that the resin must have a high viscosity at room temperature to prevent the cold flow of the resin. At the same time, during the cure cycle, the resin must also reach a sufficiently low viscosity, so that the fiber layer can be fully impregnated before the gelation and final cure of the resin, so as to ensure that there is enough resin to impregnate all the initial dry areas while still maintaining a high final fiber volume fraction, which is particularly important for aerospace applications.

In terms of OOA prepreg reinforcement, the compatibility between its structural form and resin system is mainly considered. That is, the fiber volume fraction and permeability of the reinforcing material must be combined to allow partial impregnation in the initial state before the resin gel and complete saturation during cure. The following aspects should be paid attention to in the selection of reinforcement structure: (1) Selecting the appropriate weight of prepreg. Since the number of layers to be laid is small, although the higher weight prepreg can improve the efficiency, the ratio of its initial thickness to the final thickness is higher, and it is more difficult to compact under the process pressure of only 0.1MPa. (2) The reinforcements with uneven surface morphology, such as woven fabrics, are easier to entrapped air in the interlayer area than the reinforcements with smooth surface morphology such as unidirectional tapes. During OOA cure, air must be completely evacuated under vacuum to reduce the porosity of cured parts. (3) Unidirectional reinforcements and woven fabrics with denser weaves are typically less drapable than fabrics with a looser weave. In the absence of autoclave pressure, such materials may be difficult to conform to tool geometries with tight curvatures[6, 7].

Tab. 1 Current-generation aerospace grade OOA/VBO prepreg resin systems

MANUFACTURER	RESIN FAMILY	RESIN TYPE	DESCRIPTION
ACG (now Cytec)	MTM44-1	Epoxy	Medium temperature molding (MTM) toughened epoxy. Qualified by Airbus for secondary and tertiary structure
	MTM45-1	Epoxy	Lower temperature cure system optimized for compression performance
	MTM45-1FR	Epoxy	Variant of MTM45-1 optimized for flame retardation
	MTM47-1	Epoxy	Variant of MTM45-1 optimized for hot/wet notched performance up to 130°C
Cytec	Cycom 5320	Epoxy	Toughened epoxy designed for primary structure application
	Cycom 5320-1	Epoxy	Variation on 5320 system, formulated for increased out-life.
Gurit	Sprint ST94	Epoxy	Single-sided molding prepreg for parts requiring resistance to impact damage and microcracking
Hexcel	Hexply M56	Epoxy	High performance VBO epoxy system
Toray	2510	Epoxy	Formulated to meet the requirements of general aviation primary structure
Tencate	BT250E	Epoxy	Standard VBO system used in Cirrus aircraft and unmanned vehicles. Variations for fatigue and fracture resistance for helicopter rotor blades
	TC250	Epoxy	Second generation VBO system with increased toughness and higher service temperatures
	TC275	Epoxy	Third generation system with greater inseparability, resistance to hot/wet conditioning and curable at 135° C
	TC350-1	Epoxy	Third generation system with increased out-life (45+ days), high toughness, and ability to cure at 135° C with 177° required post cure
	TC420	Cyanate ester	High temperature system (service temperatures up to 315° C)
	TC800 BMI+	Bismaleimide	High-temperature, toughened BMI prepreg formulated for cure out-of-autoclave
Henkel	Loctite BZ	Benzoxazine	VBO prepreg based on a blended epoxy-benzoxazine resin formulation

2. Molding process of OOA prepreg

3.1 Debulking

The air evacuation is very important to the manufacture of high-quality parts. In OOA process, due to the lower pressure compared to the autoclave process, the air evacuation in the manufacturing process needs more attention. Before entering the oven, the air is evacuated mainly through two steps of debulking and vacuum holding.

Debulking is the process of vacuuming the prepreg layer with a temporary vacuum setup. Debulk steps are usually short (5 - 20 min) and imposed periodically, after a small number of plies (1-3) are laid down. During the debulking process, air can be extracted to promote the close geometrical conformation of newly-deposed plies to the laminate or underlying tool. In this step, bubbles in the resin migrate to the resin surface. Vacuum holding at room temperature

refers to the process of vacuuming after the parts are sealed. Vacuum holding is used to maximize the extraction of air before heat curing. The vacuum holding time is a function of part size and prepreg permeability. For large parts, the vacuum holding time can be more than 10 hours [8].

OOA prepreg layer is of porous structure and contains continuous air paths. These paths enable air extraction during debulking and/or a room-temperature vacuum hold. The degree of evacuation mainly depends on the time under vacuum, the permeability of the prepreg layer and the size of the composite parts.

3.2 Consolidation

The maximum curing pressure of OOA process is 0.1 MPa, which is not enough to prevent porosity nucleation and growth. Therefore, it is necessary to evacuate the air, evaporated water or other volatiles in the prepreg layer before the resin gel, which is very important for manufacturing composite parts with low defects. The consolidation of OOA prepreg mainly includes fiber compaction, air evacuation and resin flow. Schematic of microstructure of OOA prepreg during laying, vacuum debulking, heat curing and post curing is show in fig. 2[9].

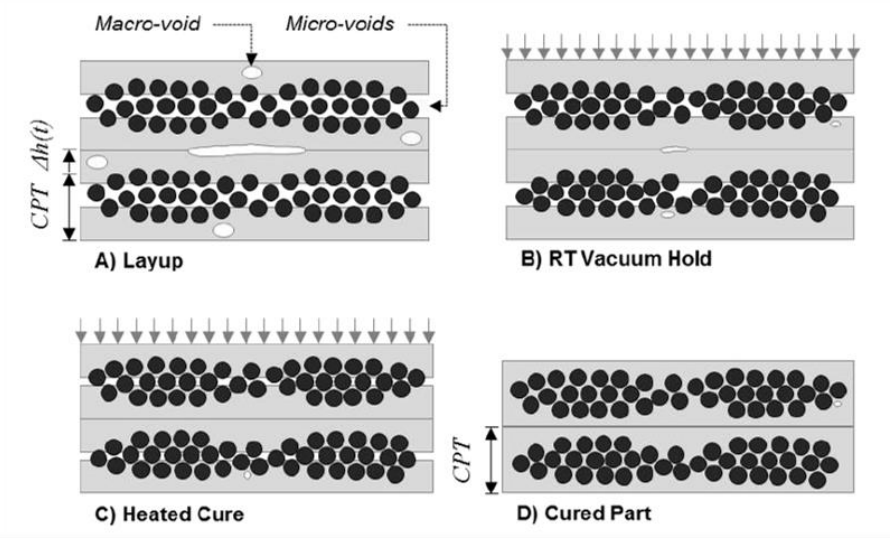

Fig. 2 Schematics of microstructure of OOA prepreg during curing

When vacuum is applied, the air is evacuated from the internal voids of the prepreg layer (Fig. 2, a and b), and the fiber volume fraction increases with compaction. At this time, the porosity and in-plane permeability of the prepreg decrease. At this stage, the flow of the resin is restricted due to its high viscosity at room temperature. After the start of heating, the resin viscosity decreased and the fibers were gradually impregnated (Fig. 2, c). The resin flows into the dry fiber bundle and fills the larger porosity or interlayer spaces therein. The thickness of the prepreg layer decreases significantly, and decreases to the thickness after curing with the porosity space. Finally, as the curing reaction was completed, the microstructure of the laminate was fixed (Fig. 2, d). It should be noted that the initial resin flow is driven by the atmospheric pressure applied on the prepreg layer. Once the resin fully impregnates the reinforcement, the resin saturation impregnation of the entire prepreg layer can only be completed through capillary flow [10]. Before the resin viscosity begins to increase and the prepreg layer undergoes the curing process, all voids between the fibers shall be saturated with resin.

3.3 Formation of defect

The prepreg of the autoclave is usually fully impregnated. In the autoclave process, the relatively high curing pressure (0.3-0.8 MPa) can prevent porosity nucleation and growth. Therefore, for the prepreg of autoclave, complete saturation reduces the possibility of dry spots and other defects due to insufficient resin flow, and helps to form a high-quality, low defect microstructure. The most common defect type in the low-pressure curing process is porosity. In OOA prepreg process, porosity can be divided into gas-induced porosity and flow-induced porosity.

(1) Gas-induced porosity

When the pressure in the core porosity exceeds the pressure of the surrounding resin, the gas-induced porosity will be formed. The factors that form the gas-induced porosity mainly include the air not evacuated before curing, the moisture absorbed by the resin, the vacuum quality reduction, the environmental pressure reduction and the air evacuation limitation.

Grunenfelder et al. [11] exposed the prepreg to elevated ambient relative humidity. The experimental results show that when the moisture content in the resin increases linearly, the void ratio of the VBO cured laminate increases exponentially. While the void content of the autoclave cured laminate was kept at a low level under all humidity conditions. A diffusion-based porosity growth model proposed by Kardos et al., the model shows that when the curing temperature is about 120 ℃, the air pressure in the porosity caused by water can exceed the maximum resin pressure of VBO curing, while the pressure applied to the resin by the autoclave is still higher than the porosity pressure, which inhibits the formation of porosity.

Centea and Hubert [12] studied the effects of ambient pressure, vacuum quality, and air entrapment on porosity. The results show that when the ratio of resin pressure to porosity pressure is low, the decrease of ambient pressure and vacuum quality leads to a linear increase of porosity in the resin rich region. The decrease of vacuum degree will hinder the resin penetration, resulting in micro porosity in the tow. During the test, the extreme case of limiting air evacuation was simulated by sealing the edge of the laminate. The results showed that this brought extremely significant porosity, which indicated that the air entrapped in the surface of the prepreg must be evacuated.

(2) Flow-induced porosity

Because the resin does not completely impregnate into the dry area of the prepreg layer, flow-induced porosity will be formed. The main factor for the formation of flow-induced porosity is the increase of resin viscosity due to exposure to environmental conditions (induced, for example, by out-time). The flow-induced porosity generally show that there are large dry areas in the fiber bundle core, which is a direct result of the existence of initial gas evacuation channels in the microstructure of OOA prepreg.

Lucas [13] et al. studied the effect of out-life on the porosity of parts produced by two VBO resin systems. For the cycom5320 system, the porosity increases with the extension of the out-life. After the cycom5320-1 system was placed outside for 33 days, the porosity of the laminate made of the resin system was less than 1%. A larger porosity content was observed at a faster heating rate, suggesting that slow ramp rates may be beneficial to VBO cure, though the underlying mechanisms of the observed porosity are unknown.

Centea [12] et al. studied the relationship between cure cycle, out-time and fiber bed architecture of prepreg. The results show that the rapid high-temperature cure cycle will lead to faster consolidation (relative to the start of the dwell period) and reduce the microporosity

caused by flow at long out-time. The results also confirmed that out-time reduces prepreg tack and can cause ply warpage, but that such changes can also improve the air evacuation capacity of the laminate and reduce gas-induced macro-porosity. Finally, the uneven surface morphology of fabric plies applied uneven pressure on adjacent layers, but ply orientation and stacking sequence showed no effect on void distribution and porosity as long as the prepreg out-time was not exceeded.

Composite structures often contain curvatures and other geometric features that complicate the layup process and introduce additional physical phenomena during consolidation. The flow and compaction phenomena occurring near such features are more complex than those that occur in flat laminates, and may lead to defects that are not observed in flat laminates, such as those shown in Figure 2.

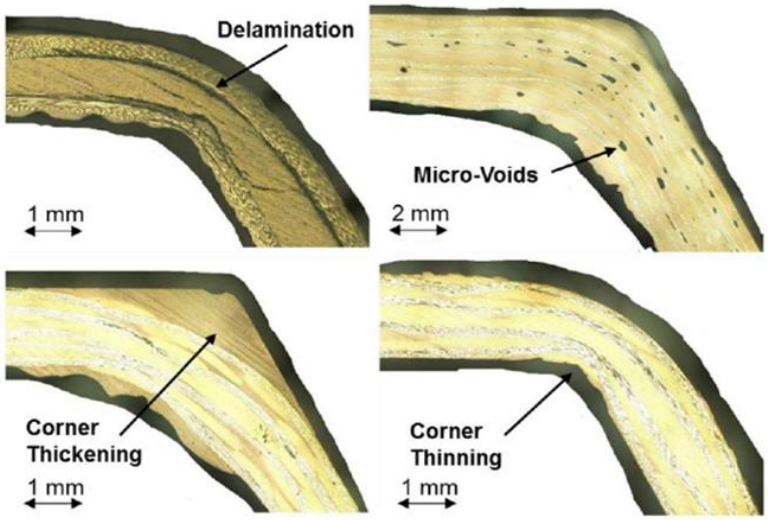

Figure 2 Examples of defects observed in OOA/VBO prepreg laminates with complex geometries (60° angles with sharp mold corner radii) [14].

In general, without an elevated pressure safeguard, OOA prepregs are vulnerable to any process deviation that reduces their void-suppression capacity, either through decreased resin pressure (from reduced ambient pressure) or, more likely, through increased void pressure caused by inadequate vacuum, insufficient air evacuation, or moisture vaporization. This sensitivity, in turn, motivates the need for strict material storage, handling and cure protocols.

3.4 Cure cycle

In the development of OOA prepreg manufacturing process, selecting the appropriate cure cycle is one of the most important choices. The cure cycle directly affects the performance of the resin, thus affecting the final quality of the parts. The proper cure cycle shall maximize the thermal and mechanical properties of the matrix, limit the defects caused by resin flow and air, minimize the curing time, energy consumption and other resources, and minimize the cost by using simple and cheap equipment and tool.

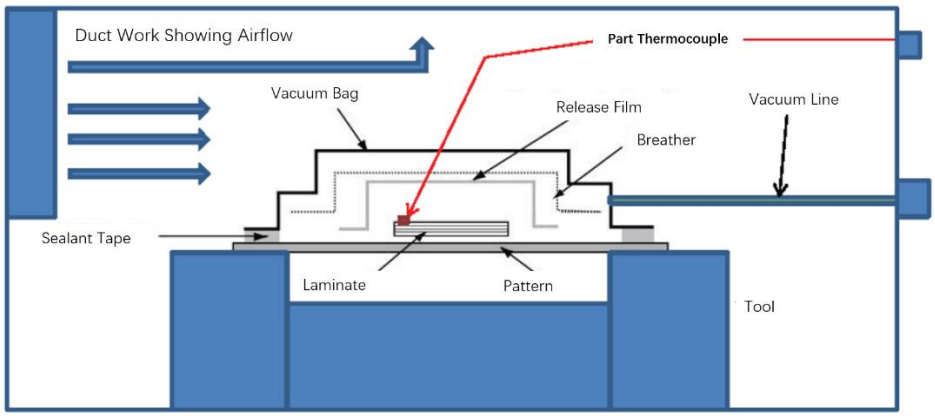

Fig. 3 Part processing in a composite cure oven

The selection of cure cycle is complex and depends on the specific situation. (1) Material factors. The cure cycle must be compatible with the matrix resin. Generally, resin systems are supplied with one (or more) manufacturer-recommended cure cycles. The selection of cure cycle must consider leaving enough time for the resin flow to ensure the gel and vitrification of the resin and not exceed the degradation temperature of the resin. (2) Thermal lag. The heat-up rate of the oven will be higher than that of the parts. Compared with the autoclave process, the internal pressure of the oven is much lower than that of the autoclave, and the heat transfer coefficient in the oven is lower than that of the autoclave. Therefore, the temperature lag during OOA curing may be higher than that of the autoclave. In OOA process, thermal lag is generally monitored and mitigated by appropriately compensating the oven cycle. (3) Thermal gradients. For OOA prepreg, if resin impregnation and air evacuation occur simultaneously, the thermal gradients may have a significant impact on the quality of the part [15]. The thermal gradients will affect the local rate of resin flow, resulting in spatially non-uniform impregnation and in-plane permeability. Generally, the internal area of the part is higher than the average temperature, so the entrapped air is driven to the edge with lower temperature, which improves the air evacuation effect of the whole part and brings low void content. It should be noted that the temperature of the part edge close to the mold is also higher than the average temperature, which easily hinders the evacuation of air and causes higher porosity in the part area with lower temperature. Literature shows that in some cases, the quality of composite parts can be improved by using multi-zone heated tools, heating blanket or improving tool design.

The selection of post-cure parameters is relatively simple because the microstructure of the parts is basically fixed after gel. The post-curr temperature should be as low as possible, or as close as possible to the expected service temperature, to limit the formation of residual stress and the deformation caused by the process during cooling.

The cure cycle of OOA prepreg is widely selected. Table 2 summarizes the main cure cycle parameters of OOA prepreg.

Tab.2 Major cure cycle parameters for OOA prepreg cure, their effects on part quality, and typical values for commercial materials

Parameter	Effects	Typical Value
Heat-up ramp(cure)	*Faster* heat-up ramps lead to: ⇓ Lower cycle times ⇓ Lower viscosity ⇓ Lower porosity (caused by out-time)	0.5 - 3°C/min

Dwell(cure)	*Higher* dwell temperatures lead to: ⇓ Lower cycle times ⇓ Lower viscosity ⇓ Lower porosity (caused by out-time) ⇑ Higher porosity (caused by moisture, air)	80 - 130°C/1-12 h
Heat-up ramp (post-cure)	*Faster* heat-up ramps (post-cure) lead to: ⇓ Lower cycle times ⇑ Higher risk of devitrification	0.5°C/min
Dwell (post-cure)	*Higher* dwell temperatures (post-cure) lead to: ⇓ Lower cycle times ⇑ Higher risk of residual stresses	180°C/1 - 2 h

3 Conclusion

In the next few years, OOA prepreg is likely to be a technology that will facilitate the transition to a fast, efficient and increasingly sustainable processing mode. At present, there are a series of non-autoclave molding processes, including resin transfer molding, vacuum assistant resin infusion and pultrusion. Each method has obvious advantages and limitations[16]. In order to meet the growing demand for composite materials, it is necessary to change the traditional autoclave method. OOA process is a step in this direction. With the development of new material systems and the development of more applications, OOA prepreg technology will continue to develop [17].

(1) Prepreg design and inspection. Specially designed OOA prepregs can improve process robustness. Through the optimization of resin system, customized impregnation can be provided for different composite parts. As the batch variation of prepreg impregnation quality may have a significant impact on the final part quality, more work needs to be done in this field. The quality control of OOA prepreg can only be realized after the development of reliable detection technology.

(2) High temperature curing resin system. At present, OOA prepreg is basically limited to the medium temperature curing epoxy resin, and the development of high-temperature curing BMI resin system is less. With the development of OOA prepreg, it is believed that polyimide, cyanate ester, bismaleimide, benzoxazine and other high-temperature resistant OOA resin systems will be developed[18].

(3) Prepreg used for automatic production. The combination of automatic placement and OOA process has great potential for cost saving. At present, foreign countries are studying the material system used for automatic manufacturing represented by Automated Tape Layer and Automated Fiber Placement.

References

1. Yang Maowei, Liu Jian, Liu Zhenpu, et al. Research Progress of Out of Autoclave Technology for Low Porosity Composite[J]. Aerospace Materials and Technology, 2016（6）: 21-25.
2. Liu Yawei. Development of prepreg non autoclave manufacturing technology based on Out of Autoclave Technology[J]. Defense manufacturing technology, 2013（5）: 17-21.
3. GU Yizhuo, LI Min, LI Yanxia, WANG Shaokai,et al. Progress on manufacturing technology and process theory of aircraft composite structure[J]. ACTA AERONAUTICAET ASTRONAUTICA SINICA, 2015, 36(8): 2773-2797.
4. Pascal Hubert, Timotei Centea, Lessa Grunefelder, et al.. Out-of-Autoclave Prepreg Processing[J].

Comprehensive Composite Materials II Elsevier, 2018(2), 63-94.
5. Thomas A. Cender, John J. Gangloff Jr., Pavel Simacek, et al. Void reduction during out-of-autoclave thermoset prepreg composite processing[C]// Sampe Seattle conference amp, 2013, 1-13.
6. Centea T, Grunenfelder LK, Nutt SR. A review of out-of-autoclave prepregs -material properties, process phenomena and manufacturing considerations[J]. Composites Part A: Applied Science and Manufacturing, 2015(70): 132–154.
7. Centea T, Nutt SR. Manufacturing cost relationships for vacuum bag-only prepreg processing[J]. Journal of Composite Materials, 2016, 50(17): 2305-2321.
8. Yuan Chao, Cheng Wenli, Chen Jing. Research Progress of Out of Autoclave Composite Porosity [J]. Composites Science and Engineering, 2019（12）: 89-93.
9. Centea T, Grunenfelder LK, Nutt SR. A review of out-of-autoclave prepregs - material properties, process phenomena and manufacturing considerations[J]. Compos Part A Appl Sci Manuf [Internet], 2014(70): 132–154.
10. Cender, T.A., Simacek, P. & Advani, S.G. Resin Film Impregnation in Fabric Prepregs with Dual Length Scale Permeability[J]. Composites Part A: Applied Science and Manufacturing, 2013 (53): 118–128.
11. Grunenfelder LK, Centea T, Hubert P, Nutt SR. Effect of room-temperature out-time on tow impregnation in an out-of-autoclave prepreg[J]. Composites Part A: Applied Science and Manufacturing, 2015(45): 119–126.
12. Centea T, Hubert P. Modelling the effect of material properties and process parameters on tow impregnation in out-of-autoclave prepregs[J]. Composites Part A: Applied Science and Manufacturing, 2012(43): 1505–1513.
13. Lucas, S, Howard S, Senger J. Vacuum Bag Only Processing: Improving Prepreg Out-Time and Porosity for Large Composite Structure [J]. Proc. SAMPE 2010 Conf., Seattle, WA: SAMPE.
14. Ma Y, Centea T, Nilakantan G, Nutt SR. Vacuum Bag Only Processing of Complex Shapes: Effect of Corner Angle, Material Properties and Process Conditions. Proc. 29th Tech. Conf. Am. Soc. Compos. US-Japan Conf. Compos. Mater. D-30 Meet., La Jolla, CA: American Society for Composites; 2014.
15. Centea T, Peters G, Nutt SR. Thermal gradients during out-of-autoclave prepreg cure: case study using a heated tool[J]. Proc. SAMPE 2015 Tech Conf., Baltimore, MD: SAMPE.
16. Witik RA, Gaille F, Teuscher R, Ringwald H, et al. Economic and environmental assessment of alternative production methods for composite aircraft components. J Clean Prod 2012;29–30:91–102.
17. Ling Hui，Zhou Yu，Cheng Shangyuan，et al. Research Progress of Out of Autoclave Technology[J]. Aerospace Materials and Technology, 2019（5）：6-11.
18. Anandan S, Nagarajan S, Chandrashekhara K, et al. Cure and process optimization for manufacturing BMI composites using OOA process. Proc. SAMPE 2013 Conf., Long Beach, CA: Society for the Advancement of Materials and Process Engineering; 2013.

Study on the additive manufacturing of carbon fiber reinforced silicon carbide composite based on vat photopolymerization

Hu Chuanqi[1], Li Shan[1], Wang gong[1], Liu Bingshan[1], Zhao Tingting[1], Duan Wenyan[1], Li Xin[1], Li Yuan[2] , Cui Congcong[3], Li Wei[3]*

[1]Technology and Engineering Center for Space Utilization,Chinese Academy of Sciences, PR China

[2]Science and Technology on Advanced Functional Composites Laboratory, Aerospace Research Institute of Material and Processing Technology;

[3]Key Laboratory of Optical System Advanced Manufacturing Technology, Chinese Academy of Sciences

Abstract: This paper explored the feasibility of 3D printing of carbon fiber reinforced silicon carbide composites (C_f/SiC) that based on vat photopolymerization, and analyzes the microstructure and mechanical properties of C_f/SiC composites. The research demonstrates it is feasible to prepare C_f/SiC by 3D printing technology based on vat photopolymerization, but the addition of carbon fiber will improve the viscosity of the slurry, reduce the fluidity of the slurry, improve the absorbance value of the slurry, and have an adverse impact on the 3D printing of the slurry. By optimizing the composition of photosensitive resin, slurry preparation process, 3D printing process and the debinding process of C_f/SiC preform, the C_f/SiC components with complex fine structure can be realized. It is found that the addition of carbon fiber has a great impact on the strength and toughness of the the C_f/SiC, and it has the anisotropy of strength and shrinkage, the linear shrinkage rate in the X-axis direction (parallel to the moving direction of the scraper) is the lowest (1.22%-1.62%), and the linear shrinkage rate in the Y-axis direction (perpendicular to the moving direction of the scraper) is the highest (3.35%-3.99%). When the carbon fiber is distributed along the length direction, it is beneficial to realize the strengthening and toughening of the preform. The strength of the test strip reaches 10.68 MPa. When the carbon fiber is distributed along the direction perpendicular to the length, the strength of the test strip is 5.15 MPa, the arrangement direction of the carbon fiber has little help to the strengthening and toughening of the preform.After debinding, the strength of C_f/SiC decreases (7.32 MPa), and the brittleness increases. We took natural gas and nitrogen as raw materials,via Chemical vapor infiltration (CVI) process under 1040℃ and realized the densification, toughness and structural homogenization of C_f/SiC samples. After CVI, the density of C_f/SiC samples is increased, the weight of samples is increased by ~50 wt%, the

density is increased from 1.40 g/cm^3 to 2.06 g/cm^3, the three-point bending strength is increased from 7.32 MPa to 121.22 MPa, and the Weibull modulus is increased from 0.25 to 5.19.

Key words: carbon fiber reinforced silicon carbide composite, vat photopolymerization, microstructure and mechanical properties, microstructure and mechanical properties.

1 INTRODUCTION

Carbon fiber reinforced silicon carbide composite (C_f/SiC) is a high-performance ceramic matrix composite (CMC). It has advantages of high melting point, high strength, high elastic modulus, high thermal conductivity, low thermal expansion coefficient and high chemical stability, and the thermal shock resistance and fracture toughness of SiC ceramic matrix are improved through carbon fiber reinforcement, which endows C_f/SiC with low density, high temperature resistance, ablation resistance and oxidation resistance, and C_f/SiC has broad application prospects in aerospace aircraft thermal protection systems, high thrust to weight ratio aeroengines, satellite attitude control engines, hypersonic ramjets, cruise missile engines, liquid and solid rocket engines and other weapon equipment fields; In addition, C_f/SiC also has great application potential in nuclear energy, high-speed braking, gas turbine hot end components, high-temperature gas filtration and heat exchange.

Vat photopolymerization (VP) is an advanced additive manufacturing technology that can fabricate ceramic parts based on the photo-polymerization of photosensitive resin-based ceramic slurry or photo curable ceramic precursor. It can build the ceramic green body with fine-complex structure layer by layer through the selective ultraviolet (UV) irradiating process, with the advantages of high strength, fine surface quality, and high dimension accuracy, which are the best among the existing ceramic additive manufacturing technologies. VP offers a new way to fabricate fine complex ceramic parts with integrated structure and function. Currently, it has been widely applied in constructing Al_2O_3, ZrO_2, SiO_2, multiphase ZrO_2-Al_2O_3 ceramics **错误!未找到引用源。** parts, etc.

Compared with the additive manufacturing of Al_2O_3 and ZrO_2 ceramics, VP of C_f/SiC parts with photosensitive resin-based C_f/SiC slurry is much more difficult due to the high absorbance value and refractive index of C_f and SiC particle, which make it harder to be cured in high dimension accuracy under the same parameters.

This paper explored the feasibility of 3D printing of carbon fiber reinforced silicon carbide composites (C_f/SiC) that based on vat photopolymerization, and analyzes the microstructure and mechanical properties of C_f/SiC composites. It is feasible to prepare C_f/SiC composite parts by CVI process, C_f/SiC materials can be densified, strengthened and toughened, and homogenized in structure.

2 EXPERIMENT

We take resin as the dispersion medium, table 2-1 shows the composition of the resin and the manufacturer of them;The SiC powder and carbon fibre is added as the solid phase, table 2-2 shows the mass fraction and the manufacturer of them.Fig.1-1 shows the process follow chart of fabricating C_f/SiC preform in this paper.

Table 2-1 The composition of the resin and the manufacturer in this paper

Monomer of resin	Mass fraction	Manufacturer

	(wt%)	
Acryloyl morpholine (ACMO)	25	China Taiwan Changxing Chemical Industry Co., Ltd
1,6 hexanediol diacrylate (HDDA)	60.9	Royal DSM group
Trimethylolpropane triacrylate (TMPTA)	14.1	Royal DSM group

Table 2-2 The composition of the solid phase and their manufacturer in this paper

Composition of solid phase	Mass fraction(wt%)	Manufacture
Silicon carbide (SiC,D_{50}=40 μm)	90	Weifang Xinfang fine powder Co., Ltd
200 μm Carbon fibre (C_f)	7.0	Korea Carbon Co., Ltd
5 mm carbon fibre (C_f)	3.0	Korea Carbon Co., Ltd

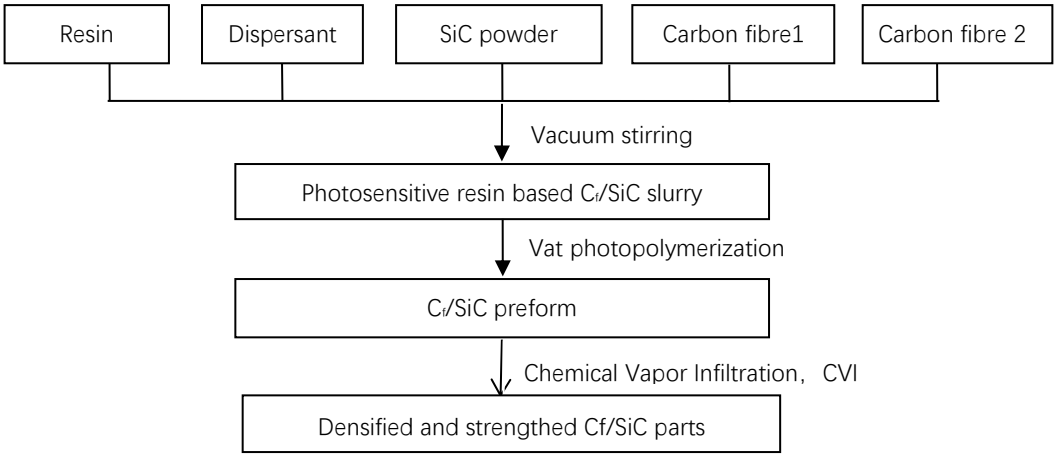

Fig.2-1

The process follow chart of fabricating C_f/SiC preform

Fig.2-2 shows the diagrammatic sketch of the additive manufacturing equipment based on digital light processing (DLP) technology. First, convert the three-dimensional solid model into two-dimensional slice graphics, then project the two-dimensional slice graphics to the surface of ceramic slurry in a "top-down" style through a projector based on digital mirror device (DMD) technology, making the slurry occurs the selective light curing. DMD has the advantages of high resolution and high switching rate, which can achieve the micron level characteristic resolution of the projector, giving it higher precision and higher efficiency of surface exposure; Then, under the computer control, the printing platform descends a certain distance through the stepping motor, the feeding system and scraper spreading system in the equipment perform the uniform tiling of ceramic slurry, and the exposure system performs the new surface exposure action to complete the curing of the new layer. In this way, the photo curing 3D printing of complex fine structure C_f/SiC green bodies is realized layer by layer.

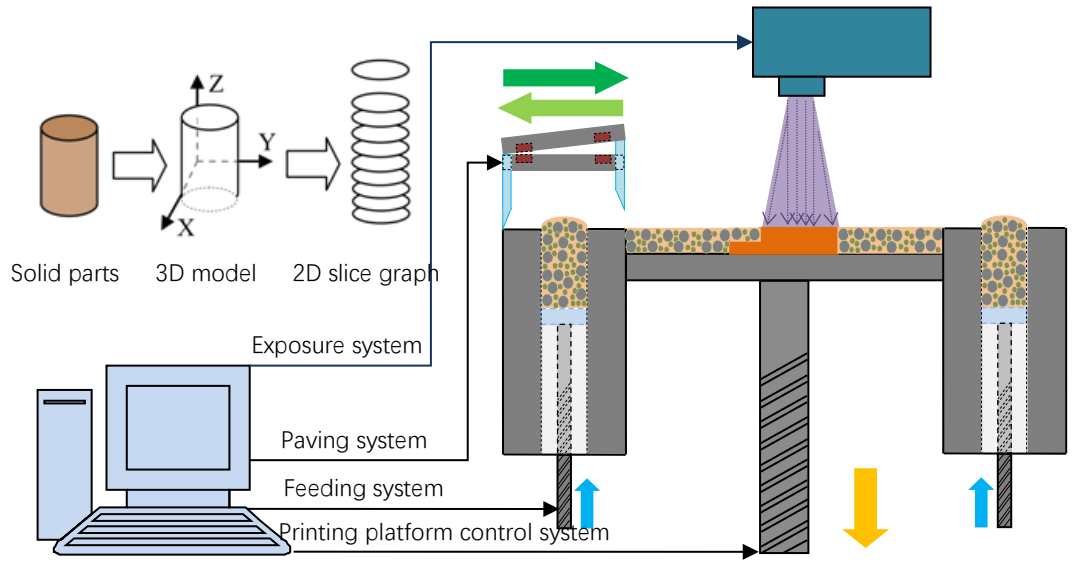

Fig.2-2 Diagrammatic sketch of C_f/SiC preform prepared by vat photopolymerization

The three-point bending strength of C_f/SiC preform before and after debinding is tested with the mechanical testing machine (American Instron, model:5965) according to GBT6569-2006 Test Method for Bending Strength of Fine Ceramics, and the Weibull modulus of bending strength is calculated. The size of the test strip is 3.00 mm × 4.00 mm × 36.00 mm, the test span is 30 mm, loading rate is 0.5 mm/min; Weigh the test strip, measure the size of the sample, calculate the volume of the test strip, and use the volume method, that is ρ= m/v calculate the sample density. The C_f/SiC preform was debinded by the high-temperature tube furnace (Hefei Kejing Material Technology Co., Ltd, model:GSL-1700X), and its microstructure was observed by field emission scanning electron microscope (Carl Zeiss, Germany, model:Sigma 300).

3 RESULT AND DISCUSS

3.1 Preparation process and phenomena of light cured C_f/SiC preform

Fig.3-1 is the appearance of the resin based SiC slurry (A, 52vol%), two kinds of carbon fibers (B) and the morphology after adding fibers (C, D and E). It can be seen that after adding carbon fibers, the fluidity of the slurry decreases and the color becomes darker.When adding the chopped carbon fiber 1 that the length of it is 200 μm, the viscosity of the slurry changes little and the fluidity of the slurry is good, but the color of the slurry changes from light green to light gray; When adding the short carbon fiber 2 with a length of 3-5 mm, the viscosity of the slurry rises sharply, the fluidity of the slurry decreases significantly, and the color of the slurry deepens further, indicating that the addition of long carbon fiber will affect the fluidity of the slurry, thereby affecting the structural homogeneity of the light cured SiC preform; At the same time, due to the high absorbance of carbon fiber, the photo curing reaction activity of the slurry will be reduced, which will adversely affect the photo curing reaction efficiency and precision of the slurry.

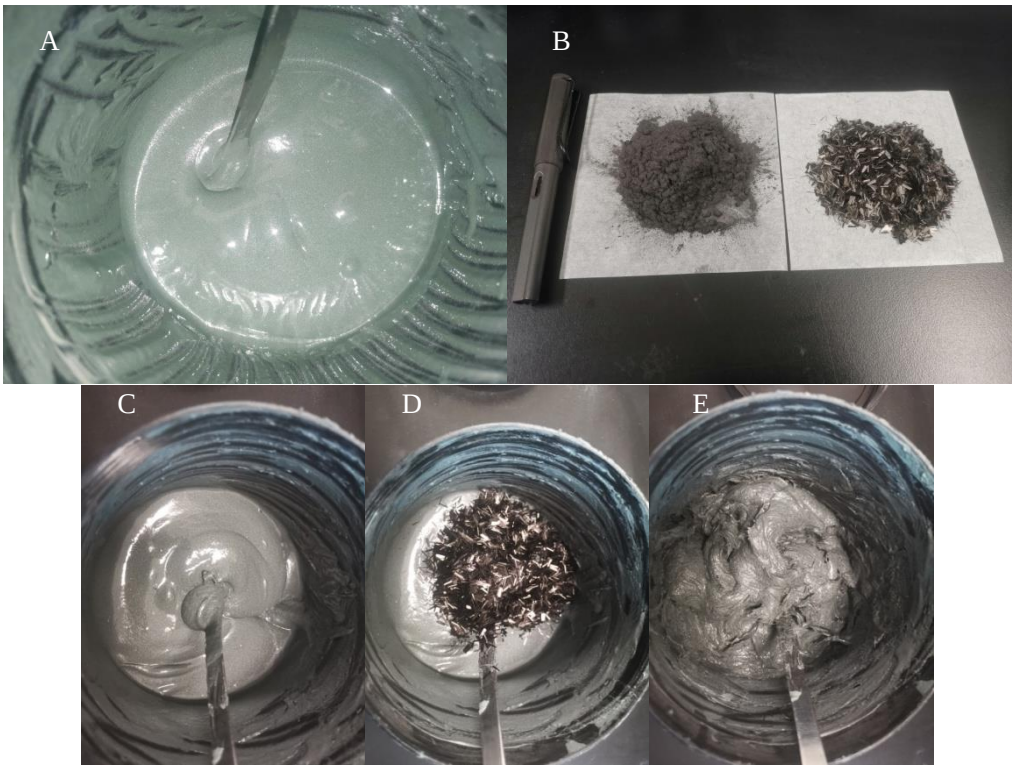

Fig.3-1 Resin based SiC slurry (A，52vol%), two kinds of carbon fibers (B) and the morphology of slurry after adding fibers (C，D and E)

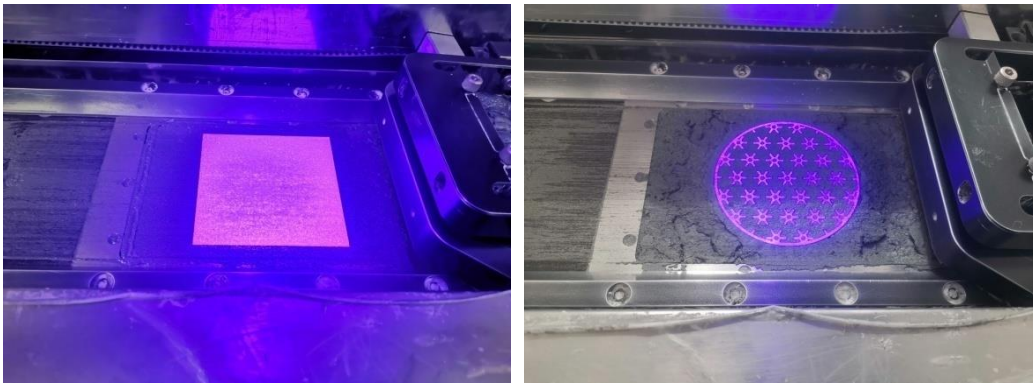

Fig. 3-2 Photos when printing samples on self-developed ceramic 3D printing equipment that based on vat photopolymerization

This paper has verified the photo curing performance of the slurry. Fig.3-2 shows the photos when the paste is printed on the self-developed ceramic photo curing equipment; Fig.3-3 shows printed C_f/SiC preforms. It can be seen that when the carbon fiber content is 10 wt.%, the photosensitive resin based C_f/SiC slurry prepared with 70% chopped carbon fiber 1 and 30% chopped carbon fiber 2 can realize the photocuring molding of complex fine structure under the optimized conditions of photosensitive resin, slurry preparation process and photocuring 3D printing process, and the C_f/SiC preform has the advantages of high curing strength and high curing precision.

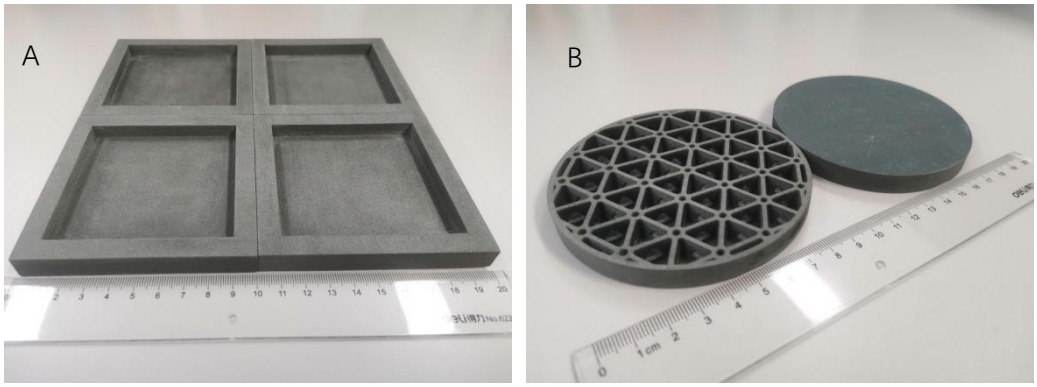

Fig. 3-3 The C_f / SiC samples prepared by ceramic 3D printing equipment based on vat photopolymerization: A, wind tunnel ablation test piece (100mm × 100mm × 12 mm); B mirror (Φ100 mm×10 mm)

3.2 Microstructure and mechanical properties of C_f/SiC before debinding

Fig.3-4 shows the printed document of the light cured C_f/SiC preform.

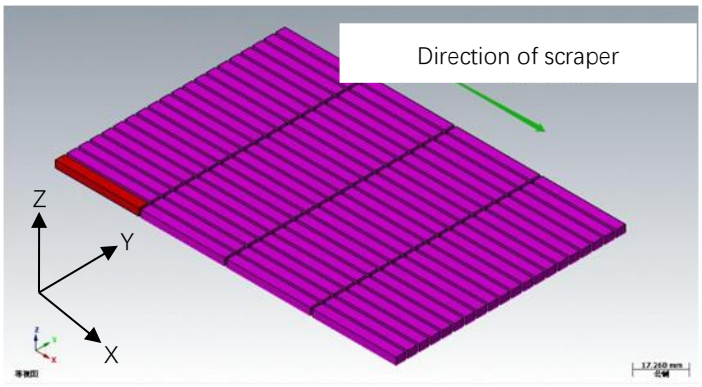

Fig.3-4 Print file diagram of light cured C_f/SiC preform

Fig. 3-5 is the scanning electron microscope diagram of XZ section of light cured C_f/SiC preform. It can be seen that two kinds of carbon fibers interspersed in the C_f/SiC preform in a disordered state; It can be seen from Figure 3-5 (D) that the carbon fiber is wrapped by the cured resin, the light cured resin is not compact, and there are small pores with a diameter about 0.2-0.3 μm on the whole, such micropores may be caused by chemical additives that do not participate in the photocuring reaction in the slurry, such as dispersant, or small bubbles mixed in the resin, or some photoinitiator BAPO particles that are not completely dissolved. In the process of preform debinding, such micro pores can provide a channel for the removal of volatile matter from resin pyrolysis and carbonization, which is conducive to reducing the pressure inside preform and is helpful for the low stress debinding of preform.

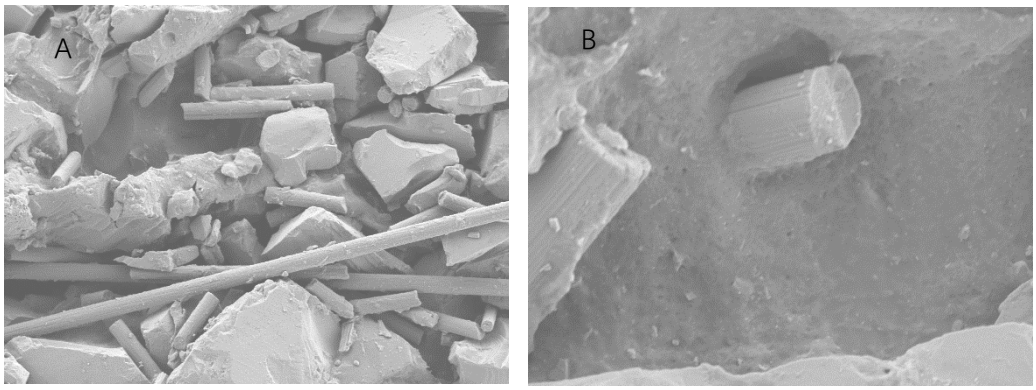

Fig.3-5 Scanning electron micrograph of XZ section in light cured C_f/SiC preform: A, 500×; B, 3000×

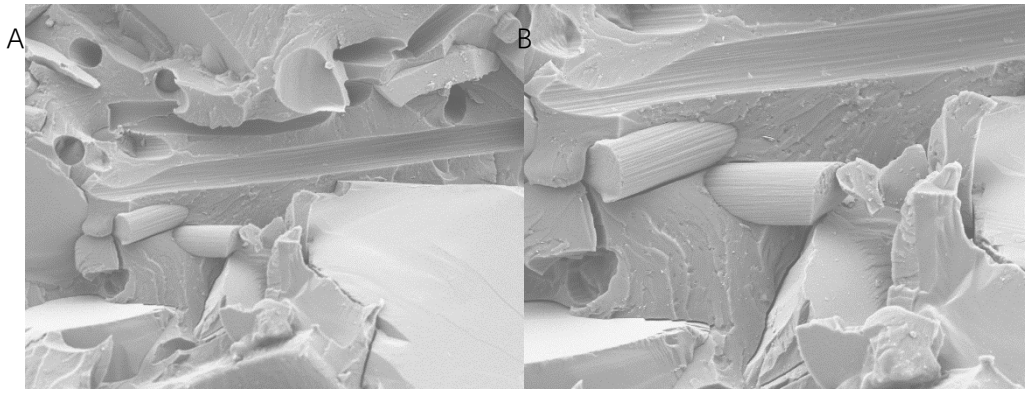

Fig.3-6 Scanning electron micrograph of YZ section in light cured C_f/SiC preform: A, 1000×; B, 2000×

Fig. 3-6 is the scanning electron microscope picture of YZ section (manually cut section) of light cured C_f/SiC preform. It can be seen from Fig. 3-6 (A) and Fig. 3-6 (B) that there are holes left on this section due to carbon fiber pulling out and silicon carbide particle peeling, in which carbon fiber pulling out leaves regular round holes with a diameter of about 7 μm; SiC particles peeled off and left irregular holes; The contour of the round hole is very regular, and the peeling surface of the particles is relatively smooth, which indicates that the photosensitive resin has a high degree of crosslinking polymerization, strength and curing accuracy, and can achieve a strong encapsulation effect on carbon fibers and silicon carbide particles; It can be seen from Fig. 3-6 (A) and Fig. 3-6 (B) that there are strip shaped grooves on the surface of carbon fiber along the length direction of the fiber. When the carbon fiber is pulled out, traces are left in the preform (Fig. 3-6 D). The grooves on the surface of carbon fiber make it difficult for the carbon fiber to be pulled out, which is conducive to the strengthening and toughening of the light cured C_f/SiC preform.

To sum up, the resin in the C_f/SiC preform has a bonding effect on carbon fiber and silicon carbide particles. There is a mechanical biting force between carbon fiber carbon fiber, carbon fiber silicon carbide particles and silicon carbide silicon carbide particles. At the same time, there is a van der Waals force (molecular force) between each silicon carbide particle and carbon fiber. The interaction of the three forces endows the C_f/SiC preform with strength and toughness.

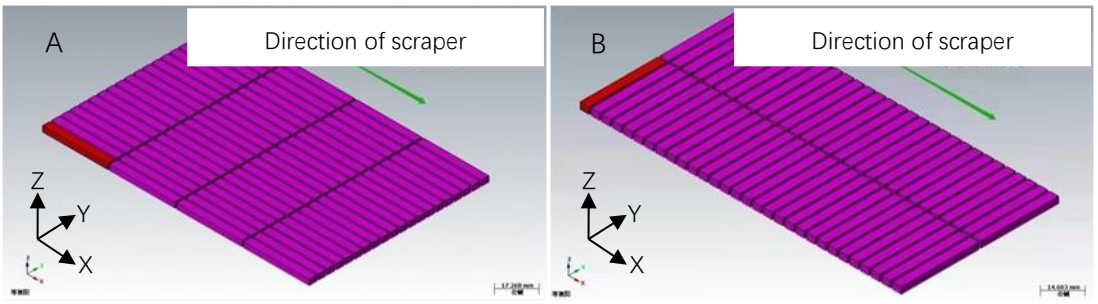

Fig.3-7 Design drawings of C_f/ SiC test samples: A, The length direction is parallel to the moving direction of the scraper ; B, The length direction is perpendicular to the moving direction of the scraper

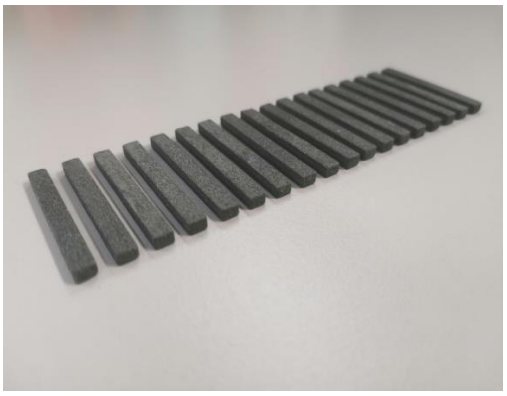

Fig.3-8 Photo of C_f/ SiC test samples

In order to investigate the influence of the arrangement direction of carbon fiber on the three-point bending strength and structural homogeneity of the light cured C_f/SiC preform before and after debinding, two kinds of test strip drawings (Fig. 3-7) were designed; Figure 3-8 is the appearance of the test strip; Table 3-3 shows the density and bending strength of them.

It can be seen from Table 3-1 that the difference of density between the two test strips is small, both of them are 1.81 g/cm^3, but the strength difference is large. The strength of test strip A is 10.68 MPa, and the strength of test strip B is 5.15 MPa, which is mainly related to the distribution of carbon fibers in the preform. In the test strip A, carbon fibers are distributed along the length direction, which is benefit for strengthening and toughening of the preform; In the B test strip, the carbon fiber is distributed along the direction perpendicular to the length, which has little help to improve the preform strength. According to the standard deviation of the density of test strips A and B in Table 3-1, the dispersion of the density of test strips A is much lower.

Table 3-1 The density and strength of the C_f/SiC preform before debinding

number	density（g/cm3）		Three points bending strength （MPa）	
	A sample	B sample	A sample	B sample
1	1.82	1.81	10.07	4.63
2	1.82	1.78	11.96	5.72
3	1.79	1.75	10.38	5.69
4	1.83	1.83	11.26	3.78
5	1.83	1.82	11.83	6.34
6	1.81	1.79	9.28	4.60
7	1.84	1.74	10.08	4.60
8	1.80	1.76	10.72	5.98
9	1.79	1.78	11.70	5.80
10	1.76	1.83	9.93	4.17
11	1.78	1.84	10.32	5.81
12	1.80	1.80	11.22	6.24
13	1.76	1.82	11.44	6.24
14	1.80	1.86	10.23	5.53
15	1.85	1.81	11.48	4.44
16	1.82	1.84	11.47	4.04
17	1.85	1.84	8.90	5.41
18	/	/	10.37	3.76
19	/	/	10.91	4.80
20	/	/	10.11	5.34
average	1.81	1.81	10.68	5.15
standard deviation	0.026	0.034	0.852	0.849

According to Griffith's microcrack theory, there are always small cracks and other defects in actual materials. Under the action of external forces, stress concentration will occur near these cracks and defects. When the stress concentration reaches a certain degree, the cracks begin to expand and cause fracture. Therefore, fracture originates from the most dangerous crack existing in the material. Fracture toughness K_{Ic}, fracture stress (or critical stress) of materials σ_C has the following relationship with the crack length c in the specific tensile stress zone:

$$K_{Ic} = Y \times \sigma_c \times \sqrt{c} \qquad (3\text{-}1)$$

In Formula (3-1), K_{Ic} is the fracture toughness, which represents the ability of materials to prevent crack growth and is a quantitative indicator to measure the toughness of materials. When the loading speed and temperature are fixed, it is a constant for a certain material. It is independent of the size and shape of the crack itself and the size of the applied stress, and it is an inherent property and intrinsic parameter of the material; Y is the geometric shape factor, which is also a constant after a given test method. According to formula (3-1), the critical stress of the material σ_C only varies with the maximum crack length c in the material. Because the distribution of crack length in the material is random, there are large cracks and small cracks, so the critical stress is also large and small, with scattered statistics, so the strength of the

material is also statistical.

This study also counts the Weibull modulus m of the preform strength to characterize the homogeneity of the material structure. The larger m, the more homogeneous the material, the lower the dispersion of the material strength (Fig. 3-9). It can be seen from the figure that the Weibull modulus of test strip A is 1.68, which is higher than that of test strip B (0.54), indicating that the lower the strength dispersion of test strip A is, the more uniform its internal structure is.

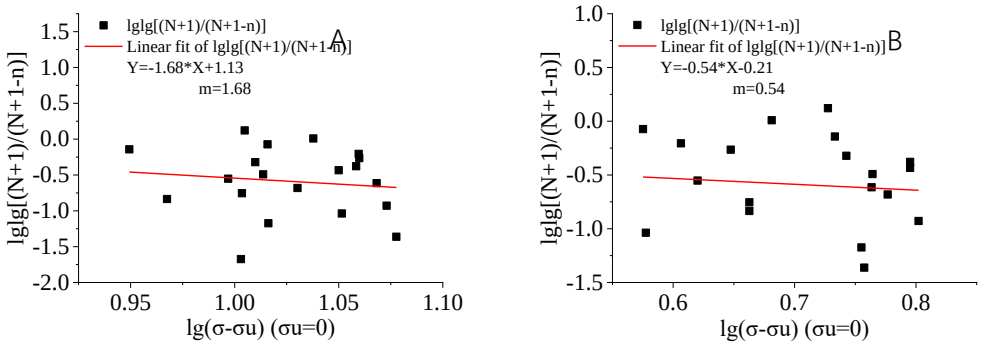

Fig.3-9 The Weibull modulus m of light cured C_f/SiC preform (before debinding) A and B

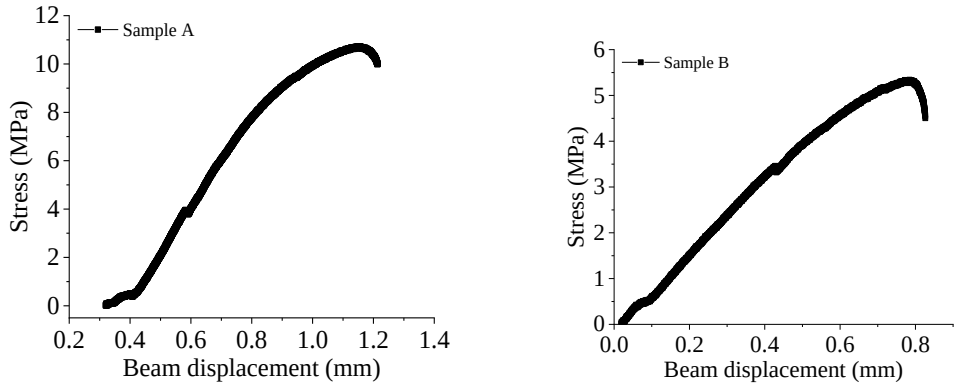

Fig.3-10 The displacement-stress curve of light cured C_f/SiC preform before debinding

Fig.3-10 shows the beam displacement stress curve of the light cured C_f/SiC test strip. It can be seen that the beam displacement stress curve of test strip A has a large radian. There is a plastic deformation stage before the fracture, and the preform does not undergo transient brittle fracture, indicating that the sample has good toughness, mainly because the preform contains photosensitive resin with certain flexibility, In addition, the directionally arranged carbon fibers in the sample also have a positive effect on the strengthening and toughening of the preform; The beam displacement stress curve of test strip B is approximately a straight line, and only a small radian appears before the fracture. The beam displacement stress of the preform presents a nonlinear relationship. The preform undergoes plastic deformation, and then the preform breaks. The preform has a certain toughness, but the toughness is not as good as that of test strip A.

To sum up, the directional arrangement of carbon fibers in the preform has a great impact on the toughness of the light cured C_f/SiC preform. The directional arrangement of carbon fibers in the length direction is conducive to improving the toughness of the preform and achieving the strength and toughness of the preform.

3.3 Microstructure and mechanical properties of C_f/SiC after debinding

Fig. 3-11 is the scanning electron microscope structure of XZ section of the debinded preform, the C_f/SiC preform becomes loose after debinding, it has good structural homogeneity, and there is no interlayer interface on XZ surface.

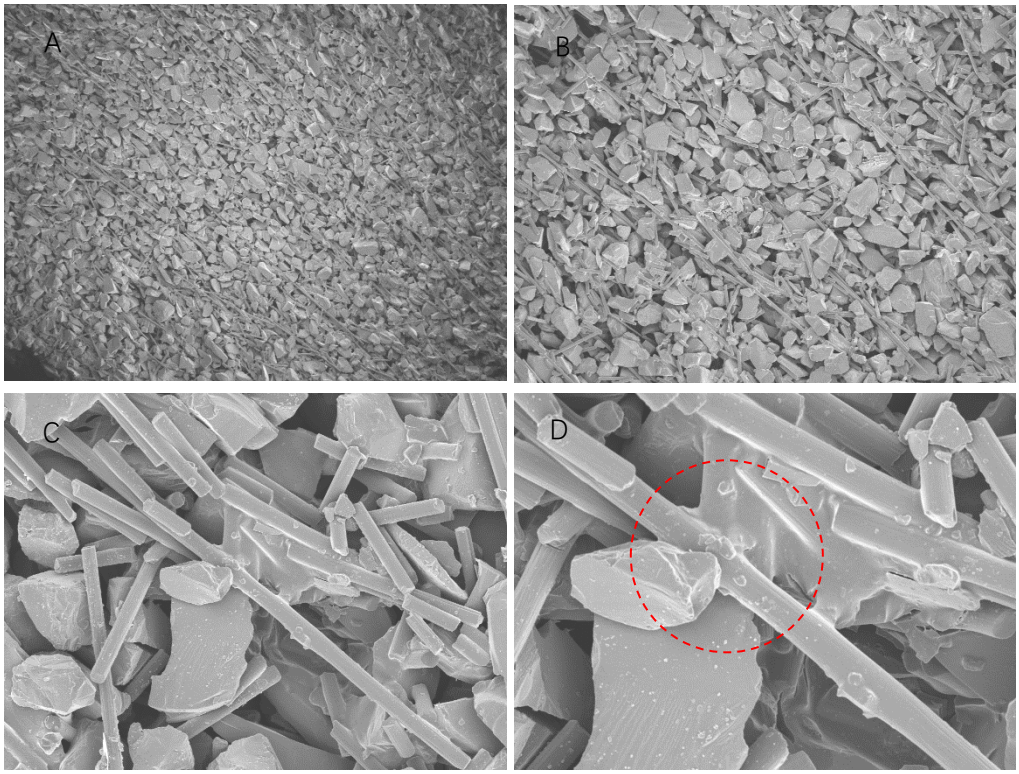

Fig.3-11 Scanning electron micrograph of XZ section in light cured C_f/SiC preform after debinding: A, 50×; B, 100×; C, 500×; D, 1000×

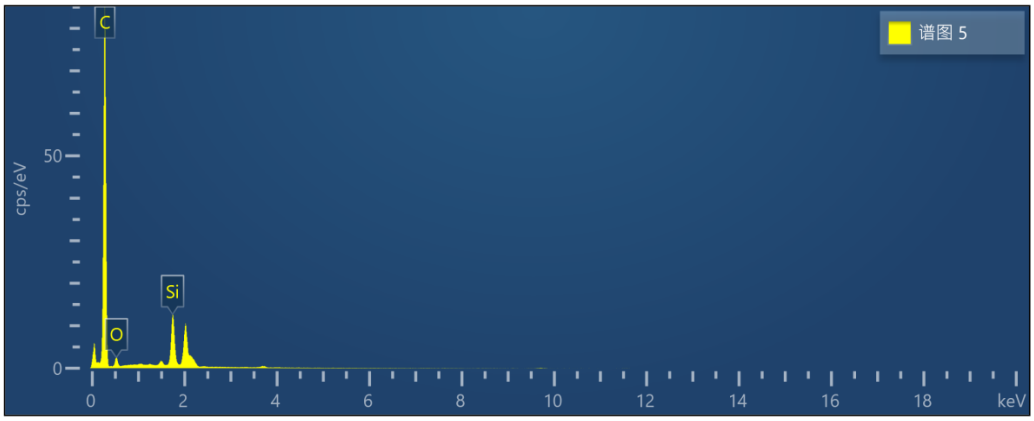

Fig.3-12 Energy spectrum analysis diagram of XZ section in light cured C_f/SiC preform after debinding

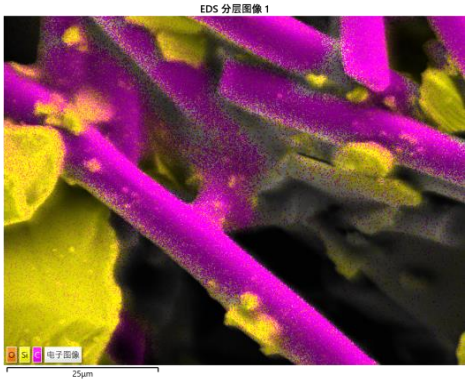

Fig.3-13 The energy spectrum analysis diagram of XZ section in light cured C_f/SiC preform after debinding

Table 3-2 Results of energy spectrum analysis for the cycle marked area in the C_f/SiC preform after debinding

Element	Line Type	Weight percentage	Wt % Sigma	Atomic percentage
C	K Series	88.74	0.18	93.17
Si	K Series	6.03	0.06	2.71
O	K Series	5.23	0.18	4.12
total		100.00		100.00

The resin in the preform undergoes pyrolysis and carbonization reaction during debinding, producing loose pore structure, The pyrolytic carbonization products are discharged from the porous structure, and the debinded body is composed of silicon carbide particles, carbon fibers, pyrolytic carbon and pores, in which carbon fibers are interspersed in the silicon carbide particles and pores; It can be seen from Fig. 3-11 (E) and (F) that pyrolytic carbon generated by resin will be generated between carbon fiber and silicon carbide particles, and will be bonded together, which improves the strength of debinded preform to a certain extent.

Fig. 3-12 is the energy spectrum analysis diagram at the circle mark in Fig. 3-11 (F), and Table 3-2 is the energy spectrum analysis results at the circle mark; Fig. 3-13 is the energy spectrum analysis diagram of XZ section of light cured C_f/SiC preform after debinding. It can be seen that the element at the position shown in the circle of Fig. 3-11 (F) is mainly carbon, which confirms that the resin in the preform is pyrolytic carbonized after debinding to produce pyrolytic carbon, and the carbon fiber and silicon carbide particles are bonded together.

Fig.3-14 Scanning electron micrograph of YZ section in light cured C_f/SiC preform after debinding: A, 50×; B, 100×; C, 200×; D, 500×

Fig.3-14 shows the scanning electron microscope structure of YZ section (manually cut section) after debinding of light cured C_f/SiC preform. It can be seen that the section is mainly composed of silicon carbide particles, carbon fibers, pyrolytic carbon and pores. Compared with the YZ section of preform before debinding, the section structure is more uniform; The strength of the debinded preform is mainly maintained by the mechanical bite force between carbon fiber and silicon carbide particles.

Table 3-3 The dimensional change, weight loss and density of the C_f/SiC preform after debinding

Number of sample	Linear shrinkage (%)			Volume shrinkage (%)	Weightlessness rate (wt.%)	density (g/cm^3)	
	X	Y	Z			Before debinding	After debinding
A	1.22	3.35	4.24	7.47	27.22	1.88	1.48
B	1.62	3.99	2.40	6.66	27.58	1.91	1.48

It can be seen that this experiment has designed two kinds of C_f/SiC samples(Fig.3-7), one is that the length direction is parallel to the moving direction of the scraper (sample A), the other is that the length direction is perpendicular to the moving direction of the scraper (sample B). Table 3-3 shows the size and mass changes of the two kinds of C_f/SiC samples after debinding. It can be seen that the two kinds of C_f/SiC samples have anisotropy of shrinkage after debinding, and their linear shrinkage in the X, Y and Z directions are different. Among them, the linear shrinkage in the X direction (parallel to the direction of scraper movement) is the lowest (1.22% - 1.62%), and the linear shrinkage in the Y direction (perpendicular to the direction of scraper movement) is higher (3.35% - 3.99%), This may be related to the grain accumulation state in both directions.

When the scraper moves, it will produce certain squeezing and shearing effects on the slurry, enabling the particles in the slurry to achieve optimal rearrangement, thus achieving the densification and accumulation in the X-axis direction. At the same time, it will make the carbon fibers directionally arranged in the X-axis direction, leading to the densification of the structure of the light cured C_f/SiC preform in the X-axis direction, and finally making the X-axis and Y-axis directions appear the anisotropy of linear shrinkage; The shrinkage of the UV cured C_f/SiC preform in the Z-axis direction is mainly related to the interlayer bonding state. During the 3D printing process, if the content of photosensitive resin in the slurry is high and the UV curing activity is good, it can achieve high strength bonding between layers, thus making the preform have a high curing density. As shown in Table 3-3, the curing density of sample B (1.91g/cm^3) is higher than that of sample A (1.88g/cm^3), indicating that the interlayer bonding strength of sample B is high, therefore, its linear shrinkage (2.40%) and volume shrinkage (6.66%) in the Z-axis direction are both low. However, due to the high resin content in sample B, its weight loss rate is high (27.58%). The density of C_f/SiC samples prepared under this process condition after debinding is 1.48 g/cm^3.

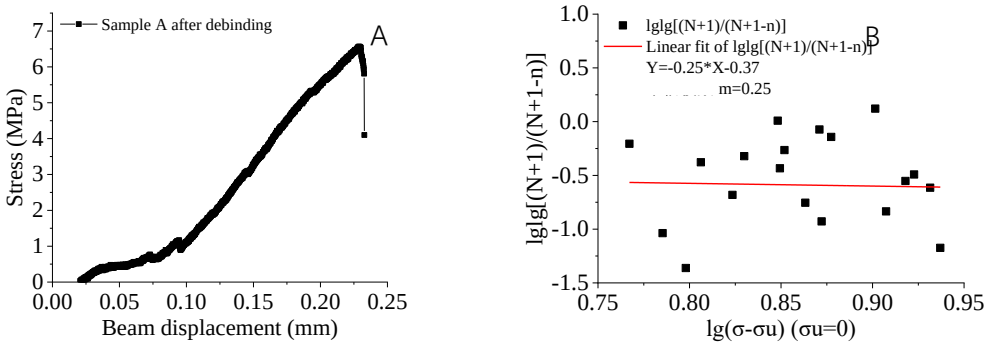

Fig.3-15 The displacement-stress curve (A) and Weibull modulus of C_f/SiC preform after debinding(B)

In this experiment, the three-point bending strength of light cured C_f/SiC test strips after debinding was tested, and the Weibull modulus of strength, shrinkage and density of debinded green bodies were calculated (Table 3-3). Fig.3-15 shows the beam displacement stress curve (A) and Weibull modulus (B) of the debinded light cured C_f/SiC test strip, we can see that the beam displacement stress curve of the debinded C_f/SiC test strip is approximately a straight line, indicating that the toughness of the debinded body decreases and the brittleness increases. The strength of the debinded body is mainly maintained by the mechanical bite force between carbon fiber and silicon carbide particles.

3.4 Microstructure and mechanical properties of C_f/SiC after CVI

Chemical vapor infiltration (CVI) is an important way to realize the densification, strengthening, toughening and structural homogenization of C_f/SiC samples.Fig.3-16 shows the photos of C_f/SiC sample after CVI.

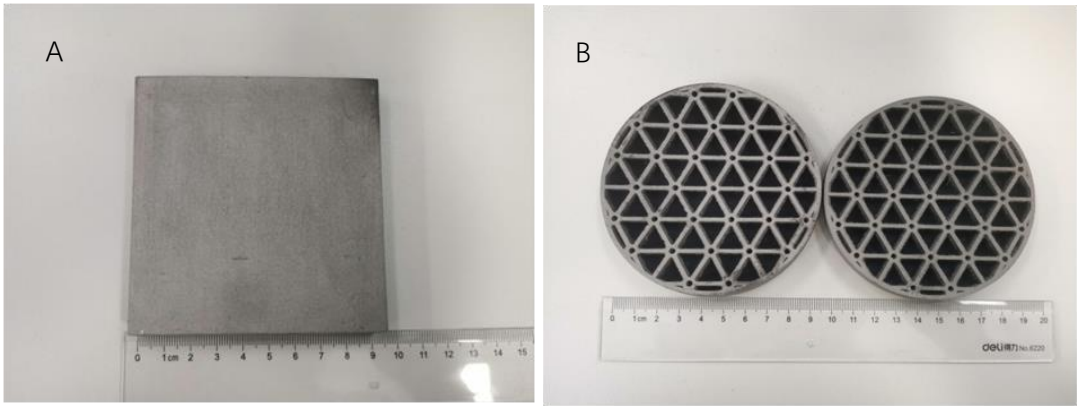

Fig.3-16 C_f/ SiC samples after CVI: A, wind tunnel ablation sample (100mm) × 100mm × 12 mm）; B, mirror（ Φ 100 mm × 10 mm）

It can be seen from Table 3-4 that the quality of the sample is improved after carburizing, with a weight increase of about 50 wt%; The density increased from 1.48 g/cm^3 after debinding to 2.01 g/cm^3, indicating that the carburizing effect was good. Carbon molecules invaded the sample and filled the pores inside the sample, realizing the densification of the sample.

Table 3-4 Shrinkage, mass and density of the ablation C_f/ SiC sample in wind tunnel test after carburizing

C_f/SiC	Mass（g）			Gain	Density（g/cm^3）		
Sample number	Before debinding	After debinding	After CVI	weight （wt%）	Before debinding	After debinding	After CVI
0	129.42	93.53	141.27	51.04	1.87	1.48	1.97

1	131.04	95.14	143.24	50.56	1.92	1.48	2.00
2	129.22	93.81	140.49	49.75	1.89	1.48	2.06
3	128.90	93.58	137.13	46.54	1.90	1.48	1.96
4	129.42	93.96	142.06	51.19	1.87	1.48	2.06
Average	129.60	94.00	140.84	49.82	1.89	1.48	2.01

Fig. 3-17 is the scanning electron microscope (SEM) diagram of the surface of carburized C_f/SiC sample. It can be seen that the thermal cracking carbon of natural gas (mainly methane CH_4) is deposited on the surface of C_f/SiC sample, forming a steamed bread like carbon layer, wrapping carbon fibers and silicon carbide particles, making the C_f/SiC sample show metallic luster; Fig. 3-18 is the SEM diagram of the section of carburized C_f/SiC sample. It can be seen that the natural gas pyrolytic carbon intrudes into the porous C_f/SiC preform and deposits on the surface of carbon fibers and silicon carbide particles, forming a thickness of 4-7 μm layer. It can be seen from Fig. 3-18 (D) that the sedimentary layer of m has an interlayer interface, indicating that the sedimentary layer is formed by the accumulation of thermally cracked carbon layers layer by layer, similar to the growth ring of trees. This deposition layer plays an important role in densification, strengthening and toughening, and structural homogenization of C_f/SiC samples. The strength of carburized C_f/SiC samples is mainly maintained by the adhesion and mechanical bite force between pyrolytic carbon pyrolytic carbon, pyrolytic carbon carbon fiber, pyrolytic carbon silicon carbide particles.

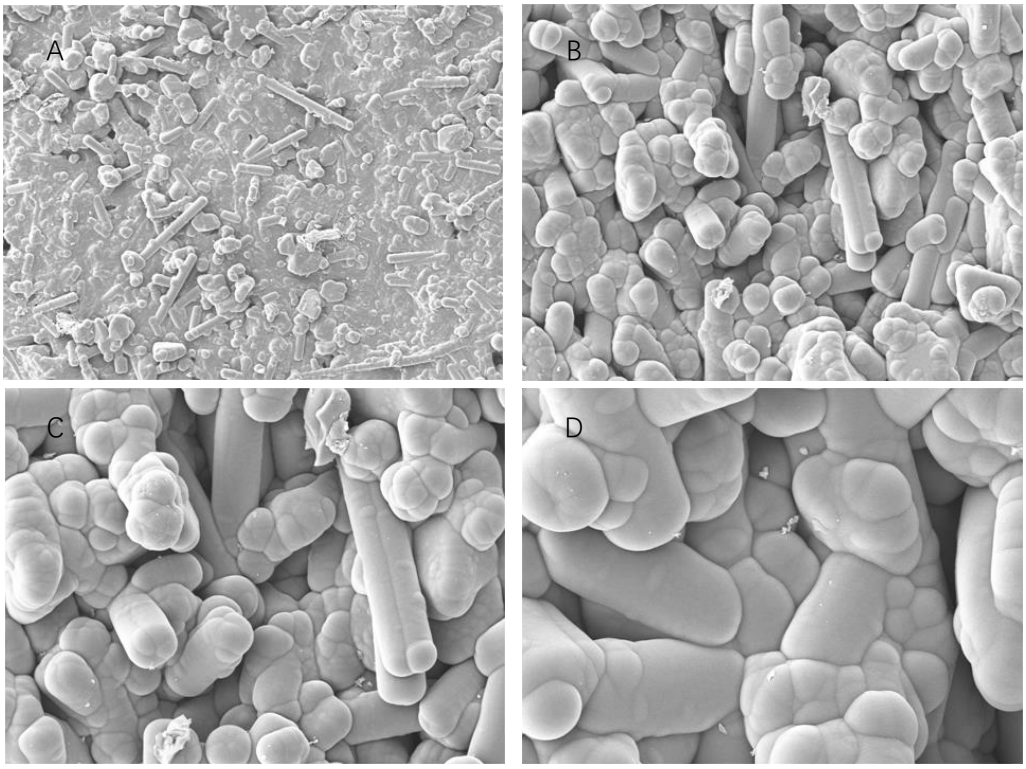

Fig. 3-17 SEM of carburized C_f/SiC sample surface: A, 100 ×； B，300 ×； C，500 ×； D，1000 ×

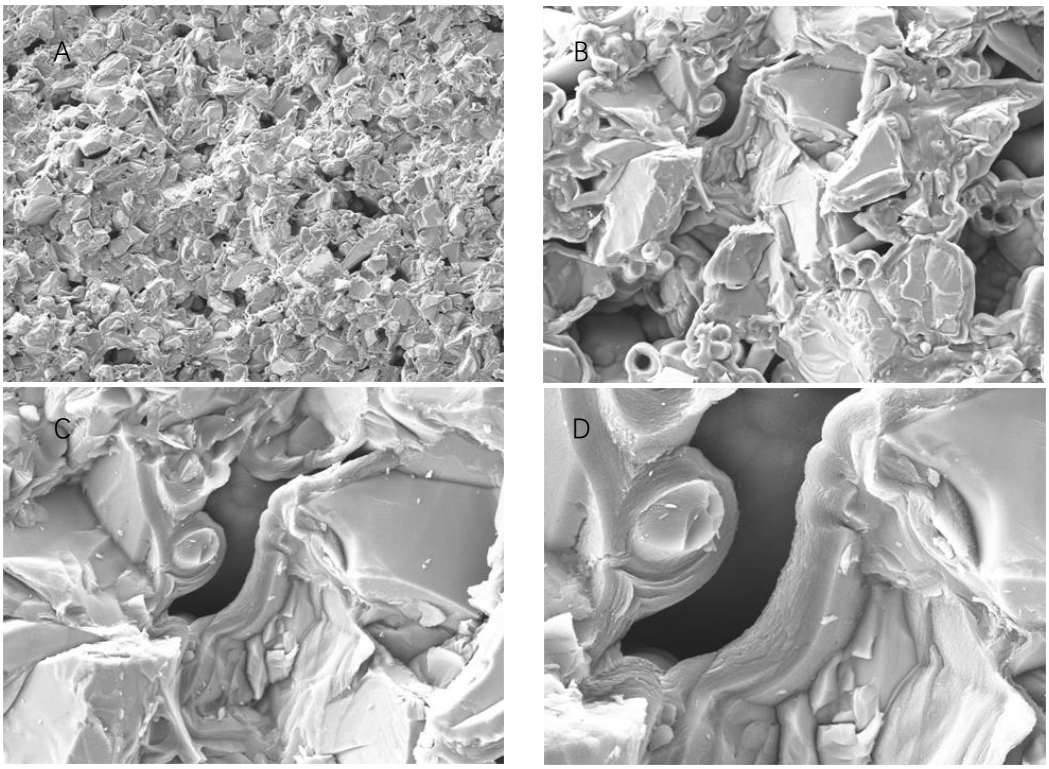

Fig. 3-18 SEM of carburized C_f/SiC sample surface: A, 100 ×； B，500 ×； C，1000 ×； D，2000 ×

Six test strips were prepared in this experiment. Table 3-5 shows the density, three-point bending strength and Weibull modulus of the six test strips.

Table 3-5 Mechanical Properties of C_f/SiC samples after CVI

Sample number	density （g/cm^3）	Three points strength （MPa）	Weibull modulus	remarks
1	2.00	116.78	1.45	The length direction is parallel to the moving direction
2	2.06	106.61	0.13	of the scraper
3	1.96	113.28	4.78	The length direction is perpendicular to the moving
4	2.06	101.49	2.11	direction of the scraper
5	2.06	128.29	1.64	The length direction is parallel to the moving direction
6	2.13	121.22	5.19	of the scraper

It can be seen from Table 3-5 that although the slurry composition for preparing C_f/SiC green bodies is roughly the same, the mechanical properties of carburized C_f/SiC prepared by different processes are different. In general, compared with the three-point bending strength of light cured carburized C_f/SiC samples and debinded carburized C_f/SiC samples, the influence of carbon fiber arrangement direction on the strength of carburized C_f/SiC samples is reduced, There is no anisotropy of mechanical properties due to different arrangement directions of carbon fibers, which indicates that the densification, strengthening, toughening and homogenization of C_f/SiC samples can be achieved by carburizing process; The carburized C_f/SiC samples prepared with resin rich slurry have higher Weibull modulus, because the resin rich C_f/SiC samples can produce higher porosity after debinding, and the high porosity provides

a three-dimensional connecting channel for carburizing, which is conducive to the densification and homogenization of C_f/SiC samples.

Figure 3-19 shows the beam displacement stress curve (A) and strength Weibull modulus (B) of the carburized C_f/SiC sample. It can be seen that the fracture stress of the carburized C_f/SiC sample is 121.22 MPa, and the Weibull modulus is 5.19; Table 3-6 shows the comparison of mechanical properties of C_f/SiC samples after debinding and carburizing. It can be seen that the density of C_f/SiC samples after carburizing is increased by~50 wt%, and the density is increased from 1.40 g/cm^3 to 2.06 g/cm^3; The three-point bending strength was increased from 7.32 MPa to 121.22 MPa, and the Weibull modulus was increased from 0.25 to 5.19. To sum up, the densification, strengthening and toughening, and structural homogenization of C_f/SiC are achieved through carburizing process.

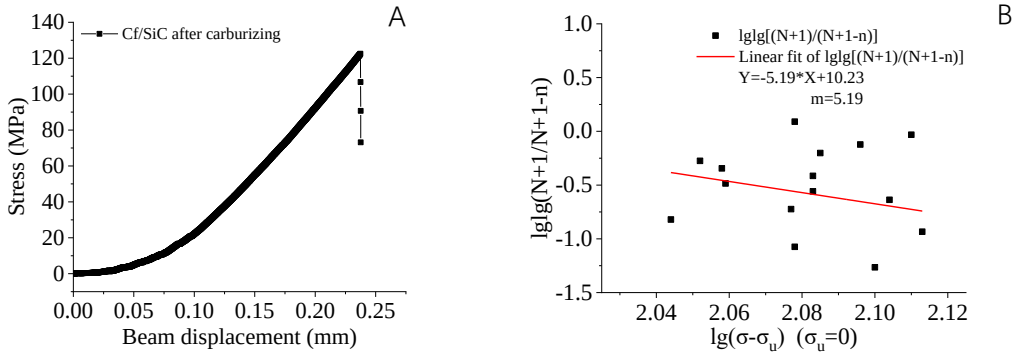

Fig.3-19 Three point bending strength (A) and Weibull modulus (B) of C_f/ SiC test strip sample after CVI

Table 3-6 Comparison of mechanical properties of C_f/SiC samples before and after CVI

C_f/SiC sample	Weight （g）	Density （g/cm^3）	Three point bending strength （MPa）	Weibull modulus
Before CVI	95.12	1.40	7.32	0.25
After CVI	143.24	2.06	121.22	5.19
Change	Increased 50.59%	Increased 47.14%	Improved 16.56	Improved 20.76

4 CONCLUSIONS

(1) The cross section of the light cured C_f/SiC preform has no layered interface, and the structure of the preform is uniform, which is mainly composed of silicon carbide particles, carbon fibers and cured resin; Carbon fiber, like pencil lead of miniature version, intersperses among silicon carbide particles in an irregular distribution, which plays a role in strengthening and toughening of light cured C_f/SiC preform; The cured resin has a strong bonding effect on carbon fiber/silicon carbide particles. There is a mechanical biting force between carbon fiber carbon fiber, carbon fiber silicon carbide particles and silicon carbide silicon carbide particles. At the same time, there is a van der Waals force (molecular force) between each silicon carbide particle and carbon fiber. The interaction of the three forces together endows the strength and toughness of C_f/SiC preform;

(2) After debinding, the light cured C_f/SiC preform will become loose, but its sectional structure is more uniform than that before debinding; The resin in the preform undergoes pyrolysis and carbonization reaction in the process of debinding to produce loose pore structure, and the pyrolysis and carbonization products are discharged from the loose pore structure. The debinded preform is composed of silicon carbide particles, carbon fibers, pyrolytic carbon and

pores, in which carbon fibers are interspersed in silicon carbide particles and voids; The pyrolytic carbon produced by resin will bond the carbon fiber and silicon carbide particles together, which can improve the strength of the debinded preform; The strength of the debinded preform is mainly maintained by the strong mechanical bite force between carbon fiber and silicon carbide particles;

(3) After debinding, the light cured C_f/SiC preform has anisotropy of shrinkage. Its linear shrinkage in the X, Y and Z directions is different. The linear shrinkage in the X direction (parallel to the moving direction of the scraper) is the lowest (1.22% - 1.62%), and the linear shrinkage in the Y direction (perpendicular to the moving direction of the scraper) is the highest (3.35% - 3.99%) Interlayer bonding state is related to grain accumulation state;

(4) When the carbon fiber is distributed along the length direction, it is beneficial to realize the strengthening and toughening of the preform. The strength of the test bar reaches 10.68MPa. There is a plastic deformation stage in the beam displacement stress curve before the fracture of the sample, and no transient brittle fracture occurs. The sample has good toughness. The directionally arranged carbon fiber has a positive effect on the strengthening and toughening of the preform; When the carbon fiber is distributed along the direction perpendicular to the length, the strength of the test bar is 5.15MPa, and the displacement stress curve of the beam is approximately a straight line. A small arc appears before the fracture, and the preform has a certain toughness. At this time, the arrangement direction of the carbon fiber has little help to the strength and toughness of the preform;

(5) After debinding, the strength of the light cured Cf/SiC preform decreases (7.32MPa), the brittleness increases, and the Weibull modulus of the strength decreases (0.25), indicating that the structural homogeneity of the debinded preform decreases.

(6) The C_f/SiC sample after debinding and carburizing has anisotropy of shrinkage, which is mainly related to the directional arrangement of silicon carbide particles and carbon fibers in the preform. The shrinkage parallel to the moving direction of the scraper is small, while the shrinkage perpendicular to the moving direction of the scraper is large; The resin content has a great influence on the microstructure and mechanical properties of the C_f/SiC sample after carburizing. Reducing the resin content in the slurry and increasing the solid content of the slurry can weaken the warpage and deformation of the slurry UV curing printing, reduce the density of the UV curing 3D printing preform, increase the porosity of the preform after debinding, and provide a channel for carburizing. After CVI, the preform can be densified to obtain high-density C_f/SiC samples;

(7) The carburizing process can realize the densification, strengthening and toughening, and structural homogenization of C_f/SiC samples. After carburizing, the density of C_f/SiC samples increases, the sample weight increases by~50 wt%, the density increases from 1.40 g/cm^3 to 2.06 g/cm^3, the three-point bending strength increases from 7.32 MPa to 121.22 MPa, and the Weibull modulus increases from 0.25 to 5.19.

ACKNOWLEDGMENT

The authors gratefully acknowledge the finical support of Key Laboratory Fund (NO.6142906210204) from Science and Technology on Advanced Functional Composites Laboratory, Aerospace Research Institute of Material and Processing Technology; Youth Innovation Promotion Association of Chinese Academy of Sciences (NO.2022160) ; Key Laboratory Fund (NO.2022KLOMT02-03) from Key Laboratory of Optical System Advanced

Manufacturing Technology, Chinese Academy of Sciences.

REFERENCES

[1] Lu Youjun, Wang Yanmin, Wu Laner. Research and application progress of carbon/silicon carbide ceramic matrix composites [J]. Materials Bulletin, 2010, 24 (11): 14-19.

[2] Fang Jinming, Mei Min, Li Junping, Ye Mingxin, Pan Yong. Preparation and properties of ultra-high temperature ceramic modified C/SiC composites [J]. Aerospace Materials Technology, 2021,51 (04): 120-125.

[3] He Bolin, Sun Jia. Research progress and application of carbon fiber reinforced silicon carbide ceramic matrix composites [J]. Silicate Bulletin, 2009, 28 (06): 1197-1202+1207.

[4] Su Chunlan, Zhou Changling, Xu Hongzhao, Yang Fanghong, Jiang Kai, Liu Futian. Research Progress of Carbon Fiber Toughened Ceramic Matrix Composites [J]. Foshan Ceramics, 2020,30 (02): 10-21

[5] Wen Zhangping, Zhang Cheng, Zhang Yonggang. Research progress and application of carbon fiber reinforced silicon carbide ceramic matrix composites [J]. Artificial Fiber, 2018, 48 (01): 18-24.

[6] Michelle L. Griffith John W. Halloran, Freeform fabrication of ceramics via stereolithography, Journal of the American Ceramic Society. 79 (1996) 2601-2608.

[7] Zak C.Eckel, Chaoyin Zhou, John H. Martin, etc,.Additive manufacturing of polymer-derived ceramics, Science.351(2016) 58-62.

[8] Shan Li, Wenyan Duan, Tong Zhao, Weijian Han, Li Wang, Rui Doua, Gong Wang. The fabrication of SiBCN ceramic components from preceramic polymers by digital light processing (DLP) 3D printing technology[J]. Journal of the European Ceramic Society, 2018, 38(4):4597-4603.

[9] Andrea Zocca, Paolo Colombo, Cynthia M. Gomes, etc,. Additive Manufacturing of Ceramics: Issues, Potentialities, and Opportunities , J. Am. Ceram.Soc.. 98 (2015) 1983–2001.

[10] Zhangwei Chen, Ziyong Li, Junjie Li, etc,. 3D printing of ceramics: A review, Journal of the European Ceramic Society. 39 (2019) 661-687.

[11] Keqiang Zhang, Rujie He, Guojiao Ding, Xuejian Bai, Daining Fang.Effects of fine grains and sintering additives on stereolithography additive manufactured Al2O3 ceramic [J].Ceramics International,2021,47(2):2303-2310.

[12] Martin Schwentenwein and Johannes Homa, Additive Manufacturing of Dense Alumina Ceramics, Int. J. Appl. Ceram. Technol.. 12 (2015) 1-7.

[13] Keqiang Zhang,Qiaoyu Meng,Xueqin Zhang,Zhaoliang Qu,Shikai Jing,Rujie He. Roles of solid loading in stereolithography additive manufacturing of ZrO2 ceramic[J].International Journal of Refractory Metals

and Hard Materials, 2021,99:105604.

[14] Xiangsong Fu, Bin Zou, Hongyu Xing, Lei Li, Yishang Li, Xinfeng Wang. Effect of Printing Strategies on Forming Accuracy and Mechanical Properties of ZrO2 Parts fabricated by SLA Technology[J]. Ceramics International, 2019, 45(14):17630-17637.

[15] C.J. Bae, D. Kim, J.W. Halloran, Mechanical and kinetic studies on the refractory fused silica of integrally cored ceramic mold fabricated by additive manufacturing, J. Eur. Ceram. Soc. 39 (2019) 618-623.

[16] XiaoyanLiu,Bin Zou, Hongyu Xing et al, The preparation of ZrO2-Al2O3 composite ceramic by SLA-3D printing and sintering processing, Ceramics International. 46(2020) 937-944.

[17] Jie Tang, Haotian Chang, Xiaotian Guo, Meng Liu, Yuquan Wei, Zhengren Huang, Yong Yang.Preparation of carbon fiber-reinforced SiC ceramics by stereolithography and secondary silicon infiltration[J].Ceramics International,2022,48(17): 25159-25167.

[18] Fan-Fan Li, Ning-Ning Ma, Jian Chen, Ming Zhu, Wen-Hui Chen, Chang-Cong Huang, Zheng-Ren Huang .Stereolithography-based additive manufacturing of lightweight and highstrength Cf/SiC ceramics[J].Additive Manufacturing,2020,34:101199-101212 .

[19]]Guojiao Ding, Rujie He, Keqiang Zhang, Niping Zhou, Hao Xu. Stereolithography based additive manufacturing of gray-colored SiC ceramic green body[J]. Journal of the American Ceramic Society, 2019, 102(12):1-12.

[20] JieTang, XiaotianGuo, Haotian Chang, Kehui Hu,Zhen Shen,WeixingWang,MengLiu,YuquanWei,ZhengrenHuang,Yong Yang. The preparation of SiC ceramic photosensitive slurry for rapid stereolithography[J]. Journal of the European Ceramic Society,2021,41(5):1-9.

[21] Chuanqi Hu,YufengChen,TaishengYang,HailinLiu,XiaotingHuang,YanliHuo,etc. Effect of SiC powder on the properties of SiC Slurry for Stereolithography [J]. Ceramics international, 2021, 47（9）: 12442-12449.

[22] Jie Tang, Meng Liu, Yuquan Wei, Yong Yang, Zhengren Huang.An efficient and low-cost liquid silicon infiltration method to prepare SiC-coated carbon short fiber for fiber protection of Cf/SiC ceramic matrix composites[J].Ceramics International,2021,47:13235–13241.

[23] Zhenduo, Zhang Zhongtai, Jiao Jinsheng. Physical Properties of Inorganic Materials [M]. Beijing: Tsinghua University Press, 2003: 1-103.

A study on 3D printing short-continuous carbon fiber synergistic reinforcement thermoplastic composites：pre-impregnated string manufacturing and its tensile performance testing

Jianming Zhou, Gongshuo Wang, Bo Wu, Shouyan Guan, Hongquan Wang, Fuji Wang*

Key Laboratory of High-performance Manufacturing for Advanced Composite Materials，Liaoning Province

School of Mechanical Engineering, Dalian University of Technology, Dalian 116024, China

Abstract: The 3D printing technology of carbon fiber reinforced thermoplastic composites can realize the integrated manufacturing of complex structural parts with excellent performance, such as light-weight and high-strength. Therefore, this technology owns broad application prospects in the field of high-end equipment manufacturing. For its application, it is essential to ensure the superb mechanical properties of 3D printed carbon fiber reinforced thermoplastic composite (CFRTP) parts. To further improve it, both short and continuous carbon fibers were used in the CFRTP 3D printing process to manufacture short carbon fiber-assisted continuous carbon fiber thermoplastic composites (S/C-CFRTP) at the same time. The sufficient impregnation between continuous carbon fibers and the thermoplastic resin matrix containing short fibers in the 3D printed S/C-CFRTP parts is extremely important for performance improvement. To achieve that, this paper proposes a manufacturing method for short fiber-assisted continuous fiber thermoplastic composite pre-impregnated string. The melt mixing module, rolled impregnation module, and mold setting module are designed to develop the pre-impregnated string manufacturing equipment. Then, the process experiments are conducted to determine the optimal manufacturing procedure. The maximum load-bearing tensile force of the pre-impregnated string is nearly 114N. Finally, compared with the S/C-CFRTP parts printed

by in situ impregnated process, the tensile strength and tensile modulus of S/C-CFRTP parts printed with this pre-impregnated string are increased by nearly 19% and 12%, respectively.

Key words: 3D printing, S/C-CFRTP, Pre-impregnated string, Mechanical property

1. Introduction

As a cutting-edge technology in the third industrial revolution, 3D printing can realize rapid and low-cost manufacturing of complex parts, and has been widely used in high-end equipment manufacturing [1]. However, parts printed with traditional materials are difficult to meet the requirements of high-end equipment for weight reduction, efficiency enhancement and high-reliability service, thus limiting the performance of printed parts. Carbon fiber reinforced thermoplastic composites (CFRTP) have the advantages of light-weight and high-strength, and the matrix can be repeatedly heated, melted, cooled and hardened [2,3], which is highly complementary to 3D printing technology. The use of 3D printing technology to manufacture CFRTP can not only retain the excellent properties of CFRTP, but also give full play to the flexible process characteristics of 3D printing, which can realize the efficient and low-cost forming of CFRTP parts with complex geometric shapes [4,5].

As the reinforcing phase of CFRTP, carbon fiber has excellent axial load-bearing properties. According to the length of carbon fibers, CFRTP can be divided into short carbon fiber reinforced thermoplastic composites (S-CFRTP) and continuous carbon fiber reinforced thermoplastic composites (C-CFRTP). Since the manufacturing process of S-CFRTP is similar to that of resin materials, it was first used in the field of 3D printing to improve the mechanical properties of 3D printed parts. Therefore, researchers first carried out the study on the optimization of 3D printing process parameters, they found that with the decrease of printing

speed, the increase of printing temperature and the decrease of printing layer thickness, the tensile properties of the printed parts also increased [6-7]. What is more, Fuda Ning et al. [8] measured the mechanical properties of 3D printed composite parts with different carbon fiber content (3~15wt%), and found that with the increase of fiber content, the tensile strength of parts first increased and then decreased. When the content of short carbon fiber is 5%, the mechanical properties are the best (42MPa). Although the increase in the content of short carbon fibers makes the content of the reinforcement phase higher, it also leads to a decrease in the flow properties of the molten S-CFRTP material during the manufacturing process, and the porosity in the manufactured S-CFRTP parts increases significantly, which in turn leads to the decreased performance of S-CFRTP parts. Although the 3D printed S-CFRTP parts have higher porosity than traditional molded parts, because of their higher fiber orientation, the strength loss due to the high porosity is basically compensated [9]. In addition, some scholars have significantly improved the performance of parts by means of fiber surface treatment and annealing of manufactured parts [10-11]. However, the tensile strength of the 3D printed S-CFRTP parts is about 43.3 MPa [12], which is much lower than the current high-end equipment performance requirements for such parts. To this end, the C-CFRTP 3D printing process was proposed [13]. Through a large number of process experiments, researchers optimized process parameters such as printing speed, forming temperature, and interlayer thickness. In view of the poor impregnation of continuous carbon fibers by the matrix and the poor bonding between layers, plasma laser-assisted heating and ultrasonic impregnated processes have been developed, which have promoted the improvement in performance to a certain extent [14-16]. However, the mechanical properties (644.8 MPa) [17] of 3D printed C-CFRTP parts are still far

lower than those of C-CFRTP parts manufactured by lay-up curing (752 MPa) [18].

Previous studies have found that in order to further improve the performance of composite parts, short carbon fibers are introduced in the manufacture process of traditional CFRTP [8]. Inspired by this, Denizhan Yavas et al. [19] replaced the resin material of the Mark two printer with a composite material containing short carbon fibers, and printed it together with the continuous carbon fiber string. It was found that due to the addition of short carbon fibers, the interlaminar shear strength of the printed parts was significantly improved. What is more, Wu Bo et al. [20] realized the 3D printing of short carbon fiber-assisted continuous carbon fiber composites based on the in situ impregnated process. The measurement found that the tensile strength of the printed parts containing short carbon fibers was increased by 13.50%, and the bending strength was increased by 29.97%. However, studies have found that the 3D printed short carbon fibers assisted by reinforced continuous carbon fiber composite parts are prone to voids due to insufficient impregnation, which significantly eliminates the effect of reinforcement [21].

To tackle this problem, this paper proposes a manufacturing method of pre-impregnated string of thermoplastic composite reinforced by short carbon fiber and continuous carbon fiber synergistically, a supporting principle prototype was developed, and the tensile properties of different continuous carbon fibers through manufacturing region of impregnated string was compared, the optimal manufacture route of pre-impregnated string was determined. Based on this, by comparing the mechanical properties of short carbon fiber-assisted continuous carbon fiber composite parts manufactured by in situ impregnated 3D printing process and pre-impregnated 3D printing process, the effectiveness of the synergistically reinforced pre-

impregnated manufacturing method proposed in this paper was verified. The results provide a novel method for further improving the performance of 3D printed CFRTP parts.

2. Experimental setup and experimental methodology

2.1 Experimental setup and its fabrication mechanism

Melt impregnation method [22] is one of the commonly used methods for manufacturing pre-impregnated strings. It uses molten thermoplastic resin to directly impregnate continuous carbon fibers to manufacture continuous carbon fiber pre-impregnated strings. Previous studies have shown that increasing the external pressure during the impregnated process is beneficial to promote the impregnation of continuous carbon fibers with molten resin [23-24]. Therefore, based on the melt impregnation method, this paper designs a special rolling device (as shown in Figure 1) to increase the external pressure during the impregnated process, and then develops the manufacture equipment for the pre-impregnated string of the thermoplastic composite reinforced by the short carbon fiber and the continuous carbon fiber synergistically (as shown in the figure 2). The main components of the pre-impregnated string manufacturing equipment and their functions are shown in Table 1. Under the pressure of the rolled impregnation module, the shape of the pre-impregnated string becomes flat (as shown in Figure 3(a)) and cannot be used for the next step of printing. To this end, a mold setting module is added to the equipment, through heating and mold reshaping, the flat string is turned into a cylindrical string with a specified diameter (as shown in Figure 3(b)).

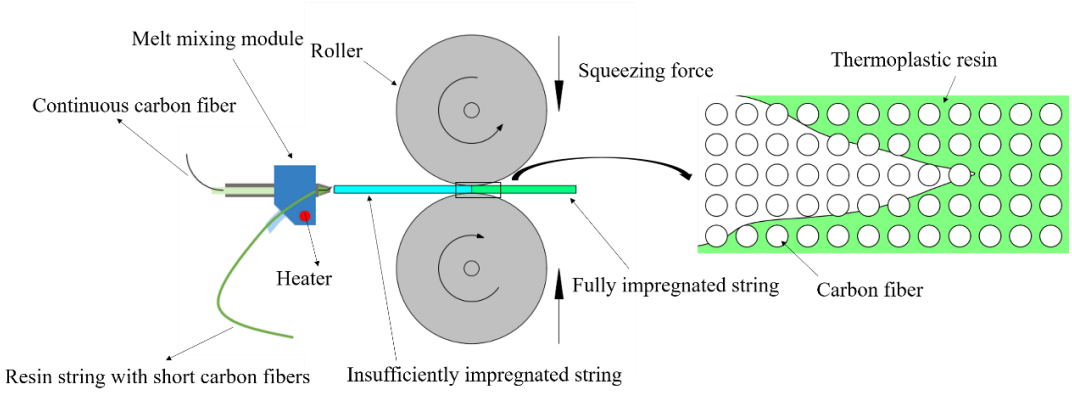

Fig.1. Schematic diagram of the rolling impregnation method

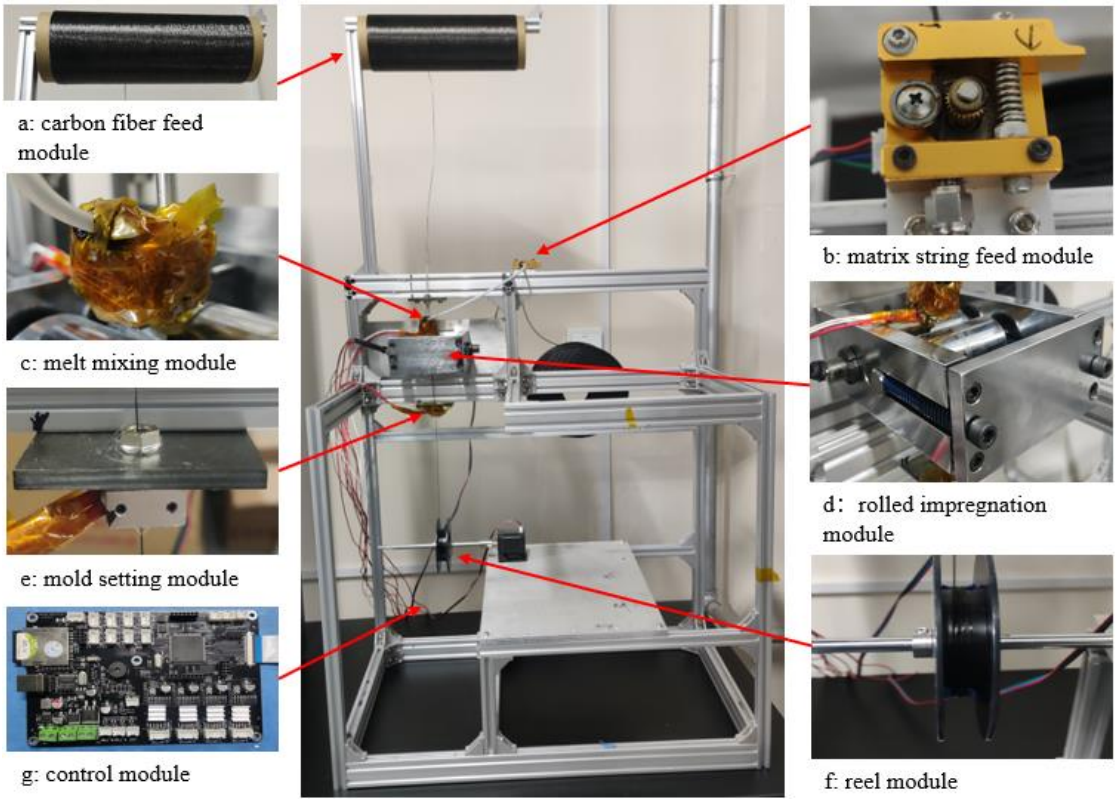

Fig.2. Pre-impregnated strings manufacture principle prototype

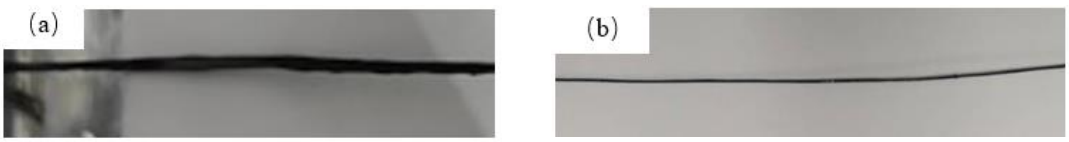

Fig.3. Comparison of whether continuous carbon fibers have passed through the mold setting module. (a) continuous carbon fibers have passed through the mold setting module, (b) continuous carbon fibers have not passed through the mold setting module.

Table 1 Main parts and functions of pre-impregnated string manufacturing equipment

Module name	Effect

A	Carbon fiber feed module	Assisting carbon fiber feeding under the action of traction
B	Matrix string feed module	Feeding short carbon fiber reinforced thermoplastic resin string
C	Melt mixing module	Fusing short carbon fiber reinforced thermoplastic resin string and realizing its blending and initial impregnation with continuous carbon fibers
D	Rolled impregnation module	Providing sufficient external pressure to promote adequate impregnation of the short carbon fiber reinforced thermoplastic resin and continuous carbon fibers heated
E	Mold setting module	Reshaping the pre-impregnated string
F	Reel module	Collecting the impregnated string and providing some traction
G	Control module	Controlling the operation of equipment

2.2 Experimental procedures

The experimental materials used in this paper are shown in Table 2. Before manufacturing the pre-impregnated string, the short carbon fiber reinforced thermoplastic resin string was dried at 90 °C for 4 hours.

Table 2 manufacture of pre-impregnated string experimental materials

Type of material	Material properties	
Short carbon fiber reinforced thermoplastic resin string	Carbon fiber percentage	15%
	Resin type	PA6
	Manufacturer	Self made
Continuous carbon fiber	Type	1K
	Manufacturer	Teigin carbon

In order to determine the optimal manufacture process of pre-impregnated string, this paper designs relevant experiments on whether the continuous carbon fiber passes through the rolled impregnation module and the mold setting module. The specific experimental settings

are shown in Table 3. In case a, the continuous carbon fiber only passes through the melt mixing module. In the case b, the continuous carbon fiber passes through both the melt mixing module and the mold setting module. In case c, the continuous carbon fiber passes through the melt mixing module, the rolled impregnation module and the mold setting module.

Tab. 3 Condition of continuous carbon fiber passing through the area

Groups	Whether through the matrix attachment module	Whether through the rolled impregnation module	Whether through the mold shaping module
a	Yes	No	No
b	Yes	No	Yes
c	Yes	Yes	Yes

Referring to the experimental settings of S/C-CFRTP in situ impregnate printing, the experimental parameters are shown in Table 4. This paper manufactured tensile strength test pieces according to the ISO 10618:2004 test standard, and used the universal tester (WDW-100E, Wenteng Corp., Jinan, China) equipped with a 200N range force sensor. The tensile properties of the pre-impregnated string were tested (as shown in Figure 4). The specific parameters are shown in Table 4.

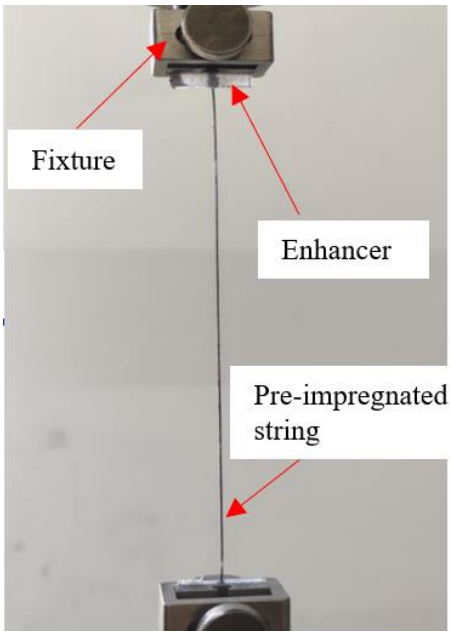

Fig. 4 Tensile test of impregnated string

Table 4 pre-impregnated string manufacture parameters and tensile test experimental parameters

Parameter name	Pre-impregnated string manufacture parameters			
	Temperature of the mold setting block	Feeding speed	Melt mixing module nozzle diameter	Mold setting module nozzle diameter
Parameter value	270℃	4mm/s	0.8mm	0.6mm
Parameter name	Test sample basic parameters			Test parameters
	Sample length	Enhancer	Enhancer bonding method	Loading speed
Parameter value	200mm	24mm×20mm paper enhancer	A-B epoxy glue Curing 16 hours	2mm/min

3. Results and discussion

3.1 Experimental results

The test results of the mechanical properties of the S/C-CFRTP pre-impregnated string manufactured under three different conditions are shown in Figure 4. The pre-impregnated

string manufactured only by the melt mixing module (case a) has the lowest tensile strength. The external load at tensile fracture is only about 91.43N, the fracture section is extremely uneven, and there are a large number of continuous carbon fibers pulled out (Figure 4). The tensile strength of the pre-impregnated string manufactured through the melt mixing module and the mold setting module (case b) is slightly improved. Compared with the pre-impregnated string manufactured in case a, the external load at tensile fracture is increased by about 8.94%, and the fiber pull-out phenomenon at the fractured section is significantly reduced. The fracture cross-section of the pre-impregnated string manufactured by the melt mixing module, the rolled impregnation module and the mold setting module (case c) is relatively flat. There is only a small amount of fiber pull-out at the fracture, and the external load at tensile fracture reaches nearly 114N, which is about 25% and 15% higher than the pre-impregnated string manufactured in case a and case b.

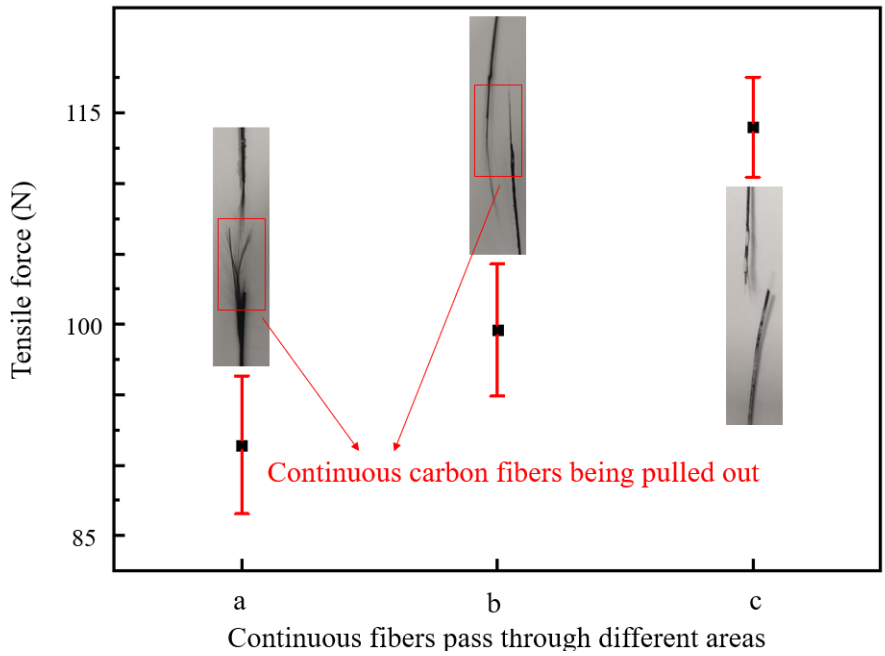

Fig.4. Test results of mechanical properties of S/C-CFRTP pre-impregnated string

3.2 Discussion

Due to the insufficient impregnation of the fibers by the resin in the 3D printed composite parts, the continuous carbon fibers are in different impregnation states, which lead the continuous carbon fibers are subjected to different stress when carrying external loads. For fibers that are insufficiently impregnated, they are only stretched by external loads. While for sufficiently impregnated fibers, under the action of the load transmitted by the nearby matrix material, they bear the external tensile load together with other sufficiently impregnated fibers. This different stress state leads to different fracture positions of continuous carbon fibers, which in turn leads to fiber pull-out at the fractured section. Therefore, the amount of fiber pullout can be used as an important indicator of the quality of the internal impregnation state of the composite. It can be seen that the pre-impregnated string manufactured in case c has the best impregnation degree, followed by case b, and the string manufactured in case a has the worst impregnation state.

Through analysis, it can be found that the reason for the above-mentioned different impregnation situations is caused by the different modules passed through during the manufacture of the pre-impregnated string. The pre-impregnated string manufactured in case a is only preliminarily impregnated in the melt mixing module, and its impregnation degree is the worst due to the lack of sufficient external pressure. In case b, the pre-impregnated string is preliminarily impregnated in the melt-mixing module, and then enters the mold setting module. Through that, the string is not only reshaped, but also promotes another impregnation behavior to a certain extent, so the impregnation degree of the pre-impregnated string manufactured in case b is improved. In case c, the pre-impregnated string has undergone the rolled impregnation module, which provides sufficient external pressure for the matrix to

impregnate the continuous carbon fiber. It leads to a significant increase in the degree of impregnation of the pre-impregnated string. At the same time, this result also proves that the rolled impregnation module designed in this paper can effectively promote the impregnation of continuous carbon fiber by the matrix material.

The degree of impregnation of the pre-impregnated string directly determines its load-bearing performance [25]. In the insufficiently impregnated string, most of the continuous carbon fibers are in the bare state with no matrix attached. Compared with the continuous carbon fiber wrapped with the resin matrix, the load-bearing performance of the continuous carbon fiber in the bare state is weaker. Therefore, when the external tensile load is applied, the continuous carbon fibers in the bare state fail soon, which in turn leads to a decrease in the overall performance of the 3D printed part. This corresponds exactly to the tensile property measurements: the most impregnated string (manufactured in case c) had the best mechanical properties, while the least impregnated string (manufactured in case a) had the worst mechanical properties.

4. Comparison of in-situ impregnation and pre-impregnation

4.1 Experimental setup and procedures

The employ of strings with excellent mechanical properties is one of the prerequisites for high-performance 3D printing of S/C-CFRTP. In order to further verify the superiority of the S/C-CFRTP pre-impregnated string manufactured, this paper uses the string manufactured in case c (section 2.1) to print the S/C-CFRTP sample through the pre-impregnated process. At the same time, the short fiber reinforced thermoplastic resin string and continuous fiber shown in Table 2 are used to manufacture S/C-CFRTP samples by in-situ impregnate process, the

properties of the samples manufactured by two different processes were compared.

The S/C-CFRTP pre-impregnated 3D printing principle and equipment used in this paper are shown in Figure 5(a) and (c). The pre-impregnated strings manufactured above directly enter the nozzle. Under the heating action of the heater, the thermoplastic matrix is in a molten state. Under the dragging action of the continuous fibers, the strings are continuously formed from the nozzle and accumulated on the printing platform. The S/C-CFRTP in situ impregnate 3D printing equipment and its principle are shown in Figure 5(b) and (d), the resin string containing short fibers and continuous fibers are distributed into the nozzle through a channel, the molten resin containing short fibers is impregnated into the continuous fiber under the action of the heating rod. Finally, because of the drag force of the continuous fiber, the forming material is piled up and formed on the printing platform.

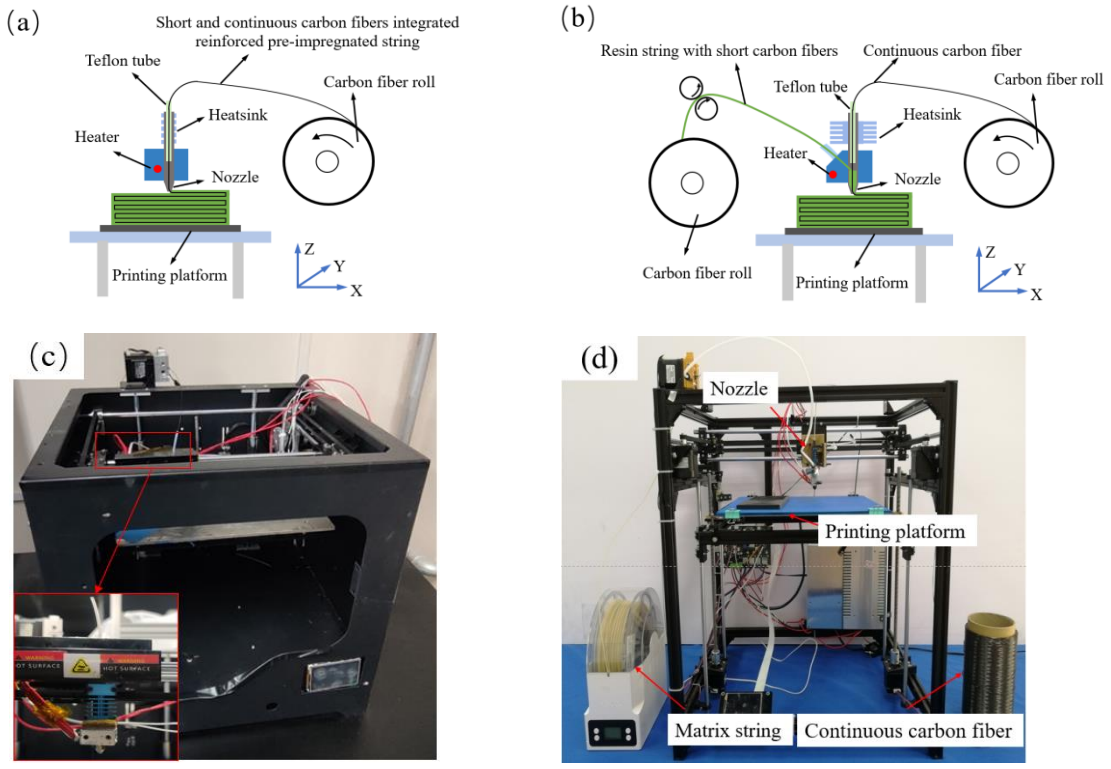

Fig.5. Different S/C-CFRTP 3D printing principle and equipments. (a) S/C-CFRTP pre-impregnate 3D printing principle, (b) S/C-CFRTP in-situ impregnate 3D printing principle, (c) S/C-CFRTP pre-impregnate 3D printing equipment, (d) S/C-CFRTP in-situ impregnate 3D printing equipment.

Tensile properties of S/C-CFRTP parts manufactured by two different processes are tested following the ISO 527-5:2009 standard [26]. The specific printing parameters and measurement parameters are shown in Table 5.

Table 5 S/C-CFRTP 3D printing experimental parameters and measurement parameters

Printing parameters				Test piece size	Loading speed
Printing speed	Printing temperature	Layer thickness	Line width		
270mm/min	270℃	0.3mm	0.8mm	250mm×15.2mm×1.2mm	2mm/min

4.2 Results and discussion

Figure 6 shows the S/C-CFRTP parts manufactured by the two processes before and after tensile test. Clearly, the S/C-CFRTP parts manufactured by the in situ impregnated process have a large amount of fiber pull-out after the test, while the S/C-CFRTP parts manufactured by the pre-impregnated process have significantly reduced fiber pull-out after the test. It shows that the manufacturing method of S/C-CFRTP pre-impregnated string proposed in this paper can effectively improve the degree of impregnation of continuous carbon fibers by the matrix. At the same time, the test results of mechanical properties (Fig. 7) show that the performance of the S/C-CFRTP parts manufactured by the pre-impregnated process is significantly improved. Compared with the parts manufactured by the in situ impregnated process, the tensile strength and tensile modulus were increased by nearly 19% and 12%, reaching 430.45MPa and 38.51GPa, respectively.

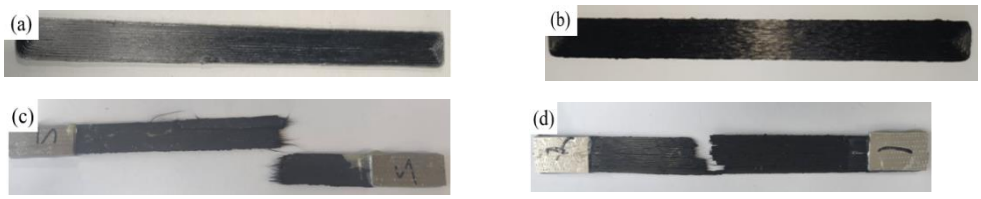

Fig.6. Comparison of S/C-CFRTP 3D printing parts manufactured by different 3D printing principle before and after tensile test. (a) S/C-CFRTP 3D printing parts manufactured by in situ impregnated strings before tensile test, (b) S/C-CFRTP 3D printing parts manufactured by pre-impregnated strings before tensile test, (c) S/C-CFRTP 3D printing parts manufactured by in situ impregnated strings after tensile test, (d) S/C-CFRTP 3D printing parts manufactured by pre-impregnated strings after tensile test.

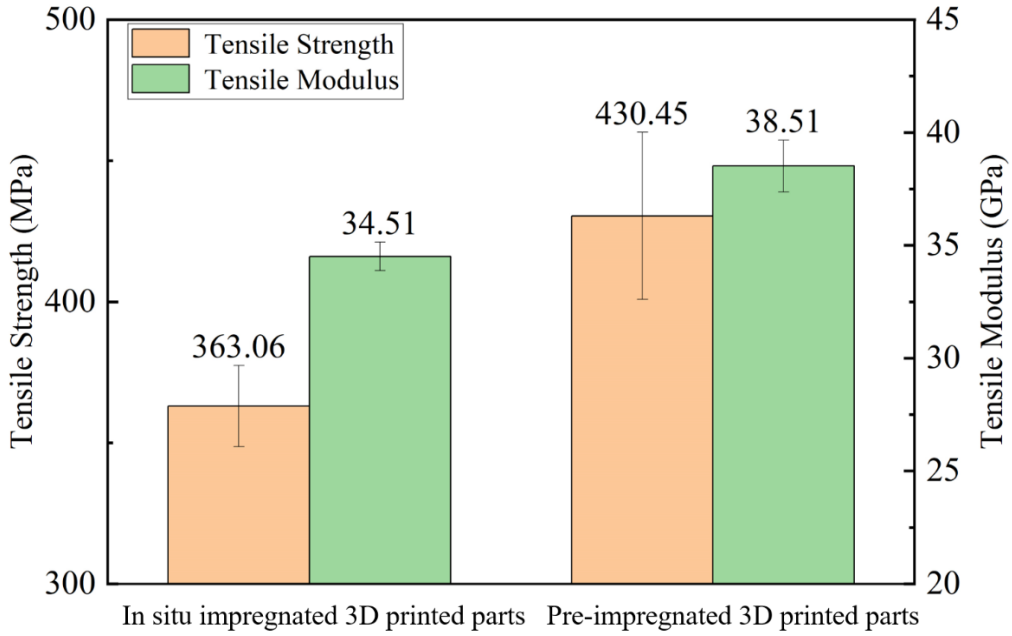

Fig.7 Comparison of tensile properties of S/C-CFRTP 3D printing parts manufactured by different 3D printing principle.

Therefore, the manufacturing method of S/C-CFRTP pre-impregnated string proposed in this paper can manufacture pre-impregnated string with high impregnation degree, which is suitable for 3D printing process and helpful to improve the performance of 3D printed S/C-CFRTP parts.

5. Conclusion

To tackle the problem of insufficient continuous carbon fiber impregnation in 3D printed S/C-CFRTP parts, this paper proposes a manufacturing method for the pre-impregnated string

of thermoplastic composite reinforced by short carbon fiber and continuous carbon fiber synergistically. A supporting principle prototype was developed. The feasibility of this method and the superiority of the manufactured S/C-CFRTP pre-impregnated string were verified by process experiments. The specific conclusions are as follows:

(1) The pre-impregnated string manufactured through the melt mixing module, rolled impregnation module and mold setting module (case c) has the best impregnation condition and the minimal fiber pull out after tensile failure. The tensile performance is also the best (about 114MPa), which is nearly 25% higher than that of case a;

(2) The optimal manufacture route of S/C-CFRTP pre-impregnated string is to go through the melt mixing module, the rolled impregnation module and the mold setting module respectively;

(3) The tensile strength and tensile modulus of the S/C-CFRTP parts printed by the pre-impregnated string manufactured in case c are about 430.45Mpa and 38.51Gpa, respectively, which are higher than those printed by situ impregnated S/C-CFRTP parts, the increase of percentage is nearly 19% and 12%, respectively.

6. References

[1] Lin D, Nian Q, Deng B, et al. Three-dimensional printing of complex structures: man made or toward nature?[J]. ACS Nano, 2014, 8(10): 9710-9715.

[2] Perrin F, Bureau M N, Denault J, et al. Mode I interlaminar crack propagation in continuous glass fiber/polypropylene composites: temperature and molding condition dependence[J]. Composites Science and Technology, 2003, 63(5): 597-607.

[3] Bureau M N, Denault J. Fatigue resistance of continuous glass fiber/polypropylene composites:

consolidation dependence[J]. Composites Science and Technology, 2004, 64(12): 1785-1794.

[4] Cerneels J, Voet A, Ivens J, et al. Additive manufacturing of thermoplastic composites[J]. Composites Week@ Leuven, 2013: 1-7.

[5] Dickson A N, Abourayana H M, Dowling D P. 3D printing of fibre-reinforced thermoplastic composites using fused filament fabrication—A review[J]. Polymers, 2020, 12(10): 2188.

[6] Somireddy M, Singh C V, Czekanski A. Mechanical behaviour of 3D printed composite parts with short carbon fiber reinforcements[J]. Engineering Failure Analysis, 2020, 107: 104232.

[7] Ning F, Cong W, Hu Y, et al. Additive manufacturing of carbon fiber-reinforced plastic composites using fused deposition modeling: Effects of process parameters on tensile properties[J]. Journal of Composite Materials, 2017, 51(4): 451-462.

[8] Ning F, Cong W, Qiu J, et al. Additive manufacturing of carbon fiber reinforced thermoplastic composites using fused deposition modeling[J]. Composites Part B: Engineering, 2015, 80: 369-378.

[9] Tekinalp H L, Kunc V, Velez-Garcia G M, et al. Highly oriented carbon fiber–polymer composites via additive manufacturing[J]. Composites Science and Technology, 2014, 105: 144-150.

[10] Bhandari S, Lopez-Anido R A, Gardner D J. Enhancing the interlayer tensile strength of 3D printed short carbon fiber reinforced PETG and PLA composites via annealing[J]. Additive Manufacturing, 2019, 30: 100922.

[11] Jing W, Hui C, Qiong W, et al. Surface modification of carbon fibers and the selective laser sintering of modified carbon fiber/nylon 12 composite powder[J]. Materials & Design, 2017, 116: 253-260.

[12] Zhang Z, Liu R, Li W, et al. Frontal polymerization-assisted 3D printing of short carbon fibers/dicyclopentadiene composites[J]. Journal of Manufacturing Processes, 2021, 71: 753-762.

[13] Matsuzaki R, Ueda M, Namiki M, et al. Three-dimensional printing of continuous-fiber composites by

in-nozzle impregnation[J]. Scientific Reports, 2016, 6(1): 1-7.

[14] Li N, Li Y, Liu S. Rapid prototyping of continuous carbon fiber reinforced polylactic acid composites by 3D printing[J]. Journal of Materials Processing Technology, 2016, 238: 218-225.

[15] Luo M, Tian X, Shang J, et al. Bi-scale interfacial bond behaviors of CCF/PEEK composites by plasma-laser cooperatively assisted 3D printing process[J]. Composites Part A: Applied Science and Manufacturing, 2020, 131: 105812.

[16] Qiao J, Li Y, Li L. Ultrasound-assisted 3D printing of continuous fiber-reinforced thermoplastic (FRTP) composites[J]. Additive Manufacturing, 2019, 30: 100926.

[17] Zhang J, Zhou Z, Zhang F, et al. Performance of 3D-printed continuous-carbon-fiber-reinforced plastics with pressure[J]. Materials, 2020, 13(2): 471.

[18] Toray industries, inc, (https://www.toraytac.com/media/221a4fcf-6a4d-49f3-837f-9d85c3c34f74/smphpw/TAC/Documents/Data_sheets/Thermoplastic/UD%20tapes,%20prepregs%20and%20laminates/Toray-Cetex-TC1100_PPS_PDS.pdf).

[19] Yavas D, Zhang Z, Liu Q, et al. Interlaminar shear behavior of continuous and short carbon fiber reinforced polymer composites fabricated by additive manufacturing[J]. Composites Part B: Engineering, 2021, 204: 108460.

[20] Wu B, Wang G, Wang H, et al. Coaxial extrusion—based additive manufacturing of nylon matrix composites synergistically reinforced by multi—phase fibers[J]. Fiber Composites, 2021, 38(02): 15-23.

[21] Oztan C, Karkkainen R, Fittipaldi M, et al. Microstructure and mechanical properties of three dimensional-printed continuous fiber composites[J]. Journal of Composite Materials, 2019, 53(2): 271-280.

[22] Hu Q, Duan Y, Zhang H, et al. Manufacturing and 3D printing of continuous carbon fiber prepreg filament[J]. Journal of Materials Science, 2018, 53(3): 1887-1898.

[23] Liu T, Tian X, Zhang Y, et al. High-pressure interfacial impregnation by micro-screw in-situ extrusion for 3D printed continuous carbon fiber reinforced nylon composites[J]. Composites Part A: Applied Science and Manufacturing, 2020, 130: 105770.

[24] Tian X, Zhang Y, Liu T, et al. Prepreg preparation and 3D printing of continuous carbon fiber reinforced nylon composite[J]. Aeronautical Manufacturing Technology, 2021, 64(15): 24–33.

[25] Wang F, Zhang Z, Ning F, et al. A mechanistic model for tensile property of continuous carbon fiber reinforced plastic composites built by fused filament fabrication[J]. Additive Manufacturing, 2020, 32: 101102.

[26] ISO 527-5, Plastics - Determination of Tensile Properties - Part 5: Test Conditions for Unidirectional Fibre-reinforced Plastic Composites, 2009. (https://www.iso.org/standard/52991.html).

7. Acknowledgement

This work was supported by National Natural Science Foundation of China (Grant No. 52130506), Innovation Fund Program from National Research Center for Manufacturing Engineering Technology of Commercial Aircraft (Grant No. COMAC-SFGS-2021-602), Liaoning Revitalization Talents Program (Grant No. XLYC1801008， XLYCYSZX1901, XLYC1902014), Science and Technology Innovation Foundation of Dalian (Grant No. 2019CT01, 2021RD08). The authors would like to acknowledge the above financial supports.

Effect of Low-Velocity Impact Times on Residual Compressive Strength of 3D Printed Continuous Carbon Fiber Honeycomb Structure

*Wenguang YE, Hao DOU, Dinghua ZHANG, Fuqiang YANG, Yunyong CHENG**

School of Mechanical Engineering, Northwestern Polytechnical University, Xi'an, Shaanxi, China

Key Laboratory of High Performance Manufacturing for Aero Engine (Northwestern Polytechnical University), Ministry of Industry and Information Technology, Xi'an, Shaanxi, China

Abstract: Continuous fiber-reinforced composites are widely used in aerospace and automotive fields due to their high specific strength and high specific stiffness. 3D printing technology has the advantages of rapid manufacturing without mold, which makes up for the shortcomings of traditional composite material processing technology that it is difficult to form complex structures. In this paper, the continuous carbon fiber reinforced honeycomb structure (CCFRHS) was prepared based on fused filament fabrication (FFF). The effect of low-velocity impact (LVI) times on the residual compressive strength of honeycomb structures was also studied. The results show that the CCFRHS has higher impact resistance and compressive strength than the pure matrix honeycomb structure. At the same time, when the total impact energy is 10J, with the increase of impact times, the residual compressive strength gradually increases. Compared with a single impact, the damage caused by small-energy impacts is smaller, so it has a higher residual compressive strength. The cracks after LVI mainly occurred in the matrix part without fiber reinforcement between the two printing paths, and the carbon fiber in the honeycomb structure did not break obviously. Therefore, compared with pure matrix honeycomb structure, CCFRHS has higher residual compressive strength after low-velocity impact. The research in this paper is of great significance for the application of 3D-printed CCFRHS in complex environments.

1 INTRODUCTION

Continuous fiber composites have been widely used in aviation, aerospace, construction, and other fields due to their high specific strength and high specific stiffness [1–3]. In recent years, the rapid development of additive manufacturing (AM) technology for continuous fiber-reinforced composites has attracted extensive interest from researchers [4–6]. For 3D printed continuous fiber composites, a large number of studies have studied their mechanical properties from the aspects of the manufacturing process, including the influence of fiber content [7,8], fiber arrangement direction [9,10], and interface bonding effect [11,12] on mechanical properties. On the basis of mechanical research, many studies have studied shape

memory [13], electromagnetic shielding [14], self-healing [15], and other properties of 3D printed continuous fiber reinforced composites from the perspective of function.

Based on the preparation of solid parts, researchers have prepared continuous fiber-reinforced composite lightweight structures with excellent mechanical properties through 3D printing, such as lattice structures [16–18], honeycomb structures [19–22], etc. Among them, the honeycomb structure is more widely concerned and studied due to its simple process and excellent mechanical properties. Among them, Zeng et al. [23] studied the fabrication of continuous fiber-reinforced composite honeycomb structures (CFRCHSs) with excellent shape memory properties by fused filament fabrication (FFF) technology, and experimentally studied their out-of-plane / in-plane compression behavior and energy absorption characteristics.

At present, most studies focus on the preparation methods of 3D printed continuous fiber composite lightweight structures and basic compression experiments. There are few studies on impact response and residual strength after impact, and there is a lack of strain and damage perception during impact and compression. In this paper, a continuous carbon fiber reinforced composite honeycomb structure (CCFRHS) was prepared by 3D printing, and the response of low-velocity impact (LVI) times to its residual compression was studied.

2 MATERIALS AND METHODS

2.1 Materials specimen fabrications

Composite materials are divided into reinforcement phase and matrix phase, the reinforcement phase used in this paper is 1K continuous carbon fiber (HTA 40 E15 1K, Toho Tenax Co., Ltd, Japan). The matrix phase material is polylactic acid (PLA 1.75, Flash Forge, Hangzhou, Zhejiang, China) commonly used in FFF printing. Table 2 shows the mechanical properties of continuous carbon fiber and PLA.

Table 2 Performance of continuous carbon fiber and PLA.

	Tensile strength	Tensile modulus	Elongation at break	Density
HTA40	3800 MPa	238 GPa	1.7%	1.77 g/cm^3
PLA filament	64.63 MPa	3.2 GPa	4.43%	1.24 g/cm^3

2.2 Specimen fabrications

As shown in *Fig. 11*(a), this paper modified the traditional FFF delta 3D printer to realize the in-situ extrusion of continuous carbon fiber composites. The main modified parts include the selection of larger diameter nozzles and throats, and the addition of carbon fiber inlets on the feed pipe. Under the action of the extruder, the PLA wire drives the continuous carbon fiber into the nozzle for in-situ impregnation, and the additive manufacturing of the CCFRHS is realized according to the printing path of the honeycomb structure. As shown in *Fig. 11*(c), in order to facilitate the experiment, the redundant parts at both ends of the honeycomb sample are cut off, and the test piece shown in *Fig. 11*(d) is finally obtained. At the same time, the honeycomb structure of pure PLA and the CCFRHS were printed for comparative experiments.

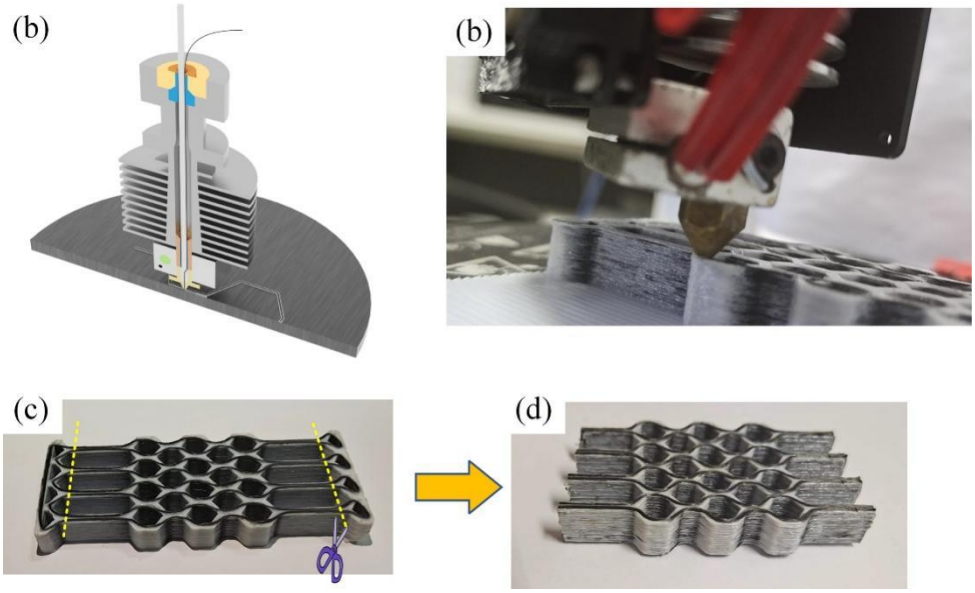

Fig. 11 Preparation process of specimen. (a) 3D printer modification. (b) honeycomb structure printing. (c) specimen treatment. (d) final specimen.

2.2 Characterizations

Fig. 12(a) shows the LVI experiment process of the honeycomb structure. The drop-weight impact system (INSTRON-CEAST 9340, Boston USA) was used to perform LVI experiment on the honeycomb structure using a hemispherical impactor. As shown in *Fig. 12*(b), the residual compressive strength of the honeycomb was measured by a universal testing machine (Instron 3382). Cone beam computed tomography (CBCT) was used to examine the LVI damage inside the honeycomb structure. Industrial cameras were used to record the experimental process.

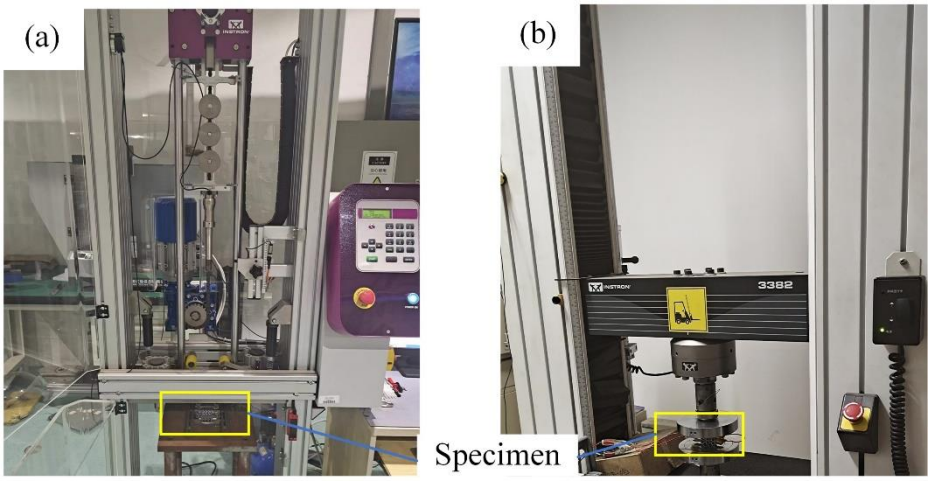

Fig. 12 Experimental process. (a) LVI experiment. (b) compression experiment after LVI.

3 RESULTS AND DISCUSSION

3.1 LVI response

For CCFRHS, the honeycomb structure is subjected to single and multicycle impact at a total energy of 10 J. As shown in *Fig. 13*(a,c,e), the impact load fluctuates greatly for many times during the first impact, indicating that the honeycomb structure is damaged in multiple

positions during the impact process. In the process of repeated impact, the impact load fluctuates little, indicating that the number of damage does not increase except for the damage caused by the first impact. As shown in *Fig. 13*(b,d,f), in the process of repeated impact, the maximum displacement increases gradually, which indicates that repeated impact leads to the deepening of damage.

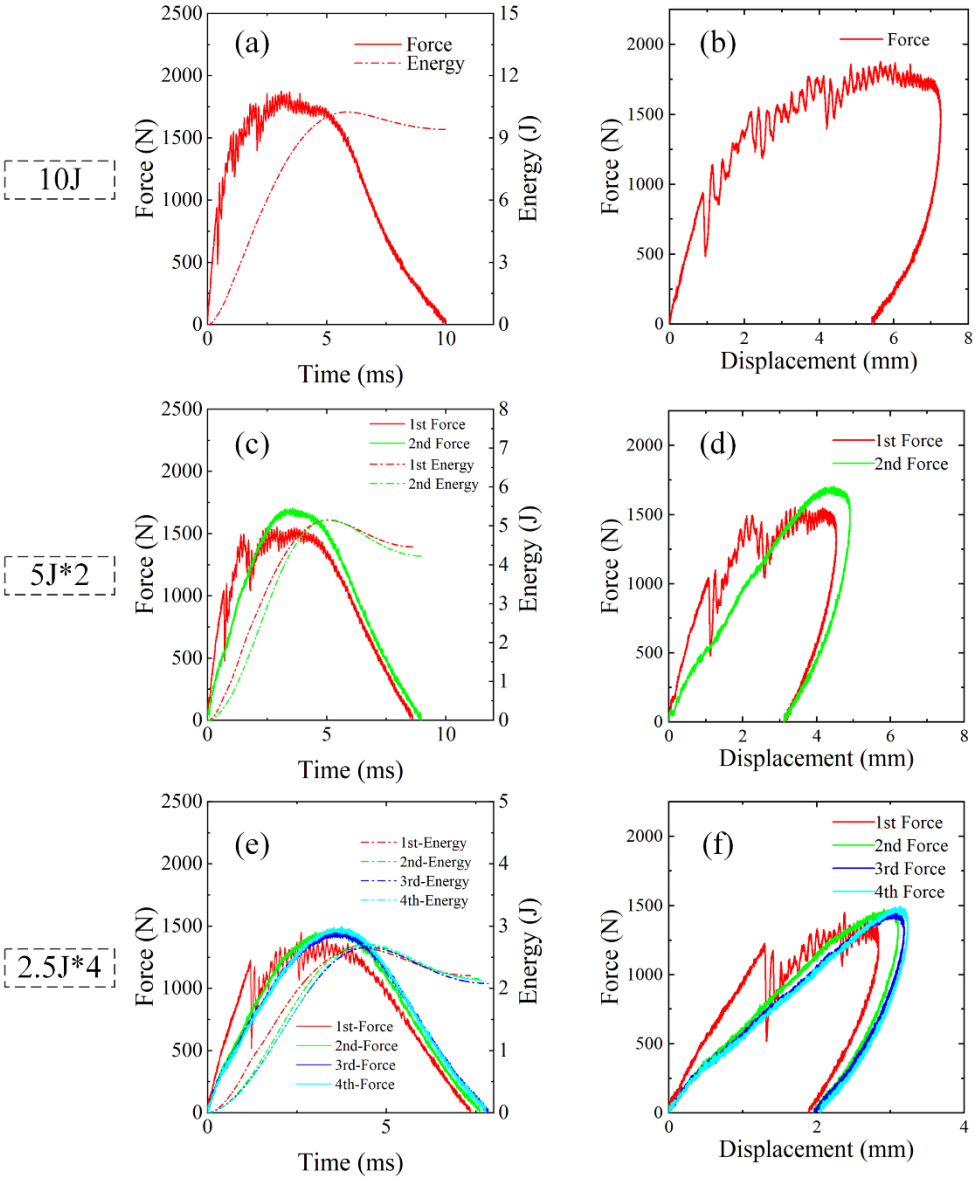

Fig. 13 LVI experiment of CCFRHS.

As shown in *Fig. 14*, for the pure PLA honeycomb structure, when the initial impact is carried out with 3J and 1.5J energy, the load fluctuates obviously many times, which indicates that many large damages have occurred in the pure matrix material. When the second impact of 1.5J energy, the impact load still fluctuates greatly, which indicates that new damage is generated inside the pure PLA honeycomb structure during the repeated impact process, which makes the maximum displacement at the second impact higher than the first impact.

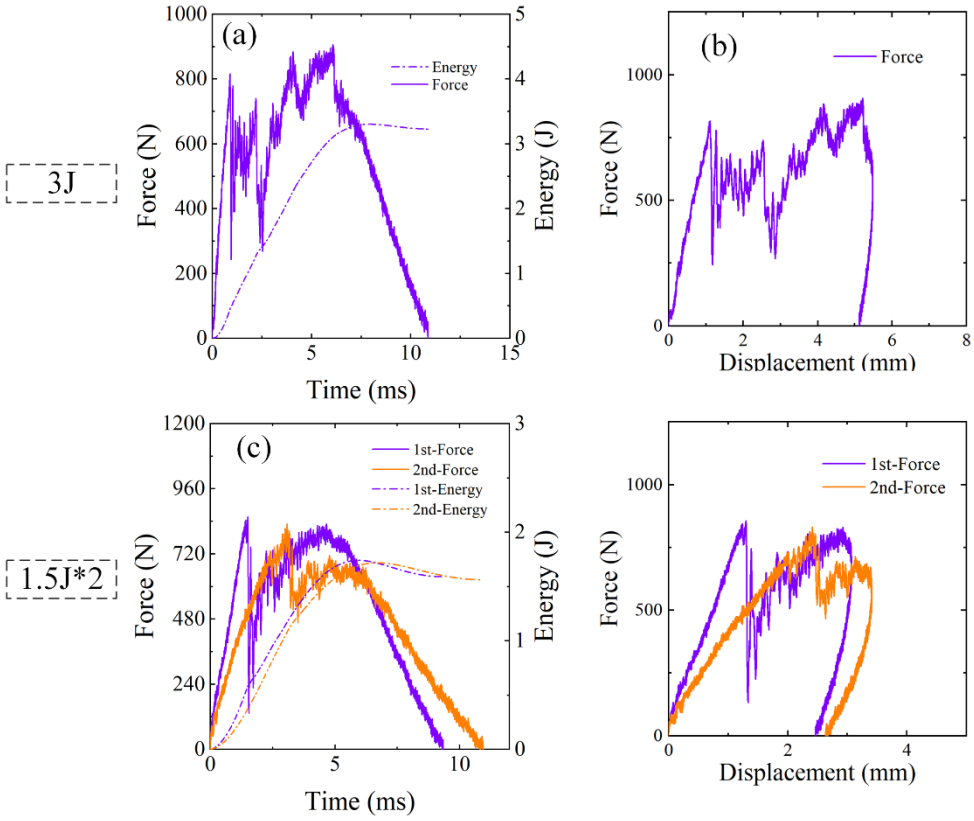

Fig. 14 LVI experiment of pure PLA honeycomb structure.

3.2 Low-velocity impact damage characterization

Fig. 15 shows the sliced image of the honeycomb structure obtained by industrial CBCT after impact. In CCFRHS, cracks are mainly produced in the matrix material between adjacent printing paths. The hindrance of continuous carbon fiber makes only the matrix material in the thinner wall partially crack, which makes the CCFRHS still have good integrity during compression. When the total impact energy is constant, with the increase of impact times, the width and number of cracks decrease, which indicates that the cumulative damage of multicycle small energy impact is smaller than that of single large energy impact.

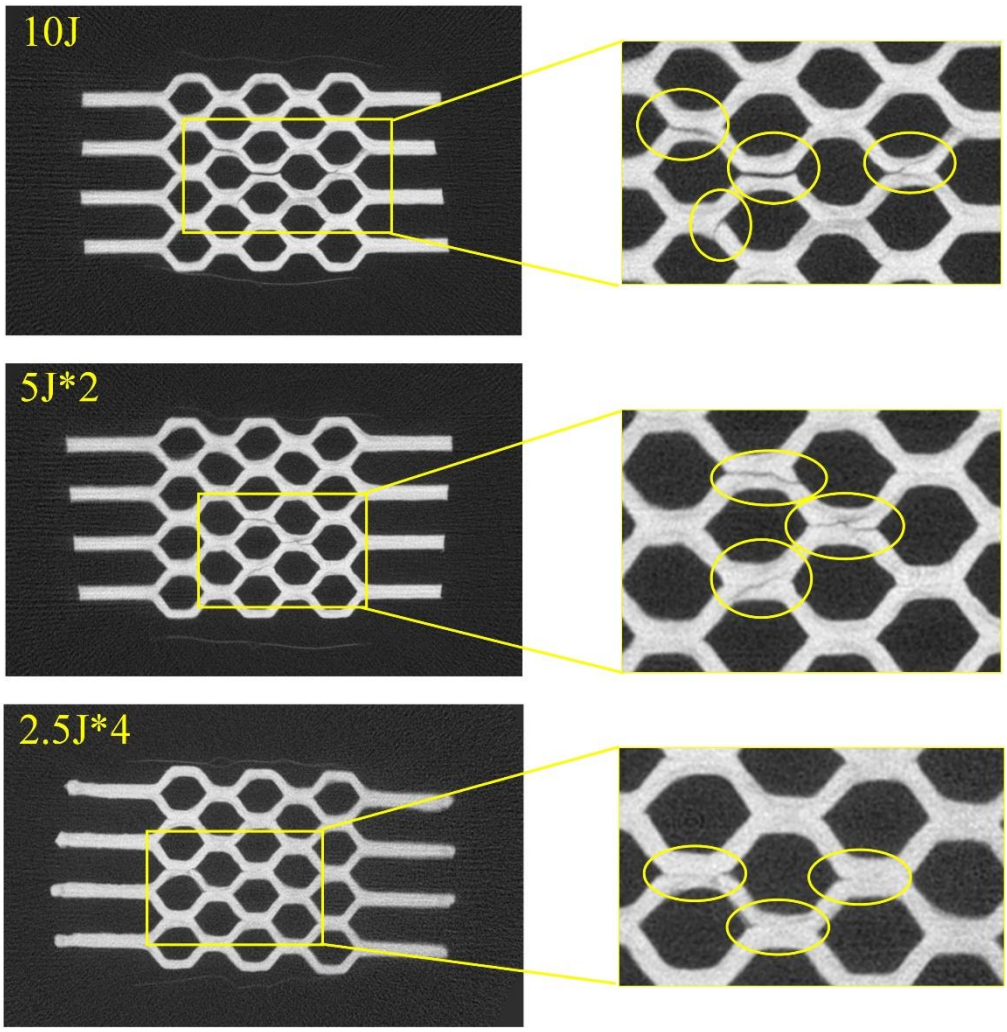

Fig. 15 Damage degree of CCFRHS after impact.

Fig. 16 shows the damage image of pure PLA honeycomb structure after impact. The impact causes the honeycomb wall of pure PLA honeycomb structure to break. Compared with a single 3J energy impact, the damage caused by 1.5J energy impact twice is widely dispersed in the honeycomb structure. This shows that the cumulative effect of multicycle small energy impact damage is more obvious, and the damage is dispersed in the honeycomb structure.

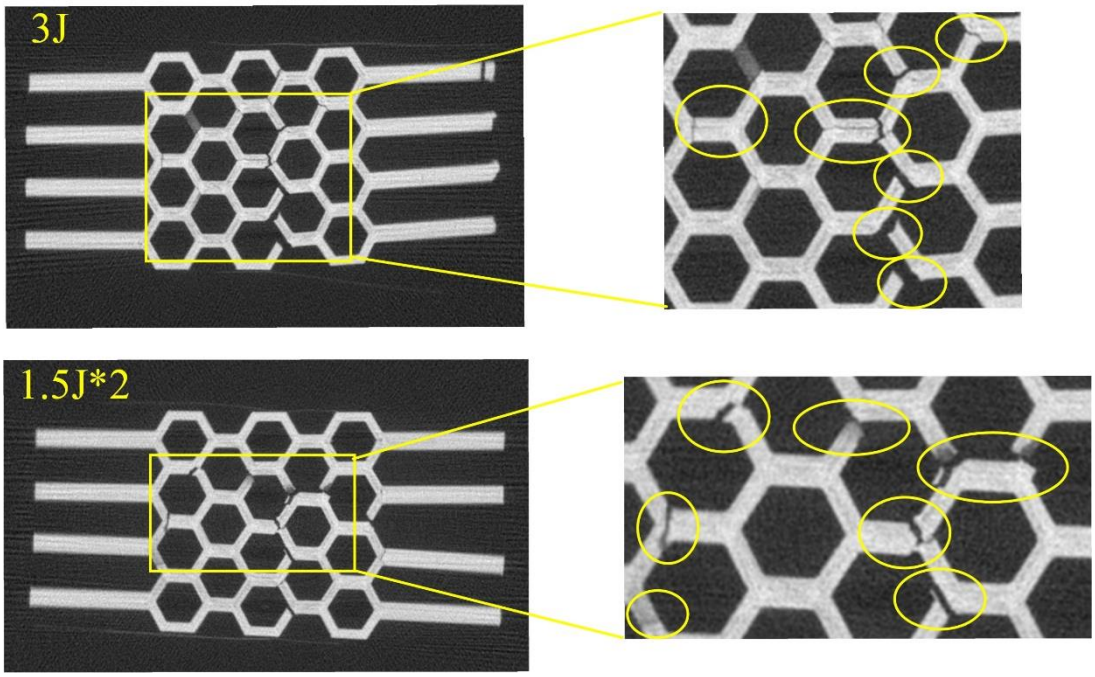

Fig. 16 Damage degree of pure PLA honeycomb structure after LVI.

3.3 Compression behavior after LVI

As shown in *Fig. 17*(a), the number of impact times does not change the compression deformation process of CCFRHS. *Fig. 17*(b) shows that the impact leads to a decrease in its strength and stiffness, but with the increase of the number of impact times, its compressive strength and stiffness gradually increase, which indicates that the more the number of small energy impact times, the better the integrity of the honeycomb structure after impact. As shown in *Fig. 17*(c), the impact changes the compression deformation process of the honeycomb structure. Compared with the honeycomb structure without impact, the impact leads to the disappearance of the enhancement stage (strain ≈ 0.2) in the compression process. *Fig. 17*(d) shows that the compressive strength and stiffness decrease with the increase of impact times, which indicates that the more the number of small energy impact times, the more the internal cumulative damage of the honeycomb structure after impact.

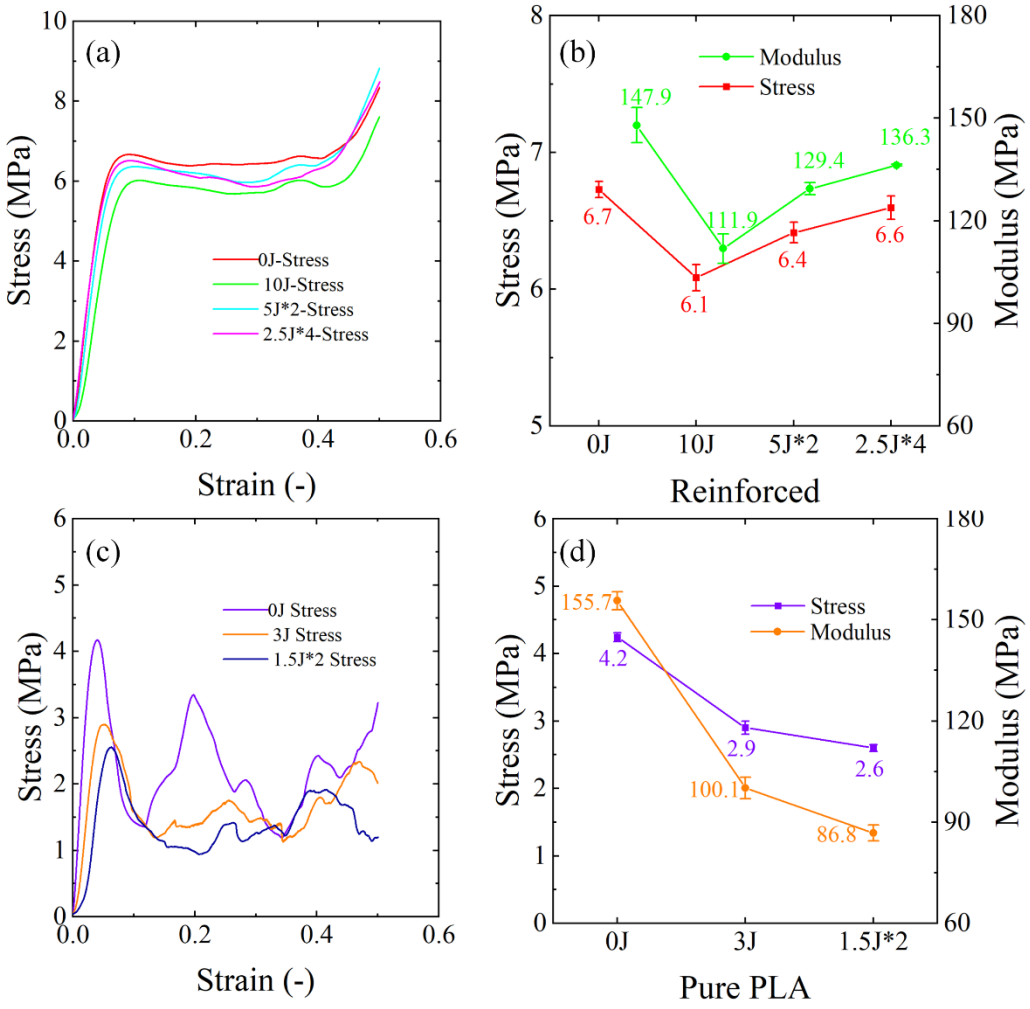

Fig. 17 Residual compressive strength of honeycomb structure after impact.

4 CONCLUSION

In this paper, the effect of LVI times on the residual compressive strength of 3D printed CCFRHS is studied. The results show that the first impact will cause more damage. Repeated impact will deepen the first damage, but cause less new damage. Impact leads to wall breakage in pure PLA honeycomb structures. Impact will cause matrix cracking between paths and matrix fracture on honeycomb wall in CCFRHS. Continuous carbon fiber will hinder the transmission of fracture so that the honeycomb structure still maintains good structural integrity after impact. Compared with pure matrix material, the damage accumulation effect of repeated impact on honeycomb structure is not obvious.

ACKNOWLEDGMENT

This work was financially supported by The Fundamental Research Funds for the Central Universities (HXGJXM202216).

REFERENCES

[1] Brenken B, Barocio E, Favaloro A, Kunc V, Pipes RB. Fused filament fabrication of fiber-reinforced polymers: A review. Addit. Manuf. 2018;21:1–16. https://doi.org/10.1016/j.addma.2018.01.002.

[2] Ferreira I, Machado M, Henriques E, Leite M, Peças P, Marques AT. State-of-the-Art Review and Roadmap. Springer; 2020.

[3] Hu Y, Li Y, Li B, Shen S. 3D printed fibre-reinforced polymer composites—Review of the fused deposition modeling process and mechanical performance of products. Fuhe Cailiao Xuebao 2021;38(4):979–96. https://doi.org/10.13801/j.cnki.fhclxb.20210118.003.

[4] Kabir S, Mathur K, Seyam A-F. A critical review on 3D printed continuous fiber-reinforced composites: History, mechanism, materials and properties. Compos. Struct. 2020;232. https://doi.org/10.1016/j.compstruct.2019.111476.

[5] Pandelidi C, Bateman S, Piegert S, Hoehner R, Kelbassa I, Brandt M. The technology of continuous fibre-reinforced polymers: a review on extrusion additive manufacturing methods. Int J Adv Manuf Technol 2021. https://doi.org/10.1007/s00170-021-06837-6.

[6] Zhang H, Huang T, Jiang Q, He L, Bismarck A, Hu Q. Recent progress of 3D printed continuous fiber reinforced polymer composites based on fused deposition modeling: a review. J Mater Sci 2021;56(23):12999–3022. https://doi.org/10.1007/s10853-021-06111-w.

[7] Zh A, Xt A, Zz A, Jz A, Lu ZA, Dl A et al. A constitutive model for 3D printed continuous fiber reinforced composite structures with variable fiber content. Compos Part B: Eng 2020;189.

[8] Chacón JM, Caminero MA, Núñez PJ, García-Plaza E, García-Moreno I, Reverte JM. Additive manufacturing of continuous fibre reinforced thermoplastic composites using fused deposition modelling: Effect of process parameters on mechanical properties. Composites Science and Technology 2019;181:107688. https://doi.org/10.1016/j.compscitech.2019.107688.

[9] Shafighfard T, Cender TA, Demir E. Additive manufacturing of compliance optimized variable stiffness composites through short fiber alignment along curvilinear paths. Additive Manufacturing 2021;37. https://doi.org/10.1016/j.addma.2020.101728.

[10] Chen X, Fang G, Liao W-H, Wang CC. Field-Based Toolpath Generation for 3D Printing Continuous Fibre Reinforced Thermoplastic Composites. Additive Manufacturing 2022;49:102470. https://doi.org/10.1016/j.addma.2021.102470.

[11] Fan C, Shan Z, Zou G, Zhan L, Yan D. Interfacial Bonding Mechanism and Mechanical Performance of Continuous Fiber Reinforced Composites in Additive Manufacturing. Chin. J. Mech. Eng. 2021;34(1). https://doi.org/10.1186/s10033-021-00538-7.

[12] Pappas JM, Thakur AR, Leu MC, Dong X. A parametric study and characterization of additively manufactured continuous carbon fiber reinforced composites for high-speed 3D printing. Int J Adv Manuf Technol 2021;113(7-8):2137–51. https://doi.org/10.1007/s00170-021-06723-1.

[13] Dong K, Ke H, Panahi-Sarmad M, Yang T, Huang X, Xiao X. Mechanical properties and shape memory effect of 4D printed cellular structure composite with a novel continuous fiber-reinforced printing path. Materials and Design 2021;198.

[14] Yin L, Tian X, Shang Z, Wang X, Hou Z. Characterizations of continuous carbon fiber-reinforced composites for electromagnetic interference shielding fabricated by 3D printing. Appl. Phys. A 2019;125(4). https://doi.org/10.1007/s00339-019-2566-0.

[15] Luan C, Yao X, Zhang C, Fu J, Wang B. Integrated self-monitoring and self-healing continuous carbon fiber reinforced thermoplastic structures using dual-material three-dimensional printing technology. Composites Science and Technology 2020;188:107986. https://doi.org/10.1016/j.compscitech.2019.107986.

[16] Li N, Link G, Jelonnek J. Rapid 3D microwave printing of continuous carbon fiber reinforced plastics. CIRP Annals 2020;69(1):221–4. https://doi.org/10.1016/j.cirp.2020.04.057.

[17] Liu S, Li Y, Li N. A novel free-hanging 3D printing method for continuous carbon fiber reinforced thermoplastic lattice truss core structures. Materials & Design 2018;137:235–44.

https://doi.org/10.1016/j.matdes.2017.10.007.
[18] Wang Z, Luan C, Liao G, Yao X, Fu J. Mechanical and self-monitoring behaviors of 3D printing smart continuous carbon fiber-thermoplastic lattice truss sandwich structure. Composites Part B: Engineering 2019;176:107215. https://doi.org/10.1016/j.compositesb.2019.107215.
[19] Wei X, Xiong J, Wang J, Xu W. New advances in fiber-reinforced composite honeycomb materials. Sci. China Technol. Sci. 2020;63(8):1348–70. https://doi.org/10.1007/s11431-020-1650-9.
[20] Quan C, Han B, Hou Z, Zhang Q, Tian X, Lu TJ. 3d printed continuous fiber reinforced composite auxetic honeycomb structures. Compos Part B: Eng 2020;187:107858. https://doi.org/10.1016/j.compositesb.2020.107858.
[21] Dou H, Ye W, Zhang D, Cheng Y, Huang K, Yang F et al. Research on drop-weight impact of continuous carbon fiber reinforced 3D printed honeycomb structure. Materials Today Communications 2021;29:102869. https://doi.org/10.1016/j.mtcomm.2021.102869.
[22] Cheng Y, Li J, Qian X, Rudykh S. 3D printed recoverable honeycomb composites reinforced by continuous carbon fibers. Composite Structures 2021;268:113974. https://doi.org/10.1016/j.compstruct.2021.113974.
[23] Zeng C, Liu L, Bian W, Leng J, Liu Y. Compression behavior and energy absorption of 3D printed continuous fiber reinforced composite honeycomb structures with shape memory effects. Additive Manufacturing 2021;38:101842. https://doi.org/10.1016/j.addma.2021.101842.

A 3D printed stucture with negative Poisson's ratios

Wenjie Dai[1], Huiyu Sun[1]*

[1]College of Aerospace Engineering, Nanjing University of Aeronautics and Astronautics, Nanjing, China
*Corresponding authors: Huiyu Sun (E-mail: hysun@nuaa.edu.cn, 29 Yudao Street, Nanjing, 210016, Jiangsu, China)

Abstract: In this paper, a 3D six-link chiral structure with negative Poisson's ratios is proposed based on the 2D four-link chiral cell-structure. The connecting nodes are arranged at specific positions (not endpoints) of the central sphere, and the direction of the connecting rod is oriented along the axial direction of stretching (not tangential direction). The 3D cell-structure is employed to obtain the chiral model by array arrangement and the antichiral model by mirror arrangement. The effects of the geometric parameters and cell-structure numbers on the Poisson's ratios of the chiral and antichiral models are investigated by finite element method. Then, the chiral and antichiral specimens are prepared by 3D printing, and tested by the Universal Testing Machine, and the validity of the simulation results is verified by comparing with the experimental results.

1 INTRODUCTION

The Negative Poisson's ratio metamaterials (also known as auxetic materials) are a special kind of materials that can expand laterally under longitudinal tensile loading (or shrink laterally under longitudinal compression loading). Duo to the unique property, metamaterials with negative Poisson's ratios also show some useful properties that exceed other materials in the field of physics and mechanics, such as high shear stiffness, great impact resistance, high fracture resistance, indentation resistance, great sound absorption and permeability variability[1]. These advantages make them have broad potential application in many fields, such as aerospace, construction, biomedicine, textile materials and noise absorption [2].

The possibility of materials with negative Poisson's ratios was proposed in the classical elastic theory 160 years ago[3]. In 1944, Love et al.[4] first discovered the negative Poisson's ratio property in pyrite crystals, and estimated that the Poisson's ratios of them were about -0.17. In 1987, Lakes et al.[5] first produced an artificial negative Poisson's ratio metamaterial by treating polyester foam in aluminum containers, and obtained negative Poisson's ratio

polyurethane foam with special concave structures. The Poisson's ratio of the concave structure is -0.7. This groundbreaking research drew widespread attention to the materials with negative Poisson's ratios, and opened the way for extensive research on metamaterials in the past thirty years.

After Lakes's pioneering work, researchers further analyzed the various cell-structures of the metamaterials with negative Poisson's ratios. The mechanical theory and finite element method were employed to analyze the mechanism of the negative Poisson's ratios. Negative Poisson's ratio metamaterials can be divided into 2D cell-structures and 3D cell-structures according to the Poisson's ratios in different directions. Comparing to 3D cell-structures, 2D cell-structures have more simple structures and easier preparation. Researchers made many breakthroughs in the field of 2D negative Poisson's ratio metamaterials. In 1988, Gibson et al. [6] proposed a concave hexagonal structure with negative Poisson's ratios. In 1991, Lakes et al.[7] first proposed a negative Poisson's ratio chiral structure. Alderson et al. [8] designed a rotating polygonal structure with negative Poisson's ratios. In 2010, Grima et al. [9] put forward a negative Poisson's ratio structure with diamond or star perforation.

3D chiral cell-structures are generally designed based on 2D chiral cell-structures. In 2016. Ha et al. [10] designed a 3D chiral negative Poisson's ratio isotropic cell-structure, which was composed of sixteen inclined rods connected to each node of the central cube. In 2017, Lu et al. [11] proposed a 3D cross chiral cell-structures with negative Poisson's ratios, and enhanced its Young's modulus by adding a star structure. In 2018, Fu et al. [12] put forward a new 3D chiral honeycomb structure with negative Poisson's ratios based on the rotation mechanism. The cell-structure consists of 2D chiral cell-structures and eight inclined rods connected to the upper and lower surfaces of the cell-structures.

In this paper, a 3D six-link chiral structure with negative Poisson's ratios is proposed based on the 2D four-link chiral cell-structure. The connecting nodes are arranged at specific positions (not endpoints) of the central sphere, and the direction of the connecting rod is oriented along the axial direction of stretching (not tangential direction). The effect of negative Poisson's ratios is generated by the rotation of the central sphere under tensile and compressive loading. By introducing the spherical geodesic theory, the displacement trajectories of connecting nodes are studied, by which the Poisson's ratios in each direction can be calculated.

The 3D cell-structure is employed to obtain the chiral model by array arrangement and the antichiral model by mirror arrangement. The effects of the geometric parameters and cell-structure numbers on the Poisson's ratios of the chiral and antichiral models are investigated by finite element method. Then, the chiral and antichiral specimens are prepared by 3D printing, the Poisson's ratios are measured by the Universal Testing Machine, and the validity of the simulation results is verified by comparing with the experimental results.

2 DESIGN

Multi-link chiral cell-structures with negative Poisson's ratios generally consist of a central circle and connecting rods. In this study, the design of 3D chiral cell-structures is developed from 2D chiral cell-structures with nontangential connecting rods as shown in Fig.1a. The 2D chiral cell-structures consist of connecting rods and circular loops with each loop joined by rods. The 2D chiral cell-structures can also be seen in the section of 3D cell-structure models. To obtain the 3D chiral cell-structure on the basis of the 2D four-link chiral structure, the circular loops are transformed into a hollow sphere, and the connecting rods are connected at the six nodes on the surface of the central sphere along the six directions of the coordinate axes as shown in Fig. 1b. The geometry of the 3D cell-structure is determined by five primary geometrical parameters: the inner diameter (r) and outer diameter (R) of the hollow sphere, the length of the connecting rod (L), the thickness of the connecting rod (T) and the width of the connecting rod (W), as shown in Fig. 1c. The cross-sectional shape of the connecting rod is assumed to be square in this cell-structure, so it can be assumed that T=W.

(a) (b)

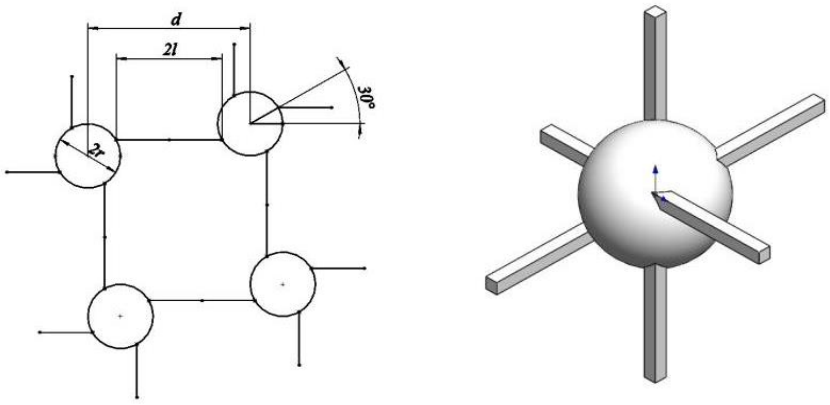

(c)

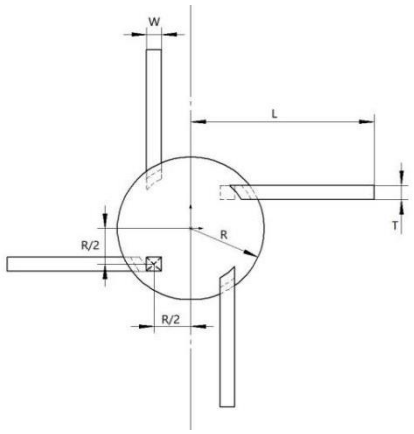

Fig. 1. Cell-structures. (a) 2D chiral cell-structure. (b) 3D chiral cell-structure. (c) geometrical parameters of 3D cell-structure.

The chiral cell-structure model can be got by connecting the basic cell-structure in pairs with the cross sections of the connecting rods through array arrangement. Assuming that the number of cells on the sides of each 3D model is N, M and K, respectively, this model is defined as the chiral model with N×M×K cells. Similarly, the antichiral model with N×M×K cells can be obtained by connecting 3D chiral cell-structure through mirror arrangement. Among them, the minimum repeating unit of the chiral model is one cell, while the minimum repeating unit of the antichiral model is composed of two cells per side (2×2×2). In order to display the opposite side, Fig. 2 shows the chiral model and the antichiral model with 2×2×2 cell-structure.

(a) (b)

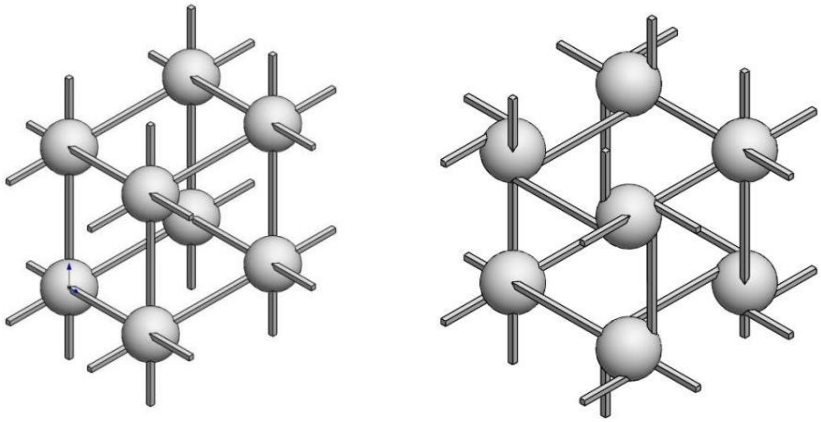

Fig. 2. 2×2×2 cell-structure. (a) the chiral model. (b) the antichiral model.

4. FINITE ELEMENT METHOD

In order to study the influence of the geometric parameters and cell-structure numbers on the Poisson's ratios of the 3D chiral model, the chiral and antichiral models with different geometric parameters and cell-structure numbers are calculated by the finite element method. In order to compare with experiments, an isotropic elastic resin is selected as the material for the finite element model, whose elastic modulus and Poisson's ratio are 13.333 MPa and 0.43, respectively. The displacement loading in the X direction and fixed boundary condition are applied at each end of the chiral and antichiral models.

Fig. 6 shows the Poisson's ratio-strain curves of the 3D chiral model with different numbers of the unit cell-structures. The unit cell-structures on the surface and in the center of the same model have different deformation under strain loading, which is caused by the different loading condition on the connecting rods. When the number of the cell-structure is small, the deformation of the cell-structures on the surface will influence the deformation of the cell-structure in the center. As shown in Fig. 6, when n>3, the influence is smaller, so we choose the chiral and antichiral models with the 4×4×4 cell-structure as the finite element models for the following research.

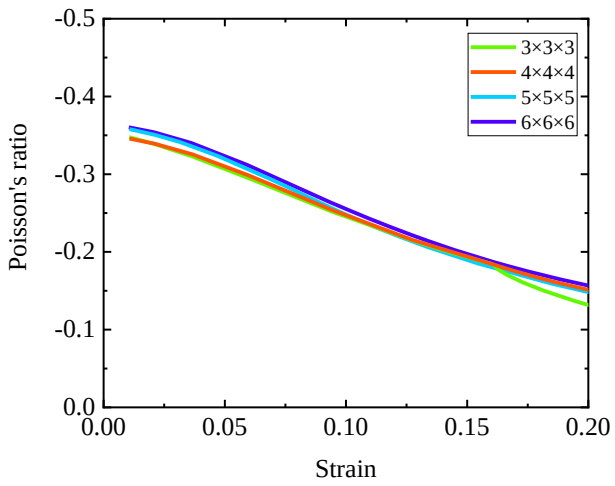

Fig. 6. The Poisson's ratio-strain curves of the 3D chiral model with different numbers of the unit cell-structures.

The influence of the geometric parameters on Poisson's ratios of the chiral and antichiral

models under tensile and compressive loadings is evaluated. For the chiral cell-structure designed in this paper, three parameters have decisive influences on the Poisson's ratios, which are the length of the connecting rod L, the outer radius R of the hollow sphere, and the section width W of the connecting rod. The finite element models with different L/R and W/R are established, and the inner radius is set as 5mm.Fig. 9 shows the chiral cell-structures with W of 2mm, 2.5mm, 3mm, 3.5mm and 4mm, in which R and L are 10mm and 25mm, respectively. The 4×4×4 chiral and antichiral models are obtained from the unit cell-structure with different W/R by array arrangement and mirror arrangement.

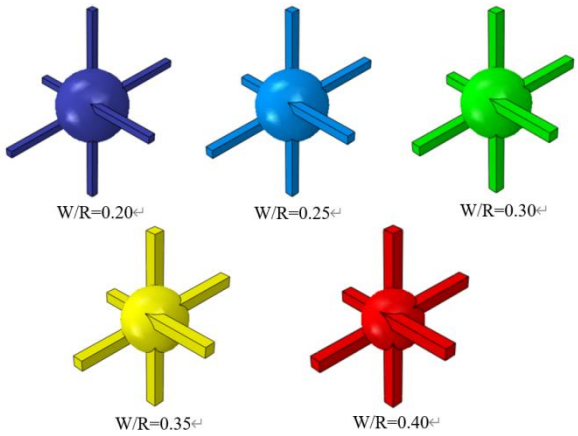

Fig. 9. Chiral cell-structure with different *W*/*R*

Figs.10a-b show the Poisson's ratio-strain curves of the chiral cell-structures under tensile loading in the Y and Z directions. The Poisson's ratios in the Y and Z directions are basically the same during loading. When *W* is 2mm and 2.5mm, the Poisson's ratios decrease at the beginning and then increase as the tensile strains increase. When *W* is 3mm, 3.5mm and 4mm, The Poisson's ratios monotonicly increase as the tensile strains increase. At the beginning of the curves, the Poisson's ratio is inversely proportional to *W*/*R*. When the negative Poisson's ratio effect is lost, the corresponding strain is directly proportional to *W*/*R*.

Figs.10c-d show the Poisson's ratio-strain curves of the antichiral cell-structures under tensile loading in the Y and Z directions. In Y direction, the Poisson's ratio is inversely proportional to *W*/*R*, and the Poisson's ratios decrease at the beginning and then increase as the tensile strains increase. When the negative Poisson's ratio effect is lost, the corresponding strain is directly proportional to *W*/*R*. In Z direction, the Poisson's ratio is also inversely proportional

to *W*/*R*, the Poisson's ratios monotonicly increase as the tensile strains increase, and the larger *W*/*R* is, the faster the Poisson's ratio increases. When the negative Poisson's ratio effect is lost, the corresponding strain is also directly proportional to *W*/*R*.

Figs.10e-f show the Poisson's ratio-strain curves of the antichiral cell-structures under compressive loading in the Y and Z directions. In Y direction, the Poisson's ratio is inversely proportional to *W*/*R* during loading, and the Poisson's ratios monotonicly increase as the compressive strains increase. In Z direction, the Poisson's ratio is also inversely proportional to *W*/*R* during loading, and the Poisson's ratios monotonicly decrease as the compressive strains increase.

(a) (b)

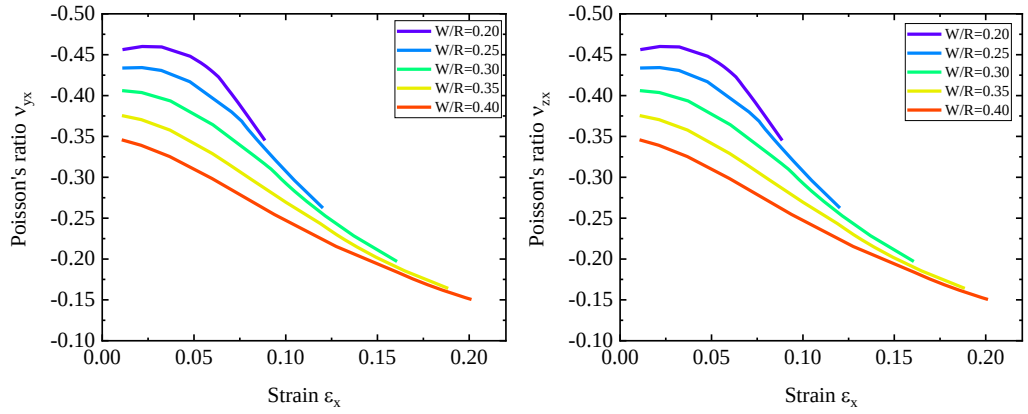

(c) (d)

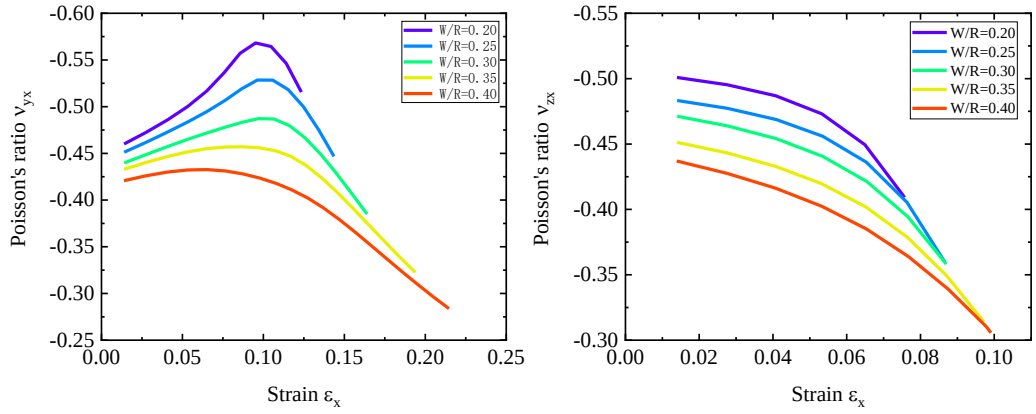

(e) (f)

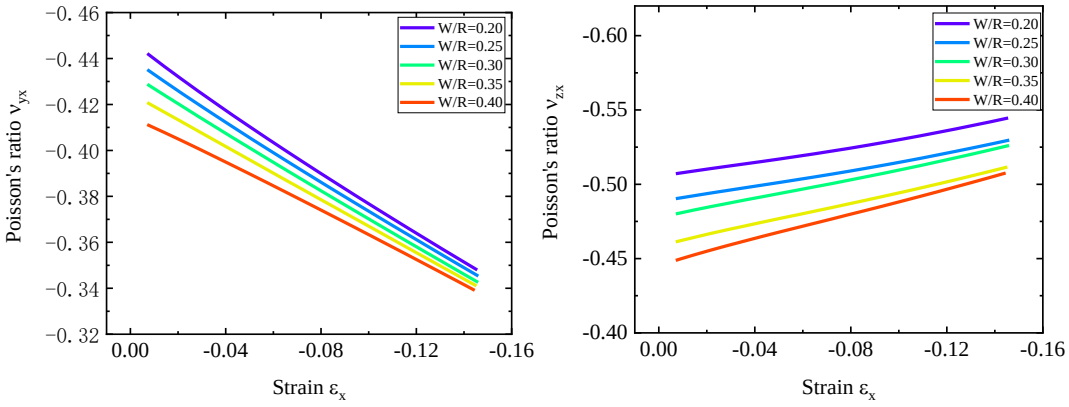

Fig.10. Poisson's ratio-strain curves of the cell-structures with different *W/R*. (a) the chiral model under tensile loading in Y direction. (b) the chiral model under tensile loading in Z direction. (c) the antichiral model under tensile loading in Y direction. (d) the antichiral model under tensile loading in Z direction. (e) the antichiral model under compressive loading in Y direction. (f) the antichiral model under compressive loading in Z direction.

3 EXPERIMENTAL VERIFICATION

In order to experimentally verify the Poisson's ratio data by the finite element method, the 4×4×4 chiral and antichiral models are chosen as the experimental models, in which *R*, *r*, *L*/*R* and *W*/*R* are 10mm, 5mm, 2.5 and 0.4, respectively. The experimental specimens are manufactured by 3D printing technonlogy with the UV Curable Resin as the base material, in which the elastic modulus, Poisson's ratio and density are 2680Mpa, 0.43 and 1.15g/cm^3, respectively. In order to make the displacements of the connecting rods under loading to be the same in the experiment, the chiral and antichiral specimens under tensile loading are connected to two rectangular plates at the two ends in the loading direction, and two clamping parts are connected to these plates, as shown in Fig. 11a-b. As for the antichiral model under compressive loading, two rigid plates are placed at two ends in the loading direction, as shown in Fig. 11c.

(a) (b)

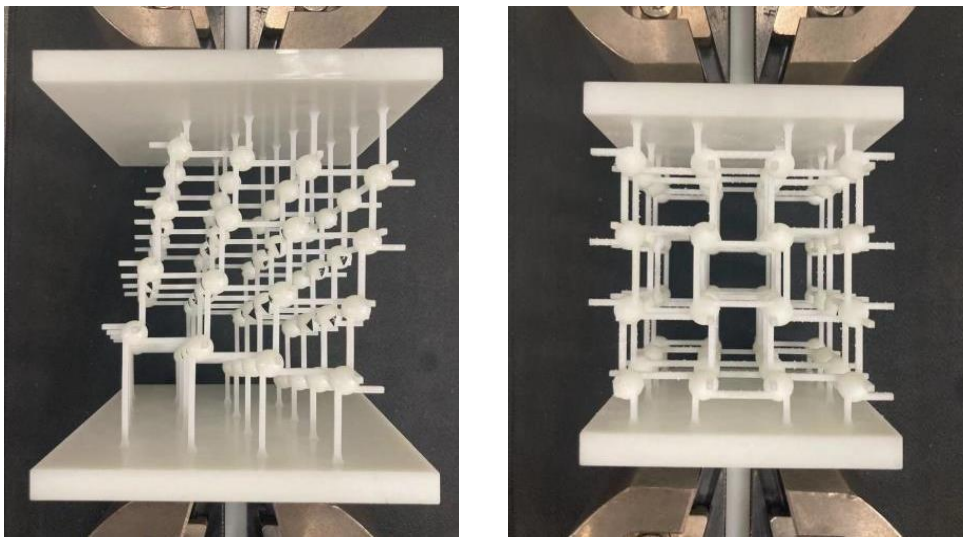

(c)

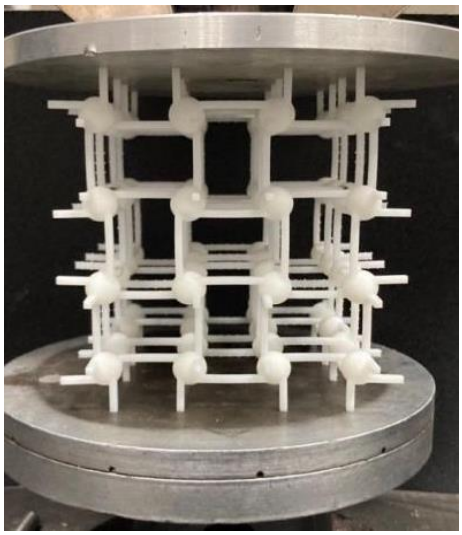

Fig. 11. The experimental specimens. (a) the chiral model under tensile loading. (b) the antichiral model under tensile loading. (c) the antichiral model under compressive loading.

The experiments for the 3D chiral model are carried out by using Universal Testing Machine. The four measuring points of the chiral and antichiral specimens are marked out. The strain of the specimens in the two directions perpendicular to the loading one can be calculated by measuring the distance of the four points with different displacement conditions, and the data can be utilized to calculate the Poisson's ratios of the specimens.

The deformation of the specimens and the finite element models is shown in Fig. 13. The bending of the connecting rods of two models is almost the same, which proves that the finite

element method is a reliable way to predict the deformation of the 3D chiral cell-structure.

(a)

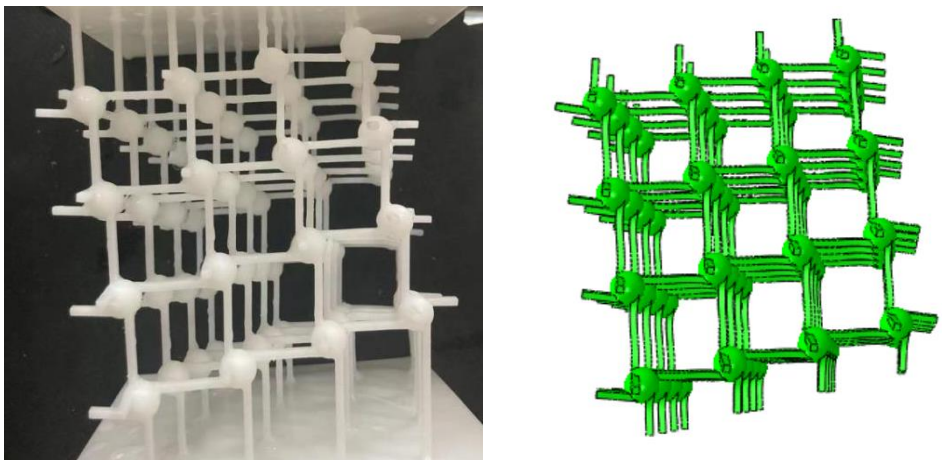

(b)

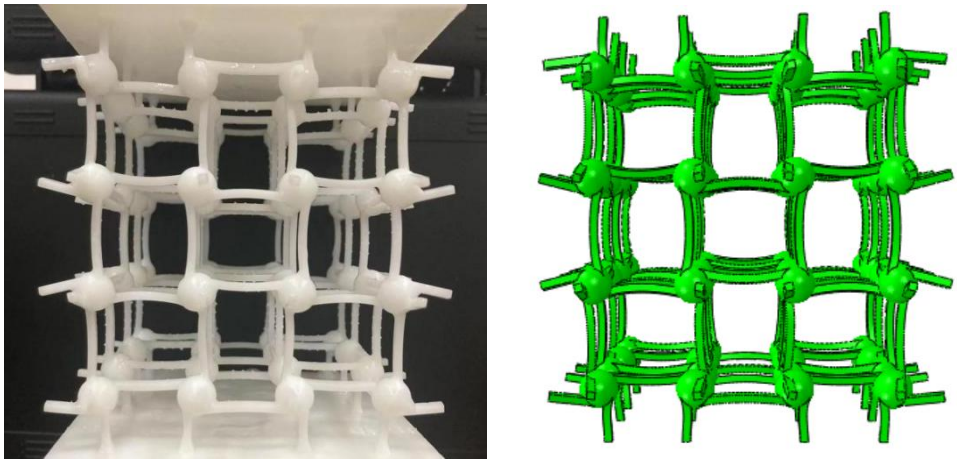

(c)

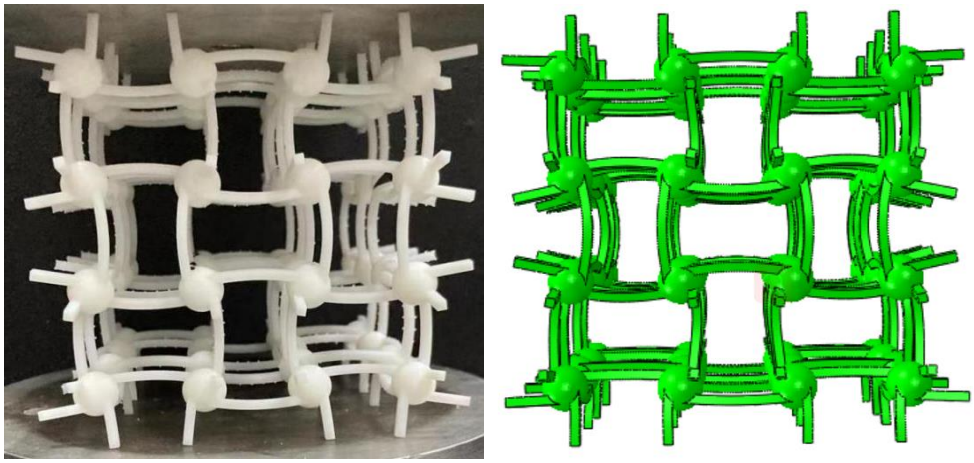

Fig. 13. The deformation of the specimens and the finite element models. (a)the chiral model under tensile loading. (b)the antichiral model under tensile loading. (c)the antichiral model under compressive loading.

4 CONCLUSION

In this paper, a 3D six-link chiral structure with negative Poisson's ratios is proposed based on a 2D chiral cell-structure. The chiral and antichiral models are obtained from the 3D cell-structure by array and mirror arrangement. The Poisson's ratio-strain curves of these structures are calculated based on the finite element method and experiment.

The influence of the geometric parameters and cell-structure numbers on the Poisson's ratios of the 3D chiral and antichiral models is investigated by the finite element method. It turns out that the chiral models have same Poisson's ratios in Y and Z directions, which can verify the results by the theoretical model. The antichiral models have different Poisson's ratios in Y and Z directions. The chiral models only possess negative Poisson's ratios under tensile loading, while the antichiral models possess negative Poisson's ratios under both tensile and compressive loading. The experimental specimens of the chiral and antichiral models are manufactured by 3D printing, and the experimental results verify the validity of the finite element method. The 3D chiral metamaterial with auxetic properties has potential applications in noise absorption and construction industry.

REFERENCES

1. R. S. Lakes, Design Considerations for Materials with Negative Poisson's Ratios[J]. Journal of Mechanical Design, 115(4): 696-700,1993.
2. C. A. Lira, A Gradient Cellular Core for Aeroengine Fan Blades Based on Auxetic Configurations[J]. Journal of Intelligent Material Systems and Structures, 22(9): 907-917, 2011.
3. E. K. Evans . Auxetic polymers[J]. Membrane Technology, 2001(137): 9, 2001.
4. A. Love . A Treatise on the Mathematical Theory of Elasticity[J]. Nature, 105(2643), 1920.
5. R. S. Lakes. Foam Structures with a Negative Poisson's Ratio[J]. Science (New York, N.Y.), 235(4792): 1038-1040, 1987 .
6. G. J. Lorna , F. Michael . Cellular solids: Structure and properties[J]. Pergamon, 1988: 358, 1988.
7. R. S. Lakes, Deformation mechanisms in negative Poisson's ratio materials: structural aspects[J]. Journal of Materials Science, 26(9): 2287-2292, 1991.
8. A. Alderson , K. E.Evans, Rotation and dilation deformation mechanisms for auxetic behaviour in the α-cristobalite tetrahedral framework structure[J]. Physics and chemistry of minerals, 28(10):711-718, 2001.
9. N. Joseph, R. G. Grima, Perforated Sheets Exhibiting Negative Poisson's Ratios[J]. Advanced Engineering Materials, 12(6): 460-464, 2010.
10. C. S. Ha , M. Plesha , R. S. Lakes, Chiral three-dimensional lattices with tunable Poisson's ratio[J]. Smart Materials and Structures, 25(5)：054005, 2016.
11. Z. X. Lu , Q. S. Wang , X. Li , Z. Y. Yang, Elastic properties of two novel auxetic 3D cellular structures[J]. International Journal of Solids and Structures, 124：46-56, 2017.
12. M. H. Fu , F. M. Liu , L. L. Hu, A novel category of 3D chiral material with negative Poisson's ratio[J]. Composites Science and Technology, 160: 111-118, 2018.

Compressive characteristics of 3D-printed continuous fiber-reinforced auxetic structures with different Poisson's ratios

X. Zhang[1,2,3], X.T. Zheng[1,2], L.Y. Song[1,2], Y.Y. Tian[4,5], D. Zhang[6], L.L. Yan[1,2]*

[1]School of Aeronautics, Northwestern Polytechnical University, Xian 710072, China

[2]Institute of Aircraft Composite Structures (ACOS), Northwestern Polytechnical University, Xian 710072, China

[3]School of Materials Science and Engineering, Nanyang Technological University, Singapore 639798, Singapore

[4] State Key Laboratory of Advanced Design and Manufacturing for Vehicle Body, Hunan University, Changsha, Hunan 410082, China

[5] School of Mechanical and Aerospace Engineering, Nanyang Technological University, 50 Nanyang Avenue, 639798, Singapore

[6]School of Mechanical, Engineering, Xi'an Jiaotong University, Xi'an 710049, China

Abstract: Continuous fiber-reinforced (CFR) 3D printing technology is one of the youngest and most promising composite fabrication process. It can meet the booming demands of the lightweight design and structural diversity in advanced transportation industries. In the present work, the CFR 3D printing is introduced to design and manufacture auxetic structures with different Poisson's ratios. The compressive performances of four types of auxetic composite structures were tested and characterized for compressive performances under the quasi-static condition and the deformation processes were also investigated. The failure mechanisms were comprehended through the capture of compression processes and the observation of fracture microstructure. Finite element models were established to further comprehend the failure mechanisms. The results reveal that the bend-induced damage, including four levels that evolving from whitish of resins to complete breakages of fibers, is the main failure mechanism of CFR 3D-pringting auxetic structures. This research paves the way for the practical engineering applications of 3D-printed auxetic structures of composite materials reinforced by continuous fibers.

1. INTRODUCTION

Auxetic structures with excellent mechanical properties, including high effective elastic modulus, high specific energy absorption (SEA) and negative Poisson's ratio, are more widely

† E-mail address: yanleilei@nwpu.edu.cn (Yan L.)

used in many fields such as advanced traffic transportations, actuators, hydrophones [1]. Generally, these auxetic structures are designed and fabricated based on homogeneous materials such as polymers and metals. With the innovative development of 3D printing of continuous carbon fiber reinforced composites, it is possible to take full the significant advantages of carbon fibers with high stiffness and strength-to-weight ratios by combining with polymers [2].

Variations of Poisson's ratio, which are caused by different structural design and geometry parameters, have led to significant changes of deformation processes and failure mechanisms during compression processes. Recently, for 3D-printing auxetic structures, most of current studies about compressive deformations and failure modes are focused on the polymers or metal materials. Under static and impact loads, Yang et al [3] compared compressive characteristics of 3D-printed auxetic structures made of polylactic acid (PLA) and thermoplastic polyurethane (TPU) materials. The results show that the deformation patterns could either stay constant or change with the force depending on the level of applied loads and the materials used. Through experimental and numerical studies, Alomarah et al [4] examined the compressive properties of re-entrant chiral auxetic (RCA) and three auxetic structures. It is noted that the RCA structure exhibited larger stress than other honeycomb auxetic structures, due to the lateral contraction came mainly from the inward movement of the inclined walls and rotation of cylinders. Najafi et al [5] discussed about the energy absorption capacity and failure mechanisms of 3D-printing auxetic structures, including re-entrant, arrowhead and anti-tetra chiral, in both static and impact loading conditions. The layer-wise pattern of collapse contributes to the larger the peak force for re-entrant structure than other two structures. While the deformation and failure mechanisms of auxetic structures have been demonstrated in many isotropic materials, the relative researches of anisotropic composite materials with negative Poisson’s ratio, especially continuous fiber-reinforced (CFR) 3D-printed materials, are still limited.

As one of the youngest manufacturing technologies of composites materials, CFR 3D printing has received considerable attention since Van et al [6] proposed it at 2016. It has been proved that embedding continuous fibers could significantly enhance the mechanical proprieties [7-9]. Previous work of CFR 3D-printed auxetic structures focused primarily on the designing of geometry and investigations of elastic properties. Chen et al [10] proposed an integrated design method with 3D printing with continuous carbon fibers to endow a base polymer for unique mechanical properties. Quan et al [11] combining continuous fibers and PLA matrixes by fused deposition modelling (FDM) to fabricate auxetic honeycomb structures. Results show that even the addition of continuous is relatively low (6%), the increase of compressive stiffness and energy absorption could reach 86.3% and 100%, respectively. Existing research has led to design of auxetic structures and investigation of their compressive properties. However, there has been little research regarding deformation processes and failure mechanisms of CFR 3D-printing auxetic structures, which were heavily influenced by the variation of Poisson's ratio.

In this study, continuous fiber-reinforced 3D printing technology is introduced to design and manufacture the auxetic structures with different Poisson's ratios. By quasi-static compression testing, four types of CFR 3D-printing auxetic composite structures are investigated. Deformation processes and failure mechanisms were analyzed experimentally.

The observations of fracture microstructure and finite element analysis are further performed to comprehend the failure mechanisms. Moreover, the effects of negative Poisson's ratio on mechanical proprieties and energy absorption are investigated.

2. MATERIALS AND METHODS

The process of 3D printing is depicted in Figure 1 (a). By adopting fused deposition Modelling (FDM) process, the PLA filaments with 1.75mm in diameter and the reinforcing fiber filaments, carbon fiber bundles (equivalent to T300-1K with linear density of 66 tex) were in-site extruded. Carbon fibers are coated with resins in a hot tank, meanwhile the prepreg process is completed as well. Then, the semifluid thermoplastic composite materials are extruded from the nozzle tip and adhere to the platform or former layers. As shown in Figure 1(b), a COMBAT-200 desktop 3D printer (based on a commercial platform, Shaanxi Fibertech Technology Development Co., Ltd.) was introduced to manufacture specimens of the 3D-printed CFR auxetic structures. Correspondingly, the parameters of 3D printing are listed in Table 1.

Table 1. The parameters of 3D printing

Parameter	Value
Nozzle temperature	220 ℃
Platform temperature	60 ℃
Printing speed	170 mm/min
Hatch space	2 mm
Layer thickness	0.4 mm
Total number of layers	40

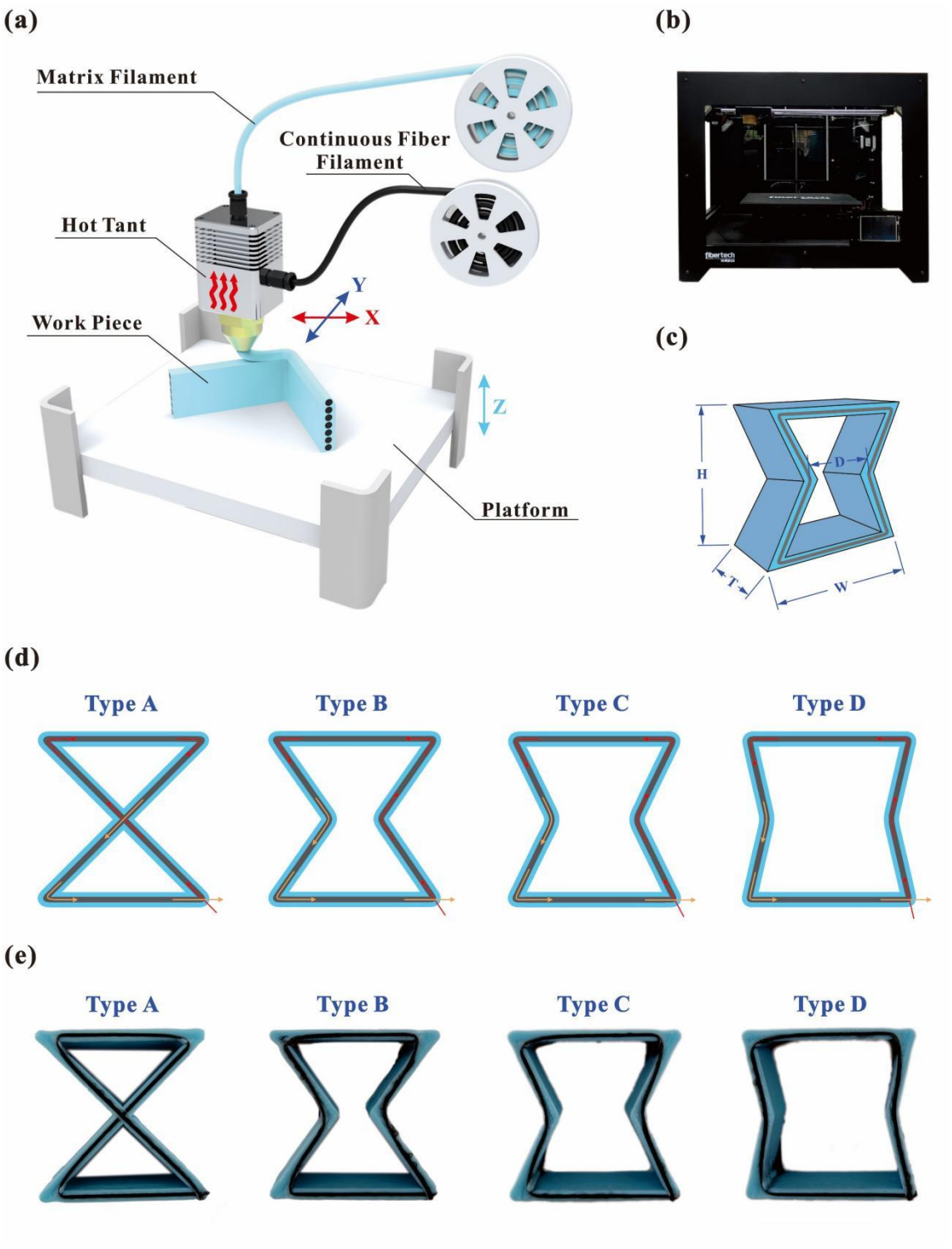

Figure.1 Schematics of 3D printing process and geometry parameters of the auxetic structures: (a) illustration of 3D printer and the extrusion process; (b) the COMBAT-200 desktop 3D printer; (c) the geometry parameters; (d) the printing paths; (e) the snapshots of fabricated structures.

The structural parameters of auxetic structures are listed in Table 2 and simultaneously shown in Figure 1 (c), in which H, W, T and D denotes the height, the weight, the thickness and the distance between re-entrant points, respectively. Besides, 3D printing paths and snapshots of these structures are correspondingly demonstrated in Figure1 (d)&(e). Taking into

account the size of the platform and the printing efficiency, there were two auxetic structures printed at one process. Although the negative Poisson's ratio (υ) is constantly changing in experiments, here, we still take the Poisson's ratio at the initial moment as the index of design and the benchmark of experiments. For the auxetic structures, when the time $t = t_0$, their Poisson's ratio (υ_0) were listed in Table 2. It should be noted that the Poisson's ratio is defined for an infinite structure composed of basic structural units (Type A to D).

Table 2. Parameters of CFR 3D-printed auxetic structures

Type	H /mm	W /mm	T /mm	D /mm	υ_0
A	32	32	16	0	0.000
B	32	32	16	7.5	-0.766
C	32	32	16	15	-0.531
D	32	32	16	22.5	-0.297

Compression tests were performed following a mode of the quasi-static process (2mm/min). The experimental setups including a loading cell and two disc-shaped clamps. The diameter of these clamps is 100 mm. The tests were conducted by an electronic universal testing machine (UTM8104 from Shenzhen Suns Technology Co., Ltd.) with a 10 kN load cell. In addition, a 4K camera (IMX686 from Sony Corporation Co., Ltd.) was introduced to capture the deformation process at a 3.33Hz frequency. After the compression, the morphology of fractures was photograph by an optical microscope with 3 million pixels (IMX766 from Sony Corporation Co., Ltd.). Four specimens were performed for each type of structures, so the total number of samples is 4×4=16.

To qualitatively demonstrate the pulling-out process of a bundle of fibers, the printed specimens were modelled by CPS4R shell element in Abaqus 6.14, and cohesive element (COH2D4) was employed to characterize the interface between fibers and resins. Figure 2 illustrate geometric parameters of the finite element model. And corresponding loads and boundary conditions are shown in Figure 3, of which the left end of the model is fixed, while the right end is subjected to displacement boundary conditions.

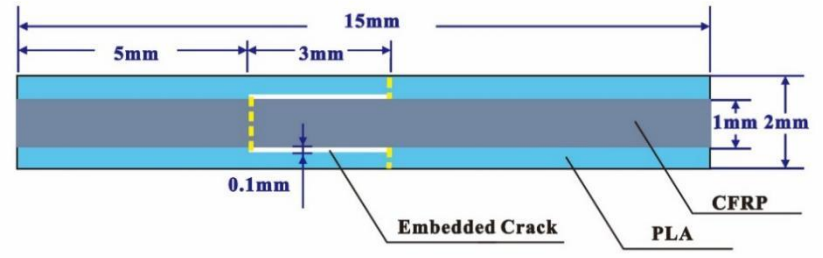

Figure 2. The geometric configuration and parameters of the finite element model

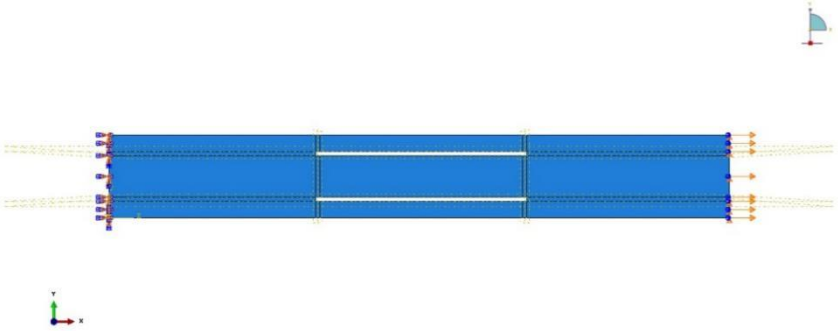

Figure 3. Loads and boundary conditions of the finite element model

3. RESULTS AND DISCUSSION

Compressive characteristics of auxetic structures (Type A, υ_0= 0) are presented in Figure 4. The type-A structures are statically and determinate structures, which consists of two closed chambers. Correspondingly, as shown in Figure 4(a), the stress-strain relationship consists of two relatively similar stages. For the first stage, the structure undergone beam buckling under compressive loading at the strain of 0.026 (Figure 4 (d)). Then, the stress rises rapidly to 4.16MPa at the strain of 0.047, where the first breakage happened. This breakage is a kind of tensile-induced damage of links as schemed in Figure 4(e), of which the directions of loads are parallel to lay-up of fibers. Originally, cracks initiated from delamination between fiber-PLA interfaces. With the increase of the strain, the cracks extended until the fibers are pulled out. At this point, the link broken, causing a rapid drop in stress and then enter the first platform of stress (ε = 0.064). Figure 4(f) shows the corresponding damage mechanisms (bend-induced) during this platform. Due to the fractures of the link, the structure transformed into a non-statically and indeterminate structure. Under the compressive loads, the beams experienced bending moments and gradually expanded (rotated around the central intersection). After the beams was fully expanded and perpendicular to the direction of the loads, it means that the closed cell had failed completely. At this densification point (ε = 0.345), the structure was densified when the energy absorption efficiency reached its first maximal value. Noted that the first stage ended and the second stage begun here.The deformation processes and failure mechanisms of the second stage are similar to those of the first stage. However, as presented in Figure 4(b)&(c), the structures exhibited stiffness softening (129.5 to 107.3 MPa) and a decrease in SEA (0.668 to 0.475 $J \cdot g^{-1}$).

Compressive characteristics of auxetic structures (Type B, υ_0 = -0.766) are presented in Figure 5. The type-B structures are un-statically and indeterminate structure and they are also symmetrical. Correspondingly, as shown in Figure 5(a), the stress-strain relationship consists of two stair-step stage. For the first stage, the structure experienced linear process and entered the first platform at a strain of 0.036. Because of the degrees of freedom, the structural deformation mode was that the central points gradually approached each other. During this stage, the stress tardily reached its first peak of 0.718 MPa (ε = 0.078), and undergone the first breakage (ε = 0.120). Then the stress had a sudden drop and then the platform stress was significantly lower. When the central points touched (ε = 0.078), there was a sudden rise of stiffness, meaning that the first stage was ended. At this time, the structure transformed to a statically and determinate structure, so the stress could continue to climb. After the linear

process, the structure bulked at a strain of 0.238. Then, it reached the second maximum stress of 2.080 MPa at a strain of 0.248. It is noted that the structure transformed at a strain of 0.278 when the central points were staggered and gradually separated. It means that the structure regained the degrees of freedom after convert to a zigzag configuration, followed by a sudden drop of stress. Finally, the structure was densified at a strain of 0.441. Although Type-B auxetic structures also have two stage, they are observably different in the amplitude level of stress. As shown in Figure 5(b)&(c) shows, the structure exhibited stiffness hardening (15.8 to 19.3 MPa) and an increase of SEA (0.225 to 0.599 $J \cdot g^{-1}$).

As for the failure mechanisms, the bend-induced damage was dominated because of the rotation of beams during transformation processes. Figure 5 (e)&(f) scheme the mechanisms of two kind of bend-induced damage. For the bend between one beam and another beam (Figure 5 (e)), they both have degrees of freedom to rotate. But for the bend between a beam and a link (Figure 5(f)), the rotation was mainly experienced by the beam due to the link was constrained by clamps. Although the boundary conditions are different, the evolution of cracks are similar for bend-induced damage: On level one, the local surface was damaged because of tensile failure and the crack initiated; On level two, the crack propagated and run through the resin area; On level three, the crack was deep into the fiber area, which cause serious damaged.

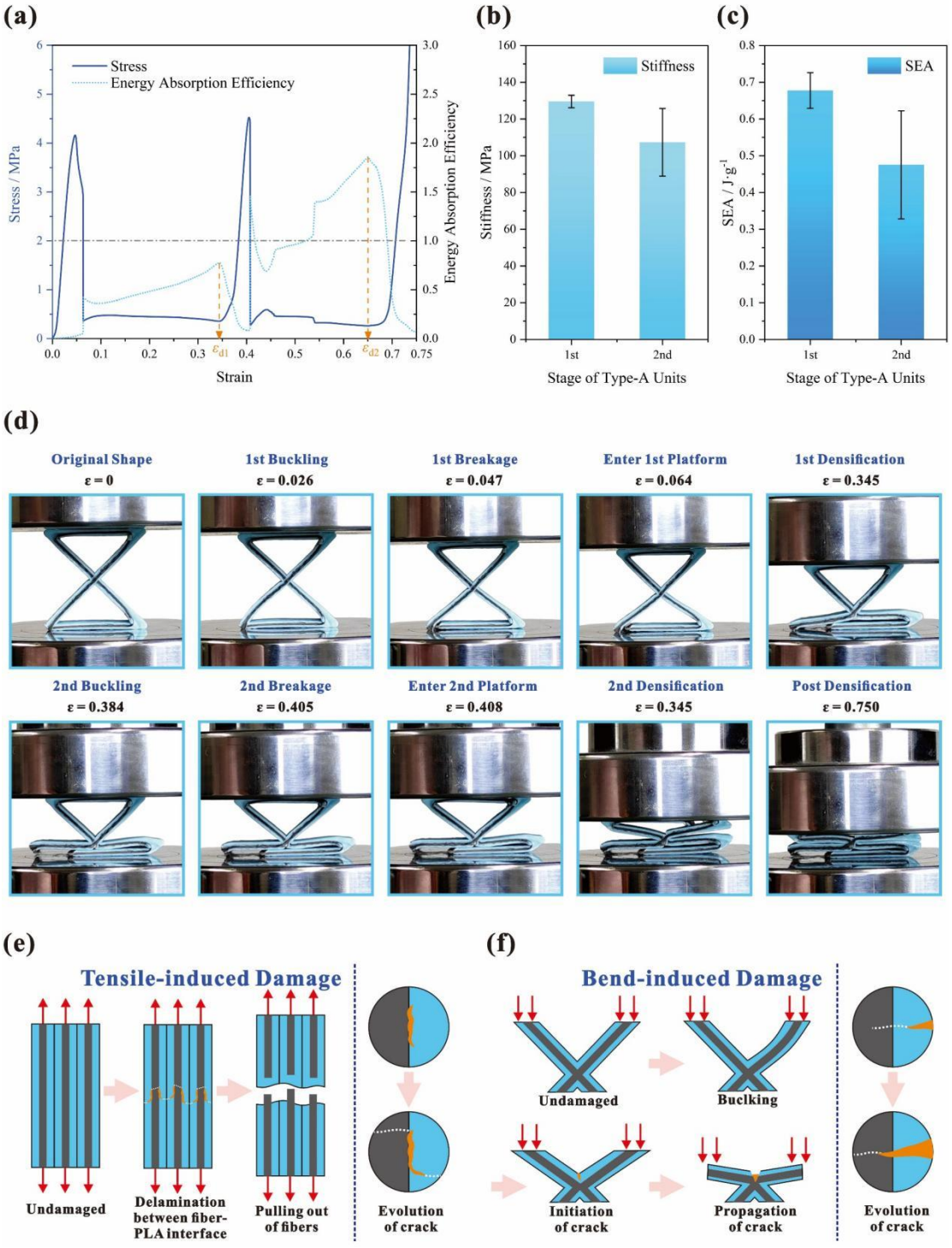

Figure 4. Compressive characteristics of auxetic structures (Type A, υ_0= 0): (a) the stress-strain relationship and the energy absorption efficiency; (b) the stiffness; (c) the SEA; (d) the deformation processes; (e) the schematic representations of the mechanisms of tensile-induced damage; (f) the schematic representations of the mechanisms of bend-induced damage.

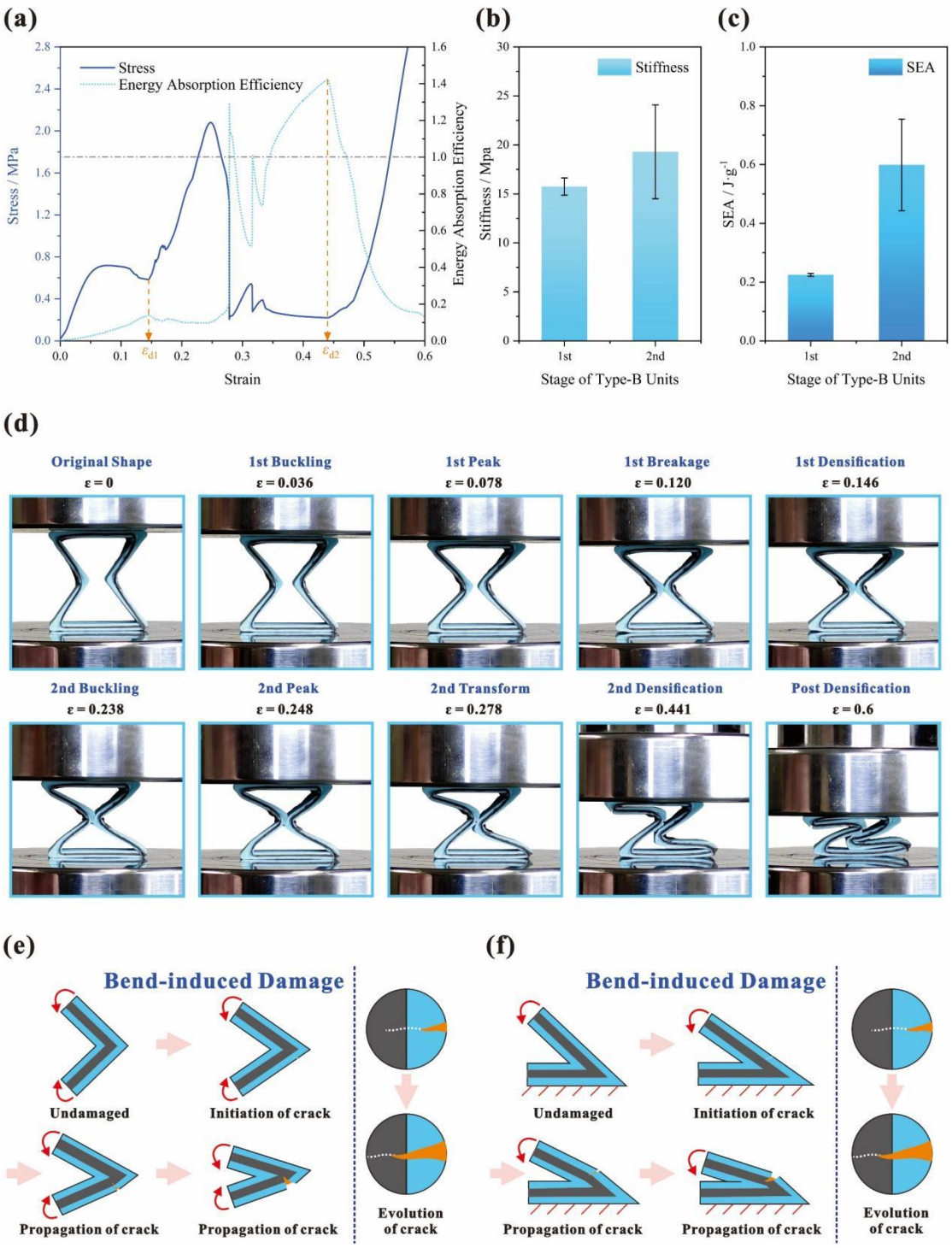

Figure 5. Compressive characteristics of auxetic structures (Type B, υ_0 = -0.766): (a) the stress-strain relationship and the energy absorption efficiency; (b) the stiffness; (c) the SEA; (d) the deformation processes; (e) the schematic representations of the mechanisms of bend-induced damage between beams; (f) the schematic representations of the mechanisms of bend-induced damage between a beam and a link.

Compressive characteristics of auxetic structures (Type C, υ_0 = -0.531) are presented in Figure 6. The type-C structures are un-statically and indeterminate structures that are also symmetrical. Correspondingly, as shown in Figure 6(a), the stress-strain relationship consists of three stage. At the first stage, the Type-C structure also experienced linear process as the Type-B structure, but reached its first peak faster (σ = 1.255, ε = 0.060). Because of the degrees of freedom, the structural deformation mode was that the central points gradually approached each other. However, comparing to type-B structures, the distance between central points of Type-C structures are increased by 7.5mm, indicating that the central points could not contact each other. After the first breakage at a strain of 0.016, the deformation mode was changed from the mutual approaching of the central points in X direction to the oppositely opposite moving in Y direction. Then, the structure was densified (ε = 0.421) while its energy absorption efficiency reached the first peak value. At this time, the structures transformed to a zigzag configuration, which indicates that the first stage ended here. During the second stage, the zigzag configuration was compressed until beams touched each other (ε = 0.542), followed by the second peak stress of 0.683 MPa (ε = 0.469). Then, the structure entered the third stage, of which the peak stress was 4.512 MPa at a strain of 0.645. Finally, the structure was densified (ε = 0.645) after a sudden drop of the stress. The dominated mechanism of Type-C structures was also bend-induced damage. As Figure 6(b)&(c), noted that not only did Type-C structures experienced more stages, but they also absorbed more energy (2.302 $J \cdot g^{-1}$) than Type-A structures (1.171 $J \cdot g^{-1}$) and Type-B (0.825 $J \cdot g^{-1}$) structures. For Type-B structures, there was no complete disconnection (level-four damage) took place. Actually, the damage of level four could happen if the crack extended continuously. As an example, Figure 6 (e) presents the morphology of the Type-C structures that undergone post densification, of which the red boxes highlight fractures of the level-four bend-induced damage.

Compressive characteristics of auxetic structures (Type D, υ_0 = -0.297) are presented in Figure 7. The type-D structures are un-statically and in-determinate structures that are also Symmetrical. Correspondingly, as shown in Figure 7(a), the stress-strain relationship consists of two stage. During the first stage, the Type-D structure buckled at strain of 0.029 and reached the peak of stress (σ = 2.323, ε = 0.060). This deformation mode was the same as Type-B and Type-C structures due to the degrees of freedom. Then, the first breakage happened at the strain of 0.155, where the stress drops drastically. The central points were gradually approaching each other until the structure transformed into zigzag configuration (ε = 0.250). After a stress platform, the structure deified at a strain of 0.372 while the energy absorption efficiency reached it first maximum value. On the basis of the compressed zigzag configuration, the structure entered the second stage and buckled at a strain of 0.410. Comparing to type-B structures, the distance between central points of Type-D structures are increased by 15mm, resulting in a change in deformation modes. As the compressive loads increased, the structure was flatting continuously and eventually was densified (ε = 0.646) after went through the second buckling (ε = 0.410) and the peak of stress (σ = 0.985, ε = 0.417).

As shown in Figure 7 (b)&(c), for Type-D structures, both the stiffness and the SEA of the second stage are significantly lower than the first stage. Although bend-induced damage still dominated, there was no level-four damage was observed. This also explains that the SEA of the Type-D structures (1.411 $J \cdot g^{-1}$) is also lower than that of the Type-B structures (2.302 $J \cdot g^{-1}$).

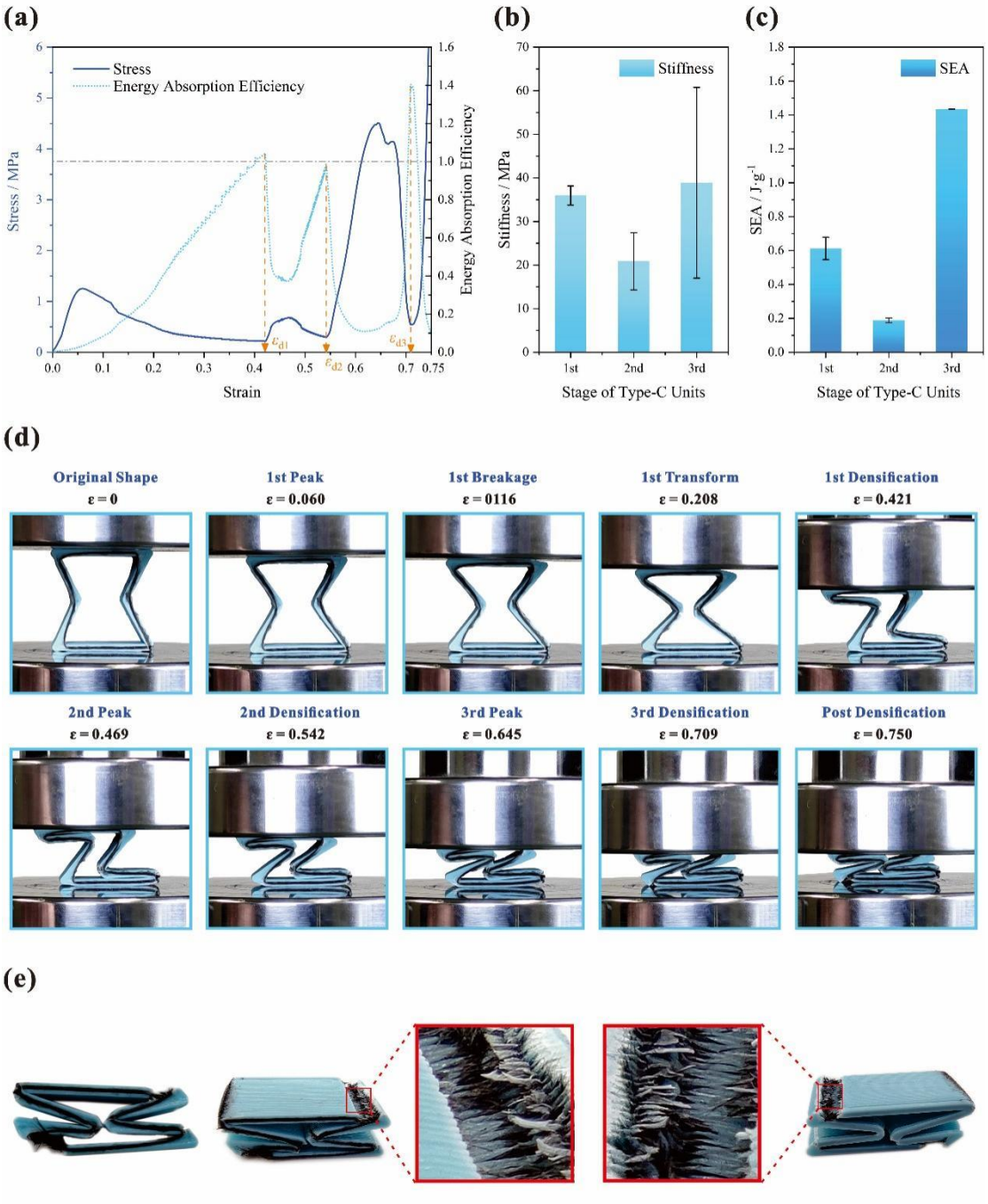

Figure 6. Compressive characteristics of auxetic structures (Type C, υ_0 = -0.531): (a) the stress-strain relationship and the energy absorption efficiency; (b) the stiffness; (c) the SEA; (d) the deformation processes; (e) the morphology of post-densified structures.

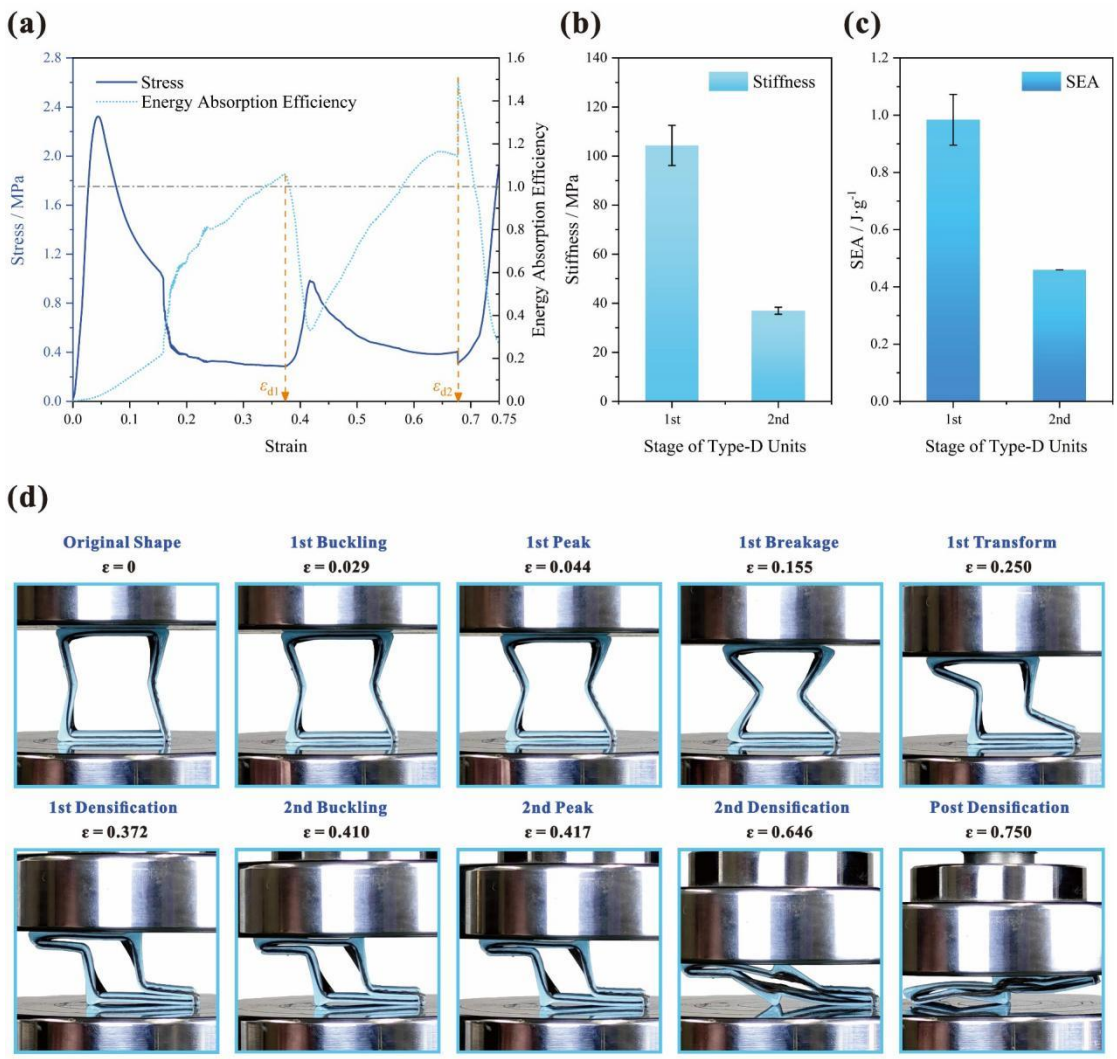

Figure 7. Compressive characteristics of auxetic structures (Type D, υ_0 = -0.297): (a) the strain-stress relationship and the energy absorption efficiency; (b) the stiffness; (c) the strength; (d) the deformation processes.

To further illustrate the Poisson's ratio effect, the variations of stiffness, strength and SEA were summarized and presented in Figure 8. Obviously, both strength and stiffness increase with the rise of the Poisson's ratio (Figure 8. (a)&(b)). The reason is that the central points are closer when the Poisson's ratio is larger, allowing for faster contacting to form closed cells. Comparing with structures with degrees of freedom, the statically and determinate structures (closed cells) have more capabilities to withstand compressive loads. However, as presented in Figure 8 (c), the variation of SEA with the Poisson's ratio is not monotonic. When υ_0 = -0.531 (Type-C), the SEA reaches its maximum value. This is because the Type-C structures have undergone larger deformation and bear higher load than other structures before densification, and the appropriate transformed configuration provides more opportunities for adequate energy absorption.

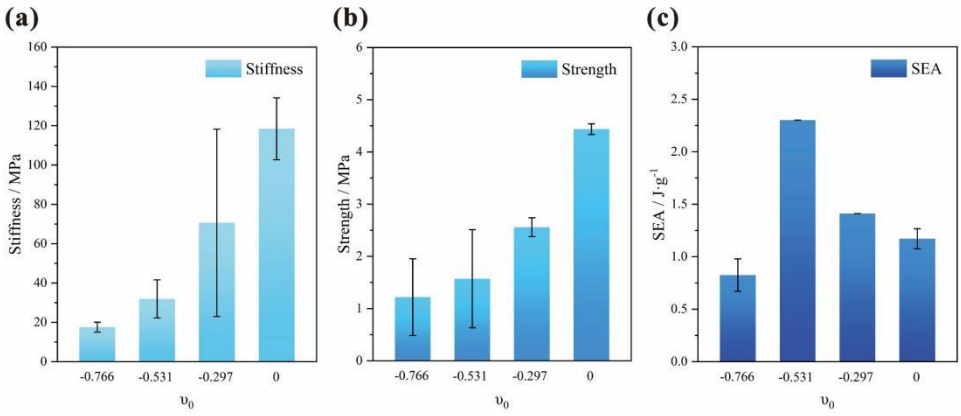

Figure 8. The variation of the stiffness, the strength and the SEA causing by different Poisson's ratio

Figure 9 shows the failure mechanism of the tension-induced damage. It can be seen from both the snapshots and optical microscopic images (Figure 9(a)&(b)) that the fracture morphology of the PLA matrixes was parallel and level with whitish edges. There were no obvious neck retractions, which indicates that the failure mode of the matrix was brittle damage. As for carbon fibers, they were pulling out with little resin residues. It is also verified that poor interfaces are the primary cause of tension-induced damage. As shown in Figure 9(c), the finite element analysis results present the damage evolution of pulling-out process that had not been captured in the previous experiments. Before the breakage (Deplanement U = 0.04mm), significant stress concentrations were generated around the interface damage (embedded cracks). Subsequently, the crack started to propagate in the direction perpendicular to the tensile loads, accompanied by a decrease in the maximum stress. This is consistent with the sudden drop in stress when fracture occurs during compression testing.

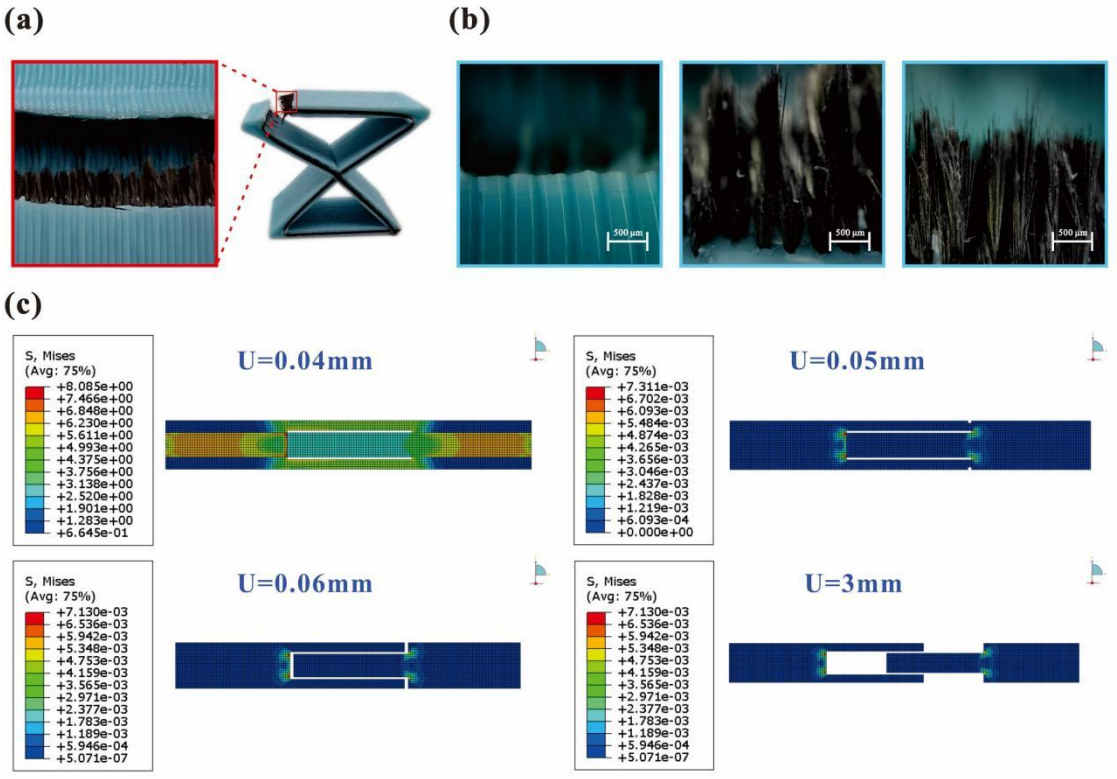

Figure 9. The failure mechanism of the tension-induced damage: (a) snapshots of the compressed Type-A structure (ε = 0.2); (b) optical microscopic images of fracture topography and (c) finite element simulation of the pulling-out process.

Figure 10 illustrates the failure mechanisms of the bend-induced damage that including four levels of damage degrees. In first level, the damage initiated from the surfaces of PLA matrixes accompanied by the sprouting of tiny white creases. Subsequently, the white creases further evolved into open matrix cracks, which also marked the begin of level-two damage. The opening expanded further as the compression proceeds, reaching a level-three damage, of which the breakages of fibers firstly occurred. Eventually, the fibers are completely severed (level-four damage) with serrated fractures. Moreover, a certain number of resins remained on the broken fibers, indicating that the poor interface is not the main cause of the bend-induced damage.

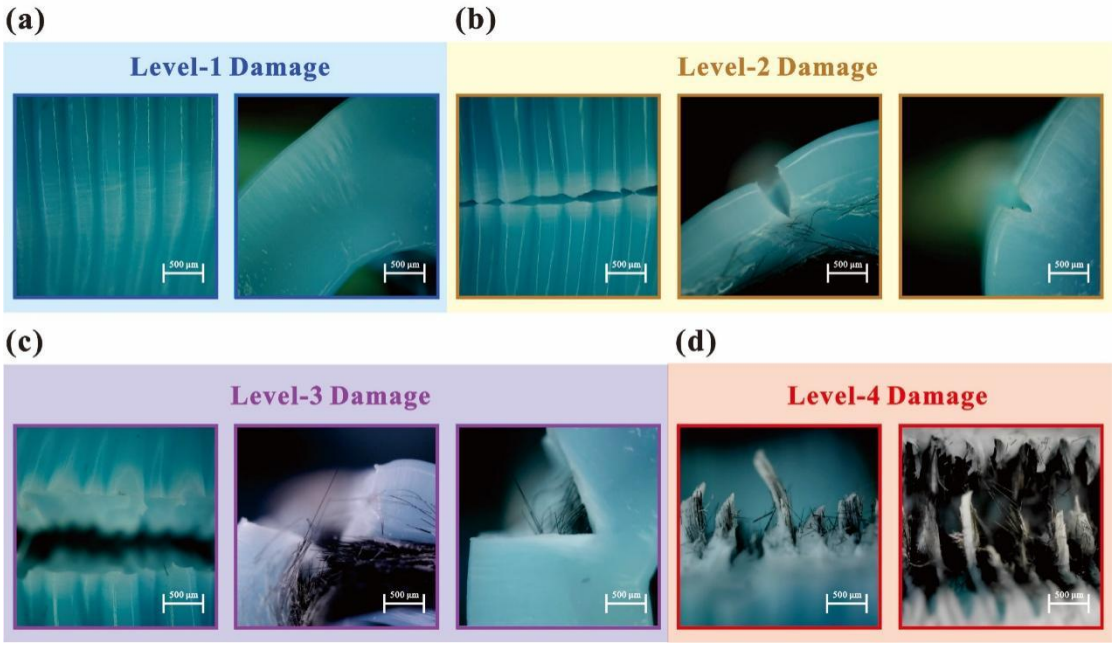

Figure 10. The failure mechanism of the bend-induced damage: optical microscopic images of fracture topography

4. CONCLUSION

In this work, we combine experiments and finite element analysis to investigate the compressive properties of 3D-printed continuous fiber-reinforced auxetic structures with different Poisson's ratios (Type A, B, C and D auxetic structures). The following conclusions can be drawn:

1. The strength and stiffness of the continuous fiber-reinforced auxetic structure present a monotonous rise with the increase of the tailored Poisson's ratio from -0.766 to 0 via varying the geometric parameters of the auxetic structures;
2. Poisson's ratio affects the deformation process by controlling the minimum distance of the central during compression, which determines whether the transformed configuration is a statically and determinate structure or not;
3. Poisson's ratios do affect the failure mechanism. When the Poisson's ratio is 0 (Type A), the failure mode is mainly tension-induced damage, which is caused by interfacial debonding;

With the negative Poisson's ratio, bend-induced damage dominates;

4. The present work reveal that the transformed configuration of continuous fiber-reinforced auxetic structure during compression is beneficial to improve energy absorption capacity. The design of this structure should focus on the effectively controlling the transformed configurations so that bear high load continually before fracture for 3D-printed continuous fiber-reinforced structures.

ACKNOWLEDGMENT

The full content of the paper was supported by the Aeronautical Science Foundation of China (201909053001), Fundamental Research Funds for the Central Universities (D5000220029), National Natural Science Foundation of China (11702326), Fundamental Research Funds for the Central Universities (G2019KY05106) and the State Scholarship Fund of China Scholarship Council (202006290188).

REFERENCES

1. Surjadi J U, Gao L, Du H, et al. Mechanical metamaterials and their engineering applications[J]. *Advanced Engineering Materials*, 2019, 21(3): 1800864.
2. Heidari-Rarani M, Rafiee-Afarani M, Zahedi A M. Mechanical characterization of FDM 3D printing of continuous carbon fiber reinforced PLA composites[J]. *Composites Part B: Engineering*, 2019, 175: 107147.
3. Yang C, Vora H D, Chang Y. Behavior of auxetic structures under compression and impact forces[J]. *Smart Materials and Structures*, 2018, 27(2): 025012.
4. Alomarah A, Masood S H, Sbarski I, et al. Compressive properties of 3D printed auxetic structures: experimental and numerical studies[J]. *Virtual and Physical Prototyping*, 2020, 15(1): 1-21.
5. Najafi M, Ahmadi H, Liaghat G. Experimental investigation on energy absorption of auxetic structures[J]. *Materials today: proceedings*, 2021, 34: 350-355.
6. Van Der Klift F, Koga Y, Todoroki A, et al. 3D printing of continuous carbon fibre reinforced thermo-plastic (CFRTP) tensile test specimens[J]. *Open Journal of Composite Materials*, 2016, 6(01): 18.
7. Heidari-Rarani M, Rafiee-Afarani M, Zahedi A M. Mechanical characterization of FDM 3D printing of continuous carbon fiber reinforced PLA composites[J]. *Composites Part B: Engineering*, 2019, 175: 107147.
8. Pyl L, Kalteremidou K A, Van Hemelrijck D. Exploration of the design freedom of 3D printed continuous fibre-reinforced polymers in open-hole tensile strength tests[J]. *Composites Science and Technology*, 2019, 171: 135-151.
9. Zhang Y, Qiao J, Zhang G, et al. Prediction of deformation and failure behavior of continuous fiber reinforced composite fabricated by additive manufacturing[J]. *Composite Structures*, 2021, 265: 113738.
10. Chen Y, Ye L. Designing and tailoring effective elastic modulus and negative Poisson's ratio with continuous carbon fibres using 3D printing[J]. *Composites Part A: Applied Science and Manufacturing*, 2021, 150: 106625.
11. Quan C, Han B, Hou Z, et al. 3d printed continuous fiber reinforced composite auxetic honeycomb structures[J]. *Composites Part B: Engineering*, 2020, 187: 107858.

Three-dimensional progressive damage analysis of the tightening process of composite bolted joints considering the real thread structure

*Qingyuan Lin [a, b], Yong Zhao [a, b, *], Yuming Liu [a, b]*

[a] State Key Laboratory of Mechanical System and Vibration, School of Mechanical Engineering，Shanghai Jiao Tong University

[b] Shanghai Key Laboratory of Digital Manufacture for Thin-walled Structures, School of Mechanical Engineering，Shanghai Jiao Tong University

Abstract: Bolted joints are the dominant connection method in assembling composite structures. Assembly quality of the bolted joint has an important effect on the mechanical properties of the whole composite structure. To investigate the stress, deformation and failure mechanism of composite bolted joints during the process of assembly, a three-dimensional progressive damage model for the real assembly process of composite bolted joints was developed and implemented using the subroutine VUMAT in Abaqus. This model takes into account the real thread structure in the composite bolted joint and simulates the real assembly process by tightening the nut during the calculation. In this model, the friction behavior of the thread contact surface is simulated by the penalty function, and the damage evolution analysis of the intra-face is realized based on the Hashin criterion. At the same time, the interface properties are characterized by cohesive model. The stress and strain field of composite bolted joint in the real assembly process was obtained by this method. The analysis results show that with the continuous of the tightening process, various damage modes will occur, including matrix compression damage, matrix tensile damage and interface damage. Among them, interface damage is the key damage type in the assembly process of composite bolted joints. The stress-strain field and damage obtained by this method can provide accurate initial state for subsequent analysis of the composite bolted joint.

Keywords: Composite bolted joints; Tightening process; 3D progressive damage analysis; Torque-bolt tension relationship; Non-linear pressure distribution; Initial assembly damage

1. Introduction

With excellent properties such as high strength-to-weight ratio, stiffness-to-weight ratio,

fracture toughness and corrosion resistance, carbon fiber reinforced polymer (CFRP) have been widely used in aeronautics, aerospace, marine, automobile and other areas in the past decades [1]. Bolted joints are widely used in various connection scenarios for composite structures due to their low cost, simplicity and ease of removal, repair and replacement of parts [2]. Composite bolted joints (CBJ) face more challenges than those in metal structures [3]. The non-linear stress field generated by the helical structure of the thread and the complex material properties of the composite laminates couple together [4]. Stress concentration around the hole edge and the interaction between the linked components reduce the load-bearing capacity of the joints and adversely affect the structural integrity [5]. 60-85 percent of failures occurring at the fastening joint [6].

The influence of the assembly results of CBJ on their subsequent performance has attracted much attention. The bolt tension is one of the crucial influencing factors. First, the bolt tension puts the joint in axial compress state, which enhances the friction. The proper bolt tension is beneficial to delay the damage of the composite laminates [7]. However, excessive bolt tension may produce initial damage and lead to premature joint failure [8–10].

In order to study the effect of bolt tension on the joint performance, numerous methods of varying complexity have been proposed to simulate the assemble state. These methods can be divided into two categories: analytical methods [11] and finite element methods [12–14]. The analysis method is often used for rough calculations in large projects, which require extensive simplification and cannot be used to analyze the complex assembly state of bolted joints. Obtaining the assembly stress distribution state by the finite element simulation method is common method in current research on composite bolted joints [15].

Modeling of fasteners is a key process in the finite element simulation. For large structures containing numerous fasteners, simplified modeling of fasteners is necessary. Several simplified modeling methods for fasteners have been proposed by researchers, including simplified solid fasteners models, connector beam models, spider fasteners models, coupled fasteners models, hybrid fasteners models and no-fasteners models [16]. Detailed models are more common in studies that focus on the local properties of the bolted joint [17]. The detailed model is generated using solid mesh, which can characterize the elastic-plastic and fracture damage of the material and obtain the accurate state of stress, strain and contact force [18]. However, there are still some problems that are difficult to solve.

First, current simulation methods are difficult to accurately predict the relationship between tightening torque and bolt tension during the assembly of composite bolted joints (CBJ). In practical engineering, the bolt tension of CBJ is indirectly controlled by controlling the torque applied to the nut [19]. However, most studies tend to give the value of bolt tension in the theoretical analysis directly without stating its specific source. Surprisingly, the relationship between tightening torque and bolt tension of CBJ has not been closely examined. Information on the simulation methods for predicting this relationship is scarcely available. There are many factors affecting the torque-bolt tension relationship of CBJ, including lubrication conditions, washers, etc. [20]. It is unrealistic to conduct experimental tests on all CBJ [7]. Accurate finite element simulation analysis is an important method to predict the relationship between tightening torque and bolt tension [15]. At the same time, the non-linear distribution state of bolt tension formed after the assembly of CBJ is difficult to accurately obtain. In the current simulation analysis, the distribution law of the bolt tension is usually summarized according to

the test results, and then set in the simulation process. However, the non-linear distribution state is formed by the interaction of bolt, nut, washers and the composite laminates [21]. The consideration of the inhomogeneity of the pressure distribution is insufficient [22]. Simulating the real assembly process is an effective means to get closer to the actual pressure distribution state.

To solve the above problems, this study proposes a three-dimensional progressive damage analysis method for the assembly process of composite bolted joints considering the detailed thread structure. This method can simulate the real assembly process, predict the relationship between tightening torque and bolt tension and obtain the non-linear distribution state of bolt tension after the assembly of composite bolted joint. With the combination of 3D progressive damage analysis method for composite laminates, the initial damage generated during the assembly of composite laminates can be effectively analyzed to provide an accurate initial assembly state for the subsequent analysis.

First, the unique mechanical behavior of bolt joints is caused by the helical structure of the threads. In this study, a program that can automatically build a finite element mesh model of the fastener with a detailed thread structure is developed. The program is highly parametric, and all the user needs to do is to input the structural parameters. Then, the pre-processing method and parameter settings to simulate the real assembly process are introduced in detail. This method enables 3D progressive damage analysis of composite materials while simulating the assembly process. Finally, the assembly process and results of the composite bolted joint are tested by tightening test, pressure distribution test and CT scan to verify the accuracy of the proposed method.

2. Simulation methods

2.1. Finite element modeling for fasteners with detailed thread structure

There are generally two types of methods to obtain a finite element mesh model. The first type is based on the existing solid structure, and the mesh is formed by virtual cutting. This type of method is general, and the mesh quality is relatively bad. The second type is to obtain the coordinates of all nodes and the node numbers of all elements by direct calculation, called mesh stacking. This type of method is more flexible and suitable for parametric mesh modeling of a series of parts with similar shapes. In this study, the mesh stacking method is used to build the fastener finite element mesh model.

Thread is a helical structure essentially. The thread profile lines (TPL) have the same shape and different directions in the profiles at different locations perpendicular to the thread axis direction.

The equation of TPL in the plane polar coordinate system [23] is shown in Eq. (1).

$$r=\begin{cases}\dfrac{d}{2}-\dfrac{7}{8}H+2\rho-\sqrt{\rho^2-\dfrac{P^2\theta^2}{4\pi^2}} & 0\le\theta<\theta_1\\ \dfrac{H}{\pi}\theta+\dfrac{d}{2}-\dfrac{7}{8}H & \theta_1\le\theta<\theta_2\\ \dfrac{d}{2} & \theta_2\le\theta<\pi\end{cases} \quad (3)$$

$$\theta_1=\frac{\sqrt{3}\pi}{P}\rho \qquad \theta_2=\frac{7\pi}{8} \qquad \rho=\frac{\sqrt{3}\pi}{12} \qquad H=\frac{\sqrt{3}}{2}P \quad (4)$$

where r is the polar diameters, θ is the polar angles, d is the nominal diameter of the

thread, and P is the thread pitch.

TPL rises and rotates simultaneously along the thread axis in three-dimensional space. The spatial surface formed is the outer contour surface of the thread structure. The relationship between the rise distance ΔL_{th} and the rotation angle $\Delta\theta_{th}$ is shown in Eq. (3).

$$2\pi \cdot \Delta L_{th} = P \cdot \Delta\theta_{th} \quad (5)$$

As shown in Fig. 1, the density of the mesh model is controlled by the circumferential mesh density coefficient n_c, the radial mesh density coefficient n_r and the axial mesh density coefficient n_P. The number of meshes is controlled by the circumferential mesh number N_c, the radial mesh number N_r and the axial mesh number N_P.

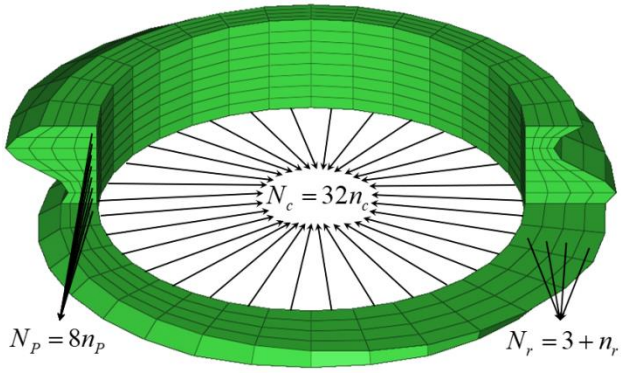

Fig. 1. Mesh model of the thread region

Due to the helical structure and curvature variation, a fine meshing is required in the thread region to ensure computational accuracy. For simple areas such as thread cores and bolt rods, relatively coarse meshing is performed to balance computational accuracy and computational efficiency. As shown in Fig. 2, the transition of the mesh density is performed using the "4-2-1" method in the direction perpendicular to the axis and parallel to the axis simultaneously.

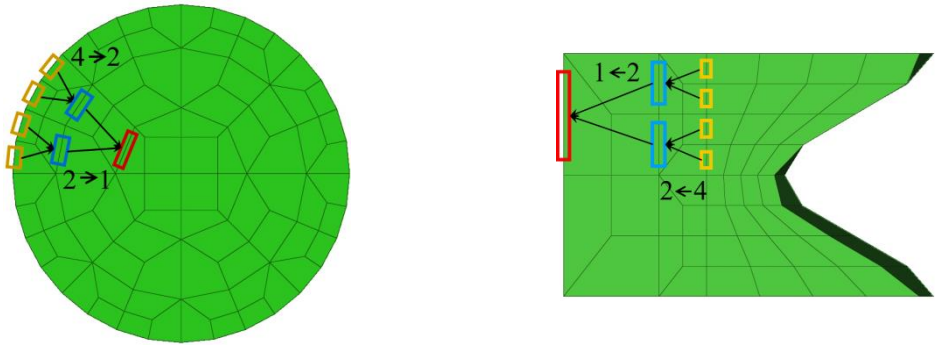

Fig. 2. "4-2-1" method for mesh density transition

For fasteners such as nuts with internal thread structure, the above method is also applicable. Based on the above modeling method, a parametric modeling program was written. The program flow is shown in Fig. 3, and the modeling results are shown in Fig. 4.

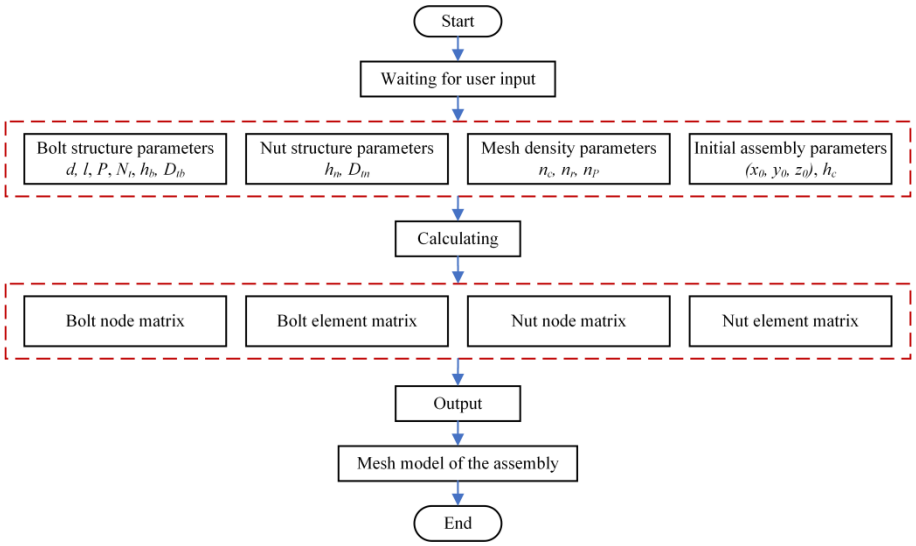

Fig. 3. Flow of the parametric modeling program

where l is the bolt length, N_t is the number of bolt threads, h_b is the bolt head height, D_{tb} is the equivalent diameter of bolt head, h_n is the nut thickness, D_{tn} is the equivalent diameter of nut, (x_0, y_0, z_0) is the initial assembly coordinates, h_c is the clamping thickness of fasteners.

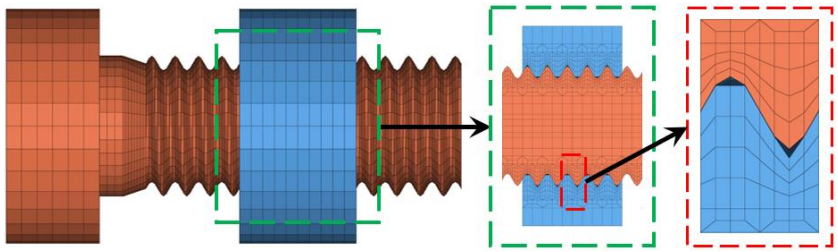

Fig. 4. Fastener mesh models with detailed thread structure

2.2. 3D progressive damage model for composite laminates

2.2.1. Intra-laminar modeling

Continuous carbon fiber reinforced plastics (CFRP) are used as the object of analysis in this study. Characterize the intra-laminar damage behaviors of CFRP using the continuum damage model (CDM) [24].

Judgment of whether damage has occurred based on damage initiation criteria. The progressive damage behaviors are characterized by modifying the stiffness matrix of the material. The stress- strain relationship of orthotropic material is shown below,

$$\begin{bmatrix} \sigma_{11} \\ \sigma_{22} \\ \sigma_{33} \\ \sigma_{12} \\ \sigma_{13} \\ \sigma_{23} \end{bmatrix} = \begin{bmatrix} C_{11} & C_{12} & C_{13} & 0 & 0 & 0 \\ C_{12} & C_{22} & C_{23} & 0 & 0 & 0 \\ C_{13} & C_{23} & C_{33} & 0 & 0 & 0 \\ 0 & 0 & 0 & C_{44} & 0 & 0 \\ 0 & 0 & 0 & 0 & C_{55} & 0 \\ 0 & 0 & 0 & 0 & 0 & C_{66} \end{bmatrix} \begin{bmatrix} \varepsilon_{11} \\ \varepsilon_{22} \\ \varepsilon_{33} \\ \varepsilon_{12} \\ \varepsilon_{13} \\ \varepsilon_{23} \end{bmatrix} \quad (6)$$

where C_{ij} represents the stiffness matrix, linking stress tensor σ_{ij} and ε_{ij}. The value of C_{ij}

is related to the damage state, which can be described by the fiber tension damage variable d_{ft}, fiber compression damage variable d_{fc}, matrix tension damage variable d_{mt} and matrix compression damage variable d_{mc}:

$$
\begin{aligned}
C_{11} &= (1-d_f)E_{11}(1-\nu_{23}\nu_{32})\Delta \\
C_{22} &= (1-d_f)(1-d_{mt})(1-d_{mc})E_{22}(1-\nu_{13}\nu_{31})\Delta \\
C_{33} &= (1-d_f)(1-d_{mt})(1-d_{mc})E_{33}(1-\nu_{12}\nu_{21})\Delta \\
C_{12} &= (1-d_f)(1-d_{mt})(1-d_{mc})E_{11}(\nu_{21}+\nu_{31}\nu_{23})\Delta \\
C_{13} &= (1-d_f)(1-d_{mt})(1-d_{mc})E_{11}(\nu_{31}+\nu_{21}\nu_{32})\Delta \\
C_{23} &= (1-d_f)(1-d_{mt})(1-d_{mc})E_{22}(\nu_{32}+\nu_{12}\nu_{31})\Delta \\
C_{44} &= 2(1-d_f)(1-s_{mt}d_{mf})(1-s_{mc}d_{mc})G_{12} \\
C_{55} &= 2(1-d_f)(1-s_{mt}d_{mf})(1-s_{mc}d_{mc})G_{13} \\
C_{66} &= 2(1-d_f)(1-s_{mt}d_{mf})(1-s_{mc}d_{mc})G_{23}
\end{aligned}
\tag{7}
$$

$$
d_f = 1-(1-d_{ft})(1-d_{fc}) \tag{8}
$$

$$
\Delta = \frac{1}{1-\nu_{12}\nu_{21}-\nu_{23}\nu_{32}-\nu_{13}\nu_{31}-2\nu_{21}\nu_{32}\nu_{13}} \tag{9}
$$

where E_{ij} is the Young's modulus, G_{ij} is the shear modulus, ν_{ij} is the Poisson ratio, s_{mt} and s_{mc} are the shear fractions in matrix tension or compression mode, respectively.

Hashin criteria is one of the most widely used failure criterion [21]. The 3D Hashin criteria is used to calculate the intra-laminar damage variables:

a) Fiber failure in tension ($\sigma_{11}>0$):

$$
d_{ft} = \begin{cases} 0, & \left(\frac{\sigma_{11}}{X_T}\right)^2+\left(\frac{\sigma_{12}}{S_{12}}\right)^2+\left(\frac{\sigma_{13}}{S_{13}}\right)^2<1 \\ 1, & \left(\frac{\sigma_{11}}{X_T}\right)^2+\left(\frac{\sigma_{12}}{S_{12}}\right)^2+\left(\frac{\sigma_{13}}{S_{13}}\right)^2\geq 1 \end{cases} \tag{10}
$$

b) Fiber failure in compression ($\sigma_{11}<0$):

$$
d_{fc} = \begin{cases} 0, & \left(\frac{\sigma_{11}}{X_C}\right)^2<1 \\ 1, & \left(\frac{\sigma_{11}}{X_C}\right)^2\geq 1 \end{cases} \tag{11}
$$

c) Matrix failure in tension ($\sigma_{22}+\sigma_{33}>0$):

$$d_{mt}=\begin{cases}0, & \left(\dfrac{\sigma_{22}+\sigma_{33}}{Y_T}\right)^2+\dfrac{\sigma_{23}^2-\sigma_{22}\sigma_{33}}{S_{23}^2}+\dfrac{\sigma_{12}^2+\sigma_{13}^2}{S_{12}^2}<1\\ 1, & \left(\dfrac{\sigma_{22}+\sigma_{33}}{Y_T}\right)^2+\dfrac{\sigma_{23}^2-\sigma_{22}\sigma_{33}}{S_{23}^2}+\dfrac{\sigma_{12}^2+\sigma_{13}^2}{S_{12}^2}\geq 1\end{cases} \quad (12)$$

d) Matrix failure in compression ($\sigma_{22}+\sigma_{33}<0$):

$$d_{mc}=\begin{cases}0, & \left[\left(\dfrac{Y_C}{2S_{23}}\right)^2-1\right]\left(\dfrac{\sigma_{22}+\sigma_{33}}{Y_C}\right)+\dfrac{(\sigma_{22}+\sigma_{33})^2}{4S_{23}^2}+\dfrac{\sigma_{23}^2-\sigma_{22}\sigma_{33}}{S_{23}^2}+\dfrac{\sigma_{12}^2+\sigma_{13}^2}{S_{12}^2}<1\\ 1, & \left[\left(\dfrac{Y_C}{2S_{23}}\right)^2-1\right]\left(\dfrac{\sigma_{22}+\sigma_{33}}{Y_C}\right)+\dfrac{(\sigma_{22}+\sigma_{33})^2}{4S_{23}^2}+\dfrac{\sigma_{23}^2-\sigma_{22}\sigma_{33}}{S_{23}^2}+\dfrac{\sigma_{12}^2+\sigma_{13}^2}{S_{12}^2}\geq 1\end{cases} \quad (13)$$

where X_T , X_C , Y_T and Y_C are longitudinal tensile strength, longitudinal compressive strength, transverse tensile strength and transverse compressive strength, respectively. S_{12} , S_{13} and S_{23} are in-plane shear strength and vertical plane shear strength, respectively.

2.2.2. Inter-laminar modeling

During the progressive damage analysis of composite laminates, intra-laminar damage and inter-laminar damage are performed simultaneously.

Characterize the inter-laminar damage behaviors of CFRP using the cohesive contact method (CCM) [25,26]. As shown in Fig. 5 and Eq. (12), a bilinear traction-separation law characterizes the cohesive contact is adopted to account for the delamination processing. Symbol meanings are shown in Table 1.

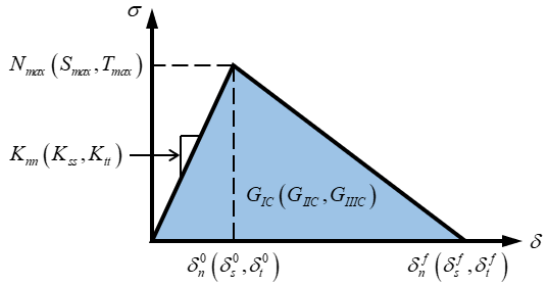

Fig. 5. Bilinear traction-separation law

$$\begin{Bmatrix}\sigma_n\\ \sigma_s\\ \sigma_t\end{Bmatrix}=\begin{bmatrix}K_{nn} & & \\ & K_{ss} & \\ & & K_{tt}\end{bmatrix}\begin{Bmatrix}\delta_n\\ \delta_s\\ \delta_t\end{Bmatrix} \quad (14)$$

Table 1

Symbol meanings of the bilinear traction-separation law.

Meanings	Model I	Model II	Model III
Separation displacement	δ_n	δ_s	δ_t
Traction stress	σ_n	σ_s	σ_t
Separation displacement at the initiation of damage	δ_n^0	δ_s^0	δ_t^0
Separation displacement at complete damage	δ_n^f	δ_s^f	δ_t^f

Stiffness coefficient	K_{nn}	K_{ss}	K_{tt}
Strength	N_{max}	S_{max}	T_{max}
Fracture toughness	G_{IC}	G_{IIC}	G_{IIIC}

The quadratic stress failure criterion is used to estimate damage initiation, while the BK failure criterion is used to predict delamination propagation [27]. The fracture toughness for the mixed fracture mode is expressed as:

$$G_C = G_{IC} + (G_{IIC} - G_{IC})(\frac{G_{II} + G_{III}}{G_I + G_{II} + G_{III}})^{\eta} \qquad (15)$$

where G_I, G_{II} and G_{III} denote the energy release rates for Modes I, II and III, respectively. G_C represents the equivalent fracture toughness. η is the damage factor.

2.3. Finite element implementation

According to the modeling and analysis method described above, the assembly process of the composite bolted joints (CBJ) is analyzed by finite element simulation.

2.3.1. Part and mesh

As shown in Fig. 6, the mesh models of composite laminates, washers, bolt and nut with real detailed thread structure are created, and all the element types are C3D8R.

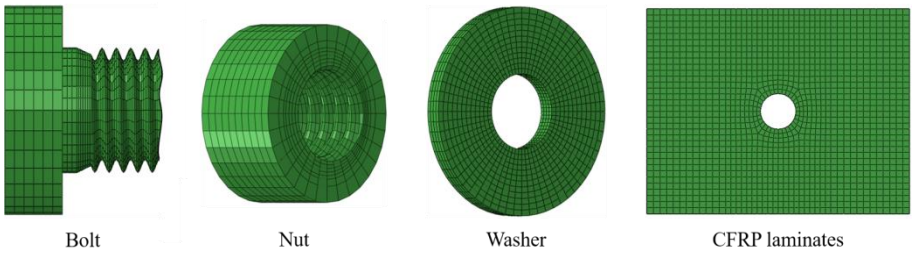

Fig. 6. Mesh models

2.3.2. Material

The material of the bolt, nut and washer is 40CrMo, and its material parameters are shown in Table 2. The CFRP material type is T800/X850. Its lay-up design is shown in Table 3, and the material parameters are shown in Table 4.

Table 2

Material parameters of 40CrMo.

Young's modulus	Poisson ratio	Mass density
210000 MPa	0.28	7.89E-09 t/mm^3

Table 3

Composite lay-up ratio and stacking sequence.

Lay-up ratio [0 / ±45 / 90]	Stacking sequence	Total lay-ups
(11%/67%/22%)	$[45/-45/0/45/90/-45/45/90/-45]_s$	18

Table 4

Material parameters of T800/X850 laminate.

Material properties		Strength	
E_{11} (MPa)	165000	X_T	3071

E_{22} (MPa)	9730	X_C	1747
E_{33} (MPa)	9730	Y_T	88
G_{12} (MPa)	4570	Y_C	271
G_{13} (MPa)	4570	Z_T	88
G_{23} (MPa)	2900	Z_C	271
υ_{12}	0.33	S_{12}	143
υ_{13}	0.33	S_{13}	143
υ_{23}	0.48	S_{23}	102

2.3.3. Assembly and interaction

As shown in Fig.7, the composite bolted joint assembly contains bolt, nut, washers, composite laminates and different types of contact surfaces. The specific contact properties and parameter settings are shown in Table 5.

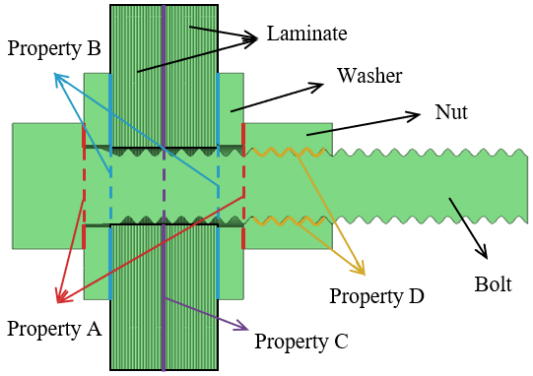

Fig. 7. Diagram of the assembly relations and contact settings

Table 5

Contact properties and parameter settings

Contact region	Property	Contact materials	Interaction type	Friction Coefficient
Bolt/nut with washer	A	40CrMo	Surface to surface	0.156
with laminate	B	40CrMo with CFRP	Surface to surface	0.340
Laminate	C	CFRP	Surface to surface	0.400
Thread	D	40CrMo	General contact	0.213

Characterize the inter-laminar properties of CFRP laminates using the cohesive contact method. The parameter settings are shown in Table 6.

Table 6

Inter-laminar cohesive parameter settings

K_{nn} (MPa)	K_{ss} (MPa)	K_{tt} (MPa)	N_{max} (N/m^3)	S_{max} (N/m^3)	T_{max} (N/m^3)	G_{IC} (N/m)	G_{IIC} (N/m)	G_{IIIC} (N/m)	η
10^6	5×10^5	5×10^5	33.51	56.29	56.29	0.28	0.79	0.79	1.45

2.3.4. Step and boundary

A dynamic explicit step is established to simulate the real assembly process of the composite bolted joint by controlling the nut boundary conditions. As shown in Fig. 8, the freedom of rotation of the nut around its axis is controlled by inputting the angle curve. At the same time,

no control will be performed on its translational freedom along the axis direction.

As the detailed thread structure is considered in the modeling process, the nut automatically moves in the direction of the axis during rotation, thus compressing the washers and the laminates and finally resulting in the tightened state.

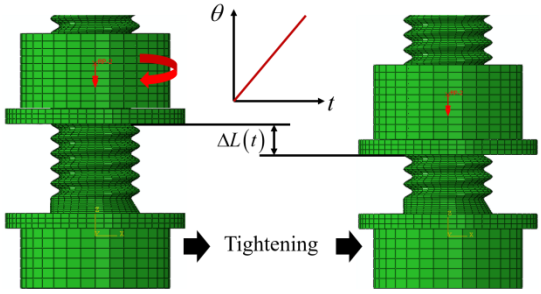

Fig. 8. Diagram of the nut tightening process

3. Simulation analysis results

As shown in Fig. 9, three different types of composite bolted joints are created according to the method in Chapter 2, which use double large washers, double large washers, and no washers. The assembly process is simulated and analyzed.

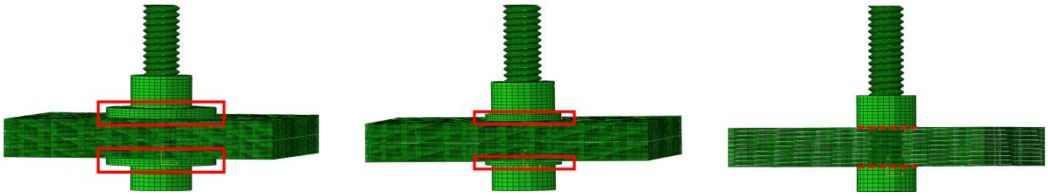

(a) Double large washers (b) Double small washers (c) No washers

Fig. 9. Finite element model of composite bolted joints

3.1. Torque-bolt tension relationship from simulations

Record the tightening torque T and bolt tension F_B during the tightening process and plot the F_B-T curve. As shown in Fig. 10, the slope of the curve is calculated as the value of the tightening coefficient α.

The calculation results show that the three types of CBJ have different tightening coefficients, and the tightening coefficient of the type of no washers is significantly different from the other two types.

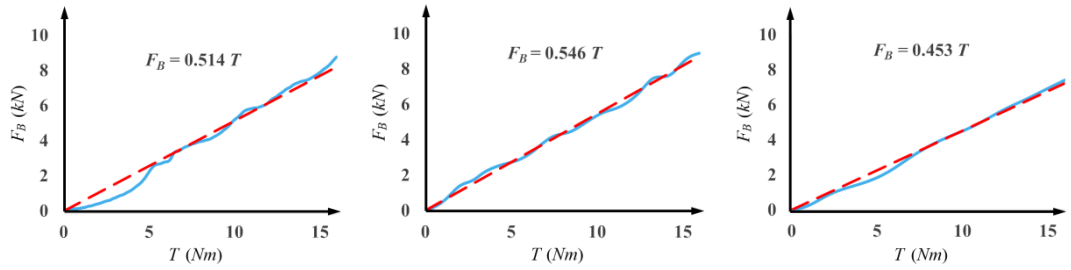

(a) Double large washers (b) Double small washers (c) No washers

Fig. 10. Torque-bolt tension relationship from simulations

3.2. Non-linear distribution state of bolt tension from simulations

Record the distribution of pressure on the outer surface of the composite laminates during the tightening process.

As shown in Fig. 11, for the same joint type, the pressure distribution state changes as the bolt tension increases. Specifically, the distribution range and the stress concentration increase with the increasing of bolt tension.

At the same level of bolt tension, washers have a significant effect on the distribution of surface pressure. The use of washers significantly increases the range of pressure distribution, lessens the stress concentration effect, and reduces the risk of initial assembly damage of CBJ. At the same time, large washers demonstrate better results than small washers.

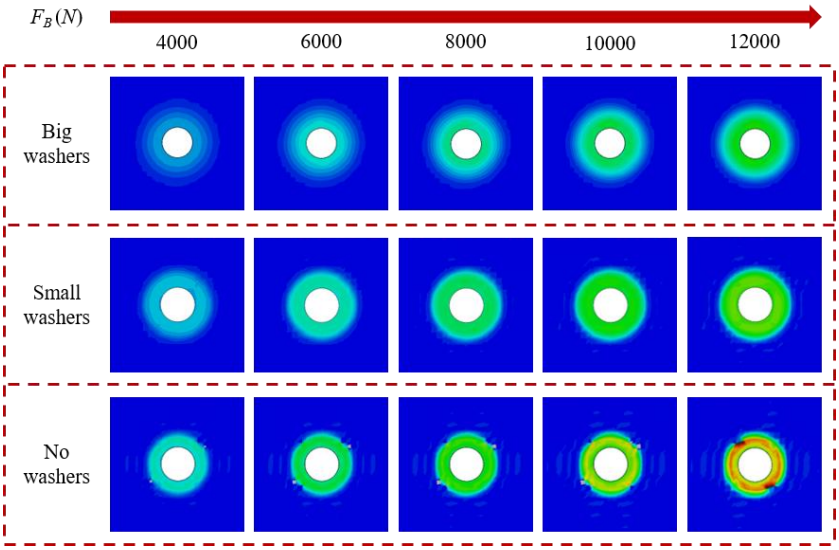

Fig. 11. Distribution state of bolt tension during the tightening process

3.3. Initial assembly damage of the composite laminates from simulations

The mechanical properties of the CFRP joint can be improved by increasing the bolt tension appropriately [28]. However, when the bolt tension is too large, microcracks tend to form, leading to local delamination [7].

The initial delamination damage due to the assembly of the composite bolted joint is analyzed according to the method proposed above. Taking the CBJ without washers as an example, as shown in Fig. 12, after the assembly, both composite laminates produced initial delamination damage. The damage is mainly concentrated between the layers adjacent to the fasteners, and no initial delamination damage occurred in the area away from the fasteners.

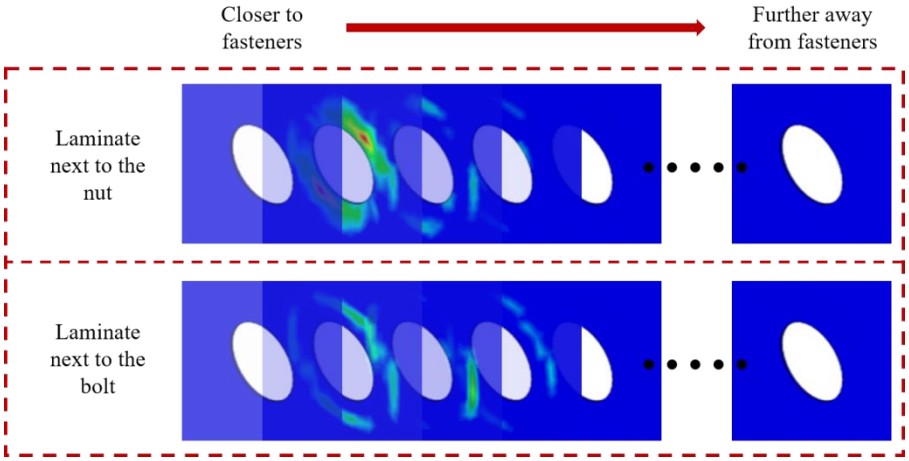

Fig. 12. Distribution state of bolt tension during the tightening process

4. Experimental verification

4.1. Experimental procedures

Assembly tests are carried out on three types of CBJ to verify the simulation results.

As shown in Fig. 13, tightening torque is applied to the nut by a torque wrench and its value is recorded. Monitoring of the bolt tension by an ultrasonic measurement system. Obtain the pressure distribution on the outer surface of the composite laminates using the pressure sensitive paper. And the delamination damage is examined using CT scan after the assembly.

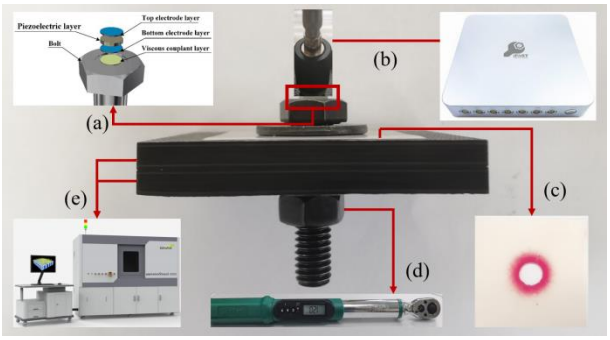

Fig. 13. Schematic of CBJ assembly tests

4.2. Experimental results

4.2.1. Torque-bolt tension relationship from experiments

As shown in Fig. 14, the values of the bolt tension at different tightening torques are recorded during the tightening process. Three repeated samples are set up for each type of CBJ.

The tightening coefficients for all samples are shown in Table 7. The results show that the tightening coefficients obtained from the simulation are basically consistent with the experimental test results, and the error does not exceed 5%.

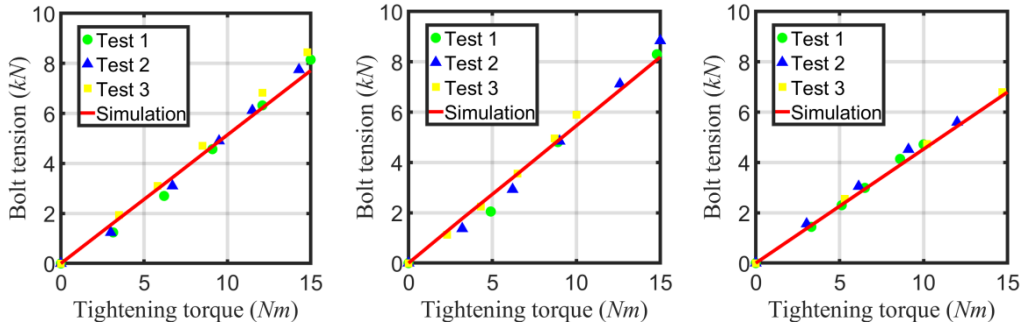

(a) Large washers (b) Small washers (c) No washers

Fig. 14. Torque-bolt tension relationship from experiments

Table 7

Experimental results of tightening coefficients

Joint type	Tightening coefficient	Mean value	Variation coefficient	Simulation result	Simulation error
Large washers	0.530 0.525 0.551	0.5352	0.021	0.514	4.0%
Small washers	0.545 0.562 0.570	0.5589	0.018	0.546	2.3%
No washers	0.447	0.4658	0.031	0.453	2.7%

0.482

0.469

4.2.2. Non-linear distribution state of bolt tension from experiments

The pressure sensitive paper is placed between the washer and the laminate before the assembly starts, and the pressure distribution is observed by the image displayed on the pressure sensitive paper after the assembly.

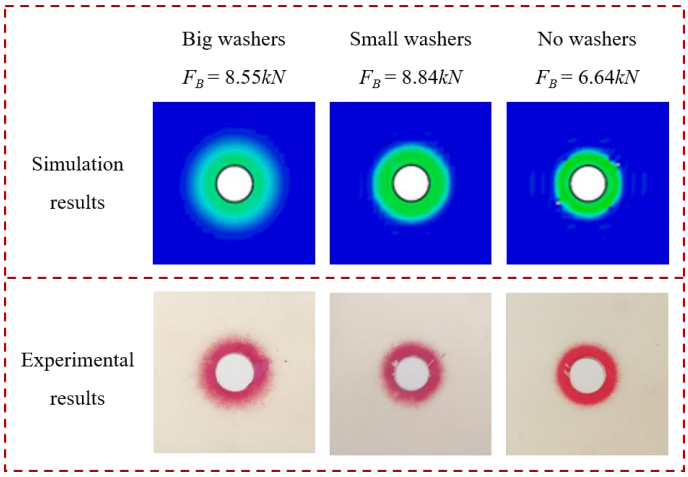

Fig. 15. Distribution state of bolt tension from experiments

As shown in Fig. 15, test results show that the pressure distribution of CBJ without washers is more concentrated and the pressure peak is higher. Washers are effective in increasing the range of pressure distribution and reducing pressure peaks. The large washers exhibited more significant effects than the small ones. The experimental test results remain consistent with the conclusions obtained from the simulation analysis.

4.2.3. Initial assembly damage of the composite laminates from experiments

After the assembly, the outer surface of composite laminates is damaged, including indentation and wear. As shown in Fig. 16, significant damage occurred to composite laminates without washers, while composite laminates with large washers showed only minor wear at the edge of the washer. Washers have a positive effect on preventing initial damage to the outer surface of the composite laminates.

(a) Large washers (b) Small washers (c) No washers

Fig. 16. Damage of the outer surface after the assembly

To observe the delamination damage inside the composite laminates, non-destructive testing is performed using CT scan. As shown in Fig. 17, all three types of CBJ produced initial delamination damage after the assembly. The damage is mainly concentrated in the area near the fasteners, and there is no delamination damage in the area away from the fasteners, which is consistent with the results of the simulation analysis in Fig. 12. In addition, type of large washers has the least delamination damage and type of no washers has the most severe delamination damage, further confirming the inhibitory effect of the washers on the initial

assembly damage of CBJ.

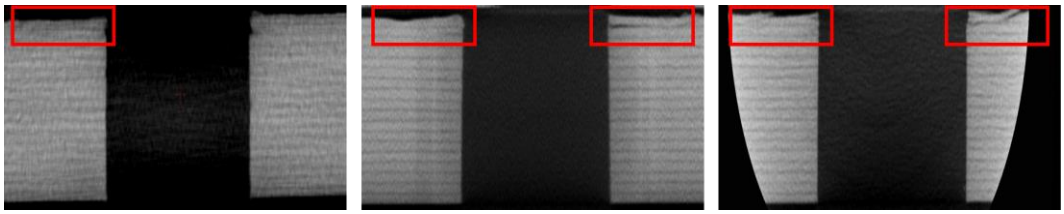

(a) Large washers (b) Small washers (c) No washers

Fig. 17. Delamination damage results tested using CT scan

5. Conclusion

In this study, a three-dimensional progressive damage analysis method for the assembly process of composite bolted joint considering the detailed thread structure is proposed. Three different types of composite bolted joints were selected as examples for simulation analysis and experimental tests. The experimental results proved the accuracy of the proposed method and finally the following conclusions are obtained.

The developed parametric modeling program can be used to build finite element mesh models of bolted joints with the detailed thread structure in a very short time, and users can easily import the mesh models into their own simulation tasks.

Simulation analysis and experimental tests were taken for the assembly process of three types of composite bolted joints: large washers, small washers and no washers. Their torque-bolt tension relationship, non-linear pressure distribution state, and initial assembly damage were obtained. There are significant differences in the torque-bolt tension relationship for the three types of joints. At the same time, the large bolt tension may lead to initial damage such as indentation, wear, and delamination of the composite laminates. The washers make the range of the pressure distribution wider and the pressure peak smaller, which has a significant inhibiting effect on the initial assembly damage of the composite laminates.

The proposed simulation method can effectively simulate the real tightening process of the composite bolted joint. It helps researchers to predict torque-bolt tension relationship, non-linear pressure distribution state, and initial assembly damage of the composite bolted joint. The stress-strain state and material damage state obtained from the simulation can be the initial input for subsequent analysis.

Acknowledgement

This work is supported by the National Natural Science Foundation of China (Grant No. 51975349) and the National Key Research and Development Program of China (Grant No. 2019YFA0709000).

References

[1] Liu Q, Lin Y, Zong Z, Sun G, Li Q. Lightweight design of carbon twill weave fabric composite body structure for electric vehicle. Composite Structures 2013;97:231–8. https://doi.org/10.1016/j.compstruct.2012.09.052.

[2] Sun Q, Lin Q, Yang B, Zhang X, Wang L. Mechanism and quantitative evaluation model of slip-induced loosening for bolted joints. AA 2020;40:577–88. https://doi.org/10.1108/AA-08-2019-0152.

[3] Obradovic J, Boria S, Belingardi G. Lightweight design and crash analysis of composite frontal impact energy absorbing structures. Composite Structures 2012;94:423–30. https://doi.org/10.1016/j.compstruct.2011.08.005.

[4] Shah SZH, Karuppanan S, Megat-Yusoff PSM, Sajid Z. Impact resistance and damage tolerance of fiber

reinforced composites: A review. Composite Structures 2019;217:100–21. https://doi.org/10.1016/j.compstruct.2019.03.021.
[5] McCarthy CT. An analytical model for the prediction of load distribution in highly torqued multi-bolt composite joints. Composite Structures 2011:12.
[6] Cao Z, Cardew-Hall M. Interference-fit riveting technique in fiber composite laminates. Aerospace Science and Technology 2006:4.
[7] Yue X, An L, Chen Z, Cai Y, Wang C. Effect of preload and shim types on the mechanical properties of composite-aluminium bolted joints. Proceedings of the Institution of Mechanical Engineers, Part C: Journal of Mechanical Engineering Science 2022;236:1099–118. https://doi.org/10.1177/09544062211007172.
[8] Marques GP, Campilho RDSG, da Silva FJG, Moreira RDF. Adhesive selection for hybrid spot-welded/bonded single-lap joints: Experimentation and numerical analysis. Composites Part B: Engineering 2016;84:248–57. https://doi.org/10.1016/j.compositesb.2015.09.002.
[9] Xu P, Zhou Z, Liu T, Pan S, Tan X, Zu S, et al. Propagation of damage in bolt jointed and hybrid jointed GLARE structures subjected to the quasi-static loading. Composite Structures 2019;218:79–94. https://doi.org/10.1016/j.compstruct.2019.03.047.
[10] Yoon D, Kim S, Kim J, Doh Y. Study on bearing strength and failure mode of a carbon-epoxy composite laminate for designing bolted joint structures. Composite Structures 2020;239:112023. https://doi.org/10.1016/j.compstruct.2020.112023.
[11] Xu XW, Man HC, Yue TM. Strength prediction of composite laminates with multiple elliptical holes. International Journal of Solids and Structures 2000;37:2887–900. https://doi.org/10.1016/S0020-7683(99)00033-5.
[12] Liu F, Lu X, Zhao L, Zhang J, Xu J, Hu N. Investigation of bolt load redistribution and its effect on failure prediction in double-lap, multi-bolt composite joints. Composite Structures 2018;202:397–405. https://doi.org/10.1016/j.compstruct.2018.02.043.
[13] Sharos PA, McCarthy CT. Novel finite element for near real-time design decisions in multi-fastener composite bolted joints under various loading rates. Composite Structures 2020;240:112005. https://doi.org/10.1016/j.compstruct.2020.112005.
[14] Zhang F, Hu Z, Gao L, Wan Y, Jin L, Jia X, et al. Investigation on in-plane shear behavior of large-size composite plates with multi-bolt joints. Composite Structures 2020;232:111553. https://doi.org/10.1016/j.compstruct.2019.111553.
[15] Zhang H, Zhang L, Liu Z, Qi S, Zhu Y, Zhu P. Numerical analysis of hybrid (bonded/bolted) FRP composite joints: A review. Composite Structures 2021;262:113606. https://doi.org/10.1016/j.compstruct.2021.113606.
[16] Tanlak N, Sonmez F, Talay E. Detailed and simplified models of bolted joints under impact loading. The Journal of Strain Analysis for Engineering Design 2011;46:213–25. https://doi.org/10.1177/0309324710396997.
[17] Yang B, Sun Q, Lin Q, Wang L, Zhang X, Ma Y. Influence mechanism of bolted joint with geometric irregularity bearing surface on anti-loosening performance. International Journal of Pressure Vessels and Piping 2021;191:104364. https://doi.org/10.1016/j.ijpvp.2021.104364.
[18] Marannano G, Zuccarello B. Numerical experimental analysis of hybrid double lap aluminum-CFRP joints. Composites Part B: Engineering 2015;71:28–39. https://doi.org/10.1016/j.compositesb.2014.11.025.
[19] Lin Q. Reliability evaluation method of anti-loosening performance of bolted joints. Mechanical Systems and Signal Processing 2022:17.
[20] Lin Q, Zhao Y, Sun Q, Chen K. Viscous Friction Effect During the Process of Tightening and Loosening

of Bolted Joints 2021:8.
[21] Liao J, Zhang J, Feng P, Yu D, Wu Z. Interface contact pressure-based virtual gradient material model for the dynamic analysis of the bolted joint in machine tools. J Mech Sci Technol 2016;30:4511–21. https://doi.org/10.1007/s12206-016-0919-6.
[22] Liu H. Modeling and free vibration analysis for bolted composite plate under inconsistent pre-tightening condition. Composite Structures 2022:19.
[23] Fukuoka T, Nomura M. Proposition of helical thread modeling with accurate geometry and finite element analysis[J]. Journal of Pressure Vessel Technology, 2008, 130(1):135-140.
[24] Li W, Guo S, Giannopoulos IK, He S, Liu Y. Strength enhancement of bonded composite laminate joints reinforced by composite Pins. Composite Structures 2020;236:111916. https://doi.org/10.1016/j.compstruct.2020.111916.
[25] Isbilir O. Numerical investigation of the effects of drill geometry on drilling induced delamination of carbon fiber reinforced composites. Composite Structures 2013:8.
[26] Singh H, Mahajan P. Modeling damage induced plasticity for low velocity impact simulation of three dimensional fiber reinforced composite. Composite Structures 2015;131:290–303. https://doi.org/10.1016/j.compstruct.2015.04.070.
[27] Benzeggagh ML, Kenane M. Measurement of mixed-mode delamination fracture toughness of unidirectional glass/epoxy composites with mixed-mode bending apparatus. Composites Science and Technology 1996;56:439–49. https://doi.org/10.1016/0266-3538(96)00005-X.
[28] Liu L, Zhang J, Chen K, Wang H. Combined and interactive effects of interference fit and preloads on composite joints. Chinese Journal of Aeronautics 2014;27:716–29. https://doi.org/10.1016/j.cja.2014.04.014.

3D modeling the material flow and induced fiber orientation for polymer composites made via large area extrusion deposition additive manufacturing

Z. Wang[1], X. Yin[1], and C. Luo[1]

[1]Dalian Maritime University, China

Abstract: Material flow and associated fiber orientation are one of the most important features in Large Area extrusion deposition Additive Manufacturing (LAAM) of short fiber-filled composites. Endeavors have been done in 2D flow models, where significant knowledges are achieved in explaining the material anisotropy of the deposited composite parts. Nevertheless, 2D flow models are limited by a couple assumptions that losing significant characters of the deposition flow. This study presents a 3D flow model focusing on the polymer composite melt flow within the nozzle and the subsequent 90-degree turning deposition onto the material substrate. Different rheology flow models are applied to quantify the flow kinematics. The fiber orientation is evaluated using the Advani-Tucker orientation tensor approach, via the one-way weakly-coupled flow/orientation analysis formulation. Computed results show the fiber orientation state on the entire cross-section of a deposited bead, which yields a clear view of how the material anisotropy is affected by the locally varied fiber orientation. 3D-model predicted orientation results exhibit a more favorable agreement with the reported experimental data than that yielded by the conventional 2D models. Additionally, it is found that the initial fiber orientation state in the nozzle inlet produces noticeable influences on the resulting fiber alignment within the LAAM-deposited composites.

1. INTRODUCTION

Large Area extrusion-based Additive Manufacturing (LAAM) develops rapidly, and has been employed in the manufacture of large-scale parts and tooling [1]. Typical thermoplastic polymer LAAM is a process where polymer feedstock materials are melted through a screw-extruder, and deposited on a heated platform, layer-by-layer, to form three-dimensional (3D) objects [2]. To achieve a relatively high dimensional accuracy and superior mechanical performances in large scale parts, carbon fiber filled polymers are employed. Duty, et al. show that adding short carbon fibers into the neat ABS polymer yields a composite with improved elastic properties, especially along the printing direction, and less distortion in the printed part following the bead deposition process of the LAAM system [3,4]. A key factor in the polymer composite deposition AM process is the flow-induced fiber orientation within the printed composite (c.f. Figure 1) since material properties of solidified parts depend on the fiber alignment within the printed bead [5]. Therefore, the prediction of fiber orientation during the polymer extrusion process in the short fiber polymer composite extrudate is of great importance.

Fiber orientation studies in LAAM applications (and similar applications of material extrusion additive manufacturing) have recently become of interest. Nixon, et al. [11] simulated fiber orientation in three fused deposition modeling (FDM) nozzle geometries (convergent, straight and divergent) using Moldflow (Moldflow Corporation, Framingham, MA, USA) and the Folgar-Tucker isotropic rotary diffusion (IRD) model [12]. Their work, which ignored die swell, showed that a converging geometry yielded the highest principal fiber alignment and the divergent geometry resulted in the lowest. Additionally, at the exit of the straight and the converging nozzle, a higher alignment was predicted near the center than at the edge, unlike the experimental result reported by Kunc [13]. Heller, et al. [14] computed the fiber orientation tensors in a conventional small scale FDM nozzle and extruded filament. In their work, die swell was computed by minimizing the integrated normal stress on the free surface using COMSOL Multiphysics (Comsol, Inc., Burlington, MA, USA). Their approach modeled the molten polymer as an isothermal Newtonian fluid in a creeping flow, and assumed an axisymmetric velocity field. Orientation tensors (c.f. e.g., Advani and Tucker [15]) were computed along streamlines within the flow domain from velocity and velocity gradient information. Their results showed that fiber alignment reached its peak at the outer edge of the nozzle, and then decreased towards the center of the flow. The above reviewed articles employed a weakly-coupled method where the fiber presence is ignored in the computation of flow fields. Alternatively, researches are carried out where the coupled flow/fiber-orientation effects are evaluated. The Smoothed Particle Hydrodynamics (SPH) approach is effective in simulating the flow-orientation coupling behaviors in the additive manufacturing deposition process [20-23]. Moreover, Wang and Smith presented a Finite-Element-Method (FEM) based algorithm to capture flow/orientation coupling nature in extrusion deposition processes [24] and later employed it to a LAAM deposition flow simulation [25].

Through an exhausted literature review, we see that the fiber orientation analysis for LAAM polymer flows are mainly limited in 2D flow domains, to our best knowledge. This study, in contrast, evaluate the effect of assumed polymer melt rheology on predicting fiber orientation via a 3D flow modeling of the extrusion-deposition process of LAAM systems. The weakly coupled formation is used to compute the fiber orientation within the polymer melt flow where we first obtain the flow kinematic in an isothermal axisymmetric large scale AM nozzle. Our flow model is created in two-dimension and solved with the finite element suite ANSYS-Polyflow (ANSYS Inc., Canonsburg, Pennsylvania, USA) [24], and includes melt flow within the nozzle in addition to a short section of post-nozzle extrudate, which enables the prediction of die swell at the nozzle exit. We consider a Newtonian fluid model, and a Carreau-Yasuda model (i.e., a generalized Newtonian fluid model) in separate flow simulations. The fiber orientation states along streamlines within the flow domain are computed from the velocity field computed within the melt flow domain. The Advani-Tucker fiber orientation tensor evaluation equation [15] and the Folgar-Tucker Isotropic Rotary Diffusion (IRD) model [12] are employed to solve the fiber orientation problem. In addition, the Orthotropic Closure (ORT) [5] is used to address the closure problem encountered in the fiber orientation computation.

2. MATERIAL and METHOD

In this study, we consider the material rheology of acrylonitrile butadiene styrene (ABS) fabricated by the PolyOne Corporation (Avon Lake, OH, USA). The rheological properties are adopted from a companion paper of the authors [17] (cf. Figure 1). With the rheological data, parameters of the applied Newtonian and Carreau-Yausda models are gained via curve-fitting procedures with ANSYS-Polymat (ANSYS Inc., Canonsburg, Pennsylvania, USA) [27]. Note, with Newtonian model, the shear viscosity is a constant, 1000 $\mathrm{Pa} \cdot \mathrm{s}$. And for the Carreau-Yasuda model, we have the following relationship,

$$\eta(\dot{\gamma}) = \eta_\infty + (\eta_0 - \eta_\infty)(1 + (\kappa\dot{\gamma})^a)^{\frac{n-1}{a}}, \tag{1}$$

where $\eta_0 = 204064\ \mathrm{Pa} \cdot \mathrm{s}^{\frac{n-1}{a}}$, $\eta_\infty = 0$, $\mu = 0.3333\ \mathrm{s}{-}1$, $n = 0.000001455$, and $a = 0.2398$, as computed via Polymat [27].

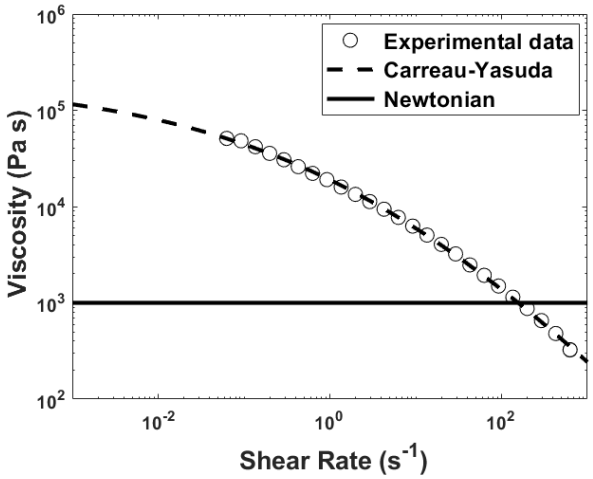

Figure 1. Shear viscosity curve fitting using applied rheology models.

We use ANSYS-Polyflow [24] to evaluate the flow kinematics in the polymer melt flow domain based on conservation of momentum

$$-\nabla p + \nabla \cdot \mathbf{T} + \mathbf{f} = \rho \mathbf{a}, \tag{2}$$

and conservation of mass

$$\nabla \cdot \mathbf{v} = 0, \tag{3}$$

where we have assumed an isothermal incompressible fluid represent the polymer melt as often appeared in extrusion die flow numerical studies [19,21,30]. In the above, p is the pressure, $\mathbf{T}$ is the total stress tensor, $\mathbf{f}$ is the body force, ρ is the density of the fluid and $\mathbf{a}$ is acceleration.

The geometry of the flow domain in our study is based on the Strangpresse Model-19 large-scale additive manufacturing extruder nozzle [41], as appearing in Figure 2. The nozzle walls are assumed to be non-slippery. One layer of deposited bead is modeled, where the two boundaries connecting the nozzle end are set as free surfaces. The bottom of the deposited bead is assumed to be perfectly bonded to the material substrate (it is the same if a subsequently-deposited bead is down below). The flow inlet is imposed with an averaged normal velocity of 6.25 mm/s, simulating a large volume deposition rate of ~700 mm3/s. To

form a smooth transition between extrusion and deposition, a tangential velocity of 101.6 mm/s is imposed to the bottom of the deposited, which is the average velocity at the nozzle exit. The flow end is set to be pressure-free. In addition, the layer thickness of the deposited bead (i.e., the distance between nozzle end and deposition substrate) is set as 3 mm. The deposition bead length is set as ten times the bead thickness, by which a steady-state condition of material flow and associated fiber orientation is expected to be achieved at the flow end. To save computational resources, we employ a symmetry plane in the middle of the flow domain.

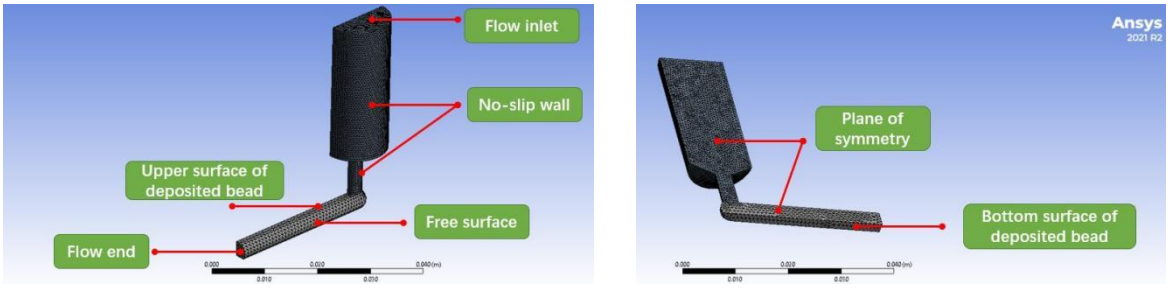

(a) (b)

Figure 2. Mesh and boundary condition of the flow domain: (a) view A; (b) view B.

The direction of a single rigid fiber within a polymer matrix is commonly described by a unit vector $\mathbf{p}(\varphi, \phi)$, as shown in Figure 3, with coordinates

$$\mathbf{p}(\varphi, \phi) = \begin{Bmatrix} \sin\varphi\cos\phi \\ \sin\varphi\sin\phi \\ \cos\varphi \end{Bmatrix}, \tag{4}$$

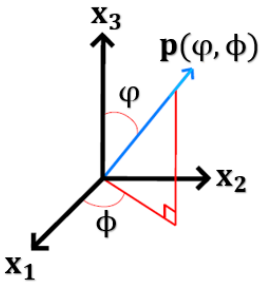

Figure 3. Coordinates of the vector $\mathbf{p}(\varphi, \phi)$ defining by the angles φ and ϕ.

Advani and Tucker [15] considered the statistical behavior of the fibers using the computationally efficient orientation tensor approach where the orientation tensor evolution equation is written as

$$\frac{D\mathbf{A}}{Dt} = (\mathbf{A}\cdot\mathbf{W} - \mathbf{W}\cdot\mathbf{A}) + \beta(\mathbf{D}\cdot\mathbf{A} + \mathbf{A}\cdot\mathbf{D} - 2\mathbb{A}:\mathbf{D}) + 2\,C_I\dot{\gamma}(\mathbf{I} - 3\mathbf{A}), \tag{5}$$

which assumes isotropic rotary diffusion first proposed by Folgar and Tucker [12]. Here, $\mathbf{A}$ and $\mathbb{A}$ are the second and fourth order orientation tensors, respectively, written as

$$\mathbf{A} = A_{ij} = \oint_{\mathbb{S}} p_i p_j \delta(\varphi, \phi)\, d\,\mathbb{S}, \text{ and } \mathbb{A} = A_{ijkl} = \oint_{\mathbb{S}} p_i p_j p_k p_l \delta(\varphi, \phi)\, d\,\mathbb{S}, \tag{6}$$

where $\delta(\varphi, \phi)$ is a probability distribution function and $\mathbb{S}$ is unit sphere surface. Note that

due to the normalization condition, the integral of $\delta(\varphi,\phi)$ over the surface $\mathbb{S}$ equates to unity, making the trace of A equal to 1 (see e.g., [25,26]). It can also be shown that A is symmetric, yielding just 5 independent components in Equation (5). In additional, the vorticity tensor W and the rate of deformation tensor $\mathbf{D}$ appearing in Equation (5) are given as

$$\mathbf{W} = \frac{1}{2}[(\nabla\mathbf{v}) - (\nabla\mathbf{v})^{\mathrm{T}}], \text{ and } \mathbf{D} = \frac{1}{2}[(\nabla\mathbf{v}) + (\nabla\mathbf{v})^{\mathrm{T}}], \tag{7}$$

We evaluate the tensors $\mathbf{W}$ and $\mathbf{D}$, from the velocity vector $\mathbf{v}$ computed along streamlines within the polymer melt flow field obtained from our ANSYS-Polyflow simulation result. The constant β in Equation (5) depends on the fiber aspect ratio as

$$\beta = \frac{\alpha^2-1}{\alpha^2+1}, \tag{8}$$

where α is the fiber aspect ratio. The interaction coefficient C_I is used to capture the effect of fiber-fiber interaction, and $\dot{\gamma}$ represents the scalar magnitude of the rate of deformation tensor $\mathbf{D}$. The last term in Equation (5) written as $2\,C_I\dot{\gamma}(\mathbf{I} - 3\mathbf{A})$ results from the the Folgar-Tucker Isotropic Rotary Diffusion (IRD) model [12]. Fu, et al. [32] experimentally observed that molten short fiber polymer composite exhibited an asymmetric profile of fiber length distribution with a peak skewed toward small values of fiber length. In addition, we experimentally measured the fiber aspect ratio of the sample prepared by performing a burn-off test on the 13 wt % carbon fiber filled ABS (manufactured by PolyOne Inc., Avon Lake, OH, USA) and found that the values of the fiber aspect ratio are in a range of 10 to 60. Following Fu, et al., we define β = 0.9802, corresponding to α = 15 in Equation (8). Bay and Tucker [9] defined an empirical formula for evaluating C_I which depends on the values of the fiber volume fraction and aspect ratio as

$$C_I = 0.0184\exp(-0.7148 v_f \alpha), \tag{9}$$

where v_f is the fiber volume fraction. Herein, the material model is selected as 13% CF/ABS (i.e. carbon fiber filled ABS). With above equations, we end up have C_I=0.0044.

The fourth order fiber orientation tensor, $\mathbb{A}$, is typically computed with a closure approximation in fiber orientation simulations. Prior studies have focused on the natural–type closure [33,34] and the orthotropic-type closure [35,36]. In this paper, we employ the Orthotropic Closure (ORT) to compute for $\mathbb{A}$ from A as defined in [5].

3. RESULTS and DISCUSSIONS

We compute the flow fields of the 3D extrusion-deposition flow by separately employing the Newtonian and Carreau-Yasuda models via Polyflow. In the view of the symmetric plane, Figure 4 provides the velocity magnitudes of the flow domain are provided for Newtonian and Carreau-Yasuda models, respectively. It can be seen clearly that the velocity profiles exhibit notable differences at the nozzle tip, where the maximum of the Newtonian model is 25.9% higher than that of the Carreau-Yasuda. While the profile of the Carreau-Yasuda model is more uniform as compared to that of the Newtonian, which is just as expected [43]. In addition, we plot the in-plane (i.e., in the symmetric plane) front side of the free surface extrudate computed from the two simulations in Figure 5. We see that the planar extrudate swell of the

Carreau-Yasuda flow is much less than that of the Newtonian flow, which is similar to that has been seen in a companion related study [17]. From the above comparison, it is expected that the differences of the flow fields would yield different fiber alignment pattern in the deposited bead flow.

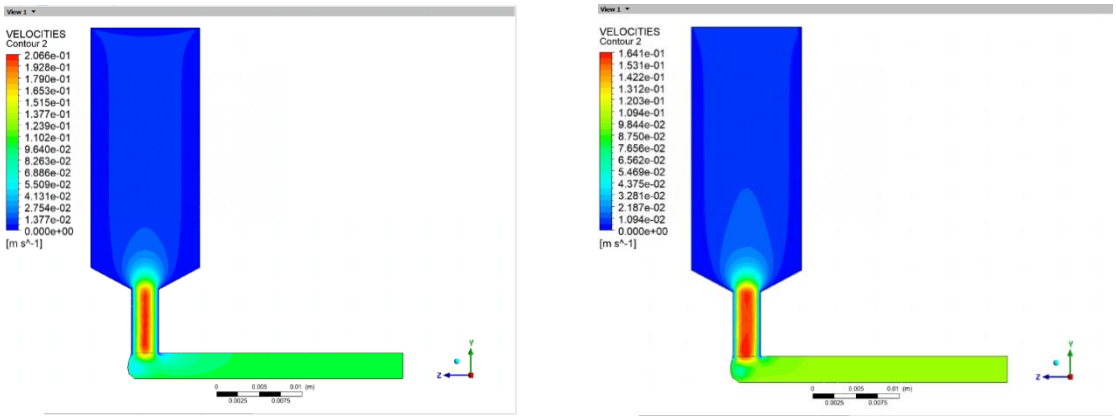

(a) (b)

Figure 4. Velocity profiles at the view of symmetric plane: (a) Newtonian model; Carreau-Yasuda model.

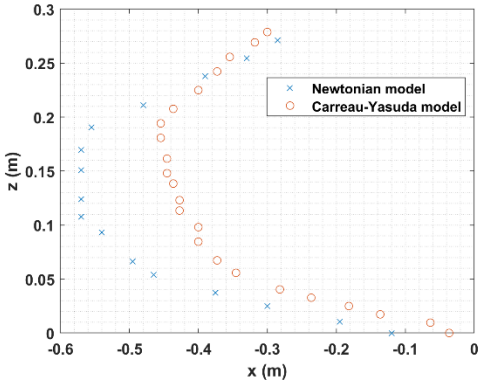

Figure 5. In-plane (i.e., in the symmetric plane) front side of the free surface extrudate.

The assumption of the initial fiber orientation state at the nozzle inlet directly influences the fiber orientation throughout the flow domain (cf. Equation (5) is a hyperbolic equation). Herein, we assume a fully 3D random alignment for the inlet condition. As mentioned, we employ a one-way weakly coupled model, where the fiber orientation tensors are evaluated along flow streamline using the uncoupled flow fields data. The diagonal component A_{33} is plotted in Figure 6, indicating how well the fibers are expected to align along the direction of material loading. In addition, the locations of flow streamlines are provided in Figure 7, where the results of the Newtonian and Carreau-Yasuda models are provided. From results shown in Figure 6, it is clearly seen that the Carreau-Yasuda model resulted flow-induced fiber orientation exhibits a higher fiber alignment along the direction of material loading as compared to that of the Newtonian model, which is also similar to the results reported in a related article [17]. In addition, the orientation states reach a steady-state in the deposited bead flow, which can be used further to represent the fiber orientation of a deposited bead. We also plot the A_{33} components within the cross-section of the flow end (i.e., the end of the deposited bead flow) in Figure 8, where the results of the Newtonian and Carreau-Yasuda models are included, respectively. We see again that the fiber orientation state resulted by the Carreau-Yasuda model exhibits a higher flow-direction alignment than that of the Newtonian. In

addition, the high fiber alignment is seen in the core region of the Carreau-Yasuda model, while the Newtonian flow exhibits the high fiber alignment among the boundary regions of the flow. With above discussions, it is seen that the rheological models of the flow directly impact the predicted fiber orientation of the extrusion-deposition flow.

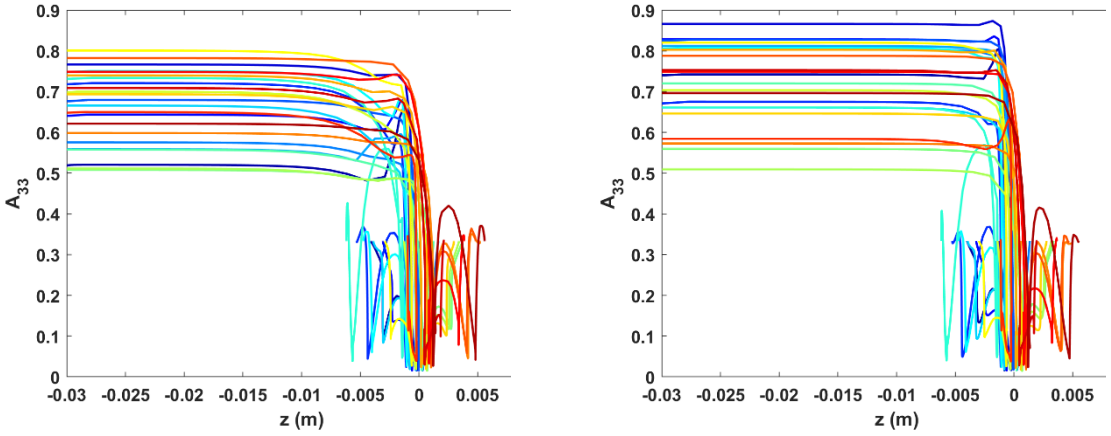

(a) (b)

Figure 6. A_{33} components computed along flow streamlines: (a) Newtonian model; (b) Carreau-Yasuda model.

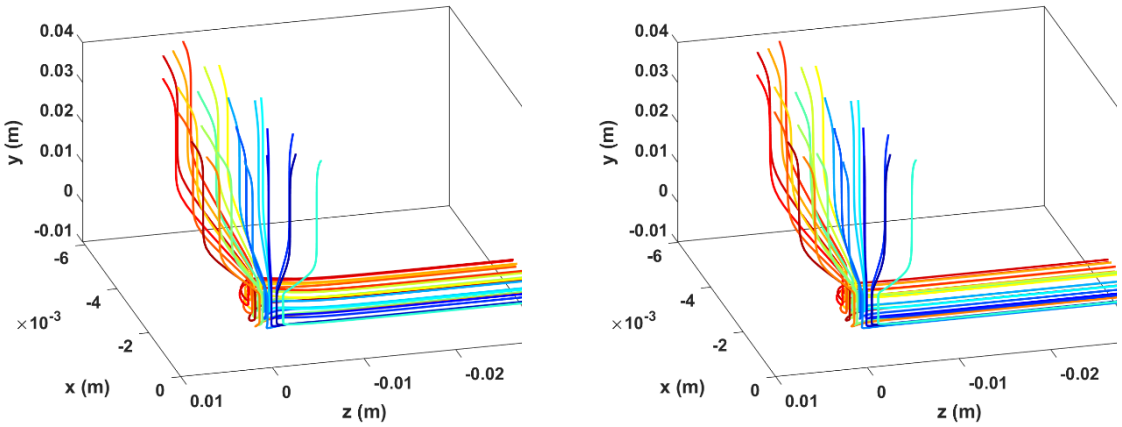

(a) (b)

Figure 7. Flow streamlines computed along flow streamlines: (a) Newtonian model; (b) Carreau-Yasuda model.

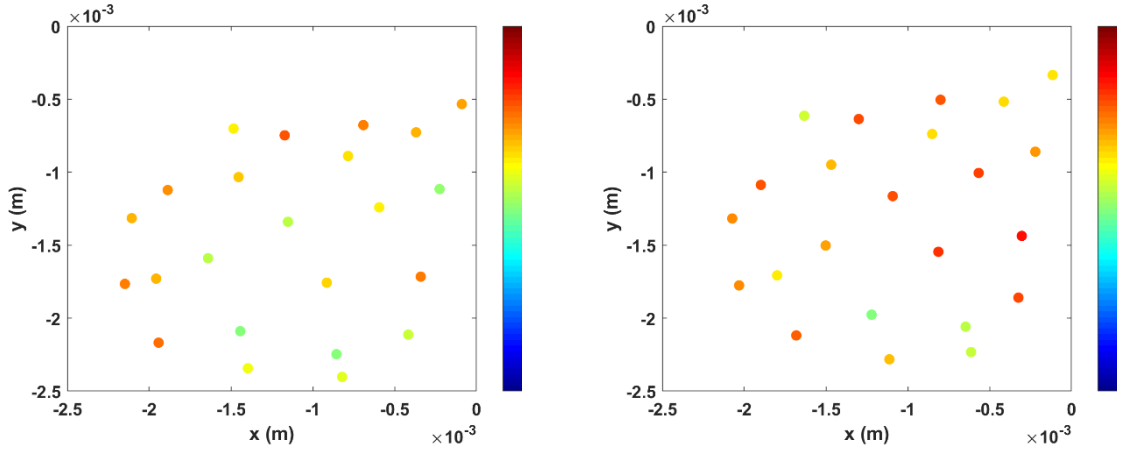

(a) (b)

Figure 8. A_{33} component results computed along flow streamlines at flow end: (a) Newtonian model; (b) Carreau-Yasuda model.

4. CONCLUSION

A 3D flow model is employed to simulate the vital extrusion-deposition process in the LAAM systems. We apply a one-way weakly coupled analysis to compute the flow and induced fiber orientation states within the flow domain. From the Polyflow-computed flow fields, it is seen that the maximum velocity magnitude of the Newtonian model is 25.9% higher than that of the Carreau-Yasuda, while the Carreau-Yasuda flow yields a more uniform velocity profile in the nozzle tip region. The Newtonian-model-predicted planar extrudate swell of the front free surface is larger than that of the Carreau-Yasuda model. In addition, the predicted fiber orientation results show that the Carreau-Yasuda model predicted results exhibit a higher fiber alignment trend along the direction of material loading, as compared to that of the Newtonian. The computed results from the 3D flow model show a similar trend as reported by a related 2D study [17]. It is also concluded that the rheological models of the flow directly impact the predicted fiber orientation of the extrusion-deposition flow, and thus should be considered seriously.

ACKNOWLEDGMENT

The author appreciates the financial supports from the National Natural Science Foundation of China (52101381), the National Research Center for International Subsea and Engineering Technology and Equipment (3132022346), and Dalian Human Resources and Social Security Bureau (Dalian City innovation and entrepreneurship support program for returned overseas students).

REFERENCES

1. Love, L. J. Utility of Big Area Additive Manufacturing (baam) for the Rapid Manufacture of Customized Electric Vehicles; Oak Ridge National Laboratory (ORNL); *Manufacturing Demonstration Facility* (MDF), **2015**.
2. Brenken, B.; Favaloro, A.; Barocio, E.; Denardo, N.; Kunc, V.; Pipes, R. B. Fused Deposition Modeling of Fiber-Reinforced Thermoplastic Polymers: Past Progress and Future Needs. In *Proceedings of the American Society for Composites: Thirty-First Technical Conference*; **2016**.
3. Love, L. J.; Kunc, V.; Rios, O.; Duty, C. E.; Elliott, A. M.; Post, B. K.; Smith, R. J.; Blue, C. A. The importance of carbon fiber to polymer additive manufacturing. *J. Mater. Res.* **2014**, *29*, 1893–1898.
4. Duty, C. E.; Kunc, V.; Compton, B.; Post, B.; Erdman, D.; Smith, R.; Lind, R.; Lloyd, P.; Love, L. Structure and mechanical behavior of Big Area Additive Manufacturing (BAAM) materials. *Rapid Prototyp. J.* **2017**, *23*, 181–189.
5. Verweyst, B. E.; Tucker, C. L. Fiber suspensions in complex geometries: flow/orientation coupling. *Can. J. Chem. Eng.* **2002**, *80*, 1093–1106.
6. Evans, J. G. The effect of non-Newtonian properties of a suspension of rod-like particles on flow fields. *Theor. Rheol. Halstead Press N. Y.* **1975**, 224–232.
7. Lipscomb, G. G.; Denn, M. M.; Hur, D. U.; Boger, D. V. The flow of fiber suspensions in complex geometries. *J. Non-Newton. Fluid Mech.* **1988**, *26*, 297–325.
8. Tucker, C. L. Flow regimes for fiber suspensions in narrow gaps. *J. Non-Newton. Fluid Mech.* **1991**, *39*, 239–268.
9. Bay, R. S.; Tucker, C. L. Fiber orientation in simple injection moldings. Part I: Theory and numerical methods. *Polym.Compos.* **1992**, *13*, 317–331.

10. Jackson, W. C.; Advani, S. G.; Tucker, C. L. Predicting the orientation of short fibers in thin compression moldings. *J. Compos. Mater.* **1986**, *20*, 539–557.
11. Nixon, J.; Dryer, B.; Lempert, I.; Bigio, D. I. Three parameter analysis of fiber orientation in fused deposition modeling geometries. In *Proc. of PPS conference*; **2014**.
12. Phelps, J. H.; Tucker, C. L. An anisotropic rotary diffusion model for fiber orientation in short-and long-fiber thermoplastics. *J. Non-Newton. Fluid Mech.* **2009**, *156*, 165–176.
13. Kunc, V. Advances and Challenges in Large Scale Polymer Additive Manufacturing. In *15th SPE Automotive Composites Conference, Novi, MI*; **2015**.
14. Heller, B.; Smith, D. E.; Jack, D. A. The Effects of Extrudate Swell, Nozzle Shape, and the Nozzle Convergence Zone on Fiber Orientation in Fused Deposition Modeling Nozzle Flow. In *American Society of Composites-30th Technical Conference*; **2015**.
15. Advani, S. G.; Tucker III, C. L. The use of tensors to describe and predict fiber orientation in short fiber composites. *J. Rheol.* **1987**, *31*, 751–784.
16. Crochet, M. J.; Keunings, R. Die swell of a Maxwell fluid: numerical prediction. *J. Non-Newton. Fluid Mech.* **1980**, *7*, 199–212.
17. Luo, X.-L.; Tanner, R. I. A streamline element scheme for solving viscoelastic flowproblems part II: integral constitutive models. *J. Non-Newton. Fluid Mech.* **1986**, *22*, 61–89.
18. Luo, X.-L.; Mitsoulis, E. An efficient algorithm for strain history tracking in finite element computations of non-Newtonian fluids with integral constitutive equations. *Int. J. Numer. Methods Fluids* **1990**, *11*, 1015–1031.
19. Béraudo, C.; Fortin, A.; Coupez, T.; Demay, Y.; Vergnes, B.; Agassant, J. F. A finite element method for computing the flow of multi-mode viscoelastic fluids: comparison with experiments. *J. Non-Newton. Fluid Mech.* **1998**, *75*, 1–23.
20. Thien, N. P.; Tanner, R. I. A new constitutive equation derived from network theory. *J. Non-Newton. Fluid Mech.* **1977**, *2*, 353–365.
21. Ganvir, V.; Lele, A.; Thaokar, R.; Gautham, B. P. Prediction of extrudate swell in polymer melt extrusion using an Arbitrary Lagrangian Eulerian (ALE) based finite element method. *J. Non-Newton. Fluid Mech.* **2009**, *156*, 21–28.
22. Limtrakarn, W.; Pratumwal, Y.; Krunate, J.; Prahsarn, C.; Phompan, W.; Sooksomsong, T.; Klinsukhon, W. Circular Die Swell Evaluation of LDPE Using Simplified Viscoelastic Model. *King Mongkut's Univ. Technol. North Bangk. Int. J. Appl. Sci. Technol.* **2013**, *6*, 59–68.
23. Clemeur, N.; Rutgers, R. P. G.; Debbaut, B. Numerical simulation of abrupt contraction flows using the Double Convected Pom–Pom model. *J. Non-Newton. Fluid Mech.* **2004**, *117*, 193–209.
24. ANSYS Polyflow User's Guide. Ansys Inc., **2013**.
25. Jack, D. A.; Smith, D. E. The effect of fibre orientation closure approximations on mechanical property predictions. *Compos. Part Appl. Sci. Manuf.* **2007**, *38*, 975–982.
26. Jack, D. A. Advanced analysis of short-fiber polymer composite material behavior, PhD Dissertation, University of Missouri–Columbia, **2006**.
27. ANSYS Polymat User's Guide. Ansys Inc., **2013**.
28. Tadmor, Z.; Gogos, C. G. *Principles of polymer processing*; John Wiley & Sons, **2013**.

29. Ajinjeru, C.; Kishore, V.; Liu, P.; Hassen, A. A.; Lindahl, J.; Kunc, V.; Duty, C. Rheological Evaluation of High Temperature Polymer. In *28th Annual International Solid Freeform Fabrication Symposium*; **2017**.
30. Michaeli, W. *Extrusion dies for plastics and rubber: design and engineering computations*; Hanser Verlag, 2003.
31. Reddy, J. N.; Gartling, D. K. *The finite element method in heat transfer and fluid dynamics*; CRC press, **2010**;32.
32. Fu, S.-Y.; Yue, C.-Y.; Hu, X.; Mai, Y.-W. Characterization of fiber length distribution of short-fiber reinforced thermoplastics. *J. Mater. Sci. Lett.* **2001**, *20*, 31–33.
33. Verleye, V.; Couniot, A.; Dupret, F. Prediction of fiber orientation in complex injection molded parts. In *ICCM/9.*; **1993**; Vol. 3, pp. 642–650.
34. Dupret, F.; Verleye, V.; Languillier, B. Numerical prediction of the molding of composite parts. *ASME-Publ.-FED* **1997**, *243*, 79–90.
35. Cintra Jr, J. S.; Tucker III, C. L. Orthotropic closure approximations for flow-induced fiber orientation. *J. Rheol.* **1995**, *39*, 1095–1122.
36. Chung, D. H.; Kwon, T. H. Improved model of orthotropic closure approximation for flow induced fiber orientation. *Polym. Compos.* **2001**, *22*, 636–649.
37. Meyer, K. J.; Hofmann, J. T.; Baird, D. G. Initial conditions for simulating glass fiber orientation in the filling of center-gated disks. *Compos. Part Appl. Sci. Manuf.* **2013**, *49*, 192–202.
38. Mase, G. T.; Smelser, R. E.; Mase, G. E. *Continuum mechanics for engineers*; CRC press, **2009**.
39. Tandon, G. P.; Weng, G. J. The effect of aspect ratio of inclusions on the elastic properties of unidirectionally aligned composites. *Polym. Compos.* **1984**, *5*, 327–333.
40. Reddy, K. R.; Tanner, R. I. Finite element solution of viscous jet flows with surface tension. *Comput. Fluids* **1978**, *6*, 83–91.
41. ANSYS CFD-Post User's Guide. Ansys Inc., **2012**.
42. Chapra, S. C. *Applied Numerical Methods with MATLAB for Engineers and Scientists*; McGraw Hill Publications, **2012**.
43. Gogos C G, Tadmor Z. Principles of polymer processing. John Wiley & Sons, 2013.

Evaluating the recent advances in finite element models tailored for fused deposition modeling

*Zhenyu Fang[1], Zhaogui Wang[1]**

[1]Dalian Maritime University, China

Abstract: Fused Deposition Modeling (FDM™) gains increasing popularity globally owing to its high-capability for building up intricate structures with low costs in time and materials. Nevertheless, complex material behaviors of thermoplastics feedstock yield extensional difficulties (e.g., low surface roughness and poor dimensional precision) for obtaining excellent quality of the fabricated products. To enhance performance and qualified rate of FDM parts, numerical analysis and predictive simulation tools are developed, which provide significant insights in better understanding the complicated physics occurred during FDM processes. This study evaluates the existing literature discussing the numerical simulations for FDM and related technologies. We explore four stages within a typical process of FDM, i.e., the material flow in the nozzle, material deposition and bonding, post-treatments, structural performance evaluation and prediction. Throughout our investigations, it is found that the physical modeling studies on the post-treatments nearly remain blank, while the post-treatments (e.g., thermal annealing and abrasive machining) have been proved as an efficient method to reduce the staircase effect of FDM parts through various experiments. The strongly anisotropic material properties exhibited by the composite feedstock are under-considered in a couple of literature. Meanwhile, it is suggested to develop more complete simulation process with consideration of continuous time sequence based on the existed single FDM process numerical model.

1. Introduction

Additive Manufacturing (AM), commonly known as 3D printing, is a combination of computer-aided design, material processing and molding technology, based on digital model files. Compared with conventional subtractive method, AM has good competitiveness in production efficiency and is cost-effective. Also, FDM is well known for its customized production, such as functional and personalized elements of wooden furniture industry [1]. Currently, there has been Big Area Additive Manufacturing (BAAM) systems developed from desk-level printer, designed for large scale molds and products, such as aerospace and automotive [2]. Essentially, FDM is a typical 3D printing technology achieved by repeating sequences of melting and cooling linear material strands according to the routes set in advance. In detail, first the product is created in Computer-Aided Design (CAD) file, which then is converted into (.STL) format [3]. The specific software slices the file and generates G-codes which is used to determine the moving path of the nozzle. FDM has made it real to

manufacture complex structural parts directly without fabricating the molds first, like injection molding. This can critically remove the expenditure of producing complex contour parts. Need to add that, there are some support materials applied into printing process to prevent the structures from dropping or falling into substrate [4]. These additional support materials can be separated manually or dissolved into liquid, promising the dimensional accuracy to some certain extent. In addition to high degree of freedom, user-friendly is one of another vital characteristics of the FDM, enabling less experienced people to operate the machine. This factor remarkably contributes to the great popularity of FDM in the domestic and overseas.

The basic principle of FDM states that the process begins with the fiber-reinforced materials fed into extruder, and then materials are deposited on the substrate or previously laid down material after being heated into semi-molten state as shown in Figure 1. Subsequently, the deposited materials begin to cool down and solidify under influenced by heat convection and conduction from the environment [5]. In addition, according to the practical production process, the fabricated parts are supposed to be assessed, so as to determine whether the performance of the products conform the expected requirements.

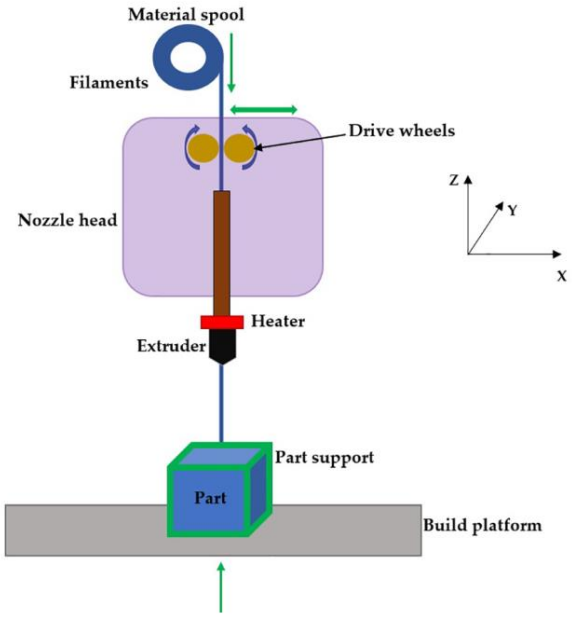

Figure 1. The schematic diagram of FDM process [4].

In spite of great potential, the durability and stability of parts created by FDM now are unable to meet many serving requirements. The reason are the defects, like distortions [6] provoked by non-uniform thermal gradients and stress build-up [7] during FDM process. In this context, simulation have proven time-effective [8] and economical to help improve the mechanical performance of FDM products, with great potential in discovering the implicit mechanisms of the FDM process. Over the years, a variety of extended methods have been put forward, while Finite Element Methods (FEM) are widely adopted on this area among various simulation methods. By dividing the model into finite units with relatively regular shapes, sophisticated mechanical responses of the project can be further simulated by iterative calculations in both micro [9] and macro [10] scopes, including many time-transient FDM processes [11]. For a systematic perception, FEM can generally be categorized into

four procedures corresponding to the actual FDM process, including the material flow in the nozzle, material deposition and bonding, post-treatments, structural performance evaluation and prediction.

Thereby, researches about FEM, which are mainly concerned with exploring mechanism via numerical tools in separate processes will be discussed in section 2. Herein, the conclusions are given in section 3, followed by summarized future works in the last section.

2. Simulations on the entire printing process

2.1 Flow in the nozzle

Nozzle zone actually is a process that can be depicted as the process that the thermoplastic filaments were fed into extruder, and heated into semi-molten state after through liquefier. Also, the process before materials depositing on the bed or previous deposited layers is also referred to nozzle zone, which indicates the overhanging portion of the continuous filament. For raw materials with no fillers, the physical parameters (e.g., pressure and the temperature distributions [12]) and phenomena (e.g., die swelling [13]) are focused. Costa et al., applied the Radial Point Interpolation Method (RPIM) into simulating the extrusion process for non-newtonian materials in FDM process. In research, RPIM was proven efficient to avoid the distortion of mesh encountered in the regular FEM [14]. Jahandardoost et al. focused on high-viscosity and non-newtonian materials in aspect of multi-physics modeling [15]. In this study, ANSYS©-CFX was utilized to conduct for the coupled fluid dynamics and heat transfer analysis, which were validated by experiments eventually. Phan et al. concentrated on the melting behaviors of flow in the nozzle as shown in Figure 2. Their simulation presented a recirculation vortex with a large viscosity in the entrance of the melting region which explained the phenomenon of no material overflow under great squeezing-pressure. In spite of some inconsistences between simulations and experiments, it was certain that nozzle design could limit printing speed. Shadvar et al. studied the relationships between die swelling, the flow rates, pressure and thermal distributions [13]. The rheological properties of selected Acrylonitrile Butadiene Styrene (ABS) were computed by ANSYS©-Polyflow software. The results revealed that the increasing flow rate led to much more significant die swelling and pressure drop of the extruder, while the temperature variation had the opposite effects.

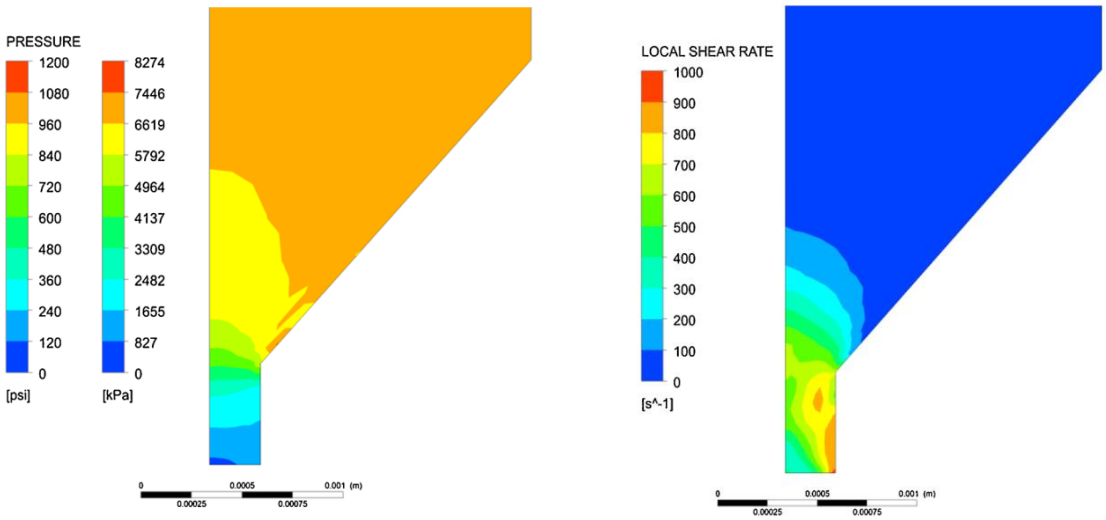

(a) (b)

Figure 2. The contour maps for (a) pressure and (b) shear rate under a specific temperature [12].

Sukindar et al. studied the effect of nozzle diameter with respects to pressure drop, geometrical error as well as extrusion time via FEM while Polylactic Acid (PLA) was taken as the sample material [16]. Analysis presented that pressure drop along the liquefier was affected notably by the diameter of the nozzle and low pressure drop is beneficial for the excellent product quality. The result was valuable in selecting the optimum nozzle diameter for 3D printing. With investigations into the melt flow behavior of 10% Iron material mixed with various polymers, the simulation results presented velocity and temperature profiles to different material compositions [17]. It was found that the material velocity increase in the case of the nozzle diameter is smaller than the entrance diameter. Similarly, melt flow behavior of the ABS-iron composite through the 90-degree bent tube of the liquefier head was simulated using ANSYS© FLOTRAN and CFX finite element packages [18]. This presented process and data helped develop the melt flow modelling of metal-plastic composites, as well as optimizing the FDM settings for better component performance with such composites. Instead of concentrating the material behavior itself, the thermal behavior of RepRap 3D printer liquefier was studied, mainly about the accompanied convective heat dissipation along the liquefier body during printing [19]. Finite elements model utilized here was to calculate the theoretical temperature distribution of the liquefier in a steady state. The obtained heat transfer mechanism can be the support for practical application.

When fillers embedded (e.g., short carbon fiber), the fiber orientation in the viscous suspension flow will be additionally concerned [20]. Since the fillers can bring great inhomogeneity to material properties as shown in Figure 3. Various divergent nozzle geometries had been tested by Garcia [21], so as to explore the possibility of making a 3D random fiber orientation into isotropic properties via a nozzle geometry. Heller et al. [22, 23] integrated the nozzle geometry and the extrudate swell to investigated the fiber orientation at the nozzle exit in the FDM process. It was revealed that extrudate swell had the modest impact on the extruded polymer's modulus of elasticity, while the influence of nozzle geometry was remarkable.

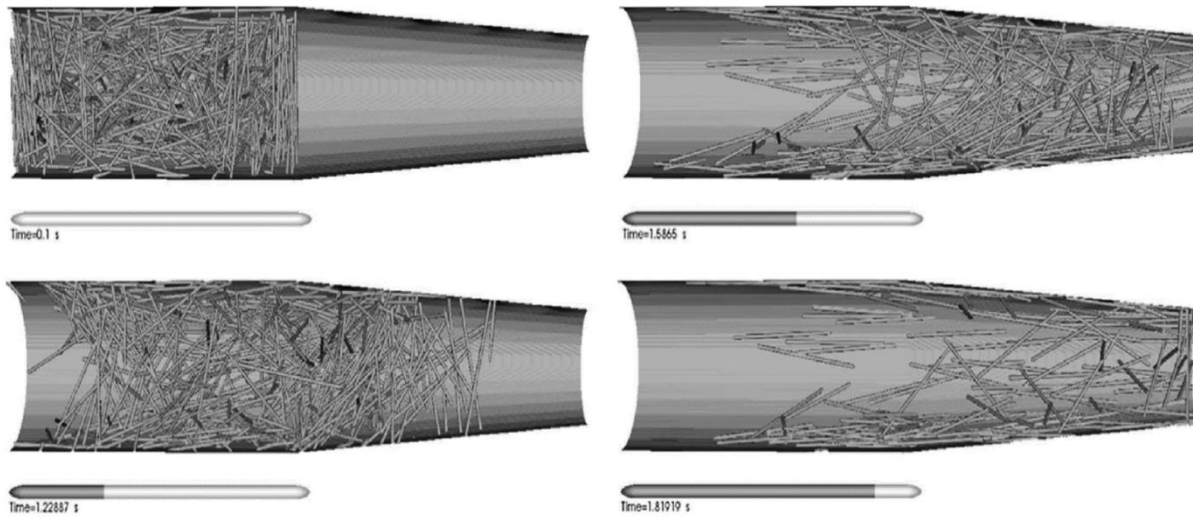

Figure 3. Three-dimensional evolution of fiber orientation in filling materials in specific domain [24].

2.2 Material deposition and bonding

After the flowing through the nozzle exit, the materials will deposit on the laid down materials or the substrate. With the sequential layer-by-layer process, the parts are molded, ultimately cooled and solidified. During this process, a number of phenomena contribute to the fusion bonding of polymer composites as shown in Figure 4. The interaction between different physical parameters (e.g., traveling speed of nozzle and heat convection [25]), integrated with the coalescence [26, 27] between different layers and adjoining filaments, as well as the formation of voids [28], will affect the final performance of the product. In terms of the traveling speed of nozzle, high speed is prone to uneven distribution of extruded materials, producing unexpected traction on the deposited materials. This will damage the adhesion between materials and causes undesired deformation as object cools later to release the accumulated stress. Different from the numerical simulation tool, Lou et al. proposed a transient updated Lagrangian finite element formulation to simulate the bond formation between molten filaments [29]. Validated by sintering experiments both qualitatively and quantitatively, it was suggested that fidelity to configuration and boundary is crucial to the prediction of bond formation and gravity should be weighed between enhancing bond formation and keeping dimensional accuracy of the printing process.

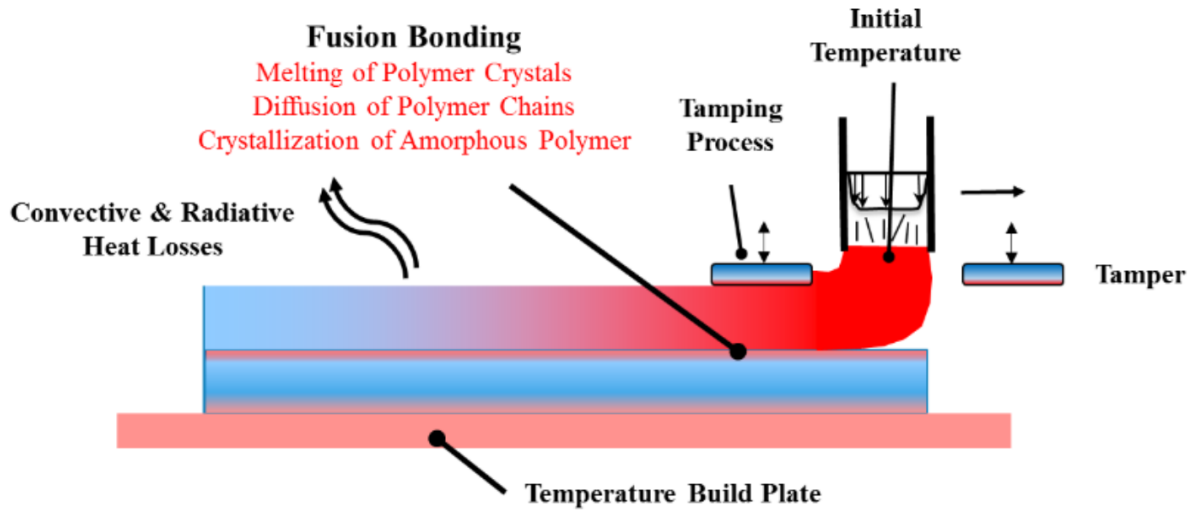

Figure 4. The phenomena involved in the material deposition and bonding process [30].

Bonding force between the layers is one of the paramount factors affecting the quality of printed parts. Barocio et al. proposed the concept that the degree of bonding, termed as the ratio of the recovered mode-I Critical Energy Release Rate (CERR) to the mode-I CERR measured from a joint bonded under ideal conditions, which is a measure of the interlayer bond strength [30]. A method to predict the degree of bonding between layers in the FDM process with semi-crystalline polymer composites was implemented in a UMATHT user subroutine. From the simulated results, crystallization is regarded as the retardation to enhance the degree of bonding. This simulation work was seen as the preparation for further predict the delamination and cracking of the printed parts.

Figure 5 illustrates the coalescence between filaments, which is dominant in structural strength and part failures. Viscosity and surface tension of polymers are two dominant factors in the level of coalescence. In the work by Lepoivre, et al., the viscosity and coalescence

were characterized by apparatus [31]. Besides, the coalescence was simulated by coupling an existing semi-analytical model with a 2D heat transfer finite element simulation model. It was revealed that the importance of applying thermal dependency of the surface tension in simulation, as well as sensitivity to the final degree of coalescence for different parameters. Also, this study demonstrated that high temperature heating chambers can reduce the porosity level of parts.

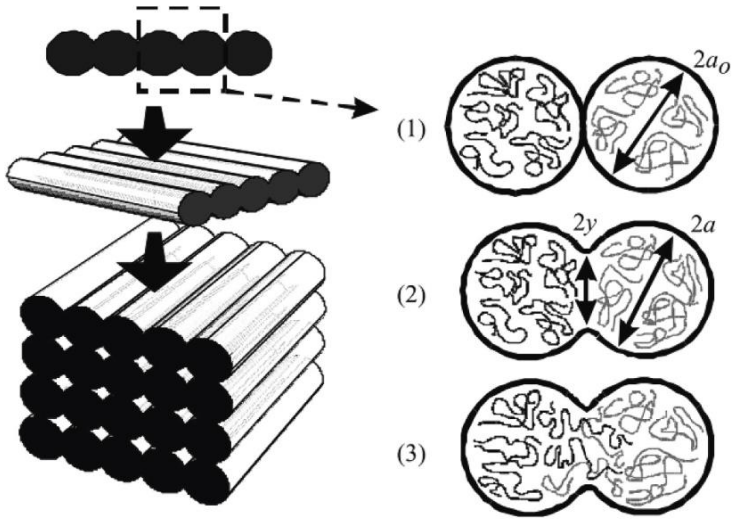

Figure 5. The microscopic bonding mechanism between adjacent filaments. (1) Contact, (2) coalescence and (3) the spread of mutual fusion between two filaments [32].

The internal voids formed in the process of material deposition has a great influence on material performances. Huang et al. focused on the formation mechanism of macroscopic defects such as voids, where time-dependent thermal simulations were conducted via CAE-Software ANSYS© on grounds of reduce the experimental efforts as shown in Figure 6. By simulating and comparing two typical cases, the relationship between the local temperature evolution and the morphology of the voids was basically elucidated, that is in the case of more heat input, the effects of interdiffusion will be greater and ultimately result in the formation of a homogeneous morphology. A three-dimensional time and spatial transient mathematical model of temperature was presented, integrated with a boundary-adjusting finite difference method by Zhang et al [33], where some significant conclusions were gained (e.g., it is universal for newly coated filaments to heat previously placed ones, which most frequently occurs in the direction of layer thickness). This research provided insights into FDM process with the scope of energy balance. Khanafer et al. also developed a 3D computational model to simulate the transient heat transfer and explore the inter-layer adhesion behavior [34]. This model can be utilized to predict temperature evolution in the area where layers interact as well as the bonding formation. In addition, it can be applied to investigate the connection between important parameters and how they affect output variables, or extended for further thermomechanical analysis. To overcome the difficulty in monitoring and modeling the solid-liquid-solid state transformation, Zhou and Hsieh introduced infrared thermography imaging method to capture temperature evolution of the filaments at the contact and associated cooling mechanism [35]. With the aid of life and death technology, a 3D finite element model was constructed to simulate the process and the maximum difference reached 13% compared with experimental data. This work

demonstrated the potential of the model in facilitating comprehension of bead spreading and filament bonding mechanics during FDM process.

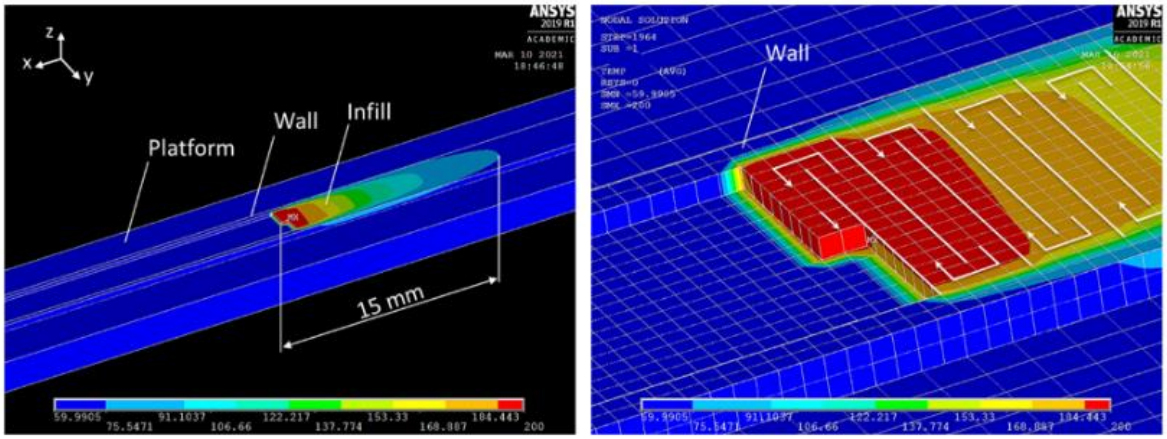

Figure 6. Illustrations of simulating dynamic FDM process with temperature evolution [28].

Ramos et al. concentrated on the accuracy and efficiency of heat transfer in deposition process . In the work, three ways of heat transfer were concluded in analysis, and the ambient temperature and convective coefficient were determined and fitted by experiments. The simulation of heat transfer was conducted in ANSYS© (Mechanical APDL 19.2). Moreover, how to simplify the model of air-filled and complex infill structures have been investigated. The results showed that infill density is the paramount factor, while the introduced method of discretization influenced less to the simulated accuracy.

To have a better understanding on the morphological evolutions of filaments, especially with temperature variation, Zhou et al. investigated the process, including flow, deposition, bonding, and heat transfer, by micro-structure simulation of deposition [37]. Confirmed by experiments, the results showed that the higher reheating temperature from subsequent deposited filaments and substrate can obviously improve the bonding condition. Moreover, it was provided that due to differences in viscosity and fluidity of different materials, filament-to-filament distance should be set appropriately to improve the adhesion and surface roughness. As printing speed and gap distance grew, the bonding degree reduced and the porosity rose. In addition, the qualitative connections between tensile strength, bonding intensity, and porosity were developed.

2.3 Post-treatments

When the printing process completed, post-treatment is seen as one of the key steps to bridge the laboratory applications to commercialization. Since systematic implementation of post processing technique can improve the roughness value of parts [38]. The formation of FDM parts is the procedure of filament materials stacking in 2D repetitively, which will cause the poor surface finish led by “Stair Casing Effect” [38] as shown in Figure 7. In terms of experiments, some researches related to improving the surface finish have already gained achievements. Regarding the semi-crystalline or crystalline plastics, annealing has proven efficient to improve the inter-layer cohesion by rising the crystallinity percentage [39]. Some chemicals were validated to be useful when applied to reduce roughness of FDM plastic parts [40, 41, 42]. Baran and Erbil reviewed various permanent surface modification approaches of FDM products fabricated by PLA for different application scenarios in terms [43].

Galantucci, et al. analyzed the effect of some machining parameters on surface roughness. Also, better performance was obtained after chemical treatment [41].

Furthermore, physical treatments (e.g., abrasive machining [44]) are common in improving the surface mechanical behaviors of FDM products. A disc finishing equipment presented the possibility of smoothing FDM components produced using Ultem™ 9085 [45]. Hotter Cutter Machining (HCM) showed its effectiveness in ABS [46]. Moreover, laser micromachining is regarded as one promising tool among post treatment methods for different types of materials [47]. In contrast to extra machining tools above, a simple way to add the filler into FDM fabricated tool has been validated effective [48].

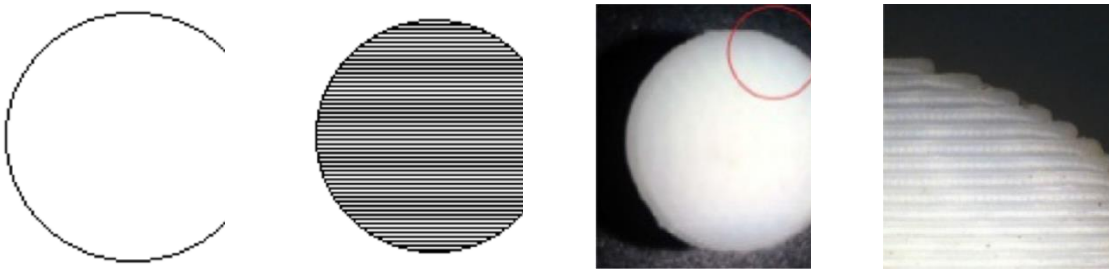

(a) (b) (c) (d)

Figure 7. The formation process of stair casing effect. (a) CAD model, (b) slicing, (c) printed part and (d) stair casing effect [38].

When adding the key words "simulation" along with "fused deposition modeling" "post treatment" in google scholar, there were few researches on this specific. It is reasonable since post treatment is trying to overcome the components' microscopic defects, integrated with complex physical phenomena. Hence, there is no established knowledge system or numerical tools to support simulation researches on this field.

2.4 Structural performance evaluation and prediction

Fabricated FDM components are prone to gain some undesirable defects or deformation after cooling under various conditions, which can have negative impact on in-service lifespan and performance. Accordingly, FEM has been extended for the numerical structural performance evaluation and prediction tool, which exhibit great potential. On the one hand, researchers use these numerical tools to evaluate the mechanical performance and defects (e.g., distortion [49], warpage [50] and fracture [51]) in advance, which can offer guidance for further structural optimization. On the other hand, these tools are applied into predicting the mechanical responses (e.g., elastic [52] and stress-strain [53] response) and properties of components under different types of loading without experimental tests, which also enable to have a better insight of the defect generated mechanism of the structure [54]. These published methods all exhibit good correlation to the experiments as shown in Figure 8. In general, these numerical tools generated from FEM can be translated between prediction and evaluation.

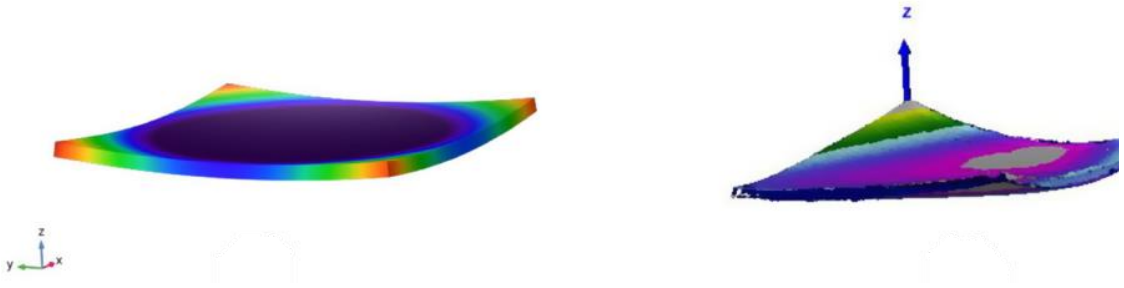

(a) (b)

Figure 8. Comparison warpage between (a) a simulated and (b) an actual printed sample [49].

Ghandriz, et al. proposed an anisotropic Cohesive Zone Model (CZM) based on the Extended Finite Element Method (XFEM) can help reveal the fracture mechanism of materials [55]. For different types of factures, specialized models were established to predict and characterize as shown in Figure 9. With parametric studies of varying the ratios between fracture parameters for the two failure criteria, different crack propagation patterns were revealed and the best agreement between numerical and experimental results was then achieved. Bouaziz et al. investigated and compared different method to study the fracture properties for specific specimen manufactured by FDM of ABS, with combination of experiments and simulation based on Digital Image Correlation (DIC) measurements [56, 57]. One is to measure only the kinematic fields, and the other is assisted by finite element simulation. Their work presented that with the aid of FEM, crack tip location can be accurately predicted and J-integral was utilized and verified. Compared with the simulated results, the method has access to figure out some connections between the material microstructure and its mechanical properties, and can be extended to the determination of other mechanical properties.

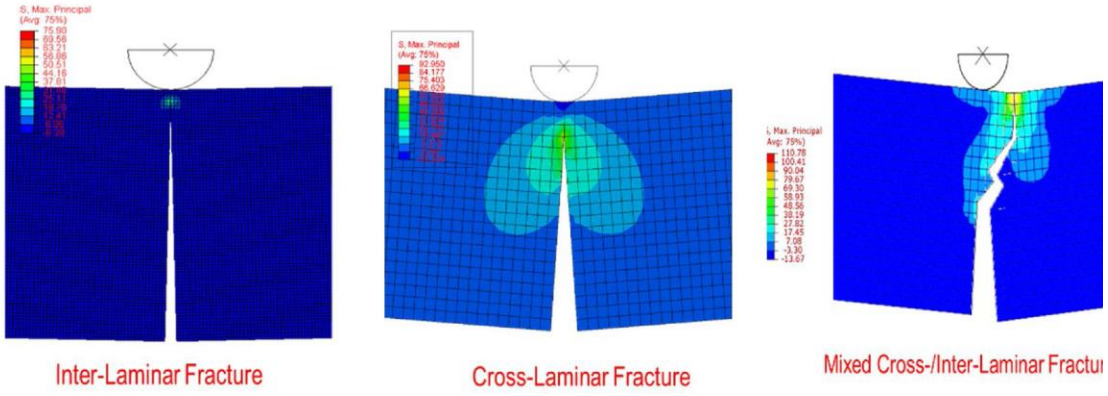

(a) (b) (c)

Figure 9. Numerical results of max principal stress and crack contours for (a) vertically layered samples, (b) horizontally layered samples, (c) obliquely layered samples [55].

Not only used to predict the failure mechanism of parts, numerical simulations are also utilized to test the mechanical performance some peculiar structure or parts designed by special material, like materials with Negative Poisson's Ratio (NPR) or Enhanced Effective Elastic Modulus (EEEM). Chen et al. investigated the mechanical behaviors of parts manufactured by CCF/PA and SCF/PA composites with either NPR or EEEM under in-plane

compression [58]. The results of simulation and experiments have been obtained and showed good correlations, which proved the potential of this numerical model to capture the key mechanism. To make up the left discrepancies, the material properties and other factors, such as fiber-orientation, are supposed to better develop.

Courter et al. took the Mobius arm part as the example to illustrate the numerical prediction based on ABAQUS© [59]. The temperature history was obtained from the coupled thermo-mechanical analysis and subsequently utilized to forecast residual stress and probable part deformation. The method from Gopsill et al. to optimize the infill structure of FDM parts based on the data from FEM demonstrated the generalizability and capacity to tackle with different complicated geometries and loading, as well as fabricating constraints [60]. Through locally adjusting the composition of the infill based upon the numerical calculated stress values, the updated sample reached by a three and a half times increase in strength, where the internal stress distributions were well defined. In the research by Jungivala and Gurrala, finite element analysis has been implemented for investigate the fracture resistance mechanism of CT-specimen made of ABS [61]. With orthotropic definition of material, load and fracture toughness with respect to J-integral was calculated, while the value of J-integral arose significantly with the increase in build orientation ranging from 0 to 90 degrees. Zhou et al. established knowledge-based library with utilization of the meso-structure numerical model and artificial neural network to predict the modulus of elasticity of FDM parts manufactured by PLA [62]. In spite of limited infill patterns, the result came with an average prediction error of 14.80% under any infill density.

3. Conclusions

This article mainly focuses on the parts made by different types of polymers, where many FEM works on FDM field are presented and discussed. During the analysis of FDM process via FEM, the factories existed in the actual environment can be divided into two categories, which reflected on the parameters set in the software. One category contains all kinds of exterior interactions, including the coalescence between adjoining deposited filaments, heat convection between material, ambient air and so on. This part occupies a great portion of current researches, especially in the material deposition and bonding. The other category refers to the interior interactions of materials due to the innate properties, like porosities and anisotropic mechanical responses, which are always investigated in the part flow in the nozzle. Besides, there are several conclusions obtained from the literature review:

1) Concerning with the simulation of flow in the nozzle, the researches on the anisotropic materials (e.g., fiber-reinforces materials) mostly are centered on the micro-structure. In the meanwhile, the simulation for anisotropic flow should be tested with consideration of fully coupled fields, and develop the methods for simplifying the material property into appropriate forms which can be applied into simulation.

2) There are research gaps between the studies on the anisotropic material properties and the material properties applied to simulation for different parts of the FDM process. In other words, the homogeneous material properties are dominant in the FEM analysis for FDM process, while the anisotropic fiber-reinforced materials' properties are found to have a considerable impact on the simulated mechanical responses of productions [63].

3) The researches focused on the post-treatments mainly utilize experimental methods, such as chemicals and physical tools, to improve the surface accuracy. There is no established knowledge system or numerical tools to support simulation researches on this field, due to sophisticated microscopic interactions.

4) The researches related to structural performance evaluation and prediction are more on investigation of internal formation mechanism and optimization of the structural performance, with some values of features as input variables. Additionally, it can be found that these numerical tools generated can be further developed from evaluation tool to prediction tool. However, it is advised to integrate the assessment process into the entire FDM simulation procedure, which takes previous accumulated mechanical responses into consideration. Also, the fiber-orientations are suggested to be added into estimating the products' performance made by composite materials.

5) Many of the existed researches on FEM analysis for the FDM process are generally isolated, which means that the time-sequential nature of the entire FDM is ignored. The previous procedures are presumed in advance, offering prerequisites for the focused FDM part. To suit the actual manufacture, complete FEM model tailored for FDM process are suggested to develop more, in spite of possible increasing computational cost.

4. Future work

For the FDM processes of fiber-filled composites, it is noticed the anisotropic material properties of the printed beads are often assumed as isotropic to reduce the computational costs. Nevertheless, employing homogenized isotropic material properties in numerical analysis and simulation can result significant bias as compared to the alternative simulations. To this end, it is important to establish the inter-connections Among the material anisotropy, thermal-mechanical responses (e.g., thermal deflection, residual stress), and structural performance of FDM-produced polymer composites. The advanced numerical tools with the suggested features can make it closer to fully exploit the advantages of FDM in cost and time effectiveness.

In addition, FEM has the potential to benefit the manufacturers economically and efficiently. Compared with the practical manufacture, there is still a remarkable gap between simulation and actual production. In addition to thermal plastics, FEM can be extended to more types of materials. The existed researches have discussed a lot about the single process. More efforts can be made to investigate how to integrate these procedures together appropriately to have the complete numerical analysis with more continuous time sequence.

ACKNOWLEDGMENT

The author appreciates the financial supports from the National Natural Science Foundation of China (52101381), the National Research Center for International Subsea and Engineering Technology and Equipment (3132022346), and Dalian Human Resources and Social Security Bureau (Dalian City innovation and entrepreneurship support program for returned overseas students).

REFERENCES

1. D. Thomas, "Costs, benefits, and adoption of additive manufacturing: a supply chain perspective," *The International Journal of Advanced Manufacturing Technology*, Vol.85, No.5, 1857-1876, 2016.
2. N. Grujovic, F. Zivic, M. Zivkovic, M. Sljivic, A. Radovanovic, L. Bukvic, M. Mladenovic, and A. Sindjelic, "Custom design of furniture elements by fused filament fabrication," *Proceedings of the Institution of Mechanical Engineers, Part C: Journal of Mechanical Engineering Science*, Vol.231, No.1, 88-95, 2017.
3. P. Chennakesava and Y. S. Narayan, "Fused deposition modeling-insights," *Proceedings of the international conference on advances in design and manufacturing ICAD&M*, 1345, December 2014.
4. M. L. Dezaki, M. K. A. M. Ariffin, and S. Hatami, "An overview of fused deposition modelling (FDM): Research, development and process optimisation," *Rapid Prototyping Journal*, 2021.
5. B. Brenken, E. Barocio, A. Favaloro, V. Kunc, and R. B. Pipes, "Fused filament fabrication of fiber-reinforced polymers: A review," *Additive Manufacturing*, Vol.21, 1-16, 2018.
6. Q. Sun, G. M. Rizvi, C. T. Bellehumeur, and P. Gu, "Effect of processing conditions on the bonding quality of FDM polymer filaments," *Rapid prototyping journal*, 2008.
7. T. N. A. T. Rahim, A. M. Abdullah, and H. Md Akil, "Recent developments in fused deposition modeling-based 3D printing of polymers and their composites," *Polymer Reviews*, Vol.59, No.4, 589-624, 2019.
8. J. Go, S. N. Schiffres, A. G. Stevens, and A. J. Hart, "Rate limits of additive manufacturing by fused filament fabrication and guidelines for high-throughput system design," *Additive Manufacturing*, Vol.16, 1-11, 2017.
9. S. Guessasma, S. Belhabib, and H. Nouri, "Printability and tensile performance of 3D printed polyethylene terephthalate glycol using fused deposition modelling," *Polymers*, Vol.11, No.7, 1220, 2019.
10. Y. Zhang, and K. Chou, "A parametric study of part distortions in fused deposition modelling using three-dimensional finite element analysis," *Proceedings of the Institution of Mechanical Engineers, Part B: Journal of Engineering Manufacture*, Vol.222, No.8, 959-968, 2008.
11. A. A. Samy, A. Golbang, E. Archer, and A. McIlhagger, "Simulation on Influence of Environmental Conditions on Part Distortion in Fused Deposition Modelling," *International Journal of Materials and Metallurgical Engineering*, Vol.16, No.4, 22-25, 2022.
12. D. D. Phan, J. S. Horner, Z. R. Swain, A. N. Beris, and M. E. Mackay, "Computational fluid dynamics simulation of the melting process in the fused filament fabrication additive manufacturing technique," *Additive Manufacturing*, Vol.33, 101161, 2020.
13. N. Shadvar, E. Foroozmehr, M. Badrossamay, I. Amouhadi, and A. S. Dindarloo, "Computational analysis of the extrusion process of fused deposition modeling of acrylonitrile-butadiene-styrene," *International Journal of Material Forming*, Vol.14, No.1, 121-131, 2021.
14. R. O. S. S. Costa, J. Belinha, R. N. Jorge, and D. E. S. Rodrigues, "Optimizing a meshless method for the simulation of the extrusion of non-Newtonian materials," *International Journal of Mechanical Sciences*, Vol.208, 106688, 2021.

15. M. Jahandardoost, and A. S. Milani, “Multiphysics Modeling and Experimental Investigation of the Deposition Process in Fused Filament Fabrication Method, under High-Viscosity and Non-Newtonian Material Flow,” *Journal of Materials Engineering and Performance*, Vol.30, No.9, 6913-6923, 2021.
16. N. A. Sukindar, M. K. A. Ariffin, B. H. T. Baharudin, C. N. A. Jaafar, and M. I. S. Ismail, “Analyzing the effect of nozzle diameter in fused deposition modeling for extruding polylactic acid using open source 3D printing,” *Jurnal Teknologi*, Vol.78, No.10, 2016.
17. N. Sa'ude, M. Ibrahim, and M. H. I. Ibrahim, “Melt flow behavior of polymer matrix extrusion for fused deposition modeling (FDM),” *Applied Mechanics and Materials*, Vol. 660, 89-93, 2014.
18. N. Mostafa, H. M. Syed, S. Igor, and G. Andrew, “A study of melt flow analysis of an ABS-Iron composite in fused deposition modelling process,” *Tsinghua Science & Technology*, Vol.14, 29-37, 2009.
19. R. Jerez-Mesa, J. A. Travieso-Rodríguez, X. Corbella, R. Busqué, and G. Gómez-Gras, “Finite element analysis of the thermal behavior of a RepRap 3D printer liquefier,” *Mechatronics*, Vol.36, 119-126, 2016.
20. J. Nixon, B. Dryer, I. Lempert, and D. I. Bigio, “Three parameter analysis of fiber orientation in fused deposition modeling geometries,” *Proc. of PPS conference*, June 2014.
21. A. Garcia, “Nozzle geometry effects on fiber orientation,” *SAMPE Conf Proc.*, Seattle, USA, 2017.
22. B. P. Heller, D. E. Smith, and D. A. Jack, “Effect of extrudate swell, nozzle shape, and convergence zone on fiber orientation in fused deposition modeling nozzle flow,” *2015 International Solid Freeform Fabrication Symposium*, University of Texas at Austin, 2015.
23. B. P. Heller, D. E. Smith, and D. A. Jack, “Effects of extrudate swell and nozzle geometry on fiber orientation in Fused Filament Fabrication nozzle flow,” *Additive Manufacturing*, Vol.12, 252-264, 2016.
24. J. P. Lewicki, J. N. Rodriguez, C. Zhu, M. A. Worsley, A. S. Wu, Y. Kanarska, J. D. Horn, E. B. Duoss, J. M. Ortega, and W. Elmer, “3D-printing of meso-structurally ordered carbon fiber/polymer composites with unprecedented orthotropic physical properties,” *Scientific reports*, Vol.7, No.1, 1-14, 2017.
25. C. Nahar, and P. K. Gurrala, “Transient thermal finite-element analysis of fused filament fabrication process,” *Rapid Prototyping Journal*, 2022.
26. E. Barocio, B. Brenken, A. J. Favaloro, M. Ramirez, J. Ramirez, and R. B. Pipes, “Prediction of the degree of bonding in the extrusion deposition additive manufacturing process of semi-crystalline polymer composites,” *Science in the Age of Experience*, 18-21, 2018.
27. A. Lepoivre, A. Levy, N. Boyard, V. Gaudefroy, and V. Sobotka, “Coalescence in fused filament fabrication process: Thermo-dependent characterization of high-performance polymer properties,” *Polymer Testing*, Vol.98, 107096, 2021.
28. M. Huang, Y. Xu, and A. K. Schlarb, “Mechanical performance and supermolecular morphology of void free polypropylene manufactured by fused filament fabrication,” *Journal of Applied Polymer Science*, Vol.138, No.47, 51409, 2021.

29. R. Lou, H. Li, J. Zhong, C. Zhang, and D. Fang, “A transient updated Lagrangian finite element formulation for bond formation in fused deposition modeling process,” *Journal of the Mechanics and Physics of Solids*, Vol.152, 104450, 2021.
30. E. Barocio, B. Brenken, A. J. Favaloro, M. Ramirez, J. Ramirez, and R. B. Pipes, “Prediction of the degree of bonding in the extrusion deposition additive manufacturing process of semi-crystalline polymer composites,” *Science in the Age of Experience*, 18-21, 2018.
31. A. Lepoivre, A. Levy, N. Boyard, V. Gaudefroy, and V. Sobotka, “Coalescence in fused filament fabrication process: Thermo-dependent characterization of high-performance polymer properties,” *Polymer Testing*, Vol.98, 107096, 2021.
32. Q. Sun, G. M. Rizvi, C. T. Bellehumeur, and P. Gu, “Effect of processing conditions on the bonding quality of FDM polymer filaments,” *Rapid prototyping journal*, 2008.
33. J. Zhang, X. Z. Wang, W. W. Yu, and Y. H. Deng, “Numerical investigation of the influence of process conditions on the temperature variation in fused deposition modeling,” *Materials & Design*, Vol.130, 59-68, 2017.
34. K. Khanafer, A. Al-Masri, I. Deiab, and K. Vafai, “Thermal analysis of fused deposition modeling process based finite element method: Simulation and parametric study,” *Numerical Heat Transfer, Part A: Applications*, Vol.81, No.3-6, 94-118, 2022.
35. X. Zhou, and S. J. Hsieh, “Thermal analysis of fused deposition modeling process using infrared thermography imaging and finite element modeling,” *Thermosense: Thermal Infrared Applications XXXIX*, Vol.10214, 51-64, May 2017.
36. N. Ramos, C. Mittermeier, and J. Kiendl, “Experimental and numerical investigations on heat transfer in fused filament fabrication 3D-printed specimens,” *The International Journal of Advanced Manufacturing Technology*, Vol.118, No.5, 1367-1381, 2022.
37. M. Zhou, L. Si, P. Chen, M. Li, Y. Zhang, H. Zhou, and D. Li, “Experimental investigation and numerical simulations of temperature and morphology in material extrusion additive manufacturing,” *The International Journal of Advanced Manufacturing Technology*, Vol.119, No.7, 4863-4876, 2022.
38. N. N. Kumbhar, and A. Mulay, “Post processing methods used to improve surface finish of products which are manufactured by additive manufacturing technologies: a review,” *Journal of The Institution of Engineers (India): Series C*, Vol.99, No.4, 481-487, 2018.
39. B. Akhoundi, M. Nabipour, F. Hajami, and D. Shakoori, “An experimental study of nozzle temperature and heat treatment (annealing) effects on mechanical properties of high-temperature polylactic acid in fused deposition modeling,” *Polymer Engineering & Science*, Vol.60, No.5, 979-987, 2020.
40. L. M. Galantucci, F. Lavecchia, and G. Percoco, “Quantitative analysis of a chemical treatment to reduce roughness of parts fabricated using fused deposition modeling,” *CIRP annals*, Vol.59, No.1, 247-250, 2010.
41. L. M. Galantucci, F. Lavecchia, and G. Percoco, “Experimental study aiming to enhance the surface finish of fused deposition modeled parts," *CIRP annals*, Vol.58, No.1, 189-192, 2009.

42. G. Percoco, F. Lavecchia, and L. M. Galantucci, “Compressive properties of FDM rapid prototypes treated with a low cost chemical finishing,” *Research Journal of Applied Sciences, Engineering and Technology*, Vol.4, No.19, 3838-3842, 2012.
43. E. H. Baran, and H. Y. Erbil, “Surface modification of 3D printed PLA objects by fused deposition modeling: a review,” *Colloids and Interfaces*, Vol.3, No.2, 43, 2019.
44. J. D. Spencer, “Vibratory finishing of stereolithography parts,” *1993 International Solid Freeform Fabrication Symposium*, 1993.
45. M. Fischer and V. Schöppner, “Some investigations regarding the surface treatment of Ultem* 9085 parts manufactured with fused deposition modeling,” *2013 International Solid Freeform Fabrication Symposium*, 2013.
46. Pandey P M, Reddy N V, Dhande S G. Improvement of surface finish by staircase machining in fused deposition modeling[J]. Journal of materials processing technology, 2003, 132(1-3): 323-331.
47. M. C. Gower, “Industrial applications of laser micromachining,” *Optics Express*, Vol.7, No.2, 56-67, 2000.
48. C. C. Kuo, and S. J. Su, “A simple method for improving surface quality of rapid prototype,” 2013.
49. A. A. Samy, A. Golbang, E. Harkin-Jones, E. Archer, and A. McIlhagger, “Prediction of part distortion in Fused Deposition Modelling (FDM) of semi-crystalline polymers via COMSOL: Effect of printing conditions,” *CIRP Journal of Manufacturing Science and Technology*, Vol.33, 443-453, 2021.
50. D. Syrlybayev, B. Zharylkassyn, A. Seisekulova, A. Perveen, and D. Talamona, “Optimization of the Warpage of Fused Deposition Modeling Parts Using Finite Element Method,” *Polymers*, Vol.13, No.21, 3849, 2021.
51. N. Aliheidari, R. Tripuraneni, A. Ameli, and S. Nadimpalli, “Fracture resistance measurement of fused deposition modeling 3D printed polymers,” *Polymer Testing*, Vol.60, 94-101, 2017.
52. H. Gonabadi, Y. Chen, A. Yadav, and S. Bull, “Investigation of the effect of raster angle, build orientation, and infill density on the elastic response of 3D printed parts using finite element microstructural modeling and homogenization techniques,” *The International Journal of Advanced Manufacturing Technology*, Vol.118, No.5, 1485-1510, 2022.
53. R. Rezaei, M. Karamooz Ravari, M. Badrossamay, and M. Kadkhodaei, “Mechanical characterization and finite element modeling of polylactic acid BCC-Z cellular lattice structures fabricated by fused deposition modeling,” *Proceedings of the Institution of Mechanical Engineers, Part C: Journal of Mechanical Engineering Science*, Vol.231, No.11, 1995-2004, 2017.
54. T. W. Kerekes, H. Lim, W. Y. Joe, and G. J. Yun, “Characterization of process–deformation/damage property relationship of fused deposition modeling (FDM) 3D-printed specimens,” *Additive Manufacturing*, Vol.25, 532-544, 2019.
55. R. Ghandriz, K. Hart, and J. Li, “Extended finite element method (XFEM) modeling of fracture in additively manufactured polymers,” *Additive Manufacturing*, Vol.31, 100945, 2020.
56. M. A. Bouaziz, J. M. Djouda, and F. Hild, “J-integral evaluation of additively manufactured polymer using local kinematic field measurements and finite element simulations,” *Procedia Structural Integrity*, Vol.28, 393-402, 2020.

57. M. A. Bouaziz, J. Marae-Djouda, M. Zouaoui, J. Gardan, and F. Hild, “Crack growth measurement and J-integral evaluation of additively manufactured polymer using digital image correlation and FE modeling,” *Fatigue & Fracture of Engineering Materials & Structures*, Vol.44, No.5, 1318-1335, 2021.
58. Y. Chen, L. Ye, Y. Zhang, and K. Fu, “Compression behaviours of 3D-printed CF/PA metamaterials: Experiment and modelling,” *International Journal of Mechanical Sciences*, Vol.206, 106634, 2021.
59. B. Courter, V. Savane, J. Bi, S. Dev and C. J. Hansen, “Finite element simulation of the fused deposition modelling process,” *Proceedings of the NAFEMS World Congress*, 11-14, 2017.
60. J. A. Gopsill, J. Shindler, and B. J. Hicks, “Using finite element analysis to influence the infill design of fused deposition modelled parts,” *Progress in Additive Manufacturing*, Vol.3, No.3, 145-163, 2018.
61. D. Jungivala, and P. K. Gurrala, “Finite element analysis of fused filament extrusion build part using different build orientation,” *Materials Today: Proceedings*, Vol.38, 3264-3268, 2021.
62. X. Zhou, S. J. Hsieh, and C. C. Ting, “Modelling and estimation of tensile behaviour of polylactic acid parts manufactured by fused deposition modelling using finite element analysis and knowledge-based library,” *Virtual and Physical Prototyping*, Vol.13, No.3, 177-190, 2018.
63. Z. Wang, Z. Fang and D. E. Smith, “Effects of Local Fiber Orientation State on Thermal-Mechanical Behaviors of Composite Parts Made by Large Area Polymer Deposition Additive Manufacturing,” *2021 International Solid Freeform Fabrication Symposium*, 2021.

The failure study of post-buckled composite single-stringer panel

*CHENG Linan[1**], WANG Houbing[1], WANG Yuan[2]*

1.Aeronautics Science and Technology Key Laboratory of Full Scale Aircraft Structure and Fatigue, Aircraft Strength Research Institute of China, Xi'an 710065, China

2.Shanghai Aircraft Design and Research Institute, Commercial Aircraft Corporation of China, Ltd. Shanghai 201210, China

Abstract: Non damage and with low-velocity impact damage specimens under uniaxial compression and tension of stiffened composite panel was conducted to study the failure load and failure modes. The interface de-bonding between stringer and skin was simulated by using the Cohesive Zone Model（CZM） in the commercial software ABAQUS. The numerical result is in good agreement with experimental one. The results indicate that: non damage specimen has comparatively large load capacity of the structure after buckling, and the interface de-bonding leads to damage evolution quickly, the load of crack initial occurred equal to failure load. Low-velocity impact damage has significant influence on the buckling load , failure load, and failure mode. This study further shows that from 10°to 30°angles of stringer run-out, the buckling load and failure load gradually increases.

Key words: composite; cohesive zone model; post-buckling; panel-stiffener; interface de-bonding

Introduction

Because of its high specific strength, large specific modulus and good fatigue resistance, carbon fiber composites have become an advanced material widely used in the fields of aviation, spaceflight and shipbuilding, structural integration has become an important way to realize the lightweight, high efficiency and low cost of composite structures [1] . As a typical integrated structure of composite materials, composite stiffened panels can achieve the advantages of strong design, high load-bearing efficiency and light weight of the structure by bonding different types of stiffeners to the composite laminate.

At present, composite panels are widely used in aerospace and other lightweight structures (such as fuselage, wing and tail) , and the safety of fuselage structure directly affects the safety of aircraft. Due to the influence of manufacturing process and assembly operation, there may be local defects at the interface of skin and rib, which become the starting point of cracking

and have a significant effect on its bearing capacity and failure behavior, is an important part of structural integrity assessment [2-5] .

The impact of composite structure is always a hot spot at home and abroad because of its outstanding engineering application value. The adhesive interface between skin and rib is usually the weak link of reinforced structure, the initial debonding load is the most concerned load in the design of the panel structure, and its size directly affects the design load level of the structure. In the process of aircraft service, the debonding defect of the adhesive interface between skin and rib will easily expand under the action of out-of-plane load, which will cause large-area debonding of the adhesive interface and delamination of the laminate, and force the structure to fail ahead of time, a threat to structural integrity. It is very important to study the influence of debonding defect on the failure process, failure form and bearing capacity of stiffened panel structure to ensure aircraft safety, improve the structural design of stiffened panel and repair the damage. It has been shown that the initial debonding load can be improved by beveling at the end of stiffeners, but few studies have been done on the beveling angle at the end of cap stiffened panels [6-10].

In this paper, the impact damage is introduced to the impact specimen, and the tensile and compressive un-iaxial tests of intact and damaged cap stiffened panel specimens are carried out, the failure modes and loading curves of the cap stiffened panels under corresponding loads are obtained. The de-bonding of the truss-skin bonding interface and delamination of the laminates are observed. At the same time, based on the finite element software ABAQUS, the cohesion model (CZM-technique is used to simulate the de-bonding of the stiffener-skin of the composite stiffened panel structure, and the effect of the debonding of the stiffener-skin on the failure load and failure mode of the structure is obtained, the influence of the cut-off angle on the buckling load and failure load of the structure is also studied.

1 Test piece

In order to simulate the actual supporting conditions of the structure, the two-truss end-points are designed in this paper, and the dimensions of the two-truss end-points are shown in Figure 1, the material of the test piece is M21E/IMA, the layer of steel bar is [45/0/0/-45/90/-45/0/0/45] , the layer of skin is [45/-45/45/90/0/90/-45/0] s, the theoretical thickness of single layer is 0.1867 mm after curing. The length of the skin is 800mm, the width is 240mm, the height of the hat truss is 32mm. There are 8 test pieces in 4 groups. The No. 2 test piece in each group is the impact damage test piece. The angles between the cap bottom and the hat waist of the 4 groups are 10 ° , 20 ° , 25 ° and 30 ° respectively.

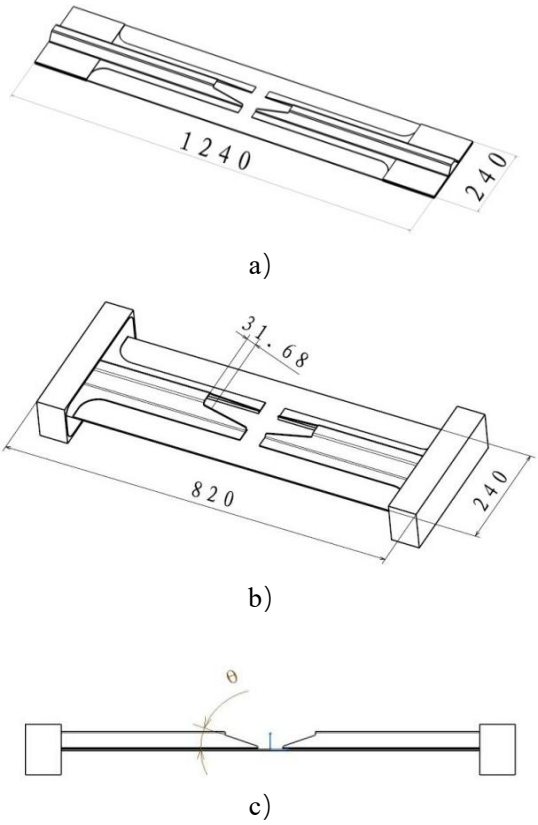

Fig.1 Geometry and dimensions for panel-stiffener

2 Impact damage introduced

The impact damage was introduced to each group of 2 # test pieces by using the hammer impact testing device, and the diameter of the hemispherical punch was 16mm. The impact energy is 35J at the joint of the hat-shaped ribs and the skin, and the impact point is at the skin surface. The impact energy is 3J at the hat waist at the end of the truss, and the impact point is at the center of the hat waist, in this paper, the support frame is designed and the out-of-plane support is applied to the specimen. The concrete impact position of the specimen is shown in Fig. 2.The impact test of panel-stiffener is shown in Fig.3. The typical NDT results after impact damage are shown in Fig. 4.

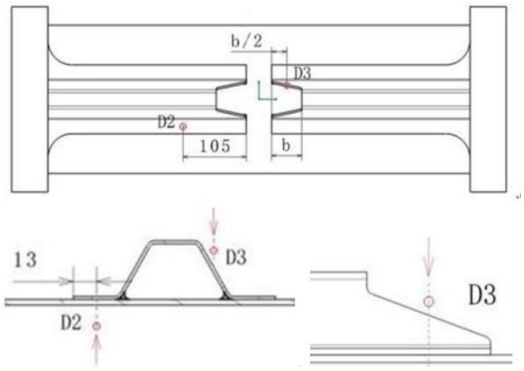

Fig.2 The impact test of panel-stiffener

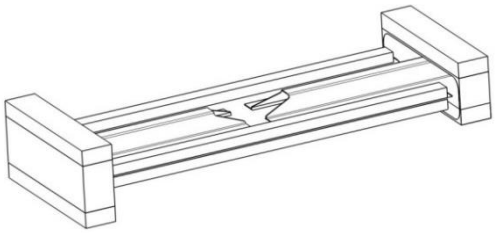

Fig.3 The impact test of panel-stiffener

The nondestructive test showed that the impact of the inclined cut-off area caused local delamination at the rib waist, and the maximum delamination area was 20mm ×10mm. No debonding of the truss skin was observed. The maximum delamination area is 30mm× 25mm, the pit depth is 0.12 mm, and the maximum debonding area is 140mm ×25mm for the bonding interface between flange and skin at the impact point, at the same time caused the other side flange and skin adhesive debonding, debonding area of the largest 83mm×25mm. Detailed record results are shown in Table 1.

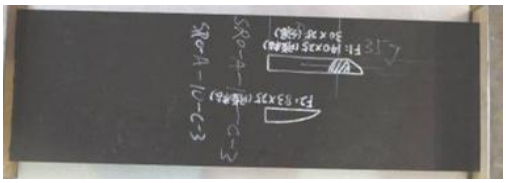

a）D2

b）D3

Fig.4 The result of non-destructive testing

Table 1 The detail results of non-destructive testing

Specimen number	Impact energy /J	Pit Depth/mm	Area of damage/ mm×mm	Nature of damage
Com -A- -20-2	35	0.11	F1：140×25 F2：83×25	stringer-skin debonding
			30×25	skin lamination
	3	/	F3：10×6	stringer lamination

3 Test of composite single-stringer panel

3.1 Test method

The number and position of the strain gauge are shown in Fig. 5. The position of the strain gauge is divided into four sections: A, B, C and D, back-to-back position of the skin surface strain gauge number + 1000. For example: a section of the rib section strain gauge No. 1001, corresponding to the skin surface strain gauge no. 2001.

The compression test of composite cap stiffened panel was carried out on Zwick Z2000E compression testing machine, and the tensile test was carried out on 150T self-balanced tensile frame. At the free side of the panel skin, a side support fixture is arranged to prevent the side from the unexpected failure such as instability, and a special side follow-up support fixture is used to simulate the simple support of the frame at the docking frame of the cut-off end. During the test, first adjust the positive pressure center, after the low-load test completed the formal test, the test piece installation support status as shown in Figure 6. When carrying out damage test, take 5kN as one stage loading, load to 30kN unload, check the working state of jig, loading equipment and measuring instrument, then take 5kN as one stage loading to 80kN, then it is loaded step by step at the level of 2kN until the structure breaks down.

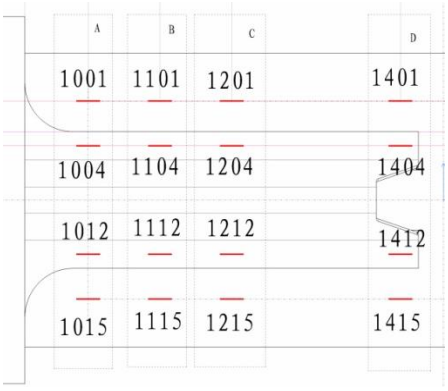

Fig.5 Number of strain gauges on stiffener plane

a)

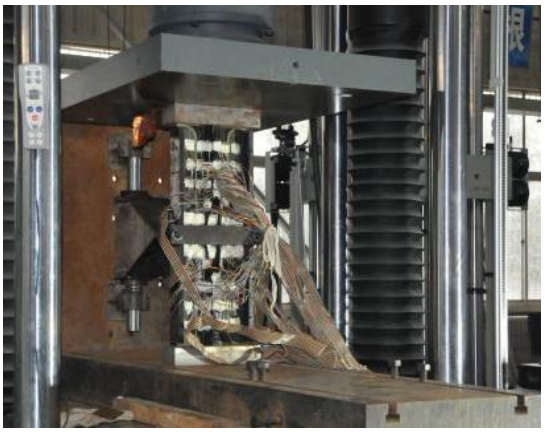

b)

Fig.6 Supporting and loading methods of stiffened composite panel specimen

3.2 Test results of intact specimens

In this paper, all the intact specimens in the test phenomenon is similar, because the different cut angle at the end of the bevel lead to stiffened panel structure buckling load and bearing capacity is different, the buckling loads and failure loads of all intact specimens are shown in Table 2, so take the Com-A-20-1 specimen as an example. Figure 7 shows the load-strain curve during the test of the COM-A-20-1 specimen, as can be seen from the figure, the strain increases linearly with the load at the initial stage of the test. When the load reaches 55 kN, the slope of the strain gauges of D section 1408 # and back-to-back 2408 # (located in the skin at

the end of the rib) changes, the results show that the structure has local buckling and the wave shape is located in the skin area at the cut-off end, and no abnormal condition is found when the specimen is loaded further, and the crisp sound can be heard during the test when the load reaches 213kN ~ 217kN, the slope of the 1404 # strain gauge and the 1412 # strain gauge located on the rib flange at the cut-off end) D section changes to 0, and the strain of the 1412 # strain gauge changes in reverse, where the load is borne by the skin, it can be observed that the rib flange-skin debonding at the cut-off point, the slope of 1204 # strain gauge and 1212 # strain gauge does not change, indicating that the debonding only takes place at the cut-off point, and the buckling wavelength of the skin at the cut-off point increases after debonding, the skin at the cut-off end is broken along the width direction of the specimen, and the structure rapidly fails under high compressive load.

Table2 Buckling load and failure load of non damage specimen under uniaxial compression

Specimen number	Buckling load/kN	Failure load/kN
Com-A-10-1	60	155
Com-A-20-1	76	185
Com-A-25-1	80	198
Com-A-30-1	85	226

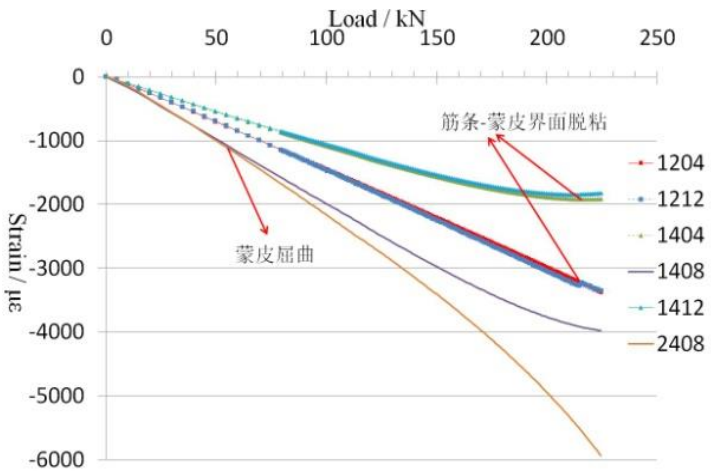

Fig.7 Load-strain curve of non damage specimen under uniaxial compression

The failure mode of the intact specimen under axial loading is shown in Fig. 8. In the intact specimen test, the buckling of the skin is first observed at the skin surface at the cut-off end, and the skin bulges in the opposite direction to the truss, the post-buckling process of the composite stiffened plates is demonstrated by the fact that the specimens do not fail immediately after buckling and can continue to bear load, after debonding, the local flexural modulus at the cut-off point decreases, and the load on the original rib gradually transfers to

the skin, and the skin continues to buckle, subsequently, the skin at the cut-off point collapses rapidly within a small load range, and the adhesive layer at the cut-off point of the intact specimen completely debonders as shown in Figure 9.

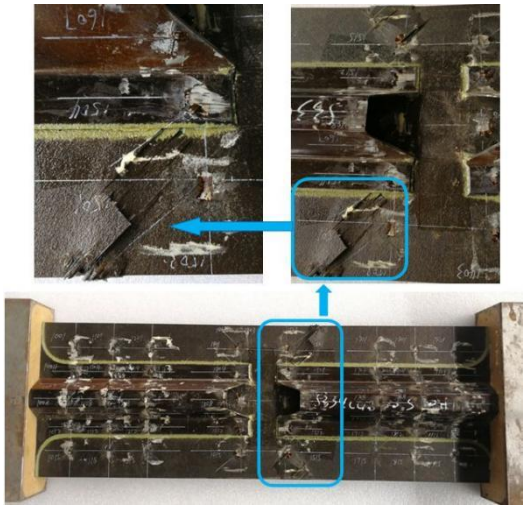

Fig.8 Failure mode of non damage specimen under uniaxial compression

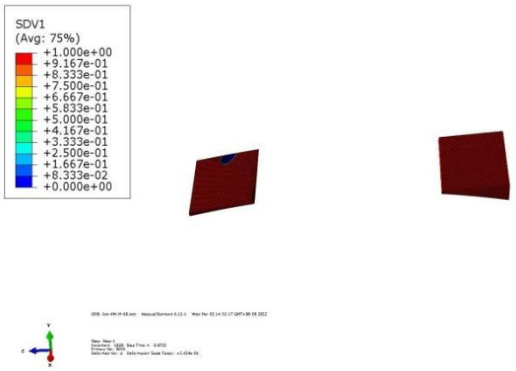

Fig.9 De-bonding of cohesive non damage specimen under uniaxial compression （Dis=3.6mm）

The failure pattern of the intact specimen under tensile loading is shown in Fig. 10. In the intact specimen test, the buckling of the skin is first observed at the cut-off skin surface, and the skin of the specimen bulges in the direction of the truss, the post-buckling process of the composite stiffened plates is demonstrated by the fact that the specimens do not fail immediately after buckling and can continue to bear load, after debonding, the local bending modulus at the cut-off point decreases, and the load on the original rib gradually transfers to the skin, the skin continues to buckle.

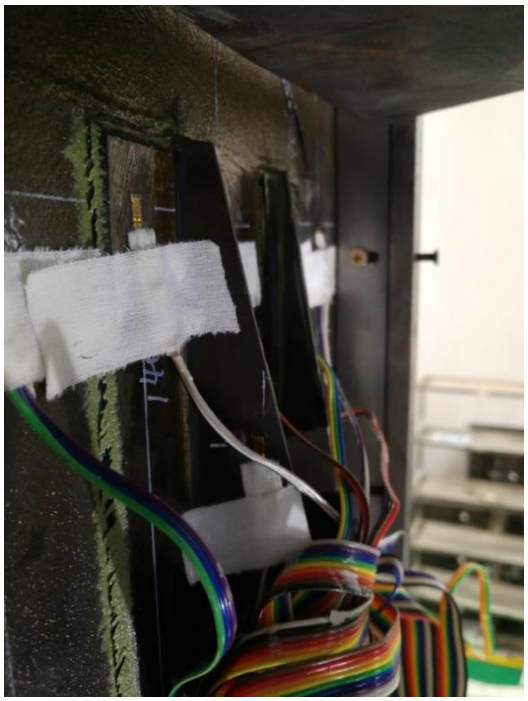

Fig.10 Failure mode of non damage specimen under tension compression

3.3 Test results with damaged specimens

In this paper, all damaged parts of the test phenomenon is similar, buckling load and failure load is basically the same, all damaged parts of the buckling load and failure load as shown in table 3. Therefore, taking the COM-A-30-2 specimen as an example, fig. 11 shows the load-strain curve during the non-destructive test. From the diagram, it can be seen that the strain increases linearly with the load at the initial stage of the test, and when the load reaches 30kN, the strain gauges of D section 1408 # and back-to-back 2408 # (located in the center of the skin at the bottom of the rib) and C Section 1215 # and back-to-back 2215 # (located in the skin) appear to be inflected, it shows that the structure has local buckling, and the wave shape is located in the skin region from the cut-off end to the impact-induced debonding, the slope of C Section 1215 # strain Gage and back-to-back 2215 # strain gage (located in the skin) changed suddenly, and the specimen made continuous sound. It was found that the adhesive interface between the strain gage and the skin was damaged. When loading to 97kN, continuous crisp sound can be heard during the test, the slope of a section 1001 # strain gauge and back-to-back 2001 # strain gauge (on the skin surface) and B section 1101 # strain gauge and back-to-back 2101 # strain gauge (on the skin surface) suddenly increases, it is found that the debonding damage extends along the truss to the bonding interface between the edge strip and the skin near the strain gage, the steel strip completely loses its bearing capacity, and the skin at the filling end rapidly loses its stability under high compression load.

Table3 Buckling load and failure load of low-velocity impact damage specimen under uniaxial compression

Specimen number	Buckling load/kN	Failure load/kN
Com-10-A-2	30	102
Com-20-A-2	35	102
Com-25-A-2	40	122
Com-30-A-2	35	100

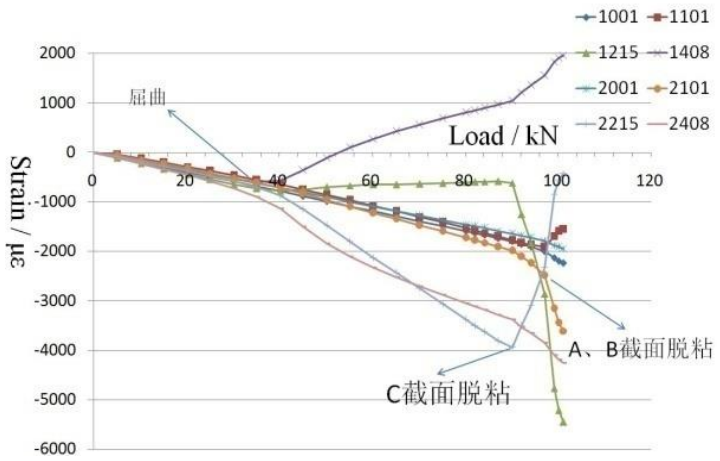

Fig.11 Load-strain curve of low-velocity impact damage specimen under un-iaxial compression

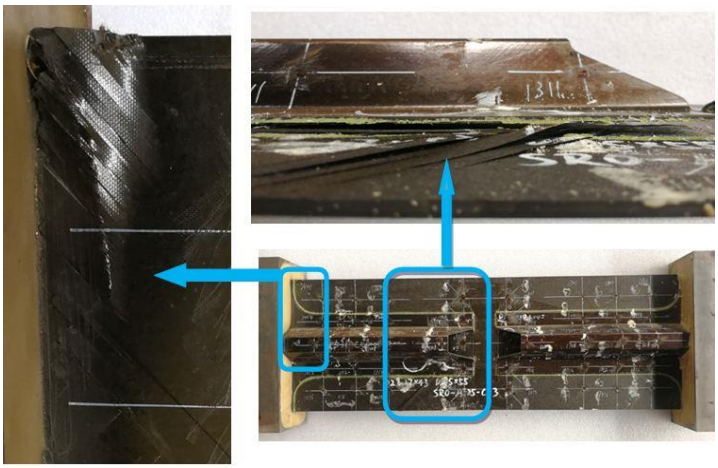

Fig.12 Failure mode of low-velocity impact damage specimen under uniaxial compression

The failure pattern of the impact damaged specimen under axial loading is shown in Fig. 12. After loading to a certain load, it is observed that the skin of the damaged specimen buckles from the cut-off point to the debonding position caused by the impact, the specimen skin bulges in the opposite direction of the truss, and with the load increasing, the band-skin debonding gradually extends to the loading end, and with the continuous crisp sound, the load-bearing capacity of the skin continues to increase, after debonding the rib flange and the skin completely, the rib and the skin are separated, and the high stability structure which the rib and the skin bear together is destroyed.

It is found that the failure load of the test piece is much greater than the buckling load, which indicates that the cap stiffened panel structure studied in this paper has a strong post-buckling capacity, the advantages of this kind of structure should be fully utilized in engineering applications.

4 Analysis of influencing factors

4.1 Impact damage effects

As shown in Fig. 13, the load-displacement curves of the test and finite element calculation for the intact and damaged specimens show that the stiffness of the damaged specimen is less than that of the intact specimen, the main reason is that the impact damage of the skin caused a certain range of debonding of the rib flange-skin bonding surface at the cut-off point, the initial buckling load decreases about 53% when the buckling wave length of the skin increases to the point of tendon-skin debonding, and the exfoliation stress of the rib flange-skin bonding surface increases, which results in the decrease of the bending stiffness of the structure, the post-buckling capacity of the structure is limited, and the average failure load of the structure is reduced by 43% .

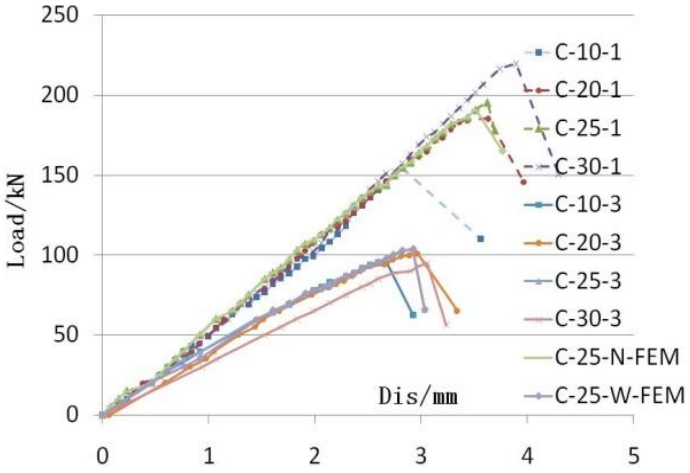

Fig.13 Load-displacement curve of test and FEM of non damage and low-velocity impact damage specimen

After the test, the nondestructive test shows that the delamination of the skin caused by the impact damage on the skin surface has not been expanded, and the delamination caused by the impact damage on the waist and cap of the cut-off end has not been expanded, it shows that the decrease of the load-bearing capacity and stiffness of the stiffened panel structure is mainly caused by the interface debonding, and the delamination of the skin and the cap-waist at the cut-off point has no effect on the structural failure.

4.2 The effect of the cut-off angle on the beveling angle

The effect of cutting angle on cut-off is studied by means of single variable method. Four groups of intact specimens are selected, and the cutting angle is 10 ° , 20 ° , 25 ° , 30 ° respectively, the failure load of the compressed intact specimen is basically the same as that of the tendon-skin debonding load, so the failure load is used instead of the debonding load. The buckling and debonding loads of the compressed specimen vary with the angle as shown in Fig 14, the initial debonding load of the tensile specimen varies with the angle as shown in figure 15.

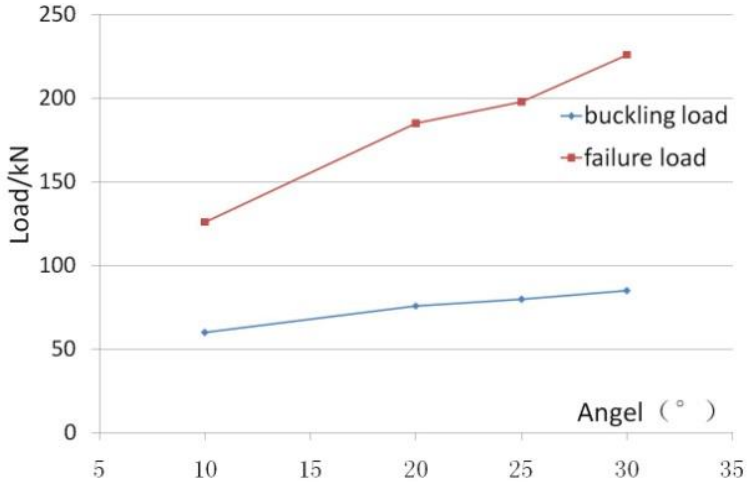

Fig.14 Buckling load and de-bonding load of non damage specimen under un-axial compression follow the angle

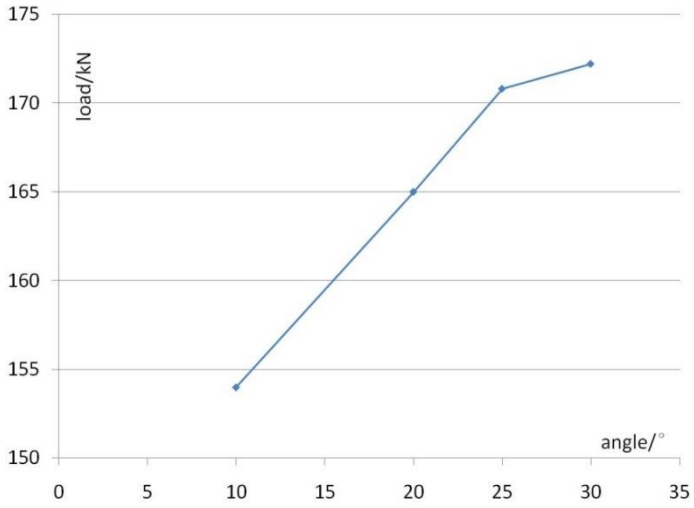

Fig.15 De-bonding load of non damage specimen under tension follow the angle

The bending modulus of the beveled section is decreased due to the beveled cutting of the end, and the local bending of the end will be aggravated under the load, the buckling load and failure load increase with the increase of bevel angle.

5 Conclusion

Through the analysis and experimental verification of composite cap stiffened panel considering impact damage and cut-off angle under compression load, the conclusions are as follows:

1) cohesive elements can be used to simulate the interface debonding of composite stiffened panels;
2) the debonding of flange-skin adhesive layer is the main cause of the structural failure of stiffened panels, which leads to the rapid damage evolution and loss of load-bearing capacity;
3) the debonding of flange-skin adhesive surface at the cut-off due to impact damage greatly reduces the buckling load and failure load of the panel structure;
4) with the decrease of the cut-off angle, the premature buckling of the skin leads to the increase of the exfoliation stress of the flange-skin adhesive surface, and at the same time, the structural bending stiffness decreases, which limits the post-buckling load-bearing capacity of the structure;
5) the research in this paper has certain reference value for the structural design of stiffened panels and the selection of structural details at the cut-off points, which need to consider the impact damage.

References

[1] Jeff W.H. Yap, Murray L. Scott , Rodney S. Thomson, Dieter Hachenberg. The analysis of skin-to-stiffener de-bonding in composite aerospace structures. Composite Structures，2002，（57）：425–435.

[2] K. Vijayaraju, P.D.Mangalgiri, B.Dattaguru. Experimental study off ailureand failure progression in T-stiffened skins. Composite Structures，2004（64）：227–234.

[3] Huang L K，Zhu L B，Zhang X M，et al. Interfacial stresses and failure simulation of composite hat-stiffened panel. Fiber Reinforced Plastics/Composites.2017（5）：34-40.

[4] Sun J J，Zhang X J，Wang H，et al. An experimental and Numerical Study on Composite Omega Stringer Debonding. 17th National Conference on Composite Materials. October，12-15，2012：80-86.

[5] Krueger R，Minguet R J. Analysis of composite skin-stiffener debond specimens using a shell/3D modeling technique. Composite Structures，2007，81（1）：41-59.

[6] van Rijn J C F N. Failure criterion for the skin-stiffener interface in composite aircraft panels.NLR-TP-98264，1998.

[7] Liu C Y，Xu X W，Chen K. Buckling，post-buckling and collapse analysis of stiffened composite panels with de-bonding damage. Acta Materiae Composite Sinica.2010，27（6）：158-166.

[8] Sun Qixing，Chen Puhui. Failure analysis of composite panels in stiffener run out region [J] . Journal of Nanjing University of Aeronautics & Astronautics: Natural Science Edition，2008，40（4）：513-516.

[9] Orifici A C, Shah S A, Herszberg I, Kotler A, Weller T . Failure analysis in post-buckled composite T-sections [J].Composite Structures, 2008, 86(1/ 3) : 146-153.

[10] Orifici A C, Thomson R S, Herszberg I, Weller T , Degenhardt R, Bayandor J. An analysis methodology for failure in post-buckling skin-stiffener interfaces [J] . Composite Structures, 2008, 86(1/3) : 186-193.

Micro-structure modeling and elastic properties prediction of 3D five-directional and full five-directional braided composites

Youlei Peng[1, 2, +], *Guangran Shao*[1, 2], *Jiatao Zhao*[1, 2], *Zhibo Wu*[1, 2], *Jian Deng*[1, 2, *]

[1]State Key Laboratory of Mechanics and Control for Aerospace Structures, Nanjing University of Aeronautics and Astronautics, No. 29 Yudao Street, Nanjing 210016, China

[2]College of Aerospace Engineering, Nanjing University of Aeronautics and Astronautics, Nanjing 210016, China

Abstract: As a third-generation fiber-reinforced composite material, 3D braided composites have become the preferred material for aircraft structural components due to the fact that the fiber bundles in the reinforcement extend along multiple directions in space and interweave with each other to form an overall network structure, which overcomes the fatal shortcomings of low inter-laminar strength and low delamination resistance of conventional laminated composites. In this paper, based on the motion law of yarn carrier in four-step braiding process, the motion trajectory and spatial direction of yarn in each unit cell area were studied for 3D five-directional and full five-directional braided composites. The inner cell yarn topology of 3D five-directional and full five-directional braided composites were given, and the inner cell model was established based on CATIA platform. At the same time, based on the theory of three-cell model and the idea of homogenization averaging, the elastic constants of 3D five-directional and full five-directional braided composites with braiding angle from 10° to 45° were predicted by numerical analysis method, and the variation of elastic properties with braiding angle and fiber volume fraction were discussed. Static tensile experiments were also carried out. The experimental data were in good agreement with the simulation results, which verified the reliability of the model. It was found that the inner cell model of the 3D five-directional and full five-directional braided structure exhibited transversely isotropic characteristics, and the braiding angle and fiber volume fraction were the main parameters affecting the elastic properties of the braided structure. The 3D full five-directional braided structure enhanced the axial tensile properties while maintaining the excellent mechanical properties of the 3D five-directional composite material due to the addition of the axial yarn in the resin-rich region.

1. INTRODUCTION

Multifunctional light-weighting of materials and structures is a key focus in the aerospace industry. Composite materials are widely used in this field due to their good designability, high specific modulus, high specific strength, good fatigue resistance, corrosion resistance, low maintenance and operating costs, and are also one of the most promising materials since the new era. However, conventional laminated composites have fatal defects such as low inter-laminar strength and low delamination resistance. As the third generation of fiber-reinforced composites, three-dimensional (3D) braided composites, in which fiber bundles extend in multiple directions and are braided to form a complete network structure, overcome the shortcomings of traditional laminated compositeswhile retaining their advantages, making them the preferred material for aircraft strucutral components. Currently, the mechanical properties of 3D braided structures with five, six, and seven directions are widely studied. However, there still exist limitations in terms of strength and stiffness, especially in 3D five-directional braided structures, which contain a large number of unidirectional gaps that affect the fiber volume fraction and mechanical properties of the material. To address this issue, researchers have begun to study 3D full five-directional braided composites, which have a more complete fiber structure, effectively improving their axial mechanical properties. The study of these materials is critical to improve their mechanical properties and application range, and to meet more complex engineering and application requirements. To date, there have been few reports on the micro-structure and mechanical properties of 3D full five-directional braided composites. Therefore, in this paper, we analyze the single cell structural parameters of both 3D braided and full five-directional braided composites, establish a single cell geometry model for the internal area of the material, predict their elastic properties, and discuss the relationship between these properties and braiding angle and fiber volume fraction. The differences between 3D five-directional and full five-directional braided composites were also studied.

2. Micro-structure analysis and modeling

2.1 Four-step 1x1 3D five-direction, full five-direction braiding process

The four-step 1×1 braiding process is the main method for manufacturing 3D braided composites. The braiding machine chassis is equipped with yarn carriers, each carrying a bundle of yarn. The yarn follows cyclic four-step movements of the machine chassis and, after being tightened, forms a 3D braided composite with a length of one flower repeat. By continuously repeating this process, the desired 3D braided composite preform can be produced. This is why it is called the four-step braiding process. For the 3D five-directional braiding process, axial yarn carriers are added to the nearby braiding yarn carriers on the basis of the four-step braiding process. The newly added axial yarn is braided by being wrapped by the adjacent braiding yarn. The arrangement and movement rules of the braiding yarn and the axial yarn carriers are shown in Figure 2.1. In the first step of machine movement, the braiding yarn and axial yarn carriers of adjacent rows move alternately one position in the x-direction. In the second step, the braiding yarn carriers of adjacent columns move alternately one position in the y-direction. The third step is the reverse of the first step, and the fourth step is the reverse of the second step. After a braiding cycle is completed, the arrangement of the yarn carriers on the chassis returns to the initial position, and the "tightening" process ensures tight contact

between the braiding yarn and the axial yarn, as well as between the braiding yarns. The preform of the 3D braided composite extends in the forming direction (z-direction) by a height of h after each braiding cycle, and can be formed through such four-step movements and the "tightening" process. It should be noted that the axial yarn carriers move only in the row direction during the four-step movements. The total number of braiding yarns in the preform is N_1, and the total number of axial yarns is N_2. Therefore,

$$N_1=mn+m+n \tag{1}$$

$$N_2=mn \tag{2}$$

In the equation, m and n are the number of rows and columns of braided yarn respectively. Therefore, the total number of yarns of 3D braided preforms can be obtained.

$$N=N_1+N_2 \tag{3}$$

As shown in Figure 2.5, the 3D full five-directional braiding process is a variation of the previously mentioned 3D five-directional braiding process, with the addition of fixed axial yarn between adjacent rows. The four-step motion pattern of the braiding yarn carriers and fixed axial yarn carrier is exactly the same as that of the 3D five-directional braiding process, while the fixed axial yarn carrier remains stationary throughout the entire braiding process. The main difference between the two braiding processes lies in the fact that the 3D full five-directional braiding process requires more axial yarn carriers, which results in the filling of more non-axial yarn voids in the 3D five-directional braiding structure with the fixed axial yarn. If the total number of braiding yarns in the 3D full five-directional rectangular preform is N_1, the total number of axial yarns is N_2, and the total number of fixed axial yarns is N_3, then:

$$N_3=(m-1)(n-1) \tag{4}$$

where m and n are the number of rows and columns of the main yarn, respectively. The total number of yarns of 3D full five-directional braided preforms can also be obtained.

$$N=N_1+N_2+N_3 \tag{5}$$

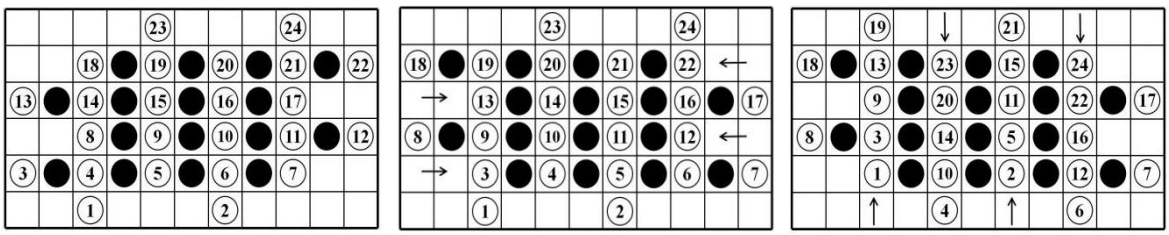

(a)Initial state (b)Step 1 (c)Step 2

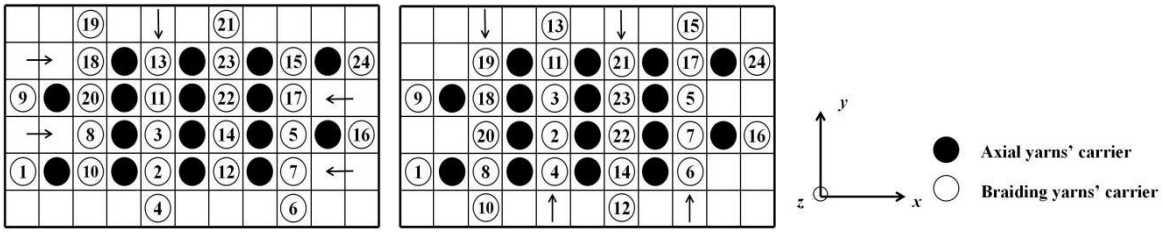

(d)Step 3 (e)Step 4

Fig. 2.1 Four-step braiding process flow chart

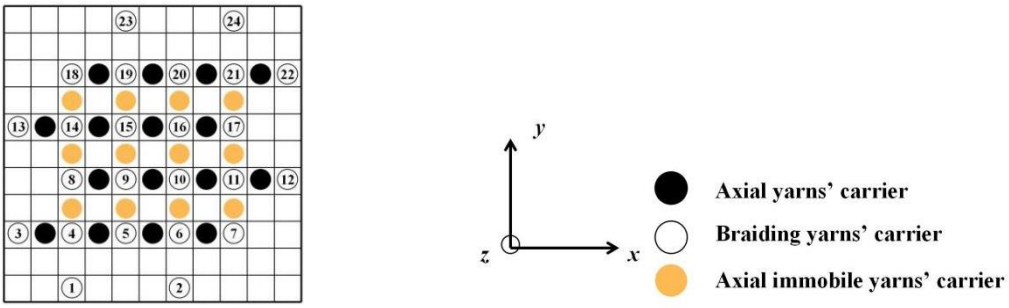

Fig 2.2 Original diagram of arrangement of yarn carriers in 3D full five-directional knitting process

2.2 Yarn movement law

The motion characteristics of yarn in braiding can be analyzed from two aspects: in-plane motion and spatial motion. In the process of braiding three-dimensional five-directional composite preforms, the take-up device of the braiding yarn moves in a "Z" shape in-plane motion, as shown in Figure 2.2. Taking the braiding yarn take-up device A as an example, after the yarn goes through a cycle of motion and the "tightening" process, the tension of the yarn makes the internal yarn in three-dimensional braiding composite material remain in a taut state. The projection of the yarn in-plane motion is the mid-point connection of adjacent positions during the yarn's motion, as shown in Figure 2.2 as A'E'. The axial yarn always moves within the QR range, and the midpoint S in QR is the projection of the axial yarn's in-plane motion trajectory.

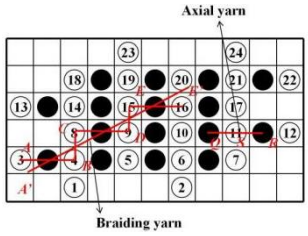

Fig 2.3 In-plane motion law of yarn carrier

From the perspective of spatial motion, the weft yarn of 3D braided composite material extends one quarter of the flower unit height in the z direction after each step of the braiding process. As shown in Figure 2.3(a), the weft yarn moves from point A to point E in space, undergoing

four steps. Under the effect of tightening and yarn tension, the trajectory of the yarn in space is a straight line A'E', located in two orthogonal planes with the cross-section of the preform at ±45°, and the angle between the trajectory and the z direction is γ. γ is defined as the internal braiding angle of the 3D braided composite material unit cell model.

For the axial yarn of 3D five-directional braided composites, since the axial yarn does not participate in the entire braiding process, the four-step motion of the axial yarn carrier Q always remains within the range of QR. Therefore, the spatial trajectory of the axial yarn is a straight line parallel to the z-axis, passing through the midpoint of the axial yarn carrier position, as shown in Fig 2.3(b).

(a)Internal yarn space direction (b)Axial yarn space direction

Fig. 2.4 Spatial movement trend of 3D five-directional braided yarn

2.3 Selection and establishment of unit cell model

The actual microscopic structure and spatial configuration of 3D five-directional and full five directional braided composites are quite complex. Therefore, the following basic assumptions are made during modeling:

(1) The internal braided yarns of the single-cell structure are assumed to extend straight in space, taking into account the influence of the "tightening" process and the compression of other direction braided yarns and axial yarns. The cross-sectional shape of the braided yarn is assumed to be a hexagon inscribed in an ellipse, with the long and short semi-axes denoted by a and b, respectively.

(2) The axial yarns are straight parallel to the z-axis in space, with a square cross-section, and the parallel edges of the cross-section form ±45° with the cross-section of the prefabricated body. The length of each edge is denoted by r_b.

(3) The braiding process remains stable and does not damage the mechanical properties of the yarns, ensuring a uniform and consistent braided component over a certain length. The projection of all yarns in the x-y plane for the 3D five-directional and full five directional braided structures is shown in Figure 2.5, where solid lines represent braided yarns, and the axial yarns are evenly distributed between them. The braided yarns are intertwined and wrapped around the axial yarns. The angle φ represents the horizontal orientation angle, which is ideally φ=±45°. The selection of the inner cell model is shown in Figure 2.4.

(a)3D five-directional braided structure (b)3D full five-directional braided structure

Fig 2.5 Horizontal projection of yarn and selection of inner cell model

Based on the basic assumptions of modeling the micro-structure and spatial configurations of each single cell yarn in various regions, the structural parameters of the single cell model can be obtained, which served as the basis for calculating the fiber volume content of the entire composite structure and establishing a parameterized solid structure model in the future. The 3D five-directional and full five directional braided composite preform, formed by the four-step braiding process, interweaves the braided yarns and axial yarns, extending in multiple directions and intertwining with each other to form a cohesive network structure. Based on the micro-structure analysis of the 3D five-directional and full five-directional braided composites, the topological relationship of yarns within the rectangular hexahedral cell is illustrated in Figure 2.6. Further characterization of the internal cell model leads to relevant parameters for the internal cell structure based on the basic modeling assumptions.

(a)3D five-directional braided structure (b)3D full five-directional braided structure

Figure 2.6 Yarn topology diagram

The braiding angle is a critical structural parameter for 3D five-directional and full five-directional braided composites. However, it is difficult to directly measure the braiding angle after material formation. In practical applications, the braiding angle α (hereafter referred to as the braiding angle) is measured, which is defined as the angle between the surface yarn pattern formed by adjacent aligned braiding yarns on the surface of the specimen and the braiding direction z. For the microscopic cell model of 3D five-directional and full five-directional braided composites, the internal braiding angle γ is related to the braiding angle α as follows:

$$\tan\alpha = W_i / (\sqrt{2}/2)\tan\gamma \tag{6}$$

For the hexagonal cell model, the width W_i, thickness T_i and height h are :

$$W_i = 2\sqrt{2}(2+r)b, \quad T_i = 2\sqrt{2}(2+r)b, \quad h = 4(2+r)b/\tan\gamma \tag{7}$$

The equation involves the axial section size factor, r. This model is based on the CATIA modeling platform and utilizes a parameterized modeling approach with V_f, α, and r as the main input variables. 3D five-directional and full five-directional braided composite material parameterized microstructural cell three-dimensional geometric model is established. For solid models under different braiding process conditions, only the basic variable parameters need to be changed in the parameterized model to generate the required internal cell model. The 3D five-directional and full five-directional braided composite material parameterized microstructural cell CATIA model is shown in Figure 2.7.

(a)3D five-directional braided composite inner cell (b)3D full five-directional braided composite inner cell

Fig 2.7 Geometric model diagram

3. Calculated results and discussion

3.1 example verification

In order to verify the effectiveness of the established single-cell model, a tensile test on 3D five-directional braided composites was carried out as a case study. The experiment was conducted at the Nanjing Fiberglass Institute Standard Research Institute, with the MTS testing machine used for loading, and the tensile test was conducted according to the standard GB/T33613-2017. The material properties of the fibers and matrix, geometric parameters of the test specimens, and corresponding inner cell structure parameters are shown in Tables 3.1.

Table 3.1 Performance parameters of fiber and matrix materials, geometric parameters of 3D five-directional braided specimens and structural parameters of inner cell finite element model

Component materials	E_{f1}/GPa	E_{f2}/GPa	G_{f12}/GPa	G_{f23}/GPa	μ_{f12}	E_m/GPa	G_m/GPa	μ_m
Carbon fiber(CCF800G)	288	22. 9	41. 5	7	0. 22	-	-	-
Resin(ACTEC						3. 53	1. 48	0. 37

H 1304)

Geometric parameters of specimen			Intracellular structural parameters				
α/°	V_f	Dimension/mm	γ/°	h/mm	r	W_i/mm	T_i/mm
27. 39	53. 61%	250×25×3. 36	36. 23	2	2	1. 036	1. 036

Table 3.2 Comparison of experimental values and simulation data of t3D five-directional braided specimens

Elastic modulus	Test times	Experimental value	Predicted value
Ez/GPa	1	87. 92	85. 87
	2	82. 66	

It should be noted that the structure of the 3D braided composite material should contain three types of structures, including inner cells, surface cells, and corner cells, from the perspective of microscopic structure analysis. However, the inner cells account for a relatively large proportion in the three single-cell model, thus this paper only analyzes the inner cells in the 3D braided composite material. From the results of the two tests, the established inner cell model in this paper is in good agreement with the experimental data verifying the reliability of the inner cell model. The comparative results also indicate that the finite element model of the inner cell established in this paper is suitable for predicting the elastic properties of 3D braided composites.

3.2 Discussion on elastic properties changing with parameters

For 3D braided composites, in addition to the influence of braiding process on the mechanical properties of materials, the braiding angle and fiber volume fraction are the main parameters that directly affect the micro-structure and mechanical properties of materials, and are also the main parameters considered in the design and optimization of 3D braided composites.

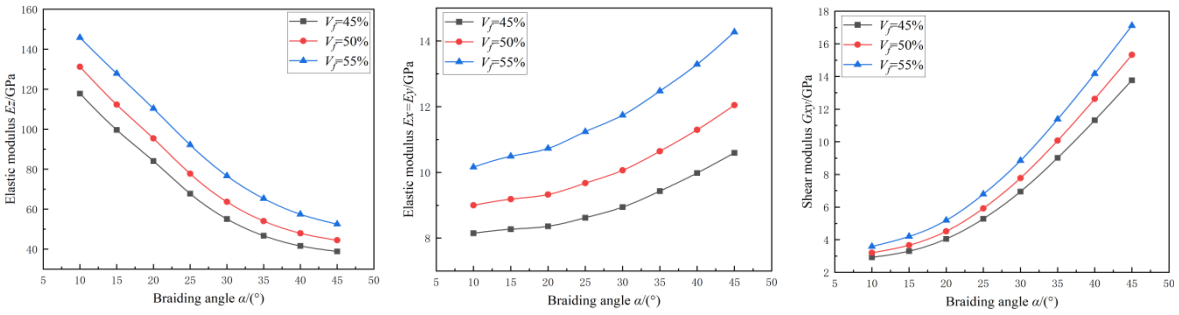

(a) (b) (c)

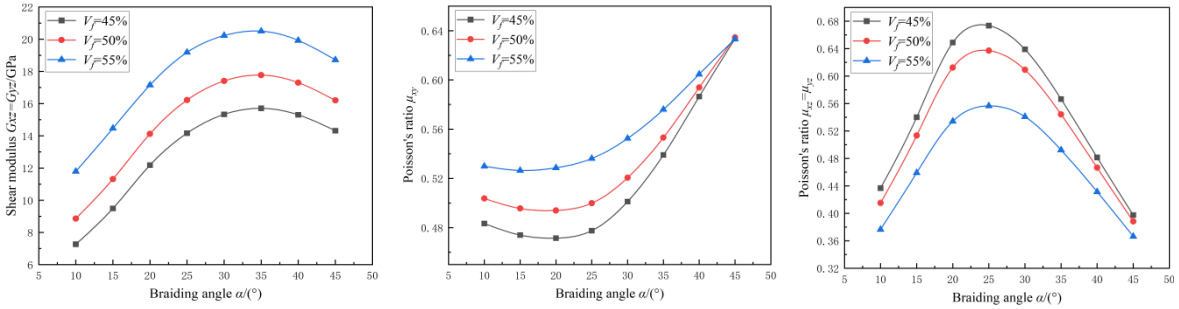

(d) (e) (f)

Fig. 3.1 Variation of elastic constant braiding angle and fiber volume fraction of 3D five-directional braided composites

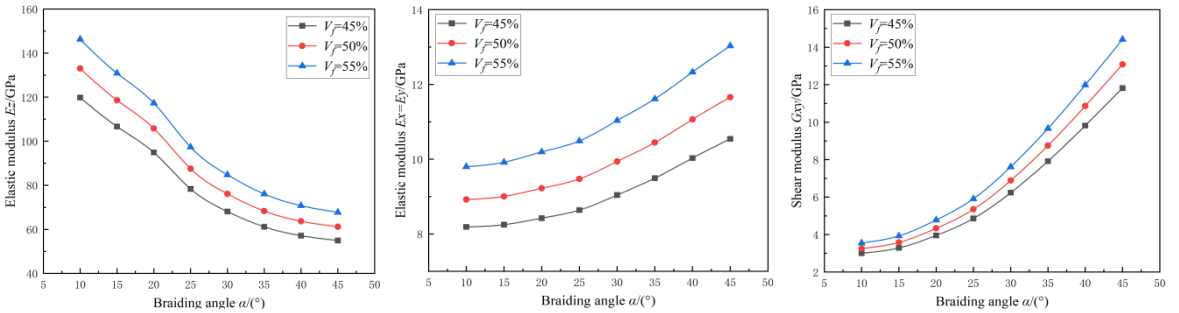

(a) (b) (c)

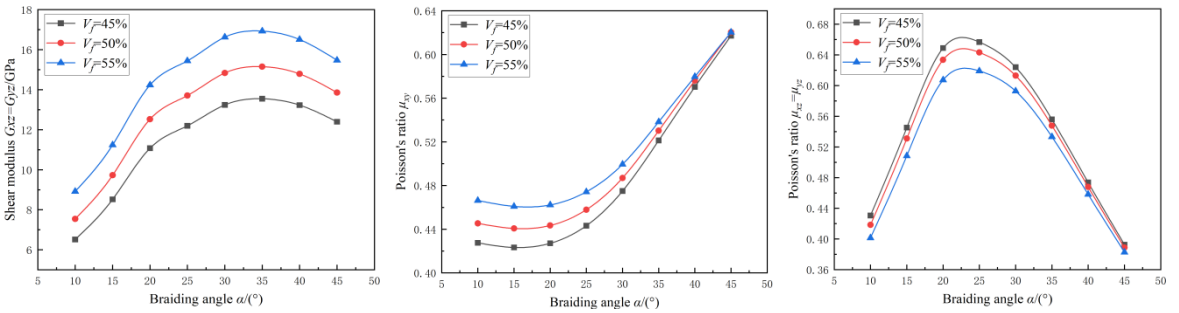

(d) (e) (f)

Fig. 3.2 Variation of elastic constant braiding angle and fiber volume fraction of 3D full five-directional braided composites

Figures 3.1and 3.2 illustrate the distribution of elastic constants of the cell in 3D five-directional and full five-directional braided composites under three different fiber volume fractions within the 10° to 45° range of braiding angle. It can be observed that the trends of the changes in the structural characteristics of 3D five-directional and full five-directional composite materials are essentially the same as the braiding angle and volume fraction change. As the braiding angle increases, the tensile strength in the axial direction (E_z) of the material decreases, particularly at lower angle (α<25°), with the greatest decrease occurring in this range. However, the rate of decrease in E_z gradually slows as the braiding angle increases

beyond 25°, eventually becoming more uniform around 45°. Additionally, both 3D five-directional and full five-directional cells exhibit isotropic characteristics in the transverse direction, with the transverse tensile modulus (E_x=E_y) increasing as the braiding angle increases. The trend is the opposite of the axial tensile modulus (E_z), and the rate of increase is small but steadily linear, accelerating in magnitude beyond 25°. Moreover, the transverse shear modulus (G_{xy}) of the material also increases with the braiding angle particularly at large angle. This result can be attributed to the gradual decrease of the stiffness component of the braiding yarn in the axial direction and the resulting decrease in the elastic modulus E_z which causes an increase in the stiffness components of the other two directions, resulting in an increase in E_x, E_y, and G_{xy}.

Figures 3.1(d) and 3.2(d) depict the axial shear modulus G_{xz}=G_{yz} of 3D five-directional and full five-directional braided composites increasing with the braiding angle α. A significant increase is observed when the braiding angle is less than 30°, but a decreasing trend emerges when the angle exceeds 40°. Similarly, Figures 3.1(e) and 3.2(e) show that the Poisson's ratio μ_{xy} of the materials first decreases and then increases with the braiding angle, exhibiting a slight decrease before 25° and a sudden increase thereafter. Meanwhile, the Poisson's ratio μ_{xz} and μ_{yz} (μxz=μyz) of the materials exhibit even more pronounced changes. When the braiding angle is less than 25°, μ_{xz} and μ_{yz} increase significantly with the increase of α. However, beyond the critical point of 25°, μ_{xz} and μ_{yz} decrease with α, and the magnitude of the decrease is also considerable, reaching the maximum value between 25° to 30°.

From the perspective of fiber volume fraction, the influence of fiber volume fraction on the 3D five-directional and full five-directional internal cell structures can be clearly observed from Figures 3.1 and 3. 2. As the fiber volume fraction increases, the elastic constants of the material also increase, and under different braiding angle, the axial tensile modulus E_z, transverse tensile modulus E_x, E_y, axial shear modulus G_{xz}, G_{yz}, and transverse shear modulus G_{xy} all increase to a similar extent. However, the trend of Poisson's ratio of the material varies slightly with the change in fiber volume fraction. The magnitude of μ_{xy} changes regularly as the fiber volume fraction increases for braiding angle less than 25°, and the increase rate becomes smaller and smaller as the braiding angle increases beyond 25°. At a braiding angle of 45°, the Poisson's ratio of the three volume fractions is similar. The influence of fiber volume fraction on Poisson's ratio μ_{xz} and μ_{yz} of the 3D five-directional and overall five-directional structures is not obvious, and there is only a slight increase in the braiding angle range of 20°-30°. The increase rate is not significant at small and large braiding angle, indicating that the influence of fiber volume fraction on the Poisson's ratio of the material is limited, but it has a significant impact on other elastic properties of the braiding structure.

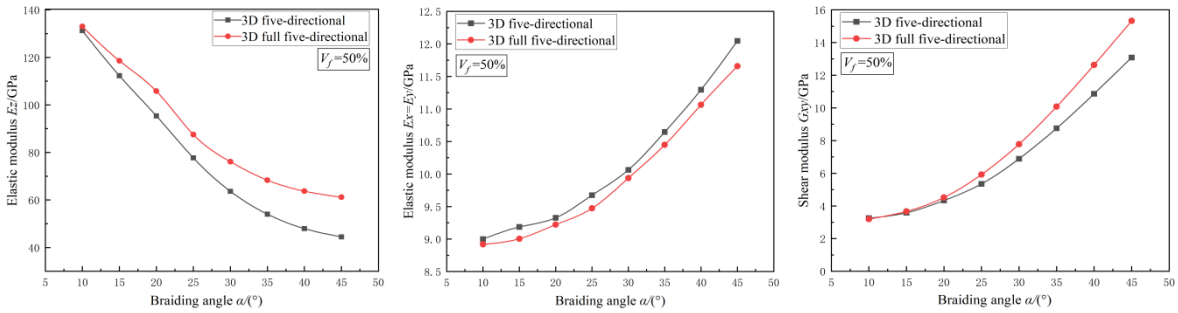

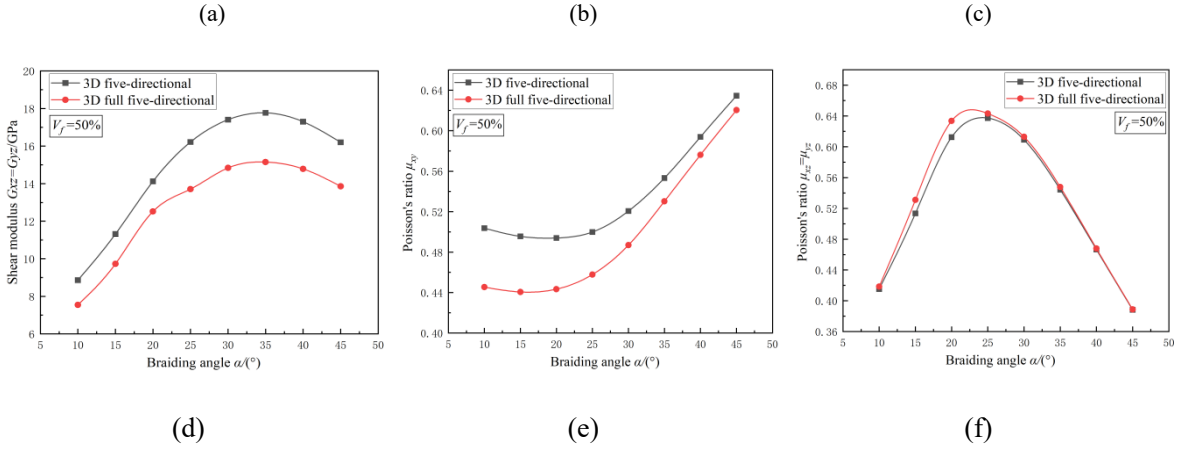

Fig. 3.3 Comparison of elastic constants of 3D five-directional and full five-directional braided composites（V_f=50%）

From Figure 3.3(a), it can be seen that under the same fiber volume fraction and braiding angle, the axial tensile performance of 3D full five-directional braided structures is higher than that of 3D five-directional braided structures, and this effect becomes more apparent with increasing braiding angle. From the perspective of the single cell structure, the reason for this is that the 3D full five-directional braided composite material fills more axial yarns in the blank areas compared to the 3D five-directional braided composite material, increasing the stiffness component in the axial direction and thus improving the axial tensile performance. However, when combined with Figures 3.3(b), (c), and (d), it can be seen that this effect leads to a decrease in the transverse tensile and shear modulus of the 3D full five-directional braided structure compared to the 3D five-directional braided structure. Under the same fiber volume fraction, the proportion of axial yarns in the 3D full five-directional braided structure is higher, while the content of other direction braided yarns is reduced, resulting in an impact on its shear performance, which is lower than that of the 3D five-directional braided structure. Similarly affected by this aspect, as shown in Figure 3.3(e), for transverse deformation resistance, the 3D five-directional braided structure still outperforms the 3D full five-directional braided structure, but with increasing braiding angle, the Poisson's ratio μ_{xy} of the two gradually approaches. Figure 3.3(f) shows that the Poisson's ratios μ_{xz} and μ_{yz} of the 3D five-directional and full five-directional braided structures are almost the same, with the 3D full five-directional braided structure slightly higher. This indicates that under the same volume fraction, the two have similar stiffness and elastic properties in the axial and transverse directions of the material.

4. CONCLUSION

(1) Based on the motion law of the yarn carrier in the 3D five-directional and full five-directional braiding processes, the in-plane and spatial motion trajectories of the yarn are analyzed. Two types of yarn topology structures for materials with inner cells are established. The 3D full five-directional braided composites fills a significant amount of the axial yarn blank position in the material, which greatly improves the fiber volume fraction of the material. The internal cell model established in this paper is basically

consistent with the experimental data, which verifies the reliability of the internal cell model.

(2) The inner cell of the 3D five-directional and full five-directional braided composites show transverse isotropic characteristics, and the braiding angle and fiber volume fraction are the main parameters affecting the elastic properties of the braiding structure. As the fiber volume fraction increases, all elastic constants of the material increase accordingly, and the changes in the braiding angle and volume fraction for both the 3D five-directional and full five-directional braided composites are basically the same. The range of 25°-30° is the boundary region for the elastic properties of the 3D braided composites.

(3) Under the same fiber volume fraction and braiding angle, the axial tensile performance of the 3D full five-directional braiding structure is higher than that of the 3D five-directional braiding structure, and this improvement becomes more significant as the braiding angle increases. The reason for this is that the 3D full five-directional braided composites fills more axial yarn in the structure's blank area than the 3D five-directional braided composites, increasing the stiffness component in the axial direction and improving the axial tensile performance.

(4) The reductions of the transverse tensile and shear modulus in 3D full five-directional braided structures are greater than those in 3D five-directional braided structures, while maintaining the same fiber volume fraction. This is due to the larger proportion of axial yarns in the full five-directional braided structure, which results in a decrease in the amount of yarns braided in other directions and negatively impacts the shear performance of the structure, leading to lower values than those in the 3D five-directional braided structure.

REFERENCES

1. Suquet P. Elements of homogenization theory for inelastic solid mechanics[A]. Sanchez-Palenci a ed. Homogenization techniques for composite media[C]. Berlin, 1987, 194-275.
2. Z Xia F Ellyi. A unified periodical boundary conditions for representative volume elements of composites and applications[J]. International Journal of Solids and Structures, 2003, 40(8):1907-1921.
3. C Zhang, X. W Xu, X Yan, General Periodic Boundary Conditions and Their Application to Micromechanical Finite Element Analysis of Textile Composites, Acta Aeronautica et Astronaut ica Sinica, 2013, 34(07):1636-1645.
4. C Zhang, X. W Xu, X Yan. Three unit-cell structure models of 3-D five-directional and full f ive-directional braided composites[J]. Journal of Nanjing University of Aeronautics & Astronaut ics, 2013, 45(2):170-178.
5. K Xu, X W Xu. Finite element analysis of mechanical properties of 3D five-directional braide d composites[J]. Materials Science & Engineering A, 2008, 487(1-2):499-509.
6. Z Lu, B Xia, Yang Z. Investigation on the tensile properties of three-dimensional full five-dire ctional braided composites[J]. Computational Materials Science, 2013, 77(Complete):445-455.

7. D S Li, Z X Lu, C Li, et al. Microstructure and mechanical properties of three-dimensional fi ve-directional braided composites[J]. International Journal of Solids and Structures, 2009, 46(1 8–19):3422-3432.

8. X B Du, H Zhu, J Ai, et al. Parameterized meso-scale modeling and experimental study on th e tensile damage evolution and strength of 3D five-directional braided composites[J]. Materials & Design, 2021(8):109702.

9. X B Pi, K Qian, H J Cao. Microstructure Analysis of 3D Full 5-Directional Braided Composi tes[J]. Aerospace Materials & Technology, 2011, 41(06):39-43.

10. F K Ko, C M Pastore. Structure and properties of integrated 3-D fabric for structural composi tes. In: Vinson J R, Taya M, (Eds), Recent Advances in Composites in the United States and Japan, Philadelphia: American Society for Testing and Materials, 1985, 428-439.

11. W Li, M Hammad, El-Shiekh A. Structure analysis of 3-D braided preforms for composites. J ournal of Textile Institute, 1990, 81(4): 491-514.

12. G Yan, J Li. Effects of braiding angle on modal experimental analysis of three-dimensional an d five-directional braided composites[J]. Composites Part B Engineering, 2012, 43(5):2423-2428.

13. J Li , Y Zhang, F Sun, et al. Mechanics analysis of three-dimensional five-directional braided composites. I: Microstructural model[J]. Fuhe Cailiao Xuebao/Acta Materiae Compositae Sinica, 2009, 26(1):150-155.

STUDY ON THE CONNECTION PERFORMANCE OF METAL SKIN/COMPOSITE STRINGER STRUCTURE

H. Q. Wang[1], T. Li[1], and C. Y. Ge[1]

[1] Department of Engineering Mechanics, Dalian University of Technology, China

Abstract: In order to study the influence of connection modes on the mechanical properties of metal skin/thermoplastic composite stringer structures, the finite element models of bolted, bonded, and hybrid joint structures are established to analyze the failure modes of joints with different connection modes and the load response curves at the loading points, based on which the nonlinear mechanical response of metal skin/thermoplastic composite stringer bearing cylinder is studied. Numerical simulations have demonstrated that, compared with bolt connection, the hybrid connection is more advantages in improving the mechanical properties and weight reduction of the bearing cylinder structure.

Key words: Thermoplastic composites; Connection modes; Finite element analysis; Structural optimization

INTRODUCTION

With advantages of light weight and excellent mechanical properties, composite materials have been widely used in the current aerospace field[1]. Compared with thermosetting composite materials, thermoplastic composite materials have lower density, higher fracture toughness and impact strength. In practical engineering applications, they usually need to be connected with metal structure by means of mechanical connection and adhesive bonding. Among them, the metal skin/thermoplastic stringer bearing structure mainly adopts the bolted connection, but the use of a large number of bolts does not meet the needs of lightweight structure, and the choice of connection mode is particularly important for the ultimate bearing capacity and other properties of the structure, so the study of the connection mode on the metal skin/thermoplastic stringer bearing performance has a very practical engineering significance.

The longitudinal connection structure of panel skin is the key connection area of fuselage, and its connection mode is generally single lap joint, which is the lightest design. Meanwhile, composite material stringer is arranged in the panel skin lap area to maintain the section stiffness of fuselage, and the stringer edge is mechanically connected with the skin through bolts[2].In order to study the influence of the connection mode on the mechanical properties of the joint structure, S. Z. Luo [3] used the cohesive force element, viscous contact and node binding constraint to simulate the bonding surface of the composite material to study the mechanical properties of the joint under the impact load, and found that the modeling method of the cohesive force element was the best match with the experimental results. Through numerical simulation, Z. H. Hu[4] found that the zero-thickness cohesive force model was the most robust in predicting the failure mechanism of bonded structures, showing the most superior numerical performance. Z. D. Liang, et al.[5] used the cohesive force model to simulate

the failure of adhesive layer when studying the numerical simulation failure process of composite single lap bonded joint. The relative error between the simulation results and the test was less than 5%, which verified the effectiveness of such finite element simulation. For the numerical model of bonding composite materials, most existing researches adopt the progressive failure method. X. Feng, et al.[6] wrote UMAT program to degenerate the modulus of damage element to the original 3% to establish a finite element model in view of the characteristics of anisotropy and progressive damage of composite materials. Y. Yao [7] wrote a USDFLD user subroutine to judge whether the structure failed according to the FV field variables in the result file, and used the Shokrieh-Hashin criterion to judge the failure, and completed the progressive failure analysis of composite single-stud bolt connection. S. Zhou [8] wrote a user subroutine to introduce a three-dimensional Hashin criterion considering shear nonlinearity to well simulate the extrusion damage evolution of bolted connection of composite laminates. All of the above studies focus on the numerical analysis of single connection structures such as adhesive and bolted connection, but lack of numerical methods for mixed connection modes with complex failure processes.

In this paper, for the composite material/metal joint structure, the numerical simulation method is used to establish the digital model of bolted, bonded and hybrid connection modes, and analyze the joint failure modes of different connection modes and the load response curves of loading points. On this basis, the hybrid bonding/bolted connection mode is used to replace the simple bonding mode in the traditional skin/stringer structure. The nonlinear mechanical response of aluminum alloy skin/thermoplastic composite stringer bearing cylinder was studied.

NUMERICAL METHOD FOR FAILURE OF COMPOSITE/METAL CONNECTION

NUMERICAL SIMULATION OF COMPOSITE FAILURE

In this paper, VUMAT user subroutine was established based on Abaqus to calculate and determine the failure of composite materials. Hashin criterion was used as the composite failure criterion in the subroutine, as shown in Equations (1) ~ (4). Camanho degradation model was used as the material degradation model[9]. In the calculation process, the corresponding material attribute reduction is carried out for the element that is judged as failure.

$$\left(\frac{\sigma_1}{X^T}\right)^2+\frac{1}{S_{12}^2}\left(\tau_{12}^2+\tau_{13}^2\right)=1 \tag{1}$$

$$-\frac{\sigma_1}{X^C}=1 \tag{2}$$

$$\left(\frac{\sigma_2+\sigma_3}{\left(Y^T\right)^2}\right)^2+\frac{\tau_{12}^2+\tau_{13}^2}{S_{12}^2}+\frac{\tau_{23}^2-\sigma_2\sigma_3}{S_{23}^2}=1 \tag{3}$$

$$\frac{1}{Y^C}\left(\left(\frac{Y^C}{2S_{23}}\right)^2-1\right)\left(\sigma_2+\sigma_3\right)+\frac{\left(\sigma_2+\sigma_3\right)^2}{4S_{23}^2}+\frac{1}{S_{23}^2}\left(\tau_{23}^2-\sigma_2\sigma_3\right)+\frac{1}{S_{12}^2}\left(\tau_{12}^2+\tau_{13}^2\right)=1 \tag{4}$$

Where, σ_i (i=1，2，3)is the stress in each principal direction of the composite material, τ_{ij} (i, j =1，2，3)is the shear stress in the corresponding plane, X, Y Is the allowable stress in each main direction of the composite material (T represents tensile, C represents compression), S_{ij} (i, j =1，2，3)is the allowable in-plane shear stress.

In this paper, two methods are adopted to delete elements with large deformation. The first method is to control by corresponding variables. When the strain of the element is obviously greater than the ultimate strain of the composite material, the element is deleted. The second method is the finite element calculation results to give a specific deformation gradient determinant. When the deformation gradient exceeds the threshold defined by Equation (5), the element is deleted to maintain the continuity of calculation[10-11].

$$\begin{cases} 0 < detF < 0.8 \\ detF > 1.2 \end{cases} \tag{5}$$

Where, $detF$ represents the volume ratio before and after unit calculation.

NUMERICAL SIMULATION OF BONDING FAILURE

In this paper, cohesion model is used to simulate the bonding surface. Parameters of the bonding surface are shown in Table 1. The damage initiation expression of the cohesion model is shown in Equation (6), Where t_i（i=1,2,3）corresponds to the stresses in Table 1 respectively.

In other contact Settings in the finite element model, mutual contact and self-contact between composite materials, metal materials and bolts are set as universal contact, and the friction coefficient of tangential contact is 0.2[10].

$$\left(\frac{t_1}{t_1^0}\right)^2+\left(\frac{t_2}{t_2^0}\right)^2+\left(\frac{t_3}{t_3^0}\right)^2=1 \tag{6}$$

Where, t_i（i=1，2，3）is the normal stress and two tangential shear stresses; t_i^o（i=1，2，3）is the normal allowable normal stress and two tangential allowable shear stresses.

Table.1 Contact failure parameters of cohesive model[12]

Parameter	value
K_t/(N/mm^3)	10^6
τ_n/MPa	45.97
τ_t/MPa	18.7
η	2.6
G_{IC}/(N/mm)	0.45
G_{IIC}/(N/mm)	0.9

NUMERICAL SIMULATION OF BOLT FAILURE

Considering that the tensile experimental model of single-layer lap joints may result in shear failure of bolts, the Johnson-Cook constitutive model was adopted for bolted connection simulation in this paper, as shown in Equation (7), and the material parameters of which are shown in Table 2.

$$\sigma=\left(A+B\varepsilon^n\right)\left[1+C\ln\varepsilon^*\right]\left[1-\left(T^*\right)^m\right] \tag{7}$$

Where, A is the initial yield stress, B is the hardening modulus, C is the strain rate constant, n is the hardening index, m is the thermal softening coefficient.

Table.2 Parameters of Johnson-Cook constitutive model [13- 14]

Parameter	value
A/MPa	782
B/MPa	498
n	0.28

C	0.028
m	1

NUMERICAL SIMULATION OF TYPICAL COMPOSITE/METAL JOINT

In this paper, numerical simulation was carried out on typical composite/metal bolt connection, adhesive connection and mixed connection modes. Ultimate bearing capacity（$F_{\max}$）and Energy Absorption（EA）were selected as reference indexes to evaluate the merits of connection modes. $F_{\max}$ could be obtained directly from peak force of load-displacement curves. EA is computed by integral of Equation (8).

$$\mathrm{EA} = \int_0^{\delta} F(x)dx \tag{8}$$

Where, $F(x)$ is the bearing capacity of the structure in the loading process, δ is the final failure displacement.

MECHANICAL MODEL OF JOINT

Composite material plate and metal plate size is $130\,\mathrm{mm} \times 30\,\mathrm{mm} \times 3.6\,\mathrm{mm}$, size and manner of lap joint as shown in Figure 1, figure of the shaded part for clamping area. The composite plate is made of continuous carbon fiber reinforced epoxy resin, and its layup sequence is [45/0/-45], wherein the fiber direction is the length direction of the plate, and the material of the metal plate is 2024 aluminum alloy. In order to study the influence of different bolt diameters on the load displacement curve and other results, the bolt specifications are M5 and M10 respectively, and the material is titanium alloy Ti6Al4V.

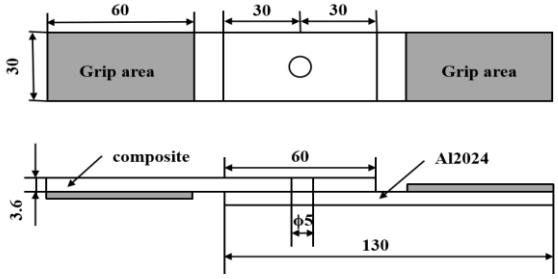

Figure.1 Schematic diagram of dimensional parameters of finite element model (mm)

The stiffness matrix of the composite material is shown in Equation (9). Poisson's ratio in all directions of the composite material is the same, which is 0.31. The strength index of the material is shown in Table 3, and the material properties of the metal plate are shown in Table 4.

$$[C] = \begin{bmatrix} 191.28 & 85.94 & 6.10 & 0 & 0 & 0 \\ & 13.61 & 6.10 & 0 & 0 & 0 \\ & & 13.61 & 0 & 0 & 0 \\ & & & 6.04 & 0 & 0 \\ & SYS & & & 6.04 & 0 \\ & & & & & 6.04 \end{bmatrix} (GPa) \tag{9}$$

Table.3 Strength parameters of composite materials

Parameter	value
X^T/MPa	2272
X^C/MPa	1386

Y^T/MPa	40
Y^C/MPa	212
$S_{12}=S_{23}$/MPa	97

Table.4 Material properties of 2024 aluminum alloy

Parameter	value
E/GPa	72
μ	0.31
ρ/(kg·m^{-3})	2700

The finite element model is shown in Figure 2, and hexahedral elements are used for calculation. At the loading end of the model, one side of the composite plate was set as the clamping part, the clamping part adopted the fixed support boundary condition, and the other end of the metal plate was set as the loading displacement end, the displacement of the loading end was 2mm, the analysis step was 0.2s, and the quasi-static analysis was carried out. In order to avoid the great influence of bolt diameter change on structural bearing capacity and energy absorption under quasi-static loading, a low-speed impact loading mode was adopted when comparing the calculation of different bolt diameters. The loading speed was selected as 1m/s, that is, the displacement of loading end was 10mm, and the analysis step size was 0.01s.

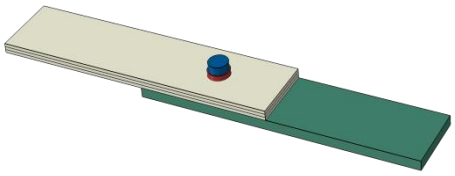

Figure.2 Schematic diagram of connection between composite material plate and metal plate

FAILURE MODE ANALYSIS

The load-displacement curves of different connection modes under quasi-static loading are shown in Figure 3. Two load peaks appear in the whole process of the hybrid connection model. Before the first load peak, the curve trend is similar to that of the bonding curve, but both in terms of failure displacement and peak force are greater than that of the bonding connection mode. The curve drops to the position of the load displacement curve of the bolted connection under the corresponding displacement, and continues to change at the same slope until the second load peak is reached and the whole structure fails. Figure 4 and Figure 5 respectively show the stress nephogram of the ultimate bearing capacity and the final failure nephogram at different connection modes, as shown in Figure 5a, adhesive surfaces play a decisive role in the bearing capacity of the overall structure, and the peeling of adhesive surfaces leads to the final failure of the structure. As shown in Figure 5b~5c, bolt shear failure eventually occurs in both bolted and hybrid connection modes, resulting in structural failure. The ultimate failure mode of tensile test model with bolt structure is shear failure of bolt. Figure 6 shows the composite matrix extrusion failure zone (red zone) where the composite extrusion failure occurs near the bolt hole.

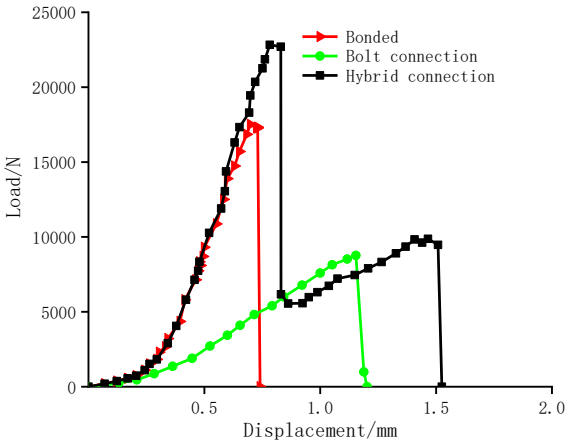

Figure.3 Load-displacement curves of three connection modes

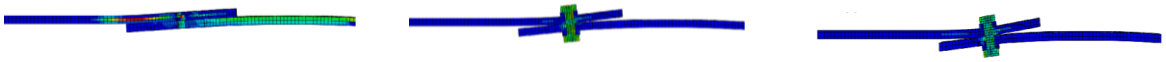

(a) Stress nephogram of adhesive joint (b) Stress nephogram of bolted joint (c) Stress nephogram of mixed connection joint

Figure.4 Stress nephogram at ultimate bearing capacity

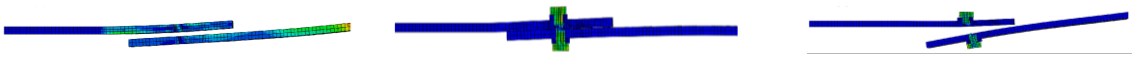

(a) Stress nephogram of adhesive joint (b) Stress nephogram of bolted joint (c) Stress nephogram of mixed connection joint

Figure.5 Sectional view of final failure

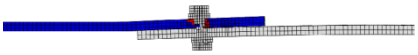

Figure.6 Failure nephogram of composite matrix

The failure model of the hybrid connection is relatively special. Figure 7-8 shows the stress nephogram and displacement nephogram of the model at the first peak load and the next moment. Combined with the load-displacement curve in Figure 3, it can be seen from the figure that before the first peak force, the adhesive joint is the main bearing part. After reaching the ultimate bearing capacity, the plate is separated, and the bolt is used as the bearing part of the next stage. Finally the second peak force is reached, the bolt shears and the model finally fails. The characteristics of the hybrid connection model, under quasi-static loading, that the adhesive joint carries first and the bolt component carries later, allow the model to produce greater displacement and deformation when the model fails. Compared with the traditional bolted connection, the energy absorption level has a greater improvement. The hybrid connection structure is superior to the bolted connection mode in ultimate bearing capacity, energy absorption and failure displacement.

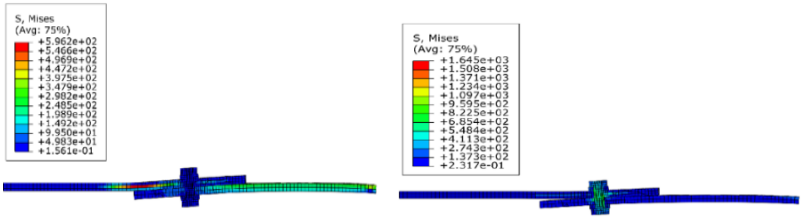

(a) Stress nephogram at the first peak force (b) Stress nephogram at the next moment

Figure.7 Stress nephogram of hybrid connections

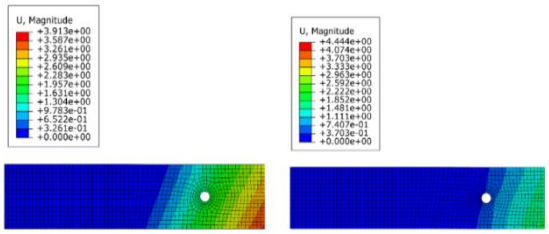

(a) Displacement nephogram at the first peak force (b) Displacement nephogram at the next moment

Figure.8 Displacement nephogram of hybrid connections

EFFECT OF BOLT SIZE ON LOW SPEED IMPACT

Figure 9 shows the load-displacement curves of bolt connection and hybrid connection with different bolt diameters. For bolts of M5 specifications, the ultimate bearing capacity and energy absorption of the structure are also improved by hybrid connection under low speed impact load, but the final failure displacement of hybrid connection is no longer larger than that of bolt connection. For bolts of different diameters, the bearing effect of M10 bolts is far better than that of M5 bolts, but the first ultimate bearing capacity of M10 hybrid connection model is not significantly improved compared with M5 hybrid connection model. It can be seen that the change of bolt size has little influence on the bearing capacity of the bonded surface, and with the increase of bolt diameter, the hybrid connection is not superior to the bolted connection model in terms of bearing capacity and energy absorption, so when the bolt size is too large, the hybrid connection mode will not necessarily improve the bearing capacity of the structure. If the bearing capacity of the overall structure is to be improved by the hybrid connection mode, different bonding methods are needed. In this paper, the bearing capacity and energy absorption of the structure can be significantly improved by forming a hybrid connection between the adhesive surface and the bolt with a small diameter.

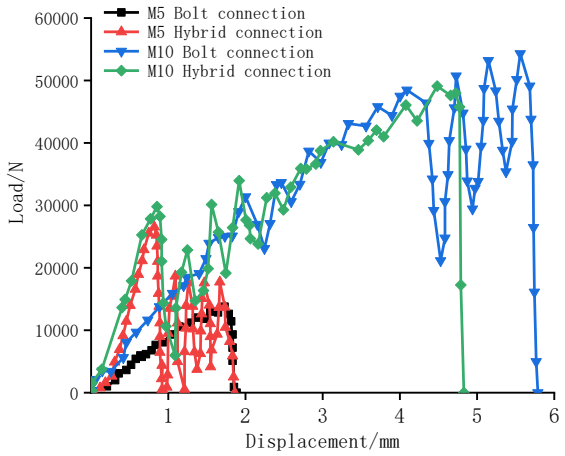

Figure.9 Load-displacement curves of two connection modes with different bolt diameters

MECHANICAL ANALYSIS OF METAL SKIN/THERMOPLASTIC STRINGER STRUCTURE

MECHANICAL ANALYSIS OF BOLT CONNECTION SKIN/STRINGER STRUCTURE

The structure of the skin and stringer of the bearing cylinder is shown in Figure 10. The diameter of the bearing cylinder is 1003mm, the height is 600mm, the thickness of the cylinder segment is 1.5mm, and the boundary height of the end frame is 50mm. The end frame of the bearing cylinder forms a certain Angle with the middle part, and the material is 2024 aluminum

alloy, parameters are shown in Table 4. The cross section of the truss structure is optimized and its length is 480mm. The material is continuous carbon fiber reinforced thermoplastic composite. According to the compression test and tensile test, the Poisson ratio of the material is $\mu_{12}=\mu_{13}=0.37$, $\mu_{23}=0.368$, The stiffness matrix of the composite material is shown in Equation (10).

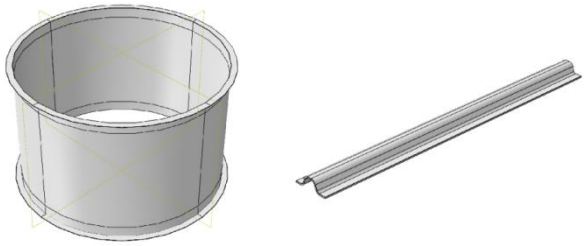

Figure.10 Schematic diagram of bearing cylinder structure

$$[C]=\begin{bmatrix} 98.10 & 57.43 & 8.48 & 0 & 0 & 0 \\ & 14.46 & 8.48 & 0 & 0 & 0 \\ & & 14.46 & 0 & 0 & 0 \\ & & & 2.20 & 0 & 0 \\ & SYS & & & 2.41 & \\ & & & & & 2.41 \end{bmatrix}(GPa) \tag{10}$$

The axisymmetric simplified model is shown in Figure 11. 16 M4 bolts are connected to the skin on the left and right sides of the stringer. The bolt spacing is 30mm, and the distance between bolt and bearing cylinder end is 15 mm. The bottom end of the model is fixated, the model considers axisymmetric constraints, the upper end is coupled with the reference point, the vertical downward displacement is applied, the explicit dynamic surface contact is set between the stringer and the skin, and the bolt is bound to the stringer and the skin respectively.

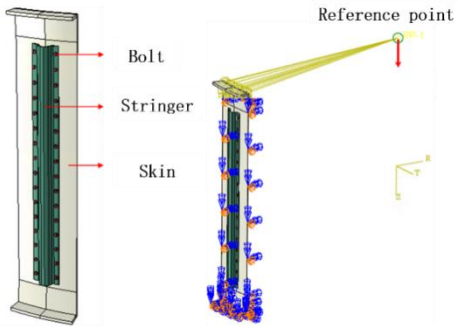

Figure.11 Finite element model of bearing cylinder

Figure 12 shows the load-displacement curve of the skin/stringer bolt connection numerical model. It can be seen that with the increase of axial displacement, the axial load increases roughly linearly, and the skin/stringer bearing cylinder first experiences local skin instability, and the bearing cylinder fails when the skin stress reaches the plastic stage, Figure 13 shows the stress nemogram of the skin/stringer bearing cylinder when it fails. It can be seen that the upper and lower sections of the stringer contact the skin and the failure occurs.

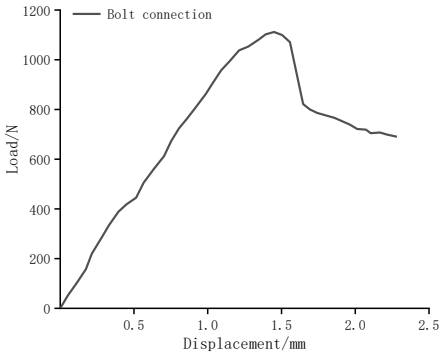

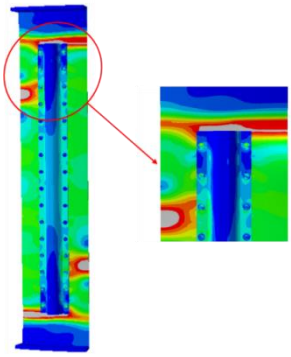

Figure.12 Load-displacement curve of bearing cylinder **Figure.13** Stress nephogram of bearing cylinder in failure

MECHANICAL ANALYSIS OF HYBRID CONNECTION SKIN/STRINGER STRUCTURE

In order to ensure that the stringer, as a bearing member, forms a hybrid connection with the metal skin, both ends of the finite element model of the stringer are in contact with both ends of the bearing cylinder, and the length is modified to 600mm, as shown in Figure 14. The skin and stringer are connected in a hybrid way. The bolt and the stringer surface and the skin surface are still bound by the node. The cohesive force model above is used to simulate the adhesive surface, parameters are shown in Table 1. The constraint mode of the load constraint end remains unchanged, and the displacement of the loading end is modified to 10mm.

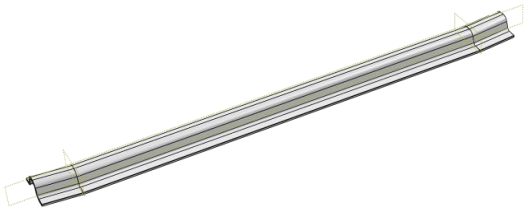

Figure.14 Schematic diagram of stringer structure

Figure 15 shows the load-displacement curves of bolt connection and hybrid connection models. The load displacement curves of bolt connected models show obvious oscillations near the peak load force, which is caused by the local buckling instability of the cylinder in the compression process. When the load displacement curve of the hybrid connection model reaches the ultimate bearing capacity, there is no obvious process of bolt continued bearing as in the hybrid connection joint model, but the trend of the curve of the hybrid connection model and the bolt connection model is very close in the descending process. The bearing cylinder model is different from the single lap tensile model. After reaching the ultimate bearing capacity, the bearing cylinder model produces buckling deformation. The cross section of some bolts is no longer parallel to the loading direction, the bolts no longer produce shear deformation, and the structural carrying capacity is greatly reduce. In addition, it can also be clearly seen from the figure that the hybrid connection is superior to the traditional bolt connection in terms of energy absorption and ultimate bearing capacity, and the use of the hybrid connection can suppress the phenomenon of structural instability caused by local buckling caused by a single bolt connection.

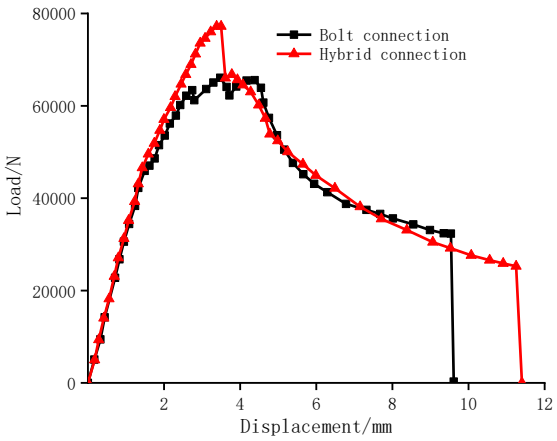

Figure.15 Load-displacement curves of two connection modes

EFFECT OF BOLT NUMBER ON BEARING CAPACITY

In order to study the possibility of reducing the number of bolts used in hybrid connection skin/stringer bearing cylinder, the number of bolts was reduced from the original 32 to 24 and 16, and three layout schemes of uniform bolt distribution were achieved, as shown in Table 5.

Table.5 Layout scheme of uniform bolts

Layout scheme	Distance between bolt and cylinder end(mm)	Bolt spacing(mm)
50% Bolt-1	75	50
50% Bolt-2	5	70
75% Bolt	85	30

The calculation results are shown in Figure 16. For the same number of bolts, the ultimate bearing capacity of 50%bolt-2 and 50%bolt-1 layout schemes is basically the same, and the difference lies in the post-buckling stage after the failure of the adhesive joint, the 50% bolt-2 scheme is better than the 50% bolt-1 scheme in terms of ductility of the structure and energy absorption due to the more dispersed bolt distribution. For the layout scheme with the same distribution characteristics but different bolt numbers, the ultimate bearing capacity of 75% bolt layout scheme is 7.4% higher than that of 50% bolt-1 scheme, indicating that increasing the number of bolts can improve the ultimate bearing capacity of the hybrid connection bearing cylinder. In addition, compared with the bolted connection results of the original model, the traditional skin stringer connection bearing cylinder can reduce the amount of bolts by 50% without affecting the original ultimate bearing capacity of the structure after the introduction of the adhesive joint to form a hybrid connection, which indicates that the skin/stringer connection bearing cylinder model can reduce the number of bolts on the basis of using the hybrid connection mode.

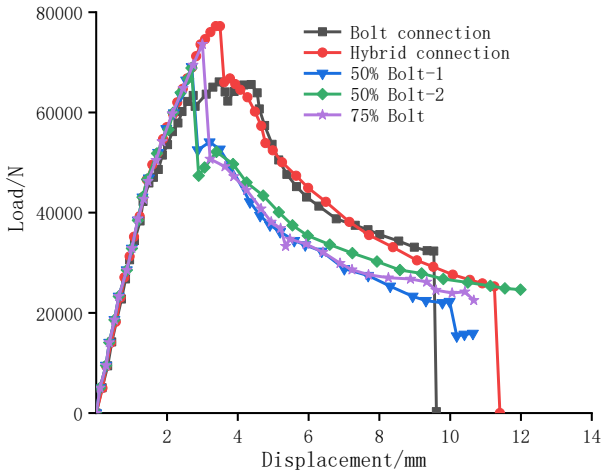

Figure.16 Comparison of results of different connection schemes

CONCLUSION

In this paper, a numerical simulation model that can consider bolted, bonded, and hybrid connection modes is established, and the failure modes of joints with different connection modes and load response curves at loading points are analyzed. On this basis, the nonlinear mechanical response of aluminum alloy skin/thermoplastic composite stringer bearing cylinder was studied. The main conclusions are as follows:

When the structure is under load, the joint with hybrid connection mode has obvious segmental deformation mode, the adhesive surface failure occurs first, and finally the bolt shear failure occurs.

The stiffness, ultimate bearing capacity and energy absorption effect of the structure can be improved effectively by adding bonding technology to the traditional bolting technology.

For the metal skin/thermoplastic stringer bearing cylinder structure, the use of hybrid connection can suppress the phenomenon of structural instability caused by local buckling caused by single bolted connection.

The traditional skin stringer connection bearing cylinder can reduce the use of metal bolts after the introduction of adhesive bonding on the premise of maintaining the overall bearing capacity of the structure, and further realize the weight reduction of the structure.

REFERENCES

S. Y. Du, Advanced composite materials and aerospace engineering[J]. Acta Materiae Composite Sinica, 24, 1, 1-12, 2007.

Y. B. Qian, X. D. Zhong, Chen Puhui, and L. Y. Liu, Longitudinal panel splice design failure analysis of composite fuselage structures. Acta Aeronautica et Astronautica Sinica, 33, 8, 1427-1433, 2012.

S. Z. Luo, Study on mechanical properties of bonded joints of carbon fiber reinforced plastics under impact loading[D]. Hunan University, 2018.

Z. H. Hu, Research on interface failure mechanisms of composite adhesive joints based on the cohesive model[D]. Zhejiang University, 2018.

Z. D. Liang, Y. Yan, and T. T. Zhang, Experimental investigation and numerical simulation of composite laminate adhesively bonded single-lap joints[J]. Journal of Beijing University of Aeronautics and Astronautics, 40, 12, 1786-92, 2014.

X. Feng, Q. Liao, and A. R. He, Numerical Failure Simulation of Composite Bolted Joint[J]. Aerospace Materials & Technology, 2013, 43(4): 87-90.

Yao Ye. Progress Failure Analysis and Strength Prediction of Composite Bolt Joint[D]. Wuhan University of Technology, 2017.

S. Zhou, Experimental and Numericial Investigation on Progressive Failure Response of Composite Bolted Joint[D]. Harbin Engineering University, 2013.
P. P. Camanho, F. L. Matthews, A progressive damage model for mechanically fastened joints in composite laminates[J]. Journal of Composite Materials, 33, 24, 2248-80, 1999.
W. Tan, B. G. Falzon, Modelling the crush behaviour of thermoplastic composites[J]. Composites Science and Technology, 134, 57-71, 2016.
W. Tan, B. G. Falzon, and M. Price, The role of material characterisation in the crush modelling of thermoplastic composite structures[J]. Composite Structures, 153,914-927, 2016.
F. A. Leone, C. G. Davila, D. Girolamo, Progressive damage analysis as a design tool for composite bonded joints[J]. Composites Part B-Engineering, 77, 474-483, 2015.
C. Sarrado, F. A. Leone, and A. Turon, Finite-thickness cohesive elements for modeling thick adhesives[J]. Engineering Fracture Mechanics, 168, 105-113, 2016.
Y. Zhang, T. Mabrouk, and D. Nelias, FE-model for Titanium alloy (Ti-6Al-4V) cutting based on the identification of limiting shear stress at tool-chip interface[J]. International Journal of Material Forming, 4, 1, 11-23, 2011.

Analysis of torsion failure behavior and its characterization of carbon fiber monofilament

Q. D. Wang[1], M. Li[1], and Y. Z. Gu[2], and S. K. Wang[1]

[1] School of Materials Science and Engineering, Beihang University, Beijing 100191, China

[2] Research Institute for Frontier Science, Beihang University, Beijing 100191, China

Abstract: Carbon fiber (CF) reinforced plastics are widely applied as structural materials. As CFRP is subjected to axial tension and compression load, it also faces a great challenge of the out-of-plane load. Therefore, the evaluation and failure analysis of torsion behaviors of CF are significant in practice. In this work, monofilament torsion test was used to characterize torsion properties of three types of CFs, i.e. normal-modulus CF300, middle-modulus CF800 and high-modulus CF40. The twisted fracture angle and the breakage elongation of CF300, CF800 and CF40 under torsion were 1.54, 3.60°, 2.15 and 0.36‰, 1.99‰, 0.71‰ respectively. According to the Raman peak analysis, AD/AG is referred as the degree of graphitization and the crystallite La is referred as the crystallite structure. The AD/AG and La of CF800 with the best tensile elongation showed great structure changes after torsion while the CF300 and CF40 changed little, which was corresponding to the torsion behavior. Furthermore, the failure mode was observed by the SEM images. The characterization indicates that torsion treatment on monofilament can evidently impact the crystalline structure of the middle-modulus and high-strength CFs, while polishing has more influence on the structure of normal-modulus and high-modulus CFs.

1. INTRODUCTION

Advanced carbon fiber reinforced polymer (CFRP) has been widely used in aerospace, military and many other fields due to its excellent properties. As CFRP is subjected to axial tension and compression load, carbon fiber (CF) as the reinforcement has been focused on its tensile property[1]. However, CF also faces a great challenge of the out-of-plane load, like torsion load[2,3], especially in the fields of textile and braiding[4]. Most research has focused on the torsional property of CFRP[5-8]. In order to investigate the structural heterogeneity and the related stress distribution, it is necessary to use a single monofilament of CF. Yanan Liu[9] proposed a novel approach and deformation model to evaluate the monofilament torsion performance and found that the toughness of CF under torsion shear stress was inferior to its resistance to tensile stress. Jianhui Hu[4] designed a high resolution torsion tester displacement for measuring the accurate torque and the angular of monofilament based on the torsion-balance method and the autocollimation principle.

Since the diameter of a carbon fiber monofilament is about 4-6 μm, it is necessary to use advanced measurement, like Raman spectroscopy[10,11] and SEM. Tuinstra and Koening[12] firstly used Raman scattering-based method to study the carbon and graphite materials. The 1360 cm^{-1} band used called the defect band (D band) and is thought to be the disordered graphitic lattice and the crystal boundary regions. The G band around 1580 cm^{-1} used called crystal band and is due to the in-plane stretching mode of the ideal graphitic lattice[13]. The D3 band around 1500 cm^{-1} attributed as defects and amorphous carbon[14]. Different parameters are useful to estimate the graphite degree and the structural heterogeneity of CFs[15]. The ratio of intensities of two bands I_D/I_G, has been shown to be related to the degree of graphitization

and the orientation of the graphite planes. The ratio of area of two bands A_D/A_G, has been referred as the degree of graphitization.

Raman spectra is often used to investigate the internal strain of carbon fiber monofilament by the characteristic paraments[16,17]. The structure damage feature by the polishing can be represented by Raman spectra, such as structural defects and formation of carbon-oxygen complexes[18]. Gen Katagir[15] found that a disordered layer existed on the surface of the polish edge plane and the spectrum measured became more intense since the disordered layer was considered to be isotropic.

During torsion test, the highly-stress-concentrated parts may accelerate the fracture of the fiber through the formation and growth of micro-voids. For different CFs, the crystallite of high-strength CF is bigger than high-strength and high-modulus CFs; the grain size of high-strength CFs is smaller than high-strength and high-modulus CFs. The orientation degree of high-strength and low-modulus CF, high-strength and middle-modulus CF and high-strength and high-modulus CF diminish in sequence[19,20]. Compared with high-strength CF, high-strength and high-modulus CF had tightly packed crystallite and the zigzag gaps between the crystallite[21]. In this way the evaluation of the torsion property in relation with the structural information is quite important for understanding of the CFs behaviors. In order to gain more understanding of the CF monofilament torsion behavior, monofilament torsion test was adapted to measure the transverse torsion-bearing capacity. The structure information of the fracture part was collected by the Raman spectroscopy and the fracture morphology was observed by SEM. Furthermore, compare torsion test with polish by the structure evolution at the fracture part to study the effect of different transverse shear loads.

2. Experimental

2.1 Materials

Three types of CFs, namely CF300, CF800 and CF40 were used. The diameter of CF300, CF800 and CF40 were 4.80, 5.30 and 4.84 μm. Other typical properties of those candidates are shown in Table 1. In order to reduce the damage during experiment, sized fibers were used without any further treatment.

2.2 Sample preparation

2.2.1 Preparation of the torsion test specimen

Take 8-cm-long CF tow and separate monofilament from the tow. Place the monofilament at the center line of the U-shaped frame paper holder and tighten the monofilament carefully to keep the collimation. The monofilament was bonded with superglue. The gauge length was 40 mm. The schematic diagram of the specimen is shown in Figure 1.

2.2.2 Preparation of polished sample

The fiber was sealed vertically into resin, and the cross section of the resin was polished sequentially with sandpaper sizes 400, 600, 800, 1000 and 1200. Finally polishing until the surface is scratch free.

2.3 Monofilament torsion failure test

The direct torsion failure tests were performed on a self-designed apparatus, shown in Figure 1(a). Three steps were involved in the monofilament torsion failure test, namely, sample placement, torsion testing and data acquisition. First, test specimen was bonded to the clamps and cut the holder of the paper frame carefully without damage the monofilament. Second turn the apparatus at the torsion speed of 20 r/min. Finally, record the turns when torsion failure happened.

The twist angle at fracture δ can be calculated from the number of torsion turns by equation (1)

$$tg\delta = \frac{\pi dN}{L} \quad (1)$$

where δ is the twist angle at fracture, d is the diameter of the fiber, N is the number of torsion turns and L is the gage length.

The elongation under torsion ε can be calculated from the twist angle at fracture δ by equation (2)[9]

$$\varepsilon = \Delta L/L = (L/(cos\delta) - L)/L = (1 - cos\delta)/cos\delta \quad (2)$$

where ε is the elongation under torsion, L is the gage length and δ is the twist angle at fracture. Ten specimens for each kind of CF were tested to obtain a mean value of the torsion properties.

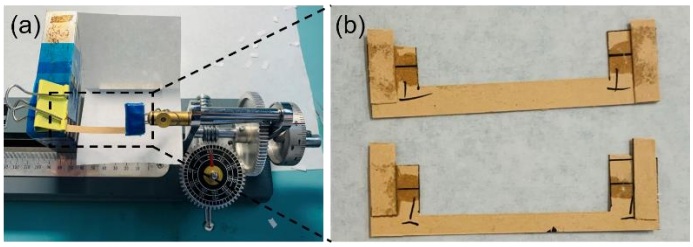

Figure 1 The self-made torsion test apparatus(a) and torsion test specimen(b)

2.4 Characterization and test

After the direct torsion failure test, the fracture of monofilament was observed by Raman spectroscopy and scanning electron microscope (SEM). The surface and fracture morphology of monofilament was observed using SEM (JSM7500, JEOL, Japan). Raman spectrum was measured by using a micro confocal laser Raman spectrometer (LabRAM HR Evolution, Horiba scientific Inc. Palaiseau, France) with a He–Ne laser excitation line. The wavelength of the exciting laser beam was 532 nm and the laser spot size was about 1 μm^2. The peaks were fitted using Lorentz function for the Raman spectra of CFs[14].

The crystallite La can be calculated from the peak intensity by equation (3)[22,23]

$$La = \frac{4.4}{I_D/I_G} \quad (3)$$

where I_D is the intensity of D-band and the I_G is the intensity of G-band.

Table 3 The mechanical properties of carbon fibers

CF types	Tensile Strength/MPa	Tensile Modulus/GPa	Elongation/%
CF300	4174	239	1.75
CF800	6573	302	2.18
CF40	4461	383	1.16

3. Results and Discussion

3.1 The torsion behavior of different kinds of carbon fiber

After the monofilament torsion failure test, the twist angle at fracture and the elongation under tension based on equation (1, 2) were adopted to characterize the torsion-bearing capacity of monofilament. Figure 2 shows the torsion test results for various CFs. The CF800 exhibited

the highest torsion-bearing capacity, with the twist angle at fracture of 3.60° and the elongation in torsion of 1.99‰. The CF300 exhibited the lowest torsion-bearing capacity, with the twist angle at fracture of 1.54° and the elongation in torsion of 0.36‰. For CF40, the torsion-bearing capacity was between CF300 and CF800, with the twist angle at fracture of 2.15°and the elongation in torsion of 0.71‰. Referring to the mechanical property listed in Table 1, it can be inferred that the order of the torsion-bearing capacity of CFs agrees well with the order of the tensile elongation at break. The torsion performance of CF800 and CF40 implicated that the higher tensile strength might exhibit better torsion properties while the higher modulus might induce worse torsion properties.

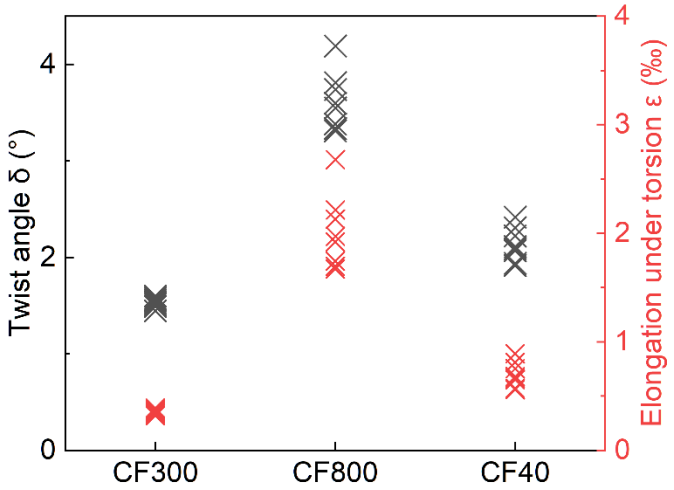

Figure 2 The torsion properties of three kinds of carbon fibers

The SEM images of fracture morphology after the torsion test are shown in Figure 3. A wedge shape fracture was shown in all the images and the fracture section differed from each other. The fracture section of CF300 shown in Figure 3(a) was relatively obtuse and the cross morphology was smooth, which suggested that the carbon fiber monofilament was destroyed by shear stress. The fracture part of CF40 shown in Figure 3(b) covered over a wide range. Different from CF300, the breakage developed along the grooves in the surface which was beneficial for the torsion behavior. Compared with CF300, the twist angle at fracture and the elongation under tension increased by 39.6% and 97.2% relatively. The wedge for the strongest CF800 with the best torsion-bearing capacity shown as a spiral shape in Figure 3(c) and was relatively sharp. More importantly obvious deformation like wave was observed in Figure 3(d), which means that the outer layer of CF800 bore great torque and the graphite structure were wrinkled under high torque. The wrinkle deformation was generated by the accumulated energy and increased the fracture surface energy. With the special fracture morphology and high fracture surface energy, the twist angle at fracture and the elongation under tension were increased to 3.60° and 1.99‰.

Those fracture morphologies suggested that the outer layer of the monofilament under larger torque was first destroyed and different failure modes were shown depending on the fiber property. Normal-modulus CF300 failed by shear stress raised by the torsion stress; high-strength and middle-modulus CF800 failed by torsion stress and the torsion stress transferred to the fiber completely; for high-strength and high-modulus CF40, the damage firstly happened in the outer layer and extended along the axial direction. Thereby, when the modulus is

relatively small, the carbon fibers failed in mixed mode, which is raised by torsion and shear stress. Along with the growing tensile modulus, the torsion gradually transferred to the whole cross section and the fiber broke in torsion mode. For high-modulus CF, the torsion stress transferred in the outer layer and along the axial direction in the outer layer.

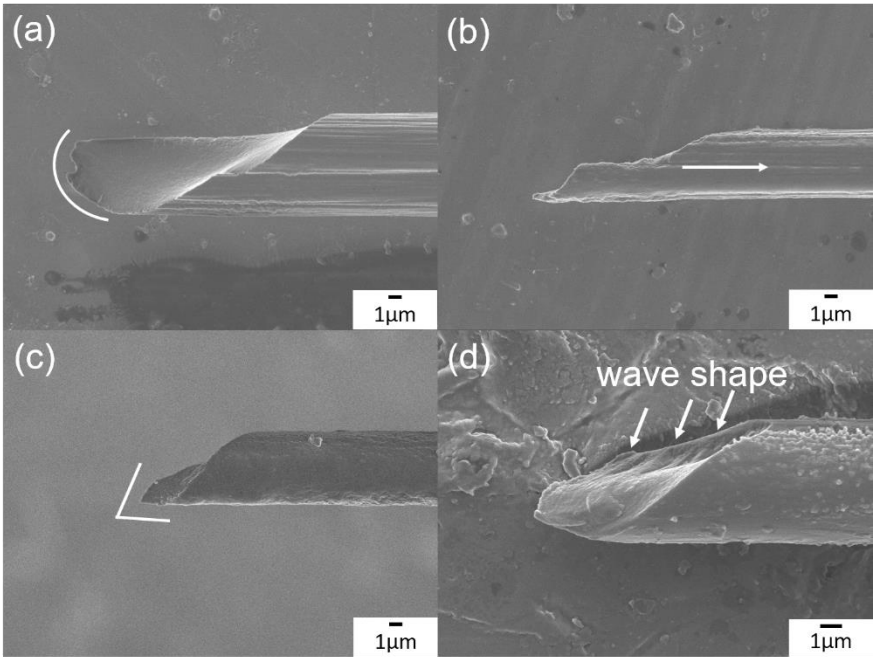

Figure 1 The image of the torsion fracture of (a)CF300, (b)CF40, and (c, d)CF800

3.2 The effects of torsion on the structure evolution of different kinds of carbon fiber

After the monofilament torsion failure test, deformation can be observed from the SEM images. The structure information was investigated using Raman spectroscopy. The Raman spectra of samples was shown in Figure 2. Generally, for carbon materials, the G-band derived from graphite structure and D-band derived from defects can be demonstrates. The G-band blue-shift can be observed obviously in all CFs and the D-band red-shift can be observed in CF800 and CF40. Those band shifts indicated that structure evolution happened during torsion. Besides, the peak of CF300 between D-band and G-band became more apparent. Quantitative research was applied to the Raman spectra in order to explore the structure change exactly inside the CFs.

The damage that the carbon fiber monofilament suffered from tension test can be represented by the area ratio A_D/A_G, which was shown in Figure 2(d). The standard A_D/A_G of CF800 is 2.79 and 3.91 after torsion. The A_D/A_G of CF800 referred as the degree of graphitization increased 40% after tension test, which demonstrated that the graphite structure was damaged greatly. The A_D/A_G of CF300 and CF40 shown a decrease by 7.4% and 20%. The A_D/A_G of CF300 decreased to 1.12 from 1.21. The A_D/A_G of CF40 decreased to 1.21 from 1.54. This indicated that the defect was introduced to CF800 fibers while the defect of CF300 and CF40 reduced by tension test.

The crystallite La calculated from equation 3 indicated the graphite structure of CFs, which was shown in Figure 2(d). The La of CF800 decreased to 3.31nm after torsion, of which the standard La was 4.1nm. The La of CF300 and CF40 shown almost no difference after tension test. The standard La of CF300 was 5.64 nm and La after torsion was 5.71 nm. The standard La of CF40 was 3.53 nm and La after torsion was 3.58 nm. This indicated that the tension stress changed the graphite structure of CF800 greatly but little of CF300 and CF40, which was

proved by the SEM images. The structure evolution of CF800 was evidently reflected by the Raman spectra and SEM images.

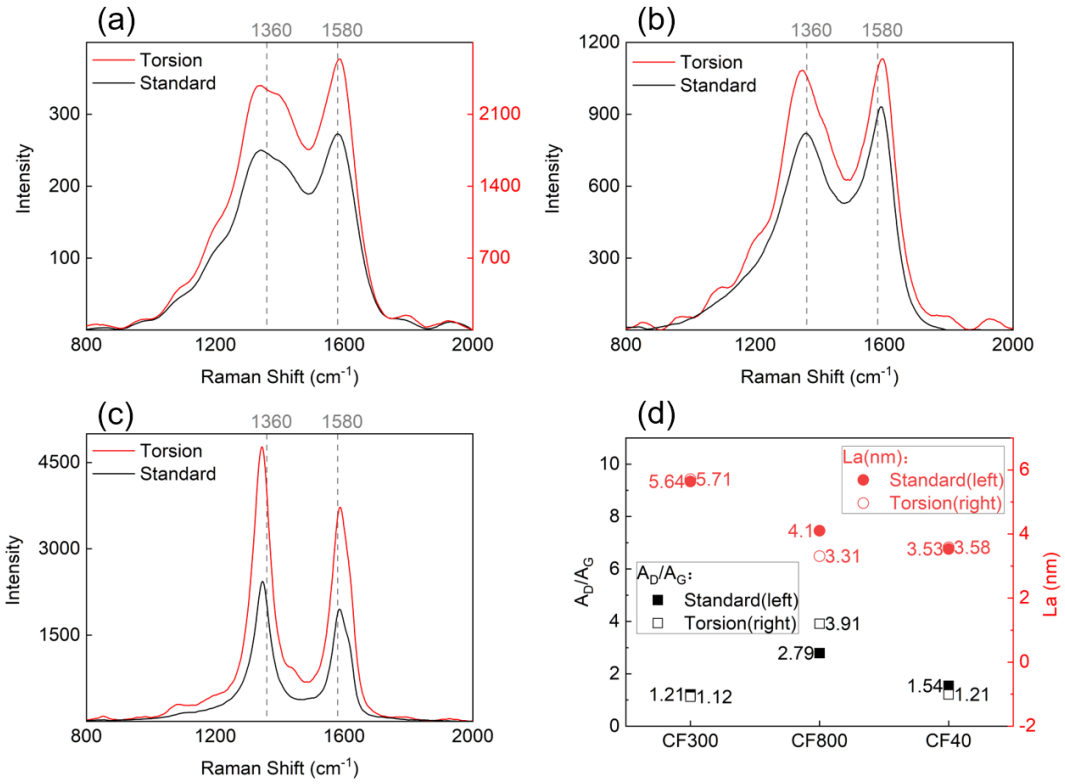

Figure 2 The Raman spectra of (a)CF300, (b)CF800 and (c)CF40 in standard condition and after torsion and (d)the structure information probed from Raman spectra

3.3 The effects of polish on the structure evolution of different kinds of carbon fiber

After the research of the monofilament torsion test, the structure change after polish process was studied using Raman spectroscopy. The Raman spectra of CF after torsion process was shown in Figure 3(a-c). The D-band and G-band shift can be observed in all CFs after polishing and was more obvious than the shift after torsion. The relative intensity of G-band was observed to be lower after two processing and was much lower after polishing. For CF300, the Raman spectra lose details in D-band after polish which can be observed after torsion. For CF800, the intensity of G-band got lower than the D-band after polish, while the intensity of G-band was higher than the D-band in other condition. For CF40, the intensity of G-band after polish process was reduced to almost half of the intensity of D-band and the G-band was wider after polish process. The spectra demonstrated that more changes happened during polish process. More structure information calculated from the Raman spectra was discussed.

The D-band referred as defect band was studied by its position, shown in Figure 3(d). The D-band position of CF300, CF800 and CF40 after polishing shifted to a similar position compared with the standard position, which were 1353.9, 1354.0 and 1349.5 cm^{-1} respectively. This suggested that on the polished surface a kind of similar disordering occurred. The D-band of CF300 exhibited red-shift after torsion and blue-shift after polish and both shifts were large. The D-band position of CF800 red-shifted to about 1354 cm^{-1} after torsion and polishing. The D-band position of CF40 exhibited red-shift after torsion and blue-shift after polish and both shifts were in a small scale. Those results demonstrated that kinds of defect inside CF propagated after different process and CF300 suffered most damages fibers after polish process.

The area ratio A_D/A_G referred as the degree of graphitization was discussed. The A_D/A_G of

CF300, CF800 and CF40 after polish were 2.67, 2.51 and 1.98 respectively. The A_D/A_G of CF800 increased by 40% after torsion, which mean that torsion had a significant influence on the degree of graphitization. The A_D/A_G of CF300 and CF40 increased after polishing but decreased after torsion like the D-band position. The A_D/A_G of CF300 increased by 121% after polish, which shown that polish damaged CF300 seriously. These results demonstrated that the A_D/A_G was influenced by process and modulus. It demonstrated that torsion had more influence to the degree of graphitization of CF800 and the polish damaged degree of graphitization of CF300 and CF40 seriously.

The intensity ratio I_D/I_G was discussed. The I_D/I_G of CF300, CF800 and CF40 after polish were 1.09, 1.10 and 2.09 respectively. The I_D/I_G of CF300 increased by 40% after polish and kept almost unchanged after torsion, which demonstrated that polishing brought more defects to CF300 than torsion. The I_D/I_G of CF40 increased by 67% after polish and kept almost unchanged after torsion like CF300, which demonstrated that polish bring more defects to CF300 than torsion. The I_D/I_G of CF800, in a opposite situation, increased after torsion and kept unchanged after polish. It demonstrated that torsion was more influential to the graphite structure of CF800 and the polish damaged the graphite structure of CF300 and CF40 seriously.

Through the analysis, some rules about the CFs can be inferred. The change of structure parameters after two processes of CF300 and CF40 was similar while the change of CF800 shown a opposite law. Associated with the mechanical properties, the tensile strength and the elongation after tensile test have an essential connection to its behavior in torsion test and polishing. For CF800, better elongation and high-strength made it possible to generate larger deformation which mean more damage was possible to propagate. Torsion test applied stress continuously with the progressively deformation and damaged the CF800 structure more seriously than the polishing, which provided transience and sudden stress. For CF300, the tensile strength and modulus were in a relatively middle level so it was easier to get broken in polishing, so the degree of graphite decreased and the defects propagated. Due to the limit of its mechanical property, the monofilament failed without the completely transferring of torsion load but of shear load, so the structure changed little but defects increased. For CF40, the high modulus made it difficult to generate great deformation, which also mean CF40 get broken easily in polishing. And in torsion test, CF40 first got damaged at the outer layer and the deformation transfer at the outer layer until the final fracture.

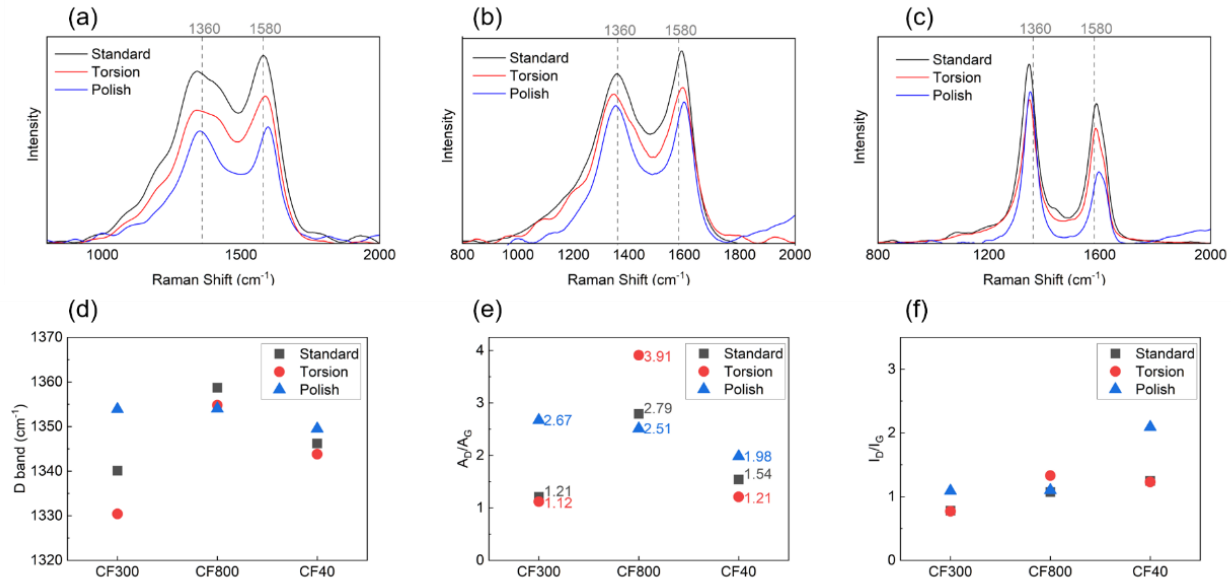

Figure 3 The Raman spectra after polish process of (a)CF300(b)CF800(c)CF40 and the structure information as indicated by the value of (d)D-band position(e) A_D/A_G and (f)I_D/I_G

4. Conclusion

In this study, three kinds of CFs were studied by monofilament torsion test and the fracture structure was characterized by SEM and Raman spectroscopy. The fracture structure after different process was studied and compared. The conclusion is as follows:

(1) The twist angle at fracture and the elongation after torsion were measured to characterize the torsion-bearing capacity of monofilament of CF. The torsion property and the fracture modes are inferior to its tension property. CF800 shows the highest elongation under tension and obvious deformation at the fracture section, indicating of the best torsion tenacity among three carbon fibers. CF300 shows shear fracture after torsion. CF40 shows a wide and straight long fracture section with the crack initiated along the grooves at the fiber surface.

(2) Structure evolution at the fracture section after torsion was probed by Raman spectroscopy, which should be ascribed to the tenacity of the CFs. With the modulus increasing, the structure paraments firstly rise and then fall. Normal-modulus CF300 failed at the shear mode because of the incomplete torsion stress transferring. The structure paraments of middle-modulus CF800 with the highest torsion properties changed mostly after torsion corresponding to the great deformation. For high-modulus CF40, it has a high degree of graphitization and the structure changed little after torsion.

(3) Torsion has more influence on the structure of the high elongation fibers, like the middle-modulus high-strength carbon fiber CF800, because larger deformation happened during the torsion test. However, polishing treatment on the cross section of CF has more influence on the structure of the low elongation fibers than torsion, like the normal-modulus CF300 and high-modulus high-strength carbon fibers CF40.

REFERENCES

1. Y. Li, W. Li, and Y. Tao, “Theoretical model for the temperature dependent longitudinal tensile

strength of unidirectional fiber reinforced polymer composites," COMPOS PART B-ENG, 161, 121-127, 2019.
2. W. Z. Zhao, N. Pei, and C. G. Xu, "Experimental study of carbon/glass fiber-reinforced hybrid laminate composites with torsional loads by using acoustic emission and Micro-CT," COMPOS STRUCT, 290, 115541, 2022.
3. F. Du, S. Alghamdi, and B. Riabbans, "An experimental study on the fracture of a unidirectional carbon fiber-reinforced composite under quasistatic torsion," COMPOS PART B-ENG, 172, 547-554, 2019.
4. J. H. Hu, L. Zeng, and P. Hu, "A new torsion tester based on an electronic autocollimator for characterizing the torsional behaviors of microfibers," Rev Sci Instrum, 92, 10, 103905, 2021.
5. Fan, H., Gu, Y., and Wang, S., "Characterization and analysis of torsion property of carbon fiber bundle combined with epoxy resin," POLYM COMPOSITE, 39, S4, E2529-E2539, 2018.
6. Y. Chai, Y. Wang, and Z. Yousaf, "Damage evolution in braided composite tubes under torsion studied by in-situ X-ray computed tomography," COMPOS SCI TECHNOL, 188, 107976, 2020.
7. T. Ogasawara, K. Onta, and S. Ogihara, "Torsion fatigue behavior of unidirectional carbon/epoxy and glass/epoxy composites," COMPOS STRUCT, 90, 4, 482-489, 2009.
8. G. Zhang, Z. Zhou, and G. Ding, "Static property analyses based on finite element method and torsion tests on carbon fibre composite motor drive shaft," Materials Research Innovations, 19, sup5, 713-717, 2015.
9. Y. N. Liu, M. Li, and Y. Z. Gu, "Characterization of torsion behavior and fracture morphology of single carbon fiber," J. Compos Mater., 48, 16, 1993-1999, 2013.
10. G. Z. Ren, C. J. Chen, and L. H. Deng, "Microstructural heterogeneity on the cylindrical surface of carbon fibers analyzed by Raman spectroscopy," NEW CARBON MATER, 30, 5, 476-480, 2015.
11. S. S. Bukalov, L. A. Leites, and A. S. Goloveshkin, "Structure of sp2-carbon fiber prepared by high-temperature thermomechanical treatment of polyacrylonitrile fiber: a Raman and X-ray diffraction study," RUSS CHEM B+, 67, 6, 1002-1009, 2018.
12. F. Tuinstra, and J. L. Koenig, "Raman Spectrum of Graphite," J CHEM PHYS, 53, 3, 1126-1130, 1970.
13. Y. L. Huang, and R. J. Young, "Microstructure and mechanical properties of pitch-based carbon fibres," J MATER SCI, 29, 4027-4036, 1994.
14. A. Sadezky, H. Muckenhuber, and H. Grothe, "Raman microspectroscopy of soot and related carbonaceous materials: Spectral analysis and structural information," Carbon, 43, 8, 1731-1742, 2005.
15. G. Katagiri, H. Ishida, and A. Ishitani, "RAMAN SPECTRA OF GRAPHITE EDGE PLANES," Carbon, 26, 4, 565-571, 1988.
16. D. H. Li, C. X. Lu, and G. P. Wu, "Heat-induced Internal Strain Relaxation and its Effect on the Microstructure of Polyacrylonitrile-based Carbon Fiber," J MATER SCI TECHNOL, 30, 10, 1051-1058, 2014.
17. T. Kobayashi, K. Sumiya, and Y. Fukuba, "Structural heterogeneity and stress distribution in carbon fiber monofilament as revealed by synchrotron micro-beam X-ray scattering and micro-Raman spectral measurements," Carbon, 49, 5, 1646-1652, 2011.
18. P. Lespade, R. Al-Jishi, and M. S. Dresselhaus, "Model for Raman scattering from incompletely graphitized carbons," Carbon, 20, 5, 427-431, 1982.
19. X. Zhang, L. Ma, and C. Q. Li, "Study of the microstructure of PAN-based carbon fibers," 5, 57-60, 2008.
20. M. Zhang, B. Zhu, and C. G. Wang, "Surface and fracture morphologies of carbon observed by SEM," J FUNCT MATER, 41, 10, 1731-1733, 2010.
21. W. W. Li, H. L. Kang, and J. Xu, "Microstructures of High-strength High-modulus Carbon Fibers and High-modulus Carbon Fibers," ACTA POLYMERICA SINICA, 3, 380-388, 2018.
22. F. Tuinstra, and J. L. Koenig, "Characterization of Graphite Fiber Surfaces with Raman Spectroscopy," Compos Mater., 4, 4, 492-499, 1970.
23. T. Jawhari, A. Roid, and J. Casado, "Raman spectroscopic characterization of some commercially available carbon black materials," Carbon, 33, 11, 1561-1565, 1995.

Real-time damage localization method for anisotropic composite materials based on multi-point acoustic emission localization technique

*Jiayin Liu[1,3], Chao Li[1], Zixi Li[1], XinXin Yan[3], Jian Zhang[2], Debo Liu[2], Huiqiang Wu[2], Wenduo Chen[1], Dazhi Jiang[1]**

1: Shenzhen Campus of Sun Yat-sen University 518107, P.R. China

2: Beijing institute of spacecraft environment engineering, Beijing 100076, PR China

3: Institute of advanced science facilities, Shenzhen 518107, PR China

Abstract: Carbon fiber reinforced composites (CFRP) are composed of various components coupling with each other, causing complexity and unpredictability of the damages, for which a reliable monitoring method is necessary. Acoustic emission (AE) technology is developing rapidly, which has been widely applied to detect and localize damages in metal materials according to the acoustic velocity and the signal receiving time by the probes. Current 3-point localize method can only guarantee the damage localization accuracy in isotropic materials. However, composite materials exhibit obvious anisotropy, the acoustic velocity is influenced when propagating through anisotropic media, proposing great challenges to the localization technique. To solve the above problems, a new acoustic emission localization method is developed in this paper. Firstly, the elastic wave velocities in various orientations on CFRP laminates are measured by two probes of AE, the data is then fitted by a function to form an anisotropic elastic wave velocity model for the CFRP laminates. The multi-point localization method is designed to localize the damage source in two-dimensional anisotropic plates with plane surface by substituting the received signal data into the anisotropic elastic wave velocity model, meanwhile, Monte Carlo method combined with mutual-correction method by multi-probe data is put forward to improve the localizing accuracy. The method is then extended to curved surface of a cylindrical shell structure, and the damage localizing accuracy is verified by lead pen breaking experiments. The results show that the anisotropic multi-point acoustic emission localization technique greatly improves the localization accuracy with the error reduced by more than 60%, compared with the traditional ones. This method is expected to form a widely applicable engineering technique of real-time nondestructie testing in the future,

which will provide a guarantee for the reliability of the composvite structures.

Key words: carbon fiber reinforced composites; real-time damage localization; anisotropy; acoustic emission technique; Monte Carlo method

1 Introduction

Composites are widely applied in spacecraft, ships, automobiles, competitive sports and other fields to achieve structural lightweight and improved performance due to their excellent properties such as high elastic modulus, excellent specific strength, corrosion resistance and fatigue resistance[1-4]. However, the composition and inner load distribution of composites are complex, taking the carbon fiber reinforced composite (CFRP) for example, the physical properties between carbon fiber and resin matrix are quite different[5, 6]. Under external load, carbon fiber acts as the load-bearing support, while the resin matrix bonds them together as a whole. This complex system corresponds to a variety of damage modes, including carbon fiber fracture, matrix cracking, interfacial debonding and so on. Various failures occur at random times and scales, which are difficult to be traced, classified or even perceived, bringing latent danger to the reliability of composite structures. Therefore, a reliable method to monitor, accurately localize and distinguish the micro-damage of composite load-bearing structures in real time has become a research hotspot at present[7-9].

Acoustic emission (AE) method as a new non-destructive testing (NDT) technology is developing rapidly in recent years[10-12]. The basic principle is that, under external load, sudden changes of microstructure occur during plastic deformation, crack formation and propagation, debonding and other non-linear-elastic processes, inevitably been accompanied by the releasing of elastic energy. Part of the energy turns into the form of elastic vibration with specific characteristics of frequency or amplitude (that is, acoustic emission signal). The acoustic emission probes are adopted to detect and analyze the vibration information so as to localize the signal emission source (damage) in real time and judge its mode.

Real-time damage localization is the highlight of acoustic emission technology[13-15]. Acoustic emission signals can be divided into continuous type and burst type, according to its separability in the time domain (in fact, acoustic emission signals are all burst types, while which is considered as a continuous one when the signal frequency is too high, acoustic waves overlapping with each other and cannot be distinguished). For continuous ones, time-domain information is difficult to obtain, the damage localization is realized by energy amplitude estimation: acoustic wave transmission process will experience reflection, scattering and absorption, resulting in acoustic wave energy attenuation which can be recorded by the probes and compared, the approximate area of damage is thus estimated. While for burst acoustic emission signals, the coordinates of damage can be calculated by geometric principle, mainly according to the acoustic velocity and receiving time by each probe. This method, known as “Time difference localization”, is the most commonly applied acoustic emission localization technology.

Fotouhi[16, 17] applied acoustic emission (AE) techniques to investigate transverse cracking mechanism in graphic/resin cross-ply composites. Plate wave propagation analysis technique was adopted to separate the signals from the noises, four probes were adopted to realize matrix localization based on the spectrum theory. The length of the crack was detected by back-scattered ultrasound, X-ray technique, destructive section and microscopic observation, respectively. The results of various tests were consistent with the AE localization, and the deviation was only 3.2 mm. Niri[18] used acoustic emission techniques to localize cracks in the pressure vessel. The time difference localization method was combined with a probability distribution algorithm, and the uncertainties of measurement system and acoustic velocity error were fully considered to realize the damage location estimation. The method was previously proved to be feasible in the plane test, which was then extended to the cylindrical surface and also achieved high localization accuracy.

With the development of AE technology, localization algorithms are becoming more and more diversified[19-23]. Liu[24, 25] proposed the region localization algorithm, as shown in Fig.1. Acoustic emission probe arrays were applied to infer the position of damage according to the signal arriving time. This method was applicable for quasi-isotropic materials and required that the distance between the probes be much less than that between the probes and the damage. While, when the damage appeared close to the probe array, the localization error turned unacceptable. Wu[26] introduced empirical mode decomposition and wavelet analysis techniques to improve the localizing accuracy. Li[27] proposed the time reversal method, which could achieve time-domain focusing and signal-noise separation. On this basis, Ciampa[28] brought in imaging algorithm to realize the damage localization in anisotropic materials.

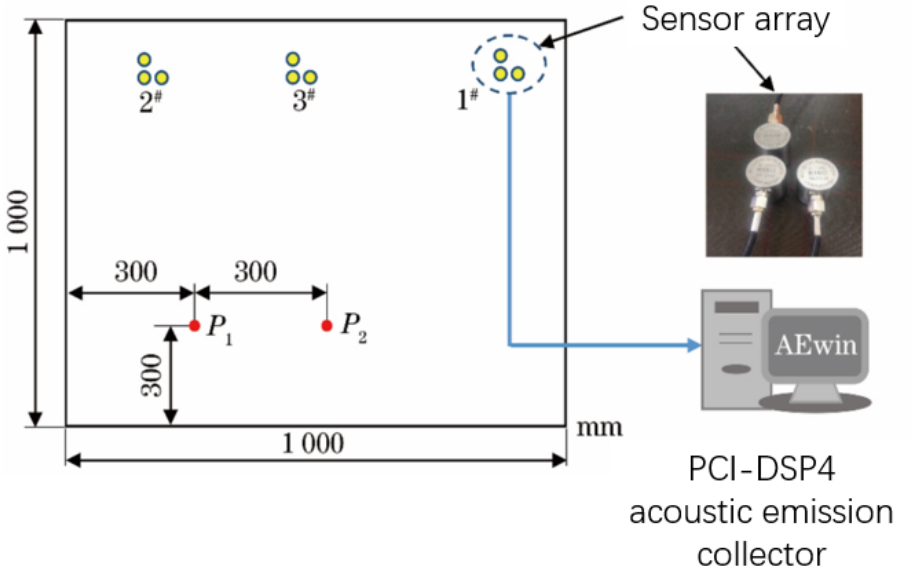

Figure 1 Schematic diagram of three-sensor array localizing test[24,25]

However, for existing acoustic emission (AE) localization techniques, there is still no widely recognized anisotropic acoustic velocity propagation mechanism in essence. Though they have exhibited high localization accuracy for isotropic or quasi-isotropic composite

materials, however, which is the other way around when comes to the materials with significant anisotropy. In this paper, the acoustic velocities in two-dimensional CFRP laminates including unidirectional and orthogonal are studied firstly. The variation law of the acoustic velocity with the orientation angle is summarized and the anisotropic acoustic velocity model is established. On the basis, a multi-point localizing verification method is proposed according to the Monte Carlo sampling theory, the approximate unbiased estimation of the damage location can be obtained by checking and correcting the multiple samples, and the discreteness of the localizing results can be decreased. Finally, the method is extended to 3D space for pressure vessel damage localization. The theoretical correctness is then verified through the significantly improved localizing accuracy by comparing with the traditional method. Which will provide technical references for nondestructive testing and health monitoring of the fiber reinforced polymer composite structures in the future.

2 Materials and equipment

In this paper, the experimental subjects include CFRP planar laminates and the space curved surface structure of a composite pressure vessel. The CFRP laminates in the size of 250×250 mm^2 are mainly composed of resin (HX3250) and carbon fiber (T300, Japan Toray) with the curing agent of m-phenylenediamine, the components' parameters are shown in Tab.1-Tab.3, respectively. The laminates can be divided into the orthogonal and unidirectional ones. The preparation methods are as follows: 8 pieces of carbon fiber unidirectional plies are cut into 250 mm×250 mm, and then laminated in the mold of corresponding size in certain orientations by sequence; resin and m-phenylenediamine are mixed according to the ration of 100:15 and then applied on the plies during the laminating process. Assemble the mold to the hot-press, set the pressure to 0.5 MPa, precure at 80℃ for 2 hours, then heat till 150℃ and cure for 2 hours, finally cool to room temperature and demould. The physical parameters of each laminated board are shown in Tab.4. The composite pressure vessel (CFRP tank) with the height of 900mm and the diameter of 800mm, shown in Fig.2, is consistent with the planar laminated plates for the same raw material, except that the former is produced by unidirectional ply winding with the top and bottom heads wound at 52° spiral angle, while the cylindric part strengthened by extra plies in circumferential direction.

Table 1 Performance parameters of T300 carbon fiber

Model	density/g·cm^{-3}	Ultimate elongation/%	Tensile strength/MPa	Tensile modulus/GPa
T300	1.76	1.50	3530	230

Table 2 Quality Index of Epoxy Resin E-51

Epoxy equivalent /g/eg	Hydrolyzable chlorine /wt%≤	Viscosity /mpa·s	Volatile fraction /≤%	Chroma /≤
184-194	0.10	11000-14000	0.20	0.5

Table 3 Performance parameters of m-phenylenediamine

Density/g·cm^{-3}	Melting point/℃	Boiling point/℃	Refractive index	Critical pressure /MPa	Ignition temperature/℃
1.139	64-66	282-284	1.6399	5.18	560

Table 4 Physical parameters of each laminated board

	Thickness/mm	mass/g	mass fraction of CF/%	volume fraction of CF/%
Orthogonal laminate	1.687	166.61	75.6	67.9
Unidirectional laminate	1.693	157.18	60.3	50.9

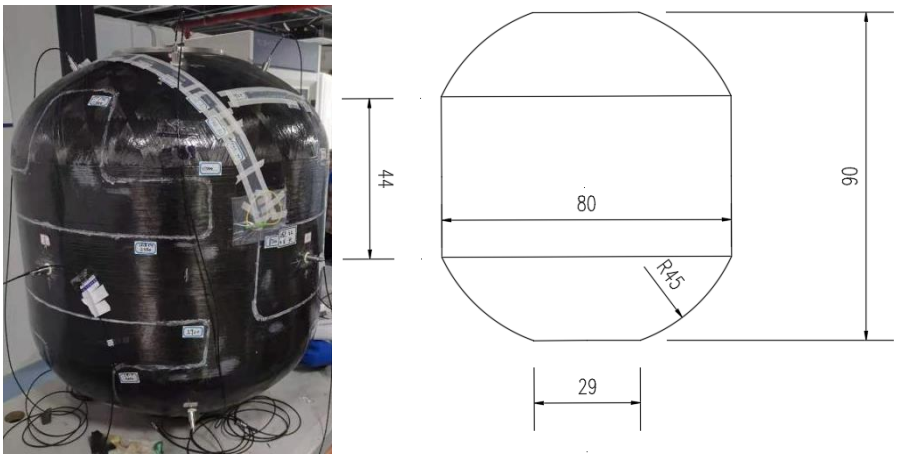

Figure 2 CFRP tank and its dimensions

In this research, the AE testing equipment adopts NetAE-2F 12-channel acoustic emission apparatus integrated by the PXAES Mulplat acoustic emission signal acquisition software from Changsha Pengxiang company in China, together with the AE154DL acoustic emission probes of Fuji Custom in Japan. The acoustic signal is simulated by lead core breaking. A 0.5 mm HB lead pen with an elongation of 3mm lead core is standardized. The tip of the lead core is gently placed on the pre-marked point on the sample, with a contact angle of 30°, then increase the pressure to break it and emit the acoustic wave. Take the 3-point AE localization system for example, as shown in Fig. 3, the blue spots represent the probes, and the red ones are the random lead-breaking test positions. The probes are distributed symmetrically, the specific coordinates and the distance between them are set according to the sample size and confessed in detail later. The lead-breaking tests are repeated at least five times at each point, in order to ensure the reliability. The expectation of the localization results is compared with the actual lead breaking point coordinates to evaluate the algorithm accuracy, and the standard deviation is taken as the evaluation index to measure data discreteness.

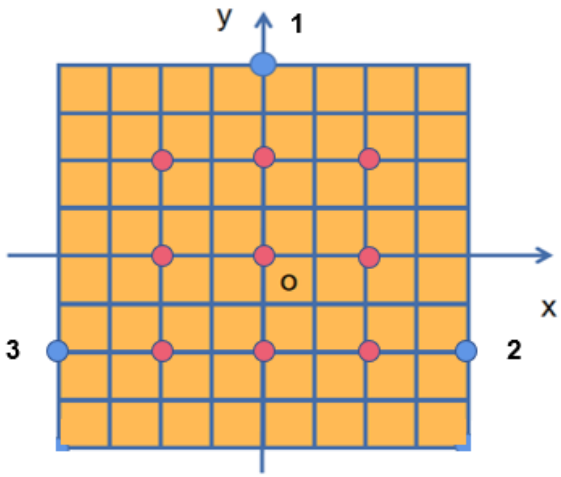

Figure 3 Schematic diagram of probe layout of three-point localizing method

3 Localization algorithm

3.1 AE localization algorithm for isotropic materials

Since the acoustic velocity in isotropic materials is constant, the time taken for acoustic waves travelling from the AE source point to the probe is proportional to the distance. The isotropic acoustic velocity model is simple, equations can be established:

$$l_1 = v \times (t_1 - t_0) = \sqrt[2]{(x_1 - x_0)^2 + (y_1 - y_0)^2} \quad (1)$$

$$l_2 = v \times (t_2 - t_0) = \sqrt[2]{(x_2 - x_0)^2 + (y_2 - y_0)^2} \quad (2)$$

$$l_3 = v \times (t_3 - t_0) = \sqrt[2]{(x_3 - x_0)^2 + (y_3 - y_0)^2} \quad (3)$$

Where,

l_i（i=1, 2 or 3）is the distance between the acoustic source/corresponding probe;

v is the isotropic propagating velocity of the acoustic wave

(x_i, y_i) （i=1, 2 or 3）is the coordinates of the probes

(x_0, y_0) is the coordinates of the acoustic source

t_i（i=1, 2 or 3）is the signal receiving time by the probes

t_0 is the signal emitting time by acoustic source

Three equations are enough to be solved simultaneously for the acoustic signal generation time t_0 and the signal source coordinates (x_0, y_0). According to geometric theory, each of the above individual formulas corresponds to a circular arc centered on one of the probes P_i (i can be 1,2,3 optional) with the radius of $v(t_i\text{-}t_0)$, and the intersection of three circular arcs should be the acoustic source location.

As mentioned above, the acoustic velocities of the anisotropic composites vary with the orientations, the wavefront profile is non-circular but has preferred orientations, which leads to the inconsistency of the isotropic velocity eigen-equation with the actual situation, resulting in large localization error. It is necessary to establish an anisotropic acoustic velocity model.

3.2 AE localization algorithm for anisotropic materials

For anisotropic composites, the acoustic velocity is a function of the orientation angle θ,

which can be obtained by experimental tests combined with mathematical function fitting method. For a straight-line path of certain length, as the fiber orientation unchanged, it is considered that the acoustic velocity stays constant which can still satisfy the linear relationship. Replace v in formula (1)-(3) with $v(\theta)$, there is:

$$l_1 = v(\theta) \times (t_1 - t_0) = \sqrt[2]{(x_1 - x_0)^2 + (y_1 - y_0)^2} \tag{4}$$

$$l_2 = v(\theta) \times (t_2 - t_0) = \sqrt[2]{(x_2 - x_0)^2 + (y_2 - y_0)^2} \tag{5}$$

$$l_3 = v(\theta) \times (t_3 - t_0) = \sqrt[2]{(x_3 - x_0)^2 + (y_3 - y_0)^2} \tag{6}$$

When θ takes plane orientation angle value of the probe position relative to the sound source, and according to the trigonometric function relationship, there is:

$$\theta_i = \tan^{-1}\frac{y_i - y_0}{x_i - x_0} \tag{7}$$

By substituting formula (7) into (4)-(6), a set of ternary equations about (x_0, y_0, t_0) is obtained, and the acoustic source coordinates can be obtained by solving the equations simultaneously.

$$l_1 = v\left(\tan^{-1}\frac{y_1 - y_0}{x_1 - x_0}\right) \times (t_1 - t_0) = \sqrt[2]{(x_1 - x_0)^2 + (y_1 - y_0)^2} \tag{8}$$

$$l_2 = v\left(\tan^{-1}\frac{y_2 - y_0}{x_2 - x_0}\right) \times (t_2 - t_0) = \sqrt[2]{(x_2 - x_0)^2 + (y_2 - y_0)^2} \tag{9}$$

$$l_3 = v\left(\tan^{-1}\frac{y_3 - y_0}{x_3 - x_0}\right) \times (t_3 - t_0) = \sqrt[2]{(x_3 - x_0)^2 + (y_3 - y_0)^2} \tag{10}$$

This method adopts the anisotropic acoustic velocity which is closer to the reality than the isotropic one for anisotropic material. However, from the view of equation solving, there are deviations in anisotropic acoustic velocity measurement, and the $v(\theta)$ equation is relatively more complex, although it can be solved iteratively by Matlab program, the calculation results are unstable which may prone to singular values in higher probability. Therefore, improvements are necessary based on the original three-point localization.

3.3 Multi-probe self-calibration method

The non-collinear three-probe information can support the acoustic source localization calculation, which embodies the necessity of the algorithm. In fact, the recorded data has certain deviation, fully depending on the reliability of the probe measurement in a single test. Furthermore, if one of the probes fails, it will be unable to localize. Acoustic emission signals in engineering are not repeatable, the fault tolerance of this method is low. In order to improve the reliability of AE localization, a multi-point localization algorithm based on Monte Carlo sampling theory is proposed in this paper.

The so-called Monte Carlo method is to construct a suitable probability model according to the law of the stochastic problem to be solved or the statistical law of the physical phenomenon itself. Conduct a large number of statistical experiments according to the model, so that some of its statistical parameters are just the solution of the stochastic problem. A classic application is the π value computation, repeated sampling finally results in high-precision unbiased estimation.

The core idea of the Monte Carlo method is to expand the sample size, which can be realized by repeated sampling or reasonable extrapolation of limited samples. When the sample size reaches a certain extent, the probability distribution of the sample tends to be consistent

with a typical probability model (the Gauss statistical theory is applied to in this paper), according to which, the expected values can be estimated, and the confidence intervals of discrete data can also be obtained. Monte Carlo simple sampling method (weight fraction is neglected) for estimating the expected value of *f*(x) in [a, b] interval is shown in formula (11), (12).

$$I = \int_a^b f(x)dx \tag{11}$$

$$< f(x) >= \frac{I}{(b-a)} \tag{12}$$

Where, *I* is the the integral value of *f*(x) in the sample space

<*f*(x)> is the no weighted mean in the sample space

While for discrete samples, there is:

$$< f(x) >= \frac{\sum_1^M f(x_i)}{M} \qquad x_i \in [a, b] \tag{13}$$

Where, *M* is the number of repeated sampling

According to Monte Carlo theory, the result of each 3-point localization can be regarded as a sample corresponding to a random error. Assuming the localization algorithm as an unbiased estimation. With the increase number of samples, the deviation vectors will cancel each other in the process of aggregation, and finally make the expected value return to the coordinate of the real, and the discreteness decreases. On the other hand, the samples can be screened first, removing the singular points. Usually the large deviation point is caused by the error of the experiment operation, while even if the exceptions, the corresponding probability of large deviation value is quite low according to the Gauss statistical theory, and the influence of the filtering process on the expectation estimation can also be ignored. Thus, the irreparable influence of the test error on the final result can be reduced.

For the localization method in this paper, we can increase the number of probes on the basis of three, for example m-point localization, and any three among the m-point can be analyzed once, a permutation combination process is taken in order to expand the sample capacity, that is a total of C_m^3 independent samples. Supposing there are n samples (C_m^3=n), the mean square deviation of localizing error can be expressed by the following:

$$d\mathrm{m} = \sqrt{[(\frac{x_{11} + x_{12} \ldots + x_{1n}}{n} - x)^2 + (\frac{x_{21} + x_{22} \ldots + x_{2n}}{n} - x)^2 \ldots . + (\frac{x_{k1} + x_{k2} \ldots + x_{kn}}{n} - x)^2]/k} \tag{14}$$

Where,

*d*m is the mean square deviation for m-point localization

k is the number of repeated times of the localization experiments

x_{ij} is the coordinate of the localization

x is the actual coordinate of the acoustic source (horizontal or vertical coordinates)

The equation can be simplified:

$$d\mathrm{m} = \sqrt{\frac{\sum_{i=1}^{i=k}\sum_{j=1}^{j=n}\Delta_{ij}{}^2 + \sum_{i=1}^{i=k}\sum_{j=1}^{j=n}\sum_{g=1}^{g=n}(\Delta_{ij} \cdot \Delta_{ig})(j \neq g)}{n^2 \cdot k}} \tag{15}$$

Where, Δ is the deviation of any 3-point localization.

According to the basic principle of sum of squares inequality, as Δ is not a constant, there is

$$\sum_{j=1}^{j=n}\sum_{g=1}^{g=n}(\Delta_{ij}\cdot\Delta_{ig})(j\neq g)<(n-1)\sum_{j=1}^{j=n}{\Delta_{ij}}^2 \tag{16}$$

Then, there is

$$dm<\sqrt{\frac{\sum_{i=1}^{i=k}\sum_{j=1}^{j=n}{\Delta_{ij}}^2}{n\cdot k}}=d3 \tag{17}$$

Where, $d3$ is the standard deviation for 3-point localization.

Thus, by taking the mean of n samples as the new statistical set, the corresponding standard deviation will be lower than the original independent sampling set. For actual damage monitoring, the signal is non-repeatable, that is, $j = 1$, while n can be increased within a certain range depending on the number of probes. Furthermore, as the number of n grows large enough, the mean of each group tends to approach the expected value of the whole set. Thus, there is:

$$\frac{x_{11}+x_{12}\ldots+x_{1n}}{n}=x\ (n\to\infty) \tag{18}$$

$$\sum_{g=1}^{g=n}(\Delta_{ij}\cdot\Delta_{ig})(j\neq g)=-{\Delta_{ij}}^2(n\to\infty) \tag{19}$$

$$\lim_{n\to\infty} d\,m=0 \tag{20}$$

The above tells that, through the sample quantity enhancement, localization accuracy is expected to be improved effectively. Under the premise of unbiased estimation, the orientation probability of single 3-point localizing error is uniformly distributed in the plane spatial, with the value conformed to the normal distribution law. As the number of probes m is large enough, in theory, the result of multi-probe simultaneous localizing can be approximated to the actual coordinates, and the dispersion approaches 0.

Multi-sample simulation will greatly increase the burden of data processing. In order to ensure the timeliness of NDT, 6-point localization is chosen in this paper, as shown in Fig.4. The localization is a kind of equation solving process, which can be realized by Matlab programming or by machine learning and other efficient technologies, thus, multi-point (6 points and above) real-time damage localizing is expected to be realized through program algorithm improvement.

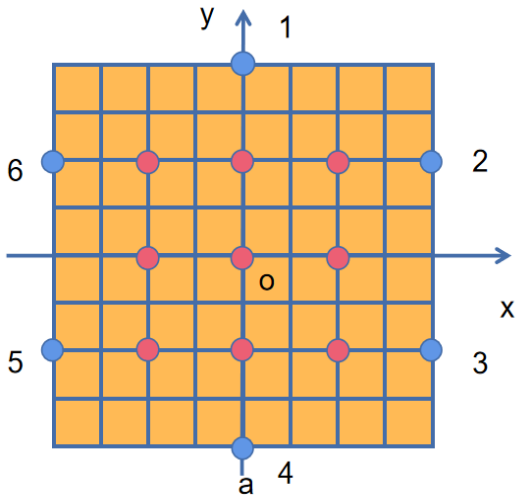

Figure 4 Schematic diagram of probe layout of six-point localizing method

4 Results and discussion

4.1 Anisotropy acoustic velocity measurement

The acoustic velocities of typical samples including the unidirectional lamination plate, orthogonal lamination plate and CFRP tank surface are measured. Acoustic velocity on the anisotropic carbon fiber reinforced epoxy composites varies with the plane orientation, the variation law is obtained by measuring the values for typical orientations and through data fitting method.

4.1.1 Anisotropic acoustic velocity of carbon fiber/epoxy unidirectional and orthotropic laminated plates

For the unidirectional/orthotropic CFRP plates, one of the carbon fiber orientation is taken as the 0° (X axis) direction. As the structure has two orthogonal symmetrical axes in the two-dimensional plane: the X axis and the Y axis. It is only necessary to investigate the variation of acoustic velocity with orientations in the range of 0-90°, and then derive the omnidirectional acoustic velocity model according to the symmetry. The typical velocity in the directions of 0°, 15°, 30°, 45°, 60°, 75° and 90° are selected, respectively. The results are shown in Tab.5.

Table 5 Acoustic velocity of T300 carbon fiber composite unidirectional and orthogonal laminate plates

orientation/°		**0**	**15**	**30**	**45**	**60**	**75**	**90**
Average acoustic velocity (m / s)	**Unidirectional**	8928.74	5726.90	3469.03	2785.45	2458.33	2299.27	2283.44
	Orthogonal	6662.94	5571.78	5393.66	5099.34	5072.16	6295.44	7186.30
Standard deviation (m / s)	**Unidirectional**	4.95	212.45	105.73	46.21	48.36	62.98	22.77
	Orthogonal	195.89	213.78	82.07	84.20	275.69	185.78	182.26

In this work, the anisotropic acoustic velocity-orientation model in two-dimensional plane is obtained by a simple method of polynomial (quadric or quantic depending on the curve complicity) curve fitting of scattered acoustic velocities in the table. Where x coordinate is the orientation angle (converted into radians for simulation convenience) of the acoustic velocity path, the y coordinate is the corresponding value of acoustic velocity. The fitting results are shown in Fig.5.

For the unidirectional CFRP plate, the equation of omnidirectional acoustic velocity from 0° to 90° is:

$$y = 76.925x^4 - 3656.1x^3 + 12993x^2 - 15947x + 8956.6 \quad (21)$$

With the fitting degree R^2=0.9983, the fitting curve is shown in Fig.5 a). the velocity reaches its lowest perpendicular to the fiber orientation, and is insensitive to the change of orientation. While, as it approaches the fiber direction, the velocity increases rapidly, the maximum is obtained parallel to the fiber direction. Obvious anisotropy is exhibited.

For orthotropic laminated plate, the fitting equation of omnidirectional acoustic velocity from 0° to 90° is:

$$y = -13477x^5 + 52548x^4 - 70989x^3 + 41345x^2 - 11072x + 6665.4 \quad (22)$$

With the fitting degree R^2=0.9986, the fitting curve is shown in Fig.5 b). the first peak acoustic velocity is 6663m/s at 0° orientation (parallel to one of the laminating directions of carbon fiber). With the orientation angle increasing, the velocity value experiences a smooth transition, firstly decrease and then increase, the minimum value is obtained at about 51°. As the orientation angle continues to approach 90°, the velocity increases rapidly to 7186m/s, which is higher than that at 0° direction. Both the probes and the lead breaking points are in direct contact with the surface ply of the CFRP where acoustic wave mainly propagates on,

thus the orientation of which has a greater influence on the acoustic velocity than the inners, resulting in the asymmetry of the acoustic velocity curve with respect to the 45° orientation of the orthogonal alternating laminate structure.

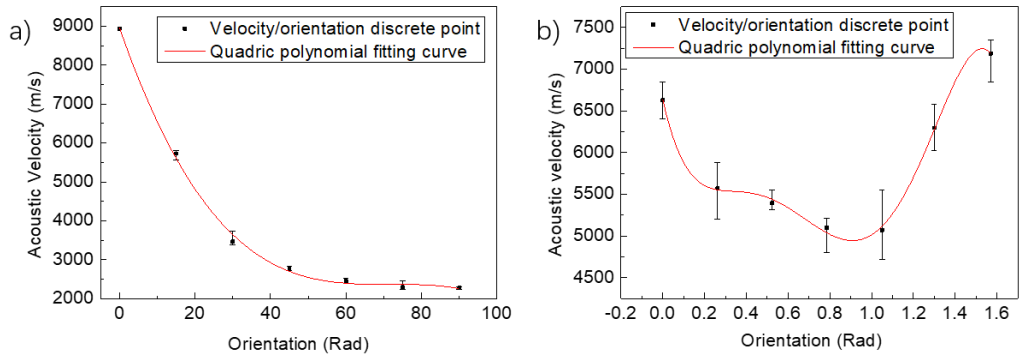

Figure 5 Velocity/orientation polynomial fitting curve of unidirectional/orthotropic laminated plate
a) unidirectional laminated plate; b) orthotropic laminated plate

4.1.2 Omnidirectional acoustic velocity of curved surface of a cylindrical shell structure

In composite materials, elastic wave transmits through solid medium such as fiber and resin, whose propagation path matches the profile of the surface. Though the laminating method of spatial curved surface is more complex than the planar structure, while the acoustic velocity testing method is basically the same. The slight difference is that, the elastic wave propagation distance and orientation should be measured along the actual path on the curved surface, instead of the simple distance between two points, however, the difference can be ignored when the radius of curvature is large enough.

Considering the symmetry, the acoustic velocities between 0°-90° are measured. As shown in Fig.6, select a point on the cylinder surface of the tank as the coordinate to install the origin probe. Draw the typical direction lines of 0°, 15°, 30°, 45°, 60°, 75°, 90°, taking the circumferential line as the reference for horizontal axis. In each direction line, a distal probe is assembled at a distance of 20cm away from the origin. The lead-breaking points are determined on each direction line between the origin and the distal, 15cm away from the origin. Thus, there is a 10cm gap for the acoustic wave arriving the two probes on the same direction line. The wave propagation velocity on each direction is repeatedly measured eight times by time difference method, and the averaging process is taken. The results are shown in Tab.6.

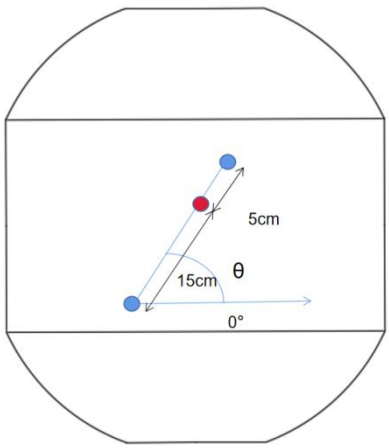

Figure 6 Schematic diagram of acoustic velocity measurement of the tank

Table 6 Acoustic velocity in all directions of tank column section

orientation/°	**0**	**15**	**30**	**45**	**60**	**75**	**90**
Average acoustic velocity （**m / s**）	6891.47	6073.26	5547.58	4878.69	4776.24	5628.48	5503.57
Standard deviation （**m / s**）	281.23	129.96	37.04	256.85	261.33	115.78	102.42

For the cylindrical shell structure, the fitting equation of omnidirectional acoustic velocity from 0° to 90° is:

$$y = -4132x^4 + 12720x^3 - 9966x^2 - 540x + 6850 \quad (23)$$

With the fitting degree R^2=0.9537, the fitting curve is shown in Fig.7. The acoustic velocity curve is complex corresponding to its lamination, and the maximum value is obtained in the direction of 0°. With the increase of orientation angle, the velocity gradually decreases, the minimum value is obtained at about 49°, which then turns to increase until 90°. The vessel lamination includes 0°, 90°, 52° and -52° orientations, and as the outer several layers are circumferential reinforcement, 0° layer dominates, thus the velocity curve deviates to 0° direction as a whole.

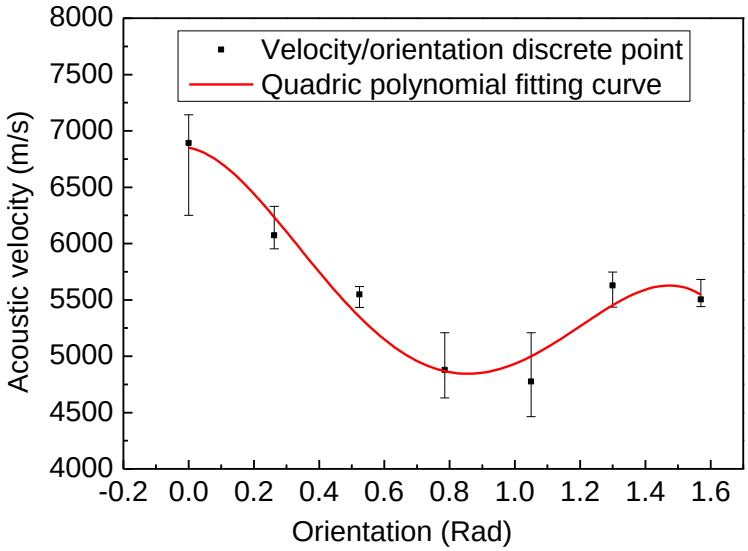

Figure 7 Velocity/orientation polynomial fitting curve of cylindrical shell structure

4.2Acoustic emission localization results

4.2.1 Acoustic emission localization of two-dimensional planar laminated composite materials

Firstly, the advantage of the anisotropic algorithm is studied by comparing the localizing accuracy with the isotropic one under three-point localization mode on the unidirectional plate. The coordinates (unit: mm) of probe 1-3 are (0, 100), (100, -50), (-100, -50), respectively. Lead-breaking is carried out at the coordinates of (0, 0), (0, 50), (0, -50), (50, 0), (-50, 0), (50, 50), (50, -50), (-50, 50), (-50, -50), respectively. The localization results by the algorithms are shown in Fig.8, and the specific coordinate values obtained by localizing calculations are shown in Tab.7. It is noticeable that the 3-point methods failed to obtain accurate localizing data every time, and singular values occur from time to time (localized coordinate far beyond the probes coverage area), for operation or equipment problems. Even if 5 repeated tests are applied, there is still a few individual points for which the localization data from the probes are

highly discrete, the localization results with guiding significance sometimes are hardly to be obtained by calculation. For the nonsingular points, the localizing deviation of the 3-point isotropic method varies from 28.8mm to 147.1mm, the expected value reaches up to 66.6mm, and the standard deviation is 77.3mm; For the anisotropic method, the lowest localizing deviation is only 5.1mm, and even the maximum is also within 20mm. The expected value is 9.5mm and the standard deviation is 10.3mm. The localizing accuracy and the discreteness are both improved obviously. The rationality of the anisotropy algorithm is fully demonstrated.

Table 7 Localization results under various localization algorithms of unidirectional board

Lead breaking coordinates (mm)	**Isotropic 3-point**		**Anisotropic 3-point**	
	Localization coordinates	Deviation	Localization coordinates	Deviation
（0，0）	(1.7, -50.6)	50.6	(8.5,3.3)	9.1
（0，50）	（-4.5，89.9）	40.1	（7.7，47.7）	8.0
（0，-50）	（-，-）	-	（-，-）	-
（50，0）	（13.9，-63.3）	78.4	（60.0，15.4）	18.3
（-50，0）	（-14.3，-75.8）	89.8	（-58.0，9.0）	12.0
（50，50）	（22.5，58.6）	28.8	（47.0，45.9）	5.1
（50，-50）	（20.4，-194.1）	147.1	（45.5，-55.6）	7.2
（-50，50）	（-18.9，49.9）	31.2	（-46.5，44.6）	6.5
（-50，-50）	（-，-）	-	（-，-）	-
Average localization deviation (mm)	66.6		9.5	
Standard deviation (mm)	77.3		10.3	

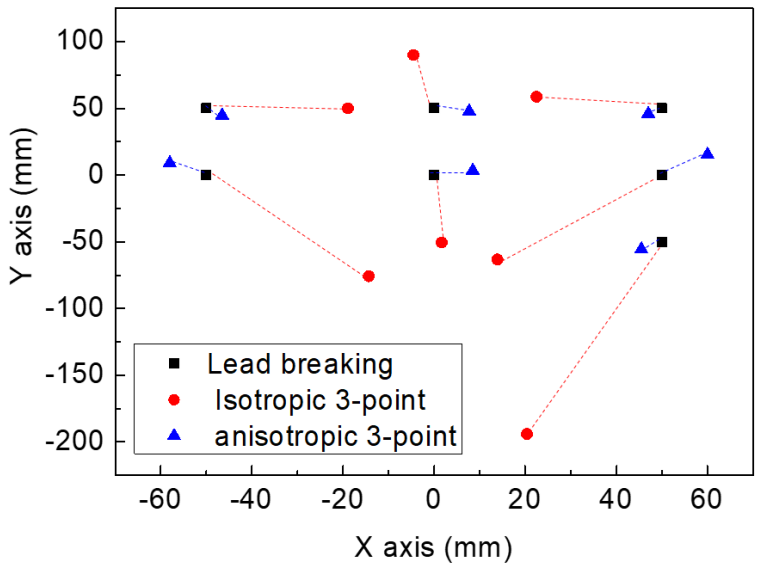

Figure 8 Localizing results by isotropic/anisotropic 3-point algorithm for the unidirectional plate

Using the time difference method, at least three-point probes data is required to solve the simultaneous equations, any probe data error will directly lead to localizing failure, the fault tolerance rate is low. However, the actual acoustic velocity is often counted in kilometers per second, and the effective localizing size of the plate is only 0.2 m×0.2 m, the time difference of the signal received by the probes is less than 10^{-4} s, thus the slight measurement error or the receiving delay by any probe will lead to a large deviation of the localization calculation result.

The multi-point localizing method is proposed expecting to make up this deficiency.

For the orthogonal plate, a 6-point anisotropic method is brought in. The coordinates (unit: mm) of probe 1-6 are (0, 100), (100, 50), (100, -50), (0, -100), (-100, -50), (-100, 50), respectively. The 3-point localization methods are carried out with the data obtained by No.1, No.3 and No.5 probes; While the 6-point method uses all the data of the 6 probes for localization calculation. The localizing results with different methods are shown in Fig.9, and the coordinate values obtained from the corresponding localization calculation algorithms are shown in Tab.8. Using 3 points for localizing, the same situation of occasional localizing failure occurs. The accuracy of isotropic three-point localizing is the lowest, but better than that on the unidirectional plate. The expected value of deviation is 27.8mm, with the standard deviation of 30.2mm. While, the accuracy of the anisotropic 3-point one is still higher than the isotropic, with the deviation values reduced by nearly 50%. The six-point positioning method has obtained reasonable localizing results for all the lead-breaking tests, the expected deviation is 8.6mm, the standard is 9.3mm (for nonsingular points), corresponding to the highest localizing accuracy and fault tolerance.

Table 8 Localization results under various localization algorithms of orthogonal plate

Lead breaking coordinates (mm)	**Isotropic 3-point**		**Anisotropic 3-point**		**Anisotropic 6-point**	
	Localization coordinates	Deviation	Localization coordinates	Deviation	Localization coordinates	Deviation
（0，0）	(4.9，30.5)	30.9	(4.8，13.5)	14.3	(-12.4, -11)	16.6
（0，50）	（-10.2，87.2）	35.6	（-4.5，69.9）	20.4	（-7.5，45.3）	8.9
（0，-50）	（1.1，-26.6）	23.4	（1.2，-39.2）	10.9	（-7.8，-46.6）	8.5
（50，0）	（59.5，17.9）	20.3	（60.4，22.7）	25.0	（41.1，6.3）	10.9
（-50，0）	（-50.6，10.5）	10.5	（-53.3，7.2）	7.9	（-44.9，2.9）	5.9
（50，50）	（74.7，74.9）	35.1	（55.7，60.3）	11.8	（44.4，49.2）	5.7
（50，-50）	（47.5，-66.3）	16.5	（56.5，-105.6）	8.6	（41.9，-50）	8.1
（-50，50）	（-55.2，99.7）	50.0	（-40.8，69.9）	21.9	（-48.9，45.9）	4.2
（-50，-50）	（-，-）		（-，-）		（-43.8，-41.2）	10.8
Average localization deviation (mm)	27.8		15.1		Nonsingular points: 8.6 All points: 8.8	
Standard deviation (mm)	30.2		16.3		Nonsingular points: 9.3 All points: 9.5	

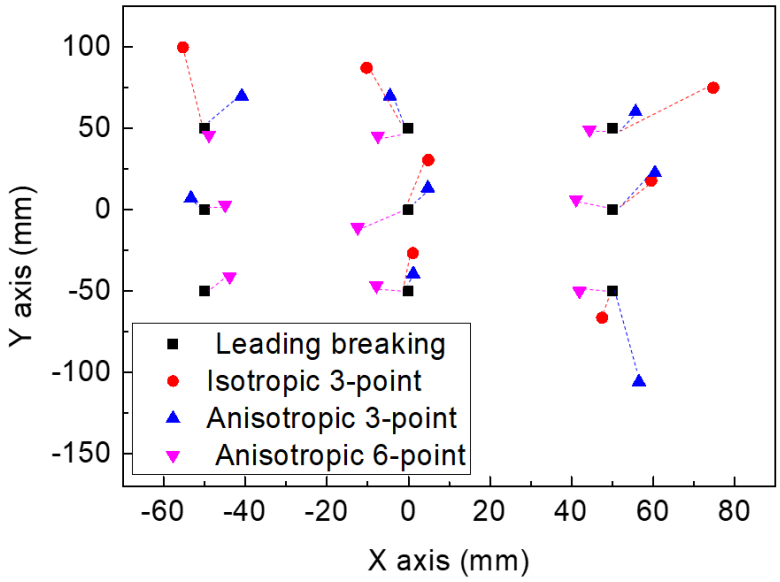

Figure 9 Localizing results by various localization algorithm for the orthogonal plate

From the view of geometric, the process of localizing solution can be regarded as the intersection of three wavefront envelope lines controlled by time parameters. The acoustic velocity of unidirectional composites varies greatly in different orientations, which changes rapidly closing to 0°orientation, but is insensitive when approaching 90°. Thus, the wavefront envelope line of unidirectional material has complex shape with sharp angles; Although the acoustic velocity on the surface of orthogonal laminates also reaches its maximum in both fiber orientations, the acoustic velocity-orientation curve is relatively more gentle. The isotropic method uses circular wavefront for approximate localization, inconsistent with the real situation. Deviations will inevitably occur and increase with the inconsistency; While, the acoustic velocity equation of anisotropic localization method is obtained from actual measurement, fully retains the anisotropy and improves the algorithm rationality. It can be inferred that the advantages of anisotropic localizing technology should be more obvious on the unidirectional plate with stronger anisotropy. The previous experimental results verify this inference.

6-point anisotropic localization algorithm is essentially the same as the 3-point anisotropic one, however the set capacity of localizing results can be enlarged by arrangement and combination of the multi-point data. The process can improve the convergence rate of the localization expectation to the true value as discussed above; Otherwise, comparisons are applied between different localizing results so as to screen and eliminate fault probe data, forming a self-correction mechanism, thus to improve the reliability and fault tolerance of the localization algorithm.

4.2.2 Acoustic emission localization of curved surface of a cylindrical shell structure

For the acoustic emission source localization on the CFRP tank, the AE probes are arranged on the cylinder section surface. The corresponding coordinates of probe 1-6 are (0, 200), (200, 100), (200, -100), (0, -200), (-200, -100), (-200, 100), unit mm. Similarly, based on the data collected by multi-probes, the localization algorithms include isotropic 3-point localization, anisotropic 3-point localization and anisotropic 6-point localization. The three-point methods use probes No. 1, 3 and 5 for localizing calculation, while the six-point method uses all the data of six probes.

Lead-breaking is carried out at the coordinates of (0, 0), (0, 100), (0, -100), (100, 0), (-100, 0) (100, 100), (100, -100), (-100, 100), (-100, -100), respectively. The results of localizing by various algorithms are shown in Fig.10, and the coordinate values are exhibited in the Tab.9.

The localizing failure rate of the 3-point methods significantly increased. The 3-point isotropic algorithm is the most discrete, and the expected value of the localizing deviation is about 65.6mm; Using 3-point anisotropy algorithm, the localization deviation is 25mm, the standard deviation is 29.5mm, the accuracy is improved significantly. The 6-point anisotropy algorithm still obtains all the localization results, and corresponds to the highest localizing accuracy, in comparison. The expected value is about 19.2mm, and the standard deviation is 23.5mm (for nonsingular points).

Table 9 Localization results under various localization algorithms of composite spatial curved surface structure

Lead breaking coordinates (mm)	**Isotropic 3-point**		**Anisotropic 3-point**		**Anisotropic 6-point**	
	Localization coordinates	Deviation	Localization coordinates	Deviation	Localization coordinates	Deviation
（0，0）	(2.3，-3.5)	4.2	(3.4，-3.1)	4.6	(0.3, -7.6)	7.6
（0，100）	（-3.7，148.1）	48.2	（-8.5，122.8）	24.3	（5.2，104.1）	6.6
（0，-100）	（-，-）	-	（-，-）	-	（-1.4，-59.4）	30.6
（100，0）	（65.4，-76.8）	84.2	（95.5，-44.0）	44.2	（98.7，-43.9）	43.9
（-100，0）	（64.8，-71.6）	179.7	（-95.0，-40.3）	40.6	（-82.8，-11.6）	20.7
（100，100）	（100.0，111.9）	11.9	（96.7，110.7）	11.2	（100.4，117.3）	17.3
（100，-100）	（-，-）		（-，-）		（52.5，-48.0）	70.4
（-100，100）	（-，-）		（-，-）		（-38.8，64.8）	70.6
（-100，-100）	（-，-）		（-，-）		（-69.5，-68.0）	44.2
Average localization deviation (mm)	65.6		25.0		Nonsingular points: 19.2 All points: 34.7	
Standard deviation (mm)	91.4		29.5		Nonsingular points: 23.5 All points: 41.6	

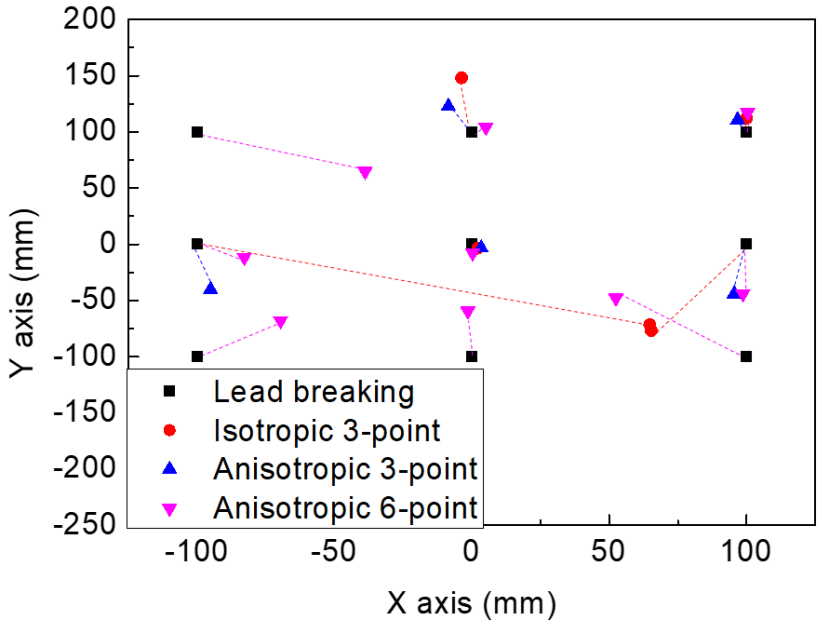

Figure 10 Localizing results by various localization algorithm for the composite spatial curved surface structure

For the spatial curved surface, the acoustic wave mainly propagates along the surface, which can be equivalent to the two-dimensional plane. Thus, the acoustic emission localizing accuracy of the spatial curved surface should be the same level as the plane, when neglecting the lamination complexity increase. On the other hand, the size of the CFRP tank sample is large enough to form a sufficient effective detection area, the affection weight of the probe size and the delay decreases, while the error caused by the localizing algorithm increases, this is also the main reason why the deviation of the 6-point anisotropic methods remains stable while that of the anisotropic 3-point localizing method increases slightly and the isotropic one greatly. When applied to practical engineering structures, the detection size will be further enlarged, and the advantages of multi-point anisotropic acoustic emission (AE) localizing technology can be more prominent.

Conclusions

In this paper, a theoretical model of anisotropic acoustic propagation velocity in composite materials is established, and a multi-probe synchronous localization algorithm is proposed according to the model and Monte Carlo sampling method. The method is compared with the traditional isotropic 3-point location technology, and its superiority is verified. The details are as following:

In composites, the acoustic propagation velocity varies greatly between fiber and matrix, and the macro velocity-orientation curve is mainly affected by the laminating method. For unidirectional laminates, the acoustic velocity along the fiber orientation is up to 8956m/s, while which decreases sharply with the increase of the orientation angle, and finally drops to 2283m/s perpendicular to the fibers. There are similarities of the acoustic velocity curves between the plane orthogonal laminated plates and the spacial surface of CFRP tank. The two fiber orientations correspond to the peaks, however there is a gap between the peak values, as the surface plies exhibit a greater influence on the acoustic velocity. The maximum of plane orthogonal structure are 7186m/s and 6662m/s, respectively; While, 6891m/s and 5503m/s respectively for the CFRP tank.

The localizing accuracy of isotropic algorithm will deteriorate with the increase of material anisotropy, while that of the anisotropic algorithm is almost unaffected. The localizing deviation is mainly composed of probe acquisition, experiment error and algorithm accuracy. While for the sample size reaching 0.4×0.4 mm^2, the algorithm accuracy becomes dominant, the localization deviation of the anisotropic algorithm is obviously lower than that of the isotropic one, the advantage will become more pronounced as the sample size continues to increase.

By using 6-point localization method, the sample capacity is enlarged basing on the Monte Carlo theory, and self-correcting can be realized to a certain extent by self-comparison, which greatly improves the fault-tolerance and localizing accuracy. In this work, 3-point localization method fails as one or more probes obtain singular data, while 6-point localization method can still achieve reasonable acoustic source coordinates, and the localizing accuracy is slightly higher than that of anisotropic 3-point method. Furthermore, in practical engineering application, it is of very high probability that various complicate factors may lead to problems for the individual probe, multi-point detection method has greater application potential for its higher reliability and accuracy.

Declaration of Competing Interest

The authors declare that they have no known competing financial interests or personal relationships that could have appeared to influence the work reported in this paper.

Acknowledgments

The authors gratefully acknowledge the financial support of the Shenzhen Science and Technology Program (Grant No. JCYJ20190807161011714).

Reference：

[1] Zhang K, Tang W, Fu K. Modeling of Dynamic Behavior of Carbon Fiber-Reinforced Polymer (CFRP) Composite under X-ray Radiation. Materials, 2018, 11(1): 143.
[2] Liu Z, Wu W, Du J, et al. Lightweight Design Of Composite Spinner For Large Wind Turbine. Journal of Physics: Conference Series, 2021, 1820(1): 012042.
[3] Muflikhun M A, Yokozeki T, Aoki T. The strain performance of thin CFRP-SPCC hybrid laminates for automobile structures. Composite Structures, 2019, 220(JUL.): 11-18.
[4] Karata M A, et al. A review on machinability of carbon fiber reinforced polymer (CFRP) and glass fiber reinforced polymer (GFRP) composite materials. Defence Technology, 2018, 14(4): 9.
[5] Totry E, et al. Effect of fiber matrix and interface properties on the in-plane shear deformation of carbon-fiber reinforced composites. Compos Sci Technol,2010, 70(6): 970-980
[6] Wachi Y, Koyanagi J, Arikawa S, et al. In Situ SEM Deformation Behavior Observation at CFRP Fiber-Matrix Interface. Springer International Publishing, 2015, 4: 67-73.
[7] Sultan M, Worden K, Pierce S G, et al. On impact damage detection and quantification for CFRP laminates using structural response data only. Mechanical Systems & Signal Processing, 2011, 25(8): 3135-3152.
[8] Yin Z, Li C, Ying T, et al. Impact Damage Detection in Patch-Repaired CFRP Laminates Using Nonlinear Lamb Waves[J]. Sensors, 2020, 21(1): 219.
[9] Seifoori S, Parrany A M, Mirzarahmani S. Impact damage detection in CFRP and GFRP curved composite laminates subjected to low-velocity impacts. Composite Structures, 2020, 261(12): 113278.
[10] Rippert L, Wevers M, Huffel S V. Optical and acoustic damage detection in laminated CFRP composite materials. Composites Science & Technology, 2000, 60(14): 2713-2724.
[11] Grigg S, Almudaihesh F, Roberts M, et al. Impact monitoring of CFRP composites with acoustic emission and laser Doppler vibrometry. Engineering Research Express, 2021, 3(1): 015012.
[12] Barile C, Casavola C, Pappalettera G, et al. Acoustic Emission Techniques for Evaluating Damage Modes in CFRP Hybrid Joints. IOP Conference Series: Materials Science and Engineering, 2021, 1038(1): 012052.
[13] Mn A, Mm A, Ma B. Using acoustic emission technique to monitor damage progress around joints in brittle materials. Theoretical and Applied Fracture Mechanics, 104:102368-102368.
[14] Rivey J C. Acoustic Emission Beamforming for Detection and Localization of Damage.. University of Washington. 2016.
[15] Kundu A, Eaton M J, Al-Jumali S, et al. Acoustic emission based damage localization in composites structures using Bayesian identification. Journal of Physics Conference Series, 2017, 842(1): 012081.
[16] Fotouhi M, Saeedifar M, Sadeghi S, et al. Investigation of the damage mechanisms for mode I delamination growth in foam core sandwich composites using acoustic emission[J]. Structural Health Monitoring, 2015, 14(3): 265-280.
[17] Saeedifar M, Fotouhi M, Najafabadi M A, et al. Prediction of quasi-static delamination onset and growth in laminated composites by acoustic emission. Composites Part B Engineering, 2016, 85: 113-122.
[18] Niri E D, Farhidzadeh A, Salamone S. Determination of the probability zone for acoustic emission source location in cylindrical shell structures. Mechanical Systems & Signal Processing, 2015, 60: 971-985.
[19] Salinas V, Vargas Y, Ruzzante J, et al. Localization algorithm for acoustic emission. Physics Procedia, 2010, 3(1): 863-871.
[20] Deng A, Li Z, Wei X. Application of quantum neural networks in localization of acoustic emission. Systems Engineering and Electronics, 2011, 22(003): 507-512.
[21] Tai J. An adaptive localization method of simultaneous two acoustic emission sources based on energy filtering algorithm for coupled array signal. Mechanical Systems and Signal Processing, 2021, 154: 107557.
[22] Xu C, Du S, Gong P, et al. An Improved Method for Pipeline Leakage Localization With a Single Sensor Based on Modal Acoustic Emission and Empirical Mode Decomposition With Hilbert Transform. IEEE Sensors Journal, 2020, 99: 1-1.
[23] Xue C, Xu G, Wang X, et al. Error analysis and correction of multi-sensor cluster methods for acoustic emission source localization. Ultrasonics, 2021, 115(12): 106438.
[24] Liu Z H, et al. Acoustic emission source localization of carbon fiber composite panels. Nondestructive testing, 2016, 10: 5.
[25]Liu Z H, et al. Time difference mapping method for locating the acoustic emission source in a composite plate. Chinese Journal of Acoustics, 2019, 38(04): 124-137.
[26] Wu X J, et al. The Location of Acoustic Emission Source of Pipeline Leakage Based on EMD and

Wavelet Transform. Nondestructive Testing, 2015 (10): 4.
[27] Li Q F, et al. Location Algorithm for Source of Acoustic Emission Based on Time Reversal. Chinese Journal of Sensors and Actuators, 2015, 28(11): 5.
[28] Ciampa F, et al. A New Algorithm for Acoustic Emission Localization and Flexural Group Velocity Determination in Anisotropic Structures. Composites Part A, 2010, 41(12): 1777-1786.

Research on Size Effect of Tensile Specimens of 3D Five-Directional Braided Composites

PU Hao YANG Sheng-chun

Aircraft Strength Research Institute of China, Xi'an 710065, China

Abstract: 3D five-directional braided composites have been widely used in recent years due to their special spatial network structure, which enables them to have excellent out-of-plane properties and good in-plane properties. However, there is a certain difference between the periodic boundary conditions imposed during the modeling and the size of the sample during the actual mechanical performance test, and the influence of the sample width on the mechanical performance testing process and results of the 3D five-directional braided composite material is not considered. In this paper, based on the three-cell model analysis method, according to the proportion and stacking method consistent with the actual material, the warp unnotched tensile specimens and the weft unnotched tensile specimens of different widths are constructed, and the stress distribution and material of the specimens under different sizes are analyzed. The elastic properties and the influence of the size effect on the 3D five-directional braided composite material provide a theoretical basis for guiding the size design of the 3D five-directional braided composite material.

Keywords: 3D five-directional braided composite material, Geometry, Finite element modeling, Elastic properties, Size effect

1 introduction

The 3D five-directional braided composite material can be considered as a combination of corner cells, face cells and inner cells in a certain stacking order according to the volume ratio[1][2]. When periodic boundary conditions are applied to the unit cell model, it has periodic The direction of the properties will be considered to be repeated to infinity in an infinite number[3], but the size of the actual sample is limited. Considering the position of the chuck of the material mechanical property testing machine, the installation of the extensometer and the arrangement of the strain gauge, the dimension in the length direction is generally longer, but cannot be approximated to be infinitely long in the width and thickness directions[4][5]. In the width direction, since the edge trimming process has no horn cells, the material is a free interface composed of face cells and inner cells at the border of the width. In the thickness direction, with the number of rows of yarn carriers in the sample weaving process With the change of the number of columns, the volume ratio of the area cells along the thickness

direction of the sample is also constantly changing.

At present, there is no special test standard for 3D five-directional braided composite materials. Testing institutions generally refer to the test method of laminated composite materials for mechanical property testing, without considering the test process and results of the mechanical properties of 3D five-directional braided composite materials by the width of the sample. Impact. Therefore, the three-cell finite element analysis model is used in this paper to construct the warp unnotched tensile and weft unnotched tensile specimen models of different widths, and analyze the stress distribution and material elastic properties of the specimens under different sizes. The effect of size effect on 3D five-directional braided composites.

2 Width design of specimens for mechanical properties of 3D five-directional braided composites

The 3D five-directional braided composite material is generally trimmed according to the required size in the width direction. The border after trimming is a free border containing only inner cells and face cells, which is no longer periodic, and the free border will affect a certain range inside the material. The stress distribution within it is affected. Therefore, according to the actual structure of the macroscopic material, an analytical model with different numbers of unit cells in the width direction after trimming (removing corner cell) is established in this paper. Due to the limitation of the curing process, the braided yarn is severely squeezed on the surface, and the braided yarn with surface unit cells can often be directly observed on the surface of the sample[6]. The analysis model of the line is more consistent, so the stress contour of the material width design analysis model in this paper is the stress contour of the fiber.

2.1 Warp Unnotched Tensile Specimens

The schematic diagram of the position selection of the warp unnotched tensile specimen model is shown in Figure 1, and the width direction includes 1 unit cell, 2 unit cells, 3 unit cells, 4 unit cells, 6 unit cells and 8 unit cells respectively.

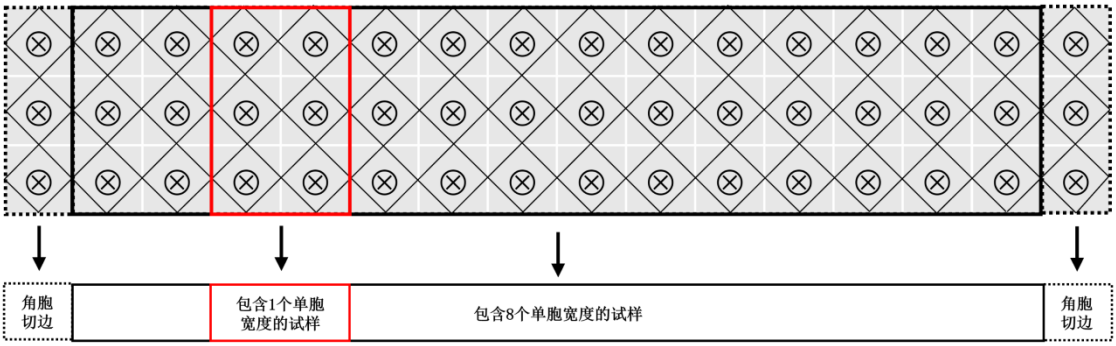

Fig. 1 Schematic diagram of position selection of warp unnotched tensile models with different numbers of unit cells (top view of weaving plane)

The mesoscopic size effect analysis model of warp unnotched tensile materials established in this paper is a combination of 2 face cells and 1/2 inner cells in the thickness direction. The actual situation of the restored sample. In the height direction (axial), since the sample size is much larger than the unit cell size, it can be considered periodic, so the model only contains one unit cell height in the height direction, and periodic boundary conditions are imposed on this direction. Figures 2 to 5 are the stress cloud diagrams of the design and analysis model of the width of the 3D five-directional braided composite sample width in the warp-direction unnotched tensile ts of 1, 2, 3, 4, 6 and 8 times the face cell width ts, respectively. When loading, a tensile displacement load of 0.2 mm is applied to the model along the axial direction to ensure that the stress results of the analysis models of specimens with different widths are comparable.

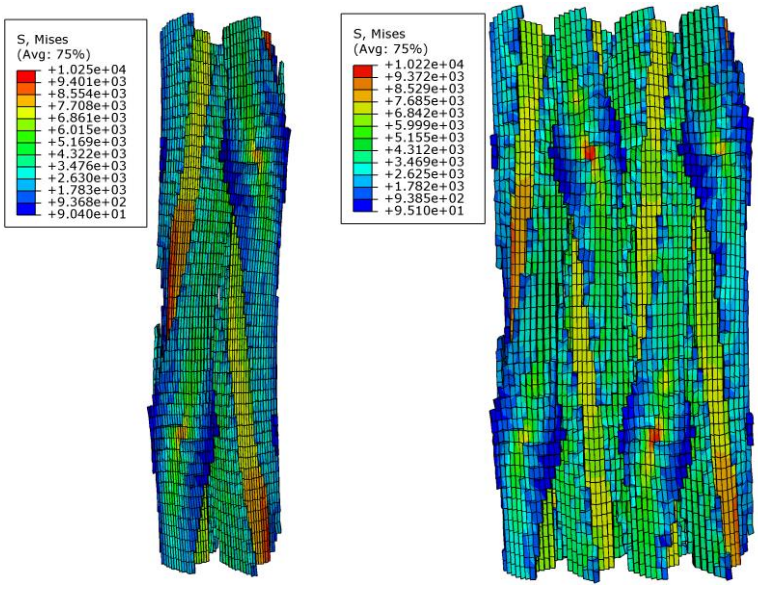

a）1 times the area cell width b）2 times the area cell width

Fig.2 The stress distribution of the meridional tensile specimens with 1 times the area cell width (2.18mm) and 2 times the area cell width (4.36mm)

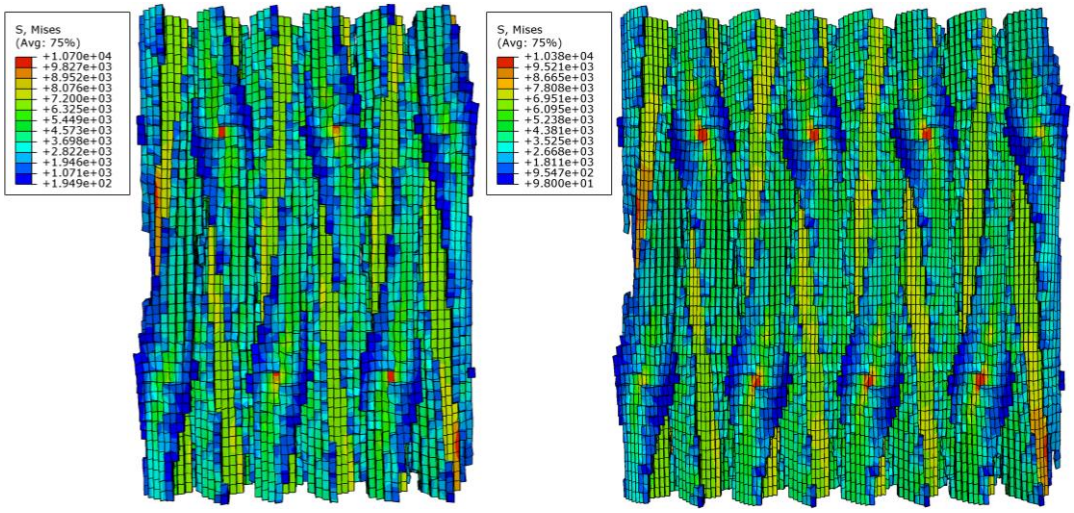

a）3 times the area cell width　　b）4 times the area cell width

Fig.3 The stress distribution nephogram of the meridional tensile specimen with 3 times the area cell width (6.55mm) and 4 times the area cell width (8.73mm)

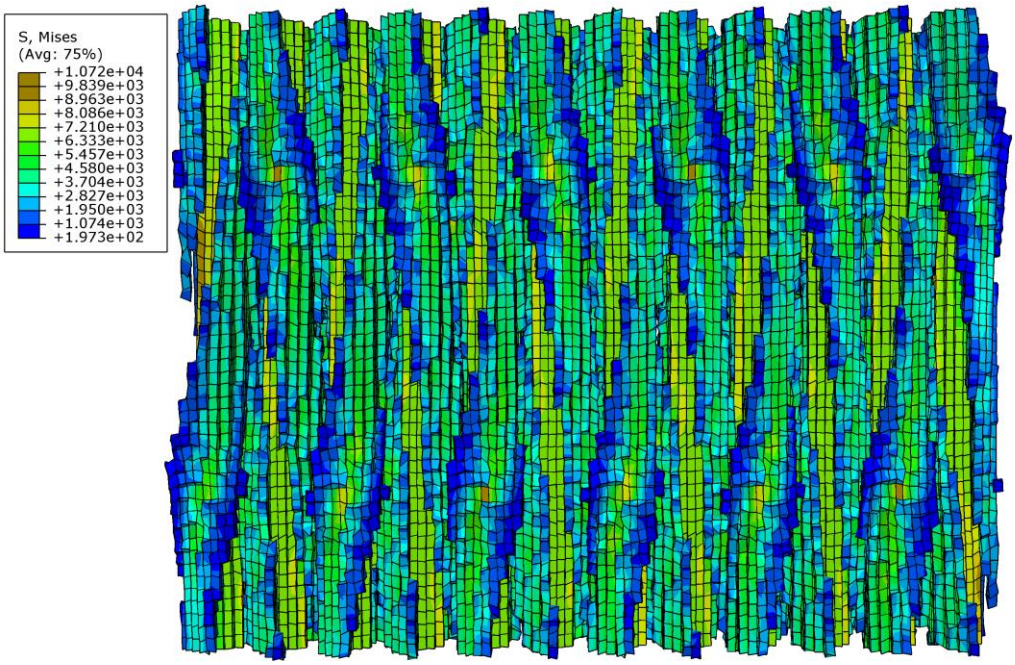

Fig. 4 The stress distribution cloud diagram of the meridional tensile specimen with 6 times the width of the area cell (13.09mm)

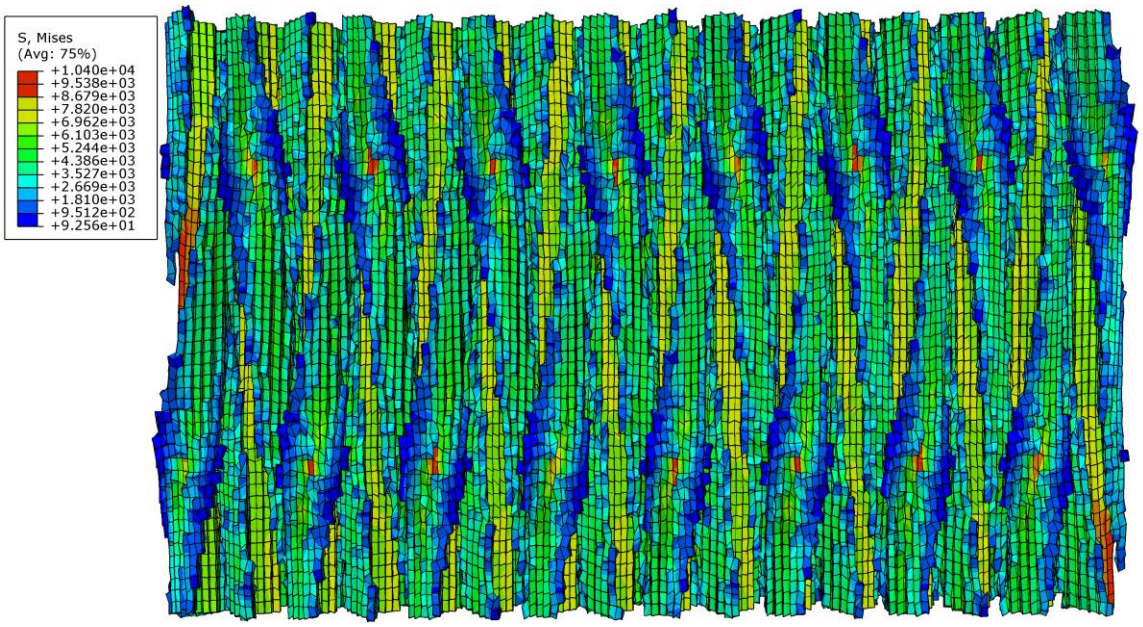

Fig.5 The stress distribution cloud diagram of the meridional tensile specimen with 8 times the cell width (17.46mm)

It can be seen from the stress nephogram of the sample with 1 times the width of the area cell that there is an obvious stress concentration area in the width direction due to the influence of the left and right free boundaries, and the influence of this area on the internal stress distribution of the sample is about $1/2t_s$. When the width of the specimen increases to 2 times the width of the area cell, due to the influence of both the free boundary and the uneven distribution of fibers inside the specimen, there is no obvious stress stabilization zone on the specimen surface, which cannot provide sufficient positions for the arrangement of strain gauges. . When the width of the sample continues to increase to 3 times the width of the face cell and 4 times the width of the face cell, it can be found that only the two sides of the sample surface are affected by the free boundary, and a large stable area appears in the center of the sample surface. Paste of strain gauges for mechanical property testing. When the sample width is 6 times and 8 times the area cell width, the uniformity of the strain field in the central area is not significantly improved compared with 3 times the area cell width and 4 times the area cell width.

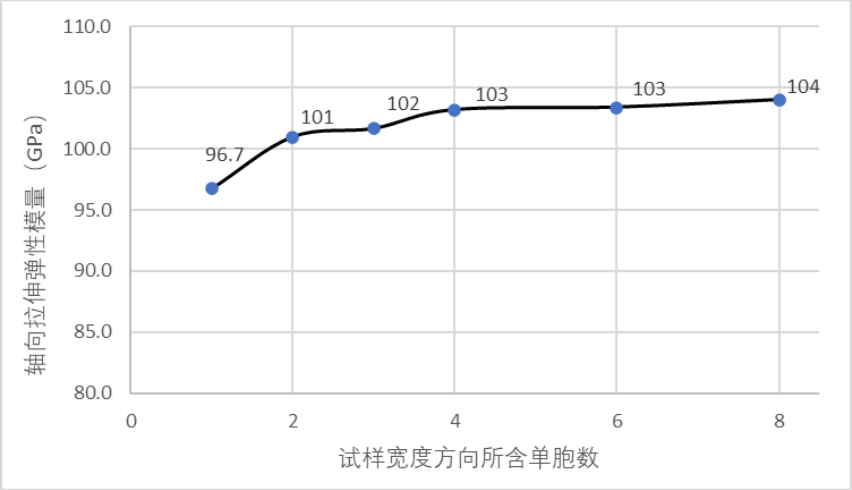

Fig.6 Calculation results of unnotched tensile modulus in warp direction with different widths

Figure 6 shows the results of the unnotched tensile modulus in the warp direction calculated by the width design analysis model of the 3D five-directional braided composite samples with 1, 2, 3, 4, 6, and 8 times the cell width. . It can be found that with the increase of the width of the sample, the meridional unnotched tensile modulus gradually increases, and tends to be stable after reaching 4 times the width of the area cell, indicating that the influence of the free boundary on the sample increases with the increase of the width. slowing shrieking.

Therefore, based on the stress distribution and calculation results of the above mesoscopic size effect analysis model, for the 3D five-directional braided composite material warp unnotched tensile specimen, the ideal specimen should exceed 4 times the area cell width.

2.2 Weft Unnotched Tensile Specimen

The unit cell size of the weft unnotched tensile specimen in the material width direction is a braided knot. The size of the braided knot of the 3D five-directional braided composite material studied in this paper is 8.48mm. The width of the weft unnotched tensile specimen is designed The width direction of the analysis model contains 1, 2, 3, 4, 6 and 8 braided knots, respectively. Figure 7 shows the selection of the position of the weft unnotched tensile model with different numbers of braided knots h. signal. The dimension in the thickness direction is consistent with the unnotched stretching in the warp direction, including 2 face cells and 1/2 inner cells. Boundary conditions are not applied in both width and thickness directions to realistically simulate real specimens. The unit cell size in the height direction is the face cell width. Since this size is small, in order to display the analysis results of the stress cloud map more intuitively, the height size of the established mesoscopic analysis model is 4 times the face cell width, and periodic boundary conditions are imposed on it.

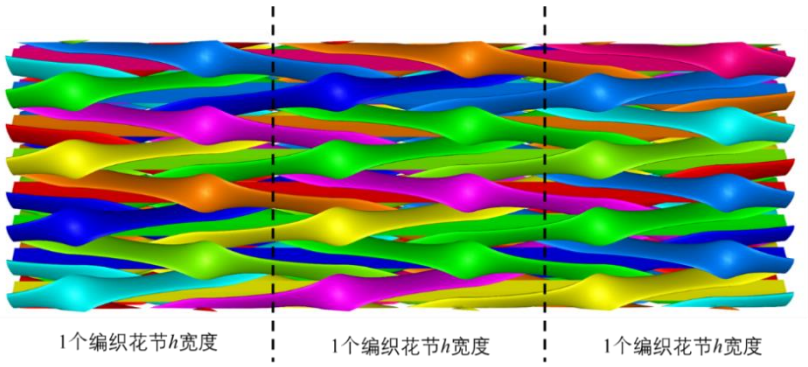

Fig.7 Schematic diagram of position selection of weft unnotched tensile model with different number of braided knuckles *h*

Figures 8 to 13 are the stress cloud diagrams of the design and analysis model of the width of the 1, 2, 3, 4, 6, and 8 times braided rosettes in the weft-direction unnotched tensile three-dimensional five-direction braided composite material. At the same time, a displacement load of 0.2 mm is applied to the model along the height direction to ensure that the stress results of the sample analysis models of different widths are comparable.

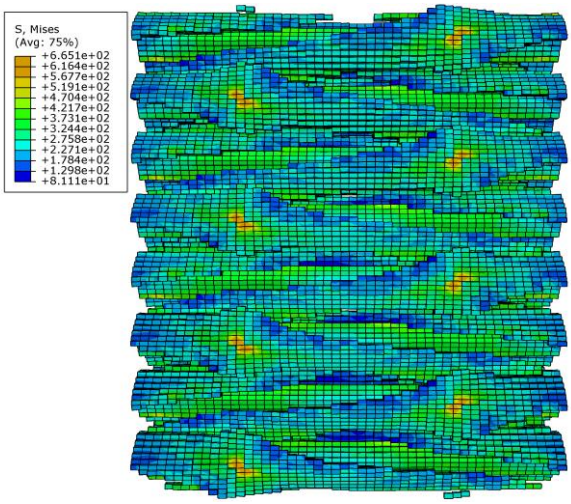

Fig.8 The stress distribution cloud diagram of the weft unnotched tensile specimen at 1 times the *h*-width of the woven rosette (8.48mm)

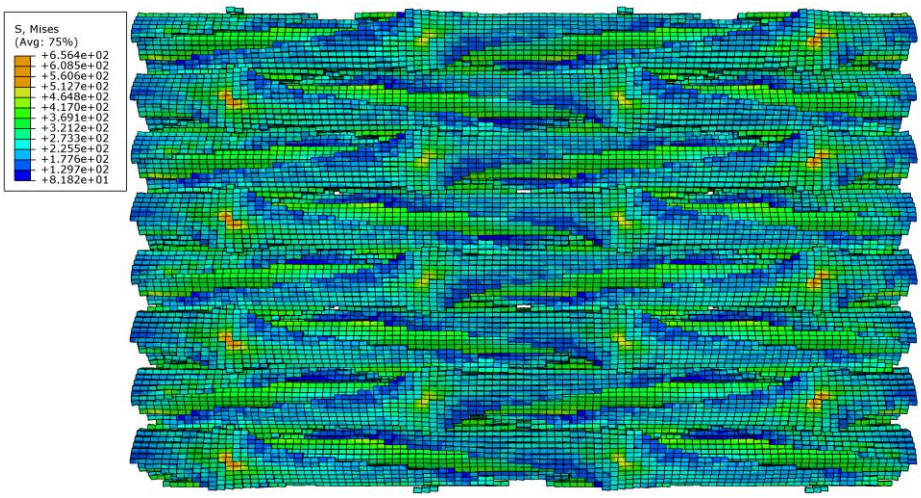

Fig.9 Stress distribution cloud diagram of 2 times the *h*-width (16.96mm) of the weft unnotched tensile specimen

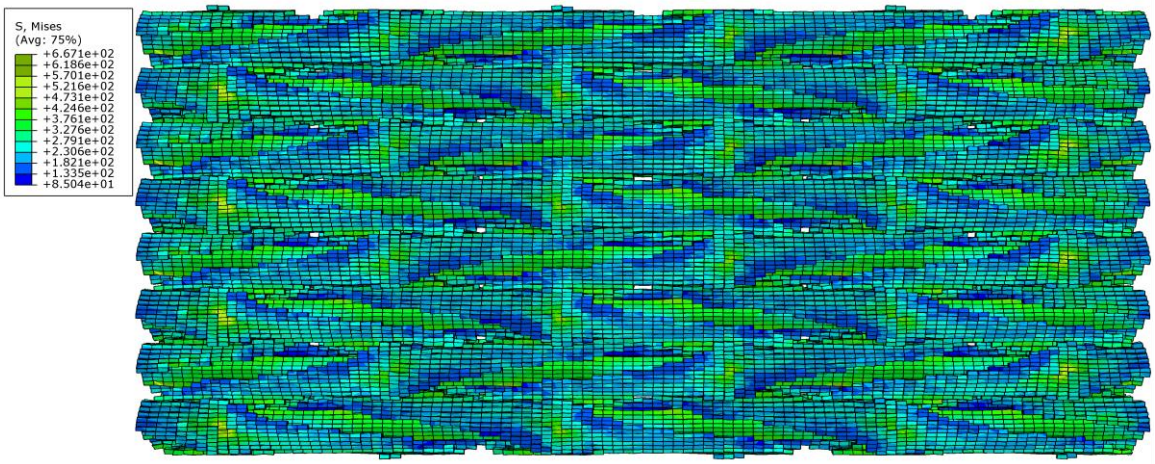

Fig.10 The stress distribution cloud diagram of the weft unnotched tensile specimen with 3 times the *h*-width (25.44mm) of the braided rosette

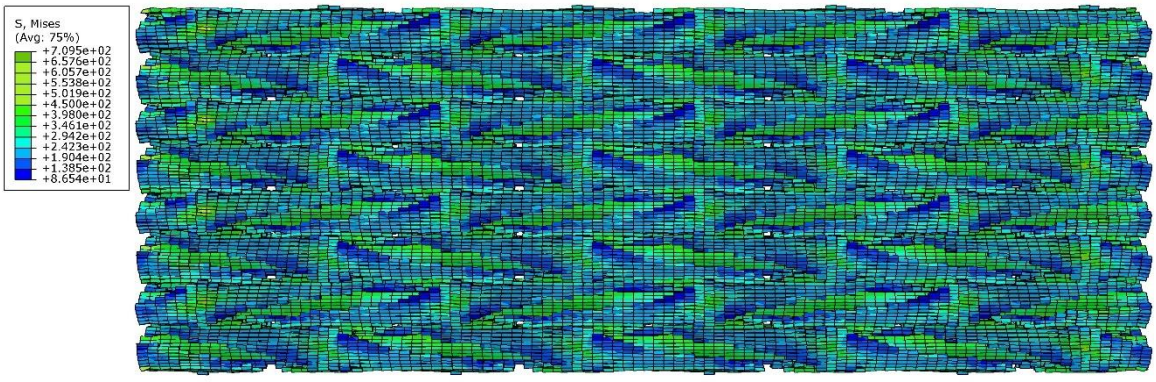

Fig.11 The stress distribution cloud diagram of 4 times the *h*-width of the braided flower section (33.92mm) in the weft unnotched tensile specimen

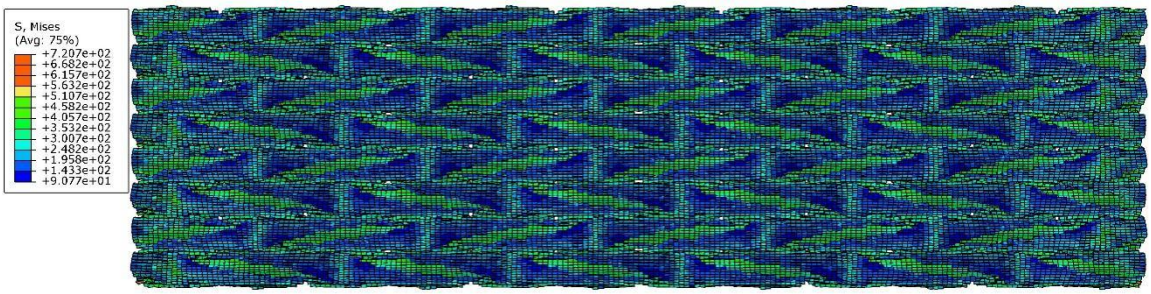

Fig.12 Stress distribution cloud diagram of 6 times the *h*-width (50.88mm) latitudinal unnotched tensile specimen

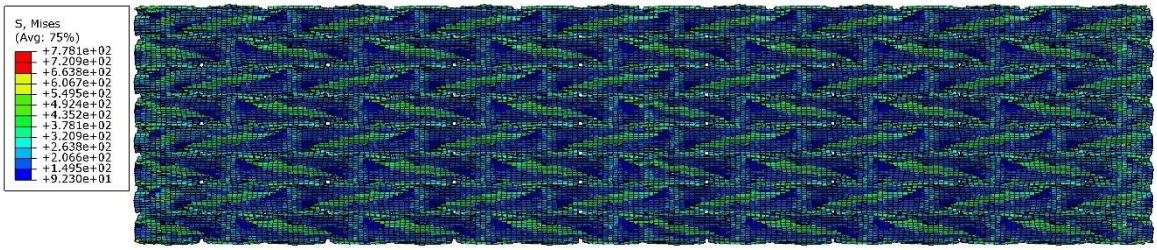

Fig. 13 Cloud diagram of stress distribution of 8 times the *h*-width (67.84mm) of the weft unnotched tensile specimen

It can be seen from the stress cloud diagram of the specimen with a width of 1 times the h-width of the braided rosette, which is the same as the unnotched tensile specimen in the warp direction. Due to the influence of the left and right free boundaries in the width direction, there is an obvious stress concentration in the middle of the specimen. position, the influence range of the free boundary on the stress distribution inside the sample is about 1/4 of the braided rosette. Observing the stress nephogram of the sample with twice the width of the braided rosette, it can be found that the stress difference level in the middle area of the sample is significantly lower than that of the sample with one width, but the obvious influence of the free boundaries on the left and right sides can still be observed. When the width of the sample is increased to 3 times the braided rosette, the stress distribution of the sample is relatively uniform, there is no obvious stress concentration area, and the influence of the free boundary on the middle of the sample can be ignored. When the sample width continued to increase to 4 times, 6 times and 8 times the braided rosette, the uniformity of the strain field in the central area did not improve significantly compared with 3 times the area cell width.

Figure 14 shows the weft-direction unnotched tensile force calculated by the dimensional design analysis model of the weft-direction specimen of the 3D five-directional braided composite material with 1, 2, 3, 4, 6, and 8 times the braided knuckle width. Modulus results. It can be found that, like the warp unnotched tensile specimen, there is an obvious size effect: as the width of the specimen increases, the weft unnotched tensile modulus gradually increases,

and tends to be stable after reaching a certain width, indicating that The influence of the free boundary on the specimen gradually decreases with increasing width.

Therefore, based on the stress distribution and calculation results of the above analysis model, for the 3D five-directional braided composite material weft unnotched tensile sample, the ideal sample should be at least 3 times the width of the braided knuckle.

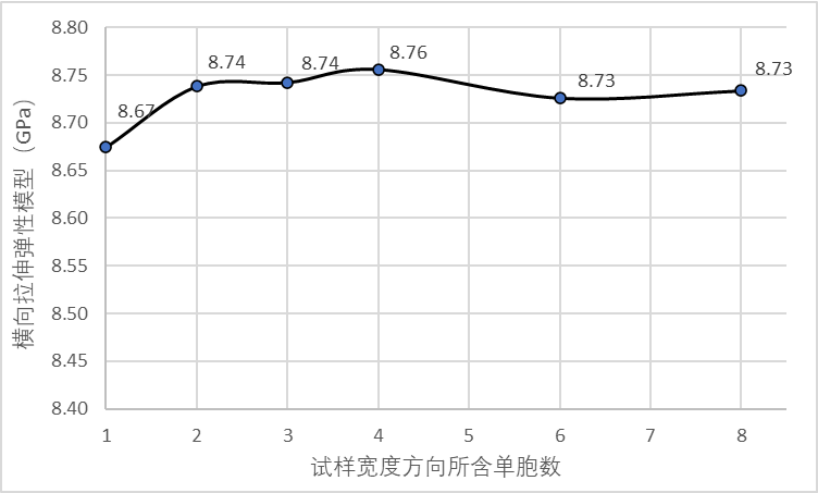

Fig.14 Calculation results of unnotched tensile modulus in weft direction of samples with different widths

3. Conclusion

In this paper, based on the three-cell finite element model, the macro-samples are constructed by using the unit cells according to the proportion and stacking method consistent with the actual materials. The mechanical properties of the samples at different cutting positions are compared, and the main conclusions are as follows:

(1) The macroscopic sample model is established by stacking different unit cells in proportion, so that the microstructure of the material can directly and quantitatively reflect its macroscopic properties.

(2) With the increase of the width of the sample, the unnotched tensile modulus of the 3D five-directional braided composite material in the warp and weft will gradually increase, and tend to be stable when the sample reaches a certain width, indicating that the free boundary is opposite to the test. The influence of the sample gradually decreases with the increase of the width. When the mechanical property test is carried out, it should be avoided that the sample width is too small and the test result will be affected by the size effect;

(3) The ideal 3D five-directional braided composite material has no gap in the warp direction. The width of the tensile sample should not be less than 4 times the

width of the face cell, and the ideal width of the 3D five-directional braided composite material without gaps in the weft direction should not be less than 3 times the braided rosette.

References:

[1] Xu Kun, Xu Xiwu.Macro and micro Mechanical Properties of THREE-DIMENSIONAL five-direction Braided Composites [J]. Journal of Astronautics(3):1053-1058.

[2] Zhang Chao, Xu Xiwu, Yan Xue.Journal of nanjing university of aeronautics and astronautics,2013,45(02):170-178.

[3] R. Pandey, H.T. Hahn. Visualization of representative volume elements for three-dimensional four-step braided composites[J]. Composites Science and Technology,1996,56(2).）

[4] D3039/D3039M Standard Test Method for Tensile Properties of Polymer Matrix Composite Materials has been revised to D3039/D3039M-14[J]. ASTM Standard.

[5] Suquet P. Elements of homogenization theory for inelastic solid mechanics[C]. Sanchez-Palencia E, Zaoui A. Homogenization Techniques for Composite Media. Berlin: Springer-Verlag, 1985: 194-275.

[6] PI Xiu-biao, QIAN Kun, CAO Hai-jian, Yu Ke-jing, Chen Hong-xia.Microstructural analysis of three-dimensional full five-direction braided composites [J]. Aerospace materials & technology,2011,41(06):39-43.

Thermal/mechanical behavior of fastened hybrid composite/metallic structures

CAO Su, WEI Jingchao, LEI Kai, CHEN Xiangming*

1.National Key Laboratory of Strength and Structural Integrity, Aircraft Strength Research Institute of China, Xi′an 710072, China

Abstract: Extreme climatic conditions, such as high temperature, low temperature and hydrothermal environment, affect the bearing performance and life expectancy of composite and metal hybrid structural components in aircraft, which have a great impact on the flight performance and safety of aircraft. Due to the large coefficient of thermal expansion mismatch between the composite and metallic structures, the temperature change in the actual flight condition induces high thermal stresses in both the composite component and metallic component. This additional stress would alter load transfer and internal stress distribution in fastened hybrids of composite and metallic structure. Thermal/mechanical behavior of the large-scale, multi-joints hybrid composite/metal structure was investigated experimentally in different temperature conditions, as well as bearing axial load under different temperatures. The internal stress distribution of different components and fasteners in hybrid composite/metal structure under different temperature/load conditions was obtained by the strain gage method.

Keywords: hybrid structure; temperature effect; thermal stress; experimental investigation

Introduction

Composite structures have been widely used in aerospace applications due to their high performance. Aircraft often experience high temperature and low temperature environment in the actual flight conditions, in which the extreme high temperature may exceed +60℃, while the extreme low temperature may below -55℃[1-2]. Because of the large coefficient of thermal expansion mismatch between the metallic and composite structures, as well as the constraint of fasteners, the temperature change in the actual flight condition induces high thermal stresses in fastened hybrids of composite and metallic structure, and then affects load transfer and stress distribution of the structure.

By experiment and finite element method, the internal stress distribution and load transfer of the fastened composite/metal structure were investigated by Guo Jushang. With the increase of temperature, the internal stress of composite laminate decreased and that of aluminum alloy plate increased, and the unevenness of load transfer increased and the load concentrated towards one bolt. Deng Wenliang et al. took the composite and aluminum alloy connection structure under tensile load as the research object, using the finite element method, to compare and analyze the load distribution of five-bolt single shear lap structure and double shear butt structure under different temperatures. The results showed that the load distribution of composite and aluminum alloy structure displayed U-shaped tendency, which is low in the middle and high on both sides. Chihdar Yang et al. studied the internal stress distribution caused by thermal load in the fastened Z-shaped aluminum beams and the composite laminate in temperature difference environment (75^{o}F on aluminum alloy beam and -65^{o}F at the bottom of composite laminate) by experimental method and finite element method. The results showed the maximum thermal stress of aluminum alloy occurred in the center of its length direction, and the fasteners at both ends of the structure bore the highest load.

In this paper, an experimental program was executed to determine the interaction between the fastened Z-shaped aluminum beams and the composite laminate. The thermal response of fastened composite/aluminum hybrid structure in high (74℃±3℃) and low (-55℃±3℃) temperature environment is investigated experimentally. Meanwhile, the elimination of thermal stress in high and low temperature environment by applying load is explored and the thermal-mechanical coupling response of structures subjected to tensile load at high and low temperatures is also investigated experimentally.

1. Material and experiment

1.1 Material

The fastened composite/aluminum hybrid structure is shown in Fig.1. No.1 is composite laminate, which is 984mm long, 210mm wide and 3.36mm thick. The composite laminate was fabricated with MTM28/T700 unidirectional fabric with 0.12mm nominal thickness, using a lay-up sequence of [45/-45/0/0/-45/0/90/45/0/-45/0/90/45/0]s. No.2 is Z-shaped aluminum alloy beam, which is made of 7050-T7451, and specific dimensions is shown in Fig.2. No.3 isφ6 bolts, which are made of low-alloy high-strength steel 16Mn.

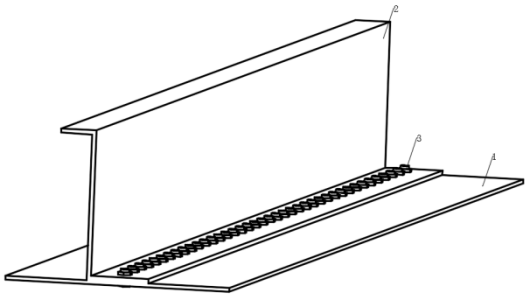

Fig1 Schematic diagram of test article

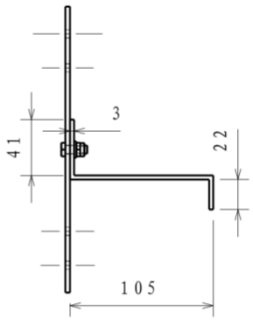

Fig2 Dimension diagram of aluminum alloy beam

1.2 Test configuration and method

An environmental chamber, as shown in Fig.3, was designed to accommodate the test article from the high temperature of 74℃±3℃ to the low temperature of -55℃±3℃. The air conditioner was used to change the temperature inside the environment chamber with the control thermocouple located inside the chamber. When the condition reached the target temperature, the test article should be placed in the chamber for at least 30 minutes to ensure the temperature distribution was uniform.

After the completion of the temperature load test, the thermal load generated by the temperature change was eliminated by mechanical loading, and then 60kN tensile load was applied on the composite laminate by hydraulic actuator.

Fig3 Environment chamber and fixture picture

Both temperature and strain data were monitored in real time by the MTS-24 data acquisition system. And the time history and steady state of temperature and strain were recorded in representative locations throughout the test article during testing. The strain gauge locations are shown in Fig.4 and Fig.5.

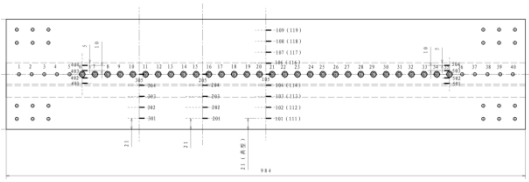

Fig4 Locations of strain gauge on composite laminate

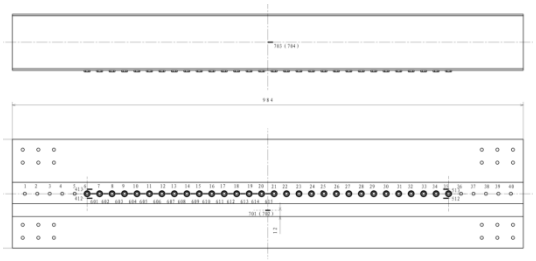

Fig5 Locations of strain gauge on aluminum alloy beam

2. Experimental results

2.1 Temperature test

2.1.1 High temperature of 74℃±3℃

The temperature-strain curves of the test article in high temperature condition are shown in Fig.6. The maximum strain appeared at the top of the Z-shaped aluminum beam, while the minimum strain appeared at the bolt at the end of the connection area. The composite laminate presented compression state as a whole and bolts at the ends bore the highest load. The aluminum alloy beam presented tensile state and the strain level at the end of the test article was higher than that at the middle. It showed that the thermal stress caused by temperature rise was mainly borne by the bolts at the end of the connecting area. The strain level of the non-connected surface of the composite laminate was slightly higher than that of connected surface, while the strain level of the non-connected part of the aluminum alloy beam was much higher than that of the connected part. Because the thermal expansion coefficient of the composite is smaller than that of aluminum alloy, and the two parts are constrained by bolts, the whole structure tended to bend toward the composite laminate with temperature rising.

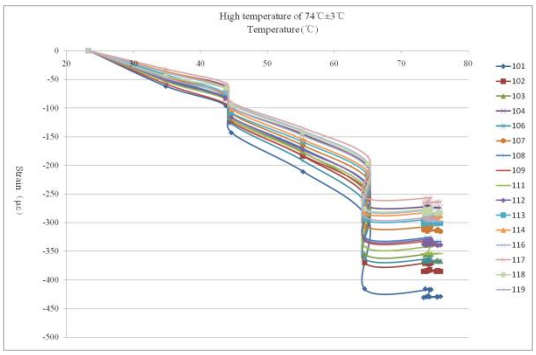

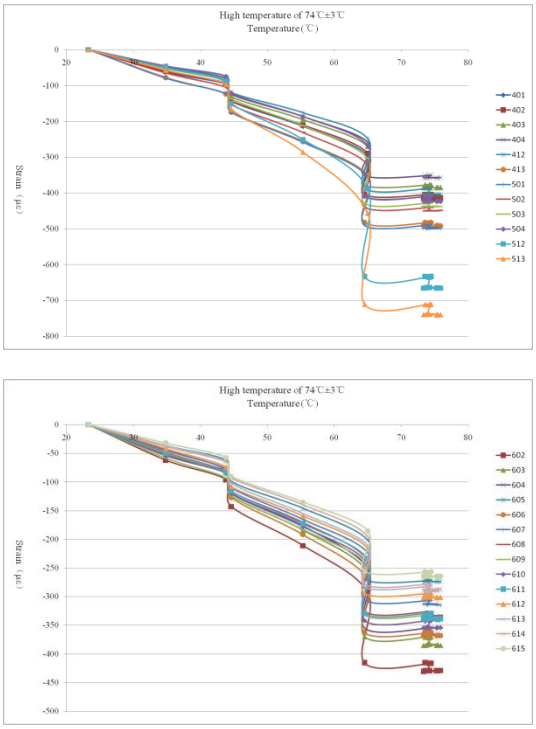

Fig5 Temperature-strain curves of high temperature test

2.1.2 Low temperature of -55℃±3℃

The temperature-strain curves of the test article in low temperature condition are shown in Fig.7. The maximum strain and the minimum strain both appeared at the bolt at the end of the connection area. The composite laminate showed a tensile state as a whole, and most of the strain values increased first and then decreased with the decrease of temperature, reaching the maximum level at about -30℃～-40℃. The strain level of the non-connected surface of the composite laminate was slightly higher than that of connected surface. The aluminum alloy beam showed a compression state, and the strain decreased with temperature decreasing. The strain level at both ends of the connecting zone was higher than that in the middle zone, and large compressive strain appeared at the top of aluminum alloy beam. The whole structure tended to bend toward the aluminum alloy beam with temperature decreasing.

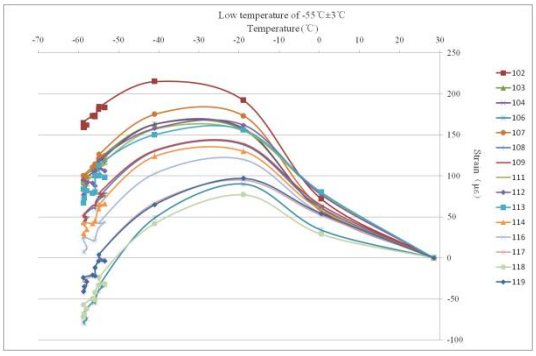

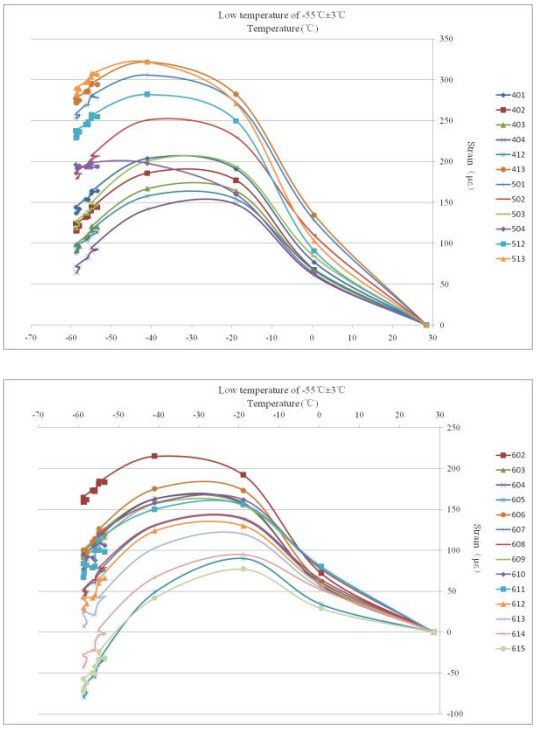

Fig7 Temperature-strain curves of low temperature test

2.2 Temperature and tensile load test

2.2.1 Tensile load under high temperature of 74℃±3℃

The load-strain curves of tensile load applied at high temperature is shown in Fig.8. The first four loading stages are the strain changes in the process of heating up to 74℃ and insulation, and the fifth stage is the strain value measured after the additional load caused by the thermal deformation of the test article is offset by loading. As the temperature rose, the composite laminate contracted while the aluminum alloy beam expanded. After the additional loading caused by thermal deformation was offset, the strain only changed slightly. During the tensile loading process, the strain changed linearly. After unloading, the test article returned to the strain level caused by high temperature. The maximum strain value appeared near the bolt at the end of the connection area, while the minimum strain value appeared between the No.10 fastener and No.11 fastener on the composite laminate. This was different from the high temperature environment test and the tensile test at room temperature, indicating that the thermal stress generated in high temperature environment affected the stress distribution of the hybrid structure subjected to mechanical loading. For the composite laminate, the strain level at the end of the connecting zone was relatively high, and the strain level of the non-connecting surface is slightly lower than that of the surface connected with aluminum alloy beam. Because the temperature rising made the whole structure bend towards the composite laminate, the compression state of the non-connected surface caused by high temperature got intensified. For aluminum alloy beam, the strain level at the end of the test article was higher than that at the middle, while the strain at the top of the beam decreased with the increase of tensile load. This is due to the fact that the tensile load alleviated the bending tendency caused by high temperature to some extent.

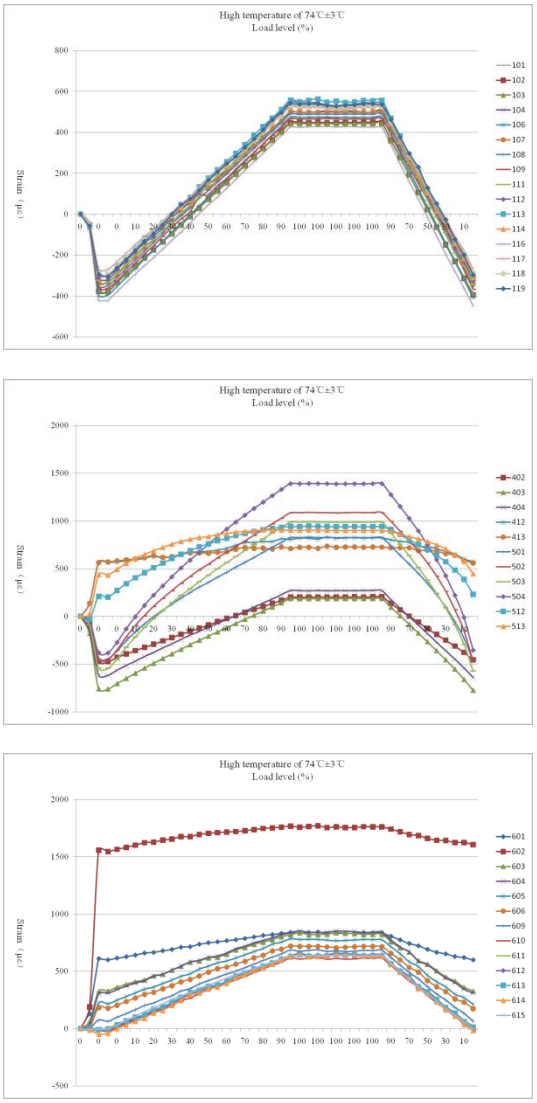

Fig8 Load-strain curves in high temperature environment

2.2.1 Tensile load under low temperature of -55℃±3℃

The load-strain curves of tensile load applied at low temperature is shown in Fig.9. The first five loading stages are the strain changes in the process of cooling down to -55℃ and insulation, and the sixth stage is the strain value measured after the thermal induced additional load is offset by loading. As the temperature decreased, the composite laminate expanded while the aluminum alloy beam contracted. After the additional loading caused by thermal deformation was offset, the change of strain was obvious. After unloading, the test article returned to the strain level caused by low temperature. The maximum strain value appeared near the bolt at the end of the connection area, while the minimum strain value appeared at the top of beam. Similar to the low temperature environment test, the whole structure tended to bend toward the aluminum alloy beam. For both composite laminate and aluminum alloy beam, the fasteners at the ends of the connecting area bore more load. On the aluminum alloy beam, with the tensile load increasing, the strain value of web decrease, while the compression strain at the top increased, due to the fact that the tensile load aggravated the bending tendency caused by low temperature.

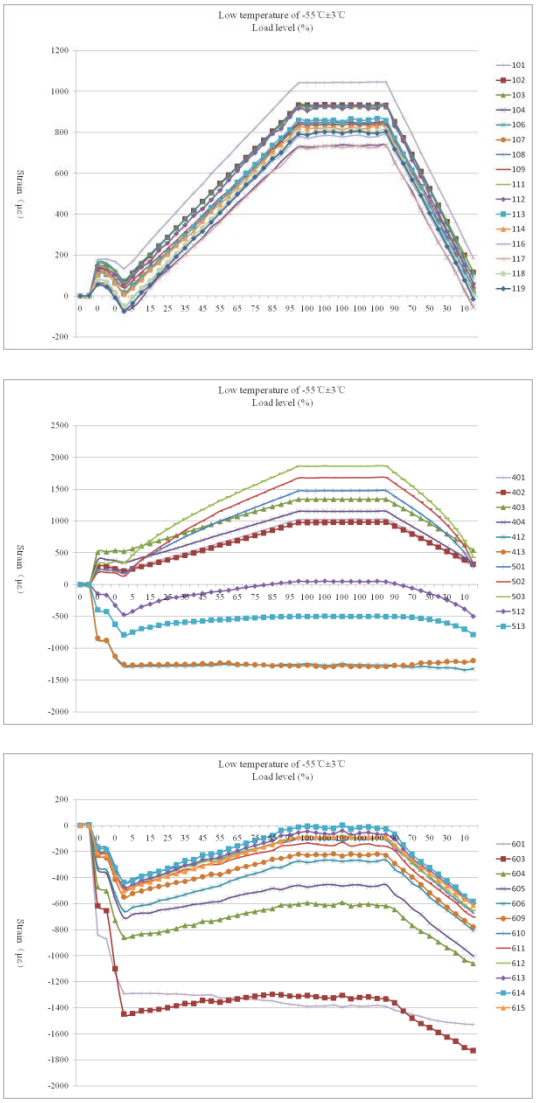

Fig9 Load-strain curves in low temperature environment

4. Conclusion

A aluminum alloy beam/composite laminate assembly was exposed to 74℃±3℃ and -55℃±3℃ separately, using a custom-designed environmental chamber. And the thermal-mechanical coupling response of structure subjected to tensile load at different temperatures was tested. Temperature and strain distributions were recorded, from which it can be found that

1. In both high temperature environment and low temperature, the thermal stress was mainly borne by the bolt at the ends of the connecting area of the test article.

2. In high temperature condition, the composite laminate presented a compression state, while the aluminum alloy beam presented a tensile state. With the temperature increasing, the whole structure had a bending tendency towards the composite laminate.

3. In low temperature condition, the composite laminate presented a tensile state, while the aluminum alloy beam presented a tensile state. With the temperature decreasing, most of the strain values on the composite laminate increased first and then decreased, and the whole structure had a bending trend towards the aluminum alloy beam.

4. In high temperature condition, the effect of loading to eliminate the additional load

induced by thermal deformation was relatively small. The thermal stress affected the stress distribution of the structure subjected to mechanical loading, meanwhile, the tensile load alleviated the bending tendency to some extent.

5. In low temperature condition, the effect of loading to eliminate the additional load induced by thermal deformation was obvious. Similar to temperature environment test, the fasteners at the ends of the connecting area bore more load. But the tensile load aggravated the bending tendency caused by low temperature.

References

[1] Liu Xiaohua Airworthiness analysis of environmental impact of composite materials[J]. Aeronautic Standardization and Quality, 2013, 04:32-34.

[2] Zheng Xiaoling. Analysis and research on the airworthiness compliance of composite structure[J]. Civil Aircraft Design and Research. 2017(1):1-6.

[3] Guo Jushang. Internal stress analysis of bolted joint composed of composite plate and aluminum plate in thermal field[D]. Harbin Institute of Technology, 2013.

[4] Deng Wenliang, Tang Hu, Cheng Zhu. Influence of Temperature on nail load distribution of composite and metal structures[J]. Engineering and Test, 2018,58(03),27-30.

[5] Chihdar Yang, Wenjun Sun, Waruna Seneviratne, and Ananthram K. Shashidhar. Thermally Induced Loads of Fastened Hybrid Composite/Aluminum Structures[J]. Journal of Aircraft. Vol.45, No.2, March-April 2008.

Study on interface debonding of reinforced composite Panel Based on seven-point bending Test

Tianjiao Qu, Houbing Wang, linan Cheng , xiangming chen, yanan chai
National Key Laboratory of Strength and Structural Integrity

Abstract: The structural failure caused by out-of-plane bending load of reinforced composite panels under post-buckling load usually occurs at the interface or maximum bending moment. In this paper, the post buckling failure of the M-stiffened panel was simulated by seven-point bending test, and the interface detachment of the composite stiffened panel was analyzed by using the cohesive force element (CZM) technique based on the finite element analysis software ABAQUS. The analysis results are in good agreement with the test results, which proves the rationality and effectiveness of the method. The results show that the initial failure of the stiffened panel is interface debonding, and the loading distance has a great influence on debonding.

Key words: M-stiffened panel, post-buckling, interface debonding , seven-point bending
Chinese library classification number：V214.8

Introduction

Carbon fiber reinforced composites are increasingly used in aircraft structures due to their high specific strength, high specific modulus, fatigue resistance, corrosion resistance and other advantages. Stiffened panel is a typical structural part of aircraft structure and has been widely used in thin-walled structures such as fuselage and wing box sections. The optimization design of carbon fiber reinforced composite reinforced panels, such as weight reduction design and load bearing improvement, has attracted much attention [1].

Debonding between stringer and skin is one of the main failure modes of composite stiffened panels. By extracting and analyzing the load on some characteristic sections of the stiffened plate, the researchers found that the shear load between the stringer and the skin was the main reason for the debonding failure of the stiffened plate[2]。 In early studies, narrow specimens and four-point bending or lateral tensile loading forms were used to simulate shear failure modes between stringer and skin[3]. However, it is difficult to obtain accurate test results because the four-point bending specimen is greatly affected by the edge effect. Rijn and Wigg Enraad[4-5] of NLR designed a seven-point bending test to solve this problem. In the seven-point bending test, load is applied to the skin by the way of point loading, so that local bending deformation is produced, and peeling load (mainly shear force and bending moment) is produced between the girder flange and the skin of the stiffened plate. In addition, the size of the test piece in the seven-point bending test is larger than that in the four-point bending test, so it is less affected by the edge stratification, and the debonding failure mainly occurs in the bonding layer between the stringer flange and the skin. In the actual structure, the failure mechanism of the composite stiffened plate in the post-buckling stage is consistent with the failure mechanism of the seven-point bending test. Therefore, if the failure criterion (i.e., the function relationship between the peeling loads) can be established when the initial failure of the reinforced plate occurs through the seven-point bending test, then the failure criterion is also suitable for the failure characterization of the reinforced plate in the post-buckling stage of the same composite material.

Kong Bin et al[6-7] studied the post-buckling load transfer mechanism of composite integral stiffened plates under axial compression, carried out a detailed analysis of internal forces and load transfer characteristics at local buckling and overall buckling stages, and summarized the failure characterization method based on finite element analysis.

On the basis of experimental research and finite element calculation, Ye Qiang et al[8]. studied and analyzed the failure mechanism of seven-point bending test. Through the analysis of a series of seven-point bending test models, the failure envelope of typical parts of composite stiffened plate is obtained, and the failure characterization method based on the relationship between shear force F B and bending moment MB and edge strip thickness and skin thickness is obtained.

Hu Botao[9-10] et al. studied the failure characterization based on six-point bending test for the interface failure of the post-buckling composite stiffened plate. The initial failure position, failure mode and internal force distribution of the rib-skin interface during post-axial buckling and six-point bending tests were compared and analyzed in Abaqus. Based on the finite element results, the calculation method of interfacial control internal forces is deduced, and the failure characterization equation and failure envelope of interfacial debonding are given.

In this paper, a seven-point bending test was performed to simulate the post-buckling failure of cap-stiffened panels. Based on the commercial finite element software Abaqus, the interface debonding of composite stiffened panels was analyzed by using the cohesion model (CZM) technology.

1. Experiment

1.1 Specimens

The material system of the carbon fiber reinforced composite seven-point bending test piece was M21E/IMA, the material specification was CMS-CP-309, and the nominal thickness of the single layer was 0.184mm. The size diagram of the test piece is shown in Figure 1, and the material properties are shown in Table 1.

The layering sequence of the skin is [45/-45/45/90/0/-45/0]s, The web of T stringer is laid in the order of [45/0/90/0/-45/0/0/-45/0/90/0/45]s. The layering order of the lower edge strip of the T stringer is [45/0/90/0/-45/0/0/-45/ 0/90/0/45/-45/0/45]s.

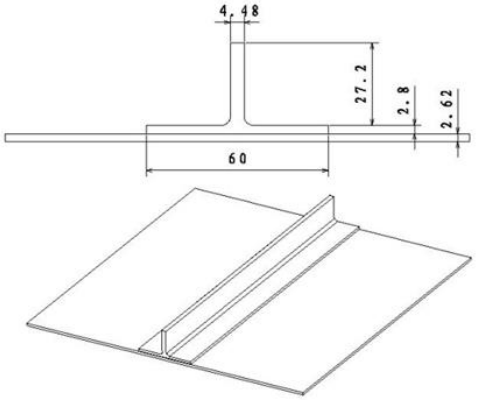

Fig.1 The Schematic diagram of specimen

Table1 Material property

Material	Longitudinal tensile modulus E_{11}(MPa)	Transverse tensile modulus E_{22}(MPa)	shear modulus G_{12}(MPa)	poisson ratio μ_{12}
M21E/ IMA	154000	8500	4200	0.35

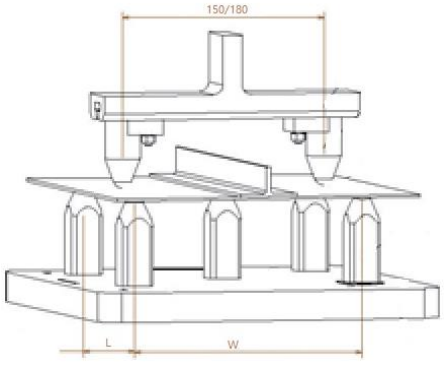

Fig.2 Schematic diagram of seven-point bending test loading

In order to adapt to different loading requirements, a set of special fixture for seven-point bending test is designed, as shown in Figure 2. A series of holes are provided on the bottom plate of the lower fixture to accommodate different support spacing requirements. The upper fixture chuck is provided with variable distance slotted holes to suit different loading spacing

requirements. The five bottom support points were symmetrically distributed at the four rectangular holes located at the support spacing and at the center point of the bottom plate, respectively. Support spacing was set in the test, that is, the length L× width W was 240mm×180mm. The two top loading points were located at the midpoint of the width direction of the symmetrical specimen on both sides of the stringer. Two loading spacing were set in the test, that is, the loading spacing was 150mm and 180mm, respectively. The load and support positions are shown in Figure 3. In order to adapt to different loading requirements, a set of special fixture for seven-point bending test is designed, as shown in Figure 2. A series of holes are provided on the bottom plate of the lower fixture to accommodate different support spacing requirements. The upper fixture chuck is provided with variable distance slotted holes to suit different loading spacing requirements. The five bottom support points were symmetrically distributed at the four rectangular holes located at the support spacing and at the center point of the bottom plate, respectively. Support spacing was set in the test, that is, the length L× width W was 240mm×180mm. The two top loading points were located at the midpoint of the width direction of the symmetrical specimen on both sides of the stringer. Two loading spacing were set in the test, that is, the loading spacing was 150mm and 180mm, respectively. The load and support positions are shown in Figure 3.

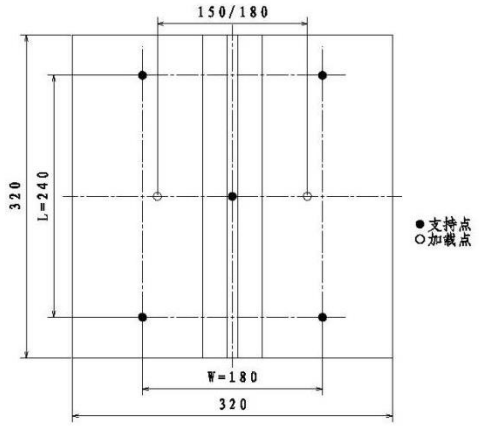

Fig.3 Loading point diagram

1.2 experimental result

Test was carried out on Intron static testing machine. Displacement control loading method was used in the formal test, and the loading rate was -1mm/min, that is, the test piece was compressed at the loading point. A total of 12 pieces were tested in 2 groups. With the loading of displacement, the test pieces gradually made a slight noise, which was caused by the change of the curvature of the skin and the inconsistency of the stiffness of the skin and the stringer. No obvious interface debonding was found. The noise of the skin and T-type stringer is relatively large during the debonding. The initial debonding position is the outer edge of the stringer in the middle of the stringer length direction. With the gradual increase of the test displacement, the test piece continuously makes a sound, and the debonding gradually expands to the inside of the stringer and both sides of the stringer. The final failure of the test part made a great noise, the load was dropped more than 30% of the maximum load, the interface between stringer and skin was debonding in 60%~80%, the skin bounced back after unloading, and the skin split wire and layering occurred only near the constraint point, without a large range of plastic deformation. Figure 4 shows the initial debonding position,

and Figure 5 shows the photo of the final failure. Table 2 shows the initial debonding and final failure results of the two groups of test pieces. The test results show that the larger the distance between loading points, the larger the initial debonding load and the smaller the final failure load.

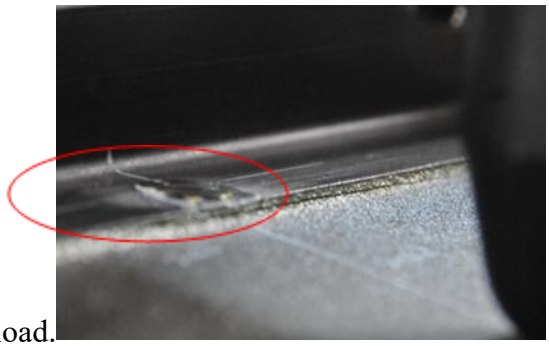

Fig.4 The initial debonding

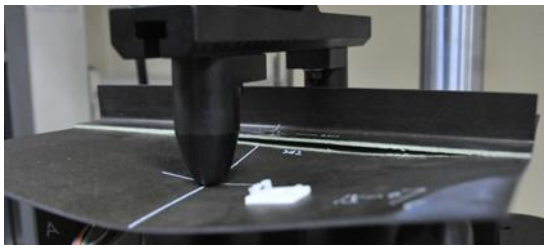

Fig.5 The final failure

Table 2 Experiment results

Test group	The loading space/mm	The supporting space /mm	Initial debonding load	Final failure load
1	150	W180	-4.54	-13.36
2	180	L240	-5.07	-12.35

2. Finite element analysis

Based on the experimental study, the failure mechanism is analyzed by finite element method. ABAQUS finite element software was used to establish the seven-point bending finite element model of the interface debonding T-type of reinforced composite panels (FIG. 6).

The boundary conditions of the seven-point bending symmetric loading finite element model are shown in FIG. 6, in which five support points (S1, S2, S3, S4 and S5) constrain the degrees of freedom of y-direction displacement and Z-direction rotation, namely, U2=UR3=0. By applying Y direction displacement load U2=Un to the two loading points (L6 and L7), Un is the displacement load applied at the loading point, and the displacement in other directions is 0, namely U1=U3 =0.

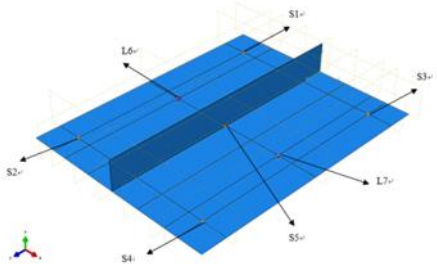

Fig.6 The finite element model

In this paper, a cohesive zone model[11] is used to simulate the interfacial debonding mechanism between skin and edge strips. Cohesive unit is a zero thickness interface element based on cohesive force model, which is mainly used to simulate and analyze the failure of bonding layer, composite interface layer, patch, etc. When used to simulate the interfacial stratification problem of composite materials, cohesive units are used based on the following assumptions :(1) material continuity; (2) Interface separation failure. The main advantages of the cohesion model are as follows :

(1) the model provides a unified description for the initiation and propagation of stratification, which overcomes the difficulty that fracture mechanics can not be used to predict the initiation of new cracks;

(2) When the scale parameter characterizing the fracture process zone is close to the characteristic geometric size of the material or structure (such as the crack length), the method of linear elastic fracture mechanics is no longer effective, and the cohesion model provides a very effective analysis method for this situation.

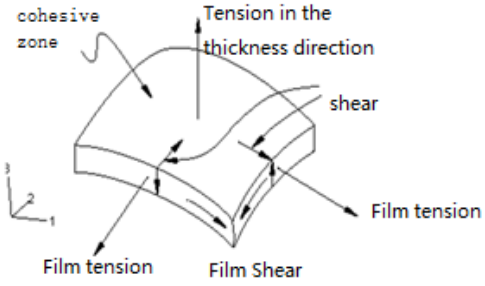

Fig.7 The force distribution of cohesive zone

The failure of cohesive zone includes two aspects: stratification initiation and expansion. Firstly, the strength criterion is used to judge the damage initiation of cohesive units. After the damage initiation, the Griffith energy failure criterion is used. Likewise, the strain criterion can be used to judge the damage initiation and failure process.

In order to accurately simulate the damage initiation of structures under complex stresses, the secondary nominal stress criterion is adopted in the model analysis, which is defined as follows:

$$d=\left\{\frac{t_n}{t_n^0}\right\}^2+\left\{\frac{t_s}{t_s^0}\right\}^2+\left\{\frac{t_t}{t_t^0}\right\}^2 \qquad (1)$$

When d=1, failure initiation occurs.

Where t_n is the normal nominal normal stress of the cohesive zone element, t_s and t_t are the two tangential shear stresses of the adhesive layer element, t_n^0, t_s^0, t_t^0 respectively the corresponding maximum stress values.

Critical strain energy release rate is an important parameter used to characterize the fracture toughness of composite laminates. It is the energy provided by the system when the laminates are extended per unit area. The critical strain energy release rates for the three failure modes of open type, slip type and staggered type are as follows:

$$G_{IC} = \int_0^{\delta_{\max 3}} \sigma_{33}(\delta) d\delta_3 \tag{2a}$$

$$G_{IIC} = \int_0^{\delta_{\max 2}} \tau_{13}(\delta) d\delta_2 \tag{2b}$$

$$G_{IIIC} = \int_0^{\delta_{\max 1}} \tau_{23}(\delta) d\delta_1 \tag{2c}$$

The damage propagation failure criterion adopts mixed failure mode:

$$D = \left\{\frac{G_{\mathrm{I}}}{G_{\mathrm{IC}}}\right\}^{\alpha} + \left\{\frac{G_{\mathrm{II}}}{G_{\mathrm{IIC}}}\right\}^{\alpha} + \left\{\frac{G_{\mathrm{III}}}{G_{\mathrm{IIIC}}}\right\}^{\alpha} \tag{3}$$

When D=1,the element failures.

Where, G_{I}, G_{II} and G_{III} are the energy release rates of the three fracture failure modes; G_{IC}, G_{IIC} and G_{IIIC} represent the critical strain energy release rates per unit length of the material under each individual load.

Table3 Mechanical property of cohesive element

E_{11}/MPa	G_{12} /MPa	G_{13} /MPa	t_n^0 /MPa
4500	1500	1500	10
$t_{s/t}^0$ /MPa	G_{IC} /J·mm^{-1}）	$G_{\Pi C}$ /（J·mm^{-1}）	t_t^0/MPa
11.5	0.25	0.66	11.5

The failure results of the strand-skin interface simulated by finite element method are shown in FIG.8. The initial debonding position is located on both sides of the edge strip, and the interface failure gradually expands inward with the increasing load. Figure 9 shows S_{11}, S_{22} and S_{12} of the skin. According to the figure 9, the failure of the bonding layer is caused by the interaction between the stress S_{11} in the first direction and the in-plane shear stress S_{12} in 1-2.

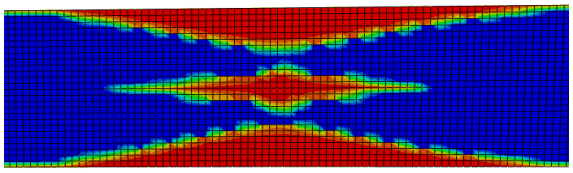

Fig.8(a) 150 Load spacing failure diagram

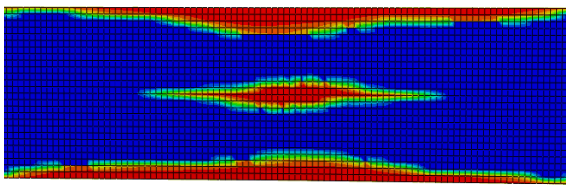

Fig.8(b) 180 Load spacing failure diagram

Fig.8 The failure diagrams

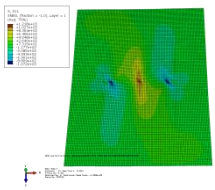

Fig.9(a) S_{11} stress diagram

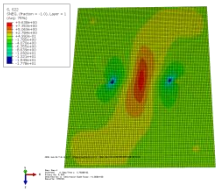

Fig.9(b) S_{12} stress diagram

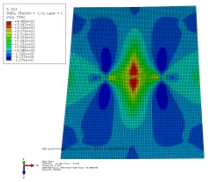

Fig.9(c) S_{22} stress diagram

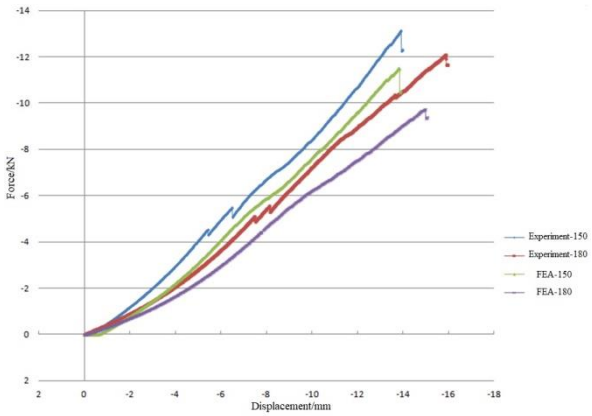

Fig.10 Load-displacement response

By comparing the FEA results of the two kinds of loading spacing, it can be seen that the increase of loading space can inhibit the initial debonding. The initial debonding position is located on both sides of the edge strip, and the interface failure gradually expands inward as the load increases gradually.

3. Conclusion

In this paper, the seven-point bending test of composite integral stiffened plate is studied by means of test and finite element analysis,and the failure characterization of typical details of stiffened plates. The following conclusions are obtained:

(1)The initial debonding position of the seven-point bending test was located on both sides of the middle edge strip. With the increasing of the load, the interface failure gradually

extended inward and outward.

(2)The cohesive zone model can effectively simulate the seven-point bending test, and the analytical results are in good agreement with the experimental results.

References

[1] Chen guijuan, Jiao guiqiong, Xiong wei, et al. Nonlinear post-buckling behavior of composite laminated plates [J]. Journal of Wuhan University of Science and Technology, 2005, 28(1):103-107.

[2]Krueger R, Cvitkovich M K. Testing and analysis of composite skin/stringer debonding under multi-axial loading [R] . NASA/ T M-1999-209097, 1999.

[3]van Rijn J C F N. Failure criterion for the skin-stiffener interface in composite aircraft panels [R]. NLR-TP-98264, 1998.

[4]van Rijn J C F N, Wiggenraad J F M. A seven-point bending test to determine the strength of the skin-stiffener interface in composite aircraft panels [R].NLR-TP- 2000-044, 2000.

[5] van Rijn J C F N. Design guidelines for the prevention of skin-stiffener debonding in composite aircraft panels[R]. NLR-T P-2000-355, 2000.

[6] KONG Bin，YE Qiang，CHEN PuHui，et al． Post － buckling load transfer mechanisms of an integrated composite panel under uniaxial compression ［J］． Acta Materiae Compositae Sinica，2010，27(5): 142-149 ．

[7]KONG Bin，YE Qiang，CHEN PuHui，et al． Post－buckling failure characteristics of an integrated composite panel under uniaxial compression［J］． Acta Materiae Compositae Sinica，2010，27(5):150-155.

[8]Ye Qiang, Xia Xiang, Xiao Shanshan, et al. Numerical and Experimental Analysis on Seven-Point Bending Test of Integrated Composite Panels[J]. Journal of Nanjing University of Aeronautics & Astronautics, 2011,43(4):470-474.

[9]HU BoTao, CHAI YaNan, CHEN XiangMing, et al.Stiffener-skin interface Failure characterization of the stiffened composite panel at post-buckling stage[J]. Journal of Mechanical Strength, 2019， 41(6) : 1473-1479.

[10]HU Botao，SUN Xiaobo，LIANG Qingxianglong. A Stringer /skin interface damage characterization method of stiffened composite structures considering effects of through － thickness Compression[J]. Fiber composites,2022, 2:37-43.

[11]CHENG Li-nan，XU Si-wen，CHEN Xiang-ming，et al. Analysis of interfacial failure in omega stiffened composite panel with embedded defect [J] Composite Materials Science and Engineering, 2022(8):28-34.

Numerical Analysis Method of Butt Connection Strength of Composite Stiffened Panels with Impact Damage

WEI Jingchao, QU Tianjiao, ZHANG Hui, CHENG Linan and CHEN-Xiangming

Aeronautics Science and Technology Key Laboratory of Full Scale Aircraft Structure and Fatigue, Aircraft Strength Research Institute of China, Xian, China

Abstract: The aircraft fuselage structure contains a large number of wall panel butt connection designs. Due to the impact of foreign objects such as runway stones, hail, and maintenance tools, it is easy to cause different degrees of impact damage to the fuselage structure, thereby affecting the strength of the aircraft structure. In this paper, the structural strength test and numerical simulation analysis of the butt area of the composite panel with impact damage are carried out. Based on the assumption of material stiffness reduction in the delaminated region caused by impact damage, a finite element model analysis method is proposed. In the model, the Hashin criterion is used to describe the failure of composite materials, and the failure of the adhesive layer between the skin and the girders is simulated based on the bilinear cohesion element model. In order to verify the validity of this method, a physical test verification study was carried out. The results show that the numerical analysis results proposed in the paper are consistent with the physical test results, and the error is less than 5%.

Key Words: Butt Connection Strength; Composite Stiffened Panel; Impact Damage; Numerical Analysis Method

1. Introduction

The fuselage structure of the aircraft contains a large number of wall panel butt connection designs. The connection of multiple parts is mainly realized through mechanical fasteners, whose connection strength directly affects flight safety and aircraft service life[1, 2]. Due to the impact of foreign objects such as runway stones, hail, and maintenance tools, it is easy to cause different degrees of impact damage to the fuselage structure, thereby affecting the strength of the aircraft structure. The low-velocity impact damage of composite materials has low visual detectability. While the damage is difficult to detect, it will significantly reduce the ultimate compressive strength of the composite structure, thus posing a serious threat to the load-bearing safety of aeronautical composite structures. Due to the importance of connection design, a large number of scholars have conducted extensive research on the connection strength of composite laminates. The three-dimensional cumulative damage calculation can vividly and objectively reflect the damage generation and evolution process at the connection, which is the current mainstream computational simulation method[3, 4].

Due to the structural characteristics of composite laminates, it is necessary to use nonlinear finite element method to calculate the damage and extension repeatedly, which makes the calculation of the connection strength large scale and long time. For large-scale composite structures, a simple and fast finite element analysis method is needed. In this paper, the structural strength test and numerical simulation analysis of the butt area of the panel with impact damage are carried out. Based on the assumption of material stiffness reduction in the impact damage delaminated region, a finite element model analysis method is proposed. In the model, the Puck criterion is used to describe the failure of the composite material, and the failure of the adhesive layer between the skin and the girder is simulated based on the bilinear cohesion element model.

2. Composite structure design and finite element model

2.1. Configuration of composite structure

Composite wing panels are usually in the form of stringer panels. The composite material laminate is made of medium-mold high-strength carbon fiber reinforced epoxy resin prepreg, the joints and connecting strips are made of titanium alloy, and the rib web is made of aluminum alloy.

The long-truss docking structure adopts three columns of long-trusses, the left and right long-trusses are connected long-trusses, and the middle is a symmetrical configuration joint. The joint end of the girders adopts the web profile of the arc at the tip and the beveled step, and adopts three rows of six bolts. The four bolts at the tip are connected with the rib shear angle piece, and the remaining two bolts are distributed on the inner side of the rib web.

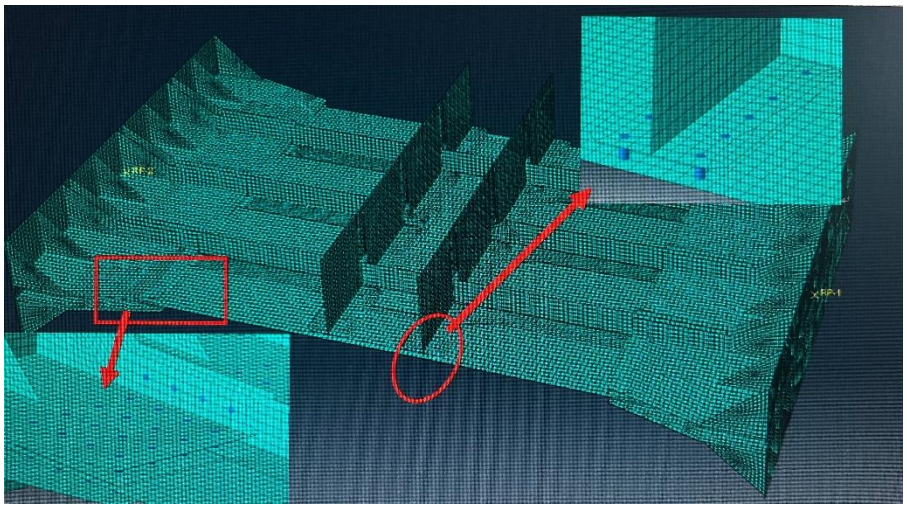

Figure 1. Finite element model of docking structure of composite sidings.

2.2. Material property

The test pieces are made of carbon fiber reinforced epoxy resin based prepreg (as shown in Table 1), and the stringer and the skin are made of co-bonded technology. Butt strap plate and butt joint material is titanium alloy Ti-6Al-4V, forged rib web material is aluminum alloy 7050.

Table 1. Mechanical properties of composite materials.

Longitudinal modulus E_{11} / MPa	Transverse modulus E_{11} / MPa	Shear modulus G_{12} / MPa	Poisson's ratio ν_{12}
178000	8260	5200	0.34

2.3. FE model

According to the structural characteristics and stress conditions, the structure of each part of the test piece is simplified according to the following principles. The long trusses are simulated by one layer of elements, in which the left/right side edge of the I-shaped long truss is the left/right layer and the bottom layer are superimposed, and the long truss web is the left and right layers. The requirements are consistent, and the direction from the truss to the skin is required to be the positive direction of the Z-axis of the element; the bolt is simulated by the Beam element; at the butt joint of the test piece, the bolt beam element and the extrusion surface of the hole side shell/solid element are connected by a common node. to simulate multi-

nail connection; for the fixture, only the loading end connected to the test piece is considered in this model, and it is not considered because the tensile and compression fatigue test platform and the actuator have no direct influence on the analysis results; the fixture adopts the shell element Simulation, the connection between the loading end and the clamping end of the test piece is also simulated by the beam element common node method.

2.3.1 Loads and boundary conditions. Loads and boundary conditions are applied to the model according to the test loading and clamping. The wing girder end selection test piece is subjected to quasi-static tensile load, quasi-static compressive load and tensile-compression fatigue load, and usually the fatigue load is much smaller than the static load, and the fatigue load can be obtained by linear reduction according to the static load. Therefore, in the virtual test, only the static tensile and quasi-static compression conditions, and the buckling analysis of the test piece under compression conditions are considered. In the process of virtual test analysis, in order to ensure equal displacement loading, a reference point RP1 for load application is set at the loading end, the concentrated force load is applied to this point, and the node and the loading end node are connected by Coupling, constrain the degrees of freedom (UY, UZ, RX, RY, and RZ) in other directions except for stretching, and at the same time load the end support on the other side, and impose full constraints on the displacement direction of 6 degrees of freedom. Release the test tensile/compression loading direction on the lateral support end face of the rib web of the test piece, and constrain five degrees of freedom in other directions.

2.3.2 Nonlinear shear relationship. The shear deformation in the fiber direction of the composite material is usually nonlinear. Hahn and Tsai gave the nonlinear shear stress-strain relationship using the higher-order elastic theory, as follows:

$$\gamma_{12} = \frac{1}{G_{12}^{o}}\sigma_{12} + \alpha\sigma_{12}^{3} \tag{1}$$

Where $G_{12}^{0}, \sigma_{12}, \gamma_{12}$ is the initial shear modulus, shear stress, and shear strain, respectively, and α is the material nonlinear constant, which can be measured by experiments. In order to facilitate the iterative calculation of the finite element program, formula (1) can be transformed into:

$$\sigma_{12}^{(i+1)} = G_{12}\gamma_{12}^{(i+1)} = \left(1-d\right)G_{12}^{o}\gamma^{(i+1)} \tag{2}$$

where *i* is the incremental step and *d* is the damage parameter, which can be expressed as

$$d = \frac{3\alpha G_{12}^{o}\left(\sigma_{12}^{(i)}\right)^{2} - 2\alpha\left(\sigma_{12}^{(i)}\right)^{3}\left(\gamma_{12}^{(i+1)}\right)^{-1}}{1+3\alpha G_{12}^{o}\left(\sigma_{12}^{(i)}\right)^{2}} \tag{3}$$

At the beginning of the model analysis, the damage parameter *d* is 0 and the shear modulus G_{12} is equal to G_{12}^{0}. The shear modulus G_{12} with the damage parameter *d* decreases linearly with loading.

2.3.3 Failure criterion. In order to better judge the various damage modes in the damage process, this paper

uses a nonlinear factor developed on the basis of the Hashin three-dimensional failure criterion[5] and the Yamada-Sun fiber matrix compressive shear failure criterion[6]. The failure judgment criterion is used to judge the various damages of composite laminates during the load-bearing process.

Matrix tensile failure（$\sigma_{22}+\sigma_{33}\geq 0$）

$$e_m^2=\left(\frac{\sigma_{22}+\sigma_{33}}{Y_T}\right)^2+\left(\frac{\sigma_{13}}{S_{XZ}}\right)^2+\left(\frac{\sigma_{12}}{S_{XY}}\right)^2+\frac{\sigma_{23}^2-\sigma_{22}\sigma_{33}}{S_{YZ}^2}\geq 1 \tag{3}$$

Matrix compression failure（$\sigma_{22}+\sigma_{33}\leq 0$）

$$e_m^2=\left[\left(\frac{Y_C}{2S_{XY}}\right)^2-1\right]\bullet\frac{\sigma_{22}+\sigma_{33}}{Y_C}+\left(\frac{\sigma_{22}+\sigma_{33}}{2S_{XY}}\right)^2+\left(\frac{\sigma_{12}}{S_{XY}}\right)^2+\left(\frac{\sigma_{13}}{S_{XZ}}\right)^2+\frac{\sigma_{23}^2-\sigma_{22}\sigma_{33}}{S_{YZ}^2}\geq 1 \tag{4}$$

Fiber tensile failure（$\sigma_{11}\geq 0$）

$$e_f^2=\left(\frac{\sigma_{11}}{X_T}\right)^2+\left(\frac{\sigma_{12}}{S_{XY}}\right)^2+\left(\frac{\sigma_{13}}{S_{XZ}}\right)^2\geq 1 \tag{5}$$

Fiber-matrix compression shear failure（$\sigma_{11}\leq 0$）

$$e_f^2=\left(\frac{\sigma_{11}}{X_C}\right)^2+\left(\frac{\sigma_{12}}{S_{XY}}\right)^2+\left(\frac{\sigma_{13}}{S_{XZ}}\right)^2\geq 1 \tag{6}$$

Table 2. Stiffness reduction methods of composite

Failure mode	Properties degradation rules
Matrix tensile failure $S_{22}\geq 0$	$E_2^d=0.2E_2$, $G_{12}^d=G_{13}^d=0.2G_{12}$
Matrix compression failure $S_{22}<0$	$E_2^d=0.4E_2$, $G_{12}^d=G_{13}^d=0.4G_{12}$
Fiber tensile failure $S_{11}\geq 0$	$E_1^d=0.07E_1$
Fiber compression failure $S_{11}<0$	$E_1^d=0.14E_1$

In order to study the delamination failure between the composite girders and the skin, this paper adopts the cohesive zone model (CZM) to predict the delamination initiation and expansion of the interface between the girders and the skin. The constitutive relation of the interface element adopts a bilinear linear elastic-linear degradation model, and the interface has two characteristics of linear loading and linear degradation during the delamination process under the action of a single type of load.

Under complex loads, the initial displacement and maximum interface stress of delamination damage can be calculated by Quads criterion of secondary failure. The interfacial tensile strength and shear strength distributions in the model are taken as 37.5MPa and 39.4MPa. When this criterion is satisfied, the interface is damaged and the performance is gradually degraded. The degradation rule is based on nonlinear softening controlled by B-K energy. In the BK criterion, the critical energy release rates of pure tensile delamination,

longitudinal shear delamination and transverse shear delamination are 0.419J/mm, 2J/mm, and 2J/mm, respectively.

2.4. Results of calculation

According to the finite element analysis results, the displacement, stress/strain and bolt load distribution of the truss end structure are firstly analyzed, and the design load of the finite element model analysis is given according to the design allowable value of the composite material, and then according to the structural The allowable value is used to check the fixture strength to obtain the structural strength margin to verify whether the test design requirements are met.

When the truss end structure is subjected to compressive load, it is usually necessary to calculate the buckling mode and buckling load of the structure first, so as to simulate the actual situation more accurately. When the compressive load is greater than the buckling load, the first-order buckling deformation occurs in the structure, resulting in structural failure. According to the buckling eigenvalues, the corresponding buckling load is 1797.5kN. Figures 2 show the E11 and E12 strain contours of the truss structure and the butt area respectively. When the compressive strain of the structural unit reaches the allowable strain of 3300με, the support reaction force at the loading point is the design load when the butt-jointed structure is compressed. When the compressive strain is 3300με, the compressive load is 815kN, which is less than the first-order buckling load of the structure, which is 1797.5kN; when the E12 strain is 6000με, the compressive load is 1232kN, which is also less than the first-order buckling load of the structure, which is 1797.5kN. The failure is later than the structural buckling invalid. When loaded to 969kN, the interface element layer has delamination failure at the butt end face of the girders, as shown in Figure 3. Considering the compressive buckling, compressive strain and debonding of the truss-skin interface at the same time, the compressive design load of the butted structure can be taken as 815kN.

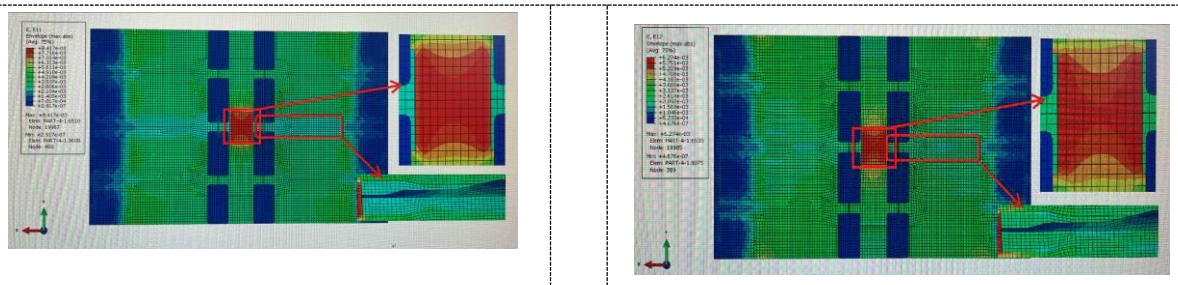

(a) E11 (b) E12

Figure 2. Strain contour of the model.

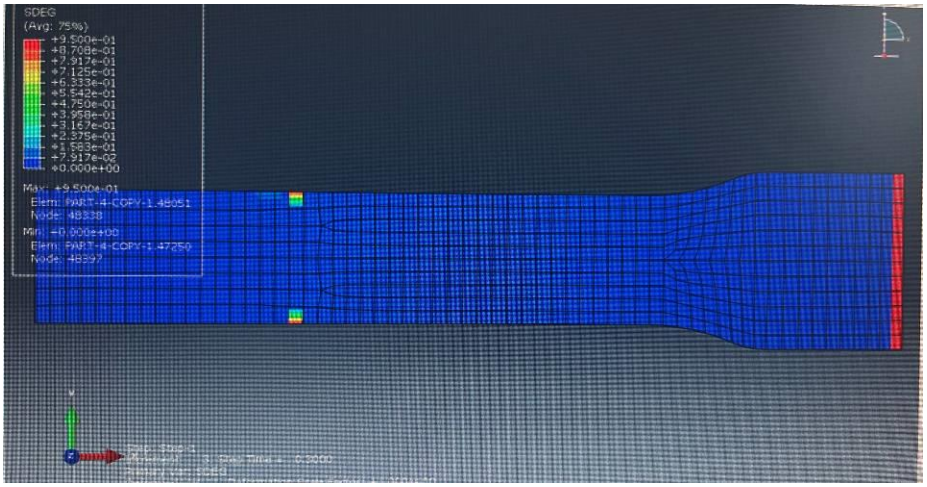

Figure 3. The initiation of delamination damage in the interface element.

2.5. Structural failure mode

According to the tensile test of the end structure of the D-shaped girders, when the load is up to 1330kN, the strain data in the physical test and the finite element results of the virtual test are compared, as shown in Table 3 below (the strain number diagram is shown in Figure 4). The error of the strain values of the first column of strain numbers 101, 110, 201, and 210 at the loading far end is all within 5%, indicating that the test loading load value and the strain feedback value are relatively consistent. The overall skin surface strain error value is small, while the long girder surface strain error is large, and the closer to the end connection area of the long girder, the greater the strain error value, this is because the fasteners close to the end connection area are densely distributed, and the holes The edge stress concentration causes a large strain error near the fastener. On the whole, the experimental strain values are in good agreement with the virtual analysis results.

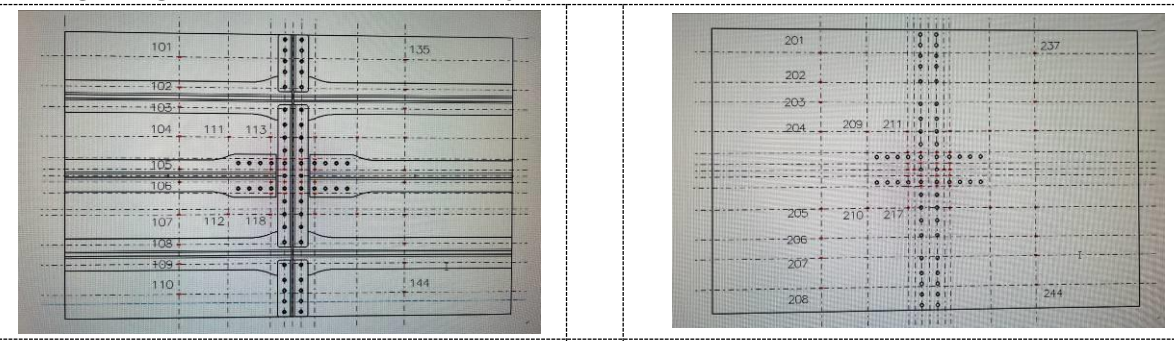

(a) Strain number for girder face

(b) Strain number of the skin surface

Figure 4. Graph of strain numbers.

Table 3. Comparison of experimental strain values and model analysis strain values

Strain number	Test value /$\mu\varepsilon$	Simulation value /$\mu\varepsilon$,	Error / %	Strain number	Test value /$\mu\varepsilon$	Simulation value /$\mu\varepsilon$,	Error / %
101	1905	1829	4	201	1974	1889	4.3
102	1666	1608	3.5	202	1820	1762	3.2
103	1676	1614	3.7	203	1786	1731	3.1

104	1745	1679	3.8	204	1731	1677	3.1
105	1385	1364	1.5				
106	1385	1345	2.9				
107	1785	1715	3.9	205	1790	1756	1.9
108	1785	1705	4.5	206	1869	1804	3.5
109	1735	1662	4.2	207	1931	1850	4.2
110	1978	1927	2.6	208	2107	2010	4.6

3. Conclusion

In this paper, the finite element analysis and strength prediction of composite stringer docking structure are carried out. According to the structural characteristics, loading and clamping methods, the model simplification principle is determined, and the finite element model of the wing truss joint structure is established. Through the progressive damage analysis, the stress and strain of the structure and the failure of the interface layer are obtained. Through experimental comparison, it is found that the strain analysis results of the model constructed in this paper are consistent with the experimental values, and the error is less than 5%, which can be used for the analysis of this type of structure.

References

[1]

[2] [1] Aviation research institute of China 2004 *Handbook of Composite Structure Design* (Beijing: Aviation industry)

[3] [2] Xie M J 2011 *Composite material connection* (Shanghai: Shanghai jiao tong university)

[4] [3] Sun HT, Qing X, Chang F-K. The response of composite joints with bolt-clamping loads, part II: model verification. J Composite Material 2002; 36(1): 69-91.

[5] [4] Binnur Goren Kiral. Effect of the clearance and interference fit on failure of the pin-loaded composites. Materials and Design 2010; 31: 85-93.

[6] [5] Hashin Z, Rotem A. A fatigue failure criterion for fiber reinforced materials. J Compos Mater 1973; 7: 448-464.

[7] [6] Yamada SE, Sun CT. Analysis of laminate strength and its distribution. J. Compos. Mater. 1978; 12: 275-284.

Study on Engineering algorithm Verification of Compression-Shear buckling of Composite T-stiffened panels

Chen Limin Zhuo Yi Xu Rongzhang Wang Houbin

China aircraft strength Research institute Xi'an 710065

Abstract：

A numerical approach was established to predict the buckling load of the composite panel stiffened by T-type stringers under compression and shear load. Analytic approaches were initially calibrated by experimental date to enable accurate predictions for the shear and compressive buckling load respectively. The buckling interaction equation was then employed to determine the buckling load for different shear-compression ratios, enabling envelopes for designers to rapidly estimate the buckling threshold for the T-stiffener panels under combined loading scenarios.

Key words: Composite T-stiffened panels, Engineering algorithm, buckling load, compression and shear load

ClC number V24.8 Document code A

Introduction

Stiffened panel structure is widely used in aircraft structure because of its good anti-instability ability and high material utilization rate. the common forms of ribs are T-type, I-shaped, L-shaped, hat-shaped, and the cross-section size of hat-shaped reinforcement is large. both sides are connected with the skin to form a closed section, which has high compression stability and can withstand high compression load.The newly developed airliners Boeing B787 and Airbus A350 adopt this structure in many parts of the fuselage.Among them, the T-type stiffened panel is an open section, which has good deformation coordination, and T-shaped reinforcement is used in many parts of the wing panel.

At present, the finite element analysis method[1-7] is mainly used to analyze the buckling and post-buckling of composite stiffened panels, and the analysis techniques include cumulative damage method. There are five kinds of methods, such as continuous damage method[8-10], VCCT, Cohesive method [11-16], extended finite element method. These methods can calculate the buckling load, buckling deformation and failure load, failure mode and so on. However, there is a high requirement for the model grid, and some methods (such as the bonding element method) also need a particularly dense grid, so that the amount of calculation of the model is very large and the operation time is very long. In addition, if the implicit algorithm is used, it is also necessary to overcome the convergence problem of calculation, usually the model will be terminated because the result is not convergent after damage. Such a costly finite element calculation method is limited in the application of structural design, designers urgently need a simple and fast engineering calculation method.

The engineering calculation method of composite stiffened panels is a simple calculation formula, curve and empirical correction coefficient summarized according to the test data, which can quickly evaluate the stability and bearing capacity of stiffened laminates[21]. The support of the composite T-shaped stiffened flange to the skin is elastic support, which belongs to simple support. How to select the plate element width of the skin in buckling calculation needs further study. In this paper, the calculated results of several buckling load algorithms of composite stiffened panels are compared with the experimental results, and a method for calculating the buckling load of

composite T-shaped stiffened panels is obtained, which is more close to the experimental results and can be used as a reference for structural design. the compression-shear buckling failure envelope of composite T-stiffened panels is formed, which can be used as a tool for structural designers to quickly evaluate the strength.

1 buckling engineering algorithm

The composite stiffened panel structure is composed of skin and long truss. before the stability calculation, the stiffened panel is divided into a series of plate elements, and then the buckling stability of the plate element is calculated separately, and the buckling of the skin is estimated according to the rectangular laminated plate.

1.1 buckling of skin under axial compression.

Method 1: for rectangular laminated plates, formula (1) can be used to calculate buckling loads under four simply supported boundary conditions.

$$N_{xcr}=\frac{\pi^2 D_{22}}{b^2}[\frac{D_{11}}{D_{22}}(\frac{b}{a})^2 m^2+2(\frac{D_{12}+2D_{66}}{D_{22}})+(\frac{a}{b})^2\frac{1}{m^2}] \quad (1)$$

In the formula:

N_{xcr} is the axial buckling load per unit length, a is the length of the plate element, b is the width of the plate element, and m is the buckling half wave number along the axial direction of the plate. In the calculation, m can be taken as an integer greater than or equal to 1, and the corresponding set of Nx is calculated, in which the smallest N_x is the buckling load N_{xcr} of the plate.

Method 2: when the ratio of the plate is ≥ 4, the buckling load of the plate can be calculated according to the following formula (2):

$$N_{xcr}=\frac{2\pi^2 D_{22}}{b^2}[\sqrt{\frac{D_{11}}{D_{22}}}+(\frac{D_{12}+2D_{66}}{D_{22}})] \quad (2)$$

Method 3: for rectangular laminated plates simply supported on four sides, the axial buckling load can also be calculated according to formula (3) below.

$$N_{xcr}=\frac{\pi^2\sqrt{D_{11}D_{22}}}{b^2}[K-2(1-\frac{D_{12}+2D_{66}}{\sqrt{D_{11}D_{22}}})]$$
$$\lambda=(a/b)(D_{22}/D_{11})^{1/4} \quad (3)$$
$$m=1,2,3,\ldots$$
$$K=(\frac{m^2}{\lambda^2}+\frac{\lambda^2}{m^2}+2)$$

In the formula: K can be queried in fig 2-3 of reference [17].

Method 4: the local buckling of reinforced laminated plate skin can also be calculated by a simplified fast calculation method, which can be used in preliminary design. For long laminates with symmetrical layers of only 0 °, 90 °and ±45 °, the buckling load can be calculated quickly according to the proportion of lamination.

$$\sigma_{xcr}=6.9k_{L0}(t/b)^2 \quad (4)$$

In the formula: It is the average axial compression buckling stress, the axial compression buckling coefficient, t is the thickness of laminate skin and b is the width of laminate skin. The buckling coefficient can be obtained from fig. 3-5 and fig. 3-6 of reference [17].

1.2 Local buckling of stiffened trusses.

When the stiffened plates are subjected to shear and transverse compression, the stringers are generally not subjected to force, so it is only necessary to check the local buckling of stringers under axial compression. the flange is generally treated as a long plate with one long edge free and the other simply supported, and the axial compression local buckling load of the flange can be calculated according to formula (5).

Generally speaking, the web of thin-walled truss can be treated as a long plate with two long edges simply supported, and the local buckling load is calculated according to formula (2).

$$N_{xcr}=\frac{12D66}{b^2}+\frac{\pi^2 D11}{L^2} \quad (5)$$

In the formula:

N_{xcr} is Axial buckling load per unit width, b is flange width. L is the length of the truss. D11, D66-bending stiffness coefficient of laminated plates.

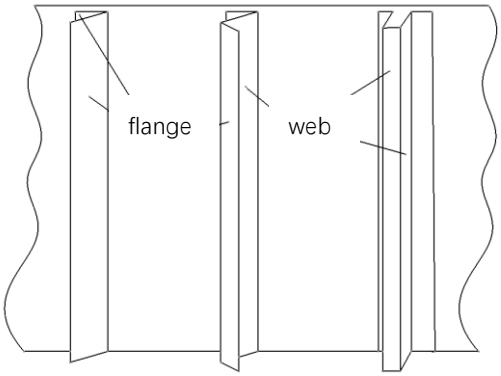

Fig.1 The flange and web

1.3 skin shear buckling algorithm

Compared with Ritz and energy variational method, the engineering calculation method of predictive shear buckling is simple and easy to understand, and it is a more preferred formula for engineers in model analysis and precalculation.

Method 1: in the case of simple support and fixed support, the calculation formula of shear buckling load is formula (6), in which the shear buckling coefficient Ks is different in the case of simple support and fixed support, which can be obtained according to the dimensionless parameters.

$$
\begin{aligned}
&N_{xycr} = K_s \frac{\pi^2 \sqrt[4]{D11 D_{22}^3}}{b^2} \\
&K_s = 3.32 + 2.17/\alpha - 0.163/\alpha^2 + \\
&\beta^2 (1.54 + 2.36/\alpha + 0.1/\alpha^2) \qquad (6) \\
&\alpha = \sqrt{D_{11} D_{22}} / D_3 \\
&\beta = (b/a) \sqrt[4]{D_{11}/D_{22}} \\
&D_3 = D_{12} + 2D_{66}
\end{aligned}
$$

1.4 Compression-shearbuckling correlation equation.

The symmetrically laminated composite plates can be simplified to orthotropic plates, which can be calculated by the buckling correlation equation (7) of orthotropic plates. When the compression-shear ration is given, the compression load and shear load of buckling under a specific compression-shear ratio can be calculated.

The buckling criteria under combined compression and shear loads are as follows:

$$R_x + R_{xy}^2 = 1 \qquad (7)$$

In the formula: $R_x = N_x / N_{xcr}$, $R_{xy} = N_{xy} / N_{xycr}$, N_{xcr}, N_{xycr} are buckling loads under uniaxial compression and pure shear, respectively.

From the compression load and shear load under the specific compression-shear ratio, the axial load and shear load are calculated from the formula (8).

$$
\begin{aligned}
&F_x = (\mathrm{N_x}/\mathrm{t}/\mathrm{E_{11}}) \times \sum_{i=1}^{n} E_i A_i \\
&F_{xy} = \mathrm{N_{xy}} \times w \qquad (8) \\
&EA_{11} = \sum_{i=1}^{n} E_i A_i
\end{aligned}
$$

In the formula: Nx is the compression load corresponding to buckling under compression-shear load, t is the thickness of the skin, E11 is the axial modulus of the skin, E_iA_i is the axial stiffness of each plate element of the stiffened panel, and w is the shear width of the specimen.

2 Compression-shear stability test

2.1 specimen

The T-shaped stiffened panel is composed of skin, 7 stringers, 4 frames and filling end. the specimen is long 2412mm, wide 1420mm and frame distance is 700mm. The cross section is shown in Fig.2.

The thickness of the skin is 4.5mm, with a total of 31 layers, which is made up of 2 layers of 0.22mm fabric and 29 layers of 0.14mm unidirectional belt. The thickness of flange is 3.16mm, with a total of 22 layers, which is made up of 1 layer of 0.22 mm fabric and 21 layers of 0.14 mm unidirectional tape. The material properties of the unidirectional belt are shown in Table 1 and the layers are shown in Table 2. The engineering constants of laminates are shown in Table 3.

The thickness of the web is twice that of the flange, and it is naturally formed by the flanging of the bottom edge on both sides, with a total of 44 layers.

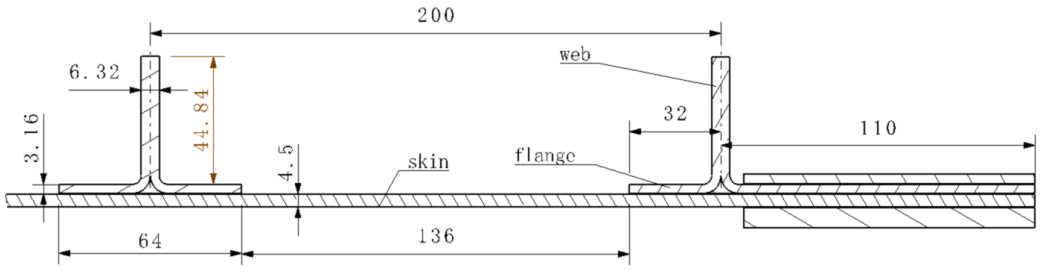

Fig.2 T-shaped specimen

Table 1 Lamina material properties parameters of T-stiffened panel

	E_{11}/GPa	E_{22}/ GPa	v_{12}	G_{12}/ GPa
unidirectional tape	147	9.23	0.33	4.4
fabric	62.5	62.5	0.047	4

Table 2 Stacking sequence of T-stiffened panel

Region	Stacking sequence
Skin	$[\pm 45/0/0/45/90/-45/0/0/45/0/-45/90/45/0/-45/0]_s$
Flange	[±45/0/-45/0/0/45/90/-45/0/0/0/45/0/0/45/0 /0/0/-45/90/45/0]

The engineering constants required for calculating local buckling of stiffened plates are shown in Table 3 ~ Table 5.

Table 3 tension stiffness of Skin and stiffener（N•mm）

Region	A_{11}	A_{12}	A_{22}	A_{16}	A_{26}	A_{66}
Skin	366811	81220	192026	0	0	87097
Stiffener	607422	96151	219010	9710	9710	104455

Table 4 Bending stiffness of Skin and stiffener（N•mm）

Region	D_{11}	D_{12}	D_{22}	D_{16}	D_{26}	D_{66}
Skin	609991	135371	295294	14464	14464	144935
Stiffener	1880000	361000	702000	-30769	-30769	388000

Table 5 Equivalent engineering parameter of Skin and stiffener

Region	E_x(GPa)	E_y(GPa)	G_{xy}(GPa)	V_{xy}
Skin	73.9	38.7	19.4	0.423
Stiffener	89.4	32.2	16.5	0.439

2.2 buckling test under compression-shear load

The test is carried out on the compression-shear composite load panel test device designed and developed by China aircraft strength Research Institute. the test device is divided into compression loading module and shear loading assembly, which can apply compression and shear load independently, and any proportion of compression and shear combined load can be applied in coordination.

A total of 3 specimens were tested, and the compression-shear composite load tests were carried out with a compression-shear ratio of 2.6. In order to obtain the strain distribution and buckling load of the test specimen, strain gauges are arranged at the intercostal skin and Stringers, shown in Fig.3. The strain flower number inside the skin starts with 1, the external number of the skin corresponding to its position begins with 2, and the web is arranged with a unidirectional strain gauge back-to-back, with strain number 501-528. Only part of the strain is shown in figure 3. In the actual test, the strain is generally arranged on three sections for each frame-distance in order to monitor the buckling time and strain distribution.

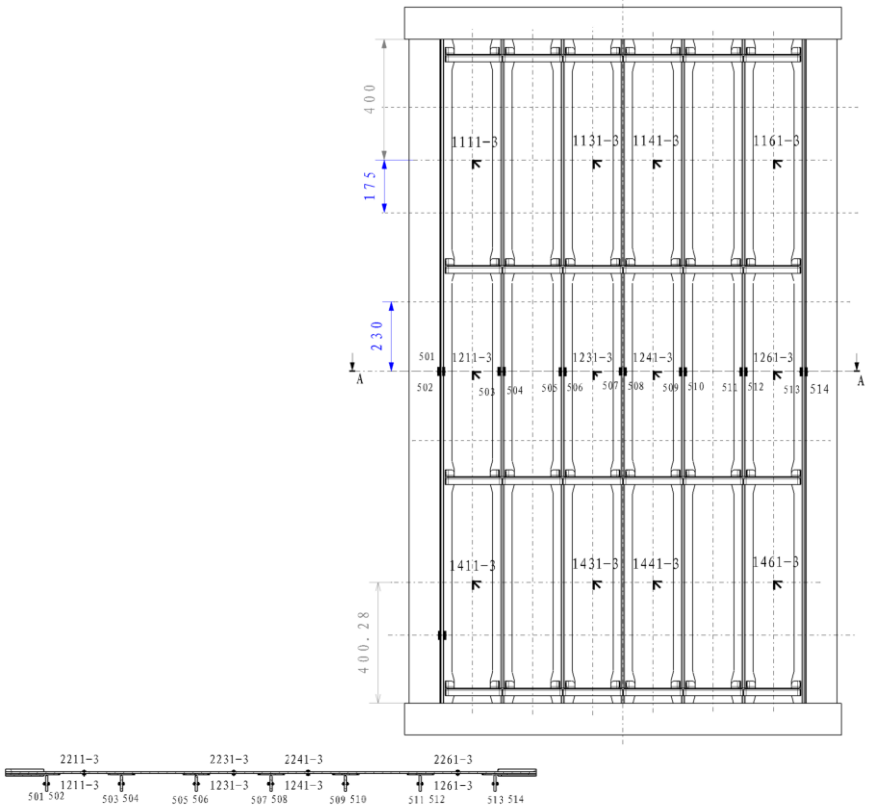

Fig.3 Arrangement of strain gage

For the support and loading mode of the specimen, see Fig.4. The specimen is simply supported on three sides and fixed at the lower end. the fixture can constraint frame out-of-plane deformation and release the degree of freedom needed for the deformation of the specimen to ensure that the buckling occurs in the effective examination area.

The upper end of the specimen is compressed by the ball hinge compression platform, and the uniformly distributed shear load is applied on both sides of the specimen. The base load of compression is 1567.2 kN(F_x), The base load of shear is 312.695 kN(F_{xy}). Load to 100% with a step size of 5% of the base load, and then continue loading to failure with a step size of 1% of the base load.

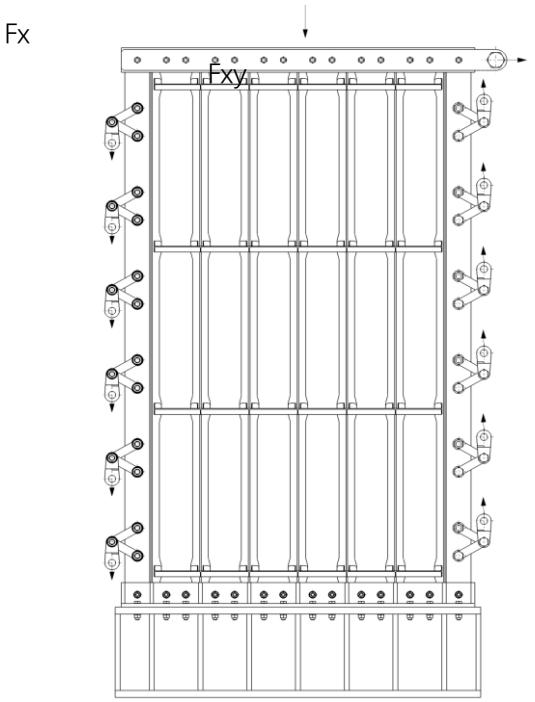

Fig.4 Support and load application of specimen

2.3 Test results

There are two ways to determine the buckling time by using the strain measured by the electric method. First, the load-strain curve is drawn one by one according to the cross section or longitudinal section, and the local initial buckling load of the skin and the web is determined by the bifurcation (or inflection point) of the strain gauge measurement curve arranged back-to-back in the corresponding section (Fig.5), and the buckling time is determined by the percentage of back-to-back strain bending of the skin exceeding a given value (10% recommended) (see formula 8). The stiffened panel skin buckles locally at all three frame-distances, and the load is redistributed after buckling, so the strain slope of the web will change at the same time after the skin buckling.

The results of compression-shear buckling test are shown in Table 6.

$$\frac{\varepsilon_1-\varepsilon_2}{\varepsilon_1+\varepsilon_2}\times 100\% \qquad (8)$$

Table 6 result under compression and shear

No	Buckling load %	Compression load kN	Shear load kN
T-1	124%	1975	394
T-2	128%	2006	400
T-3	124%	1943	388
Average load		1975	394

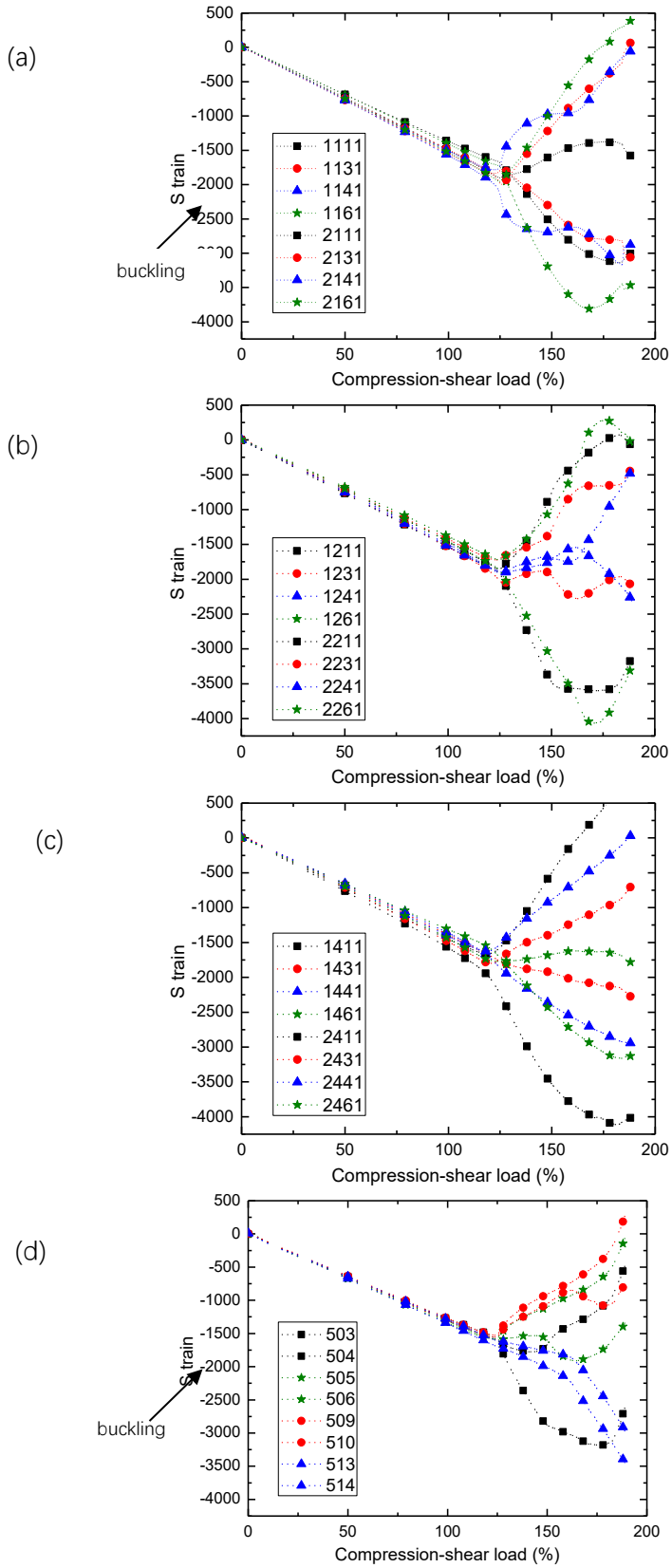

Fig.5 Load-strain curve

3 evaluate engineering algorithms

The stringer elements of T-shaped stiffened panels include flanges and webs. when analyzing the local buckling of T-shaped stiffened panels, the buckling of the skin, flange and web of stringers are analyzed respectively. T-shaped stringer is an open section, and its supporting condition can be simply supported.

In the calculation of compression buckling, there are usually three possible ways to choose the skin width (see figure 6). b1 corresponds to the net width of the skin between the bars, b3 corresponds to the root spacing of the horizontal web, b2 = (b1+b3) / 2.

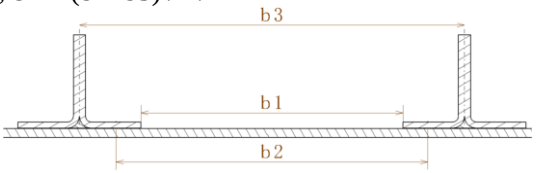

Fig.6 the values of b

The frame of the specimen is a "floating frame". There is no connection between the frame and the net width area of the skin, and the frame is only connected with the skin at the low edge of the flange. The value of b need to be verified.

When ‘a’ is 700mm, the compression buckling calculation method 1, method 2, method 3 and method 4 are used to form the buckling curve, while ‘a’ is 2400mm, the compression buckling calculation method 1 is used to form the buckling curve, as shown in Fig.7.

When the values of compression buckling method 1, method 2 and method 3 are the same, the compression buckling load is basically the same. Compared with the results obtained by the three methods, compression buckling method 4 is slightly lower, conservative and safe in structural design, but at the same time, the buckling strength potential of the structure is not fully utilized.

In the compression test of stiffened panels, the compressive buckling load is 865 N/mm. When ‘a’ is 700mm, the b value close to the test result is queried on the curve of Fig.7, When ‘b’ is 139mm, and the buckling load consistent with the test value can be obtained. the buckling calculation results are shown in Table 7. That is to say, the value of b is b1, which is close to the experimental value. The buckling calculation results are close to the experimental results, that is, while the ‘a’ is 2400mm, the value of b is 161mm between b1 and b2.

Table.7 the compression buckling load of engineering algorithm

No.	a /mm	b /mm	Compression N/mm
Method 1	700	139	870
Method 2	700	139	868
Method 3	700	139	870
Method 4	700	139	813
Method 1	2400	139	1203
Method 1	2400	161	870
Test			865

Through the comparison between the compression buckling engineering algorithms and the test results, it is concluded that in the compression buckling analysis algorithm of T-shaped stiffened panels, the boundary condition is simply supported, and the value b should be the net width of the skin . Although the frame is a floating frame, the value of ‘a’ should be the frame distance, not the length of the specimen. The results of calculating the compressive buckling load by using method 1, method 2 and method 3 are consistent.

The compression buckling estimation of the stiffened truss is carried out by using the compression buckling formula (5). The buckling of the stringer should be 4165uε, while the buckling strain of the skin is 2610 uε. The buckling of the stringer is later than the buckling time of the skin, which meets the requirement that the buckling of stringer should not be earlier than that of skin in the design of stiffened panel structure.

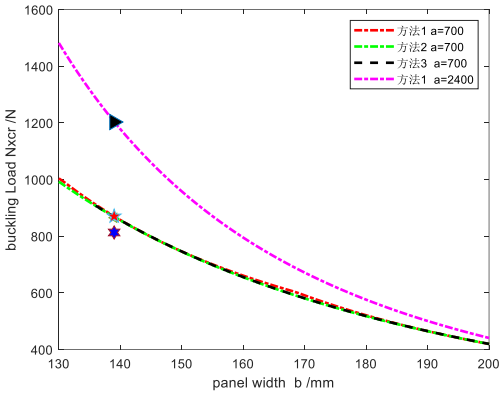

Fig.7 $N_{xcr}-b$ curves

Parameters 'a' and 'b' are taken from the values of compression engineering algorithm, and formula (6) is used to estimate the buckling load under shear load. The correlation equation (9) is used to estimate the buckling under the combined load of compression and shear. in view of the consistency of the calculation results of the compression buckling engineering algorithm 1, method 2 and method 3, it is only necessary to choose one of the methods to estimate the buckling under the combined compression-shear load.

$$\frac{Nx}{Nxcr}+\left(\frac{Nxy}{Nxycr}\right)^2=1 \qquad (9)$$

Nx/Nxy is 2.6, Nxcr is -870N/mm, Nxycr is 916 N/mm。

The total axial load and the shear load at the end of the specimen can be obtained by using the formula (8). The shear width is shown in Fig. 4, W=1318mm. However, the comparison between the estimated shear results of the two long edge of the specimen and the test results is shown in Table 8. The error is less than 3%, so the parameters of the compression buckling and shear buckling engineering algorithm are selected appropriately, on this basis, the compression-shear buckling load is solved according to different compression to shear ratio (see Table 9), thus the buckling envelope under compression-shear load is formed, as shown in Fig.8.

Table 8 result of combined load under compression and shear

	Fx /kN	*Fxy* /kN
Calculation Fxy	1913	393
Test Fxy	1959	391
Error /%	2.35%	0.5%

Table 9 the buckling load under combined load

Buckling load	Ratio						
	2.6:1	2:1	1:1	1:2	3:1	1:4	8:1
Nx	780	730	552	352	795	200	856
Nxy	300	365	552	706	265	803	107

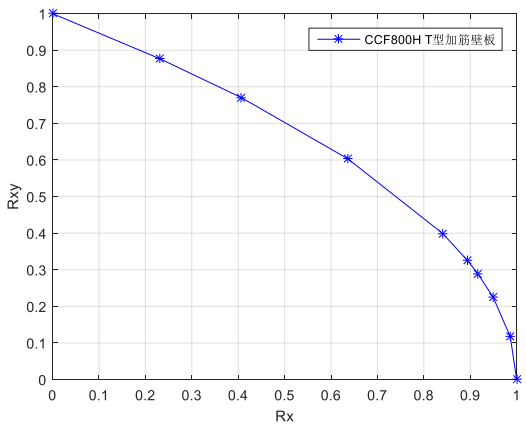

Fig.8 curve of R*x*-R*xy*

4. Conclusion

Through the buckling load analysis and experimental study of composite T-stiffened panels, the following conclusions can be drawn.The main results are as follows:

(1) the method for calculating the axial compression buckling load of composite T-stiffened panels (method 1, method 2, method 3) is a more simple and effective method, and the calculated results are in good agreement with the experimental results. it can well predict the initial buckling load of composite T-stiffened panels, and the predicted buckling error of method 4 is slightly larger than that of the former three methods. For shear buckling analysis, the prediction error of shear buckling analysis method 1 is the smallest.

(2) for the buckling analysis of T-shaped stiffened panels belonging to the open section, 'a' should be selected as the frame distance, and the buckling load can be accurately predicted (including the floating frame type), and the supporting condition is simply supported.

(3) the compression-shear buckling load is estimated by different compression-shear ratio, and the compression-shear failure buckling envelope of T-type specific material and typical geometric size is formed, which provides a quick tool for querying the buckling analysis under arbitrary compression-shear ratio in the design stage.

Reference

[1]. Basu S, Waas A M, Ambur D R. Prediction of progressive failure in multidirectional composite laminated panels [J]. Int J Solids Struct, 2007, 44(9): 2648-2676.

[2] Tang Jianmao. A review of aerospace materials [J].Spacecraft Environment Engineering, 2013, 30（4）: 352-359（in Chinese）.

[3] Maimi P, Camanho P P, Mayugo J A, Davila C G. A continuum damage model for composite laminates: Part I-constitutive model [J]. Mech Mater 2007, 39(10): 897-908.

[4] Orifici A C, de Zarate Alberdi I O， Thomson RS, Bayandor J. Compression and Post-Buckling Damage Growth and Collapse Analysis of Flat Composite Stiffened Panels [J]. Composites Science and Technology, 2008, 68: 3150–3160.

[5] Ambur D R, Jaunky N, Davila C G, Hilburger M W. Progressive failure studies of composite panels with and without cutouts, NASA/CR-2001-211223 [R], Washington: NASA, 2001.

[6] Chaiara Bisagni, Riccardo Vescovini, Dávila C G. Single-stringer compression specimen for the assessment of damage tolerance of post buckled structures [J]. Journal of Aircraft, 2011, 48(2): 495-502.

[7] Turon A, Camanho P P, Costa J, Davila C G. A damage model for the simulation of delamination in advanced composites under variable-mode loading [J]. Mech Mater, 2006, 38: 1072–1089.

[8] Chaiara Bisagni, Dávila, C G. Experimental investigation of the postbuckling response and collapse of a single-stringer specimen [J]. Composite Structures, 2014, 108: 493-503.

[9] Reinoso J, Blazquez A, Paris F, Canas J, Melendez J C. Postbuckling behaviour of a pressurized stiffened composite panel-part I: experimental study [J]. Composite structures, 2012, 94: 1533-1543.

[10] Abramovich H, Weller T, Bisagni C. Buckling Behavior of Composite Laminated Stiffened Panels Under Combined Shear–Axial Compression[J]. Journal of Aircraft, 2008, 45(2): 402-412.

[11] Bisagni C, Cordisco P. An Experimental Investigation into the Buckling and Post-Buckling of CFRP Shells Under Combined Axial and Torsion Loading[J], Composite Structures, 2003, 60(4): 391–402.

[12] Bisagni C, Cordisco P. Post-Buckling and Collapse Experiments of Stiffened Composite Cylindrical Shells Subjected to Axial Loading and Torque[J], Composite Structures, 2006, 73: 138–149.

[13] Zhu S H, Yan J Y, Wang Y Q, et al. Buckling and Postbuckling Experiments of Integrally Stiffened Panel Under Compression–Shear Loads[J]. Journal of Aircraft, 2015, 52(2): 680-691.

[14] Julien Bertolini, Bruno Castanie, Jean-Jacques Barrau, Jean-Philippe Navarro. Multi-level experimental and numerical analysis of composite stiffener debonding. Part 1: Non-specific specimen level [J]. Composite Structures, 2009, 90: 381-391.

[15] Benzeggah M L, Kenane M. Measurement of mixed-mode delamination fracture toughness of unidirectional glass/epoxy composites with mixed mode bending apparatus [J]. Compos Sci Technol, 1996, 56: 439–449.

[16] Krueger R, Cvitkovitch M K, O'Brien T K, Minguet P J. Testing and analysis of composite skin/stringer debonding under multi-axial loading [J]. J Compos Mater, 2000, 34:1263–1300.

[17] Institute of Aeronautics China. Stability handbook of composites structure design [M]. Beijing: Aviation Industry Press,2002（in Chinese）.

[18] Cui DeGang. Structural stability design manual [M].Beijing: Aviation Industrial Press,1996： 137-165 (In Chinese).

Study on nail load distribution ratio of composite - metal lap joints

*Yi Zhuo * , Baocai Pang , Zishi Shen , Lei Li*

Aircraft Strength Research Institute of China

Abstract: Multi-nail connections are a common connection method for aircraft composite structures to metal structures. These connection details are the weak points of aircraft structures and figuring out the load transfer ratio of each fastener is the key to structural strength calibration and weight reduction. The load distribution ratio of each row of nails is calculated using an empirical formula based on test strain data for the single shear structure with multi-row nail connection of composite thick plate and metal strip plate, and the results are compared with those obtained using an engineering calculation method. The findings demonstrate that the empirical formula, which is based on strain data, can calculate the load distribution ratio of multiple rows of nails. The empirical formula is easy to use and accurate enough to be used for preliminary strength analyses of composite material-metal lap joints in aircraft structures.

Key words: Aircraft structure, composite material, lap joint, nail load distribution, strain data

Because of their superior qualities, including high specific strength, particular stiffness, and designability, advanced composite materials are frequently employed in the design of aviation and aerospace structures and have established themselves as a key component of aircraft structures [1]. The design of the joint structure has become essential to the design of composite structures because of issues like anisotropy of composite materials and their multi-modal forms of defects or damage, which have a significant impact on the overall performance of composite structures. In addition, 70% of the structural damage areas of flight equipment occur in the joint section[2]. Mechanical connections are a popular connection method in composite constructions due to their benefits, including great durability and the transfer of heavier weights[3]. However, compared to metallic parts, the anisotropy of composite materials causes more complex stress distribution at the hole margins and significant inhomogeneities in nail load distribution. The effectiveness of composite multi-nail connection systems is decreased by the inhomogeneity of the nail load distribution. Therefore, by analyzing the load distribution issue of many nail joint structures, precisely anticipating the amount of each nail

load, and then optimizing joint design, it becomes one of the major ways to increase the effectiveness of joint structures[4,5].

Analytical, experimental, and numerical simulation methods are the three main approaches used to examine the load distribution of composite multi-nail joints, with the experimental approach serving as the foundation for the other two approaches[6]. A lot of study has been done by academics in order to precisely measure the nail load distribution of composite multi-nail joints. Hart-Smith, Lawlor, and others conducted numerous experiments on composite connections as early as the 1940s, when composite materials were used in aircraft structures, to examine the effects of connection geometry parameters, tightening torque, nail hole clearance, and other factors on nail load distribution, quasi-static strength, and fatigue life[7,8]. To ascertain the impact of particular stiffness on nail load distribution, Chinese researchers Xie Mingjiu, Chi Jian, and colleagues conducted a significant number of tests and presented a substantial amount of test data, graphs, and curves[9,10]. Along with conducting numerous pertinent experimental experiments, Zhao Yingmei et al. also examined the load distribution of multi-nail connections when combined with finite element models[11-14].

In this study, a composite-metal single lap joint was used to explore the nail load distribution ratio of the joint. First, a test was conducted to determine the strain variation law of four rows of four nail lap single shear joints with the applied load. The load distribution ratio for each row of nails was then determined using the strain data using empirical formulas and engineering calculation techniques. By comparing the computational analysis's findings, it was found that the empirical formula's conclusions were essentially identical to those of the engineering calculation approach and could be applied to the prediction of nail load distribution in composite-metal lap joints.

1、Test

The multi-nail single lap test piece of composite laminate and titanium alloy plate was selected to carry out the test. The composite material is a high modulus carbon fiber reinforced resin base laminate with a layup sequence of [45/0/-45/90/0/0/45/0/-45/0/-45/0]s. The strip plate is made of TC4 titanium alloy. The connecting fasteners choose high lock bolts and matching nuts with a diameter of 18mm. The size, structural form and strain measuring position of the test piece are shown in figure 1.

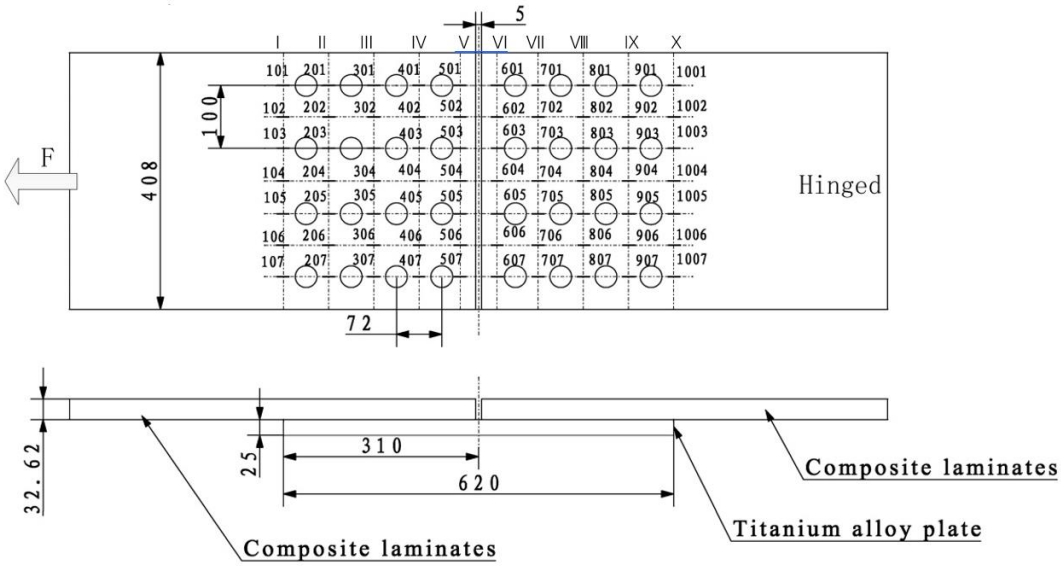

Figure 1 Structural form of the test piece

The test load is loaded by hydraulic actuator in a force-controlled manner step by step, and the variation of strain with load at each measurement point is recorded. Finally, the test piece was stretched to destruction. The strain measurement instrument ST-24 developed by China Aircraft Strength Research Institute was used for strain acquisition.

2. Test results

The specimen's tensile failure load is 3145.5 kN, the first row of the composite laminate's nail section on the loading side is where it fails, which shows the tensile failure of the laminate caused by nail hole extrusion. Figure 2 depicts the load-strain curve of the test strain measurement location.

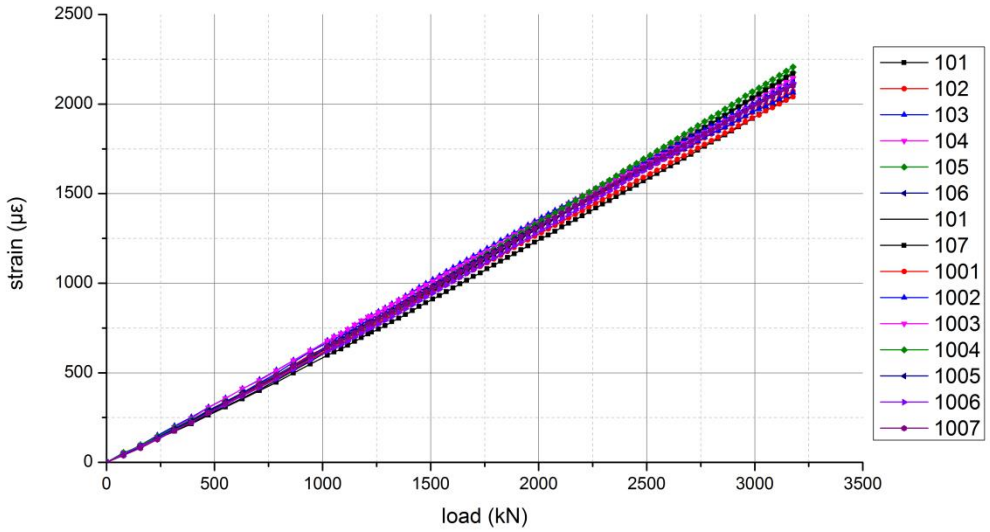

a) Section I and Section X strain gauge load-strain curves

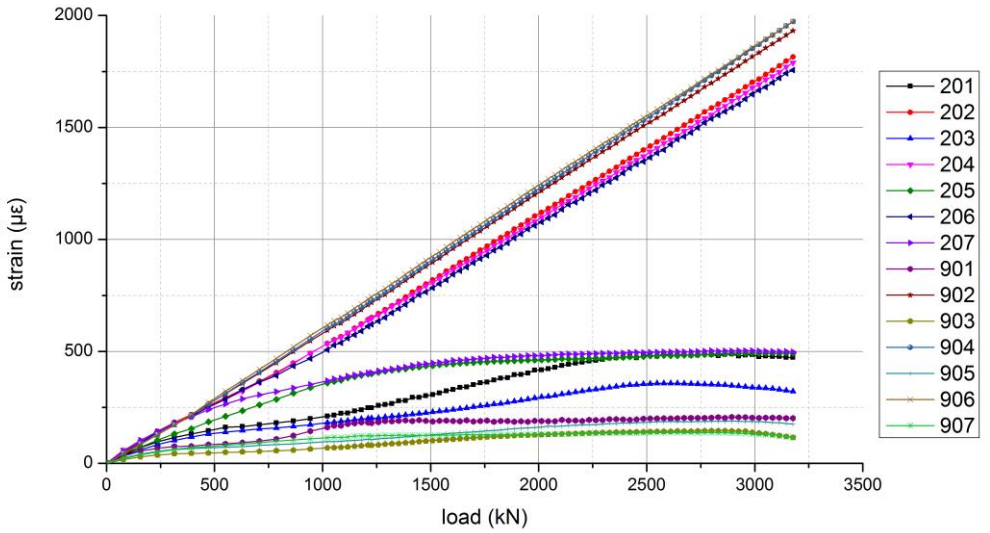

b) Section II and Section IX strain gauge load-strain curves

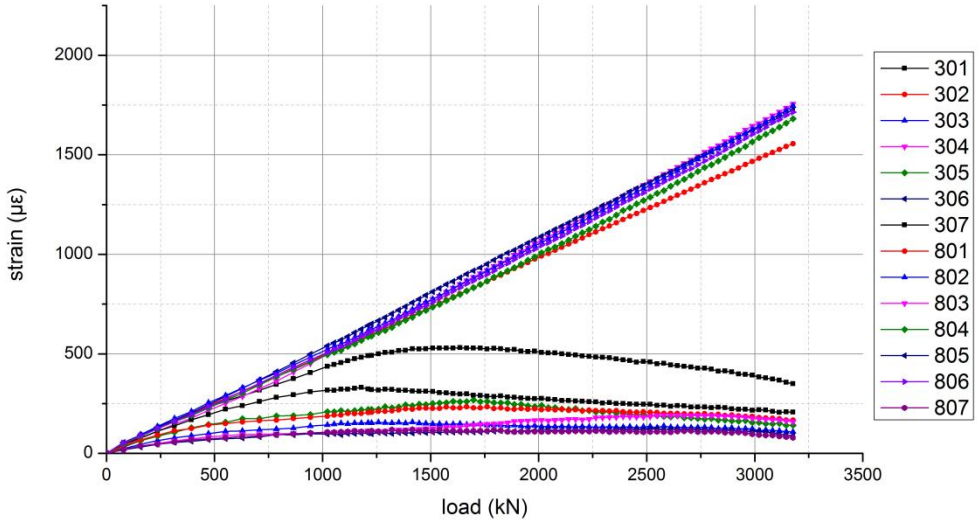

c) Section III and Section VIII strain gauge load-strain curves

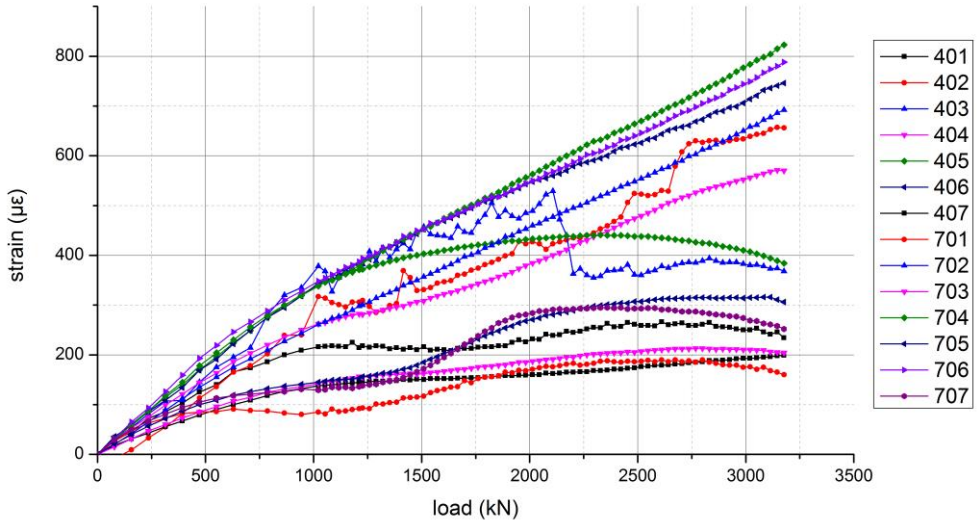

d) Section IV and Section VII strain gauge load-strain curves

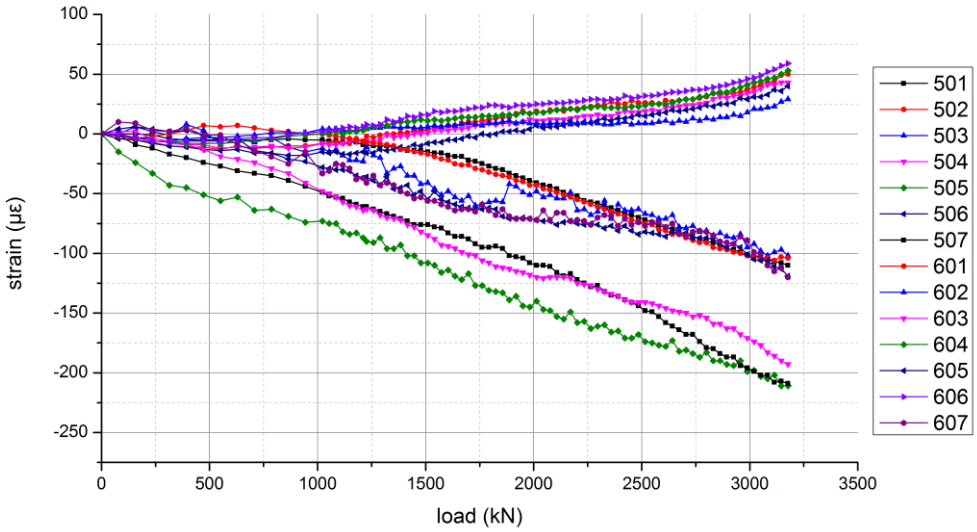

e) Section V and Section VI strain gauge load-strain curves

Figure. 3 load-strain curve of composite laminate at measuring point

The following conclusions can be reached by examining the data and the load-strain curve:

1) The strain grows linearly with an increase in load at the section I and section X measuring locations until the specimen fails.

2) The composite laminate is exposed to extrusion load at the nail, bypass tensile load between the two nails, and strain zigzag distribution on the same section in the cross sections II section IV and section VII section IX. All strain gauges in sections V and VI are negative, which is primarily due to edge effect.

3) The strain curves of the 10 cross sections of the test piece show that the strains in the first row of nail attachments at the loading and support ends are the largest, with the maximum strain values recorded in channel 202 reaching 1815 με and channel 904 reaching 1745 με . The failure of the composite-metal lap joint occurs close to the first row of nails at the loading end or the constraint end because the strain values measured by the strain gauges near the first / last row of nails are higher than those near the other nails. At the connection's end, the test laminate cracks during failure, followed by a tensile failure brought on by nail hole extrusion.

3、 Empirical calculation method of nail load distribution ratio

Figure 4 depicts the composite laminate's static analysis. The friction force(f_i) between the composite laminate and the titanium alloy strip plate and the bolt connection extrusion load(F_{u-i}) balance the overall load(F) applied by the hydraulic actuator.

The load borne by the composite laminate is transferred to the titanium alloy strip plate through the bolts, and the load borne by the composite laminate will be reduced with each bolt, and the reduced load is transferred backward through the bypass load and friction, where the bypass load is transferred to the bolts behind, and the bolt force and friction are transferred to the titanium alloy plate. Since the friction force is small in proportion to the load transferred by the bolt, it can be neglected [15].

With each bolt, the load carried by the composite laminate is transferred to the titanium alloy strip plate, and as a result, the load is reduced. The reduced load is then transmitted backward through friction and bypass load, where the bypass load is transferred to the bolts behind them and the bolt force and friction are transferred to the titanium alloy plate. Since the friction force is negligible in comparison to the load that the bolt transfers, it can be disregarded[15].

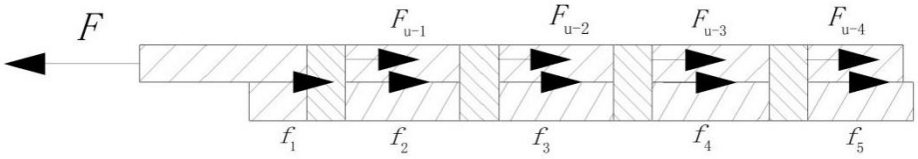

Figure 4 Load balance schematic

The strain on the composite laminate reflects the magnitude of the load at the measurement point, and the load transmitted by each bolt can be calculated indirectly through the strain, as shown in equation (1).

$$\begin{cases} R_I = (SF_I \times t_I) / (SF_{IV} \times t_{IV}) \\ R_{II} = (SF_{II} \times t_{II} - SF_I \times t_I) / (SF_{IV} \times t_{IV}) \\ R_{III} = (SF_{III} \times t_{III} - SF_{II} \times t_{II}) / (SF_{IV} \times t_{IV}) \\ R_{IV} = (SF_{IV} \times t_{IV} - SF_{III} \times t_{III}) / (SF_{IV} \times t_{IV}) \end{cases} \quad (1)$$

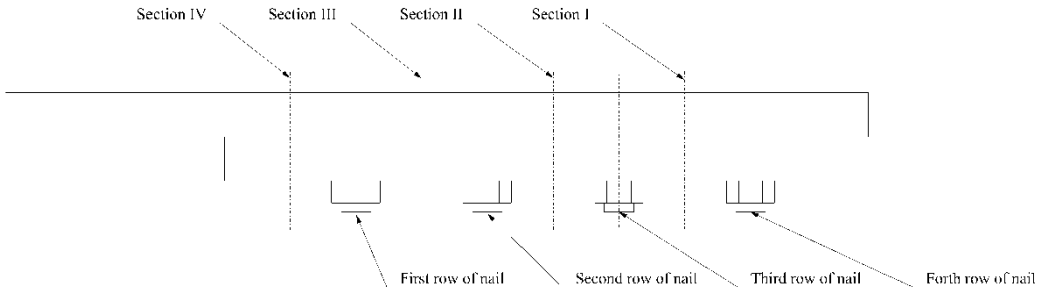

Figure 5 Schematic diagram of test piece section location

In the equation, $R_I \sim R_{IV}$ are the proportion of nail load for each section, $SF_I \sim SF_{IV}$ are the average strain of each section respectively. $t_I \sim t_{IV}$ are the thickness of the test piece for

each section of the test piece, respectively.

4. Engineering calculation of the first row of nail load [16]

According to the calculation formula and chart in 《Durability and damage tolerance design manual for the civil aircraft structures-fatigue design and analysis》, the load share of the first row of nails can be queried according to the flexibility coefficient of the plate.

For the structure shown, the flexibility calculation formula with plate, substrate and nail is

$$F_s = \frac{S}{W_s t_s E_s} \tag{5}$$

$$F_p = \frac{S}{W_p t_p E_p} \tag{6}$$

$$C = \frac{K_{dc}}{t_s E_p}(14.7 - 0.8D)\left(\frac{t_s}{t_p}\right)^{0.456} \tag{7}$$

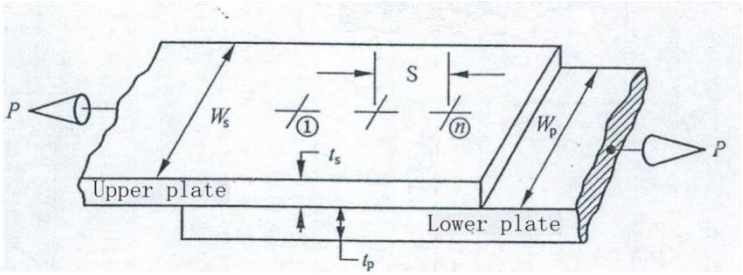

Figure 6 Schematic diagram of single shear loaded structure form

F_s ——upper plate flexibility coefficient;

F_p ——lower plate flexibility coefficient;

F_e ——bolt flexibility coefficient;

S——fastener spacing (load direction);

W——width;

E_s / E_p ——elastic modulus of the plate;

t_s ——thickness of the upper plate;

t_p ——the thickness of the lower plate;

D——bolt diameter;

K_{dc} ——fastener material correction factor, steel bolts are taken as 0.67;

After calculating the F_s and F_p, query in Figure 7 to get the load distribution ratio of the first row of nails

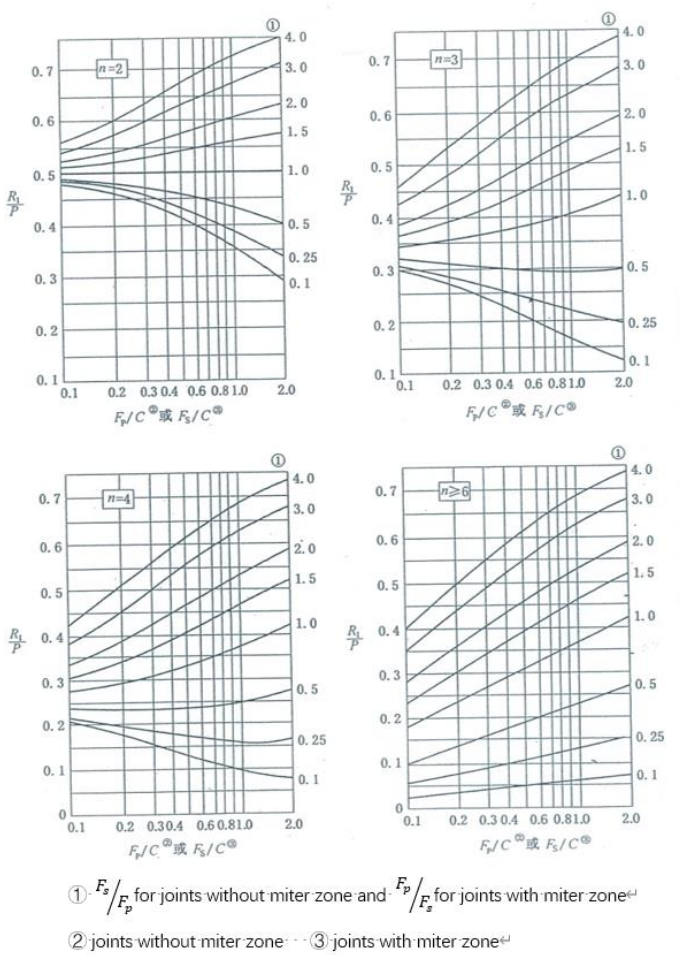

Figure 7 Single shear connector dangerous end fastener load R

5. Calculation results

According to equation (1), the nail load distribution at the loading end of the test piece can be calculated, as shown in Table 1 and Table 2. comparing the data in Table 1 and Table 2, it can be seen that the load proportion of the first row of nails increases to a certain extent as the load increases.

Table 1 nail load distribution ratio (F=1572.8kN)

Position	The row number of pin			
	First	Second	Third	Forth
Load site	0.44	0.19	0.04	0.28
Supporting site	0.52	0.14	0.06	0.28

Table 2 nail load distribution ratio (F=3177.0kN)

Position	The row number of pin			
	First	Second	Third	Forth
Load site	0.52	0.18	0.09	0.22
Supporting site	0.56	0.16	0.06	0.22

Using the engineering method, S=72mm, t_s=32. 62mm, t_p=25mm, E_s=85GPa, E_p=110Pa, W=104mm, D=18mm, according to the curve extrapolation in Figure 7, we can calculate

R_1=0. 45 .

Comparing the results of the empirical formula and the engineering method, the proportion of nail load calculated by the empirical formula is greater than that of the engineering calculation.

6. Conclusion

Composite laminate and titanium alloy plate were tested. The following results were reached after measuring the surface strain distribution of the composite laminate during the tensile process on 4 rows of nail lap test pieces and computing the load distribution for each nail.

1) The load-bearing ratio of each nail in a four-row nail connection changes slightly during stretching, with the load ratio of the first row of nails continuously increasing;

2) During the stretching process, the load-bearing ratio of each nail in a four-row nail connection varies somewhat, and the load ratio of the first row of nails steadily rises;

3) The empirical calculation approach, which depends on the logic of the strain gauge arrangement, can quickly calculate the load ratio of each row of nails. The calculation results can be used to track the test piece's structural integrity as it is being put through its paces.

References

[1]Shen Fan.Study of Composite on pinnerd-joint strength[D].Wu han of technology,2011.
[2] Xie Ming-jiu.Composite con nect ion manual[M] . Beijin g: Nat ional Defense Indus t ry Press, 1994. (in C hinese)
[3] Li Shun-lin．Composite material manual work［M］． Beijing:National Defense Industry Press， 1988 (in Chinese)
[4] Yin Yu, Li Xiaoqiang, Li Dongsheng,et al.Research Development on Mechanical Connection of Composite Laminate. Aeronautical Manufacturing Technology.2016.11:72-77
[5]Zhang Ming-xing.Load Distribution and Finite Element Calulation of T800 Carbon Fiber Hyper Joints Composite Laminates. Fiber Reinforced Plastics/Composites.2011(5):62-66.
[6]LV Guang-quan, GUO Xin, ZHANG Ji-kui,Study on pin load distribution of composite laminate single-lap joint with multi bolts. Hi-Tech Fiber & Application.2012,38(1):53-56.
[7] Hart-Smith L J. et al. Optimized bolted joint: US Patent, 4579475[P]. 1986–04–01.
[8] Lawlor, V. P., McCarthy, M. A., Stanley, W. F.. Anexperimental study of bolt–hole clearance effects in double-lap, multi-bolt composite joints [J]. CompositeStructures, 2005, 71(2): 176-190.
[9] Song En-peng，Liu Wenting，Xie Mingjiu.et al.Investigation of the Influence of Jointed Member Stiffness on Fastener Load Distribution for Composite Multiple - bolted Joint.Aircraft Design.2005,25(4):29-32
[10] Chi Jian Xie Mingjiu．Reserch on Multiple-bolted Composite Joint by Finite Element Analysis[J]．Acta Aeronautica et Astronautica Sinica.1998,19(4):499—502
[11]Zhao Mei-ying, Yang Lin g, Wan Xiaopeng. Load distribution in composit emulti fastener joints[J].Computer s& Srructures,1996, 6(2):331-342.
[12]Peng Pai，Zhao Meiying，Jiang Hongxing.Research on the Auto-modeling and Analytic Method of Load Distribution for Multi-bolt Joints in Composite Structures. Mechanical Science and Technology for Aerospace Engineering.2015,34(6):974-977
[13]Huang He yuan，Zhao Mei ying，Wan Xiaopeng，et al.osite Bolted Joints Non-Linear Stiffness Model and its Application. Journal of Northwestern Polytechnical University. 2018,36(1):66-73.

[14]Li Bo,Zhao Mei ying,Wan Xiao Peng.Research on the Secondary Bending of Composite-metal Adhesively Bonded Jionts.Advances in Aeronautical Science and Engineering.2013,4(2):170-174
[15]Liu Xingke, Li Yazhi, Liu Xiangdong,Study on Load Distribution of Multiple bolted Metal to Composite Joints.Advances in Aeronautical Science and Engineering.2011,2(2):193-198
[16]Zheng Xiaoling. Durability and damage tolerance design manual for the civil aircraft structures-fatigue design and analysis［M］. Beijing: Aviation Industry Press. 2003: 335(In Chinese) .

Prediction of the delamination of CFRPs in Mode I tests based on TPA-GRU model

Xiaoying Cheng[1, 2], Jinghua Ying[1], Zhenyu Wu[1, 2]

1 College of Mechanical Engineering, Zhejiang Sci-Tech University, Hangzhou, 310018, China.

2 Zhejiang Provincial Innovation Center of Advanced Textile Technology, Shaoxing, 312000, China.

Abstract: One of the most important tasks for acoustic emission (AE) method in non-destructive testing is to evaluate the damage status of carbon fiber composites and predict the remind service life of the key composite components. A prediction model based on temporal pattern attention mechanism is developed by combining feature evaluation algorithm with deep learning method in this work. First, the AE signal generated before the first delamination was selected to calculate the residual interlayer performance. Fifteen traditional time-domain features and nine cumulative features of AE signals were extracted. And second, the RReliefF algorithm was used to evaluate the features and the features insensitive to degradation were filtered. It is found that the cumulative features contain more information. Additionally, we compared the prediction results of the proposed temporal pattern attention (TPA) - gated recurrent unit (GRU) model and long short term memory, GRU, GRU-Attention. The results showed that the TPA mechanism focusing on feature information performed best.

Key words: Composite material, Mode I test, Acoustic emission, residual interlayer performance, TPA-GRU

1.Introduction

Carbon fiber reinforced polymer (CFRP) composites are widely taking over the traditional materials in various fields due to the high specific modulus and strength[1]. The common damage of CFRP composites is divided into interlaminar and intralaminar damage types. The occurrence and expansion of interlaminar damage will lead to the decrease of structural stiffness and strength, and even cause catastrophic accidents. Therefore, the issue of delamination has attracted considerable attention from professionals in the fields of composite structure design and strength analysis.. It is particularly important to predict the performance of the residual materials as early as possible.

Recent developments in the field of Acoustic Emission (AE) have led to a great interest in applying AE data stream in structural health monitoring (SHM) and the prognostication of future conditions. Philippidis et. al. obtained the nonlinear relationship between the residual strength of the material and the count through the tensile fatigue test of the unidirectional laminates of glass fiber/epoxy resin composites [2]. Caprino et. al. found that there is a good empirical correlation between the residual strength of glass fiber composites after four-point bending pre-fatigue test and the total AE count detected under the maximum stress applied

during the pre-fatigue cycle [3]. Compared with regression analysis, deep learning is better at capturing effective information in time series, which makes it widely used in the field of prediction. Wu et al. proposed to use long short term memory (LSTM) neural network to obtain good remaining useful life prediction accuracy under complex operation, working conditions, model degradation and strong noise, and make full use of long-term and short-term memory capabilities [4]. However, the research on the performance prediction of composite materials based on deep learning combined with AE is very limited.

In this work, a prediction model of the delamination is established by the AE signal obtained in the mode I experiment. The RReliefF [5] feature selection algorithm is used to evaluate the damage quantitative characterization ability of traditional AE features and cumulative features. Then, a gated recurrent unit network of temporal pattern attention mechanism is established. The accuracy of the proposed model is also compared with other existing models to verifying its performance.

2.Materials and experiments

The samples in the experiment were composed of 8 layers of plain carbon fiber (12K). The resin matrix was a mixture of Epolam 2040 epoxy resin and 2042 curing agent in a weight ratio of 100:32. The samples were prepared according to ASTM D5528 (2013) [6] standard, as shown in Fig.1. The initial crack was 80 mm long, initiated by inserting a layer of polyimide film in the middle of samples. The sample size was 185 × 2 × 4 mm^3. In order to transmit the load, two hinges were pasted at a distance of 50 mm from the crack tip. DCB tests were performed on a tensile test machine with a 500N load cell. At a loading rate of 5mm/min, the data acquisition system simultaneously recorded load-displacement data, and an AE sensor (NANO30, PAC) was attached above the sample at a distance of 85mm from the crack tip.

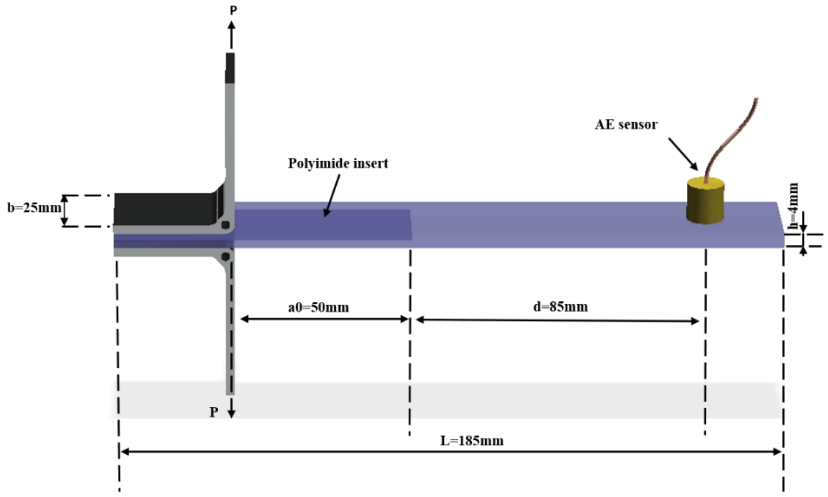

Fig. 18.The geometry and dimension of the test sample

3.Method

3.1 Data preparation

With the continuous damage inside the sample, a large number of generated AE signals indicate the degree of degradation. The goal is to estimate the residual interlayer properties of the sample based on the existing AE signals. Only AE signals recorded before the maximum load is reached are remained (Fig.2). The residual interlaminar performance from the first delamination is defined as follows:

$$y_i = \left(\max_{1\le i\le N}(F_i) - (F_i)\right) / \max_{1\le i\le N}(F_i) \quad (1)$$

where N is all the AE signals before the maximum load is reached, and F_i represents the load corresponding to the i-th AE signal.

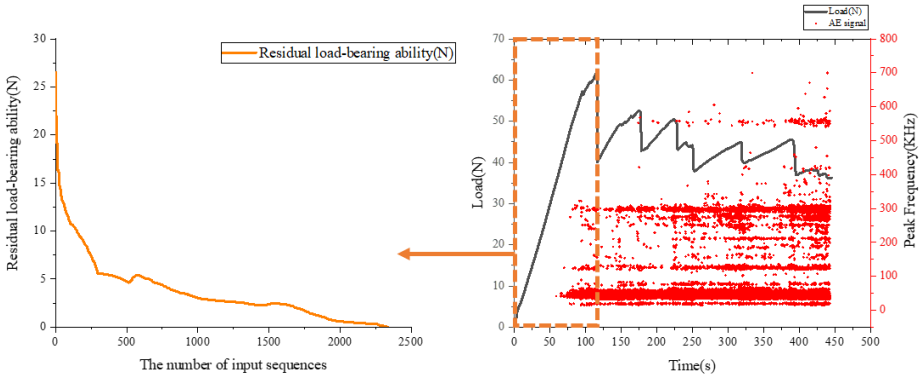

Fig. 19.The residual interlaminar performance calculated from DCB test.

3.2 Feature selection

RReliefF is an algorithm that uses contextual information to weigh the quality of features. Features are evaluated according to different values of neighbors with the same response value and neighbors with different response values. The probability of different predicted values of two instances is used to approximately evaluate the quality of features. The algorithm is as follows:

(1) The final estimation of the a-th AE feature is expressed as $w^{(a)}$, the weight of the different response values of the residual interlayer strength is w_{dy}, the weight under different AE features is $w_{df}^{(a)}$, and the weight under different responses and different AE features is $w_{dy\&df}^{(a)}$, all initialized to 0.

(2) Randomly select an AE event sample x_r and find its k nearest neighbor samples $x_{r_n}, n=1,2,...,k$, and then update the weight for each nearest neighbor x_{r_n}, each AE feature and each AE event. The calculation process is as follows:

$$\begin{cases} W_{dy} = \sum_{r=1}^{N}\sum_{r_n=1}^{k}\Delta_y\left(x_r, x_{r_n}\right)\cdot d\left(x_r, x_{r_n}\right) \\ W_{df}^{(a)} = \sum_{r=1}^{N}\sum_{r_n=1}^{k}\Delta_{f^{(a)}}\left(x_r, x_{r_n}\right)\cdot d\left(x_r, x_{r_n}\right) \\ W_{dy\&df}^{(a)} = \sum_{r=1}^{N}\sum_{r_n=1}^{k}\Delta_y\left(x_r, x_{r_n}\right)\cdot\Delta_{f^{(a)}}\left(x_r, x_{r_n}\right)\cdot d\left(x_r, x_{r_n}\right) \end{cases} \quad (2)$$

where N represents the total number of AE events, which $\Delta_y\left(x_r, x_{r_n}\right)$ is the difference between the response values of x_r and x_{r_n}, $d\left(x_r, x_{r_n}\right)$ is the normalized distance between x_r and x_{r_n}, and $\Delta_{f^{(a)}}\left(x_r, x_{r_n}\right)$ is the difference of the a-th feature between x_r and x_{r_n}. The specific calculation method is as follows :

$$\begin{cases} \Delta_y\left(x_r, x_{r_n}\right) = \left|y_r - y_{r_n}\right| / \left(\max_{1\le i\le N}(y_i) - \min_{1\le i\le N}(y_i)\right) \\ d\left(x_r, x_{r_n}\right) = e^{-\left(rank(r,r_n)/\sigma\right)^2} / \sum_{1\le r_i\le k} e^{-\left(rank(r,r_i)/\sigma\right)^2} \\ \Delta_{f^{(a)}}\left(x_r, x_{r_n}\right) = \left|x_{r,a} - x_{r_n,a}\right| / \left(max\left(f^{(a)}\right) - min\left(f^{(a)}\right)\right) \end{cases} \quad (3)$$

where $rank\left(r, r_n\right)$ is the position of x_{r_n} in the k nearest neighbors, sorted by the distance to x_r, and σ is user-defined control distance influence factor.

(3) Calculate the final weight estimate of the a-th feature:

$$W^{(a)} = W^{(a)}_{dy\&df} / W_{dy} - \left(W^{(a)}_{df} - W^{(a)}_{dy\&df}\right) / \left(N - W_{dy}\right) \quad (4)$$

3.3 Gated recurrent unit

Gated recurrent unit (GRU) has a simpler structure and comparable performance to LSTM. It consists of two gates: update gate and reset gate. The structure is shown in Fig. 3.

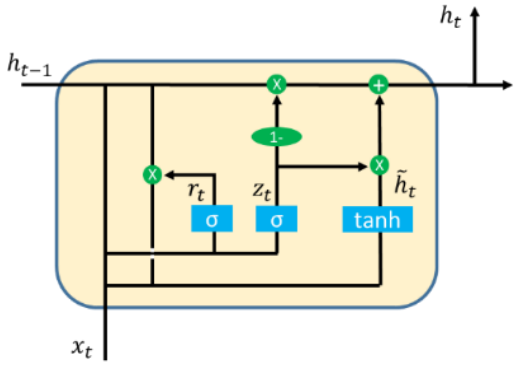

Fig. 20.The typical structure of GRU cell

where $x_t \in R^n$ is the input information of the current moment t, r_t and z_t represent the values calculated by the reset gate and the update gate respectively. h_{t-1} is the hidden state of the previous moment as the input of the next moment. The hidden state at the current moment is h_t, $\tilde{h}_t$ represents the combination of the information of the current moment and the hidden state of the previous moment. The specific calculation process is as follows:

$$z_t = \sigma\left(W_z \cdot \left[h_{t-1}, x_t\right]\right) \quad (5)$$

$$r_t = \sigma\left(W_r \cdot \left[h_{t-1}, x_t\right]\right) \quad (6)$$

$$\tilde{h}_t = \tanh\left(W_h \cdot \left[r_t * h_{t-1}, x_t\right]\right) \quad (7)$$

$$h_t = \left(1 - z_t\right) * h_{t-1} + \tilde{h}_t * z_t \quad (8)$$

where W_z, W_r, W_h is the weight matrix, σ and $\tanh$ represents the activation function.

3.4 Temporal pattern attention - gated recurrent unit

The temporal pattern attention (TPA) mechanism [7] utilizes the convolutional neural network (CNN) filter to extract the fixed-length temporal pattern in the input information, determines the weight of each temporal pattern via scoring function, and obtains the final output information according to the weight size. Compared with the typical attention module that focuses on time steps, the TPA module focuses on variables. The schematic diagram of the TPA attention mechanism is shown in Fig. 4:

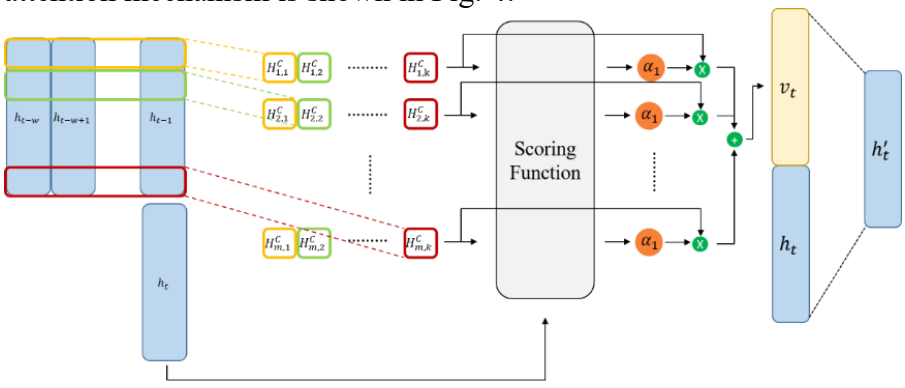

Fig. 21.The process of TPA

where h_i is the hidden layer output (column vector) of each time step, w represents the

length of the sliding window, i.e., the length of the time series, and $H=\{h_{t-w},h_{t-w+1},\ldots,h_{t-1}\}$ is the hidden layer output matrix. The row vector represents the state of a single variable at all time steps, and the column vector represents the state of a single time step.

The CNN filter is used to enhance the learning ability of the model, and the time pattern matrix H^C of the variable in the range of the convolution kernel is extracted:

$$H_{i,j}^C=\sum_{l=1}^{w}H_{i,(t-w-1+l)}\otimes C_{j,T-w+l} \quad (9)$$

where $H_{i,j}^C$ represents the eigenvalues extracted by the i-th row vector and the j-th convolution kernel, and T represents the maximum weight length of the convolution kernel extraction, usually $T=w$. The correlation between each variable is calculated by the scoring function:

$$f\left(H_i^C,h_t\right)=\left(H_i^C\right)^{\acute{u}}W_a h_t \quad (10)$$

where H_i^C is the i-th row vector of H^C, the attention weight α_i is obtained by normalizing the sigmoid activation function:

$$\alpha_i=sigmoid\left(f\left(H_i^C,h_t\right)\right) \quad (11)$$

Then, the row vectors of H^C are weighted and summed to obtain the context vector α_i:

$$v_t=\sum_{i=1}^{m}\alpha_i H_i^C \quad (12)$$

where m is the number of features. Finally, the final prediction results $y_{t-1+\Delta}$ are integrated according to equations (13) and (14):

$$h_t^{'}=W_h h_t+W_v v_t \quad (13)$$

$$y_{t-1+\Delta}=W_{h'}h_t^{'} \quad (14)$$

where W_h、W_v、$W_{h'}$ are parameter weight matrix.

3.5 Training configuration

First, the hidden state is obtained through the GRU layer, which contains two hidden layers. The number of GRU cell of each layer is 64, and then a convolutional layer is used to obtain the time mode of different time steps. The number of CNN filters is 25 and the filter size is 50. The activation function is Relu. The maximum epoch is 100. The learning rate is 0.01 and the Adam optimization algorithm is used. The training is carried out by sliding window. It is assumed that m features are obtained by feature selection, and there are n time series. The i-th sequence can be expressed as $x_i=\{a_1,a_2,a_3,\mathrm{K},a_m\}$, the length of the sliding window is t, and the step size is set to 1, then a window sequence $n-t+1$ is generated. Each input is a matrix of $t\times m$, and the output is the residual interlayer performance at the moment of $t+1$.

4.Results and discussion

In this work, 15 traditional AE features are extracted, which are Rise Time (RT), Duration Time (DT), Average Frequency (AvF), Count (C), Energy (E), Amplitude (A), Root Mean Square (RMS), Average Signal Level (ASL), Absolute Energy (AbE), Initial Frequency (IF), Center Frequency (CF), Signal Strength (SS), Peak Frequency (PF), Decay Angle (DA) and Rise Angle (RA). However, the traditional features will not change monotonously with the degradation of the composite material properties. It is difficult to predict the residual bearing capacity of the sample through this non-cumulative feature. Therefore, 9 additional interpretable cumulative features are used to qualitatively describe the degradation process of

composite materials. They are Cumulative Rise Time (CRT), Cumulative Signal Strength (CSS), Cumulative Energy (CE), Cumulative Duration (CD), Cumulative Absolute Energy (CAbE), Cumulative Average Signal Level (CASL), Cumulative Root Mean Square (CRMS), Cumulative counts (CC) and Cumulative Hit (CH). CE, CAbE, CC, CH and CSS have proved to be effective in presenting the damage evolution process of composite materials. The 24 AE features are evaluated by the RReliefF algorithm, and the features with higher weight values are used as the input of the prediction model.

The weights of the 24 AE features obtained by the RReliefF algorithm are shown in Fig. 5. The weights of most cumulative features are higher than non-cumulative features. Consistent with the above speculation, the cumulative features contain more information on the performance degradation of composite materials than non-cumulative features. Here, we selected eight cumulative AE features with relatively higher weights, i.e., CRT, CC, CE, CD, CASL, CSS, CAbE, and CH, to predict the delamination under the mode I test.

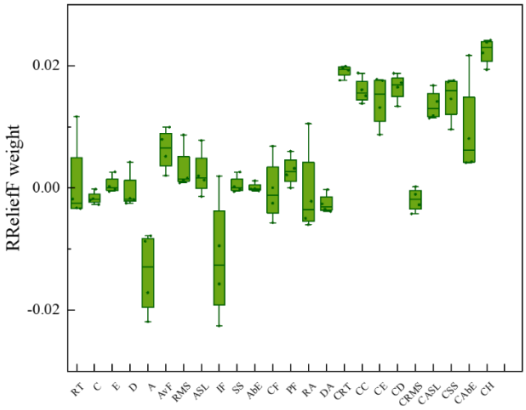

Fig. 22.The weights of 24 features evaluated using the RReliefF algorithm

The Root Mean Square Error (RMSE)[8] is used as the scoring metric of the prediction performance:

$$RMSE = \sqrt{\frac{1}{N}\sum_{i=1}^{N}\left(\hat{y}_i - y_i\right)^2} \qquad (15)$$

where $\hat{y}_i$ and y_i represents the predicted value and actual value of the residual interlayer performance.

In order to further prove the superior performance of the GRU model based on the TPA mechanism for the prediction of mode I delamination, the result is also compared with LSTM, GRU, and GRU model based on traditional attention mechanism (GRU-Attention). As shown in Fig.6, the prediction results of the three models in the samples DCB-1, DCB-2, DCB-3, and DCB-4 are compared with the real values. The RMSE of each model are shown in Fig.7. The prediction accuracy of the GRU model is significantly higher than that of the LSTM model. However, after combining the traditional attention mechanism, the prediction results of the other three groups of samples does not show comprehensive improvement except for the DCB-3 sample. Compared with the GRU-Attention model, the prediction model based on TPA-GRU reduced the RMSE on the four data sets by 31.1 %, 60.6 %, 25.8 %, and 46.3 %, respectively, which are the lowest prediction errors on the four data sets.

It is known that the traditional attention mechanism pays more attention to the information of time span, while ignoring the importance of features. However, TPA mechanism focuses on the features extracted from the row vectors of the GRU hidden state through the CNN filter, which enables the model to select relevant information across multiple time steps. The proposed model can not only learn the relationship between multiple features, but also span

previous time and sequences. Therefore, the prediction performance of the TPA-GRU model is better than the traditional attention mechanism.

The prediction results of each DCB sample as a test set are shown in Fig.6. The prediction results of the model are not just a final value, but a process of continuous degradation of the interlayer properties of the sample. As shown in the figure, each DCB prediction result here is obtained by the model trained on the other three DCB samples. It can be seen that the residual interlayer performance of mode I can be accurately predicted by the cumulative AE features combined with the TPA-GRU model. In the initial stage of loading, the main damage types are matrix cracking and fiber/matrix debonding. The generated AE signals are less and discontinuous, which makes the input sequence contain less information. Therefore, enough signals are needed to form an input sequence. However, although the sequence composed of more signals has better prediction effect, it means that the calculation and time cost are increased, and the more signals are included, the closer the distance is to the delamination, which will make the prediction meaningless. Therefore, the combinations of 50 continuous signals are used as the input sequences. It can also be found that each sample has a small increase in the residual interlayer performance. This is because before the crack propagation is observed, small cracks that are not easy to detect by the naked eye have appeared in the composite laminates, but do not affect AE features, so accurate prediction values can still be obtained.

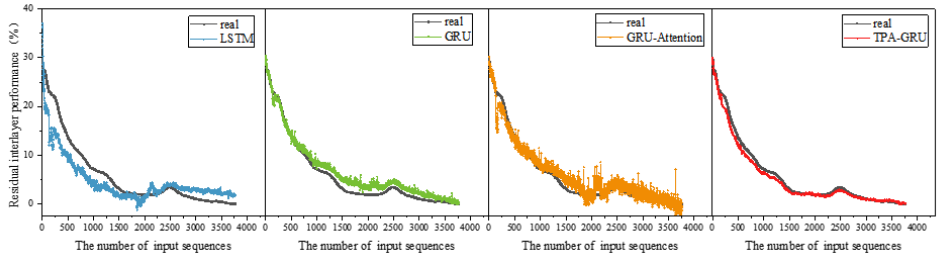

(a) DCB_1

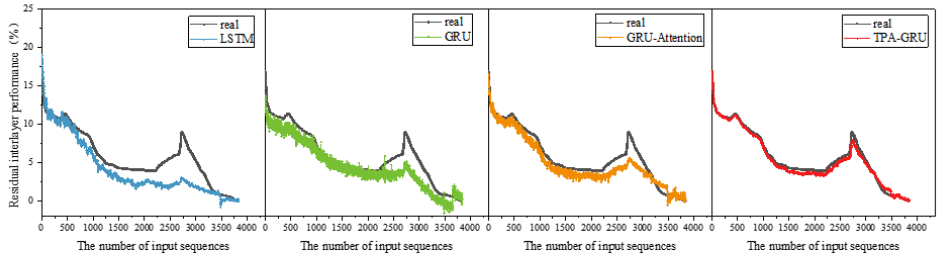

(b) DCB_2

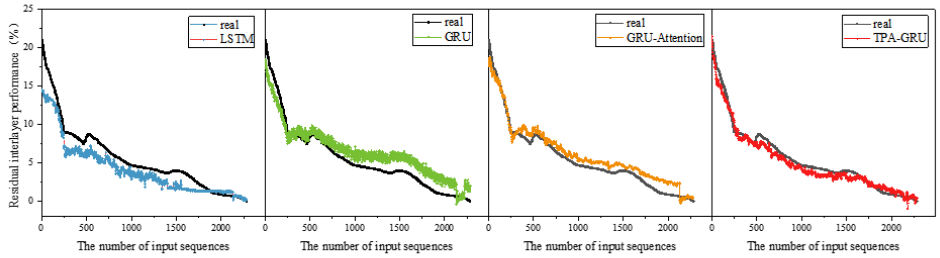

(c) DCB_3

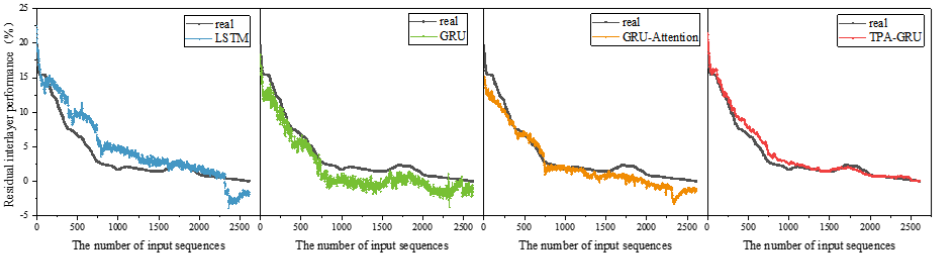

(d) DCB_4

Fig. 23.The prediction result of the residual interlayer performance for each sample.

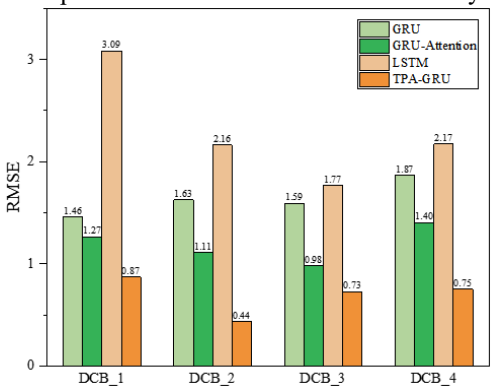

Fig. 24.Prediction errors of different samples on different models

5. Conclusion

In this work, a damage prediction model is established to predict the residual interlaminar properties of composite laminates. First, the feature evaluation algorithm RReliefF was

introduced to filter features that are insensitive to cumulative damage. The evaluation results of 24 features were discussed, and 8 cumulative features were selected. And second, based on the main features of the three training data sets, a TPA-GRU model for damage prediction was constructed and evaluated on a test data set. Last, the results of the proposed model were compared with the other three models. The following two main conclusions are drawn:

1. Compared with the traditional features, the cumulative AE features contain more information and can better describe the degradation process and damage state of DCB samples.
2. Compared with LSTM, GRU and GRU model based on traditional attention mechanism, TPA-GRU model has superior performance in predicting mode I delamination. Therefore, the combination of deep learning and feature evaluation is a feasible method to quantify the degradation process of composite materials.

Reference

[1] Shanyi DU, Guan Z. Strategic considerations for development of advanced composite technology for large commercial aircraft in China. Acta Materiae Compositae Sinica. 2008;25:1-10.

[2] Philippidis TP, Assimakopoulou TT. Using acoustic emission to assess shear strength degradation in FRP composites due to constant and variable amplitude fatigue loading. Composites Science and Technology. 2007;68:840-7.

[3] Caprino G, Teti R, Iorio ID. Predicting residual strength of pre-fatigued glass fibre-reinforced plastic laminates through acoustic emission monitoring - ScienceDirect. Composites Part B Engineering. 2005;36:365-71.

[4] Wu Y, Yuan M, Dong S, Lin L, Liu Y. Remaining useful life estimation of engineered systems using vanilla LSTM neural networks. Neurocomputing. 2018;275:167-79.

[5] Robnik-?Ikonja M, Kononenko I. Theoretical and Empirical Analysis of ReliefF and RReliefF. Machine Learning. 2003;53:23-69.

[6] D-A A. Standard Test Method for Mode I Interlaminar Fracture Toughness of Unidirectional Fiber-Reinforced Polymer Matrix Composites. 2001.

[7] Shih SY, Sun FK, Lee HY. Temporal pattern attention for multivariate time series forecasting. Machine Learning. 2019;108:1421-41.

[8] Lu D, Yu W. Predicting the tensile strength of single wool fibers using artificial neural network and multiple linear regression models based on acoustic emission. Textile Research Journal. 2020:004051752094820.

Fatigue Life Prediction of Composite Materials Based on BP Neural Networks

Yiwei Zhang, Weiling Zheng, Jiangbo Dang

YiWei Zhang Power and Energy, Northwestern Polytechnic University, China

Weiling Zheng Power and Energy, Northwestern Polytechnic University, China

Jiangbo Dang Power and Energy, Northwestern Polytechnic University, China

Abstract: To investigate the fatigue life of composite materials, a neural network model was constructed to predict the fatigue life of composite unidirectional plates based on the feature that BP (Back propagation) neural networks can handle multivariate non-linear models. Experimental values were used as the data set and parameters related to the off-axis direction were calculated and used as new features to enrich the training data. The number of hidden layer and number of nodes in the hidden layer of the network was determined using empirical methods, and four metrics were identified to assess the training effectiveness and accuracy of the BP neural network. The analysis of the training results shows that the use of BP neural networks to predict the fatigue life of composite unidirectional plates has good results, but the training accuracy is related to the network structure. It provides a way to study the fatigue life of unknown materials in engineering.

1. Introduction

Nowadays, composite materials are increasingly used in the automotive, marine and aerospace sectors. In these applications composites are often subjected to cyclic loading, leading to fatigue damage. The fatigue life of composites is therefore an important object of research into the performance of composites. So far, most studies on the fatigue life of composites have focused on the S-N curve of the material, i.e. the stress-life curve and the strain-fatigue life curve of the material[1]. According to research, the S-N curve of a material is related to certain physical properties of the material and the loading process such as the modulus of elasticity, the tensile strength and the stress ratio during loading, the maximum stress and other factors [2].

The stress-life curves of materials are generally obtained by corresponding fatigue tests, and in the long run, most materials, including composite materials, have accumulated more stress-life curves. With the development of artificial intelligence, neural networks can handle many multivariate nonlinear model problems for which it is difficult to obtain exact analytical solutions, and have been widely used in fields such as image speech recognition [3]. According to the characteristics of neural networks, this

paper through the fatigue life data of known materials and thus the prediction of materials with unknown fatigue performance, so that the time and financial cost spent on fatigue testing can be eliminated has a greater value, and can allow researchers developing materials to have a preliminary prediction of their fatigue performance.

Artymiak et al [4] demonstrated the use of ANN to predict S-N curves based on a database of fatigue properties of steel alloys.Pujol and Pinto [5] used ANN to develop cumulative fatigue damage functions based on the results of experimental tests carried out on steel alloys.Tang[6] used a BP neural network to simulate the S-N curve of a unidirectional plate by obtaining fatigue data of the glass composite S2/5208 under a constant load with a stress ratio of R=0.1. The final results obtained from the simulation were in high agreement with the experiment, where the region with a large error appeared in the low circumference fatigue region, because it was beyond the learning range of the neural network. Huo [7] constructed a BP neural network containing three hidden layers to predict the compressive strength of composite laminates containing fibre folds, and this method constructed in the paper provides some reference for the strength assessment of composites in engineering. Vassilopoulos et al [8] used a simple neural network model to simulate the multi-directional composite laminates under tensile-tensile, tensile-compression and compression-compression loading. M. Al-Assadi et al [9] investigated the effect of basic material properties on fatigue life for stress ratios R = 0.1 based on a variety of composites with different neural network algorithms, where a variety of materials were used as training inputs to predict the fatigue life of the remaining materials. Mohamed et al [10] added different stress ratios R as training features and considered the effect of stress ratio on fatigue life during loading.

All the above literature considered the use of neural networks for performance prediction of composite materials. The fatigue performance of composite unidirectional plates is related to the properties of the fibre direction and the vertical fibre direction, the loading angle, the stress ratio, the stresses applied, etc. BP neural networks can be used for fatigue life prediction of composites because they can handle many multivariate non-linear model problems for which exact analytical solutions are difficult to obtain. In this paper, a neural network model between the relevant parameters and the life is developed by using experimental data of eight composite materials, and the network is trained to predict the fatigue life of composite unidirectional plates.

2. Data processing

2.1 Fatigue test data

The learning of BP neural networks requires a certain amount of data support. In this paper, we study the fatigue life of composite unidirectional plates under transverse tensile-tensile stresses, where the data are obtained from the literature[11-17]. The data mainly include material elastic modulus, tensile strength, stress ratio, maximum stress during loading and the corresponding cycle life. The basic

physical parameters of each material are shown in Table 1

Table 1. Material physical parameters

Name of material	E_1/GPa	E_2/GPa	μ_{12}	G_{12}/GPa	X/MPa	Y/MPa	S/MPa
E-Glass/Epoxy	53.48	17.7	0.278	5.83	1140	35	61
1003 Glass/Epoxy	44.73	12.76	0.28	5.8	1060	50	72
E-Glass/Polyester	17	5.4	0.3	2.9	204	48	72
T800H/2500	155	9	0.3	4.5	2900	70	48
S2eglass/epoxy	52	8	0.28	3	1840	44	39
XAS914	150	9.5	0.263	1.07	1990	57	47
Kevlar	95	5.1	0.34	1.8	2500	30	30
AS/3501-5A	147	10.3	0.3	7	2280	57	75

In the table E_1 is the modulus of elasticity in the fibre direction of the material, E_2 is the modulus of elasticity in the vertical fibre direction, μ_{12} is the Poisson's ratio G_{12} is the shear modulus, X is the tensile strength in the fibre direction, Y is the tensile strength in the vertical fibre direction and S is the shear strength.

In the literature[9-10] E_1, X, E_2, Y the angle of declination θ and the stress ratio R and maximum stressduring loading are used as in σ_{max} puts to the network and the number of fatigue cycles N of the material as the only output. Considering that only eight materials are used as the training set, the modulus of elasticity in the off-axis direction as well as the tensile strength will be recalculated in this paper and this will be used as a new input. One of the off-axis physical properties is calculated as follows.

2.2Modulus of elasticity calculation

Under the principal direction of the material, the stress-strain can be expressed as

$$\begin{bmatrix} \varepsilon_1 \\ \varepsilon_2 \\ \gamma_{12} \end{bmatrix} = \begin{bmatrix} S_{11} & S_{12} & 0 \\ S_{12} & S_{22} & 0 \\ 0 & 0 & S_{66} \end{bmatrix} \begin{bmatrix} \sigma_1 \\ \sigma_2 \\ \tau_{12} \end{bmatrix} = S \begin{bmatrix} \sigma_1 \\ \sigma_2 \\ \tau_{12} \end{bmatrix} \quad (1)$$

Where $\varepsilon_1, \varepsilon_2, \gamma_{12}$ is the along-fibre direction, vertical fibre direction strain and shear strain respectively, $\sigma_1, \sigma_2, \tau_{12}$ is the along-fibre direction, vertical fibre direction stress and shear stress respectively, and S is the material flexibility matrix.

The performance in the off-axis direction is as follows[18].

$$
\begin{aligned}
\bar{S}_{11} &= \frac{1}{E_x} = \frac{1}{E_1}\cos^4\theta + \left(\frac{1}{G_{12}} - \frac{2v_{21}}{E_1}\right)\sin^2\theta\cos^2\theta + \frac{1}{E_2}\sin^4\theta \\
\bar{S}_{22} &= \frac{1}{E_y} = \frac{1}{E_1}\sin^4\theta + \left(\frac{1}{G_{12}} - \frac{2v_{21}}{E_1}\right)\sin^2\theta\cos^2\theta + \frac{1}{E_2}\cos^4\theta \\
\bar{S}_{12} &= -\frac{v_{yx}}{E_x} = -\frac{v_{21}}{E_1}\left(\sin^4\theta+\cos^4\theta\right) + \left(\frac{1}{E_1} + \frac{1}{E_2} - \frac{1}{G_{12}}\right)\sin^2\theta\cos^2\theta \\
\bar{S}_{65} &= \frac{1}{G_{xy}} = \frac{1}{G_{12}}\left(\sin^4\theta+\cos^2\theta\right) + 4\left(\frac{1+2v_{21}}{E_1} + \frac{1}{E_2} - \frac{1}{2G_{12}}\right)\sin^2\theta\cos^2\theta \\
\bar{S}_{16} &= \frac{\eta_{xy\text{-}x}}{E_x} = \left(\frac{2}{E_1} + \frac{2v_{21}}{E_1} - \frac{1}{G_{12}}\right)\sin\theta\cos^3\theta - \left(\frac{2}{E_2} + \frac{2v_{21}}{E_2} - \frac{1}{G_{12}}\right)\sin^3\theta\cos^2\theta \\
\bar{S}_{26} &= \frac{\eta_{xy\text{-}2}}{E_y} = \left(\frac{2}{E_1} + \frac{2v_{21}}{E_1} - \frac{1}{G_{12}}\right)\sin\theta\cos\theta - \left(\frac{2}{E_2} + \frac{2v_{21}}{E_2} - \frac{1}{G_{12}}\right)\sin\theta\cos^3\theta
\end{aligned}
\qquad (2)
$$

2.3 Off-axis strength calculation

Tsai-Hill strength criterion for composite unidirectional panels,

$$
\frac{\sigma_1^2}{X^2} - \frac{\sigma_1\sigma_2}{X^2} + \frac{\sigma_2^2}{Y^2} + \frac{\tau_{12}^2}{S^2} = 1 \qquad (3)
$$

The Tsai-Hill strength criterion in the off-axis direction[18],

$$
\frac{\cos^4\theta}{X^2} + \left(\frac{1}{S^2} - \frac{1}{X^2}\right)\cos^2\theta\sin^2\theta + \frac{\sin^4\theta}{Y^2} = \frac{1}{\sigma^2} \qquad (4)
$$

Where X is the tensile strength in the direction of the fibre, Y is the tensile strength in the direction of the vertical fibre and σ is the stress magnitude at an off-axis angle,where $X = \sigma_0$， and $Y = \sigma_{90}$.

The elasticity coefficients E_x, E_y in the off-axis direction can be derived from equation (2) and the tensile strength in the off-axis direction can be calculated from equation (4). This is used instead of the off-axis angle as a characteristic of the material.

3. BP neural network construction

3.1 BP neural network algorithm

In this paper, a BP neural network model is used, with a typical structure shown in Fig.1. BP neural network errors are continuously adjusted along the direction of fastest descent, with the goal of minimizing the error between the actual result and the network output, and the error information is propagated forward during the learning process as a way to readjust the weights [17].

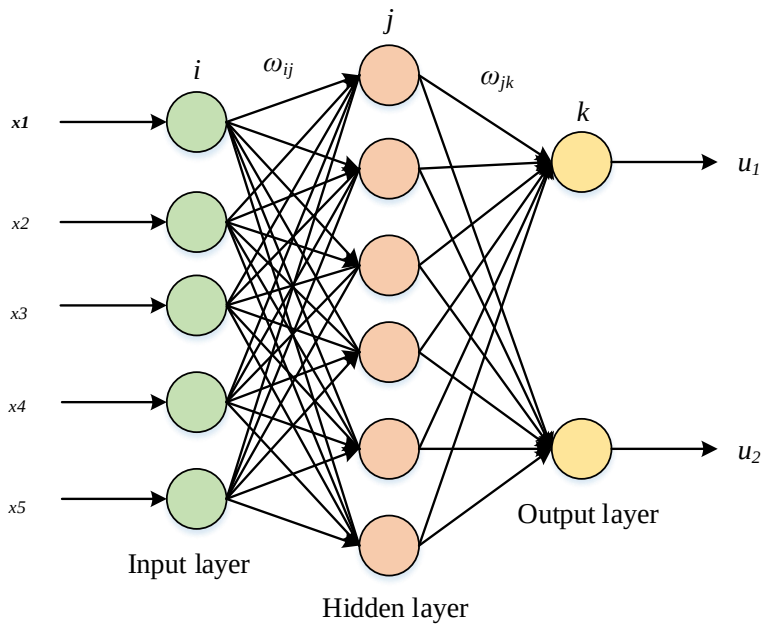

Fig.1 Typical BP neural network structure

The activation value of each neuron in the hidden layer S_j

$$S_j=\sum \omega_{i,j}x_j+b_j \tag{5}$$

Where w_{ij} is the connection weight from the input layer to the hidden layer and b_j is the threshold value of the hidden layer.

The activation function uses an S-shaped function, i.e.

$$f(x)=\frac{1}{1+exp(-x)} \tag{6}$$

Calculates the output value of cell j of the hidden layer：

$$p_j=f\left(s_j\right)=\frac{1}{1+exp\left(-\sum_{i=1}^{n} w_{ji}x_i+b_j\right)} \tag{7}$$

Similarly the activation value and the output value of the output can be found.

Calculate the activation value S_k for the k-th cell of the output value.

$$s_k=\sum_{j=1}^{p} v_{kj}b_j-\theta_k \tag{8}$$

Calculate the actual output value y_k for the kth cell of the output layer.

$$y_k=f\left(s_k\right),(t=1,2,L,q) \tag{9}$$

Where v_{kj} is the weight from the hidden layer to the output layer and b_k is the output layer cell threshold; $f(x)$ is the S-type activation function.

Using the above equations, the process of down propagation of an input pattern can be calculated.

When these values are not the same as the expected values, i.e. when the error is greater than the defined value, the grid should be corrected.

At this point the correction is done from back to front, so the error is said to be back propagated and the calculation is done from the output layer to the hidden layer and then from the hidden layer to the input layer.

The correction error for the output layer is

$$d_k = \left(o_k - y_k\right) y_k \left(1 - y_k\right), k = 1,2,L,q \tag{10}$$

where y_k is the actual output and o_k is the desired output.

The correction error for each cell in the implicit layer is

$$e_j = \left(\sum_{k=1}^{q} v_{kj} d_k\right) p_j \left(1 - p_j\right) \tag{11}$$

The correction error of each intermediate unit is generated by the transfer of the correction error from the q output layer units. Once the correction error is found, then the output layer to implied layer and implied layer to input layer weights can be adjusted layer by layer using d_k and e_j in the opposite direction.

For the output layer to implied layer join weights and output layer thresholds the correction amounts.

$$\begin{aligned} \Delta v_{kj} &= \alpha d_k p_j \\ \Delta \theta_k &= \alpha d_k \end{aligned} \tag{12}$$

Where p_j is the output of unit j in the hidden layer, d_k the correction error in the output layer, and α is the learning coefficient.

The amount of correction from the implied layer to the input layer is

$$\begin{aligned} \Delta w_{ji} &= \beta e_j x_i \\ \Delta \theta_j &= \beta - e_j \end{aligned} \tag{13}$$

Where e_j is the correction error of unit j of the hidden layer; β is the learning coefficient.

3.2 Structural parameters of neural networks

The number of nodes in the hidden layer and the number of nodes in the BP neural network are important factors affecting the accuracy of the computation, according to research, a network with one hidden layer can already approximate any rational function, increasing the number of layers can further reduce the error and improve the accuracy but also complicate the network and thus increase the training time of the network weights. For the number of nodes in the hidden layer, there is no ideal analytical formula to determine a reasonable number of neuron nodes, but the empirical formula[20] is generally

used.

$$\sum_{i=0}^{n} C_M^i > k \quad (14)$$

$$M = \sqrt{n+m} + a \quad (15)$$

$$M = log_2 n \quad (16)$$

Where k is the number of samples, M is the number of neurons in the hidden layer, n is the number of neurons in the input layer, m is the number of neurons in the output layer, and a is a constant between [0,10].

The inputs to the neural network used in this paper are the modulus of elasticity in the fibre direction (E_1), the modulus of elasticity perpendicular to the fibre direction (E_2), the tensile strength of the material in the fibre direction (X), the tensile strength of the material perpendicular to the fibre direction (Y), the loading process stress ratio (R) and the maximum stress (σ_{max}). The output is the logarithm of the number of cycles ($\lg N$). The neural network model was constructed, trained and tested using the Matlab platform with the parameters shown in Table 2.

Table 2 BP neural network parameter values

Parameters	
Input layer neurons	6
Output layer neurons	1
Hidden layer	3
First hidden layer neurons	12
Second hidden layer neurons	8
Third hidden layer neurons	5
Learning Rate	0.01
Activation functions	Sigmoid
Training algorithms	Levenberg-Marquardt

3.3 Data processing and evaluation indicators

Because the neural network minimizes the overall error of all input parameters, excessive fluctuations in the range of values can affect grid training accuracy, so the range of input values should be kept as small as possible. The number of material fatigue cycles is typically between 10 and 10,000,000. The logarithm of the cycle number is normalized to a range between 0 and 1, and because the numerical order of magnitude of the cycle cycles varies so much that the normalization process can result in very small or even close to 0 values, the fatigue cycle life of the material should be taken as lgN, and then lgN normalized. The maximum stress value, material modulus of elasticity, tensile strength, and stress ratio should all be normalized accordingly. Matlab software was used for network

construction and training.

Four metrics, mean absolute error (MAE), mean squared error (MSE), root mean squared error(RMSE) and regression value, were used to evaluate the prediction effectiveness and accuracy of the BP neural network respectively[5]. The first three metrics are an analysis of the error; the smaller the value, the smaller the error of the model. The regression value R represents the correlation between the predicted output and the actual value, the closer the R value is to 1 the closer the relationship between the prediction and the actual data, and the closer the R value is to 0 the greater the randomness of the relationship between the prediction and the output data.

$$MAE=\frac{1}{m}\sum_{i=1}^{m}\left|y_i-\hat{y}_i\right| \tag{17}$$

$$MSE=\frac{1}{m}\sum_{i=1}^{m}(y_i-\hat{y}_i)^2 \tag{18}$$

$$RMSE=\sqrt{\frac{1}{m}\sum_{i=1}^{m}(y_i-\hat{y}_i)^2} \tag{19}$$

$$R=1-\frac{\sum_{i=1}^{m}(y_i-\hat{y}_i)^2}{\sum_{i=1}^{m}(y_i-\bar{y}_i)^2} \tag{20}$$

Where y_i is the true value of the sample, $\hat{y}_i$ is the predicted value of the BP network, $\bar{y}_i$ is the mean of the true value of the sample; m denotes the number of samples.

4 Fatigue life prediction

Eight different composites were included in the data used, as the experimental data all contained off-axis tensile data for the composites. The off-axis properties of the composites at different angles were calculated for a total of 34 different moduli of elasticity, tensile strengths, and stress ratios for five different loading cases, for a total of 471 sets of tensile experimental data, according to Section 1. Because the off-axis properties were calculated for different materials at different angles, the materials under the off-axis were treated as different from the orthotropic materials for ease of description and were expressed using E_1.

The first 32 different material data were used as the training set and the remaining two different materials $E_1=17GPa$ and $E_1=5.4GPa$ were used as the test set. The final calculated values for each error and regression are shown in Table 3. The prediction results for the use of the BP neural network are shown in Figure 2 and Figure 3. Figure 2 shows the effect of predicted versus experimental values for material $E_1=17GPa$; Figure 3 shows the effect of predicted versus experimental values for $E_1=5.4GPa$. Figure 4 shows the experimental and predicted life 2-fold dispersion band plots.

Table 3 BP neural network model evaluation index values

MAE	0.55128
MSE	0.50166
RMSE	0.70828
R	0.815

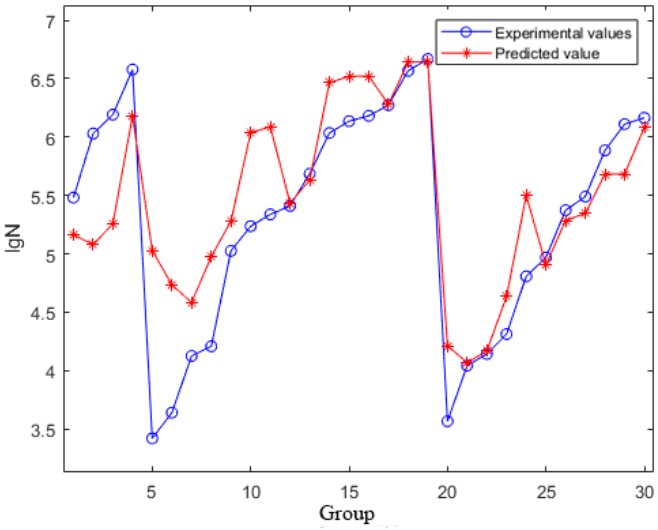

Fig.2 Comparison of predicted and actual values for E_1 = 17 GPa material

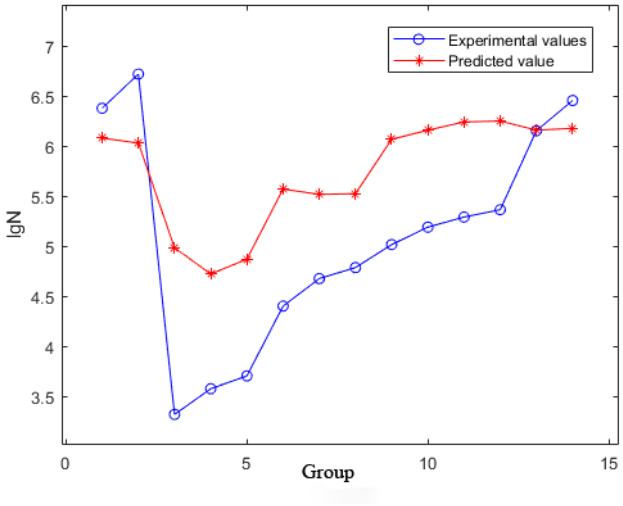

Fig.3 Comparison of predicted and actual values for E_1 = 5.4 GPa material

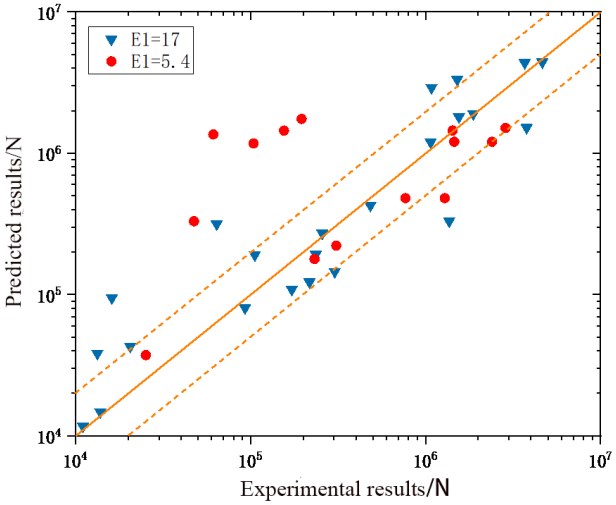

Fig.4 Neural network training values and experimental values 2-fold dispersion band

Comparing Fig. 2 and Fig. 3, it can be seen that the material with $E_1 = 5.4GPa$ has a significantly larger error between its predicted and actual values than the material with $E_1 = 17GPa$ and the predicted values are overall larger compared to the actual values. Combined with the two-fold dispersion band in Figure 4, almost 40% of the points for the $E_1 = 5.4GPa$ material fall outside the dispersion band and the prediction accuracy is not very good. From the training material parameters, it can be seen that the parameters of the two data used for testing, except for the E_1, E_2, X and Y values are smaller than the values of the material in the training set, so it can be seen that the trend of the predicted value is more consistent with the actual value, but the overall value is large.

Therefore, the network model was readjusted and the training and test sets were readjusted to include as wide a range of material parameter values as possible. Different material data were selected as the test validation and the remaining materials were used as training, three training sets were performed for a total of six materials.The results predicted using the BP neural network are shown in Figure 5-figure supplement 10, and the 2-fold dispersion band are shown in Figure 11-figure supplement 13,the test materials and errors are shown in Table 4;

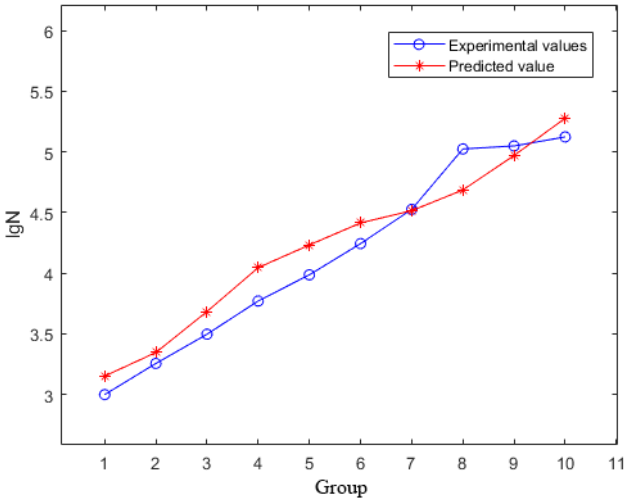

Fig.5 Comparison of predicted and actual values for E_1 =47.67GPa material

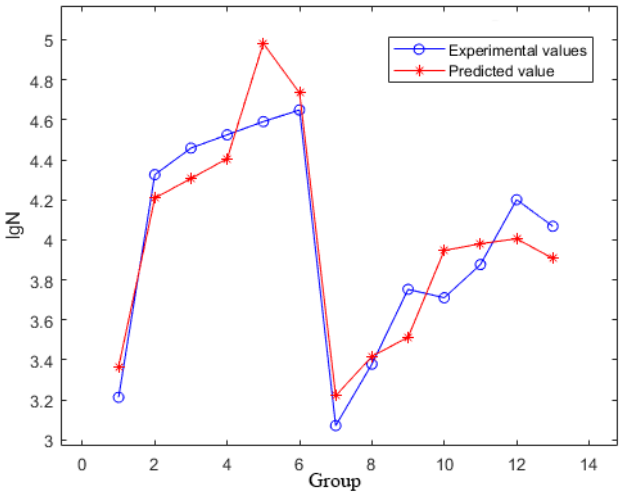

Fig.6 Comparison of predicted and actual values for E_1= 16.48 GPa material

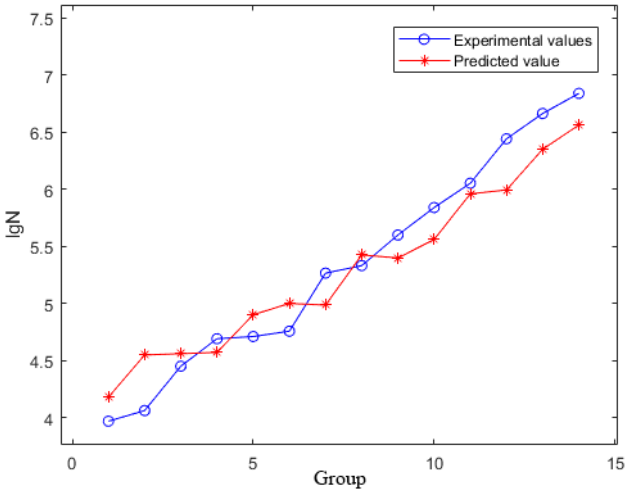

Fig.7 Comparison of predicted and actual values for E_1 =66.52 GPa material

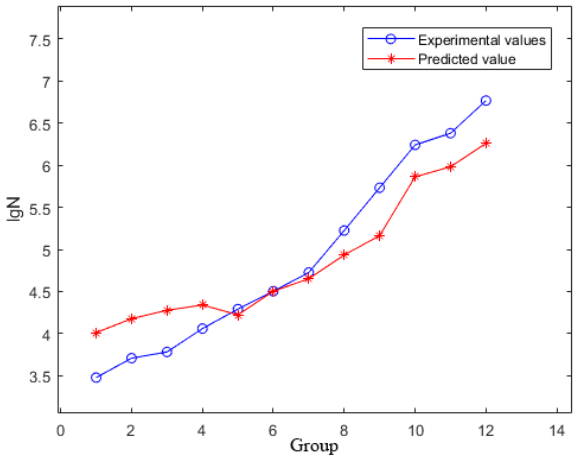

Fig.8 Comparison of predicted and actual values for E_1= 10.72 GPa material

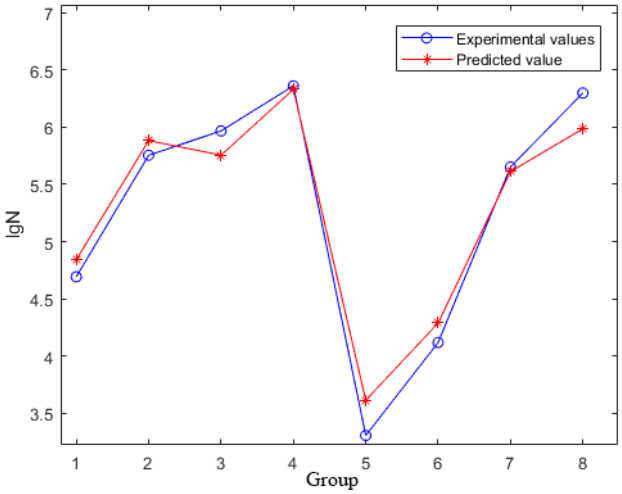

Fig.9 Comparison of predicted and actual values for E_1 =155 GPa material

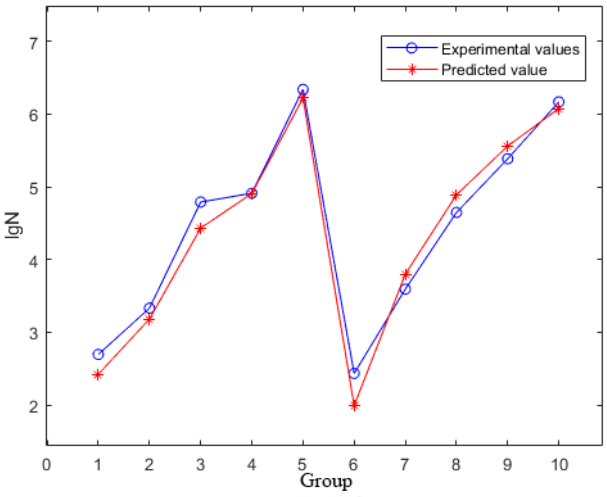

Fig.10 Comparison of predicted and actual values for E_1=79.65GPa material

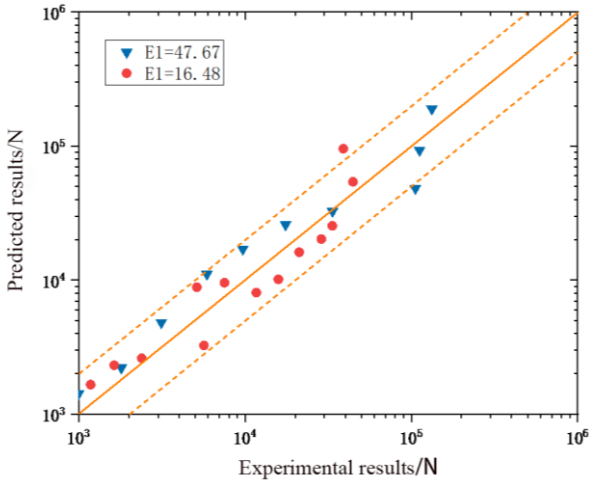

Fig.11 Group 1 neural network training values and experimental values 2-fold dispersion band

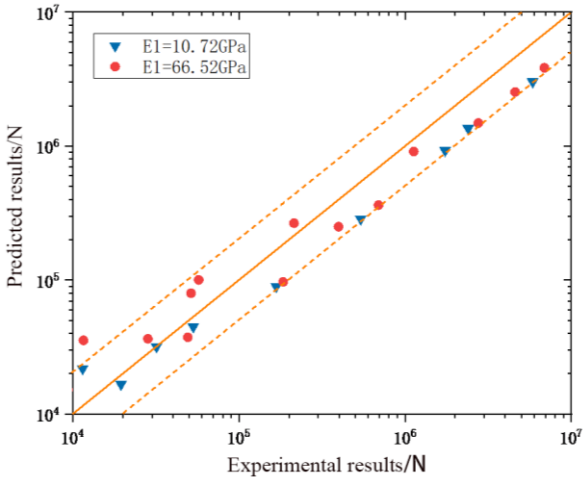

Fig.12 Group 2 neural network training values and experimental values 2-fold dispersion band

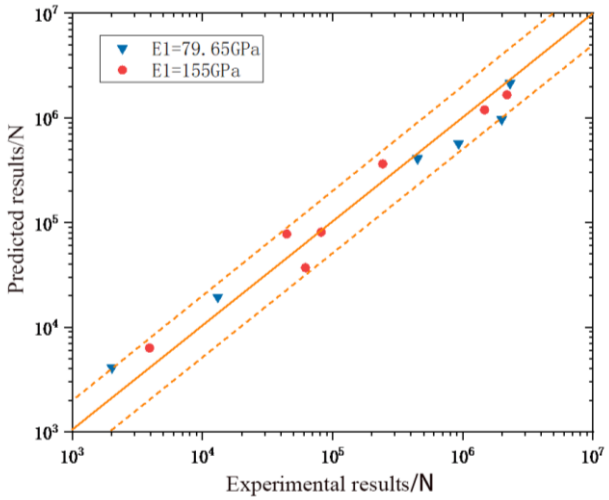

Fig.13 Group 3 neural network training values and experimental values 2-fold dispersion band

Table 4 BP neural network model evaluation index values

Group	E_1/GPa	MAE	MSE	RMSE	R
1	16.48/47.67	0.1671	0.0357	0.1891	0.9039
2	10.72/66.52	0.2409	0.0748	0.2735	0.8652
3	79.65/155	0.1896	0.0491	0.2217	0.8824

As can be seen from Table 4 and Figures 5-Figure 13, the retuned network model has predicted values that are closer to the experimental values, and compared to the first training model, there is a significant reduction in error, with all types of errors reduced by around 0.1 and regression values around 0.9, indicating that the predicted values correlate well with the experimental values. The smallest error and the best prediction is in group 1. In comparison, the other two groups have different degrees of bias and bias compared to group 1, but the overall results are acceptable. In terms of the twofold dispersion band, the predictions are above 90% of the points in the band.

5.Conclusion

Predicting the fatigue life of composite unidirectional plates by building a BP neural network, using experimental values as the dataset, and calculating parameters related to the off-axis direction and considering them as new features, enriching the variety of materials in the dataset helps to improve the BP neural network model training effect. The number of hidden layer and number of nodes in the hidden layer of the network was determined using empirical methods, and four metrics were identified to assess the training effectiveness and accuracy of the BP neural network. The analysis of the training results shows that the use of BP neural networks to predict the fatigue life of composite unidirectional plates has good results, but the training accuracy has a certain relationship with the network structure, in order to ensure the training accuracy, the data in the training set should be made to contain a wider range. The use of BP neural network algorithm provides a way to study the fatigue life of unknown materials in engineering, but the influence of the specific structure of the neural network, the algorithm and the data on the prediction accuracy should be considered more in the subsequent research process.

References

[1] R. F. Wu, "Comparison and Analysis of S-N Curves in Different Standards." *Ship Engineering*, 2017, 39(1):5.

[2] W. X. Yao, *Structural fatigue life analysis*,Press,2019.

[3] E. A. Smirnov et al, "Comparison of Regularization Methods for ImageNet Classification with Deep Convolutional Neural Networks." *AASRI Procedia* (2014).

[4] P. Artymiak, et al, "Determination of S-N curves with the application of artificial neutral networks. " *Fatigue & Fracture of Engineering Materials & Structures* 22.8(1999):723-723.

[5] P. Pujol,ea al, "A neural network approach to fatigue life prediction." *International Journal of*

Fatigue 33.3(2011):313-322.

[6] Z. W. Tang et al, "BP Neural Network Model of Composite S-N Curve." *Hot Working Technology*,45.4(2016):3.

[7] G. L. Huo, Z. H Ning, "Strength Prediction of Laminates Containing Embedded Fiber Wrinkles Using BP Neural Networks." *Journal of Nanjing University of Aeronautics & Astronautics*,52.03(2020):460-467.

[8] P. Vassilopoulos, "Modelling Fatigue Life of Multidirectional GFRP Laminates under Constant Amplitude Loading with Artificial Neural Networks." *Advanced Composites Letters*,15.2(2006):43-51.

[9] M. Al-Assadi,et al, "Predicting the Fatigue Life of Different Composite Materials Using Artificial Neural Networks" Applied composite materials.17(2010):1-14.

[10] Mohamed, et al, "Using Artificial Neural Networks to Predict the Fatigue Life of Different Composite Materials Including the Stress Ratio Effect." *Applied Composite Materials* (2011).

[11] Z. Hashin, A. Rotem, "A Fatigue Failure Criterion for Fiber Reinforced Materials."*Journal of Composite Materials*,1973, 7(4):448-464.

[12] J. Awerbuch,.H. T. Hahn, "Off-axis fatigue of graphite/epoxy composite." *ASTM special technical publications* (1981).

[13] H. E. Kadi, and F. Ellyin, "Effect of stress ratio on the fatigue of unidirectional glass fibre/epoxy composite laminae." *Composites*,25.10(1994):917-924.

[14] T. P. Philippidis, and A. P, Vassilopoulos, "Complex stress state effect on fatigue life of GRP laminates. Part I, Experimental." *International Journal of Fatigue,*24.8(2002):813-823.

[15] M. Kawai, and H. Suda, "Effects of Non-Negative Mean Stress on the Off-Axis Fatigue Behavior of Unidirectional Carbon/Epoxy Composites at Room Temperature." *Journal of Composite Materials*,38.10(2004):833-854.

[16] A. Jayantha, Epaarachchi and Philip D. Clausen, "An empirical model for fatigue behavior prediction of glass fibre-reinforced plastic composites for various stress ratios and test frequencies." *Composites Part A: Applied Science and Manufacturing* (2003).

[17] G. Fernando, et al, "Fatigue behaviour of hybrid composites - Part 1 Carbon/Kevlar hybrids." *Journal of Materials Science* 23.10(1988):3732-3743.

[18] G. L. Shen, *Composite mechanics*., Press, 2013.

[19] R. G. Kamble,N.R. Raykar , and D.N. Jadhav, "Machine learning approach to predict fatigue crack growth." (2021).

[20] B. Jiao, M. X.Ye, "Determination of Hidden Unit Number in a BP Neural Network."*Journal of Shanghai Dianji University*, 2013, 16(3):5.

Compression shear test technique for flat panel of composite material

Guangqi Huang [1], Chong Li[1]

[1]Aircraft Strength Research Institute of China,China

Abstract: The stability of fuselage panels under combined compression and shear loads has always been an important issue in fuselage strength research. In recent years, because of its high specific strength and good fatigue performance, composite materials are increasingly used in aircraft structures. In the selection stage of composite fuselage panels, the curved fuselage panels are usually simplified into flat panels for pressure shear tests. In the past, the box composed of flat plates were loaded by bending and torsion. In order to reduce costs and improve efficiency, now they are mostly tested by special pressure shear devices. The compression load and shear load are loaded separately. The two loads are applied independently and do not interfere with each other, One installation can realize the buckling load test with any compression shear ratio, and its superposition error is within 3%. It can also constrains the outer normal direction of the skin at the end of the frame, releases the degrees of freedom along the compression direction and shear direction, and simulates the support state under the whole frame, which is more realistic and effective than the previous support of simulating steel ribs in panel compression.

Keywords: compression and shear loads,composite materials,fuselage panels,flat panels,end of the frame,degrees of freedom

Composite stiffened panels are widely used in today's aircraft structures, such as wing and tail wing panels, beam webs and fuselage panels. As the main load-bearing component of aircraft structures, composite stiffened panel structures usually need to consider the stability under multiple loads. In the whole building block test verification process, the panel level test accounts for a large proportion, and the stiffened panel with curvature is usually simplified to a straight panel for strength research, shape selection, participation selection and verification [1]~[8]. Compression and shear are the main load forms for the verification of the stability of stiffened panels. In the past, the research and verification of the stability of panels under the combined action of compression and shear were usually carried out by applying bending and torsional loads to the box section, The establishment of composite compression and shear test technology and the successful development of test equipment for composite straight wall panels provide an effective and low-cost test method and way for the stability study of flat wall panels under combined compression and shear loads.

1 Specimen

The specimen is a composite fuselage "M" type long truss stiffened wallboard, which is mainly composed of skin, stringer, angle piece, floating frame and glue filling box. The stringer is bonded to the skin, and the skin, angle piece and floating frame are bolted. Both ends of the specimen sealed in the aluminum box with epoxy resin. The configuration of the test piece is shown in Figure 1.

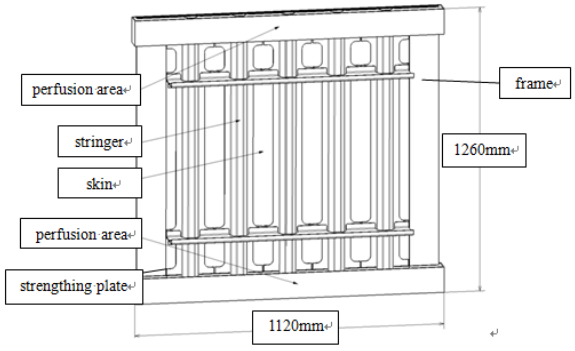

Fig.1 configuration of specimen

The skin, stringer and stiffener of the test piece are made of M21E/IMA, with a single layer thickness of 0.186mm. The frame structure is made of 2024-T42 aluminum alloy, with a thickness of 2mm. See Table 1 for material properties and Table 2 for specimen layers.

Table 1 material properties of specimen

Material	E11(MPa)	E22(MPa)	G12(MPa)	μ12
M21E/IMA	154000	8500	4200	0.35
2024-T42	72345	72345	—	0.33

Table 2 specimen layers

Name	Layers
Skin layer	[45/-45/-45/90/45/0]s
Stringer layer	[45/0/0/-45/90/-45/0/0/45]
Strengthening plate layer	[45/-45/90/-45/45/0/45/-45/-45/45/0/0/45/-45/-45/45/0/45/-45/90/-45/45]

2 The supporting and loading mode of specimen

The test is carried out on a special test fixture, as shown in Figure 2. The compression and shear loading can be loaded separately and independently, which can realize the test of any compression shear ratio.

As shown in Figure 3, the bottom edge of the specimen is fixed on the compression platform through a group of corner pieces, and the upper end is connected with a group of pull plates, which are used to apply the shear force at the upper end of the specimen. Several loading joints are installed on both sides of the specimen to apply side shear load. The frame joints are installed at both ends of the frame of the specimen to constrain the displacement of the normal direction outside the skin of the frame and simulate the support state of the real structure to the frame end.

As shown in Figure 4, the compression load is applied by the compression actuator, and the load is applied on the specimen through the load sensor and loading platform. Before the test, the position of the compression actuator shall be adjusted so that the pressure center coincides with the stiffness center (pressure center) of the cross section of the specimen in the assessment area.

Shear load shall be applied according to the principle of self balance of the frame. As shown in Figure 5, several actuators which output the same loads on both sides of the frame output compression load. The load is applied to the joints on both sides of the specimen through the direction conversion of the curved lever. The frame will rotate around the axis under the reaction force of the specimen, so that the pull plate will apply shear load to the upper end of the specimen. From the balance of moments, it can be known that the shear flow on the four sides of the test piece is equal. Before the test, the shear frame shall be adjusted so that the shear load passes through the skin center of the specimen.

As shown in Figure 6, the two ends of the frame need to be constrained in the test. Two sets of linear guide sliders in the horizontal and vertical directions are used to form a plane servo system, and a spring is installed at the bottom to counteract the influence of gravity. The compression and shear displacement can not be limited while constraining the displacement of the frame in the direction of

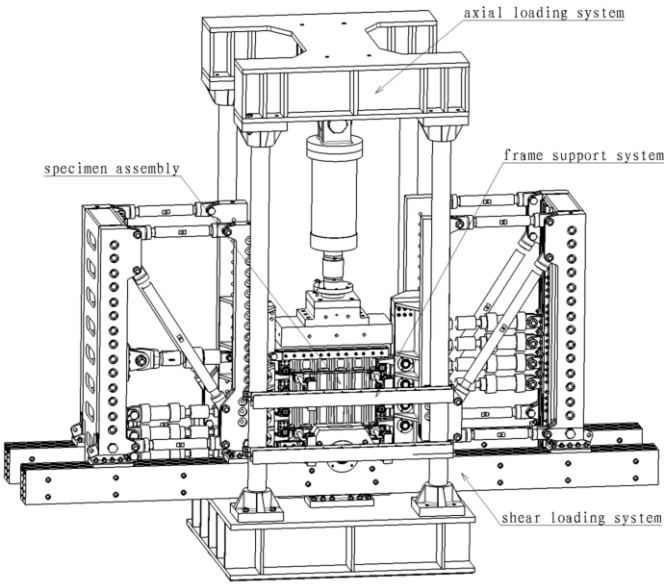

the outer normal of the skin.

Fig.2 test fixture

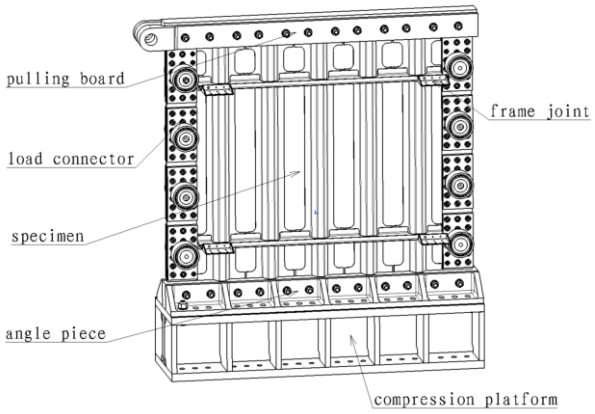

Fig.3 schematic diagram of the periphery of the specimen

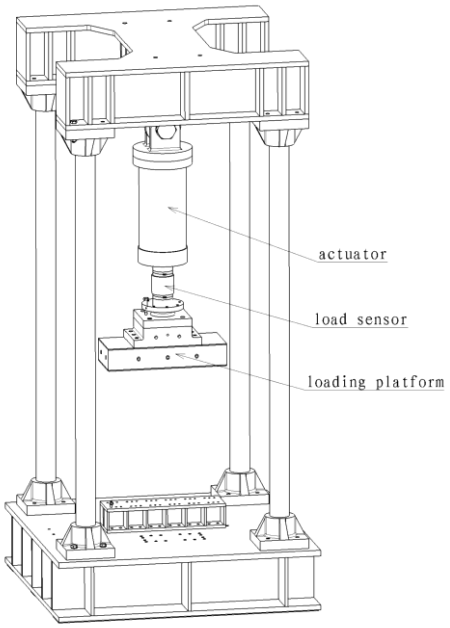

Fig.4compression loading system

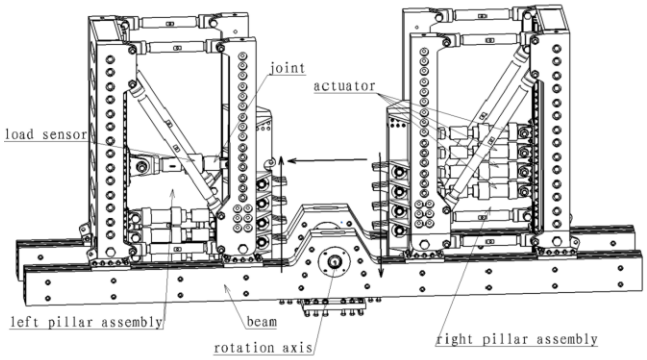

Fig.5 shear loading system

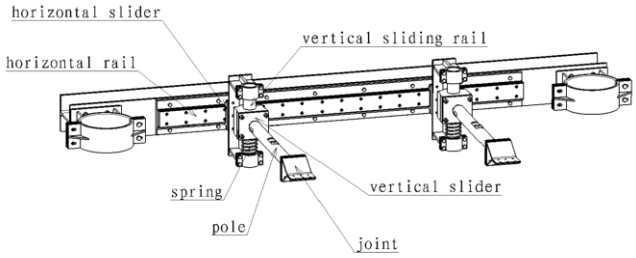

Fig.6 frame support system

3 Test measurement

A number of strain gauges are pasted in the assessment area of the specimen. See Figure 7 for the location and number of strain gauges.

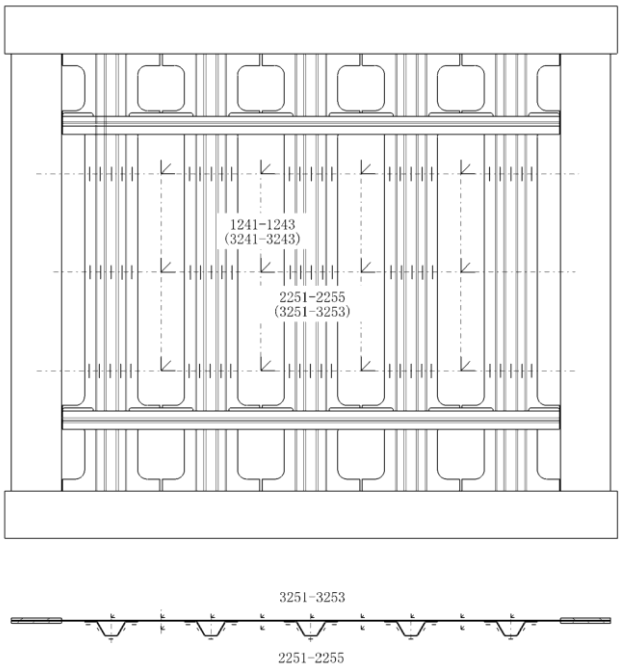

Fig. 7 Sticking position and number of strain gauge

4 Test equipment

4.1 Loading control system

The coordinated loading control system developed by MOOG-F CS Company is used for the test loading control. The control error of the loading control system is less than 1%. The system can set the alarm of out of tolerance, out of limit, power failure and other faults according to the test

requirements. The alarm limit and post alarm processing measures can be set as required, and the program, feedback, error and other data before and after the alarm can be saved according to the test requirements after the alarm.

4.2 Data acquisition system

The strain and displacement of the test are measured by the ST16 data acquisition system developed by Aircraft Strength Research Institute of China. The measurement error of the system is ± 0.5%, and the acquisition speed is 5000 points/second.

4.3 Loading execution equipment

1 set of 2000kN actuator for applying compression load.

Eight sets of 200kN actuators are used to apply shear load.

4.4 Instrument accuracy

See Table 11 for measuring instruments used in the test.

Table 3 Test equipment and measuring instruments

Device name	Specifications	quantity	Allowable error/accuracy level
coordinated loading control system	32 channels	1	≤1%
Load cell	200kN	1	0.3degree
Load cel	2000kN	1	0.3degree
ST16 data acquisition instrument	ST16/±20000με	2	±0.5%
Large range digital Dial indicator	0.01mm	1	0.01mm
Aviation DC stabilized voltage power supply	ZN24V40A*2	1	/
Pressure gauge	Y-100/40MPa	1	1.6 级
Ultrasonic A scanner	-	1	1 级

5 Test process and results

First, the specimen was pretested twice according to 50% of the estimated initial buckling load (compression - 558000N, shear 357000N) to verify the repeatability of multiple loads, as shown in Table 4, it can be seen that the absolute repeatability error is within 5%. In addition, in order to verify that the two loads can be decoupled from each other and do not interfere with each other, compression tests and shear tests were conducted separately. The strains obtained under the two working conditions were superposed, and then compared with the compression shear test strains. The results are shown in Table 5. The superposition error is within 5%, indicating that the two loads are basically non-interference.

Table 4 Repeatability error

Strain number	The first strain	The second strain	error
1241	-643	-627	2.55%
1242	-1224	-1270	-3.62%
1243	388	380	2.11%
2251	-629	-641	-1.87%
2252	-652	-638	2.19%
2253	-636	-630	0.95%
2254	-636	-624	1.92%
2255	-599	-572	4.72%
3241	-620	-602	2.99%
3242	-1290	-1283	0.55%

3243	236	230	2.61%
3251	-660	-641	2.96%
3252	-941	-939	0.21%
3253	344	324	6.17%

Table 5 superposition error

Working condition number	Compression-shear	Compression	shear	superimposition	error
1241	-643	-624	-40	-665	3.35%
1242	-1224	-139	-1137	-1276	4.22%
1243	388	289	80	369	-4.92%
2251	-629	-632	-26	-658	4.67%
2252	-652	-596	-36	-632	-3.03%
2253	-636	-563	-54	-617	-3.02%
2254	-636	-597	-21	-618	-2.79%
2255	-599	-633	52	-581	-3.02%
3241	-620	-638	40	-598	-3.52%
3242	-1290	-200	-1141	-1341	3.94%
3243	236	248	-18	230	-2.48%
3251	-660	-640	-3	-643	-2.59%
3252	-941	-156	-809	-966	2.61%
3253	344	303	45	347	1.00%

In the formal test, 5% of the test load under the compression shear ratio of 1:2 is taken as the step length, and the load is gradually loaded to 60% of the test load, and then 1% of the test load is taken as the step length, and the load strain curve is shown in Figure 8. It can be seen from the figure that the linearity of the strain curve is very good before buckling.

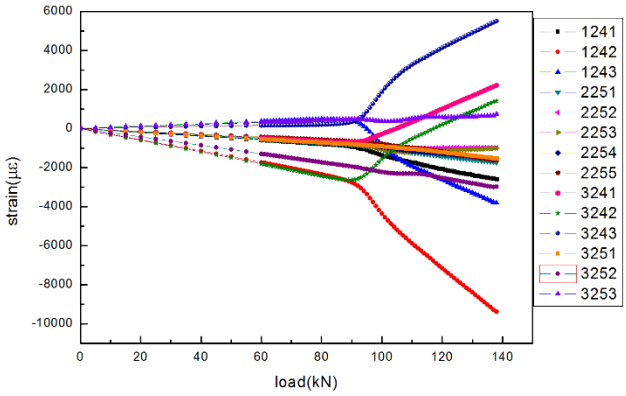

Fig.8 load-strain curve of the specimen

6 Conclusion

From the above test results, the following conclusions can be drawn:

The technology uses compression and shear separately to load, which can realize the test of any compression shear ratio. The two kinds of loads have no interference, and the repeatability of multiple loading is good. The support state of the frame end is accurately simulated.

References:

[1] A test device capable of uniformly applying axial compression and shear loads.ZL 2012 1 0528616.7

[2] Bisagni, C., and Cordisco, P. An Experimental Investigation into the Buckling and Post-Buckling of CFRP Shells Under Combined Axial and Torsion Loading, Composite Structures, 2003, 60(4): 391–402.

[3] H. Abramovich and T. Weller and C. Bisagni. Buckling Behavior of Composite Laminated Stiffened Panels Under Combined Shear–Axial Compression. Journal of Aircraft, 2008, 45(2): 402-412.

[4] D. Wilckens， F. Odermann and A. Kling, Buckling and Post Buckling of Stiffened CFRP Panels under Compression and Shear Test and Numerical Analysis. 54th AIAA/ASME/ASCE/AHS/ASC Structures, Structural Dynamics, and Materials Conference, April 8-11, 2013, Boston, Massachusetts.

[5] P. Cordisco and C. Bisagni. Cyclic Buckling Tests of Stiffened Composite Curved Panels under Compression and Shear. 49th AIAA/ASME/ASCE/ AHS/ASC Structures, Structural Dynamics, and Materials Conference, 2008, Schaumburg.

[6] Bisagni, C., and Cordisco, P. Post-Buckling and Collapse Experiments of Stiffened Composite Cylindrical Shells Subjected to Axial Loading and Torque, Composite Structures 73 (2006): 138–149.

[7] Bisagni C. Numerical analysis and experimental correlation of composite shell buckling and post-buckling. Composite Part B: Eng 2000;31(8):655–67.

[8] Joël Serra, J.E. Pierré, J.C. Passieux. Validation and modeling of aeronautical composite structures subjected to combined loadings: The VERTEX project. Part 1: Experimental setup, FE-DIC instrumentation and procedures. Composite Structures 179 (2017) 224–244.

Comprehensive Test Technology of Curved Plate

Yi An [1], Chong Li[1]

[1]China Aircraft Strength Research Institute, China

Abstract: The aircraft fuselage structure is composed of various forms of stiffened curved panels, and is the main load-bearing component of the fuselage structure, which accounts for a large proportion in the whole building block strength test process. In aircraft development, the stability, durability and damage tolerance of stiffened fuselage panels under tension/compression, bending, shear, single or combined airtight loads are usually considered, A large number of tests of wall panels under the combined action of multiple loads are required. For this reason, a series of technical research and device development work have been carried out. The self balanced loading system is adopted, and each load is relatively independent. The tension/compression, shear, and airtight loads of curved plates are single or combined, and each load is decoupled from each other without interference. The straight edge boundary of the curved plate is constrained by a V-shaped frame, which truly simulates the cylindrical boundary, and each joint is equipped with an anti instability device, which effectively prevents the instability of the free edge.

Keywords: composite curved Plate, multiple loads, instability of the free edge

In recent years, in order to save the test cost and improve the test efficiency, many countries are vigorously developing the composite fuselage panel test technology to replace the traditional box section and cylinder section tests in the advanced research stage. According to the published technical data and reports, only European and American countries with advanced aviation technology and China now have the test technology and devices for composite loading of more than three kinds of loads, and have accumulated many technologies and experience of static and fatigue and damage tolerance characteristics, and have developed several sets of serialized special test devices for wall panels[1]~[5]. The representative of these devices are the COLTS device (which can jointly apply axial compression, torsion and airtight loads) of NASA, the FASTER device (which can jointly apply airtight, tensile and shear loads) of FAA, the fuselage wall panel test device of IMA, Germany, and the domestic panel integrated test device (FPTS)[6]~[7], Large aircraft fuselage curved plate multiaxial load test device[8], these technologies and devices have been put into application, representing the international advanced level.

At present, there are two main ways to achieve the multiaxial loading of the fuselage curved plate. One is to use the D-box method to form a sealed box structure by combining the wall plate with the structural members below and the cover plates at both ends. Axial and torsional loads are applied to the box structure. The structural members below the wall plate, because of its special structure, does not bear the axial load of the wall plate, but can transmit torque. Airtight loads can also be applied to the sealed structure, Therefore, axial, shear and airtight loads can be loaded. The other scheme is to constrain the straight edge of the specimen through a V-shaped frame, and then use a shear frame to load the four sides of the specimen. The two schemes are mainly reflected in the difference of the shear load loading mode and the boundary support mode. It is difficult to design and process the

structural members under the wall panel by D-box method. At present, the method of steel profiles with rubber backing plates is used in China. The disadvantage is that it can bear part of the compression load. When applying tensile load, it is necessary to adjust the tightness of fasteners. When applying airtight load, it will warp locally. Another scheme supported by V-shaped frame can only apply shear load in one direction due to the connection mode between the shear frame and the straight edge of the specimen. Due to the structural characteristics of the shear frame, the axial and shear displacement are limited to a certain extent. And because of the use of discrete loading joints, the free edge is prone to lose stability before the assessment area under the effect of compression load.

In view of the above problems, in order to meet the growing demand for composite fuselage curved plate test and balance the advantages and disadvantages, the overall plan supported by V-shaped frame is adopted to develop the next generation of curved plate comprehensive test technology.

1 Specimen

One fuselage curved plate test configuration is selected as the specimen, and the configuration of the specimen is shown in Figure 1. The specimen has a total length of 3100mm and a total width of 2150mm (curve length), including 5 frames and 8 trusses, with a spacing of 210mm and a spacing of 620mm. The material of skin and stringer is M21E/34%/UD194/IMA-12. The number of skin layers in the assessment area is 12, and the thickness is 2.21mm. The stringer is a hat type stringer. See Table 1 for the material information of the specimen and Table 2 for the pavement information.

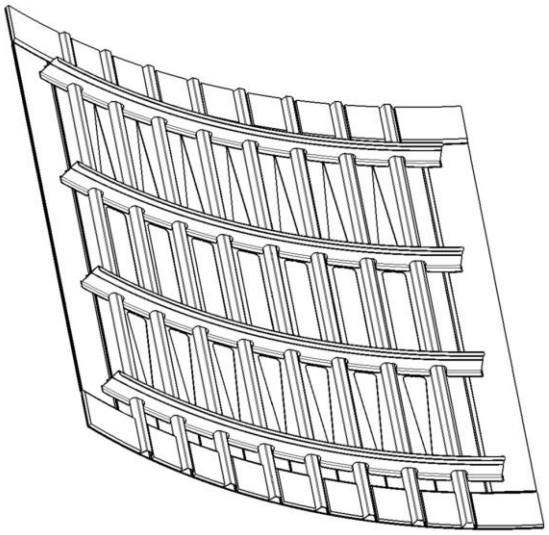

Fig.1 configuration of specimen

Table 1 material properties of specimen

Material	E11(MPa)	E22(MPa)	G12(MPa)	μ12
M21E/IMA	154000	8500	4200	0.35

Table 2 specimen layers

Name	Layer number	Thickness	Layers
Skin layer	12	2.21	[45/-45/-45/90/45/0]s
Stringer layer	9	1.66	[45/0/0/-45/90/-45/0/0/45]
Frame layer	14	2.58	[45/-45/0/90/45/-45/0]s

2 The support and loading mode

The test is carried out on a special test device, as shown in Figure 2-3. The test device can be divided into axial loading system, shear loading system, airtight circumferential loading system and specimen changing system according to its functions.

As shown in Figure 4,The two curved edges of the specimen are connected with the corner piece, and several loading joints are installed on the two straight edges. The frame end is fixed with the loading joint by the frame joint. Together they form the specimen assembly.

As shown in Figure 5,the axial load is applied by two symmetrically arranged axial actuators in the axial load application system. One end of the specimen assembly is connected to the fixed end beam and the other end is connected to the movable end beam. The movable end beam can

slide along the axis along the linear motion mechanism without limiting the axial displacement of the specimen.

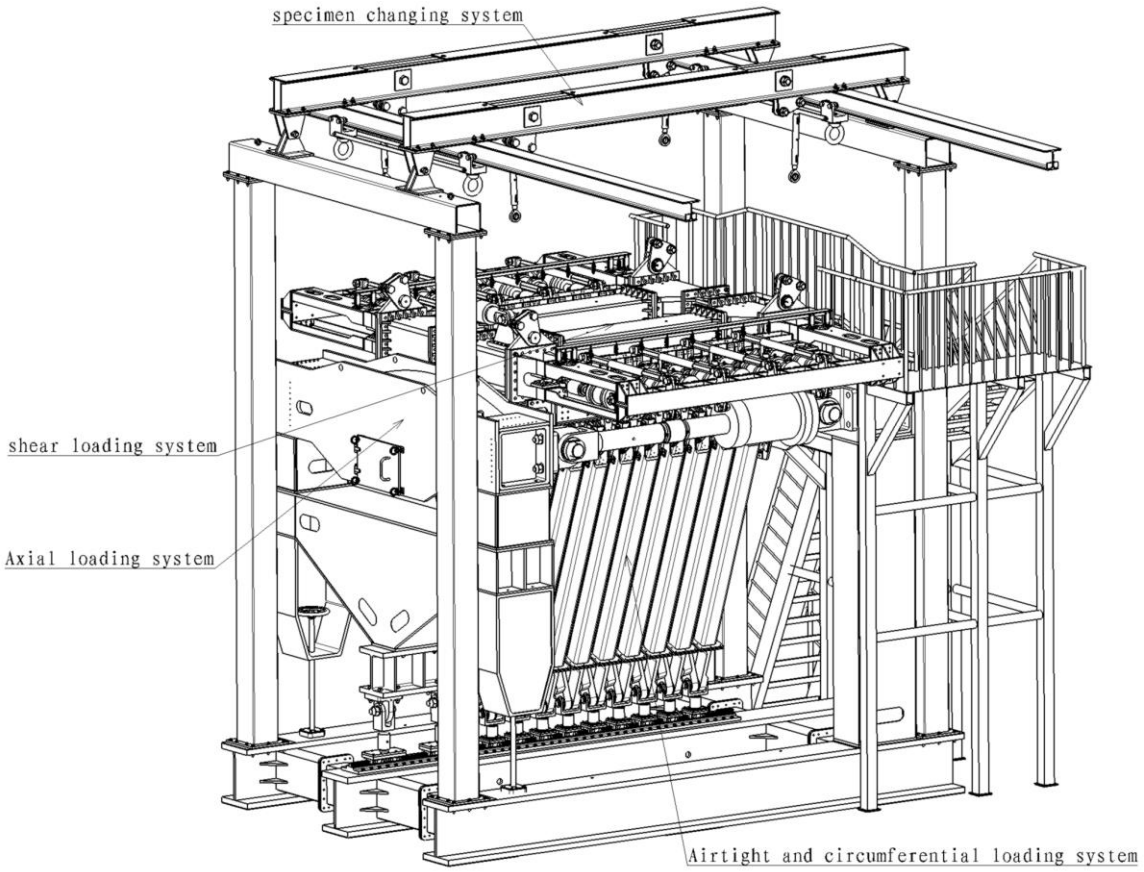

Fig.2 test device

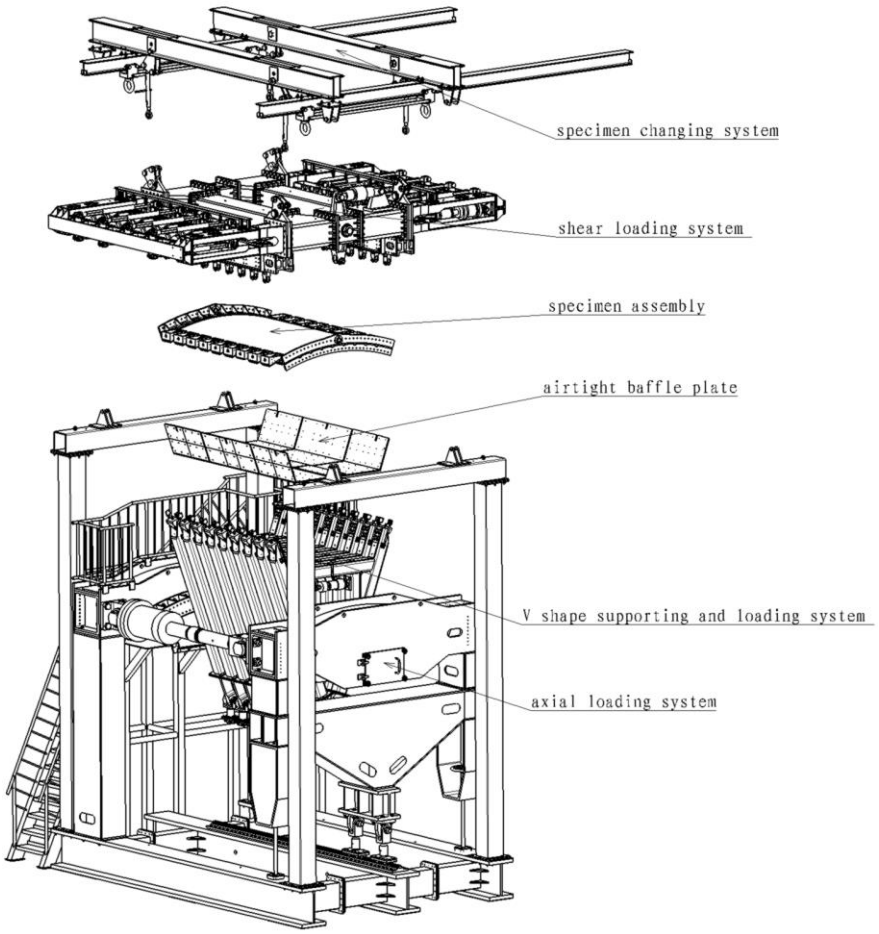

Fig.3 exploded view of the test device

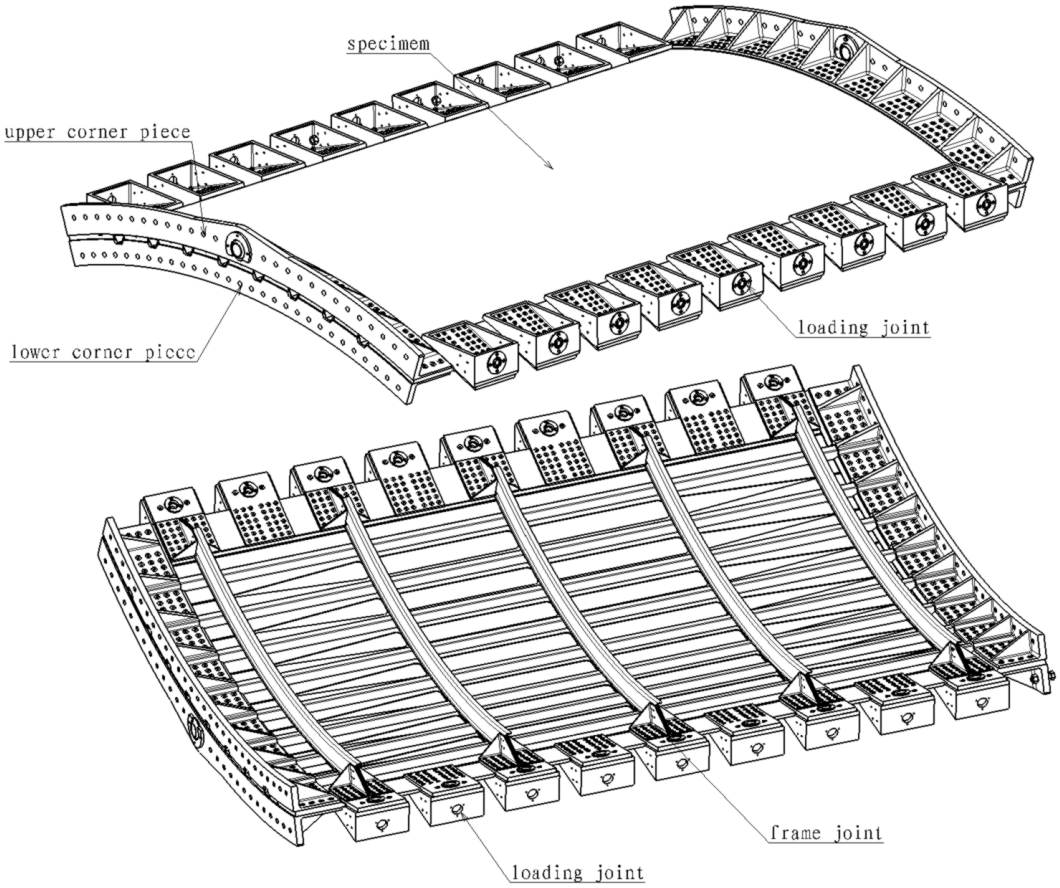

Fig.4 specimen assembly

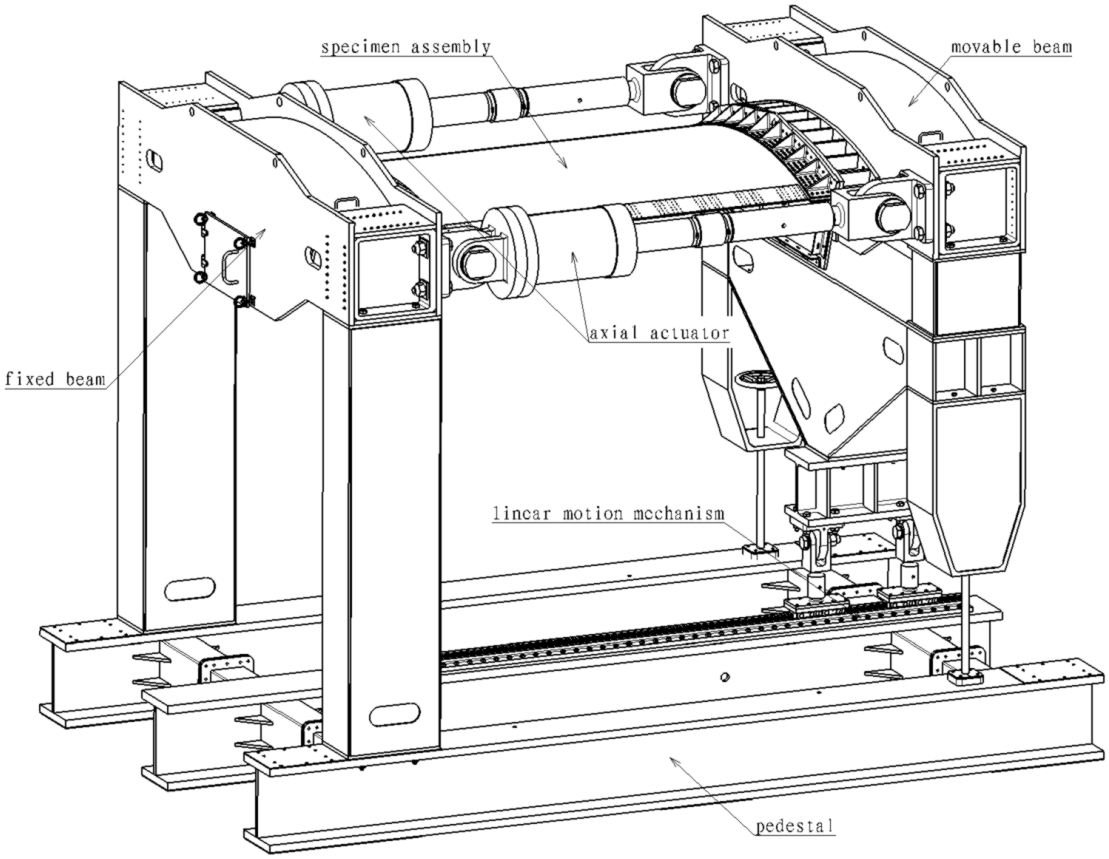

Fig.5 axial loading system

The basic idea of applying shear load is to use the self balancing frame to load on four sides respectively. As shown in Figure 6, the rear end of the shear frame is hinged with the corner piece at one end of the specimen assembly, and the front end is hinged with the other end of the specimen assembly through a swinging two-stage lever mechanism. Load sensors are installed on the lever. The oil circuits of all actuators in the loading units at both sides of the frame are in parallel, Apply shear force of equal size and opposite direction to two straight edges of the specimen. It can be seen from the connection relationship and the principle of moment balance that the specimen is subject to uniform shear force. In order not to limit the shear and axial displacement, each loading unit is designed as a two-stage lever mechanism with movable fulcrum and constant lever arm, which realizes the forward and reverse follow-up loading, as shown in Figure 7.

As shown in Figure 8, the two straight edges of the specimen are constrained by several V-shaped components. The rotation center of the V-shaped component is the center of the skin. An actuator is installed at the horizontal position in the middle of the V-shaped component to balance the circumferential force generated by the airtight load, and to open the V-shaped component without limiting the circumferential displacement of the specimen. The skin is always constrained to be cylindrical to prevent local warping and deformation at the joint, At the same time, all V-shaped components can slide along the axis without limiting the axial displacement of the specimen.

The airtight baffle on the V-shaped piece, the baffle at both ends and the specimen form a closed structure together, and the air bag is pasted inside to facilitate the application of airtight load. A pair of anti instability connecting rods are installed at the upper end of the V-shaped parts, which can effectively prevent the instability of straight edges.

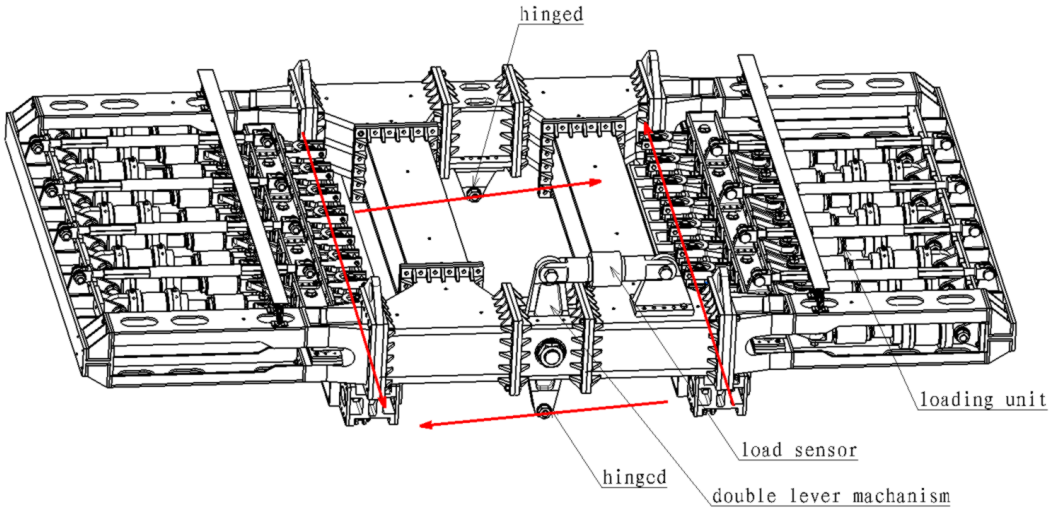

Fig.6 shear loading system

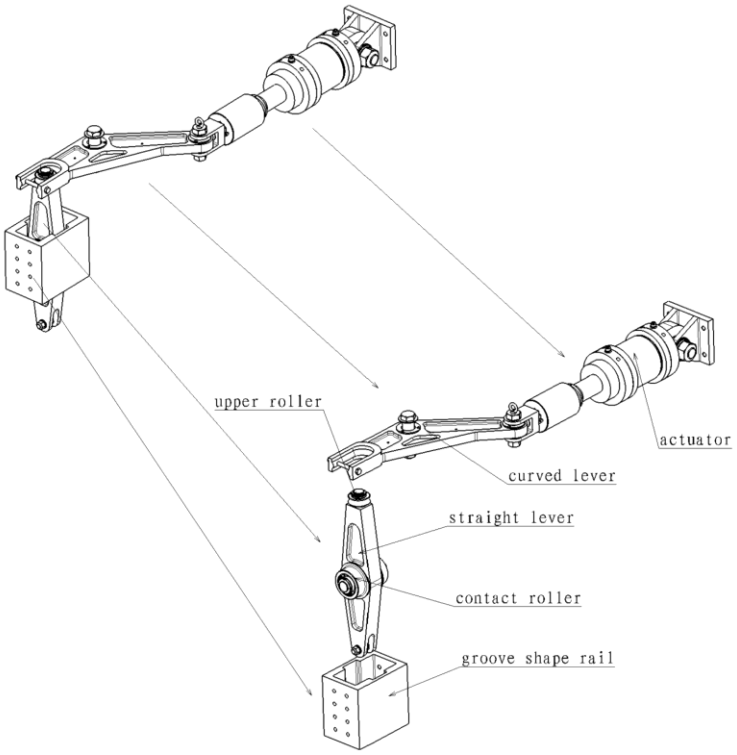

Fig.7 loading unit

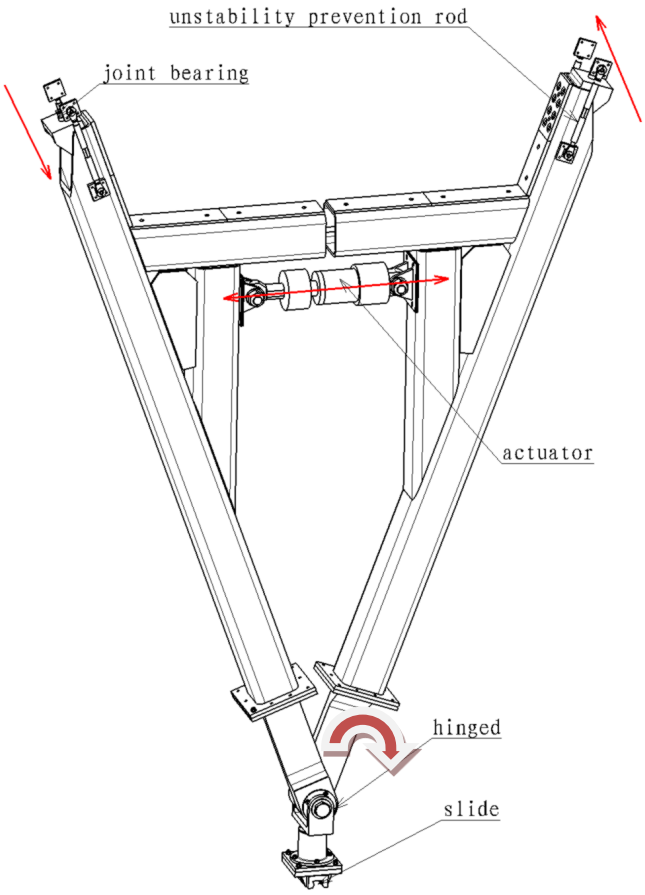

Fig.8 V-shaped component

3 Test measurement

A number of strain gauges are pasted in the assessment area of the specimen. See Figure 9 for the location and number of strain gauges.

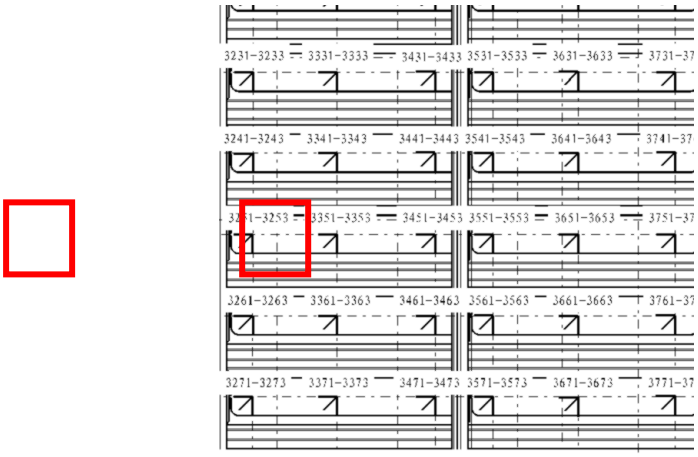

fig.9 sticking location and number of strain gauge

4 Test equipment

4.1 Loading control system

The coordinated loading control system developed by MOOG-FCS Company is used for the test loading control. The control error of the loading control system is less than 1%. The system can set the alarm of out of tolerance, out of limit, power failure and other faults according to the test requirements. The alarm limit and post alarm processing measures can be set as required, and the program, feedback, error and other data before and after the alarm can be saved according to the test requirements after the alarm.

4.2 Data acquisition system

The strain and displacement of the test are measured by the ST16 data acquisition system developed by Aircraft Strength Research Institute of China. The measurement error of the system is ± 0.5%, and the acquisition speed is 5000 points/second.

4.3 Instrument accuracy

See Table 3 for measuring instruments used in the test.

Table 3 Test Equipment and Measuring Instruments

Device name	Specifications	quantity	Allowable error/accuracy level
coordinated loading control system	32 channels	1	≤1%
Load sensor	200kN	1	0.3 level
Load sensor	2000kN	1	0.3 level
Load sensor	300kN		0.3 level
Load sensor	Z/1MPa	2	0.25 level
Precision digital pressure gauge	0.25MPa	1	0.4 level
Electric contact point pressure gauge	0.6MPa	1	1.6 level
ST16 data acquisition instrument	ST16/±20000με	2	±0.5%
Large range digital Dial indicator	0.01mm	1	0.01mm
Aviation DC stabilized voltage power supply	ZN24V40A*2	1	/
Pressure gauge	Y-100/40MPa	1	1.6 level
Ultrasonic A scanner	-	1	1 level

5 Test Results and Analysis

The compression load of - 265500N, the shear load of 287785N, and the air pressure load of 33.441KPa were taken to carry out the single load and composite load loading tests on the specimen. The test results are shown in Table 4 and Table 5. The repeatability error of multiple loading is within 1%, and the superposition error of the sum of strains under each single load and the strain under composite load is within 5%. The finite element analysis was carried out with the same load and constraint conditions, as shown in Figure10~ Figure13.The error between the test results and the finite element calculation results is within 10%，as shown in Table 6.

Table 4 Repeatability error

Strain number	The first strain	The second strain	error
1351	-796	-792	0.50%
1352	912	912	0.03%
1353	805	813	-0.97%
3351	-928	-920	0.85%
3352	926	922	0.48%
3353	730	729	0.08%
1651	-977	-982	-0.52%
1652	843	835	0.95%
1653	912	903	0.97%
3651	-891	-889	0.25%
3652	773	773	-0.04%
3653	811	810	0.16%
1351	-799	-792	0.84%

1352	906	912	-0.64%

Table 5 superposition error

Working condition / Stram number	composite	Compression	shear	airtight	superposition	error
1351	-792	-795	54	-28	-769	2.85%
1352	912	-172	968	128	924	-1.28%
1353	813	208	-35	625	798	1.85%
3351	-920	-793	-75	-20	-888	3.47%
3352	922	-168	908	135	875	5.09%
3353	729	183	-31	600	752	-3.12%
1651	-982	-782	-117	-45	-944	3.87%
1652	835	-186	951	105	870	-4.23%
1653	903	207	64	614	885	1.99%
3651	-889	-790	-39	-51	-880	1.02%
3652	773	-206	915	85	794	-2.78%
3653	810	210	-40	604	774	4.46%

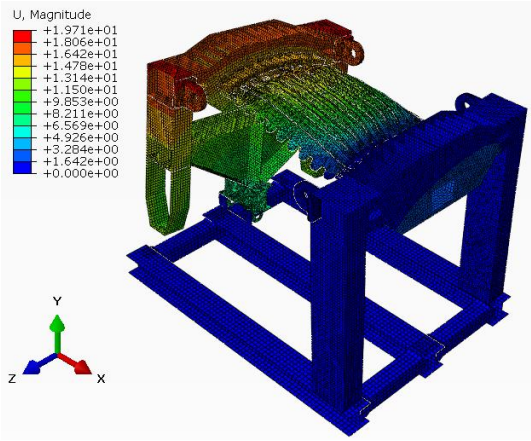

fig.10 test overall displacement diagram

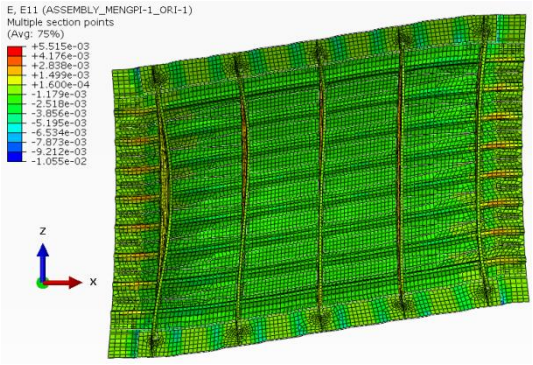

fig.11 Compression strain distribution diagram of specimen

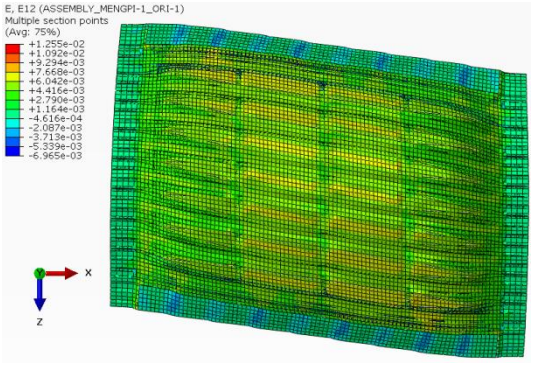

fig.12 shear strain distribution diagram of specimen

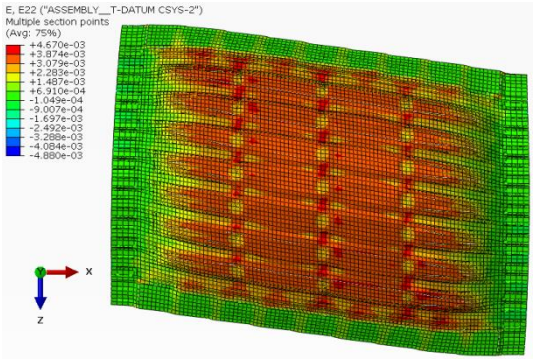

fig.13 Circumferential strain distribution diagram of specimen

Table 6 Error between test and finite element analysis

Strain number	test value	Analytical value	error
1351	-796	-828	3.82%
1352	921	981	6.15%
1353	805	780	-3.15%
3351	-928	-934	0.67%
3352	926	874	-5.91%
3353	737	751	1.88%
1651	-977	-1014	3.64%
1652	843	823	-2.41%
1653	912	933	2.22%
3651	-900	-940	4.25%
3652	765	737	-3.81%
3653	820	836	1.86%
1351	-799	-756	-5.62%
1352	897	841	-6.64%

6 Conclusion

From the above test results, the following conclusions can be drawn:
This technology can realize the loading of axial, shear and airtight loads. Each load is decoupled without interference, and the repeated loading is good.

References：

DONALD J. Baker combined load test fixture: NASA/TM-2010-216211[R]. Washington, D. C.: NASA, 2010.

OSTGAARD DOUGLAS R ; PATEL RAMANLAL A ; MCNEIL LEE A ; E-fixture:US2006101921A[P].2006-05-18

A test device capable of uniformly applying axial compression and shear loads.ZL 2012 1 0528616.7

WANG B W, CHEN X M, DENG F C, et al. Complex load test technology for aircraft panels: Review[J]. Acta Aeronautica et Astronautica Sinica, 2022, 43(3): 024987 (in Chinese).

P. Cordisco and C. Bisagni. Cyclic Buckling Tests of Stiffened Composite Curved Panels under Compression and Shear. 49th AIAA/ASME/ASCE/ AHS/ASC Structures, Structural Dynamics, and Materials Conference, 2008, Schaumburg.

CHAI Y N,DENG F C,LI C,et al A composite load test device for fuselage panel:CN104807694B[P]. 2018-01-30.

LI Z, WANG J, DENG F C, et al. Strength analysis and test verification of composite fuselage panels[J]. Acta Aeronautica et Astronautica Sinica, 2020, 41(9): 223688 (in Chinese).

ZANG W F,DONG D K,WANG J A A static/fatigue test fixture for complex load of large fuselage panel CN103149075A[P]，2015-01-28.(in Chinese)

Damage Evolution Analysis of C/SiC Composites under Biaxial Compression Based on Acoustic Emission

Jinpeng Yang[1,2], Leijiang Yao[2,], Zhiyong Tan[3], Bin Li[2], and Zelong Ma[1,2]*

[1]School of Aeronautics, Northwestern Polytechnical University, Xi′an, 710072, People's Republic of China

[2] National Key Laboratory of Science and Technology on UAV, Northwestern Polytechnical University, Xi′ an, 710072, People's Republic of China

[3]Science and Technology on Space Physics Laboratory, Beijing, 100076, People's Republic of China

Abstract—The damage behavior under complex stress condition is the key factor affecting the service performance of the thermal structure of hypersonic aircrafts. Acoustic emission was utilized to monitor the damage of satin braided C/SiC during biaxial compression tests. Pattern recognition of the acoustic emission signals was implemented by the principal component analysis and the fuzzy C-means clustering algorithm. The results showed that the damage evolution could be divided into 5 stages: (I) linear elastic stage with no damage occurs, (II) damage initiation with matrix cracking and delamination as main damage modes, (III) serious damage occurs with a large amount of delamination and fiber breakage events, (IV) all kinds of damage develop stably except fiber breakage, (V) last failure stage with active fiber breakage events.

Keywords: acoustic emission; C/SiC; biaxial compression; pattern recognition; damage evolution

1. INTRODUCTION

Carbon fiber toughened silicon carbide ceramic matrix composites (CMCs) have became candidates materials for the next generation of aerospace thermal structural components, which have exceptional high-temperature mechanical properties [1]. However, composites are typically subjected to multiple loads in actual working environments, which can lead to premature failure before reaching the ultimate load of the material [2,3]. Therefore, real-time online monitoring is necessary to understand the damage of C/SiC composites in complex stress states.

Acoustic emission (AE) is a nondestructive testing (NDT) technology, widely used for CMCs damage monitoring. Researchers have employed various pattern recognition methods [4] to cluster AE signals of CMCs during room temperature tensile tests [5,6], high temperature tensile tests [7,8], and low-velocity impact tests [9]. The damage evolution under different load conditions were illustrated by analyzing AE signal characteristics of different categories.

In this study, a biaxial compression tests of the satin weave stitched C/SiC composites were carried

out at room temperature. AE technique was used to monitor the damage of CMCs synchronously. The feature dimension of AE signal is reduced by using the principal component analysis (PCA) method [10]. The AE signals were clustered by the fuzzy C-means (FCM) clustering algorithm, which could characterize the damage process of C/SiC composites.

2. EXPERIMENTAL DETAILS

The specimen is a "cross" sample made of satin-woven weaved C/SiC composites manufactured by polymer impregnation and pyrolysis (PIP) process. The geometric dimensions of specimen are as follows: total length (L) = 150 mm, length of the holding section (W) = 50 mm, thickness (B) = 5 mm, and fillet radius of the transition zone (R) = 15 mm.

The test equipment is a vertical plane biaxial electro-hydraulic servo loading device made in Southeast University. The biaxial compression tests were conducted at room temperature under displacement control with a rate of 0.48 mm/min. The AE wide band sensors were attached to the sample to monitor the damage. The AE acquisition device parameters (PAC PCI-II) are preamplification gain 40dB, signal threshold 45dB, sampling rate 1MPS, bandpass filter 20-1200 kHz. Figure. 1 illustrates the damaged monitoring system.

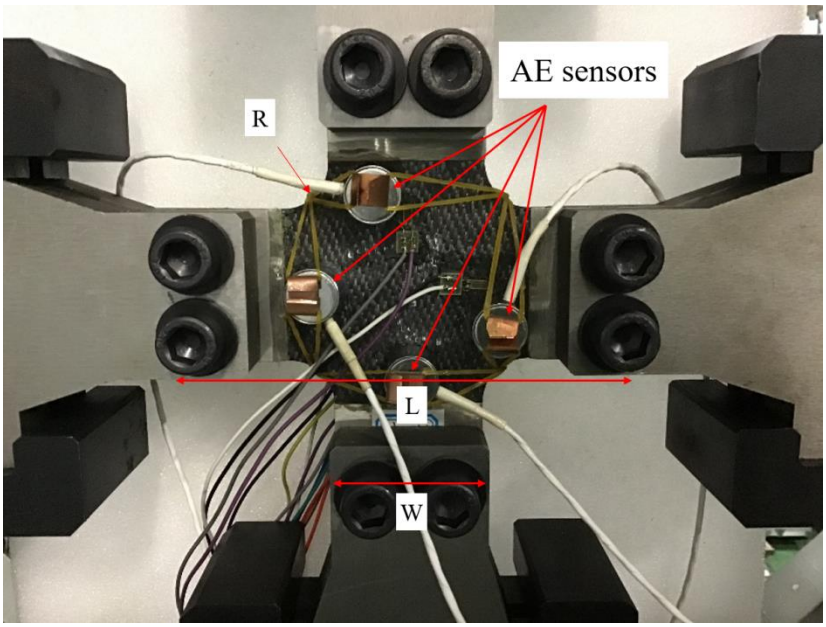

Figure 1 Damage monitoring system in biaxial compression test of CMCs.

3. PATTERN RECOGNITION TECHNIQUES

AE signals collected in the test process are analyzed by dimensionality reduction and feature extraction. 11 time-domain features (including AE rise time, AE count, AE energy, AE duration, AE amplitude, AE signal strength, AE absolute energy, AE average frequency, AE wave peak calculation frequency, AE inverse calculation frequency, AE initial frequency) and 2 frequency-domain features (including AE center frequency, AE peak frequency) were selected as the initial features of the AE signal data. The PCA method can reduce the dimensionality of AE signal data. By calculating the eigenvalue of the covariance matrix, the information contained in each dimension can be measured. Figure 2 illustrates the variance explained across these different dimensions. The cumulative contribution rate reaching 85% can represent all the information of the original AE signal based on the principal component selection. According to figure 2, the dimensions of data set were reduced to

6 by using PCA technique [10].

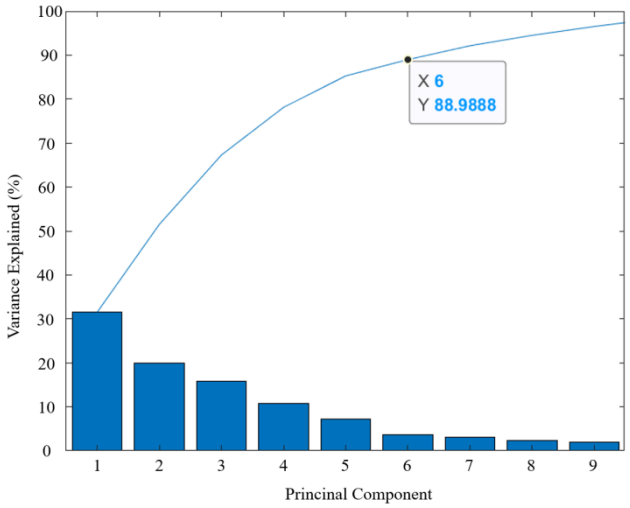

Figure 2 Variance explained with principal component.

After feature dimensionality reduction, AE signal data were clustered based on the FCM method [11]. The CH index, DB index and Silh index [12] were selected to assess the clustering results. Figure 3 shows the results of the various evaluation indicators. Based on the definitions of various evaluation indicators, the clustering effect is better if the CH index and Silh index are higher while the DB index is lower. According to the evaluation results, the features of AE signals were clustered into 4 signal types.

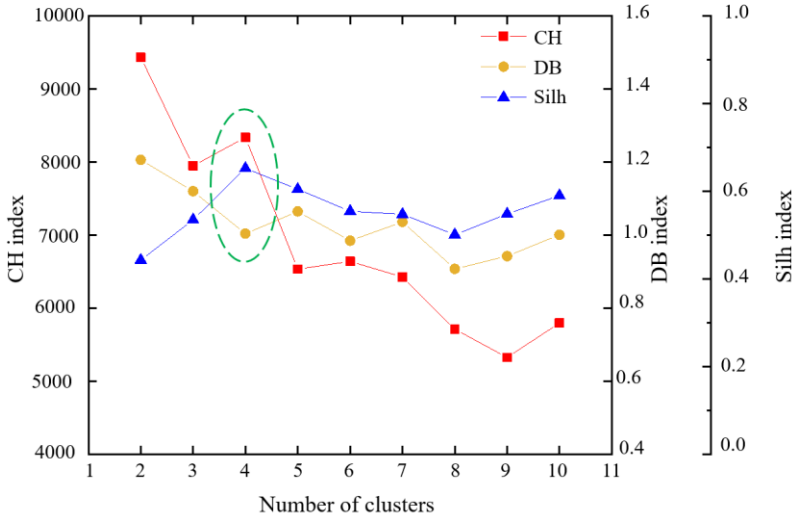

Figure 3 Number of clusters with different index.

4. RESULTS AND DISCUSSION

4.1 AE data clusters labelling

During compression testing of C/SiC composites, the SiC matrix often cracks under low stress due to its brittleness, resulting in a small amount of strain energy released by the material fracture. This characteristic corresponds to Class A signals, which have the lowest energy and average frequency. Therefore, the damage form corresponding to Class A signals is matrix cracking. Delamination, on

the other hand, is caused by relative sliding and friction between layers of materials. This type of damage typically produces AE signals with higher energy and frequency, consistent with the cluster center parameters of Class B signals. Class D signals have the highest energy and average frequency, indicating that this type of damage occurs in high stress states and typically involves a large number of fiber cluster fracture events. Therefore, the material damage form corresponding to Class D signals is fiber cluster fracture. The average frequency of Class C signals is high, but the difference between Class C and Class D signals is large, which does not conform to the AE signal characteristics generated by a small amount of fiber breakage. Combined with its low energy, the material damage form corresponding to Class C signals is interfacial damage. Table 1 shows the parameter value of each cluster center and the corresponding relationship between AE signals and damage types.

Table 1 The parameter value of each cluster center and damage form.

Clusters	Counts	Energy (mv·ms)	Amplitude (dB)	Average frequency (kHz)	Damage form
A	32	9	57	44	Matrix cracking
B	162	34	68	167	Delamination
C	90	19	63	103	Interfacial damage
D	248	71	73	246	Fiber cluster fracture

4.2 Damage evolution analysis

Combining the load data, cumulative AE energy (Figure 4) and cumulative AE events (Figure 5) during the biaxial compression process of C/SiC composites, the damage evolution process could be divided into 5 stages: (I), The material is in the linear elastic stage and there is almost no damage with little AE signals. (II), The elastic modulus of the material decreases, and the material initiates damage with matrix cracking and delamination as the main modes. At this point, the SiC matrix is the main bearing phase. (III), The elastic modulus increases, and a large number of fiber cluster fractures and delamination damages occur in the material. At this point, Carbon fibers become the main bearing phase. (IV), The elastic modulus of the material decreases again, and the internal damage of the material develops steadily, instead of the fracture damage of the fiber clusters. At this point, the SiC matrix becomes the main bearing phase again. (V), A large number of fiber cluster fracture damages occurred, and the material entered the final failure mode.

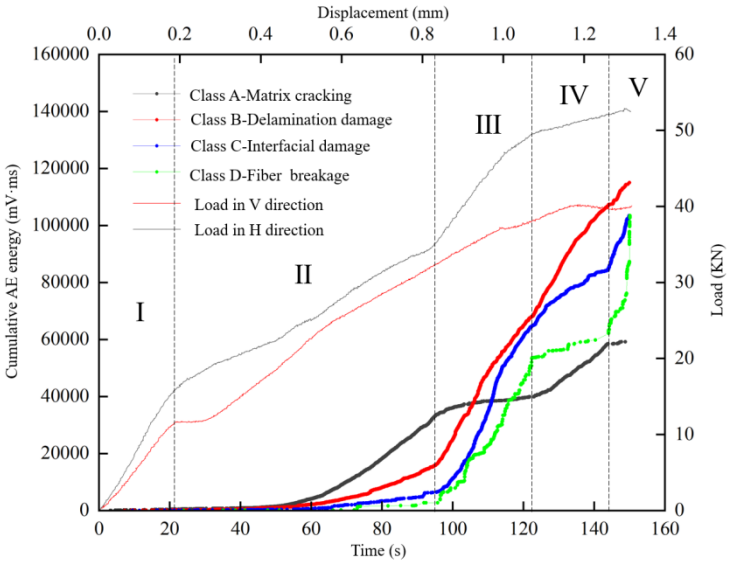

Figure 4 Cumulative AE energy with time

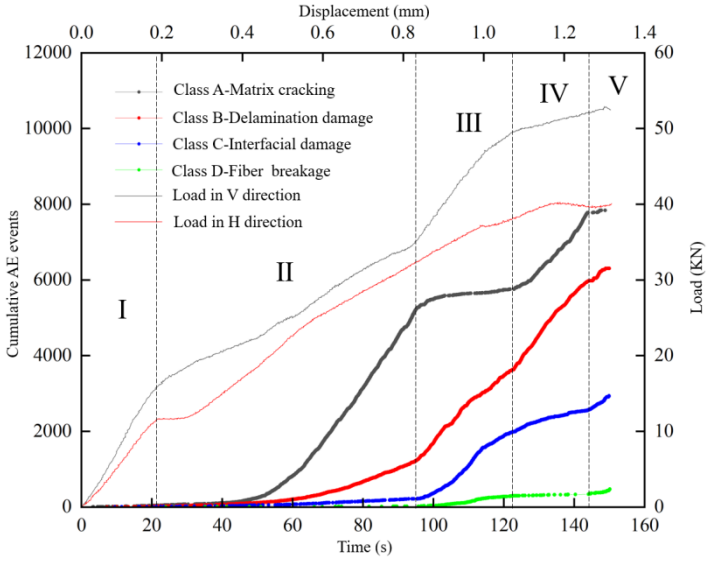

Figure 5 Cumulative AE events with time

By analyzing the internal damage evolution process of C/SiC composites under complex stress conditions, it has been revealed that the material undergoes an alternating loading process between the carbon fiber and the silicon carbide matrix. This finding provides a potential method for the failure warning of C/SiC composites under complex stress conditions in the future.

5. CONCLUSION

Through the application of the AE online monitoring technique and advanced pattern recognition methods, the damage mechanism and damage evolution of C/SiC composites are clearly identified during the biaxial compression process. The following conclusions can be drawn:

(1) AE technique can effectively monitor the damage of C/SiC composite under complex stress conditions. By extracting features and performing pattern recognition of AE signals, there are 4 types of damage occurs in C/SiC composite during the test: matrix cracking, interfacial damage, fiber cluster fracture, and delamination.

(2) Based on load data and AE data, the damage evolution of C/SiC composite under biaxial compression can be divided into 5 stages: (I) linear elastic stage, (II) matrix bearing stage, (III) fiber cluster bearing stage, (IV) damage stable develop stage, (V) final failure stage. Under complex stress conditions, C/SiC composites demonstrate an alternating load-bearing phenomenon between fibers and matrix.

REFERENCES

1. Hong Da, Zhang Tao, et al. Research and application status of C/SiC ceramic matrix composites[J]. Material guide, 16, 1-19, 2023.
2. Xu Cheng-hai, Meng He-song, et al. Mechanical behavior of three-dimensional woven carbon/carbon composites under biaxial compression[J]. Journal of Composite Materials, 29, 06, 206-211, 2012.
3. Chen Zhen, Fang Guo-dong, et al. Experimental study on biaxial tension of three-dimensional axially braided C/C composites[J]. Solid rocket technology, 38, 02, 267-272. 2015.
4. GODIN N, R'MILI M, REYNAUD P, et al. Identification of Damage Modes in Ceramic Matrix Composites by Acoustic Emission Signal Pattern Recognition[M]. 32, 2, 123-133, 2011.
5. Zhang Yong-zhen, Tong Xiao-yan, et al. Correlation between tensile strength of C/SiC and acoustic emission evolution[J]. Journal of Inorganic Materials, 49, 04, 666-672, 2021.
6. Zhang Yong-zhen, Tong Xiao-yan, et al. Acoustic emission pattern recognition of C/SiC tensile damage based on improved genetic algorithm[J]. Journal of Inorganic Materials, 35, 05, 593-600, 2020.
7. MORSCHERGN, MAILLETE. Nondestructive evaluation – use of acoustic emission for CMCs[J]. Comp Compos Mater II, 5, 308–324, 2018.
8. S. M, N. G, P. R, et al. Unsupervised and supervised classification of AE data collected during fatigue test on CMC at high temperature[J]. Composites Part A, 43, 2, 254-260, 2011.
9. Yao Leijiang, Lyu Peng, Bai Guodong, et al. Influence of low velocity impact on oxidation performance of SiC coated C/SiC composites[J], Ceramics International, 45, 16, 20470-20477, 2019.
10. ZhangBaoyin, Dong Ensheng, et al. Research on damage detection technique of composite material based on PCA-GA-RSPSVM[J]. Journal of Electronic Measurement and Instrument, 31, 9, 1402-1407, 2018.
11 PEIZHUANG W. "book-review"Pattern Recognition with Fuzzy Objective Function Algorithms. [J]. SIAM Review, 25, 3, 1983.
12. Zhang Yong-zhen. Damage identification of ceramic matrix composites based on acoustic emission’s deep learning[D]. Northwestern Polytechnical University, 2022.

Design and verification of multi-layer mechanical and thermal integrated composite plane structure

Zhang Long[*]*, Zhao Yunpeng*

Beijing Institute of Spacecraft System Engineering, China

Abstract: With the increasingly stringent requirements for thermal load-bearing and lightweight of structures in complex space missions, the mechanical & thermal integrated structure has attracted extensive attention. In this paper, a multi-level thermal integrated planar structure with a kind of "sandwich" structure composed of carbon fiber reinforced polymer (CFRP) composites panel and aluminum alloy honeycomb as the matrix, besides polyimide foam material as the main thermal bearing material was proposed. A mechanical and thermology coupling design method was adopted, which can match the heat bearing boundary of -170 ~ + 135 ℃ and achieve the vacuum thermal conductivity of the plane structure normal up to less than 1.0 w/ (m · K). Meanwhile the first-order frequency of the structure was not less than 70Hz. The method has been verified by thermal vacuum and vibration tests. The test piece had no deformation before and after the thermal vacuum test, and the normal vacuum thermal conductivity of the structure was tested as 0.52~0.88w/ (m · K); The structure had no damage before and after the vibration test, and the first-order frequency of the structure was 111hz. The test results showed that the integrated structural design method can realize the mechanical and thermal integrated design, furthermore the designed structure had process realizability, which has been applied to a spacecraft structural product already.

Keywords: sandwich structure; carbon fiber reinforced polymer (CFRP); polyimide foam; vacuum thermal conductivity.

1. INTRODUCTION

The traditional satellite structural plate was some kinds of honeycomb sandwich structure, thus carbon fiber reinforced polymer (CFRP) was selected as the material of the outer surface of the plate, but the thermal bearing capacity of the CFRP did not satisfy the operating temperature requirements of the solar cell array. Traditionally methods of thermal control were able to solve the deformation caused by the temperature cycle in-orbit. Liu presented a degradation modeling method for thermal control coatings to evaluate the influence of environmental factors for thermal control[1]. Due to the degradation in order to solve the thermal insulation problem between the solar cell sheet and the structure, thermal insulation material layers should be designed between the outer side plate and the solar cell sheet. Together with the honeycomb sandwich structure, it formed an integrated double sandwich structure, which was used as the mounting carrier of solar cells. A satellite utilized a body

mounted solar cell array. According to the requirements of the whole satellite mission, solar cells were pasted on the outer surface of the top and the other two plates. The in-orbit temperature of the structural plane where the solar array was located has been expected to be -160 ℃ ~ +115 ℃ under long-term conditions and -170 ℃ ~ +135 ℃ under short-term conditions. Jian indicated that a composite tube model based on a coefficient of thermal expansion (CTE) computed by presentative volume elements (RVE) was able to optimize composite structure of satellite under thermal-mechanical load[12]. Du proposed a platform to achieve thermal dimensional stability via providing near-zero coefficient of thermal expansion and isolating the residual thermal expansion by flexible structure connection to obtain the entire stability[13].

The principle for the design was to avoid the deformation of the thermal insulation material layer under the alternating load of the harsh high and low temperature environment, causing the deformation of the bearing part of the structural plate or the fracture of the grid panel. The thermal insulation material with low density, low modulus, low thermal conductivity and high and low temperature resistance should be selected. Through the screening of materials in the early stage, it was found that the polyimide foam material can meet the requirements of thermal and mechanical load at the same time[14]. Xiang studied that the structure flexible polyimide foams ranged with open cell ratio, which influenced the compression strength[15]. Liu compared with two kinds of foams prepared from aromatic dianhydride and isocyanate, while the thermal properties of the polyimide foam investigated by Fourier transform infrared spectroscopy (TG-FTIR) was thermally stable[16]. Wang has shown that bending strength of polyimide matrix composites was affected by various phases[17]. Therefore, an integrated structure based on polyimide foam was constructed. Configuration of integrated sandwich structure was shown in Figure 1. Due to the low modular of polyimide foam, it was necessary to design a thick layer for improve the stiffness of integrated structure. Andrews investigated that open-cell foams with hollow struts and solid strut foam to confirm that the Young's modulus and plastic collapse were relevant to power law creep deformation[18].

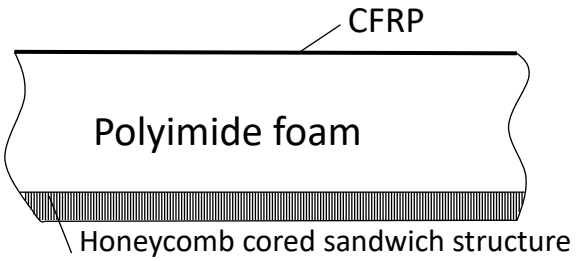

Figure 4. Schematic diagram of integrated structure

In this paper, in view of the requirements of super static and super stable structure of a certain satellite model, a body mounted solar cell array was adopted. It existed a large amount of heat exchange between the battery array and the structure. In order to meet the requirements of the thermal and mechanical environment of the structure, it was necessary to solve the heat insulation and support requirements between the structure and the solar cell array. The thermal and mechanical properties of polyimide foam sandwich structure were designed and verified by using polyimide foam as the base material. Finally the mechanical & thermal performance of the integrated structure has been evaluated by components using standard tests.

2. Integrated structural design

The parameters of the integrated structure were designed, including two aspects: thermal and mechanical loading. (1) The thermal design and analysis were carried out according to the extreme temperature working condition of -170 ℃ ~ +135 ℃. The integrated structural plate was decomposed from the material level and the component level to form the following thermal control technical indicators: the vacuum thermal conductivity (λ) in the normal direction of the insulation support integrated structure was less than 1.0 W / (m • K); The scaled down parts of space environment protection structure meet the common requirements of industrial devices (- 40 ℃ ~ 85 ℃); (2) According to the stiffness requirements and frequency distribution of the satellite structure, the fundamental frequency of the integrated thermal insulation support structure was allowed more than 70 Hz.

According to the requirements of environmental temperature of the integrated structure, and considering the heat insulation effect and process feasibility, three kinds of polyimide foam honeycomb sandwich structure configuration schemes were proposed. Specific parameters were listed in Table 1. In the table, it figures out that Scheme 1 was relatively optimal and adopted as the configuration design of the integrated structure.

Table 4. Integrated structure configuration scheme

Scheme	Design results (area ratio of polyimide foam to structural plate)	Temperature fluctuation (inside the structural plate)
1	100%	ΔT = ±15℃
2	55%	ΔT = ±12℃
3	4%	ΔT = ±7℃

2.1 Thermal design and analysis

On the basis of configuration design, by comprehensively comparing the thermal and mechanical stability of polyimide foam, multi-layer insulation components and aerogel, the thermal insulation scheme of structural outer panel with polyimide foam honeycomb sandwich was selected. In order to achieve the required thermal insulation effect (temperature fluctuation: $\Delta T \leq \pm 5$ ℃ / rail), and to consider the structural stability and spacecraft weight reduction requirements, the polyimide foam thickness of sandwich structure needed to be comprehensively considered.

Firstly vacuum thermal conductivity was determined as the key parameter of polyimide foam. The sensitivity analysis of the vacuum thermal conductivity of polyimide foam was carried out according to the analysis of 0.05 W / (m · K) and 0.01 W / (m · K). The selection of working conditions and the analysis results were shown in Table 2. It can be seen that this parameter has a great impact on the temperature stability of honeycomb structural plates, and the temperature fluctuation difference was about 40% ~ 60%.

The vacuum thermal conductivity of polyimide foam was tested in the full use temperature range according to the actual process composite state of the polyimide foam. The measured results were shown in Table 2. It can be seen that the vacuum thermal conductivity of the foam varies with temperature (λ = 0.0026 W / (m · K) @ - 170 ℃, λ = 0.018 W / (m · K) @ 25 ℃, 0.042 W / (m · K) @ 135 ℃). This result can be used as the basis for the thickness design and analysis of polyimide foam.

Table 5. Thermal conductivity of polyimide foam in vacuum

Temperature / Pressure	-170℃/10^{-3} Pa	25℃/10^{-2} Pa	135℃/10^{-2} Pa
λ（W/(m·K)）	0.0026	0.018	0.042

Considering the requirements for temperature stability of honeycomb structural plate (≤ ± 5 ℃ / rail), the foam thickness of the integrated thermal insulation support structural plate was determined to be more than 40 mm. Based on the determined integrated structural plate configuration (foam & honeycomb structure) and the designed thickness (40mm), the vacuum thermal conductivity in the vertical direction can be obtained through the analysis of one-dimensional composite based on wall thermal resistance combined model, taking into account the vacuum thermal conductivity of polyamide foam in different temperature ranges. The specific design and analysis results of the vertical vacuum thermal conductivity varied from 0.54 W / (m · K) ~ 0.92 W / (m · K).

The analysis results of the test pieces under high and low temperature in the typical conditions were shown in Figure. 2. From the analysis results, it can be seen that the inner temperature was -37 ℃ ~ 37 ℃, which satisfied the requirements of industrial devices (- 40 ℃ ~ 85 ℃). Based on the above thermal analysis results, it showed that the vertical vacuum thermal conductivity of the integrated structure and the thermal insulation effect of polyimide foam realized the requirements.

Based on the above thermal analysis results, it shows that the vertical vacuum thermal conductivity of the integrated structure and the thermal insulation effect of polyimide foam meet the requirements.

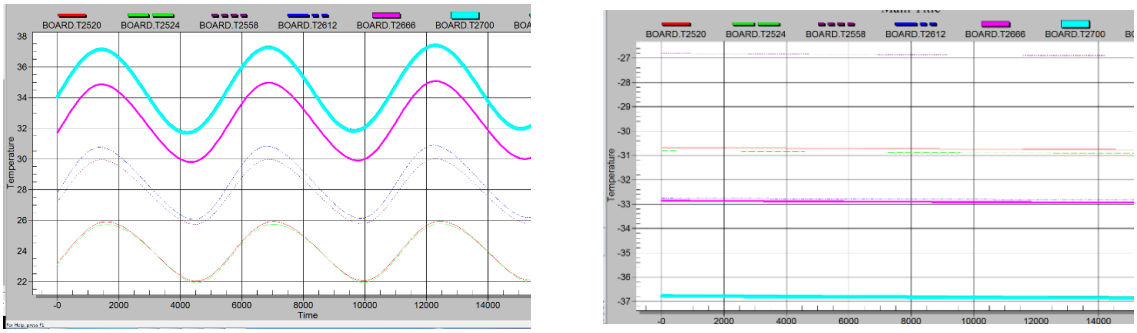

(a) Temperature in the condition of β = 73°　　(b) Temperature in the condition of β = 90°

Figure 5. Analytical results of internal and external temperature of test pieces (β was for working state of satellite)

2.2 Mechanical design and analysis

According to the configuration requirements of Scheme 1 in Table 1 and parameters of the polyimide foam listed above, the stiffness requirements of the integrated structure with the fundamental frequency not less than 70 Hz were satisfied in combination with the mechanical and thermal deformation requirements. It was determined that the polyimide foam sandwich structure adopted the structural form of sticking polyimide foam and carbon fiber panel outside the carbon fiber honeycomb panel.

In order to meet the thermal deformation and load bearing requirements of the integrated structure, high modulus fiber (M55J) was selected as the skin fiber of the integrated structure; The two layers of honeycomb sandwich structural plate adopted the same ply angle, that was, $[0\ °/\pm 45\ °/\pm 15\ °/90\ °]_s$, with a single layer thickness of 0.08mm and a total thickness of 0.96 mm; In order to ensure the optimal thermal performance of the outermost skin of the integrated structure (the skin bonded with solar cells), the lamination sequence of $[0\ ° / 60\ ° / -60\ °]_s$ was adopted. (The 0 ° direction was the

long side direction of the integrated structure).

According to parameters measured by the mechanical properties test of polyimide materials, the mechanical properties of polyimide sandwich structures were analyzed. In the principle that the larger the area of the test piece, the smaller the foam thickness, and the higher the fundamental frequency, it was determined that the size of the test piece was 500 mm × 500 mm × 62 mm (length × width × height), wherein the thickness of foam layer was 40mm. The foam modulus adopted the measured performance of the material (Young's modulus was 0.2 MPa, Poisson's ratio was 0.3, density was 6.5 kg/m^3). The boundary constraint condition was the fixed support constraint of the bottom surface. The fundamental frequency mode was shown in Figure 3. The transverse fundamental frequency was 117.9 Hz and the longitudinal fundamental frequency was 216.8 Hz, which met the stiffness requirement of not less than 70 Hz. Since the mechanical properties of polyimide foam material were less than those of honeycomb panel structure, the main mode was the deformation of polyimide foam layer.

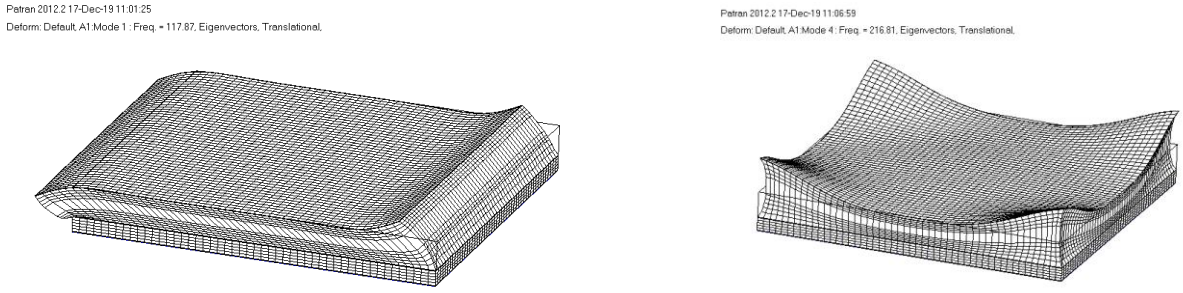

(a) The transverse vibration (b) The longitudinal vibration

Figure 6. Vibration mode of integrated structure

2.3 Summary

Based on the thermal mechanical coupling design and analysis results, the vertical vacuum thermal conductivity of the integrated structure and the thermal insulation effect of polyimide foam meet the requirements, and the stiffness of the integrated structure meets the requirements. Since the foam material was fragile and its edge and surface strength were less than the internal strength, a layer of polyimide tape was wrapped on the side wall of the integrated structure to improve the strength of the overall structure.

3. Test verification

In order to verify the design of polyimide foam sandwich structure and evaluate its mechanical and thermal characteristics, mechanical and thermal environment tests of polyimide foam sandwich structure were carried out. The test pieces were polyimide foam sandwich panels.

3.1 Mechanical test verification

There were four test pieces in total. The size of the test pieces was 500 mm x 500 mm x 102 mm, 900 mm x 600 mm x 62 mm, and the thickness of foam was 40 mm and 80 mm. And solar cells were pasted on the surface of the test pieces. Pieces were screwed to the test-bed to ensure that the fundamental frequency of the tooling was greater than 150 Hz. It was listed in Table 3 for summary of test pieces.

Table 6. Summary of test pieces

No.	Size(Length x Width x Height) / mm	Thickness of foam / mm	Hole	Covering
1.	500 x 500 x 102	80	Yes	No
2.	500 x 500 x 102	80	Yes	No
3.	900 x 600 x 62	40	No	Yes
4.	900 x 600 x 102	80	No	Yes

Each piece shall be subject to random and sinusoidal tests. Each test included two conditions: transverse and longitudinal (vertical panel). There were a total of eight working conditions for the test piece. A sinusoidal test (0.5g) shall be conducted before and after each single test condition. The test shall be conducted in the sequence of transverse sine, transverse random, longitudinal sine and longitudinal random.

The characteristic level sinusoidal vibration responses of test pieces 1 and 2 were shown in Figure 4 and Figure 5 (only listed the results of piece No.1 and No.2 because of the similarity of results). The vibration response of test pieces was low before 100Hz, which met the requirements of the product on the satellite. The longitudinal fundamental frequency of test piece No.1 (holing) was about 200 Hz, and the transverse fundamental frequency was 165 Hz. The longitudinal fundamental frequency of test piece No.2 was about 260 Hz, and the transverse fundamental frequency was 168 Hz. It can be seen from the figures that the characteristic curve of the test piece matched well before and after the test, indicating that the stiffness of the integrated structure has not changed.

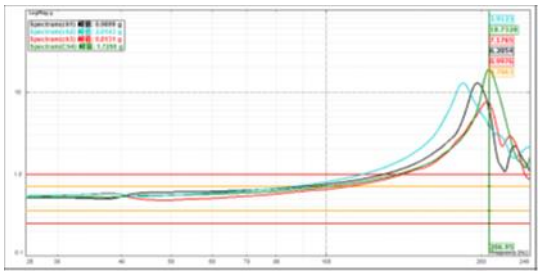

(a) Sinusoidal vibration response of longitudinal characteristic level

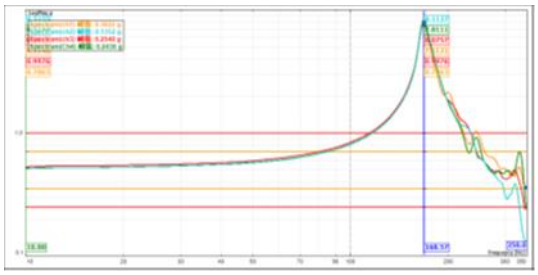

(b) Sinusoidal vibration response of transverse characteristic level

Figure 7. Characteristic level sinusoidal vibration response curve of test piece No.1

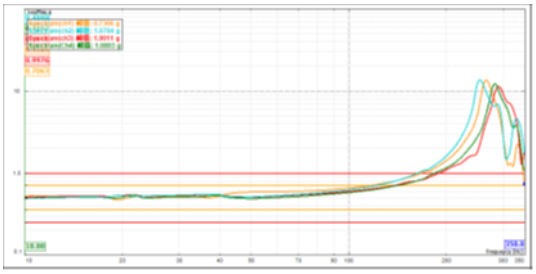

(a) Sinusoidal vibration response of longitudinal characteristic level

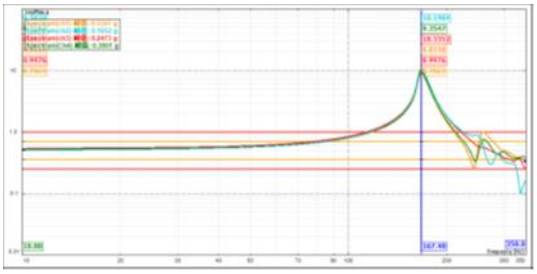

(b) Sinusoidal vibration response of transverse characteristic level

Figure 8. Characteristic level sinusoidal vibration response curve of test piece No.2

The test value of test piece No.1 was compared with the analysis value, in which the test value was 111 Hz and the analysis one was 80 Hz when it has not been covered. The analysis value was conservative. Compared with test pieces No.1 and No.2, the fundamental frequencies of test pieces

with or without hole were about 200 Hz and 260 Hz in the longitudinal direction and 165 Hz and 168 Hz in the transverse direction. The basic frequency of the test with or without covering was 168 Hz and 111 Hz respectively, which showed that covering the test piece around with polyimide tape can significantly improve the stiffness of the test piece. When the foam thickness was 40 mm and 80 mm respectively, the transverse fundamental frequency was 265 Hz and 165 Hz respectively, indicating that the thicker the foam thickness, the lower the stiffness.

3.2 Thermal test verification

In order to verify the feasibility of polyimide foam sandwich structure molding process and battery array patch process, verify the vacuum resistance of polyimide foam sandwich structure, expose the defects of materials and manufacturing process, several thermal vacuum tests were conducted with 3 pieces in total. And test conditions was listed in Table 4.

Table 7. Summary of thermal vacuum test conditions

Item	Pressure /Pa	Temperature /℃	Number of cycles	Temperature change rate /℃/min	Holding time/h
Value	$\leq 6.65\times10^{-3}$	-180 / +145	6.5	≥1	4

The installation state of the test piece in the vacuum tank was shown in Figure 6. The test pieces were connected with the tooling through two holes for releasing the lateral degrees of freedom. The temperature on both sides of the test piece was controlled respectively. After 1.5 cycles of the program, it stopped to visually checking the appearance. While there was no obvious change, it is continued to complete the cycles.

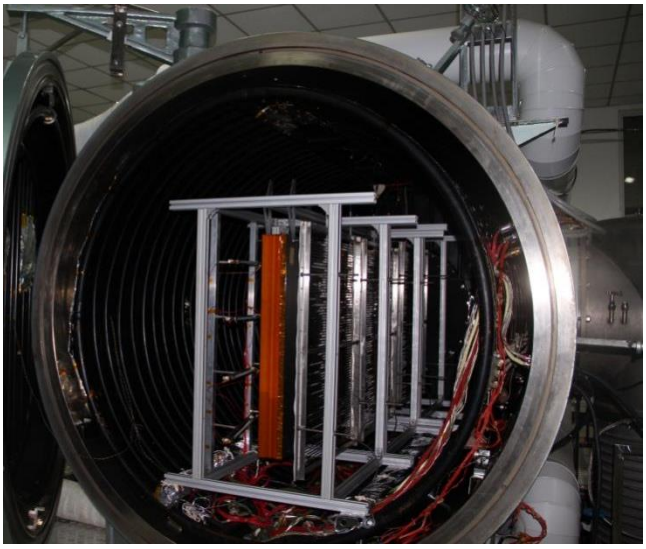

Figure 9. Status before thermal vacuum test

The surface of the test piece was visually inspected, and there was no obvious change before and after the test. The temperature record values of each temperature measuring point under high and low temperature thermal test conditions were shown in Figure 7 (Red symbols were for sensors on inner side while black ones were for sensors on the other side). The inner side temperature of the plate is 18 ℃ ~ 36 ℃ under high temperature conditions and -26 ℃ ~ -13 ℃ under low temperature conditions. The thermal insulation effect satisfied the requirements (-40 ℃ ~ 85 ℃). The vertical vacuum thermal conductivity of the insulation support integrated structural plate calculated based on

the modified thermal analysis model of the test results was 0.52 ~ 0.88 W/(m · K), which can fulfill the index request (vertical vacuum thermal conductivity was less than 1.0 W/(m · K)).

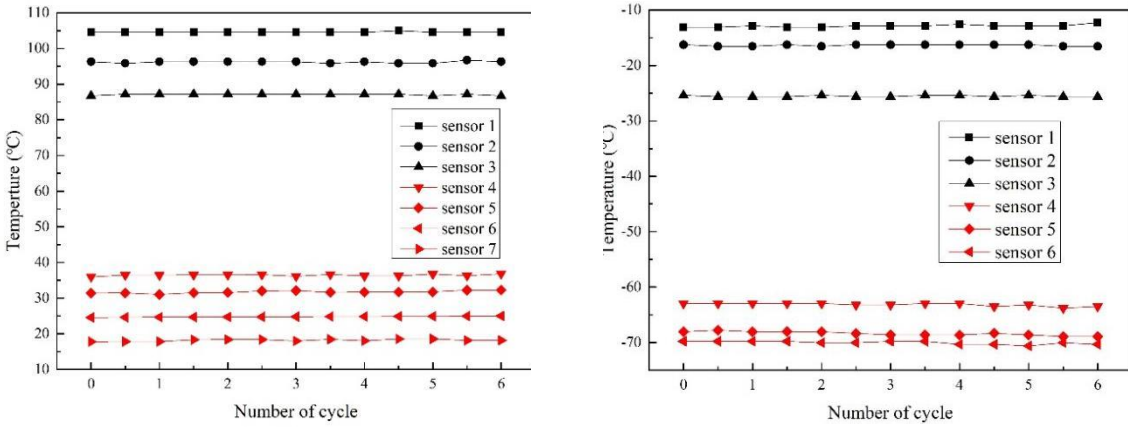

(a) High temperature (b) Low temperature

Figure 10. Temperature record of inner and outer side of test piece

3.3 Summary

After the mechanical tests, the products were checked, and every single product was not significantly damaged. The characteristic level was well overlapped before and after the qualification level test, and the battery chip did not fall off or break, indicating that the product met the mechanical requirements, and the design method and manufacture was feasible. There was no obvious change in the test pieces before and after the thermal vacuum test,, which proven that the integrated structure can withstand the thermal environmental load required and met the deformation requirements of the thermal load; The vertical vacuum thermal conductivity of the integrated structure calculated by the modified thermal analysis model based on the test results fulfilled the requirements.

4. CONCLUSION

Aiming at the contradiction that the honeycomb sandwich structure of the traditional satellite can not satisfy the temperature requirements of the mounted solar array, it proposed an integrated thermal insulation support structure based on polyimide foam material, raised the thermal and mechanical design methods of the integrated structure, and verified that the integrated structure fulfilled the requirements of thermal and mechanical load through simulation analysis and environmental testes. The main conclusions of this paper are as follows:

1). The integrated sandwich structure composed of polyimide foam and honeycomb sandwich structure bore the thermal and mechanical load of the satellite in-orbit;

2). The thickness of foam material was the main factor affecting the thermal insulation performance of the integrated structure, and was a critical factor affecting the structural stiffness;

3). The lateral stiffness of the integrated structure can be improved by using polyimide tape to cover the side of the integrated structure;

4). Due to the influence of factors such as foam material dispersion and process implementation deviation, the thermal conductivity of the integrated structure had a certain deviation from the calculated value.

REFERENCES

1. T. Y. Liu, Q. Sun, J. R. Meng, et al. " Degradation modeling of satellite thermal control coatings in a low earth orbit environment." *Solar Energy*, 139, 467-474, 2016.
2. M. A. Jian, H. Zhang, L. Yan, et al. "Thermal-mechanical Optimizing Analysis on Multi-scale Numerical Model for Composite Structure of Satellite." *Chinese Space Science and Technology*, 4, 22, 14-22, 2015.
3. Z. C. Du, M. R. Zhu, Z. G. Wang, et al. "Design and application of composite platform with extreme low thermal deformation for satellite. " *Composite Structures*, 152, 693-703, 2016.
4. E. S. Weiser, T. F. Johnson, T. Clair, et al. "Polyimide Foams for Aerospace Vehicles." *High Performance Polymers*, 12, 1, 1-12, 2000.
5. A. M. Xiang, Y. Li, L. W. Wei, et al. "Thermal degradation and flame retardant properties of isocyanate-based flexible polyimide foams with different isocyanate indices." *Thermochimica Acta*, 652, 160-165, 2017.
6. X. Y. Liu, M. S. Zhan and K. Wang. "Thermal properties of the polyimide foam prepared from aromatic dianhydride and isocyanate." *High Performance Polymers*, 24, 5, 373-378, 2012.
7. L. P. Wang, T. Zhang, L. Zhang, et al. "Thermostability, mechanical and tribological behaviors of polyimide matrix composites interpenetrated with foamed copper." *Transactions of Nonferrous Metals Society of China*, 26, 2336-2346, 2016.
8. E. W. Andrews. "Open-cell foams with hollow struts: Mechanical property enhancements." *Materials Letters*, 60, 5, 618-620, 2006.

Application of Impulse-cyclone Airflow Drying in Wood-based Composites

Feng Chen [1 *] *, Xinghua Xia* [1,2]

1. Taizhou University

2. Universiti Malaysia Kelantan

Abstract: Wood fiber/wood flour drying is an important pretreatment process of wood-based composites. The current drying methods are characterized by long drying time and high energy consumption, which do not conform to the strategic decision of developing low-carbon economy and sustainable industrialization in China. In this paper, the new features of the development of impulse-cyclone airflow drying equipment were discussed. The feasibility of using this technology as a new type of heat treatment energy-saving and environmental-friendly equipment was outlined in the industry, and case studies were conducted. The artificial neural network model was used to predict the drying water content of wood flour, and the CFD model was used to continue the optimization of the equipment to improve the drying efficiency. Finally, the future research directions are prospected and discussed.

Keywords: Impulse-cyclone Airflow Drying; Wood-based Composites; Wood flour; Moisture Content; Optimization

1.Problems in Wood Fiber Drying

Wood fibers or wood flour, as a well-known fast-growing natural material, have been used in biomass power generation, papermaking, construction, and wood fiber-plastic composites (WPCs) in China[1-3]. Despite having a natural network structure, abundant surface-active groups, excellent mechanical properties, good biocompatibility, and environmentally friendly characteristics, poplar fibers have strong hydrophilicity to cause agglomeration[4-7]. In addition, drying is a process of pretreating the fibers to remove the excess moisture from the cell wall and cell cavity of ground wood fibers[8].

Wood fiber drying is also a link with the most energy consumption of wood product processing equipment [9]. The energy consumption of wood fiber drying equipment accounts for 45% - 60% of the total energy consumption of product processing, and the wood fiber drying efficiency is low [10]. China will take reducing carbon emissions of China's industry and energy sector as the key task during the 14th Five Year Plan period. The traditional fiber drying methods will be gradually eliminated or transformed, and a low energy consumption, fast and environmentally friendly drying technology that makes wood fibers highly dispersed will be explored, which meets the requirements of today's efficient utilization of biomass

resources and the development of low-carbon circular economy [11]. Impulse cyclone high temperature airflow drying technology can use high temperature airflow to quickly complete the drying of wood fibers, which will be one of the ideal methods to ensure the drying quality of wood fibers [12].

1.1 Wood fiber drying technology and application status

The traditional methods of wood fiber drying include hot air circulation oven drying, drum drying, tube airflow drying, infrared radiation drying and microwave drying. Hot air circulation oven drying is a commonly used wood fiber drying method for research and enterprises [13]. This drying method has simple process operation and low technical requirements, but it has a long drying time, high energy consumption and large temperature difference in the box body, resulting in uneven final moisture content of materials. In the drum drying method, wood fibers are put into a drum dryer for drying. This drying method has a long drying time, generally 6h-8h, and high drying energy consumption. Tube air drying is the earliest method of wood fiber drying. In the late 1980s, a two-stage straight pipe drying process was developed on the basis of the original single-stage wood fiber drying equipment [14]. This process has played a significant role in improving the wood fiber drying quality, density board performance, and heat efficiency. However, this method occupies a large area and costs a lot [15]. The drying time of infrared radiation is short. This drying method transfers heat directly to the particle surface through the infrared generator, without directly heating the air [16]. Microwave drying refers to the direct action of penetrating particles on the interior of the object to be dried. But infrared radiation drying and microwave drying are seldom used in wood fiber drying because of their high cost.

At present, the research focuses on the selection of drying medium, energy saving utilization, and improvement of drying equipment[17]. For example, Meunier, Rasmuson, and Tong used high-temperature superheated steam as the convection drying medium to study the pipe type, drying temperature, flow rate, particle size, and the impact on the drying process of superheated steam, it can effectively reduce the size of drying equipment, and has obvious drying effect for drying non heat sensitive substances [18]. At the same time, increasing the pressure can reduce the drying time of materials and effectively play the role of superheated steam. These scholars also simulated the superheated steam drying of sawdust. For the improvement of drying equipment, scholars at home and abroad focus on improving drying efficiency and reducing energy consumption by using combined airflow drying system Vogt. The drying time and energy consumption can be reduced by improving the drum drying method to dry wood flour [19]. The basic principle is that infrared heating generator is equipped in the lower length direction of the horizontally

rotating drum, and the moisture content of materials is controlled by the drum rotation speed and infrared heating. The energy consumption can be reduced from 48% - 56% to 30%. Nimmol C et al. [20] studied the combined use of impinging stream and other dryers, and the drying characteristics of single-stage impinging stream and multi-stage dryer for materials. The results showed that the water content of single-stage impinging stream multi-stage drying could be rapidly reduced compared with single-stage impinging stream drying. Lin Jinna et al. [21] used the impinging stream drying method to effectively improve the dispersion of bamboo fiber.

According to the current situation and development trend of fiber drying equipment, the traditional wood fiber drying technology consumes more energy and has low drying efficiency. New drying technologies have developed to a certain extent with their respective applications. However, the key technical problems such as large equipment area, high energy consumption and poor dispersion of drying materials have not been completely solved.

1.2 Mechanism and Application Status of ICAD

ICAD is a new drying method being studied. Its basic principle is the combination of pulse airflow dryer and cyclone dryer. Materials are added to the pulse airflow dryer by the spiral feeder. After entering the straight pipe, the materials are accelerated by the airflow. When passing through the pulse pipe, the air velocity in this part becomes smaller due to the sudden expansion of the pipe diameter of the pulse pipe, at this time, the material continues to move due to inertial action, making the material speed greater than the air inlet velocity. When the material gradually decelerates, it moves to the next straight pipe section for accelerated motion. In the straight pipe to pulse pipe to straight pipe, the acceleration to deceleration to acceleration motion alternates the above motion process, which expands the relative speed and heat transfer area between the hot air flow and the fiber material, improves the heat and mass transfer rate, and can remove free water and some combined water. After entering the cyclone dryer, when the hot air carries the material in the tangential direction, the hot air rotates downward along the inner wall of the cyclone dryer, and the material rotates along the inner wall until it moves to the bottom of the dryer due to centrifugal force and gravity. There is an inner tube near the bottom. When the material moves to the inner tube, it is taken out of the cyclone dryer by the inner tube, The advantage of the cyclone dryer is that the difference between the material and the air inlet speed is large due to the gravity and centrifugal force. At the same time, the rotary movement results in an increase in the drying heating area, an increase in the movement distance of the material in the cyclone dryer, which can reduce the floor area, strengthen the heat transfer process, remove

the combined water and chemical water that are difficult to dry, and ensure product quality and environmental friendliness, the moisture transfer of the dried material can be completed quickly with low equipment investment and operation cost.

The prototype of ICAD derived from the combination of straight pipe airflow dryer and cyclone dryer. This kind of equipment was developed in the mid-1990s and widely used in PVC drying after 2000 [22,23]. Materials are dried by hot air and then dried in sections in the cyclone dryer. Because of its high heat and mass transfer process and long material retention time, the drying quality of PVC resin is guaranteed, this kind of equipment is easy to operate and easy to automate. This kind of drying equipment is widely used in PVC production. Wang, et al. [24] of Tsinghua University, developed a new efficient airflow cyclone combined drying technology. This type of drying equipment divides hot air into two branches. The hot air enters the straight pipe airflow dryer to contact materials for constant speed drying, while the other hot air enters the cyclone dryer for speed reduction drying, and then returns to the end of the straight pipe dryer after passing through the cyclone separator for fine particles, Finally, the hot air is exhausted through the cyclone separator together with the hot air. Compared with the Hoechst drying system, this drying method has better energy saving, can effectively reduce the investment in equipment, reduce the total power consumption and air consumption, and greatly improve the drying efficiency of materials. Due to the long drying pipeline of the straight tube dryer, the design height is generally more than ten meters high, and the relative speed of materials and air flow is low, the heat transfer coefficient is also low, resulting in low drying efficiency. To solve this problem, some R&D personnel use the pulse air flow dryer to replace the straight tube air flow dryer, and form the pulse cyclone air flow dryer with the cyclone dryer to replace the Hoechst drying system. This type of dryer has high drying efficiency, It can reduce the floor area of the pipeline and save costs. Liu [25] and others successfully used pulse cyclone airflow drying to dry m-phthalonitrile from 15% of the initial moisture content to 0.3%. Chen F et al. used pulse cyclone high temperature air flow drying to treat poplar wood fiber. The results showed that the number of free hydroxyl groups in wood components was greatly reduced and the polarity was reduced due to the high temperature effect, which improved the dispersion between materials.

The application of ICAD technology is mainly concentrated in medicine, food and other fields at present. The application in the wood fiber drying field is just in the initial stage, and there is no in-depth study on the process parameters that affect the final moisture content of wood fiber drying.

1.3 Research status of moisture content prediction model

The factors that affect the final moisture content of wood fibers dried by ICAD are very complex, including external environmental parameters such as drying method, drying temperature, wind speed, feeding speed, as well as physical parameters of wood fibers such as origin, variety, initial moisture content, fiber morphology, etc. It is difficult to establish an accurate and objective model for the final moisture content of wood fibers, In the process of ICAD, the process parameters are often determined by the experience of operators, lacking objective basis, and the drying quality of wood fibers cannot be guaranteed. Therefore, the establishment of accurate moisture content prediction model can determine the relationship between wood fiber drying process parameters and final moisture content, and provide scientific basis for efficient, intelligent and reasonable wood fiber drying.

The research on the prediction model of material moisture content mainly focuses on the research of artificial neural network method and regression analysis method. Artificial neural network (ANN) is an important branch of computer science, and also a subject with the thinking function of computer simulation [26]. ANN has the characteristics of nonlinear characteristics, learning and induction ability, and extensive combination ability, and can solve many complex problems. The research of artificial neural network in the field of wood drying mainly focuses on the prediction of wood moisture content and mechanical properties by BP (reverse transfer) neural network algorithm, RBF (radial basis function) neural network algorithm, Elman neural network algorithm modeling, etc [27]. There is no relevant research and report on the literature retrieval of wood fiber drying moisture content prediction.

2. Solution to the problem of ICAD for wood fibers

2.1 Application of ICAD in 3D Printing Materials

Polylactic acid (PLA), a biodegradable aliphatic polyester well suited for the production of disposable materials [28,29], is typically prepared from fermented plant starch, such as wheat starch, potato starch, sweet potato starch, cornstarch, and dextrin [30]. Additionally, PLA can be extruded into filaments by 3D consumable extruder products and is easy to print [31,32], making it an ideal 3D printing material. Wood fibers or flour (WF) are mainly composed of cellulose, hemicellulose, and lignin. Cellulose is a natural homopolymer consisting of D-anhydroglucose ($C_6H_{11}O_5$) [33]. In the supramolecular structure of cellulose, the hydroxyl groups of the molecular chains are bonded by hydrogen bonds to form a crystalline region with high crystallinity, thus giving WF incredible rigidity [34]. Lignin has effective and economical adhesion properties, which can be used as rubber reinforcement, plastic matrix reinforcement, adhesive, dispersant [35]. Due to the excellent performance of wood, 3D printing filaments are commercialized as WoodFill and Laywoo-D3, which consist of around 30% recycled WF and around 65% PLA [36]. However, WF with certain moisture content in the composite is heated and evaporated to cause an interface cavity layer during

fusing filament process; thus, 3D printing filaments based on wood flour/PLA composites suffer low dimensional stability, poor mechanical properties, carbonization, and filament plugging [37]. In addition, WF is highly hydrophilic and undergoes agglomeration because of its surface abundance of hydroxyl groups (–OH) [38]; thus, PLA containing nonpolar ester groups has poor interfacial compatibility with WF [39]. Hence, it is necessary take the interfacial compatibility and dispersion of WF into account. Many researchers have conducted studies on enhancing the compatibility between PLA and WF.

According to research of Chen [40]. Under acidic conditions, the selection of appropriate nucleophilic compounds (carboxylic acid or anhydride) and appropriate reaction conditions can reduce the hydroxyl content of the esterified WF and provide better thermoplasticity. They can improve the brittleness of WF/PLA composites and may also interact with polylactic acid or produce hydrogen bond. In addition, it is reported that the agglomeration and hydroxyl groups of WF can be reduced under ICAD high-temperature treatment (HT). The use of esterification and HT complex modification for PLA/WF composite preparation for 3D printing has not yet been reported. In order to increase the compatibility between WF and PLA, we used WF heat treated at high temperature, WF modified with silane coupling agent (SCA), WF esterified with glacial acetic acid/acetic anhydride (AAH), WF modified with SCA and heat treated at high temperature, and WF esterified with AAH and heat treated at high temperature. The composite materials were prepared by a 3D printing filaments extruder and 3D printer. Through the mechanical property, crystallinity, contact angle, and surface energy measurements, we aimed to determine the best method and mechanism for the synthesis of PLA/WF composites.

In order to further improve the compatibility of WF and PLA, the compatibilizers SCA and glacial acid/AAH were added to wood fiber after HT. The compatibilization mechanism of SCA and AAH was determined by infrared spectroscopy, and their effects on the mechanical, thermal, and mechanical properties of the WF/PLA composites were investigated. The effects of the WF modification treatments on the crystallization and water resistance of the WF/PLA were studied, and their section morphologies were characterized. The results are summarized below.

The infrared spectra show that the intensity of the absorption peak near 3432 cm^{-1} attributed to the O–H stretching vibration increases with increasing number of HT. This indicates that heat treatment can expose more hydroxyl groups on the surface of WF, which provides the possibility for the chemical reaction of hydroxyl groups. The characteristic peaks at 1740 and 1370 cm^{-1} of WF treated with AAH proved the WF esterification with AAH.

By observing the change of aspect ratio, it can be seen that the acetyl groups replaced some of the hydroxyl groups in WF after esterification, resulting in swelling effect and increase of aspect ratio.

Several modification methods can improve the mechanical properties of the WF/PLA composites to varying degrees. The mechanical properties of the WF/PLA composites can be improved by HT, SCA treatment, and esterification of wood fiber. However, the effect of esterification on the WF/PLA composites is not obvious.

SEM images of the tensile section of the composites show that AAH-modified WF without HT improves the dispersion of WF in the plastic matrix. However, the compatibility of WF with PLA is limited, and the tensile section still shows poor compatibility between the two components. On the other hand, the compatibility between the esterified wood fiber and PLA after HT is good as shown by the rough tensile section and obvious matrix deformation in the SEM images. The appearance of a large number of cavities and relatively flat sections shows that the HT WF/PLA composites are still brittle materials, and their compatibility is poor.

The modification method did not change the crystal form of the modified WF/PLA composites. The crystallinity of the wood fiber was reduced after four treatments, and the crystallinity and cold crystallization temperature of the heat-treated and esterified wood fiber composites were the lowest. This is due to the enhanced movement of chain segments, the enhanced ability of penetration between phases, increased interaction force between components, and reduced surface adhesion of each interface in the composites in the heat-treated and esterified WF composites, resulting in greater compatibility between WF and PLA in HF-AAH/PLA. The PLA and HT esterified WF composites exhibited the largest contact angle (97.5°) and superior hydrophobic properties. Thus, addition of a small amount of HT esterified WF to WF/PLA composites in 3D printing filament extruder enhances its plasticization property and toughness at low cost, suggesting the future wide applications of the material in 3D printing.

2.2 Prediction of moisture content of wood flour by ICAD

The moisture content prediction model of wood fibers is used for improving available drying systems, developing new designs, and optimizing process parameters. But it is difficult to establish an accurate and objective prediction model for the final moisture content of wood fiber drying. The process parameters are often determined by the experience of operators during the process of the ICAD, which lacks an objective basis and cannot ensure the quality of wood fiber drying. In optimization research, although a large number of tests are required to obtain the desired results, it is time-consuming and cumbersome, which however can be solved by appropriate mathematical models, when the correlation between various input variables and output variables is made use of for simulation [41]. The most widely used models are multiple linear regressions and the artificial neural network (ANN) [42]. Response surface methodology (RSM) is a traditional multiple regression linear model [43]. By responding to the influence of multiple variables, a reasonable experimental design of RSM is given for the arrangement and combination of various influencing factors, and then the optimal prediction results are obtained. When the delta function is quadratic, RSM is

more accurate than other techniques. When it comes to the ANN, it possesses a wide range of approximation capabilities, can be applied to various types of nonlinear problems, and links the relationship between input and corresponding output through the black box modeling method [44]. For the prediction of the ANN in wood moisture content, some scholars have adopted various methods, such as the backpropagation (BP) neural network algorithm, the recurrent neural network (RNN), and Elman neural network algorithm, but these neural network models are prone to gradient disappearance or gradient explosion [45]. For the establishment of the moisture content prediction model for wood fiber drying, there is no relevant research and report. As an improved RNN neural network, the Long Short-Term Memory neural network (LSTM-NN) can effectively learn the long-term dependence of temporal data, and besides, it is widely used in many scientific and technological fields such as machine reading, emotion analysis, and image description [46]. Moreover, the LSTM-NN model is also applied to the prediction of product performance under the interaction of multiple factors [47]. The prediction effect of the LSTM-NN model depends on the reliability of input variables, but there is no research exploring the combination of wood fibers drying process conditions and LSTM-NN. Particle swarm optimization (PSO) was first proposed by Eberhart and Kennedy in 1995[48]. Its basic concept comes from the study of birds foraging behavior. PSO algorithm is inspired by the behavior of this biological population and used to solve optimization problems [49].

The variance analysis of RSM showed that there was a highly significant relationship between the process factors of the regression model and the final moisture content of poplar fiber. The difference between the predicted value and the actual value in the analysis structure was extremely small, explaining the model fitted by the response surface method possesses good adaptability and can be adopted to explore the effect of the pulse-cyclonic airflow drying process on the final moisture content of wood fiber. Among them, three of the four influencing factors in the model are significant, and the order of significance is: initial moisture content > inlet air temperature > feed rate > inlet air velocity. Considering that, the mathematical regression equation obtained by software storage is $Y= 4.40 + 1.95A -1.35B + 1.13C + 0.17D -0.40AB + 0.40AC + 0.30AD -0.15BC + 0.050CD -0.54A^2+ 0.11B^2 -0.092C^2-0.44D^2$.

The MSE and MAPE of the LSTM-NN model were smaller than those of RSM and BP-NN models. The determination coefficients of the RSM model, the BP-NN model and the LSTM-NN model were 0.9785, 0.9350 and 0.9809, respectively, indicating that the moisture content prediction performance of the LSTM-NN model was slightly better than that of RSM model and BP neural network models, which can solve the complex nonlinear relationship and accurately reflect the mapping relationship between network input and output.

Under the PSO algorithm, the optimized ICAD process parameters of the trained BP-NN model were initial moisture content 10.6 %, inlet air temperature 238 ^oC, feed rate 90 kg/h, and inlet air velocity 9 m/s, while the optimal ICAD process parameters of the LSTM model were initial moisture content of 10.3 %, inlet air temperature of 242 ^oC, feed rate of 90kg/h and inlet air velocity of 8 m/s.

Under the optimal moisture content, the final moisture content of LSTM-NN obtained by optimization was 0.96 %, and the error was lower than 1.33 % and 1.43 % obtained by the RSM model and the BP-NN model, respectively. Therefore, the LSTM-PSO methods were more suitable for process optimization and prediction of wood fiber moisture content. Furthermore, the analysis method adopted in this study provides a reference for optimizing the process of wood fiber-plastic composites and lays a theoretical foundation for the application of ICAD technology in the biomass composite industry. In this paper, only some process parameters were considered in the study of final water content, and several factors can be considered in

further prediction, such as the length-diameter ratio and wood species. In addition, the LSTM-PSO model was combined with other models to further improve the prediction accuracy of the model.

2.3 Device optimization of ICAD

The drying rate depends on the external conditions such as particle temperature, hot air temperature, moisture content and air flow velocity. It is particularly important to exclude the non-combined moisture content, because the moisture on the wood fiber surface diffuses around through the air film on the surface in the form of steam. This mass transfer process is accompanied by heat transfer, so strengthening heat transfer can accelerate drying.

It can be seen from the analysis of simulation results that the imbalance of pressure at the elbow will lead to the concentrated collision of materials. Due to the centrifugal force and inertia at the downcomer, it is easy to cause the materials to stay and affect the forward speed. Second, the included angle between the pulse tube and the visual tube will easily cause no kinetic energy at the included angle of the pulse tube, which is not conducive to transmission. When the included angle kinetic energy at both sides is large, the deceleration effect of drying efficiency at both sides is not obvious, and the drying efficiency of materials in the middle is not good, it is easy to cause uneven moisture content.

According to the above analysis, we optimize the structure of the pulse dryer, change the inclination angle of the pulse tube, change the diameter and radian of the elbow, increase the windward space of the material, and change the elbow structure, so that there are also materials in the concave, and all of them are in high-speed gas phase movement, which can greatly reduce the vertical contact between the air flow and the wall surface, and make the air flow move steadily and at high speed.

At present, the transition angle between the pulse drying tube and the straight tube is 159 °, and the set transition angle is 135 °, 140 °, 145 °, 150 °, 155 °, 165 ° respectively. The other dimensions remain unchanged. To compare the drying effects of these drying tubes under the same conditions 155 ° 159 ° 140 ° 145 ° 165 ° 135 °, we assume that the height of the drying tube is unchanged, and changing the angle will change the diameter of the pulse tube.

The radius of the upper elbow is 310mm, we take 340mm, 370mm, 400mm and 430mm.The particles in the bend are divided into two categories according to their energy: those with larger kinetic energy and those with smaller kinetic energy. The particles with higher kinetic energy rush to the outside, and the particles with lower kinetic energy turn to the inside. We call this secondary flow.

The longer the drying time is, the better the drying effect is, under the condition of ensuring a certain speed. It can be seen from the simulation value that we choose the maximum particle phase time as the reference value. At the same time, it is necessary to ensure that there is no eddy current at the transition angle, so as to prevent the eddy current phenomenon at the transition section from causing particles to attach and accumulate at this position, affecting the drying efficiency, which is extremely unfavorable for the air flow drying process. The air flow trajectory on the central section of the dryer transition section at different transition angles is shown in the figure. It can be seen from the figure that the size of the transition angle has a significant impact on the flow field in the transition section. With the increase of the transition angle, the flow transition section becomes smoother. When the transition angle is less than 150 °, the speed (blue) in the transition section is low, and vortex is easy to form in this part. The vortex phenomenon can cause particles to attach and accumulate at this position, which affects the drying efficiency. For the drying process and its disadvantages, long time will cause wood flour to be too dry or carbonized, so the transition angle of pulse air dryer should be increased as much as possible in actual production.

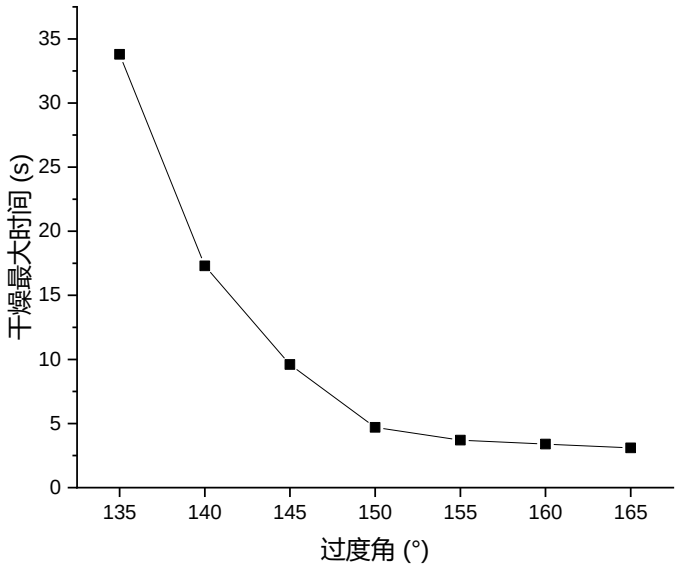

Fig. 1. Relationship between transition angle and maximum drying time

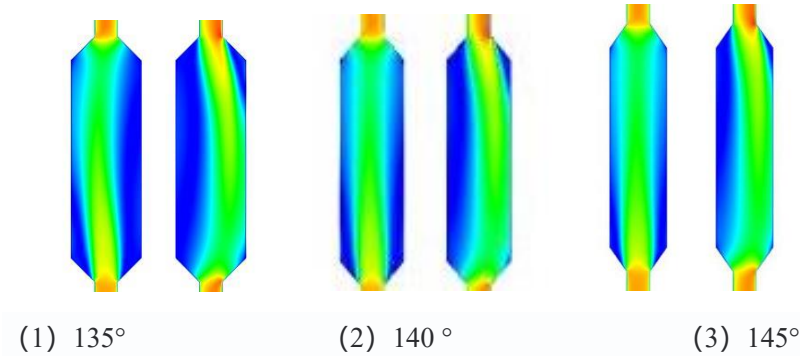

（1）135°　（2）140 °　（3）145°

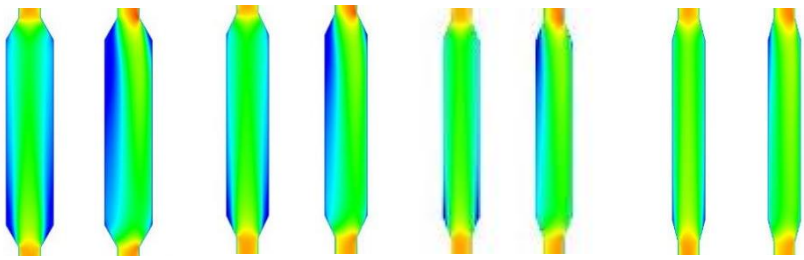

（4）150°　（5）155°　（6）160°　（7）165°

Fig. 2. Relationship between transition angle and air velocity

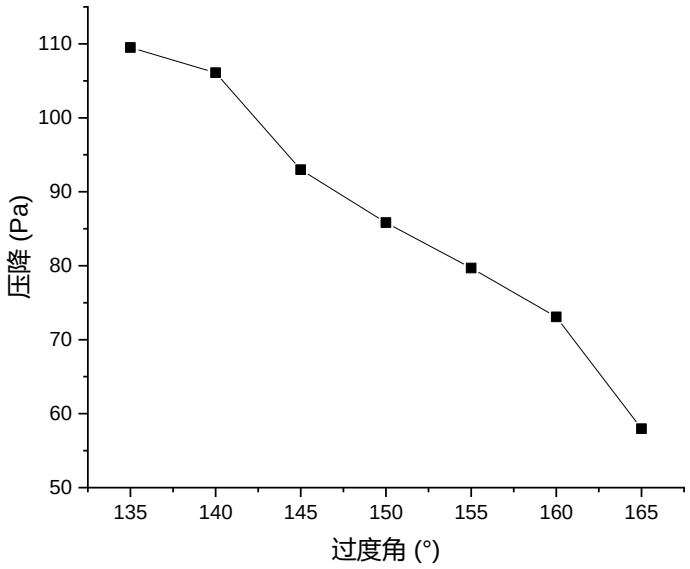

Fig. 3. Relationship between transition angle and pressure drop

The pressure drop distribution in the dryer at different transition angles is shown in Figure 1. From Figure 1, it can be seen that with the increase of transition angle, the pressure drop of the dryer decreases gradually; From the analysis of the flow field in the transition section, it can be seen that when the transition angle is large, the air flow in the transition section can transition smoothly, making the local loss at this position small. On the contrary, when the transition angle is too small, the air flow disturbance in the transition section is too large, resulting in increased local loss, then the pressure drop value and pressure drop increase, which will lead to increased energy consumption in the drying process, which is adverse to the drying process.

Considering the influence of transition angle on pressure drop value and airflow turbulence change, the transition angle of pulse airflow dryer should be smaller when the particle moisture content is satisfied. At this time, the pressure loss in the drying process is small, and vortex phenomenon is not easy to occur. Production practice shows that when the transition angle is too small, particles are easy to accumulate at the transition position of the shrinking section and the expanding section, which is extremely unfavorable for the drying process, According to the above analysis results, it is recommended to adopt a transition angle of about 165 ° in actual production from Figure 2 and Figure 3.

In the process of wood flour transmission, the force and speed at the elbow change. The loss of wind speed and pressure in the elbow will cause wood flour to fail to pass through the elbow, which will not complete the function of wood flour transmission. Increasing the fan power will increase the power loss. More importantly, the friction between wood flour and the elbow, especially the friction and erosion of the pipe wall outside the elbow, will affect the service life of the elbow. In the past, the piping design and fan selection were all estimated based on the empirical formula of pressure and velocity loss, which has certain defects. Through the finite element analysis of FLUENT, we can directly see the distribution of pressure and velocity when the air flows through the elbow, and understand the reasons for pressure loss according to the analysis results of FLUENT, as well as the factors that should be considered in the actual pipeline design.

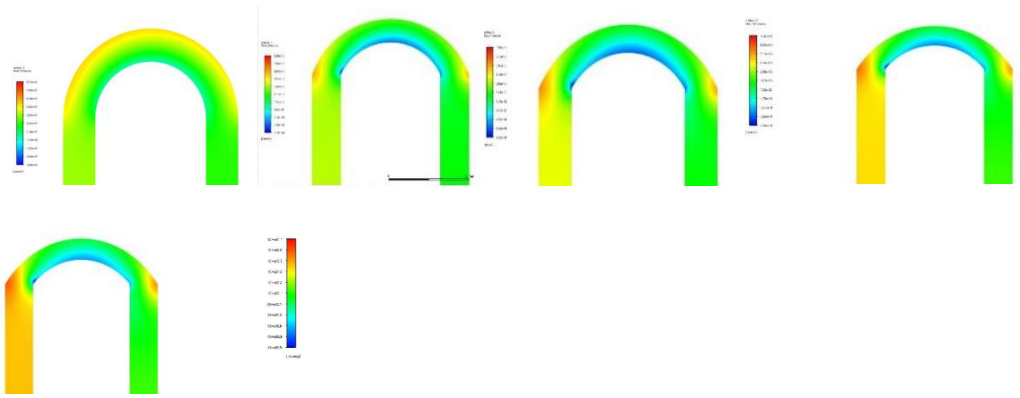

Fig. 4. Relation between bending angle and pressure

The pressure distribution cloud diagram is shown in Figure 4. With the reduction of the chamfer angle, the pressure of the elbow has changed significantly from the inlet to the outlet of the elbow. When the angle is 50 °, the pressure on the left and right sides changes the most. At the same time, it can be seen that except for the 90 ° chamfer, the pressure inside the elbow almost drops to 0. At 90 ° angle cutting, the pressure at the center line of the bend changes less than that at other angles, while the pressure increases sharply from the center line to the outside of the bend.

This is because when the gas passes through the elbow, it is subjected to the centrifugal force, forming a secondary vortex flow at the arc of the elbow, resulting in turbulence changes in the gas flow field, air flow molecules collide with each other, and ultimately leading to sharp changes in pressure and speed in the pipeline. The smaller the chamfer angle is, the more obvious the centrifugal force is, which ultimately leads to the more obvious changes in the pressure and velocity in the pipeline. It can be seen from the figure that with the increase of chamfer angle, the erosion of air flow on the wall decreases. When the particles flow, the particles with large kinetic energy rush to the outside, and the particles with small kinetic energy stay to the inside.

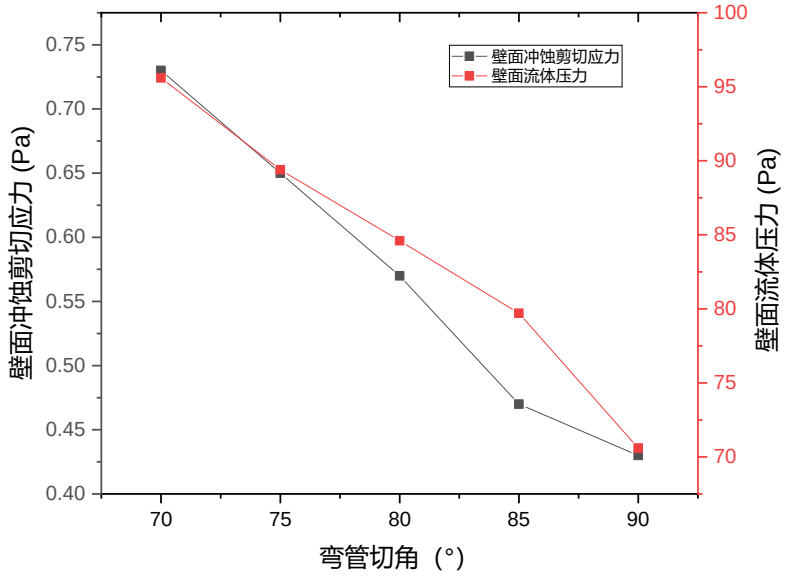

Fig.5. Relationship between bending angle, pressure and erosion

Conclusion

As the reinforcement of composite materials, the drying quality of biomass fiber can not only endow the fiber with good dispersion and moisture content, but also significantly improve the comprehensive performance of the product. This project takes low value wood, bamboo and crop straw as the research object, studies the characteristics of pulse cyclone high-temperature airflow drying, especially the drying dynamics model, establishes the artificial neural network that can predict the moisture content, improves the drying model system, and applies the optimization theory to establish the optimization method of dryer equipment, and conducts in-depth research on the application of wood fiber engineering.

References

[1] Xu H , Shen M , Shang H , et al. Osteoconductive and Antibacterial Poly(lactic acid) Fibrous Membranes Impregnated with Biobased Nanocarbons for Biodegradable Bone Regenerative Scaffolds. Industrial & Engineering Chemistry Research, 2021; 60(32), 12021-12031. https://doi.org/10.1021/acs.iecr.1c02165

[2] Gao S , Song W , Guo M . The Integral Role of Bioproducts in the Growing Bioeconomy. Industrial Biotechnology, 2020; 16(1):13-25. https://doi.org/10.1089/ind.2019.0033

[3] Rodrigues S C S, de Mesquita F A S, de Carvalho L H, et al. Preparation and characterization of polymeric films based on PLA, PBAT and corn starch and babassu mesocarp starch by flat extrusion. Materials Research Express, 2021; 8(3): 035305. https://doi.org/10.1088/2053-1591/abeaca

[4] Viidik L , Vesala J , R Laitinen, et al. Preparation and characterization of hot-melt extruded polycaprolactone-based filaments intended for 3D-printing of tablets. European Journal of Pharmaceutical Sciences, 2020; 158:105619. https://doi.org/10.1016/j.ejps.2020.105619

[5] Kananathan J , Samykano M , Kadirgama K , et al. Comprehensive investigation and prediction model for mechanical properties of coconut wood–polylactic acid composites filaments for FDM 3D printing. European Journal of Wood and Wood Products, 2022; 80(1):75-100. https://doi.org/10.1007/s00107-021-01768-1

[6] Natesan S , Samuel J S , Srinivasan A K . Design and development of Schiff's base (SB)-modified polylactic acid (PLA) antimicrobial film for packaging applications. Polymer Bulletin, 2021; (10):1-20. https://doi.org/10.1007/s00289-021-03703-z

[7] Grijpma D W , Nijenhuis A J , Wijk P , et al. High impact strength as-polymerized PLLA. Polymer Bulletin, 1992; 29(5):571-578. https://doi.org/10.1007/BF00296720

[8] Lv S , Zhang Y , Gu J , et al. Biodegradation behavior and modelling of soil burial effect on degradation rate of PLA blended with starch and wood flour. Colloids Surf B Biointerfaces, 2017; 159:800-808. https://doi.org/10.1016/j.colsurfb.2017.08.056

[9] Nh A , Ia B , Mg C , et al. The remarkable three-dimensional network structure of bacterial cellulose for tissue engineering applications. International Journal of Pharmaceutics, 2019; 566:631-640. https://doi.org/10.1016/j.ijpharm.2019.06.017

[10] Xing L , Hu C , Zhang W , et al. Transition of cellulose supramolecular structure during concentrated acid treatment and its implication for cellulose nanocrystal yield. Carbohydrate Polymers, 2019; 229:115539. https://doi.org/10.1016/j.carbpol.2019.115539

[11] Kumar A N , Kim G B , Muhorakeye A , et al. Biopolymer Production Using Volatile Fatty Acids as Resource: Effect of Feast-Famine Strategy and Lignin Reinforcement. Bioresource Technology, 2021; 326(1):124736. https://doi.org/10.1016/j.biortech.2021.124736

[12] Lam K . MO-F-CAMPUS-I-03: CT and MR Characteristics of Some Specialty 3D Printing Filaments Medical Physics, 2015; 42(6):3579-3579. https://doi.org/10.1118/1.4925469

[13] Tao Y , Wang H , Li Z , et al. Development and Application of Wood Flour-Filled Polylactic Acid Composite Filament for 3D Printing. Materials, 2017, 10(4):339. https://doi.org/10.3390/ma10040339

[14] Elrhayam Y , Elharfi A . 3D-QSAR studies of the chemical modification of hydroxyl groups of biomass (cellulose, hemicelluloses and lignin) using quantum chemical descriptor. Heliyon, 2019; 5(8): e02173. https://doi.org/10.1016/j.heliyon.2019.e02173

[15] Gallardo-Cervantes M, González-García Y, Pérez-Fonseca A A, et al. Biodegradability and improved mechanical performance of polyhydroxyalkanoates/agave fiber biocomposites compatibilized by different strategies. Journal of Applied Polymer Science, 2021; 138(15): 50182. https://doi.org/10.1002/app.50182

[16] Han G, Zhang C, Zhang D, et al. Upgrading of urea formaldehyde-bonded reed and wheat straw particleboards using silane coupling agents. Journal of Wood Science, 1998; 44(4): 282-286.

https://doi.org/10.1007/BF00581308
[17] Gao X, Li Q, Cheng W, et al. High temperature and pressurized steaming/silane coupling co-modification for wood fibers and its effect on the properties of wood fiber/HDPE composites. Macromolecular Research, 2017; 25(2): 141-150. https://doi.org/10.1007/s13233-017-5024-x
[18] Xiang E, Huang R, Yang S. Change in Micromechanical Behavior of Surface Densified Wood Cell Walls in Response to Superheated Steam Treatment. Forests, 2021; 12(6): 693. https://doi.org/10.3390/f12060693
[19] Chen F, Han G, Li Q, et al. High-temperature hot air/silane coupling modification of wood fiber and its effect on properties of wood fiber/HDPE composites. Materials, 2017; 10(3): 286. https://doi.org/10.3390/ma10030286.
[20] Nimmol C , Hirunwat A . Multistage Impinging Stream Drying for Okara[J]. Applied Engineering in Agriculture, 2017, 33(4):445-450. https://doi.org/10.13031/aea.12212
[21] Lin Jinna, Chen Lihui, Huang Zutai, Xie Dayong. Study on impinging stream drying of bamboo explosive pulp [J]. Journal of Shaanxi University of Science and Technology, 2004 (04): 21-26. CNKI:SUN:XBQG.0.2004-04-006
[22] Stamm A J , Tarkow H . Dimensional Stabilization of Wood. The Journal of physical and colloid chemistry, 1947; 51(2):493-505. https://doi.org/10.1021/j150452a016
[23] Matsuda H . Preparation and utilization of esterified woods bearing carboxyl groups. Wood Science & Technology, 1987; 21(1):75-88. https://doi.org/10.1007/BF00349719
[24] Wang R, Sun S, Wang W, Zhu Z (2019) Investigation on the thermophoretic sorting for submicroparticles in a sorter with expansion-contraction microchannel. J International Journal of Heat Mass Transfer 133 (APR.): 912-919. https://doi.org/10.1016/j.ijheatmasstransfer.2018.12.126
[25] Liu R, Luo S, Cao J, et al. Mechanical properties of wood flour/poly (lactic acid) composites coupled with waterborne silane-polyacrylate copolymer emulsion. Holzforschung, 2016; 70(5): 439-447. https://doi.org/10.1515/hf-2015-0064
[26] Jebrane M, Sèbe G. A new process for the esterification of wood by reaction with vinyl esters. Carbohydrate Polymers, 2008, 72(4): 657-663. https://doi.org/10.1016/j.carbpol.2007.10.001
[27] Lee S H, Ohkita T, Kitagawa K. Eco-composite from poly (lactic acid) and bamboo fiber. 2004; 58(5): 529-536. https://doi.org/10.1515/HF.2004.080
[28] Chen, F., Han, G., Li, Q., Gao, X., Cheng, W. (2017a). "High-temperature hot air/silane coupling modification of wood fiber and its effect on properties of wood fiber/HDPE composites," J Materials, 10(3), 286.10.3390/ma10030286.
[29] Chen, F., Li, Q., Gao, X., Han, G., Cheng, W. (2017b). "Impulse-cyclone drying treatment of poplar wood fibers and its effect on composite material's properties," J BioResources, 12(2), 3948-3964.10.15376/biores.12.2.3948-3964.
[30] Elrhayam, Y., Elharfi, A. (2019). "3D-QSAR studies of the chemical modification of hydroxyl groups of biomass (cellulose, hemicelluloses and lignin) using quantum chemical descriptors," J Heliyon, 5(8), e02173.
[31] Gallardo-Cervantes, Miguel, et al. "Biodegradability and improved mechanical performance of polyhydroxyalkanoates/agave fiber biocomposites compatibilized by different strategies." Journal of Applied Polymer Science 138.15 (2021): 50182. 10.1002/app.50182
[32] Gao, S., Song, W., Guo, M. (2020). "The integral role of bioproducts in the growing bioeconomy," J Industrial Biotechnology, 16(1), 13-25.
[33] Gao, X., Li, Q., Cheng, W., Han, G., Xuan, L. (2017). "High temperature and pressurized steaming/silane coupling co-modification for wood fibers and its effect on the properties of wood fiber/HDPE composites," J Macromolecular Research, 25(2), 141-150.
[34] Grijpma, D., Nijenhuis, A., Van Wijk, P., Pennings, A.J.P.b. (1992). "High impact strength as-polymerized PLLA," 29(5), 571-578.
[35] Guo, Y., Chen, J.-Q., Su, M., Hong, J.-G.J.J.o.W.C., Technology. (2018). "Bio-based plastics with highly efficient esterification of lignocellulosic biomass in 1-methylimidazole under mild conditions," 38(4), 338-349.
[36] Han, G., Zhang, C., Zhang, D., Umemura, K., Kawai, S. (1998). "Upgrading of urea formaldehyde-bonded reed and wheat straw particleboards using silane coupling agents," J Journal of Wood Science, 44(4), 282-286.
[37] Jamaluddin, N. , Hsu, Y. I. , Asoh, T. A. , & Uyama, H. . (2021). Effects of acid-anhydride-modified cellulose nanofiber on poly(lactic acid) composite films. Nanomaterials, 11(3), 753. 10.3390/nano11030753
[38] Jebrane, M., Sèbe, G.J.C.P. (2008). "A new process for the esterification of wood by reaction with vinyl esters," 72(4), 657-663.
[39] Kerner, D., Vinnikov, V. (2010). "Decomposability of local determinantal representations of hypersurfaces,"

J Mathematics.
[40] Kumar, A. N. , Kim, G. B. , Muhorakeye, A. , Varjani, S. , & Kim, S. H. . (2021). Biopolymer production using volatile fatty acids as resource: effect of feast-famine strategy and lignin reinforcement. Bioresource Technology, 326(1), 124736. 10.1016/j.biortech.2021.124736
[41] Bledzki A.K., Faruk O. Creep and impact properties of wood fibre–polypropylene composites: influence of temperature and moisture content. J Composites Science Technology. 2004; 64(5): 693-700. DOI: 10.1016/S0266-3538(03)00291-4.
[42] Ou R., Xie Y., Wolcott M.P., Sui S., Wang Q. Morphology, mechanical properties, and dimensional stability of wood particle/high density polyethylene composites: effect of removal of wood cell wall composition. J Materials Design. 2014; 58: 339-345. DOI: 10.1016/j.matdes.2014.02.018.
[43] Khan M.A., Ali K.I. Effect of moisture and heat on mechanical properties of wood and wood-plastic composite. J Polymer-Plastics Technology Engineering. 1993; 32(1-2): 5-13. DOI: 10.1080/03602559308020151.
[44] Karthi N., Kumaresan K., Sathish S., Gokulkumar S., Prabhu L., Vigneshkumar N. An overview: Natural fiber reinforced hybrid composites, chemical treatments and application areas. J Materials today: proceedings. 2020; 27: 2828-2834. DOI: 10.1016/j.matpr.2020.01.011.
[45] Lee S.Y., Yang H.S., Kim H.J., Jeong C.S., Lim B.S., Lee J.N. Creep behavior and manufacturing parameters of wood flour filled polypropylene composites. J Composite Structures. 2004; 65(3-4): 459-469. DOI: 10.1016/j.compstruct.2003.12.007.
[46] Soucy et al. 2014 Soucy J., Koubaa A., Migneault S., Riedl B. The potential of paper mill sludge for wood–plastic composites. J Industrial Crops Products. 2014; 54: 248-256. DOI:10.1016/j.indcrop.2014.01.013.
[47] Dev SR., Raghavan VG. Advancements in Drying Techniques for Food, Fiber, and Fuel. Drying Technology. 2012; 30:11-12, 1147-1159. DOI: 10.10.80/07373937.2012.692747.
[48] Dx A., Fan Y.B., Hj B., Jsc C., Yu G.B. An investigation of heat transfer of flexible fibers in a rotating drum dryer using the Discrete Element Method. Powder Technology. 2020; 364: 494-506. DOI: 10.1016/j.powtec.2020.02.024.
[49] Granström K. Emissions of monoterpenes and VOCs during drying of sawdust in a spouted bed. Forest Products Journal. 2003; 53(10): 48-55. DOI: 10.1046/j.1439-0329.2003.00334.x.

Funding Statement

The National Natural Science Foundation of China (Grant No.31901243) financially supported this research.

Declaration of Conflicting Interests

The author(s) declared no potential conflicts of interest with respect to the research, authorship, and/or publication of this article.

Research on tensile failure mechanism of unidirectional CFRP tendons under high temperatures based on fractal characteristics of AE signals

Weixin Wang[1], Xiao Wang[1], Jie Xu[1,2,3], Qinghua Han[1,2,3]*

[1] School of Civil Engineering, Tianjin University, Tianjin 300350, China

[2] Key Laboratory of Earthquake Engineering Simulation and Seismic Resilience of China Earthquake Administration (Tianjin University), Tianjin 300350, China

[3] Key Laboratory of Coast Civil Structure Safety (Tianjin University), Ministry of Education, Tianjin 300350，China

Abstract: In view of the problem that the mechanical properties of Unidirectional (UD) carbon fiber-reinforced polymer (CFRP) tendons at high temperature deteriorates significantly and it is difficult to give timely damage warning, this paper carried out four groups of acoustic emission (AE) monitoring tests for tensile failure process of UD CFRP tendons under different temperature conditions (i.e. 20 ºC, 300 ºC, 450 ºC and 500 ºC). By analyzing the time domain characteristics and fractal characteristics of AE signal sequences at different temperatures, it was found that the AE count and cumulative energy sequence can be better used to describe the whole failure process of UD CFRP tendons. The Hurst index of AE count sequence could reflect the meso-damage evolution law of UD CFRP tendons, which provided a theoretical basis for establishing the advanced warning mechanism for structural health monitoring (SHM). In addition, the multi-fractal spectrum could help us to understand the tensile failure mechanism of UD CFRP tendons at different temperatures from microscopic perspective. Finally, the reliability of the analysis based on multi-fractal spectrum was verified by using scanning electron microscopy (SEM).

Keywords: Unidirectional CFRP tendon; Acoustic emission; High temperature; Multi-fractal; Hurst index; Failure mechanism

1. Introduction

Unidirectional (UD) carbon fiber-reinforced polymer (CFRP) tendons have a bright application prospect in civil engineering due to its excellent tensile properties, favourable

corrosion resistance and fatigue resistance [1-4]. At present, the UD CFRP tendons are mainly used in structural strengthening [5, 6], prestressed concrete [7] and cable bridges [4, 8, 9]. Although the application of UD CFRP tendons can largely compensate for the defects of steel such as corrosion and low specific strength, the fire resistance of the former still has a certain gap compared with steel [10, 11]. As is known to all, fire is one of the most common disasters endangering public safety, which can not be ignored in structural design [12, 13]. More attention should be paid to structures with UD CFRP tendons as the main load-bearing component under fire threat [4, 14]. In recent decades, a large number of scholars have carried out experimental and theoretical studies on the high temperature mechanical properties of this building material, which provides a basis for the design of structural fire resistance [14-19]. However, due to the complexity of the microstructure of UD CFRP tendons and the remarkable influence of temperature on their mechanical properties, it is difficult to fully evaluate the reliability of structures under fire condition by relying on macro-mechanical parameters only. Therefore, it is very important to further study the tensile failure mechanism of UD CFRP tendons at elevated temperature and establish the corresponding health monitoring system.

Acoustic emission (AE) technology is a reliable and efficient nondestructive monitoring method, which is widely used in material damage research and civil engineering health monitoring [20-25]. Scholars have carried out time-frequency domain analysis on AE signals of UD CFRP tendons and cables, and found that the amplitude, frequency, energy and other AE characteristic parameters can be related to the complex damage mechanism inside the material [26-32]. These research results have important guiding effect on health monitoring of UD CFRP tendons in engineering application. However, most of the above research were

carried out at room temperature, and there are few studies on AE signal characteristics of tensile failure of UD CFRP tendons under high temperature conditions. In order to establish the health monitoring mechanism of UD CFRP tendons under fire condition, it is necessary to explore the AE characteristics during tensile process at elevated temperatures.

On account of the existence of multiple AE sources in the failure process of UD CFRP tendons, the signals received by the monitoring terminal are characterized by multi-moding, non-stationarity, and nonlinearity [26, 32]. Moreover, the influence of temperature on AE characteristics of UD CFRP tendons during tensile process is not clear, which undoubtedly brings new challenges to the processing and analysis of AE signals. In the early 1970s, the concept of fractal was firstly proposed by Mandelbrot [33]. After half a century of accumulation and development, fractal theory has gradually become an independent branch of nonlinear science, which is widely used in the field of biomedicine [34], geography [35] and finance [36]. Since the 21st century, scholars have studied the fractal characteristics of AE signals generated by steel [37], concrete [38] and coal rock [39] in the failure process, proving that the AE signals have fractal characteristics in time and space scales. Therefore, fractal theory has become one of the effective ways to process AE signals, and the evolution process of material damage can be described by using fractal dimension and multi-fractal spectrum [40, 41]. Some studies have shown that fractal theory has obvious advantages in dealing with complex nonlinear signals [42]. Kong et al. [43] used the fractal theory to process the AE characteristic parameter series of sandstone uniaxial compression tests at different temperatures, and proved that the changes of fractal dimension and multi-fractal spectrum were significantly correlated with the damage evolution of materials. Li et al. [26] used fractal dimension to analyze AE signals from fatigue

tests of UD CFRP cables, and found that the cumulative damage index based on fractal dimension could well reflect the material fatigue cumulative damage process, which indicated the feasibility of fractal method for quantifying the damage condition of UD CFRP tendons.

Based on the high temperature tensile test of UD CFRP tendons conducted by the author before [18], this paper carried out single fractal and multi-fractal analysis on AE signals under four temperature conditions of 20 ºC, 300 ºC, 450 ºC and 500 ºC respectively according to the different failure modes. On the basis of periodic fluctuation of Hurst index, the meso-damage evolution of UD CFRP tendons at different temperatures was analyzed, and the advanced warning mechanism for structural health monitoring (SHM) was established. Furthermore, the tensile failure mechanism of UD CFRP tendons at different temperatures was explored by multi-fractal spectrum of AE signals. The scanning electron microscopy (SEM) images of UD CFRP samples verified the validity of multi-fractal analysis results.

2. Experimental methods

2.1. Preparation of specimens

The UD CFRP tendon specimens were prepared by pultrusion manufacturing process [11] with the use of domestic T700-12K PAN-based carbon fibers and multifunctional epoxy resin as raw materials, in which the fiber volume content was 65%. The parameters of raw materials can be seen in Table 1. As is shown in Fig. 1(a), the total length (L) of the specimen is 1000 mm with a diameter of 5 mm. The anchorage length (l_a) at both ends of the specimen is 180 mm and the length of the heating zone in the middle part (l_h) is up to 400 mm. In order to prevent the high temperature from affecting the signal received by the sensor, a flat-plate anchoring system is adopted as shown in Fig. 1(b). A hole was arranged on the side far away from the heating end for the AE sensor so as to contact the UD CFRP tendons under test. The

specific design parameters of the anchorage system can be found in the article [32].

Table 1. Properties of the raw material of the UD CFRP tendon.

Material	Type	Tensile modulus(GPa)	Tensile strength(MPa)	Density(g/cm^3)	T_g (°C)
Carbon fibre	T700	230	4900	1.8	—
Resin	CP-02A/B	-	35～45	1.18	220～230

Note: The data is provided by the manufacturer.

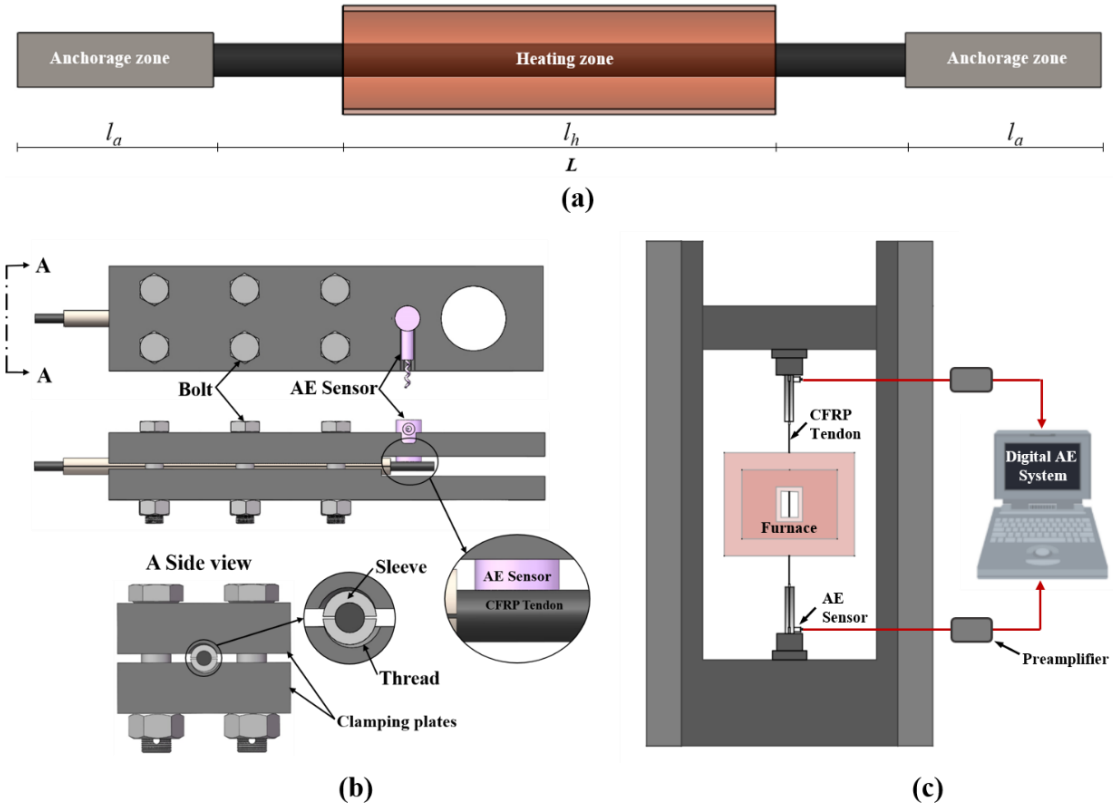

Fig. 1. Schematic of high temperature tensile test: (a) Tensile specimen (b) Installation of anchorage and AE sensor (c) Test set-up.

2.2. Test set-up

The set-up for this high temperature tensile test is shown in Fig. 1(c). The tests were conducted using an AG-250kN electronic testing machine. The heating equipment was DZL-10 high-temperature test furnace with a highest working temperature of 700 °C. The furnace

was equipped with a 10kW ceramic heater with a temperature rise accuracy of ±1 ºC. The temperature of hot air in the furnace was monitored by K-type thermocouple. A multichannel AE monitoring system produced by Physical Acoustics Company (PAC) and two R15α sensors were used to collect AE signals during the test. The gain of the pre-amplifier was set as 40dB and the threshold was set at 45dB to ensure a high signal to noise ratio (SNR). The test sampling rate was set as 3MHz. In order to ensure the normal signal acquisition of the AE sensors during the test, the couplant was applied between the AE sensors and the tested specimens. Moreover, the operating performance of the sensor was verified by pencil lead break procedure prior to each tensile process[44]. More detailed parameters of the test set-up can be found in [18, 32].

2.3. Experimental procedure

In order to prevent the effect of thermal deformation of the specimen on the test results during high temperature tests, only the upper anchor of the specimen was connected to the test machine before the heating process. Adjust the position of crosshead of the test machine and install the lower anchorage after the heating process was completed. The heating rate was 15 ºC/min. After reaching the target temperature, the heat preservation process was carried out for 20 minutes to ensure uniform heating inside and outside the specimens. The tensile rate of the test was controlled by displacement and the loading rate was set as 6 mm/min (≈ 0.01 strain/min) [45, 46]. The AE system was started when the universal testing machine began to load.

3. Calculation method

Calculation methods of multi-fractals mainly include partition function method [47], structure function method [48], wavelet transform modulus maximum method [49] and multifractal detrended fluctuation analysis [50].

Determine the profile of the time series $\{x_i; i = 1,2,3,\cdots,N\}$:

$$y(k) = \sum_{i=1}^{k}(x_i - \bar{x}) \tag{1}$$

for $k = 1,2,\cdots,N$. Where $\bar{x}$ is the mean of the time series.

Divide the profile of length N into N_s non-overlapping segments of equal length r. The same procedure is repeated starting from the opposite end to reduce the effect of remain. Thus, $2N_r$ segments are obtained altogether and we set $9 \leq r \leq N/4$.

Remove linear (or higher order) trend for each of the $2N_r$ segments and calculate the residual variance:

$$F^2(v,r) = \frac{1}{r}\sum_{i=1}^{r}\{y[(v-1)r+i] - y_v(i)\}^2 \tag{2}$$

for $v = 1,2,\cdots,N_r$.

$$F^2(v,r) = \frac{1}{r}\sum_{i=1}^{r}\{y[N-(v-N_r)r+i] - y_v(i)\}^2 \tag{3}$$

for $v = N_r+1, N_r+2,\cdots,2N_r$. Where $y_v(i)$ is the fitting polynomial in segment v.

Define the qth order fluctuation function as:

$$F_q(r) = \left\{\frac{1}{2N_r}\sum_{v=1}^{2N_r}[F^2(v,r)]^{\frac{q}{2}}\right\}^{1/q} \tag{4}$$

for any $q \neq 0$, and when $q = 0$, the fluctuation function is:

$$F_0(r) = exp\left[\frac{1}{4N_r}\sum_{v=1}^{2N_r} lnF^2(v,r)\right] \tag{5}$$

For a certain value of q, the linear relationship between $F_q(r)$ and r can be obtained:

$$logF_q(r) = h(q)logr + c \tag{6}$$

Where, $h(q)$ is the generalized Hurst scaling function and c is a constant. For $q = 2$, the standard DFA procedure is retrieved and $h(2)$ is the Hurst index. If $h(q)$ is a constant at

a certain q value, the time series has a single regularity. Otherwise, the series has a multi-fractal regularity.

Then, the scaling exponent is derived from:

$$\tau(q) = qh(q) - 1 \quad (7)$$

The singularity spectrum of a multi-fractal measure, $f(\alpha)$ is related to $\tau(q)$ via a Legendre transform

$$f(\alpha) = q\alpha - \tau(q) \quad (8)$$

Where, α is a singularity strength or Hölder exponent and obtained numerically as the first derivative of the $\tau(q)$ function with respect to q.

We can describe the multifractal spectrum with the width of the spectrum $\Delta\alpha$, the relationship between small and large signal frequencies Δf, and the difference between the right and left half-spectrum $\Delta\alpha_0$ [51].

The width of the spectrum of $\Delta\alpha$ is calculated as follows:

$$\Delta\alpha = \alpha_{max} - \alpha_{min} \quad (9)$$

Where, α_{min} correspond to large signals and α_{max} correspond to small signals. A lower value of $\Delta\alpha$ means a smaller difference between large and small signals.

The relationship between small and large signal frequencies of Δf is defined as:

$$\Delta f = f(\alpha_{max}) - f(\alpha_{min}) \quad (10)$$

Where, $f(\alpha_{max})$ means the value of f when $\alpha = \alpha_{max}$, the opposite of $f(\alpha_{min})$. $\Delta f > 0$ means the strong AE signal dominate and $\Delta f < 0$ means the weak AE signal dominate.

The shape of the singularity spectrum can be recognized by the difference between the right width and the left width:

$$\Delta\alpha_0 = \frac{\alpha_{max} + \alpha_{min}}{2} - \alpha_p \quad (11)$$

Where, α_p is the α value at the peak point of the spectrum. $\Delta\alpha_0 > 0$ correspond to left skewed distribution, which means small signals play a dominant role in the damage evolution. $\Delta\alpha_0 < 0$ correspond to right skewed distribution, which means large signals contribute more to the damage evolution. $\Delta\alpha_0 = 0$ correspond to symmetric distribution.

4. Results and discussion

4. 1 Time histories of AE signals

In this section, the tensile failure process of UD CFRP tendons at different temperatures was analyzed by the variation of load, AE count and cumulative AE energy in the tensile process with time changes, as shown in Fig. 2. It can be seen from the comparison that the ultimate load of UD CFRP tendons decreased with the temperature rise, which was mainly caused by the softening and volatilization of the resin matrix at high temperatures. The fluctuation characteristics of AE signals in the whole process were also changed with the increase of temperature. The AE count was relatively active throughout the whole process at 20 ºC, and the cumulative AE energy curve showed a trend of continuous multi-step increase at the last stage of loading. Moreover, the cumulative AE energy increased significantly when approaching the final failure, which was also a reflection of the brittle fracture of CFRP materials at room temperature. However, the historical process of AE signals changed significantly when the temperature exceeded the glass transition temperature of the resin matrix (about 220 ºC). The activity of AE counts at 300 ºC, 450 ºC and 500 ºC could be obviously divided into two stages. At the initial stage of loading, AE signals maintained a relatively stable development and the accumulated energy was at a lower level. When the load was approaching its ultimate bearing capacity, a large number of AE signals appeared, accompanied by a rapid rise in the energy accumulation curve, showing an exponential cumulative growth trend

throughout the whole process.

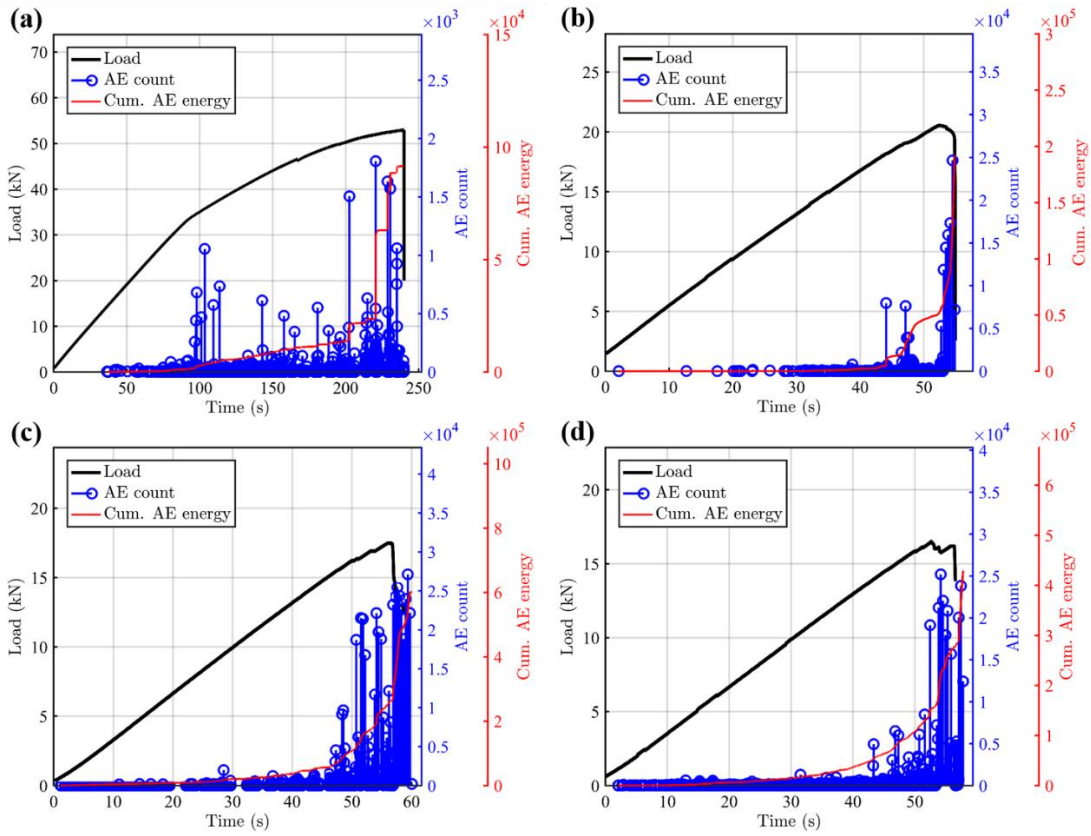

Fig. 2. Variation characteristics of load, AE count and cumulative AE energy: (a) 20 ℃ (b) 300 ℃ (c) 450 ℃ (d) 500 ℃.

4.2 Variation characteristics of the Hurst index

Previous studies have shown that a corresponding correlation mechanism can be established between the fluctuation characteristics of Hurst index and the stages of damage propagation in materials [43]. By analyzing the fluctuation of Hurst index of AE signals in the tensile process of UD CFRP tendons at different temperature, it can contribute to understanding the meso-damage development of materials at different stress levels, and establishing the advanced warning mechanism for SHM. In this study, the AE signals at each temperature were divided into 10 sections with a stress ratio of 10%. The variation characteristics of Hurst index calculated by the AE count at different stress ratio were analyzed as shown in Fig.3. It can be

seen that the Hurst index exhibited obvious periodic fluctuation with the increase of stress ratio under all temperature conditions. According to fractal theory, the higher the Hurst index, the more remarkable the increase of corresponding AE signals, and the material internal damage entered an unstable stage [43]. Moreover, when approaching the failure, the Hurst index showed a trend of increasing first and then decreasing, which provided a certain statistical rule for analyzing failure evolution and advanced warning. The curve of 20 ^{o}C in Fig. 3(a) was taken as an example to analyze the relationship between Hurst index and material damage. Initially, no internal damage occurred due to the good mechanical properties of the material at a lower stress level (0-0.2). The Hurst index rose significantly as the stress level increased to 0.3, which indicated that internal meso-damage would occur, and the number of signals increased obviously. Subsequently, the Hurst index curve sloped slowly downward until the stress level increased to 0.5, indicating that the internal damage of the material developed steadily. When the stress level reached 0.7, the Hurst index began to rise until its maximum value, indicating that the internal damage has expanded more seriously, which meant a rapid increase in the number and size of cracks. When the load continued to increase until the failure, the material broke along the larger cracks already generated before. Meanwhile, the damage mode changed monotonously compared with the previous section, and the Hurst index decreased. For the remaining three working conditions, a similar trend could be found in the load level range near the fracture. And the damage warning stress levels at 300 ^{o}C (Fig. 3(b)), 450 ^{o}C (Fig. 3(c)), and 500 ^{o}C (Fig. 3(d)) are 0.8, 0.7 and 0.6 respectively.

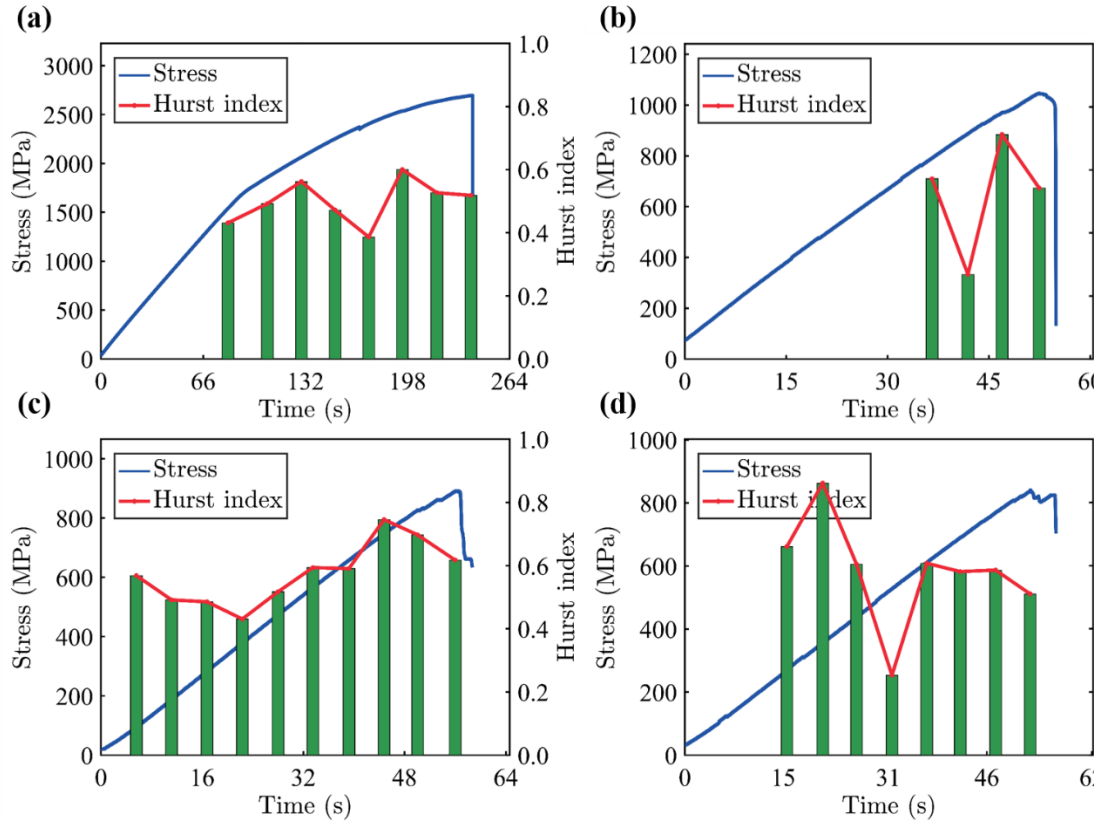

Fig. 3. Relationship between the Hurst index and stress: (a) 20 ℃ (b) 300 ℃ (c) 450 ℃ (d) 500 ℃.

It is worth noting that the “up-down” information signs of the Hurst index may not occur more than once during the entire loading process. There are two descending stages in all the four temperature conditions, which are mainly due to the change of AE signals in the fractal angel, proving the change of meso-damage state inside the material. In the first “up-down” process, “up” represented the initiation of the internal damage in the material and “down” meant that the damage had entered a stable period. But the “up” in the second “up-down” process meant that the damage had entered an unstable state, indicating that instable failure of the material is about to occur. Therefore, the second “up-down” process can be used as an advanced warning signal of failure for SHM at different temperatures.

4.3 Multi-fractal regularities of the AE signals.

Multi-fractal can further reveal the fractal structure of time series of AE signals on the basis of traditional fractal. As was shown, Fig. 5 summarized the multi-fractal spectrum of AE count sequence during the whole tensile process of UD CFRP tendons at different temperatures. Through the multi-fractal analysis, it was found that the multi-fractal characteristics of AE signals in the tensile failure process of materials are remarkable, which will be of great help to explore the meso-failure mechanism of materials.

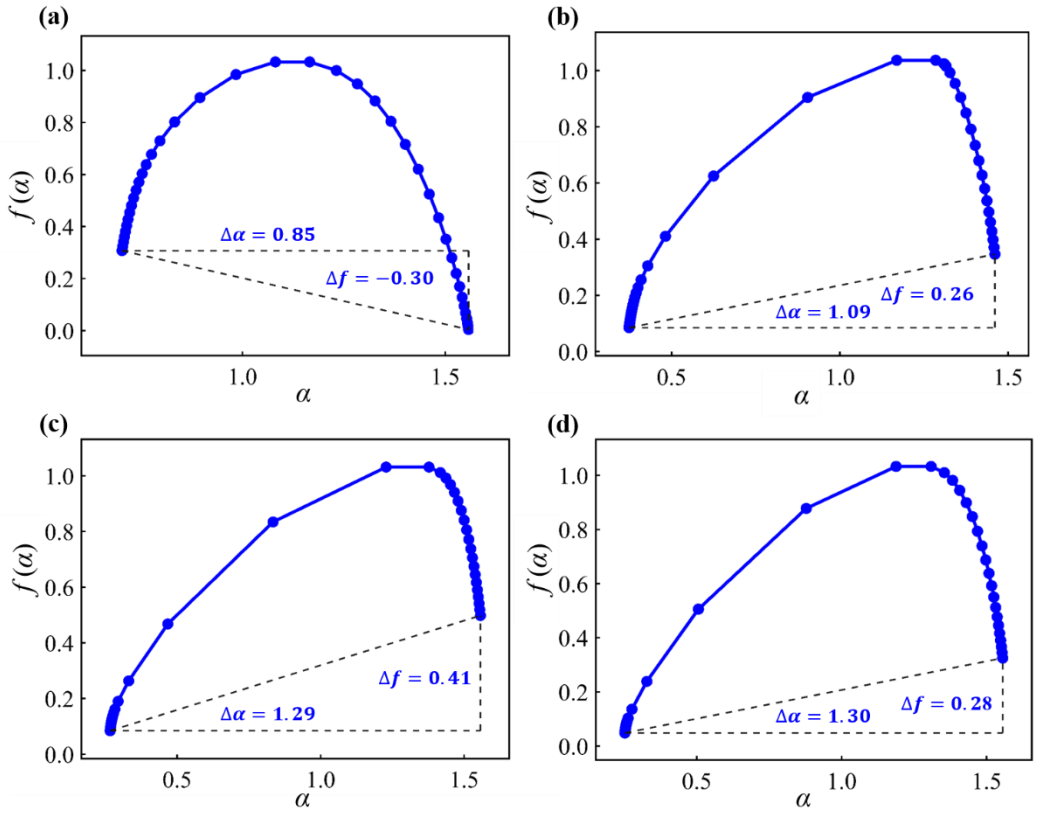

Fig. 4. Multi-fractal spectrum at different temperatures: (a) 20 ℃ (b) 300 ℃ (c) 450 ℃ (d) 500 ℃.

As can be seen from Fig. 4, with the rise of temperature, the value of $\Delta\alpha$ increases from 0.85 at 20 ℃ to 1.30 at 500 ℃, which indicates that the difference and the inhomogeneity of AE signals sequence increases. On the one hand, it can be seen from Fig. 2 that the fluctuation degree of AE signals at 20 ℃ is a multi-stage active change involving the whole process. With the increase of temperature, the activity characteristic of AE signals changes to be suddenly active only at the stage of near destruction. The inhomogeneity of AE signals in the whole

loading process explains the reason for the change of $\Delta\alpha$. On the other hand, the variation of $\Delta\alpha$ can also help to analyze the time-varying characteristics of the failure of UD CFRP tendons at different temperatures to a certain extent. According to the analysis in reference [32], the resin matrix maintains elastic state at room temperature, and the bond between the fiber and resin inside the material is stable, as shown in Fig.5. The fibers and resins in the composite unit share the load well. When the load increases, minor defects in the resin will lead to the germination of microcosmic matrix cracks in the first place. When the cracks expand to the fiber, they will develops along the interface of fiber and resin, and debonding occurs subsequently. This will result in the loss of the restraint of the resin on the fibers, and the local deformation increases. Excessive deformation will lead to tensile fracture of fibers, which will aggravate the continuous expansion of cracks along the vertical direction to the fiber, and eventually lead to the generation of macro cracks. This failure mode is brittle and the failure mechanism will not change during the tensioning process. The three types of meso-failure modes above can also be found in the scanning electron microscopy (SEM) images of UD CFRP tendon at 20 ºC, as shown in Fig. 6(a). However, when it comes to 300 ºC, which exceeds the glass transition temperature T_g (220-230 ºC) of the resin, the matrix becomes soft and its mechanical properties degrade rapidly [18]. This will result in the decrease of the ability of matrix medium to transfer the stress between the fibers. Because the fibers are not perfectly parallel inside the tendon, as shown in Fig. 7, when the load is applied, the internal shorter fibers are straightened first, resulting in stress concentration in these fibers. Due to the low carrying capacity of a single fiber wire, it is broken at a lower load level, and thus the AE signals appear. As the load increases, the relatively short fibers are gradually pulled off. When the load increases to close to the fracture limit, the parallel fiber bundles of equal length inside the tendon are gradually pulled off, resulting in a large number of AE counts and a sharp trend of the cumulative AE energy curve. Therefore, the fluctuation of AE signals in the whole time

series is more obvious than that at room temperature. As can be seen from the Fig. 6(c), when the temperature rises to 450 °C, a large amount of resin volatiles, and the remaining fibers bear the tensile load alone. For UD CFRP specimen at 500 °C (Fig. 6(d)), the resin inside the material evaporates thoroughly, as a result, the effect of the above failure mechanism is more obvious so $\Delta\alpha$ reaches the maximum.

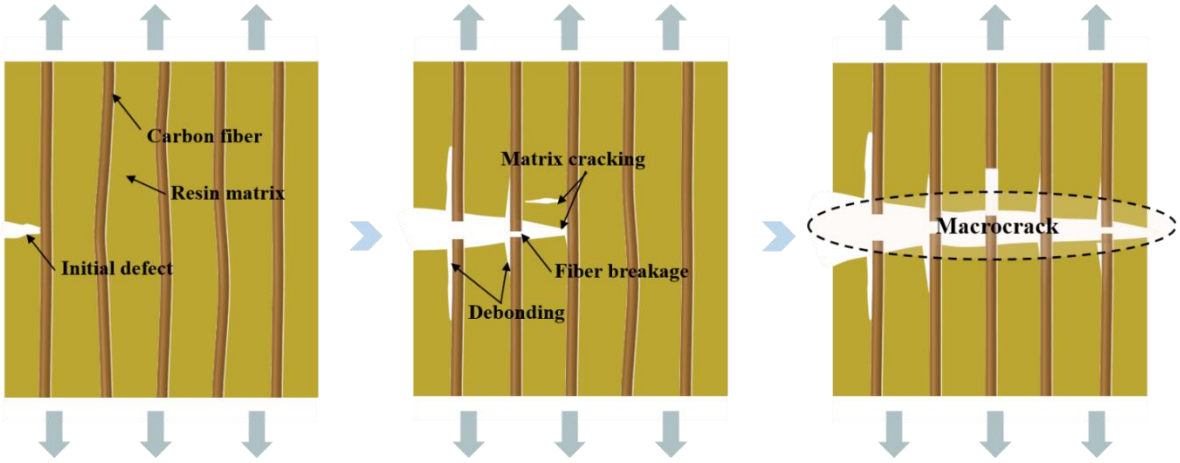

Fig. 5. Schematic of failure mechanism of UD CFRP tendons at 20℃.

In addition to the above analysis of changes in $\Delta\alpha$ values, it can be seen from Fig.4 that the value of Δf was less than 0 when the temperature was at 20 °C, which means the weak AE signals dominate [51]. While the Δf values at other three temperatures were more than 0, and AE signals were dominated by strong signals. This indicates that the data structure of AE signals and the damage mechanism reflected in the process of failure under the influence of high temperature have obvious changes. Moreover, the multi-fractal spectrum showed a left skewed distribution in time scale at 20 °C, indicating that small signals played a dominated role in material failure. While the multi-fractal spectrum at high temperature showed a right skewed distribution, manifesting that the large-signal played a dominant role in failure process [51]. Due to the complexity of meso-structure of the composite, the mode of internal damage of UD CFRP tendons is relatively complex when they are tensioned at room temperature, such as matrix cracking, debonding and fiber breakage (Fig. 5). The generation of small signals exactly reflects the initiation of micro-cracks in the material. As shown in Fig. 6(a), there are a lot of

micro-cracks in the material at room temperature, which is also the main reason for macro-fracture of the material. The diversity of the causes of these cracks and the randomness of their propagation direction also verify the complexity of AE signals reflected by multi-fractal spectrum under this temperature condition.

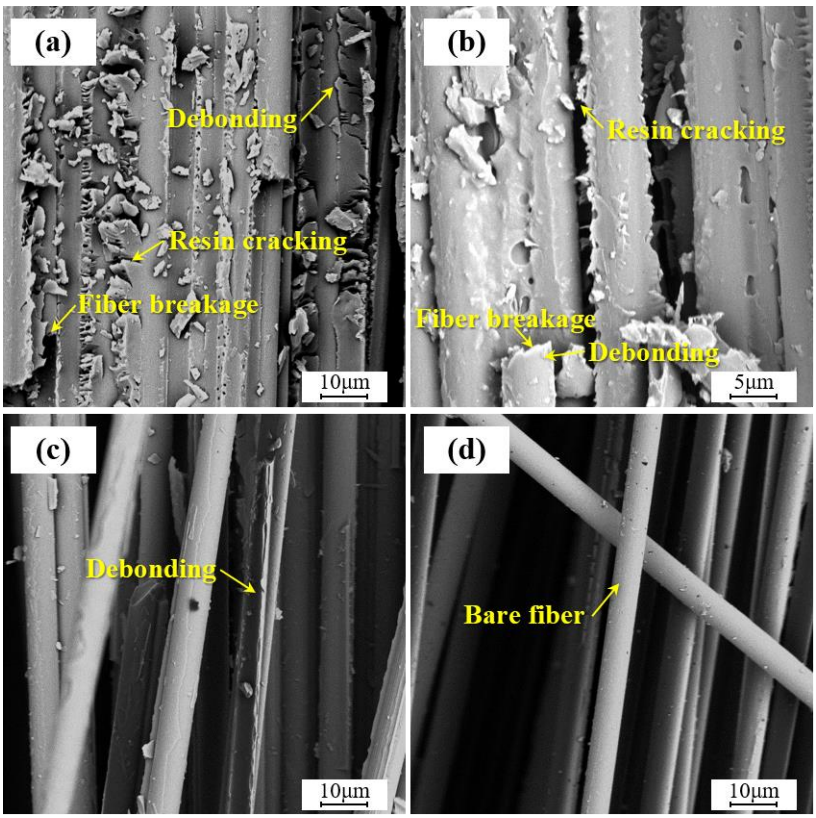

Fig. 6. SEM image of UD CFRP tendon specimen at different temperatures: (a) 20 ℃ (b) 300 ℃ (c) 450 ℃ (d) 500 ℃.

When the temperature rises to 300~500 ℃, the resins change from elastic to viscoelastic, which will lead to softening or even volatilization. As was shown in Fig. 6(b), the matrix at 300 ℃ presented a state significantly different from that at 20 ℃. After heating, the resin material showed viscous properties and the number of micro-cracks was dramatically reduced, among which only large-scale cracks occurred due to fiber misalignment. This can also prove that the larger signals are dominated in the intensive multi-fractal spectrum. As the temperature increased further, the resin began to volatilize. In consequence, both failure modes, interphase debonding and matrix cracking, will gradually decrease or even disappear, and the fiber breakage will gradually become the main failure mode during tensile process, as shown in Fig.7.

The fact that the AE count and energy triggered by fiber breakage are higher than those of other modes also confirms that the higher physical parameter events represented by the multi-fractal spectrum play a leading role.

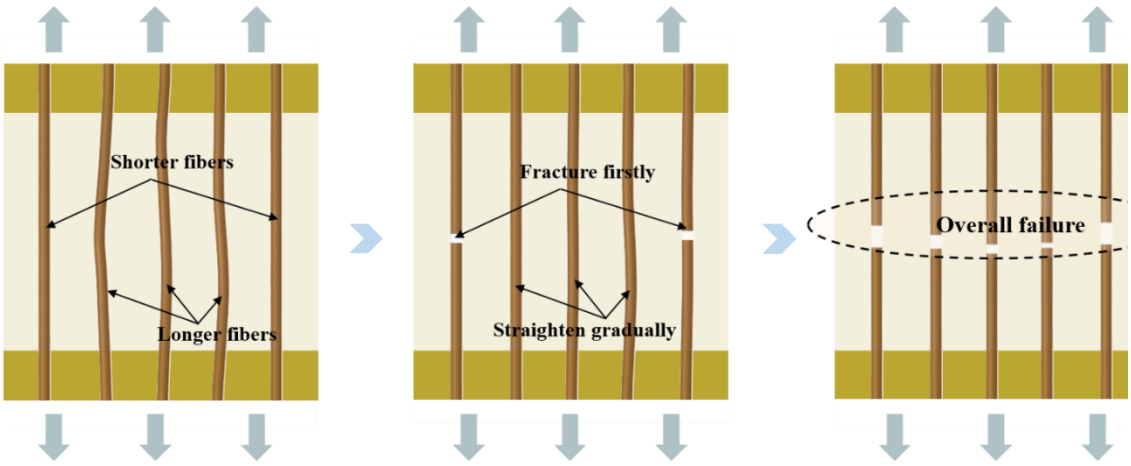

Fig. 7. Schematic of failure mechanism of UD CFRP tendons after resin failure at high temperature.

5. Conclusion

In this study, fractal theory was used to study the nonlinear characteristics of AE signals during tensile process of UD CFRP tendons at different temperatures of 20 ºC, 300 ºC, 450 ºC and 500 ºC. The damage evolution of materials at different temperatures was analyzed by using the change characteristics of the Hurst index. The tensile failure mechanism of UD CFRP tendons at high temperature was investigated by multi-fractal spectrum. The main conclusions are as follows:

1) Temperature has a significant influence on the time-domain characteristics of AE signals during the tensile process of UD CFRP tendons. The AE count remains active during the whole tensile process at 20 ºC, and the cumulative AE energy curve shows a multi-step ascending feature when approaching failure. However, for the other three high temperature conditions, AE signals are inactive under lower load, and the signal activity increases sharply when close to destruction, and the cumulative AE energy curve shows an

exponential upward trend.

2) The Hurst index of AE signals has two typical ‘up-down’ marks in the tensile process. The first rising mark indicates the initiation of meso-damage in the material, and the first falling mark indicates the stable development of damage. The second rise means that the damage changes from stable development to unstable development, indicating the forthcoming material failure. The ‘up-down’ mark in the second paragraph can therefore be used as a failure warning for health monitoring. The reference critical stress level of UD CFRP tendons at 20 ºC, 300 ºC, 450 ºC and 500 ºC are 0.7, 0.8, 0.7 and 0.6, respectively, which provides certain guidance for the fire resistance design of the structure.

3) The characteristics of multi-fractal spectrum of AE signals can well reflect the failure mechanism of UD CFRP tendons at different temperatures. At 20 ºC, the internal damage mode of the material is complex, and the initiation of micro-cracks such as matrix cracking and debonding plays a leading role in the process of failure, which leads to the left skewed distribution of the fractal spectrum and the negative value of Δf. While at other high temperatures, the multi-fractal spectrum is of right skewed distribution and Δf is positive, indicating that the fiber fracture represented by the larger signal plays a dominant role in the failure process due to the softening and volatilization of resin. Moreover, due to the loss of matrix protection under high temperature condition, the non-uniform fibers are pulled and broken successively, which resulted in the large non-uniformity of AE signals in the whole process. Therefore, $\Delta\alpha$ rises with the increasing of temperature.

CRediT authorship contribution statement

Weixin Wang: Investigation, Software, Data curation, Writing - original draft. Xiao Wang:

Validation, Investigation. Jie Xu: Conceptualization, Methodology, Writing - review &editing. Qinghua Han: Supervision, Writing - review & editing.

Declaration of Competing Interest

The authors declare that they have no known competing financial interests or personal relationships that could have appeared to influence the work reported in this paper.

Acknowledgements

The authors also would express appreciation to the financial support by: National Natural Science Foundation of China (no. 52278204), the Joint Funds of the National Natural Science Foundation of China (U1939208), and the 111 Project (B20039) and the Innovation Foundation for Postgraduate of Tianjin (Grant No. 2021YJSB128).

References

[1] Xie G, Bian Y, Feng Q, Wang CM, Liu R. Experimental study on wedge-bonded anchors for CFRP tendons under cyclic loading. Construction and Building Materials. 2020;236.

[2] Wang L, Zhang J, Xu J, Han Q. Anchorage systems of CFRP cables in cable structures—a review. Construction and Building Materials. 2018;160:82-99.

[3] Liu T, Liu X, Feng P. A comprehensive review on mechanical properties of pultruded FRP composites subjected to long-term environmental effects. Composites Part B: Engineering. 2020;191.

[4] Liu Y, Zwingmann B, Schlaich M. Carbon fiber reinforced polymer for cable structures—a review. Polymers. 2015;7:2078-99.

[5] Ye Y, Guo Z, Liu Y, Wang L. Flexural behavior of stone beams reinforced with prestressed NSM CFRP bars. Construction and Building Materials. 2014;54:466-76.

[6] Deng Y, Li Z, Zhang H, Corigliano A, Lam ACC, Hansapinyo C, Yan Z. Experimental and analytical

investigation on flexural behaviour of RC beams strengthened with NSM CFRP prestressed concrete prisms. Composite Structures. 2021;257.

[7] Badawi M, Wahab N, Soudki K. Evaluation of the transfer length of prestressed near surface mounted CFRP rods in concrete. Construction and Building Materials. 2011;25:1474-9.

[8] Xie G, Yin J, Liu R, Chen B, Cai D. Experimental and numerical investigation on the static and dynamic behaviors of cable-stayed bridges with CFRP cables. Composites Part B: Engineering. 2017;111:235-42.

[9] Yang Y, Fahmy MFM, Guan S, Pan Z, Zhan Y, Zhao T. Properties and applications of FRP cable on long-span cable-supported bridges: A review. Composites Part B: Engineering. 2020;190.

[10] Wang YC, Wong PMH, Kodur V. An experimental study of the mechanical properties of fibre reinforced polymer (FRP) and steel reinforcing bars at elevated temperatures. Composite Structures. 2007;80:131-40.

[11] Han Q, Wang L, Xu J. Experimental research on mechanical properties of transverse enhanced and high-temperature-resistant CFRP tendons for prestressed structure. Construction and Building Materials. 2015;98:864-74.

[12] Khorasani NE, Garlock M, Gardoni P. Fire load: Survey data, recent standards, and probabilistic models for office buildings. Engineering Structures. 2014;58:152-65.

[13] Peris-Sayol G, Paya-Zaforteza I, Balasch-Parisi S, Alós-Moya J. Detailed analysis of the causes of bridge fires and their associated damage levels. Journal of Performance of Constructed Facilities. 2017;31.

[14] Bazli M, Abolfazli M. Mechanical properties of fibre reinforced polymers under elevated temperatures: An overview. Polymers. 2020;12.

[15] Wang YC, Kodur V. Variation of strength and stiffness of fibre reinforced polymer reinforcing bars with temperature. Cement and Concrete Composites. 2005;27:864-74.

[16] Ashrafi H, Bazli M, Najafabadi EP, Vatani Oskouei A. The effect of mechanical and thermal properties of

FRP bars on their tensile performance under elevated temperatures. Construction and Building Materials. 2017;157:1001-10.

[17] Khaneghahi MH, Najafabadi EP, Shoaei P, Oskouei AV. Effect of intumescent paint coating on mechanical properties of FRP bars at elevated temperature. Polymer Testing. 2018;71:72-86.

[18] Xu J, Wang W, Han Q. Mechanical properties of pultruded high-temperature-resistant carbon-fiber-reinforced polymer tendons at elevated temperatures. Construction and Building Materials. 2020;258.

[19] Zhou F, Zhang J, Song S, Yang D, Wang C. Effect of temperature on material properties of carbon fiber reinforced polymer (CFRP) tendons: Experiments and model assessment. Materials (Basel). 2019;12.

[20] Ono K. Review on structural health evaluation with acoustic emission. Applied Sciences. 2018;8.

[21] Thirumalaiselvi A, Sasmal S. Pattern recognition enabled acoustic emission signatures for crack characterization during damage progression in large concrete structures. Applied Acoustics. 2021;175.

[22] Behnia A, Chai HK, Shiotani T. Advanced structural health monitoring of concrete structures with the aid of acoustic emission. Construction and Building Materials. 2014;65:282-302.

[23] Nair A, Cai CS. Acoustic emission monitoring of bridges: Review and case studies. Engineering Structures. 2010;32:1704-14.

[24] Romhány G, Czigány T, Karger-Kocsis J. Failure assessment and evaluation of damage development and crack growth in polymer composites via localization of acoustic emission events: A review. Polymer Reviews. 2017;57:397-439.

[25] Saeedifar M, Zarouchas D. Damage characterization of laminated composites using acoustic emission: A review. Composites Part B: Engineering. 2020;195.

[26] Li H, Huang Y, Chen W, Ma M, Tao D, Ou J. Estimation and warning of fatigue damage of FRP stay cables based on acoustic emission techniques and fractal theory. Computer-Aided Civil and Infrastructure

Engineering. 2011;26:500-12.

[27] Li D, Hu Q, Ou J, Li H. Fatigue damage characterization of carbon fiber reinforced polymer bridge cables: Wavelet transform analysis for clustering acoustic emission data. Science China Technological Sciences. 2011;54:379-87.

[28] Li D, Hu Q, Ou J. Fatigue damage evolution and monitoring of carbon fiber reinforced polymer bridge cable by acoustic emission technique. International Journal of Distributed Sensor Networks. 2012;8.

[29] Shateri M, Ghaib M, Svecova D, Thomson D. On acoustic emission for damage detection and failure prediction in fiber reinforced polymer rods using pattern recognition analysis. Smart Materials and Structures. 2017;26.

[30] Ghaib M, Shateri M, Thomson D, Svecova D. Study of FRP bars under tension using acoustic emission detection technique. Journal of Civil Structural Health Monitoring. 2018;8:285-300.

[31] Xu J, Liu X, Han Q, Wang W. A particle swarm optimization–support vector machine hybrid system with acoustic emission on damage degree judgment of carbon fiber reinforced polymer cables. Structural Health Monitoring. 2020.

[32] Xu J, Wang W, Han Q, Liu X. Damage pattern recognition and damage evolution analysis of unidirectional CFRP tendons under tensile loading using acoustic emission technology. Composite Structures. 2020;238.

[33] Mandelbrot B. Fractals: form, chance and dimension. 1st ed. New York: W.H. Freeman, 1977.

[34] Karperien A, Ahammer H, Jelinek H. Quantitating the subtleties of microglial morphology with fractal analysis. Frontiers in Cellular Neuroscience 2013;7:3.

[35] Mandelbrot B. How long is the coast of britain? Statistical self-similarity and fractional dimension. Science 1967;156:636–638.

[36] Jiang Z, Xie W, Zhou W, Sornette D. Multifractal analysis of financial markets: a review. Reports on Progress in Physics. 2019;82.

[37] Biancolini M, Brutti C, Paparo G, Zanini A. Fatigue cracks nucleation on steel, acoustic emission and fractal analysis. International Journal of Fatigue. 2006;28:1820-5.

[38] Lv Z, Jiang A, Jin J, Lv X, Liu W. Multifractal analysis and compressive strength prediction for concrete through acoustic emission parameters. Advances in Civil Engineering. 2021;2021:1-13.

[39] Li D, Wang E, Kong X, Ali M, Wang D. Mechanical behaviors and acoustic emission fractal characteristics of coal specimens with a pre-existing flaw of various inclinations under uniaxial compression. International Journal of Rock Mechanics and Mining Sciences. 2019;116:38-51.

[40] Kong X, Wang E, He X, Li Z, Li D, Liu Q. Multifractal characteristics and acoustic emission of coal with joints under uniaxial loading. Fractals. 2017;25.

[41] Xie H, Liu J, Ju Y, Li J, Xie L. Fractal property of spatial distribution of acoustic emissions during the failure process of bedded rock salt. International Journal of Rock Mechanics and Mining Sciences. 2011;48:1344-51.

[42] Pavlov AN, Anishchenko VS. Multifractal analysis of complex signals. Physics-Uspekhi. 2007;50:819–34.

[43] Kong B, Wang E, Li Z, Wang X, Chen L, Kong X. Nonlinear characteristics of acoustic emissions during the deformation and fracture of sandstone subjected to thermal treatment. International Journal of Rock Mechanics and Mining Sciences. 2016;90:43-52.

[44] ASTM E976–10. Standard guide for determining the reproducibility of acoustic emission sensor response. ASTMInt 2010.

[45] ASTM D3039M–14. Standard test method for tensile properties of polymer matrix composite materials. ASTM Int 2014.

[46] ACI. 440.3R-04. Guide test methods for fibre-reinforced polymers (FRPs) for reinforcing or strengthening concrete structures. American Concrete Institute 2004..

[47] Halsey TC, Jensen MH, Kadanoff LP, Procaccia I, Shraiman BI. Fractal measures and their singularities: The characterization of strange sets. Nuclear Physics B - Proceedings Supplements 1987;2:501–11.

[48] Benzi R, Paladin G, Parisi G, Vulpiani A. On the multifractal nature of fully developed turbulence and chaotic systems. Journal of Physics A: Mathematical and General 1984;17:3521–3531.

[49] Muzy JF, Bacry E, Arneodo A. The multifractal formalism revisited with wavelets. International Journal of Bifurcation and Chaos 1994;04:245–302.

[50] Kantelhardt JW, Zschiegner SA, Koscielny-Bunde E, Havlin S, Bunde A, Stanley HE. Multifractal detrended fluctuation analysis of nonstationary time series. Physica A: Statistical Mechanics and Its Applications 2002;316:87–114.

[51] Tan J, Hu C, Lyu Q, Dick JM, Ranjith PG, Li L, Wang Z. Multi-fractal analysis for the AE energy dissipation of CO2 and CO2+ brine/water treated low-clay shales under uniaxial compressive tests. Fuel. 2019;246:330-9.

Improved Adhesive Bonding Strength of Bonded Repair of Thermoplastic Composites Using Laser Surface Patterning

Sepideh Sadat Hosseini Noorabadi [1], Muhammad Bilal Asif [1], and Jinglei Yang [1, 24]

[1] Department of Mechanical and Aerospace Engineering, Hong Kong University of Science and Technology, Clear Water Bay, Kowloon, Hong Kong SAR

[2] Shenzhen Hong Kong Collaborative Innovation Research Institute, Futian, Shenzhen, China

Abstract: Composite structures are gaining more and more importance in a variety of industrial applications, thereby novel maintenance and repair techniques are required to ensure their proper operation. Surface pre-treatment is one of the key processes in the bonded repair of fiber-reinforced polymer composites. Laser surface treatment can be easily monitored and adjusted for fast, precise, scalable, and reproducible surface patterning of composites that is capable of automation. This paper, for the first time, investigates the feasibility of laser surface patterning as a surface activation method for the repair of Thermoplastic Glass Fibre/Elium® Composites. The composite adherents are structured in parallel lined-like textures using a 1064 nm pulsed nanosecond laser. The influence of laser parameters such as fluence on the produced surface microstructures and resulting bonding performance are discussed. The surface morphology and microstructure were characterized by scanning electron microscopy (SEM) and fourier transform infrared spectroscopy (FTIR) analyses were carried out to study the effect of laser texturing on the functional groups of composites' surfaces. Bonded specimens were mechanically tested using a single lap shear test. It was found that the optimum laser fluence is 12.8 J/cm^2 leading to the bonding improvement of up to 30% compared to the untreated specimens and the highest shear strength of 15.2 MPa thus reducing repair area and costs significantly. Furthermore, it is demonstrated that this improvement in adhesive strength is achieved only by selective removal of resin at controlled laser parameters without exposing or damaging fibers on the composite surface resolving the main concern about damaging the underlying plies.

Keywords: Laser Surface Treatment, Interface, Bonded Repair, Thermoplastic Composite

1. Introduction

[4] ***Email:*** *maeyang@ust.hk*

The use of fiber-reinforced polymer composites (FRPCs) in various industries is being increased during the last decades due to their superior advantages, such as high specific strength and stiffness making them suitable candidates for engineering structures. Compared with metals, the anisotropic behavior of advanced composite makes the non-destructive damage assessment, maintenance strategies, and repair verification more complicated than traditional metal construction [1]. The National Aeronautics and Space Administration clearly emphasized that the major challenges for the composite aircraft industry are FRPC structural maintenance and repair technologies[2], [3]. Metal structural repair often uses riveting and screw connecting techniques while composite repair can make use of bonded repair (sided lap or scarf based)[4]–[6]. The future trend in structural repairs is towards the adhesively bonded repair technique for a variety of reasons investigated by Baker and Wang [7].

The initial FRPC material surface is inappropriate for adhesively bonded repairs and needs an appropriate surface treatment. The purpose of surface treatment is to promote surface activity via the removal of surface contaminations, modification of surface roughness, and the improvement of surface free energy [8], [9]. Various surface treatment strategies are introduced for adhesively bonded repairs such as polishing, mechanical abrasion, grit blasting, plasma modification, peel-ply, and chemical etching[10]–[18]. However, these methods have various drawbacks that ascertain researchers to find an alternative strategy. For example, mechanical abrasion is an inefficient, long-term process that is subject to human error and inconsistencies. Corona discharge and plasma treatment can activate surface molecules by chemical modification for surface wettability improvement, but the equipment is expensive, and the treatment depth is only a very thin layer. Peel plies are for short-term storage and should be stored frozen. Regarding the chemical etching process, solutions such as strong acid/alkali/oxidant pollute the environment and are harmful to operators.

A repeatable, effective, and measurable surface treatment is a key component of a repairing methodology. Recently, laser surface treatment of adhesively bonded repairs has attracted attention, as a kind of new and high-functionality technique. In laser surface treatment, a laser beam is used to ablate the composite surface thereby creating a surface texture. The laser surface preparation is a green process, which can be easily controlled and automated to create a uniform surface texture. Madge et al [19] compared the strength and fatigue properties of laser-treated and sand-treated CFRP adhesively bonded joints demonstrating that laser treatment for the selective removal of the matrix resin prior to adhesive bonding is potentially an effective method for the improvement of bonding strength. Palmieri found that a 355 nm Nd: YAG laser could ablate about 10–20 μm depth of the laminate surface without breaking fibers and will improve the reproducibility and robustness in a production environment [20]. Li et al [21] compared the effect of laser surface treatment and polish treatment on the bonded repair of CFRP composites. It was found that laser treatment resulted in chemical and physical activation of the bonding surface which improved the adhesive bonding strength compared to

the polished ones. Zhan et al [22] investigated the effect of UV laser treatment on the adhesive joint strength of CFRP bonds. The results revealed that there is a relation between surface resin distribution after laser treatment and bonding strength which is highly dependent on the laser parameters such as scanning speed. Lim et al [23] showed that the laser treatment of Thermoplastic Carbon fiber reinforced Polyamide composites led to the improvement of the adhesive bonding strength due to the increase in surface wettability and the functional groups. The interest in Elium-based composites in recent years as a room temperature thermoplastic resin with superior mechanical properties comparable to thermoset composites [24], [25] and the advantage of recyclability reveals that it is needed to determine whether these composites are suitable for laser surface texturing or not. In this paper, for the first time, the feasibility of laser texturing as a surface treatment strategy for Elium-based composite is investigated to see how laser parameters influence the laser interaction with the composite and the resulting microstructure. Furthermore, the single lap shear strength tests were examined to investigate the effect of laser surface texturing on bonding strength improvement.

2. Material and methods

2.1. Materials and fabrication

Elium® 188, the room temperature acrylic resin, is supplied from Arkema. As recommended by the resin manufacturer 2% Benzoyl peroxide (BPO) was mixed with the Elium® resin to initiate polymerization. For each composite, 14 layers of a 200g 2×2 Twill Woven E-glass fabric (Easy Composites Ltd), were used as reinforcement. The novel composite system was developed using a cost-effective vacuum-assisted resin infusion (VARI). The kit for the VARI process consists of an aluminum mold, vacuum pump, pressure pot, inlet, and outlet hoses for infusion of resin, peel plies, mesh flow, and spiral tube, Fig. 2.1(a). After the layers of reinforcements are placed on the aluminum mold and covered by a vacuum bag, the resin inlet is locked by clamps, and the resin outlet was connected to the pressure pot of the vacuum pump. Then, the assembly was placed under maximum vacuum pressure (0.1 mbar) using the vacuum pump to remove the air trapped among the layers of the laminate, Fig. 2.1(b). Then, the Elium resin consisting of a BPO initiator was infused into the prepared layup. After the injection completion, the inlet hose was clamped, and the composite was cured in an oven at 60˚C for 2 hours. Once cured, based on the ASTM standard, the specimens with ~2.3 mm thickness were cut via an abrasive waterjet cutting machine, Fig. 2.1(c).

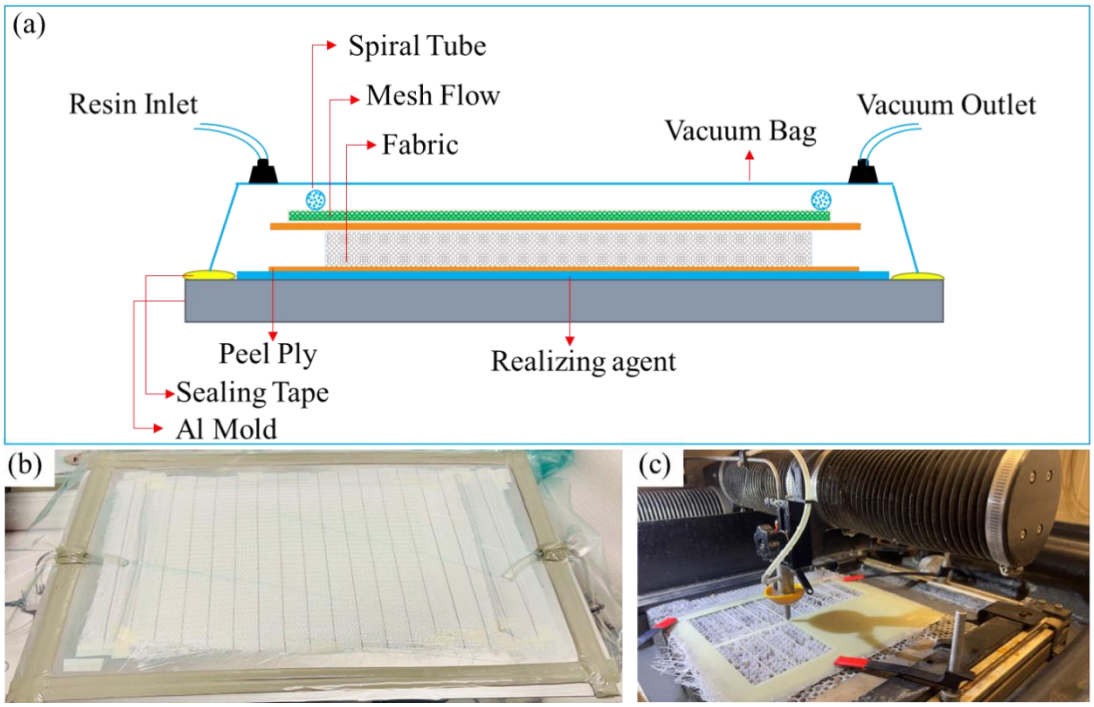

Fig. 2.1 Schematic of Vacuum Assisted Resin Infusion (VARI) (a), Glass Fiber-Elium Composite Layup (b), and Abrasive waterjet cutting (c)

2.2. Laser surface treatment

Laser texturing was performed with a 1064 nm nanosecond pulsed Han's Laser source, with nominal power and a spot diameter of 20 W and 30 µm, respectively. Laser irradiation was performed over areas of 25 × 25 mm on the composite specimens while varying the laser fluence.

Table 1

Laser system characteristics and parameters.

Wavelength	1064 ± 5 nm
Power	20 W
Spot Diameter	30 µm
M^2 Factor	< 2
Scanning Speed	1000 mm/s
Number of Scans	2
Fluence	12.8 J/cm^2 and 33.0 J/cm^2
Hatch space	100 µm

For each repetition and parameter set, two identical specimens were textured to allow the preparation of an adhesive-bonded joint between the treated surfaces. Pulse fluence, F, was calculated based on energy per unit area:

$$F = \frac{4E_p}{\pi d_0^2} \quad (1)$$

where E_p is the pulse energy and d_0 is the focused spot diameter.

The laser scanning strategy comprised parallel lines (PL) orthogonal to the direction in which force was applied during tensile tests. Preliminary tests were first performed to establish the macroscopic parameter range over which an appropriate level of laser interaction could be achieved without excessive melting or burning of Glass fiber-Elium composites. Firstly, the influence of laser treatment on the composite ablation was investigated to determine the optimum laser fluence, then the hatch spacing effect was evaluated to obtain the highest adhesive strength at optimum fluence.

2.3. Scanning electron microscopy

Scanning electron microscopy (TM3030, Hitachi) was performed with an accelerating voltage of 10 kV to observe the modified morphology of the laser-treated surfaces and their cross-section. Primarily, composites were coated with ~15 nm of Au coating for charge dissipation.

2.4. Fourier transform infrared spectroscopy (FTIR)

To investigate the effect of the laser treatment on the functional groups on the Glass Fiber-Elium surfaces, the surfaces of the laser-treated and untreated specimens were analyzed with Fourier transform infrared spectroscopy (FTIR). The FTIR was measured with a Bio-Rad FTS 6000 spectrometer based on an attenuated total absorbance unit. The collected spectral range was 400 to 4000 cm^{-1}, the resolution was 4 cm^{-1}, and 128 scans were conducted. Each measurement was performed after the acquisition of the spectrum of the surrounding air as a background.

2.5. Adhesive bonding test

Specimens of similar thickness were bonded to each other using 3M™ Scotch-Weld™ Low-Odour Acrylic Adhesive DP810 followed by oven curing at 49˚C for 30 minutes recommended by the manufacturer [26]. The shear strength of this DP810 adhesive for aluminum adherend and acrylic adherend is 26.2 MPa and 7.6 MPa, respectively [26].

Lap shear testing was carried out (Universal testing machine, MTS Sintech 10/D) to obtain the static lap shear strength of the bonded joints following the ASTM D5868-01 standard [27] at a constant speed of 13 mm/min. Fig. 2.2 shows the sample dimension for a single lap shear bonding experiment. Load-displacement curves were plotted, and the maximum LSS was obtained by dividing the peak load and the bonded area (25×25 mm^2). For each configuration of untreated or laser-treated specimens, at least 5 samples were tested.

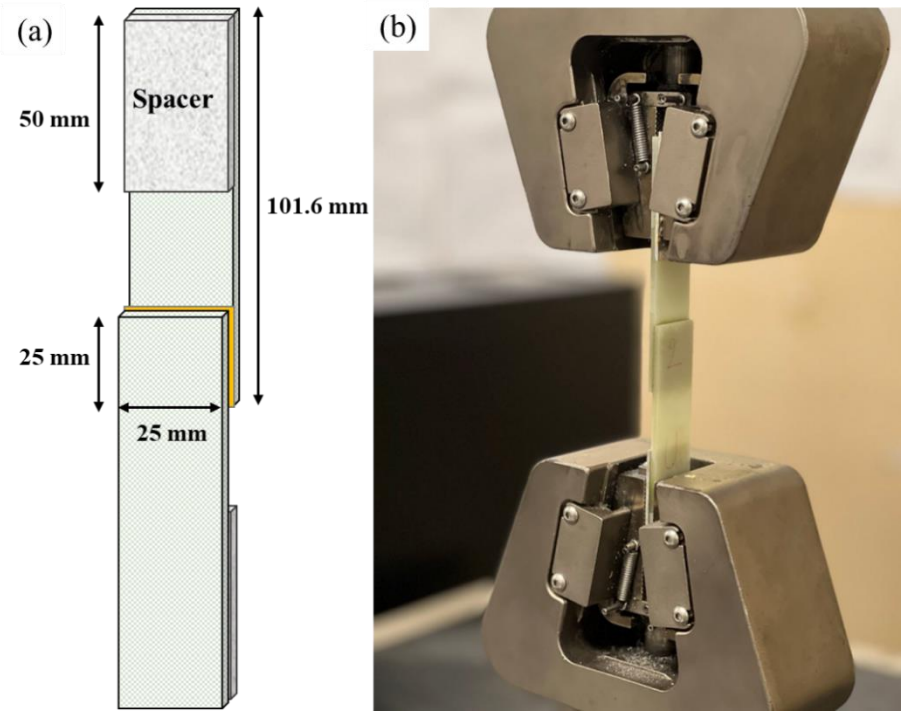

Fig. 2.2 Schematic illustration of specimen configuration for single lap shear test (a), Single lap shear test prior to the experiment (b)

3. Results and Discussion

3.1. The microstructure of laser-treated composites

The main parameter to determine the removal depth of the matrix is accumulated laser fluence during the laser ablation process. Surface resin's ablation cannot be obtained when adequate laser fluence does not accumulate on the surface[28]. On the contrary, when the laser fluence is too high, the risk of delamination arises [29]. Thus, the determination of laser fluence is vital for the working composite material specifically for Elium-based composites which there is not any information regarding its interaction with pulse laser radiation as a surface treatment method. In our experiment to determine the optimum accumulated laser fluence, Glass fiber-Elium composites were treated with 12.8 J/cm^2 and 33.0 J/cm^2 fluences. As seen in Fig. 3.1, the surface morphology of untreated samples demonstrates the typical surface of a composite with a woven pattern of glass fabric under surface resin. When the composite is treated with lower accumulated laser fluence, 12.8 J/cm^2, it is seen that most of the Elium resin remains on the surface as expected, and only a small amount of fiber surface was exposed (small white points on the SEM micrographs pointed with yellow arrow) (Fig. 3.1(b)). As laser fluence increased to 33.0 J/cm^2 the removal of much more Elium resin from the surface and severe fabric damage, exposure, breakage, and uncontrolled resin removal are obvious. A high-fidelity laser ablation process is needed to avoid exposing or damaging composite fibers [30]; hence, the laser fluences greater than 12.8 J/cm^2 cannot guarantee acceptable bonding performance.

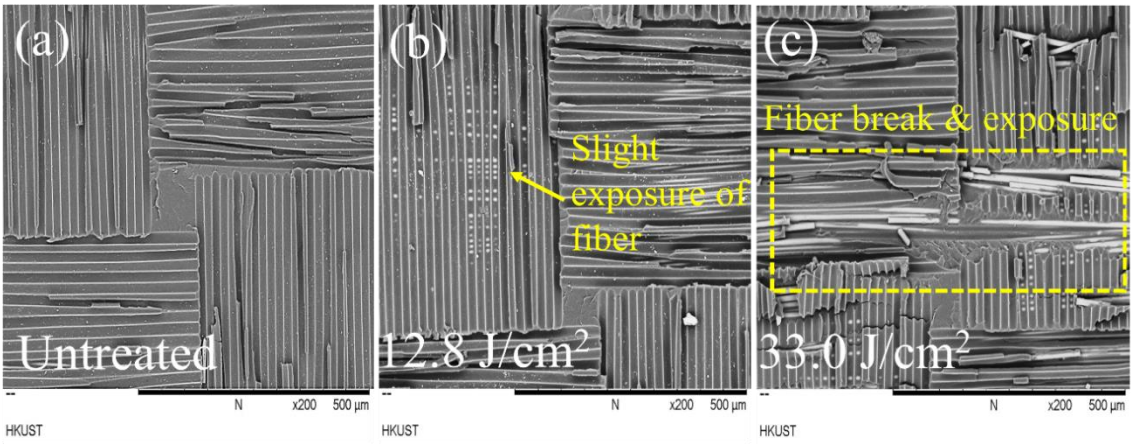

Fig. 3.1 SEM images (scale bar = 500 µm) of Glass fiber- Elium composite surfaces: untreated (a), laser-treated with 12.8 J/cm^2 fluence (b), and laser- treated with 33.0 J/cm^2 fluence (c)

3.2. Surface Chemistry

Chemical adhesion theory represents the increase in the chemical bonding activity between the adherend and the adhesive layer can obviously improve the bonding strength; hence, surface chemistry modification after various levels of laser treatment needs to be characterized [30]. FTIR results for untreated and laser-treated samples are shown in Fig. 3.2. For untreated Glass fiber-Elium composite, there was a sharp, intense peak that appeared at 1720 cm^{-1} due to the presence of ester carbonyl group (C=O) stretching vibration. The broader peak appeared ranging from 1300 to 1000 cm^{-1} due to the presence of ester bond (C–O) stretching vibration. There was also another peak observed at 2951 cm^{-1} due to the presence of alkyl group (C–H) stretching [31]. Laser-treated samples also showed curves with similar peaks to the untreated samples revealing that for 12.8 J/cm^2 and 33.0 J/cm^2 fluences the surface functional groups are still related to PMMA, but for 70.8 J/cm^2 the absorption peak changed to Glass peak with the presence of Si-O-Si group showing that for this level of fluence all surface resin is removed, and the underlying fabric is exposed to the surface. Considering the complete removal of Elium resin and exposure/ breakage of glass fibers, this fluence level was considered too high and not suitable for any improvement in adhesive bond strength. Therefore, no further testing was carried out for fluence of 70.8 J/cm^2.

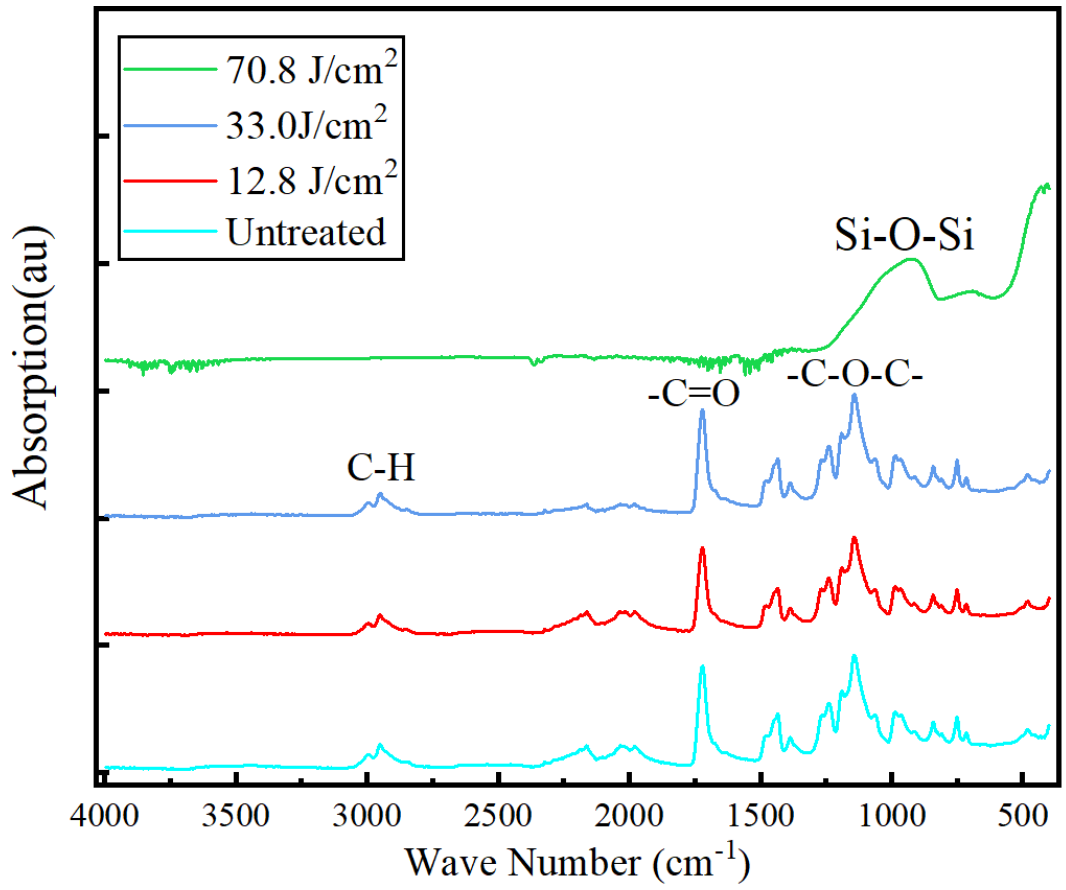

Fig. 3.2 FTIR spectra of untreated and laser-treated specimens at 12.8 J/cm^2, 33.0 J/cm^{2,} and 70.8 J/cm^2

3.3. Single Lap Shear Testing

Apparent shear strength tests have been conducted on Glass fiber- Elium composites as described in Section 2.5. To demonstrate the influence of laser fluence on the laminate surfaces, an initial composite named untreated sample was used as a base for comparison. As can be seen from Fig. 3.3, the lap shear strength of untreated adherend was determined to be 11.8 ± 0.36 MPa, while the highest shear bonding strength of 15.21 ± 0.42 MPa was observed for 12.8 J/cm^2 fluences with a 30% improvement as compared to the untreated laminate. The mechanical results are in concordance with the microstructural and surface chemistry studies described in previous sections. It illustrates that partial ablation of Elium resin by surface laser treatment at 12.8 J/cm^2 fluences resulted in better mechanical interlocking but also led to the chemical bonding activation and removal of surface contamination without damaging the composite surface. Furthermore, at 33.0 J/cm^2 fluences, a decline of 5% in adhesive bond strength was observed. This poor mechanical performance is attributed to the onset and development of surface damage (See Fig. 3.1(c)) which is further aggravated by the increase of laser fluence. Moreover, the minimum standard deviation was observed in the shear strength values at 12.8 J/cm^2 fluences, indicating the creation of a uniform and consistent surface texture.

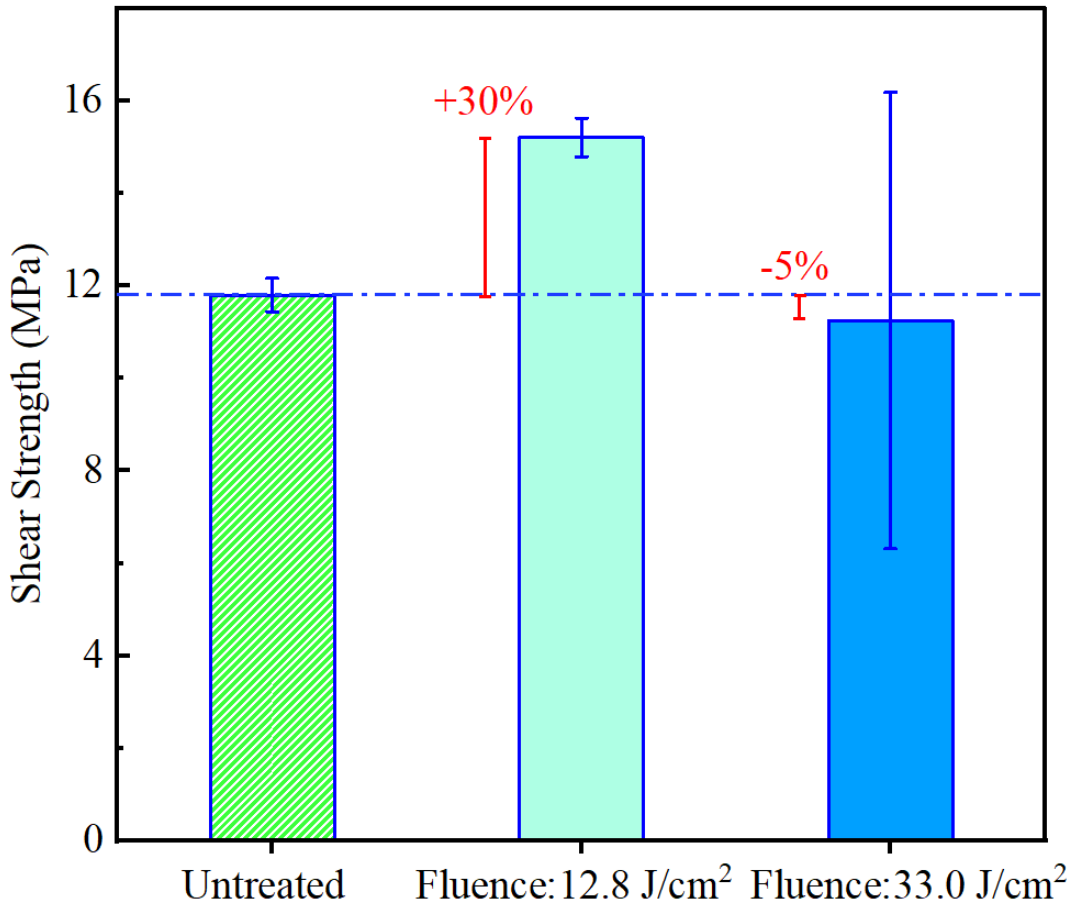

Fig. 3.3 Single lap shear results of untreated and laser-treated specimens at 12.8 J/cm^2 and 33.0 J/cm^2 fluences

4. Conclusion

In this research, activated Thermoplastic Glass fiber-Elium composite laminates were manufactured through pulsed laser treatment to study the influence of laser surface treatment on the surface behaviors and adhesion properties in the bonded repair of FRPC structures. The results demonstrate that optimization of laser parameters is crucial in creating desired texture on the surface without burning surface resin or local breakage and exposure of fibers to the surface; hence, the 12.8 J/cm^2 laser fluence is appropriate for laser texturing of this specific composite leading to significant improvement of adhesive bonding strength. Furthermore, the laser fluence at 33.0 J/cm^2 resulted in the breakage of fibers and the creation of uneven surface texture leading to poor bonding performance supporting the fact that laser treatment of FRPC needs to be conducted without the exposure and breakage of underlying fibers to the surface. It can be concluded that laser treatment is able to significantly improve the laser-based repair process and can be scalable for industrial applications by automation with may decrease time and labor costs. Initial findings are significant and demonstrate the feasibility of laser treatment as a surface preparation method. A detailed investigation on laser treatment of Thermoplastic Glass fiber-Elium composites is currently ongoing to understand the underlying adhesion

theories responsible for the bonding performance changes by hatch space and fluence variation in a broader range.

Acknowledgment

This project was partially supported by the Project of Hetao Shenzhen-Hong Kong Science and Technology Innovation Cooperation Zone (HZQB-KCZYB-2020083).

References

[1] K. B. Katnam, L. F. M. da Silva, and T. M. Young, "Bonded repair of composite aircraft structures: A review of scientific challenges and opportunities," Progress in Aerospace Sciences, vol. 61, pp. 26–42, Aug. 2013, doi: 10.1016/J.PAEROSCI.2013.03.003.

[2] C. Soutis, "Fibre reinforced composites in aircraft construction," Progress in Aerospace Sciences, vol. 41, no. 2, pp. 143–151, Feb. 2005, doi: 10.1016/J.PAEROSCI.2005.02.004.

[3] Tenney DR, Davis Jr JG, Pipes RB, and Johnston N, "Structural Framework for flight: NASA's role in the development of advanced composite materials for aircraft and space structures," NASA/CR-2011-217076 , 2009.

[4] A. Baker, Bonded repair of aircraft structures. 1988. Accessed: Sep. 12, 2022. [Online]. Available: https://books.google.com/books?hl=en&lr=&id=5WDb442rOekC&oi=fnd&pg=PR9&dq=Bonded+repair+of+aircraft+structures&ots=EzQV_lPF9F&sig=29Z2ASqq45RhNRqoGwqDyNa9_9k

[5] H. Bendemra, Compston, and PJ Crothers, "Optimisation study of tapered scarf and stepped-lap joints in composite repair patches," Compos Struct, vol. 130, 2015.

[6] I. Jölly, S. Schlögl, M. Wolfahrt, and G Pinter, "Chemical functionalization of composite surfaces for improved structural bonded repairs," Compos B Eng, vol. 69, 2015.

[7] A. Baker and J Wang, "Proposed through-life management approaches for adhesively bonded repair of primary structures," Int J Adhes Adhes, vol. 87, 2018.

[8] J. Jang and H. Yang, "The effect of surface treatment on the performance improvement of carbon fiber/polybenzoxazine composites," J Mater Sci, vol. 35, 2000.

[9] X. Li, X. Zhang, H. Zhang, J. Yang, A. Nia, and GB Chai, "Mechanical behaviors of Ti/CFRP/Ti laminates with different surface treatments of titanium sheets," Compos Struct, vol. 163, 2017.

[10] Y. Pan et al., "Improvement in interlaminar strength and galvanic corrosion resistance of CFRP/Mg laminates by laser ablation," Materials Letter, vol. 207, pp. 4–7, 2017.

[11] H. Lee and J. T. Ohsawa, "Effect of plasma surface treatment of recycled carbon fiber on carbon fiber-reinforced plastics (CFRP) interfacial properties," Appl Surf Sci, vol. 328, 2015.

[12] J. Y. Rhee, "A study on the peel and shear strength of aluminum/CFRP composites surface-treated by plasma and ion assisted reaction method," Composite Science and Technology, 2003.

[13] N. Encinas, B. Oakley, and MA Belcher, “Surface modification of aircraft used composites for adhesive bonding,” Int J Adhes Adhes, vol. 50, 2014.

[14] V. Prysiazhnyi, M. Stupavská, and C. K. Ráheľ, “A comparison of chemical and atmospheric plasma assisted copper plating on carbon fiber reinforced epoxy polymer surfaces,” Surf Coat Technol, vol. 258, 2014.

[15] J. Holtmannspötter, J. v. Czarnecki, M. Wetzel, D. Dolderer, and C. Eisenschink, “The use of peel ply as a method to create reproduceable but contaminated surfaces for structural adhesive bonding of carbon fiber reinforced plastics,” Journal of Adhesion, vol. 89, no. 2, pp. 96–110, Feb. 2013, doi: 10.1080/00218464.2012.731828.

[16] O. S. Kanerva, “The peel ply surface treatment for adhesive bonding of composites: A review,” Int J Adhes Adhes, 2013.

[17] D. Klapprott and R. W. Li, “Key factors of the peel ply surface preparation process,” compositesworld.com, 2004.

[18] M. Kurt, A. Güler, İ. Duran, and Ö. İ. Uludamar, “Effects of different surface treatments on the bond strength of glass fiber-reinforced composite root canal posts to composite core material,” J Dent Sci, vol. 7, 2012.

[19] M. Madge, E. Brousseau, M. Eaton, and C. Featherston, “Adhesive Bonding of laser processed CFRP panels,” 16th International Conference on Experimental Mechanics At: Cambridge, UK, 2014.

[20] F. Palmieri and C. W. Belcher, “Laser ablation surface preparation for adhesive bonding of carbon fiber reinforced epoxy composites,” Int J Adhes Adhes, vol. 68, 2016.

[21] S. Li, T. Sun, and W. Y. Liu, “A study of laser surface treatment in bonded repair of composite aircraft structures,” R Soc Open Sci, vol. 5, no. 3, Mar. 2018, doi: 10.1098/rsos.171272.

[22] X. Zhan, S. Chen, Y. Li, and Y. Y. Wang, “Effect of surface cold ablation on shear strength of CFRP adhesively bonded joint after UV laser treatment,” Int J Adhes Adhes, vol. 94, 2019.

[23] S. Lim, J. Cheon, and M. K. and, “Effect of laser surface treatments on a thermoplastic PA 6/carbon composite to enhance the bonding strength,” Compos Part A Appl Sci Manuf, vol. 137, 2020.

[24] M. Kazemi, L. Shanmugam, and … J. Yang, “Investigating the roles of fiber, resin, and stacking sequence on the low-velocity impact response of novel hybrid thermoplastic composites,” Composite Part B: Engineering, vol. 207, 2021.

[25] M. Kazemi, L. Shanmugam, D. Lu, and J. Yang, “Mechanical properties and failure modes of hybrid fiber reinforced polymer composites with a novel liquid thermoplastic resin, Elium®,” Compos Part A Appl Sci Manuf, vol. 125, 2019.

[26] “3M, “Scotch-Weld™ Low Odor Acrylic Adhesive DP810 Black Technical Data Sheet,” 2016, Accessed: Sep. 12, 2022. [Online]. Available: http://multimedia.3m.com/mws/media/66280O/3mscotch-weld-low-odor-acrylic-adhesives.pdf.

[27] “ASTM D5868-01; Standard Test Method for Lap Shear Adhesion for Fiber Reinforced Plastic (FRP) Bonding,” 2016. https://scholar.google.com/scholar?hl=en&as_sdt=0,5&q=ASTM+D5868-01%3B+Standard+Test+Method+for+Lap+Shear+Adhesion+for+Fiber+Reinforced+Plastic+(FRP)+Bonding (accessed Sep. 12, 2022).

[28] F. Fischer, S. Kreling, and … K. D., “Pre-treatment of CFRP for adhesive bonding using laser radiation,” ECCM15 - 15TH EUROPEAN CONFERENCE ON COMPOSITE MATERIALS, 2012.

[29] F. Fischer, S. Kreling, P. Jäschke, M. Frauenhofer, D. Kracht, and K. Dilger, “Laser surface pre-treatment of CFRP for adhesive bonding in consideration of the absorption behaviour,” Journal of Adhesion, vol. 88, no. 4–6, pp. 350–363, Apr. 2012, doi: 10.1080/00218464.2012.660042.

[30] A. B.-I. J. of A. and Adhesives and undefined 2012, “Adhesion phenomena in bonded joints,” Int J Adhes Adhes, vol. 38, pp. 95–116, 2012.

[31] P. Kalakonda and S. Banne, “Thermomechanical properties of PMMA and modified SWCNT composites,” Nanotechnol Sci Appl, vol. 10, pp. 45–52, Feb. 2017, doi: 10.2147/NSA.S123734.

Optimal selection of process parameters based on reasonable control of cutting force and cutting temperature in peripheral milling of CFRTP

Xianghe JIANG1,2 , Rao FU1,2 , Hongyan ZHOU1,2 , Gang WEI1,2 , Lianheng GE1,2 , Fuji WANG1,2*

1State Key Laboratory of High-Performance Precision Manufacturing, School of Mechanical Engineering, Dalian University of Technology, Dalian 116024

2Key Laboratory of High-Performance Manufacturing for Advanced Composite Materials, Liaoning Province, Dalian 116024

Abstract: Carbon fiber reinforced PEEK matrix composite (CFRTP) is an emerging material for aerospace industrial due to its superior properties. Milling CFRTP would be an important step during its application to achieve accurate shape for assembly. However, due to its high sensitivity on temperature, the machining surface quality is strongly affected by cutting force as well as cutting temperature. This paper conducted the studies about the effects of cutting force and cutting temperature on the quality of machined surface respectively and optimized machining parameters to improve the roughness of the machined surface. First, the suitable ranges of the cutting force and the cutting temperature are figured out, based on the specific analysis on the effects of the cutting force and cutting temperature on machined surface quality. It was found that the cutting force has a linear relationship with the feed rate. Then the relationship between cutting temperature and cutting speed under different feed rates is studied through neural network. Further, with this method, the temperature can be predicted according to cutting speed within an error of 6%. With that, the machining parameters optimization is conducted. The surface roughness is signally improved by using the optimized parameters. The research results are hope to provide guidance for high quality milling of CFRTP.

Keywords: CFRTP; Milling; Cutting force; Cutting temperature; Surface quality

1. Introduction

Carbon fiber reinforced high-performance PEEK matrix composite (CFRTP) is a material with many advantages, including excellent strength/stiffness to weight ratiotemperature resistance, recyclability and designable performance[1-4]. These properties make CFRTP an ideal material for weight reduction and efficiency enhancement of high-end equipment[5]. However, CFRTP is a difficult material to process due to its anisotropy, macroscopic lamination, and significant performance differences between the matrix phase PEEK resin and the micro-enhanced phase CF. In addition, processing damage is common, which makes it difficult to achieve high-quality processing of components. Therefore, achieving high-quality milling of thermoplastic

composites such as CFRTP is a significant challenge.

In the processing of composite materials, large cutting forces can result in significant material deformation, leading to poor surface quality.[6, 7] Temperature is also a critical factor in determining whether fiber and resin can be effectively removed. PEEK resin undergoes a phase transition from a glass state to a highly elastic state upon heating, which softens the resin and weakens the constraint on the fiber. This makes it challenging to cut the fiber effectively. Moreover, the heat-softened resin is prone to smearing on the machined surface under the extrusion of the tool[8], which results in poor surface quality. Additionally, PEEK resin exhibits strong viscosity after undergoing the thermal phase change, which can cause the chip removal ability of the tool to decrease once the resin adheres to the tool surface. In serious cases, the chip removal groove can be blocked, and the cutting temperature may rise rapidly, leading to extremely poor surface quality that does not meet the requirements for high-quality surface processing. Thus, cutting force and temperature are critical factors that significantly affect the surface quality of peripheral milling of CFRTP.

Therefore, scholars have carried out a lot of research. When investigating the influence of cutting force on the machining quality of composite materials, Wang Fuji[9] from Dalian University of Technology designed a "multi-tooth milling cutter" with end edges to enhance material removal efficiency. This cutting method of cutting CFRP with discrete "micro-tooth" is called "micro-element removal". This micro-tooth structure can reduce the cutting width, reduce the radial cutting force and achieve the purpose of reducing machining damage. NurhanizaM et al.[10] conducted research on the influence of end milling process parameters of multi-directional carbon fiber composites on the processing quality. Through the implementation of orthogonal experiments, it was found that the feed rate had the greatest impact on the surface quality, and the feed force F_x and surface roughness values increased significantly with the increase of the feed rate. Finally, the response table, variance analysis and other methods were used to obtain the milling parameters with the best processing surface roughness. In order to reduce delamination, Tsao et al.[11] established a cutting force model for CFRP drilling. Research shows that large particle sizes are beneficial to reducing thrust and delamination.

In the research of composite cutting temperature, WANG et al.[12] used the tool-workpiece thermocouple method to analyze the effect of cutting temperature on the surface quality of CFRP milling. They found that the resin softened with the increase of cutting temperature during milling. This phenomenon leads to the weakening of the binding effect of the resin on the fiber and the poor quality of the milled surface. Especially when the temperature exceeds the glass transition temperature (T_g=185 ℃), the resin degrades on and under the processed surface, resulting in a sharp deterioration of the quality of the processed surface. This shows that it is very important to avoid high cutting temperature for high-quality surface processing during CFRP milling. Based on this conclusion, researchers have proposed many methods to reduce the cutting temperature in machining. Cooling auxiliary processes such as low-temperature air[13], minimum lubrication (MQL)[14], supercritical carbon dioxide[15] and liquid nitrogen[16] have been applied to CFRP processing. The results show that different cooling processes can improve the surface quality of CFRP milling. However, due to economic and environmental reasons, composites are still processed under dry cutting conditions in most cases in actual production. To sum up, in order to achieve high-quality processing of

thermoplastic composites, it is necessary to reasonably control the cutting force and cutting temperature, and optimize the selection of process parameters.

This paper aims to achieve high-quality peripheral milling of thermoplastic composites by controlling the cutting force and temperature in the cutting zone within a reasonable range. Firstly, based on the specific analysis of the impact of cutting force and temperature on the quality of the machined surface, the appropriate range of cutting force and temperature is determined. In order to control the cutting force and cutting zone temperature within an appropriate range by optimizing process parameters, the relationship between the cutting force and cutting zone temperature and process parameters was established, and the optimal process parameters were given on this basis. The research results will provide guidance for high-quality CFRTP peripheral milling.

2. Experimental setup and experimental methodology

2.1 Experimental system

The experimental system is based on the Mikron HSM500 high-speed machining center. To obtain information about the cutting force and temperature of the cutting area during the machining process, the Kistler 9257B dynamometer is used to collect the cutting force signal, as shown in Fig. 1. The workpiece is clamped onto the dynamometer using a clamp. Additionally, the temperature of the cutting area is measured using an extremely fine thermocouple and the Topry TP560 multi-channel temperature measuring instrument.

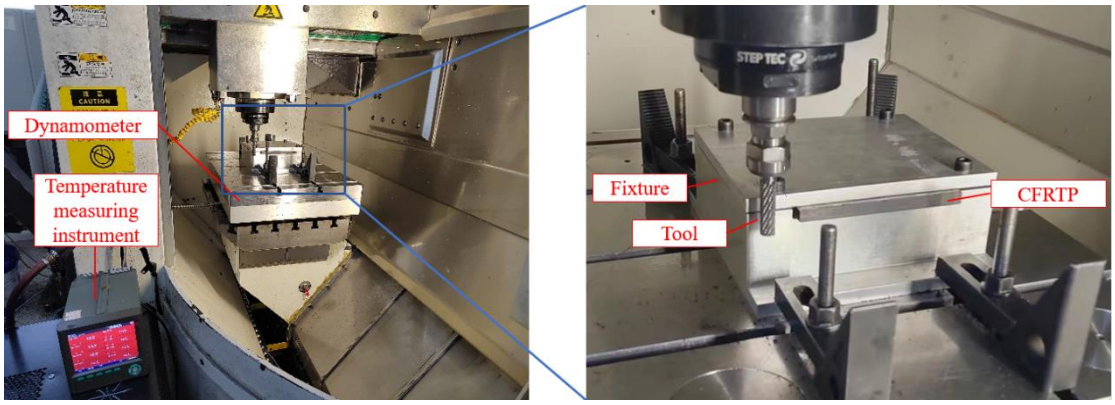

Fig.1 Experiment system for milling CFRTP

2.2 Experimental methodology

The material used for the workpiece in this experiment is a T700 grade carbon fiber/PEEK resin-based thermoplastic composite multidirectional plate, with a fiber volume fraction of 60%. The workpiece has dimensions of 120mm×120mm×8mm and a laying sequence of $[0/\pm45/90]_{8s}$, with the surface fiber direction being 90°. Tables 1 and 2 provide specific material properties and experimental conditions for the CFRTP workpiece, respectively.

As depicted in Fig. 2, three rows of small holes with a diameter of 0.6mm and uniformly distributed distance are drilled in the length direction of the CFRTP workpiece, labeled as Column A, Column B, and Column C. The depth of each hole is 4mm, and the distance between each row of holes is 10mm. T-type extremely fine thermocouples are utilized to measure the temperature in the cutting area during the experiment, as they possess high accuracy and stable performance. To prevent bubbles from affecting the thermocouple temperature measurement, the front measuring point of the thermocouple is inserted into the epoxy resin and left to stand

for 2 seconds. Once the front measuring point is wrapped by the resin, the thermocouple is buried into the small hole, and the epoxy resin is poured into the small hole before being left to stand. Once the epoxy resin is cured, the experiment can proceed.

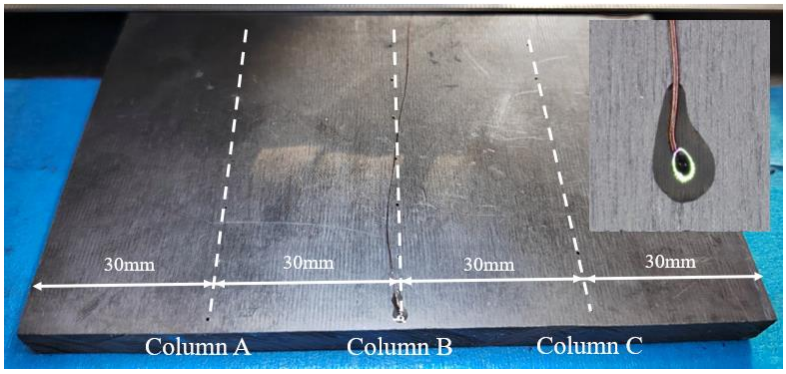

Fig. 2 Sample preparation

For this study, as there is no specialized tool available for CFRTP milling, multi-tooth milling cutter with left and right cutting edges that have proven to be effective in milling thermosetting composite materials are utilized as processing tools, as depicted in Fig. 3.

Fig. 3 Multi-tooth milling cutter with left and right cutting edges

Table. 1 Properties of CFRTP

Parameters	Value
Longitudinal tensile strength(Mpa)	2070
Transverse compressive strength(Mpa)	102
Longitudinal Young's modulus(Gpa)	127
Transverse Young's modulus(Gpa)	10.3
Poisson's ration	0.3
Glass transition temperature of resinT_g(℃)	143

Table. 2 Tool parameters and machining parameters

Parameters	Value
Tool diameter D(mm)	10
Main cutting edge rake angle γ (°)	5
Main cutting edge clearance angle α (°)	3
Cutting speed v (m/min)	50 ~ 200
Feed per revolution f (m/rev)	0.1 ~ 0.4
Radial cutting depth a_p(mm)	0.3
Milling mode	Climb milling

To investigate the influence of cutting force and cutting zone temperature on surface quality, a total milling distance of 0.36 m is used for each tool. To eliminate any potential effects of sharp tool wear at the initial stage of the experiment, each tool undergoes a preliminary test where it cuts 0.24m under the processing parameters of v=100m/min and f=0.2mm/r.

As illustrated in Fig. 4, once the tool trial cutting is completed and a radial cutting depth of

2mm is achieved using the processing parameters listed in Table 2, the surface obtained in this experiment is cut off from the workpiece and kept for observation and analysis of the milled surface. Another cutting tool with a diameter of 6mm is then used to cut the workpiece at the position indicated in Fig. 4. This step allows for the creation of an observation sample with a thickness of 2mm. The distance between the next row of holes and the edge of the workpiece remains 2mm, enabling it to be used directly for the subsequent experiments.

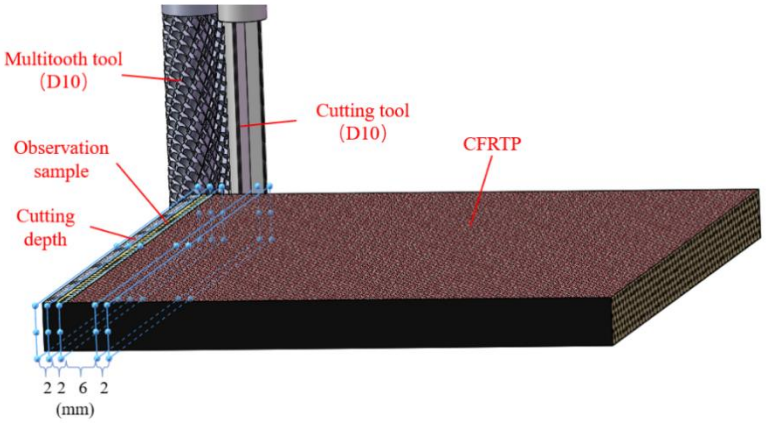

Fig. 4 Schematic diagram of milling position

During peripheral milling, the cutting force remains relatively stable except when the tool enters or exits the workpiece. To compare the impact of cutting zone temperature on the quality of the machined surface under the same cutting force, three rows of small holes for embedding thermocouples were drilled on the workpiece, allowing for the measurement of three temperature data under the same cutting force in each experiment. The Alicona 3D surface measuring instrument was used to observe the machining topography, as shown in Fig.5. The observation position was located 1 mm below the measurement point position, and the size of the observation area was approximately 4 mm × 2.7 mm. The observation area included all fiber angle layers. In the experiment, three-dimensional surface roughness Sa was used to evaluate the surface processing quality of peripheral milling.

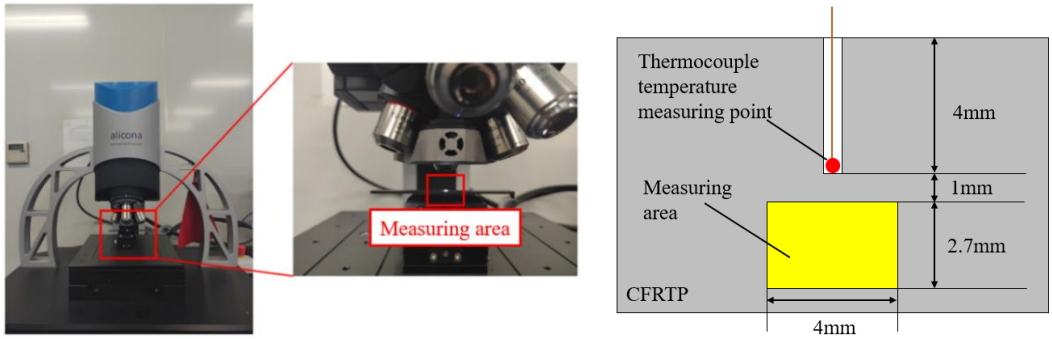

Fig. 5 Alicona 3D surface measuring instrument and schematic diagram observation area

3. Influence of cutting force and temperature on machined surface quality

3.1 Influence of cutting force on surface quality

To analyze the effect of cutting force on surface quality, the results of two groups of experiments with the same cutting zone temperature but different cutting forces are compared. Fig. 6 (a) and (b) show the surface quality when the cutting zone temperature is about 115 ℃ and the cutting forces are 268.1N and 406.2N, respectively.

The experimental findings suggest that a higher cutting force leads to a smoother and cleaner surface finish, whereas a lower cutting force (F=268.1N) causes some of the resin to remain on the machined surface, resulting in a rougher surface finish. This is because PEEK resin is a high toughness material that is difficult to effectively remove under small cutting forces. However, at higher cutting forces (F=406.2N), the resin undergoes a "strain strengthening" effect due to its viscoelastic nature, leading to easier cutting and improved surface quality. Additionally, the increase in cutting force facilitates quick chip flow along the chip removal groove, preventing chip buildup and tool adhesion, ultimately improving the cutting state of the tool and the quality of the machined surface.

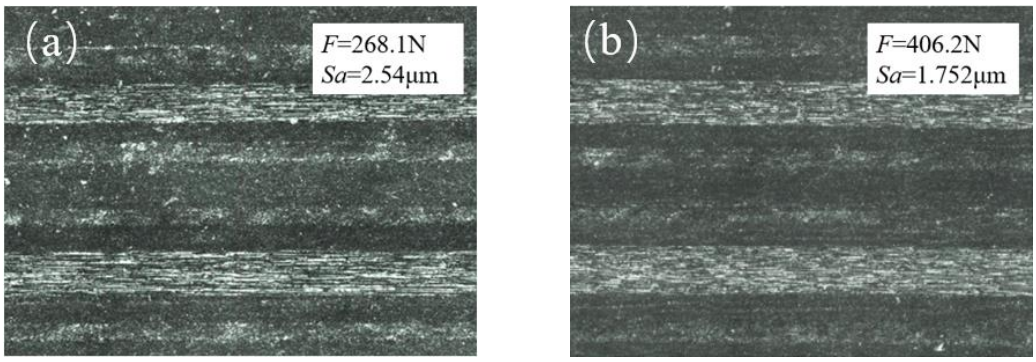

Fig. 6 Machined surface observation under different cutting forces (a)Surface under lower force (b)Surface under higher force

3.2 Influence of temperature on surface quality

In order to reveal the effect of temperature on milling surface roughness, two sets of data under the same process parameters were selected for comparison. Fig. 7 (a) and (b) show the surface morphology when the cutting force is about 201N and the cutting zone temperature is 128.5 ℃ and 200.3 ℃ respectively.

The experimental results demonstrate that when the cutting zone temperature is high (T=200.3 ℃, which is higher than the glass transition temperature T_g=143 ℃), the surface roughness of the milled material is significantly increased due to the inability to effectively remove a large number of fibers and resins. As shown in Fig. 7, there are noticeable differences in material removal among the fiber layers at various angles.

When the fiber's cutting angle is 0°, there is a phenomenon of debonding between the fiber and the matrix resin. This occurs due to the small relative angle between the cutting speed direction and the fiber direction during the material removal process of the 0° fiber layer. When the cutting zone temperature is low, the thermoplastic resin in the glass state has a strong binding effect on the fiber, causing the fiber to undergo micro buckling fracture under pressure, with the fracture surface located close to the tool tip. As the temperature in the cutting zone increases, especially when it exceeds the glass transition temperature, the binding effect of the thermoplastic resin on the fiber weakens significantly due to the resin softening. This results in a change in the fiber's fracture form from micro buckling fracture at lower temperatures to buckling fracture, with the fracture surface located away from the tool tip. A large area of debonding then occurs between the fiber and the resin.

When the fiber cutting angle is 45°, the fiber is mainly removed by extrusion fracture. The surface of the fiber layer corresponding to the 45° fiber cutting angle appears relatively flat

without any apparent damage, and a small amount of resin is coated on the surface. This is because during the machining process, friction and pressure on the flank lead to a small amount of resin being applied to the machined surface.

When the cutting angle of the fiber is 90°, the fiber is primarily removed by shear fracture. Furthermore, the fiber layer corresponding to the 90° fiber angle exhibits distinct morphological characteristics depending on the temperature. During the material removal process, the resin is applied to the machined surface due to flank extrusion. Particularly, at high cutting zone temperatures, the resin undergoes a phase change when heated, causing an increase in plasticity. As a result, the resin tends to smear and stick to the machined surface, resulting in a rougher surface morphology.

When the fiber cutting angle is 135°, the main methods of material removal are fiber matrix debonding and fiber bending. Pits are mainly caused by fiber matrix debonding, followed by fiber fracture caused by bending and shearing. When the cutting zone temperature is high, the resin matrix softens, the strength of the fiber-resin interface decreases, and the crack propagation length along the interface increases, leading to deeper damage depth. However, the surface morphology of the 135° fiber directional angle layer formed by milling does not have pits but forms a groove. This is because a large amount of fiber and resin matrix debris is generated under the action of high cutting forces. Broken fibers are removed as the chips are removed, while resin matrix debris increases in viscosity due to temperature rise, exacerbating the coating phenomenon. This fills most of the pits and forms grooves.

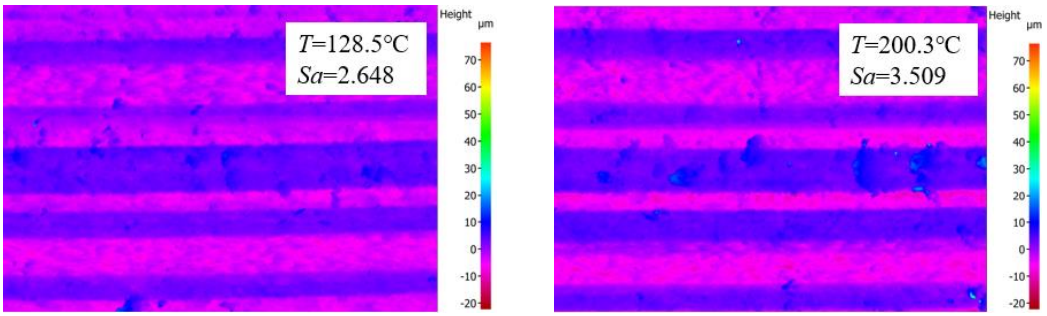

Fig. 7 Machined surface observation at different temperatures (a) Machined surface at lower temperature(b) Machined surface at higher temperature

3.3 Surface quality under different cutting forces and cutting zone temperatures

The experimental results indicate that surface roughness above Sa3.2 μm is obtained when the cutting force is between 224.8 N and 340 N, which fails to meet the requirements of high-quality CFRTP peripheral milling. However, at cutting forces between 340 N and 429.7 N, the machined surface roughness Sa is less than Sa3.2 μm at all rotating speeds, leading to better surface quality. This is due to the slow outflow of high-viscosity resin along the chip removal groove when the cutting force is small, leading to resin buildup on the tool's front face. This reduces the cutting edge's ability to effectively cut the fibers and resins, thereby increasing the surface roughness. In contrast, when the cutting force is large, the tool's surface remains clean and free of resin residue. Fig. 8 illustrates this phenomenon.

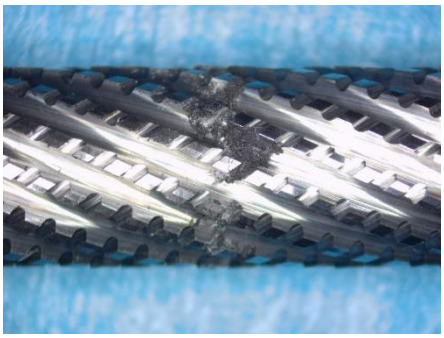

(a) Tool surface under higher cutting force

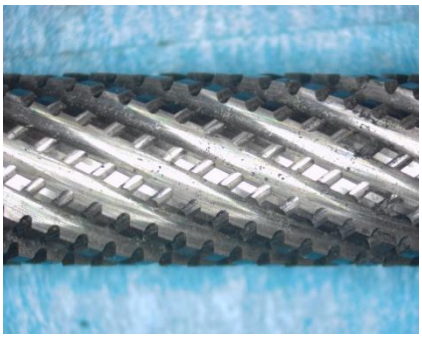

(b) Tool surface under lower cutting force

Fig. 8 Tool surface status under different cutting forces

Fig. 9 shows the relationship between cutting zone temperature and milling surface roughness under two different cutting forces. As can be seen, when the temperature is above room temperature, the temperature of the cutting zone is positively correlated with the size of the surface roughness. In other words, the lower the temperature of the cutting zone, the smaller the surface roughness. This suggests that controlling the cutting zone temperature can help improve the surface quality of the milled CFRTP.

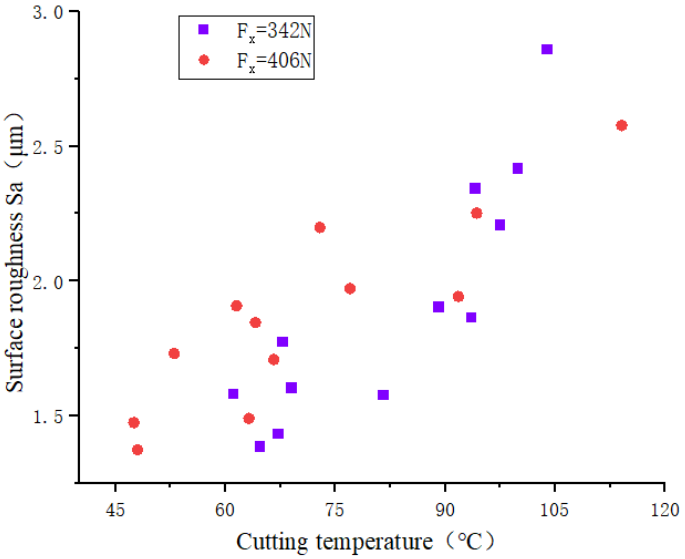

Fig.9 Relationship between surface roughness and cutting zone temperature under different cutting forces

4. Relationship between milling parameters and cutting force and cutting zone temperature

According to the influence of cutting force and cutting zone temperature on surface quality in Section 3, in order to obtain high-quality machined surface, it is necessary to reasonably control the cutting force and cutting zone temperature. Therefore, this section will establish the relationship between the cutting force and the temperature of the cutting zone and the process parameters of the peripheral milling, and give the optimized process parameters.

4.1 Relationship between cutting force and feed rate per revolution

Cutting force is a crucial parameter in assessing the performance of machining. Fig.10 (a) displays the original signal of cutting force during the milling of CFRTP. It can be observed that the feed force F_x and axial force F_z remain relatively stable throughout the cutting process, while the tangential force F_y exhibits three minor valleys. This is due to the tool passing through the pre-drilled hole that contains a thermocouple, leading to minor fluctuations in the tangential force. After analysis, the fluctuation range is found to be within 5%, indicating that the impact

of pre-drilling on the force is insignificant. The axial force F_z is much lower than the other two directions.

Fig. 10 (b) shows the relationship between the x-axis directional force F_x and the feed rate per revolution f. The feed rate per revolution of each stage corresponds to three cutting speeds. The experimental results show that in general, the resultant force F_x has a linear relationship with the feed rate per revolution, and the cutting force F_x increases with the increase of the feed rate f. The fitting equation is shown in equation (1), and the adjusted $R^2 \approx 0.95$.

$$F_x = 576.3f + 166.8 \quad (1)$$

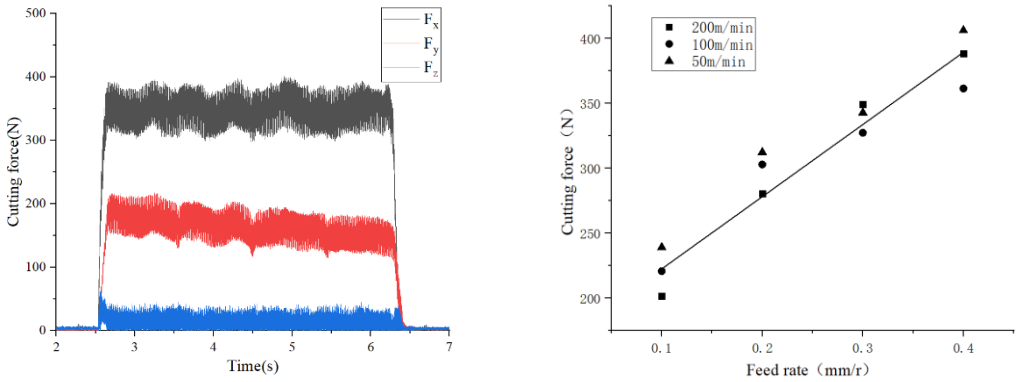

Fig. 10 Relation between feed rate per revolution and cutting force (a) Original signal of cutting force (b) Relation between feed rate per revolution and resultant force F_x

It can be seen from Section 3.3 that the cutting force should be kept within the range of 340 N~429.7 N. It can be calculated from equation (1) that the feed rate per revolution of circular milling should be selected between 0.30mm/r~0.46mm/r.

4.2 Relationship between cutting zone temperature and cutting speed under different feed rate per revolution

Because cutting speed is an important factor affecting the temperature of cutting zone. Therefore, in order to optimize the cutting zone temperature within the range of 340 N~429.7 N, the cutting speed with the feed rate f per revolution between 0.30mm/r~0.46mm/r is optimized. For this reason, the relationship between the cutting zone temperature and the cutting speed will be established under different feed rates per revolution.

Select the feed rate per revolution as 0.3 mm/r and 0.4 mm/r. Fig. 11 shows the relationship between the cutting zone temperature and the cutting speed under the same feed rate per revolution. As shown in the figure, the temperature in the cutting zone increases first and then decreases with the increase of cutting speed. As the cutting speed increases, the contact frequency between the cutting edge and the workpiece also increases, which leads to an increase in the generation of frictional heat. Additionally, as the propagation speed of plastic deformation is slower than that of elastic deformation, the higher the cutting speed, the less plastic deformation occurs and therefore, less heat is generated through plastic deformation. There exists a critical speed value, denoted as v_0, where $0<v<v_0$. When the cutting speed is within this range, the increase in friction heat generation dominates, resulting in an increase in cutting temperature. Conversely, when the cutting speed is $v>v_0$, the decrease in plastic deformation heat production dominates, leading to a decrease in cutting temperature despite the increase in friction heat production.In this experiment, the range of v_0 is approximately 35 m/min -50 m/min.

It can be seen from the figure that the relationship between cutting speed and cutting zone temperature is nonlinear. In addition, when the feed rate per revolution is different, the relationship between them is also different. Based on the above characteristics, back-propagation (BP) neural network is used to characterize the relationship between the two. The structure diagram of neural network is shown in Fig. 12.

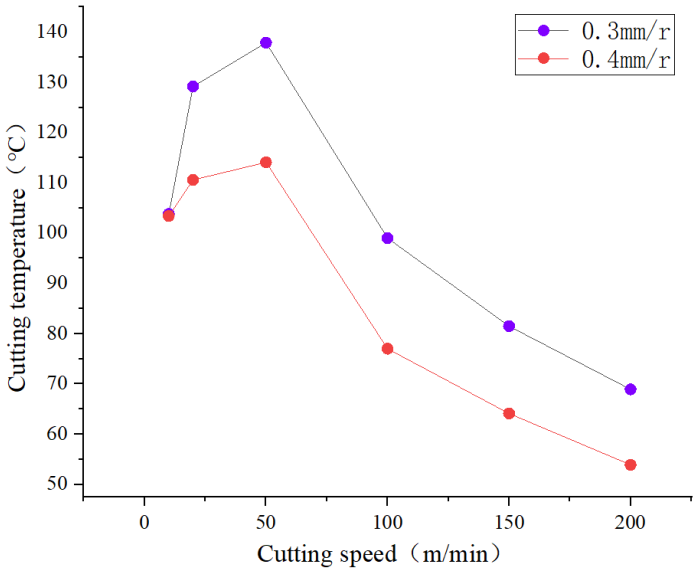

Fig. 11 Relationship between temperature and cutting speed under different feed rate per revolution

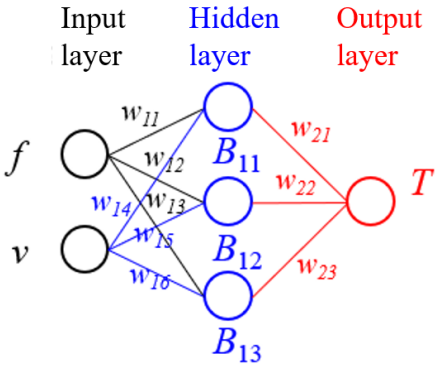

Fig. 12 Structure diagram of BP neural network

There are two elements in the input layer, namely, feed rate f and cutting speed v; There is only one element in the output layer, which is the cutting zone temperature T. w_{ij} and B_{ij} are the weights and thresholds of BP neural network respectively.

In the forward transmission of neural network, the input signal is processed from the input layer to the hidden layer and output at the output layer. If the output layer cannot get the expected output, it will turn to back propagation and adjust the network weight and threshold according to the prediction error, so that the BP neural network prediction will continue to approach the expected output. The number of hidden layers in this network is given by trial and error method. The mean square error of network prediction is 10^{-6}. Use the data in Fig. 11 for neural network, where f=0.3mm/r, v=150/min, f=0.4mm/r, v=20m/min are used as test data, and the rest data are used for network training.

In addition, in order to make the prediction of BP neural network more accurate, genetic

algorithm is used to optimize the initial weights and thresholds of the network, and the final optimization results are shown in the table.

Table. 3 Weights and thresholds of genetic algorithm optimization

Weight	w_{11}	w_{12}	w_{13}	w_{14}	w_{15}	w_{16}	w_{21}	w_{22}	w_{23}
values w	0.6111	0.6594	-0.3410	1.8480	2.2258	-2.9464	0.2419	-1.5165	-1.1992
Threshold	B_{11}	B_{12}	B_{13}	T					
values B	1.3447	0.4371	-2.5518	-2.1514					

Then, the network is trained by "traingdx" algorithm. The maximum number of training is set to 2000, the learning rate is set to 0.1, the rate of improving the learning rate is set to 1.1, and the rate of reducing the learning rate is set to 0.75. After training, compare the predicted results with the verified values, as shown in Fig. 13.

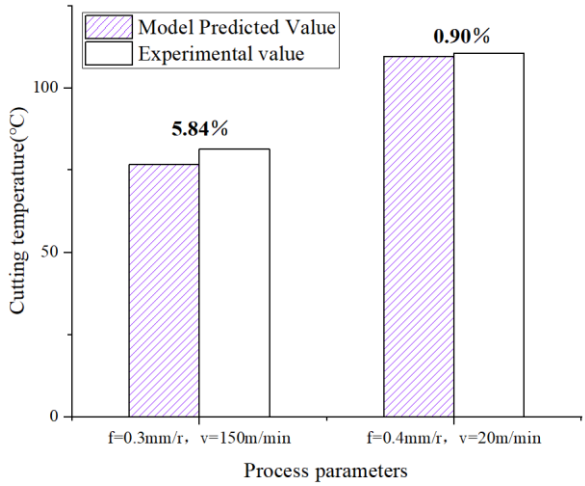

Fig. 13 Comparison between predicted results and test data

It can be seen from Fig. 13 that the network prediction error is within 6% , proving that the network prediction results are accurate.Therefore, according to the prediction relationship between cutting speed and temperature by the above neural network, when the peripheral milling processing parameter is v=200 m/min, f=0.4 mm/r, the cutting zone temperature is the lowest, that is, this parameter is the optimized CFRTP peripheral milling processing parameter.

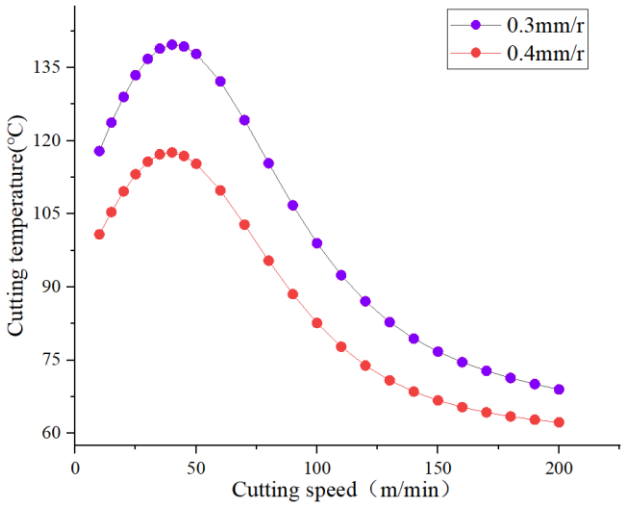

Fig. 14 Relationship between cutting speed and temperature under different feed rate per revolution

5. Conclusions

In this paper, the influence of cutting force and cutting zone temperature on the surface roughness of peripheral milling is analyzed. Based on this analysis, a relationship between cutting force, cutting zone temperature, and process parameters is established. Additionally, the paper provides process parameters that can help control cutting force and cutting zone temperature within the appropriate range. The specific conclusions are as follows:

(1) Within a certain range, increasing cutting force results in a decrease in surface roughness during peripheral milling. This is because high toughness resin absorbs more energy and is more prone to fracture when the cutting force is large. In addition, higher temperatures in the cutting area lead to greater surface roughness due to the phase change of PEEK resin. This phase change weakens the constraint on the fiber, making it more difficult to cut off. Furthermore, the resin becomes soft when heated and is not easily cut off, leading to the coating of resin on the machined surface under the action of the flank.

(2) A linear relationship exists between cutting force F_x and feed rate f per revolution. This relationship can be expressed specifically as $F_x=576.3f+166.8$. The relationship between cutting zone temperature and cutting speed v is nonlinear and can be established through neural network learning. Based on the prediction model, the lowest cutting zone temperature occurs when the peripheral milling processing parameters are v=200 m/min and f=0.4 mm/r.

(3) A critical value v_0 exists, where the cutting zone temperature increases with increasing cutting speed before the cutting speed reaches the critical speed v_0. When the cutting speed exceeds v_0, the temperature of the cutting zone decreases with increasing cutting speed. Therefore, when selecting the cutting speed for CFRTP peripheral milling, it is advisable to choose a speed far away from the critical value v_0. In this experiment, the range of cutting speed v_0 is approximately 35 m/min -50 m/min.

References

1. Stewart R (2011) Thermoplastic composites — recyclable and fast to process. Elsevier B.V, pp 22-28. http://doi.org/10.1016/S0034-3617(11)70073-X.

2. Lim SJ, Cheon J, Kim M (2020) Effect of laser surface treatments on a thermoplastic pa 6/carbon composite to enhance the bonding strength. Composites Part A: Applied Science and Manufacturing 137:105989. https://doi.org/10.1016/j.compositesa.2020.105989.

3. Yamamoto T, Terada Y (2021) Use of hollow colloids for generating nanovoids to mitigate the brittle fracture of carbon fiber-reinforced thermoplastics. Composites Part A: Applied Science and Manufacturing 149:106506. https://doi.org/10.1016/j.compositesa.2021.106506.

4. Ge J, Catalanotti G, Falzon BG et al (2022) Towards understanding the hole making performance and chip formation mechanism of thermoplastic carbon fibre/polyetherketoneketone composite. Composites Part B: Engineering 234:109752. https://doi.org/10.1016/j.compositesb.2022.109752.

5. Mazur RL, Cândido GM, Rezende MC et al (2016) Accelerated aging effects on carbon fiber pekk composites manufactured by hot compression molding. J Thermoplast Compos Mater 29:1429-1442. https://doi.org/10.1177/0892705714564283.

6. Jia Z, Fu R, Niu B et al (2016) Novel drill structure for damage reduction in drilling cfrp composites. International Journal of Machine Tools and Manufacture 110:55-65. https://doi.org/10.1016/j.ijmachtools.2016.08.006.

7. Anand RS, Patra K (2018) Cutting force and hole quality analysis in micro-drilling of cfrp. Mater Manuf Process 33:1369-1377. https://doi.org/10.1080/10426914.2017.1401715.

8. Xu J, Huang X, Davim JP et al (2020) On the machining behavior of carbon fiber reinforced polyimide andpeek thermoplastic composites. Polym Compos 41:3649-3663. https://doi.org/10.1002/pc.25663.
9. Wang F, Zhang B, Jia Z et al (2019) Structural optimization method of multitooth cutter for surface damages suppression in edge trimming of carbon fiber reinforced plastics. J Manuf Process 46:204-213. https://doi.org/10.1016/j.jmapro.2019.09.013.
10. Nurhaniza M, Ariffin MKAM, Mustapha F et al (2016) Analyzing the effect of machining parameters setting to the surface roughness during end milling of cfrp-aluminium composite laminates. International Journal of Manufacturing Engineering 2016:1-9. https://doi.org/10.1155/2016/4680380.
11. Tsao CC, Hocheng H (2007) Parametric study on thrust force of core drill. J Mater Process Technol 192-193:37-40. https://doi.org/10.1016/j.jmatprotec.2007.04.062.
12. Wang H, Sun J, Li J et al (2016) Evaluation of cutting force and cutting temperature in milling carbon fiber-reinforced polymer composites. The International Journal of Advanced Manufacturing Technology 82:1517-1525. https://doi.org/10.1007/s00170-015-7479-2.
13. Nor Khairusshima MK, Che Hassan CH, Jaharah AG et al (2013) Effect of chilled air on tool wear and workpiece quality during milling of carbon fibre-reinforced plastic. Wear 302:1113-1123. https://doi.org/10.1016/j.wear.2013.01.043.
14. Brinksmeier E, Janssen R (2002) Drilling of multi-layer composite materials consisting of carbon fiber reinforced plastics (cfrp), titanium and aluminum alloys. CIRP Annals 51:87-90. https://doi.org/https://doi.org/10.1016/S0007-8506(07)61472-3.
15. Xia T, Kaynak Y, Arvin C et al (2016) Cryogenic cooling-induced process performance and surface integrity in drilling cfrp composite material. The International Journal of Advanced Manufacturing Technology 82:605-616. https://doi.org/10.1007/s00170-015-7284-y.
16. Ishida T, Noma K, Kakinuma Y et al (2014) Helical milling of carbon fiber reinforced plastics using ultrasonic vibration and liquid nitrogen. Procedia CIRP 24:13-18. https://doi.org/10.1016/j.procir.2014.07.139.

Acknowledgement

This work was supported by National Natural Science Foundation of China (Grant No. 52090053), Science and Technology Innovation Foundation of Dalian (Grant No. 2021RD08), Science and Technology Innovation Foundation of Dalian (Grant No. 2022JJ12GX027), Science and Technology Innovation Foundation of Dalian (Grant No. 2022JJ12GX027). The authors would like to acknowledge the above financial supports.

Tribological Behaviors of Tungsten Carbide Against Ti and CFRP Under the Condition of Supercritical Carbon Dioxide Cryogenic Minimum Quantity Lubrication

*Yongkun LI[1,2], Rao FU[1,2,] *, Changlin DU[1,2], Shuai LIU[1,2], Xuepeng SHI[1,2], Meng ZHAO[1,2], Fuji WANG[1,2]*

[1]State Key Laboratory of High-Performance Precision Manufacturing, School of Mechanical Engineering, Dalian University of Technology, Dalian 116024

[2]Key Laboratory of High-Performance Manufacturing for Advanced Composite Materials, Liaoning Province, Dalian 116024

Abstract: Drilling titanium alloy (Ti) and carbon fiber reinforced polymer (CFRP) stacks is a necessary step for aircraft assembly and this process is preferably completed in one shot to ensure for production and precision purpose. However, Ti and CFRP are both hard-to-cut materials with extremely different material properties, and during drilling, the cutting tools are susceptible to rapid and severe wear; therefore, a proper cooling and lubrication process is needed. Supercritical carbon dioxide ($scCO_2$) cryogenic minimum quantity lubrication (CMQL) is an emerging cooling method for the cutting process, which is supposed to lower the temperature as well as friction. This paper has conducted an experimental study on the tribological behaviors of tungsten carbide against Ti and CFRP under CMQL condition to further understand its advantages in the application of Ti and CFRP stack. The results show that CMQL can effectively improve the severe friction between tungsten carbide and Ti and reduce the average friction coefficient by a maximum of nearly 0.065. It was found that the wear mechanism in both dry and CMQL was titanium adhesive wear, but CMQL can significantly suppress the adhesive wear under Ti case. Comparatively, the friction between tungsten carbide and CFRP was relatively steady under both dry and CMQL conditions. CMQL reduced the average friction coefficient by a maximum of nearly 0.08 and improved the degree of abrasive wear under CFRP case. This paper can provide a basis for revealing the tribological behaviors under CMQL condition.

Keywords: Ti; CFRP; Supercritical carbon dioxide; Cryogenic minimum quantity lubrication; Tribological behavior

1. INTRODUCTION

With the advantages of high specific strength/stiffness, good fatigue resistance and superior

corrosion resistance, carbon fiber reinforced polymer/plastic (CFRP) composites have found a wide range of applications in the aerospace industry [1, 2]. CFRP is often combined with titanium, aluminum and other metal materials to form a stack structure to provide improved mechanical properties and structural functions not available in the individual materials [3, 4]. Ti and CFRP are usually used as the stack structure for the main load-bearing components in the critical parts of the aircraft (such as the center wing box, wing, etc.), such as Ti/CFRP and CFRP/Ti stacks [5]. Mechanical fasteners such as bolts and rivets are typically used to better join such stacks, so drilling holes in stacked structures has become an unavoidable and important part of aircraft assembly [4, 6]. Because the quality of the hole directly affects the safety and reliability of the equipment [7].Therefore, to ensure the hole-making accuracy and improve the manufacturing efficiency, the drilling of these stacks should preferably be completed in one shot [5].However, titanium alloy and CFRP are both difficult to machine materials with different material properties [8], and it is difficult to adapt the machining tool and process parameters to both materials, making the machining of stacked structures a major challenge. The high hardness and poor thermal conductivity of titanium alloy tends to generate large amounts of cutting heat and cutting forces during machining [9-11]. While titanium alloy maintains high hardness and strength at high temperatures, it is chemically active, resulting in easy chip adhesion to the cutting edge and therefore severe tool wear during machining [12, 13]. In addition, the resin matrix in the CFRP material system is very sensitive to temperature, and the large amount of cutting heat generated during machining of the titanium phase is transferred to the CFRP phase, which can lead to glass transition or even thermal degradation of CFRP and serious damage [14, 15]. Furthermore, CFRP has anisotropic material properties in which the carbon fiber-reinforced phase has high hardness and high abrasiveness. Therefore, during the drilling and hole making process, the friction behavior between the hard points represented by the carbon fiber and the cutting edge of the tool is quite poor, resulting in rapid tool wear [16, 17]. Therefore, the serious problem of tool wear when drilling CFRP and Ti stacks is a concern [18-20].

To mitigate the thermal and mechanical effects during CFRP/Ti stack machining, cooling and lubrication applications are commonly used today. Among them, the most widely used flood technology significantly reduces the friction coefficient and temperature at the tool-work interface and improves tool life [21]. However, the use of large quantities of cutting fluid causes serious economic and environmental problems [22, 23]. Most importantly, due to the hygroscopicity of CFRP, the use of cutting fluids is not allowed when machining CFRP. [24]. In recent years, with the development of green cutting technology, cryogenic minimum quantity lubrication (CMQL) technology has emerged. CMQL is an organic combination of cryogenic cooling and minimum quantity lubrication (MQL) technology. It not only significantly reduces the temperature of the cutting area and maintains the effective lubrication capacity of the oil film, but also meets the requirements of green and clean machining, which is highly advantageous[25]. Common cooling media currently used in CMQL include liquid nitrogen (LN_2), liquid carbon dioxide (LCO_2), cold air and supercritical carbon dioxide ($scCO_2$) [26]. Among them, $scCO_2$ has the combined advantages of excellent lubricant solubility, efficient cryogenic cooling (-78.5°C), and easy preparation and storage at room temperature, which is significantly superior for cutting hard-to-cut materials.[27-29].

Studies on the application of $scCO_2$ MQL have mainly focused on the milling and turning of metals, and only in recent years has it been gradually applied to the field of composite materials processing. Stephenson et al.[30] investigated the possibility of replacing water-based (aqueous) flood coolant with $scCO_2$ MQL in rough turning of Inconel 750. The results showed that tool wear was consistently lower

with $scCO_2$ MQL than with water-based (aqueous) flood coolant, and in addition, the MRR material removal rate could be increased by 40% with $scCO_2$ MQL compared to water-based flood coolant for equivalent tool life. Wika et al. [31] compared the effects of $scCO_2$, $scCO_2$ MQL and flood coolant in Ti-6Al-4V milling. It was found that $scCO_2$ MQL provided sufficient cooling and lubrication to significantly improve tool life. Cai et al. [32] investigated the finish milling performance of Ti-6Al-4V material in four green cutting environments: dry, $scCO_2$, $scCO_2$-based MQL with water-based cutting fluid ($scCO_2$-WMQL), $scCO_2$-based MQL with oil-on-water droplets cutting fluid ($scCO_2$-OoWMQL).The experimental results showed that the cutting force, cutting temperature and surface roughness were minimized in $scCO_2$-OoWMQL environment due to its good cooling/lubrication and chip removal performance. An et al. [28] investigated the application of dry, $scCO_2$, $scCO_2$-WMQL and $scCO_2$-OoWMQL in side milling of Ti-6Al-4V . It was shown that the lowest tool wear, minimum cutting torque and optimal surface topography were obtained under $scCO_2$-OoWMQL condition. Zou et al. [26] investigated the machining performance of CFRP laminates under $scCO_2$ and vegetable oil-based CMQL conditions. Lower cutting temperature, lower cutting forces, lower surface roughness and higher machining efficiency can be achieved under CMQL condition. Chen et al. [33] explored the feasibility of CMQL in finish milling of in-situ TiB_2/7075 composite. The results showed that $scCO_2$-OoWMQL combined good cooling and lubrication properties and excelled in suppressing adhesive wear and slowing down abrasive wear, resulting in a 198.08% improvement in tool life over dry condition.

Most of the existing studies are based on cutting experiments under various working conditions, which lack information on the wear process and have limitations in revealing the tool wear mechanism. In contrast, friction and wear experiments can obtain the behavior of the friction process in real time[24, 26, 33],which is advantageous in revealing the wear mechanism. However, there are still relatively few studies in this area.

In this paper, in order to investigate the advantages of CMQL application in Ti and CFRP stack drilling, a study on the tribological behavior of cemented carbide with Ti and CFRP under CMQL conditions was carried out. A ball-on-disk reciprocating friction and wear tester with CMQL was built, and tribological experiments were conducted under different normal loads and sliding velocities. The friction coefficients of tungsten carbide against Ti and CFRP under dry and CMQL conditions were obtained, and the effect of CMQL on the wear mechanism of carbide was analyzed.

2. EXPERIMENT SETUP

2.1 Experimental materials

The tribological experiments in this study were performed in the form of a ball-disk contact. The upper specimen was a 6-mm diameter tungsten carbide ball of the material grade German Guhring K40UF, whose properties are shown in Table 1. The lower specimen was Ti-6Al-4V titanium alloy and T800/X850 composite material (lay-up sequence is $[0/45/90/-45/]_S$, fiber volume fraction is 65%). The material properties of both are shown in Table 2 and Table3. The sizes were all 30mm×15mm×8mm. The Ti was finish milled, ground and polished to a surface roughness of Sa≤0.8μm. The CFRP was finish milled to a surface roughness of Sa≤4.0. The upper and lower specimens were ultrasonically cleaned with anhydrous ethanol and deionized water for 20 min, and dried in a drying oven at 50°C for backup.

Table 1 Main chemical composition and properties of K40UF tungsten carbide

Parameter	Value	Parameter	Value
CO (%)	10.0	K_{IC} ($MNm^{-3/2}$)	10.5
WC+Cr_3C_2+VC (%)	90.0	Bending strength (N/mm^2)	> 4000
Density (g/cm^3)	14.4	Porosity-Class A(μm)	<02
HRA	92.1	WC grain size (μm)	0.6

Table 2 Mechanical properties of CFRP laminates

Parameter	Value
Longitudinal tensile strength (MPa)	2984
Transverse compressive strength (MPa)	265
Longitudinal Young's modulus (GPa)	170
Transverse Young's modulus(GPa)	8.1
Poisson's ration	0.355

Table 3 Mechanical properties of Ti-6Al-4V

Parameter	Value
Yield Strength (MPa)	910
Tensile Strength (MPa)	923
Elongation (%)	13.5
Hardness (HV5)	314

2.2 CMQL System

The $scCO_2$ cryogenic cooling system (provided by Conprofe Green Tools Co., Ltd.) was used to provide CMQL condition. Fig. 1 shows a schematic diagram of a CMQL system. LCO_2 becomes a supercritical fluid when it is above 31.26°C and pressurized to above 72.9 bar. $scCO_2$ has a high diffusion coefficient and low viscosity similar to that of a gas. It is the most widely used supercritical fluid solvent in the industry, capable of dissolving various cutting fluids (soluble vegetable oil, water-based cutting fluid, etc.). The vegetable oil is pumped into the mixing chamber by an oil pump and mixed with $scCO_2$ to form a high pressure $scCO_2$-oil mixture. Based on the Joule-Thomson effect, a high pressure scCO2-oil fluid mixture is ejected from the nozzle to form a mixed jet of gaseous CO_2/oil atomized particles/solid CO_2. The nozzle exit temperature is theoretically up to -78.5°C, resulting in cooling and lubrication of the sprayed area.

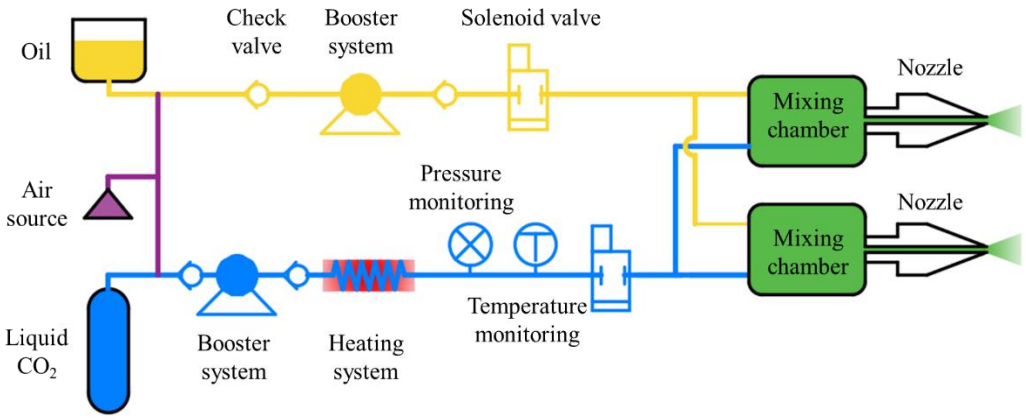

Fig. 1. Schematic diagram of CMQL system

2.3 Tribological experiments under CMQL condition

In order to study the tribological properties of tungsten carbide under CMQL condition, the existing MDW-02G high-speed reciprocating friction wear tester (provided by Jinan Yihua Tribology Testing Technology Co., Ltd.) was modified as shown in Fig. 2(a). Two independent nozzles of the CMQL system were fixed on the linear reciprocating slider of the tester through the connecting plate and bolts, which can follow the movement of the upper specimen. The lower specimen is fixed to the special fixture by two bolts, and the CMQL medium is injected into the friction area through the nozzles. Nozzle 1 and nozzle 2 are distributed along the sliding velocity direction, the inclination angle between the nozzles and the horizontal plane is 10°, and the distance between the nozzles and the center of the upper specimen is 25 mm, as shown in Fig. 2(b).

(a)

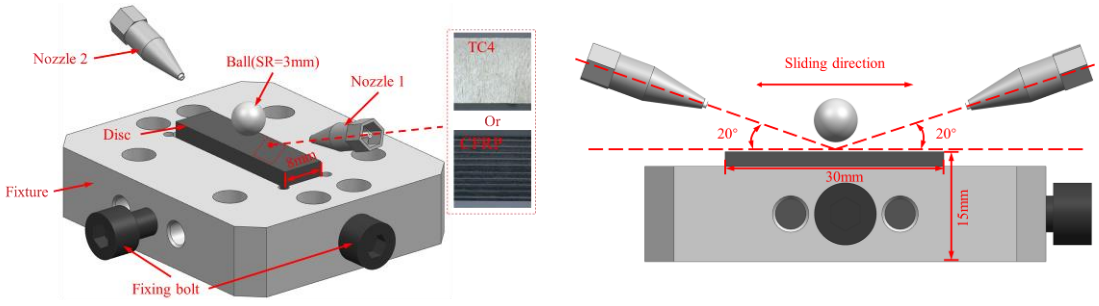

(b)

Fig. 2. Tribological experiments under CMQL conditions: (a) friction and wear tester with CMQL system, (b) schematic diagram of CMQL nozzle angle

The process parameters are shown in Table 4. Experiments were designed to investigate the effects of normal load and sliding velocity on the tribological properties of tungsten carbide under dry and CMQL conditions. The load and velocity were set by special software, and the friction coefficient was recorded in real time. The length of the wear marks was 20 mm, and the temperature was room temperature. The friction time was 10 min, and the friction coefficient was recorded at a frequency of 1 Hz. The morphology of the worn surface was measured by Alicona InfiniteFocus G5 at the end of the experiment.

Table 4 Process parameters for tribological experiments

Lower specimen material	Normal load F (N)	Sliding velocity ν (m/s)
CFRP	25/50/75/100	0.20
TC4	25/50/75/100	0.04

3. RESULTS AND DISCUSSION

3.1 Friction coefficient

3.1.1 Friction coefficient of tungsten carbide against Ti

Fig. 3(a) shows the effect of different normal loads on the friction coefficient curves under dry condition. It can be seen that in the initial stage of the experiment, the friction coefficient suddenly increases within a few seconds, which was due to the need for a running-in process between the ball-on-disk friction pair. As the tungsten carbide ball gradually ground into the titanium alloy, the friction coefficient tended to be steady in a certain time, but still fluctuated in a certain range. With the increase of time, the friction of the tungsten carbide ball caused the depth of the wear marks on the Ti to increase. The friction contact area increased, and the friction coefficient showed an overall increasing trend. In addition, a violent and uneven noise can be heard during the experiment. It can be seen that the friction between Ti and tungsten carbide was very severe and can not maintain a steady friction state.

In addition, the local fluctuations in the coefficient of friction were as high as 0.13 under the lower load of 25N. The overall friction curve increased slowly. As the friction time increased, the friction coefficient increased steadily. As the load increased, the fluctuation of the coefficient of friction became smaller, less than 0.05 at 100N load. However, there were jumps of the friction coefficient, such as 50N load at 338s the friction coefficient was 0.4540, suddenly increased to 0.5802 at 339s. Similar phenomena occurred at 238s and 497s for 75N load and at 516s and 541s for 100N load. This may be due to the following: as the friction process progressed, the titanium adhesion accumulated on the surface of the tungsten carbide ball. The friction interface became titanium adhesion and titanium alloy contact. When the accumulation of titanium adhesion reached a certain value, the shear stress on the titanium adhesion was greater than the adhesive force. The titanium adhesion was detached, causing the friction interface to change abruptly and the friction coefficient to jump. It can be seen that although the fluctuation of the local stability phase decreased with the increase of the load, it will be extremely unstable during the whole friction process. In the experimental normal load range, the maximum friction coefficient was about 0.6.

Fig. 3(b) shows the effect of different normal loads on the friction coefficient curves under CMQL condition. The variation of friction coefficient curve was similar to that of the dry. At the lower loads of 25 N and 50 N, the friction coefficients showed significant jumps, such as 282s and 503s at 25 N and 403s and 464s at 50 N. While at 75 N and 100 N, the friction coefficients were steadier.

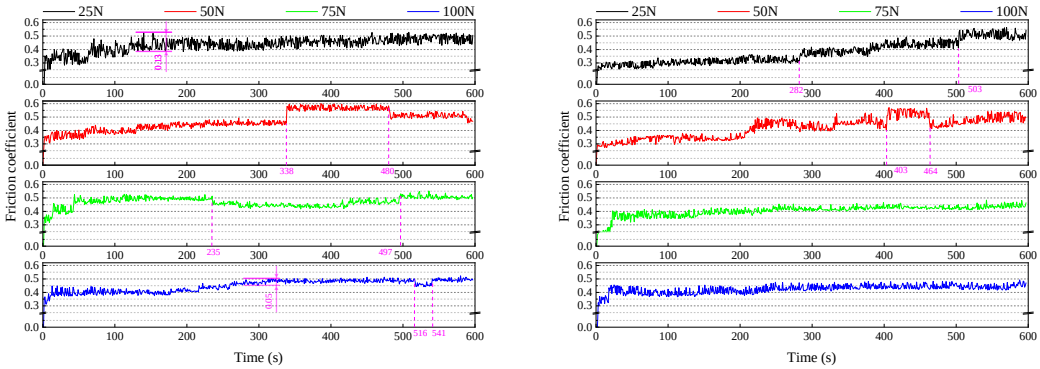

(a) (b)

Fig. 3. Friction coefficient curves of tungsten carbide against Ti under different normal loads: (a) Dry, (b) CMQL

Fig. 4(a) shows the comparison of the friction coefficients under dry and CMQL conditions. Under different loads, CMQL caused the friction coefficient to decrease to different degrees, which was attributed to the excellent cooling and lubricating effect of CMQL. At 25N load, the friction coefficient of CMQL was about 0.1 lower than that of the dry type for the first 400s, while after 400s, the two coefficient frictions were of similar magnitude. At 100N load, the friction coefficient curve of CMQL was close to that of the dry. This was due to the fact that, as the friction time increased and the normal load increased, the depth of the wear marks increased. The CMQL jet did not easily enter the friction region, so the friction coefficient converged to the dry condition. In the experimental normal load range, the maximum friction coefficient was about 0.55. The friction coefficients were averaged for the whole friction process to obtain the average friction coefficients under dry and CMQL conditions as shown in Fig. 4 (b). As the load increased, the average friction coefficient under dry increased and then decreased, while the friction coefficient under CMQL fluctuated and increased. CMQL significantly reduced the average friction coefficient between tungsten carbide and Ti by a minimum of about 0.025 and a maximum of about 0.065.

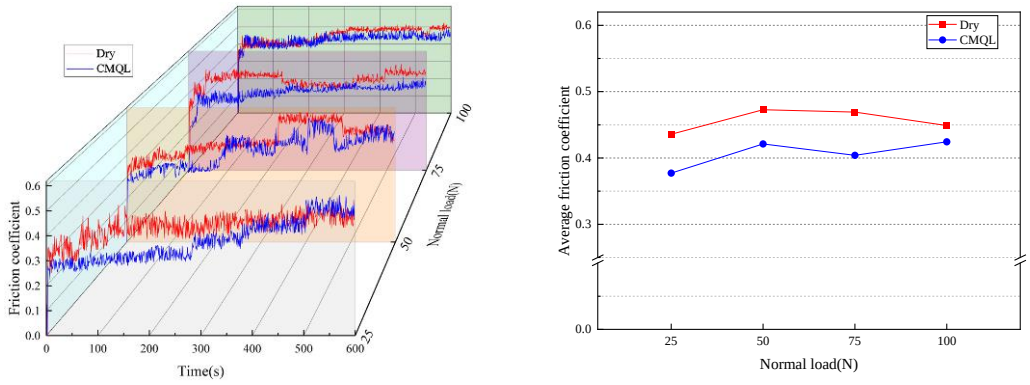

(a) (b)

Fig. 4. Comparison of friction coefficients of tungsten carbide against Ti under dry and CMQL conditions (under different normal loads): (a) friction coefficient curves, (b) average friction coefficients

3.1.2 Friction coefficient of tungsten carbide against CFRP

Fig. 5(a) shows the effect of different normal loads on the friction coefficient curves under dry

condition. It can be seen that the friction of tungsten carbide against CFRP was steadier than that of tungsten carbide against Ti. The friction coefficient entered the steady stage after a short running-in stage in the early. The overall friction coefficient fluctuated very little, and there was no jump in the friction coefficient. In the later stage of friction, the friction coefficient showed a decreasing trend, which was most obvious under 25N load. This was probably because: with the friction process, the carbon fiber and resin material on the surface of the composite material were worn out, producing carbon powder and resin particles. The longer the friction time, the greater the accumulation of both. The large amount of carbon powder and resin particles acted as a good lubricant and the friction coefficient decreased as a result. In the experimental normal load range, the friction coefficient was about 0.4 at the maximum.

Fig. 5(b) shows the effect of different normal loads on the friction coefficient curves under CMQL condition. The variation of the friction coefficient curve under 25N and 50N loads was similar to that of the dry, passing through three stages: running-in, steady and decreasing process. And the friction coefficient under 75N and 100N load went through a longer running-in and increasing stage before entering the steady stage. In the experimental normal load range, the friction coefficient was about 0.45 at the maximum.

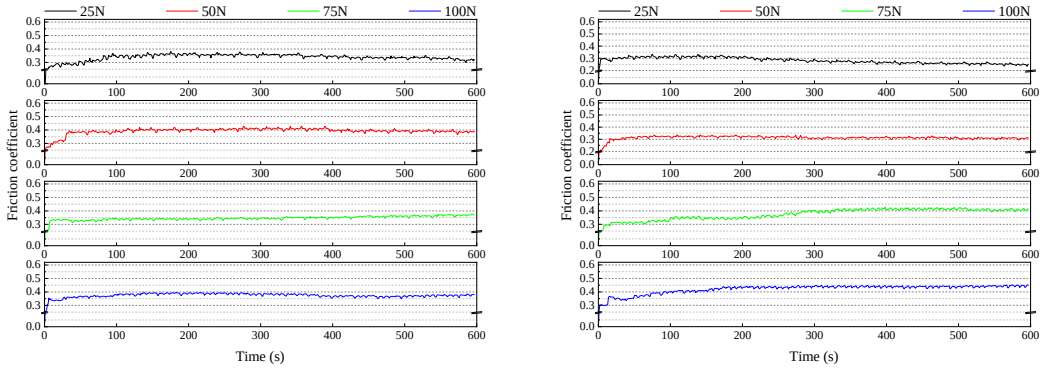

Fig. 5. Friction coefficient curves of tungsten carbide against CFRP under different normal loads: (a) Dry, (b) CMQL

Fig. 6(a) shows the comparison of the friction coefficient curves under dry and CMQL conditions. It can be seen that the overall friction coefficient curves of CMQL were lower than those of the dry and significantly lower under 25N and 50N loads. And under 50N and 75N loads, the friction coefficient of CMQL was slightly larger than that of the dry in the initial process. However, as the friction process progressed, the friction coefficient of CMQL increased significantly around 100s. This may be due to: the cooling effect of CMQL hardened the CFRP, and the interaction between the tungsten carbide and CFRP friction interface became more intense under higher load, which caused the friction coefficient to increase. And the lubricating effect of CMQL was not enough to improve this condition, so the friction coefficient would be larger than that of the dry. As the friction process progressed, the depth of the wear marks increased. It was more difficult for the lubricating fluid of CMQL to penetrate. The friction coefficient would become larger.

Fig. 6(b) shows the comparison of the average friction coefficients under dry and CMQL conditions. As the load increased, the average friction coefficient under dry condition increased, but there was a fluctuation when the normal load was 50N. The average friction coefficient under CMQL

condition increased approximately linearly. CMQL significantly reduced the coefficient of friction at lower normal loads, by about 0.06 and 0.08 at 25 N and 50 N loads, respectively. While at 75 N and 100 N loads, CMQL increased the friction coefficient by about 0.03 and 0.05, respectively.

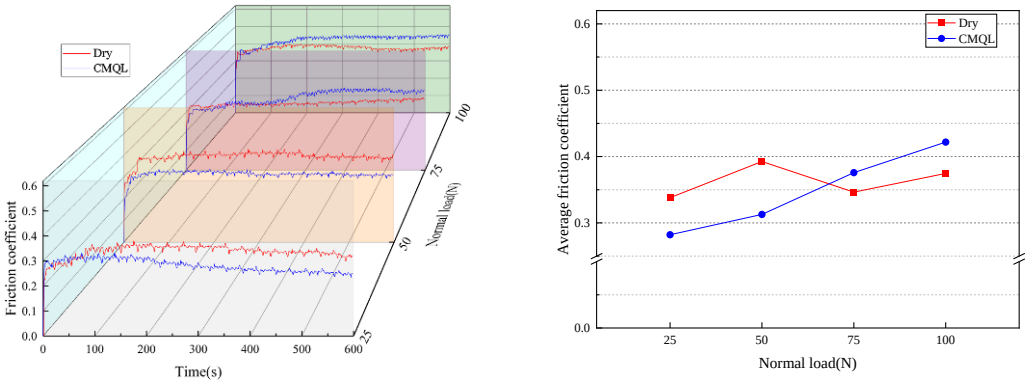

(a) (b)

Fig. 6. Comparison of friction coefficients of tungsten carbide against CFRP under dry and CMQL conditions (under different normal loads): (a) friction coefficient curves, (b) average friction coefficients

3.2 Wear morphology

3.2.1 Typical wear morphology of tungsten carbide under dry condition

The initial morphology of the tungsten carbide surface is shown in Fig. 7(a). The Alicona InfiniteFocus G5 is an optical measuring instrument. The surface finish of the tungsten carbide ball was almost mirror-like, it reflected light when the light source shined on the surface. This resulted in a circular, high-gloss area appears in the center region. Due to the grinding accuracy, the tungsten carbide surface had concaves of varying sizes. Fig. 7(b) shows the typical wear morphology of the tungsten carbide against Ti under dry condition. Clear wear areas were visible on the tungsten carbide surface. The original concaves on the surface were worn away, exposing the new rougher tungsten carbide surface. And multiple areas and larger pieces of titanium adhesion were observed, extending overall in the sliding direction. Fig. 7(c) shows the typical wear morphology of the tungsten carbide against CFRP under dry condition. The wear level of tungsten carbide against CFRP was significantly lower than that of tungsten carbide against Ti. The original surface concaves were flattened by the reciprocal friction of the high hardness carbon fiber and carbon fiber scratches along the sliding direction can be observed.

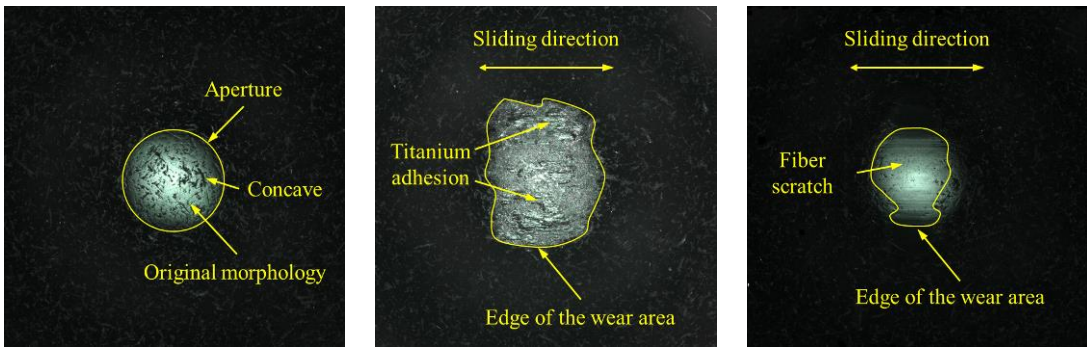

(a) (b) (c)

Fig. 7. Typical wear morphology of tungsten carbide against Ti and CFRP under dry condition: (a) initial morphology, (b) tungsten carbide against Ti (F=50N), (c) tungsten carbide against CFRP（F=100N）

3.2.2 Wear morphology of tungsten carbide against Ti

Fig. 8 shows the wear morphology of tungsten carbide against Ti under dry and CMQL conditions. The normal loads had a significant effect on the wear morphology. As the normal load increased, the wear area on the tungsten carbide surface increased and the degree of titanium adhesion showed an overall increasing trend. This indicated that the increase in contact stress leads to increased wear. Comparing the wear morphology under dry and CMQL conditions, CMQL significantly reduced the wear area and decreases the degree of titanium adhesion. It can be seen that CMQL significantly improved the wear of tungsten carbide against Ti.

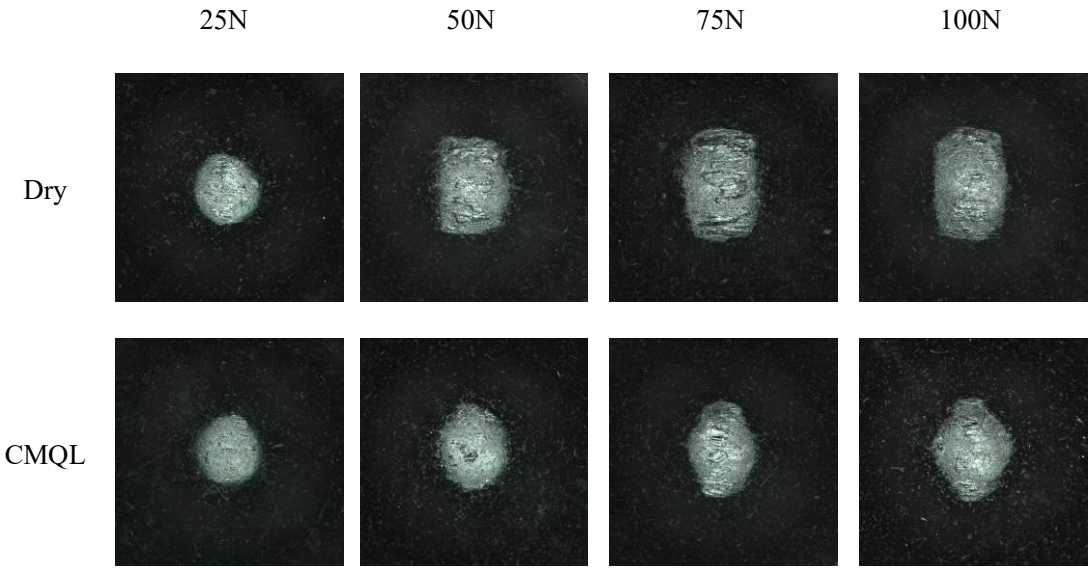

Fig. 8. Wear morphology of tungsten carbide against Ti under dry and CMQL conditions (under different normal loads)

3.2.3 Wear morphology of tungsten carbide against CFRP

Fig. 9 shows the wear morphology of tungsten carbide against CFRP under dry and CMQL conditions. No significant wear was observed on the tungsten carbide surface under the dry and CMQL conditions at the lower 25N load. Minor fiber scratches were not observed for CMQL only up to 50 N load. As the load increased, the scratches on the carbide surface were gradually smoothed out and the wear area became larger. This was because that an increase in normal load led to an increase in contact stress, which in turn led to an increase in wear. By comparing the wear morphology under dry and CMQL conditions, it was found that CMQL significantly reduced the area of the wear. CMQL improved the wear of tungsten carbide against CFRP.

25N 50N 75N 100N

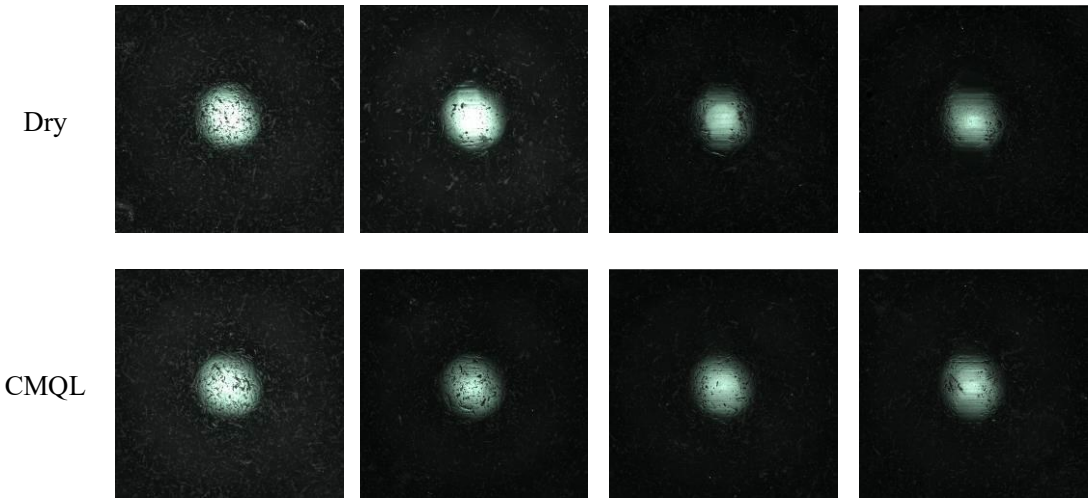

Fig. 9. Wear morphology of tungsten carbide against CFRP under dry and CMQL conditions (under different normal loads)

4. CONCLUSIONS

The possibility of applying CMQL to suppress tool wear during drilling of Ti and CFRP stack structures was investigated. The tribological properties and wear mechanisms of tungsten carbide under dry and CMQL conditions were studied. The conclusions of the study were as follows:

(1) Under dry condition, the friction of tungsten carbide against Ti was severe. The friction coefficient fluctuated widely and friction jumps occurred. The maximum friction coefficient was about 0.6. The friction of tungsten carbide against CFRP was tender, the friction coefficient was steady, and the maximum was about 0.45.

(2) CMQL had excellent cooling and lubricating effect, which can obviously improve the friction of tungsten carbide against Ti and CFRP and reduce the friction coefficient. The average friction coefficient can be reduce by a maximum of about 0.065 for tungsten carbide against Ti and 0.08 for tungsten carbide against CFRP.

(3) Under the dry condition, the wear mechanism of tungsten carbide against Ti was titanium adhesive wear. The wear morphology was a rough tungsten carbide surface covered with irregular titanium adhesion. The wear mechanism of tungsten carbide against CFRP was abrasive wear. The wear morphology was a flat tungsten carbide surface and fiber scratches on it.

(4) CMQL can effectively inhibit the wear of tungsten carbide, especially in the case of Ti. CMQL reduced the area of the wear, the degree of titanium abrasive wear and CFRP abrasive wear.

ACKNOWLEDGMENTS

This work is supported by National Natural Science Foundation of China (Grant No. 52105432 and 52090053), Science and Technology Innovation Foundation of Dalian (Grant No. 2021RD08), Science and Technology Innovation Foundation of Dalian (Grant No. 2022JJ12GX027), Science and Technology Innovation Foundation of Dalian (Grant No. 2022JJ12GX027).

REFERENCES

1. R. Fu, Z. Jia, F. Wang, Y. Jin, D. Sun, L. Yang, and D. Cheng, “Drill-exit temperature characteristics in drilling of UD and MD CFRP composites based on infrared thermography,” *Int. J. Mach. Tools Manuf*, 135,

24-37, 2018.
2. F. Wang, B. Qian, Z. Jia, R. Fu, and D. Cheng, “Secondary cutting edge wear of one-shot drill bit in drilling CFRP and its impact on hole quality,” *Compos. Struct*, 178, 341-352, 2017.
3. J. Xu, M. Ji, J. Paulo Davim, M. Chen, M. El Mansori, and V. Krishnaraj, “Comparative study of minimum quantity lubrication and dry drilling of CFRP/titanium stacks using TiAlN and diamond coated drills,” *Compos. Struct*, 234, 2020.
4. J. Xu, A. Mkaddem, and M. El Mansori, “Recent advances in drilling hybrid FRP/Ti composite: A state-of-the-art review,” *Compos. Struct*, 135, 316-338, 2016.
5. Z. Jia, C. Zhang, F. Wang, R. Fu, and C. Chen, “Multi-margin drill structure for improving hole quality and dimensional consistency in drilling Ti/CFRP stacks,” *J. Mater. Process. Technol*, 276, 2020.
6. R. Hussein, A. Sadek, M. A. Elbestawi, and M. H. Attia, “Low-frequency vibration-assisted drilling of hybrid CFRP/Ti6Al4V stacked material,” *Int. J. Adv. Manuf. Technol*, 98, 9-12, 2801-2817, 2018.
7. Q. Wang, F. Wang, C. Zhang, and C. Chen, “Combined effects of various materials on tool wear in drilling of Ti/CFRP stacks,” *Proc. Inst. Mech. Eng. Part C-J. Eng. Mech. Eng. Sci*, 234, 14, 2750-2759, 2019.
8. J. Xu, C. Li, M. Chen, and F. Ren, “A comparison between vibration assisted and conventional drilling of CFRP/Ti6Al4V stacks,” *Mater. Manuf. Process*, 34, 10, 1182-1193, 2019.
9. N. Manikandan, D. Arulkirubakaran, D. Palanisamy, and R. Raju, “Influence of wire-EDM textured conventional tungsten carbide inserts in machining of aerospace materials (Ti–6Al–4V alloy),” *Mater. Manuf. Process*, 34, 1, 103-111, 2018.
10. N. DuyTrinh, Y. Shaohui, N. Nhat Tan, P. Xuan Son, and L. A. Duc, “A new method for online monitoring when grinding Ti-6Al-4V alloy,” *Mater. Manuf. Process*, 34, 1, 39-53, 2018.
11. A. Prabukarthi, V. Krishnaraj, M. Santhosh, M. Senthilkumar, and R. Zitoune, “Optimisation and tool life study in drilling of titanium (Ti-6Al-4V) alloy,” *Int. J. Mach. Mach. Mater.* 13, 2-3, 138-157, 2013.
12. X. Yang, and C. Richard Liu, “Machining Titanium and Its Alloys,” *Mach. Sci. Technol.*, 3, 1, 107-139, 1999.
13. R. Li, P. Hegde, and A. J. Shih, “High-throughput drilling of titanium alloys,” *Int. J. Mach. Tools Manuf*, 47, 1, 63-74, 2007.
14. S. Morkavuk, U. Köklü, M. Bağcı, and L. Gemi, “Cryogenic machining of carbon fiber reinforced plastic (CFRP) composites and the effects of cryogenic treatment on tensile properties: A comparative study,” *Compos. Pt. B-Eng*, 147, 1-11, 2018.
15. T. Yashiro, T. Ogawa, and H. Sasahara, “Temperature measurement of cutting tool and machined surface layer in milling of CFRP,” *Int. J. Mach. Tools Manuf*, 70, 63-69, 2013.
16. J. Xu, “A review on tool wear issues in drilling CFRP laminates,” *Front. Mater*, 9, 2022.
17. X. Wang, P. Y. Kwon, C. Sturtevant, D. Kim, and J. Lantrip, “Tool wear of coated drills in drilling CFRP,” *J. Manuf. Process*, 15, 1, 127-135, 2013.
18. O. Isbilir, and E. Ghassemieh, “Comparative Study of Tool Life and Hole Quality in Drilling of Cfrp/Titanium Stack Using Coated Carbide Drill,” *Mach. Sci. Technol.*, 17, 3, 380-409, 2013.
19. K.-H. Park, A. Beal, D. Kim, P. Kwon, and J. Lantrip, “Tool wear in drilling of composite/titanium stacks using carbide and polycrystalline diamond tools,” *Wear*, 271, 11-12, 2826-2835, 2011.
20. X. Wang, P. Y. Kwon, C. Sturtevant, D. Kim, and J. Lantrip, “Comparative tool wear study based on drilling experiments on CFRp/Ti stack and its individual layers,” *Wear*, 317, 1-2, 265-276, 2014.
21. J. Xu, M. Ji, M. Chen, and F. Ren, “Investigation of minimum quantity lubrication effects in drilling CFRP/Ti6Al4V stacks,” *Mater. Manuf. Process*, 34, 12, 1401-1410, 2019.
22. Chetan, S. Ghosh, and P. Venkateswara Rao, “Application of sustainable techniques in metal cutting for

enhanced machinability: a review," *J. Clean Prod.*, 100, 17-34, 2015.
23. K. K. Gajrani, P. S. Suvin, S. V. Kailas, and M. R. Sankar, "Hard machining performance of indigenously developed green cutting fluid using flood cooling and minimum quantity cutting fluid," *J. Clean Prod*, 206, 108-123, 2019.
24. X. Liang, and D. Wu, "Tribological properties of carbon-fibre-reinforced plastic against tungsten carbide under dry condition," *Tribol. Int*, 134, 118-128, 2019.
25. M. Liu, C. Li, Y. Zhang, Q. An, M. Yang, T. Gao, C. Mao, B. Liu, H. Cao, X. Xu, Z. Said, S. Debnath, M. Jamil, H. M. Ali, and S. Sharma, "Cryogenic minimum quantity lubrication machining: from mechanism to application," *Front. Mech. Eng*, 16, 4, 649-697, 2022.
26. F. Zou, J. Dang, X. Wang, H. Zhang, X. Sun, Q. An, and M. Chen, "Performance and mechanism evaluation during milling of CFRP laminates under cryogenic-based conditions," *Compos. Struct*, 277, 2021.
27. N. R. Putra, M. A. Che Yunus, and S. Machmudah, "Solubility model of arachis hypogea skin oil by modified supercritical carbon dioxide," *Sep. Sci. Technol*, 54, 5, 731-740, 2018.
28. Q. An, C. Cai, F. Zou, X. Liang, and M. Chen, "Tool wear and machined surface characteristics in side milling Ti6Al4V under dry and supercritical CO_2 with MQL conditions," *Tribol. Int*, 151, 2020.
29. Y. Yuan, C. Wang, J. Yang, L. Zheng, and X. Weiqiang, "Performance of supercritical carbon dioxide ($scCO_2$) mixed with oil-on-water (OoW) cooling in high-speed milling of 316L stainless steel," *Procedia CIRP*, 77, 391-396, 2018.
30. D. A. Stephenson, S. J. Skerlos, A. S. King, and S. D. Supekar, "Rough turning Inconel 750 with supercritical CO_2-based minimum quantity lubrication," *J. Mater. Process. Technol*, 214, 3, 673-680, 2014.
31. K. K. Wika, O. Gurdal, P. Litwa, and C. Hitchens, "Influence of supercritical CO_2 cooling on tool wear and cutting forces in the milling of Ti-6Al-4V," *Procedia CIRP*, 82, 89-94, 2019.
32. C. Cai, X. Liang, Q. An, Z. Tao, W. Ming, and M. Chen, "Cooling/Lubrication Performance of Dry and Supercritical CO_2-Based Minimum Quantity Lubrication in Peripheral Milling Ti-6Al-4V," *Int. J. Precis Eng Manuf-Green Technol*, 8, 2, 405-421, 2020.
33. J. Chen, W. Yu, Z. Zuo, Y. Li, D. Chen, Q. An, H. Wang, and M. Chen, "Tribological properties and tool wear in milling of in-situ TiB_2/7075 Al composite under various cryogenic MQL conditions," *Tribol. Int*, 160, 2021.

Evaluation of Failure Criteria for Tensile Strength of Composite Laminates with Open Cracks

Botao Hu[1], Fanchen Deng[1], Xinhao Tang[1],and Qingxianglong Liang[1]

[1]National Key Laboratory of Strength and Structural Integrity, Aircraft Strength Research Institute of China, Xi' an , 710065, China

Abstract—In order to evaluate the effect of crack notches on the mechanical properties of composite laminates with different sizes and aperture sizes, static tensile fracture tests were carried out on four different layups and aperture sizes of composite laminates. The test results showed that for the four types of layup, the strength of the specimens with a crack length of 6.35mm decreased by 46.3%, 59.0%, 47.9%, and 39.7%, respectively, compared to intact specimens. The larger the proportion of 0° layup, the greater the strength decrease of the cracked specimens. Under the same layup, when the crack length to plate width ratio is constant, the tensile strength decreases rapidly with the increase of crack length. Based on the test results, three commonly used models for predicting the residual strength of composite laminates with open cracks, the point stress criterion, the average stress criterion, and the stress field intensity method, were evaluated. The results showed that the average stress criterion had higher accuracy than the point stress criterion and the stress field intensity method.
Key words: crack, composite, failure criterion, tensile strength.

5. INTRODUCTION

In the application of composite material structures, various forms of openings are inevitably present at process separation surfaces and inspection cover plates, and crack damage may also occur due to external environmental effects. The presence of openings breaks the continuity of the long fibers, changes the force transmission path in the structure, and can also cause stress concentration in the area around the hole due to the sudden change of the structure stiffness. Therefore, the existence of holes seriously affects the mechanical performance of the structure and affects the service performance of composite materials [1].

The core issue in the study of residual strength of cracks is the selection and use of the fracture criteria[2]. Among the fracture criteria proposed, the characteristic distance method is currently widely accepted and used which is based on the elastic stress field description of the equivalent orthotropic plate notch root, expressed by characteristic distances. In these methods, the most important are the point stress criterion (PSC) and the average stress criterion (ASC) proposed by Whitney and Nuismer[3], as well as other modified criteria derived from these criteria[4-5].

ASC assumes that the laminate of the composite material layer plate will fail when the average stress within a characteristic distance a_0 from the crack tip reaches the ultimate strength of the undamaged laminate layer plate. PSC assumes that the stress level at a characteristic distance d_0 from the crack tip of the composite material layer plate reaches the ultimate strength of the undamaged laminate layer plate. The "material properties" a_0 and d_0 required in PSC and the ASC need to be determined by physical experiments, and these "material properties" are related to material properties, layup sequence, notch shape, and sample size.

Yao proposed a stress field intensity (SFI) analysis method[6-7], taking into account the influence of stress gradient at the root of the defect. Tang developed a damage influence failure criterion (DI) based on a large amount of experimental data, using parameter analysis and fitting methods[8]. This criterion no longer requires "material properties" determined by experiments, except for unidirectional laminated material performance data. Chen developed a fiber damage failure criterion (FD) and proposed a fiber fracture criterion for predicting the notch strength of fiber-reinforced composite materials by predicting the fracture of 0° fibers[9]. Wu proposed an engineering simplified model for predicting the residual strength of composite laminates containing circular holes based on the stress field intensity method [10].

In terms of numerical analysis methods, Chang first proposed a two-dimensional progressive damage finite element model, considering the influence of shear nonlinearity, transverse tensile strength, and shear in-place strength, analyzing the stress concentration at the hole edge of composite laminates with holes, and predicting the tensile and compressive strength [11-12]. Li developed the LaRC05 criterion for failure analysis of planar stress problems and proposed a corresponding continuous damage evolution method, which effectively predicted the tensile strength of composite laminates with holes [13-14].

Most of the above research focuses on laminated composites with circular holes and less on the effects of proportionally increasing specimen hole size and width and crack defects. Moreover, there is little comparison between different failure criteria. Therefore, four types of laminated composite plates containing center cracks were selected for tensile testing, with four different crack lengths to plate width ratios for each laminate and three different crack lengths for each. Based on the test results, the characteristic distance of PSC, ASC, and SFI were calculated. Through the analysis of the characteristic distance, the advantages and disadvantages of the three criteria in predicting the residual strength of composite plates with cracks were compared.

6. Estimation model for residual strength of composite laminates

2.1 Point stress criterion (PSC)

For an infinitely anisotropic plate with a crack length of 2c under uniform Y-direction stress σ at infinity, PSC assumes that when the stress at a characteristic distance from the crack edge reaches the ultimate strength of the intact laminated plate, the laminated plate fails, i.e.

$$\sigma_y(x,0)\big|_{R+d_0} = \sigma_b \tag{1}$$

where, $\sigma_y(x,0)$—Y-direction stress distribution on the smallest cross-section containing the crack, d_0—characteristic distance determined by experiments.

For an orthotropic infinitely plate with a central crack under uniaxial tension, the same formula for calculating the strength of a laminated plate with a circular hole is used [15], i.e.

$$\sigma_c^{\infty} = \frac{2\sigma_b}{2+\zeta_4^2+3\zeta_4^4-(K_T^{\infty}-3)(5\zeta_4^6-7\zeta_4^8)} \tag{2}$$

where, $\zeta_4 = c/(c+d_0)$, K_T^{∞}—stress concentration factor at the hole edge of the infinitely wide laminated plate, which is calculated by the formula

$$K_T^{\infty} = 1 + \left[\frac{2}{A_{22}} \left(\sqrt{A_{11}A_{22}} - A_{12} + \frac{A_{11}A_{22} - A_{12}^2}{2A_{66}} \right) \right]^{\frac{1}{2}} \quad (3)$$

where A_{ij} is the in-plane stiffness coefficient of the laminated plate.

The critical failure strength of an infinitely wide plate is $\sigma_c^{\infty} = \eta\sigma_c$, σ_c is the failure strength of a finite width plate corrected by a finite width correction factor η. When the ratio of the defect length to the plate width is not greater than 1/3, for a laminated plate with a central crack of length 2c, we have

$$\eta = \sqrt{(W/(\pi c))\tan(\pi c/W)} \quad (4)$$

Where, W is the width of the plate.

2.2 Average stress criterion (ASC)

ASC assumes that when the average stress within a characteristic distance a_0 from the crack edge reaches the ultimate strength of the intact laminated plate, the laminated plate fails, i.e.

$$\frac{1}{a_0}\int_R^{R+a_0} \sigma_y(x,0)dx = \sigma_b \quad (5)$$

Where, a_0—characteristic distance determined by experiments.

For an orthotropic infinitely plate with a central crack under uniaxial tension, the same formula for calculating the strength of a laminated plate with a circular hole is used, i.e.

$$\sigma_c^{\infty} = \frac{2\sigma_b(1-\zeta_2)}{2-\zeta_2^2-\zeta_2^4+(K_T^{\infty}-3)(\zeta_2^6-\zeta_2^8)} \quad (6)$$

Where $\zeta_2 = c/(c+a_0)$.

1.3 Stress field intensity method (SFI)

SFI assumes that the failure of a component with stress concentration depends not only on the peak stress but also on the stress-strain field caused by the stress concentration zone. This method takes into account the influence of stress gradients in the damage zone at the root of the notch, and considers the combined contribution of stress at different material points to the failure of the notch root by allocating weight functions to the stress vectors of all material points in the field strength area.

For a laminated plate with a crack, the formula for calculating the failure strength can refer to the formula for calculating the strength of a laminated plate with a central circular hole, i.e.

$$\sigma_c = \frac{2(1-\lambda)\sigma_b}{\eta\lambda[m_1 + Dc(m_1 - m_2)]} \quad (7a)$$

$$m_1 = 2\lambda^{-1} - \lambda - \lambda^3 + (K_T^{\infty} - 3)(\lambda^5 - \lambda^7) \quad (7b)$$

$$m_2 = \lambda^{-2} - \ln\lambda - \frac{3}{2}\lambda^2 + (K_T^{\infty} - 3)(\frac{5}{4}\lambda^4 - \frac{7}{6}\lambda^6) - \frac{K_T^{\infty}}{12} + \frac{3}{4}$$ (7c)

Where, d_s ——characteristic distance determined by experiments; $\lambda = c/(c+d_s)$; $D = \frac{2}{W-2c}$。

7. TEST

3.1 Test specimens

The test specimens are smooth composite laminates made of medium modulus carbon fiber reinforced M21C epoxy resin unidirectional tapes with a nominal thickness of 0.187mm per layer. The adhesive film is a composite structural adhesive cured at 180°C. The material properties of the specimens are shown in Table 1.

Table 1 Elastic properties of unidirectional M21C/IMA

E_{11}/GPa	E_{22}/ GPa	v_{12}	G_{12}/ GPa
179	8.11	0.317	4.14

Note: E_{11} - Elastic modulus in the fiber direction; E_{22} - Elastic modulus in the perpendicular direction to the fibers; v_{12} - Poisson's ratio; G_{12} - Shear modulus.

The specimens were manufactured using automatic fiber placement and autoclave curing auxiliary process. Two configurations were used: without notch and with a centrally located crack, as shown in Figure 1.

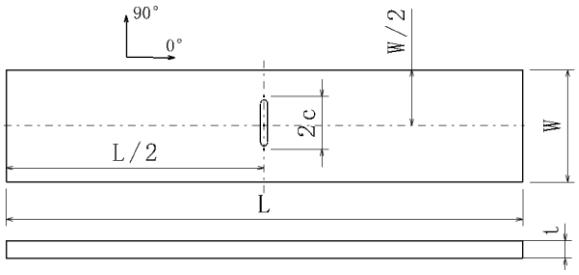

Figure 1 Specimen with crack

The specimens contain 4 typical ply configurations, as shown in Table 2. Configuration A is quasi-isotropic, Configuration D mainly contains 45° plies, Configuration B and C are similar, with only a slight difference in the proportion of 0° and 90° plies.

Table 2 Ply configurations of test specimens

Lay code	Ply ratio (0/±45/90)	Ply order	Number of layers	Total thickness (mm)
A	25/50/25	$[45/0/-45/90]_{2s}$	16	2.99
B	50/40/10	[45/0/-45/0/90/0/45/0/-45/0]s	20	3.74
C	40/40/20	$[45/0/-45/90/0]_{2S}$	20	3.74
D	10/80/10	[45/-45/90/45/-45/45/-45/0/45/-45]s	20	3.74

According to the different configurations and ply layups, the specimens were divided into 28 groups, totaling 96 specimens, as shown in Table 3.

Table 3 Test specimen configurations, quantity, and dimensions

Lay code	Notch type	Crack length/mm	Width/ mm	Length/ mm	Quantity
A/B/C/ D	Without notch	N/A	31.75	247	6
	Crack	6.35	31.75	247	3
	Crack	6.35	25.4	247	3
	Crack	6.35	38.1	247	3
	Crack	12.7	63.5	374	3
	Crack	25.4	127	628	3
	Crack	50.8	254	1136	3

The end of the specimens with a width of 254mm was reinforced with a patch made of the same material as the specimen, with a ply layup of $[45/0/-45/90]_{2S}$ and a length of 120mm. The patch had the same width as the specimen and was bonded to the specimen with adhesive.

3.2 Test method and environment

The test was conducted in a dry environment at room temperature. Prior to the test, the specimens were placed in the laboratory environment (temperature at 23℃±3℃ and humidity not exceeding 85% RH) for at least 24 hours. The unnotched tensile strength test followed the ASTM D3039 standard test method for tensile properties of polymer matrix composite materials, while the notched tensile strength test followed the ASTM D5766 standard test method for open-hole tensile strength of polymer matrix composite laminates.

The tests were conducted on an electro-hydraulic servo material testing machine MTS100T, with a loading error of no more than ±1% and a relative error of strain measurement of no more than ±1%. The specimen with a width of 254mm was connected to the test fixture by bolts, and the specimen-fixture assembly was clamped between the upper and lower grips of the testing machine, while the remaining specimens of other widths were clamped directly in the testing machine grips, and the centerline of the specimen was aligned with the centerline of the testing machine grips. The schematic of the test loading is shown in Figure 2.

Figure 2 Test site photo

Four strain gauges were attached to each test specimen. The positions of the strain gauges were shown in Figure 3, where W is the width of the test specimen, c is the half length of the crack, and H is the clamp length. The clamp length of the test specimen with a width of 254mm was 120mm, while the clamp length of other specimens was 50mm. Strain gauges were symmetrically attached to the back of each specimen. During loading, the data acquisition system ST24 was used for continuous measurement of strain.

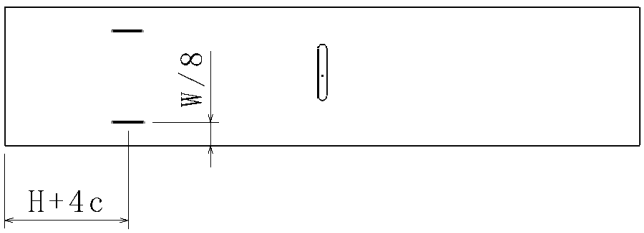

Figure 3 Schematic diagram of the paste position of the strain gauges

The specimens were inspected for defects before the test, using an ultrasonic flaw detector named EPOCH XT with a dynamic range of 34dB, a horizontal linear error of 0.1%, and a vertical linear error of 1.1%.

The strains of preload tests were not greater than 1000με, and the loading was carried out in 5 levels, recording and comparing the strain measurement results. The preload tests ended until the relative error of the strain measurement values at symmetric positions were not more than 10%. The formal test was conducted with displacement control loading at a loading rate of 2mm/min until the specimen was fractured. During the test, the test load, grip displacement, and strains were recorded.

3.3 Test results

The far-field fracture strains of the intact specimen were about 16000με, while that of notched specimens decreased to between 5000-8000με. The test fracture loads are shown in Table 4, where e is the ratio of the crack length to the plate width, F_{max} is the average breaking load, σ_c is average value of failure stress, CV

is the coefficient of variation of failure load.

Table 4 Summary of test fracture information

Lay code	Notch type	Plate width/mm	Crack length/mm	e	F_{max}(kN)	σ_c (MPa)	CV
A	Without notch	31.75	/	/	90.2	948.7	5.38%
A	Crack	31.75	6.35	0.2	48.3	509	0.76%
A	Crack	63.5	12.7	0.2	90.6	477.3	0.96%
A	Crack	127	25.4	0.2	163.7	431	2.84%
A	Crack	254	50.8	0.2	302.2	398	2.31%
A	Crack	25.4	6.35	0.25	36.7	482.7	2.4%
A	Crack	38.1	6.35	0.17	60.6	531.7	0.87%
B	Without notch	31.75	/	/	200.4	1687.8	1.53%
B	Crack	31.75	6.35	0.2	98.6	692	4.17%
B	Crack	63.5	12.7	0.2	160.5	676	2.84%
B	Crack	127	25.4	0.2	287	604.3	3.47%
B	Crack	254	50.8	0.2	462	486.3	4.81%
B	Crack	25.4	6.35	0.25	70.1	738	0.77%
B	Crack	38.1	6.35	0.17	113.1	793.7	8.68%
C	Without notch	31.75	/	/	158.5	1334.5	3.7%
C	Crack	31.75	6.35	0.2	82.6	695.3	2.0%
C	Crack	63.5	12.7	0.2	147.4	620.7	0.9%
C	Crack	127	25.4	0.2	256.1	539.0	1.38%
C	Crack	254	50.8	0.2	419.0	441.3	5.06%
C	Crack	25.4	6.35	0.25	59.3	624.3	1.06%
C	Crack	38.1	6.35	0.17	97.9	687.0	4.71%
D	Without notch	31.75	/	/	65.4	550.7	1.16%

D	Crack	31.75	6.35	0.2	39.4	332	1.1%
D	Crack	63.5	12.7	0.2	75.0	316.0	1.32%
D	Crack	127	25.4	0.2	141.6	298	0.73%
D	Crack	254	50.8	0.2	251.1	264.3	1.43%
D	Crack	25.4	6.35	0.25	29.1	305.7	0.53%
D	Crack	38.1	6.35	0.17	49.3	346	0.53%

It is found through the test that the dispersion of the test results was low, and the maximum coefficient of variation was 8.68%, indicating that the test results were reliable. For the four types of laminates A, B, C, and D, the strength of the notched specimens with a crack length of 6.35mm decreased by 46.3%, 59.0%, 47.9%, and 39.7%, respectively, compared with the intact specimens. It can be seen that the greater the proportion of the 0° laminate, the greater the strength decrease of the notched specimen. With the constant ratio of crack length to plate width, the tensile strength decreased with the increase of the crack length.

Fracture photos of the four types of laminates are shown in Figure 4. The fracture mode of the specimen with with A laminate was the delamination fracture on the hole section, showing strong symmetry due to its special laminate. For the specimens of B and C laminates, the failure mode was a cross-sectional fracture in the working area, mixed with angular fracture. As the specimen size increases, there is a greater tendency towards cross-sectional fracture. The failure mode of specimens with D laminate was layer separation along the 45-degree direction, due to the 80% proportion of 45-degree layers.

a） A laminate　　b） B laminate

c） C laminate　　d） D laminate

Figure 4 Photographs of the specimens' failure

8. Evaluation of failure criterion

The estimation models of PSC, ASC, and SFI method were validated based on the obtained test data. The test specimens included four types of laminates, each consisting of intact specimens, four different crack length specimens with the same crack length to plate width ratio, and three plate width specimens with the same crack length for each configuration. Each type of specimen configuration included at least three test specimens to ensure the accuracy of the test results.

Three types of failure criteria require obtaining the corresponding characteristic distances through experiments. For each laminate type, the characteristic distances for different aperture sizes and plate widths can be calculated. The relative average error(RAE) is defined as the maximum relative error between the characteristic distance value obtained for the same type of specimen and the characteristic distance average value, by taking the average of the characteristic distances for different crack length. The relative mean error can be used to evaluate the effectiveness of the failure criteria.

The obtained characteristic distances are shown in Table 5. It can be seen that the characteristic distances obtained for different crack lengths and plate widths are different. Overall, when the ratio of crack length to plate width is constant and the crack length is less than 25.4mm, the larger the crack length, the greater the characteristic distance. When the crack length is constant, the difference in characteristic distance is relatively small, but it still shows a decreasing trend with increasing plate width.

Table 5 Summary of characteristic distances

Lay code	Plate width/mm	Crack length/mm	e	Characteristic distances/mm		
				d_0(PSC)	a_0(ASC)	d_s(SFI)
A	31.75	6.35	0.2	0.93	2.36	1.85
A	63.5	12.7	0.2	1.54	3.72	3.02
A	127	25.4	0.2	2.16	4.95	4.18

A	254	50.8	0.2	3.10	6.82	5.89
A	25.4	6.35	0.25	0.82	2.01	1.52
A	38.1	6.35	0.17	1.04	2.71	2.17
B	31.75	6.35	0.2	0.41	0.99	0.88
B	63.5	12.7	0.2	0.76	1.81	1.62
B	127	25.4	0.2	1.03	2.30	2.11
B	254	50.8	0.2	0.49	1.01	0.95
B	25.4	6.35	0.25	0.51	1.28	1.07
B	38.1	6.35	0.17	0.60	1.55	1.37
C	31.75	6.35	0.2	0.81	2.19	1.77
C	63.5	12.7	0.2	1.18	2.96	2.52
C	127	25.4	0.2	1.50	3.48	3.09
C	254	50.8	0.2	1.14	2.42	2.23
C	25.4	6.35	0.25	0.62	1.56	1.26
C	38.1	6.35	0.17	0.77	2.06	1.75
D	31.75	6.35	0.2	1.44	3.55	2.50
D	63.5	12.7	0.2	2.51	5.89	4.32
D	127	25.4	0.2	4.22	9.39	7.12
D	254	50.8	0.2	5.50	11.02	8.69
D	25.4	6.35	0.25	1.17	2.70	1.85
D	38.1	6.35	0.17	1.58	4.07	2.95

The average characteristic distance and relative error are shown in Table 6, where $\overline{d_0}$ is the average characteristic distance of PSC, $\overline{a_0}$ is the average characteristic distance of ASC, $\overline{d_s}$ is the average characteristic distance of SFI, RAE is the relative average error. It can be seen that the accuracy of the average stress criterion prediction is better than that of the point stress criterion and stress field intensity method.

Table 6 Summary of relative errors

Lay	PSC		ASC		SFI	
code	$\overline{d_0}$ /mm	RAE	$\overline{a_0}$ /mm	RAE	$\overline{d_s}$ /mm	RAE
A	1.60	94.0%	3.76	81.3%	3.11	89.7%
B	0.63	62.6%	1.49	54.4%	1.33	58.3%

C	1.00	49.5%	2.45	42.3%	2.10	46.9%
D	2.74	101.0%	6.10	80.6%	4.57	90.1%

In fact, by substituting the average characteristic distance into the corresponding residual strength calculation formula, the errors between the predicted results of the three criteria and the experimental results can be obtained. The maximum errors for each type of laminate were listed in Table 7. It can be seen that in any case, the average stress criterion is a better criterion, and for A and D laminates, the error obtained by the stress field intensity method has made it unusable. For D laminate, which has an absolute advantage for the 45° laminate, all three criteria show a large error.

Table 7 Maximum error for each type of laminate

Lay code	Error(PSC) /%	Error(ASC) /%	Error(SFI) /%
A	26.4	18.8	30.9
B	16.6	12.7	14.2
C	19.2	13.9	20.3
D	35.8	23.5	45.0

9. Conclusion

Static tensile tests were carried out on composite laminates with four different stacking sequences, different crack lengths and widths, and the failure mode and failure load of each specimen were obtained. The extremely small coefficients of variation confirm the accuracy of the test results. Evaluation of the three failure criterion was finished based on the test results, and the following conclusions were drawn:

a) For the same stacking sequence, when the ratio of crack length to plate width is constant, the tensile strength decreases rapidly with the increase of crack length；

b) For the same stacking sequence, when the crack length is constant, the characteristic distance slightly increases with the increase of plate width. When the ratio of crack length to plate width is constant and the crack length is less than 25.4mm, the larger the crack length, the larger the feature distance.

c) Compared with the point stress criterion and stress field strength method, the average stress criterion is always the better criterion for predicting the residual strength of laminates with crack holes under any circumstances.

In summary, the experimental results and evaluation conclusions of this study can provide reference and guidance for the design and manufacture of composite laminates, and also provide new ideas and methods for the performance research of similar materials.

Acknowledgments

The authors gratefully acknowledge the support of Commercial Aircraft Corporation of China for specimens used in this work.

REFERENCES

1. Z. H. Sun, Y. Tie, L. Cheng, and Y. L. Hou, “Damage analysis experimental study of Open-hole CFRP composite laminates,” *FRP /CM*, No.1, 5-10, 2019.
2. N. B. Yang, Y. N. Zhang, *Design of Composite Aircraft Structures*, Aviation Industry Press, 2004.
3. J. M. Whitney，R. J. Nuismer, “Stress fracture criteria for laminated composites containing stress concentrations,”*Journal of Composite Materials*, 8(3) : 253-265, 1974.
4. R. J. Nuismer, J. D. Labor, “Applications of the average stress failure criterion: Part Ⅰ:Tension,” *Journal of Composite Materials*，12(3) : 238-249, 1978.
5. R. J. Nuismer, J. D. Labor, “ Applications of the average stress failure criterion: Part Ⅱ: Compression,” *Journal of Composite Materials*，13(1) : 49-60, 1979.
6. W. X. Yao, “On the notched strength of composite laminates,” *Composite Science and Technology*, 45(2):105-110, 1992.
7. W. X. Yao, Y. N. Yan, and X. L. Yu, “The method of stress field intensity for predicting notched strength of composites,” *ACTA Materiae Compositae Sinica*, 11(1):67-72, 1994.
8. X. D. Tang, Z. Shen, P. H. Chen, and S. C. Yang, “Residual strength estimation of composite laminates with damage,” *ACTA Aeronautica et Astronautica Sinica*,18(2):146-152, 1997.
9. P. H. Chen，Z. Shen，and J. Y. Wang, “Prediction of the strength of notched fiber-dominated composite laminates,” *Composites Science and Technology*，61(9) : 1311-1321, 2001.
10. Y. T. Wu, W. X. Yao, “Simplified engineering model for predicting residual strength of notched laminates based on stress field intensity method,” *Journal of Nanjing University of Aeronautics & Astronautics*，48(4) : 551-557, 2016.
11. F. K. CHANG，K. Y. CHANG, “A progressive damage model for laminated composites containing stress concentrations,” *Journal of Composite Materials*，21(9) : 834-855, 1987.
12. K. Y. CHANG, S. LIU，F. K. CHANG, “Damage tolerance of laminated composites containing an open hole and subjected to tensile loading,” *Journal of Composite Materials*，25(3) : 274-301, 1991.
13. B. LI，Y. Z. LI，and R. X. DING, “Physically based failure analysis method for laminated composites,” *Acta Materiae Compositae Sinica*，30（supplement）,158-162, 2013.
14. B. LI，Y. Z. LI，and F. YANG, “Theoretical methodology for laminated composite strength including insitu effect,” *Acta Aeronautica et Astronautica Sinica*，35(11)：3025-3036, 2014.
15. Chinese Aeronautical Establishment, *Design Handbook of Composite Material Structure*, Aviation Industry Press, 2001.

Experimental Study on Compressive Strength of Composite Stiffened Curved Plate after Repaired

LILI WANG[1]，SHENGCHUN YANG[1*]，YUMING JIA[2], PENGFEI CHENG[1]

([1]National Key Laboratory of Strength and Structural Integrity，Aircraft Strength Research Institute of China，Xi'an，Shaanxi，710065，China

[2]First Aircraft Design and Research Institute，Xi'an，Shaanxi，710089，China)

Abstract: In this paper, the compressive strength of aircraft composite fuselage structure after repair is studied. First of all, according to the structural characteristics of the fuselage, two kinds of composite stiffened curved plates are designed and processed, which are nondestructive and damaged, and repaired by patching and gluing. Then according to the loading characteristics of the fuselage, the compressive strength tests of two kinds of composite stiffened curved plates under simply supported boundary conditions are designed and completed. Finally, the two test results are compared and analyzed from the aspects of initial buckling behavior, failure mode and failure load, and the effectiveness of patching and gluing repair of composite stiffened curved plates is evaluated. The results indicated that the repair scheme can meet the design requirements for damage repair of composite fuselage panel of civil aircraft, and can provide reference for strength verification and research of composite fuselage structure after repair.

Key words: composite fuselage　curved plate　repair design　experimental research

1 Introduction

The proportion of composite materials used in airframes has become an important indicator to evaluate the progressiveness and market competitiveness of aircraft to some extent[1]. In recent aircraft models of Boeing, Airbus and other companies, composite materials have been successfully introduced into main load-bearing structures such as airframes and wings. The strength of these structures is closely related to flight safety. Composite laminates, as the most commonly used aviation composite structure, are highly sensitive to lateral impact loads due to their low interlayer strength. However, during production, operation, and maintenance, composite structures are often subjected to impact loads such as bird strikes, ice and tool drops, which can lead to matrix cracking and delamination damage, leading to a decrease in structural strength and stiffness, posing a great threat to the safety and reliability of aircraft during service [2-3].

To ensure the reliability and integrity of composite material structures during use and extend their service life, it is necessary to repair or replace severely damaged structures or parts. Due to the high cost of composite structural components and the trend of integrated and integrated composite material design, the replacement of damaged structures is not an economic choice, so the research on composite material repair technology is becoming increasingly important. The repair technology of patching and bonding has become a mainstream composite structure repair method in the aviation field due to its advantages of restoring the aerodynamic shape of components, generating small repair stress, basically eliminating eccentric loads, and reducing weight gain[4]. Currently, there have been a large number of studies on patching and bonding repair of aircraft composite reinforced plates[5-7], However, the research and evaluation of the mechanical properties of composite material structures after repair is still one of the key issues in the research of composite material

structure repair technology, especially for the reinforced curved plates of large-sized composite material fuselage of civil aircraft, the failure behavior after repair has not been fully and deeply studied due to cost constraints.

This article conducts research on the compressive strength of aircraft composite fuselage structures after repair. Firstly, based on the structural characteristics of the fuselage, two types of composite material reinforced curved plates, non-destructive and damaged, were designed and processed, and repaired by patching and bonding. Then, based on the load-bearing characteristics of the fuselage, compression strength tests were designed and completed for two types of composite material reinforced curved plates under simply supported boundary conditions. Finally, a comparative analysis was conducted on the initial buckling behavior, failure mode, failure load, and other aspects of the two test results, The effectiveness of patching and bonding repair for composite reinforced curved plates was evaluated. The results indicate that the design repair plan can meet the design requirements for repairing damage to composite material fuselage panels in general civil aircraft, and can provide reference for strength verification and research of composite material fuselage structures after repair.

2 Specimens design

Taking the top wall panel of a certain passenger aircraft fuselage as a typical part, a 3-stringer composite hat shaped reinforced curved plate was designed as shown in Figure 1. The test pieces were divided into two types: undamaged and damaged, and repaired by patching and bonding. Each type had 3 pieces, totaling 6 pieces. The repair part was located at the skin between the two stringers.

The overall size of the test piece is 1275mm × 978mm × 135mm, laid with T800 grade carbon fiber reinforced resin matrix composite material, with a single layer thickness of 0.19mm. The numbering rules for test pieces are: PDT400Z0024-1-A-1 #~3 # (non-destructive parts), PDT400Z0024-1-B-1 #~3 # (repair parts).

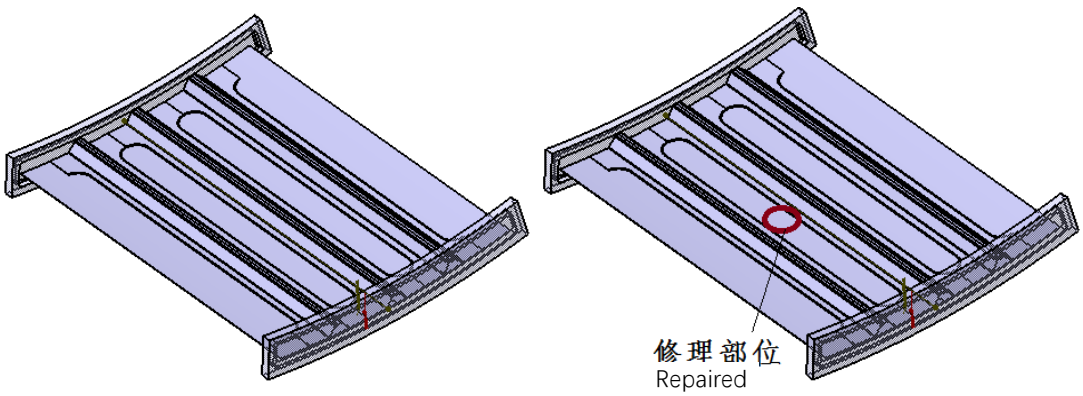

Figure 1 Schematic diagram of composite material reinforced curved plate test piece

3 Experimental Method

The experiment was completed on a ZWICK-2000kN compression testing machine, supported by a designed specialized fixture. Simple support constraints were applied at the end of the test piece, and lateral constraints were applied on both sides of the test piece. The test load was uniformly applied at the end of the test piece, and the combined force of the load passed through the

centroid of the test piece section to achieve pure compression. The schematic diagram of the centr oid structure of the section is shown in Figure 2, and the test support and loading scheme is sho wn in Figure 3.

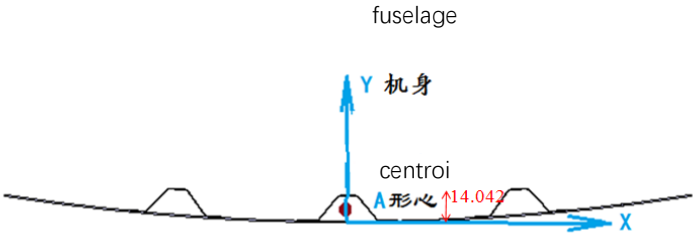

Figure 2 Schematic diagram of the cross-section centroid of the test piece

The estimated ultimate load for the test is 290kN, and a step-by-step loading method is used during the test. The loading level difference and test sequence are shown in Table 1.

Table 1 Loading Level Difference and Order

Test sequence	Loading level difference and related requirements
1.Pre test	Using the 5% ultimate load as the level difference, after loading to the 30% ultimate load, unload step by step, and check the stress on the test piece and the operation of the fixture, loading equipment, and measuring instruments.
2.Limited load test	Using 5% ultimate load as the level difference, load to 65% ultimate load, then use 2% ultimate load as the level difference, load to 67% ultimate load, hold for 30 seconds, and unload after loading is completed.
3.Destructive test	Using a 5% ultimate load as the level difference, load to 65% ultimate load, then load to 67% with a 2% ultimate load as the level difference, continue to load to 70% with a 3% ultimate load as the level difference, then load to 80% with a 5% ultimate load as the level difference, and then load to 100% with a 2% ultimate load as the level difference. After holding for 3 seconds, load to 1% ultimate load until failure.

Figure 3 Test Support and Loading Scheme

Arrange a resistance strain gauge at the position shown in Figure 4- Figure 5 to track the strain changes in the key areas of the test piece throughout the entire testing process. The strain measurement mainly adopts the electrical measurement method, and the strain gauge used complies with GB/T13992 (Class A standard). The uniaxial strain gauge model BE120-3AA and strain flower model BE120-3CA are used. The adhesion and curing of the strain gauge were completed at room temperature.

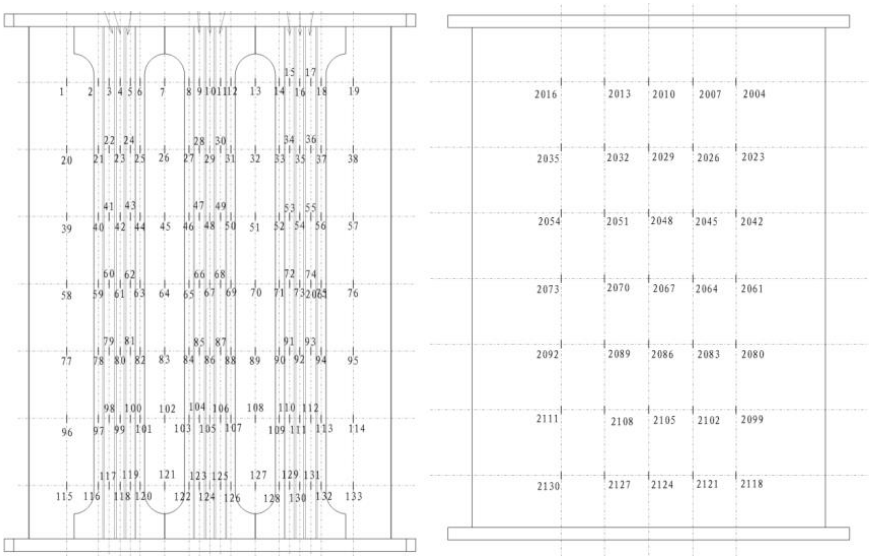

Figure 4 Layout of strain gauges for non-destructive test pieces

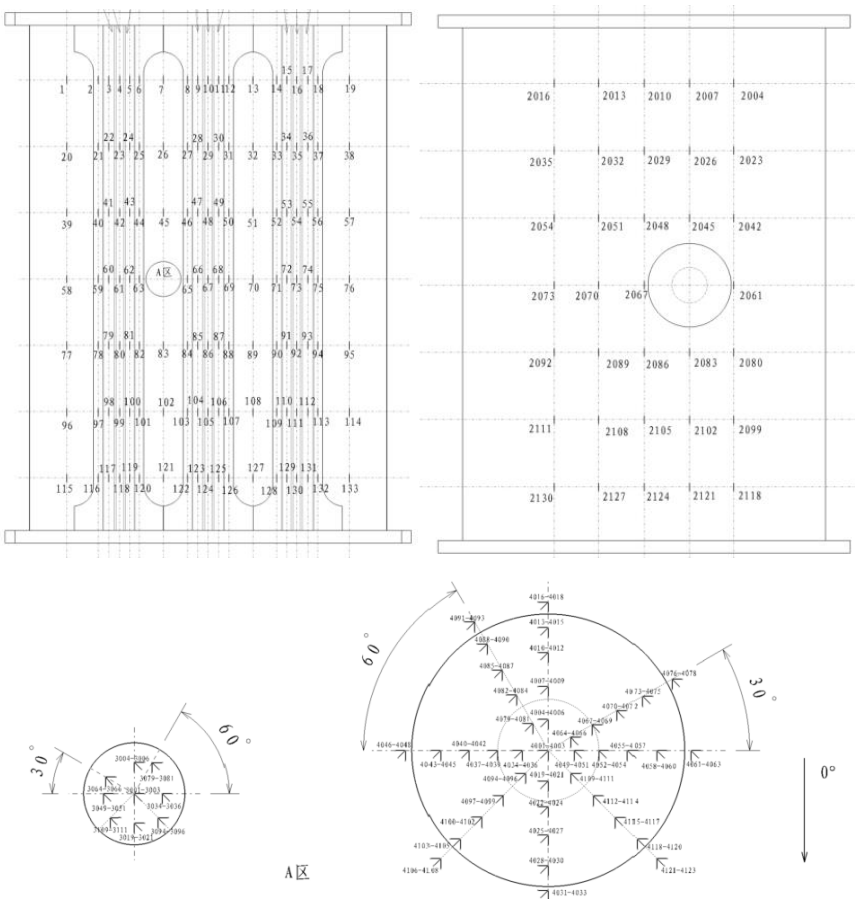

Figure 5 Layout of strain gauges for test pieces after repair by patching and bonding

4 Experimental results and analysis

4.1 Compression failure result of non-destructive components

All tests were completed in the order shown in Table 1. The initial buckling load and final failure load of each test piece are shown in Table 2. It can be seen that the average failure load of each test piece is 222.8kN, and the test results of the three samples have little dispersion, with a dispersion

coefficient of 6.1%.

Table 2 Compression Failure Test Results of Non Destructive Parts

Specimen number	Damage, failure mode	buckling load /kN	Failure load /kN
PDT400Z0024-1-A-1#	Skin buckling, long truss fracture, long truss to skin debonding	101.28	237.47
PDT400Z0024-1-A-2#	Skin buckling, long truss fracture, long truss to skin debonding	115.77	210.66
PDT400Z0024-1-A-3#	Skin buckling, long truss fracture, long truss to skin debonding	100.33	220.13

The failure process and mode of each test piece are basically consistent, as shown in Figure 6. The strain distribution in key areas of each test piece during the failure test process is shown in Figures 7-9, and the strain analysis is shown in Table 3. It can be seen that each test piece is the initial buckling of the free edge skin, followed by the buckling of the skin between the long trusses. Changes in structural stiffness result in load redistribution, and ultimately the long trusses and skin detach, causing the long trusses to buckle, and the stiffened plate to lose its load-bearing capacity.

Figure 6 Failure mode of non-destructive components

Table 3 Strain Analysis of Key Areas of Non Destructive Parts

Specimen number	Initial buckling site	Initial buckling strain
PDT400Z0024-1-A-1#	Free edge skinning	−758με
PDT400Z0024-1-A-2#	Free edge skinning	−768με
PDT400Z0024-1-A-3#	Free edge skinning	−710με

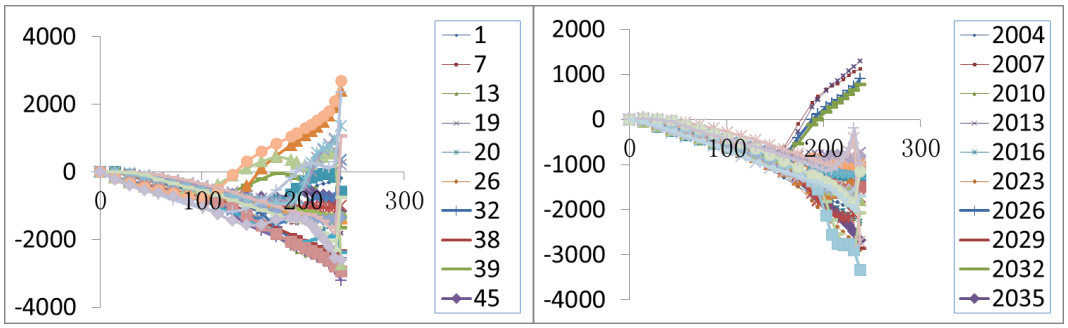

a) Rib surface skin b) Smooth skinning

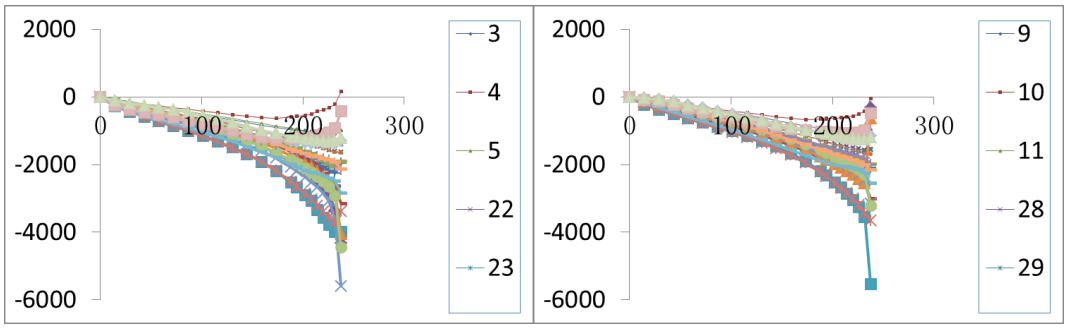

c) Left stringer d) Intermediate stringer

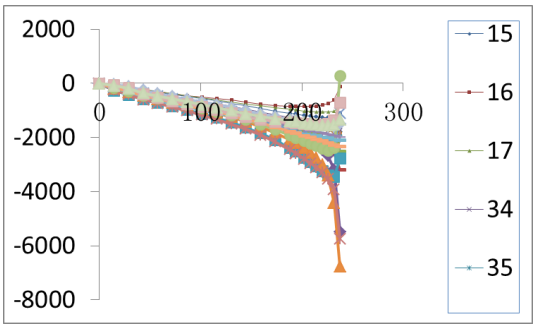

e) Right stringer

Figure 7 PDT400Z0024-1-A-1 # Key Measurement Point Load Strain Curve

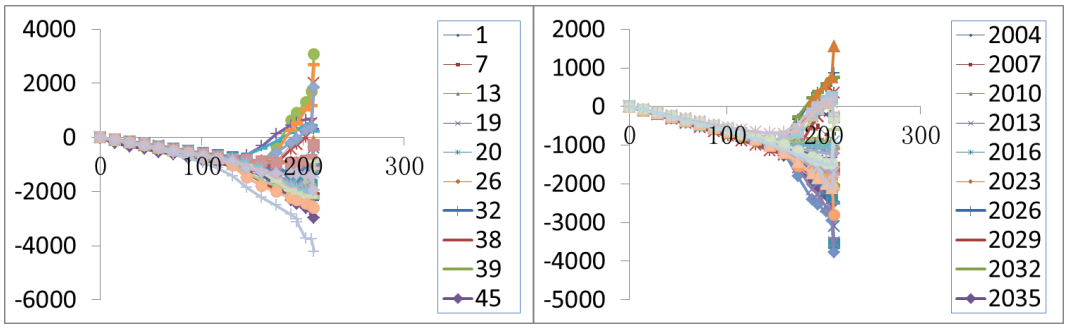

a) Rib surface skin b) Smooth skinning

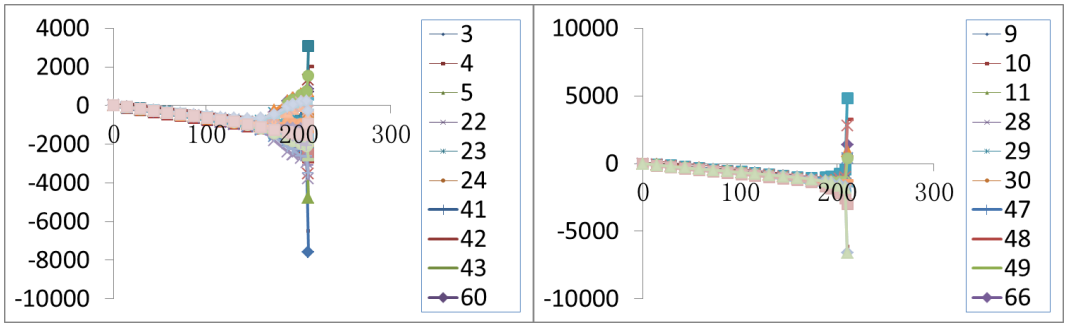

c) Left stringer d) Intermediate stringer

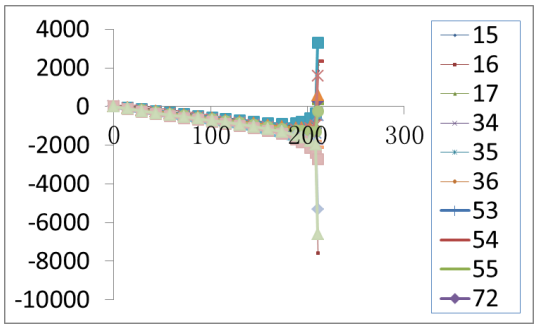

e) Right stringer

Figure 8 PDT400Z0024-1-A-2 # Key Measurement Point Load Strain Curve

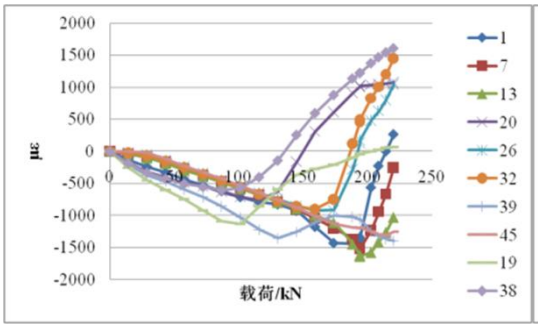

a) Rib surface skin

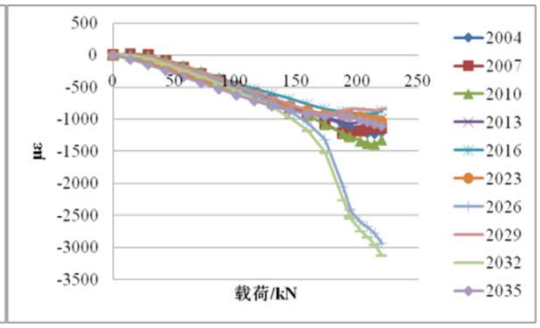

b) Smooth skinning

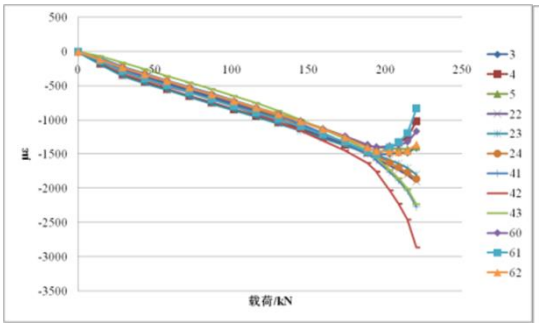

c) Left stringer

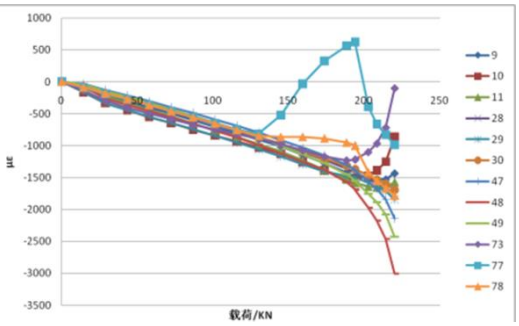

d) Intermediate stringer

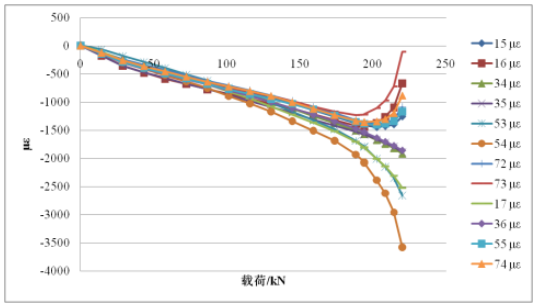

e) Right stringer

Figure 9 PDT400Z0024-1-A-3 # Key Measurement Point Load Strain Curve

4.2 Compression failure result of repaired components

All tests were completed in the order shown in Table 1. The initial buckling load and final failure load of each test piece are shown in Table 4. It can be seen that the average failure load of each test piece is 224.4kN, which is basically equivalent to the average failure load of non-destructive parts. The test results of the three samples have little dispersion, with a dispersion coefficient of 9.8%.

Table 4 Compression Test Results of Repair Parts

Specimen number	Damage, failure mode	buckling load/kN	Failure load/kN
PDT400Z0024-1-B-1#	Skin buckling, long truss fracture, long truss to skin debonding, patch debonding	115.9	248.0
PDT400Z0024-1-B-2#	Skin buckling, long truss fracture, long truss to skin debonding, patch debonding	120	221.1
PDT400Z0024-1-B-3#	Skin buckling, long truss fracture, long truss to skin debonding, patch debonding	124	204

The failure process and mode of each test piece are basically consistent, as shown in Figure 10. The strain distribution in the key areas of each test piece during the failure test process is shown in Figure 11- Figure 13, and the strain analysis is shown in Table 5, which is basically consistent with the stiffness response of the non-destructive component. It can be seen that each test piece is the initial buckling of the free edge skin, followed by the buckling of the skin between the long trusses, resulting in load redistribution due to changes in structural stiffness. Finally, the long trusses and skin detach, the long trusses break, the adhesive patches and skin detach, and the reinforced plate loses its load-bearing capacity.

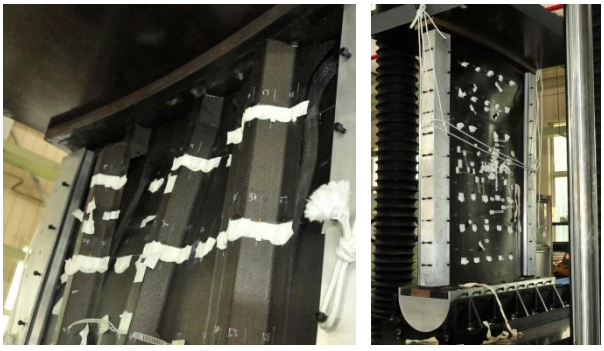

Figure 10 Failure Mode of Repair Parts

Table 5 Strain Analysis of Key Areas of Repair Parts

Specimen number	Initial buckling site	Initial buckling strain
PDT400Z0024-1-B-1#	Free edge skinning	−783με
PDT400Z0024-1-B-2#	Free edge skinning	−790με
PDT400Z0024-1-B-3#	Free edge skinning	−795με

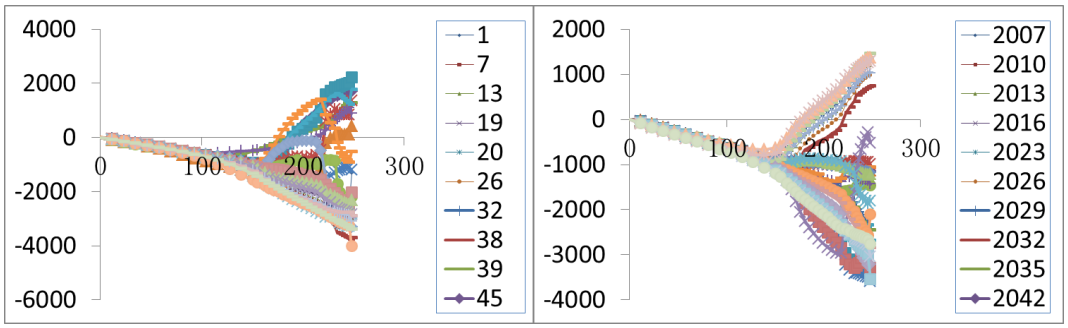

a) Rib surface skin

b) Smooth skinning

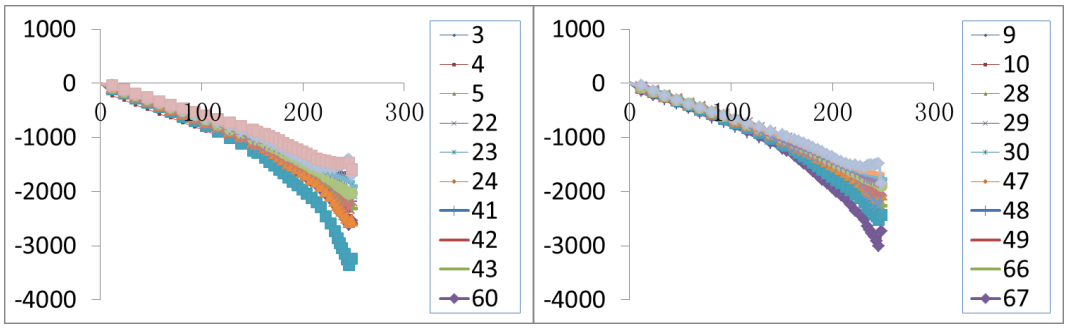

c) Left stringer

d) Intermediate stringer

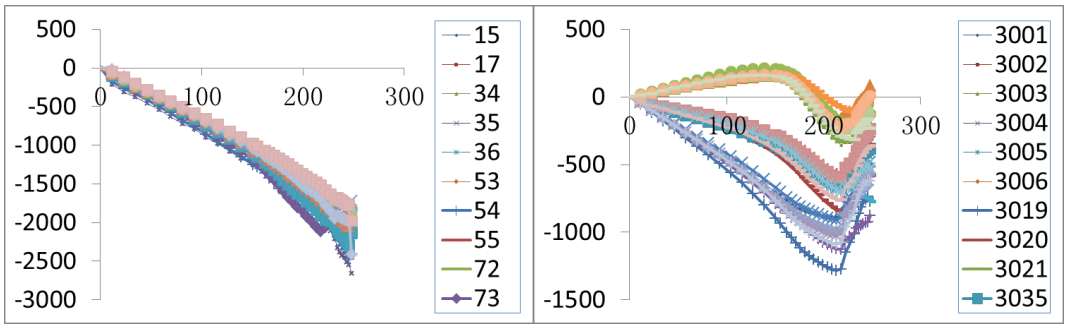

e) Right stringer

f) Reinforcement surface repair area

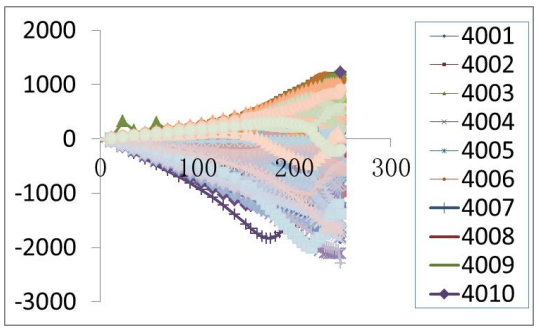

g) Smooth repair area

Figure 11 PDT400Z0024-1-B-1 # Key Measurement Point Load Strain Curve

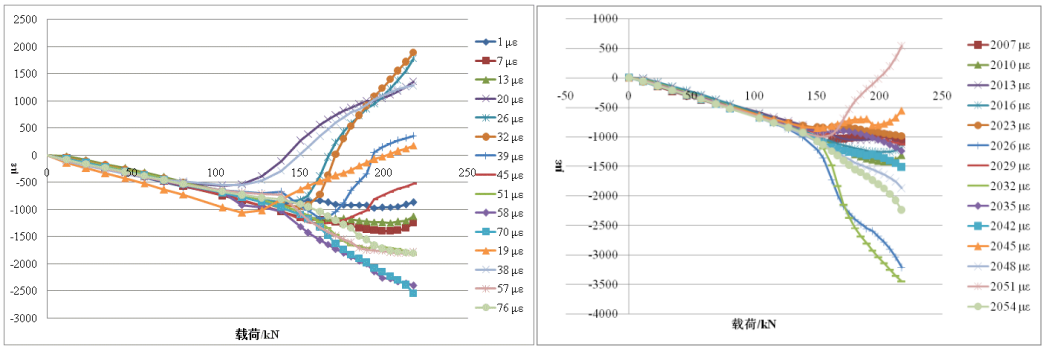

a) Rib surface skin

b) Smooth skinning

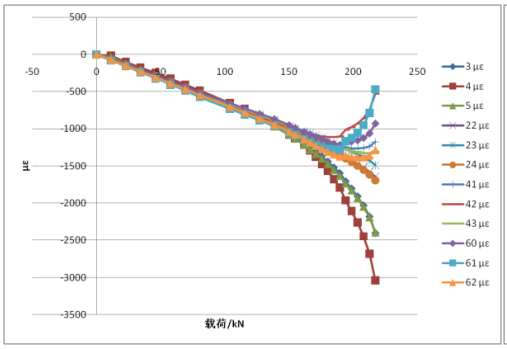

c) Left stringer

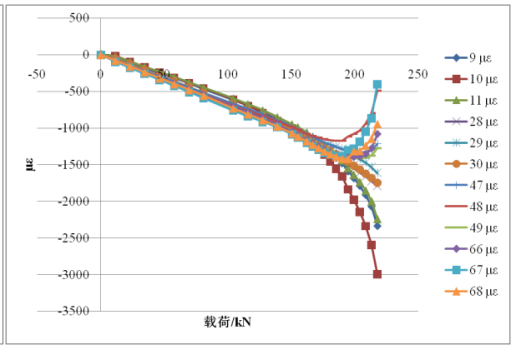

d) Intermediate stringer

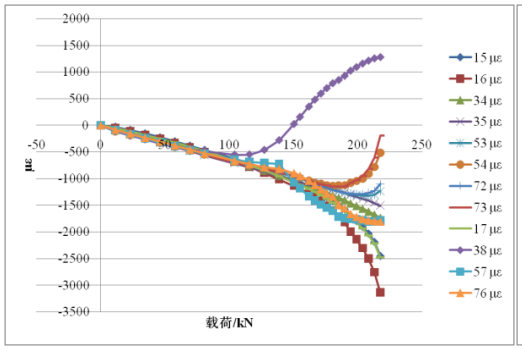

e) Right stringer

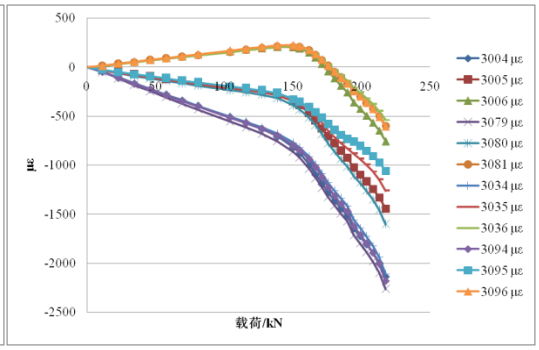

f) Reinforcement surface repair area

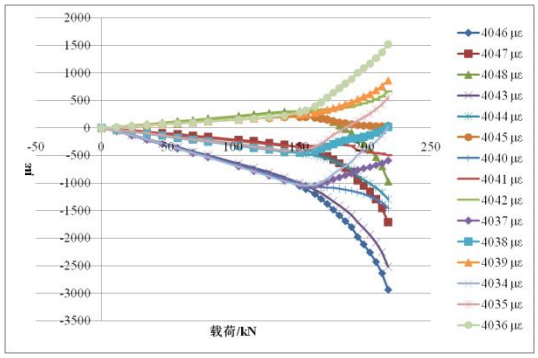

g) Smooth repair area

Figure 12 PDT400Z0024-1-B-2 # Key Measurement Point Load Strain Curve

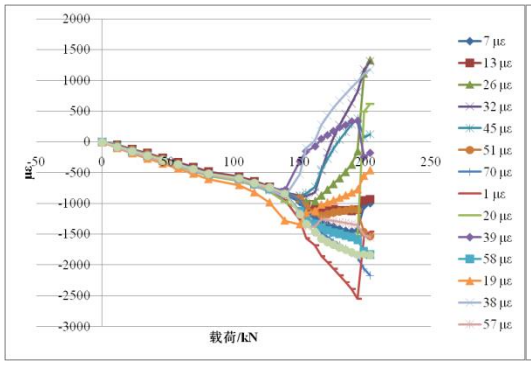

a) Rib surface skin

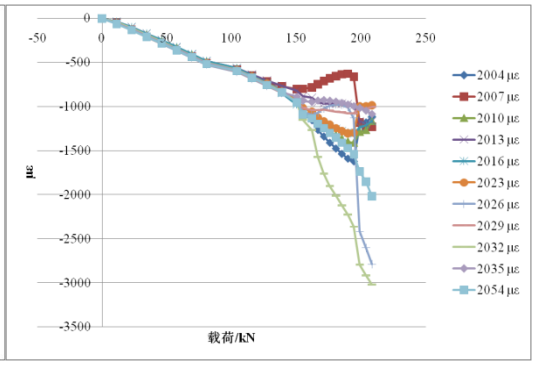

b) Smooth skinning

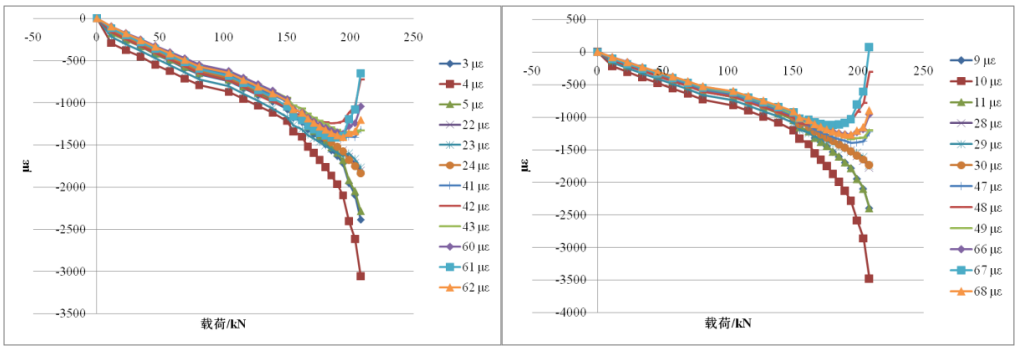

c) Left stringer d) Intermediate stringer

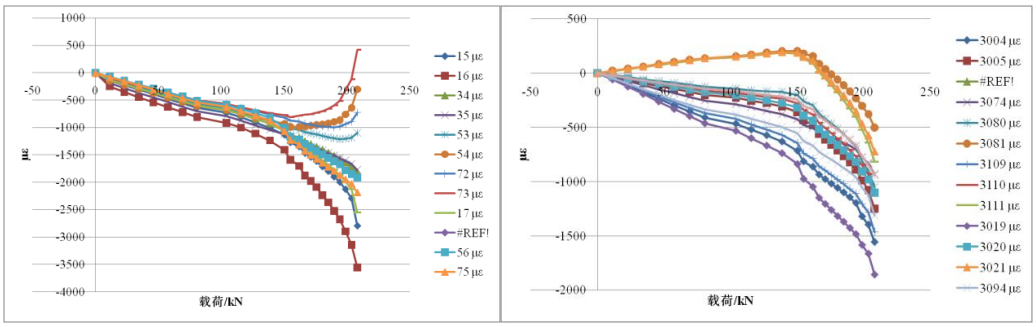

e) Right stringer f) Reinforcement surface repair area

Figure 13 PDT400Z0024-1-B-3 # Key Measurement Point Load Strain Curve

5 Conclusion

[1] Through compression tests on intact and repaired parts, the compressive strength of composite material fuselage structures after repair was studied, and the following conclusions can be drawn:

[2] a) The average axial compressive failure strength of composite reinforced curved plates after repair by patching and bonding is basically the same as that of undamaged parts, and the structural stiffness response is basically the same;

[3] b) The designed repair plan can meet the design requirements for repairing damage to composite material fuselage panels in general civil aircraft, and can provide reference for strength verification and research of composite material fuselage structures after repair.

References

[1] Ma Limin, Zhang Jiazhen, Yue Guangquan, et al. Application of composite materials in the new generation of large civil aircraft [J]. Journal of Composite Materials, 2015,32 (2): 317-322

[2] Chen Xiangbao. Repair of Composite Material Structure Damage [M]. Beijing: Chemical Industry Press, 2001

[3] Chen Shaojie. Guidelines for Damage in Composite Material Structures [M]. Beijing: Aviation Industry Press, 2001

[4] Wang Yuequan. Progressive Damage Analysis of Aircraft Composite Structure Repair Design [D]. Nanjing: Nanjing University of Aeronautics and Astronautics, 2010

[5] Xu Jianxin, Cao Xiaomei, Li Dinghe. Stability analysis of stepped excavation repair of composite material reinforced plates [J]. Journal of Civil Aviation University of China, 2011,29 (4): 1-3
[6] Wang C H， Gunnion A J. On the design methodology of scarf repairs to composite laminates[J].Composite Science and Technology，2008,68（1）：35-46.
[7] Zheng Xitao, Zhang Xin, Zhang Ye. Residual strength analysis of composite material bonding repair structures [J]. Aerospace Manufacturing Technology, 2017 (21): 68-72